THE JOINT 22ND INTERNATIONAL HEAT PIPE CONFERENCE AND 16TH INTERNATIONAL HEAT PIPE SYMPOSIUM

24 - 28 NOVEMBER 2024
NAKHON PATHOM, THAILAND

PROCEEDINGS

THE JOINT 22ND INTERNATIONAL HEAT PIPE CONFERENCE AND 16TH INTERNATIONAL HEAT PIPE SYMPOSIUM

24 - 28 NOVEMBER 2024

NAKHON PATHOM, THAILAND

PROCEEDINGS

Title: The Joint 22nd International Heat Pipe Conference and 16th International Heat Pipe Symposium

Published by: Mr. Nattawut Tharawadee

Printing Manager: Heat Pipe and Heat System Association

Edition: 1, dated April 10, 2025, quantity 200 copies

National Library of Thailand Cataloging in Publication data

Nattawut Tharawadee.
The Joint 22nd International Heat Pipe Conference and 16th International Heat
Pipe Symposium.-- Bangkok : Mean Service Supply, 2025.
498 p.

1. Engineering -- Research. I. Title.

016.62
ISBN 978-616-623-535-7

Printed by: MEAN SERVICE SUPPLY LIMITED PARTNERSHIP
Head Office, 88/8 Chalongkrung Road, Lamplatiew Sub-district, Latkrabang District, Bangkok 10520, Thailand.

Price: 2,750 Baht

Contents

Welcome messages

Dear distinguished guests, esteemed researchers, and participants,

It is my great honor, as a Member of Parliament representing Nakhon Pathom Province, to extend a warm welcome to all of you at the 22nd International Heat Pipe Conference and 16th International Heat Pipe Symposium (22IHPC & 16IHPS). This prestigious gathering of minds in the fields of heat pipe research and thermal technology brings together scholars, scientists, and experts from across the globe. We are truly delighted to host this significant event here in our province.

Nakhon Pathom is a province rich in culture, history, and innovation. Over the years, we have worked tirelessly to develop our infrastructure and facilities to support global events like this. Our goal is to establish Nakhon Pathom as a new hub for international academic conferences. We believe that through events like 22IHPC & 16IHPS, we can demonstrate our capability and readiness to become a center of knowledge exchange, collaboration, and academic excellence on the world stage.

We hope that this conference will not only foster fruitful discussions and groundbreaking discoveries but also provide you with an opportunity to experience the charm and hospitality of our province.

Once again, welcome to Nakhon Pathom, and I wish you all a successful and inspiring conference.

Thank you.

Dr. Panuwat Sasomsap,

Member of Parliament for Nakhon Pathom Province, THAILAND

Welcome Messages

I still remember when the 6IHPS-2000 has been successfully organized in Chiang Mai Thailand with great appreciation of research exchanging as well as our northern Thai culture and cuisine in November 2000. By this special occasion of the 22nd IHPC and 16th IHPS here in Silpakorn University, Nakhon Prathom Province, we, in the same manner, cordially welcome all participants in this conference. We wish this occasion of exchange of research information will be in a friendly environment among variety of expert researchers, scientists and engineers from different institutions and industries around the world. Moreover, an unforgettable experience in several activities, nature, cultural, performance and Central Thai food in this beloved province of Nakhon Prathom can be unforgettable. The city represents Dvaravati civilization that once flourished here in the central plain of Thailand. The name Nakhon Prathom technically means the very first city here in this land. Silpakorn University (SU) is firmly established in this very first city of Nakhon Prathom. SU was originally established as the School of Fine Arts under the Fine Arts Department in 1933. Its inception and development owed much to an almost lifetime devotion of Professor Silpa Bhirasri, an Italian sculptor with original name of Corrado Feroci, who was commissioned during the reign of King Rama VI to work in the Fine Arts Department. SU presents its vision as a leading university in fostering creativity and integrating science and arts for the sustainable development of society.

I, therefore, would like to declare that on this occasion of 22IHPC and 16IHPC, we, on behalf of SU, will foster science and engineering for the sustainable development of our world. Let us, I mean all of you participants, contribute this fostering through out the 22IHPC and 16IHPS in this special week of November. Again, ladies and gentlemen, let me cordially welcome you all to our international Heat Pipe Conference.

Prof.Pradit Terdtoon

Honorary Chair of Local Organizing Committee

Welcome messages

Dear Conference Participants,

On behalf of the organizing committee, it is my great honor, as the Chairman of the Joint 22nd IHPC (International Heat Pipe Conference) and the 16th IHPS (International Heat Pipe Symposium), to warmly welcome researchers, academics, and experts from around the world to this significant conference, which will be held from November 24 to 28, 2024, in Nakhon Pathom, Thailand.

Thailand is rich in diverse cultures and a long history that harmoniously blends art, architecture, traditions, and a unique way of life. Hosting this conference here not only provides an opportunity for academic knowledge exchange but also offers a wonderful chance for all attendees to experience the charm of Thai culture, whether through exquisite Thai cuisine, the beauty of Thai music, or the breathtaking landscapes and cultural heritage sites.

This conference is an important platform for presenting research and exchanging the latest knowledge in heat pipes, heat transfer, and energy management. We aim to foster innovative solutions that meet current industrial demands and establish sustainable collaborations among researchers and experts worldwide.

As the chairman, I sincerely thank everyone for their participation. I hope each of you will gain invaluable insights from the conference and enjoy the richness of Thai culture. May this event be a successful gathering that promotes knowledge exchange and fosters sustainable innovations.

Best regards,

Asst. Prof. Dr. Nattawut Tharawadee

Chairman of Local Organizing Committee

Curriculum Vitae of Prof. Aliakbar Akbarzadeh

Founder and Past Leader of the Energy Conservation and Renewable Energy Group

School of Engineering, RMIT University, Melbourne, Australia

Aliakbar was born in Iran. He completed his schooling in Mashhad and received his BSc in Mechanical Engineering from Tehran University, Iran (1966). Later, he earned his MSc (1972) and PhD (1975) from the University of Wyoming, USA. Over the past 50 years, he has held academic positions at Shiraz University, the University of Melbourne, UC Berkeley, and RMIT University in Melbourne, Australia.

In 1988, Aliakbar established the Energy Conservation and Renewable Energy Group in the School of Engineering at RMIT University, where he was its leader until his retirement in 2020. He supervised approximately 40 PhD candidates to completion and has authored over 200 refereed publications and four books, accumulating more than 7,000 citations. A thermodynamicist, Aliakbar's research interests span a wide range of areas, including the use of salinity gradient solar ponds as a source of industrial process heat, the application of thermoelectric generators for power generation from waste heat and renewable sources, and the use of heat pipes for cooling electric and electronic devices. His pioneering work on developing heat pipe heat exchangers for waste heat recovery systems in bakeries earned him the Australia National Energy Award in 1992.

Many of the PhD students he trained now work for companies manufacturing computer components and their cooling devices, or as academics in engineering schools in Australia, Thailand, Iran, and Saudi Arabia. Aliakbar has been an active participant in International Heat Pipe Symposia and International Heat Pipe Conferences, chairing the first IHPS held outside of Japan in 1991. He also served as the Honorary Chair of the joint IHPC/IHPS in 2022, held in Melbourne, Australia.

After more than 50 years in academia, Aliakbar retired in 2020 to focus on voluntary work, studying philosophy, and playing music. He is currently an Honorary Professor at RMIT University, mentoring younger academics. Aliakbar is blessed with a supportive partner, Nasrin, two children, their spouses, and two grandchildren. As a volunteer, he supports several not-for-profit organizations dedicated to the care of the elderly and the welfare of refugees and newcomers to Australia.

Curriculum Vitae of Prof. G. P. "Bud" Peterson

G. P. "Bud" Peterson is currently President Emeritus and Regents Professor in the Woodruff School of Mechanical Engineering at the Georgia Institute of Technology. He served as the 11th president of Georgia Tech from April 1, 2009 through August 31, 2019. Under his leadership Georgia Tech exceeded the $1.5 billion goal for Campaign Georgia Tech by 20%, grew innovative collaborations and strategic partnerships, expanded the campus infrastructure, and increased national and global visibility.

Prior to joining Georgia Tech, he served as Chancellor at the om the University of Colorado at Boulder, where he served as Chancellor. Prior to that he s Chancellor at CU, he served as provost for six years at Rensselaer Polytechnic Institute (RPI) in New York, where he played a key role in the institutional transformation and the dramatic improvement in the faculty's quality, size, and diversity; and at Texas A&M University for 19 years, where he held a number of leadership positions, including Associate Vice Chancellor for Engineering for the Texas A&M University System, Executive Associate Dean of Engineering, and Head of the Department of Mechanical Engineering. Prior to his service at Texas A&M, he served as a visiting research scientist at NASA-Johnson Space Center in Houston, Texas.

Throughout his career, Peterson has played an active role in helping to establish the national research and education agendas, serving as a member of a number of congressional task forces, research councils, and advisory boards, including the Office of Naval Research (ONR), the National Aeronautics and Space Administration (NASA), the Department of Energy (DOE), the National Research Council (NRC), and the National Academy of Engineering (NAE). In addition, he has served as a member of the Board of Directors of the American Institute of Aeronautics and Astronautics (AIAA), a member of the Board of the Association of Public and Land-grant Universities (APLU), a member of the Executive Committee of the Association of American Universities (AAU), a member of the Board of Directors of the American Council on Education (ACE), and currently serves on the AIAA Board of Trustees, a member of the Knight Commission on Intercollegiate Athletics, and Chair of the NCAA Board of Governors.

A distinguished scientist, he was appointed in 2008 by President George W. Bush to the National Science Board (NSB), which oversees the NSF and advises the President and Congress on matters related to science and engineering research and education, and in 2014 was reappointed to the board by President Barack Obama. He has served on the U.S. Council on Competitiveness, the National Advisory Council on Innovation and Entrepreneurship (NACIE), and was appointed by President Obama to the the Advanced Manufacturing Partnership (AMP) 2.0 Steering Committee.

In 2018 he was appointed by Vice President Mike Pence to the National Space Council – User Advisor Group.

Peterson's research interests have focused on the fundamental aspects of phase-change heat transfer, including the heat transfer in reduced-gravity environments, boiling from enhanced surfaces, and some of the earliest work in the area of flow and phase-change heat transfer in micro/nanochannels. Early investigations focused on applications involving the thermal control of manned and unmanned spacecraft and progressed through applications of phase-change heat transfer, to the thermal control of electronic components and devices. His current research includes fundamental applications of phase-change heat transfer to the field of biotechnology; including the in-situ treatment of cancerous tissue using hypo- and hyper-thermia to arrest epileptic seizures through the rapid cooling of localized brain tissue; the cooling of the leading edges of hypersonic vehicles utilizing phase-change processes; and heat dissipation from personal and wearable technologies.

He is a fellow of both the American Society of Mechanical Engineers and the American Institute of Aeronautics and Astronautics and is the author or co-author of 17 books or book chapters, 260 refereed journal articles, and 145 conference publications. He has 22 patents, with two others pending.

Peterson earned a bachelor's degree in Mechanical Engineering, a second bachelor's degree in Mathematics, and a master's degree in Engineering, all from Kansas State University. He earned a Ph.D. in Mechanical Engineering from Texas A&M University. He and his wife, Val, have four adult children, two of whom are Georgia Tech alumni and eight grandchildren.

History of the International Heat Pipe Conference (IHPC)

No	LOCATION	YEAR
1st IHPC	Stuttgart, Germany	1973
2nd IHPC	Bologna, Italy	1976
3rd IHPC	Palo Alto, USA	1978
4th IHPC	London, UK	1981
5th IHPC	Tsukuba, Japan	1984
6th IHPC	Grenoble, France	1987
7th IHPC	Minsk, Belarus	1990
8th IHPC	Beijing, China	1992
9th IHPC	Albuquerque, USA	1995
10th IHPC	Stuttgart, Germany	1997
11th IHPC	Tokyo, Japan	1999
12th IHPC	Moscow, Russia	2002
13th IHPC	Shanghai, China	2004
14th IHPC	Florianopolis, Brazil	2007
15th IHPC	Clemson, USA	2010
16th IHPC	Lyon, France	2012
17th IHPC	Kanpur, India	2013

History of the International Heat Pipe Symposium (IHPS)

No	LOCATION	YEAR
1st IHPS	Tokyo, Japan	1985
2nd IHPS	Osaka, Japan	1987
3rd IHPS	Tsukuba, Japan	1988
4th IHPS	Tsukuba, Japan	1994
5th IHPS	Melbourne, Australia	1996
6th IHPS	Chiangmai, Thailand	2000
7th IHPS	Jeju, Korea	2003
8th IHPS	Kumamoto, Japan	2006
9th IHPS	Kuala Lumpur, Malaysia	2008
10th IHPS	Taipei, Taiwan	2011
11th IHPS	Beijing, China	2013

History of the Joint International Heat Pipe Conference and International Heat Pipe Symposium (IHPC&IHPS)

No	LOCATION	YEAR
18th IHPC and 12th IHPS	Jeju, Korea	2016
19th IHPC and 13th IHPS	Pisa, Italy	2018
20th IHPC and 14th IHPS	Gelendzhik, Russia	2021
21st IHPC and 15th IHPS	Melbourne, Australia	2023

International Committee Members

Honorary Chairperson

Prof. M. Groll, Stuttgart, Germany

Past-Chairpersons

Prof. J. Bonjour, Lyon, France (interim chairperson)

Prof. Y. Maydanik, Ekaterinburg, Russia

Chairperson

Prof. S. Khandekar, Kanpur, India (deceased)

Members

Prof. J. H. Boo, Seoul, Korea

Assoc. Prof. A. Date, Melbourne, Australia

Prof. S. Filippeschi, Pisa, Italy

Prof. S. W. Kang, Taipei, Taiwan

Prof. M. Mantelli, Florianopolis, Brazil

Prof. M. Marengo, Pavia, Italy

Prof. H. Nagano, Nagoya, Japan

Prof. J. M. Ochterbeck, Clemson, USA

Prof. K. S. Ong, Kuala Lumpur, Malaysia

Prof. W. Qu, Beijing, China

Assoc. Prof. N. Soponpongipat, Nakhon Pathom, Thailand

Mr. W. Supper, Leiderdorp, Netherlands

Prof. L. L. Vasiliev, Minsk, Belarus

Local Committee Members

Honorary Chair

Prof. Dr. Pradit Terdtoon, Chiang Mai University

Chair

Asst. Prof. Dr. Nattawut Tharawadee, Silpakorn University

Co-chair

Assoc. Prof. Dr. Nitipong Soponpongppipat, Silpakorn University

Members

Assoc. Prof. Dr. Pracha Yuenyongkul Rajamangala, University of Technology Lanna

Assoc. Prof. Dr. Piyanan Charoensawan, Naresuan University

Asst. Prof. Dr. Kridsadakorn Budachan, King Mongkut's University of Technology North Bangkok

Assoc. Prof. Dr. Phrut Sakulchangsajathai, Chiang Mai University

Dr. Tanad Katapradit, Engineo Co.LTD.

Assoc. Prof. Dr. Niti Kammuang-Lue, Chiang Mai University

Dr. Sura Tandee, Rajamangala University of Technology Isan

Asst. Prof. Dr. Narong Srihajong, Rajamangala University of Technology Isan

Asst. Prof.Surapin Phromdan Rajamangala, University of Technology Lanna

Dr. Nat Thuchayapong, Silpakorn University

Asst. Prof. Dr. Weeranut Intagun, Silpakorn University

Dr. Paisan Comsawang, Silpakorn University

Advisory committee

Prof. Budsaba Kanoksilpatham, Silpakorn University

22nd IHPC and 16th IHPS Conference Program, November 24-26, 2024

Time	Day 1 (Sunday) November 24, 2024
10:00-17:00	Registration and Welcome Party **Remark** Service Van Available at Suvarnabhumi Airport

Time	Day 2 (Monday) November 25, 2024	
8:30-10:10	Open Ceremony MC : Prof.B. Kanoksilpatham	
10:10-10:20	Coffee Break	
	Oral presentations - Parallel sessions	
	Room1	Room2
	Chair: Prof.M. Marengo Co-Chair: Dr.P. Sakulchangsajathai	Chair: Prof.J. Bonjour Co-Chair: Dr.P. Yuenyongkul
10:20-10:40	Paper ID 003(S2B)	Paper ID 005(S7)
10:40-11:00	Paper ID 012(S2B)	Paper ID 015(S7)
11:00-11:20	Paper ID 040(S2B)	Paper ID 029(S7)
11:20-11:40	Paper ID 049(S2B)	Paper ID 033(S7)
11:40-12:00	Paper ID 081(S2B)	Paper ID 047(S7)
12:00-13:00	Lunch	
	Chair: Prof.A. Pattamatta Co-Chair: Dr.N. Kammuang-Lue	Chair: Prof.P. Terdtoon Co-Chair: Dr.P. Yuenyongkul
13:00-13:20	Paper ID 085(S2B)	Paper ID 004(S2C)
13:20-13:40	Paper ID 090(S2B)	Paper ID 011(S2C)
13:40-14:00	Paper ID 093(S2B)	Paper ID 013(S2C)
14:00-14:20	Paper ID 128(S2B)	Paper ID 017(S2C)
14:20-14:40	Coffee Break	
	Chair: Prof.A. Pattamatta Co-Chair: Dr.N. Kammuang-Lue	Chair: Prof.P. Terdtoon Co-Chair: Dr.P. Yuenyongkul
14:40-15:00	Paper ID 021(S2A)	Paper ID 022(S2C)
15:00-15:20	Paper ID 024(S2A)	Paper ID 064(S2C)
15:20-15:40	Paper ID 043(S2A)	Paper ID 067(S2C)
15:40-16:00	Paper ID 080(S2A)	Paper ID 088(S2C)
16:00-16:20		Paper ID 131(S2C)
16:30-18:00	IOC Meeting	
18:30-20:00	Dinner	

Time	Day 3 (Tuesday) November 26, 2024	
	Oral presentations - Parallel sessions	
	Room1	Room2
	Chair: Prof.M. Mantelli Co-Chair: Dr.T. Khamdaeng	Chair: Prof.W. Supper Co-Chair: Dr.P. Charoensawan
9:00-9:20	Paper ID 083(S2A)	Paper ID 045(S3)
9:20-9:40	Paper ID 097(S2A)	Paper ID 069(S3)
9:40-10:00	Paper ID 103(S2A)	Paper ID 084(S3)
10:00-10:20	Paper ID 104(S2A)	Paper ID 106(S3)
10:20-10:40	Coffee Break	
	Chair: Prof.M. Mantelli Co-Chair: Dr.T. Khamdaeng	Chair: Prof.W. Supper Co-Chair: Dr.P. Charoensawan
10:40-11:00	Paper ID 112(S2A)	Paper ID 107(S3)
11:00-11:20	Paper ID 115(S2A)	Paper ID 126(S3)
11:20-11:40	Paper ID 132(S2A)	Paper ID 036(S6)
11:40-12:00	Paper ID 133(S2A)	Paper ID 061(S6)
12:00-13:00	Lunch	
	Chair: Prof.S.W. Kang Co-Chair: Dr.P. Charoensawan	
13:00-15:00	Poster sessions (13Posters: Paper ID 10,32,35,50,55,62,78, 79,82,102,108,114,125) : authors will be invited to introduce their poster through a pitch presentation.	
16:00-18:00	Woodland Museum	
18:00-21:00	Conference Banquet	

22nd IHPC and 16th IHPS Conference Program, November 27-28, 2024

Time	Day 4 (Wednesday) November 27, 2024		Time	Day 5 (Thursday) November 28, 2024	
9:00-9:20	Keynote Lecture: Prof.G.P. Peterson Chair: Prof.P. Terdtoon, Co-Chair: Prof.B. Kanoksilpatham		9:00-9:20	Keynote Lecture: Prof.N. Hirotaka Chair: Prof.P. Terdtoon, Co-Chair: Prof.B. Kanoksilpatham	
9:20-9:40	Coffee Break		9:20-9:40	Coffee Break	
	Oral presentations - Parallel sessions			Oral presentations - Parallel sessions	
	Room1	Room2		Room1	Room2
	Chair: Prof.M. Marengo Co-Chair: Dr.P. Sakulchangsajathai	Chair: Prof.J. Bonjour Co-Chair: Dr.P. Yuenyongkul		Chair: Prof.P. Terdtoon Co-Chair: Dr.P. Sakulchangsajathai	Chair: Prof.M. Mantelli Co-Chair: Dr.T. Khamdaeng
9:40-10:00	Paper ID 054(S5)	Paper ID 028(S8)	9:40-10:00	Paper ID 041(S1)	Paper ID 092(S7)
10:00-10:20	Paper ID 073(S5)	Paper ID 030(S8)	10:00-10:20	Paper ID 048(S1)	Paper ID 099(S7)
10:20-10:40	Paper ID 095(S5)	Paper ID 058(S8)	10:20-10:40	Paper ID 105(S1)	Paper ID 109(S7)
10:40-11:00	Paper ID 044(S4)	Paper ID 071(S8)	10:40-11:00	Paper ID 025(S2D)	Paper ID 110(S7)
11:00-11:20	Paper ID 051(S4)	Paper ID 087(S8)	11:00-11:20	Paper ID 026(S2D)	Paper ID 111(S7)
11:20-11:40	Paper ID 070(S4)	Paper ID 096(S8)	11:30-12:00	Closing ceremony MC : Prof.B. Kanoksilpatham	
11:40-12:00	Paper ID 124(S4)	Paper ID 118(S8)			
12:00-13:30	Lunch				
13:30-15:00	Wat Phra Kaew and Grand Palace				
15:30-19:30	ICONSIAM				
19:45-21:45	Dinner Cruise along Chao Phraya River				

List of Session Topics

S1 Fundamental studies on thermal-fluid phenomena associated with heat pipes and closed two-phase thermosyphons

S2 Theoretical and experimental studies on heat pipes and thermosyphons, including capillary pumped loops (CPL), loop heat pipes (LHP), oscillating (or pulsating) heat pipes (OHP-PHP), mini-micro-heat pipes, etc.

- S2A is a session on Pulsating Heat Pipe (PHP)
- S2B is a session on Loop Heat Pipe (LHP)
- S2C is a session on Heat Pipe and Vapor Chamber (HP&VC)
- S2D is a session on Thermosyphon (TS)

S3 Electronics and battery cooling applications, including thermal control of microelectronics and power electronics, cooling of CPU, LED system.

S4 Heat pipe and thermosyphon applications in energy industry, including heat exchangers, new and renewable energy systems, etc.

S5 Aerospace applications of heat pipes, including spacecraft thermal control, space power systems, aircraft thermal control, avionics cooling, etc.

S6 Heat pipes for special applications, including biomedical instruments, precision metrology, agricultural facilities, environmental systems, etc.

S7 Manufacturing processes and material processing associated with heat pipes and thermosyphons, including new developments of wicks, working fluids, materials, modeling of corrosion and life tests

S8 State-of-the-art heat pipe development and applications, novel ideas of heat pipe development

Detailed Program Schedule of Parallel Sessions

Day 1 (Sunday) November 24, 2024	
10:00-17:00	-Registration and Welcome Party -Service Van Available at Suvarnabhumi Airport
Day 2 (Monday) November 25, 2024	
8:30-10:10	Open Ceremony, MC : Prof. B. Kanoksilpatham, Silpakorn University
10:10-10:20	Coffee Break
	Oral presentations - Parallel sessions
	Room 1 Chair: Prof.M. Marengo Co-Chair: Dr.P. Sakulchangsajathai
10:20-10:40	**[ID003-S2B]** Copper-Water Loop Heat Pipes with Flat Evaporators: Development, Tests and Application *Yury F. Maydanik, Sergey V. Vershinin and Maria A. Chernysheva*
10:40-11:00	**[ID012-S2B]** Visualization of vapor-liquid interface in vapor grooves of loop heat pipe *Xue Zhou, Lingji Hua, Nanxi Li, Zhenhua Jiang, Yan Lu*
11:00-11:20	**[ID040-S2B]** Numerical and experimental study on heat and mass transfer in the secondary wick of a loop heat pipe *Le Liu, Zhenhua Jiang, Bo Shao, Bingyao Lin, Nanxi Li and Deping Dong*
11:20-11:40	**[ID049-S2B]** Thermal Vacuum Testing of Loop Heat Pipe Controlled by Electrohydrodynamic Conduction Pump *Genki Seshimo, Masahito Nishikawara, Takeshi Miyakita and Hiroshi Yokoyama*
11:40-12:00	**[ID081-S2B]** Measurement of Impact Force of Geyser Boiling in Two-Phase Closed Thermosyphon *JinHyeuk Seo and Jungho Lee*
	Room 2 Chair: Prof.J. Bonjour Co-Chair: Dr.P. Yuenyongkul
10:20-10:40	**[ID005-S7]** Experimental Investigation of the Structure of SiC Porous Ceramic in Application to LHP Evaporator Working in Medium-Temperature Heat Rejection Systems *Pawel Szymanski, In-Hyuck Song, Jae-Ho Jeon, Piotr Radomski, Tadeusz Miruszewski and Dariusz Mikielewicz*
10:40-11:00	**[ID015-S7]** Heat transport characterization of a loop heat pipe with primary/secondary wick-integrated evaporator by additive manufacturing *Yuki Akizuki, Kimihide Odagiri, Hiroshi Yoshizaki, Masahiko Sairaiji, Hosei Nagano and Hiroyuki Ogawa*
11:00-11:20	**[ID029-S7]** Development of a Vapor Chamber with Hybrid Wick Structure by Additive Manufacturing Technology *Yawei Xu, Hongxing Zhang, Jinyin Huang and Jianyin Miao*
11:20-11:40	**[ID033-S7]** Novel Ultra-Thin Vapor Chambers with Composite Triple (Mesh, Grooves and Powders) Wicks Having Cooling Capacity of 860 W under 40×40 mm^2 Heating *Shwin-Chung Wong, Chih-Yuan Fu, Lian-Qi Huang, Ting-Yun Kuo, Jo-Ting Tang, Chih-Chao Hsu and Chung-Yen Lu*

11:40-12:00	**[ID047-S7]** Numerical investigation of the hierarchical micro pore-channel composite evaporator for high-performance heat dissipation devices *Jiaxi Du, Jialin Liang, Binjian Ma, Huizhu Yang, Yue Yang and Yonggang Zhu*
12:00-13:00	Lunch
	Room 1 Chair: Prof.A. Pattamatta Co-Chair: Dr.N. Kammuang-Lue
13:00-13:20	**[ID085-S2B]** Modeling Ultra-Thin Flat Loop Heat Pipes using a 1-D Lumped Parameter Approach *Marco Bernagozzi, Kelvin Guessi Domiciano, Larissa Krambeck, Marcia B. H. Mantelli and Marco Marengo*
13:20-13:40	**[ID090-S2B]** Fabrication Procedures and Experimental Study of a Sodium Rod-Plate Heat Pipe *Elvis Falcão de Araújo, Alice Toledo de Castro, Juan Pablo Flórez Mera, Luis H.R. Cisterna and Marcia Barbosa Henriques Mantelli*
13:40-14:00	**[ID093-S2B]** Experimental studies on startup behavior of cylindrical evaporator nickel bi-porous wicked miniature loop heat pipe *Toni Kumari, Chandan Nashine and Manmohan Pandey*
14:00-14:20	**[ID128-S2B]** Multievaporator Cold Plate (MECOP) Heat Loop characterization with butane and R134a *Luka Ivanovskis, Igors Ušakovs, Donatas Mishkinis,Marco Gottero, Albino Quaranta and Stéphane Lapensée*
	Room 2 Chair: Prof.P. Terdtoon Co-Chair: Dr.P. Yuenyongkul
13:00-13:20	**[ID004-S2C]** Start-up characteristics of a high-temperature liquid metal heat pipe with fins: An experimental study *Zhi-Hu XUE, Yin Yu and Wei Qu*
13:20-13:40	**[ID011-S2C**] Thermal Performance Evaluation of Tower Type Vapor Chamber *Harutoshi Hagino, Phan Thanglong, Tsuyosi Koshio, Yuji Saito and Yoji Kawahara*
13:40-14:00	**[ID013-S2C]** Temperature Uniformity Characteristics of a Sodium Heat Pipe-Based Isothermal Heat Pipe Liner Eunsueng An, Kyungsoo Park, Pyungsoon Kim, Wukchul Joung
14:00-14:20	**[ID017-S2C]** The effect of gradient structure wick on the heat transfer performance of polyurethane flexible flat heat pipe *Hongling Lu, Li Jia, Liaofei Yin and Chao Dang*
14:20-14:40	Coffee Break
	Room 1 Chair: Prof.A. Pattamatta Co-Chair: Dr.N. Kammuang-Lue
14:40-15:00	**[ID021-S2A]** Mono-sized Cryogenic Pulsating Heat Pipe Operational with both Neon and Helium – an Experimental Study *Tisha Dixit, Gilles Authelet, Charles Mailleret, Florian Gouit, Vadim Stepanov and Bertrand Baudouy*
15:00-15:20	**[ID024-S2A]** Advancements in Commercialization of Oscillating Heat Pipes *Corey A. Wilson*

15:20-15:40	**[ID043-S2A]** Visualization Study of a Unique Heat Transfer Mechanism in an Ultra-Low Fill Rate Heat Pipe with a Single Serpentine Channel Resembling Pulsating Heat Pipes *Koji FUMOTO, Kento OKUBO, Shotaro OSHIMA, Asami HATAMOTO, Keisuke KURITA, Isao HARAYAMA and Hiroshi IIKURA*
15:40-16:00	**[ID080-S2A]** Heat Transfer Characteristics of Oscillating Heat Spreader with Petal-shaped Topological Channel Layout *Guoqing Zhou, Ziang Li and Jian Qu*
	Room 2 Chair: Prof.P. Terdtoon Co-Chair: Dr.P. Yuenyongkul
14:40-15:00	**[ID22-S2C]** Development of Cryogenic Methane Constant Conductance Heat Pipe *Sandeep Hatte, Kuan-Lin Lee and Calin Tarau*
15:00-15:20	**[ID064-S2C]** Experimental study of heat transfer characteristics of bent high-temperature heat pipe *Zhipeng Zhang, Hongyu Yang, Chenglong Wang, Kailun Guo, Wenxi Tian, Suizheng Qiu and Guanghui Su*
15:20-15:40	**[ID067-S2C]** Visualization Experiments and Numerical Analyses of Ultra-thin Heat Pipes Using a Wick Structure with Non-uniform Shape *Yasushi Koito, Junichi Akiyama and Hiroto Ueno*
15:40-16:00	**[ID088-S2C]** An Experimental Investigation of Aluminum/Ammonia Heat Pipe with Rectangular Smooth Edge Axial Groove Wick *Amawasee Rukruang, Sajad Mishkhas, Meng-Hao Chen, Tzu-Hui Yu, Yen-Ting Chen, Jong-Shinn Wu, Piyatida Trinurak, Somchai Wongwises and Chi-Chuan Wang*
16:00-16:20	**[ID131-S2C]** The Heat Pipe with Variable Size of Pores *V.V. Cheverda, A.A. Lukyanov and I.S.Vozhakov*
16:20-18:00	Free time
18:00-20:00	Dinner
Day 3 (Tuesday) November 26, 2024	
	Oral presentations - Parallel sessions
	Room 1 Chair: Prof.M. Mantelli Co-Chair: Dr.T. Khamdaeng
9:00-9:20	**[ID083-S2A]** Novel Pulsating Heat Pipe Composed of Wire-Plate Grooves *Larissa Krambeck, Kelvin Guessi Domiciano, Kênia Warmling Milanez and Marcia Barbosa Henriques Mantelli*
9:20-9:40	**[ID097-S2A]** Experimental study of low cost extruded aluminum profiles as pulsating heat pipes for long distance heat transfer *Claus Brede, Stefan Becker and Florian Schwarz*
9:40-10:00	**[ID103-S2A]** Detection and Measurement of Non-Equilibrium States in Pulsating Heat Pipes *Mauro Mameli, Mauro Abela, Davide Della Vista and Sauro Filippeschi*
10:00-10:20	**[ID104-S2A]** Deployable Pulsating Heat Pipe: Experiments on Ground and onboard Parabolic Flight *Roberta Perna, Mauro Mameli, Maksym Slobodeniuk, Luca Pagliarini, Cyril Romestant, Vincent Ayel and Fabio Bozzoli and Sauro Filippeschi*

	Room 2 Chair: Prof.W. Supper Co-Chair: Dr.P. Charoensawan
9:00-9:20	**[ID045-S3]** Study on On-Board Inverter Cooling Loop Heat Pipe for Electronic Vehicles *Makoto Kamata, Yuta Shimada, Noriyuki Watanabe, Shinobu Aso, Kazuki Sadakata, Shigeyuki Tanabe and Hosei Nagano*
9:20-9:40	**[ID069-S3]** Experimental study of pulsating heat pipes for cooling the stator of an electrical machine *Halima Aziza, Riadh Boubaker, Safouene Ouenzerfi, Naoko Iwata, Vincent Dupont, Souad Harmand*
9:40-10:00	**[ID084-S3]** Electric Vehicle Battery Cooling via Loop Heat Pipes coupled with Underbody Aerodynamics *Marco Bernagozzi, Marco Marengo and Anastasios Georgoulas*
10:00-10:20	**[ID106-S3]** Antiparallel Flat Plate Pulsating Heat Pipe for the Cooling of Electronic Enclosures *Davis T Vempeny, Laxman Kumar Malla, Hemanth Dileep, Pankaj Srivastava, Pallab Sinha Mahapatra and Arvind Pattamatta*
10:20-10:40	Coffee Break
	Room 1 Chair: Prof.M. Mantelli Co-Chair: Dr.T. Khamdaeng
10:40-11:00	**[ID112-S2A]** Comparative Study on Operational Characteristics of Polymer Pulsating Heat Pipes in Different Orientations *Zhengyuan Pei and Yasushi Koito*
11:00-11:20	**[ID115-S2A]** Effect of bending angle on the thermal performance of a polymeric flat plate pulsating heat pipe *Marco Marengo, Ayse Candan Candere, Francois Clemens, Nicolas Miché, Marco Bernagozzi, Mehmet Saglam, Anastasios Georgoulas and Orhan Aydin*
11:20-11:40	**[ID132-S2A]** Feasibility Study on the Application of a Novel Three-Dimensional Structured Pulsating Heat Pipe *Jongmin Jung and Yongseko Jeon*
11:40-12:00	**[ID133-S2A]** The Effect of Unidirectional Circulation Mechanism of Asymmetric and Interconnecting Channels on the Heat Transfer Performance of Pulsating Heat Pipe *Junseok Kim and Yongseok Jeon*
	Room 2 Chair: Prof.W. Supper Co-Chair: Dr.P. Charoensawan
10:40-11:00	**[ID107-S3]** Design and Evaluation of Remote Loop Thermosyphon for High Heat-flux 2U Servers *Abdolmajid Zamanifard, Piyatida Trinurak, Somchai Wongwises and Chi-Chuan Wang*
11:00-11:20	**[ID126-S3]** Identifying Niche of Heat Pipe Technology in Electric Vehicle Battery Cooling Applications *Randeep SINGH, Takeshi KOSHIO, Harutoshi HAGINO, Phan Thanh LONG, Tsuyoshi OGAWA, Tien NGUYEN, Masataka MOCHIZUKI, Thanudej AUSSAWINWONG, Charoenrath CHANSIRISATHAPORN and Kanokwan CHAICHANA*

11:20-11:40	**[ID036-S6]** Two-phase Thermosyphon with Horizontal Evaporator and Radiative Sky Cooling at the Condenser *Aalekh Srivastava, Prem Kumar, Amrit Ambirajan, Pradip Dutta, Zubin Varghese, Rohith B L and Praveena Subrahmanya*
11:40-12:00	**[ID061-S6]** Thermal performance of the geothermal thermosyphon for snow melting on paved roads *Hyunmuk Lim, Seokjin Lee, Sukkyung Kang, and Jungho Lee*
12:00-13:00	Lunch
	Poster session Chair: Prof.S.W. Kang, Co-Chair: Dr.P. Charoensawan
13:00-15:00	**[ID010]** Pore Network Simulation for Design of Biporous Structures in Loop Heat Pipe Evaporators *Masahito Nishikawara*
	[ID032] Optimization of capillary structures for loop heat pipes based on multiscale carbonyl nickel powder *Qi Wu, Guoguang Li, Zhichao Jia, Hanli Bi, Hongxing Zhang and Jianyin Miao*
	[ID035] Experimental and Numerical Studies of a Loop Thermosyphon *Prem Kumar, Jayant Kathuria, Aalekh Srivastava, Susmita Dash, Amrit Ambirajan and Pradip Dutta*
	[ID050] Evaluation of Heat Transfer Characteristics in Pulsating Heat Pipes under Ultralow Filling Ratios: Effect of the Working Fluid Type *Atsushi Shiokawa, Asami Hatamoto and Koji Fumoto*
	[ID055] Spreading Thermal Resistance of Boiling-driven Heat Spreader *Jung Chan Moc, Su Yoon Doh1 and Jungho Lee*
	[ID062] Thermal Performance of Surface Characterization for Two-phase Immersion Cooling using HFE-7200 *Sanghyeon Shin and Jungho Lee*
	[ID078] Thermal Performance Enhancement of Two-Phase Closed Thermosyphon by Thread Tapping inside the Evaporator *Sukkyung Kang, Seokjin Lee and Jungho Lee*
	[ID079] Experimental Study on Oscillating Heat Spreader with Topology Optimization Channels for the Cooling of Multiple Heat Source Electronics *Ziang Li, Guoqing Zhou and Jian Qu*
	[ID082] Thermal Performance of a LHP (loop heat pipe) for Ultra-high Heat Flux Cooling *Hee Soo Myeong and Seok Pil Jang*
	[ID102] Study of the Pool Boiling Heat Transfer Coefficient in a Thermosyphon *Souza, Fernando Gonçalves, Ribeiro, Andreza Sousa, Pabon, Nelson Yurako Londoño1 and Mantelli, Marcia Barbosa Henriques*
	[ID108] Pseudo steady state temperature predictions for a bottom heated pulsating heat pipe utilizing a correlation based tool *K. Nandakumar Chandran, Kailash Choudhary, Jason Chetwynd-Chatwin, June Kee Min and Man Yeong Ha*

	[ID114] Current development of the thermal hydraulic code AC^2/ATHLET for the high-temperature heat pipe simulation *Daniel Eckert, Fabian Weyermann and Jörg Starflinger*
	[ID125] Performance Evaluation of a Bi-porous Wicked Flat Miniature Loop Heat Pipe *Chandan Nashine, Toni Kumari and Manmohan Pandey*
16:00-18:00	Woodland Museum
18:00-21:00	Conference Banquet
Day 4 (Wednesday) November 27, 2024	
9:00-9:20	Keynote Lecture: Prof.G.P. Peterson Topic: An Historical Overview of the use of Heat Pipes in the Thermal Control of Hypersonic Vehicles Chair: Prof.P. Terdtoon, Co-Chair: Prof.B. Kanoksilpatham
9:20-9:40	Coffee Break
	Oral presentations - Parallel sessions
	Room 1 Chair: Prof.M. Marengo Co-Chair: Dr.P. Sakulchangsajathai
9:40-10:00	**[ID054-S5]** Reliable Startup and Continuous Oscillation Conditions of OHP *Nagai Hiroki and Kawaguchi Ayumu*
10:00-10:20	**[ID073-S5]** Experimental Study on thermal performance of a 3D printed Titanium-Water Heat Pipe *Shuaiting Lu, Huizhi Wang, Yuandong Guo, Jinyin Huang, Jianyin Miao and Guiping Lin*
10:20-10:40	**[ID095-S5]** Heat Transfer Performance of a Six-turn Pulsating Heat Pipe for Aeronautical Application under Vibration Environment *Naoko Iwata, Vincent Dupont and Antoine de Ryckel*
10:40-11:00	**[ID044-S4]** Numerical and Experimental Investigation of a 10 kW Flat-Type LHP for Waste Heat Recovery *Shawn Somers-Neal, Tatsuki Tomita, Noriyuki Watanabe, Ai Ueno, Hosei Nagano*
11:00-11:20	**[ID051-S4]** Optimal Heat Pipe Operation for Efficient Latent Energy Exchanger *Helen Skop and Darrell Klammer*
11:20-11:40	**[ID070-S4]** Heat pipe assisted combined power generation and water desalination *Oranit Traisak, Aliakbar Akbarzadeh and Abhijit Date*
11:40-12:00	**[ID124-S4]** Heat transfer performance of a prototypically 8 m-long two-phase closed thermosyphon for spent fuel pool passive cooling *Sergio Iván Cáceres Castro, Rudi Kulenovic and Jörg Starflinger*
	Room 2 Chair: Prof.J. Bonjour Co-Chair: Dr.P. Yuenyongkul
9:40-10:00	**[ID028-S8]** Influence of the liquid lifting height on the performance of an inverted two-phase thermosyphon *Ricardo Schneider Calomeno, Fernando Henrique Milanez and Marcia Barbosa Henriques Mantelli*

10:00-10:20	**[ID030-S8]** Experimental Study on Two-Phase Loop Driven by Osmotic Pressure and Capillary Force *Hanli Bi, Zheng Peng, Chenpeng Liu, Zhichao Jia, Guoguang Li, Yuandong Guo, Hongxing Zhang and Jianyin Miao*
10:20-10:40	**[ID058-S8]** The aluminum boiling-driven heat spreader *Su-Yoon Doh, Junyoung Choi, Seung M. You and Jungho Lee*
10:40-11:00	**[ID071-S8]** Low Pressure Drop Biomimetic Manifold Microchannels for Cooling Electronic Devices *Keyi Huang, Guiping Lin, Kai Tang and Yuandong Guo*
11:00-11:20	**[ID087-S8]** Thermal Characteristics of Concentric Annular Thermosyphon with Phase Change Material *Weeranut Intagun, Paisan Comsawang, Nattawut Tharawadee and Nat Thuchayapong*
11:20-11:40	**[ID096-S8]** Experimental investigation of the effect of the vibration on the operation of the direct contact condensation “box” component of a Capillary Jet Loop *V. Dupont, C. Popper, M. Bertha, S. Hoffait and A. de Ryckel*
11:40-12:00	**[ID118-S8]** Enhancing the Performance of Single-Loop Pulsating Heat Pipe by Creating a Novel Asymmetry *Anoop Kumar Shukla and Subrata Kumar*
12:00-13:30	Lunch
13:30-15:00	Wat Phra Kaew and Grand Palace
15:30-19:30	ICONSIAM
19:45-21:45	Dinner Cruise along Chao Phraya River
Day 5 (Thursday) November 28, 2024	
9:00-9:20	Keynote Lecture: Prof.N. Hirotaka Topic: Cryogenic Heat Pipes Chair: Prof.P. Terdtoon, Co-Chair: Prof.B. Kanoksilpatham
9:20-9:40	Coffee Break
	Oral presentations - Parallel sessions
	Room 1 Chair: Prof.P. Terdtoon Co-Chair: Dr.P. Sakulchangsajathai
9:40-10:00	**[ID041-S1]** Effect of evaporation and orientation on surface tension-induced liquid penetration in a porous medium *Rampally Srirama, Chandra Murthy and Navneet Kumar*
10:00-10:20	**[ID048-S1]** High-speed microscopic observation of thermo-fluid behavior in a porous wick under saturated vapor condition for loop heat pipes *Taito Kato, Kimihide Odagiri, Yuki Akizuki, Hosei Nagano and Hiroyuki Ogawa*
10:20-10:40	**[ID105-S1]** Two-phase Pressure Drop Experimental Study for Small Capillary Tubes *Kelvin G. Domiciano, Mauro Mameli, Larissa Krambeck, Sauro Filippeschi and Marcia B. H. Mantelli*
10:40-11:00	**[ID025-S2D]** Enhancing Condensation and Evaporation Performance in Two-Phase Closed Thermosyphons through Inner Surface Treatment: An Experimental Investigation *Marc Kirsch, Rudi Kulenovic and Jörg Starflinger*

11:00-11:20	**[ID026-S2D]** Aluminum Loop Thermosyphon with two Evaporators and One Condenser for Electronic Cooling *Leonard L. Vasiliev, Alexander S. Zhuravlyov, Alyona A. Gasparovich and Dmitry S. Sadchenko*
	Room 2 Chair: Prof.M. Mantelli Co-Chair: Dr.T. Khamdaeng
9:40-10:00	**[ID092-S7]** Experimental studies and analytical mathematical modeling of the evaporation rate of the sintered-grooved wick *Wanchai Pileug, Pradit Terdtoon, Niti Kammuang-lue and Phrut Sakulchangsatjatai*
10:00-10:20	**[ID099-S7]** Accommodating Thermal Stress in High-temperature Heat Pipes *Longfei Hu, Bo Li, Wei Qu, Xiaoguang Luo, Jijun Yu, Bangcheng Ai and Mohan zhang*
10:20-10:40	**[ID109-S7]** Additive Manufacturing of Vapor Chamber *Chen K. L, Hsu S. C and Kang S. W*
10:40-11:00	**[ID110-S7]** Numerical Simulation of Fluid Dynamics Characteristics in 3D printed TPMS Structures *Senthilkumar S., Kishore Bhaskar S., Penubarthi Guru Varun, Chen K. L. and Kang S. W.*
11:00-11:20	**[ID111-S7]** Experimental Investigation of An Air-Cooled Roll-Bond Flat Thermosyphon Module *Mohsen Khandan Bakavoli, Piyatida Trinurak, Somchai Wongwises and Chi-Chuan Wang*
11:30-12:00	Closing ceremony MC : Prof.B. Kanoksilpatham

List of papers

Paper ID 003(S2B)

Copper-Water Loop Heat Pipes with Flat Evaporators: Development, Tests and Application

Yury F. Maydanik*[1], Sergey V. Vershinin[1], and Maria A. Chernysheva[1]

[1] *Institute of Thermal Physics of the Ural Branch of the Russian Academy of Sciences, Ekaterinburg, Russia*
Corresponding author email address: lhtd@itpuran.ru

Abstract

The results of the development and research of copper-water LHPs with flat evaporators are presented. The tests were conducted with heat sources with different heating surface areas and under different conditions of condenser cooling. The maximum heat load achieved when testing a miniature LHP with a 2.3 mm thick evaporator and a 6.6 cm^2 heat source was 20 W with natural air cooling of the condenser and 44 W with forced convection. The total thermal resistance of the LHP was at the level of 0.6 °C/W and 1.3 °C/W, respectively. When testing an LHP with a 10 mm thick flat-oval evaporator with a 34 cm^2 heat source, the maximum heat load was restricted to 700 W, which was not the limiting value. When the condenser was cooled with water with a temperature of 40 °C, the evaporator temperature was 78 °C, and its thermal resistance was 0.016 °C/W. An LHP with a 19 mm thick and 50 mm diameter disk-shaped evaporator was tested with a 16 cm^2 heater. The minimum evaporator thermal resistance of 0.043 °C/W was obtained at a heat load of 460 W. Examples of the use of copper-water LHPs in various electronics cooling systems are also presented.

Keywords: Heat-transfer device; Loop heat pipe; Cooling system

1. Introduction

Loop heat pipes (LHPs) are highly efficient heat-transfer devices that are increasingly being used in various fields of technology. LHPs are made in the form of a closed loop, including an evaporator and a condenser, connected by separate smooth-walled pipelines for the movement of vapor and liquid, having a relatively small diameter. The fine-pored capillary structure (wick) with which these devices are equipped has a special shape and is located only in the evaporator. Evaporators can be cylindrical or flat. Flat evaporators can be rectangular, disk-shaped, or flat-oval. In flat-oval evaporators, longitudinal replenishment of the wick evaporation zone is realized, while others use opposite replenishment [1]. The advantage of flat evaporators is that they have a flat thermal contact surface. Unlike cylindrical evaporators, they usually do not require any additional intermediate interface elements to provide thermal contact with heat sources. Flat evaporators are usually used in LHPs with working fluids that have a pressure at the operating temperature not greater than or slightly greater than the external atmospheric pressure. The most effective of them is water in combination with a copper body and a wick. The results of the development and testing of a copper-water LHP with a 3.2 mm thick flat-oval evaporator were first published in 2004 [2]. Even then, these tests demonstrated the high efficiency of copper-water LHPs. When this device was tested with a heat source with a heating surface area of 4 cm^2 and forced air cooling of the finned condenser, the heat load was increased from 10 to 160 W. The temperature of the evaporator varied from 35 to 98 °C. The minimum value of the evaporator thermal resistance of 0.05 °C/W was reached at the maximum heat load, which was not the limit. At present, the results of the development and testing of LHPs with flat-oval evaporators with a thickness of 2 to 15 mm are known, confirming their high efficiency [3-8]. The thickness of evaporators with opposite replenishment, which are most often disk-shaped, is typically in the range of 15-30 mm. Disadvantages of copper-water LHPs with flat evaporators include the limited temperature range of 0 to 100 °C at which they can be stored, transported and operated. The lower temperature limit is associated with the risk of water freezing, which can cause deformation of the thin flat walls of the evaporator. The upper limit is due to the fact that at temperatures above 100 °C, the water vapor pressure inside the LHP exceeds the external atmospheric pressure, which can also cause deformation. To avoid these undesirable effects, it is necessary to increase the wall thickness, which increases the thermal resistance of the evaporator. Another limitation of copper-water LHPs is the strong dependence of the operating temperature on the inner diameter of the vapor line, which should be sufficiently large [9]. As a result, there is a decrease in the possibilities for configuring the vapor line when placing the LHP in constrained conditions. However, copper-water LHPs with flat evaporators currently have the best thermal characteristics and high potential for practical applications in electronic cooling systems.

2. LHPs with flat-oval evaporators

Figure 1 shows the external view of a miniature copper-water LHP with a flat evaporator measuring 45 mm × 26 mm × 2.3 mm and an active zone measuring 30 mm × 22 mm.

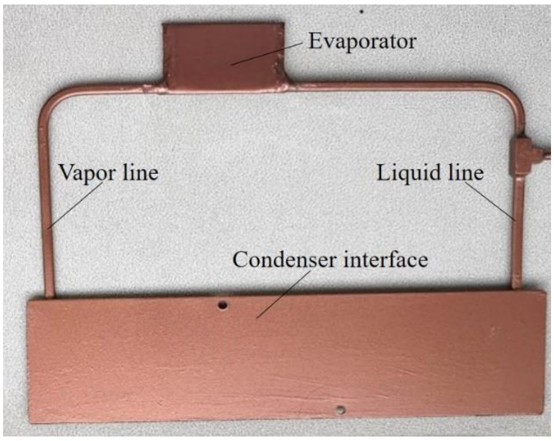

Figure 1. A miniature LHP.

The vapor line, liquid line and condenser of this device are 120 mm, 130 mm and 210 mm long, respectively. They are made of a 3/2.5 mm diameter copper tube, flattened to the thickness of the evaporator. The condenser was connected to the interface, a copper plate with dimensions of 185 mm × 50 mm × 0.5 mm. The tests were carried out with the device in a horizontal position. The heat source was a copper block with a heating surface area of 6 cm^2 equipped with an electric heater. The condenser was cooled by natural and forced air convection at a rate of 6 m/sec at a temperature of 22-24 °C. Figure 2 presents the experimental dependence of the evaporator temperature on the heat load under the specified conditions.

Figure 3 shows the external view of an LHP with a 10 mm thick flat-oval evaporator that was tested with a heat source with a heating surface of 34 cm^2 when the condenser was directly cooled with water at a flow rate of 4 L/min and a temperature of 20 °C and 40 °C.

The LHP vapor line is 300 mm long and 6/5 mm in diameter. The condenser is 500 mm long and has the same diameter. The liquid line is 630 mm long and 4/3 mm in diameter. The condenser is made in the form of a loop and is has a polyvinyl cooling jacket. Figure 4 demonstrates the experimental dependence of the temperature at the heating surface of the heat source (T_j) on the heat load at different cooling water temperatures.

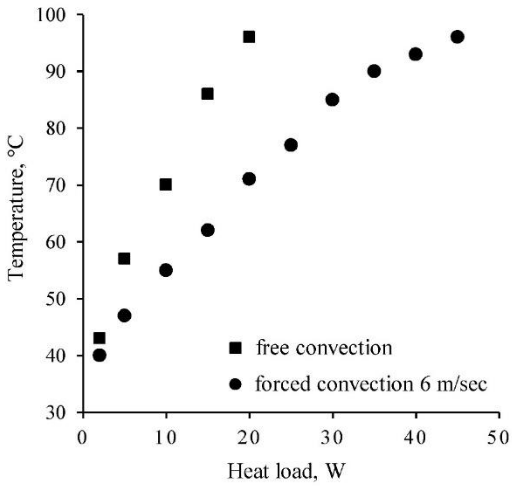

Figure 2. Dependence of the evaporator temperature on the heat load under different condenser cooling conditions.

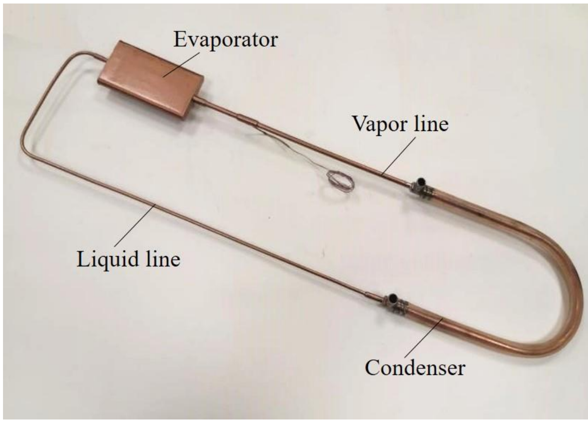

Figure 3. An LHP with a 10 mm thick flat-oval evaporator.

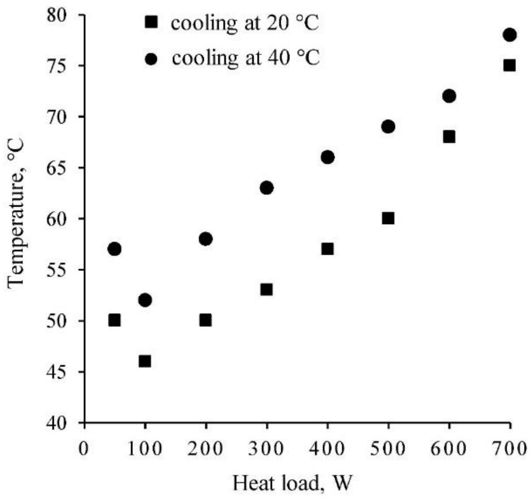

Figure 4. Dependence of the temperature at the heating surface of the heat source on the heat load at different condenser cooling temperatures.

Analysis of the graphs shows that there is no direct proportional dependence of the operating temperature on the condenser cooling temperature, which is typical for copper-water LHPs. In this case, at a maximum heat load of 700 W, the temperature difference is only 3 °C, while the cooling temperature difference is 20 °C. This fact has an important practical meaning, especially when using LHPs in cooling systems of servers in data centers, where the so-called "free cooling" is implemented, where it is necessary to use warm water with a temperature of 40 °C or more. It should also be noted that the heat load of 700 W, which in this case is limited only by the power of the heat source, is not the limit for this LHP. This follows from the fact that the vapor temperature is significantly below 100 °C. In addition, the analysis of the thermal resistance dependence $R_j = T_j – T_v/Q$ presented in Figure 5 shows a tendency for its further decrease below the achieved minimum value of 0.016 °C/W.

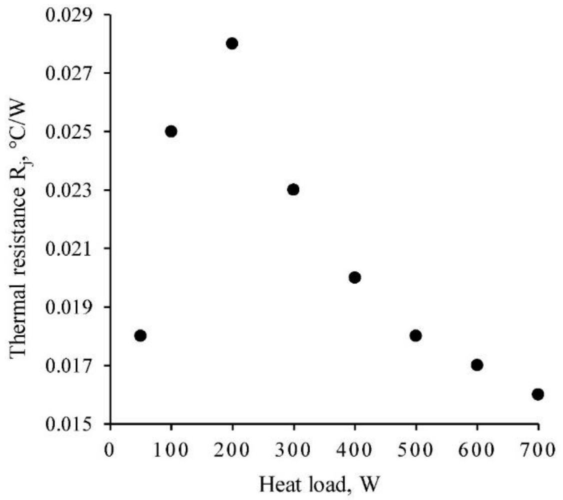

Figure 5. Dependence of the thermal resistance R_j on the heat load at a cooling temperature of 40 °C.

3. LHPs with disk-shaped evaporators

Figure 6 shows a copper-water LHP with a disk-shaped evaporator with a diameter of 50 mm and a thickness of 19 mm.

The LHP vapor line is 330 mm long and 6/5 mm in diameter. The condenser is 200 mm long and has the same diameter. The liquid line is 345 mm long and 4/3 mm in diameter. The condenser is connected to a copper interface with dimensions of 100 mm × 75 mm × 4 mm. During the LHP tests, a heat source with a heating area of 16 cm^2 was used. The condenser interface was pressed against a heat exchanger, through which water was pumped at a flow rate of 4 L/min and a temperature of 20 °C, 40 °C and 60 °C. The test results are presented in Figure 7.

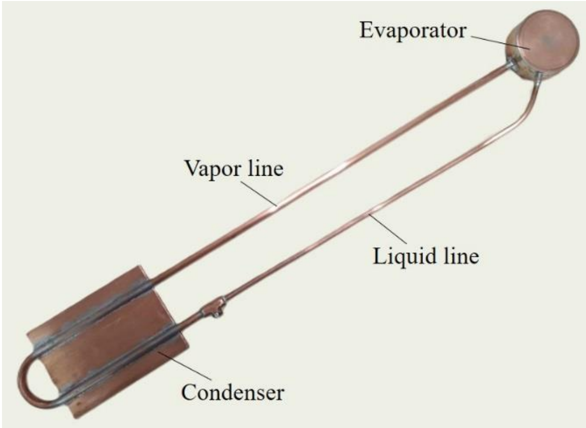

Figure 6. An LHP with a disk-shaped evaporator.

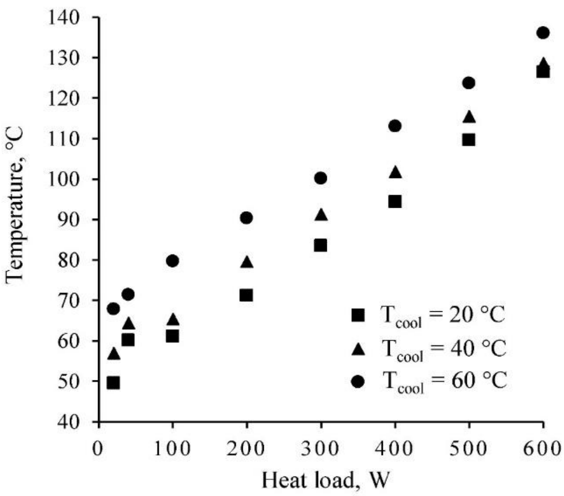

Figure 7. Dependence of the temperature at the heating surface of the heat source on the heat load at different condenser cooling temperatures.

Here it can also be seen that the temperature of the heat source is weakly dependent on the cooling temperature of the condenser. When the latter changed by 40 °C, the temperature of the heat source changed by only 10 °C at the maximum heat load of 600 W, and the maximum difference of 19 °C was observed at a heat load of 200 W. It should also be noted that the vapor temperature in the LHP exceeded normal atmospheric pressure only at a cooling temperature of 60 °C with a heat load above 450 W. At its maximum value, this excess reached 43 kPa, which was not critical for such an evaporator, whose flat wall thickness was double that of the flat-oval evaporator. This led, as expected, to an increase in the thermal resistance R_j, whose minimum value was 0.042 °C/W at a heat load of 400 W. At the same heat load and with the same heat source, the R_j value with the flat-oval evaporator was 0.030 °C/W.

4. Practical application of copper-water LHPs with flat evaporators

For the first time, such LHPs were used in coolers designed to cool powerful CPUs and GPUs in personal computers and servers. One such cooler with an LHP equipped with a 7 mm thick flat-oval evaporator and 6 mm diameter pipelines is shown in Figure 8.

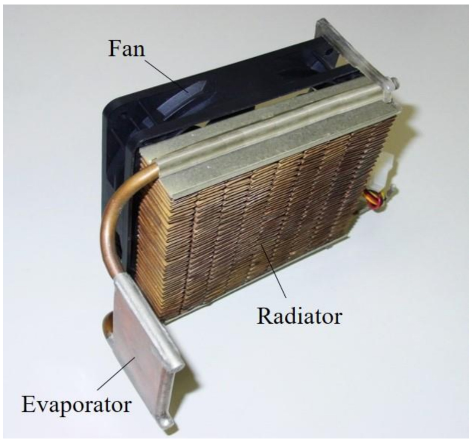

Figure 8. A CPU cooler for a personal computer.

The cooler had copper fins with an area of 0.328 m^2 connected to a 120 mm fan. The overall dimensions and weight of the cooler with the fan are 150 mm × 120 mm × 85 mm and 380 g, respectively. The operating characteristic of the cooler at a fan speed of 980 rot/min is demonstrated in Figure 9.

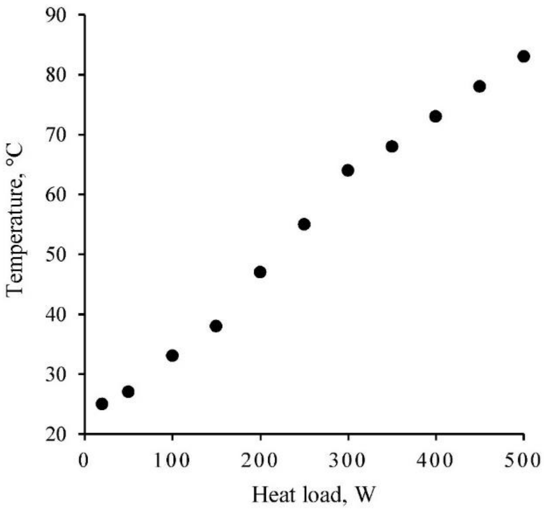

Figure 9. Dependence of the temperature at the heating surface of the CPU simulator on the heat load.

Here it is clear that the maximum allowable temperature of 70 °C is reached at a heat load of 370 W, and a comfortable temperature of 50 °C is achieved at a heat load of 200 W, which is in good agreement with the actual demand with a good reserve for further increases in the heat load.

Figure 10 shows another cooler developed on the basis of an LHP with the same evaporator for the GPU of a powerful gaming computer. The diameters of the vapor and liquid lines were 5/4 mm and 4/3 mm, respectively.

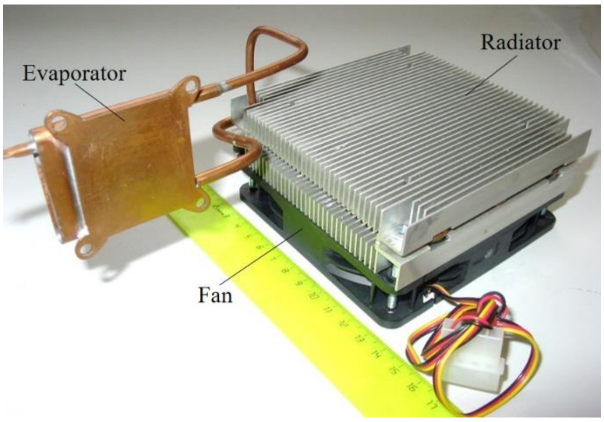

Figure 10. A GPU cooler.

The cooler was equipped with a double-sided aluminum radiator with 0.5 m^2 fin area and a 120 mm fan with a speed of 1800 rot/min. Figure 11 shows the cooler's operating characteristics obtained with the GPU thermal simulator.

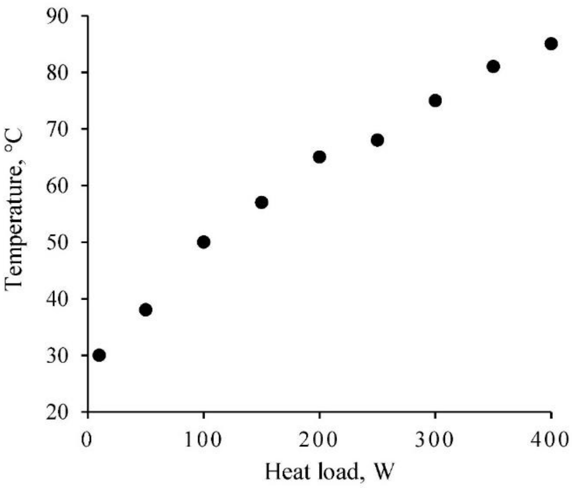

Figure 11. Dependence of temperature at the heating surface of the GPU simulator on the heat load.

A reference temperature of 70 °C was achieved here at a heat load of 270 W, and a temperature of

50 °C was reached at a heat load of 120 W. These parameters fully meet the specified requirements for the cooler.

Figure 12 shows another cooler that was developed on the basis of a copper-water LHP with a 7 mm thick flat-oval evaporator for a cooling system of CPUs in a 1U server.

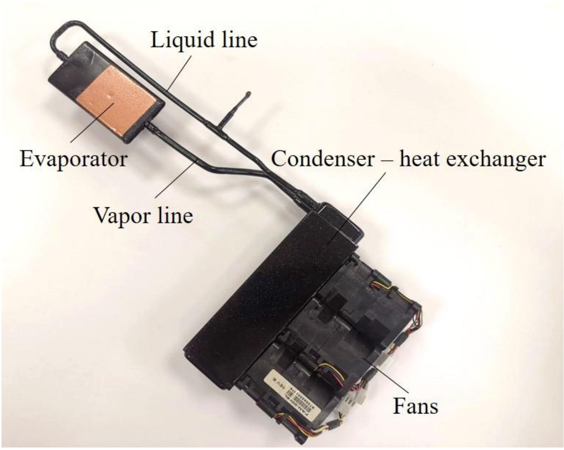

Figure 12. A cooler for a CPUs cooling system in a 1U server.

The LHP here has a vapor line with a diameter of 5/4 mm and a liquid line with a diameter of 4/3 mm. A modified serial "Alphacool" heat exchanger with dimensions of 145 mm × 40 mm × 40 mm, equipped with three high-speed "Nidec Ultra Flo" fans with a maximum speed of 12000 rot/min and a blowing rate of 7 m/sec was used as the LHP condenser.

Figure 13 demonstrates the temperature dependence of the CPU simulator on the heat load at the maximum blowing rate.

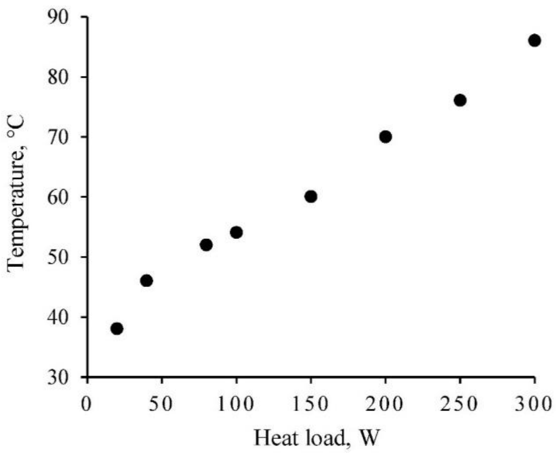

Figure 13. Dependence of the temperature at the heating surface of the server CPU simulator on the heat load.

The test results of the cooler show that the reference temperature of 70 °C is achieved under the given cooling conditions at a heat load of 200 W. This also meets the specified technical requirements for the cooling system with some margin. Figure 14 shows a 1U server equipped with such coolers, one of which has flexible lines made of bellows tube with a nominal inner diameter of 6 mm.

Figure 14. A 1U server with cooling systems based on copper-water LHPs with "Aphacool" heat exchangers.

Figure 15 shows a hybrid server cooling system where copper-water LHPs with 7mm thick flat-oval evaporators were used to dissipate heat from two CPUs with a TDP of 95 W. A vertical liquid heat exchanger located outside the server was acted as a heat sink. At a cooling water temperature of 40 °C, the temperature of CPU1 and CPU2 was maintained at 61 °C and 68 °C, respectively.

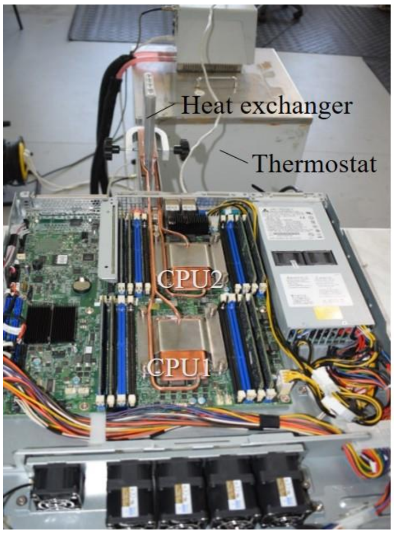

Figure 15. A hybrid 1U server cooling system.

5. Conclusions

The paper presents the results of development, experimental studies and practical application of copper-water loop heat pipes with flat-oval evaporators with a thickness of 2.3 mm, 7 mm and 10 mm, and with a disk-shaped evaporator with a diameter of 50 mm and a thickness of 19 mm. The tests were carried out under different condenser cooling conditions with cooling water temperatures of 20 °C, 40 °C and 60 °C. It is shown that the cooling water temperature does not significantly affect the temperature of the heat load source. A maximum heat load of 700 W was achieved with a 10 mm flat-oval evaporator with a minimum thermal resistance of 0.016 °C/W. The minimum thermal resistance of the disk-shaped evaporator of 0.030 °C/W was obtained at a heat load of 400 W. Examples of different variants of cooling systems for electronic components based on LHPs with flat-oval evaporators are also presented.

References

[1] Yu.F. Maydanik, M.A. Chernysheva, and V.G. Pastukhov, Review: Loop heat pipes with flat evaporators. Applied Thermal Engineering, 2014. 67 (1-2): p. 294.
[2] Yu.F. Maydanik, Miniature loop heat pipes. in the 13th International Heat Pipe Conference, 2004. Shanghai, China.
[3] Yu. Maydanik, S. Vershinin, M. Chernysheva, and S. Yushakova, Investigation of a compact copper-water loop heap pipe with a flat evaporator. Applied Thermal Engineering, 2011. 31 (16): p. 3533.
[4] M.A. Chernysheva, S.I. Yushakova, and Yu.F. Maydanik, Copper-water loop heat pipes for energy-efficient cooling systems of supercomputers. Energy, 2014. 69: p. 534.
[5] Y. Maydanik, M. Chernysheva, and S. Vershinin, High-capacity loop heat pipe with flat evaporator for efficient cooling systems. Journal of Thermophysics and Heat transfer, 2020. 34 (3): p. 465.
[6] Y. Maydanik, S. Vershinin, and M. Chernysheva, Investigation of thermal characteristics of an LHP evaporator with heat sources having different heating surface areas. Applied Thermal Engineering, 2021. 199: p. 117533.
[7] V.I. Dmitrin and Yu.F. Maydanik, Development and experimental investigation of a miniature loop heat pipe with a thin flat evaporator. Thermal processes in engineering, 2017. 8: p. 346. (in Russian).
[8] Kangning Xiong, Like Meng, and Shuangfeng Wang, Design, fabrication, investigation and analysis of a novel flat evaporator loop heat pipe for cooling high heat flux server chips. Applied Thermal Engineering, 2022. 201: p. 117775.
[9] S. Yushakova, M. Chernysheva, Yu. Maydanik, and S. Vershinin, On the lowering of the operating temperature of a copper-water loop heat pipe. in the 16th International Heat Pipe Conference, 2012. Lyon, France.

Paper ID 005(S7)

Experimental Investigation of the Structure of SiC Porous Ceramic in Application to LHP Evaporator Working in Medium-Temperature Heat Rejection Systems

Pawel Szymanski[1*], In-Hyuck Song[2], Jae-Ho Jeon[1], Piotr Radomski[1], Tadeusz Miruszewski[3], and Dariusz Mikielewicz[1]

[1] *Faculty of Mechanical Engineering and Ship Technology, Gdansk University of Technology, Gdansk, Poland*
[2]*Ceramic Materials Division, Korea Institute of Materials Science, Republic of Korea*
[3]*Faculty of Applied Physics and Mathematics, Gdansk University of Technology, Gdansk, Poland*
**Corresponding author email address: pawel.szymanski2@pg.edu.pl*

Abstract

This study investigates the structure and microstructure of a mullite-bonded SiC porous ceramic disk intended to function as a wick in a flat-type Loop Heat Pipe (F-LHP) operating within medium temperature ranges. The analysis focused on critical physical properties, including pore distribution, size, and permeability, to evaluate their influence on the performance of the LHP. Porosity was assessed using both percolation and Archimedes methods, while pore size was determined through Scanning Electron Microscopy (SEM) and Mercury Intrusion Porosimetry. The chemical composition of the wick was characterized using Energy Dispersive X-ray Spectroscopy (EDX) and X-ray diffraction (XRD), which identified the presence of silicon, aluminum, and oxygen. These chemical constituents have significant implications for the selection of chemically compatible medium temperature working fluid for use in the LHP system.

Keywords: Loop Heat Pipe, wick, working fluid, chemical compatibility.

1. Introduction

This paper discusses the effect of ceramic porous wick microstructure properties and chemical composition on the performance of a F-LHP operating in medium-temperature applications. The wick is made of mullite-bonded SiC developed as a disc.

In the experiment, the wick structure with multiple physical properties, including pore size distribution, total and effective porosity, and permeability across different structural topologies, was measured and tested to precisely determine the capillary performance necessary for heat and mass transport in LHP. The chemical composition of the wick was analyzed to identify its chemical elements and further precisely qualify its chemical compatibility with potential working fluids. Table 1 presents a list of working fluids that are recommended or not recommended for use with specific construction materials, serving as a guide in selecting potential working fluids.

The function of the wick is to provide the necessary capillary pressure to the working fluid for continuous circulation in the loop and to direct the flow of liquid through a permeable medium to the evaporation area, while preventing the backflow of vapor.

The pressure drop across the wick is determined by the wick's structural parameters, including open porosity, permeability, mean pore radius, and the properties of the working fluid. An important function of the LHP evaporator is that the meniscus inside the wick automatically adjusts due to heat load by reducing its radius of curvature to match the effective pore radius of the wick, thereby creating the highest possible capillary pressure to counter the total pressure drop in the system. This maximum pressure is determined by the Young-Laplace equation:

$$\Delta P_{cap,max} = \frac{2\sigma\cos\theta}{\mathrm{r}_p} \qquad (1)$$

where r_p is the wick meniscus curvature radius, σ is the liquid surface tension and Θ is the liquid-solid contact angle [8].

Another important parameter that determines a wick's performance is the pressure drop it can create. This pressure drop is characterized by the liquid's viscosity and the wick's permeability and can be approximated by the Darcy equation;

$$\Delta P_{wick} = \frac{l\mu_l}{\rho_l A_l \kappa_l}\dot{m}_l \qquad (2)$$

where $\frac{A_l}{l}$ is the average area for the flow divided by the length of the flow path, μ_l is the liquid dynamic viscosity, κ_l is the liquid permeability and $\dot{m}_l$ is the liquid mass flow rate across the porous wick. The Carman-Kozeny equation provides a simple model that relates permeability to the average pore diameter, such that:

$$\kappa_l = \frac{r_p^2 \varepsilon^3}{37.5(1-\varepsilon)^2} \qquad (3)$$

where ε is the porosity of the wick.

Table 1. Materials and working fluids compatibility table [1-7]

	Compatible	**Non - Compatible**
Aluminum	C_7H_8 $^{(137°C)}$, $C_{10}H_8$$^{(215°C)}$	S, $C_{18}H_{14}$, $C_{12}H_{10}$, $SnCl_4$, $TiCl_4$, $AlBr_3$, $SbBr_3$, $SbCl_3$, S/I10%
Copper	C_7H_8 $^{(280°C)}$,$C_{10}H_8$$^{(350°C)}$, $H_2O$$^{(200°C)}$	Dowtherm A, Cs
Nickel	$TiCl_4$$^{(300°C)}$,$AlBr_3$$^{(400°C)}$, $C_5H_9NO$$^{(320°C)}$, NaK$^{(650°C)}$	$SnCl_4$, $GaCl_3$, Cs, Na
Molybdenum	$C_7H_8$$^{(250°C)}$,$C_{12}H_{10}$$^{(250°C)}$, $C_{10}H_8$$^{(270°C)}$	
Niobium	K$^{(600°C)}$	S/I10%
Iron	Dowtherm A$^{(420°C)}$, $C_{18}H_{14}$$^{(380°C)}$, $C_8H_{18}N_2$$^{(250°C)}$, $C_7H_8$$^{(280°C)}$, $C_{12}H_{10}$$^{(400°C)}$, $C_{10}H_8$$^{(380°C)}$, $C_{10}H_7F$$^{(257°C)}$, $SnCl_4$$^{(227°C)}$, $TiCl_4$$^{(159°C)}$, $H_2O$$^{(165°C)}$, S/I10%$^{(350°C)}$, NaK$^{(795°C)}$, Hg$^{(600°C)}$,	$SbCl_3$
Titanium	Dowtherm A$^{(406°C)}$, $C_7H_8$$^{(250°C)}$, $C_{10}H_8$$^{(320°C)}$, $TiCl_4$$^{(227°C)}$, $H_2O$$^{(252°C)}$,	$TiBr_4$, $GaCl_3$, $AlBr_3$, $SbBr_3$, S/I10%, K, Cs

2. Wick analysis

The mullite-bonded SiC disc was manufactured by uniaxial pressing of a powder mixture containing 80 wt% SiC and 20 wt% kaolin, followed by conventional sintering at 1500°C for 2 hours in air. Photos of the wick, evaporator, and its elements are presented in Figures. 1, 2, and 3.

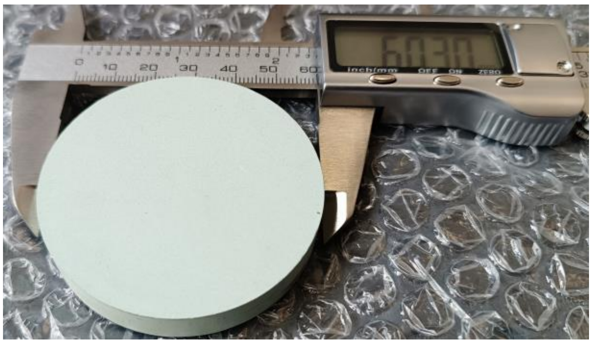

Figure 1. Photograph of the ceramic disc.

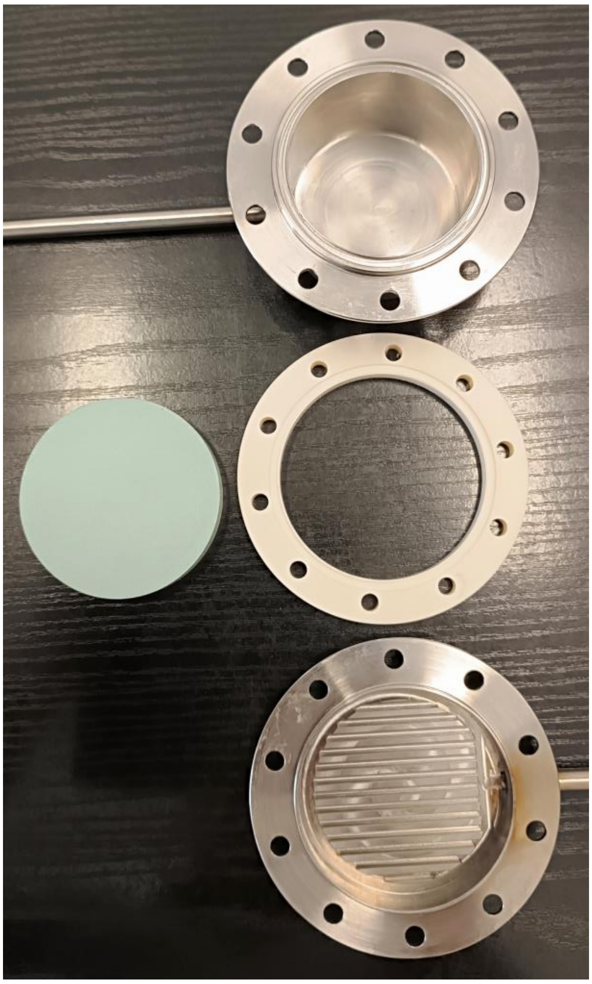

Figure 2. Photograph of the evaporator elements.

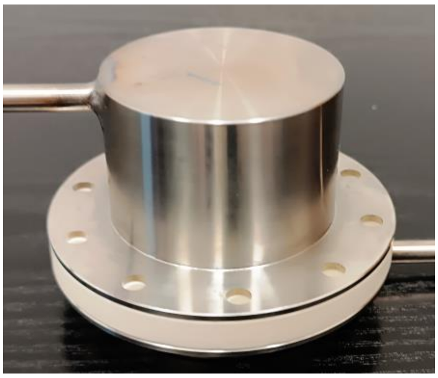

Figure 3. Side view of the evaporator.

2.1. Porosity measurement

The wick has been measured and weighted to evaluate its open porosity. Porosity has been calculated using two methods, i.e. perlocation theory to determine total porosity:

$$\varepsilon = \left(1 - \frac{\rho_{measured}}{\rho_{theoretical}}\right) \cdot 100\% \qquad (2)$$

where $\rho_{theoretical}$ is the density of mullite-bonded SiC, determined by the X-ray crystallography analysis allowing to obtain the atomic and molecular structure of the material and in consequence determine its concise molecular-theoretical density of a structure that is $\rho_{theoretical}$= 0,0031 g/mm^3. The $\rho_{measured}$ is the density measured experimentally:

$$\rho_{measured} = \frac{m_{dry\ sample}}{V} \qquad (3)$$

The second method to calculate porosity is the Archimedes method, which allows for the calculation of open porosity (a.k.a. 'effective' porosity), responsible for pumping the working fluid around the loop. The procedure involves first measuring the dry weight m_1 of the wick using the electronic scale, then, saturating the wick with acetone (CH_3COH_3, CAS:67-64-1 – density 0.00079 g/mm^3) for 6 hours, and finally measuring the weight of the saturated wick in the air m_2 and in the acetone m_3:

$$\varepsilon_o = \frac{m_2 - m_1}{m_2 - m_3} \cdot 100\% \qquad (5)$$

Porosity calculation results are presented in Table 2.

Table 2. Wick properties.

Diameter [mm]	60.3
Thickness [mm]	9.9
Volume [mm^3]	28193
Mass of dry sample m_1 [g]	56.8
Mass of sample saturated in acetone and weighed in air m_2 [g]	61.9
The apparent mass of the sample saturated and weighted in acetone m_3 [g]	41.3
Total porosity calculated using the perlocation theory [%]	36.6
Effective porosity calculated by the Archimedes method [%]	24.8

2.2 Pore size measurement and permeability calculation

The pore size of the wick was determined using two methods: scanning electron microscopy (SEM) and mercury intrusion porosimetry. SEM images of the wick samples are presented in Figure 4. The first method, using SEM, allows for the measurement of pore sizes only at the external cut surface of the wick and thus represents only the largest pores. Moreover, the pore channels inside the material change their dimensions due to the irregular microstructure, which could enhance the capillary pressure. Therefore, it is necessary to measure pore sizes inside the sample using porosimetry evaluation.

a)

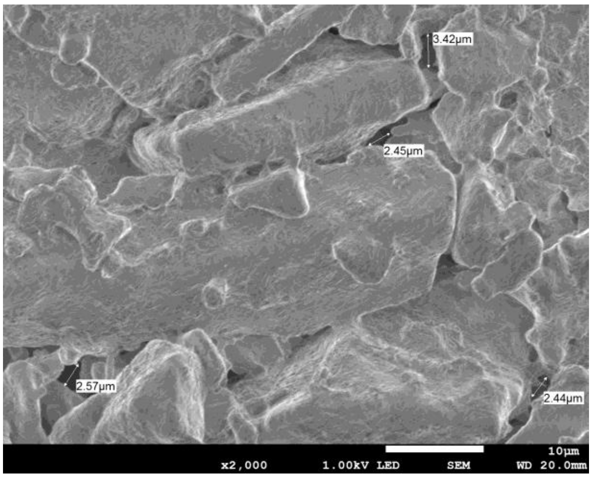

b)

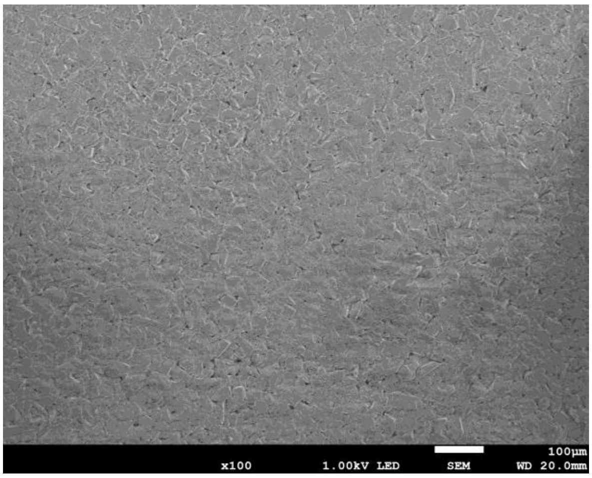

Figure 4. SEM images of the wick sample at (a) 2000x magnification (b) 100x magnification.

Mercury porosimetry, a.k.a mercury intrusion porosimetry (MIP), is a technique used to measure the porosity and pore size distribution of a material. In this method, the non-wetting properties of mercury, a non-wetting liquid, are utilized by forcing it into the pores of a material under increasing pressure. Due to its high surface tension, mercury does not spontaneously enter the pores; it requires external pressure. The pressure required to intrude mercury into a pore is inversely proportional to the pore diameter, as described by the Washburn equation:

$$P = \frac{2\gamma cos\theta}{r} \tag{6}$$

where

P is the pressure, γ is the surface tension of mercury, θ is the contact angle, and r is the pore radius.

As the pressure increases, mercury intrudes into progressively smaller pores. The volume of mercury intruded at each pressure is measured, allowing for the determination of the pore size distribution. By analyzing the volume of mercury intruded at various pressures, a pore size distribution curve can be generated, providing insights into the material's porosity, pore size distribution, and total pore volume. Figure 5 presents the pore size distribution in a ceramic disc obtained through porosimetry analysis.

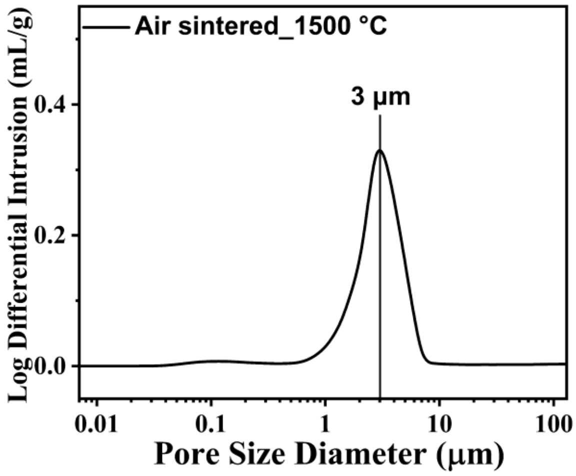

Figure 5. Pore size distribution obtained by porosimeter analysis.

As it can be seen from Figure 5, the mean diameter of the single pore is around 3 μm. Therefore using Eq. (3) the permeability can be calculated to be 6.4 $\times 10^{13}$ m^2.

2.3 Chemical composition analysis

Energy Dispersive X-ray Spectroscopy (EDX) measurements allow for the determination of the chemical composition of each element in the ceramic structure. An example of the EDX spectrum obtained for the studied SiC sample is shown in Figure 6, while the corresponding weight percentages of the analyzed elements are listed in Table 3. As can be seen, the studied sample consists mainly of silicon, aluminum, and oxygen. Since carbon is too light an element to be detected by the EDX method, it was not included in Table 3. The weight proportions indicate the dominance of silicon in the structure, with aluminum present at 10 wt%. The presence of aluminum likely results from the SiC manufacturing process, indicating that the analyzed sample contains impurities. The oxygen detected during EDX analysis probably comes from trace amounts of silicon dioxide (SiO_2), formed during the silicon oxidation in the SiC manufacturing process.

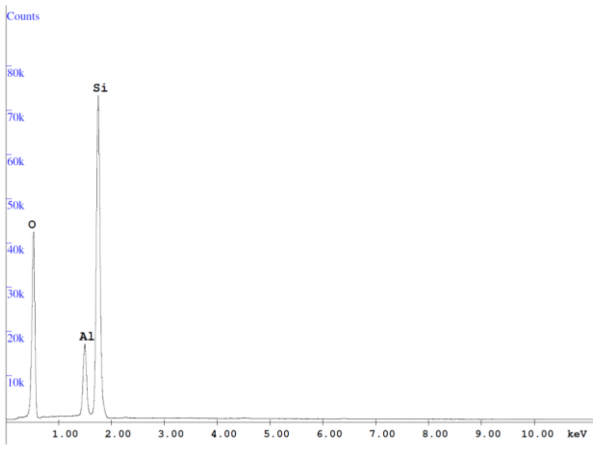

Figure 6. EDX spectra of mullite-bonded SiC disc collected from the surface.

Table 3. Weighted composition of elements of which the wick is made.

Element	Weights (%)
O	33.8
Al	10.1
Si	56.1
Total	100.00

X-ray diffraction (XRD) studies were also carried out in a 10–90° range to check the phase purity of studied material. The measurements were performed on the surface of the cylindrical sample. Figure 7 shows the XRD diffractogram for the investigated SiC sample, measured in different atmospheres – argon and air. As observed in both atmospheres, the main diffraction peak (visible for ~36°) corresponds to the α-SiC phase crystallized in a hexagonal crystal structure [9]. The other reflections are from silicon dioxide (~22°) and a mullite phase of probably unknown stoichiometry $xAl_2O_3{:}ySiO_2$ (visible at ~27°). It was also observed that when the samples were fabricated in an air atmosphere, the amount of the SiO_2 phase was significantly higher, which is related to the oxidation of silicon in the structure. The amount of mullite phase observed, and SiC, does not depend on the atmosphere.

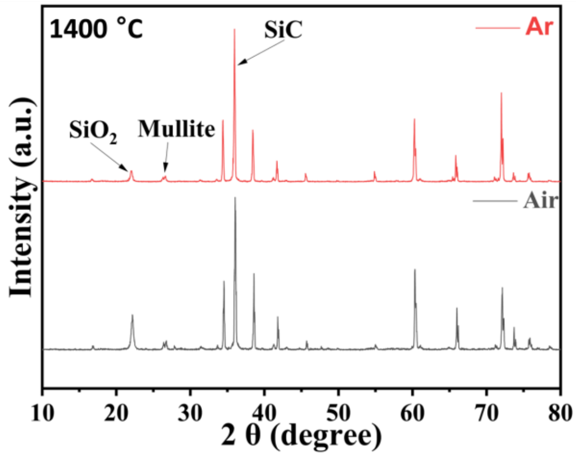

Figure 7. XRD patterns of studied SiC sample as a function of atmosphere.

Figure 8 presents the XRD pattern for the pellet with a composition of 80 wt% SiC and 20 wt% kaolin, sintered at 1500°C for 2 hours in air. The chemical composition of kaolin is mainly aluminum and silicon, classifying it as a natural aluminosilicate. Kaolin is added to silicon carbide (SiC) for several reasons, primarily to improve the material's mechanical properties and chemical resistance, as well as to reduce costs [10]. As can be seen, the addition of kaolin did not significantly change the XRD pattern, as it is mainly composed of aluminum and silicon, which were also detected in the unmodified SiC (see Figure 7).

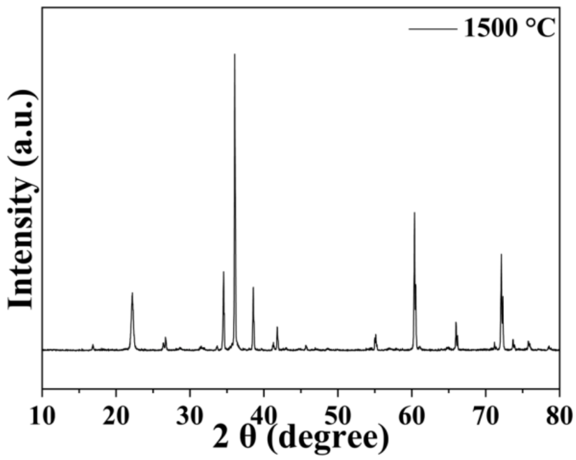

Figure 8. XRD pattern of analyzed pellet with composition 80 wt% SiC (α-SiC ~30 μm) + 20 wt% Kaolin, processed at 1500°C for 2 h in air.

3. Conclusions

This study investigates the structure and microstructure of a porous ceramic material shaped into a disk, intended to function as a wick in a F-LHP operating at medium temperatures. The research focuses on evaluating the physical parameters, such as pore distribution and size, as well as permeability, to assess their impact on the subsequent performance of the LHP.

The porosity of the material was examined using two methods: percolation and the Archimedes method. The pore size was measured using Scanning Electron Microscopy (SEM) and Mercury Intrusion Porosimetry. Additionally, Energy Dispersive X-ray Spectroscopy (EDX) was employed to determine the chemical composition of the elements within the ceramic structure. The EDX results revealed that the material contains silicon, aluminum, and oxygen.

X-ray diffraction (XRD) analysis revealed that the main diffraction peak corresponds to the α-SiC phase, with additional peaks for silicon dioxide and a mullite phase, where the presence of SiO2 increased when the material was fabricated in air due to silicon oxidation. The addition of kaolin (20 wt%) to SiC did not significantly alter the XRD pattern, as kaolin's primary components, aluminum and silicon, were already present in the unmodified SiC.

Given that the wick contains aluminum, this affects the final selection of the working fluid. After preliminary analysis, it was determined that suitable working fluids could include C_7H_8 (Toluene) and $C_{10}H_8$ (Naphthalene), while fluids such as S (Sulfur), $C_{18}H_{14}$ (O-Terphenyl), $C_{12}H_{10}$ (Diphenyl), $SnCl_4$ (Tin Tetrachloride), $TiCl_4$ (Titanium tetrachloride), $AlBr_3$ (Aluminum Bromide), $SbBr_3$ (Antimony Tribromide), $SbCl_3$ (Antimony Trichloride), and S/I10% were deemed unsuitable.

ACKNOWLEDGEMENTS

The research was funded by a project supported by the Poland National Science Centre, named OPUS 24 (2022/47/B/ST8/01490), as well as by two projects funded by Gdansk University of Technology's Excellence Initiative—Research University: the Argentum Triggering Research Grants (17/1/2021/IDUB/I3b/Ag) and the Radium Learning Through Research Program (1/1/2023/IDUB/III.1a/Ra).

References

[1] M. Barbosa and H. Mantelli, Thermosyphons and Heat Pipes: Theory and Applications. 2021.

[2] H. Jouhara, D. Reay, R. McGlen, P. Kew, and J. McDonough, Heat Pipes Theory, Design and Applications, 7th ed. Butterworth-Heinemann, Elsevier Science, 2023.

[3] Y. Zhang, Heat Pipes Design Application and Technology. Nova Science Pub Inc, 2018.

[4] D. Mishkinis, P. Prado, R. Sanz, A. Radkov, A. Torres, and T. Tjiptajardja, Loop Heat Pipe working fluids for intermediate temperature range: from -40ºC to +125ºC, in Proc. International Conference Heat Pipes for Space Applications, Moscow, Russia, 2009.

[5] W. G. Anderson, J. J. Bland, Y. Fershtater, K. A. Goncharov, M. Nikitkin, and A. Juhasz, High-temperature Loop Heat Pipes, IECEC Paper No. AP-18, ASME, 1995.

[6] W. G. Anderson, J. H. Rosenfeld, D. Angirasa, and Y. Mi, Evaluation of Heat Pipe Working Fluids In The Temperature Range 450 to 700K, AIP Conference Proceedings, vol. 699, p. 20, 2004.

[7] T. C. Werner, Y. Yan, T. Karayiannis, V. Pickert, R. Wrobel, and R. Law, Medium temperature heat pipes – Applications, challenges and future direction, Applied Thermal Engineering, vol. 236, Part A, 2024.

[8] P. Szymanski, D. Mikielewicz, and S. Fooladpanjeh, Current Trends in Wick Structure Construction in Loop Heat Pipes Applications: A Review, Materials, vol. 15, p. 5765, 2022.

[9] V. A. Izhevskyi, L. A. Genova, A. H. A. Bressiani, and J. C. Bressiani, Liquid Phase Sintered SiC. Processing and Transformation Controlled Microstructure Tailoring, Materials Research, vol. 3, no. 4, pp. 131-138, 2000.

[10] M. S. Prasad, K. J. Reid, and H. H. Murray, "Kaolin: processing, properties and applications, Applied Clay Science, vol. 6, pp. 87-119, 1991.

Paper ID 010

Pore Network Simulation for Design of Biporous Structures in Loop Heat Pipe Evaporators

Masahito Nishikawara[1*]

[1] *Nagoya University, Nagoya, Japan*
**Corresponding author email address: nishikawara@nagoya-u.jp*

Abstract

With the rapid development of additive manufacturing technology, the optimal design of microstructure for evaporative heat transport is increasingly necessary; however, no established method currently exists. In this study, thermal hydraulic simulations of biporous wicks with different pore-size ratios were performed using a pore network model to obtain information for designing the pore-size distributions in loop heat pipe evaporators. The calculated permeabilities of all biporous wicks were adjusted to isolate the influence of pore-size ratios. Results indicated that a smaller pore-size ratio led to higher maximum heat fluxes and improved heat-transfer coefficients of the evaporator. As observed in monoporous wicks, longer three-phase contact lines at the contact surface between the evaporator casing and the wick enhanced heat transfer performance. The findings suggest that adjusting the radius ratio of biporous wicks could design heat fluxes with higher heat-transfer coefficient.

Keywords: Additive manufacturing; Biporous wick; Heat-transfer coefficient; Pore network simulation

1. Introduction

Thermal control devices, known as loop heat pipes (LHP), have recently gained attention in various fields. Capillary pressure develops, and liquid evaporates in the porous media of the evaporator. The configuration of the evaporator is a critical factor in performance design. However, establishing an optimal design method remains challenging due to the complexity of two-phase thermal hydraulics within the capillary evaporator.

The heat transfer mechanism in an evaporator using both analytical and experimental approaches was investigated. Three-dimensional pore network simulations and a visualized evaporator with an observable contact surface between the heated casing and the wick were used in this study [1, 2]. The pore network simulation elucidated the relationship between the shape of the liquid-vapor interface and the heat transfer performance of the evaporator. Specifically, it was found that the length of the three-phase contact line (TPCL) at the contact surface between the evaporator casing and the wick was linearly related to the heat-transfer coefficient of the evaporator [1]. This result highlights the importance of considering the three-dimensional microstructure of porous media, marking the first such clarification by this study. In addition, this study experimentally validated the linear relationship between TPCL length and heat-transfer coefficient of the evaporator, as revealed by a pore network simulation, using custom observation equipment [2].

In addition, pore network simulations, validated by experiments, were performed by changing the shape of a simple pore-size distribution (called a monoporous wick). The results showed that a moderate pore-size distribution increased the heat-transfer coefficient of the evaporator [1]. This result suggests that the microstructure itself directly affects thermal performance rather than inducing indirect changes in macroscopic properties such as permeability. This study introduces a new research direction focused on improving the performance of LHPs through the microstructural design of porous media. With recent advances in additive manufacturing, it is now possible to fabricate porous materials with tailored microstructures. As a result, there is growing interest in using pore network simulations to design porous media.

This study investigated biporous wicks, which are characterized by double peaks in pore-size distribution. Experimental evidence has shown that biporous structures improve evaporator performance [3-5]. Mottet et al. [6] performed pore network simulations on LHP/CPL evaporators with clustered biporous wicks, showing that under high heat flux conditions, monoporous wicks exhibited a completely vapor-filled region immediately below the heating surface, creating a thermal resistance layer. In contrast, biporous wicks maintained a two-phase state, resulting in an increased heat-transfer coefficient. However, the correlation between the pore-size distribution in biporous wicks and the thermal hydraulics of the liquid and vapor phases, as well as the influence of the physical properties of the working fluid, remains unresolved.

In this study, three-dimensional pore network simulations were performed on dissolving-type biporous wicks [3, 5], which are considered easy to produce using additive manufacturing technology. The pore-size distribution was varied to investigate its effect on the heat-transfer coefficient of the evaporator. These results can be used to formulate design methodologies for optimizing pore-size distributions in biporous structures. This study is divided into sections that cover the numerical model, porous sample generation, results, discussion, and conclusions. The numerical model describes the governing equations, evaporator geometry, and pore network model. Porous samples were generated by varying the pore radius ratio while maintaining constant permeability. The results section presents the effect of the pore radius ratio on heat-transfer coefficients and compares the findings with monoporous wicks.

2. Numerical model

The computational domain, representing part of the periodic structure of the capillary evaporator is shown in Figure 1. It is a cuboid with the size of 4.0 × 3.5 × 1.5 mm ($L_x \times L_y \times L_z$), consisting of a stainless-steel (SS) casing, wick, and grooves. The groove height was 1.0 mm, the casing thickness was 1.0 mm, and the contact surface between the casing and the wick was 50% of the $L_x \times L_z$ area. Although the domain can be reproduced in two dimensions, the liquid-vapor interface shape has a distribution in the z-direction due to the disordered porous structure, necessitating 3D simulations.

In the simulation, the porous structure flow was represented using a pore network model (Figure 2), and the energy conservation of the casing and wick was solved. Depending on the heat flux applied to the evaporator, the state of the wick phase is divided into saturated with liquid for low heat flux and a liquid-vapor two-phase for high heat flux. In the simulation, the transition conditions for the two-phase state were decided based on the boiling critical superheat. The wick liquid-vapor interface was calculated such that the pressure difference

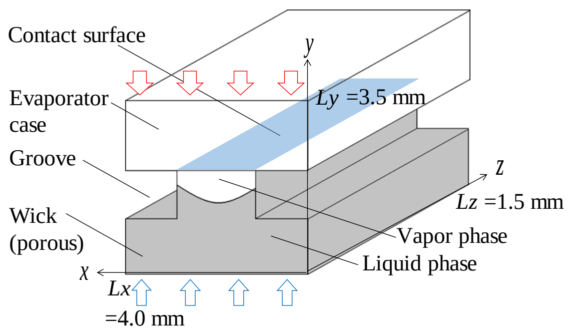

Figure 1. Computational domain (not-to-scale).

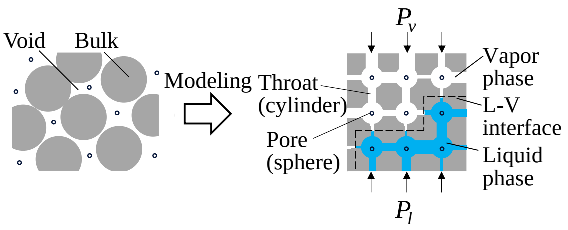

Figure 2. Overview of pore network model.

between the vapor and liquid at the interface balanced the local capillary pressure. The local capillary pressure P_{cap} is expressed as follows:

$$P_{cap} = \frac{2\sigma \cos\theta}{r_{th}} \quad , \tag{1}$$

where, σ is surface tension, θ is the contact angle, r_{th} is the throat radius. The throat mass flow rate between neighboring pores was proportional to the pressure difference between the pores. The mass conservation is expressed as follows:

$$\sum_{n=1}^{6} \frac{g_{i,n}}{\nu}\left(P_i - P_n\right) = 0 \quad , \tag{2}$$

where ν is the kinetic viscosity and $g_{i,n}$ is the flow conductance, which is proportional to the quadruplicate throat radius and inversely proportional to the throat length. The details of the numerical model are available in [1].

Constant saturation temperature and pressure were applied to the groove and compensation chamber (CC). Zero-pressure loss was assumed through the transport line and a constant heat flux was applied at the top of the casing. The applied heat fluxes increased to the operating limit of the upper temperature range. Ammonia was used as the working fluid, and porous polytetrafluoroethylene (PTFE) porous media were used as wicks.

3. Porous sample

Three porous samples with different pore radius ratios (= r_L/r_S) were generated, as shown in Figure 3. The porosity characteristics of the samples are listed in Table 1. The ratio of the pore radius at the peak on the small side (= r_S) to the pore radius at the peak on the large side (= r_L) is defined as r_L/r_S , which was adjusted by changing r_L, while keeping r_S constant for each sample. The frequencies at r_S and r_L are defined as f_S and f_L, respectively, with the ratio f_L/f_S set to 1.0, 0.25, and 0.10 for r_L/r_S = 4, 10, and 16, respectively. The throat radii were generated based on the designed pores. Diameter distribution was then randomly allocated to the wick. The computational permeability was fitted to match the permeability measured in [5].

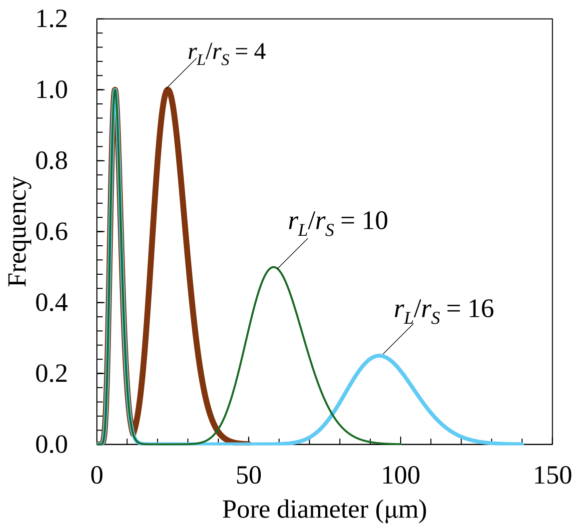

Figure 3. Pore-size distribution of the three biporous samples.

Table 1. Porous characteristics of the biporous samples.

Sample	r_S(μm)	r_L(μm)	f_L/f_S	K(m^2)
$r_L/r_S = 4$	3.0	12	1.0	9.6×10^{-13}
$r_L/r_S = 10$	3.0	29	0.50	9.8×10^{-13}
$r_L/r_S = 16$	3.0	47	0.25	9.7×10^{-13}

4. Results and discussion

The results of the evaporator heat-transfer coefficients are shown in Figure 4. The heat-transfer coefficient was calculated using the heat flux applied to the evaporator casing and the temperature difference between the average temperature of the evaporator casing surface and the saturation temperature of the vapor. The sample with a small r_L/r_S demonstrated a high

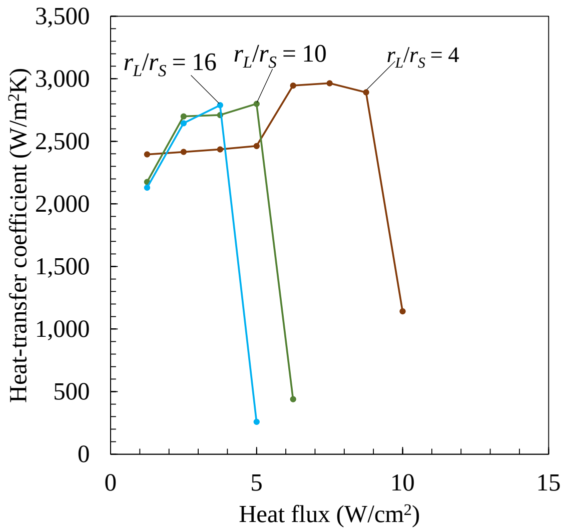

Figure 4. Computed heat-transfer coefficients of the evaporator for each sample.

maximum heat flux and heat-transfer coefficient.

The computed liquid-vapor interfaces and phase distributions at the contact surface between the casing and wick for the sample with $r_L/r_S = 4$ are shown in Figure 5. For reference, the liquid-vapor interface of a liquid-saturated wick is also shown for reference, although this state was not simulated. At low heat fluxes, the liquid-vapor interface within the wick exists only near the contact surface. At 6.25 W/m^2, the liquid-vapor interface extended in the depth direction, and the length of the TPCL (the boundary line between the two phases at the contact surface) increased. At 8.75 W/cm^2, the liquid-vapor interface shape became more complex, and the TPCL became longer. In addition, some Haines jumps, local breakthroughs at the pore scale, occurred at the liquid-vapor interface between the grooves and wick. This phenomenon does not occur in monoporous wicks. At 10 W/cm^2, the interface receded across the plane, and the TPCL became

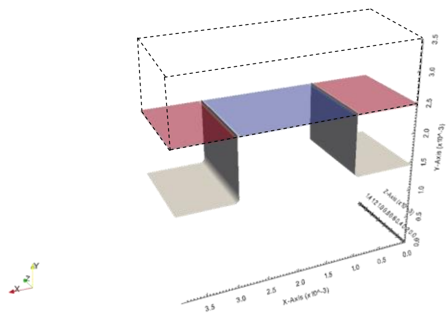

(a) Saturated

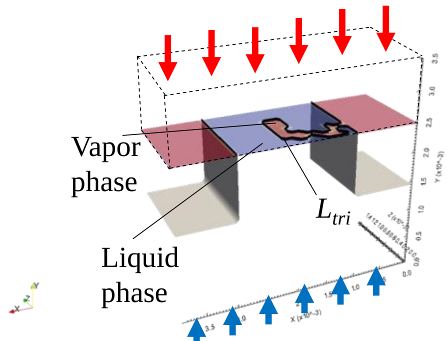

(b) 1.25 W/cm^2

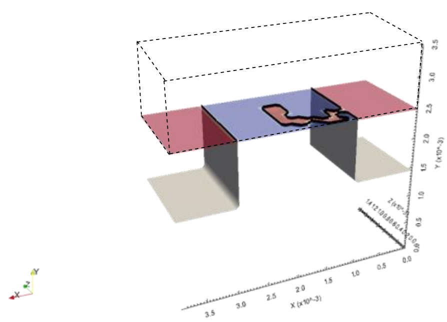

(c) 3.75 W/cm^2

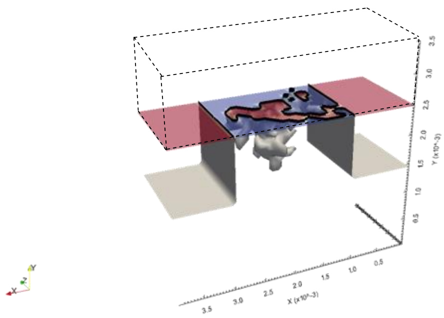

(d) 6.25 W/cm^2

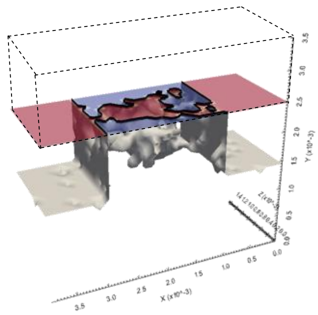

(e) 8.75 W/cm^2

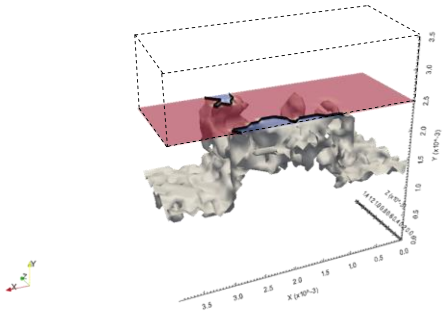

(f) 10 W/cm^2

Figure 5. Liquid-vapor interface for the sample with r_L/r_S = 4. (a) Saturated wick and (b) 1.25 W/cm^2, (c) 3.75 W/cm^2, (d) 6.25 W/cm^2, (e) 8.75 W/cm^2, (f) 10 W/cm^2 of applied heat flux.

significantly shorter, causing a reduction in heat-transfer coefficient. Numerous local Haines jumps occurred below the grooves, resulting in a complex liquid-vapor interface.

Three main modes of phase distribution were classified: (1) shallow vapor pockets with relatively short TPCL lengths (Low-h_{evap}), as shown in Figures 5b and c; (2) locally deep vapor pockets with long TPCL lengths (High-h_{evap}), as shown in Figures 5d and e; and (3) deep vapor pockets throughout the plane with short TPCL lengths (Pre-dryout). These three-phase distribution modes are clearly observed in Figure 6, where the TPCL length and maximum depth of the vapor pocket are shown.

Figure 7 shows the temperature distribution at the contact surface at 8.75 W/cm^2, where the heat-transfer coefficient was high. The temperature was lower near the TPCL areas, where evaporation occurred, and higher in regions farther from the TPCL. Evaporation at the TPCL was the dominant heat transport mechanism in the evaporator in the two-phase state, particularly in wicks with low thermal conductivity. As shown in Figure 8, the heat-transfer coefficient of the evaporator was linearly related to the TPCL length. This characteristic is consistent with that of monoporous wicks.

Figure 9 shows the phase distributions with the samples of r_L/r_S = 10, 16 at high heat fluxes where the heat-transfer coefficients are high. Both distributions have the long TPCL similar to Figure 5d, e and can be classified as the High-h_{evap} mode.

Compared to monoporous wicks, while the shapes of the liquid-vapor interface and TPCLs differed, there was no difference in the

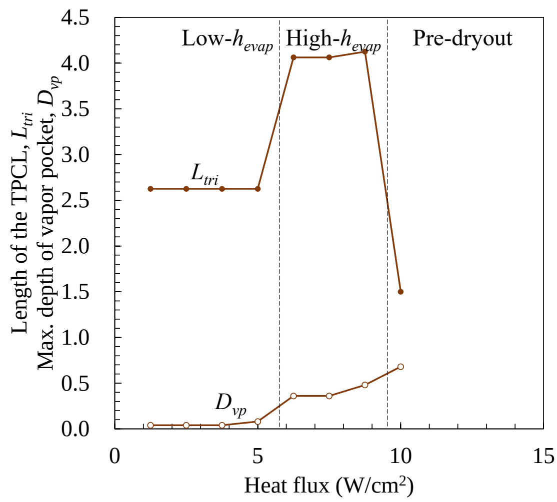

Figure 6. The TPCL length of each sample. L_{tri} are normalized with the TPCL length in the case of the liquid-saturated wick. D_{vp} are normalized with the wick height.

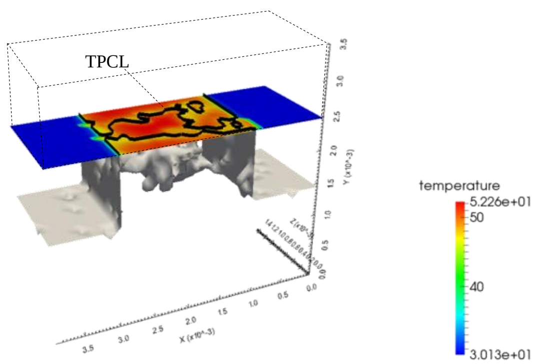

Figure 7. Temperature distribution at the contact surface between the casing and wick at 8.75 W/cm^2 of heat flux for the sample with r_L/r_S = 4.

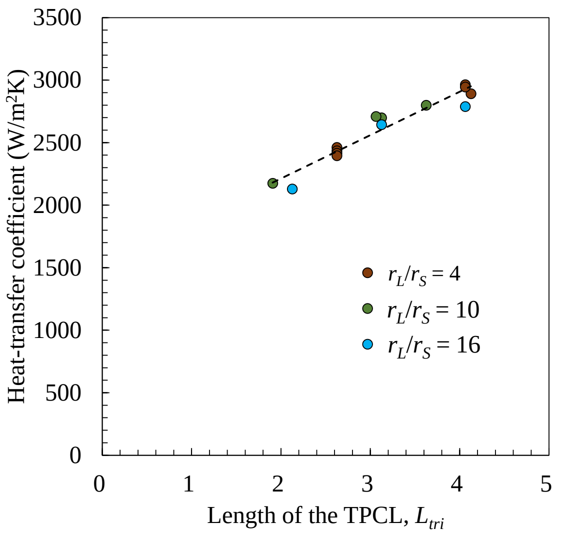

Figure 8. Relationship between the TPCL length and heat-transfer coefficient of the evaporator.

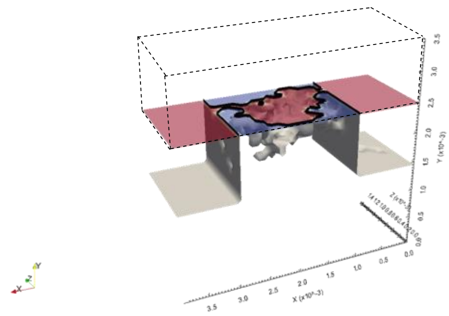

(a) r_L/r_S = 10, 5.0 W/cm^2

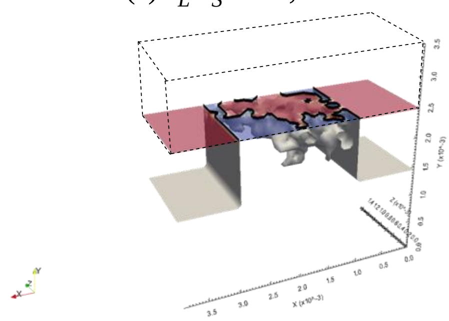

(b) r_L/r_S = 16, 3.75 W/cm^2

Figure 9. Liquid-vapor interfaces for the samples with r_L/r_S = 10 and 16.

fundamental heat transport mechanism; the heat-transfer coefficient increased with TPCL length. Figure 4 shows that the heat flux at which the phase distribution mode transitions to the High-h_{evap} mode varies with the pore radius ratio. A higher pore radius ratio corresponds to a low transition heat flux to the High-h_{evap} mode. This suggests that the high heat-transfer coefficient can be optimized by adjusting the pore-radius ratio of the biporous wick. Future research should focus on the influence of pore-size distribution and fluid properties.

5. Conclusions

To optimize the pore-size distribution of biporous wicks, the thermal hydraulics of the LHP evaporator were calculated using a pore network simulation for three different pore radius ratios while keeping permeability constant. The sample with a small pore radius ratio exhibited a high maximum heat flux and a high heat-transfer coefficient of the evaporator. The relationship between the TPCL and the heat-transfer coefficient was linear for biporous wicks, and there was no difference in the fundamental heat transport mechanism; a longer TPCL showed a higher heat-transfer coefficient compared to monoporous wicks. A high pore radius ratio indicated a lower transition heat flux to the high heat-transfer coefficient mode. This suggests the heat-transfer coefficient can be deliberately increased at specific heat fluxes, potentially expanding the use of low-heat-flux sources such as solar and geothermal heat.

Acknowledgement

This work was supported by TEPCO Memorial Foundation and Mayekawa Houonkai foundation.

References

[1] M. Nishikawara, Pore network simulation of loop heat pipe evaporator with different pore size distribution, International Journal of Heat and Mass Transfer, 2024. 218: p. 124739.
[2] M. Nishikawara, S. Tomita, Hiroshi Yokoyama and H. Yanada, Relationship between phase distribution and heat-transfer coefficient of loop heat pipe evaporator investigated by lateral observation of porous media, Applied Thermal Engineering, 2024. 236: p. 121524.
[3] C.C. Yeh, B.H. Liu, Y.M. Chen, A study of loop heat pipe with biporous wicks, Heat Mass Transfer, 2008. 44: p.1537.
[4] F.C. Lin, B.-H. Liu, C.-C. Juan, Y.-M. Chen, Effect of pore size distribution in bidisperse wick on heat transfer in a loop heat pipe, Heat Mass Transfer, 2011. 47: p. 933.
[5] S.C. Wu, B.H. Hsieh, D. Wang, Y.M. Chen, Manufacture of a biporous nickel wick and its effect on LHP heat transfer performance enhancement, Heat Mass Transfer, 2015, 51: p. 1549.
[6] L. Mottet, M. Prat, Numerical simulation of heat and mass transfer in bidispersed capillary structures: application to the evaporator of a loop heat pipe, Applied Thermal Engineering, 2016. 102: p. 770.

Paper ID 011(S2C)

Thermal Performance Evaluation of Tower Type Vapor Chamber

Harutoshi Hagino[1*], Phan Thanglong, Tsuyosi Koshio, Yuji Saito and Yoji Kawahara

[1] *Fujikura,1440, Mutsuzaki, Sakura-shi, Chiba, Japan*
* *harutoshi.hagino@jp.fujikura.com*

Abstract

Tower heat sink is used for high power electronic device cooling solution. There are tower type heat pipe and vapor chamber design. Tower type heat pipe have multiple heat pipes on solid metal base. Tower type vapor chamber have multiple heat pipe on vapor chamber base and bottom of pipe and vapor chamber is integrated. Tower type vapor chamber's thermal resistance is lower than tower type heat pipe because there is no interface between pipe and base and large vapor space. Experimentally, thermal resistance of tower type vapor camber is 12% lower and dry out limit is around 14% higher than tower type heat pipe. Tower type vapor chamber's performance is depended on internal water flow path and amount of fluid charging. Especially heat transfer coefficient and dry out limit is affected. Internal flow path between condensation and evaporation area and high amount of fluid charging is necessary for high power heating solution.

Keywords: Vapor Chamber; Heat Spreader; High Heat Flux; Chip packaging

1. Introduction

Tower heat sink is used for high power cooling solution. It is made from metal base, heat pipe and fin. Heat pipe is connected on top side of metal base with bending and the other side of HP is connected to fin. Recently power density of chip is increasing and heat dissipation capacity of tower heat sink may not be enough for high power electronics like a high density CPU/GPU. Heat pipe is bended and heat transport property is decreased due to decreasing of vapor path at bending area. Furthermore, there is contact thermal resistance of bonding layer between heat pipe and metal base. Recently tower type vapor chamber is attracting attention as an air-cooling solution. Vapor chamber is well-known two-phase heat transfer device, which spreads heat from small area of heat sources to large area of heatsink. Appearance of tower type vapor chamber is similar to tower heat sink but inside of metal base is vapor chamber and heat pipe is connected to vapor chamber directly. Vapor space of vapor chamber and heat pipe is continuously and there is no thermal resistance between vapor chamber and heat pipe. Fluid and vapor flow paths in tower vapor chamber is complex than tower heat sink because the direction of vapor and liquid flow in tower vapor chamber is changed to horizontally or vertically in internal space. A comparison between tower vapor chambers and tower heat pipes and the effect of the tower vapor chamber's internal structure on the heat transport characteristics and the effect of water charging to evaporation and condensation condition will be reported.

2. Structure of Tower Type Vapor Chamber

Fig. 1 shows a schematic of a typical vapor chamber[1]. Vapor chamber is made from container, wick and column. Air in inside of vapor chamber is evacuated and the working fluid is charged with keeping vacuum for make saturated condition. When one area of the vapor chamber is heated, working fluid is vaporized and vapor is flowed to the other area. Vapor is condensed to fluid at condensation area and latent heat is released. Condensed fluid is spread on column or wall surface or moved in wick by capillary force. It is returned to the evaporator area and vaporized again. The vapor chamber can transport heat from heating area to cooling side by using this cycle of evaporation and condensation and thermal resistance of vapor chamber is kept lower than that

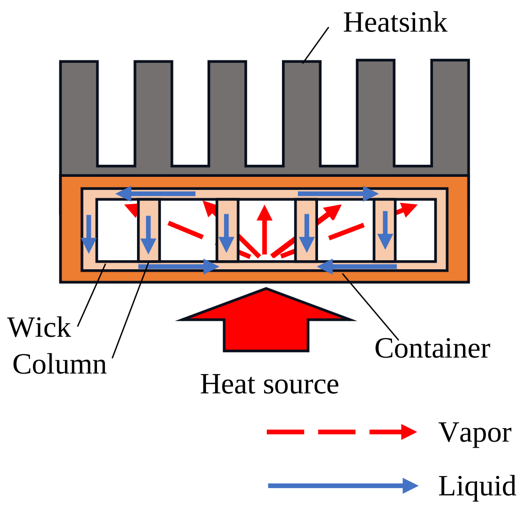

Figure 1. Fundamental of Vapor Chamber

of heat sink. When it is used to high heat generation solution like a CPU/GPU, it is need to increase heat dissipation [2]. Tower type heat sink solution is used for increase heat dissipation. Fig.2 is shown a schematic of a tower heat pipe heat sink. It has multiple heat pipes. It is bended to L shape or U shape. Bottom side of heat pipe is on base plate and other side is extended to vertical direction for set fin. Heat is conducted from base and moved to fin by heat pipe. Appearance is tower like and fin volume is high for large amount of dissipation heat. The dissipation heat of tower type heat pipe solution is depended on the number of pipes. As a result, size of tower type heat pipe is easily increased when it is used high power heat source. Fig.3 and Fig.4 show tower type vapor chamber. Vapor chamber is used as a base and heat pipe is connected on the top side of vapor chamber base as a condensation area. Vapor space in pipe and base is combined and heat sink is attached to the outside of pipe. Vapor chamber base is contacted to heat source and working fluid in inside of vapor chamber is vaporized by heat from heat source. Vapor is rising in pipe and condensed. As a result, heat is dissipated through the fins. Condensed fluid on the surface of pipe is returned to the evaporator area by wick's capillary force. The heat transport capacity of tower type vapor chamber is higher than tower heat sink and tower heat pipe due to large internal vapor space. The design of liquid and vapor flow paths is important for performance because the direction of vapor and liquid flow in tower vapor chamber is changed to horizontally or vertically in vapor space.

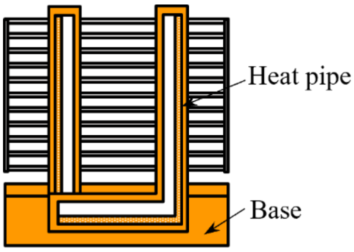

Figure 2. Tower type heat pipe

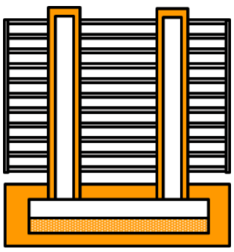

Figure 3. Tower vapor chamber.

3. Simplified vapor chamber model

The main difference between the tower type vapor chamber and heat pipe is evaporator structure. Fig. 5 show thermal circuit schematic of tower type heat pipe and vapor chamber. In general, the heat pipe is soldered to the base on the other hand, the space in heat pipe and vapor chamber is integrated. Thermal resistance of tower type heat sink is high due to the effect of heat conduction of the solder layer and base. There is no solder layer in tower type vapor chamber and heat is conducted to vapor chamber base directly. As a result, tower vapor chamber can kept low thermal resistance. Furthermore there is difference in evaporation area. Tower type heat pipe's evaporator is made from multiple heat pipes and evaporation area is internal surface of heat pipe. It is separated and vapor and liquid flow in heat pipe is limited to pipe length direction due to pipe wall. Considering the thickness of the pipe wall, the apparent area of the evaporation area is decreased. There is no interface like wall of pipe in evaporator area of vapor chamber and effective evaporator area is larger than tower heat pipe. As a result, vapor chamber base is effective for decrease evaporation thermal resistance.

4. Sample and test condition

The tower heat pipe consists of 8 pcs of L-shape bended heat pipe, and it is fixed by solder to solid Cu base. Fin is connected to

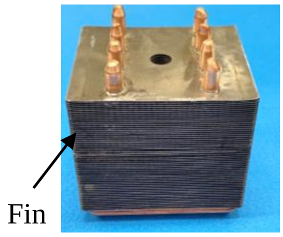

(a) Tower type vapor chamber

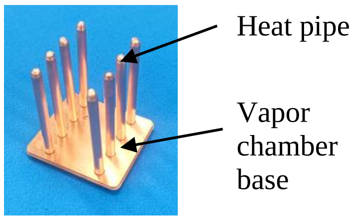

(b) Vapor chamber base and hipe condensation structure.

Figure 4. Tower type vapor chamber

each pipe for cooling side (Fig.2). Inside of tower vapor chamber base have space as vapor chamber and heat pipe are connected to the top of base. Wick is formed to the inner wall of pipe for condensed water flow path. It is extended from the pipe inside wall to bottom surface for contact wick in pipe and bottom wick on the surface of base wall (Fig.6). In order to evaluate the effect of the wick to water flow, a sample without a wick in the pipe was evaluated (Fig.3).Samples were tested in wind tunnel (Air temperature is 25℃ and air flow rate is 60 CFM) with 50 mm x 30 mm heater. Heater is fixed under center of base and thermal grease is printed between base and heater. Thermal resistance R_t [°C/W] is defined from the base temperature T_{base} [°C], inlet air temperature T_{air} [°C] and heater power Q [W] as below.

$$R_t = (T_{base} - T_{air})/Q \quad (1)$$

The evaporation heat transfer coefficient *hevp* [W/(m² · K)] was calculated from tube top temperature T_{top} [°C] as below.

$$hevp = Q/((T_{base} - T_{top})A_{evp}) \quad (2)$$

where A is the area of the evaporation area [m²]. The condensation heat transfer coefficient h_{con} [W/(m² · K)] was calculated from tube top temperature $T_{HP\ top}$ [°C] and VC top temperature $T_{VC\ top}$[°C].

$$hevp = Q/((T_{HP\,top} - T_{VC\_top})A_{con}) \quad (3)$$

6.Experimentalresult

6.1. Heat transport property consideration

Figure 8 and 9 shows the measured value of R_t and h_{evp}. *Rt* of sample without a wick in pipe was increased from 200W and h_{evp} was decreased. It shows dryout was happen from low power [2]

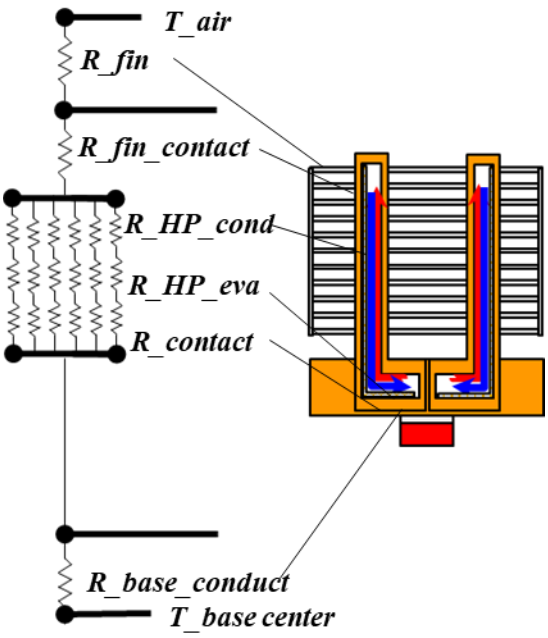

(a)Tower type heat pipe

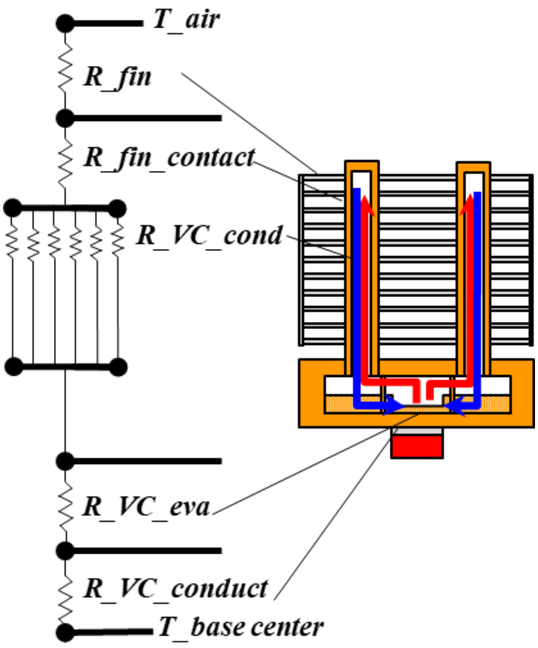

(b)Tower type vapor chamber

Figure 5. Tower type vapor chamber

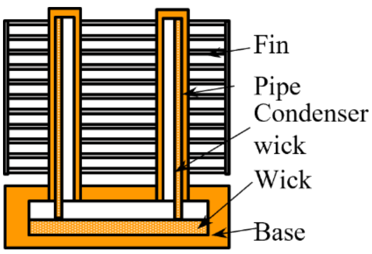

Figure 7. Temperature measurement point

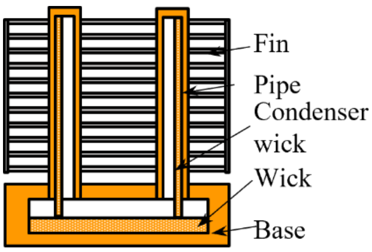

Figure 6. Tower type vapor chamber

This case fluid returning direction and vapor condition. On the other hand, Rt of sample with wick in HP is kept steady condition with increasing power and dryout does not occur until 800W. In case of no wick on the surface of inner pipe, the condensed liquid must either slip out from the pipe or return to the evaporation zone along the wall surface. It is considered that dryout occurred because the liquid condensed in the pipe was not returned sufficiently and there was not enough liquid in the evaporation area. flow direction is different. Fluid and vapor is affected and fluid returning is impeded by counter flow effect[2]. Extending wick from pipe to bottom wick act as liquid reflux flow path from condensation area to evaporation area. As a result, condensed liquid move from condensation area to evaporator and dryout limit is increased due to the amount of liquid reflux increasing. Comparing the thermal resistance of the tower vapor chamber with that of the tower heat pipe, the thermal resistance of the tower vapor chamber is about 15% lower. The evaporative heat transfer coefficient for the tower heat pipe was about 30,000[W/(m2-K)], while that for the tower vapor chamber was about 90,000[W/(m2-K)]. In the tower type heat pipe, each vapor space in pipe is independed and the vapor transport path is restricted to the inside of the pipe. It means heat spreading is one-dimensional. In the tower-type vapor chamber, the pipe and the base are combined and the vapor diffuses in the plane direction and then rises in the pipe to dissipate heat. Heat dissipation is three-dimensional transport. Therefore, it is considered that the evaporative heat transfer coefficient is larger than that of the tower type heat pipe due to the larger vapor space and lower pressure drop in vapor transport, resulting in lower thermal resistance.

6.2. Effect of charging liquid

Fig.10 show the water charging ratio dependence of thermal resistance of tower type vapor chamber. When charging water is 5.4 cc, it was worked until 400 W and thermal resistance is increased at high input power condition. Working power limit is increased to 800W by increasing amount of charging liquid. Rt of sample with 6.5cc charging is decreased with increasing input power until 800W and it is increased over 800W. Rt of sample with 7.3cc charging have same property. Fig.10 and Fig.11 show the results of evaporation and condensation heat transfer coefficient for various liquid volumes. Peak of h_{evp} of sample with 5.4cc charging is 400W and h_{evp} is decreased with

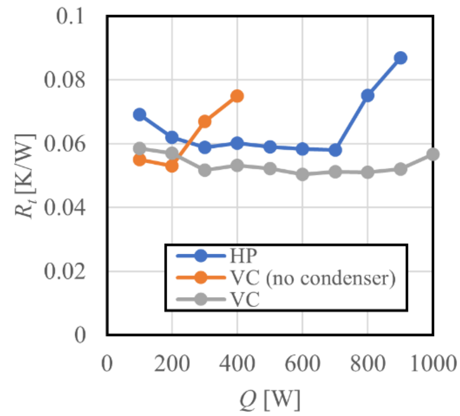

Figure 8. Thermal resistance: R_t .

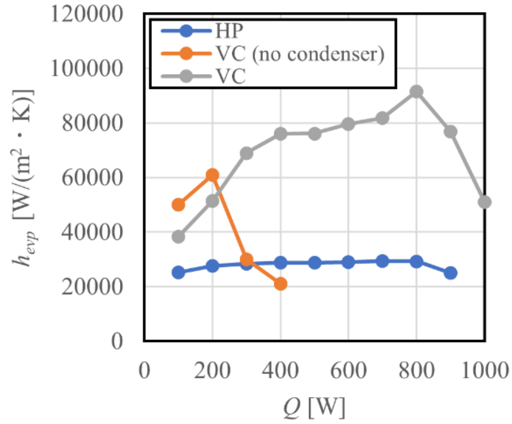

Figure 9. Evaporation heat transfer coefficient: h_{evp} .

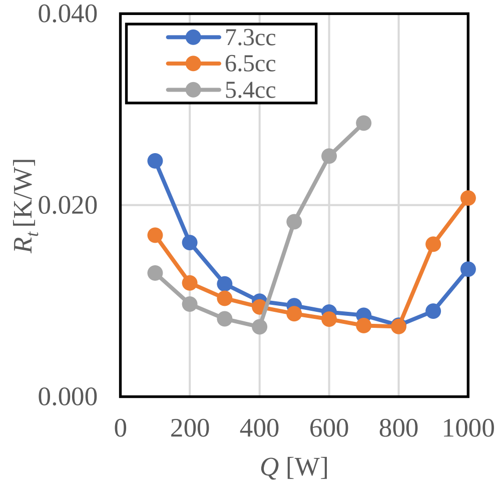

Figure 10. The amount of charging fluid dependence of thermal resistance

increasing power. It means water charging level is low level and the dryout limit of vapor chamber is 400W level. The dryout limit of sample with charging of 6.5cc and 7.3cc is 800W level but decreasing in h_{evp} of sample with 7.3cc is smaller than sample with charging 5.4cc. It show dryout condition is different due to high water charging and it is partial dryout condition. Any case of liquid charging level, peak of h_{evp} is same level. h_{con} have same property. When amount of charging fluid is increased, peak of h_{con} is shifted to high input power condition. It means tower type vapor chamber's performance and dryout limit is depended on charging water level.

7. Conclusion

Heat transfer property of tower type vapor chamber and heat pipe is evaluated and compare property of same size of tower type heat pipe. Thermal resistance of tower type vapor camber is 12% lower and dry out limit is around 14% higher than tower type heat pipe. Tower type vapor chamber's performance is depended on internal water flow path and amount of fluid charging. Especially heat transfer coefficient and dry out limit is affected. Internal flow path between condensation and evaporation area and high amount of fluid charging is necessary for high power heating solution.

References

[1] Thanh-Long Phan, Y. Saito and M. m ochizuki, "Integrated vapor chamber heat spreader for high power processors," 2014 International Conference on Electronics Packaging (ICEP), Toyama, Japan, 2014, pp. 424-428, doi: 10.1109/ICEP.2014.6826719.
[2] Weibel, Justin A., and Suresh V. Garimella. "Recent advances in vapor chamber transport characterization for high-heat-flux applications." Advances in Heat Transfer 45 (2013): 209-301.
[3] Shabgard, Hamidreza, et al. "Heat pipe heat exchangers and heat sinks: Opportunities, challenges, applications, analysis, and state of the art." International Journal of Heat and Mass Transfer 89 (2015): 138-158.

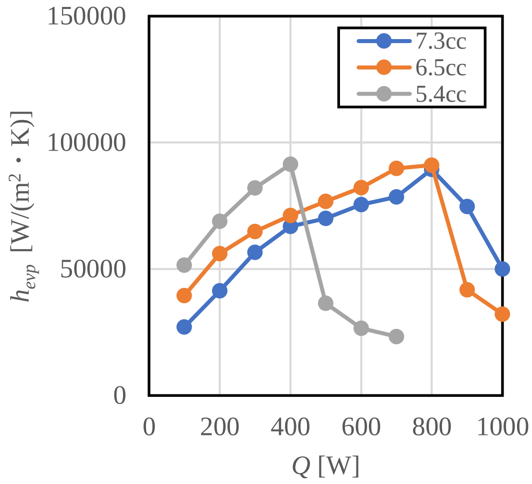

Figure 11. The amount of charging fluid dependence of h_{evp}

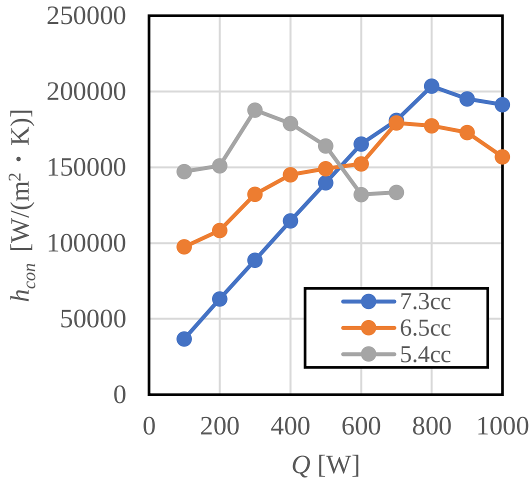

Figure 12. The amount of charging fluid dependence of h_{con}

Paper ID 012(S2B)

Visualization of vapor-liquid interface in vapor grooves of loop heat pipe

Xue Zhou[1,2], Lingji Hua[1], Nanxi Li[1], Zhenhua Jiang[1,2*], Yan Lu[1,2]

[1] *Shanghai Institute of Technical Physics, Chinese Academy of Sciences,Shanghai, PR China*
[2] *University of Chinese Academy of Sciences, Beijing, PR China*
**Corresponding author email address: jiangzhenhua@mail.sitp.ac.cn*

Abstract

Loop heat pipes (LHPs), utilizing the capillary force of the porous wick to circulate the working fluid internally, has been widely employed as an efficient thermal management device in both aerospace industries and household technologies. Thanks to the endeavors of the pioneering researches, various optimization methods, especially regarding to the pivotal component – evaporator with the wick inside, have been proposed to improve the heat transfer performance of LHPs. Despite these advances, there are still divergence on the optimal size of groove dimensions in the wick, presumably due to the common neglect on the influence imposed by the changing vapor-liquid interface. In this work, therefore, a three-dimensional numerical simulation model based on CFD method, as well as a visual experiment, is established to simultaneously observe the vapor-liquid distribution and the thermal efficiency of the LHPs in the vapor grooves. The experimental results and simulation have shown that there is thin-film evaporation in the vapor groove when the evaporator is applied with a low heat load. However, such liquid film will gradually attenuate or even retract into the solid wick when the heat load is above a threshold value. Particularly, the change in liquid film leads to the altering in the evaporator heat-transfer coefficient.

Keywords: Loop heat pipe; Visualization; Vapor-liquid distribution; Heat-transfer coefficient

1. Introduction

The loop heat pipe (LHP) is an efficient two-phase heat transfer device that utilizes the evaporation and condensation of the working fluid internally [1]. Different from the traditional heat pipe (HP), LHPs separate the liquid and vapor lines and leverage the porous wick in the evaporator to drive the circulation of the working fluid [2]. This special structure renders anti-gravity ability, long-distance, and high heat transfer capacity for LHPs, making them widely used for the payloads in satellites [3], battery thermal management [4], and electronic devices [5].

As a key component of LHP, the evaporator plays a pivotal role in both organizing evaporation and providing the driving force for the LHP system. Consequently, enhancing the heat transfer performance of the evaporator is a key strategy in optimizing the design of LHPs. The heat transfer capability of the evaporator can be characterized by an evaporative heat transfer coefficient. The evaporative heat transfer coefficient is considered to have a significant relationship with the liquid-vapor distribution in the vapor groove and the wick. Anand [6] pointed out that the thermal resistance from the evaporator wall to the liquid-vapor interface is a major factor affecting the evaporative heat transfer coefficient. Kissev [7] concluded that when the evaporator operates in the meniscus evaporation mode, an enhancement in both the evaporative heat transfer coefficient and the maximum heat flux can be achieved.

Nevertheless, the relationship between the liquid-vapor interface behaviors under different heat loads and the evaporator heat-transfer coefficient has not been verified by the combination of visualization and simulation. In this work, a visualization experiment on a LHP was conducted to observe the internal working fluid state in the vapor grooves from the radial circumferential surface of the evaporator. At the same time, a 3-D numerical simulation of the evaporator was established based on CFD methods, comprehensively considering the capillary force and phase change. The relationship between the liquid film thickness inside the vapor grooves and the evaporation heat transfer coefficient under varying heat loads was analyzed by the visualization experiment and the 3-D numerical simulation.

2. Experimental setup

2.1. LHP with visualized evaporator and experimental apparatus

The LHP used in the experiment is shown in Fig. 1 (a). It consists of a cylindrical evaporator containing a PTFE wick, a CC, a condenser, a vapor line, and a liquid line. The envelope of the evaporator is made of quartz glass to facilitate the visualization of the vapor-liquid interface in the wick grooves. Fig. 1 (b) presents a detailed view of the internal structure of the visualized evaporator and CC. Both the radial circumferential surfaces of the evaporator and CC, as well as their axial planes, are all fabricated with high-transparency quartz glass as the visualization windows. The various components are securely fastened and sealed using flanges and O-rings, ensuring tight connections between the evaporator and CC. A pressure test has demonstrated that this structure can withstand a pressure of 1.2 MPa. The loop heat pipe employs R245fa, an eco-friendly refrigerant, as its working fluid. Its saturation pressure ranges from 0.053 MPa to 1.006 MPa within the temperature span of 0 to 90°C, fulfilling the pressure-bearing capability of the visualized evaporator. The detailed structural parameters of the LHP are presented in Table 1.

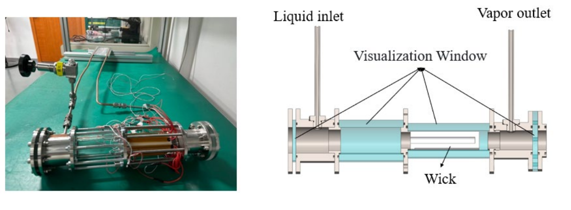

(a) LHP (b) Cross-sectional view of the visualized evaporator

Figure 1. The LHP and the visualized evaporator diagram

Table 1. Main geometric parameters of the LHP

Components	Parameters	Dimensions
Evaporator	ID/OD×L (mm)	22/40×95
CC	ID/OD×L (mm)	32/50×83
Wick	ID/OD×L (mm)	8/22×80
	Porosity	33%
Vapor grooves	W/H×L (mm)	1/1×80
	Quantity	12
Vapor line	ID/OD×L (mm)	4/6×740
Liquid line	ID/OD×L (mm)	4/6×570
Condenser	ID/OD×L (mm)	4/6×420

The schematic diagram of the experimental setup and the distribution of the temperature sensors are depicted in Fig. 2. During the experiment, the LHP is placed horizontally. Four-wire Pt1000 platinum resistance temperature sensors are assigned along the LHP to measure local temperature at crucial points along the LHP. Polyethylene film heaters are uniformly affixed to the circumferential wall of the evaporator covering an area of 72 cm^2 to provide various heat loads. It is worth mentioning that the polyethylene film heaters which are not transparent would block out the view of the evaporator wall. To facilitate clear observation of the vapor-liquid distribution within the axial vapor grooves of the evaporator, the polyethylene film heaters are only put on the outer surface of the evaporator corresponding to the locations of the wick fins. The condenser is thermally coupled to a water-cooled plate using a thermal pad and secured with C-clamps to minimize contact thermal resistance. Serving as a heat sink, the temperature of the water-cooled plate is regulated by the temperature control module of the water chiller, maintaining a constant sink temperature of 15 ± 0.1°C throughout the experiment. A high-speed camera operating at 1000 frames per second (fps) is utilized to record the vapor-liquid distribution in the vapor grooves.

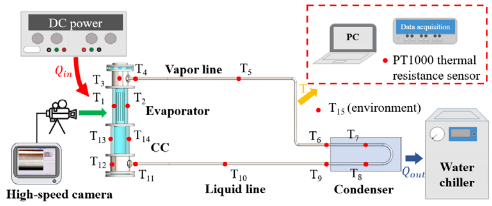

Figure 2. Experiment system & temperature sensor distribution

2.2. Data Processing and Uncertainty Analysis

The following steps are employed to visually record and extract liquid film thickness characteristic parameters in the vapor grooves:

(1) Adjust the focus of the high-speed camera so that it can clearly discern the vapor-liquid distribution features within the vapor grooves.

(2) Given the known groove width W_v, compare the number of pixels occupied by the channel width in the image (N_v), and convert this to determine the actual size represented by each pixel in the image.

(3) Process the captured images for grayscale and binarization, enhancing the visual distinction between the vapor and liquid phases.

(4) Utilize image processing software to measure the total number of pixels occupied by the liquid film (N_l), thereby the liquid film thickness (d_l) can be obtained by:

$$d_l = \frac{W_v}{Nv} \times N_l \tag{1}$$

The operating temperature T_e is utilized to assess the heat transfer performance of the LHP.

$$T_e = \frac{T_1 + T_2}{2} \tag{2}$$

The evaporator heat-transfer coefficient is a critical parameter for assessing the heat transfer performance of the LHP, which is defined as the evaporator heat-transfer coefficient between the inner wall of the evaporator shell and the vapor:

$$h_{evap} = \frac{Q_{apply}}{A_{apply}(T_w - T_v)} \tag{3}$$

$$Q_{apply} = IU \tag{4}$$

Where, T_w denotes the temperature of the evaporator's inner shell, and T_v signifies the temperature of the vapor. The temperature of the evaporator inner shell T_w is obtained by subtracting the temperature difference caused by heat conduction through the evaporator shell from the average surface temperature of the evaporator T_e:

$$T_w = T_e - \frac{Q_{apply} ln(D_o/D_i)}{2\pi\lambda L_e} \quad (5)$$

Where, D_o and D_i denote the outer and inner diameters of the evaporator wall respectively, λ signifies the thermal conductivity of the quartz glass, and L_e stands for the length of the evaporator.

In the experiment, the liquid film thickness, temperature, voltage, and current are directly measured parameters. After an appropriate focal length of the high-speed camera is determined, the real size of one pixel in the recorded image can be calculated, which is about 15.4 μm. The uncertainty of liquid film thickness measured is determined as one pixel at the direction vertical to the vapor grooves, corresponding to ± 15.4 μm. The uncertainty of the PT1000 platinum resistance temperature sensor with an accuracy is ± 0.15 K. The accuracy grades of both the ammeter and voltmeter are 0.5%. The heat load and thermal resistance are indirect measurement parameters, with their uncertainties primarily stemming from directly measured parameters such as temperature, resistance, and voltage. According to the standard uncertainty analysis [8], the uncertainty of heat load and evaporator heat-transfer coefficient are 5.31%, and 5.53%, respectively.

3. Numerical simulation model

Fig. 3 shows the schematic of the computational domain for the LHP evaporator. As shown in Fig. 3, the computational domain comprises wall, wick, and vapor groove. The vapor grooves are several rectangle grooves milled on the outer surface of the wick, whose width and height are presented as W_v and H_v. The region where the inner surface of the wick comes into contact with the evaporator wall is called as fin. The length of the fin in the cross section is described as W_{fin}. To reduce the computational burden, a half-domain model is adopted with symmetric boundary conditions along the axes of θ = 0 and θ = $\theta_v/2$, as depicted in Fig. 3 (b). A uniform heat load is applied to the outer wall of the evaporator. The influence of gravity is neglected in this work. Notably, the wick is assumed as homogeneous and isotropic porous material.

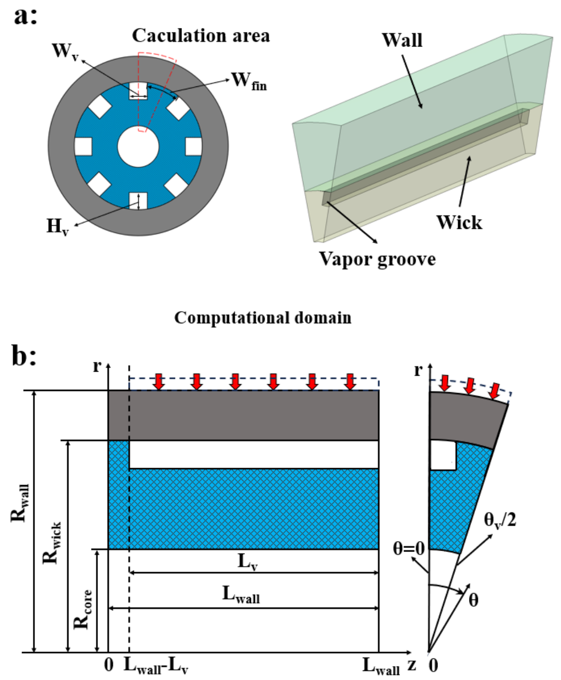

Figure 3. Computational domain & coordinate system

3.1. Governing equation

The Volume of Fluid (VOF) method, intended to track vapor-liquid interfaces, is commonly employed in computations involving multiphase flows with immiscible phases [9]. In the VOF model, the phase interface within each infinitesimal is implemented by means of the introduction of the volume fraction variable. The governing equations encompass the continuity equation, momentum equation, and energy equation.

Continuity equation:

$$\sum_i \alpha_i = 1 \quad (6)$$

$$\frac{\partial}{\partial t}(\varepsilon\alpha_p\rho_p) + \nabla\cdot(\varepsilon\alpha_p\rho_p\overrightarrow{u_p}) = S_p \quad (7)$$

Where, ρ, $\vec{u}$, and α respectively denote the density, velocity, the volume fraction of vapor or liquid. The state of the fluid is designated by the subscript p, containing the vapor phase or liquid phase. ε signifies porosity. In the zone of wick, ε is the porosity of the porous PTFE. In the other fluid zone, the value of ε is set at 1. The right term S_p is represents the mass source term, which is described in Section 3.2 in detail.

Momentum equation:

$$\frac{1}{\varepsilon}\left[\nabla\cdot\left(\frac{\rho_m}{\varepsilon}\overrightarrow{u_m u_m}\right)\right] = -\nabla P + \frac{1}{\varepsilon}\nabla\cdot\left[\mu_m\left(\nabla\overrightarrow{u_m} + \nabla\overrightarrow{u_m}^T\right)\right] + S_{cap} + S_r + \vec{F}_{CS} \quad (8)$$

Where, S_{cap} and S_r represent respectively the momentum source term contributed by the capillary force and the momentum source term accounting for flow resistance in the porous medium zone, which are detailed with their exact expressions further elaborated in Section 3.3 and Section 3.4. P in Eq. (8) denotes the pressure. The subscript m indicates the mixture phase of liquid and vapor. $\vec{F}_{CS}$ refers to the volumetric force caused by interfacial surface tension. This force can be computed using the Continuum Surface Force (CSF) model, which was proposed by Brackbill et al. [10].

$$\vec{F}_{CS} = \sigma \cdot \frac{\rho r_l \nabla \alpha_l}{\frac{1}{2}(\rho_l + \rho_v)} \quad (9)$$

Where, σ and r_l respectively denote the surface tension coefficient and the curvature of the liquid phase surface.

Energy equation:

$$\nabla \cdot \left(\varepsilon v \rho_m \overrightarrow{u_m} C_{p,m} T_m\right) = \varepsilon \nabla \cdot (\lambda_m \nabla T_m) + (1-\varepsilon)\nabla \cdot (\lambda_s \nabla T_m) + S_E \quad (10)$$

Where, the subscript s and S_E refer to the solid portion of the wick and the energy source term associated with phase change.

3.2. Phase-change model

The primary function of the phase-change model is to compute the phase-change mass source term S_p, which is then incorporated into the continuity equation to simulate the phase-change process. In this study, the Lee model [11] is employed, utilizing the saturation temperature T_{sat} as the criterion of condensation and evaporation, to accurately predict the occurrence of phase change.

$$S_p = \begin{cases} \dfrac{C_l \alpha_l \rho_l (T_m - T_{sat})}{T_{sat}}, & T \geq T_{sat} \\ \dfrac{C_v \alpha_v \rho_v (T_m - T_{sat})}{T_{sat}}, & T < T_{sat} \end{cases} \quad (11)$$

Where, C_l and C_v are mass transfer time parameters with unit s-1. According to the work of Wu et al. [12] and De Schepper et al. [13], Cl and Cv are set to 0.1. Particularly, both the numerical simulation and experimental observation are consistent with each other in the work of Wu et al. [12].

$$S_E = S_p h_{lv} \quad (12)$$

Where, h_{lv} represents the latent heat of vaporization of the fluid.

3.3. Porus media model

The wick within the evaporator constitutes a porous medium zone, with its pressure drop conforming to the Forchheimer equation [14]. As a result, the resistance source term within the porous medium can be captured by:

$$S_r = -\frac{\mu}{K}\vec{u} - C_2 \cdot \frac{1}{2}\rho|\vec{u}|\vec{u} \quad (13)$$

Where, μ is dynamic viscosity. C_2 is the Forchheimer factor (inertial force factor), which can be calculated by:

$$C_2 = \frac{3.5}{D_p} \cdot \frac{1-\varepsilon}{\varepsilon^3} \quad (14)$$

Where, D_p denotes the average particle diameter. Generally, the second term on the right of Eqn. (8) can be omitted due to the small mass flow rate in the LHP [15]. K is the permeability of the porous material, obtained by the Ergun equation [16]:

$$K = \frac{D_p^2}{150} \cdot \frac{\varepsilon^3}{(1-\varepsilon)^3} \quad (15)$$

3.4. Capillary force model

The capillary force formed at the evaporating meniscus drives the return of liquid from the central core back to the evaporation interface, playing a crucial role in the LHP cycle. However, since the solid skeleton that is physically present is not represented in the porous media model, the capillary force formed by the surface tension on the three-phase contact line between solid, liquid, and vapor cannot be calculated in the model. In the present work, capillary force is represented as a momentum source term added to the momentum equations, which is applied only at the vapor-liquid interface within the porous zone through the use of a User Defined Function (UDF). Although capillary force manifests as a volume force in the momentum equation, it is in essence surface forces acting perpendicular to the vapor-liquid interface. The capillary force is determined by the Young-Laplace equation as follows:

$$S_{cap} = \frac{2\sigma cos\phi}{R_{eff}} \nabla \alpha_v \quad (16)$$

Where, ϕ, R*eff*, and $\nabla\alpha_v$ represent the contact angle, the effective radius of the wick, the gradient of the vapor phase volume fraction, respectively. In the porous medium zone, $\nabla\alpha_v$ is always perpendicular to the vapor-liquid interface. Apparently, the magnitude of the capillary force varies with the gradient of the vapor volume fraction and the area of vapor-liquid interface caused by changes in heat loads.

3.5. Initial and boundary conditions

The heat transfer between the vapor groove, wick and wall is a mutually coupled process. The boundary conditions are represented as following.

At $r = R_{wick} + \delta_w$, for heated surface ($L_{wall} - L_v < z < L_{wall}$),

$$-\lambda \times \frac{\partial T}{\partial \vec{n}} = \frac{Q_{apply}}{A_{heat}} \quad (17)$$

At $r = R_{wick} + \delta_w$, for other surface ($z < L_{wall} - L_v$)

$$-\lambda \times \frac{\partial T}{\partial \vec{n}} = 0 \tag{18}$$

At $r = R_{core}$, for inlet surface ($0 < z < L_{wall}$), a velocity has been set as the inlet condition. The velocity is determined by the input heat load and the latent heat of vaporization of the fluid:

$$v = \frac{Q_{apply}}{2h_{lv}\rho_l \pi R_{core} L_{wall}} \tag{19}$$

At $z = 0$, for adiabatic surface ($R_{core} < r < R_{wall}$)

$$-\lambda \times \frac{\partial T}{\partial \vec{n}} = 0 \tag{20}$$

At $z= L_{wall}$, for outlet surface ($R_{core} < r < R_{wick}$), we set pressure as the outlet condition (the gauge pressure):

$$P_{out} = 0\ Pa \tag{21}$$

At $z= L_{wall}$, for other surface ($R_{wick} < r < R_{wall}$)

$$-\lambda \times \frac{\partial T}{\partial \vec{n}} = 0 \tag{22}$$

At $\theta = 0$ and $\theta = \theta_v/2$, symmetry boundaries ($0 < z < L_{wall}$) are set in this model.

The vapor-liquid distribution in the initial state of the evaporator is depicted in Fig. 4. In the legend, 0 denotes liquid and 1 represents vapor. As shown in Fig. 4, the vapor groove is filled with vapor, and the wick is flooded with liquid in the initial state of the evaporator.

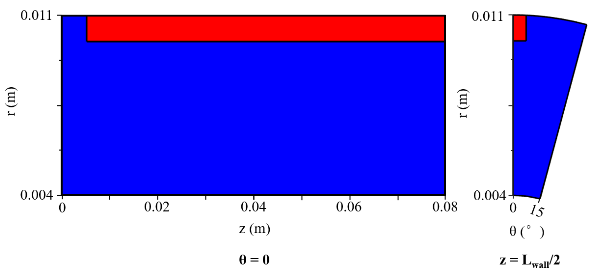

Figure 4. Initial vapor-liquid distribution of the evaporator

3.6. Mesh Independence Verification

The computational domain is divided into three zones: the wall as the solid zone, and the vapor groove and wick as the fluid zones. The overall domain is primarily discretized using hexahedral volume meshes, with coarser volume meshes employed for areas distant from the vapor groove in both the wall and wick zones, while mesh refinement is applied near the vapor groove and throughout the entire vapor groove zone. The total numbers of meshes resulting from this domain division are 100300, 123600, 155378, and 173148, with corresponding minimum mesh lengths of 0.09 mm, 0.08 mm, 0.07 mm, 0.06 mm, and 0.05 mm, respectively. Mesh independence verification calculations are performed for the average temperature of the evaporator outer wall at a heat load of 40 W using these four meshes, as depicted in Fig. 5. In consideration of the accuracy of the computational results, as well as the conservation of computational resources and time, the mesh with a minimum cell length of 0.07 mm is ultimately selected for the simulation calculations.

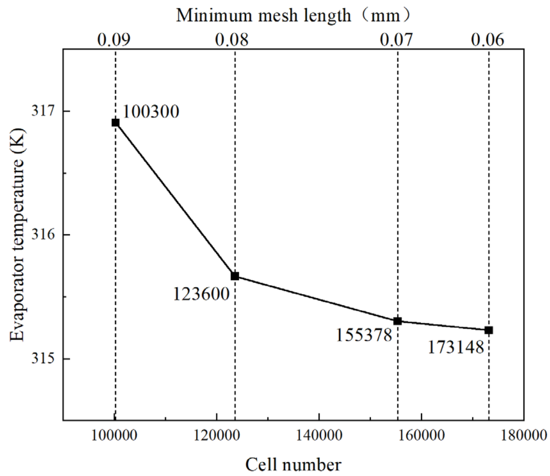

Figure 5. Mesh independence verification

4. Results and discussions

4.1. Experiment results

The temperature distribution along the LHP and vapor-liquid phase interface of the working fluid are experimentally observed under the heat load range from 5 W to 45 W. As shown in Fig. 6, under the heat load of 5 W, temperatures T1 and T2 gradually increased from ambient temperature to around 320 K. Concurrently, there were slight increases in the temperatures of the evaporator vapor chamber T3, evaporator outlet T4, and CC inlet T11, as well as the CC temperatures T12-T14. Conversely, the temperatures of the condenser T6-T9 remained virtually unchanged. The observed temperature rise can be attributed to heat leakage between the evaporator and CC and thermal conduction through the connecting lines. After 50 minutes, the evaporator outlet temperature T4 did not exhibit an appreciable tendency to increase, indicating no vapor output. Namely, the LHP failed to startup under the heat load of 5 W. Consequently, the LHP is considered to have failed to startup under a heat load of 5 W.

When increasing the heat load to 10 W, the evaporator temperature skyrocketed immediately rose, followed by a rapid decline after 175 seconds, indicative of the substantial generation of vapor in the evaporator and its subsequent escaping along the vapor line. As a result, the temperatures of the vapor line and condenser inlet also increased. After 190 seconds, the temperatures of the liquid line and CC inlet began to decrease. Such a decrease suggested that the vapor produced by the evaporator was driving the working fluid into the CC, initiating the circulation of the working fluid within the LHP successfully.

Successful LHP startup is thus confirmed. Following the successful startup, stepwise increases of the heat load from 10 W to 45 W are successively exerted on the LHP. As a response, the temperatures of the LHP evaporator consistently exhibited an initial rapid rise within 10 minutes and then followed by a gradual stabilization plateau. The LHP demonstrated response times within 10 minutes and is capable of maintaining steady-state temperatures for 30 minutes before each change in the heat load.

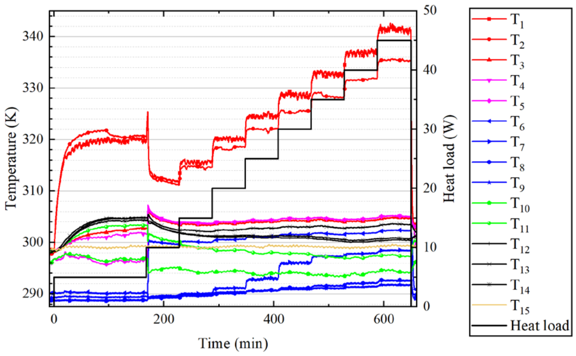

Figure 6. Temperature of the LHP in the experiment

Fig. 7 demonstrates the vapor-liquid distribution images in the vapor groove of the visualized LHP under the heat load range from 10 W to 45 W. As shown both in the visualized images, it is evident that a thin liquid film of approximately 0.169 mm thick covers resided on the outer surface of the wick within the vapor grooves when the heat load is 10 W. Due to the influence of gravity, the liquid film layer at the upper part of the vapor groove is significantly thinner than the lower part. Also notably, small bubbles sporadically emerge from the thin liquid film layer on the wick surface under the heat load of 10 W and 15 W, which means that nucleate boiling is dominant in this state [17]. As the heat load gradually increases, the thickness of the thin liquid film layer decreases, and it eventually disappears after the heat load reaches 35 W.

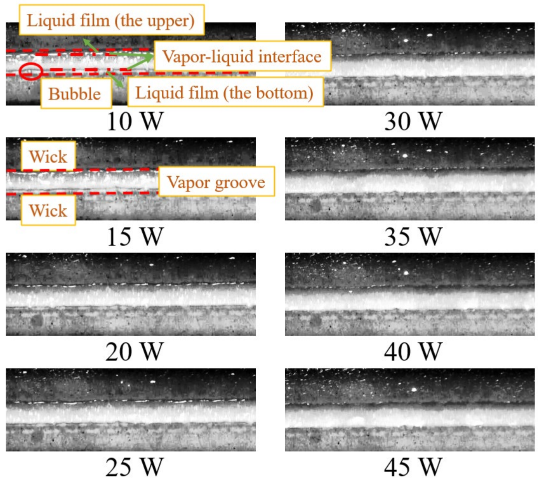

Figure 7 Vapor-liquid distribution diagrams in the vapor groove under varying heat loads

4.2. Model validation

Fig. 8 presents a comparison of model simulation results for the experimental and numerical data of the average wall temperature of the evaporator under various heat loads with the experimental data, which exhibited a monotonous increase against the heat load. A constant offset no larger than 2K is observed between the experiment and simulation. This offset is attributed to the neglect of the heat leakage through the evaporator wall to the CC and the surroundings in the simulation. Given the small thermal conductivity of the quartz glass composing the evaporator wall, heat loss to the environment via this wall constitutes a consistently significant proportion. Despite this small disparity, the numerical and experimental data exhibit strong consistency, indicating that the model possesses a certain degree of feasibility in predicting the operating conditions of the LHP evaporator.

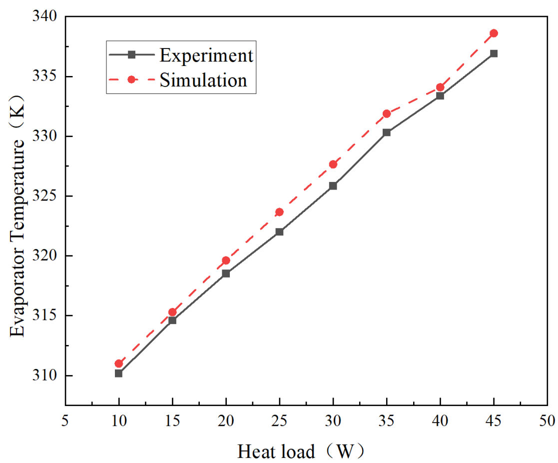

Figure 8 The comparison between the experimental and numerical data

To further validate the simulation method, the numerical picture of the vapor-liquid distribution in the evaporator at different heat load is also presented and compared with the visualization experiments in Fig. 9. It should be noted that when the heat load exceeds a threshold value, the vapor penetrates in to the wick and the vapor-liquid interface becomes experimentally invisible. The corresponding experimental data of the liquid layer thickness is therefore recorded as 0. Numerical simulation can be employed to trace the exact vapor-liquid interface inside the wick.

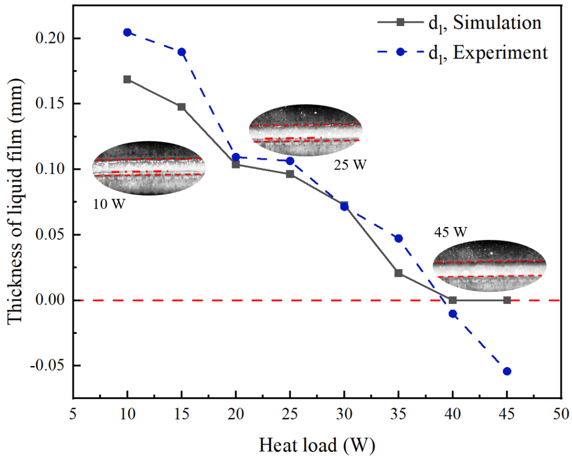

Figure 9 The comparison between the experimental and numerical data

4.3. Simulation results

Fig. 10 presents the temperature contour for the symmetry plane at $\theta = 0$ and $\theta = \theta_v/2$, as well as the axial cross-section at $z = L_w/2$, under a heat load of 15 W. In Fig. 10 (a) and (b), the wall temperature distribution is similar at both the symmetry planes $\theta = 0$ and $\theta = \theta_v/2$. The outer wall temperature gradually increases along the z-axis and eventually levels off, reaching a maximum of 315.46 K on the evaporator's outer surface. Along the radial direction, the temperature decreases from the outer surface inward. In the gap between the evaporator's inner surface and the wick, temperatures in the region with groove (z = 0.005 ~0.08 m) are slightly lower than those without groove between z = 0 ~ 0.005 m. Moreover, the temperature distribution of the wick below the vapor groove exhibits slight variations along the z-axis at both $\theta = 0$ and $\theta = \theta_v/2$, showing a good uniformity of the temperature along the z-axis. The temperature contour in Fig. 10 (c) further displays that the temperatures near the vapor groove interface are lower than those beneath the vapor groove. Additionally, a slightly lower temperature at the symmetry plane $\theta = 0$ with a vapor groove is observed when compared to the symmetry plane $\theta = \theta_v/2$ without a vapor groove. The temperature distribution pattern within the evaporator at other heat loads follows similar trends as those observed at 15 W, hence further elaboration is omitted.

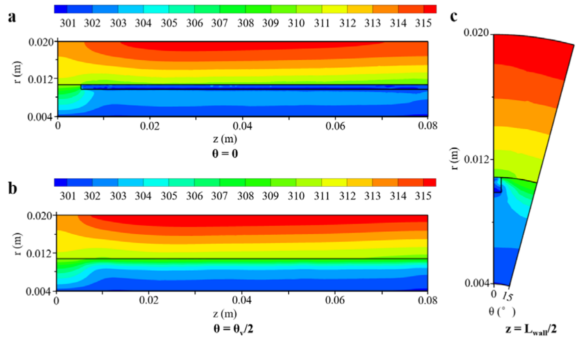

Figure 10 Temperature contour of the evaporator under 15 W

Fig. 11 presents the phase fraction contour and velocity vector in the z $=L_{wall}/2$ plane when the heat load is 15 W. The working fluid in the wick is entirely liquid, while the vapor-liquid interface exists in the vapor groove. A thin liquid film is present at the bottom of the vapor groove. The three-dimensional velocity vector in the vapor groove is shown in Fig. 11 (b). Due to the presence of the thin liquid film near the vapor groove interface, the velocity of the working fluid in this region is slightly lower than that at the center of the vapor groove. The two-dimensional velocity vector in the wick is depicted in Fig. 11 (c), indicating that the flow velocity of the working fluid inside the wick is significantly lower than that in the vapor groove. Fig. 12 displays the phase fraction contour in the evaporator for the symmetry plane at $\theta = 0$ under the heat load of 15 W. As shown, a uniform layer of thin liquid film extends along the z-axis in the vapor groove, with an average thickness of 0.19 mm.

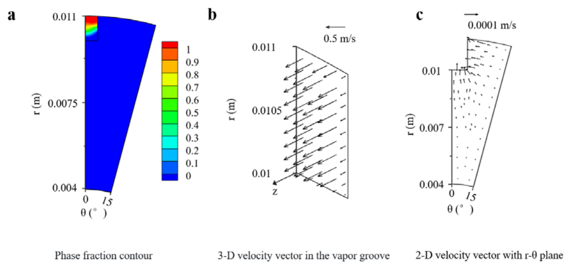

Figure 11 Temperature contour of the evaporator under 15 W

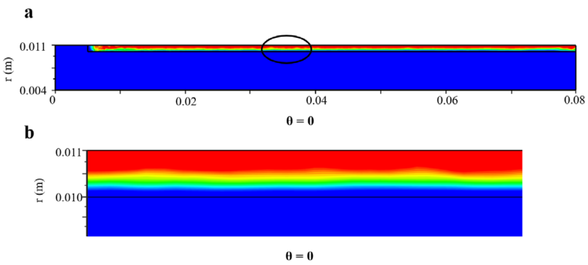

Figure 12 Phase fraction contour at θ = 0 under 15 W

When the heat load exceeds 40 W, its phase fraction distribution is significantly different compared to that at 15 W, as shown in Fig. 13. Under the heat load of 40 W, the vapor-liquid interface penetrates in to the wick, allowing an increased evaporation surface area and enhanced evaporation rate. The increased evaporation rate, in turn, raises the flow resistance of the liquid in the wick and decreases the replenishment rate from the CC. The combined effect of these two factors—the increased evaporation rate and the reduced replenishment rate—causes the vapor-liquid interface to penetrate even deeper into the wick.

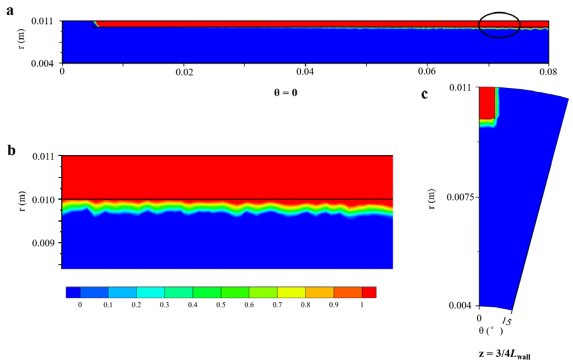

Figure 13 Phase fraction contour in the evaporator under 40 W

4.4. The effect of vapor-liquid distribution on the evaporator heat-transfer coefficient

The evaporator heat-transfer coefficient is a key parameter to assess the heat transfer performance of the evaporator. The numerical calculation results for the evaporator heat-transfer coefficient, along with experimental data are depicted in Fig. 14. It is clear that there is a common tendency in both simulation and experiment results that the evaporator heat-transfer coefficient experiences a rapid increase, a short plateau, and a sharp decline with the increasing heat load. The reason behind this can be explained by the observation of vapor-liquid interface mentioned above. The vapor-liquid interface is formed at the boundary between the evaporator wall, wick and vapor groove under a lower heat load. It is characterized by liquid film thickness in this paper. By connecting Fig. 9 and Fig. 14, it is considered that there are two modes for the relationship between the vapor-liquid interface behavior and evaporator heat-transfer coefficient: Fig. 15 and Fig. 16 show images of these:

(a) Lower heat load

As depicted in Fig. 16 (a), the evaporation occurs at the vapor-liquid interface which forms at the surface of the liquid film in the vapor grooves. From the schematic diagram of thermal resistance in Fig. 16 (b), there are some constant thermal resistances caused by the thermal properties of materials and fluids, as well as the structure. They are the thermal conduction resistance of wall R_{wall}, the thermal convection resistance between vapor groove and the inner surface of wall $R_{e,in-v}$, the thermal resistance from wall to the interface of the vapor grooves R_{hc}, the thermal resistance for heating the liquid working fluid replenished from the CC R_{wick}. In this mode, the vapor-liquid interface retreats towards the boundary of vapor groove with the increasing of heat loads, which characterized by the thinning of liquid film. The thermal conduction resistance of liquid film (R_{int-lv}) and interfacial evaporative thermal resistance R_{l-v} due to the movement of the vapor-liquid interface are the main reason for the increasing of evaporator heat-transfer coefficient. The thermal resistances in the liquid film can be written as follows when they are assumed as one-dimensional in the normal direction of the vapor-liquid interface [18].

$$R_{int-lv} + R_{l-v} = A^{-1}\left(\frac{\lambda_l}{d_l}\right)$$

$$+A^{-1}\left\{\frac{2\gamma}{2-\gamma}\left(\frac{h_{lv}^2\rho_v}{T_{lv}}\right)\left(\frac{1}{2\pi R_g T_{lv}}\right)^{0.5}\right\}^{-1} \quad (23)$$

Where, γ is the evaporative accommodation coefficient, R_g is the gas constant. As the heat load increases, the liquid film thickness within the vapor groove is observed to decrease, leading to the decrease of the R_{int-lv} and R_{l-v} and the increase of the evaporator heat-transfer coefficient.

(b) Higher heat load

As shown as Fig. 16 (a), the liquid film in vapor groove disappears and the vapor penetrates into the wick region, leading to the vapor-liquid interface recede into the wick once the heat load exceeds a threshold value. A different transfer mechanism exists in the wick and vapor grooves as depicted in Fig. 16 (b). A vapor blanket is formed in the vicinity of vapor groove and the contact surface between the wall and wick. The thermal resistance from wall to the interface of the vapor grooves R_{hc} becomes dominant. With further increase in heat load, the vapor-liquid interface extends deeper into the wick, augmenting the rapid decline of the evaporator heat transfer coefficient.

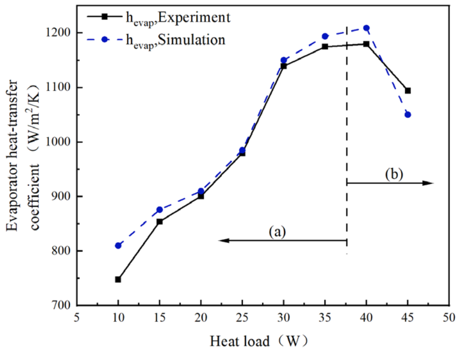

Figure 14 Evaporator heat-transfer coefficient in simulation and experiment

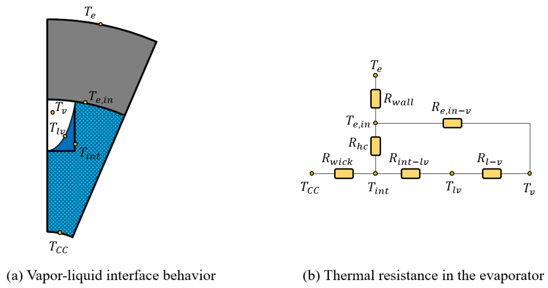

Figure 15 Schematic diagram of vapor-liquid interface behavior and thermal resistance in the evaporator when liquid film in the vapor groove

Other research of LHP evaporator have investigated the similar phenomena. Nishikawara et al. [19] manufactured a cylindrical evaporator sealed with a glass window and observed a transition from a liquid-saturated state to a two-phase state of the wick. Anand et al. [20] performed an experiment of a flat evaporator with a visualized CC and found the formation of bubble in the CC when the capillary limit is reached. They explained it as the movement or recession of the vapor-liquid interface in the wick. Liao et al. [21] carried out a visual study on the phase change behaviors in a vertical two-dimensional porous structure. The results illustrated that a high frequency cyclic process of the bubble growth-collapse and liquid replenishment behaviors virtually led to a vapor-liquid co-existing zone under a lower and moderate heat load. And a stable vapor film formed with a further increase of heat load. Such observation explained that the heat transfer coefficient increased with the increase of heat flux until a peak value occurred. What they have in common is that the vapor blanket is formed in the wick as the heat load increases in the visualized observation. This phenomenon explains why the evaporator heat-transfer coefficient increases first, then reaches its peak, and drops afterwards, when combined with the experimental observation and simulation on the vapor–liquid distribution in the condenser in this work. The thermal resistance in the liquid film becomes dominant under a lower heat load, while the thermal resistance between wall to the evaporation interface plays an essential role in deteriorating the evaporator performance.

5. Conclusions

In this work, a three-dimensional numerical model based on CFD method is established to predict the temperature and vapor-liquid distribution in the evaporator. The applicability of this simulation model is validated by visualized experiments and the relationship between the vapor-liquid distribution and the heat transfer characteristics is summarized: At lower heat loads, a thin liquid film is present inside the vapor groove, upon which evaporation takes place. The evaporator heat-transfer coefficient exhibits a close relationship with the vapor-liquid distribution (characterized by liquid film thickness) in the vapor grooves. As the heat load increases, the thickness of this liquid film gradually decreases, correspondingly causing the evaporator heat-transfer coefficient to increase. The film is progressively attenuated until the vapor-liquid interface retreats into the interior of the wick. At this point, the evaporator heat-transfer coefficient reaches a peak and then rapidly declines.

ACKNOWLEDGEMENTS

This project is supported by National Key Research and Development Program of China – Civil Space Technology Advance Research Project under Grant D010202.

References

[1] Maydanik YF: Loop heat pipes. Applied Thermal Engineering 2005, 25(5-6):635-657.

[2] Ku J: Operating Characteristics of Loop Heat Pipes. In.: SAE International 1999.
Applied Catalysis A: General, 2001. 207(1): p. 355.

[3] Swanson TD, Birur GC: NASA thermal control technologies for robotic spacecraft. Applied Thermal Engineering 2003, 23(9):1055-1065.

[4] Hashimoto M, Akizuki Y, Sato K, Ueno A, Nagano H: Proposal, transient model, and experimental verification of loop heat pipe as heating device for electric-vehicle batteries. Applied Thermal Engineering 2022, 211.
[5] Zhou D, Chen Y, Gao W, Xin G: A novel thermal management scheme of 3D-IC based on loop heat pipe. International Journal of Thermal Sciences 2024, 199.
[6] Anand, A.R.; Ambirajan, A.; Dutta, P. Investigations on vapor blanket formation inside capillary wick of loop heat pipe. International Journal of Heat and Mass Transfer. 2020, 156, 119685.
[7] Kissev VM, Vlassov VV, Muraoka I. Experimental optimization of capillary structures for loop heat pipes and heat switches [J]. Applied Thermal Engineering. 2010, 30(11-12): 1312-1319.
[8] Moffat RJ: Describing the uncertainties in experimental results. Experimental Thermal and Fluid Science 1988, 1(1):3-17.
[9] Hirt CW, Nichols BD: Volume of fluid (VOF) method for the dynamics of free boundaries. Journal of Computational Physics 1981, 39(1):201-225.
[10] Brackbill JU, Kothe DB, Zemach C: A continuum method for modeling surface tension. Journal of Computational Physics 1992, 100(2):335-354.
[11] Lee WHJMtf, reactor safety, applications: A pressure iteration scheme for two-phase flow modeling. 1980, 1:407-431.
[12] Wu HL, Peng XF, Ye P, Eric Gong Y: Simulation of refrigerant flow boiling in serpentine tubes. International Journal of Heat and Mass Transfer 2007, 50(5-6):1186-1195.
[13] De Schepper SCK, Heynderickx GJ, Marin GB: Modeling the evaporation of a hydrocarbon feedstock in the convection section of a steam cracker. Computers & Chemical Engineering 2009, 33(1):122-132.
[14] Joseph DD, Nield DA, Papanicolaou G: NON-LINEAR EQUATION GOVERNING FLOW IN A SATURATED POROUS-MEDIUM. Water Resources Research 1982, 18(4):1049-1052.
[15] Shao B, Jiang Z, Xu G, Liu L, Li N, Dong D: Numerical and experimental study on the vapor-liquid distribution of loop heat pipe with varying density of working fluid. Applied Thermal Engineering 2023, 226.
[16] Ergun S, Orning AA: FLUID FLOW THROUGH RANDOMLY PACKED COLUMNS AND FLUIDIZED BEDS. Industrial and Engineering Chemistry 1949, 41(6):1179-1184.
[17] Odagiri K, Nishikawara M, Nagano H: Microscale infrared observation of liquid–vapor interface behavior on the surface of porous media for loop heat pipes. Applied Thermal Engineering 2017, 126:1083-1090.
[18] Schrage RW: A theoretical study of interphase mass transfer: Columbia University Press; 1953.
[19] Nishikawara M, Tomita S, Yokoyama H, Yanada H: Relationship between phase distribution and heat-transfer coefficient of loop heat pipe evaporator investigated by lateral observation of porous media. Applied Thermal Engineering 2024, 236.
[20] Anand AR, Jaiswal A, Ambirajan A, Dutta P: Experimental studies on a miniature loop heat pipe with flat evaporator with various working fluids. Applied Thermal Engineering 2018, 144:495-503.
[21] Liao Q, Zhao TJIJoH, Transfer M: A visual study of phase-change heat transfer in a two-dimensional porous structure with a partial heating boundary. 2000, 43(7):1089-1102.

Paper ID 013(S2C)

Temperature Uniformity Characteristics of a Sodium Heat Pipe-Based Isothermal Heat Pipe Liner

Eunsueng An[1], Kyungsoo Park[2], Pyungsoon Kim[2], Wukchul Joung[1, 3*]

[1] *Department of Intelligent Robot Engineering, Pukyong National University, Busan, Republic of Korea*
[2] *Green Energy Materials Research Team, Hyundai Motor Group, Uiwang, Republic of Korea*
[3] *Department of Mechanical Engineering, Pukyong National University, Busan, Republic of Korea*
**Corresponding author email address: wukchuljoung@pknu.ac.kr*

Abstract

In this work, a heat pipe-based isothermal furnace liner (HPL), employing sodium (Na) as a working fluid, was fabricated to enhance temperature uniformity of a high-temperature furnace. The HPL was constructed with two concentric stainless-steel (316 L) tubes to have external dimensions of approximately 101.6 mm × 70 mm × 410 mm (outer diameter × inner diameter × length). The HPL possessed two 1 mm thick wicks on the internal surfaces of the HPL; the wicks were directly sintered on the internal surfaces of the inner and outer tubes with approximately 100 µm diameter stainless-steel (316 L) powder. Approximately 175 g of 99.8 % pure Na was injected into the evacuated HPL, which corresponded to approximately 170 % of the void volume of the wick. The temperature uniformity of the HPL, which was defined as the maximum temperature change over a 200 mm distance from the bottom of the working space, was tested at diverse temperatures in the range from 800 K (530 °C) to 1100 K (830 °C). Test results showed that the temperature uniformity of the HPL was improved with increasing temperature, attaining 0.63 K ± 0.31 K (approximately 95 % level of confidence) at 1100 K.

Keywords: High-temperature heat pipe liner; Sodium; Sintered wick; Isothermal furnace liner, Temperature uniformity

1. Introduction

Realisation of a uniform temperature field at elevated temperatures is essential in numerous high-value industries and precision thermometry [1-5]. Representative applications include semiconductor manufacturing processes [1], reactors in chemical plants [2], hydrogen production facilities [3], and precision furnaces for thermometer calibration and realisation of the reference temperatures (i.e., the fixed points of the International Temperature Scale of 1990) [4, 5]. Conventionally, multi-zone furnaces have been widely used to realise a working space of a high degree of temperature uniformity. However, due to the increased heat loss at elevated temperatures and finite thermal conductivity of diffusion-based furnace liners, a temperature inhomogeneity of several tens of kelvins is considered inevitable at temperatures above the aluminium freezing temperature (i.e., 660.323 °C) [5, 6]. In this circumstance, a highly conductive isothermal furnace liner, such as an isothermal furnace liner made of an annular heat pipe (hereafter the heat pipe liner, HPL), has been extensively employed to improve the temperature uniformity of the heated space of the conventional high-temperature furnaces [2, 3, 5]. Figure 1 shows the schematic of the HPL having an annular cross section.

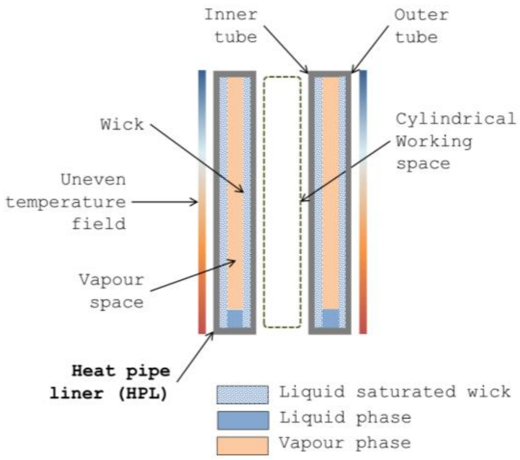

Figure 1. Schematic diagram of the annular HPL.

Heat pipes are undisputedly the most effective two-phase passive heat transfer devices which utilise saturation pressure difference between the heated section (evaporator) and cooled section (condenser) for vapour flow from the evaporator to the condenser and the capillary pressure difference across the evaporating meniscuses of the wick in the evaporator for the liquid return from the condenser to the evaporator, respectively [7]. As shown in Fig. 1, the HPL realises a cylindrical working space of enhanced temperature uniformity due to the internal circulation and continuous evaporation and condensation of the working fluid. Due to their excellent isothermalisation characteristics, heat pipes have extensively been used for temperature homogenisation of the conventional furnaces in a form of the annular heat pipe (i.e., the HPL) [8-12]. In particular, due to the unsatisfactory temperature uniformity of the conventional furnaces at elevated temperatures, the HPLs are finding their niches for high-temperature furnaces in precision thermometry [5, 11, 12].

High-temperature HPLs are characterised by their working fluids, which are predominantly alkali metals such as potassium (K) and sodium (Na) due to their proper saturated vapour pressure characteristics at high temperatures [5, 10-15]. The traditional high-temperature HPLs were generally fabricated with grooves or meshes as the wick structure for ease of the machining and accessibility, respectively [5, 13, 14, 16]. However, the low available capillarity of the groove wick and the difficulties in the firm attachment of the mesh wick to the HPL wall have rendered the HPLs with grooves or meshes unsatisfactory in terms of the temperature uniformity and the manufacturability [7, 17]. In this circumstance, a sintered wick, which has widely been used for mass production of commercial room-temperature heat pipes, can possibly be used as the wick of the high-temperature HPL due to their high capillarity and superior manufacturability.

In this work, a stainless-steel HPL, employing sodium (Na) as a working fluid (Na HPL), was fabricated for use at elevated temperatures. In particular, two porous layers were directly sintered on the inner surfaces of the HPL to form a sintered porous wick on each of the inner and outer tubes of the HPL. The temperature uniformity characteristics of the fabricated Na HPL were systematically investigated at different temperatures in the range from 800 K (530 °C) to 1100 K (830 °C) to examine the effect of the operating temperature on the temperature uniformity of the Na HPL.

2. Sodium heat pipe liner

Figure 2 shows the dimensions and section view of the fabricated HPL. The HPL had external dimensions of 101.6 mm × 70 mm × 410 mm (outer diameter × inner diameter × length); two concentric inner and outer tubes of approximately 3 mm thickness comprised the main body of the HPL with 5 mm thick bottom and lid plates. For enhanced temperature uniformity of the cylindrical working

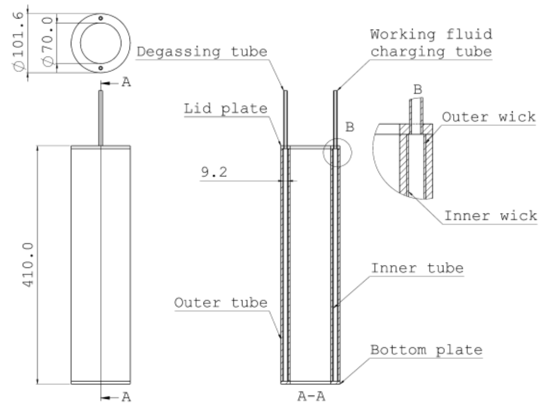

Figure 2. External-dimensions and section view of the tested HPL (dimensions in mm).

space formed by the HPL, the wick was sintered on the internal surfaces of both the inner and outer tubes; the outer wick on the outer tube was expected to absorb external thermal disturbances, and the inner wick on the inner tube was employed to further uniformise the temperature field of the cylindrical working space [18]. For the wick of the HPL, stainless steel (316 L) powder of approximately 100 μm diameter was directly sintered on the inner surface of the outer tube (the outer wick) and the outer surface of the inner tube (the inner wick) at a thickness of approximately 1 mm. Two 6.4 mm (1/4 inch) diameter tubes were attached to the upper lid of the HPL; one was used for injection of the working fluid into the HPL, and the other was used to evacuate or degas the HPL; after completion of the working fluid injection and degassing of the HPL, the two tubes were pinched off from the HPL and welded for hermetic sealing.

Figure 3 shows the schematic of the working fluid injection apparatus used for fabrication of the Na HPL. 99.8 % pure sodium was used as the working

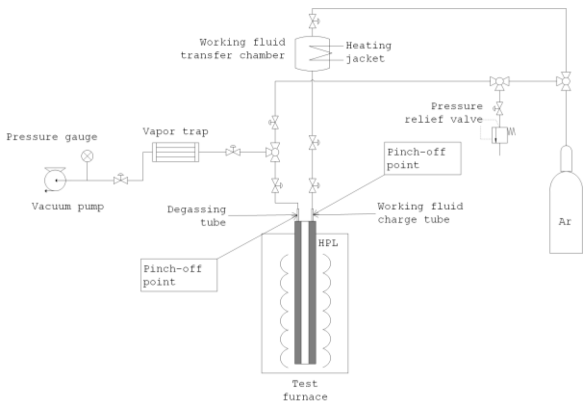

Figure 3. Schematic of the working fluid injection apparatus.

fluid of the HPL for use at high temperatures. The HPL was filled with approximately 175 g of Na, which corresponded to approximately 170 % of the wick void volume. Due to the reactive nature in the air and higher melting temperature than the room temperature (i.e., approximately 98 °C) of sodium, a predetermined mass of sodium was first injected into a sealed transfer chamber in an inert atmosphere, and then the molten sodium in a heated transfer chamber was guided to flow into an evacuated HPL, which was maintained at a temperature above the melting temperature of sodium; when the working fluid was injected into the HPL, the working fluid injection tube was pinched off and welded.

After the working fluid injection, the HPL was degassed by heating the HPL to an elevated temperature with the degassing tube closed and then by evacuating the HPL at room temperature. The degassing of the HPL was repeated until the pressure indicated by the vacuum gauge did not change with successive repetition of the degassing process. When the degassing was finished, the degassing tube was also pinched off and welded, completing the fabrication of the Na HPL.

3. Test setup and method

In this work, to test the temperature uniformity characteristics of the HPL, immersion temperature profiles of the working space of the HPL (i.e., axial distributions of temperature changes from bottom of the working space to a certain height) were measured. In particular, to investigate the effect of the operating temperature on the immersion characteristics of the HPL, the axial temperature profiles were measured at temperatures in the range from 800 K (530 °C) to 1100 K (830 °C) with an increment of 100 K. The lower limit of the temperature range was determined based on the wetting characteristics of sodium on a stainless-steel surface and the continuum start-up temperature of sodium heat pipe, both of which require to use a sodium heat pipe at a temperature above approximately 500 °C (770 K) [19, 20]; the upper limit was set by the maximum service temperature of 316 stainless steel, which was approximately 870 °C (1140 K) [21].

To perform the immersion temperature profile test, the HPL was located in a single-zone furnace, which had a heated zone measuring approximately 150 mm × 600 mm (diameter × length). In addition, to accurately measure the axial temperature distribution of the working space, a cylindrical alumina (Al_2O_3) block, having dimensions of 65 mm × 12 mm × 350 mm (outer diameter × inner diameter × length), was place in the working space

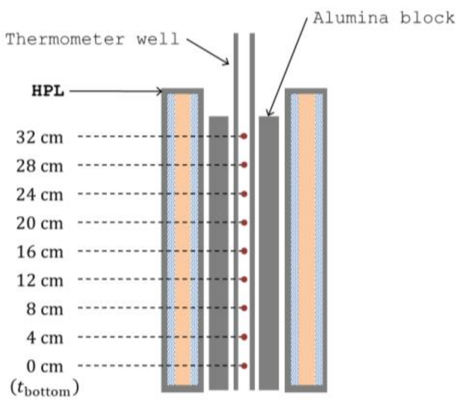

Figure 4. Locations of the temperature measurements along the centre axis of the working space.

of the HPL; at the centre of the alumina block, an alumina thermometer well with dimensions of 10 mm × 6 mm × 500 mm (outer diameter × inner diameter × length) was inserted into the alumina block to allow a thermometer to scan the axial temperature distribution. The remnant of the working space was filled with a ceramic wool insulator to reduce unnecessary heat loss.

The immersion characteristics of the working space was assessed by measuring temperature changes along the thermometer well from the bottom of the working space, and this was carried out by pulling out a thermometer located in the thermometer well from the bottom. Figure 4 shows the measurement locations of the temperature distributions along the central axis of the working space. As shown in the figure, the height of the thermometer, at which temperatures were measured, was increased from 0 cm (i.e., the bottom) to 32 cm with an increment of 4 cm. Together with the assessment of the immersion characteristics of the Na HPL, immersion temperature profiles of an empty HPL, which was not injected with the working fluid but filled with argon (Ar) at an atmospheric pressure, were also measured for comparison purpose.

Type N thermocouple with an Inconel sheath of 5 mm diameter and 610 mm length was used to measure the axial temperature distribution with a precision potentiometer, and their stated accuracies were approximately 0.8 % of reading and ±0.12 °C, respectively. The temperature uniformity of the working space was characterised by temperature deviations from the bottom of the working space (i.e., temperature differences). In this circumstance, using the same (i.e., single) thermometer and potentiometer, due to the correlations of the measurand, the systematic uncertainty components (e.g., uncertainties due to calibration, potentiometer, etc.) were eliminated, and repeatability was the only influencing uncertainty factor, thus enabling precise measurements of the temperature difference [22]. The measurement of the immersion profile was repeated three times to estimates the repeatability at an approximately 95 % level of confidence.

4. Test results

The temperature uniformity of the working space of the Na HPL was characterised by the temperature distribution along the central axis of the working space (i.e., the immersion temperature profile), and to demonstrate the effectiveness of the Na HPL as an isothermal furnace liner, comparisons of the immersion profiles between the Na HPL and the empty HPL were carried out. The immersion temperature profiles measured with the empty HPL and the Na HPL are provided in Figures 5 (a) and (b), respectively. As shown in Figure 5 (a), at all the tested temperatures, the immersion temperature profiles of the empty HPL revealed monotonic decrease in temperature with increasing distance from the bottom of the working space, reproducing the non-uniform temperature field outside the HPL. At 1100 K, the temperature depression, measured with the empty HPL over 20 cm from the bottom, was 11.2 K ± 0.3 K (at approximately 95 % level of confidence).

On the other hand, as shown in Figure 5 (b), the immersion profiles of the Na HPL demonstrated apparent improvement in the temperature uniformity at elevated temperatures (e.g., at 1000 K and 1100 K). At temperatures less than 1000 K, the Na HPL produced immersion profiles similar to the temperature profiles of the empty HPL, but at temperatures above 1000 K, the temperature uniformity of the working space was greatly improved with increasing temperature. For example, at 1100 K, the maximum temperature change of the working space of the Na HPL over 20 cm from the bottom was 0.63 K ± 0.31 K (at approximately 95 % level of confidence), manifesting itself as a clear indication of the effectiveness of the Na HPL as an isothermal furnace liner.

The outstanding enhancement in the temperature uniformity of the Na HPL at elevated temperatures were attributed to the formation of the dual liquid–vapor phase interfaces on the inner and outer wicks and the internal convection of the working fluids inside the HPL [18]; the outer phase interface on the outer wick absorbed thermal disturbances from the external thermal environment outside the HPL (i.e., the heated zone of the single-zone furnace), thus allowing the inner phase interface on the inner wick to have a more stable and uniform temperature field. In particular, as the isothermal characteristics of the Na HPL was further enhanced at 1100 K than the case at 1000 K (e.g., 0.63 K ± 0.31 K versus 7.5 K ± 1.9 K), the optimum operating temperature of the Na HPL was expected to be above 1100 K (830 °C), necessitating tests of the Na HPL, made of more effective heat-resistant materials (e.g., Inconel), at temperatures above 1100 K. At lower temperatures than 1000 K, due to the insufficient saturated vapour pressure inside the HPL, the internal vapour flow was supposed to be ineffective, resulting in the poor temperature homogenisation characteristics at 800 K and 900 K. Overall, the Na HPL, employing the sintered dual wicks on its internal surfaces, demonstrated its potential as an isothermal furnace liner at temperatures above 1100 K.

(a)
(b)
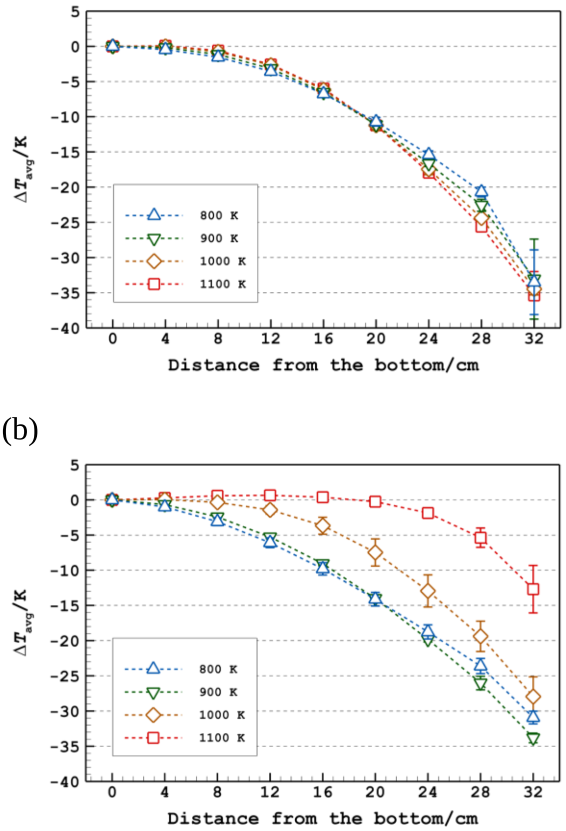

Figure 5. Immersion temperature profiles of the working spaces formed by (a) the empty HPL and (b) the Na HPL. The error bars indicate the expanded measurement uncertainties at approximately 95 % level of confidence.

5. Conclusions

In this work, a stainless-steel HPL, employing sodium as a working fluid, was fabricated to homogenise the uneven temperature field of the conventional high-temperature furnace. The HPL was constructed with two concentric tubes to have an annular cross section and had outer dimensions of 101.6 mm × 70 mm × 410 mm (outer diameter × inner diameter × length), thus forming a cylindrical working space inside the HPL. Dual stainless-steel sintered porous wicks of approximately 1 mm thickness were directly sintered on the internal surfaces of the concentric tubes to generate the dual liquid-vapour phase interfaces on both of the outer and inner wicks, thus to further uniformise the temperature field of the working space formed by the HPL. 99.8 % pure sodium was injected into the HPL (i.e., the Na HPL), which corresponded to approximately 170 % of the void volume of the wick, for use at elevated temperatures.

The temperature uniformity characteristics of the Na HPL was assessed by measuring the immersion temperature profiles along the central axis of the working space at diverse temperatures from 800 K to 1100 K. Test results showed that effective temperature homogenization of the working space was attained with the Na HPL with the dual sintered wick structure, and at 1100 K, a maximum temperature change of approximately 0.63 K was measured over 20 cm distance from the bottom of the working space, demonstrating the effectiveness of the Na HPL as an isothermal liner for high-temperature furnaces.

6. ACKNOWLEDGEMENTS

This work was supported by the National Research Foundation (NRF), South Korea, under project BK21 FOUR (Smart Robot Convergence and Application Education Research Centre).

References

[1] A. Su, J. Jeng, H. Huang, C. Yu, S. Hung, C. Chao, Control relevant issues in semiconductor manufacturing: Overview with some new results, Control Eng. Practice, 2007. 15: p. 1268.
[2] D. Reay, A. Harvey, The role of heat pipes in intensified unit operations, Appl. Therm. Eng., 2013, 57: p. 147.
[3] S. Wong, H. Hsiao, K. Lo, Improving temperature uniformity of CO preferential oxidation for hydrogen-rich reformate with a heat pipe, Int. J. Hydrog. Energy, 2014. 39: p. 6492.
[4] K. D. Hill, D. J. Woods, Characterizing the NRC Blackbody Sources for Radiation Thermometry from 150 °C to 962 °C, Int. J. Thermophys., 2009. 30: p. 105.
[5] A. Merlone, et al., Gas-controlled heat pipes in metrology: More than 30 years of technical and scientific progresses, Measurement, 2020. 164: 108103.
[6] D. I. Head, J. Gray, M. de Podesta, Current Work on Furnaces and Data Analysis to Improve the Uniformity and Noise Levels for Metal Fixed Points, Int. J. Thermophys., 2009. 30: p. 296.
[7] D. A. Reay, P. A. Kew, R. J. McGlen, Heat Pipes: Theory, Design and Applications, 6th Ed. (Butterworth-Heinemann, Amsterdam, 2014).
[8] X. K. Yan, Y. N. Duan, W. Wang, J. Li, J. H. Yang, Thermal Characteristics of a Sealed Glass-Water Heat Pipe from 0 °C to 60 °C, Int. J. Thermophys., 2011. 32: p. 224.
[9] J. Choi, Y. Yuian, D. Boca-Tascius, H. Kang, Design, construction, and performance testing of an isothermal naphthalene heat pipe furnace, Rev. Sci. Instrum., 2014. 85: 095105.
[10] H. Zhang, F. Ye, H. Guo, X. Yan, Effects of Heating Temperature on the Isothermal Performance of a Potassium Concentric Annular Heat Pipe, Energies, 2022. 15: 2367.
[11] K. S. Gam, A stable microcomputer-controlled heat pipe furnace and test of new noble metal thermocouples, Measurements, 1996. 18: p. 101.
[12] X. K. Yan, Y. N. Duan, C. F. Ma, Z. F. Lv, Construction of Sodium Heat-Pipe Furnaces and the Isothermal Characteristics of the Furnaces, Int. J. Thermophys., 2011, 32: p. 494.
[13] C. Wang, et al., Experimental study on heat transfer limit of high temperature potassium heat pipe for advanced reactors, Ann. Nucl. Energy, 2021. 151: 107935.
[14] Y. Ma, et al., Experimental study on sodium Screen-Wick heat pipe capillary limit, Appl. Therm. Eng., 2023. 227: 120397.
[15] H. Jouhara, A. Chauhan, T. Nannou, S. Almahmoud, B. Delpech, L. C. Wrobel, Heat pipe based systems - Advances and applications, Energy, 2017. 128: p. 729.
[16] J. Zhao, D. Yuan, D. Tang, Y. Jiang, Heat transfer characteristics of a concentric annular high temperature heat pipe under anti-gravity conditions, Appl. Therm. Eng., 2019, 148. P. 817.
[17] N. N. Babu, H. C. Kamath, Materials used in Heat Pipe, Mater. Today: Proceedings, 2015. 2: p. 1469.
[18] B. Nam, C. Park, W. Joung, Temperature uniformity characteristics of a hybrid pressure-controlled loop heat pipe with a heat pipe liner, Int. Comm. Heat Mass Transf., 2024. 156: 107656.

[19] C. K. Day, R. W. Smith, Under Sodium Viewing, Rep. HEDL-SA-615, Hanford Engineering Development Laboratory, 1973.
[20] X. Wang, T. Ma, Y. Zhu, H. Chen, J. Zeng, Experimental investigation on startup and thermal performance of a high temperature special-shaped heat pipe coupling the flat plate heat pipe and cylindrical heat pipes, Exp. Therm. Fluid Sci., 2016. 77: p. 1.
[21] J. R. Davis, ASM Specialty Handbook: Stainless Steels (ASM International, Materials Park, Ohio, 1994).
[22] Joint Committee for Guides in Metrology (JCGM), Evaluation of measurement data - Guide to the expression of uncertainty in measurement, JCGM 100:2008 (BIPM, Paris, 2008).

Paper ID 015(S7)

Heat transport characterization of a loop heat pipe with primary/secondary wick-integrated evaporator by additive manufacturing

Yuki Akizuki[1*], Kimihide Odagiri[1], Hiroshi Yoshizaki[2], Masahiko Sairaiji[2], Hosei Nagano[3] and Hiroyuki Ogawa[1]

[1] *Japan Aerospace Exploration Agency (JAXA), Sagamihara, Japan*
[2] *SOLIZE Corporation, Yokohama, Japan*
[3] *Nagoya University, Nagoya, Japan*
**Corresponding author email address: akizuki.yuki@jaxa.jp*

Abstract

This paper reports the design, fabrication, and testing of a loop heat pipe (LHP) with an additive manufacturing evaporator integrated with an evaporator/reservoir and primary/secondary wick. Conventional LHP evaporators have been made with their evaporator case and wick separate, then joined by shrink fitting or other means. This study applied additive manufacturing (AM) to designing and fabricating a wick-integrated evaporator that provides high performance and reliability at low cost. Step-up heat load tests were conducted with different tilt angles to evaluate the heat transport capability of LHPs with an AM evaporator and the effectiveness of a secondary wick. The LHP with the AM evaporator achieved a maximum heat transport capability of 170 W (heat flux: 11.3 W/cm^2) and a minimum thermal resistance of 0.24 °C/W (at 90 W) at a 0 deg tilt angle. The study demonstrated a heat transport of 20 W at a 90 deg tilt angle, the most difficult orientation for LHP operation. The heat transfer coefficient of evaporation and the heat leak ratio were calculated, and the test results were evaluated. This demonstrated that the AM evaporator offers high evaporative performance and that the secondary wick in the evaporator can reduce the heat leak ratio.

Keywords: Loop heat pipe, additive manufacturing, secondary wick, spacecraft thermal control

1. Introduction

A loop heat pipe (LHP) is a two-phase fluid loop driven by capillary force [1],[2]. The efficient heat transport device utilizes latent heat, is lightweight, powerless, long distance, and anti-gravity operation. It is gaining attention for space and terrestrial applications. In space application, this device is now being applied to thermal control for spacecraft, especially for waste heat from space telescope cryocoolers and temperature control of electric propulsion systems for deep space probe.

Figure 1 is a schematic diagram of LHP operation. The LHP driving force is the capillary force generated by the primary wick, but a secondary wick may be equipped to move the working liquid from the reservoir to the evaporator. In microgravity, the surface tension of a fluid causes the fluid to stick to the reservoir wall, making it difficult to supply liquid to the primary wick. This can easily lead to dryout. A secondary wick enables a stable fluid supply to the primary wick and is essential when LHPs are used for space application, where operation in a microgravity environment and high reliability are required.

LHP evaporators have been manufactured with the evaporator case and primary/secondary wick separate, joining them using shrink fitting, welding, or another process. This method, however, causes some variation in the evaporator performance. In addition, manufacturing is expensive due to the large number of steps in manufacturing and verification, the manufacturing difficulty, and the long development period, all of which limit the device's scope of use. We conducted this research to develop a low-cost, high-performance, high-reliability LHP with an evaporator made by additive manufacturing (AM). Utilizing AM reduces the work of producing the primary/secondary wick and of joining the wick with the evaporator case, which has been the rate-limiting step in the cost and schedule.

Table 1 shows the previous research on LHPs utilizing AM. Although several LHPs have been developed utilizing additive manufacturing [3]-[7], many are fabricated separately from the evaporator case and wick. There is no research for developing and evaluating the thermal performance of a wick-integrated evaporator with a secondary wick. In addition, the unique evaporation ability of the AM evaporator has not been studied, now have the heat transport characteristics of the LHP using an AM evaporator. There has been no comprehensive clarification of these.

Based on the above background, this study reports on the development of an LHP with a primary and secondary wick-integrated evaporator for space applications and our evaluation of its heat transport characteristics.

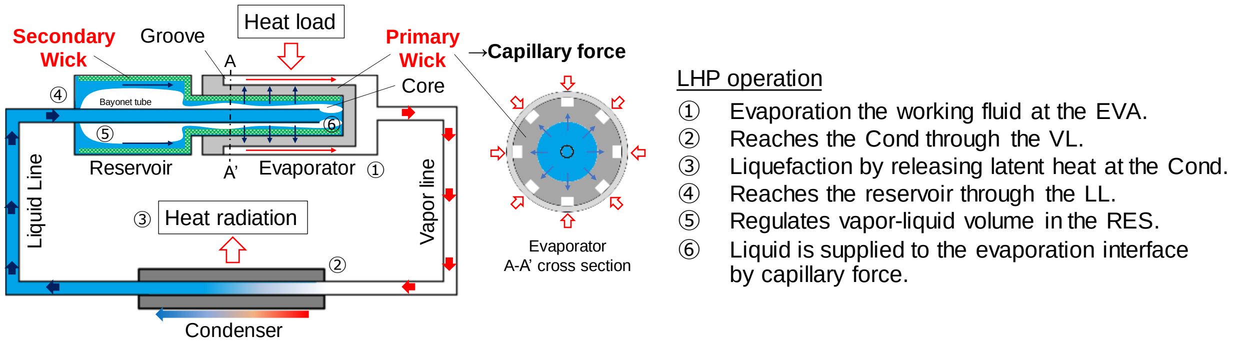

Figure 1. LHP operation schematics.

Table 1. Previous research on LHPs utilizing AM.

Authors	Year	EVA case and wick printing method	Secondary wick	Working fluid	Heat transport capability, W	Heat transport length, mm
J. Esarte et al. [3]	2017	Separate	With (separate)	Methanol	80	100
B. Richard et al. [4]	2017	Integrated	With (separate)	Ammonia	45	300
Z. Hu et al. [5]	2020	Separate	Without	Water	160	220
R. Gupta et al. [6]	2022	Integrated	Without	Ammonia	70	3000
J. Corrochano et al. [7]	2023	Separate	Without	Ammonia	236	1000

*The porous material is SUS 316L in each reference.

2. Development of an Additive Manufactured Evaporator

2.1. Printing with porous media

Laser powder bed fusion (LPBF) was adopted for the AM, and SUS316L powder with an average particle diameter of 10 μm was used as the base material. Before the evaporator was fabricated, a condition search was performed for fabricating high-performance porous media with high porosity and a small pore radius. The laser energy flux was varied to obtain the correlation between the laser energy flux and the porosity and pore radius by measuring the porosity and pore radius of the fabricated samples. The porosity was calculated from the mass measurement results using Equation (1), and the pore radius was calculated from the maximum capillary force obtained in the bubble point test using Equation (2).

$$\phi_{wick} = \frac{M_{eva} - M_{ec}}{\rho_{SUS} V_{wick}} \tag{1}$$

$$r_{pore} = \frac{2\sigma \cos\theta_{cont}}{P_{cap}} \tag{2}$$

Figure 2 shows the relationship between porosity and pore radius during primary wick conditioning (top) and secondary wick conditioning (bottom). The figure also shows a correlation between the porosity and pore radius. It was clarified that printing conditions by changing printing parameters other than laser energy flux had to be optimized for high-performance porous media. This study chose a porosity of 23% and a pore radius of 4.6 μm for the primary wick, and a porosity of 66% and a pore radius of 70 μm for the secondary wick.

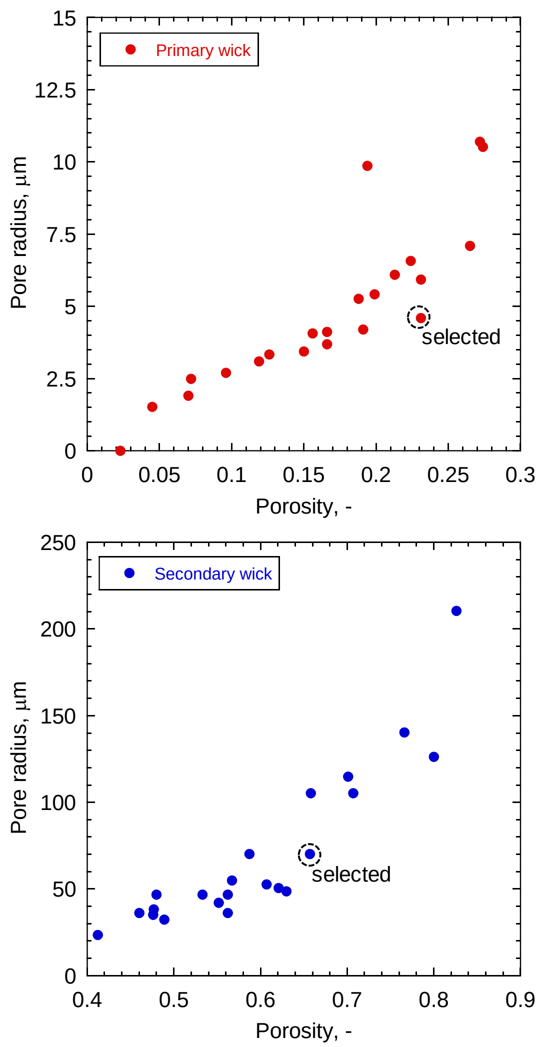

Figure 2. The relationship between porosity and pore radius obtained from condition search.

2.2. Primary/secondary Wick-integrated Evaporator/reservoir

Figure 3 and Figure 4 show an external view and a 3D CAD cross-section of the evaporator and reservoir fabricated by AM. Table 2 shows the AM evaporator specifications. The evaporator was cylindrical shape. The evaporator case, reservoir, primary wick, and secondary wick were all made in a single piece. The secondary wick was formed continuously along the reservoir wall and the inner wall of the primary wick and is designed to transport the working fluid in the reservoir to the primary wick.

The secondary wick on the inner wall of the primary wick also reduces the heat leakage from the evaporator. The effective thermal conductivity of the sintered wick can be calculated using Maxwell's equation, shown in Equation (3) [8].

$$k_{wick} = k_s \left[\frac{2 + k_l/k_s - 2\varepsilon(1 - k_l/k_s)}{2 + k_l/k_s + \varepsilon(1 - k_l/k_s)} \right] \quad (3)$$

where k_s is the thermal conductivity of the solid phase, k_l is the thermal conductivity of the liquid phase, and ε is the wick porosity. Figure 5 shows the thermal conductance through the wick when the thickness of the primary and secondary wick changes. Since the porosity of the primary wick is lower than the secondary wick, the thermal conductance of the entire wick can be reduced by adding a thickness of the secondary wick. However, making the primary wick too thin reduces the capillary force. In this study, the wick thickness was determined so that the thermal conductance through the wick was below 10% of the expected evaporative thermal conductance, and the primary and secondary wick thicknesses were 1.5 mm each.

A babble point test was conducted on the fabricated units, and the maximum pore radius was calculated to be 5.2 µm. This result confirmed that the wick with the same pore radius as the porous sample fabricated in the condition search was formed during evaporator fabrication.

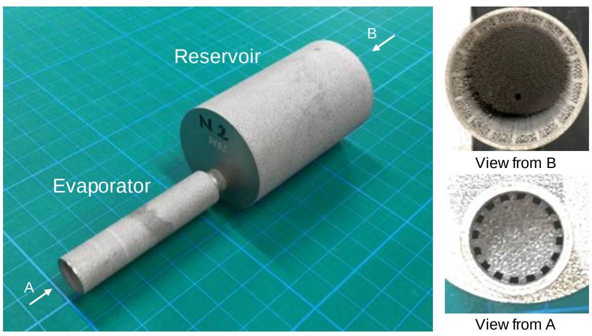

Figure 3. Appearance and side view from evaporator/reservoir of an AM evaporator.

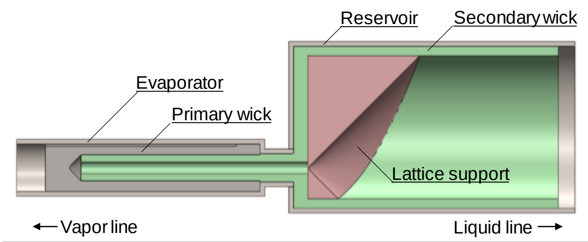

Figure 4. 3D CAD cross-section of an AM evaporator.

Table 2. Specifications of an AM evaporator.

Component	Dimension
Evaporator	ID/OD: 10/12 mm Length: 50 mm
Reservoir	ID/OD: 34/36 mm Length: 60 mm
Primary wick	ID/OD: 5.5/10 mm Thickness: 1.5 mm Pore radius: 4.6 µm (5.2 µm) Porosity: 23%
Secondary wick	ID/OD, Thickness: 2.5/5.5 mm, 1.5 mm (EVA side) 30/34 mm, 2.0 mm (RES side) Pore radius: 70 µm Porosity: 66%
Vapor grooves	W/H/L: 1/ 0.75/40 mm Number: 16

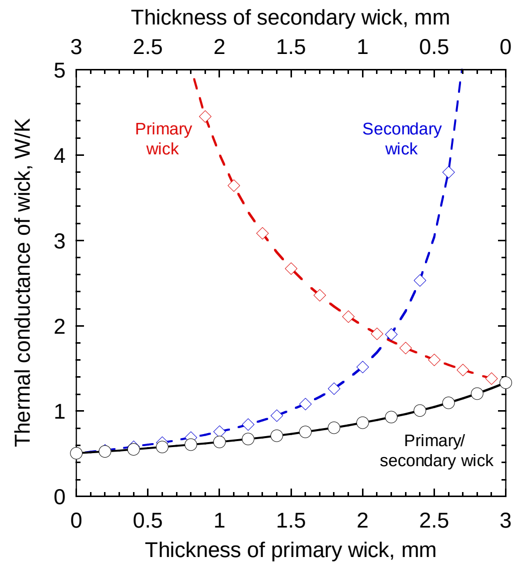

Figure 5. Dependence of thermal conductance through the primary and secondary wick on thickness.

3. Test Specimens and Conditions

The LHP system was developed by combining a fabricated AM evaporator with a transport line and condenser. The appearance and specifications of the LHP are shown in Figure 6 and Table 3. Acetone was selected as the working fluid and charged to 36 g (volume ratio: 63%). Table 3 lists the main specifications for the LHP with an AM evaporator. Thermal performance tests were conducted under atmospheric pressure and room temperature conditions (25°C). Temperatures were measured by 20 T-type thermocouples (accuracy ±1.0°C) and collected with a data logger at two-second intervals. The condenser was temperature-controlled by a copper cooling line parallel to the condenser line, and a chiller unit controlled the cooling fluid temperature. The evaporator, transport lines, and condenser were all insulated with thermal insulators to reduce heat loss to the environment. The heat source was simulated by an aluminum heater block heated by four rod heaters attached to the evaporator and a DC power supply was used to apply heat load.

The test conditions are shown in Table 4. Nos. 1-4 were conducted by changing the LHP tilted angle, as shown in Figure 7, and step-up heat load tests were conducted until the heater block rose to 150 °C or until dryout occurred in the evaporator. No. 5 was conducted by changing the sink temperature with a constant heat load of 80 W.

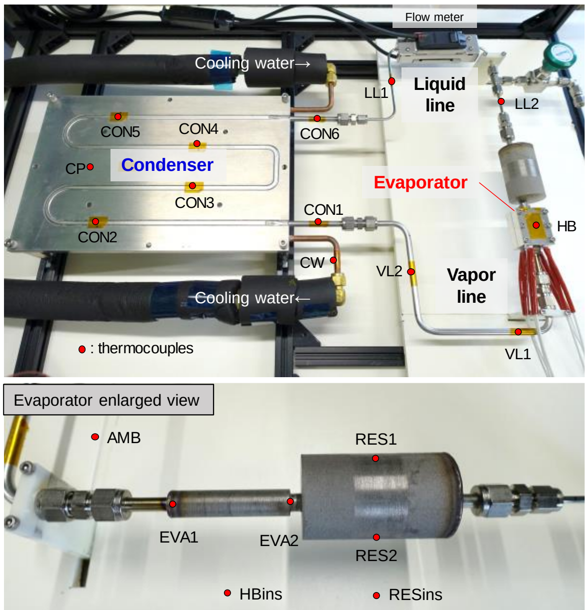

Figure 6. Appearance and thermocouple position of LHP system.

Table 3. Specifications of LHP system.

Component	Dimension
Heating area	OD, Length: 12/40 mm (Area: 15.1 cm^2)
EVA/RES	(Refer to Table 2.)
Vapor line	ID/OD: 4.57/6.35 mm Length: 400 mm
Condenser line	ID/OD: 4.57/6.35 mm Length: 1067 mm
Liquid line	ID/OD: 1.76/3.18 mm Length: 400 mm
Bayonet tube	ID/OD, Length: 1.5/1.7 mm, 55 mm (EVA side) 1.76/3.18 mm, 50 mm (RES side)
Working fluid	Acetone, 36 g

Table 4. Test conditions.

No.	Heat load, W	Sink temperature, °C	Tilt angle, deg (θ)
1	10-180 (10 W steps)	20	0 deg
2	10-180 (10 W steps)	20	45 deg
3	10-20-30	20	90 deg
4	10-190 (10 W steps)	20	-90 deg
5	80	0-50 (10 °C steps)	0 deg

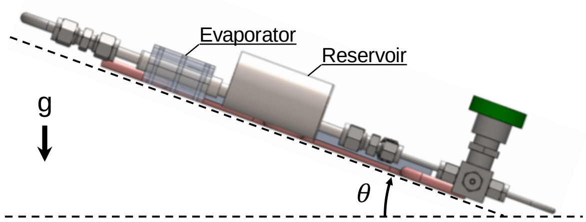

Figure 7. Test configuration.

4. Results and Discussion

4.1. Effect of the LHP tilt angle (Results of Nos. 1-4)

The temperature profile of No. 1 is shown in Figure 8, with the graph for startup at the top and for the entire test at the bottom. The temperature profile at startup shows that the LHP started up successfully because the temperature at the condenser inlet (CON1) rose rapidly 3.5 minutes after the start of the 10 W heat load to the heater block. The temperature of CON2 increased at a heat load of around 70-80 W, indicating an extension of the two-phase length at the condenser. When the heat load reached 180 W, the evaporator temperature (EVA1) rose rapidly due to dryout, and the test was terminated.

The temperature profile of No. 3 is shown in Figure 9 for startup at the top and for the entire test at the bottom. The temperature profile at startup shows that LHP started up 8 minutes after a heat load of 10 W was applied to the heater block. Compared to No. 1, it took longer to start due to the difficult tilt angle. Temperature oscillations occurred at CON1 and LL2 at a heat load of 10 W due to a low mass flow rate. As the heat load was increased, the evaporator temperature rose sharply at 30 W, resulting in a dryout. Since a maximum heat transport capability of 170 W was observed in No. 1, we believe the liquid supply to the primary wick was cut off due to the secondary wick's capillary limit rather than the primary wick's capillary limit, thus causing a dryout. The performance evaluation of the secondary wick is discussed in Section 5.2.

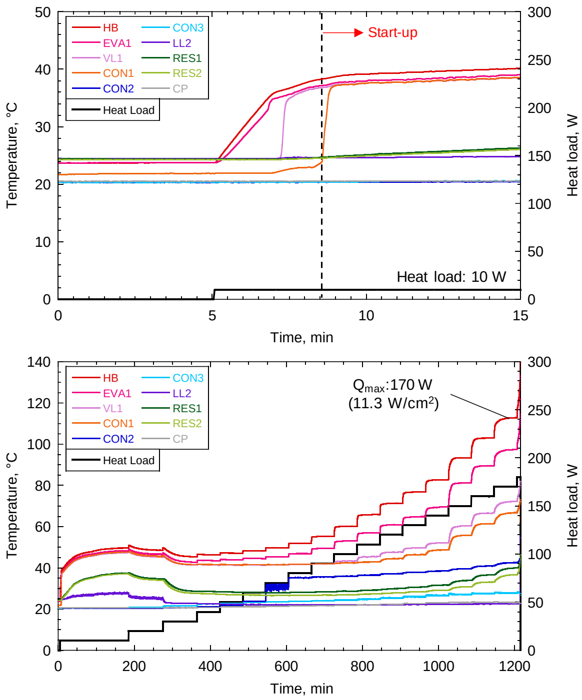

Figure 8. No. 1 temperature profile (top: startup, bottom: entire test).

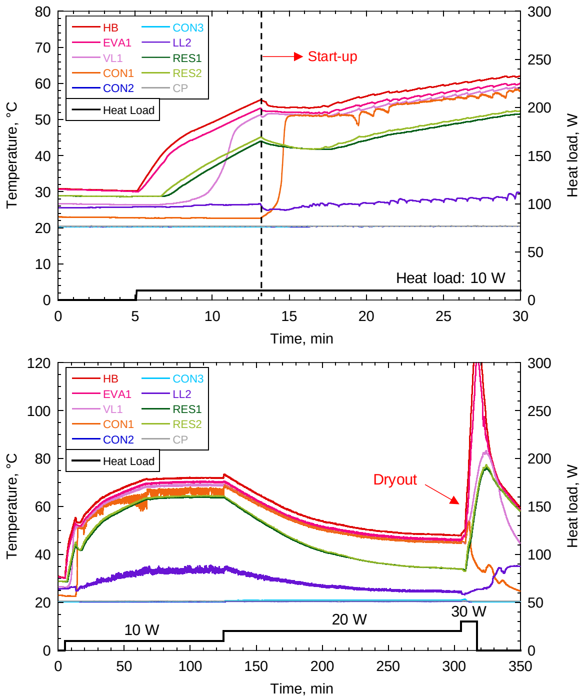

Figure 9. No. 3 temperature profile (top: startup, bottom: entire test).

Next, the operating temperature (EVA1) and LHP thermal resistance at the steady state of Nos. 1-4 are summarized to compare the heat transport performance at each tilt angle. The relationship between the heat load and the operating temperature and that of the LHP thermal resistance at steady state is shown in Figure 10, where the LHP thermal resistance was calculated from the

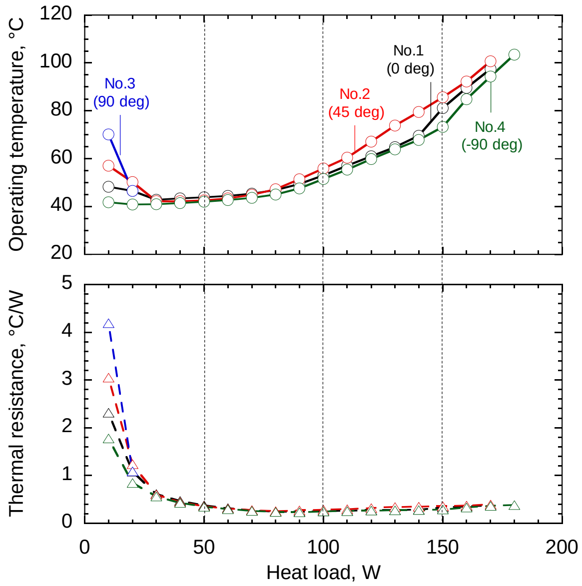

Figure 10. Operating temperature and LHP thermal resistance at steady state of Nos.1-4.

operating temperature, average condenser temperature, and heat load using the following equation.

$$R_{LHP} = \frac{T_{EVA1} - T_{CON\_ave}}{Q_{load}} \quad (4)$$

Nos. 1 and 2 found a maximum heat transport capability of 170 W, and No. 4 achieved 180 W. The effectiveness of the secondary wick was confirmed partially by the result that heat transport capability at a tilt angle of 45 deg was equivalent to that at an tilt angle of 0 deg. Compared with the results of No. 3, the tilt angle of No. 2 was such that the liquid returned through the bayonet tube was easily supplied directly to the evaporator. Therefore, we inferred that the heat transport capability of No. 2 was as high as that of No. 1. Conversely, in No. 4, the liquid was more easily supplied to the evaporator than at other tilt angles, and thus dryout was less likely to occur.

The operating temperatures of Nos. 1 and 2 were higher than those of No. 4 at low heat loads. In the low heat load region where the flow velocity is small, the liquid cooled by the condenser is less likely to flow back to the reservoir than in No. 4, and the heating effect by heat transfer between the liquid line and the ambient was larger.

All test results show similar operating temperatures in the medium heat load range of 30-100 W. However, in the high heat load range of 100 W and above, the operating temperatures increase in the order of No. 2, No. 1, and No. 4. This is due to the insufficient liquid near the wick tip in No. 2, where liquid supply is difficult, causing the operating temperature to rise. No. 4 is less likely to run out of liquid and thus maintains a low operating temperature up to the high heat load region.

The LHP thermal resistance of No. 1 had a minimum of 0.24 °C/W at 90 W. It was confirmed that the LHP thermal resistance was equivalent in the high heat load region, although there were differences at low heat loads for each tilt angle.

4.2. Effect of the sink temperature, No. 5 results

The temperature profile of No. 5 is shown in Figure 11, where the top shows representative temperature points and the bottom is an excerpt of condenser measurement points. This shows that heat transport is stable for sink temperatures from 0 to 50 °C. This result shows that the two-phase length extended as the sink temperature increased. Since the temperature difference between the internal fluid and the condenser is smaller, a longer two-phase length is required to increase the heat transfer area of the condenser tube and keep the heat dissipation amount to the condenser.

Figure 12 shows the steady-state LHP thermal resistance, evaporator thermal resistance, and condenser thermal resistance. The evaporator thermal resistance and condenser thermal resistance are calculated from the following equations.

$$R_{eva} = \frac{T_{EVA1} - T_{VL1}}{Q_{load}} \tag{5}$$

$$R_{con} = \frac{T_{VL1} - T_{CON\_ave}}{Q_{load}} \tag{6}$$

Figure 12 shows that the LHP thermal resistance decreases with increasing sink temperature; a minimum thermal resistance of 0.094 °C/W is achieved at a sink temperature of 50 °C. Similar to the LHP thermal resistance, the condenser thermal resistance also decreases with increased sink temperature, which is attributed to an increase in the condenser temperature with the extension of the two-phase length. However, the evaporator thermal resistance was stable at 0.06-0.07 °C/W for each temperature range, indicating a small dependence on the sink temperature. With a sink temperature of 50 °C, the evaporator thermal resistance accounted for 70% of the LHP thermal resistance, thus confirming it is the rate-limiting factor of thermal resistance.

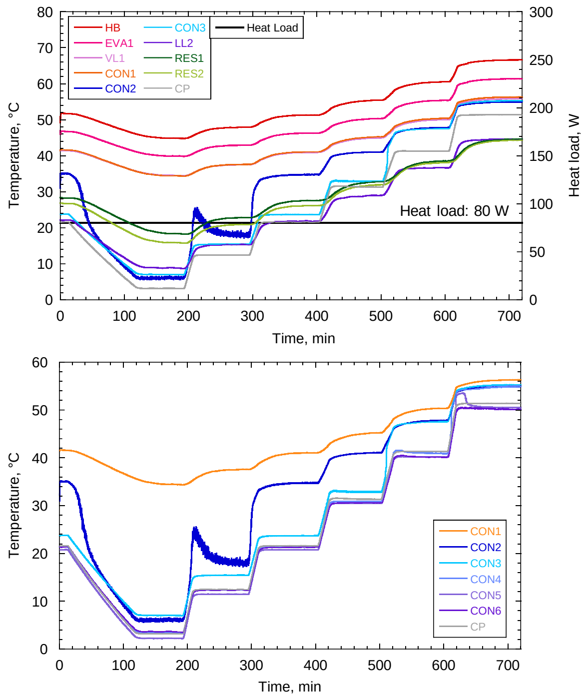

Figure 11. No. 5 temperature profile (top: representative temperature points, bottom: excerpt of condenser measurement points).

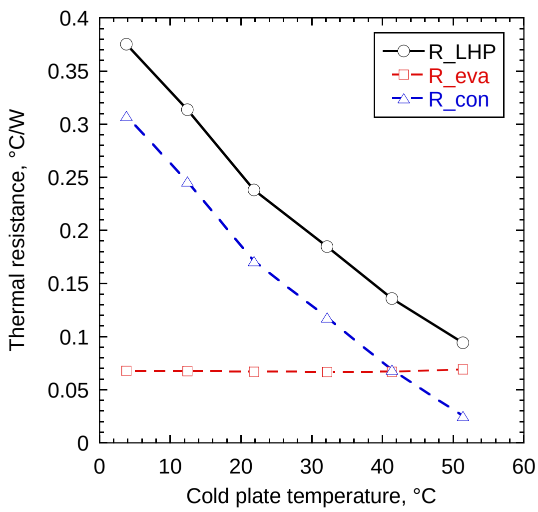

Figure 12. Thermal resistance at steady state of No. 5.

5. Thermal Performance Evaluation of Evaporator

5.1. Heat transfer coefficient of evaporation

The thermal performance of the AM evaporator was evaluated by calculating the evaporative heat transfer coefficient. This coefficient is calculated from Equation (7), where the evaporative heat amount Q_{ev} in Equation (7) can be expressed as shown in Equation (8), based on energy conservation in the evaporator.

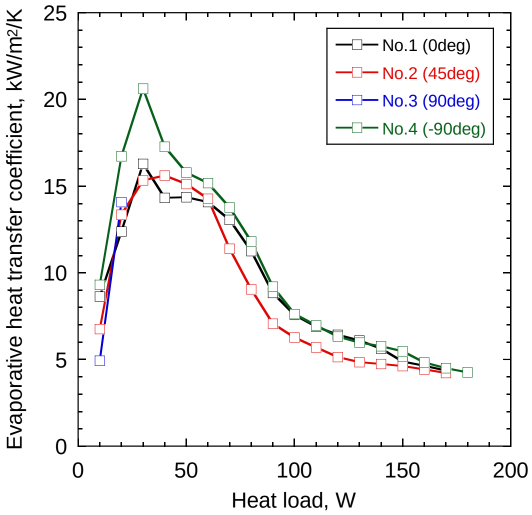

Figure 13. Evaporative heat transfer coefficient of the AM evaporator for each tilt angle.

$$h_{evap} = \frac{Q_{ev}}{A_{evap}(T_{EVA1} - T_{VL1})} \quad (7)$$

$$Q_{ev} = \frac{Q_{apply} - Q_{loss}}{1 + \frac{C_p}{\lambda}(T_{VL1} - T_{LL2})} \quad (8)$$

where A_{evap} represents the contact area between the wick and groove and the evaporator case, and Q_{loss} represents the heat loss amount released to the atmosphere through the evaporator insulation.

The dependence of the evaporative heat transfer coefficient on the heat load for each tilt angle is shown in Figure 13. The trend in the evaporative heat transfer coefficient with heat load is similar for each tilt angle. In all cases except for No. 3, the heat transfer coefficients are high at 12-15 kW/m^2/K in the 30-70 W heat load range but then gradually decrease and stabilize at 5 kW/m^2/K after 100 W. This is because the recession of the vapor-liquid interface occurs on the wick surface as the heat flux increases [9]. From the viewpoint of the tilt angle, the decrease in heat transfer coefficient is particularly noticeable in No. 2, where the liquid is not easily supplied to the evaporator.

5.2. Thermal performance of secondary wick

A simplified pressure drop calculation was performed when designing the secondary wick. This section compares the design results with the test results.

In the vertical orientation above the evaporator and below the reservoir tested in No. 3, when the total pressure drop generated in the secondary wick exceeds the maximum capillary force, it becomes difficult to supply liquid to the primary wick, and dryout occurs. Thus, the LHP can operate as long as Equation (9) is valid. The capillary force generated at the wick is expressed by Equation (10), and the total pressure drop can be expressed as the sum of the flow pressure drop through the wick and the volumetric force of the liquid held in the wick, as shown in Equations (11) and (12).

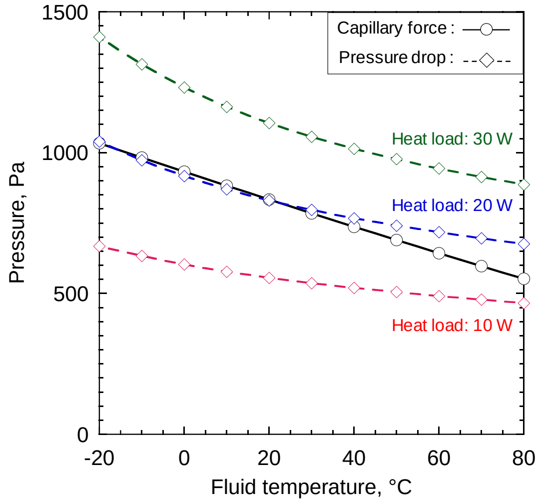

Figure 14. Capillary force and pressure drop at the secondary wick.

$$\Delta P_{cap\_sw} > \Delta P_{loss\_sw} + \Delta P_{loss\_g} \quad (9)$$

$$\Delta P_{cap\_sw} = \frac{2\sigma \cos\theta_{cont}}{r_{pore\_sw}} \quad (10)$$

$$\Delta P_{loss\_sw} = \frac{\mu Q_{ev}}{K_{sw} A_{sw} \rho_l} L_{sw} \quad (11)$$

$$\Delta P_{loss\_g} = \rho_l g h \quad (12)$$

Figure 14 compares the capillary force and total pressure drop at the secondary wick at 10-30 W. The reservoir temperature is about 35 °C at 20 W from the No. 3 result, and the figure shows that the pressure drop at the secondary wick is about the same as the capillary force. At a heat load of 30 W, the pressure drop is larger than the capillary force. This confirms that there is no significant discrepancy between the test results and the calculated results for the heat transport capability of the secondary wick. To increase the heat transport capability, it is necessary to reduce the pore size while maintaining a high porosity.

Next, the heat transport performance of the evaporator was evaluated based on the heat balance in the evaporator. The heat load Q_{load} applied to the evaporator is roughly divided into the evaporative heat amount Q_{evap} expressed by Equation (8), heat leakage Q_{wick} and Q_{case} into the reservoir through the wick and evaporator case,

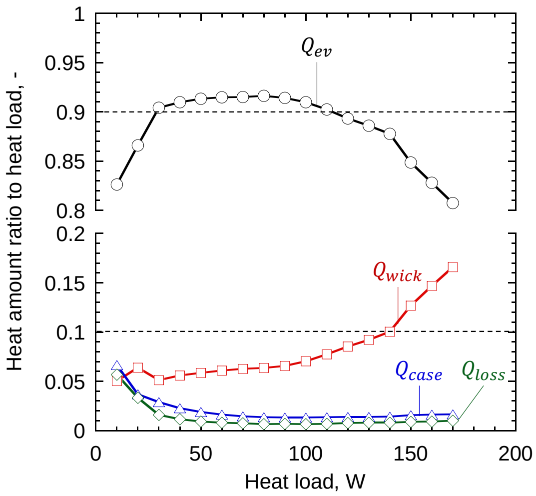

Figure 15. Breakdown of the heat balance in the evaporator at steady state for No. 1.

and heat loss Q_{loss} released to the ambient through the evaporator's insulation. Each heat amount can be calculated from the following equations.

$$Q_{case} = G_{case}\left(T_{EVA\_ave} - T_{RES\_ave}\right) \quad (13)$$

$$Q_{loss} = G_{loss}(T_{HBins} - T_{AMB}) \quad (14)$$

$$Q_{wick} = Q_{apply} - Q_{ev} - Q_{case} - Q_{loss} \quad (15)$$

The breakdown of the heat balance in the evaporator at steady state for test result No. 1 is shown in Figure 15. It was confirmed that 80-95% of the heat load was used as the evaporative heat in each heat load region. The heat leakage through the wick was also suppressed to less than 10% in the heat load of 140 W or less, indicating that the secondary wick effectively suppresses heat leakage to the reservoir. To further reduce heat leakage through the wick, the porosity of the primary wick should be increased.

6. Conclusions

In this study, a primary/secondary wick-integrated evaporator/reservoir was fabricated by AM. LHP system was developed, and its heat transport performance was demonstrated and evaluated. The knowledge gained from this study is listed below.

i) A primary and secondary wick-integrated evaporator/reservoir was fabricated by AM with a pore radius of 5.2 μm.

ii) A step-up heat load test was conducted, and a maximum heat transport capability of 170 W (heat flux: 11.3 W/cm^2) and minimum thermal resistance of 0.24 °C/W (at 90 W) were achieved in the tilt angle of 0 deg.

iii) The secondary wick's effectiveness was verified by performing the step-up heat load tests at different tilt angles. The heat transport of up to 20 W was successfully achieved at the tilt angle of 90 deg, and it was confirmed that the test result largely agreed with the calculation results.

iv) The effect of sink temperature on heat transport performance was verified, and it was found that the evaporator thermal conductance was independent of sink temperature.

v) The evaporative heat transfer coefficient was calculated, showing that a high heat transfer coefficient of 15 kW/m^2/K was achieved. The secondary wick thermal performance was evaluated, and it was shown that the heat leakage through the wick was sufficiently reduced.

ACKNOWLEDGMENTS

This work was supported by JSPS KAKENHI Grant Number JP 23K26306.

References

[1] J. Ku, "Operating Characteristics of Loop Heat Pipes," SAE technical paper series, 1999-01-2007, 1999

[2] Y.F. Maydanik, "Loop heat pipes," Applied. Thermal Engineering, 25, 2005, pp.635-657

[3] J. Esarte, J.M. Blanco, A. Bernardini, and J.T. San-Jose, "Optimizing the design of a two-phase cooling system loop heat pipe: Wick manufacturing with the 3D selective laser melting printing technique and prototype testing", Applied. Thermal Engineering, 111, 2017, pp.407-419

[4] B. Richard, D. Pellicone, and B. Anderson, "Loop Heat Pipe Wick Fabrication via Additive Manufacturing," 47th International Conference on Environmental Systems proceedings, 2017

[5] Z. Hu, D. Wang, J. Xu, and L. Zhang, "Development of a loop heat pipe with the 3D printed stainless steel wick in the application of thermal management", International Journal of Heat and Mass Transfer, 161, 2020, 120258

[6] R. Gupta, C.H. Chen, and W.G. Anderson, "Experiments on a Loop Heat Pipe with a 3D Printed Evaporator", 51th International Conference on Environmental Systems proceedings, 2022

[7] J. Corrochano, F.Romera, C. Gallesuillos, A. Perinan, F. Lasagni, M. Gottero, and S. Lapensee, "Development and Characterization of Additive Manufacturing Flat Loop Heat Pipe Evaporator", 52nd International Conference on Environmental Systems proceedings, 2023

[8] P. D. Dunn and D. A. Reay, "HEAT PIPES third edition", Pergamon Press, 1982, p.100

[9] K. Odagiri and H. Nagano, "Investigation on liquid-vapor interface behavior in capillary evaporator for high heat flux loop heat pipe", International Journal of Thermal Science, 140, 2019, pp.530-538

Paper ID 017(S2C)

The effect of gradient structure wick on the heat transfer performance of polyurethane flexible flat heat pipe

Hongling Lu[1], Li Jia[2*], Liaofei Yin[3], Chao Dang[4]

[1] *Beijing Jiaotong University, Beijing, China*
[2] *Beijing Jiaotong University, Beijing, China*
[3] *Beijing Jiaotong University, Beijing, China*
[4] *Beijing Jiaotong University, Beijing, China*
**Corresponding author email address: ljia@bjtu.edu.cn*

Abstract

To address the heat dissipation challenges of foldable wearable electronic devices, in this paper, we prepared polyurethane flexible flat heat pipe using pouring technology, employing copper wire mesh as the wick and machining it into a strip structure to achieve gas-liquid coplanarity. Infrared thermography was used to observe the capillary climb phenomenon of the working fluid, and the gradient structure with different mesh counts of the wire mesh was identified as the optimal wick structure through comparative experiments. The heat transfer performance of the heat pipe at different tilt and bending angles was experimentally investigated. The results showed that the heat pipe could achieve the optimal balance between evaporation and condensation processes when the filling ratio (*fr*) was 100% and the tilt angle was 90°, thus constructing an efficient and stable two-phase circulation mechanism. However, with the increase of the bending angle, the flow resistance of the working fluid inside the heat pipe increases and the heat transfer path became more complicated, leading to the increase in the overall thermal resistance of the heat pipe.

Keywords: Polyurethane flexible flat heat pipe; Infrared thermography; Capillary climb; Gradient structure wick; Heat transfer performance

1. Introduction

With the rapid development of foldable and wearable electronics in recent years, microelectronic devices gradually exhibited a trend towards high performance and miniaturization. However, as the functionality and integration of the devices increased, the heat flux generated internally also surged significantly [1], particularly during the dynamic processes of folding and unfolding, posing a particularly tricky heat dissipation problem. Within small and compact spaces and in complex operating environments, traditional rigid heat pipes struggled to keep pace with the escalating demand for heat dissipation [2, 3]. To confront this challenge, flexible flat heat pipe technology commenced its rapid development and gradually emerged as the premier choice for solving the thermal management problems of such electronic devices [4].

Current research on flexible flat heat pipes centered on optimizing the shell material and the design of the wick structure. Yang et al [5] utilized a metal cavity in conjunction with a flexible copper foil as the shell material for the evaporating, condensing, and adiabatic sections, respectively, and employed UV-curing adhesive sealing technology to fabricate a novel flexible flat heat pipe. They thoroughly examined the impacts of the filling ratio, bending curvature, and bending angle on its heat transfer performance. The study revealed that, under the optimal filling ratio and horizontal operation, the heat pipe was capable of transferring up to 25 W with a minimum thermal resistance of 0.99 K/W, and maintained the ability to transfer 15 W even under 180° bending and a curvature diameter of 30 mm. Zhang et al. [6] utilized copper as the evaporating and condensing section shell material and epoxy resin pouring in the adiabatic section to manufacture the heat pipe, and investigated the thermal performance of the heat pipe with varying filling ratios under different tilting and bending conditions. It was found that the most significant factor influencing the heat transfer performance of the ultra-thin flexible flat plate heat pipe was its internal volume, whereas the tilt angle and bending angle had less impact. In addition, Liu et al. [7] and Sun et al. [8] both utilized aluminum-plastic film for the shell material, but the structure of the wick differed. The former employed three layers of sintered stainless-steel mesh accompanied by hot pressing technology to achieve sealing, thereby reducing the contact thermal resistance, while the latter combined multi-layer copper mesh with porous microcolumns and utilized hot pressing and bonding technology for encapsulation. The results indicated that the flexible flat heat pipe designed by Liu et al. not only achieved a bending angle of 180°, but also maintained a stable heat transfer performance after repeated bending, exhibiting a minimum thermal resistance of 0.525 °C/W and a maximum effective thermal conductivity of 1499 W/m·K. Meanwhile, the heat pipe developed by Sun et al., with a thickness of 0.8 mm, boasted a maximum thermal conductivity of 1943.5 W/m·K and a maximum heating power of 17.1 W. Within a bending range of 0° to 180°, the thermal conductivity fluctuation remained minimal, preserving excellent heat transfer stability. It is evident that the design of the internal wick structure exerts a crucial influence on the heat transfer performance of the heat pipe.

It is worth noting that, in the heat transfer process, the flexible flat heat pipe required the utilization of the high permeability of the wick to ensure rapid transport of the working fluid, while also employing high capillary force to guarantee adequate supply and distribution of the working fluid within the wick structure. However, a single wick structure inherently exhibited either high capillary force but low permeability, or high permeability with limited capillary force. A composite wick structure, though capable of balancing the relationship between capillary force and permeability, was more complex to process, and its enhancement of heat transfer performance was limited. Consequently, this paper proposed the use of a gradient structure wick, achieved by combining different mesh counts, to optimize the matching of capillary force and permeability. Furthermore, an integrated pouring process was utilized to fabricate a flexible shell with a tight structure and excellent performance.

2. Experimental investigations

2.1. Experimental samples and systems

Due to the superior performance of polyurethane material in terms of thermal stability, flexibility, and strength, it was selected as the substrate of the flexible flat heat pipe shell in this paper. In order to further enhance the airtightness of the shell, the shell in this study was poured using polyurethane solvent, with the size of 90 mm × 50 mm × 1.6 mm. The specific pouring process was as follows: the polyurethane solvent was mixed with the curing agent at the mass ratio of 1:1 through a mixer, and then the mixed solvent was slowly poured into the well-designed shell plate mould of the heat pipe, with a 3 mm diameter hole pre-drilled for the filling tube. The mould was evacuated using a vacuum drier until all air bubbles were removed. Finally, the filled mould was transferred to the oven for curing, with the oven temperature set at 60 °C for 90 minutes. Once cured, the mould was allowed to cool naturally to room temperature, and then it was removed for demoulding, thus completing the casting and resulting in a complete polyurethane flexible flat heat pipe (PFFHP) shell.

In order to ensure that the wick could maintain its structural integrity during the bending and deformation of the flexible flat heat pipe, and at the same time possess good flexibility and capillary properties, copper wire mesh was used as the material for it in this study. Two types of structures were designed: a single structure of wick (with the same count of mesh) and a gradient structure of wick (a combination of two different mesh counts). In order to further optimize the flow paths of the gas and liquid phases within the wick and reduce the flow resistance, the copper wire mesh wick was designed in a strip structure. The strip structure wick is illustrated in Figure 1a, while the gradient structure wick is shown in Figure 1b. Based on the relevant research results, the optimal widths of the gas-phase and liquid-phase channels were determined to be 1.5 mm and 2.5 mm, respectively, at the wick height of 0.8 mm in this experiment.

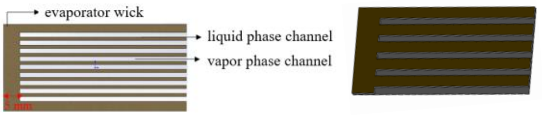

(a) strip structure (b) gradient structure

Figure 1. Schematic structure.

The specific mesh counts for the single and the gradient structure wicks are detailed in Table 1.

Table 1. Type and parameters of the wick

Wick number	Type A	Type B
Wick material	copper mesh	
Wick size	80 × 40 × 0.8 mm^3	
Wick mesh count	10#250	8#250+2#350
Note: a#b, where “a” represents the number of layers and “b” represents the mesh count.		

The designed wick structure was embedded directly into the PFFHP shell, and the heat pipe was sealed using a secondary pouring technique.

A capillary climb test setup, as depicted in Figure 2, was constructed to accurately evaluate the influence of two types of the wick on the capillary climb rate of the working fluid. This setup primarily consisted of an infrared thermal imaging camera, a lifting platform, a glass petri dish, a ruler, clamps, wick samples, a computer, and a data acquisition instrument.

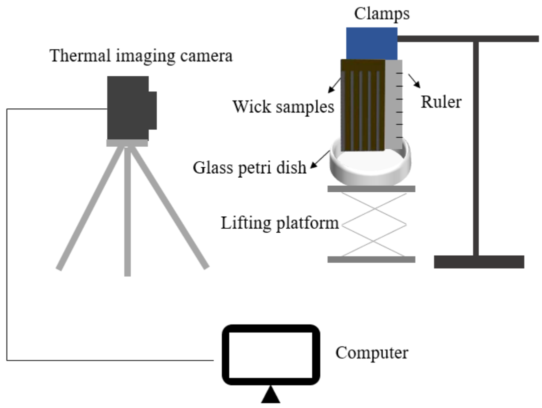

Figure 2. Schematic diagram of the capillary climb test setup.

The experimental setup for the heat transfer performance of the PFFHP was constructed, as previously shown in Figure 3, and the entire system consisted of a heating module, a data acquisition module, a vacuum module, and a heat pipe sample. The heat source was a ceramic heating plate (10 mm × 10 mm), which was stably powered by a DC power supply. On the surface of the heat pipe, in the boxed area depicted in Figure 3, eight thermocouples were arranged to monitor its temperature distribution. Specifically, T1 and T2 were positioned near the heat source to measure the evaporating section temperature, whereas T3, T4, and T5, T6, T7, T8 were uniformly distributed along the axial position of the upper shell of the heat pipe, tasked with measuring the temperatures of the adiabatic section and the condensing section, respectively. Furthermore, to simulate the actual operating conditions of electronic equipment, the system employed a natural convection cooling method, utilizing common deionized water as the working fluid. In order to minimize the impact of heat loss on the heat transfer performance of the heat pipe, the remaining portion of the PFFHP, excluding the condensing section, was wrapped in thermal insulation wool.

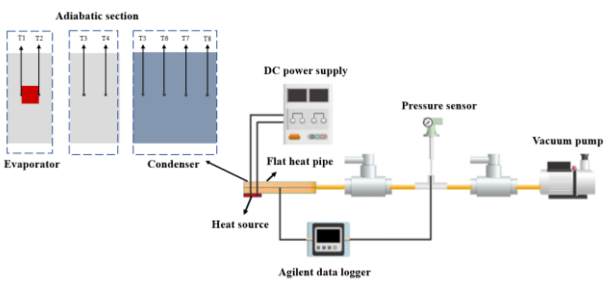

Figure 3. Experimental setup for the heat transfer performance of the PFFHP.

2.2. Data reduction and uncertainty analysis

The thermal resistance, a crucial metric in assessing the heat transfer performance of polyurethane flat heat pipes, is derived through the following formula:

$$R = \frac{T_{\text{e-ave}} - T_{\text{c-ave}}}{Q} \tag{1}$$

In the formula, $T_{\text{e-ave}}$ represents the average temperature at the evaporation section, $T_{\text{c-ave}}$ represents the average temperature at the condensation section, and Q represents the heating power.

To thoroughly investigate the impact of the bending process on the overall heat transfer performance of flat heat pipes, the following equation can be utilized to calculate the vapor pressure drop incurred as the vapor flows from the evaporation end to the condensation section [9]:

$$\Delta P_{\text{v}} = \left(\frac{C\left(f_{\text{v}} - \text{Re}_{\text{v}}\right)\mu_{\text{v}}}{2\left(r_{\text{h,v}}\right)^2 A_{\text{v}}\rho_{\text{v}} h_{\text{fg}}} \right) L_{\text{eff}} Q \tag{2}$$

In the formula, C represents the constant related to the Mach number, f_{v} represents the vapor friction coefficient, Re_{v} represents the vapor Reynolds number, μ_{v} represents the vapor viscosity, $r_{\text{h,v}}$ represents the hydraulic diameter, A_{v} represents the cross-sectional area of the channel, ρ_{v} represents the vapor density, h_{fg} represents the latent heat of vaporization, and L_{eff} represents the effective length of the heat pipe.

When steam flows through curved sections, additional hydraulic losses occur, which can be quantified using the following equation:

$$h_{\text{m}} = \left[0.131 + 0.159 \left(\frac{D}{R} \right)^{3.5} \right] \frac{\theta}{90^{\circ}} \frac{v^2}{2g} \tag{3}$$

In the formula, v represents the steam velocity, and g represents the gravitational acceleration.

The filling ratio, defined as the ratio of the filling volume to the pore volume of the wick structure, is crucial for understanding the performance of the heat pipe. Its calculation formula is as follows:

$$fr = \frac{V_{\text{l}}}{V_{\text{c}}} \tag{4}$$

Before the experiment commenced, all measuring devices were calibrated to ensure data accuracy. The pressure sensors had a precision of ±0.25%, the T-type thermocouples had a precision of ±0.10°C, and the DC power supply voltage and current readings had precisions of ±1% and ±0.50%, respectively. Based on the formula proposed by Moffat R J [10], the uncertainty of the thermal resistance of the polyurethane flat heat pipe was calculated to be 1.03%.

$$\delta X = \left[\sum_{i=1}^{N} \left(\frac{\partial X}{\partial V_i} \delta V_i \right)^2 \right]^{1/2} \tag{5}$$

3. Results and discussion

3.1. Influence of the wick structure on the heat transfer performance of the PFFHP

Figure 4 showed infrared thermal image observations, illustrating the rate of capillary climb of the working fluid in the structures of type A and B wicks. Given the different infrared emissivity of water and copper at room temperature, the region where water climbed appeared dark blue in the infrared thermal image. The observation revealed that the working fluid inside the gradient structure reached a higher climb height within the same time frame, clearly indicating that the gradient structure significantly improved the capillary performance of the type B wick compared to the type A wick.

This improvement stemmed from the gradient structural design of the type B wick. The upper layer, featuring a large porosity, facilitated the rapid entry and filling of the working fluid by providing sufficient flow space; while the lower layer, designed with a smaller porosity, significantly strengthened the capillary force, ensuring stably maintained and slowly release of the working fluid within the wick. This gradient distribution of porosity not only directly improved the capillary performance of the wick, enabling continuous and stable climbing of the working fluid, but also facilitated rapid flow through the high permeability of the upper layer while ensuring the uniform distribution within the wick through the low permeability of the lower layer.

In the heat transfer process, the gradient structure leveraged the capillary force to drive the transport of the working fluid, accelerating the heat transfer and diffusion, and effectively improving the heat transfer efficiency of the system. Additionally, the gradient design reduced the resistance encountered by the working fluid during the transport process, allowing for smoother flow and even distribution within the wick. This optimized distribution further enhanced the contact area between the wick and the heat source, ultimately improving the overall heat transfer performance of the system.

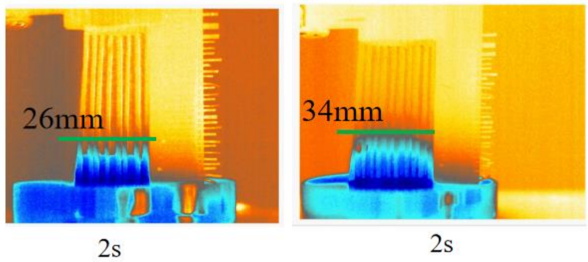

(a) Type A (b) Type B

Figure 4. Capillary rise conditions.

Consequently, we conducted the heat transfer performance test on the polyurethane flexible flat heat pipe equipped with a gradient structure wick (G-PFFHP).

3.2. Effect of the tilt angle on heat transfer performance

Firstly, we tested the effect of the filling ratio (50%, 70%, and 100%) on the heat transfer performance of G-PFFHP at the tilt angle of 0°, as depicted in Figure 5, and the results indicated that G-PFFHP exhibited the optimal heat transfer performance at this angle when *fr* was set to 100%.

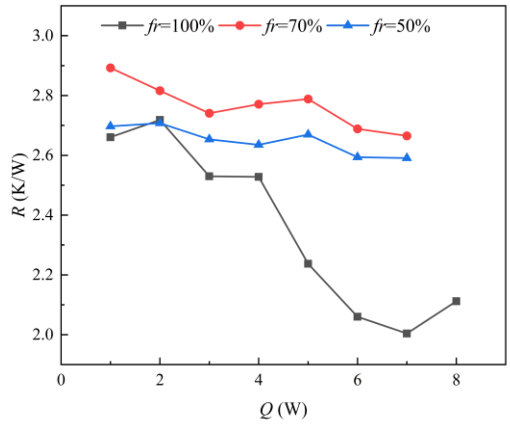

Figure 5. Trend of thermal resistance with heating power at different filling ratios.

Subsequently, we further investigated the influence of inclination angles (90° and -90°) on the heat transfer performance of G-PFFHP at *fr*=100%, and the trend of thermal resistance changes was depicted in Figure 6. At the tilt angle of 90°, the G-PFFHP showed the best heat transfer performance, which was primarily attributed to the synergistic effect of gravity and the gradient structure wick. Gravity assisted the flow of the working fluid, as its direction aligned with the direction of the working fluid's return from the condensing end to the evaporating end, effectively reducing the risk of drying out at the evaporating end and ensuring continuous wetting of the evaporating interface, thereby significantly enhancing the heat transfer efficiency. Moreover, the gradient structure of the wick design amplified this benefit: the lower layer of 350-mesh copper wire mesh, with its fine mesh structure, imparted robust capillary force, becoming the crucial driving force for the working fluid's return flow, even under high thermal loads, ensuring its efficient pull-back to the evaporating end. Meanwhile, the upper layer of 250-mesh copper wire mesh accelerated the flow rate of the working fluid through its high permeability, shortening the retention time in the wick and enabling the evaporation-condensation cycle to proceed faster.

However, when the thermal load surpassed 4 W, the thermal resistance of the G-FFHP at 90° tilt abruptly increased. This was most likely due to the extreme evaporation phenomenon triggered by overheating at the evaporation end, rapidly depleting the working fluid near the evaporation interface. Despite the potent capillary force of the wick's gradient structure, timely replenishment of sufficient working fluid to meet the evaporation demand became challenging, leading to partial or complete drying out of the evaporation interface, diminishing heat transfer efficiency and elevating thermal resistance. Furthermore, a copious amount of vapor bubbles generated at the evaporation end under heavy heat load may have accumulated in the wick, forming a blockage that further impeded the flow of the working fluid and heat transfer. Simultaneously, the capillary force of the lower layer of 350-mesh copper wire mesh may have reached saturation, unable to further accelerate the reflux of the working fluid; whereas the upper layer of 250-mesh copper wire mesh, despite its high permeability, could not fully function due to the vapor bubble blockage or insufficient working fluid.

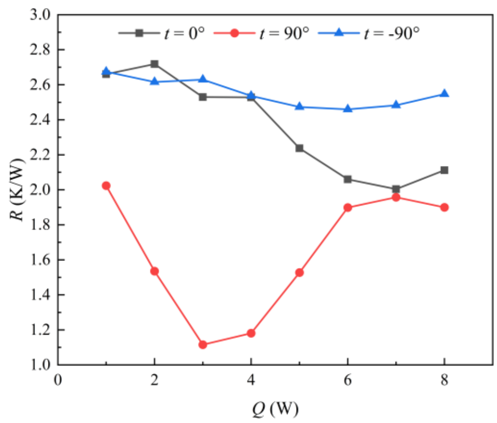

Figure 6. Variation of thermal resistance with heat load at different tilt angles.

3.3. Effect of the tilt angle on heat transfer performance

Since flexible flat heat pipes were usually bent in practice, we further investigated the effect of the bending angle (45° and 90°) on the heat transfer performance of the G-PFFHP at *fr*=100%, and the trend of its thermal resistance is shown in Figure 7. As shown in the figure, it could be seen that the thermal resistance increased with the bending angle at different bending angles. This was due to the fact that at small bending angles (e.g., 0° and 45°), the vapor-phase and liquid-phase channels within the G-PFFHP remained relatively straight or were slightly curved, which facilitated the smooth flow of the working fluid (a mixture of liquid and vapor) in the wick, thereby reducing flow resistance and ensuring efficient heat transfer. However, as the bending angle grew, particularly when it reached 90°, the internal channels of the heat pipe underwent significant bending, which not only shortened the length of the straight sections but also enlarged the radius of curvature of the flow channels. This resulted in increased centrifugal and frictional forces that had to be overcome by the flow of the working fluid. The formation of local vortexes or reflux zones at the bends further aggravated the flow resistance, slowing down the circulation speed of the working fluid and impairing the effective transmission of heat.

From a heat transfer perspective, the heat transfer path at small bend angles was relatively direct and efficient, relying on the efficient conduction and convection of the liquid in the vapor chamber and the wick. However, as the bending angle increased, the heat transfer path became more complicated, and heat had to bypass additional bending segments, increasing the path length and complexity while decreasing heat transfer efficiency. Simultaneously, the augmentation of flow resistance and the complexity of the heat transfer path led to heightened energy loss and heat loss during the heat transfer process. Additionally, there might have been heat accumulation and an increase in the temperature gradient at the bending sections. These factors, in concert, contributed to the rise in thermal resistance.

Furthermore, the enlargement of the bending angle also impacted the phase transition process within the heat pipe. At the evaporating end, heat was absorbed to convert the liquid mass to a gaseous state, while at the condensing end, the gaseous mass released heat and condensed. The increase in the bending angle disrupted the equilibrium and efficiency of the phase change process. Moreover, the heightened flow resistance may have diminished the pressure difference between the evaporating end and the condensing end, thereby affecting the steam flow rate and condensation effect, and ultimately, adversely influencing the heat transfer performance of the heat pipe.

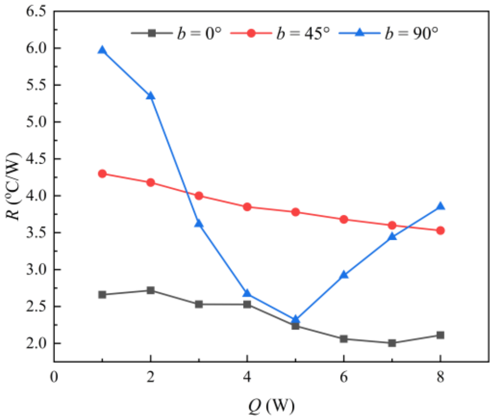

Figure 7. Variation of thermal resistance with heat load at different bending angles.

4. Conclusions

In this paper, a new type of flexible flat heat pipe was manufactured by the pouring method, and its internal wick was constructed from copper wire mesh. The influence of the wick structure on the transport of the working fluid was analyzed using infrared thermography, and the effects of tilt angle and bending angle on the heat transfer performance of the PFFHP under the optimal filling ratio were experimentally investigated. The primary conclusions that were drawn are as follows:

(1) In comparison to the single-structure wick with uniform mesh count, the gradient-structure wick featuring varying mesh counts was more adept at balancing the mutually constraining relationship between capillary force and permeability. Consequently, the working fluid ascended to a greater height within the same timeframe, ensuring a more robust transport capacity.

(2) The PFFHP exhibited optimal heat transfer performance at a filling ratio of 100% and a tilt angle of 90°. The tilt angle significantly impacted the flow of the working fluid and the efficiency of heat transfer. By optimizing the filling ratio and tilt angle, an efficient and stable two-phase circulation mechanism could be established.

(3) The increase in the bending angle led to a significant increase in the thermal resistance of the heat pipe due to impeded working fluid flow, vortex phenomena, complexity of the heat transfer paths, and a decrease in the efficiency of the phase change process.

5. ACKNOWLEDGEMENTS

Special thanks are given to the support from the Key Project of the Fundamental Research Funds for the Central Universities of the Ministry of Education (Project No.: 2022JBCG002).

References

[1] J. Lim, and S. J. Kim, Fabrication and Experimental Evaluation of a Polymer-based Flexible Pulsating Heat Pipe. Energy Conversion and Management, 2018. 156: p. 358-364.

[2] J. L. Huang, W. Zhou, J. H. Xiang, C. Z. Liu, Y. Gao, S. L. Li, and W. S. Ling, Development of novel flexible heat pipe with multistage design inspired by structure of human spine. Applied Thermal Engineering, 2020. 175: p. 115392.

[3] J. L. Huang, J. H. Xiang, X. Y. Chu, W. J. Sun, R. L. Liu, W. S. Ling, W. Zhou, and S. L. Tao, Thermal performance of flexible branch heat pipe. Applied Thermal Engineering, 2021. 186: p. 116532.

[4] M. J. Gibbons, M. Marengo, and T. Persoons, A Review of Heat Pipe Technology for Foldable Electronic Devices. Applied Thermal Engineering, 2021. 194: p. 117087.

[5] X. Yang, T. Liu, W. Yan, and S. Wang, Design, fabrication and heat transfer performance study of a novel flexible flat heat pipe. International Communications in Heat and Mass Transfer, 2023. 142: p. 106673.

[6] X. C. Zhang, J. Li, and Q. Chen. Preparation method and thermal performance of a new ultra-thin flexible flat plate heat pipe. Heat Transfer Research, 2024. 55: p. 1.

[7] C. Liu, Q. Li, and D. Fan. Fabrication and performance evaluation of flexible flat heat pipes for the thermal control of deployable structure. International Journal of Heat and Mass Transfer, 2019. 144: p. 118661.

[8] Y. L. Sun, F. Y. Liang, H. Tang, Y. Tang, S. W. Zhang, and K. J. Chua, Ultrathin flexible heat pipes with Microsorum fortunei structural-like wick for cooling flexible electronic devices. International Journal of Heat and Mass Transfer, 2023. 202: p. 123743.

[9] P. Naphon, S. and Wongwises, A Review of flow and heat transfer characteristics in curved tubes. Renewable and Sustainable Energy Reviews, 2006. 10: p. 463-490.

[10] R. J. Moffat, Describing the uncertainties in experimental results. Experimental Thermal and Fluid Science, 1988. 1: p. 3-17.

Paper ID 021(S2A)

Mono-sized Cryogenic Pulsating Heat Pipe Operational with both Neon and Helium – an Experimental Study

Tisha Dixit[1*], Gilles Authelet[1], Charles Mailleret[1], Florian Gouit[1], Vadim Stepanov[1], and Bertrand Baudouy[1]

[1]*Université Paris-Saclay, CEA, IRFU, Département des Accélérateurs, de la Cryogénie et du Magnétisme 91191, Gif-sur-Yvette, FRANCE*

**Corresponding author email address: tisha.dixit@cea.fr*

Abstract

A single pulsating heat pipe (PHP), having an inner diameter tube of 1 mm, has been experimentally tested at low temperature with two different cryogens. The tests consist of measuring the thermal performance of this heat pipe with neon and helium as working fluids. For neon, the Bond number is around 2.5 and for helium, it is close to 12. The idea behind this study is to investigate the functioning of a cryogenic PHP at Bond number much higher than 4 – the well-accepted design limit. This paper presents the results in vertical and horizontal orientations and for different filling ratios. It has been demonstrated that at a diameter well above the classical Bond number criterion, a cryogenic PHP is operational. At best, the helium PHP is able to transfer heat with a thermal resistance in the range of 1 K/W in vertical orientation. Although the evaporator enters the supercritical regime at few instances, it is observed to successfully transport heat – perhaps not in "true" PHP mode. The neon PHP exhibits a thermal resistance four times lower in vertical orientation and, unlike helium PHP, always remains within the saturation dome. Horizontally both PHPs showcase relatively higher thermal resistance values.

Keywords: Cryogenics; Pulsating heat pipe; Bond number criteria; Experimental study

1. Introduction

For small size and low power (below 20 W) cryogenic system, such as superconducting magnet, alternative solutions to liquid cryogen cooling using refrigerators (generally called cryocoolers) are pursued to simplify the cryogenic scheme and operation. It has also the advantage to make the overall system compact and autonomous. The cryogenic design is therefore different and requires the use of efficient and passive thermal link between the cryocooler's cold tip and the system to be cooled. Several solutions exist and are under investigation. One of the most promising thermal link, developed by CEA Paris-Saclay, is the cryogenic fluid based Pulsating Heat Pipes [1-5].

The working physics of room temperature and cryogenic PHPs remains the same except for the differences due to the intrinsic properties of cryogenic fluids [6]. However, the experimental measurements of cryogenic PHPs are relatively more complex and dissimilar. The tests have to be conducted at temperatures below 120 K (- 153.15 °C) and as low as 2.3 K (- 270.85 °C) if helium is employed. The foremost challenge is the cool-down from room temperature to such low values which is a time-consuming process (one week for our study). Moreover, the PHP must be placed in a cryostat where high vacuum of the order of 10^{-6} mbar is maintained to annihilate thermal convection. Additionally, radiation shield and multi-layer insulation are employed to enclose the PHP thereby inhibiting radiation heat in-leak, which can be of the order of several watts if not intercepted.

These PHPs have cryocoolers connected to the condenser for the cold source. As a result, maximum performance capacity of cryogenic PHPs is at the moment limited by the cryocooler capacities provided by the manufacturers. This necessitates the optimization of the performance of cryogenic PHPs based on the geometric dimensions.

The present study focuses on development of a single cryogenic PHP that can operate with two working fluids. The target application is High-Temperature Superconducting (HTS) magnet that can operate around 20-30 K but would produce high magnetic field at helium temperature [7, 8]. The main idea is use the same PHP to permit the superconducting magnet to work at neon and helium temperature (27 K and 4 K respectively at saturation condition and 1 atm. pressure). These cryogenic fluids are chosen for working temperature range and safety reason (no hydrogen). The design for the capillary tube diameter for neon is obtained from the classical Bond number criterion [9-11]. Accordingly, the PHP is fabricated from a 1 mm inner diameter tube that equates to Bo ≈ 2.5 [12-13]. In the goal of studying large Bond number PHP performance, the same PHP has been tested in helium [14]. This tube size renders a relatively very high Bond number of 12 if helium is employed. This work presents the experimentally measured thermal and hydraulic performance of the same cryogenic PHP operational with both neon and helium in horizontal and vertical orientation and at varying filling ratios.

2. Cryogenic PHP design

The PHP tube is made of stainless steel SS316L and is wound between the evaporator and condenser in 10 turns. The total length of the PHP tubing is around 8.5 m with only one soldered connection at the T-joint as shown in Figure 1. This T-joint connects the PHP to the feeding tube. The overall PHP length is 0.44 m long with an adiabatic part of 0.2 m. The tubing wound is only 0.4 m long, so the bends are completely embedded in the evaporator and condenser (depicted in Figure 1). The condenser and evaporator, made of oxygen free electronic (OFE) copper, are identical in length with 0.12 m and are specifically machined to embed the PHP tubes. Details of the cryogenic PHP have been specified in Table 1.

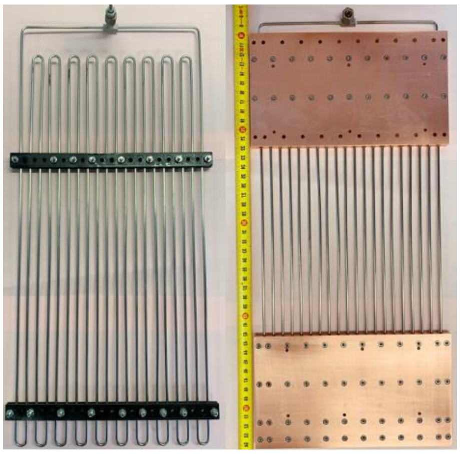

Figure 1. Pictures of the tubing alone (left) and with the evaporator and condenser (right).

Table 1. Specifications of the fabricated cryogenic PHP.

Working fluids (condenser temperature)	Neon (27.1 K) Helium (2.3-5.1 K)
PHP tube inner diameter	1 mm
Number of PHP tubes	20
PHP tube material	SS316L_ann
Projected PHP tube length	0.40 m
Projected overall length	0.44 m
Length of PHP embedded in condenser/evaporator	0.10 m
Condenser/evaporator material	OFE copper
Condenser/evaporator length	0.12 m
Adiabatic part length	0.20 m

3. Experiment test-rig

In order to experimentally investigate the cryogenic PHP, a test-rig has been developed in-house. 3D rendering of the cryostat is shown in Figure 2. The two-stage Gifford-McMahon cryocooler (Make: Sumitomo, Model: RDE 418-D4 4 K) at the condenser provides a maximum cooling capacity of 18 W for neon and 1.8 W for helium temperature range (@ 50 Hz). Flexible Kapton thermofoil heaters are glued onto the evaporator to stimulate the heat load. Specialized cryogenic low temperature sensors (Cernox®) record the temperature evolution of the condenser and the evaporator while a room pressure transducer located at the entry of the gas feedthrough pipe displays global pressure of the PHP.

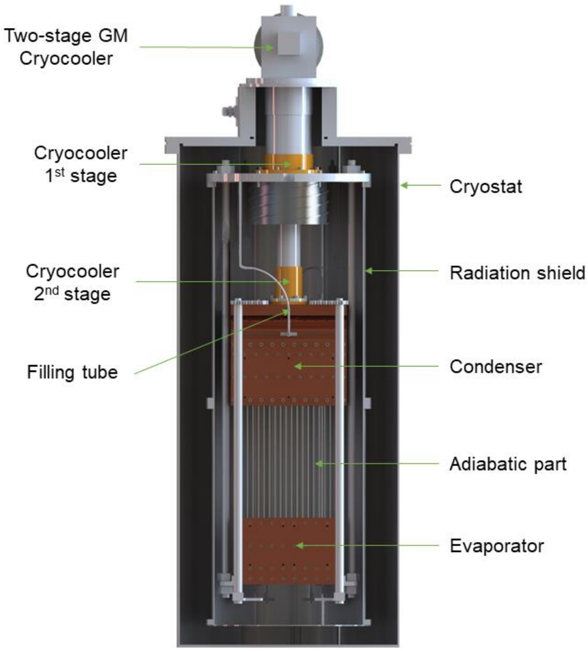

Figure 2. 3D rendering of cryostat for experimental testing of cryogenic PHP.

To intercept the room radiation, radiation shield combined with fifteen layers of superinsulation are thermally connected to the first stage of the cryocooler which is at around 50 K. The PHP itself is wrapped around superinsulation to minimize parasitic heat load that are in the order of ~33 mW and for neon and ~50 mW for helium temperatures. Another heat load that must be inhibited is the incoming heat in-leak from the wiring running between the room temperature feedthrough and cryogenic instrumentation. The wires, therefore, have larger length (few meters long) and thermalized intermittently resulting in heat in-leak of ~40 mW for neon and ~310 mW for helium respectively.

External to the cryostat (Figure 2), the test-rig consists pumping units for vacuum insulation and

PHP filling ratio adjustment, a data acquisition system and a gas filling equipment for both fluids as pictorially shown in Figure 3. The filling ratio (FR), defined as the ratio of the volume of liquid to the total PHP volume, is adjusted via a controlled pressure buffer fed by the gas reserve. The rig also allows changing the orientation of the cryostat from vertical to horizontal and vice-versa for both fluids. Some of the intrinsic fluid properties of neon and helium have been enlisted in Table 2.

Figure 3. Picture of the test-rig with the cryostat in horizontal orientation (top). Pumping system and the two gas buffers (left center), DAQ (right center) and gas reserves (right).

Table 2. Thermophysical properties of neon and helium.

Working fluid	Neon	Helium
Saturation temperature*	27.1	4.22
Critical temperature (K)	44.4	5.2
Critical pressure (bar)	26.53	2.27
Freezing temperature (K)	24.5	< 2
Freezing pressure (bar)	0.43	25.3
Density liquid (kg/m^3)**	1207	125
Density vapor (kg/m^3)**	9.58	16.8

* at atmospheric pressure
** at saturation and atmospheric pressure

The foremost task is to cool-down the PHP from room temperature to the desired cryogenic temperature. As the cryocooler is turned on, the PHP condenser takes about 8 hours to reach low temperatures while the evaporator takes few days (owing to the SS316L adiabatic part). The cryostat vacuum is maintained in the range of 10^{-6} mbar. Another flexible Kapton thermofoil heater is added on the cryocooler second stage so that its temperature can be controlled when neon is employed in the PHP. Once all the equipment within the cryostat has reached steady cryogenic temperatures, the PHPs are ready to be filled with the working fluid.

4. Results and Discussion

The tests are commenced with neon as the working fluid – first in vertical orientation having bottom heating mode followed by horizontal orientation. Same PHP configuration is then tested with helium as the operating fluid. The PHP thermo-hydraulic performance is mapped for different filling ratios and at varying evaporator heat load (0-20 W for neon and 0-1.5 W for helium).

For the first test set of neon PHP, the condenser temperature is regulated at 27.1 K (- 246.05 °C) – which corresponds to the saturation temperature of neon at atmospheric conditions. Several FRs in range of 10% to 90% are tested with systematic addition of evaporator heat load (each step held for 30 minutes).

The temperature of the evaporator and the global pressure are seen to rise with increase in the evaporator heat load. Figure 4 (a) and 4 (b) illustrate sample time-evolution profiles of the experimentally recorded temperature difference between evaporator and condenser (ΔT) and the global pressure respectively for neon PHP with FR of 20%, 40% and 60% both in vertical and horizontal orientation.

Below FR of 20%, dry-out of the PHP is observed. Lower is the FR, smaller is the heat load at which the dry-out occurs. Horizontally oriented, dry-out occurs at relatively lower heat loads with the same FR values as of vertical orientation. Above FR of 20%, this heat pipe is able to transfer up to 18 W before reaching the maximum extraction power of the cryocooler. However, at few instances of higher heat load with higher FR, the pressure reaches above the mechanical safety pressure limit which is when the test is immediately terminated.

It can be seen from Figure 4 (a) that at no evaporator heat load, the PHP condenser and evaporator are in equilibrium. Their temperature difference is in the order of ~40-120 mK. During the functional range of up to 18 W, depending on the PHP orientation, a maximum ΔT of 6 K is recorded. Beyond 18 W, cryocooler is unable to regulate the condenser temperature and its temperature rises rapidly reflecting a drop in ΔT. In regards to the global pressure, it rises to 2.5 times that of the atmospheric pressure.

Comparing the performance of the neon PHP between its vertical and horizontal placement, for same FR and evaporator heat load, the PHP evidentially maintains a higher ΔT in horizontal orientation than vertical. Likewise, the PHP oscillations are more distinctly seen in horizontal orientation.

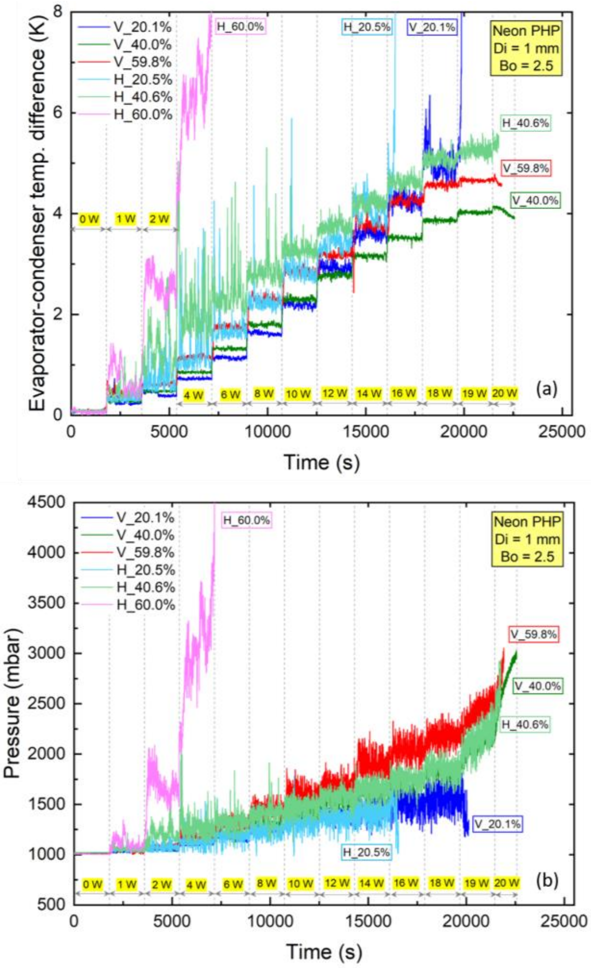

Figure 4. Time-evolution of **(a)** evaporator-condenser temperature difference **(b)** global pressure across the neon PHP as a function of evaporator heat load, filling ratio and orientation (V=Vertical and H=Horizontal).

Literature review reveals that few works have experimentally reported a functional cryogenic pulsating heat pipe at diameters above that of the critical diameter based on the Bond number criterion [3-5, 15-18]. The diameters corresponds to Bond number values in the range of 5 to 6 [14]. This prompted the authors' interest in exploring the functionality of cryogenic PHPs with relatively high Bond number. Using the PHP diameter of 1 mm with helium renders a Bond number value close to 12. Initial trial tests conducted with helium PHP in vertical orientation showcased it to be indeed operational. Furthermore, the helium PHP was also observed to function in horizontal orientation. Systematic tests were thereafter conducted at various FRs. Figure 5 (a) and 5 (b) presents the time-evolution curves of evaporator-condenser temperature difference (ΔT) and the global pressure for helium PHP both in vertical and horizontal orientation depicted at few FRs (20%, 35% and 65%).

As the cryocooler second stage can attain a lowest temperature of 2.3 K (- 270.85 °C), the condenser temperature is not regulated for testing the PHP with helium. Its cooling capacity in this temperature range is also significantly lower than that of neon which is why the imposed evaporator heat load range is only until 1.5 W. From no load condition, the heat load is gradually increased by 0.1 W and held constant for 30 minutes. Beyond 1.0 W, each heat load is imposed for 15 minutes. Both the condenser as well as the evaporator temperature rise with the gradual addition of evaporator heat load. The PHP is observed to re-adjust itself at larger evaporator-condenser temperature difference and pressure for higher heat load (Figure 5).

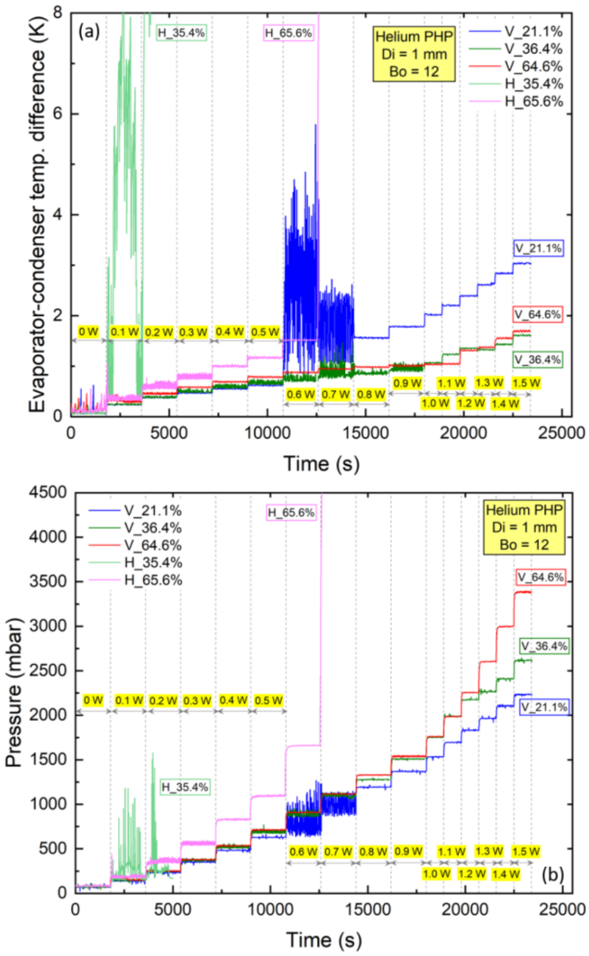

Figure 5. Time-evolution of **(a)** evaporator-condenser temperature difference **(b)** global pressure across the helium PHP as a function of evaporator heat load, filling ratio and orientation (V=Vertical and H=Horizontal).

The helium PHP also undergoes dry-out at FRs below 20% in vertical orientation. Around FR of 20%, sudden large amplitude oscillations are recorded (at 0.6 W and 0.7 W) in which the fluid in the evaporator is seen to oscillate between the super-critical and saturation/superheated states of helium. This peculiar behavior is validated by multiple repeatability tests conducted on different days. It has also been found by other authors [19, 20] that have experimentally tested helium PHP but with tube diameter satisfying the Bond number criterion of Bo < 4. At all other FRs up to 90%, helium PHP is operational and does not experience dry-out.

However, for heat load from 1.0 W, the evaporator temperature or the global pressure (or both) rise above the helium supercritical temperature and pressure values while the condenser remains in the saturation region. Even so, at some instances, the characteristic pulsations of PHP are recorded and it still successfully transfers heat. This is again similar to the characteristics reported by other works on helium PHP where the Bond number criterion is respected [19-22]. Even for some room-temperature fluids like ethanol [23] and FC-72 [24], the transition to supercritical states has been observed – but under micro-gravity!

In horizontal orientation, the PHP fails to start until 35% FR (this is why there is no data for H_20% in Figure 5) – in which case too the PHP sees a quick dry-out at just 200 mW of heat load. Furthermore, unlike the vertical orientation in which the PHP operates until 1.5 W of evaporator heat load, horizontally a maximum of 1.0 W could be imposed at 55% FR [14]. It is observed to function in supercritical state at much lower heat loads than when operated vertically.

The experimentally obtained thermal performance data for neon as well as helium PHP is expressed in terms of thermal resistance which is evaluated as the ratio of evaporator-condenser temperature difference and the imposed evaporator heat load. This has been depicted graphically in Figure 6 against varying evaporator heat load for both neon and helium PHP oriented vertically and horizontally.

For the fabricated PHP geometry and neon as the working fluid, the lowest thermal resistance has been found at maximum heat load of 18 W for FR of 40%. This is why, so as to highlight the difference, data for 40% FR has been showcased for all cases except for helium-horizontal for which the data was not available at 40%. Instead, it has been presented at 35% and 45% FR.

It can be evidently seen from Figure 6 that neon PHP has thermal resistance quantitatively in lower range than the same diameter helium PHP (0.20 – 0.72 K/W vs 0.91 – 24 K/W respectively). For both working fluids, PHP in horizontal orientation is observed to have higher thermal resistance than when placed in a gravity-assisted vertical orientation. Furthermore, while the neon PHP always functions within the saturation regime, the helium PHP is seen to enter supercritical state (marked in Figure 6) at several instances and still operate.

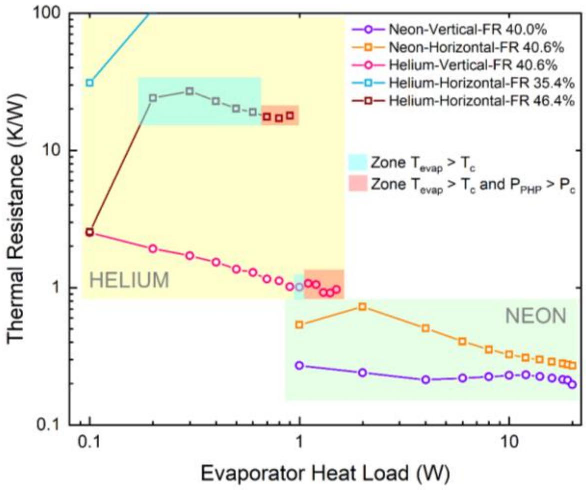

Figure 6. Thermal resistance against homogenous evaporator heat load for mono-sized PHP operational with both neon (shaded green zone) and helium (shaded yellow zone) at FR of approximately 40%. For helium, zone where only the evaporator temperature and where both pressure as well as the evaporator temperature are in supercritical regime are marked.

It is interesting to note that neon-vertical, neon-horizontal and helium-vertical have thermal resistance values of 0.27 K/W, 0.53 K/W and 1.01 K/W respectively at 1.0 W of evaporator heat load. In other words, neon-horizontal has 2 times and helium-vertical has 3.7 times higher thermal resistance than that of neon-vertical for same PHP configuration, filling ratio and evaporator heat load.

On another note, successful long duration tests stretching several hours (~100 hours for neon PHP and ~65 hours for helium PHP) with constant filling ratio and evaporator heat load have been conducted [13,14]. The PHP pressure and evaporator temperature are observed to be in steady range throughout the test duration. This demonstrates the stability and reliability of this cryogenic PHP in long run.

5. Conclusions

This work establishes that a helium-based cryogenic PHP is operational even when the Bond number considerably overshoots the conventionally-set limit value of 4. This PHP, initially designed to meet Bond number criterion for neon as the working fluid, exhibits the same characteristics as those observed generally in helium PHPs. However, the exact effect is difficult to ascertain and needs visualization aide to determine when and if the PHP is in 'true' pulsating mode. This is not a straightforward task in cryogenics owing to the complexities associated in barring the undesired heat in-leaks. Similar large diameter tests must be conducted with other cryogens as well in order to explore usage of a single PHP working with several cryogenic fluids thereby attracting more applications of cryogenic PHPs.

6. ACKNOWLEDGEMENTS

Authors would like to thank Département des Accélérateurs, de la Cryogénie et du Magnétisme (DACM) of IRFU at CEA Paris-Saclay for internal R&D grant 2019.

References

[1] M. Barba, R. Bruce, A. Bonelli, and B. Baudouy, Experimental study of large-scale cryogenic pulsating heat pipe. IOP Conference Series: Materials Science and Engineering, 2017. 278: 012156.
[2] R. Bruce, M. Barba, A. Bonelli, and B. Baudouy, Thermal performance of a meter-scale horizontal nitrogen pulsating heat pipe. Cryogenics, 2018. 93: p. 66-74.
[3] M. Barba, R. Bruce, F. Bouchet, A. Bonelli and B. Baudouy, Thermal study of one-meter long neon cryogenic pulsating heat pipe. IOP Conference Series: Materials Science and Engineering, 2019. 502: 012152.
[4] M. Barba, R. Bruce, F. Bouchet, A. Bonelli, and B. Baudouy, Effects of filling ratio of a long cryogenic pulsating heat pipe. Applied Thermal Engineering, 2021. 194: 117072.
[5] M. Barba, R. Bruce, F. Bouchet, A. Bonelli, and B. Baudouy, Effect of the thermo-physical properties of the working fluid on the performance of a 1-m long cryogenic horizontal pulsating heat pipe. International Journal of Heat and Mass Transfer, 2022. 187: 122458.
[6] J.M. Pfotenhauer, Recent developments in cryogenic pulsating heat pipes. ES Energy & Environment, 2019. 3: p. 1-3.
[7] P. Fazilleau, X. Chaud, F. Debray, T. Lécrevisse, and J.B. Song, 38 mm diameter cold bore metal-as-insulation HTS insert reached 32.5 T in a background magnetic field generated by resistive magnet. Cryogenics, 2020. 106: 103053.
[8] M. Durante, P. Fazilleau, T. Lecrevisse, C. Lorin, M. Segreti, and O. Tellier, Overview of HTS accelerator magnet developments at CEA Saclay. IEEE Transactions on Applied Superconductivity, 2024. 34(5): 4002905.
[9] S. Khandekar, Thermo-hydrodynamics of closed loop pulsating heat pipes, Doctoral dissertation, IKE Germany, 2004.
[10] E.T. White, and R.H. Beardmore, The velocity of rise of single cylindrical air bubbles through liquids contained in vertical tubes. Chemical Engineering Science, 1962. 17: p. 351-361.
[11] M. Marengo, and S. Nikolayev, Pulsating heat Pipes: Experimental analysis, design and applications. In Encyclopedia of Two-Phase Heat Transfer and Flow IV Volume 1: p. 1-62 (World Scientific, Singapore, 2018).
[12] T. Dixit, G. Authelet, C. Mailleret, F. Gouit, and B. Baudouy, Experimental investigation of vertical neon pulsating heat pipe for superconducting magnet cooling application. IOP Conference Series: Material Science and Engineering, 2022. 1240: 012076.
[13] T. Dixit, G. Authelet, C. Mailleret, F. Gouit, V. Stepanov, and B. Baudouy, High performance and working stability of an 18 W class neon pulsating heat pipe in vertical/horizontal orientation. Cryogenics, 2023. 132: 103670.
[14] T. Dixit, M. Daval, G. Authelet, C. Mailleret, F. Gouit, V. Stepanov, and B. Baudouy, Oversized diameter helium pulsating heat pipe. Applied Thermal Engineering, 2024. 251: 123613.
[15] K. Natsume, T. Mito, N. Yanagi, H. Tamura, T. Tamada, K. Shikimachi, N. Hirano, and S. Nagaya, Heat transfer performance of cryogenic oscillating heat pipes for effective cooling of superconducting magnets. Cryogenics, 2011. 51: p. 309-314.
[16] T. Mito, K. Natsume, N. Yanagi, H. Tamura, T. Tamada, K. Shikimachi, N. Hirano, and S. Nagaya, Achievement of high heat removal characteristics of superconducting magnets with imbedded oscillating heat pipes. IEEE Transactions on Applied Superconductivity, 2011. 21(3): p. 2470-2473.
[17] K. Natsume, T. Mito, N. Yanagi, H. Tamura, T. Tamada, K. Shikimachi, N. Hirano, and S. Nagaya, Development of cryogenic oscillating heat pipe as a new device for indirect/conduction cooled superconducting magnets. IEEE Transactions on Applied Superconductivity, 2012. 22(3): 4703904.
[18] K. Natsume, T. Mito, N. Yanagi, and H. Tamura, Development of a flat-plate cryogenic

oscillating heat pipe for improving HTS magnet cooling. Physics Procedia, 2013. 45: p. 233-236.
[19] L.D. Fonseca, J. Pfotenhauer, and F. Miller, Results of a three evaporator cryogenic helium pulsating heat pipe. International Journal of Heat and Mass Transfer, 2018. 120: p. 1275-1286.
[20] M. Li, L. Li, and D. Xu, Effect of filling ratio and orientation on the performance of a multiple turns helium pulsating heat pipe. Cryogenics, 2019. 100: p. 62-68.
[21] D. Xu, L. Li, and H. Liu, Experimental investigation on the thermal performance of helium based cryogenic pulsating heat pipe. Experimental Thermal and Fluid Science, 2016. 70: p. 61-68.
[22] M. Li, L. Li, and D. Xu, Effect of number of turns and configurations on the heat transfer performance of helium cryogenic pulsating heat pipe. Cryogenics, 2018. 96: p. 159-165.
[23] S. Jun, and S.J. Kim, Experimental investigation on the thermodynamic state of vapor plugs in pulsating heat pipes. International Journal of Heat and Mass Transfer, 2019. 134: p. 321-328.
[24] M. Mameli, A. Catarsi, D. Mangini, L. Pietrasanta, N. Michè, M. Marengo, P.D. Marco, and S. Filippeschi, Start-up in microgravity and local thermodynamic states of a hybrid loop thermosyphon/pulsating heat pipe, Applied Thermal Engineering, 2019. 158: 113771.

Paper ID 022(S2C)

Development of Cryogenic Methane Constant Conductance Heat Pipe

Sandeep Hatte[1*], Kuan-Lin Lee[1], and Calin Tarau[1]

[1]Advanced Cooling Technologies, Inc., Lancaster, PA, 17601

**Corresponding author email address: sandeep.hatte@1-act.com*

Abstract

Cryogenic heat pipes have been of great interest for thermal management of space applications involving cooling and thermal control of optical surfaces, infrared scanning systems, large superconducting magnets, etc. However, the development of cryogenic heat pipes is more challenging than ambient temperature or liquid metal heat pipes, due to the relatively low surface tension of candidate working fluids and their high-pressure values that present the safety challenges during the storage. In this study, the design, fabrication, and demonstration of a constant conductance heat pipe (CCHP) that uses methane as the working fluid is conducted to carry a design power of 15 Watts in the operational cryogenic temperature range of 100 – 140 K. Funded by NASA Goddard Space Flight Center (GSFC), Advanced Cooling Technologies Inc (ACT) has developed a methane CCHP using axial grooved structures for efficient capillary pumping of otherwise low surface tension methane working fluid. The thermal performance testing demonstrated that the cryogenic heat pipe can carry about 3 times the required power, i.e., 45 Watts, for up to 0.762 cm (0.3”) of inclination against gravity, about three times the space qualification of 0.254 cm (0.1”). Steady isothermal heat pipe operations were observed with less than 5 Kelvin temperature drop for a 1.42-meter (56”) length heat pipe.

Keywords: Cryogenic heat pipe; methane; thermal management; grooves

1. INTRODUCTION

Various space applications and instruments require efficient thermal management at low (cryogenic) temperature levels.[1-5] Therefore, the development of cryogenic heat pipes is of great interest. Primary challenges in the design of cryogenic heat pipe based thermal management system is the high pressures of the working fluids at room temperature or storage temperatures. In addition, popular cryogenic working fluids such as nitrogen, methane, etc., have low surface tension thereby offering additional challenges particularly in space configurations where the liquid return to evaporator is governed by the capillary action. As a result, significant attention has been given to wick structures that enable efficient pumping of cryogenic liquids. Existing studies[6,7] have identified the lack of appropriate wick structure designs to efficiently pump low surface tension fluids such as methane, nitrogen, argon, etc. as the most critical aspect of cryogenic heat pipe development. In this NASA GSFC-funded work, ACT developed a cryogenic constant conductance heat pipe using *axial* groove structures and methane as a working fluid. Using ACT’s proprietary groove design, detailed investigation into the performance of methane constant conductance heat pipe is conducted.

2. DESIGN AND FABRICATION

Figure 1 shows the design of the Methane CCHP and associated components. The design requirements identified for the development of methane CCHP are as follows:

1. Operating temperature: 100 – 140 K
2. Minimum power carrying capacity: 15 Watts.
3. Steady state operations at space orientation i.e., 0.254 cm inclination against gravity during ground testing.
4. Heat pipe dimensions: 1.1 meters (44”) evaporator and 0.3 meters (12”) condenser with no adiabatic section.
5. Storage temperature of about 333 K
6. Factor of safety of 4 or higher

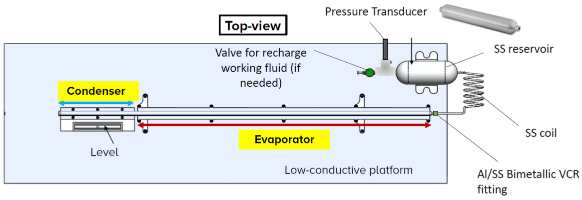

Figure 1. Schematic representation of methane CCHP design and associated components

Figure 1 shows that the aluminum envelope of methane CCHP is connected to a stainless-steel reservoir via a stainless-steel to aluminum bimetallic Vacuum Coupling Radiation (VCR) fitting. Higher operating pressures of methane gas at ambient and storage temperatures require the addition of a reservoir. Figure 1 shows a stainless-steel reservoir used to accommodate the higher pressure of methane gas at room temperature and temperature values suitable for transport. Assuming a storage temperature of 333 K, reservoir sizing is determined by the maximum pressure in the system.

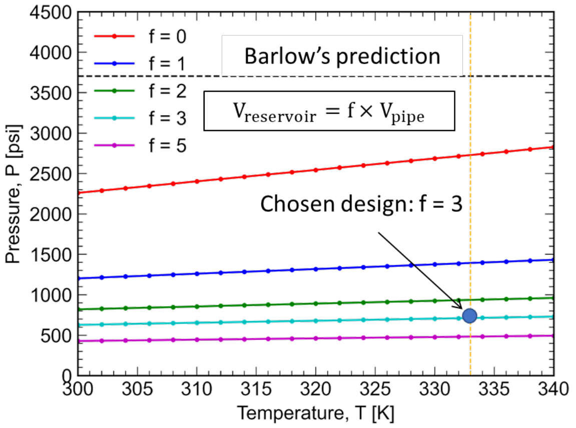

Figure 2. Reservoir sizing.

Figure 2 shows the variation of pressure in the system with maximum temperature for various sizes of the reservoir. The reservoir size is decided by designing the system for a factor of safety of 4. The maximum allowable pressure in the system is calculated using Barlow's prediction. For a maximum temperature of 333K, the maximum allowable pressure in the system is calculated to be around 3700 psi. Accordingly, a reservoir size with volume that is three times the volume of heat pipe, is chosen to generate a maximum pressure in the system to be below 750 psi, thereby achieving a factory of safety of 4 or higher.

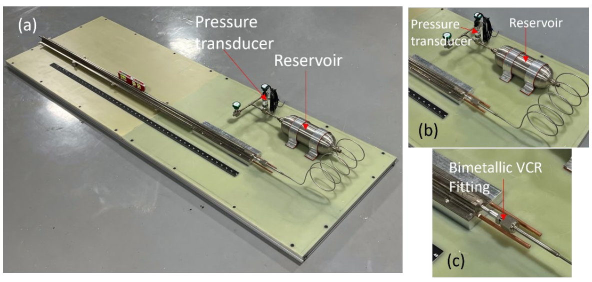

Figure 3. Fabrication and assembly of methane CCHP system.

Figure 3 shows the as-fabricated methane CCHP with associated components. The heat pipe side is made of aluminum with a bimetallic fitting in between to connect to the components made of stainless steel. A pressure transducer is installed to monitor pressure at all times, during testing and storage. The heat pipe assembly is positioned on a non-conductive platform to minimize conductive heat losses.

3. RESULTS AND DISCUSSION

The performance characterization of the methane CCHP was conducted by monitoring the temperature profiles on the heat pipe assembly.

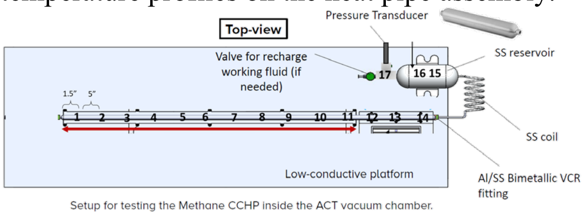

Figure 4. Thermocouple map

Figure 4 shows the relative position of all the thermocouples on the heat pipe system. A total of 11 thermocouples are located on the evaporator, three on the short condenser, and three on the reservoir and pressure transducer. During testing, it was observed that reservoir and pressure transducer remain relatively warm with temperature above 288 K due to lack of working fluid and very low thermal conductivity of the SS coil.

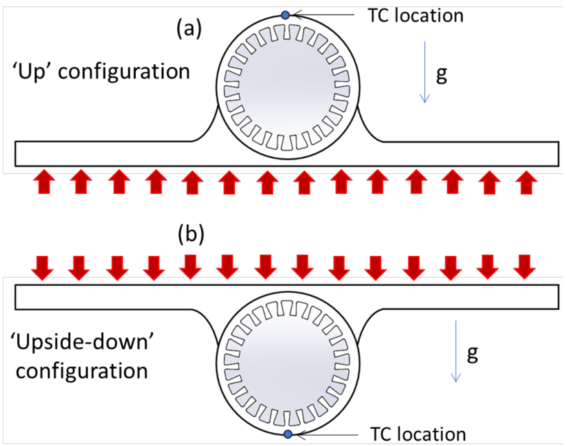

Figure 5. two configurations studied: 'up' and 'upside down'.

The testing was conducted for two configurations of the heat pipe, namely, up and upside down. These two configurations enable us to characterize the effects of potential puddle formation due to de-wetting of the grooves, as discussed later.

During testing, a number of parameters are varied to study the performance of the methane heat pipe. Given the primary objective of the study is to develop methane CCHP for space applications, the testing is conducted at several inclinations against gravity. It is noted that in this paper, a select set of results are discussed in which the values of inclination against gravity are 0.1° (i.e., ~0.1"), 0.2° (i.e., ~0.2"), and 0.4° (i.e., ~0.4"). In an against gravity inclination case, the condenser end is below the evaporator end. For reference, it is noted that inclination against gravity of 0.1" corresponds to the space qualification. Next, a working fluid (methane) amount with 2% margin of undercharged heat pipe is used. For a cryogenic heat pipe with low surface tension working fluid such as methane, the possibility of puddle formation due to excess liquid is high. To avoid this situation, an undercharged heat pipe configuration is suitable. For each set of parameters, both the up and upside down configurations are testes. For each test, the power is varied from 10 Watts to 75 Watts. For each case transient variation of temperature is noted along with maximum temperature difference on the heat pipe.

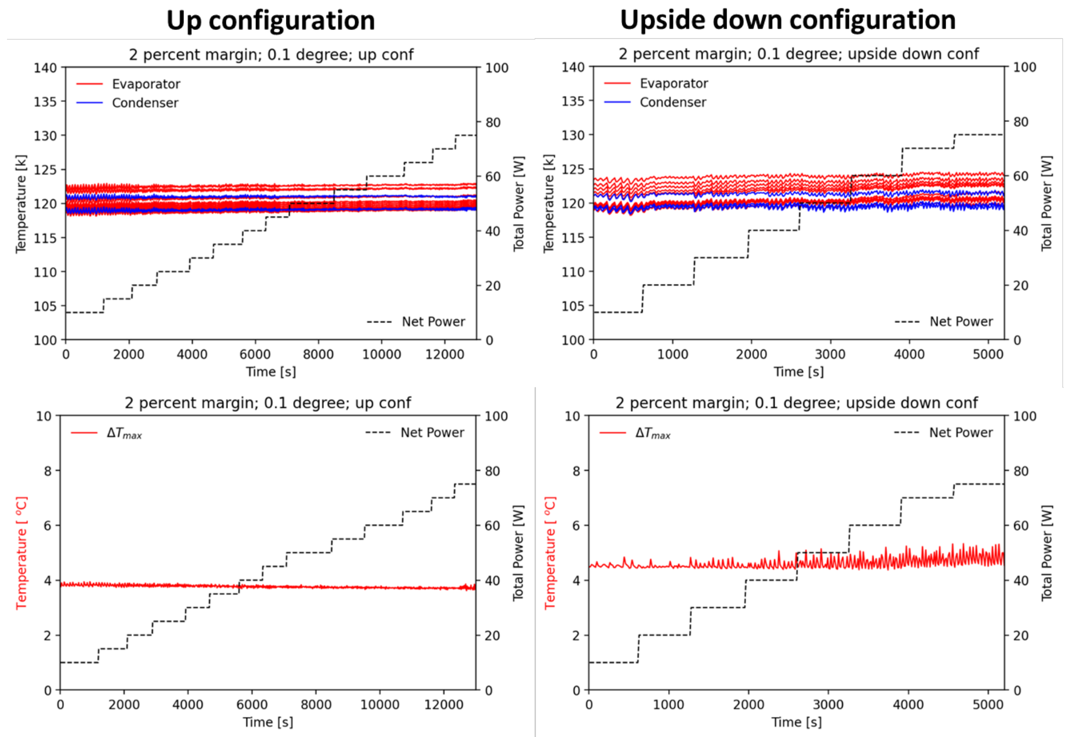

Figure 6. Performance of methane CCHP for 0.1° inclination against gravity orientation.

Figure 6 shows the case of 0.1° inclination against gravity with both up and upside-down configurations. It is evident from Figure 6 that the evaporator and condenser temperatures are close to 120K. For all power values covered in the test, the maximum temperature difference any two locations on the heat pipe are less than 5K. For a 56" long heat pipe a maximum temperature difference of less than 5K indicates an isothermal performance. For both up and upside-down configuration, the heat pipe is working with minimum temperature gradient between the evaporator and condenser sections of the heat pipe. However, the maximum temperature difference between any two locations on the heat pipe is higher for the case of upside-down configuration compared to up configuration. The slight variation in the maximum temperature difference indicates towards the puddle formation. To elucidate the effects of puddle formation of the working fluid, the inclination against gravity is increased as follows.

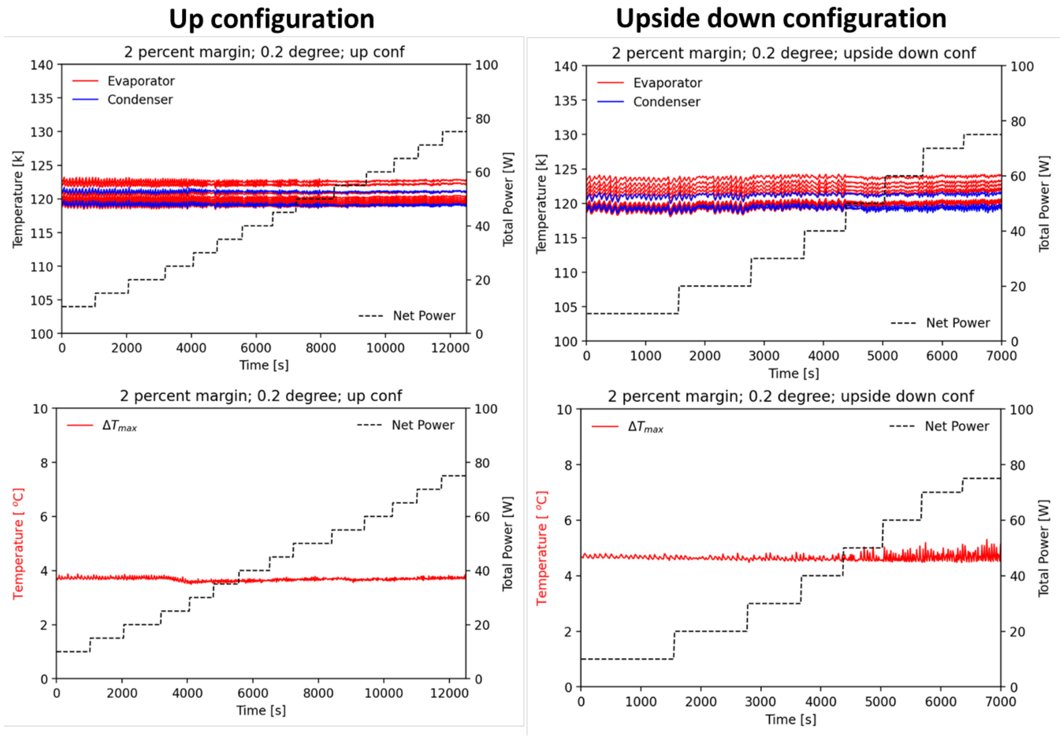

Figure 7. Performance of methane CCHP for 0.2° inclination against gravity orientation.

For the case of 0.2° inclination against gravity, the performance of heat pipe remains same with close to isothermal behavior and a maximum temperature difference of less than 5K for both up and upside-down configuration. However, the maximum temperature difference on the heat pipe is greater for upside-down configuration than in up configuration. The continued similar difference in the maximum temperature difference on the heat pipe is an indication of potential puddle formation. To gather more information, and to highlight the effects of puddle formation, the inclination angle is increased to 0.4°.

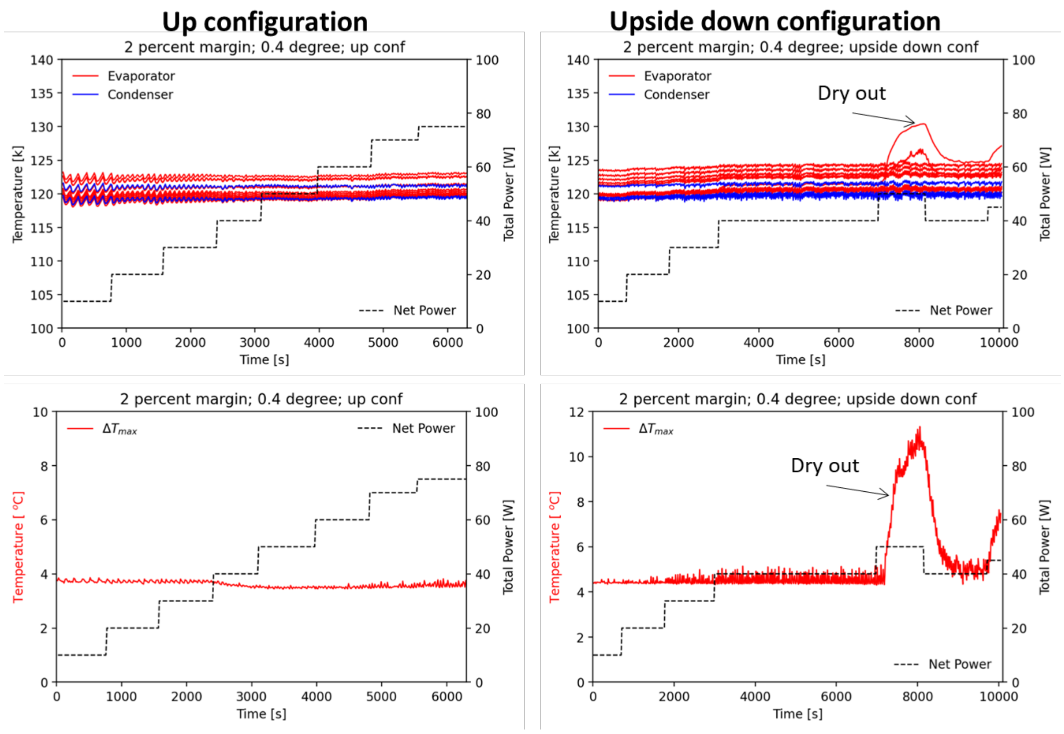

Figure 8. Performance of methane CCHP for 0.4° inclination against gravity orientation.

Figure 8 shows the variation of temperature with time for various power increments. For the up configuration at 0.4 ° inclination of the pipe against gravity, isothermal conditions with maximum temperature difference of less than 5K are observed. This consistent performance in comparison to lower inclination angles indicates normal operations. However, in the upside-down configuration, a local dry out is observed at about 50 Watts power input. Figure 8 shows that temperatures at two locations on the evaporator are rising with time uncontrollably. In addition, thermocouple 1 begins showing an abrupt rise in temperature followed by thermocouple 2. Both thermocouples are located at the beginning of the evaporator. In a local dry out, a section of the evaporator is dried of liquid leading to superheated region and sudden rise in temperature. The local dry out is mitigated by reducing the power back to 40 Watts when the thermocouples 1 and 2 are replenished with liquid and normal operations resume. The difference in performance between the upside-down configuration and up configuration indicates higher chances of puddle formation.

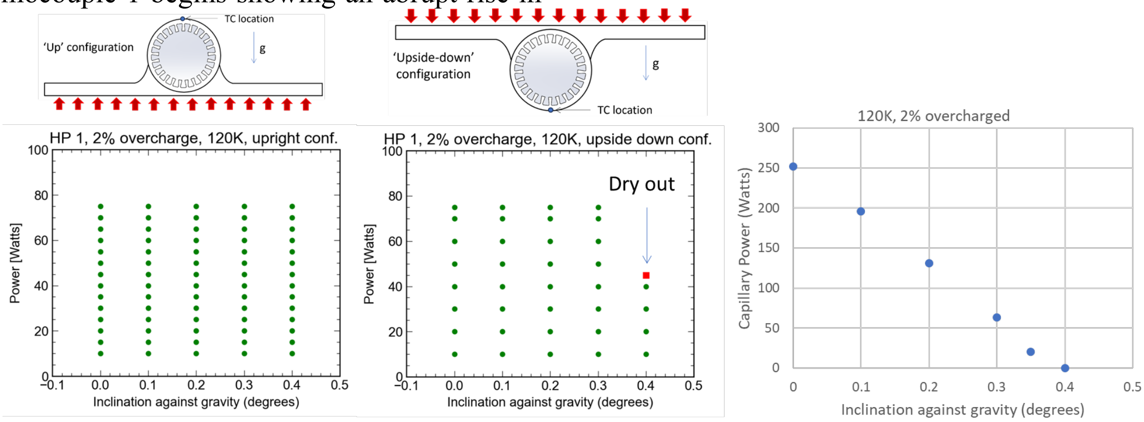

Figure 9. Summary of methane CCHP performance and comparison against predictions.

Figure 9 offers a summary of the methane CCHP tests conducted at various powers, inclinations, and two configurations. The overall performance of the methane CCHP is compared against a theoretical prediction. It is seen from Figure 9 that for the case of 0.4° inclination against gravity, the theoretical prediction indicates that the heat pipe should not carry any power. However, the pipe carried about 75 Watts of power without drying out in up configuration, and up to 40 Watts of power before drying out in upside-down configuration. Such significant difference points to two possibilities: 1. Partial drainage of grooves leading to puddle formation, 2. Huge errors in the theoretical predictions.

In figures 6, 7, and 8, insignificant variation of temperature with time for increasing power is investigated through numerical analysis. The evaporator and condenser sections of the heat pipe are analyzed by conducting numerical simulation. Figure 10 shows the numerical simulation setup and discusses the results in terms of temperature variation with time for various power input values. It is evident from Figure 10 that due to lower heat flux values, the rise in temperature with time as the power increases in insignificant. The non-dominating temperature rise can be verified by overlapping the experimental performance in the results obtained from numerical analysis, as shown in Figure 10.

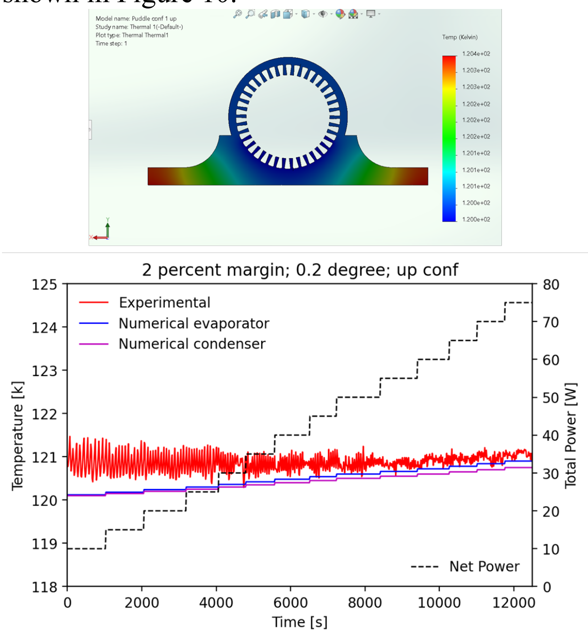

Figure 10. Numerical simulation of temperature rise in evaporator and condenser sections.

The effects of puddle formation that affects the performance of methane heat pipe is illustrated through the following figure. Assuming complete drainage of the grooves, the condenser end is filled with working fluid and evaporator end shows multiple grooves drained of liquid.

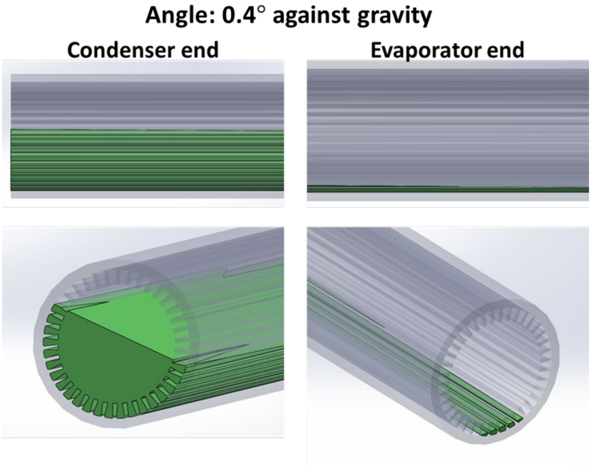

Figure 11. Puddle formation resulting from complete drainage of grooves.

Such as configuration with complete drainage of grooves leading to the formation of puddle could significantly hinder the performance of cryogenic heat pipe. Further investigation, possibly with significant undercharging of heat pipe, and careful considerations of the effects of puddle formation on the performance of heat pipes are needed.

4. CONCLUSIONS

In this study, Advanced Cooling technologies, Inc. demonstrated design, fabrication, and detailed testing of a cryogenic constant conductance heat pipe (CCHP) that used methane as a working fluid. Using proprietary groove design, the performance of the methane CCHP is evaluated for various inclinations against gravity, various power input values, and two configurations namely up and upside-down. Through testing it was observed that the pipe operated with maximum temperature difference of less than 5K and carried about 75 Watts of power as opposed to the design requirement of 15 Watts. In addition, extensive testing revealed that there is a possibility of partial or complete drainage of working fluid leading to puddle formation.

5. ACKNOWLEDGEMENTS

ACT acknowledges the funding offered by NASA GSFC under contract 80NSSC23PA518 and support from program managers - Eric Silk and Howard Tseng. Justin Boyer and Eugene Sweigart helped with the fabrication and testing, along with support from ACT's production team.

References

[1] Gully, P., Mo, Q., Yan, T., Seyfert, P., Guillemet, L., Thibault, P., & Liang, J. (2011). Thermal behavior of a cryogenic loop heat pipe for space application. *Cryogenics*, *51*(8), 420-428.

[2] Lee, J., Kim, D., Mun, J., & Kim, S. (2020). Heat-transfer characteristics of a cryogenic loop heat pipe for space applications. *Energies*, *13*(7), 1616.

[3] Bai, L., Zhang, L., Lin, G., He, J., & Wen, D. (2015). Development of cryogenic loop heat pipes: A review and comparative analysis. *Applied Thermal Engineering*, *89*, 180-191.

[4] Peterson, G. P., & Compagna, G. L. (1987). Review of cryogenic heat pipes in spacecraft applications. *Journal of Spacecraft and Rockets*, *24*(2), 99-100.

[5] Shukla, K. N. (2015). Heat pipe for aerospace applications—an overview. *Journal of Electronics Cooling and Thermal Control*, *5*(01), 1.

[6] Beam, Jerry, PATRICK BRENNAN, and Mel Bello. "Design and performance of a cryogenic heat pipe experiment (CRYOHP)." In *27th Thermophysics Conference*, p. 2867. 1992.

[7] Peterson, G. P., and G. L. Compagna. "Review of cryogenic heat pipes in spacecraft applications." *Journal of Spacecraft and Rockets* 24, no. 2 (1987): 99-100.

Paper ID 024(S2A)

Advancements in Commercialization of Oscillating Heat Pipes

Corey A. Wilson[1*]

[1]*ThermAvant Technologies, Columbia, Missouri, USA*
**Corresponding author email address: Corey.Wilson@ThermAvant.com*

Abstract

Commercial adoption of oscillating heat pipes (OHPs) has been slow due to challenges in operational predictability and stability. Since 2007, ThermAvant Technologies has focused on developing manufacturing processes, operational modeling, and qualification testing for a wide range of OHP applications. These OHPs vary from small high-flux heat spreaders to over 1-meter long heat transporters and can serve as dual-purpose structural and thermal systems. The operational limits model was essential for creating a predictable design and was validated using extensive data from both ground and orbital testing, including an on-orbit experiment conducted between 2017 and 2019. In 2021, these efforts culminated in the integration of an OHP into a commercial satellite, marking a significant advancement in OHP technology for space-based thermal management solutions. This paper presents these advancements and discusses these commercial OHP applications.

Keywords: Oscillating Heat Pipe; Pulsating Heat Pipe; Commercialization; Heat Spreader; Heat Transporter

1. Introduction

The oscillating heat pipe (OHP), also called a pulsating heat pipe (PHP), was invented and patented in 1990 by Akachi [1–4]. Since then, substantial progress has been made in academia and industry to better understand OHP operating characteristics. Despite these advancements, commercialization remained limited until recently [5–10]. This hesitation stemmed from concerns over the OHP's predictable operating limits, operational stability, repeatability, and limited heritage.

Since 2007, ThermAvant Technologies has sustained focus on addressing these concerns regarding the OHP's commercial viability. Initial work focused on extensive testing of a wide range of OHPs, and developing manufacturing and modeling capabilities. This testing included an on-orbit experiment from 2017 to 2019 [11–15]. In 2018 ThermAvant began developing and delivering OHPs for integration into terrestrial, airborne, and on-orbit commercial systems and in 2021 the first commercial satellite using an OHP, developed by ThermAvant, was launched [16]. Over the years, the company has undertaken hundreds of demonstration, qualification, and system integration projects including over 10 orbital flight qualification campaigns.

These OHPs' sizes range in lengths from less than 2 cm to over 1 m and in thicknesses from less than 2 mm for thin, two-dimensional spreading to over 10 cm for more complex form factors with three-dimensional channel routing for heat transfer in all three planes. Dissipated powers managed by these OHPs vary from a few watts to several kilowatts.

As part of their commercial qualification, they have been designed to meet various industry standards such as ANSI/AIAA S-080A-2018 [17] and SMC-S-016 [18], and pass additional customer specific tests including mechanical and thermal shock, mechanical vibration, temperature cycling, high acceleration loading, aging, non-condensable gas injection, cold soaking, repeat cycle testing, long-duration testing, part-to-part performance consistency, and operational limits testing.

To date, ThermAvant has delivered over 5,000 OHPs, primarily for commercial aerospace and U.S. government end-uses, with over 1,000,000 hours of successful on-orbit operation. This paper presents ThermAvant's work on OHP design and manufacturing, OHP modeling, and OHP applications.

2. OHP Manufacturing

ThermAvant primarily develops flat-plate OHPs, as shown in Figure 1. These OHPs are highly customizable to meet customer specifications and can be manufactured with tight tolerances using standard metalworking techniques.

Figure 1. 3U OHP heat spreader with corner removed for inspection.

These OHPs are most commonly manufactured via computer numerical control (CNC) machining to create channels in individual plates of material. These channel plates are then stacked to form a complex three-dimensional channel path, after which the plates are hermetically joined to create a sealed monolithic structure. Finally, the external surfaces are machined into their final shape, and the working fluid is introduced.

This form factor offers high structural integrity, largely due to the frequent bridging of channel walls. As a result, the stiffness of the OHP is typically only 6% lower than a solid, channel-less version, while the modal frequencies increase by just 3–5%. Additionally, the internal channels reduce the overall density by 10–30% compared to a solid structure. These OHPs are typically made from aluminum to minimize mass while ensuring high thermal conductivity in the support structure.

This method allows ThermAvant to develop OHPs in a wide range of two-dimensional and three-dimensional geometries with integral mounting features, support structures such as isogrids, and coatings. In addition, this method allows for complex and precise channel routing predicted by the in-house OHP Limits of Operation model.

3. OHP Limits Of Operation Model

Many OHP models have been developed to predict operation and performance. For commercial development, a model that allows for rapid design iteration and optimization was essential. As a result, a model was created similar to the constant conductance heat pipe (CCHP) operational limits model to predict a set of operational limits for the OHP.

The initial version of this model was published in Drolen and Smoot defining the Bond number limit, sonic limit, swept length limit, and vapor inertia limit [19]. In addition to these limits, the viscous-temperature-difference contour is defined to predict the portion of operational temperature difference due to viscous losses. The startup limit was defined in a subsequent presentation [20]. The combined limits are shown in Figure 10 with the operational envelope defined as the region above the startup limit and below the sonic, vapor inertia, swept length, and bond number limits.

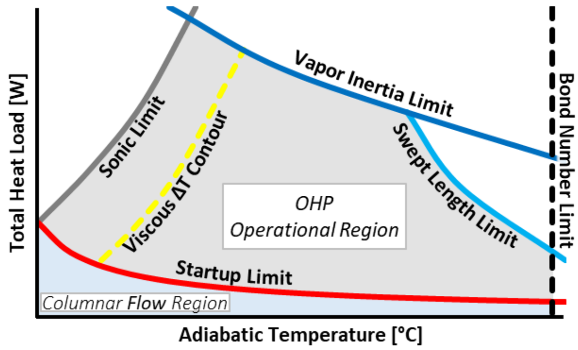

Figure 2. Example OHP limits of operation chart.

The Bond number limit is a well-established limit for the OHP that determines when the liquid no longer bridges the channel in a gravity field and instead forms a stratified flow [21–23]. In a constant gravitational field this limit defines the maximum operating temperature. This maximum operating temperature is the temperature at which the working fluid thermophysical properties for the surface tension, σ, and liquid and vapor densities ρ_l and ρ_v resolve the following equation,

$$D_h = 2.74\sqrt{\frac{\sigma}{g(\rho_l - \rho_v)}} \quad (1)$$

where D_h, is the hydraulic diameter of the channel and g is the OHP's acceleration.

The sonic limit occurs when the fluid velocity is choked at the speed of sound for the two-phase mixture. It is defined as,

$$Q_{sonic} = \frac{C_N N \pi D^2}{8\gamma\left[f\frac{\rho_l}{\rho_v} + (1-f)\right]\left(\frac{1}{\rho_v} - \frac{1}{\rho_l}\right)} \frac{{h_{fg}}^2}{\sqrt{c_v T_{sat}}} \quad (2)$$

where C_N is the number of condensers, N is the number of channels, γ is the evaporative fraction as further defined in Drolen et al. [24], f is the fill fraction, h_{fg} is the latent heat of vaporization, c_v specific heat at a constant volume, and T_{sat} is the saturation temperature. This limit is rarely encountered and has minimal experimental validation.

The startup limit is the inception of boiling in the OHP, when the incident heat flux is sufficient to create the necessary superheat at the wall to create nucleation in a flowing two-phase mixture. Once nucleation begins in the OHP, fluid flow is much more rapid and continuous. At heat loads below this limit, heat is transported by non-nucleating convective flow that transports significantly less heat than above the limit.

$$Q_{start} = \frac{\pi C_N N_h L_h}{2\beta\varepsilon\gamma \ln\left(\frac{r_{in}}{r_{in} - \delta}\right)} \quad (3)$$

where N_h is the number of heaters, L_h is the length of the heater, β is a startup figure of merit which is a function of the fluid properties , ε is the surface roughness, r_{in} is the channel inner radius, and δ is the liquid film thickness.

The vapor inertia limit is defined as when the vapor generation rate is high enough to allow vapor to penetrate the liquid slug resulting in annular flow,

$$Q_{vap} = \frac{1.924 N C_N r_{in} h_{fg}}{\gamma}\sqrt{\sigma\rho_v r_{in}(cos\theta_r - cos\theta_a)} \quad (4)$$

where θ_r is the receding contact angle and θ_a is the advancing contact angle.

The swept length limit is defined as when the nucleation frequency is too high preventing liquid from fully circulating through an evaporator channel. The swept length limit is a modifier on the vapor inertial limit resulting in reduced heat transport,

$$Q_{swept} = Q_{vap}\left[\frac{C_N U}{\alpha L_{htr} f}\right]^{1.35} \quad (5)$$

where U is the bulk flow speed, f is the frequency of nucleation, and α is the conduction correction factor when heat spreading occurs in the OHP.

In addition to these limits, the viscous flow losses in the OHP are also frequently a limiting factor for OHP operation. At lower temperatures, the viscous drag results in an added pressure head to the OHP which must be overcome by an increase in temperature rise across the OHP. When this added temperature difference exceeds the customer requirement or in a worst case scenario approaches the solid conduction of the base material, the OHP is no longer viable.

This model is continually being refined from the initial published framework. The limits models presented in this paper are from a more recent iteration of the model.

4. Limits Model Validation

The OHP limits of operation model was developed and validated with thousands of datasets collected from a wide range of OHP designs and test conditions. Two key experiments were selected from this larger collection to demonstrate the model's accuracy: the ASETS-II experiment for the swept length and vapor inertia limits, and the high flux OHP experiment for the startup limit.

The ASETS-II experiment was an important study for validating the swept length and vapor inertia limits in a range of operating conditions [13]. The experiment was conducted by the Air Force Research Laboratory (AFRL) using three OHPs developed by ThermAvant. The experiment aimed to assess the long-term on-orbit operation of the OHPs, validate their operational limits, and compare performance to on-ground horizontal operation. The testing included six months of on-ground evaluation before launch, followed by 780 days of on-orbit testing. All three OHPs performed as expected in orbit, demonstrating that horizontal on-ground operation is equivalent to on-orbit operation. Additionally, the operational limits and performance remained consistent throughout the entire testing period [11–14]. The complete dataset is available on the *NASA Physical Sciences Informatics (PSI) website:* *https://psi.ndc.nasa.gov* [15].

While all ASETS-II OHPs were important for validating the limits model, the OHP charged with R-134a and using the small heater was specifically designed to cross the vapor inertia and swept length limits. The dimensions of the OHP are shown in Figure 3 and the heat map is shown in Figure 4.

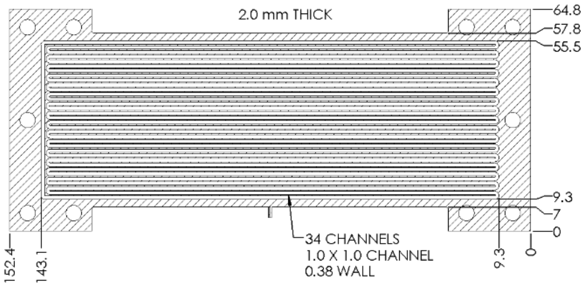

Figure 3. ASETS-II OHP dimensions (units: mm)

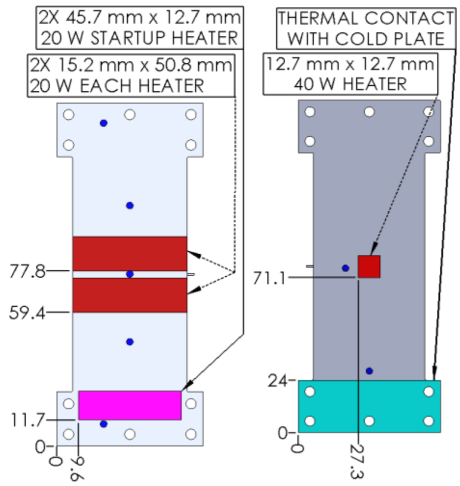

Figure 4. Heat map for ASETS-II OHP charged with R-134a where (a) is the top surface and (b) is the bottom surface with the active heater (units: mm).

Figure 5, based on Drolen et al. [13], shows the on-ground and on-orbit experimental data overlaid on the OHP limits chart. Each dataset was analyzed for stable operation, unstable operation with partial dryout, and runaway conditions with full dryout. The experiment demonstrates close alignment between the predicted limits and experimental results. Some working and non-working results overlap in the dataset, this is attributed to the stochastic nature of the OHP where the OHP is assumed to be in a quasi-stable state.

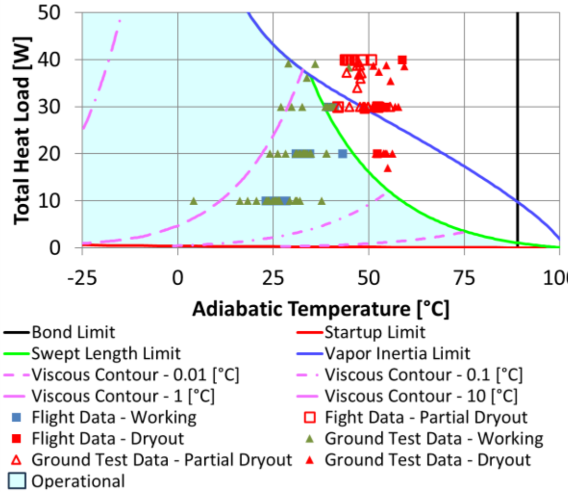

Figure 5. ASETS-II OHP #3 with small heater limits model and test results, based on Drolen et al. [13].

The high flux OHP experiment was important in validating the startup limit, as it required a relatively high heat load to initiate operation [25]. The OHP was designed to spread heat from a high heat flux heat source to a larger rejection area on the opposite surface. The heat source was 1 cm x 1.3 cm centered on the 3.7 cm x 7.6 cm x 0.4 cm copper OHP with heat rejection on the entire surface opposite the heat source (Figure 6). The OHP, charged with methanol, was tested to 330 W (254 W/cm^2). The OHP was evaluated with a rejection temperature from 10 °C to 80 °C. Figure 7 shows the time series data of the OHP's transition across the startup limit when the cold plate was set to 40 °C. The transition across the startup is visible in the change in temperature amplitude as it crosses the limit. This amplitude change is not measurable with all OHP designs. Figure 8 shows that the conductance significantly increases as the OHP crosses above the startup limit. Figure 9 shows close alignment of the startup limit to the experimental data.

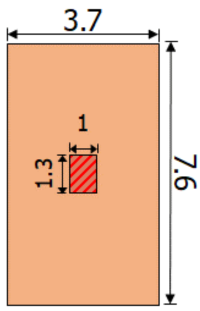

Figure 6. Copper OHP dimensions in centimeters and heat map.

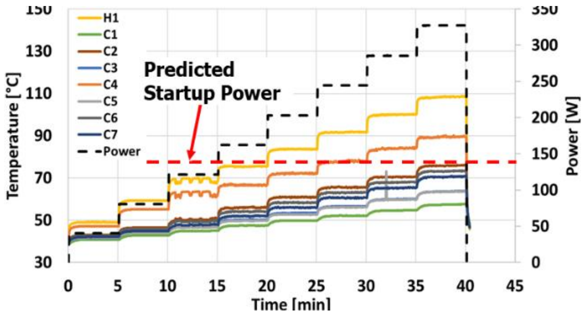

Figure 7. Timeseries results for 40 °C rejection showing transition across startup limit.

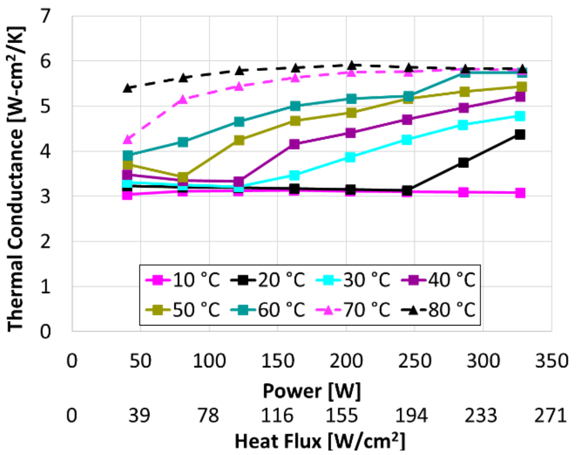

Figure 8. OHP Experimental data at a range of cold plate temperatures showing conductance transition at startup limit.

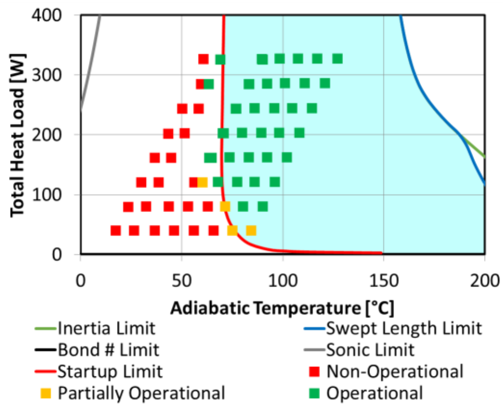

Figure 9. OHP limits chart with experimental data showing alignment of startup limit.

5. Case Study: 3U VPX Heat Frame OHP

The manufacturing and predictive modeling of an OHP's operational limits has enabled ThermAvant to develop commercially viable OHPs for a wide range of applications. Because OHPs provide efficient heat transport in thin, structural form-factors and can handle high fluxes, one natural application is a heat spreader for electronics cooling. This case study will present an OHP heat spreader designed for a standardized form factor and a comparison with existing solutions.

The ANSI/VITA 48.2 3U VPX heat frame is a standardized heat spreader for ruggedized electronics boxes used in terrestrial, airborne, and on-orbit applications [26]. The heat frame is designed to attach to one side of a circuit card to conduct heat from the tops of high heat flux components on the card to the perimeter of the card at heat sink locations, called cold rails, in the electronics box.

The attachment between the heat spreader and the circuit card often requires screw holes near high-flux components and around the perimeter of the plate. Additionally, the design may necessitate cut-outs or varying planes to accommodate components or allow for electrical connections. Due to alignment requirements between the cold rails and the circuit board, the heat spreader may need to jog out of plane by less than 1 cm to effectively transport heat to the cold rail.

These heat frames are commonly solid aluminum heat spreaders, however more efficient heat transporters are required for high flux applications, such as encapsulated graphite heat spreaders [27], heat pipe embedded spreaders [28], or OHP heat spreaders. Each has their advantages and limitations.

Encapsulated graphite heat frames can inherently operate across a wide range of temperatures due to lack of two-phase heat transport. They are however inherently 2D heat spreaders in the plane of the graphite. The performance does not degrade beyond the reduction in transport path with through holes and cut-outs in the design. However, they are typically single plane heat spreaders, or if the graphite is in multiple planes, it is not continuous and therefore has a thermal break with solid metal between. This leads to reduced performance when multiple planes are required.

Heat pipe-embedded heat frames usually utilize one or more flattened copper-water heat pipes embedded in an aluminum plate to transport heat from electronic components to cold rails [29]. These heat pipes serve as axial heat spreaders along the tube path and are ideally routed directly from the heat source to the heat sink. Consequently, their heat transport efficiency is limited by their formability. A typical heat pipe has a minimum bending radius of at least 2.5 times its outer diameter [30]. Many heat frames require frequent holes for mounting circuit cards and other components, which can limit heat pipe routing options and may sacrifice thermal performance. Additionally, heat frames often have out-of-plane cold rails for heat rejection. Due to tight offsets, the heat pipes may not bend sufficiently to route to a cold rail, leading to a final conduction distance of about 1 cm through the lower conductance aluminum plate [31].

OHP heat frames are inherently 3D heat spreaders, as their highly flexible channel routing allows heat transport from multiple planes and orientations. Through-holes and changes in planes do not pose significant complications. Therefore, an OHP heat frame can transport thermal energy in the working fluid from the heat source to the sink with less than 1 mm of solid aluminum conduction. However, a significant number of through-holes or other constrictions may limit the number of OHP turns for stable operation. Additionally, the OHP requires sufficient thickness for the fluid channel, typically between 1 to 3 mm. Figure 10 shows a 6U VPX OHP heat frame. These OHPs are generally designed for heat fluxes of less than 30 W/cm² but can be engineered to handle at least 250 W/cm².

Figure 10. 6U VPX heat frame OHP

An unfeatured 3U VPX heat frame OHP was developed to demonstrate these operational capabilities (Figure 11). The aluminum OHP was heated uniformly across three heat sources and cooled at rails along the edges of the heat frame in a horizontal orientation (Figure 12). The heat map and OHP dimensions can be seen in Figure 13a. The OHP was tested under a combined total heat load of 130 W, with the highest heat flux measuring 3.1 W/cm². Three working fluids were evaluated: ammonia, butane, and propyne and a solid aluminum version was also tested as a baseline. Ammonia proved to be the highest-performing working fluid, achieving a conductance of 53 W/K—nearly ten times the conductance of the solid aluminum envelope (Figure 13b).

Figure 11. Three unfeatured 3U VPX heat frames.

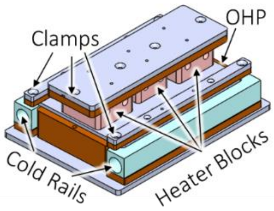

Figure 12. Experimental setup for the 3U VPX heat frame.

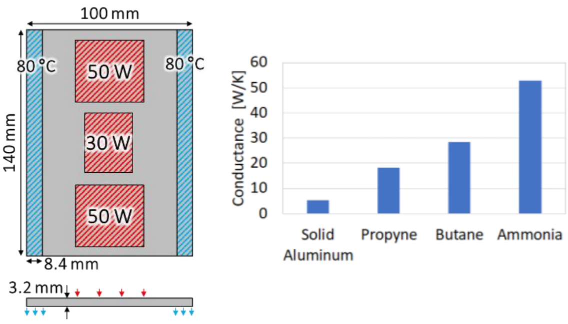

(a) (b)

Figure 13. Heat map (a) and thermal performance data for 3U VPX heat frame with a combined heat load of 130 W.

The time series data for the ammonia OHP is shown in Figure 15, showing the rapid transition to steady-state without overshoot and low thermal amplitude of the oscillating motion. Figure 14 shows the limit chart for the ammonia OHP with the experimental results overlaid, indicating significant margin to the operating limits.

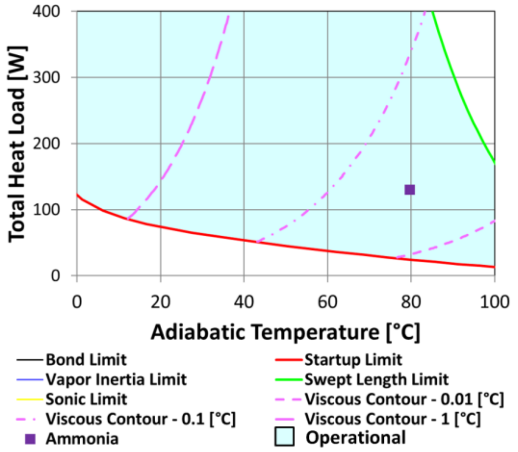

Figure 14. Limits of operation for the ammonia 3U VPX heat frame with experimental results.

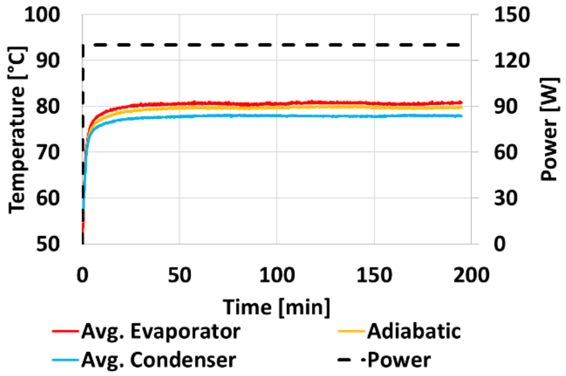

Figure 15. Timeseries data of 3U VPX heat frame charged with ammonia.

Case Study: OHP Base Plate Heat Transporter

Many of the same reasons for using an OHP with a heat spreader are applicable to heat transporters. Such as in applications that are space constrained, require the thermal device to be structural, and/or transport a high heat load or acquire a high heat flux. This case study will compare an OHP heat transporter with the status quo CCHP heat transporter, and a design that incorporates the unique capabilities of an OHP.

The most common high-performance passive heat transporter for satellite applications is the CCHP, which operates efficiently in both gravity-neutral and gravity-aided orientations, allowing it to transport heat over multiple meters [32,33]. For on-orbit applications, CCHPs are frequently utilized as thermal linkages between payloads and radiator panels, helping to thermally balance the satellite by transporting heat across its structure. These CCHPs typically have a diameter of at least 10 mm and can be bent to form complex routing, with bend radii at least 3-5 times the outer diameter, typically ranging from 30 to 35 mm [32–34].

OHP-based transporters offer several advantages and some disadvantages compared to CCHPs. OHP transporters generally have a thickness between 1.5 mm and 7 mm, depending on design requirements, heat load, and transport distance. They can be bent or machined into various shapes, including branching structures to collect heat from multiple locations. For example, a 1.5 mm thick OHP can be bent with a 4.6 mm inner diameter radius, while a 5.6 mm thick OHP can achieve a bend radius of 28 mm. If tighter curvature is needed, the OHP can be machined to create the required sharp angles. Moreover, OHPs can operate against gravity over distances of at least 1 m, with the heat source positioned above the heat sink [35].

The primary disadvantage of OHPs is that their transport length is inherently limited compared to CCHPs. In an OHP, the two-phase mixture flows along the entire transport length at high velocity, resulting in higher viscous losses. This added pressure loss leads to a greater temperature gradient along the transport length. Depending on the fluid and design constraints, an OHP has been demonstrated to be competitive with other heat pipes for lengths of up to approximately 1 m. At lengths longer than 1 m, manufacturing limits prevent a full evaluation. Therefore, at multi-meter scales and low heat loads, CCHPs may present a more effective solution.

In one application, ThermAvant designed an OHP heat transporter to spread heat from an electronics box in a satellite to a CCHP-embedded radiator panel. In this scenario, the OHP was designed to evenly remove heat from the electronics box and to then evenly distribute the heat across multiple CCHPs. Furthermore, the OHP had to function effectively in any orientation, allowing for ground testing after integration without requiring satellite reorientation.

The OHP heat transporter (Figure 16a) was 1067 mm long by 152 mm wide at its widest point, and 5.6 mm thick. The narrow section was 280 mm long by 50 mm wide. This region was designed to remove heat from a 280 mm x 50 mm heat source and the entire opposite surface of the OHP was designed to reject the heat to ten 30.5 mm wide cold rails evenly spaced (Figure 16b).

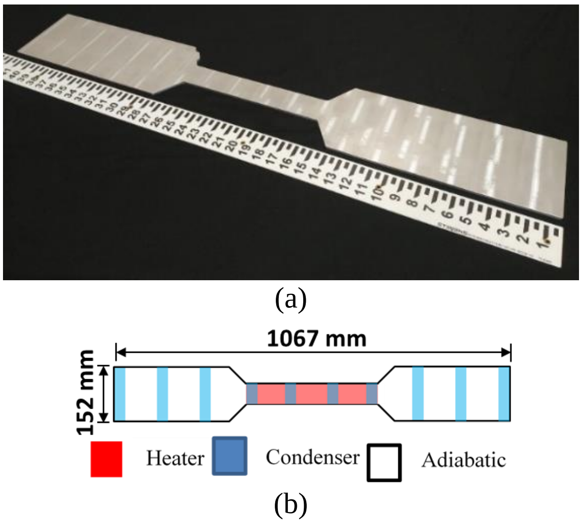

Figure 16. (a) OHP Heat Transporter next to inch ruler and (b) heat map of experiment

The OHP was tested at 75 W, 100 W, and 200 W in horizontal, 5° and a vertical orientation. The highest thermal performance was in the horizontal orientation at 200 W (1.4 W/cm^2) with a conductance of 129 W/K.

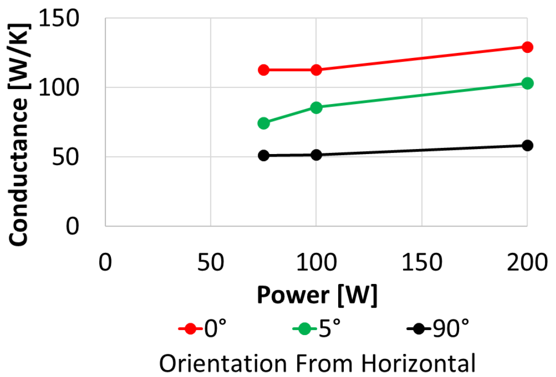

Figure 17. Experimental results for OHP transporter at different orientations and heat loads.

Figure 18 shows the transporter OHP's limits model with experimental results. The experimental results for the three orientations occur at nearly the same adiabatic temperature and therefore are overlapping. The OHP operated well within the safe operational region with margin for higher heat loads.

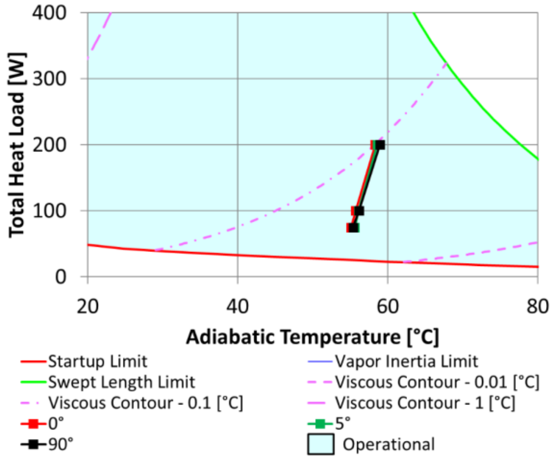

Figure 18. Limits model for OHP transporter with experimental results.

CCHPs could be designed to transport this heat flux, however they are not able to transport this heat load in a 5.6 mm thick structural form factor, transform the high flux to a lower flux in the rejection region, and do so in all orientations [32].

6. Conclusions

ThermAvant has developed and demonstrated OHPs with a wide range of capabilities:

- Heat acquisition from less than 1 W/cm^2 to over 250 W/cm^2
- Transport lengths ranging from less than 2 cm to 3 m
- Heat rejection fluxes of less than 1 W/cm^2 to 10s of W/cm^2.
- Thicknesses less than 1 mm to several mm for multi-kilowatt thermal transporters
- Operating temperatures from -196 °C (77 K) to 1200 °C
- A wide range of working fluids and envelope materials
- Operate as a thermal-structural multi-functional material
- Producible in complex three-dimensional thermally active shapes

Extensive work was conducted to predictively model OHPs, design and manufacture them to industry standards, and commercially produce them for a wide range of applications. With thousands of OHPs fielded, over 10 space flight qualification campaigns completed, and over 1 million hours of on-orbit flight time, the OHP is an important new tool for thermal management in commercial systems.

7. Acknowledgements

Special thanks to the ThermAvant Team, consultant Dr. Bruce Drolen, and the Small Business Innovation Research grants through the Air Force Research Laboratory, NASA, Navy, and Army Research Laboratory.

References

[1] H. Akachi, Structure of a heat pipe, 4921041, 1990.
[2] H. Akachi, Tunnel-plate type heat pipe, 5697428, 1997.
[3] H. Akachi, Structure of micro-heat pipe, 5219020, 1993.
[4] H. Akachi, Ribbon-like plate heat pipes, 5642775, 1997.
[5] JJ Cooling Innovation, (n.d.). https://www.jjcooling.com/ (accessed April 18, 2023).
[6] Pulsating Heat Pipe, Novark (2018). https://www.novarktechnologies.com/pulsating-heat-pipes/ (accessed September 9, 2022).
[7] Pulsating Heat Pipes, Advanced Cooling Technologies (n.d.). https://www.1-act.com/thermal-solutions/passive/heat-pipes/pulsating/ (accessed April 23, 2024).
[8] ThermAvant Technologies, ThermAvant Technologies (n.d.). https://www.thermavant.com (accessed April 23, 2024).
[9] Pulsating Heat Pipe-ALVC Industries Limited_Fold FIN sheet_Aluminium VC, (n.d.). https://www.alvcfactory.com/Products_dt/Pulsating_Heat_Pipe.html (accessed June 11, 2024).
[10] IcePipe, 아이스파이프 (n.d.). https://icepipeled.com/?lang=en (accessed March 4, 2024).
[11] B.S. Taft, S.M. Smith, ASETS-II Oscillating Heat Pipe Space Flight Experiment: Ground Truth Results, in: American Society of Mechanical Engineers Digital Collection, 2017. https://doi.org/10.1115/HT2017-4706.
[12] B. Taft, K. Irick, ASETS-II Oscillating Heat Pipe Space Flight Experiment: The First Six Months On Orbit, Frontiers in Heat and Mass Transfer (FHMT) 12 (2018). http://dx.doi.org/10.5098/hmt.12.24 (accessed September 9, 2022).
[13] B.L. Drolen, C.A. Wilson, B.S. Taft, J. Allison, K.W. Irick, Advanced Structurally Embedded Thermal Spreader Oscillating Heat Pipe Micro-Gravity Flight Experiment, Journal of Thermophysics and Heat Transfer 36 (2022) 314–327. https://doi.org/10.2514/1.T6363.
[14] C.A. Wilson, B. Drolen, B. Taft, J. Allison, Advanced Structurally Embedded Thermal Spreader II (ASETS-II) Oscillating Heat Pipe Flight Experiment and Database, in: Melbourne, Australia, 2023: p. 7.
[15] J. Allison, B. Taft, Advanced Structurally Embedded Thermal Spreader II (ASETS-II) Oscillating Heat Pipes (OHP), NASA Physical Sciences Informatics (PSI) (n.d.). https://psi.ndc.nasa.gov/app/record/164634.
[16] AFRL, industry launch revolutionary spacecraft technology - Oscillating Heat Pipes, ONE AFRL / TWO SERVICES (n.d.). http://www.afrl.af.mil/News/Article-Display/Article/2817283/afrl-industry-launch-revolutionary-spacecraft-technology-oscillating-heat-pipes/ (accessed May 20, 2022).
[17] ANSI/AIAA S-080A-2018 - Space Systems—Metallic Pressure Vessels, Pressurized Structures, and Pressure Components, (n.d.). https://webstore.ansi.org/standards/aiaa/ansiaiaa080a2018 (accessed October 24, 2024).
[18] Test Requirements for Launch, Upper-Stage, and Space Vehicles, (2014).
[19] B.L. Drolen, C.D. Smoot, Performance Limits of Oscillating Heat Pipes: Theory and Validation, Journal of Thermophysics and Heat Transfer 31 (2017) 920–936. https://doi.org/10.2514/1.T5105.
[20] D.A. Pounds, L. Ellebracht, B. Drolen, An Empirical Study of a Long, High Temperature Oscillating Heat Pipe for Next Generation Spacecraft Thermal Control, in: Spacecraft Thermal Control Workshop, El Segundo, California, 2018.
[21] H. Akachi, Structure of micro-heat pipe, US5219020A, 1993. https://patents.google.com/patent/US5219020A (accessed May 26, 2022).
[22] A.A.M. Delil, Thermal-Gravitational Modelling and Scaling of Heat Transport Systems for Applications in Different Gravity Environments: Super-Gravity

Levels & Oscillating Heat Transfer Devices, in: Toulouse, France, 2000: p. 21.
[23] S. Khandekar, An Introduction to Pulsating Heat Pipes, Electronics Cooling (2003). https://www.electronics-cooling.com/2003/05/an-introduction-to-pulsating-heat-pipes/ (accessed July 31, 2024).
[24] B.L. Drolen, C.D. Smoot, Performance Limits of Oscillating Heat Pipes: Theory and Validation, Journal of Thermophysics and Heat Transfer 31 (2017) 920–936. https://doi.org/10.2514/1.T5105.
[25] C. Wilson, S. Hayden, Ultra-Low Thermal Resistance Structural Heat Spreaders Built With The OHP Technology, in: Advancements in Thermal Management 2019, Denver Colorado, 2019.
[26] VITA - Online store product, (n.d.). https://www.vita.com/Sys/Store/Products/258937 (accessed October 18, 2024).
[27] Heat Spreaders & Conductive Chassis, Boyd | Trusted Innovation (n.d.). https://www.boydcorp.com/thermal/conduction-cooling/heat-spreaders-conductive-chassis.html (accessed October 2, 2024).
[28] VME/ VPX Card Frames, Advanced Cooling Technologies (n.d.). https://www.1-act.com/thermal-solutions/embedded-computing/vme-vpx/ (accessed October 2, 2024).
[29] VME/ VPX Card Frames, Advanced Cooling Technologies (n.d.). https://www.1-act.com/thermal-solutions/embedded-computing/vme-vpx/ (accessed October 18, 2024).
[30] Heat Pipe Bending Tool | Q ATS, (n.d.). https://www.qats.com/Products/Heat-Pipes/Heat-Pipe-Bending-Tool (accessed October 18, 2024).
[31] S.K. Hota, K.-L. Lee, G. Hoeschele, T. Mcfarland, S. Rokkam, R.W. Bonner, Experimental Comparison of Two-Phase Heat Spreaders for Space Modular Electronics, in: 52nd International Conference on Environmental Systems, Calgary, Canada, 2023.
[32] Euro Heat Pipes - Technical Data Sheet N 1A: EHP AGXXX Heat Pipes, n.d. http://www.ehp.be/ehpcontent/CCHP-techdata-2020.pdf (accessed June 21, 2022).
[33] W.G. Anderson, C. Tarau, TFAWS Heat Pipes Short Course, in: Thermal & Fluids Analysis Workshop, NASA Langley Research Center, Hampton, VA, 2019. https://tfaws.nasa.gov/wp-content/uploads/Heat-Pipes-Short-Course.pdf (accessed October 2, 2024).
[34] Constant Conductance Heat Pipes Design/Manufacturing Notes and Extrusion Catalog, n.d. https://www.1-act.com/wp-content/uploads/2012/12/cchpcat.pdf (accessed June 22, 2022).
[35] D.S. Hilsenbeck, D.B. Drolen, M. Merwin, Development of Thermal Switching Oscillating Heat Pipes for an Enhanced Lunar Thermal Wadi, in: Spacecraft Thermal Control Workshop, 2021.

Paper ID 025(S2D)

Enhancing Condensation and Evaporation Performance in Two-Phase Closed Thermosyphons through Inner Surface Treatment: An Experimental Investigation

Marc Kirsch[1*], Rudi Kulenovic[2] and Jörg Starflinger[3]

[1,2,3] *Institute of Nuclear Technology and Energy Systems, University of Stuttgart, Stuttgart, Germany*
**marc.kirsch@ike.uni-stuttgart.de*

Abstract

Straight stainless steel two-phase closed thermosyphons (TPCTs) of 3 m length with deionized water as the working fluid are experimentally investigated. The TPCTs with an inner diameter of 35 mm and a wall thickness of 1,5 mm consist of an evaporator, an adiabatic and a condenser section of equal length. In this study, TPCTs with five different inner surface treatments have been investigated: two sandblasted with surface roughness of R_a = 6030 nm resp. R_a = 9020 nm, one polished with R_a = 900 nm, one with a laser-structured condenser section exhibiting a superhydrophobic contact angle, and an untreated TPCT as a reference. The influence of the filling ratios $V+$ (20 %, 30 %, 40 %, 56 %, 75 %, 100 %) at different evaporator temperatures T_e (45 °C, 60 °C and 80 °C) and condenser temperatures T_c (10 °C, 20 °C and 30 °C) on the heat transfer performance of the TPCT has been investigated. The results show that inner surface treatment significantly improves the heat transfer rate of the TPCT by up to 35 % at the maximum operating point.

Keywords: thermosyphon; inner surface treatment; sandblasting; polished; laser structuring; coating; stainless steel-water

1. Introduction

Two-phase closed thermosyphons (TPCT) are a widely used system for heat transfer. Their stand out attribute is their straightforward design combined with low-cost production and high level of reliability in operation. Due to these advantageous properties, they have been tested and used for years in a wide variety of applications such as de-icing roads, maintaining permafrost soils or turbine blade cooling [1]. Considering the Fukushima reactor accidents, research endeavors have pivoted towards the development of passive safety devices for cooling of spent fuel pools of nuclear power plants. TPCTs emerge as promising candidates for this purpose due to the above-mentioned properties. Within the PALAWERO research project at the Institute of Nuclear Technology and Energy Systems (IKE), University of Stuttgart [2; 3], the feasibility of TPCTs for the cooling of spent fuel pools was comprehensively investigated and validated [4; 5].

However, the use of untreated steel pipes as the base of the TPCT does not fully utilise the possible heat transfer potential. It is well known that an improvement in the evaporation and condensation properties can be achieved by e.g. mechanical treating the inner heat transferring surface [6; 7]. The objective of this study is to evaluate the efficacy of various processing methods namely laser structuring, sandblasting, and polishing in comparison to an untreated reference condition across a spectrum of operational parameters and filling ratios of the TPCTs. To achieve this objective, an extensive experimental investigation for five different TPCTs has been undertaken.

2. Experimental setup and test procedure

2.1. Experimental setup

The experimental setup can be seen schematically in Figure 1. The TPCT measured in the test stand consist of three zones, a 1 m long evaporation zone, a 1 m long adiabatic zone, and a 1 m long condensation zone. For the construction of the TPCT, pipes made of 1.4301 (ANSI 304) steel with an inner pipe diameter of 35 mm and a wall thickness of 1.5 mm were used. A cover was welded on each end of the TPCT, which is equipped with two 1/4-inch connection pieces. This enables evacuation and filling via a connected valve. Furthermore, a pressure transducer and invasive temperature measurement sensors are additionally attached here.

The measurement setup of the five TPCT is identical. At equal distances of 250 mm, 12 PT-100 temperature sensors are mounted on the outside of the TPCT to determine the TPCT surface temperature. In the evaporation and condensation zones, the tube surfaces at the sensor positions were milled to a depth of approx. 1 mm to improve the measuring accuracy. The resulting flat surfaces ensure that the attached temperature sensors measure the surface temperature without an undercutting by the fluid of the thermostat circuit. Inside the TPCT there are 4 invasive temperature measuring points, 2 in the condensation zone and 2 in the evaporation zone, which are equipped with PT 100 measuring sensors inserted into the TPCT via the 1/4-inch connection described above. The absolute pressure is also measured here by means of a cross piece attached to the connection pieces. A Lauda T 4600 thermostat is used on the heating side and a Huber CC525 on the cooling side, both using water as working fluid. For heating the evaporation zone and cooling the condensation zone, identical semi-circular heat exchangers with an internal diameter of 47 mm are used. The heat exchangers have 11 baffle plates guiding the working fluid of the thermostat circuits along the TPCT in a meandering pattern. For calorimetric heat flow measurements, the temperatures at the outlet and inlet of each heat exchanger are measured by PT-100 temperature sensors.

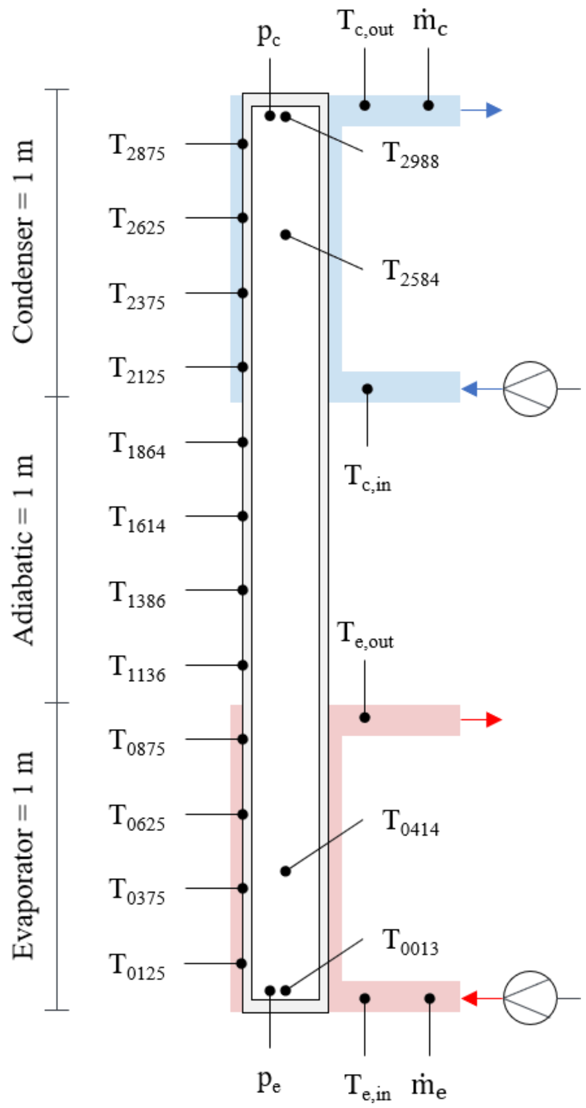

Figure 1 Scheme of the test stand design

The volume flows of the two thermostat circuits are determined by means of ultrasonic flow meters. The mass flow rate of the temperature control circuit is adjusted via a bypass. This also ensures that fluctuations greater than 0.2 l/s due to the pump do not occur. The accuracies of the measuring sensors used are as follows. The absolute pressure sensors of type PAA-33x from Omega have an accuracy of ± 0.15 % FS, where FS stands for full scale. All PT-100 temperature sensors have class A accuracy and thus a measurement uncertainty of ± (0.15 + 0.002 T). The measurement uncertainty of the volumetric flow meter is ± (0.7 % RD + 0.7 % FS), where RD stands for reading. The measurement data acquisition is carried out via a Keysight 34970A data logger, and the measurement software is based on Agilent VEE.

The entire measurement setup was insulated with Amaflex XG with a thermal conductivity of 0.042 W/(mK). The ambient and the insulation temperature was also measured with a PT-100 sensor.

2.2. Surface treatment

For the 5 TPCTs analysed, different methods of processing the inner surface were selected. One TPCT is used as an untreated reference TPCT in order to be able to evaluate the influence of the surface treatments. The other methods can be divided into two groups, those aimed at optimising condensation, laser-functionalisation and polishing, and those aimed at improving evaporation due to surface roughness, in this study with the help of sandblasting [8–10]. Their manufacturing will be described now in more detail. The first internally processed TPCT is a laser-functionalized pipe in the 1m long condensation area. The rest of the TPCT is made out of the reference pipe. In general, this processing method uses texturing with ultrashort laser pulses [7] to change the contact angle and thus the wettability. The contact angle defined according to Young's equation changes from 72°±3° for the reference TPCT to 153°±3° for the laser-functionalized TPCT, as can be seen in the lower part of Figure 2. The upper part of the figure shows the behaviour of a water droplet in the cut-open pipe half-shell with laser-functionalized internal machining.
The second inner machined TPCT was polished using a cylindrical grinding machine to reduce the roughness alongside the 3 m pipe. The realisation can be seen in Figure 3. A roughness value R_a

(average roughness) of 900 nm was achieved using this process. In all cases, the roughness values indicated in this paper were determined in collaboration with the Materials Testing Institute (MPA), University of Stuttgart and the highest R_a value was selected from the multi-point measurements carried out.

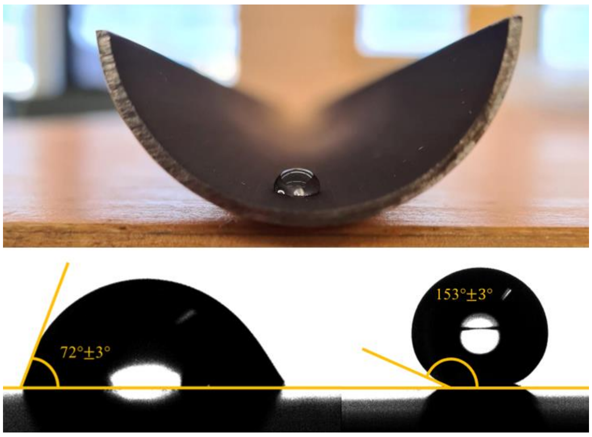

Figure 2 Above, water droplets in the laser-functionalized TPCT; below, change in contact angle due to laser functionalisation

The third and fourth internally machined tubes shown in Figure 4 were sandblasted with different coarse abrasives. Roughnesses R_a of 6030 nm and 9020 nm were achieved. Again, the entire 3 m pipe was machined internally.

Figure 3 Polished TPCT tube

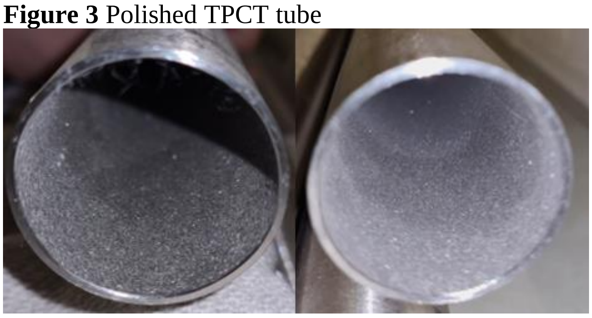

Figure 4 Sandblasted tubes with $\boldsymbol{R_a}$ 9020 nm (left) and $\boldsymbol{R_a}$ 6030 nm (right)

2.3. Test Procedure

The experimental investigations were performed with $V+$ of 20 %, 30 %, 40 %, 56 %, 75 % and 100 % at three fluid inlet temperatures of the heat exchanger at the evaporation zone (45°C, 60 °C and 80 °C) and the condensation zone (10 °C, 20 °C, 30 °C). Each TPCT is filled according to a uniform procedure. For this purpose, the TPCT is evacuated before the filling procedure and then leakage tested with helium. Afterwards, a leak test is carried out with the help of the attached pressure sensors. This ensures that the pressure does not exceed 3 mbar, the maximum error of the pressure sensor. Deionized and degassed water is used for. After the TPCT has been filled, it is degassed. For this purpose, only the evaporation side is heated up to 60 °C. In this state, the valve in the upper area of the TPCT is opened and the non-condensable gas, that accumulates there, is released into an attached, vacuumed expansion tank. This process with the expansion tank reliably prevents the ingress of outside air, as it is still a closed system. The non-condensable gas comes from air dissolved in the working fluid which cannot be completely removed during the degassing process before filling. A check is made via the upper of the two invasive temperature sensors mounted in the condensation zone. After degassing, the temperature of the lower sensor adjusts to the temperature of both sensors. The measurements on the filled TPCT were carried out in measurement series with predefined filling levels and predefined temperature at the flow inlet of the condensation zone. The flow inlet temperature to the evaporation zone was then raised from 45 °C to 80 °C in 5 °C steps. However, to keep this paper concise and focused, only the key temperatures of 45 °C, 60 °C, and 80 °C were selected for detailed analysis. The measurement was carried out according to the following principle. After reaching the selected inlet temperature in the evaporation zone, 10 min were waited to ensure that the system was completely thermally settled. After that, measurements were taken for 10 min. After completion of this measuring point, the next evaporator temperature was adjusted for the subsequent measurement.

2.4. Data reduction

The heat transfer $\dot{Q}_c$ is determined calorimetrically for the condenser section. This is done via the difference of the inlet temperature $T_{c,in}$ to the outlet temperature $T_{c,out}$, the specific heat capacity c_p, the density ρ and the volume flow $\dot{V}_c$ of the coolant water of the thermostat circuits.

$$\dot{Q}_c = \dot{V}_c \cdot \rho \cdot c_p (T_{c,out} - T_{c,in}) \quad (1)$$

Based on this, the average heat transfer coefficient of the condenser h_c can then be calculated.

$$h_c = \frac{Q_c}{2 \cdot \pi \cdot r_o \cdot L_c \cdot (T_{Vsat} - T_{c\,w})} \quad (2)$$

The variables required for this are the TPCT radius r_o of 19 mm, the length L_c of the condenser of 1000 mm, the temperature of the steam in the condenser T_{Vsat}, which in this case is determined by the saturation temperature of the vapour based on the pressure p_c present in the condenser, and the wall temperature of the condenser $T_{c\,w}$. For the wall temperature $T_{c\,w}$, the average value of the 4 PT-100 temperature sensors T_{2125}, T_{2375}, T_{2625} and T_{2875}, which can be seen in Figure 1, is used. Specific property data for water and steam are determined by using the Industrial Formulation 1997 for the Thermodynamic Properties of Water and Steam IAPWS R7-97.

2.5. Error calculation

The measurement uncertainty is calculated using the Gaussian error propagation approach.

$$\Delta y = \sqrt{\sum_{i=0}^{n} \Delta x_n^2 \left(\frac{\partial y}{\partial x_n}\right)^2} \quad (3)$$

Here Δy is the total error of the parameter y, x_n is the independent measured variable and Δx_n is the measurement error.

3. Results

The presented graphs show the heat transfer rate $\dot{Q}_c$ as a function of the filling ratio $V+$ at three different evaporator temperatures T_e of 45 °C, 60 °C and 80 °C under three different condenser temperatures T_c of 20 °C, 10 °C, and 30 °C. The experimental investigations were carried out for five different inner surface conditions: polished surface (R_a = 900 nm), rough surfaces (R_a = 6030 nm and R_a = 9020 nm), a laser-structured surface and an untreated reference surface

In Figure 5 the results for T_c = 20 °C are shown. In general, the highest heat transfer rate is at $V+$ of 20 and 30 % for R_a = 6030 nm with an absolute value of 4.45 kW. For T_e = 45 °C, it can be stated that, with the exception of the filling level of 30 %, any internal surface treatment brings a significant improvement. The reference TPCT still in an unstable operation point has a heat transfer rate of 0.195 kW, while the R_a = 6030 nm TPCT operates stable at 1.05 kW. Across all filling levels, the TPCT with R_a = 6030 nm has the highest heat transfer rate. Another striking aspect is the difference of maximum heat transfer rates depending on the inner surface treatment method and $V+$. For example, it is 20 % for the laser-functionalized tube, 30 % for the two sandblasted tubes and the reference TPCT and 40 % for the polished tube. At T_e = 60 °C, the differences between the reference, polished and laser functionalized TPCT are within the range of the measurement error. The difference between the two sandblasted TPCTs could not be greater. For R_a = 9020 nm, the heat transfer rate is 10 to 15 % below the reference TPCT, whilst for R_a = 6030 nm there is a maximum improvement of over 25 % compared to the reference TPCT. With the exception of V + = 100 %, the improvement is at least 10 %. For T_e = 80 °C again R_a = 6030 nm stands aside of the other inner surface treatments. The heat transfer rate increases by at least 13.5 % compared to the reference TPCT, and even 20 % at V +=100 %. Additionally, the polished TPCT shows promising heat transfer improvements of about 5 to 10 % at $V+$ of 30, 40 and 75 %. At $V+$ of 20 % however, both the polished and R_a = 9020 nm TPCTs show lower heat transfer rates than the reference TPCT due to a higher dry-out possibility.

In Figure 6 the results for T_c = 10 °C can be seen. For R_a = 6030 nm, results are presented only for $V+$ = 20, 30 and 56 %. Measurements were only conducted for $V+$ of 20 % and 30 % - where the maximum heat transfer rate is expected based on measurements at 20 °C and prior findings from the other TPCTs - and 56 % was included as a reference value in general, the highest heat transfer rate of about 5 kW is at T_e = 80 °C and $V+$ of 20 % resp. 30 % for R_a = 6030 m . For T_e = 45 °C and V + of 20 % and 30 %, the reference TPCT shows better results than any other surface treatment. With 2.15 kW at $V+$ = 30 % it is also the highest total heat transfer rate achieved at this T_e. At $V+$ above 30 % the results change drastically and the polished and the R_a = 6030 nm TPCT have more than 160 % higher heat transfer rates than the reference TPCT. As seen for T_c = 20 °C, it should be noted that the large percentage difference is due to the unstable operation of the reference TPCT. At $V+$ = 100 %, the differences even out more or less, and there is no superior TPCT. For T_e = 60 °C, the TPCT behave in a similar way then seen in Figure 5 for T_c = 20 °C. The best results can be seen for R_a = 6030 nm with a peak value of 3,45 kW at $V+$ = 20 %. The overall improvement rate is 13 %, 4,5 % and 7,3 % at $V+$ of 20, 30 and 56 %. The polished and the laser functionalized TPCTs behave similar to the reference TPCT with the exception of $V+$ = 20 % for the polished TPCT with a heat transfer drop of - 21 %. Again, the R_a = 9020 nm TPCT is below the heat transfer rate of the reference TPCT with - 6 to - 34 %. The results for T_e = 80 °C show a heat transfer improvement of 6 to 9 % for R_a = 6030 nm. Besides this there is only a significant change in contrast to the reference TPCT for the laser functionalized and the polished TPCT at $V+$ = 20 % with a heat transfer decrease of - 7,5 % and - 12,9 %.

In Figure 7 the results for T_c = 30 °C are given. For R_a = 6030 nm, results are again presented only for $V+$ = 20,30 and 56 %. In general, the highest heat transfer rate of 3.95 kW is at $V+$ of 20 % for R_a = 6030 nm(note that the scale of the y-axis is adapted to the lower heat transfer rates for the middle and lower part of the figure).

For T_e = 45 °C, the reference and the laser functionalized TPCTs are not in a working state. Therefore, a comparison of the heat transfer increase in percentage does not provide a valuable result. After all, it is to be seen that for R_a = 6030 nm a stable TPCT operation occurs, with a maximum heat transfer rate of 1,2 kW at $V+$ = 30 %. Also, a working state of the TPCT can be seen for the R_a = 9020 nm with heat transfer rates between 0.5 kW and 0.7 kW for $V+$ up to 56 %. In this $V+$ area the polished TPCT also shows heat transfer rates of around 0.5 kW.

At T_e = 60 °C, all surface treatments with the exception of R_a = 9020 nm show improvements in the heat transfer rate at any $V+$. For polished and laser functionalized TPCTs, with one exception at $V+$ of 20 %, the heat transfer improvement lies between 8,5 % and 12,5 %. R_a = 9020 nm shows only an improvement at a $V+$ of 20 % with around 11,5 %. For the other $V+$, the heat transfer rate decreases compared to the reference from - 10,5 % to – 20 % and at 100 % even as high as - 53 %. The highest heat transfer rate can be achieved with the R_a = 6030 nm TPCT at $V+$ = 20 %. It shows a 59 % better result at a total value of 2.45 kW. For $V+$ of 30 % and 56 %, the improvements are high with 37 % and 41 %.

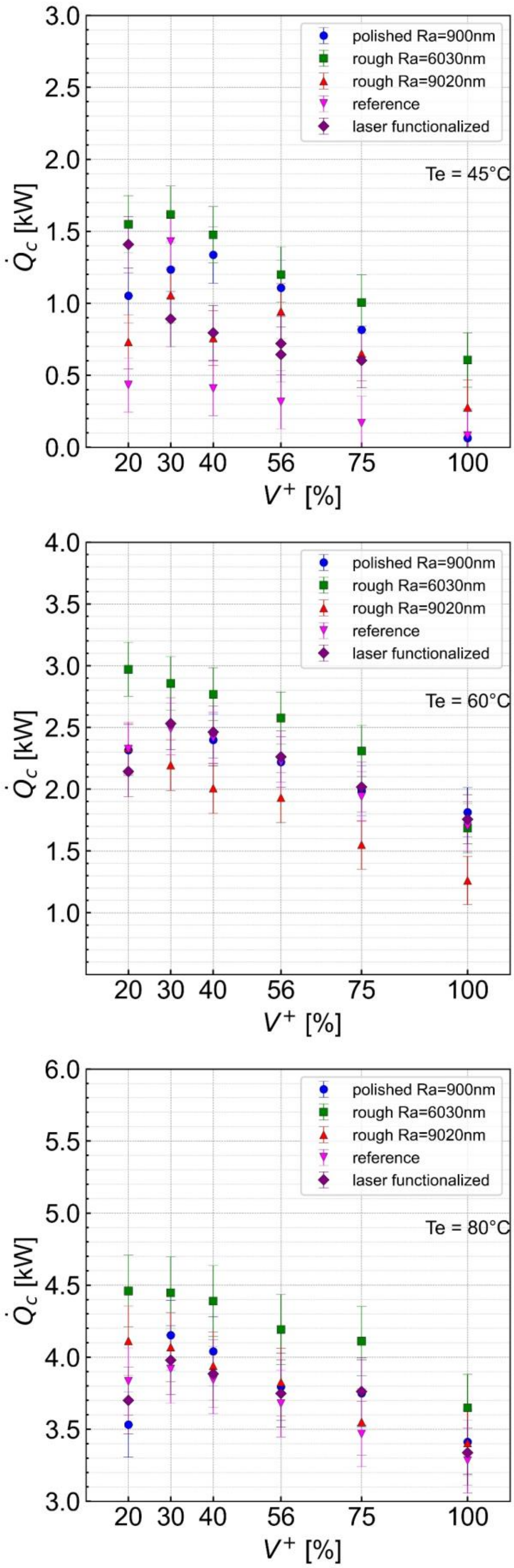

Figure 5 Heat transfer rate at T_c = 20 °C vs. V^+

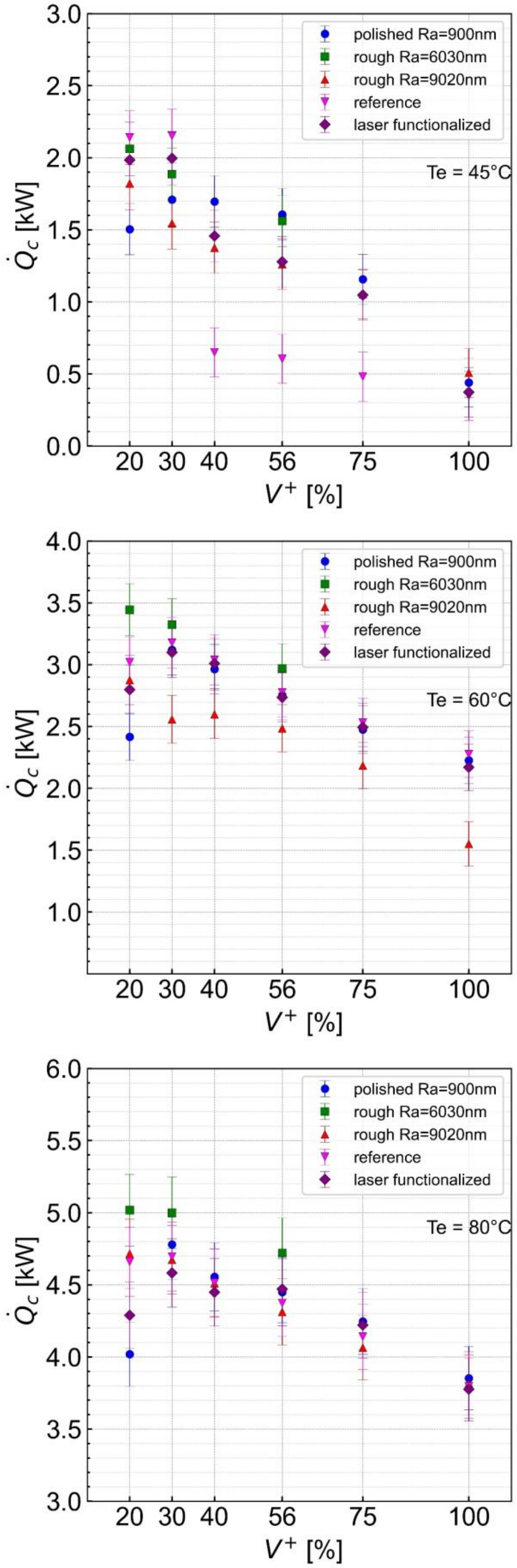

Figure 6 Heat transfer rate at T_c = 10 °C over all $V+$

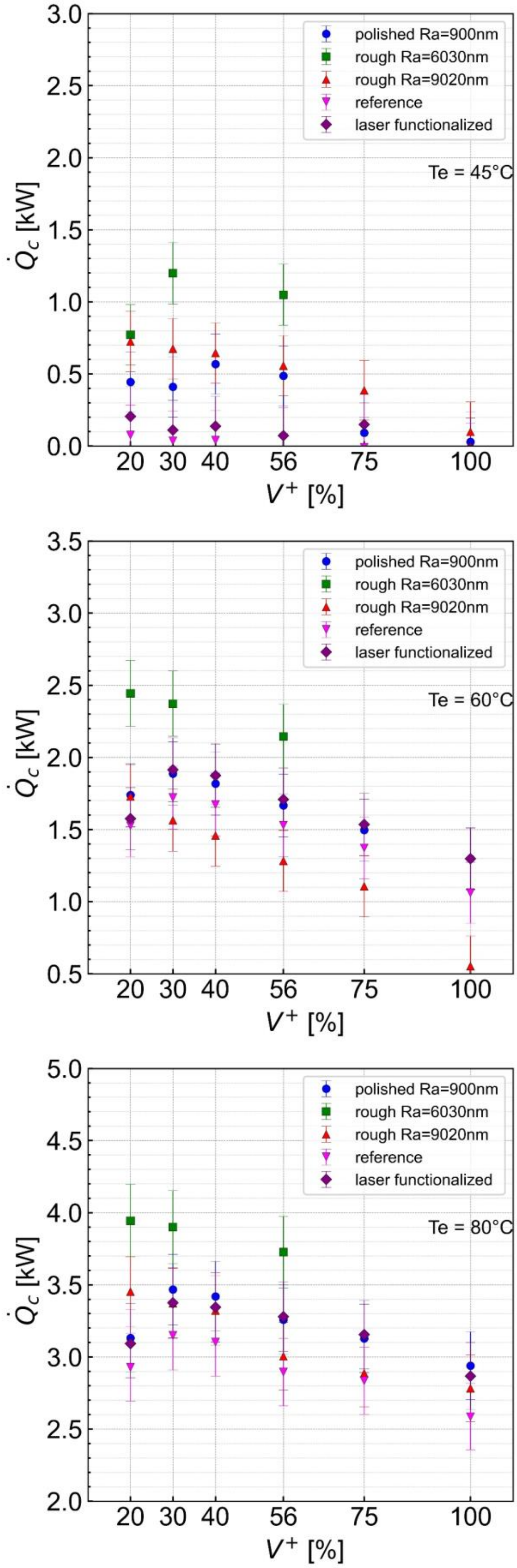

Figure 7 Heat transfer rate at T_c = 30 °C over all $V+$

At T_e = 80 °C all surface-treated TPCTs show an improvement compared to the reference TPCT. The most significant improvement is achieved for R_a = 6030 nm with a maximum of 35 % and a heat transfer rate of 3.95 kW at $V+$ = 20 %. For 30 % and 56 % $V+$, an improvement of around 25 % is reached. For the polished and the laser functionalized TPCTs, a heat transfer increase between 6,5 % and 12,5 % can be attained. The TPCT with R_a = 9020 nm reaches for 20 % $V+$ an improvement of 17,5 %, which flattens out to 7,5 % improvement rate for 30 % and 40 % $V+$. For $V+$ of 56 % and 75 % it goes down even more so it is within the error margin. In Figure 8 the average heat transfer coefficient $\bar{h}_c$ in the condenser section as a function of the heat flux $\dot{q}_c$ is given and provides an insight into the effect of surface treatment with sandblasting at R_a = 6030 nm compared to the reference TPCT.

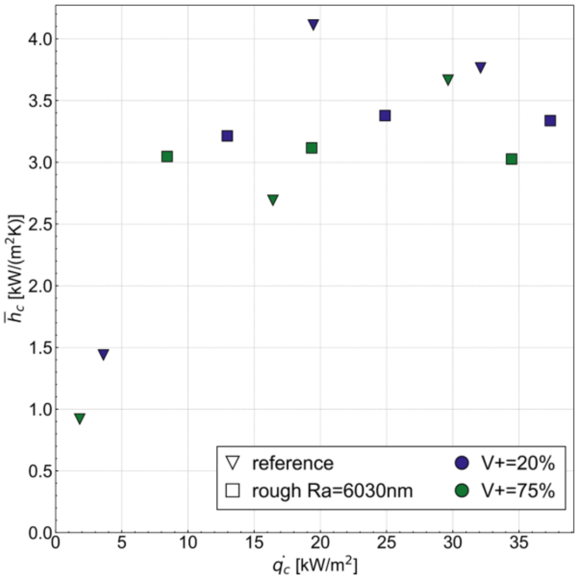

Figure 8 Heat transfer coefficients vs. heat flux for the reference and the $\boldsymbol{R_a}$ = 6030 $\boldsymbol{nm}$ TPCT at $\boldsymbol{V+}$ = 20 % and 75 % for $\boldsymbol{T_e}$ of 45 °C, 60 °C and 80 °C

The R_a = 6030 nm TPCT was selected due to its overall high improvement in heat transfer rate. Two $V+$ of 20 % and 75% where chosen, due to the significant difference in their influence on the heat transfer rate. The general impact of varying T_e of 45 °C, 60 °C and 80 °C can be easily observed, as it strongly correlates with the value of $\dot{q}_c$. Additionally, the higher heat transfer rate of the R_a = 6030 nm TPCT and the higher heat transfer rate for both surfaces at $V+$ = 20 % is evident. Beyond these expected effects, the influence of the rougher surface R_a = 6030 nm on the condenser compared to the reference TPCT is highlighted. Despite having a higher heat transfer rate at any of the inspected T_e and $V+$, the heat transfer coefficient is significantly lower for the R_a = 6030 nm TCPT for $\dot{q}_c \geq$ 20kW/m². The $\bar{h}_c$ decrease in comparison to the reference TPCT is in the range of - 11 % to - 18,5 %. An explanation for this could be that the surface roughness prevents a good backflow of the condensate and therefore reducing the effective condensation there. As mention in chapter 2.2 the expected positive influence of the sand blasting should be improving the evaporation. For $\dot{q}_c$ < 20 kW/m², the behavior is reversed, as at this point, stable operational behavior of the TPCT becomes the more influential factor. The influence of stable operational behavior of the TPCT can also be observed for the reference TPCT at $\dot{q}_c$ between 15 and 20 kW/m². At a $V+$ = 75 % the TPCT operates in an unstable and pulsating manner, which directly results in a lower average heat transfer coefficient $\bar{h}_c$ compared to the $\bar{h}_c$ at $V+$ = 20% during stable operation.

4. Comparison and Conclusions

The results of this study demonstrate that surface treatment significantly influences the heat transfer performance of TPCTs under various operating conditions. The TPCT with a surface roughness of R_a = 6030 nm consistently exhibited the highest heat transfer rates at most of the investigated conditions, particularly at the low evaporator temperature T_e = 45 °C. The most significant improvement was observed for the filling ratios $V+$ = 20 % and 30 %, where a stable operation of the TPCT resulted in a significant higher heat transfer rate compared with the untreated reference TPCT. The study revealed that while intermediate surface roughness R_a = 6030 nm produced the best overall heat transfer rates, the TPCT with a rougher surface R_a = 9020 nm generally underperformed, often showing lower heat transfer rates than the reference TPCT, particularly at high filling ratios and evaporator temperatures. This suggests that an excessive roughness may be counterproductively for the condensation process by inhibiting the condensate backflow, reducing the effective heat transfer.

At higher evaporator temperatures T_e = 80 °C, the polished and laser-functionalized TPCTs demonstrated notable improvements, achieving heat transfer rates up to 20 % higher than the reference TPCT. However, these gains were not as pronounced as those achieved by the R_a = 6030 nm TPCT, highlighting the advantage of a moderate roughness level for the thermal performance.

In conclusion, this study confirms that surface treatment is a critical factor in enhancing TPCT heat transfer rate, and that a surface roughness of around R_a = 6030 nm provides the most consistent improvements. However, the effectiveness of surface treatments varies depending on the specific combination of operating temperatures and filling ratios. Therefore, further research is necessary to explore the long-term effects of surface treatments and possible influence of combined inner surface treatments.

5. Acknowledgements

The presented work was funded by the Federal Ministry for the Environment, Nature Conservation, Nuclear Safety and Consumer Protection (BMUV, project no.1501612A) on basis of a decision of the German Bundestag.

6. References

[1] A. Faghri. Heat Pipes: Review, Opportunities and Challenges. Frontiers in Heat Pipes. 2014. 5(1).

[2] C. Graß and R. Kulenovic. Abschlussbericht / Final Report Reaktorsicherheitsforschung-Vorhaben-Nr./ Reactor Safety Research Project No.: 1501515. 2020.

[3]. C. Graß; R. Kulenovic; J. Starflinger. Experimental study on heat transfer characteristics of long two-phase closed thermosiphons related to passive spent fuel pool cooling. in Joint 19th IHPC and 13th IHPS. 2018. Pisa, Italy.

[4]. A. Krüssenberg; A. Schaffrath; A. Wielenberg; M. Kirsch; S.I. Cáceres Castro; R. Kulenovic; J. Starflinger. Long Straight Closed Two-Phase Thermosiphons - Experiments of IKE and Validation of ATHLET models. in 14th International Topical Meeting on Nuclear Reactor Thermal-Hydraulics, Operation and Safety (NUTHOS-14). 2024. Vancouver,

[5]. A. Krüssenberg; F. Weyerman; A. Wielenberg; A. Schaffrath; C. Graß; R. Kulenovic; J. Starflinger. Experimental and Numerical Study on Two-Phase Closed Thermosiphons related to Passive Spent Fuel Pool Cooling. in 12th International Topical Meeting on Nuclear Reactor Thermal-Hydraulics NUTHOS-12. 2018. Qingdao.

[6]. M.Kirsch, S. Cáceres, R. Kulenovic, J. Starflinger. Experimental investigation on two-phase closed thermosyphons with laser-structured coating in the condenser section. in Joint 21st IHPC and 15th IHPS. 2023. Melbourne.

[7] Holder, Daniel, Peter, Alexander, Kirsch, Marc, Cáceres, Sergio, Weber, Rudolf, Onuseit, Volkher, Kulenovic, Rudi, Starflinger, Jörg and Graf, Thomas. Enhancing heat transfer at low temperatures by laser functionalization of the inner surface of metal pipes. Nature Scientific Reports. 2024. 14(1): p. 2557.

[8] D. Sarker, W. Ding, C. Schneider and U. Hampel. Single bubble dynamics during nucleate flow boiling on a vertical heater: Experimental and theoretical analysis of the effect of surface wettability, roughness and bulk liquid velocity. International Journal of Heat and Mass Transfer. 2019. 142: p. 1–15.

[9] A. A. Alammar, F. N. Al-Mousawi, R. K. Al-Dadah, S. M. Mahmoud and R. Hood. Enhancing thermal performance of a two-phase closed thermosyphon with an internal surface roughness. Journal of Cleaner Production. 2018. 185: p. 128–136.

[10] D. Glushkov, E. Orlova, A. Islamova, D. Nikitin, Y. Lyulin and D. Feoktistov. Influence of the Metal Surface Texture on the Possibility of Controlling the Phase Transition of Water Droplets in the Single-Phase Regime. Applied Sciences. 2022. 12(23): p. 12155.

Paper ID 026(S2D)

Aluminum Loop Thermosyphon with two Evaporators and One Condenser for Electronic Cooling

Leonard L. Vasiliev, Alexander S. Zhuravlyov, Alyona A. Gasparovich, Dmitry S. Sadchenko

Luikov Heat and Mass Transfer Institute, Minsk, Belarus

Abstract

This paper presents the results of investigation of the parameters of a new flat aluminum thermosyphon, the evaporator of which contains two identical panels operating in parallel, each of which has eight mini-channels. The panels are combined by single vapor and liquid collectors. On each of the evaporator panels there are heat sources (chips) of varying power, a cooling of which is carried out using loop thermosyphon condenser. The working fluid is acetone. The influence of the heat load and the working fluid volume on the heat transfer coefficients of the evaporator, condenser and the thermal resistance of the thermosyphon was determined and investigated. The system's optimal filling ratio is found to be around 30-50%, and the lowest evaporator thermal resistance is 0.15 K/W for the heat load range 20-80 W. The test results showed that the thermal resistance of the thermosyphon decreases with an increase in the transferred heat flux due to an increase in a speed of a circulating working fluid and intensification of heat transfer. The thermosyphon has good dynamics of quick access to the operating mode. It is stable in operation in a wide range of heat fluxes.

Keywords: Thermosyphon; Evaporator; Condenser; Heat transfer coefficient

1. Introduction

Modern electronic chips are minidevices with a high packing density inside electronic or electrical cabinets. Active thermal management of chips using heat pipes and thermosyphons ensures their reliable operation and maximizes the mean time between failures of minielectronic devices. As a result of the miniaturization of highly integrated electronic components packed inside electronic cabinets, the heat flux density generated by them reaches 100–200 W/cm^2. Chip miniaturization increases the density of the heat flux, which must be dissipated into the environment (air). Two-phase thermal regulation systems (heat pipes and thermosyphons) play a vital role in the efficient cooling of electronic or electric cabinet components due to their ability to transfer heat at high speed over long distances without significant heat losses [1-5]. Thermosyphon and its integrated system have distinct advantages over other free cooling methods and have great application potential. A two-phase loop thermosyphon (TPLT) is a type of passive heat transfer device which has the ability of efficient heat transfer over a long distance without any external power supply [6-9]. Loop thermosyphons can be effectively used in cooling systems for powerful electronic components, in particular, central and graphic processors, thyristors, IGBT modules, LEDs, the maximum operating temperature of which is in the range of 70–100 °C. It has been widely used in various thermal engineering application, including data center [10-14].

The full information about the thermosyphon is given in Table 1.

Table 1. Specifications of the thermosyphon

Specifications	Size/Material
Working fluid	Acetone
Filling volume	15-63%
Evaporator	
Material	Aluminum
Number of panels	2
Number of mini-channels in one panel	8
Dimensions of one mini-channel (length × width × height)	7 mm × 3 mm × 110 mm
Hydraulic diameter	4.2 mm
Condenser	
Type	Tube in tube
Material	Aluminum
External dimensions (length × external diameter)	200 mm × 24 mm
Wall thickness	2 mm
Dimensions of vapor and liquid collectors	160 mm × 9 mm × 9 mm
Cooling liquid	Water
Liquid temperature	20 °C

Thus, it can be concluded that at the present time, the development and study of the possibilities of introducing highly efficient thermosyphons is a promising and relevant line of research. In recent years, mini-channel heat exchangers have been used as compact evaporators in both the automobile system of air conditioning and heat pumps [15, 16]. TPLT consists of an evaporator, condenser, a compensation chamber (second panel, transient time of switch on) , vapor and liquid pipes, Fig. 1. The working fluid is acetone. At the low filling ratio, the flow pattern changes as slug, flow-churn, flow-annular, flow with the heat load increase and the gas – liquid flow shifts to slug flow – geyser boiling – been revealed as well, Fig. 2. The panels are united by single vapor and liquid collectors.

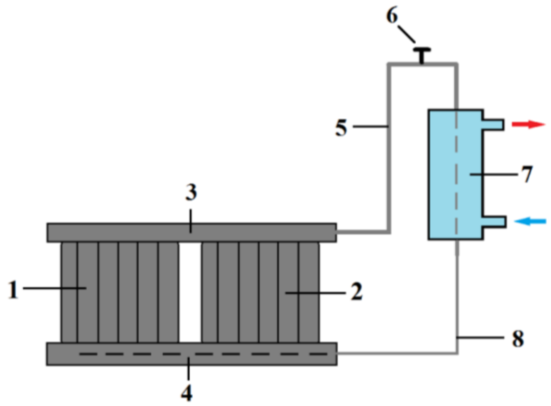

Fig.1. Schematic diagram of the thermosyphon: 1, 2) evaporator panels; 3) vapor collector; 4) liquid collector; 5)vapor tube; 6)filling connection; 7) condenser; 8) liquid tube.

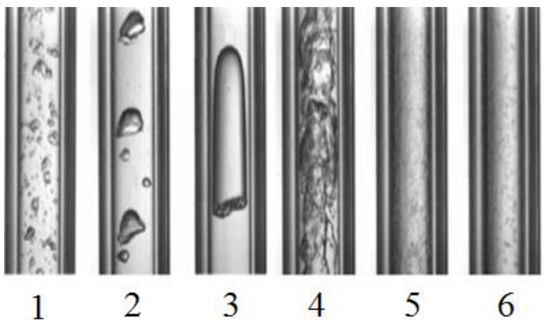

Fig. 2. Characteristic features of boiling of liquid in the vertical channels of the thermosyphon (*d* = 4 mm) as a function of the heat load [5]:
1) nucleation of mini-bubbles on the channel wall; 2) merging of mini-bubbles into larger ones, 3) separation of the liquid flow into vapor plugs and liquid cuffs; 4) the development of turbulence in a two-phase vapor – liquid flow; 5) annular separation of the vapor-liquid flow with formation of thin liquid films on the wall, accompanied by an increase in the vapor content of the two-phase flow; 6) wet vapor flow (fog).

The evaporator and condenser of thermosyphon are connected to each other by means of a vapor (5) and liquid (8) tubes. The inner diameter of the vapor tube is 8 mm and that of the liquid one is 4 mm. In each panel the mini-channels are separated by thin walls (ports) 1 mm thick. The ports in the mini-channels are used as internal fins. They increase the heat exchange surface area and the evaporation rate of the working fluid. Multichannel loop thermosyphons have advantages over single-channel ones. They are more compact, have a larger ratio of the inner surface of the channel to its volume, a smaller volume of working fluid and mass, which leads to more intensive and efficient heat transfer [17-19].

Depending on the heat load, the two-phase process of hydrodynamics and heat transfer of the working fluid in mini-channels is accompanied by the nucleation and development of vapor bubbles.

The thermosyphon condenser is made in the form of a water double-tube heat exchanger and is cooled by a water flow from a LOIP FT-316-40 thermostat. The evaporator is heated by a HY10010E DC power supply. T-type thermocouples (copper-constantan) are installed at the main points of the thermosyphon. The thermocouple signals are processed by an Agilent 34980A multimeter and transferred to a computer for further processing. To minimize heat losses, the evaporator, vapor and liquid tubes are covered with a layer of thermal insulation. The liquid tube connects the condenser with the evaporator and runs inside the lower evaporator collector of the thermosyphon along its entire length to ensure uniform supply of the working fluid to both panels. The general view of the experimental setup is shown in Fig. 3.

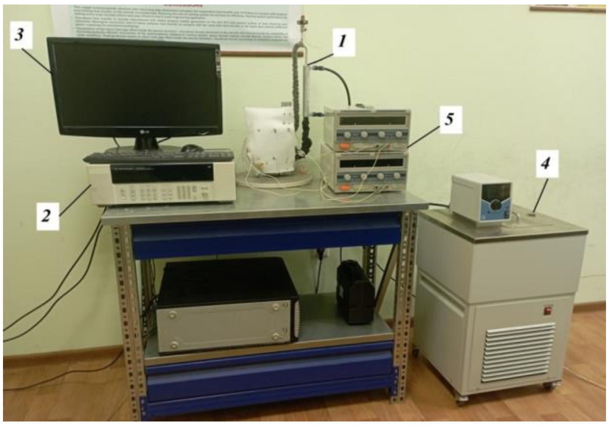

Fig. 3. Loop thermosyphon with two evaporator panels: 1) thermosyphon; 2) multimeter; 3) personal computer; 4) thermostat; 5) power supplies.

The location of the thermocouples on the surface of the thermosyphon is shown in Fig. 4, where the main numbers of thermocouples are circled in red. The experimental setup is designed to study heat transfer processes during evaporation, boiling, and condensation in thermosyphons. In the process of research, the temperatures along the thermosyphon, the thermal resistance of the thermosyphon components, the heat transfer efficiency, and the critical heat flux were determined. All tests were carried out under the same conditions at an air temperature in the room of 18-20 °C. The water coolant temperature was 20 °C. The time intervals between two successive tests were at least 12 hours, which made it possible to completely cool the setup down to room temperature.

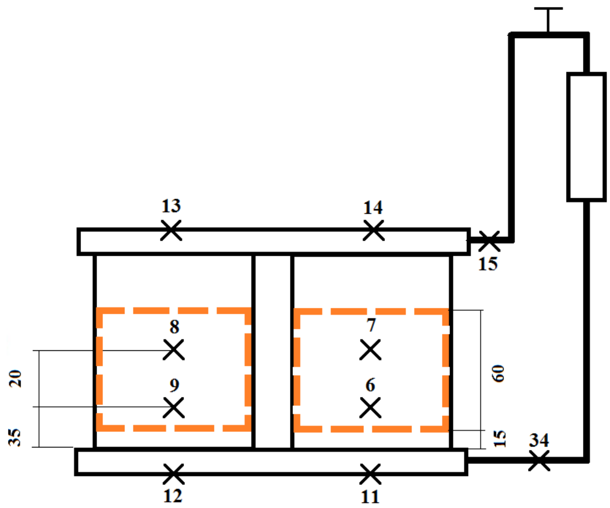

Fig. 4. Arrangement of the thermocouples on the evaporator panels with two heaters, condenser, vapor and liquid collectors, vapor and liquid tubes.

2. Experimental study of the parameters of the thermosyphon with a thermal load on one or two panels

2.1. Panel No. 1

Figure 5 shows a graph of the evolution of the temperature field on the surface of the annular thermosyphon over time when 33% of its volume is filled with acetone. The heat flux (Q = 40 W) is supplied to panel 1; initially panel 2 is used as a compensation chamber, contributing to a successful and reliable start of the thermosyphon as an auxiliary analog of the condenser. Non stationary heating of the thermosyphon panel 1 occurs in the transitional period of time (number 1 in Fig. 5). Vapor does not enter the thermosyphon vapor tube until the time when the saturation temperature in the vapor collector reaches 60 °C.

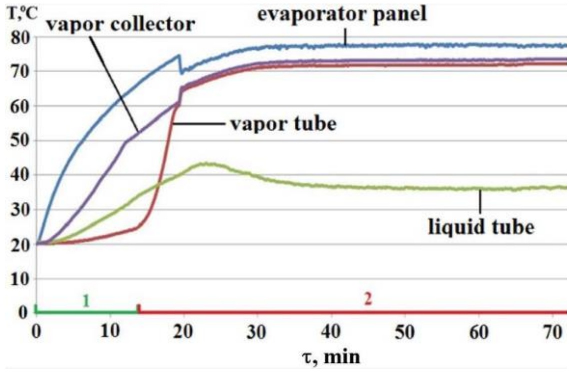

Fig. 5. Graph of temperature distribution in time for filling 33% of acetone at a heat load of 40 W: 1) nonstationary heating process; 2) stationary process of heat transfer in the thermosyphon.

During the transient process of heat transfer from panel 1 to panel 2 of the evaporator, the thermosyphon condenser remains passive, as evidenced by the constancy of its temperature in the vapor tube (Number 1, Fig. 5). After the temperature of the panel 2 rises to the saturation temperature (60 °C), the operation of the thermosyphon condenser is activated, and the heat transfer in the thermosyphon becomes stationary (Number 2, Fig. 5). The end of the transitional period of operation of the thermosyphon and the beginning of the stationary period of heat transfer of the annular thermosyphon can be determined by the change in the temperature at entry of the liquid coming from the condenser to the liquid collector of the evaporator (thermocouple 34 on the liquid tube of the thermosyphon, Fig. 4).

The evolution of the thermosyphon launching in time and the transition from the nonstationary operation mode to a stationary one is shown in Fig. 6.

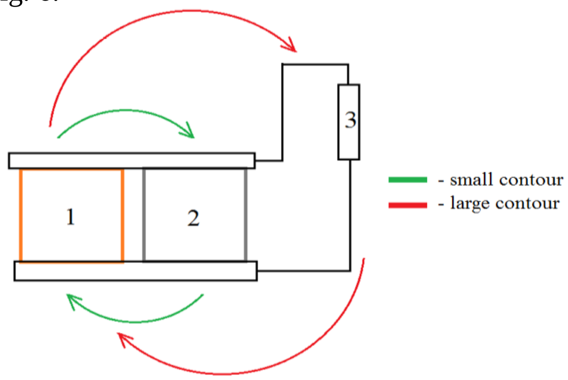

Fig. 6. Scheme of operation of the thermosyphon: the transient mode of operation is indicated by a green contour 1 (small contour of operation), the stationary mode of operation of the thermosyphon with the active participation of the condenser (heat sink) is indicated by a red contour 2 (large contour of operation).

Fig. 7 shows the temperatures along the thermosyphon.

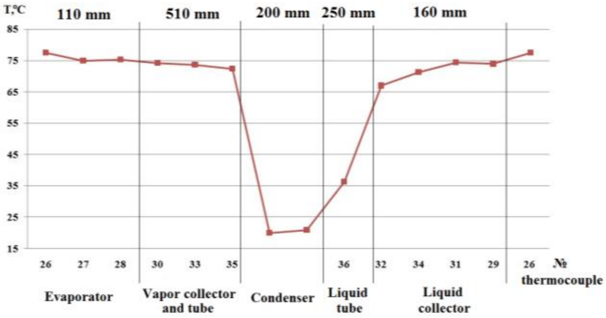

Fig. 7. Temperature distribution along the thermosyphon in the stationary mode of operation, Q = 80 W.

The average heat transfer coefficient in a thermosyphon is determined from the Newton–Richman equation:

$$h = \frac{Q}{\Delta T \cdot F} = \frac{q}{\Delta T}. \qquad (1)$$

The heat transfer coefficient calculated for different fillings of the thermosyphon with the working fluid is shown in Fig. 8.

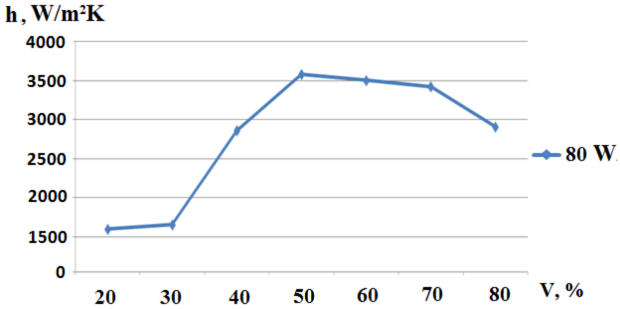

Fig. 8. Graph of the dependence of the heat transfer coefficient on the volume of filling the evaporator with acetone (percentage).

From the analysis of Fig. 8 it can be concluded that significant changes in the heat transfer coefficient are observed when 30% to 50% of the evaporator are filled with acetone. With a further increase in the filling volume, the heat transfer coefficient remains near constant. Thus, the optimal filling of the thermosyphon with the working fluid is 50% at a nominal thermal load on the thermosyphon of 40 W.

The thermal resistance of the evaporator R_e, condenser R_c, and the total thermal resistance R_t, shown in Fig. 9, are calculated by formulas (2)-(4):

$$R_e = \frac{T_e - T_v}{Q}, \qquad (2)$$

$$R_c = \frac{T_v - T_c}{Q}, \qquad (3)$$

$$R_t = \frac{T_e - T_c}{Q}. \qquad (4)$$

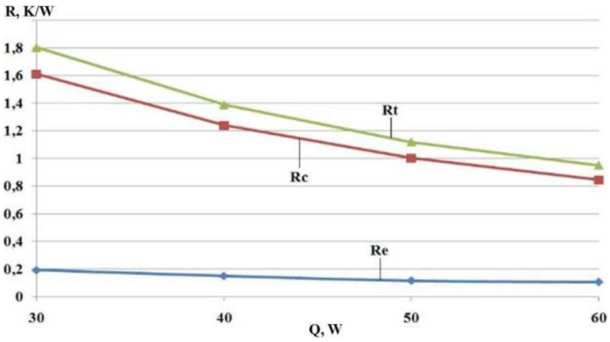

Fig. 9. Thermal resistance of evaporator (R_e), condenser (R_c) and total thermal resistance (R_t) vs. heat load Q.

2.2. Heat load on two thermosyphon panels

The loop thermosyphon with two evaporator panels is capable of removing the heat flux from two identical or different heat sources, which may differ in the heat flux value.

To study the effect of the load on two panels of the thermosyphon, an experiment was carried out during which the main panel (1) was activated at a heat flux of 40 W. After reaching the stationary mode, an additional panel (2) with a heat flux of 20 W was activated too. The graph of temperature distribution is shown in Fig. 10.

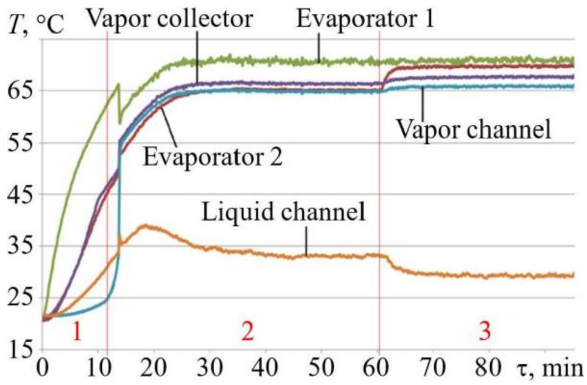

Fig. 10. Graph of the temperature distribution on the surface of the thermosyphon evaporator in time. Both panels are active, the total heat load is 60 W.

Figure 10 is divided into three parts. The first part shows the startup process of panel 1 at a heat flow of 40 W. The second part displays the startup of the thermosyphon and the emergence into the stationary mode of operation.

The third part displays the emergence into the stationary mode of operation of the thermosyphon with the inclusion of additional panel 2 at a heat flux of 20 W. When a heat load was applied to panel 2, the temperature of the main panel 1 remained practically unchanged, there was a slight increase in the vapor temperature and a significant decrease in the temperature at the condenser outlet, which indicates an intensification of the heat exchange of the condenser. The graph of the temperature distribution along the thermosyphon in the stationary mode of operation with the supply of 40 W to panel 1 and the supply of 20 W to panel 2 is shown in Fig. 11.

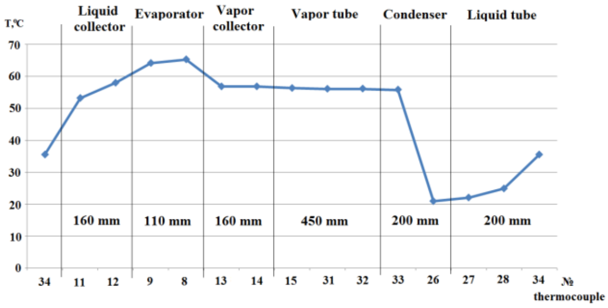

Fig. 11. Temperature distribution along the thermosyphon in the stationary mode of operation of both panels of the thermosyphon.

Results of experimental study of the thermosyphon with two parallel panels found that it operation is related to the difference in heating power between the two panels. The hydraulic resistance of the high-load panel is higer than the low-load panel. When there is a significant difference in the loads of the two panels, the high-load panel experiences overheating due to insufficient flow, while the low-load panel incurs some flow wastage.

3. Conclusions

A new flat aluminum loop thermosyphon with two multi-channel evaporator panels has been developed and tested. Thermal characteristics of the thermosyphon have been studied experimentally when the volume of filling the evaporator with the working fluid is minimal (30-50% of the total volume of the evaporator). The evaporators have the common collectors for the transfer of vapor and working fluid. The test results showed that the thermal resistance of the thermosyphon decreases with an increase in the transferred heat flux due to the increase in the speed of the circulating working fluid and intensification of the heat transfer. Stability of the thermosyphon parameters is maintained even with highly nonstationary and asymmetric heat inputs to the evaporator surface in a wide range of heat fluxes. The thermosyphon has a good dynamics of quick access to the operating mode. The flat evaporator of the thermosyphon has good thermal contact with the objects to be cooled. Consequently, a number of cooled elements, such as IGBTs, cryogenic infrared sensors, electronic circuits, LEDs, etc., can be attached to the thermosyphon evaporator, consisting of several multichannel panels.

References

[1] B. Albertsen and G. Schmitz, Experimental parameter studies on a two-phase loop thermosyphon cooling system with R1233zd(E) and R1224yd(Z). International Journal of Refrigeration, 2021. 131: p. 146.

[2]. A. J. Robinson, J. Colenbranderb, G. Byrnec, P. Burke, J. McEvoy, and R. Kempers, Passive two-phase cooling of air circuit breakers in data center power distribution systems, Electrical Power and Energy Systems. 2020. 121: art. 106138.

[3] Dongliang Zhao, Christine Elizabeth Martini, Siyu Jiang, Yaoguang Ma, Yao Zhai, Gang Tan, Xiaobo Yin, and Ronggui Yang, Development of a single-phase thermosiphon for cold collection and storage of radiative cooling. Applied Energy, 2017. 205: p. 1260.

[4] M. Polačiková, P. Nemec, M. Malcho, and J. Jandačka, Experimental investigations of a passive cooling system based on the gravity loop heat pipe principle for an electrical cabinet. Applied Sciences. 2022: 12 p. 1634.

[5] TG Karayiannis, MM Mahmoud, Flow boiling in microchannels: Fundamentals and applications. Applied Thermal Engineering, 2017. 115: pp. 1372–1397.

[6] L. Wang, W. Zhong, W. Min, Z. Wang, and X. Cao, Experimental study on the thermal performance of a novel two-phase loop thermosyphon under low-heat-flux conditions. Applied Thermal Engineering, 2024. 236: Art. 121447.

[7] C. Sarno, C. Tantolin, R. Hodot, Yu. F. Maydanik, and S. Vershinin, Loop thermosyphon thermal management of the avionics of an in-flight intrrtainment system. Applied Thermal Engineering. 2013. 51: p. 764.

[8] J. Cao, Z. Zheng, M. Asim, M. Hu, Q. Wang, Y. Su, G. Pei, and M. K. H. Leung, A review on independent and integrated/coupled two-phase loop thermosyphons. Applied Energy, 2020. 280: p. 306.

[9] Y.-G. Lv, Y.-T. Wang, T. Meng, Q.-W. Wang, W.-X. Chu. Review on thermal management technologies for electronics in spacecraft environment. Energy Storage and Saving. 2024. 3: p. 153.

[10] S. Manova, L. G. Asirvatham, R. Nimmagadda, J. R. Bose, and S. Wongwises, Cooling of high heat flux electronic devices using ultra-thin multiport minicgannel thermosyphon. Applied Thermal Engineering, 2019. 169(2): art. 114669.

[11] L. L. Vasiliev, A. S. Zhuravlyov, M. A. Kuz'mich, V. K. Kulikovskii, and V. A. Olekhnovich, Loop thermosyphon for cooling heat-loaded electronics components. Journal of Engineering Physics and Thermophysics. 2023. 96(7): p. 1708.

[12] E. Oró, M. Codina, and J. Salom, Energy model optimization for thermal energy storage system integration in data centres. Journal of Energy Storage, 2016. 8: p. 129.

[13] L. Ling, Q. Zhang, Y. Yu, and S. Liao, Experimental investigation on the thermal performance of water cooled multi-split heat pipe system (MSHPS) for space cooling in modular data centers. Applied Thermal Engineering, 2016. 107: p. 591.

[14] X. Wang, Q. Wen, J. Yang, J. Xiang, Z. Wang, C. Weng, et al., A review on data centre cooling system using heat pipe technology. Sustainable Computing: Informatics and Systems. 2022. 35: art. 100774.

[15] G. Previati, G. Mastinu, and M. Gobbi, Thermal management of electrified vehicles – a review. Energies. 2022. 15(4): art. 1326.

[15] Y. Liu, Z. Yan, Z. Jiang, N. Li, B. Yang, and Y. Wu. Experimental study on the small two-phase thermosyphon loop with minichannel evaporator. Journal of Thermal Science and Engineering Applications. 2023. 16(2): art. 021006.

[16] Y. He, C. Hu, H. Li, X. Hu, and D. Tang, Experimental investigation on air-cooling type loop thermosyphon thermal characteristic with serpentine tube heat exchanger. International Journal of Refrigeration. 2022. 138: p. 52.

[17] T. G. Karayiannis and M. M. Mahmoud, Flow boiling in microchannels: Fundamentals and applications. Applied Thermal Engineering, 2017. 115: p. 1372.

[18] Y. A. Kuzma-Kichta, A. V. Lavrikov, E. A. Kustova, and E. A. Kuleshov, Research of water boiling in microcnannel. Journal of Physics: Conference Series. 2019. 1370(1): art. 012058.

[19] M. Piasecka and K. Strąk, Boiling Heat Transfer during Flow in Vertical Mini-Channels with a Modified Heated Surface. Energies. 2022. 15(9): art. 7050.

Paper ID 028(S8)

Influence of the liquid lifting height on the performance of an inverted two-phase thermosyphon

Ricardo Schneider Calomeno[1*], Fernando Henrique Milanez[1], Marcia Barbosa Henriques Mantelli[1]

[1] *Heat Pipe Laboratory, Federal University of Santa Catarina, Florianópolis, SC, Brazil*
* *Corresponding author email address: ricardoschneider@labtucal.ufsc.br*

Abstract

The use of passive heat transfer technologies, such as thermosyphons and heat pipes, to transfer heat from a source located above a heat sink is not straightforward, as the capacity of returning liquid from the condenser to the evaporator is deeply affected. An alternative solution is the inverted two-phase thermosyphon, which uses the pressure difference between hot and cold components to pump the working fluid and transfer heat through a closed loop, with liquid flowing up against gravity. The condensate lifting height is one of the main operational parameters and is related to the vertical distance between evaporator and condenser. The control of the aperture and closure of valves directs the flow inside the loop. In the present work, an inverted two-phase thermosyphon prototype is tested under thermal load ranging from 2.0 to 12.0 kW and for liquid lifting heights of 2.0, 3.0 and 5.0 m, with water as the working fluid. The prototype showed a large capacity to adapt well to various operation conditions, with stable operation for all tested configurations. The results demonstrate that the evaporator temperature is the parameter that most affect the lifting height, as the higher temperature, the higher is the saturated vapor pressure and so its difference to the accumulator. Actually, this pressure difference is the driving force for the condensate lifting. However, the thermal load level did not affect the capacity of liquid lifting.

Keywords: Inverted two-phase thermosyphon; downward heat transfer; periodic operation; passive technology

1. Introduction

In the design of thermal systems for industrial applications, the use of passive technologies to transfer heat, like heat pipes and thermosyphons, is very convenient. These devices are efficient and reliable, when the heat source is below the heat sink and the return of condensed liquid, from the condenser to the evaporator, occurs in the gravity direction. For horizontal operation, in which the heat source and sink are at the same level, wick structures are used to displace the liquid and the liquid lifting height is limited by the capillary pumping capacity of the media. The major concern, is when liquid needs to be lifted, against the gravity, when the heat source is above the heat sink.

A passive alternative technology to transfer heat downwards is the inverted two-phase thermosyphon, in which the heat transfer process can be continuous or periodic.

The continuous process is represented by the bubble pump technology, in which vapor bubbles formed in the evaporator mix with the working fluid, resulting in a fluid with lower density, that pushes the working fluid through a closed loop [1-3]. Alternatively, in periodic processes, the fluid flow is displaced against gravity by the pressure difference between the hot and cold components of the device [4-9].

Inverted thermosyphons can be applied for the thermal control of electronics [10-11], of solar collectors [12], for the air condition systems in house cooling systems [13], for cooling of marine propulsion engines [14], for oil and gas rigs, among others.

Over the last few years, the number of works regarding inverted two-phase thermosyphons have increased, either for the bubble pump or for the component pressure difference technologies [12].

Both vapor and liquid are used to carry heat, for the devices driven by pressure differences. Some prototypes employed as working fluids the HCFC 141b [4, 8-9] and water [15], for lifting the liquid to heights ranging from 2.0 m to 3.3 m, and R114 [5] for liquid lifting from 7.0 m to 15.0 m. In these works, thermal loads ranged from 50 W to 1.2 kW. For electronics cooling, FC72 [10-11] was used for lifting heights ranging from 0.35 m to 0.7 m and for thermal loads from 14 W to 45 W. Prototypes in which the liquid carries the heat normally use water [7,16]. With this working fluid, a prototype [16] transferred heat in the horizontal direction, being able to lift the returning liquid up to 0.4 m.

In the present work, the thermal and hydraulic performance of a prototype of an inverted two-phase thermosyphon is analyzed under thermal loads ranging from 2.0 kW to 12.0 kW, different operation conditions and for different liquid lifting heights. The prototype is adaptable, allowing tests with different liquid lifting heights. Three configurations were tested: liquid heights of 2.0 m, 3.0 m and 5.0

m. The geometry of the prototype is based on a previous study [17].

2. Experimental Apparatus

The inverted two-phase thermosyphon prototype investigated in the present work is shown in Figures 1 and 2. The device is composed by an evaporator, a condenser and an accumulator, along with connecting pipes (lines) and valves. Four lines are used to connect these components: equalization L_1, drainage L_2, vapor transport L_3 and liquid lifting L_4. Lines L_1 and L_2 connects the accumulator to the evaporator, line L_3 connects the evaporator outlet to the condenser inlet while line L_4 connect the condenser outlet to the accumulator. Distilled water is used as the working fluid.

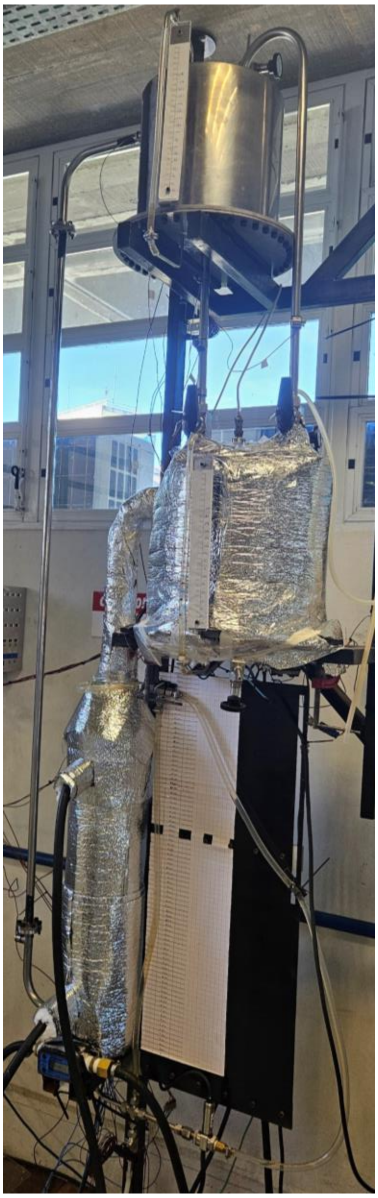

Figure 1. Experimental Apparatus, configuration with liquid lifting height (ΔH_{CA}) of 2.0 m.

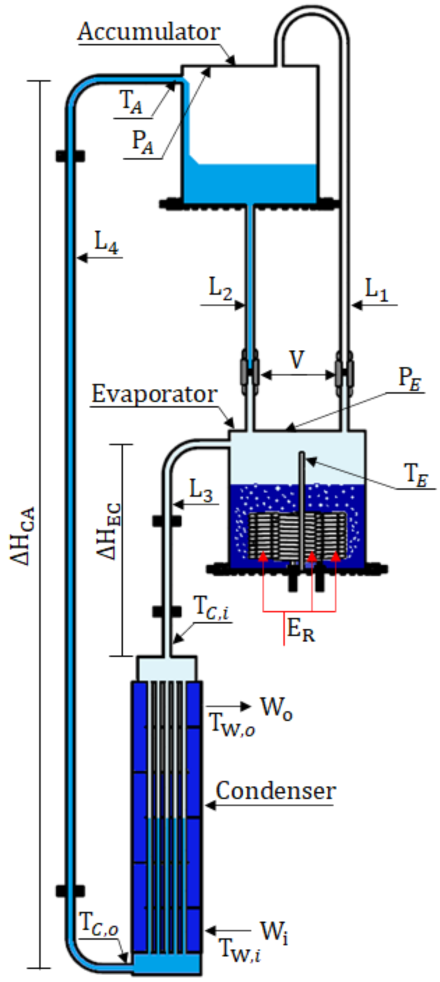

Figure 2. Inverted two-phase thermosyphon sketch (during vapor transport process): E_R – electric heaters, T – thermocouples, P – pressure transducer, V – sphere valves, W_i and W_o – cooling fluid inlet and outlet, respectively, lines: L_1 – equalization, L_2 – drainage, L_3 – vapor transport and L_4 – liquid lifting, ΔH – height variation.

Both evaporator and accumulator have the same geometry: cylindrical tanks with 30.0 cm height and 30.0 cm internal diameter, with an internal volume of 21.2 L. Inside the evaporator, in the bottom, three electric heaters are immersed in a working fluid liquid pool, as shown in Figure 2. The resistances are controlled by a Variac transformer, providing heat power of up to 4.2 kW. The maximum input of power in the evaporator, i.e., the thermal load, is of 13.2 kW. The evaporator is filled with (v_e) 16.0 L of the working fluid. The condenser is actually a cylindrical shell-and-tube heat exchanger. The shell has an internal diameter of 15.0 cm and contains 25 parallel tubes of 60.0 cm long, with external and internal diameters of 1.27 cm and 1.06 cm respectively, in a 5x5 arrangement. In the shell side, five baffles, with a baffle cut of 18%, are employed.

Water, from a cooling tower, flows through the heat exchanger shell, removing heat from the condenser tube bundle. Sphere valves are used in lines L_1 and L_2 to control the passage of working fluid between evaporator and accumulator. The tubes of lines L_3 and L_4 are flanged, as indicated in Figure 2, enabling the change of the tube, so that the height difference between the condenser in relation to both evaporator and accumulator can be increased or reduced. The evaporator, line L_3 and condenser are insulated with a 3.0 cm thick Isoglas™ blanket, externally covered by a 0.5 cm aluminized low-density polyethylene (LDPE) blanket.

2.1. The Operation Cycle

This inverted two-phase thermosyphon prototype operates with a periodic cycle composed by two processes: vapor transport and drainage. The vapor transport, illustrated in Figure 2, begins with the closure of the sphere valves in lines L_1 and L_2, while the electric heaters are turned on. The liquid pool inside the evaporator is heated, vapor is formed resulting in pressurized vapor that flows downwards, carrying heat to the condenser through line L_3. In the shell side of the condenser, water is continuously supplied from a cooling tower during the entire cycle. Therefore, the vapor that enters the tubes condenses. A liquid pool is formed at condenser bottom and accumulates in line L_4. During the working fluid condensation, the liquid level inside L_4 rises forced by the vapor pressure produced in the evaporator, being able to reach the accumulator, forming another pool. The liquid also fills the line L_2 region above the valve. Therefore, to lift liquid against gravity, the hydraulic pressure of the liquid column in line L_4 needs to be overcame by the vapor pressure. So, a proper temperature difference between the working fluid inside the evaporator and the accumulator is required.

After some time, then the liquid level inside the evaporator is low, the electric heaters are turned off and the vapor transport process ends. Then, the drainage process starts with the opening of the sphere valves on lines L_1 and L_2. As the vapor flows from the evaporator to the accumulator through line L_1, the pressure difference between these components is equalized, and the liquid lifting from the condenser to the accumulator ceases. Once the pressure difference between the evaporator and the accumulator is lower than the hydraulic head within line L_2, the liquid flows back to the evaporator by gravity through line L_2. When the liquid level inside the evaporator is restored, both sphere valves are closed in order to start a new cycle.

2.2. Data Acquisition

To measure the temperature at different locations of the device, thirteen T-type thermocouples were used. Six of them can be seen on Figure 2. The other seven thermocouples were for measurements of: ambient, accumulator (top and bottom positions), three on line L_2 (top, middle and bottom) and one on the middle of line L_1. For pressure measurements, two absolute transducers were used, one at the evaporator and the other at the accumulator, as seen in Figure 2. The pressure difference between condenser inlet and outlet was measured with a differential transducer, as seen in Figure 3. The liquid level inside the accumulator, the evaporator and the condenser were monitored with transparent graduated scale hoses. The flow rate of cooling fluid supplied to the condenser by the cooling tower was measured with a flowmeter. The power applied to each electric heater was measured with a wattmeter.

Readings of temperature and pressure were made using the data-acquisition hardware platform from National Instruments™ with LabVIEW.

Figure 3. Equipment for condenser liquid level and differential pressure measurements. Prototype at 5.0 m lifting liquid height (ΔH_{CA}) configuration.

2.3. Experimental Procedure

For all the analyzes, a common procedure was followed before the first operation cycle. A vacuum pump is used to reduce the internal pressure of the inverted two-phase thermosyphon prototype, with both sphere valves opened, in order to remove non-condensable gases inside the device. A standard initial condition in terms of the pressure inside the evaporator and the accumulator was then established. The amount of working fluid removed from the device in this procedure was minimal.

In the beginning of every start-up cycle, all the liquid was inside the evaporator. After the reduction of the internal pressure, both sphere valves were closed, then, the electric heaters were turned on. The thermal load applied to the evaporator was on, until the evaporator liquid level decrease below 12.9 cm, which was equivalent to 10 L of working fluid. After that, the electric heaters were turned off and both sphere valves were opened, so the drainage process could begin.

After the start-up cycle described above, a certain amount of liquid remained at the condenser bottom and inside line L_4. Thus, in the following cycles, the volume of the evaporator liquid pool was lower than that of the start-up cycle. All the other cycles after the start-up cycle (regular cycles), begun with a liquid pool at the condenser bottom and inside line L_4.

As already mentioned, the applied thermal load ranged from 2.0 kW to 12.0 kW. Three different testing configurations were tested. The height differences between: evaporator and condenser inlet (ΔH_{EC}), condenser outlet and accumulator (ΔH_{CA}), and accumulator bottom and evaporator top (ΔH_{EA}) can be seen on Table 1, along with the average volume of the liquid pool on the condenser bottom and line L_4, v_p.

Table 1. Height difference between components of the inverted two-phase thermosyphon prototype and average volume of liquid pool on condenser bottom and line L_4 in each configuration.

Configuration	1st	2nd	3rd
ΔH_{CA} [m]	2.0	3.0	5.0
ΔH_{EC} [m]	0.55	1.55	3.55
ΔH_{EA} [m]	0.5	0.52	0.52
v_p [L]	2.2	2.8	3.2

After the start-up cycle and some regular cycles were finished, the evaporator was refilled, until the liquid pool was restored to an average of 16 L. The liquid pool inside at the condenser bottom and line L_4 are drained only if, in a following analysis, another start-up cycle will be done. So, for analysis with only regular cycles, the total amount of working fluid in the prototype is given by the sum of v_e and v_p.

3. Results and Discussion

In the first analysis, the device was submitted to a single regular cycle in order to evaluate the operational conditions in terms of temperature and pressure. In this analysis, the second configuration (Table 1) was tested, with the lifting liquid height of 3.0 m, while the condenser was cooled at an average flow rate of 4.95 L/min. During the vapor transport process, a thermal load (Q_E) of 4.0 kW was continuous applied in the evaporator. The volume of the evaporator liquid pool before the electric heaters were turned on was approximately 16.4 L. Figure 4 shows temperature and pressure measured with time obtained during this cycle.

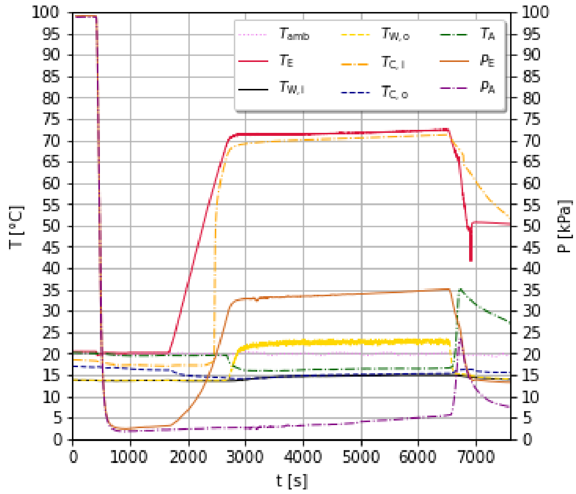

Figure 4. Temperature and pressure as a function of time for a single regular cycle with Q_E =4.0 kW and lifting height of 3.0 m.

As observed in Figure 4, initially, the internal pressure of the device is approximately at the atmospheric level. A vacuum pump connected to the prototype was used to remove non-condensable gases and to reduce the pressure between t = 410 s and t = 930 s. Then, the vacuum pump was disconnected from the device and both sphere valves were closed. The electric heaters were turned on at t = 1650 s, resulting in the heating of the working fluid (and so increasing of T_E), raising the pressure of the vapor inside the evaporator, P_E. Vapor flowed downwards through line L_3 and reached the condenser inlet at t =2340 s, when the temperature $T_{C,i}$ increased. During this process, the condenser liquid level decreased from 52 cm to 12.7 cm. In the shell side of the condenser, the temperature of the cooling liquid at the inlet was $T_{W,i}$ and at the outlet it was $T_{W,o}$. In the tube side, as vapor condenses, liquid is subcooled and leaves at the condenser outlet with temperature $T_{C,o}$. Then, cold liquid was lifted inside line L_4, where it absorbed heat from the ambient at a slightly higher temperature T_{amb} because line L_4 was not thermally insulated, until the accumulator inlet height was reached. At t =2683 s, cold liquid reached the accumulator inlet, decreasing the temperature T_A. A liquid pool was formed at the bottom of the accumulator. During the vapor transport process, the internal pressure of the accumulator (P_A) presented a smooth increase with time, which was caused by air leakage through the transparent hoses used to measure the liquid levels inside the components. Also P_E, T_E and $T_{C,i}$ showed a smooth increase. It is also important to observe that, despite the continuous increase with time of the absolute pressure due to air leakages, the pressure difference between evaporator and accumulator (ΔP_{EA}) remained constant. This is the pressure difference responsible for the liquid lifting, which is constant for a given configuration and thermal load.

As the evaporator liquid level reached 12.9 cm, the electric heaters were turned off, ending the vapor transport process. At $t = 6565$ s, the drainage process begun with the opening of the sphere valve on line L_1, so hot vapor flowed directly from the evaporator to the accumulator, equalizing the pressure between components, increasing T_A while T_E and $T_{C,i}$ decreased and the liquid lifting stopped. As the pressure equalized, the liquid level in the condenser rose, so temperature $T_{W,o}$ decreased and approached $T_{W,i}$. When ΔP_{EA} decreased below 2 kPa, the sphere valve of line L_2 was opened. Then, T_A and P_A decreased. Once the ΔP_{EA} fell below the hydraulic head of the accumulator liquid pool, the return of liquid though line L_2 begun. The cold liquid reduced the evaporator temperature. Natural convection on the accumulator surface cooled down this component. After all liquid had returned from the accumulator to the evaporator, both sphere valves were closed and the cycle was completed.

In the second analysis, the three configurations were submitted to different thermal loads along consecutive regular cycles. For each configuration, the applied thermal load, Q_E, ranged from 2.0 kW to 12.0 kW, with 2.0 kW steps. Thermal load was applied until a certain volume of liquid was evaporated from the evaporator (ΔV_E). These test parameters are listed on Table 2. The average cooling fluid flow rates (V_f) were: V_f =11.91 L/min for ΔH_{CA} =2.0 m, V_f =20.61 L/min for ΔH_{CA} = 3.0 m and V_f = 10.31 L/min for ΔH_{CA} =5.0 m. Temperature measurements along the prototype are shown in Figure 5, while Figure 6 shows the measurements of pressure, thermal load into the evaporator and heat transfer rate in the condenser (Q_C), calculated with the following equation:

$$Q_C = \rho c_p V_f \left(T_{W,o} - T_{W,i}\right) \tag{1}$$

where ρ and c_p are the density and the specific heat of the cooling fluid, respectively.

Table 2. Thermal load (Q_E), volume of liquid evaporated (ΔV_E) and cycle numbering for each liquid lifting height (ΔH_{CA}).

ΔH_{CA} [m]		2.0		3.0 and 5.0	
Test	Q_E [kW]	Cycle	ΔV_E [L]	Cycle	ΔV_E [L]
1	2.0	1st	2	1st	3
2	4.0				
3	6.0			2nd	3
4	8.0	2nd	3		
5	10.0			3rd	6
6	12.0	3rd	6	4th	6

Right after the initial pressure reduction period of the device with the vacuum pump, the sphere valves were closed and the electric heaters were turned on, heating the working fluid, very similar to the test presented before.

The operational conditions for liquid lifting were achieved in this prototype when $T_E \cong$ 59.1°C in the first configuration ($\Delta H_{CA} = 2.0$ m), $T_E \cong$ 70.1°C for the second configuration ($\Delta H_{CA} = 3.0$ m) and $T_E \cong$ 81.2°C for the third configuration ($\Delta H_{CA} = 5.0$ m).

When the thermal load Q_E was increased, from 2.0 kW to 4.0 kW, a new operational condition was quickly achieved with the increase of T_E, $T_{C,i}$, $T_{C,o}$, P_E and Q_C, then all become smooth as observed in Figure 5. Once the evaporator liquid level reached 12.9 cm, the electric heaters were turned off and the drainage process begun with the opening of the sphere valves, just like the previous test. The average total time lapse required to the drainage process was smaller for the first configuration ($\Delta H_{CA} = 2.0$ m), with equalization and liquid return time of 45 s. For the second and third configurations with ΔH_{CA} of 3.0 m and 5.0 m, respectively, the sphere valves were replaced by valves with a lower flow coefficient and that are better suited for operation at high temperatures. For these two configurations, the equalization last 180 s and the liquid returned within 200 s, in average.

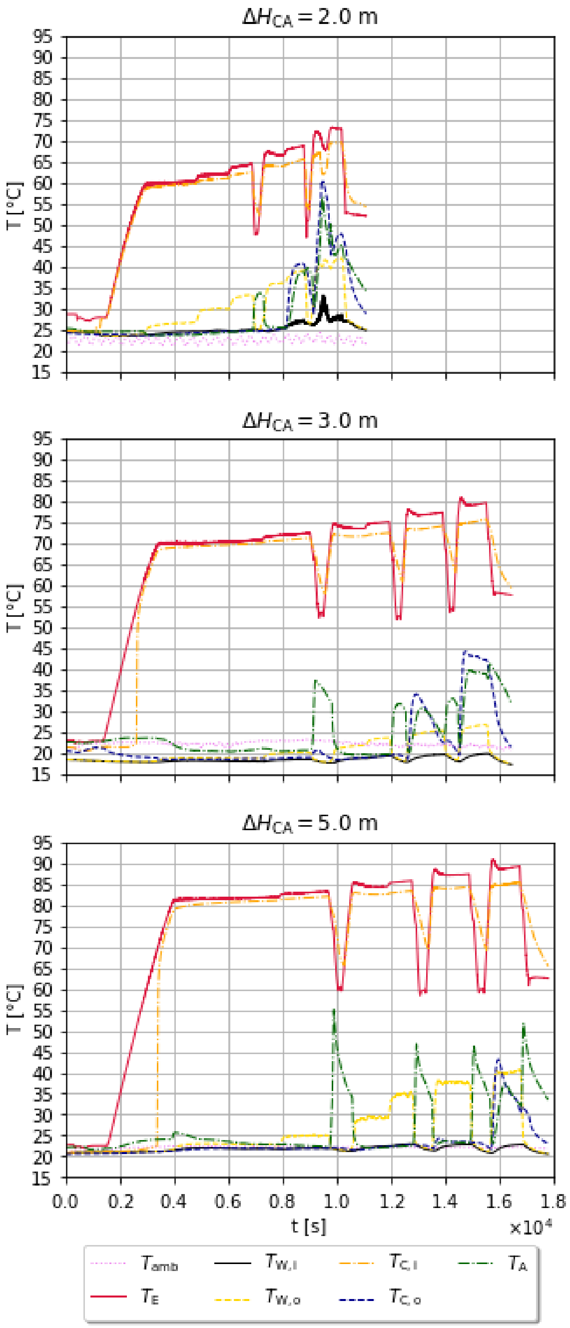

Figure 5. Temperatures measurement as a function of time for the three tested configurations and for thermal load Q_E ranging from 2.0 kW to 12.0 kW, at 2.0 kW steps.

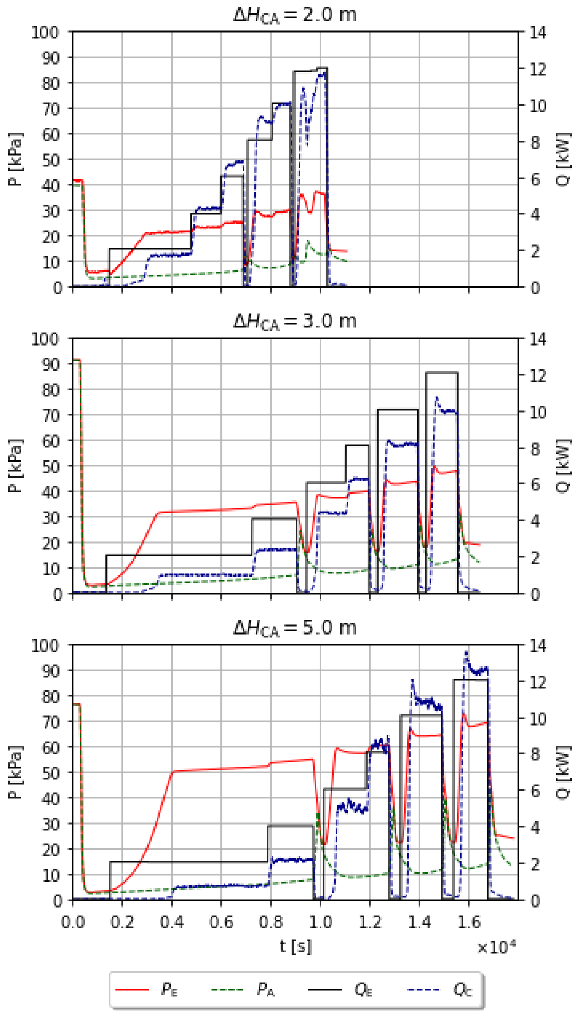

Figure 6. Measured pressures, thermal load input and heat transfer rate at the condenser as a function of time for the three tested configurations and for thermal load Q_E ranging from 2.0 kW to 12.0 kW, at 2.0 kW steps.

After the liquid had returned to the evaporator, both sphere valves were closed, the electric heaters were turned on again, corresponding to the first thermal load of the second cycle. The temperature behavior was again similar to the cycles presented before. Once operation conditions were achieved again, the accumulator was cooled by the liquid that enters this component and by natural convection on the exterior surface, reducing the pressure P_A. A small decrease was observed at T_E, $T_{C,i}$ and P_E, in Figure 5 and 6, while the pressure difference between evaporator and accumulator remained constant.

The larger was the height difference between the evaporator and the condenser (ΔH_{EC}), the larger was the temperature difference between T_E and $T_{C,i}$ This was due to the pressure drop of the vapor flow through line L_3, which also increased with the increase of the applied thermal load.

When the fifth thermal load, $Q_E = 10.0$ kW was applied, the condenser was not capable to promote subcooling of the condensate in the first (ΔH_{CA} =2.0 m) and the second (ΔH_{CA} =3.0 m) configuration. Therefore, hot liquid started to be delivered to the accumulator, increasing T_A. Also, the condenser liquid level was not stable and oscillated between 30.0 and 32.5 cm. A bubble implosion noise could be heard from the bottom of the condenser. This behavior lasted until the end of the cycle for the first configuration. For the second configuration the noise could be heard which was much lower than the first configuration, and it progressively reduced as the temperature of the liquid leaving the condenser reduced, decreasing $T_{C,o}$ and T_A. After 820 s, this noise vanished.

In the last cycle, the sixth thermal load, of $Q_E = 12.0$ kW, was applied. Soon after the operational conditions were reached again, the bubble implosion noise was heard again from the condenser bottom for all the three configurations tested. For the first configuration, with $\Delta H_{CA} = 2.0$ m, a part of the vapor did not condensate within the condenser, and so, inside line L_4 a two-phase flow was formed, which could be heard through the sound of vapor flow while the condenser liquid level oscillated between 17.0 to 38.5 cm. During this process, there was a sharp increase in $T_{C,o}$ and T_A with the intake of hot vapor and liquid in the accumulator which led to an increase of P_A, while a decrease was observed in pressure P_E and in temperatures T_E and $T_{C,i}$. The pressure difference between evaporator and accumulator decreased and was not large enough to maintain the liquid lifting, which stopped, and the noise ceased. Right after that, the temperature of the working fluid rose again, as can be seen in T_E and $T_{C,i}$, increasing back the pressure P_E, while the accumulator and line L_4 were cooled, decreasing the temperatures $T_{C,o}$ and T_A and pressure P_A. Soon after, the pressure difference between evaporator and accumulator was enough to continue the liquid lifting, although the noise was heard again until the end of the vapor transport process.

For the second and third configurations, the two-phase flow did not occur. In the second configuration, with $\Delta H_{CA} = 3.0$ m, the condenser had not completely subcooled the liquid and the hot liquid was lifted to the accumulator until the end of the cycle. The noise was heard during the entire vapor transport process, but much lower than the first configuration. The condenser liquid level varied from 22.0 to 27.0 cm after the noise started, up to 24.0 to 27.0 cm at the end of the cycle. In the third configuration, with $\Delta H_{CA} = 5.0$ m, the behavior observed was similar to what was observed in the second configuration with the thermal load $Q_E = 10.0$ kW, where after 960 s the noise vanished. The condenser liquid level oscillated from 22.5 to 27.0 cm at the beginning and was stable at 24.2 cm at the end. In this configuration, the noise was considerably lower than in the other two configurations. Also, the time period between bubble implosions noises was considerably larger.

In all configurations, it was observed that the device was able to adapt to changes, especially the pressure variations in the accumulator. The temperature and pressure of the working fluid inside the evaporator, T_E and P_E respectively, varied as well, so that the liquid lifting heigh was maintained. The pressure difference between evaporator and accumulator, ΔP_{EA}, was very stable when the power input was kept constant, as it can be seen in Figure 7.

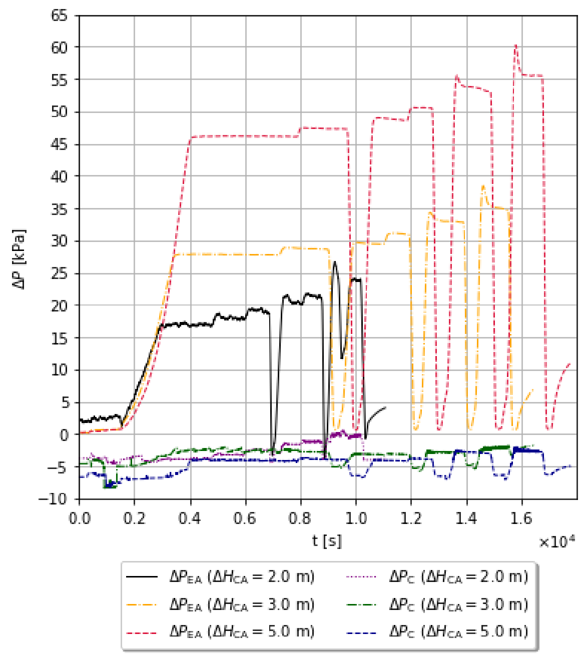

Figure 7. Pressure differences as a function of time between evaporator and accumulator (ΔP_{EA}) and condenser inlet and outlet (ΔP_C) for all the three tested configurations.

With air leaking into the device through the hoses during the operation cycles, a smooth increase in the accumulator pressure P_A was observed. Due to this effect, the device adapted constantly by increasing the evaporator pressure P_E and the vapor temperature T_E, while ΔP_{EA} remained stable, according to the hydraulic head of the liquid column that was being lifted inside line L_4. No sign of interference in the condensation process due to air infiltration was observed, as the pressure difference between condenser inlet and outlet ΔP_C also remained stable during the vapor transport process, which could also be observed in Figure 7.

As hot vapor flowed downwards carrying latent heat from the evaporator to the condenser, where it condensed and the liquid was subcooled. The heat transferred from the working fluid to the cooling fluid, Q_C, was measured for all the configurations.

In the first configuration, lifting height of 2.0 m, small heat losses were observed as there were small differences between the power input and the condenser heat transfer rate.

For the second configuration, with lifting height of 3.0 m, larger heat losses were observed, as the heat transfer rate at the condenser was considerably smaller (up to 50%) than the heat input to the condenser. For the thermal load of Q_E =2.0 kW, it was measured $Q_C \cong 1$ kW, with the average temperature difference between condenser inlet and outlet less than 1°C. The measurement uncertainty in the condenser heat transfer was approximately 30%. As the thermal load increased, average heat transfer differences between evaporator and condenser of 1.6 kW to 1.8 kW was observed, corresponding to differences in heat transfer rates of less than 16%.

For the third configuration, with lifting height of 5.0 m, the measured Q_C approached the applied thermal load for Q_E between 8.0 and 12.0 kW. The first and second thermal loads steps, 2.0 kW and 4.0 kW, a relatively small temperature difference between condenser inlet and outlet of less than 3.5 °C was observed.

4. Conclusions

Three configurations of an inverted two-phase thermosyphon prototype were tested in this work to evaluate the thermal and hydraulic performance. The length of lines L_3 and L_4 of this prototype can be varied, thus, enabling tests with different liquid lifting heights.

Experiments were carried out at thermal loads ranging from 2.0 kW to 12.0 kW along consecutive regular operational cycles for the three configurations. The device has worked well for all the liquid lifting heights tested. A self-regulation capacity was observed in this inverted two-phase thermosyphon, that is, the system is able to adapt to changes in the operation conditions in order to maintain operation. The third configuration tested, with the maximum lifting height of 5.0 m, have shown the best performance with a very stable operation along all the six thermal loads levels tested.

The constant infiltration of non-condensable gases through the transparent hoses used as visors to measure liquid level in different components lead to a smooth increase of the absolute pressure inside the components, although the pressure difference between evaporator and accumulator is constant during the vapor transport process.

As the distance between evaporator and condenser increased, higher was the temperature difference between the evaporator and the accumulator required to achieve the pressure difference ΔP_{EA} to surpass the hydraulic head of the lifting liquid. So, for devices with a heat source with prescribed temperature, special attention must be taken about the height between the components in order to secure operation.

Additional experiments will be carried out with the third configuration, with $\Delta H_{CA} = 5.0$ m, with thermal loads ranging from 1.0 kW to 13.0 kW to evaluate the thermal and hydraulic behavior of the prototype for other operation conditions. The experimental data collected will be then used to development of thermal and hydraulic models to predict the performance of the inverted two-phase thermosyphon under study here.

5. Acknowledgements

The authors would like to acknowledge the financial support from CNPq in the development of this work.

References

[1] S. Ito, K. Tateishi and N. Miura. Studies of a thermosyphon system with a heat source near the top and heat sink at the bottom, 2007. In proceedings of ISES Solar World Congress 2007: Solar Energy and Human Settlement: p. 930-938.

[2] M.C. Tsai, S. W. Kang, H. Y. Li and W. F. Tsai. Operation of a two-phase reverse loop thermosyphon, 2015. Journal of Applied Science and Engineering, 18(3): p. 259-264.

[3] D. Chlusziński and M. Duda. A new concept and a test of a bubble pump system for passive heat transport from solar collectors. Energies, 2020. 13(5), 1185.

[4] F. Fantozzi and S. Filippeschi. Analisi teorico sperimentale di un termosifone bifasico in controgravità, 2000. 18th UIT Congress, Cernobbio, Italy.

[5] G. De Beni and R. Friesen. Passive downward heat transport: Experimental results of a technical unit. Solar Energy, 1985. 34(2): p. 127-134.

[6] K. Kadoguchi and M. Yamazaki. Intermittent heat transportation by discharge of accumulated vapor. Applied Thermal Engineering, 2004. 24: p. 2761-2775.

[7] Y. Dobriansky and Y. G. Yohanis. Cyclical reverse thermosiphon. Archives of thermodynamics, 2010. 31(1): p. 3-32.

[8] F. Fantozzi and S. Filippeschi. Pulsated two-phase thermosyphons for electronic equipment thermal control. In Proceedings of International Conference on Environment Systems – ICES 2002, 2002. San Antonio, Texas, United States of America.

[9]. F. Fantozzi, S. Filippeschi, V. J. Sasin and N. M. Savchenkova. Heat transport device based on pulsing thermosyphons with forced fluctuation of pressure. In Proceedings of 12th International Heat Pipe Conference -12th IHPC, 2002. Moscow, Russia.

[10] S. Filippeschi, E. Latrofa and G. Salvadori. On the possibility of evaporator drastic scale reduction in a periodically operating two-phase thermosyphon. In Proceedings of 3rd International Symposium on Two-Phase Flow Modelling and Experimentation, 2004. Pisa, Italy.

[11] F. Fantozzi, S. Filippeschi and E. M. Latrofa. Upward and downward heat and mass transfer with miniature periodically operating loop thermosyphons. Superlattices and Microstructures, 2004. 35: p. 339-351.

[12] Y. Dobriansky and R. Wojcik. State of the art review of conventional and anti-gravity thermosyphons: Focus on two working fluids. International Journal of Thermal Sciences, 2019. 136: p. 491-508.

[13] S. Filippeschi, Y. Su and S. B. Riffat. Feasibility of periodic thermosyphons for environmentally friendly ground source cooling applications. International Journal of Low-Carbon Technologies, 2013. 8: p.117-123.

[14] S. W. Chang, T. M. Liou and Y. R. Jiang. Thermal performance of two-phase reciprocating anti-gravity closed thermosyphon. International Journal of Heat and Mass Transfer, 2016. 100: p.704-717.

[15] Y. Koito, Y. Ikemizu, T. Tomimura and M. Mochizuki. A vapor-pressure-driven heat pipe for sideward long-distance heat transportation. Frontiers in Heat Pipes – FHP, 2010. 1, 013005.

[16] Y. Koito, M. S. Ahamed, S. Harada and H. Imura. Applied Thermal Engineering, 2009. 29: p. 259-264.

[17] R. S. Calomeno, F. H. Milanez and M. B. H. Mantelli. Simplified hydraulic and thermal models for inverted two-phase thermosyphons, 2023. In Proceedings of Joint 21st International Heat Pipe conference and 15th International Heat Pipes Symposium – 21st IHPC and 15th IHPS, 2023. Melbourne, Australia.

Paper ID 029(S7)

Development of a Vapor Chamber with Hybrid Wick Structure by Additive Manufacturing Technology

Yawei Xu[1], Hongxing Zhang[1], Jinyin Huang[1], Jianyin Miao[1*]

[1]National Key Laboratory of Spacecraft Thermal Control, China Academy of Space Technology, Beijing, P.R. China
*Corresponding author email address: miaojianyin@sina.cn

Abstract

This article introduced a novel method for developing vapor chamber based on additive manufacturing (AM). Leveraging the advantages of AM in forming complex geometries, a composite capillary wick material was designed. The microstructure was analyzed using SEM (Scanning Electron Microscopy) and MicroCT (Micro-Computed Tomography). The results indicated that a continuous, interconnected porous structure was obtained. Thermal performance tests showed that 3D printed capillary wick can significantly enhance the heat transfer capability and ultimate heat flux density of vapor chamber. The 2D vapor chamber can accommodate a heat flux density of 88W/cm² with a thermal resistance of only 0.024℃/W. The 3D vapor chamber exhibited significant changes in thermal resistance under different orientations. Relevant data can provide guidance for the thermal design and experiment of spaceborne high-power electronic equipment.

Keywords: Additive Manufacturing, Composite Capillary Wick, Vapor Chamber, Heat Transfer Enhancement

1. Introduction

With the development of electronic integration technology, satellite-borne electronic equipment exhibits characteristics of high power and high heat flux, making thermal dissipation technology one of the bottlenecks that constrain the performance and reliability of satellite-borne electronic equipment [1]. In the space vacuum environment, the convective cooling measures commonly used in ground consumer electronic products cannot function [2]. Based on the classic integrated architecture of electronic products, reducing the thermal resistance from the heat-generating device to the heat dissipation panel is the focus of thermal design. The main technical approaches include high thermal conductivity materials, thermal interface materials, heat pipe products, and so on [3, 4]. Among them, vapor chambers, while possessing the advantages of high thermal conductivity, small temperature gradient, simple structure, and high reliability of traditional heat pipes, also have a unique two-dimensional structural feature that can achieve multi-point isothermalization, high heat flux heat spreading, and other functions. Research on vapor chamber technology for thermal dissipation of high-power electronic equipment has been one of the research hotspots in recent years.

Similar to heat pipes, vapor chambers are composed of a shell, capillary wick, and working fluid. The capillary wick has strong structural design capabilities and significantly affects the thermal performance of the vapor chamber. Therefore, novel capillary wick structures are a hot topic of research for scholars all the time. Hamdy [5] studied the mesh and powder composite capillary wick, which had outstanding advantages in thermal performance compared to a single mesh or powder capillary wick. Oshman [6] combined the wire mesh with micro-channel, significantly enhancing the thermal performance of the vapor chamber. Peng [7] and others, drawing inspiration from the vein structure of leaves, developed a biomimetic capillary wick with vein-like patterns. The experimental results showed that the new structural form can improve the transport efficiency of the working fluid. Additive manufacturing (AM) technology is a manufacturing method developed in recent years. It possess prominent advantages in forming complex and irregular structures. Based on the method described in the literature [8], a titanium-water heat pipe for thermal management of high-power spacecraft has been successfully developed, preliminarily verifying the technical feasibility of additive manufacturing technology in the production of heat pipes.

From the above, it is evident that the heat transfer capability of the vapor chamber is constrained by the single type of capillary wick. By combining different types of porous structures, the capillary force and the transport efficiency of the working fluid can be synergistically improved, which is expected to significantly enhance the heat transfer performance of Vapor Chambers. In this paper, a nine-square micro-channel composite capillary wick structure was fabricated through AM. And based on this structure, two-dimensional and three-dimensional vapor chambers were developed. The test results showed that the 3D printed composite capillary wick can significantly improve the critical heat flux density of the vapor chamber.

2. Design and Fabrication

Based on AM technology, a vapor chamber with a composite capillary wick was developed. Both the shell material and the capillary wick material are AlSi10Mg, which are integrated and printed in one piece. Ammonia was chosen as the working fluid. To verify the feasibility of the AM technology, two different configurations of vapor chambers were developed, namely the 2D vapor chamber and the 3D vapor chamber.

2.1 2D vapor chamber

The structural diagram of the 2D vapor chamber is shown in Fig. 1. The wall thickness of the AlSi10Mg shell is 1.5mm. To ensure the pressure-bearing capacity and rigidity of the shell, a cylindrical pressure-bearing dot matrix is set between the two shell bodies. To achieve the interconnection of the liquid working fluid between the capillary wicks on both sides, a porous capillary wick annulus is set around the pressure-bearing cylinder. To enhance the working fluid transport capacity of the 3D printed capillary wick, thereby improving the thermal conduction capability of the vapor chamber, a staggered nine-square micro-channel is set on the surface of the capillary wick. The size of the micro-channels is 0.5×0.5mm.

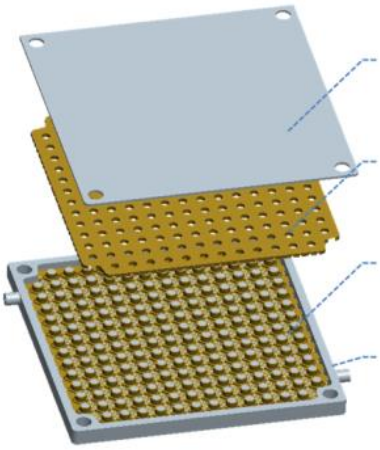

Fig. 1 Schematic diagram of the internal structure of the 2D vapor chamber

2.2 3D vapor chamber

In this study, a 3D vapor chamber was designed and developed, and the schematic diagram of its internal structure is as follows. The 3D vapor chamber is a five-sided box structure, with the cavity at the bottom of the box connected to the cavities on the sides. The internal structure of the ground and the surrounding areas is similar to that of the 2D vapor chamber.

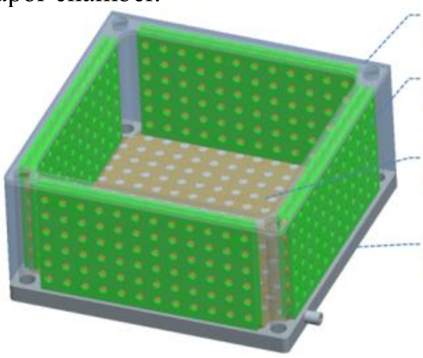

Fig. 2 Schematic diagram of the internal structure of the 3D vapor chamber

2.3 Characterization of Wick Parameter

The morphological characteristics of the 3D printed capillary wick are characterized using a Phenom XL electron microscope, and the microstructure photos are shown below. By controlling the AM scanning parameters and laser energy, a loose through-hole structure can be obtained, with macroscopic pores formed by large particle pores, adhering to small particle spherical powders that are not completely fused.

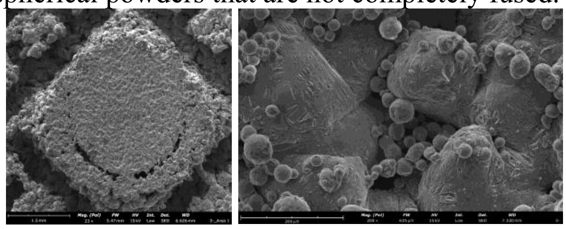

Fig. 3 SEM photos of wick material

To further characterize the pore structure of the 3D printed capillary wick, the microstructure unit of wick was inspected using the NEOSCAN N70 micro-CT. The inspection results were shown in the figure below. It can be seen that both the nine-square micro channels and porous skeleton were formed. The shell and the pressure-bearing structural columns were dense sintered, while the capillary wick is a non-dense sintered structure. A well-connected interface between the two structure is formed. The nine-square micro-channel feature on the surface of the capillary wick is consistent with the design model. The interconnected pore structure inside the capillary wick was mainly composed of gaps between incompletely fused powder particles.

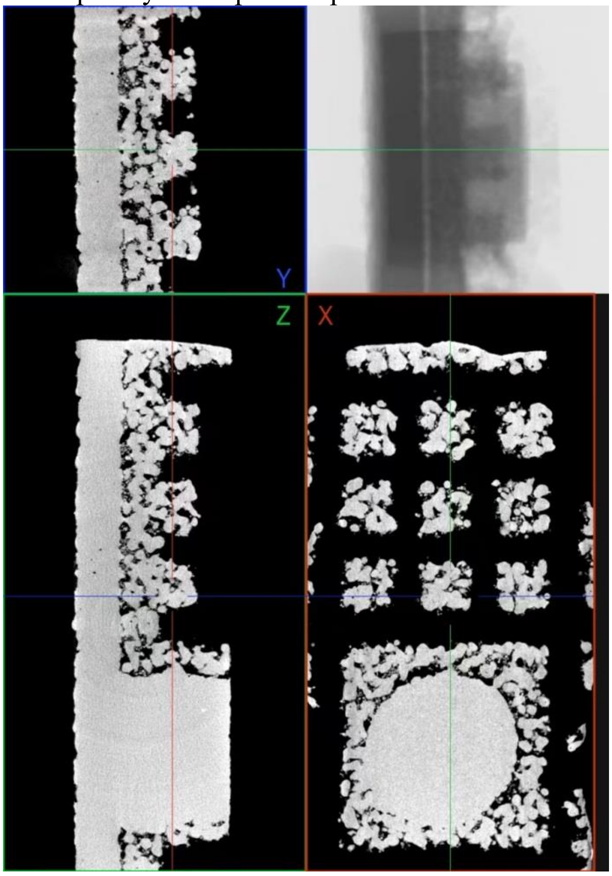

Fig. 4 CT photos of wick material

The pore parameters of the vapor chamber were tested using the PMI Parameter device. By examining the curve of the flow rate change with pressure after the capillary wick was wetted by a liquid medium, the bubble point pressure and the corresponding bubble point pore size of the porous medium material can be determined. The pore parameters of the capillary wick were statistically obtained by testing multiple samples. The bubble point pore size is about 25 μm, and the effective flow pore size is about 40 micrometers. According to Darcy's law of permeation, the permeability of the capillary wick is measured to be approximately 5×10^{-12} m^2.

Table 1 Porosity parameter of wick material

No. unit	mean flow pore pressure kPa	mean flow pore diameter microns	bubble point pressure kPa	bubble point pore diameter microns	permeability constant 1E-12m2
Sample 1	7.05	12.66	3.69	24.19	4.98
Sample 2	6.02	14.82	2.40	37.16	6.03
Sample 3	6.24	14.29	3.45	25.89	4.11
Sample 4	6.87	12.99	3.61	24.73	6.16
Sample 5	6.66	13.41	3.62	24.65	5.28
Sample 6	6.80	13.13	3.72	23.97	5.31
Sample 7	6.90	12.94	3.60	24.81	4.62
Sample 8	4.99	17.90	2.08	42.90	6.79
Sample 9	6.54	13.64	3.34	26.69	4.34
Sample 10	5.98	14.93	2.92	30.57	6.73
Average	6.40	14.07	3.24	28.56	5.43
STDEV	0.56	1.41	0.53	5.87	0.87

3. Experimental Setup and Method

3.1 Experimental setup of 2D vapor chamber

As shown in Figure 5(a), the test setup consists of a simulated heating system, a simulated cooling system, and a temperature signal acquisition system. The simulated heating element is a ceramic heating plate measuring 15mm by 15mm, and the power loading is controlled by a programmable power supply. The cooling system is composed of a cold plate and a chiller. Under the heat transfer mode test conditions, the coupling area between the vapor chamber and the cold plate is approximately 20mm. Under the heat spreading mode test conditions, the entire surface of the vapor chamber is in contact with the cold plate. Figure 5(b) provides a photograph of the test system. Thermocouples are placed at various characteristic locations of the vapor chamber, and the temperature data is collected through the Agilent temperature measuring instrument KaySight 34970A. The positions of the temperature measurement points under the heat transfer mode and heat spreading mode are shown in Figures 5(c) and (d), respectively.

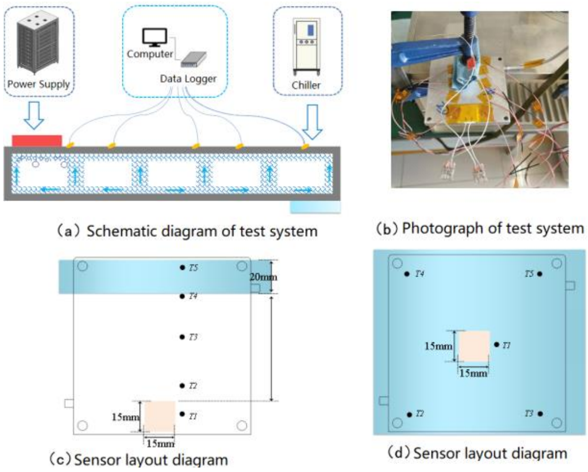

Fig. 5 Schematic diagram of 2D vapor chamber experimental setup

3.2 Experimental setup of 3D vapor chamber

To test the effect of gravity on the heat transfer performance of three-dimensional vapor chambers, four different orientations were compared. As shown in Figure 6, in orientation 1, the heating element is located at the center of the bottom of the vapor chamber, with the cold plates on either side of the vapor chamber cavity. The evaporation section is positioned higher than the condensation section, with the vapor chamber operating in an anti-gravity mode. Orientation 2 is implemented in the same state as orientation 1, with the difference being that the test object is flipped, with the heating surface lower than the condensation surface, and the vapor chamber operating in a pro-gravity mode. Orientations 3 and 4 place the test object vertically, with the cold plates located on the upper or lower sides or the left and right sides of the surrounding vapor chamber cavities, respectively.

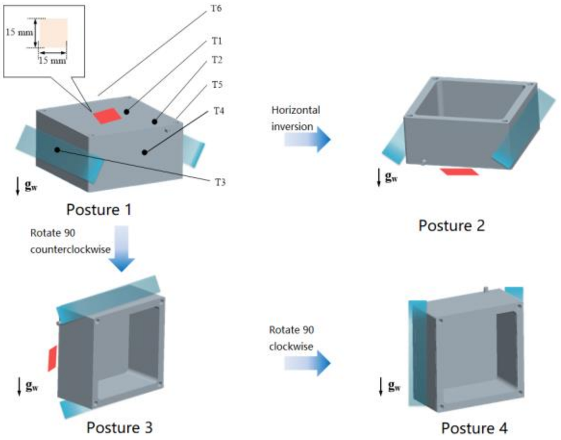

Fig. 6 Schematic diagram of 3D vapor chamber experimental setup

3.3 Data Processing

In the text, two physical quantities, the temperature difference across the heat transfer and the thermal resistance, are used to characterize the heat transfer performance of the vapor chamber. The calculation method for the temperature difference across the heat transfer is the difference between the evaporation section temperature and the condensation section, as shown in the following formula. Where T_e and T_c represent the temperatures of the evaporation section and the condensation section, respectively.

$$\Delta T = T_e - T_c$$

Here, ΔT represents the temperature difference across the heat transfer.

The calculation method for thermal resistance is shown in the following formula, where R represents the thermal resistance, ΔT represents the temperature difference across the heat transfer, and Q represents the heat power provided by the direct current (DC) regulated power supply.

$$R = \frac{\Delta T}{Q}$$

4. Results and Discussion

4.1 2D vapor chamber

In the heat transfer mode, the heat load is incrementally increased by 10W steps up to 200W. The temperature rise curve at the typical measurement points is shown in Figure 7. T1 to T4 are located near the heat source and the adiabatic section, while T5 is located in the condensation section. Under various test conditions, the temperature difference between T1 to T4 is small. When the load power is between 10W and 120W, there is almost no temperature difference across the four temperature measurement points. Under the condition of loading 200W, the heat flux density in the evaporation zone is as high as 88W/cm^2, and the temperature difference between the evaporation zone and the adiabatic zone is only 1.3 ºC. The small temperature difference between the evaporation zone and the adiabatic zone is mainly attributed to three factors. Firstly, the shell and the wick are an integrated structure made by 3D printing, with the porous structure of the wick and the shell forming a metallurgical bond, resulting in a low thermal resistance. Secondly, the nine-grid composite wick shortens the liquid supply path in the evaporation zone, which helps to enhance the capillary heat transfer limit. Thirdly, the internal structure of the 3D printed porous structure contains partially unmelted spheres, and the secondary pore structure formed between these unmelted spheres increases the specific surface area of the evaporation surface. The temperature difference between the condensation measurement point T5 and the other four measurement points continues to widen with the increase of the load power. Under the condition of loading 200W, the condensation heat transfer temperature difference is 4.75 ºC. The T5 measurement point is located above the condensation section. The coupling length between the condensation section and the cold plate is 20mm, considering the shell side wall thickness of 5mm, the effective condensation heat transfer surface area is approximately 13.5cm^2, and the condensation heat transfer heat flux density is about 14.8W/cm^2. The condensation temperature difference is relatively larger compared to the evaporation temperature difference, which is believed to be due to the wider pore size distribution of the 3D printed porous wick. As the heat transfer increases, the liquid in the larger pore size decreases and accumulates in the condensation zone, reducing the number of condensation nucleation sites on the wick surface, leading to a decrease in condensation heat transfer efficiency.

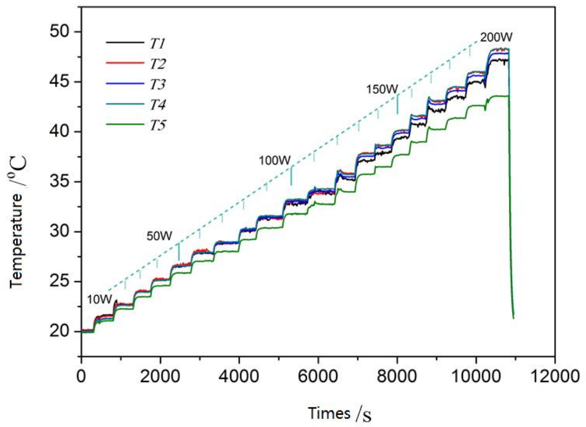

Fig. 7 Temperature Rise Curve of 2D Vapor Chamber in Heat Transfer Mode

In the heat transfer mode, the trend of the temperature difference and thermal resistance of the vapor chamber with the increase of loading power is shown in Figure 8. The temperature difference across the heat transfer continuously widens as the loading power increases, and an inflection point appears in the temperature rise slope when the power is increased to 200W. At a loading power of 10W, the thermal resistance of the heat transfer is about 0.06 °C/W, and it quickly decreases to 0.015 °C/W (at a loading power of 40W). Between 40W and 180W, the thermal resistance of the heat transfer remains approximately constant. At 200W loading, the thermal resistance of the heat transfer increases to 0.024 °C/W. It is analyzed that at 200W, the heat transfer capacity limit of the vapor chamber is approached, the temperature rise slope shows an inflection point, and the thermal resistance begins to rise.

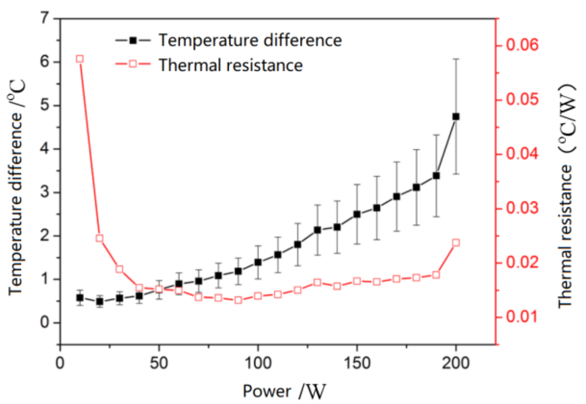

Fig. 8 Temperature Difference and Thermal Resistance Curves of 2D Vapor Chamber in Heat Transfer Mode

In the heat spreading mode, the power is incrementally increased by 20W steps up to 200W. The temperature rise curve at the typical measurement points is shown in Figure 9. The vapor chamber is horizontally placed on the cold plate, with T1 located near the heat source and T2 to T5 located at the four corners of the vapor chamber. As the loading power increases, the temperature difference among the five measurement points continues to widen. The temperature at T4 is significantly lower than the other measurement points, and the temperature difference continues to expand with the increase in loading power. At 200W loading, a sudden drop in temperature is observed at T4, and the temperature difference with other measurement points expands to about 6.5 °C. Combined with the test results in the heat transfer mode, it is analyzed that in the heat spreading mode, the condensation heat transfer area increases, and the mechanism of liquid plug formation is somewhat alleviated, but not eliminated. Due to the wide distribution of capillary pore sizes, at high power levels, the working fluid in the large capillary pores decreases under the action of capillary pressure, and the working fluid accumulates at the condensation position. When the loading power reaches 200W, the accumulated working fluid at T4 exceeds a critical value and forms a liquid plug, causing a sudden drop in temperature at that point.

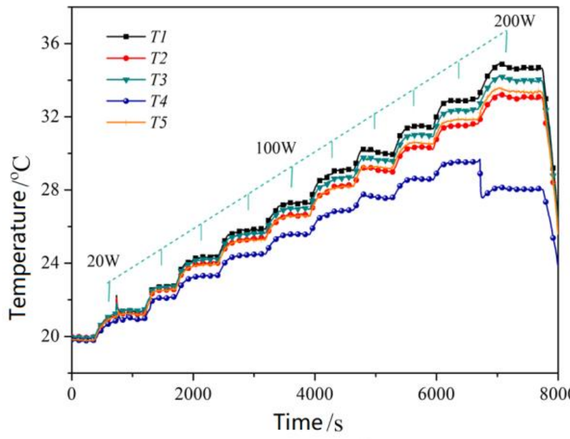

Fig. 9 Temperature Rise Curve of 2D Vapor Chamber in Heat Spreading Mode

The statistical results of the temperature difference and thermal resistance of the vapor chamber in the heat spreading mode are shown in Figure 10. The patterns of change for both are similar to the test results in the heat transfer mode. The temperature difference across the heat transfer continuously widens as the loading power increases, and an inflection point appears in the slope of the temperature difference increase at 200W. The thermal resistance curve shows a pattern of decreasing first and then increasing, with a thermal resistance of about 0.015 ℃/W between 40W and 180W. At 200W, due to the formation of a liquid plug in a local cavity, the temperature at the T4 measurement point drops sharply, causing the thermal resistance to soar to 0.033 ℃/W.

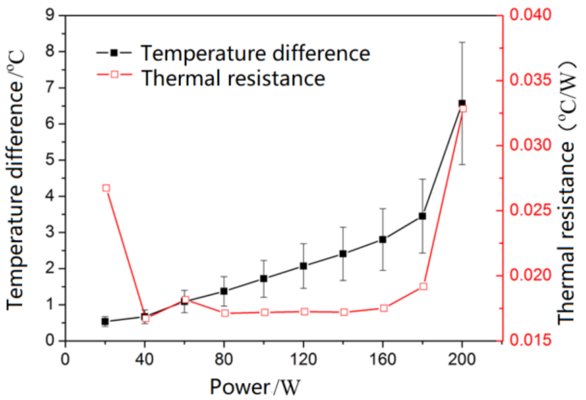

Fig. 10 Temperature Difference and Thermal Resistance Curves of 2D Vapor Chamber in Heat Spreading Mode

In summary, the additively manufactured two-dimensional vapor chamber was tested in both the heat transfer mode and the heat spreading mode, and the sample has a heat transfer capacity of 200W. Thanks to the unique porous structure of the additively manufactured capillary wick, the sample can adapt to a heat flux density of 88W/cm^2, with an evaporation temperature difference of only 1.3 ℃. At the same time, due to the wide distribution of pore sizes in the additively manufactured porous structure, with the interlacing of large and small pore sizes, it is easy for liquid plugs to form in the condensation section at high power, which in turn leads to an increase in the heat transfer temperature difference.

4.2 3D vapor chamber

The heat transfer performance of 3D vapor chamber was tested in four different orientations. The patterns of change in temperature difference and thermal resistance are shown in Figures 11 and 12. In orientation 1, the temperature difference across the heat transfer and thermal resistance began to soar when the loading power exceeded 80W. In orientation 2, the temperature difference across the heat transfer increased approximately linearly with the loading power, and the thermal resistance remained stable at around 0.048 ℃/W between 20W and 200W. For orientations 3 and 4, where the heated surface is placed vertically, the patterns of change in the temperature difference across the heat transfer with the loading power are the same. Between 20W and 120W, the temperature difference across the heat transfer increased approximately linearly with the loading power, and the thermal resistance remained approximately constant, at 0.052 ℃/W (orientation 3) and 0.042 ℃/W (orientation 4). When the loading power exceeds 120W, the slope increases, and the thermal resistance rises.

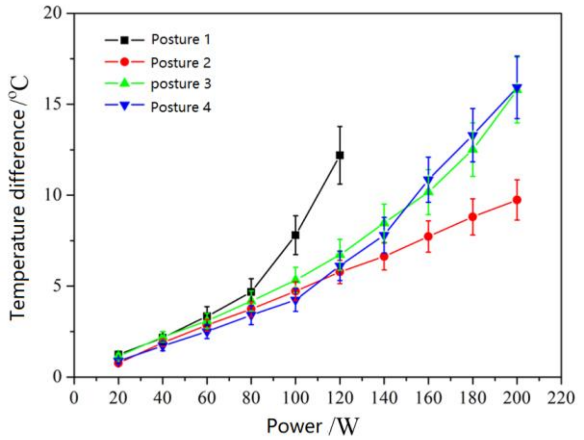

Fig. 11 Temperature Difference Curves of 3D Vapor Chamber Under Different Orientations

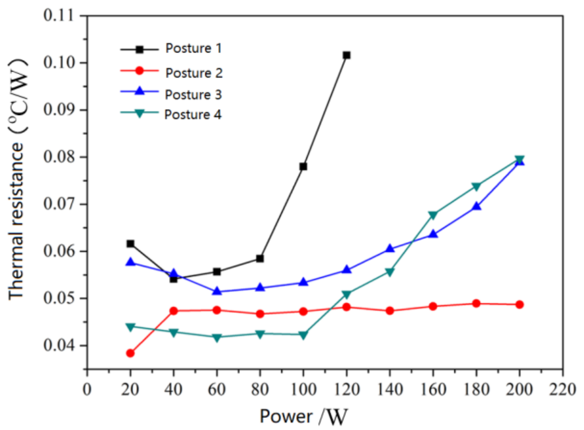

Fig. 12 Thermal Resistance Curves of 3D Vapor Chamber Under Different Orientations

Based on the criterion that overheating occurs at the evaporation section measurement point and there is an abrupt change in thermal resistance, the heat transfer capacity of the three-dimensional vapor chamber under different orientations is as follows. Under horizontal anti-gravity conditions, the heat transfer capacity is about 80W (orientation 1), under horizontal pro-gravity conditions, the heat transfer capacity is greater than 200W (orientation 2), with the heated surface vertical and the cooling cold plate arranged above and below, the heat transfer capacity is about 180W (orientation 3), and with the heated surface vertical and the cooling cold plate arranged left and right, the heat transfer capacity is about 100W (orientation 4). It should be noted that although the power at which overheating occurs at the T1 measurement point is relatively low during the orientation 4 test, the overall temperature at the other measurement points is lower than that in orientation 3. At a loading power of 100W, the thermal resistance of orientation 4 is lower than that of orientation 3, and at a loading power of 200W, the thermal resistance of both is the same. The results of the multi-orientation heat transfer performance tests indicate that the heat transfer capacity of the three-dimensional vapor chamber is significantly affected by the gravitational field (orientation).

5. Conclusion

This article introduced a method for developing vapor chambers by additive manufacturing techniques. Taking advantage of the benefits of additive manufacturing technology in forming complex geometries, a composite capillary wick structure was designed, which interweaves a nine-square micro-channel with a powder porous material. Both 2D and 3D vapor chambers were developed. The quality of the microstructure formation was analyzed using SEM (Scanning Electron Microscopy) and MicroCT methods. The results showed that by controlling the scanning parameters at different locations, it was possible to simultaneously achieve a dense shell structure and a continuously interconnected non-dense porous structure. Thermal performance tests indicated that the 3D printed capillary wick can significantly enhance the heat transfer capability and the maximum heat flux density of the vapor chamber. Test results under different orientations showed that the thermal resistance was highest under the condition against gravity, followed by the condition with gravity, and the lowest under the vertically oriented condition, which is less affected by gravity. This phenomenon was owning to the uneven porosity of the 3D printed porous structure, leading to inadequate working fluid supply in anti-gravity attitude.

References

[1] H. Tang, Y. Tang, Z. Wan, J. Li, W. Yuan, L. Lu, Y. Li, K. Tang, Review of applications and developments of ultra-thin micro heat pipes for electronic cooling, Appl. Energy 223 (2018) 383e400.

[2] R.J. McGlen, R. Jachuck, S. Lin, Integrated thermal management techniques for high power electronic devices, Appl. Therm. Eng. 24 (8e9) (2004) 1143e1156.

[3] Y. Xiang, W. Yao, J. Li. The one-dimensional analysis of heat and mass transfer processes in loop heat pipe evaporator. Chinese space science and technology, 2005. 2: p. 16-21.

[4] F. Tavakkoli, S. Ebrahimi, S. Wang, K. Vafai, Analysis of critical thermal issues in 3D integrated circuits, Int. J. Heat Mass Tran. 97 (2016) 337e352.

[5] H. Hamdy, H. Souad, An experimental and numerical study on the effects of the vapor chamber wick structure on its thermal performance, Heat Transfer Eng. 36 (3) (2015) 278–289.

[6] C. Oshman, B. Shi, L. Chen, R.G. Yang, Y.C. Lee, G.P. Peterson, V.M. Bright, The development of polymer-based vapor chambers (PFHP), J. Microelectromech. S. 20 (2) (2011) 410–417.

[7] Y. Peng, W. Liu, N. Wang, Y. Tian, X. Chen, A novel wick structure of vapor chamber based on the fractal architecture of leaf vein, Int. J. Heat Mass Tran. 63 (63) (2013) 120–133.

Paper ID 032

Optimization of capillary structures for loop heat pipes based on multiscale carbonyl nickel powder

Qi Wu[1], Guoguang Li[1], Zhichao Jia[1], Hanli Bi[1], Hongxing Zhang[1*], Jianyin Miao[1]

[1] *National Key Laboratory of Spacecraft Thermal Control, Beijing Institute of Space System Engineering, Beijing, P.R. China*

**Corresponding author email address: redlincoco@hotmail.com*

Abstract

The wick is the core component that provides driving force for the operation of the loop heat pipe, and its capillary force determines the heat transfer capacity of the loop heat pipe. It is very important to know the performance characteristics and adaptation range of wicks of different scales for the practical application of wicks in different types of loop heat pipes. In this paper, the performance parameters of loop heat pipe wick prepared by micron carbonyl nickel powder, submicron carbonyl nickel powder and nanoscale carbonyl nickel powder were characterized and compared, and the problems of different scale wick in practical application were analyzed. By optimizing the scale of carbonyl nickel powder, the capillary driving force is greatly increased from 55 kPa to 130 kPa. The experiment proves that this optimization can make the loop heat pipe better meet the needs of high-power and long-distance heat transmission, and has obvious application advantages.

Keywords: Loop heat pipe; Capillary structure; Multiscale; Carbonyl nickel powder

1. Introduction

Since Maidanik Y. F. et al. first proposed the concept of loop heat pipe in 1971, it has become one of the key technologies for the heat dissipation of high-power spacecraft loads due to its features such as high-power long-distance heat transfer, no vibration, long life and high reliability. It has been widely used in the field of space thermal control and has broad application prospects [1-4]. As the core component of loop heat pipe, wick provides driving force for loop heat pipe operation, and its capillary force determines the heat transfer capacity of loop heat pipe [5]. It is generally believed that the small-pore capillary structure can provide greater capillary driving force to overcome the loop pressure drop. But at the same time, the permeability of wick will be reduced, thereby increasing the flow resistance of the working medium [6-7]. Therefore, it is very important to define the performance characteristics and adaptation range of wicks of different scales for the practical application of wicks in different types of loop heat pipes.

In this paper, the performance parameters of the loop heat pipe wicks prepared by micron carbonyl nickel powder, submicron carbonyl nickel powder and nanoscale carbonyl nickel powder were characterized, and the problems in the practical application of the above wicks of different scales were analyzed. The performance of the loop heat pipe was optimized by adjusting the scale of carbonyl nickel powder, and the suitable application range was given.

2. Wicks based on carbonyl nickel powder with different scales

2.1. Micron carbonyl nickel powder

The particle size of the common micron carbonyl nickel powder is 1.2~1.8 μm, as shown in the figure below. The experimental results show that the maximum pore size of the prepared wick is generally 0.9~1.3 μm; permeability range: 1.0×10^{-14}~5.0×10^{-14} m^2; and the capillary driving force of the corresponding loop heat pipe is about 55 kPa.

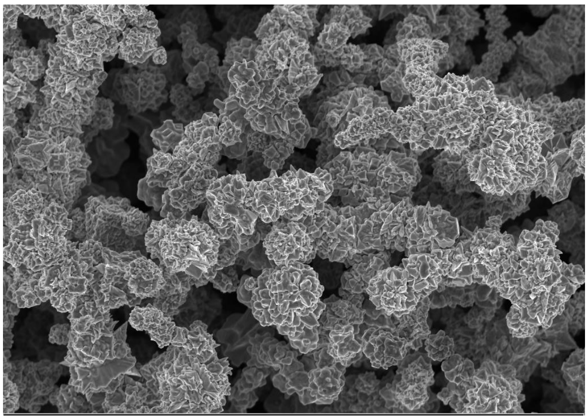

Figure 1. SEM image of micron carbonyl nickel powder.

Although increasing the pressing pressure can reduce the maximum pore diameter of the wick and thus increase the capillary driving force, micron carbonyl nickel powder cannot achieve more than 100 kPa capillary driving force, due to the limitation of the size of the powder. Therefore, the use of smaller particle size powder is the key to improve the capillary driving force.

2.2. Nanoscale carbonyl nickel powder

The particle size of nanoscale powder is much smaller than that of micron powder, but if nanoscale powder is used as wick raw material alone, it will cause extremely low permeability and great resistance, which is not conducive to the overall performance of the evaporator. Therefore, the pore size was reduced by mixing nanoscale nickel powder into micron carbonyl nickel powder. The use of nanoscale mixed powder can effectively reduce the maximum pore size and improve the capillary force. The experimental results show that the capillary force of the wick can reach 210 kPa with the addition of 15% nanoscale carbonyl nickel powder (with a particle size of 50 nm), which is four times of the 55 kPa capillary driving force of the micron wick. But at the same time, its permeability drops to the order of 10^{-15} and the resistance is much greater.

In addition, it is also found that there are serious problems of low-temperature sintering of nanoscale mixed powders during the study. The manufacturing process of loop heat pipe usually includes high-temperature welding process, and it is necessary to ensure that the capillary force of the evaporator does not decrease after welding and other processes. Therefore, the capillary force changes of the wick prepared by nanoscale mixed powder before and after heating at 200℃/1h were compared. The test results showed that after heating at 200℃/1h, the capillary force decreased from 210 kPa to 150 kPa.

In order to confirm the reason for the change of capillary force of the wick prepared by nanoscale mixed powder before and after heating, scanning electron microscopy was conducted to observe the microscopic morphology of the powder before and after heating, as shown in Figure 2. It can be seen from the figure that after heating, the powder shrinks and aggregates to a certain extent, and the pores formed between the powders become larger. It can be inferred that the low-temperature sintering of nanoscale powders occurs [8-9], which leads to a significant reduction in capillary force.

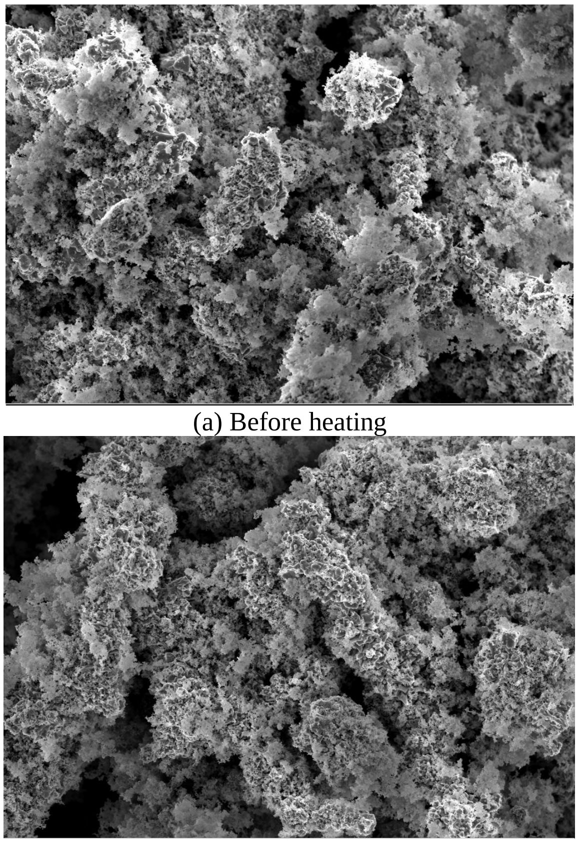

(a) Before heating

(b) After heating

Figure 2. Comparison of nano-scale mixed powder before and after heating.

2.3. Submicron carbonyl nickel powder

From the above analysis, it can be inferred that the use of a single particle size of submicron powder can simultaneously improve the capillary force, reduce the problem of low-temperature sintering and ensure a certain permeability. Therefore, the capillary structure of the loop heat pipe was optimized by using submicron carbonyl nickel powder. Carbonyl nickel powder with particle size of 0.69 μm was pressed under conventional pressure, as shown in Figure 3. The experimental results showed that the permeability range was as follows: 6.86×10^{-15}~8.22×10^{-15} m^2, the capillary driving force of the wick can reach 130 kPa at room temperature, which is more than twice the capillary driving force of the micron carbonyl nickel powder wick pressed under the same pressure. In addition, the submicron wick was heated at 200℃/1h, and the results showed that the capillary force did not change after heating.

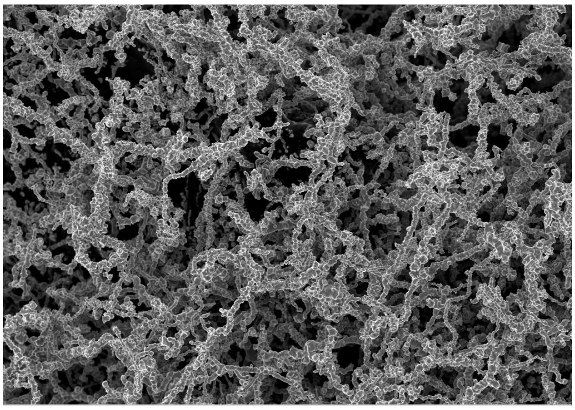

Figure 3. SEM image of submicron carbonyl nickel powder.

In addition, the thermal conductivity of the wick directly affects the heat leakage inside the loop heat pipe evaporator. So the thermal conductivity of micron carbonyl nickel powder wick and submicron carbonyl nickel powder wick formed by the same process were tested respectively. The measurement was carried out by laser pulse method according to ASTM E1461. The test results show that the thermal conductivity of micron carbonyl nickel powder wick is 3.89 W/m·K, while that of submicron carbonyl nickel powder wick is only 0.96 W/m·K, showing better thermal insulation characteristics.

In summary, although the capillary driving force of the wick prepared by submicron powder is lower than that prepared by nanoscale mixed powder, it can achieve the improvement of the capillary driving force without introducing defects, and has a low thermal conductivity, which has obvious application advantages.

3. Experimental verification of heat transfer performance

In order to verify the influence of the above optimization on the heat transfer performance of the loop heat pipe, the evaporator of the loop heat pipe was fabricated by using micron carbonyl nickel powder and submicron carbonyl nickel powder as the raw material of the wick. The two evaporators were connected to the test system respectively to test the heat transfer performance. The dimensions of the two evaporators are the same. The vapor pipe, liquid pipe and condensing pipe used in the test system are small-diameter pipes with an inner diameter of 2 mm (high resistance). The test results are shown in Table 1.

Table 1. Comparison of heat transfer performance of loop heat pipe before and after optimization.

Evaporator	Heat transport distance (m)	Maximum heat transfer capacity (W)	Permeability (m^2)	Capillary force (kPa)
Evaporator based on micron carbonyl nickel powder	0.5	450	1.1×10^{-14}	55
	10	215		
Evaporator based on submicron carbonyl nickel powder	0.5	410	1.2×10^{-15}	130
	10	300		

It can be seen that compared with the evaporator based on micron carbonyl nickel powder, the evaporator based on submicron carbonyl nickel powder has no advantage in short-distance heat transfer, because the flow resistance in the evaporator is dominant at this time, and the permeability of submicron carbonyl nickel powder is lower and the resistance is larger. However, the evaporator based on submicron carbonyl nickel powder has obvious advantages in long-distance heat transfer, when the external loop resistance is the main resistance, and the large capillary driving force can significantly improve the overall heat transfer capacity. Therefore, it is verified that the above optimization design for loop heat pipe evaporator can better meet the needs of high-power and long-distance heat transmission.

In order to more comprehensively compare the application range of loop heat pipes based on two sizes of carbonyl nickel powder, the relationship between the maximum heat transfer capacity and transmission distance of the two evaporators was theoretically calculated. The calculation results are shown in the figure below. As can be seen from the figure, only in the case of short-distance heat transfer of less than 1m, the evaporator based on micron carbonyl nickel powder will show application advantages. When the heat transfer distance is greater than 1m, with the increase of the transmission distance, the advantage of the evaporator based on submicron carbonyl nickel powder will become more and more obvious.

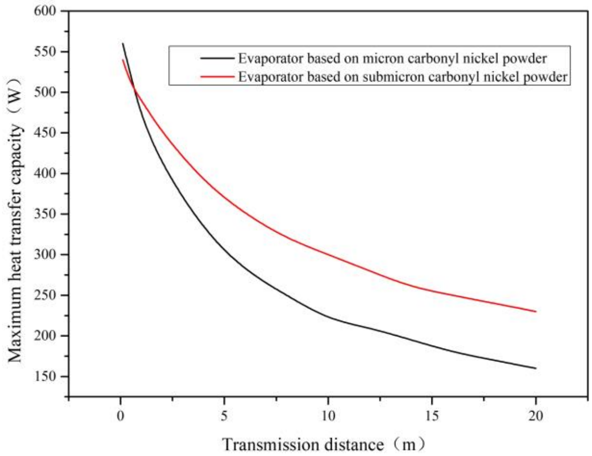

Figure 4. The relationship between maximum heat transfer capacity and transmission distance.

4. Conclusions

In this paper, the properties of the loop heat pipe wick prepared by micrometer carbonyl nickel powder, submicron carbonyl nickel powder and nanoscale carbonyl nickel powder were characterized and compared. The results show that the use of smaller particle size powder is the key to improve the capillary driving force. The use of nanoscale mixed powder can effectively reduce the maximum pore size and increase the capillary force. But at the same time, its permeability is very low, the resistance is large, and there are problems of low-temperature sintering. Relatively speaking, the submicron carbonyl nickel powder can achieve the improvement of capillary driving force without introducing defects. The experiment proves that it can better meet the needs of high-power and long-distance heat transfer, and has obvious application advantages.

5. ACKNOWLEDGEMENTS

The authors would like to thank Huanyu Lv and Fengshi Zheng for their help with the experiment and the raw material.

References

[1] Z. Y. Wang, W. S. Yang. A review on loop heat pipe for use in solar water heatin. Energy & Buildings, 2014. 79: p. 143-154.
[2] P. Gully, Q. Mo, T. Yan, et al. Thermal behavior of a cryogenic loop heat pipe for space application. Cryogenics, 2011. 51 (8): p. 420-428.
[3] A. Okamoto, T. Miyakita, H. Nagano. On-orbit experiment plan of loop heat pipe and the test results of ground test. Microgravity Science and Technology, 2019. 31 (3): p. 327-337.
[4] T. D. Swanson, G. C. Birur. NASA thermal control technologies for robotic spacecraft. Applied Thermal Engineering, 2003. 23 (9): p. 1055-1065.
[5] Y. Xiang, W. Yao, J. Li. The one-dimensional analysis of heat and mass transfer processes in loop heat pipe evaporator. Chinese space science and technology, 2005. 2: p. 16-21.
[6] J. Cho, Y. Yua, W. Sano, D.-A. Borca-Tasciuc. Low temperature sintering of copper biporous wicks with improved maximum capillary pressure. Materials Letters, 2014. 132: p. 349-352.
[7] T. Semenic, I. Catton. Experimental study of biporous wicks for high heat flux applications. International Journal of Heat and Mass Transfer, 2009. 52: p. 5113–5121.
[8] S. A. Paknejad, A. Mansourian, J. Greenberg, et al. Microstructural evolution of sintered silver at elevated temperatures. Microelectronics Reliability, 2016, 63: p. 125-133.
[9] C. H. Hsiao, W. T. Kung, J. M. Song, et al. Development of Cu-Ag pastes for high temperature sustainable bonding. Materials Science and Engineering A, 2017, 684: p. 500-509.

Paper ID 033(S7)

Novel Ultra-Thin Vapor Chambers with Composite Triple (Mesh, Grooves and Powders) Wicks Having Cooling Capacity of 860 W under 40 × 40 mm^2 Heating

Shwin-Chung Wong[1*], Chih-Yuan Fu[1], Lian-Qi Huang[1], Ting-Yun Kuo[1], Jo-Ting Tang[1], Chih-Chao Hsu[2], and Chung-Yen Lu[3]

[1]*Department of Power Mechanical Engineering, National Tsing Hua University, Hsin-Chu, 300, Taiwan, ROC*

[2]*Dual-Use Technology Development Center, National Chung-Shan Institute of Science & Technology, Taoyuan, Taiwan, ROC*

[3]*Chemical Systems Research Division, National Chung-Shan Institute of Science & Technology, Taoyuan, Taiwan, ROC*

**scwong@pme.nthu.edu.tw*

Abstract

140 × 80 × 1.0 mm^3 ultra-thin vapor chambers (UTVCs), to be used in air-cooling modules for high-power AI servers, are fabricated and tested horizontally under a heating area of 30 × 30 or 40 × 40 mm^2. The measured maximum heat transfer rates with the thermal resistances of the UTVCs are 696.8 W with 0.027 K/W and 860 W with 0.016 K/W, respectively. In contrast, the UTVC with a 2×200 mesh wick can reach only 259 W [3]. Accordingly, the air-cooling UTVC module may reach 1400 W if four Ø8 mm composite heat pipes are used, or reach > 1900 W if eight Ø8 mm heat pipes are used. Higher Q_{max} and lower R can be expected for a 50 × 50 mm^2 heating area. These results indicate that the proposed air-cooling UTVC module will very likely stand out and be chosen for high-power AI server cooling among the cold-plate cooling modules.

Keywords: Vapor chamber; Composite wick; Air-cooling module; AI server; Triple composite wick

1. Introduction

This work tests the ultra-thin vapor chambers (UTVCs) with novel composite triple (mesh-groove-powder) wicks under high heating rates up to 700 W at a heating area of 30 × 30 mm^2 or 40 × 40 mm^2. Recent power dissipations of AI GPUs have exceeded 1000 W and are claimed to be unsolvable using air cooling method. However, the liquid cooling method adopting cold plates requires extremely complex liquid piping for servers, racks, and infrastructure of the data centers. Above all, the installation and maintenance costs are extremely high and inconvenient for cold-plate liquid cooling. If air cooling can solve such high-power consumptions, nothing needs to be changed. The only drawback is to maintain the large heat sink height to deal with the > 1000 W high powers. If air cooling method is plausible, direct installation of the data center with low cost can be easily realized. Hence, we propose a thermal module, as shown in Fig. 1, that can reach a cooling capacity of 1500 W with a core unit of high-power UTVC under a heating area of 40 × 60 mm^2. In Fig. 1, the UTVC lies at the 40 × 40 mm^2 bottom center of the module, and four (or eight) ϕ8 mm heat pipes (HPs) with a composite groove-powder wick compressed to 3.5 mm, two (or four) HPs at each side with a 40 × 10 mm^2 area but remain cylindrical when penetrating through the heatsink plate fins. If eight HPs are used, a heat spreader made of oxygenless copper is needed. The HPs are flattened to 3.5 mm at the evaporator section. Subtracting the ineffective end of 5 mm, the heated area of a HP is 15 × 9 mm^2. We have measured the cooling capacity of a vertically-oriented bent HP to be about 140–150 W. Thus, with a high cooling capacity of 860 W and a rather low thermal resistance of about 0.016 K/W for a high-power UTVC with a triple composite wick, the total cooling capacity may reach > 1400 W (or 1900 W when eight HPs are used). without exceeding the chip temperature limit of 85 °C.

The composite-wick UTVC is the core unit of an air-cooling module, for AI server management, as shown in Fig. 1. The UTVC lies under the bottom of this module to contact the AI heater. To dissipate an amount of heat larger than 1 kW, a large fin area is needed. Using a large fin height, the fin efficiency may be lowered. Consequently, four (or eight) Ø8 mm heat pipes are used to co-cool the AI chip laying at both sides of the heater. The heat pipes are flattened to 3.5 mm at their evaporator and their 8 mm cylindrical condenser penetrates through the heatsink fins. Each bent heat pipe has been tested to solve a heat load up to 140–150 W.

The excellent thermal performance of the present novel UTVC mainly results from the fact that the condensate can return to the evaporator wick directly via the numerous pillars, as shown in Fig. 2. The low-power applications of it are mostly on smartphones. Since this novel design adopts a rather thin container wall and mesh wick to reach a sufficient heat transfer capability and a low vapor chamber resistance (R) under a thickness of 0.2–0.4 mm, it has been widely applied in commercial smartphones. As to its high-power capability, the greatly shortened return distance, and hence much lowered liquid flow resistance, is of crucial importance. It makes possible a high maximum heat load (Q_{max}) of 140 W and a low minimum thermal resistance (R_{min}) of 0.03–0.05 K/W for a 140 × 80 × 0.6 mm^3 UTVC which adopted only a single layer of #200 mesh wick [2]. When a mesh-groove composite wick is adopted, a Q_{max} near 487 W and an R_{min} as low as about 0.03 K/W can be obtained with the UTVC thickness slightly increased to 0.7 mm [3].

The objective of this study is to test a kind of triple composite wick consisting of one layer of #200 mesh over the grooves with powders added in the evaporator [4]. Outside the evaporator, only double composite mesh-groove is employed to avoid excessive liquid flow resistance. The thermal performance of these UTVCs with the triple composite wick will be compared with the double composite wick under a fixed UTVC footprint and thickness. The tests results reveal that a Q_{max} as high as 860 W with a low thermal resistance (R) of 0.016 K/W can be obtained for the triple-wicked UTVC heated under 40 × 40 mm^2.

2. Experiments

2.1. Preparation of the triple composite-wicked UTVC

The schematic structure of the triple composite-wicked UTVC is depicted in Fig. 3. The footprint (or condenser) area of the UTVC is 140 × 80 mm^2. The UTVC thickness is fixed at 1.0 mm. The material is copper alloy C5191. After thorough cleaning, the top and bottom plates were integrated by diffusion bonding in an 800 ℃ environment with 15% hydrogen under 50 kg/cm^2 for 2 h. The static contact angles of outer flat UTVC surfaces were kept as small as 12±2°. The filling tube was mounted using a high-frequency welder. Evacuation of the non-condensable gas (NCG) was conducted before sealing of the filling tube.

The Ø1.0 mm pillars at a pitch of 3.0 mm were formed by chemical etching on the inner surface of the top plate. On the top plate, a 0.10 mm-thick recess over the whole inner chamber was etched out to accommodate the originally 0.11 mm-thick #200 mesh wick. The pillar depth or the vapor duct thickness was 0.6 mm. The wire diameter of the #200 copper mesh is 0.055 mm and the wire distance is 0.072 mm. The porosity of the mesh wick is estimated to be 0.607 [1]. Parallel grooves similar to those shown in [2] were etched on the bottom plate.

For an AI chip without a hot spot, the highest heat flux occurs at the chip center. In the triple composite wick, the composite mesh-powder wick has the highest capillarity but the lowest permeability. So, it is applied at the center of the heater with a small area (Region A in Fig. 3). Some pillars are made in Region A for its anti-compression strength. Outside the powder wick is a 40 × 40 mm^2 region of a densified double composite mesh-groove wick (Region B). This heated region must have a sufficiently strong capillarity to avoid early dryout. So, the groove width is lowered to 0.10 mm here. Yet, the groove wall thickness cannot be too small to maintain a low evaporator resistance. Outside Region B is Region C with a double composite wick, Further outside is Region D with another double composite wick having a highest permeability K. Both Regions C and D can have a large K with wider and deeper grooves without concern of capillarity. But the groove length of Region C is in line with that of Region B, at 0.5 mm. The groove length of Region D can be longer, selected as 5 mm. All these groove depths and widths depend on the etching technique of the producer.

2.2. The test setup

The schematic of the experimental setup is shown in Fig. 4. The UTVC was tested under a horizontal orientation. The heating block was made of oxygenless copper C30100 with a thermal conductivity of 391±3 W/(m·K). A uniform heating surface of 30 × 30 mm^2 is attached to be bottom center of the UTVC, while a cold plate with running water of 50±1 ℃ at $2 \cdot 10^{-5}$ m^3/s covers the top surface (i.e., the condenser) of the UTVC. A total load of 3.6 kg, including the weight of the cold plate, was applied on the test sample to minimize the TIM resistances. This load has been proved to be non-influential to the test results [3].

K-type thermocouples (Omega, Inc.) were used in this work. In Fig. 4, thermocouples T_1 and T_2 are implanted 10 mm apart along the centerline of the heating rod to measure the actual heat input (Q). The temperature measured at the center of the top surface of the heating rod (T_3) was assigned as the junction temperature (T_j). Q_{max} is defined as the largest Q prior to dryout.

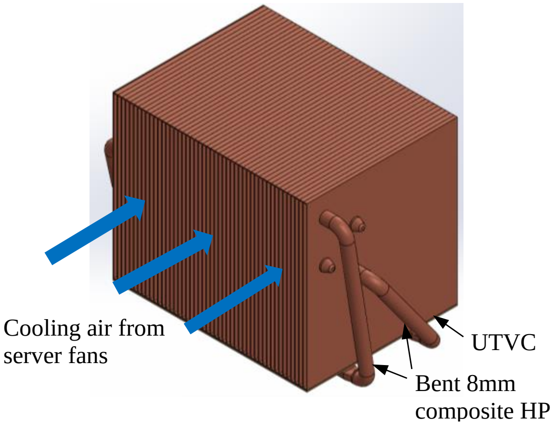

Figure 1. A proposed air-cooling thermal module for air-cooling of AI servers.

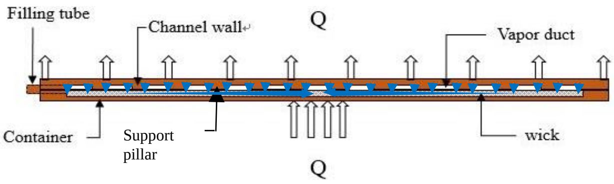

Figure 2. The novel UTVC and the liquid cycling route.

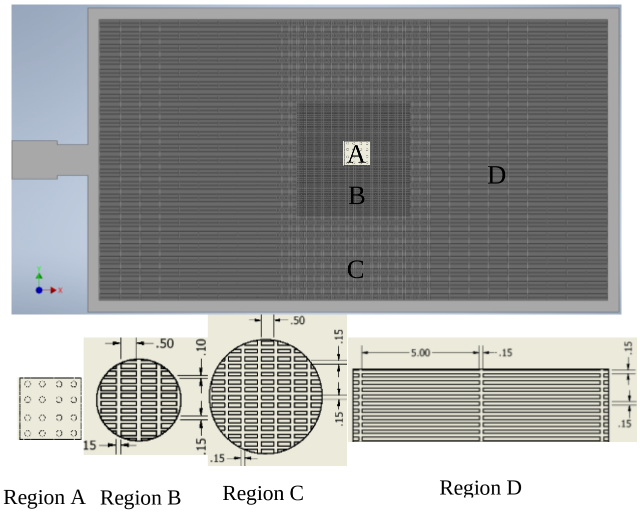

Figure 3. The triple composite wick structure.

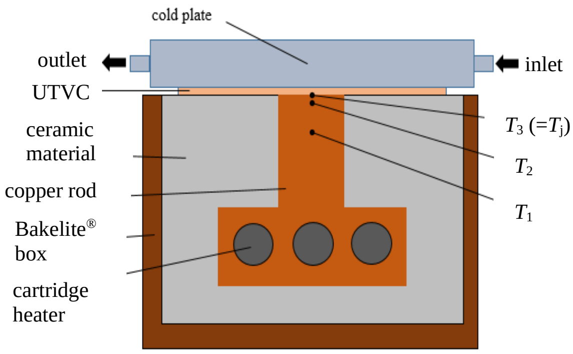

Figure 4. The test setup for the UTVCs.

As shown in Fig. 5, seven thermocouples (T_4–T_{10}), spreading over the bottom surface of the cold plate, measured the condenser temperatures. The cold plate has two symmetric serpentine ducts, each with one inlet and outlet. The outlet temperature was higher than the inlet temperature by 4 K. A thin layer of thermal grease (DOWSIL TC-5021, thermal conductivity of 3.5 W/(m·K)) was laid between every contact interface. The measured values of R involved the resistance associated with the thermal grease, which occupied a small fraction of the total R. The experimental Q and R are defined as

$$Q = 35.19 \times (T_1 - T_2) \ (30 \times 30 \text{ mm}^2) \text{ or} \quad (1a)$$

$$Q = 62.56 \times (T_1 - T_2) \ (40 \times 40 \text{ mm}^2). \quad (1b)$$

The thermal resistance of the UTVC (including R_{tim}) is calculated as

$$R = (T_j - T_{c,\text{avg}})/Q, \quad (2)$$

where $T_{c,\text{avg}} = \frac{\sum_{i=4}^{10} T_i}{7}$. (3)

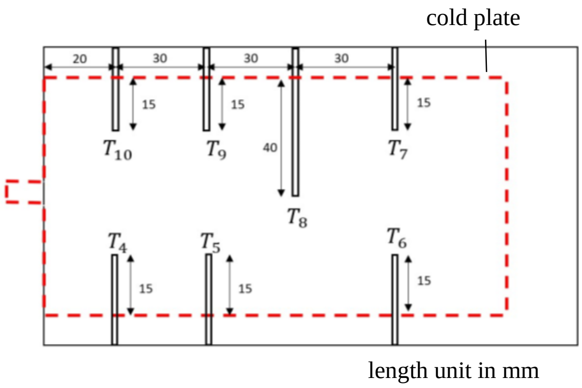

Figure 5. The thermocouple positions on the bottom surface of the cold plate.

3. Results and Discussion

Fig. 6 shows the thickness of the UTVC. Fig. 7 shows the R-Q performance for a triple composite wick at 30 × 30 mm^2, along with a two-layer 2×200 mesh wick [2]. Obviously, the triple composite wick displays superior thermal performance to the ordinary 2×200 mesh wick. Fig. 8 presents the R-Q performance for a densified triple composite wick, along with a double composite mesh-groove wick, at 30 × 30 mm^2 or 40 × 40 mm^2. Heated at 30 × 30 mm^2, the $Q_{\max}$ for the triple-wick UTVC reaches 700 W, while that of the densified double composite wick and the 2×200 mesh wick are only 632 W [1] and 259 W

[3], respectively. At a larger heating area of 40 × 40 mm^2, the Q_{max} may reach 860 W with an R as low as 0.016 K/W. The triple composite wick obtains a higher Q_{max} and slightly better in R than the double composite mesh-groove wick. In the triple composite-wicked UTVC, the largest differences among the condensation temperatures were less than 6.4 K. This value may be affected by the water temperature different in the cold plate. We will use a new cold plate with a much smaller temperature difference between the inlet and outlet for improvement.

Figure 6. The thickness of a UTVC with a triple composite wick.

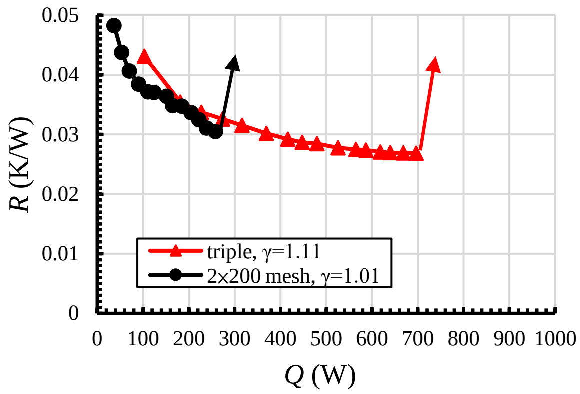

Figure 7. The R-Q relation for a triple composite wick in comparison with a two-layer 2×200 mesh wick heated at 30 × 30 mm^2.

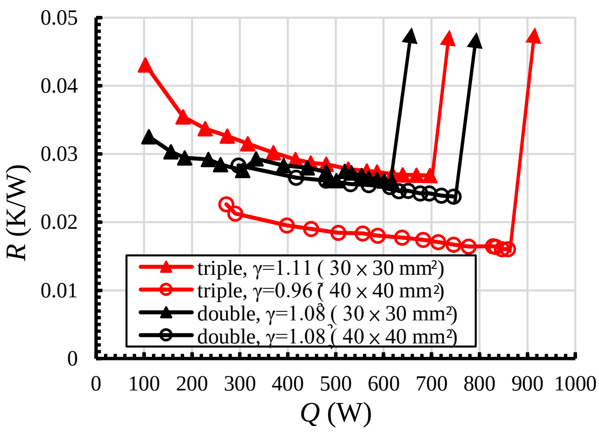

Figure 8. The R-Q relation for a triple composite and a double composite wick heated at 30 × 30 mm^2 or 40 × 40 mm^2.

4. Concluding Remarks

140 × 80 × 1.0 mm^3 ultra-thin vapor chambers (UTVCs), to be used in air-cooling modules for high-power AI servers, were fabricated and tested horizontally under a heating area of 30 × 30 mm^2 or 40 × 40 mm^2. The measured maximum heat transfer rates with the thermal resistances of the UTVCs are 696.8 W with 0.027 K/W and 860 W with 0.016 K/W, respectively. We will optimize the design to improve the Q_{max} and R. In contrast, the UTVC with a 2×200 mesh wick can reach only 259 W [3]. We will also test the UTVC with a 50 × 50 mm^2 heater, which corresponds to the heating area for the UTVC for the 58 × 63 mm^2 GB200 heater. Accordingly, the air-cooling UTVC module may reach 1400 W if four ϕ8 mm heat pipes are used, or reach > 1900 W if eight ϕ8 mm heat pipes are used. These results indicate that the proposed air-cooling UTVC module will stand out and be chosen for high-power AI server cooling among the cold-plate cooling modules.

5. ACKNOWLEDGEMENTS

This work is supported financially in part by Ministry of Science and Technology under MOST 111-2221-E-007-057 and in part by National Chung-Shan Institute of Science & Technology under NCSIST-702-V205.

References

[1] S.-C. Wong, C.-Y. Fu, K.-W. Tseng, L.-Q. Huang, C.-C. Hsu, and C.-Y. Lu, Ultra-thin vapor chambers with composite mesh-groove wick having a cooling capability up to 700 W under 40×40 mm^2 heating, 2024, to be submitted for publication.

[2] S.-C. Wong, Y.-C. Li, C.-Y. Sung, L.-Q. Huang, C.-Y. Fu, and C.-C. Hsu, Effects of vapor duct thickness on the thermal performance of ultra-thin vapor chambers under forced-convection cooling. Thermal Science and Engineering Progress, 2024. 47: 102285.

[3] K.-W. Tseng, S.-C. Wong, C.-Y. Fu, L.-Q. Huang, C.-C. Hsu, and C.-Y. Lu, Thermal performance of 0.7mm-thick ultra-thin vapor chambers with composite mesh-groove wick, ITHERM 2024, Colorado, USA, May 28-31, 2024.

[4] S.-C. Wong and M.-S. Deng, Performance tests on triple composite mesh-groove-powder wicks in a visualizable flat-plate heat pipe, International Journal of Heat and Mass Transfer, 2024. 219: 124912.

Paper ID 035

Experimental and Numerical Studies of a Loop Thermosyphon

Prem Kumar*, Jayant Kathuria, Aalekh Srivastava, Susmita Dash, Amrit Ambirajan, Pradip Dutta

Indian Institute of Science, Bangalore, India
**premkumar@iisc.ac.in:*

Abstract

A two-phase loop thermosyphon is a passive two-phase heat transfer device. In the literature, mathematical modeling is carried out with the assumption that a two-phase flow is present in the riser and the downcomer is fully filled with liquid. In the present work, a 1D mathematical model is developed for fully-filled and partially filled downcomers. The mathematical model successfully modeled the trend of mass flow rate with input heat as observed in the literature. An experimental setup is also designed to compare the predicted results with experimental results. The model predicted the trend mass flow rate pattern with heat loads, as observed in the literature. The model predicts a higher operating temperature than the experimental results. Visualization studies are also carried out to observe the flow pattern in the riser. The visualization study showed that in the riser, vapor dragged the liquid to some height and the liquid returned to the evaporator and only vapor went to the loop. Higher predicted temperature can be attributed to the invalidity of the assumption of two-phase flow throughout the riser.

Keywords: Loop Thermosyphon; Modelling; Partially Filled Downcomer; Visualization

1. Introduction

Loop thermosyphon is a hermetically sealed passive two-phase device that transports heat from the evaporator to the condenser with liquid return facilitated by gravity. It consists of an evaporator, a condenser, and separate tubes for vapor flow (riser) and liquid flow (downcomer), as shown in Figure 1 [1].

Modelling is a tool to estimate the performance of the loop thermosyphon. In the open literature, various studies have been done with steady-state thermo-hydraulic mathematical models of the loop thermosyphon. Normally, 1D mass, momentum, and energy equations are solved using an iterative scheme [2]. Mathematical models are available with the assumption that the downcomer is filled with liquid [3, 4]. The flow in the riser is generally assumed to be two-phase [5, 6]. The output parameters are the mass flow rate, temperatures, and pressures in the loop [3, 4, 7, 8, 9]. Literature shows the increasing and decreasing trend of mass flow rate with an increase in heat loads. The increase in mass flow rate with load at lower heat loads is termed as *gravity-dominated* regime. Beyond a certain heat load, the mass flow rate in the loop decreases with increase in heat load which is termed *friction-dominated* regime.

Song et al. [8] analytically studied the loop normalized mass flow rate for different heat inputs. They observed a gravity and frictional-dominated regime. Chehade et. al. [10] modeled a loop thermosyphon for telecommunication cabinet cooling and validated it with experimental data. They observed two-phase flow in the vapor and liquid lines. Aung et al. [11] modeled a loop thermosyphon to investigate the effect of riser diameter and inclination angle on collector efficiency for solar heating applications. They assumed a fully filled downcomer and two-phase flow in the riser in the model. It was observed that collector efficiency increased with an increase in riser diameter and inclination. During the above studies, two-phase flow is assumed in the riser and the downcomer is considered to be fully filled with liquid. The liquid level in the downcomer depends on the heat load, fluid charging, and dimensions of the loop. The level can be *partially filled* in some cases. Zhang, et al. [3] formulated a one-dimensional steady-state model for a two-phase thermosyphon loop (TPTL) with both fully and partially filled downcomer. For partially and fully filled downcomers, the state at the condenser outlet will be saturated and subcooled, respectively.

For low thermal loads and low filling ratio, the downcomer is partially filled. Increasing the thermal load and the refrigerant charge both leads to an increase in liquid height in the downcomer and finally fully filled downcomer operation is achieved [4]. Zhang et al. [4] experimentally investigated the thermal performance of loop thermosyphon and compared it with a mathematical model. They observed that the actual driving force is less than that of fully filled downcomer. Visualization showed that the downcomer can be partially filled.

As discussed above, few modeling studies are available that solve the governing equations for both partially or fully filled downcomers [3, 4]

In this paper, a 1D mathematical model of a constant conductance loop thermosyphon (i.e., without a reservoir) is developed for the general case of no constraints on the boundary conditions or the imposition of any fixed states. It also considers the conditions where the downcomer is fully and partially filled. An experimental setup is also fabricated to validate the model by comparing the predicted results from the model with experimental data.

2. Mathematical model

One-dimensional steady-state mass, momentum, and energy equations are iteratively solved using MATLAB. It is assumed that a two-phase flow is present in the riser. The model is developed for situations when the downcomer is either partially filled or fully filled. The steady-state equation for the conservation of mass is:

$$\dot{m} = constant \tag{1}$$

Where $\dot{m}$ is the mass flow rate of the working fluid. The steady-state momentum equation after integrating around the loop is [4]:

$$\oint \phi_{lo}^2 \frac{2 f_{lo} G^2}{D_h \rho_l} ds + \oint \left((1-\alpha)\rho_l + \alpha \rho_v \right) g \sin\theta \, ds = 0 \tag{2}$$

G is the mass flux, α is the void fraction, φ_{lo}^2 and f_{lo} are respectively the two-phase friction multiplier and Fanning frictional factor when the entire flow is liquid, and s is the length variable *along* the loop. Equation (2) states that the gravity head balances the frictional pressure drop. The void fraction α and is calculated using Thom's correlation [12].

$$\alpha = \left(1 + \left(\frac{1-x}{x}\right) \left(\frac{\rho_v}{\rho_l}\right)^{0.89} \left(\frac{\mu_l}{\mu_g}\right)^{0.18} \right)^{-1} \tag{3}$$

The two-phase multiplier is calculated using Freidel's corrections [5]

$$\phi_{lo}^2 = C_{F1} + \frac{3.24 C_{F2}}{Fr^{0.045} We^{0.035}} \tag{4}$$

$$C_{F1} = (1-x)^2 + x^2 \left(\frac{\rho_l}{\rho_v}\right) \left(\frac{f_{vo}}{f_{lo}}\right) \tag{5}$$

$$C_{F2} = x^{0.78} (1-x)^{0.24} \left(\frac{\rho_l}{\rho_v}\right)^{0.91} \left(\frac{\mu_v}{\mu_l}\right)^{0.19} \left(1 - \frac{\mu_v}{\mu_l}\right)^{0.7} \tag{6}$$

$$Fr = \frac{G^2}{g D_i \rho_{tp}^2} \tag{7}$$

$$We = \frac{G^2 D}{\rho_{tp} \sigma} \tag{8}$$

$$\rho_{tp} = \left(\frac{x}{\rho_v} + \frac{1-x}{\rho_l} \right)^{-1} \tag{9}$$

The equation for conservation of energy is [3]:

$$\dot{m} \frac{dh}{ds} = q \; ; \tag{10}$$

where h is the enthalpy and q is the supplied heat per unit length. The current model used Shah correlation for condensation which is a function of vapor quality [12].

The mass of fill *constraint* within the loop is given by

$$\oint \rho A ds = M_{fill} \tag{11}$$

Note that M_{fill} is the quantity of working fluid filled in the loop, ρ is the local density, and A is the cross-sectional area of the tube. The details of the loop and working fluid are given in Table 1.

Table 1. Dimensions of the loop thermosyphon.

Height of loop	750 mm
Width of loop	300 mm
Length of evaporator	150 mm
Length of condenser	220 mm
Inner tube diameter	9.2 mm
Working fluid	Methanol
Charging volume	100 ml

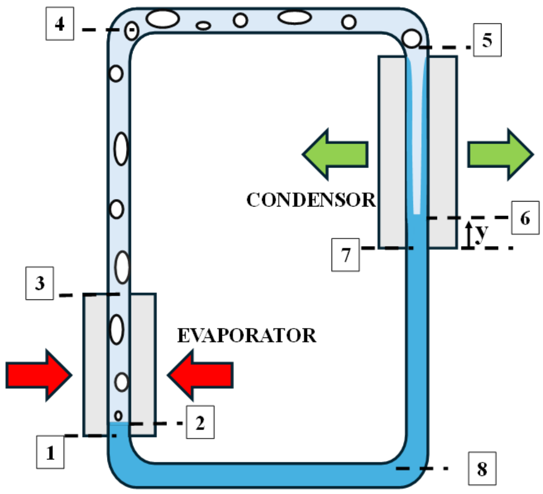

Figure 1. Schematic for loop thermosyphon for modeling with fully filled downcomer

The loop is divided into different zones based on the state of the working fluid for fully-filled and partially-filled downcomers, as shown in Figure 1 and Figure 2. Table 1 and Table 2 describe the zones for the fully filled and partially filled cases, respectively. Each zone is further divided into a large number of small elements and an assumption is made that the properties do not vary within the element. Enthalpy and pressure at node points are calculated using the energy and momentum conservation equations mentioned above. The flow charts to solve the equations for fully-filled and partially-filled downcomers are given in Figure 3 and Figure 4, respectively.

Initially, the model is run assuming the downcomer is filled with liquid. If the model does not converge, then the downcomer is partially filled and the relevant algorithm for that case is then used.

Table 1. Zones for fully filled downcomer case

ZONE	DESCRIPTION
1-2	Subcooled liquid flow in evaporator
2-3	Two-phase flow in evaporator
3-4	Two-phase fluid flow in vertical riser
4-5	Two-phase fluid flow in horizontal riser
5-6	Two-phase fluid flow in condenser
6-7	Subcooled liquid flow in a condenser
7-8	Subcooled liquid flow in vertical downcomer
8-1	Subcooled liquid flow in horizontal downcomer

* 1-2 is the region between points 1 and 2 in Figure 1.

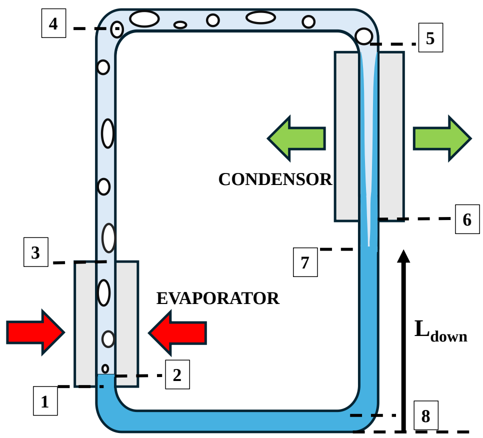

Figure 2. Schematic for loop thermosyphon for modeling with partially filled downcomer

Table 2. Zones for partially filled downcomer case

ZONE	DESCRIPTION
1-2	Subcooled liquid flow in evaporator
2-3	Two-phase flow in evaporator
3-4	Two-phase fluid flow in vertical riser
4-5	Two-phase fluid flow in horizontal riser
5-6	Two-phase fluid flow in condenser
6-7	Liquid film in downcomer
7-8	Liquid flow in vertical downcomer
8-1	Liquid flow in horizontal downcomer

* 1-2 is the region between points 1 and 2 in Figure 2.

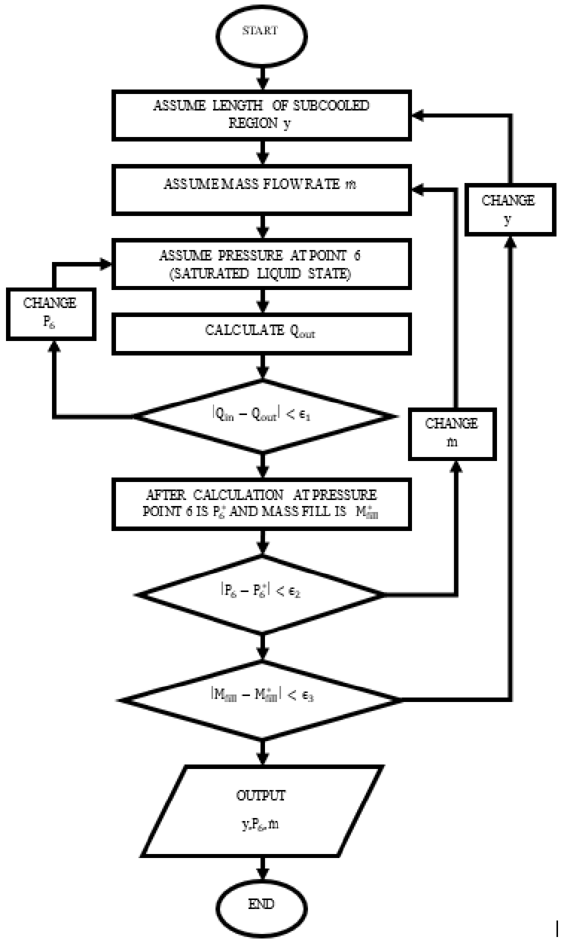

Figure 3. Flow chart to solve the mathematical model when the downcomer is full.

3. Experimental Details

A schematic of the loop thermosyphon is given in Figure 5. The experimental setup of the loop thermosyphon has the same general dimensions as the mathematical model. The dimensions of the loop components are given in Table 1. The loop is made using copper tubing of (outer diameter [OD] -12.7 mm, inner diameter [ID]-9.2 mm). The evaporator and condenser are oriented vertically. The evaporator is heated with the help of aluminum saddle and cartridge heaters. The condenser is a tube-in-tube type heat exchanger. The cold water from the chiller is circulated in the annular section to cool the thermosyphon condenser. Thirteen T-type thermocouples are placed at different locations on the loop for temperature measurement. The details of the instruments used in the experimental set-up are given in Table 2.

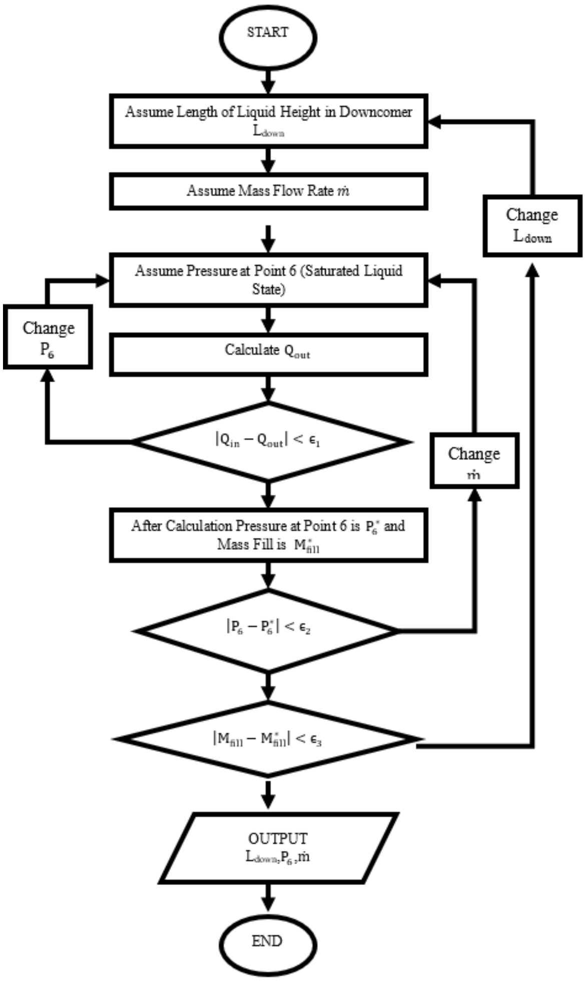

Figure 4. Flow chart to solve the mathematical model when the downcomer is partially filled.

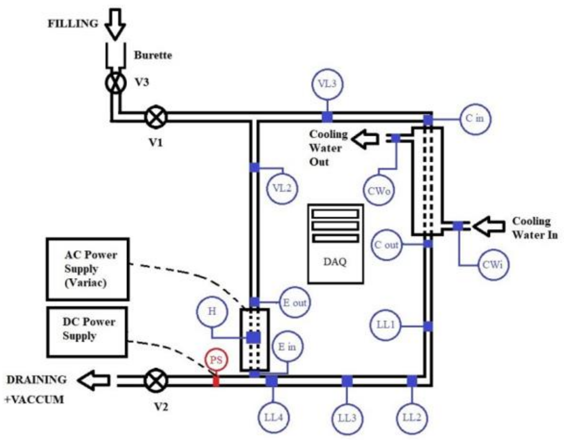

Figure 5. Schematic of experimental set-up for loop thermosyphon

Table 3. Details of the sensors and instruments used

Thermocouples	Company	TC Direct
	Type	T-Type, Welded Tip
	Bead Diameter	0.3 mm
	Accuracy	±0.4°C
Pressure Transducer	Company	Omega
	Model	PX309-500A5V
	Operating Temperature	-40°C to 85°C
	Output	0-5Vdc
Constant Temperature fluid circulator	Company	Siskin
	Model	RCC2500-RT3
	Maximum Pressure	2 bar
	Cooling Capacity	2 kW @ 20°C
	Heating Capacity	2.5 kW
Insulation	Evaporator	Glass Wool (0.023 – 0.04 W/mK)
	Loop	Black Nitrile (0.034W/mK)
Saddle	Dimensions	150 mm x 50 mm x 50 mm
	Material	Aluminium
Heater	Type	Cartridge Heater
	Maximum Power	250 W @ 230Vac
	Dimension	Ø 8 mm x 140 mm
Data Acquisition System	Company	Keithley
	Model	7708 - 40 Channel Differential Multiplexer
	Sampling Rate	5 seconds
Power Supply (Heater)	Company	DENKO Variac-Single Phase
	Type	AC
	Voltage/current	0-270V/0-6A
Power Supply (Pressure Transducer)	Company	APLAB
	Model	L3202
	Voltage	0-32Vdc
	Current	0-2A

4. Results

The results of the mathematical model are presented in Figure 6 with 100 ml of methanol as the working fluid (fill ratio: 35%). The model predicts similar trends for mass flow rate and vapor quality at the evaporator outlet as reported in the open literature [2, 3, 7].

With an increase in heat load, the mass flow rate increases reaching a maximum, and then decreases. The first portion (increase in flow rate) is termed as *gravity-dominated regime* and the second portion (decrease in flow rate) is called the *friction-dominated regime* as shown in Figure 6.

In gravity-dominated mode, with a small increase in vapor quality, there is a large increase in void fraction and a large decrease in mean density of the two-phase flow. After a certain value of vapor quality, driving pressure force reached nearly a constant value. The mass flow rate keeps increasing till the driving force increases.

With an increase in heat loads, vapor quality increases, which causes an increase in frictional losses. The mass flow has to decrease in order to satisfy the constant driving force. The mass flow rate decreases with an increase in heat load, this regime is termed a frictional-dominated regime.

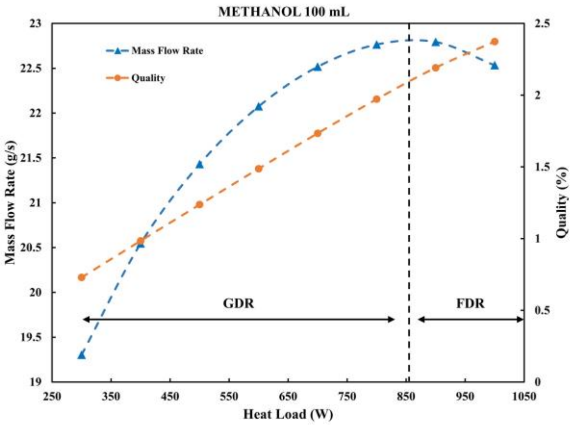

Figure 6. Mass flow rate and vapor quality in the loop at various heat loads

The measured transient temperatures obtained from the experiments with methanol are shown in

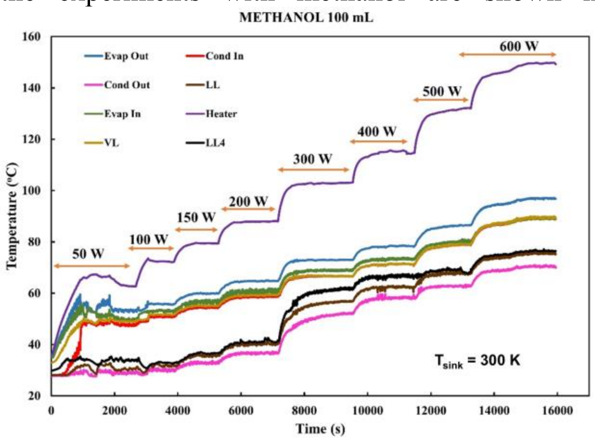

Figure 7. The loop successfully started at 50W, the heat load is varied up to 600W. The variation of temperature at different locations of the loop is shown in

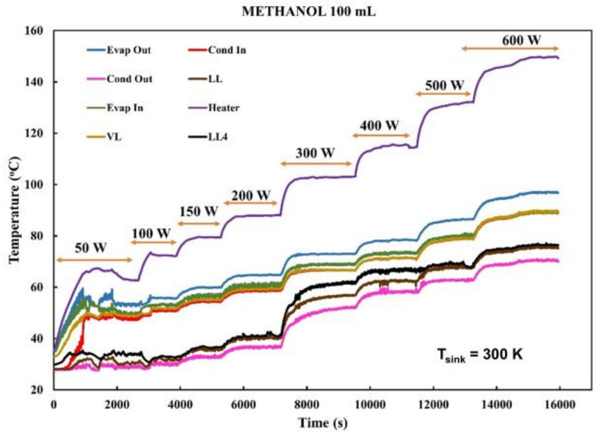

Figure 7. It is also noticed that there is geysering in the loop indicated by the fluctuation of pressure in loop [13] and increases with increase in heat load as shown in Figure 8.

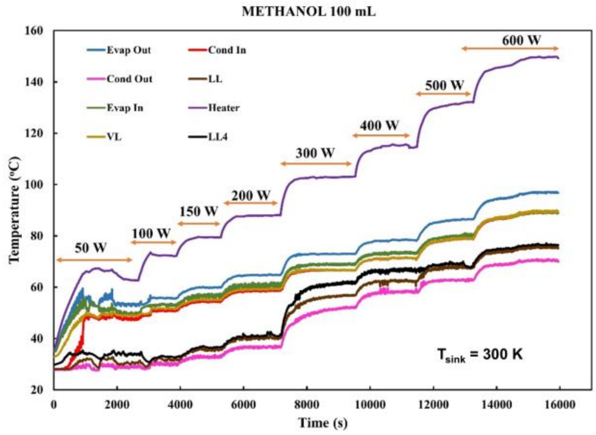

Figure 7. Variation of temperature at different locations with time

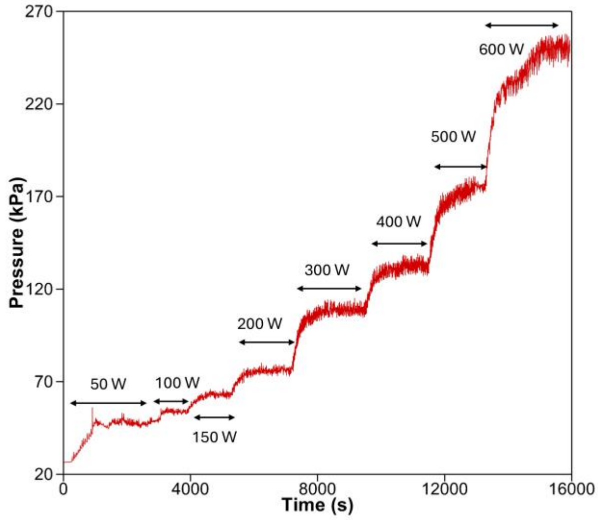

Figure 8. The variation of pressure in the loop at different heat load.

The experiments were performed with pentane, methanol, and water and the results for the steady-state thermal resistance are summarized in Figure 9. It is observed that pentane had lower thermal resistance at low heat loads whereas water had a lower thermal resistance at higher heat loads. Pentane exhibited dry-out at heat loads above 300W. Experiments with methanol were stopped at 600W since the heater temperature exceeded 160°C. The experiments with water were terminated at 900W due to a limitation with the power supply.

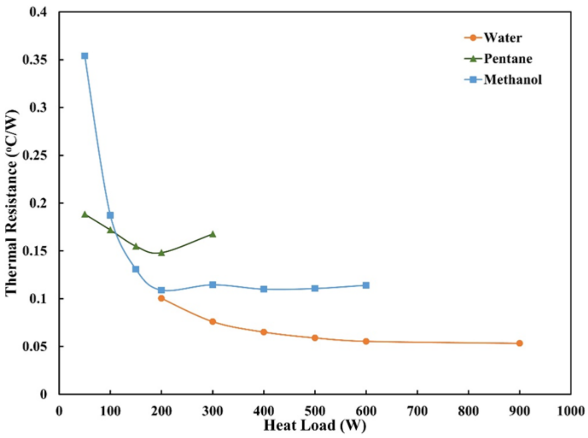

Figure 9. Comparison of thermal performance of loop thermosyphon with different working fluid

The modeling *and* experimental results are shown in Figure 10. There is a clear discrepancy between the results. The model predicts higher temperatures than the experiments. The predicted temperature behavior is nearly isothermal. The temperature depends on the saturation pressure in the loop which is a function of the heat transfer coefficient in the condenser.

In the model, it is assumed that a two-phase flow is present throughout the riser. To validate this, a visualization study is carried out.

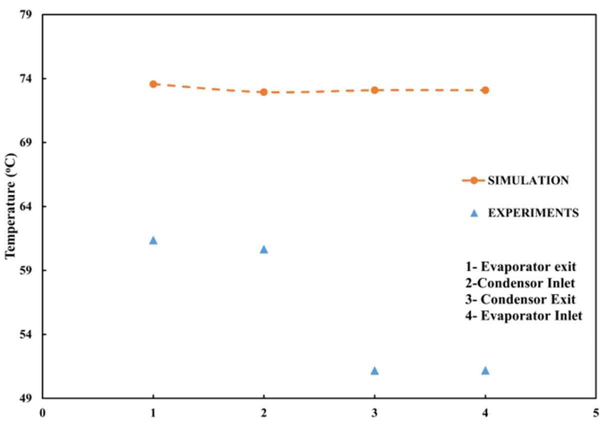

Figure 10. Comparison of results from experiments and modeling at heat load of 300 W.

4.1 Visualization study

In the modified experimental setup, a transparent tube is placed in the riser at the exit of the evaporator to visually observe the flow, as shown in Figure 11. Flow visualization in the transparent riser was carried out using a DSLR camera (Canon M50 mark 2).

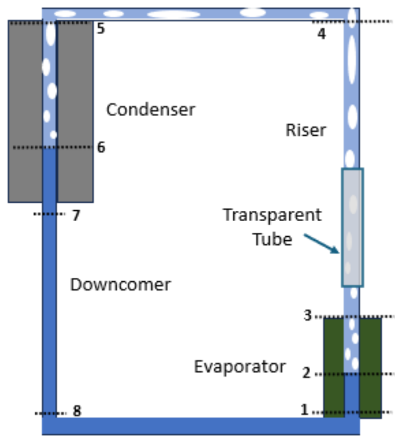

Figure 11. Schematic of loop thermosyphon for fully filled downcomer with a glass tube in the riser.

Figure 12 shows the flow pattern in the transparent tube at a heat load of 300 W with working fluid as methanol for a fill ratio of 35% (100 ml). It was observed that geysering occurred in the riser, wherein liquid plugs rise to some height and then fall back to the evaporator, resulting in only vapor reaching the condenser. This is akin to *geysering* [13, 14]. The standard two-phase models with separated flow do not account for this counter-flow effect. This suggests that the conventional mathematical modeling approach needs to be modified.

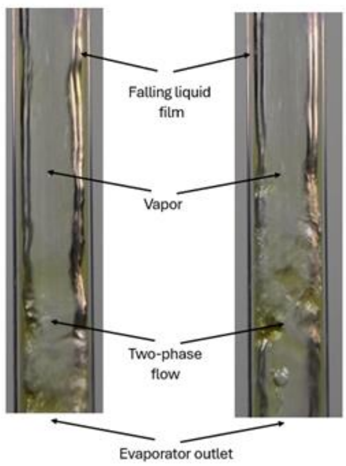

Figure 12. Visualization of fluid flow in the riser of the small loop thermosyphon at 300 W with

methanol.

5. Summary and Conclusion

In the present work, a 1D mathematical model is developed for fully and partially filled downcomers. An experimental setup is also built to compare the predicted results and experimental results. Visualization studies are also carried out to observe the flow pattern in the riser. The following observations were drawn from the present study.

- The mathematical model exhibited an increasing then decreasing trend in the mass flow rate with heat input indicating a transition from gravity dominated to friction dominated regimes.
- The experiments showed that the pentane had the lowest thermal resistance for heat loads below 200 W whereas water had the lowest thermal resistance above this (200 W).
- The mathematical model predicts a higher operating temperature than the experimental data. This is attributed to the assumption of *steady* two-phase flow in the riser.
- The visualization study showed that geysering was occurring in the riser. This may explain the discrepancy between the experimental data and the mathematical model.

Nomenclature	
A	Area (m^2)
D	diameter (m)
F	Friction factor
Fr	Froude number (-)
G	mass flux (kg/m^2)
g	Acceleration due to gravity (m/s^2)
h	Enthalpy (J/kg)
L	Length (m)
m	Mass flow rate (kg/s)
M	Mass (kg)
P	Pressure (Pa)
Q	Heat per unit length (W/m)
S	Local space variable
We	Weber number (-)
x	Vapor Quality (-)
Greek Symbols	
α	void fraction (-)
Θ	Angle (^{o})
M	Viscosity (Pa.s)
P	Density (kg/m3)
Σ	Surface tension (N/m)
φ_{lo}^2	Two-phase frictional multiplier (-)
Subscript	
Tp	Two-phase (homogeneous model)
Vo	Vapor only
Lo	Liquid only
Fill	Filled
l	Liquid
v	Vapor
h	Hydraulic

6. ACKNOWLEDGMENT

This research is funded by the Department of Science and Technology, Government of India (Project no. CRG/2022/008337)

Reference

[1] F. Milanez, and M.B.H. Mantelli, Heat transfer limit due to pressure drop of a two-phase loop thermosyphon, Heat Pipe Science Technology, An International Journal, 2010, 1(3).

[2] J. Zhang, G. Song, Z. Qiu, and H. Li, Thermal analysis and effects study of evaporator exit vapor quality in a separate heat pipe. Applied Thermal Engineering, 2020, 181, p. 115716.

[3] P. Zhang, B. Wang. W. Shi, L. Han, and X. Li, Modeling and performance analysis of a two-phase thermosyphon loop with partially/fully liquid-filled downcomer, International Journal of Refrigeration, 2015, 58: pp. 172-185.

[4] P. Zhang, B. Wang, W. Shi, and X. Li, Experimental investigation on two-phase thermosyphon loop with partially liquid-filled downcomer, Applied Energy, 2015, 160, 10-17.

[5] R. Khodabandeh, Pressure drop in riser and evaporator in an advanced two-phase thermosyphon loop, International Journal of Refrigeration, 2005, 28(5), 725-734.

[6] N. M. Rao, C. C. Sekhar, B. Maiti, and P. K. Das, Steady-state performance of a two-phase natural circulation loop, International Communications in Heat and Mass Transfer, 2006, 33(8), 1042-1052.

[7] P. K. Vijayan, M. R. Gartia, G. S. S. P. Rao, D. S. Pilkhwal, and D. Saha, Steady state behaviour of single-phase and two-phase natural circulation loops. 2nd RCM on the IAEA CRP, 2005, Corvallis, Oregon State University, USA.

[8] J. Song, Performance and scaling analysis for a two-phase natural circulation loop, International Communications in Heat and Mass Transfer, 2008, 35(9), pp. 1084-1090.

[9] C. Nadjahi, H. Louahlia-Gualous, and S. Le Masson, Experimental study and analytical modeling of thermosyphon loop for cooling data center racks, Heat and Mass Transfer, 2020, 56, pp. 121-142.

[10] A. Chehade, H. Louahlia-Gualous, S. Le Masson, and E. Lépinasse, Experimental investigations and modeling of a loop thermosyphon for cooling with zero electrical consumption. Applied Thermal Engineering, 2015, 87, 559-573.

[11] N. Z. Aung, and S. Li, Numerical investigation on

effect of riser diameter and inclination on system parameters in a two-phase closed loop thermosyphon solar water heater, Energy Conversion and Management, 2013, 75, 25-35

[12] V. P. Carey, Liquid-vapor phase-change phenomena, 3rd edition CRC Press.

[13] C. Tecchio, J. Oliveira, K. Paiva, M. Mantelli, R. Galdolfi, and L. Ribeiro, Geyser boiling phenomenon in two-phase closed loop-thermosyphons, International Journal of Heat and Mass Transfer, 2017, 111, 29-40.

[14] T. Zhang, J. Qu, and Y. Hua, Heat transfer characteristics and operational visualization of two-phase loop thermosyphon, Applied Thermal Engineering, 2023, 228, 120520.

Paper ID 036(S6)

Two-phase Thermosyphon with Horizontal Evaporator and Radiative Sky Cooling at the Condenser

Aalekh Srivastava[1], Prem Kumar[1*], Amrit Ambirajan[1], Pradip Dutta[1], Zubin Varghese[2], Rohith B L[2], Praveena Subrahmanya[2]

[1] *Indian Institute of Science, Bengaluru, India, 560012*
[2] *Trane Technologies, Bengaluru, India, 560029*
[*]*premkumar@iisc.ac.in*

Abstract

Radiative sky cooling (RSC) is a passive technique of heat transfer with outer space and can achieve temperature below ambient. This technique has a variety of applications, including cooling of buildings, small warehouses, etc. The constraint of this technique is to keep the system under the sky to have a sufficient view for heat transfer. There are options for transferring the heat from a source using a pumped loop system coupled with the RSC sink kept under open sky. However, electric energy is required for this operation. This paper provides a solution for passive heat transfer using a two-phase closed tubular thermosyphon (TPCTT) with low startup requirements under low heat flux. This paper presents the design study and on-field testing of such thermosyphon. Different parameters, like orientation, working fluids, sink temperature and heat flux, are studied in the design aspects.

A lab experimental setup is fabricated to test the best combination of parameters for RSC application. The tests are made in evaporator control and condenser control mode. In the former, heat flux is applied in the evaporator at a fixed condenser temperature and thermal resistance is calculated for performance. In latter, the condenser temperature drops below ambient, keeping the evaporator dipped in a thermal storage tank filled with water. The relative closeness of the TST-filled water temperature to the sink defines the performance.

The optimum design parameters are used to fabricate an on-field testing setup of TPCTT, coupled with RSC. The on-field testing has been done under the open sky, and the experiment result shows that this design can help transfer heat from one location to the RSC sink.

Keywords: Heat Transfer, Thermosyphon, Two-Phase, Radiative Sky Cooling.

1. Introduction

Radiative sky cooling (RSC) is the cooling of objects on Earth by emitting infrared radiation to space through the atmospheric window, which is transparent to radiation for wavelengths in the range of 8-13µm [1]. Unlike losing heat to the ambient by cooling using forced or natural convection, this system exchanges heat with outer space which is at approximately 4K. Recent developments in RSC-based coatings demonstrate that surface temperatures below ambient can be achieved [2]. This is possible because of the lower absorption of solar and atmospheric radiation and the higher emission of radiation in the 8-13µm range from terrestrial objects to space. As a result, a net cooling effect is produced at night and during the day. Many researchers focusses on using this passive technique to cool buildings, establish cold storage systems, etc., thus reducing energy consumption [3]. Generally, the heat source (building space or chamber) is in thermal contact with the RSC sink using either direct contact, a passive heat transport system or a pumped cooling system. Using pumped loops for flow of fluid requires electricity for operation. A survey of the open literature shows that passive heat transfer from a source to the RSC sink is accomplished with single-phase thermosyphons [4]. The main limitation is that flow initiation happens only when the temperature difference between inlet and outlet of RSC panel is sufficient to generate the density difference required to overcome the pressure drop. That is why, single-phase solar water heaters are replaced by two-phase thermosyphon-equipped solar water heaters [5]. This paper explores the potential of a two-phase thermosyphon to transfer heat from a source to an RSC sink due to the low-temperature difference between the source and sink compared to a single-phase thermosyphon.

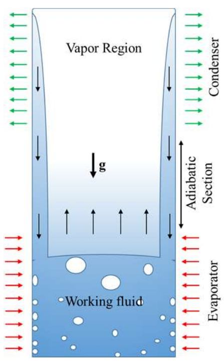

Figure 1. Schematic of thermosyphon

Two-phase closed tubular thermosyphon (TPCTT), being a passive heat transfer device, has been widely used in various thermal management applications [6]. It consists of an evaporator connected to a heat source, a condenser thermally attached to the heat sink and an adiabatic section that connects the evaporator and condenser. Figure 1 presents a schematic of the TPCTT. The working fluid in the evaporator takes the heat from the source by a phase change of liquid to vapour. The vapour rises to the condenser and releases the heat to sink by condensation. The condensed liquid returns to the evaporator because of gravity. Thus, phase change led to a high thermal conductance of this device. In the literature, substantial work has been done on the startup and operational characteristics of TPCTTs. Various parameters such as working fluid, fill ratio (ratio of working fluid filled to the evaporator volume), operating temperature, heat load, sink temperature, inclination, internal surface texture, etc., affect the performance of thermosyphons. The selection of working fluid is decided by the operating temperature range, figure of merit (FOM), working pressure and chemical compatibility [7].

Russo et al. [8] studied a vertical thermosyphon using several working fluids with an FR of 40%. The condenser was air-cooled, and the evaporator was heated from 0 to 25 W (evaporator heat flux 0 to 10500 W/m^2). Among water, ethanol, acetone, and methanol, the authors found that acetone performs the best, while water is the worst in thermal resistance. Rongchai et al. [9] explored the use of thermosyphons in air-water heat recovery systems, comparing R134a, water, and a hybrid of water and R134a. The condenser was cooled by water flow in their setup, while the evaporator absorbed heat from the airflow. Their findings indicated that R134a outperformed water, achieving the highest heat transfer rate. Naresh et al. [10] conducted an experimental study on thermosyphons using R134a, water, and acetone as working fluids, with heat loads ranging from 0 to 150 W. Their results showed that R134a exhibited the lowest heat resistance, followed by acetone and then water. Anand et al. [11] investigated thermosyphons using R134a and water as working fluids, with heat loads varying from 0 to 300 W ($0 < q'' < 75200$ W/m²). They concluded that R134a maintained lower evaporator temperatures at low heat loads ($Q < 100$ W), whereas water achieved lower evaporator temperatures at higher heat loads.

The amount of working fluid in the thermosyphon, often expressed as the Fill Ratio (FR), affects the performance of the thermosyphon. Lower thermal resistance can be obtained in thermosyphon with low FR. This has been experimentally validated by Choi et al. [12], tested 25%, 50% and 75% FRs, and Reji et al. [13], tested 50%, 60% and 70% FRs. A study conducted by Naresh et al. [10] on different fill ratios of R134a varied from 20% to 80%. Results showed that 50% is the optimum FR, resulting in the lowest thermal resistance compared to FRs of 20% and 80%, respectively. Jiao et al. [14] concluded that low FR will lead to quicker startup of the thermosyphon and observed that shaking and reversing can further reduce startup time.

Tilting the straight thermosyphon relative to its horizontal plane significantly affects its performance. This change influences both the distribution of the working fluid and the liquid return head within the system. The thermal resistance decreases at smaller angles because the working fluid covers a larger evaporator area than vertical thermosyphons, however, this also reduces the gravity head for liquid return. Wang et al. [15] investigated a thermosyphon, using ammonia as the working fluid filled with 40% FR, at various inclination angles and found that the lowest thermal resistance was at a 10° inclination relative to the horizontal. Kim et al. [16] studied a thermosyphon with water as the working fluid and determined that the lowest thermal resistance occurred at 50% FR and a 30° inclination angle. Zhang et al. [17] studied thermosyphons by controlling the condenser temperature and noted a lower startup temperature difference in the horizontal position. However, the minimum "operating" thermal resistance was observed at a 20° inclination. Reji et al. [18] tested a copper thermosyphon with R600a as the working fluid, comparing smooth and grooved evaporators under heat loads from 0 W to 50 W (heat flux ~ 8000 W/m²). The grooved evaporator showed a lower thermal resistance of 0.19 °C/W than the smooth one had 0.26 °C/W. This highlights the importance of internal surface modifications and thermosyphon's inclination in reducing startup superheat. Choi et al. [12] found that coating the evaporator's inner surface with cellulose nanofiber reduced thermal resistance by about 30% compared to an uncoated flat surface. Researchers also explored thermosyphon by modifying the design with a horizontal evaporator. DenHartog [19] investigated a thermosyphon designed for permafrost cooling, featuring a horizontal evaporator and a vertical condenser, with R12 as the working fluid. In this testing, the evaporator was submerged in water and the condenser sink was maintained at -15°C. This setup successfully transformed the water surrounding the evaporator into ice. These findings have also been verified by Haynes et al. [20], who studied a horizontal evaporator-based thermosyphon in which the evaporator is 37 m long and filled with CO_2 as the working fluid. Jouhara et al. [21] tested a thermosyphon with a horizontal evaporator and an inclined condenser at various inclination angles, using two working fluids: pure water and an azeotropic mixture of water and ethanol. At low heat loads, the horizontal evaporator exhibited significantly lower thermal resistance compared to larger inclination angles. However, at higher heat loads, the thermal resistance showed less sensitivity to changes in inclination angle. Zhang et al. [22] investigated thermosyphons for permafrost cooling and recommended a 20° inclination from horizontal to maintain the stability of the permafrost stratum. A recent numerical study by Chen et al. [23] on permafrost cooling suggested that a horizontal evaporator thermosyphon could be a viable alternative, providing 72% better heat transfer than inclined thermosyphons. A summary of the literature suggests that at low heat flux, refrigerants, acetone, and methanol offer lower thermal resistance; however, at high heat load, water performs the best by offering lower thermal resistance. A lower fill ratio, surface modification, and more tilt towards the horizontal increase the performance by reducing the startup superheat and the thermal resistance of the thermosyphon. However, as the heat load increases, horizontal orientation lacks the gravity head required for liquid return.

In literature, the utilization of TPCTT has not been explored for an RSC application. RSC applications possess great potential for cooling along with convective cooling media. For RSC applications, a thermosyphon with minimal startup superheat is required due to the limited temperature difference these passive devices generate. In these scenarios, where the condenser temperature governs heat transfer rather than the evaporator, it is crucial to understand the effects of orientation, working fluid, and fill ratio (FR). A literature survey suggests that refrigerants, methanol, and acetone are effective for low-temperature differences. However, it is of interest to know which among them gives lower thermal resistance and improved startup when the condenser temperature drops below ambient.

This paper presents a comparative study of horizontal and vertical evaporator TPCTTs for RSC applications with R134a and methanol. In this study, the adiabatic and condenser configurations remain unchanged by altering orientations. These tests aim to identify a thermosyphon configuration/design for RSC applications; hence, the condenser is designed to cool the condenser below ambient temperature. Based on the trials with small thermosyphons, a larger thermosyphon is fabricated and field-tested with actual RSC film.

2. Design and Development of thermosyphon

The thermosyphon design includes an evaporator, an adiabatic section, and a condenser. The radiative sky cooling and the requirement of a gravity head influenced the condenser design. It is inclined at 15° with the horizontal to have the gravity head for liquid return and sufficient view of the sky to have efficient RSC [24].

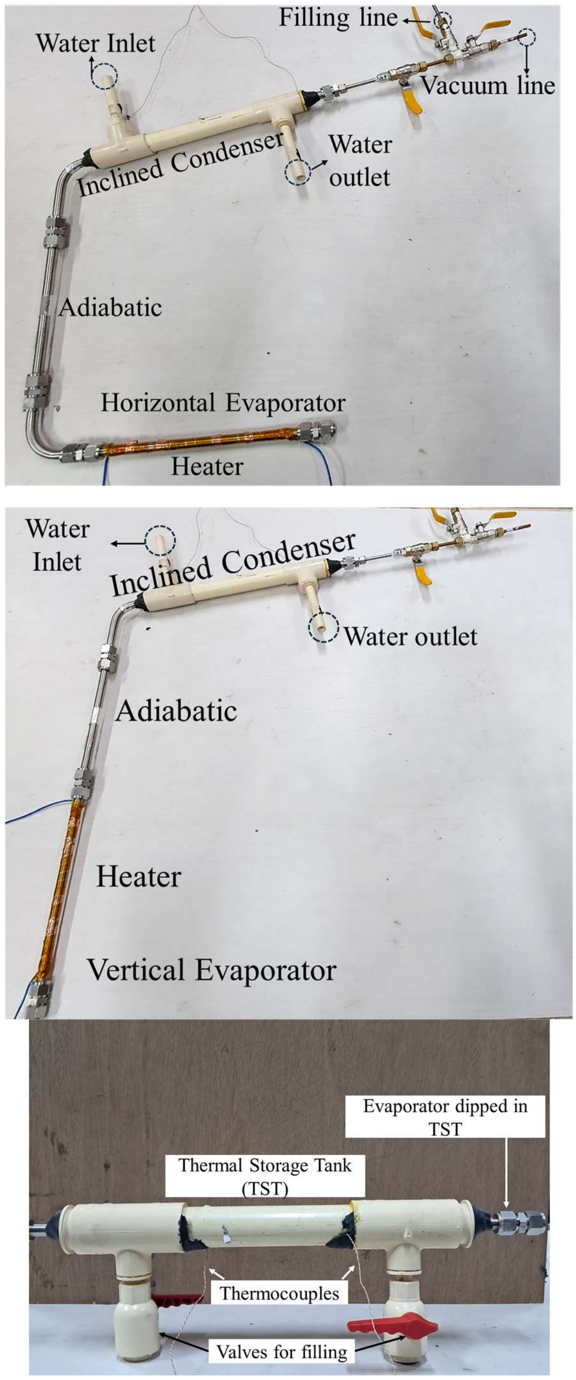

Figure 2. Actual photo of thermosyphon at different orientations and TST

The adiabatic section connects the evaporator and condenser and is vertical in orientation. Generally, in most applications, the evaporator is oriented vertically, and inclination effects are studied by tilting the whole thermosyphon. Tilting the thermosyphon changes orientation and the gravity head. To study the influence of evaporator orientation, a setup is fabricated that can incorporate horizontal and vertical evaporators with the same condenser design, as shown in Figure 2. The TST shown in figure 2 is used in testing methods explained later. The schematics of these thermosyphons and positions of thermocouples are shown in Figure 3. Miniature thermosyphon is fabricated with stainless steel material. Table 1 summarises the details of thermosyphon.

Table 1. Summary of thermosyphon parameters

Parameter	Description
Evaporator length	300 mm
Adiabatic length	300 mm
Condenser length	310 mm
Working fluids	R134a, Methanol
Fill Ratios	25%
Angle of condenser with horizontal	15°
Material of tubes	Stainless Steel
Inner Diameter	10 mm
Outer Diameter	12.5 mm
Thermocouples	T-type

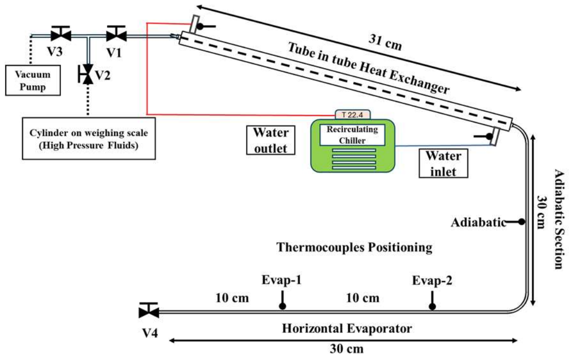

(a) TPCTT with horizontal evaporator

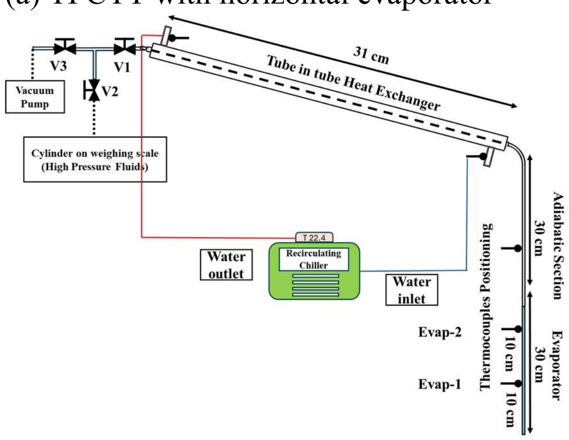

(b) TPCTT with vertical evaporator

Figure 3. Schematic of TPCTT with different evaporator arrangements

A diffusion pump pumping station evacuates the thermosyphon to a pressure of 10^{-5} mbar before filling. It should be noted that the fill ratio is defined as the ratio of the volume occupied by the working fluid as a liquid to the volume of the evaporator.

2.1 Testing Methodology

The testing of horizontal and vertical evaporator-based thermosyphon has been made in two ways:

1. **Condenser Control Mode (CCM)**: In this method, the condenser temperature drops below the evaporator temperature (ambient condition) by circulating a fluid through a cold fluid circulator. The boundary conditions on the condenser side are to simulate a condenser attached to the RSC film by dropping the temperature below ambient (depending on atmospheric and ambient conditions). In this case, the evaporator is dipped in a water tank (made of CPVC material shown in Figure 2) filled with (0.3 kg) of water. The drop in condenser temperature causes the startup of the thermosyphon. The rate of temperature drops of water from ambient and minimum temperature attained describes the performance of thermosyphon. In this test, the sink temperature is dropped and maintained at 16°C, while the ambient temperature varies from 29°C to 30°C.
2. **Evaporator Control Mode (ECM):** In this experiment, the evaporator is heated using a heater made of nichrome wire wrapped around the evaporator. The evaporator is wrapped in ceramic fibre tape and encased in black nitrile insulation. The average sink temperature is maintained at 25°C for all sets of ECM experiments. The heat load varies from 0 W to 58 W (heat flux ~5140 W/m^2) using an AC Variac (max. Current capacity: 6A). Multimeter and clamp meter measure the voltage and current, respectively. Thermal resistance is used to characterise the performance of thermosyphon. It is expressed as:

$$R_{th} = \frac{\overline{T_e} - T_{cf}}{Q} \qquad (1)$$

where, $\overline{T_e}$ is the average temperature of evaporator, T_{cf} is the average temperature of cold fluid circulator (referred as average sink temperature) and Q is the heat supplied.

2.2 Uncertainty Analysis:

To estimate the uncertainty in the temperature difference between the thermocouples, they are all immersed in a well-stirred constant temperature bath that is maintained in the range of 15°C to 55°C. The standard deviation among them is determined to be 0.1°C. Consequently, the uncertainty in the temperature difference with 95% confidence is 0.3°C. The voltage and current measurements uncertainties are ±1% and ±4%, respectively. Table 2 summarizes the various measurement uncertainties. Using the method of Kline and McClintock, the uncertainty in thermal resistance is estimated as follows:

$$R = \frac{\Delta T}{Q} \qquad (2)$$

$$Q = VI \qquad (3)$$

$$\left(\frac{\Delta R}{R}\right)^2 = \left(\frac{\Delta[\Delta T]}{\Delta T}\right)^2 + \left(\frac{\Delta V}{V}\right)^2 + \left(\frac{\Delta I}{I}\right)^2 \qquad (4)$$

Table 2 summarizes the uncertainty in various measuring parameters.

Table 2. Uncertainty in Parameters

S. No.	Measured Parameters	Uncertainty
1	Temperature	±0.5°C
2	Temperature difference	±0.3°C
3	Voltage	±1%
4	Current	±4%

Figure 4 shows the uncertainty in calculating thermal resistance for TPCTT at different orientations.

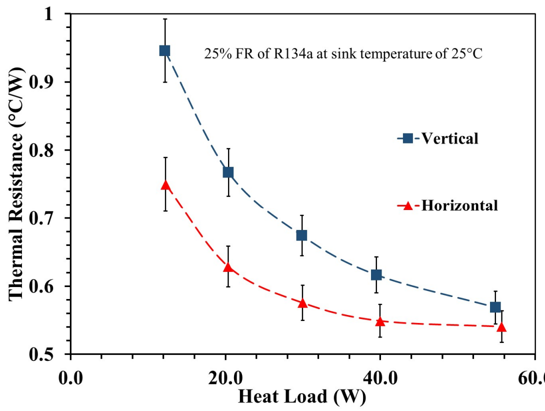

Figure 4. Uncertainties in Thermal Resistance Calculation

3. Results and discussion

This section presents the effect of evaporator orientation on thermal performance at a FR of 25%. The tests have been performed for R134a and methanol in both CCM and ECM, respectively. The effect of the orientation of the evaporator on startup and thermal resistance for each TPCTT is presented. As discussed subsequently, horizontal evaporator thermosyphon has lower thermal resistance and improved startup behaviour.

3.1 Effect of evaporator orientation in ECM

In evaporator control mode, the effect of orientation on methanol and R134a is examined. Figure 5 (a and b) illustrates methanol tested at 25% FR and a sink temperature of 25°C. The heat load varies from 0 to 58 W (heat flux~ 5180 W/m^2) using an AC variac. In a vertical orientation, methanol exhibits oscillation at all heat loads. At 12 W, the evaporator temperature reaches 80°C. The temperature drops suddenly when the condensed liquid film reaches the condenser, indicates the start-up. As the heat load increases, the degree of overshoot decreases because the frequency of bubble formation increases.

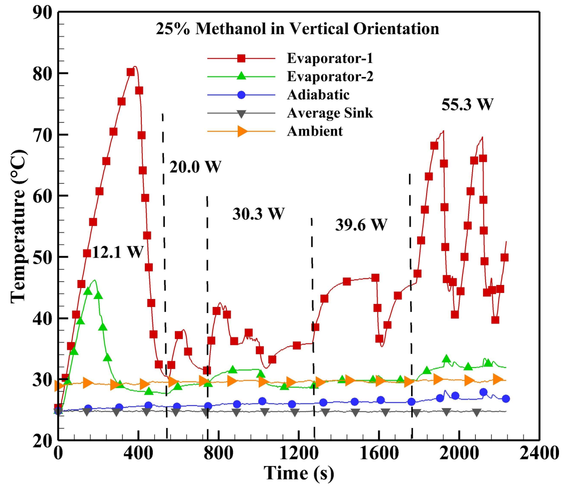

(a) Vertical

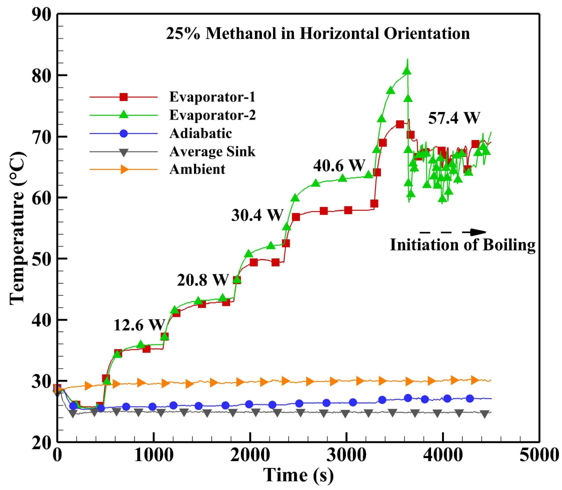

(b) Horizontal

Figure 5. TPCTT with methanol at 25% FR for horizontal and vertical evaporators.

This is evident from Figure 5(a) that at 55 W, the frequency of oscillation rises. Conversely, a smooth temperature profile is achieved at each heat load in a horizontal orientation of evaporator. This can be attributed to the availability of large liquid-vapor interface area, evaporation mode of phase-change dominates over boiling mode (up to heat load of 40 W). Further increase in heat load, at 57W, a transition of phase-change mode occurs, indicating the initiation of boiling (indicated by fluctuation and drop in temperature). Because of the evaporation mode of phase-change, no temperature overshoot is observed at horizontal compared to vertical orientation showing start-up.

Figure 6 (a and b) represents the transient temperature profile at different heat loads of R134a in vertical and horizontal orientations. The sink temperature is maintained at 25°C. In Figure 6-a, the temperature shows start-up at 12W, a relatively less temperature overshoot (~ 5°C) compared to methanol (~ 50°C). This also shows that, for low heat loads R134a is better than methanol.

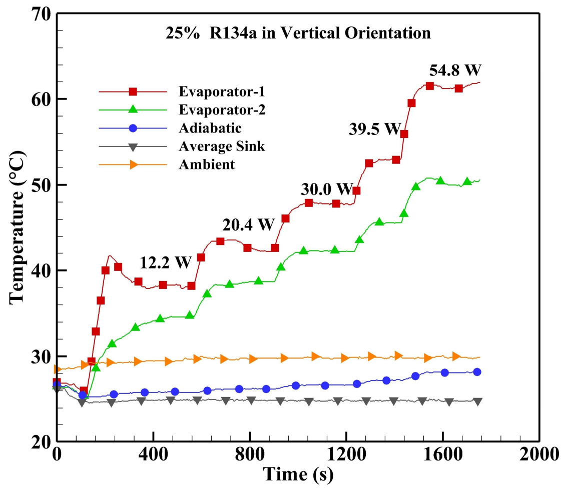

(a) Vertical

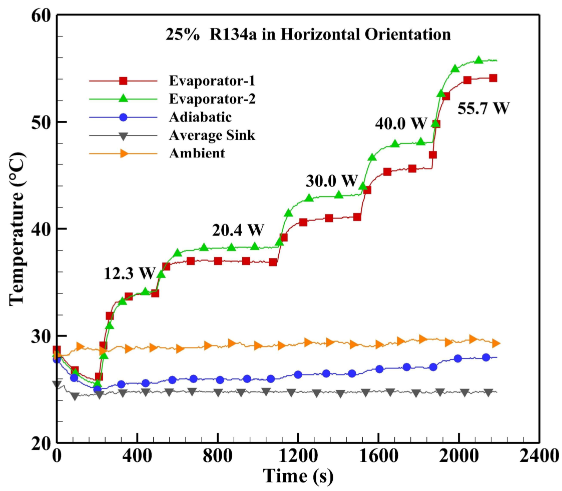

(b) Horizontal

Figure 6. TPCTT with R134a and 25% FR for horizontal and vertical evaporators.

However, in the horizontal orientation shown in Figure 6-b, TPCTT achieves a steady state temperature for each heat load. It is also seen that two thermocouples of the evaporator in horizontal conditions are almost similar, while in vertical, the difference persists for each heat load. It is also seen in figure 6a, that as the heat load is increased, there is a slight kink in the evaporator temperature is observed as the heat load is increased, however that is not present in figure 6-b.

Figure 7 compares the thermal resistance for methanol and R134a at different orientations of the evaporator. Since the steady-state temperature is not achieved in a vertical orientation for methanol, it is not included in the comparison. When R134a is compared in TPCTT with different orientations, it is observed that the horizontal configuration provides lower thermal resistance compared to the vertical one. However, as the heat load increases, the difference between them decreases. The effect of evaporation, in case of unavailability of superheat, lowers the thermal resistance at low heat load (12W, 20W etc.). At heat load of 55 W, the thermal resistance of both orientations for R134a lies in the uncertainty range of each other (shown in Figure 4).

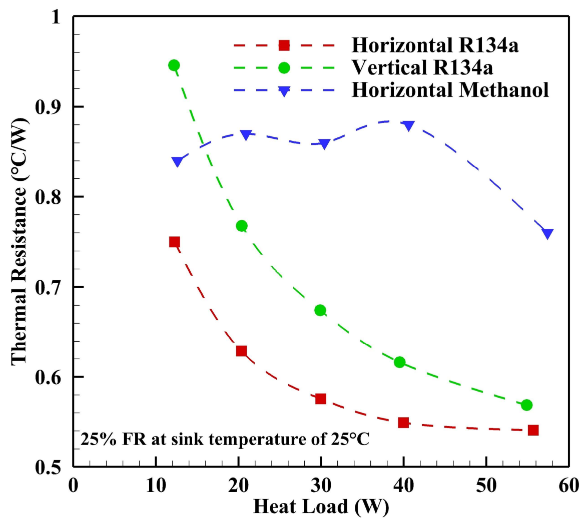

Figure 7. Thermal resistance of R134a and methanol at different orientations

When R134a and methanol are considered at horizontal evaporator configuration, R134a performs better at all heat loads than methanol regarding thermal resistance. Also, it is seen that thermal resistance is almost constant at all heat loads, and sudden drops occur when boiling initiates in the case of methanol. From the study it is concluded that, at low heat load, the horizontal offers better performance, due to evaporation mode of phase change compared to boiling, which requires superheat.

3.2 Effect of evaporator orientation in CCM

In CCM, the evaporator is dipped in a thermal storage tank (TST), filled with 0.3 kg of water. The performance of TPCTT is defined by the rate of temperature drop of water, and the temperature attained by water at equilibrium.

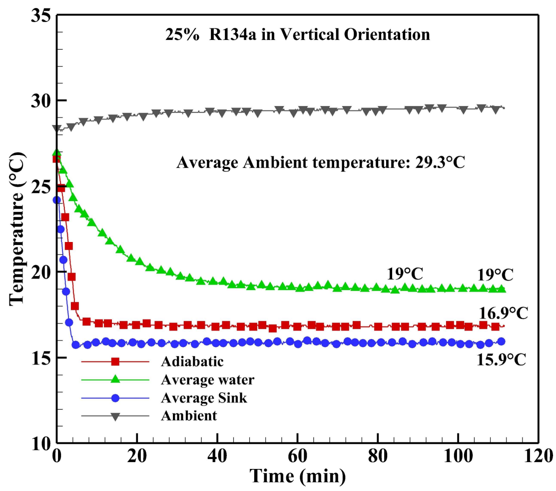

Figure 8. Transient temperature of water in vertical orientation filled with R134a

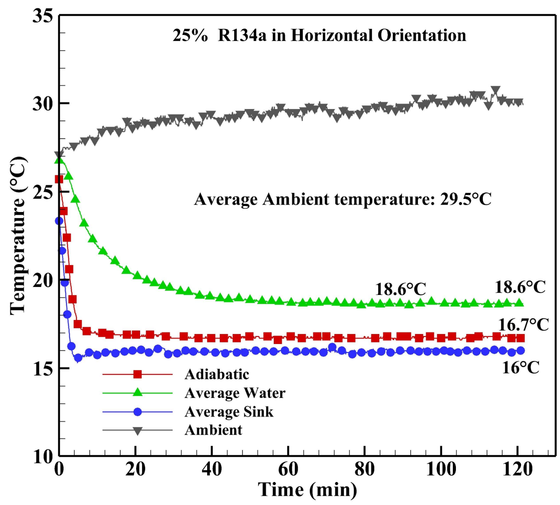

Figure 9. Transient temperature of water in horizontal orientation of evaporator filled with R134a

Figure 8 shows the temperature drop of water in TST, where TPCTT is filled with R134a (25%FR) in vertical orientation of evaporator. The average sink temperature is maintained at 15.9°C, while the water was initially at 25°C. The minimum temperature attained by the water is 19°C which is average of two thermocouples places in TST (shown in figure 2). Figure 9 represents the transient behaviour of water when evaporator is in horizontal orientation. The TPCTT is filled with R134a with 25% FR. The minimum temperature reached by the water at sink temperature of 16°C, is 18.6°C. From figure 8 and 9 it can be concluded that, in CCM, the results are validating the ECM, showing horizontal leads to more relative closeness to sink compared to vertical one.

Figure 10 illustrates the transient temperature profile of water in a TST with a vertically oriented evaporator containing methanol at 25% FR. The sink temperature decreased to 15.9°C, while the average ambient temperature was 30.3°C. The cooling behavior of methanol differs from that of R134a. Initially, methanol cools down rapidly, but a slight kink is observed, after which the cooling rate changes. This may happen because, initially the condensed subcooled liquid film falling along the wall of evaporator, would start evaporating. Since the evaporator is filled with 25% only, therefore, 75% of it is left with the liquid film. This phenomenon is not observed with R134a in a vertical orientation. This may happen, due to methanol's specific heat being 1.8 times that of R134a, requiring more heat to change the temperature of the subcooled liquid. However, for complete understanding of this phenomenon, it needs further investigation. The adiabatic line shows the film temperature, which is nearer to sink temperature. Once the water reaches a temperature, which causes the evaporator to rather depend on evaporation, or reduced boiling. This causes the water to cool down at a less rate compared to the initial one.

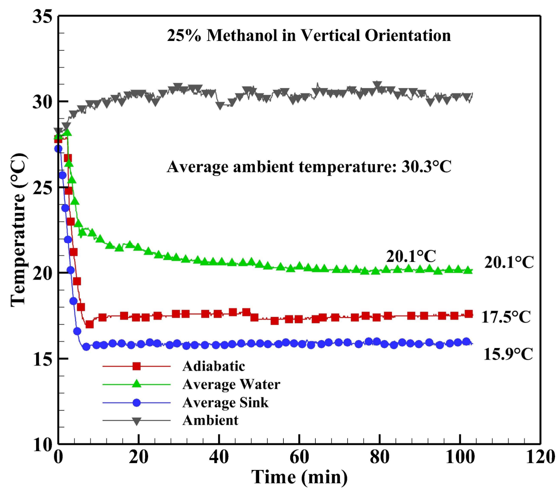

Figure 10. Transient temperature of water in vertical orientation of evaporator filled with methanol

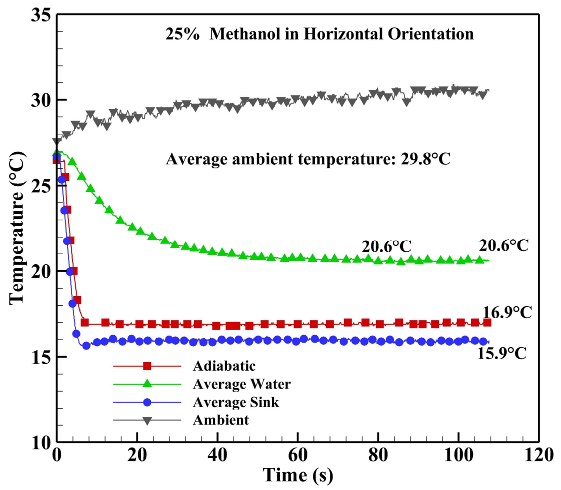

Figure 11. Transient temperature of water in horizontal orientation filled with methanol

The minimum temperature attained by the water after two hours of test is 20.1°C at sink temperature of 16°C. which is better than horizontal case of methanol

Figure 11 illustrates the transient temperature of water when the TST, equipped with an evaporator, is in a horizontal orientation. The TPCTT is filled with methanol at 25% FR, and the sink is maintained at 16°C. The minimum temperature achieved by the water was 20.6°C, with the sink temperature at 16°C. The cooling is governed mainly by evaporation mode of phase change and a similar cooling rate can also be seen in Figure 9.

The section led to the conclusion that TPCTT performed better in case of horizontal, compared to vertical oriented evaporator in case of R134a. However, in the case of methanol, initially, the subcooled liquid film offers higher cooling rate to water in vertical as compared to horizontal orientation and later it is reduced.

4. Field testing of TPCTT with RSC

This section describes an experimental setup and tests with a thermosyphon wherein the condenser is coupled a radiator that is covered with RSC film. The tests are carried out with a direct view of the sky. The evaporator is horizontal, as decided from the above. Based on earlier results [25] and the above experimental studies a horizontal evaporator thermosyphon filled with R134a was chosen. Further, since the effect of FR is insignificant for a longer evaporator, and threading influences the performance, an FR of 40% is used. The schematic of the experimental setup is shown in Figure 12. The TPCTT is made of a copper tube with an inner diameter of 9.5 mm and a thickness of 1 mm as described in [25]. Threading improved performance in condenser control mode and has been experimentally verified by Aalekh et al. [25] and study of FR is insignificant for these applications. The horizontal evaporator has internal circumferential threads with a pitch of 0.5 mm to enhance the wetting area of the working fluid. The condenser is inclined at a 15° angle relative to the horizontal plane, providing a gravity head for the liquid to return and allowing the RSC sink to have a good view of the sky.

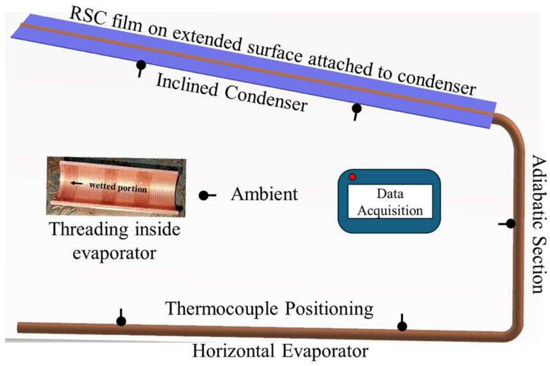

Figure 12. Schematic of the experimental setup for testing thermosyphon with RSC sink

Table 4 summarizes details of the fabricated thermosyphon for on-field testing.

Table 4. Description of thermosyphon fabricated for on-field testing

Parameter	Description
Container material	Copper
Evaporator length	1920 mm
Adiabatic section	838 mm
Condenser length	1920 mm
Angle of inclination of condenser	15
Inner diameter	9.5 mm
Wall thickness of tube	1 mm
Pitch of threading	0.5 mm
Working fluid	R134a
Fill ratio	40%
Thermocouples	T type

The radiator is an aluminum sheet that is covered with RSC film on the top surface. The radiator is in physical/thermal contact with the condenser. Tests are performed to check the response of the evaporator temperature corresponding to the *sub-ambient* temperature produced by the RSC film at the condenser end. Figure 13 illustrates the test results demonstrating that the evaporator temperature closely tracks the RSC sink temperature, which is sub-ambient. The novel feature of this thermosyphon is that even a small drop in condenser temperature is tracked by the evaporator. This test was conducted over two consecutive days on the terrace of the ICER building of IISc. At the two highlighted points, the RSC film was 2.9°C and 2.6°C below ambient, while the difference between the evaporator and RSC film temperature was 1.5°C and 2.2°C, respectively.

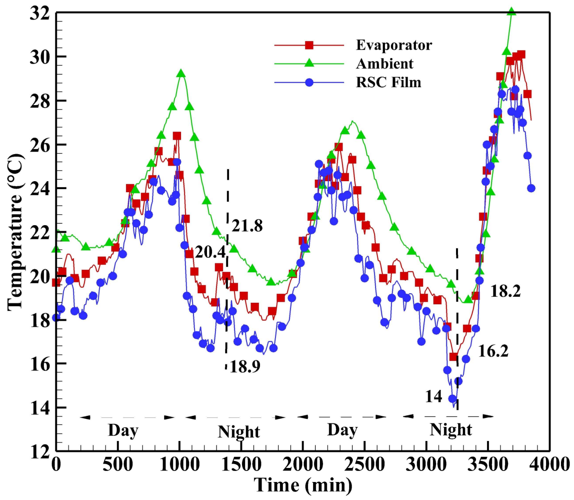

Figure 13. Response of the evaporator to the radiator temperature.

The RSC sink did not have a convective cover, hence lower sub-ambient temperatures could not be achieved.

5. Summary and Conclusions

A two-phase closed tubular thermosyphon is tested with horizontal and vertical evaporator orientation in ECM and CCM mode. Methanol and R134a are used as working fluid. Another setup was also fabricated to field test a horizontal evaporator TPCTT with the condenser coupled to a radiator covered with radiative sky cooling film. The following conclusions can be drawn from the present study.

- It is observed that horizontal evaporator TPCTT lowers thermal resistance in ECM and lowers the temperature difference between the water and sink for R134a.
- In CCM, for methanol, the subcooled condensed falling film causes higher cooling rate in vertical orientation as compared to horizontal orientated evaporator.
- In horizontal orientation, evaporation mode of phase-change dominant over the boiling mode at lower heat load in ECM. After a certain heat load, boiling becomes the dominant mode of phase-change.
- R134a performed better than methanol in the given heat range and sink temperature.
- The evaporator closely tracked the condenser temperature. Thus, this thermosyphon-based approach has the potential to transfer heat passively from a heat source to an RSC-covered radiator.
- A on-field testing of thermosyphon is shown with RSC application and evaporator tracks well the condenser temperature, which was below ambient.

Acknowledgement

The authors would like to acknowledge the generous support of Trane Technologies Ltd. for this work.

References

1. Zhao D., Aili A., Zhai Y., Xu S., Tan G., Yin X. and Yang R., Radiative sky cooling: Fundamental principles, materials, and applications, Applied Physics Reviews, 2019. *6*(2).
2. Zhao D, Aili A, Zhai Y, Lu J, Kidd D, Tan G, Yin X, Yang R. Subambient cooling of water: toward real-world applications of daytime radiative cooling, Joule, 2019. 3(1):111-23.
3. Wu Y., Zhao H., Sun H., Duan M., Lin B., Wu S., A review of the application of radiative sky cooling in buildings: Challenges and optimization, Energy Conversion and Management, 2022. 265: p. 115768.
4. Zhao D., Martini CE., Jiang S., Ma Y., Zhai Y., Tan G., Yin X., Yang R., Development of a single-phase thermosiphon for cold collection and storage of radiative cooling, Applied Energy. 2017. 205: pp.1260-1269.
5. Chow T.T., Bai Y., Dong Z., Fong K.F., Selection between single-phase and two-phase evacuated-tube solar water heaters in different climate zones of China, Solar energy, 2013. 98: pp.265-74.
6. Jafari D., Franco A., Filippeschi S., Di Marco P., Two-phase closed thermosyphons: A review of studies and solar applications. Renewable and Sustainable Energy Reviews, 2016. 53: pp 575-593.
7. Mantelli, Marcia Barbosa Henriques, Thermosyphons and heat pipes: theory and applications. Switzerland: Springer International Publishing, 2021.
8. Russo G. M., Rambeck L. K, Nishida F. B., Santos P. H. D., and Antonini A. T., Thermal performance of thermosyphon for different working fluids, Revista de Engenharia Térmica 15, 2016. 1: pp 03-08.
9. Rongchai K. and Tundee S., Development, testing and design optimisation of a water and R134a based thermosyphon heat exchanger for air-water heat recovery systems, Case Studies in Thermal Engineering, 2022. 39: p.102453.

10. Naresh Y., and Balaji C., Thermal performance of an internally finned two phase closed thermosyphon with refrigerant R134a: A combined experimental and numerical study, International Journal of Thermal Sciences, 2018. 126: 281-293.
11. Anand R.S., and Shibin D., A prognostic analysis on experimental evaluation of thermosyphon using refrigerant R134a and water based on machine learning and optimization techniques, Heat and Mass Transfer, 2021. 57: pp. 481-493.
12. Choi D., Gyosik J., Woonbong H., and Kwon-Yeong L., Heat transfer enhancement of small-diameter two-phase closed thermosyphon using cellulose nanofiber and hydrophilic surface modification, Nanomaterials, 2021. 11(3): 647.
13. Reji A.K., Kumaresan G., Sarathi A., Arasappa G.S., Kumar R.S., Matthew M.S., Analysis of thermosiphon working with eco-friendly refrigerant under various fill ratios, Materials Today: Proceedings, 2021. 45: pp.2618-21.
14. Jiao Q., and Tao H., Experimental research of startup process of two-phase closed thermosyphon (TPCT), In Proceedings of ISES Solar World Congress 2007: Solar Energy and Human Settlement, 2007. 1: pp. 18-21.
15. Wang Y., Wang X., Wang J., Liu Y. and Chen J., Heat transfer performance of a two-phase closed thermosyphon with different inclination angles based on the core-tube monitoring, Case Studies in Thermal Engineering, 2023. 42: p. 102738.
16. Kim Y., Shin D.H., Kim J.S., You S.M. and Lee J., Boiling and condensation heat transfer of inclined two-phase closed thermosyphon with various filling ratios, Applied Thermal Engineering, 2018. 145: pp. 328-342.
17. Zhang M., Lai Y., Pei W. and Jin L., Effect of inclination angle on the heat transfer performance of a two-phase closed thermosyphon under low-temperature conditions, Journal of Cold Regions Engineering, 2014. 28(4): p. 04014007.
18. Reji A.K., Kumaresan G., Kaushik N., Karthi V.N. and Naveen M.K., Thermal analysis of grooved heat pipe with eco-friendly refrigerant for low heat loads in comparison to an ordinary thermosyphon, Materials Today: Proceedings, 2022. 66: pp.878-882.
19. DenHartog S.L., A thermosyphon for horizontal applications, Cold Regions Science and Technology, 1988. 15(3): pp. 319-321.
20. Haynes F.D., Zarling J.P. and Gooch G.E., Performance of a thermosyphon with a 37-meter-long, horizontal evaporator, Cold Regions Science and Technology, 1992. 20(3): pp. 261-269.
21. Jouhara H., Ajji Z., Koudsi Y., Ezzuddin H. and Mousa N., Experimental investigation of an inclined-condenser wickless heat pipe charged with water and an ethanol–water azeotropic mixture, Energy, 2013. 61: pp.139-147.
22. Zhang M., Yan Z., Pei W., Lai Y., Qin Y. and Yu F., Experimental study on the startup and heat transfer behaviours of a two-phase closed thermosyphon at subzero temperatures, International Journal of Heat and Mass Transfer, 2022. 190: p.122283.
23. Chen K., Jin M., Li G., Liu Y., Lu J., Zhao Y. and Yu Q., Thermal performance and heat transfer process of an expressway embankment with horizontal-thermosyphons in permafrost regions, Cold Regions Science and Technology, 2023. 212: p. 103887.
24. Hu M., Zhao B., Cao J., Wang Q., Riffat S., Su Y. and Pei G., Quantitative characterization of the effect of inclination angle on flat-plate radiative cooling performance in buildings, Journal of Building Engineering, 2022. 59: p.105124.
25. Srivastava A., Kumar P., Ambirajan A., Dutta P., Varghese Z., Rohith BL, Subrahmanya P. Experimental investigation of thermosyphons with horizontal evaporator for low heat flux applications. Applied Thermal Engineering, 2024. 257: p. 124249.

Paper ID 040(S2B)

Numerical and experimental study on heat and mass transfer in the secondary wick of a loop heat pipe

Le Liu[1,2], Zhenhua Jiang[1,2*], Bo Shao[1,2], Bingyao Lin[1], Nanxi Li[1], Deping Dong[1,2]

[1] *Shanghai Institute of Technical Physics of the Chinese Academy of Sciences, Shanghai, China*
[2] *University of Chinese Academy of Sciences, Beijing, China*
**Corresponding author email address: jiangzhenhua@mail.sitp.ac.cn*

Abstract

In this paper, the effects of secondary wicks on the performance of loop heat pipe were investigated under different evaporator tilts, and the corresponding physical mechanism was analyzed based on the results of the experiments and CFD numerical simulations. The detachable structure in the compensation chamber was designed and constructed to realize the disassembly or installation of a secondary wick. A 3D model of the whole LHP was built and numerical simulations of steady state operation were conducted by ANSYS software. According to the experimental results, increasing the evaporation tilt would make the LHP without a secondary wick in a more unfavorable operating state and even dry out. After adding a secondary wick, it operated smoothly under all the same conditions. The numerical and experimental results showed that the secondary wick could play a role in stabilizing the return flow of the working fluid, improving working fluid redistributions and making the LHP system operate more stably. When designing and utilizing LHP, the impact of the secondary wick should be carefully taken into account.

Keywords: Loop heat pipes; Secondary wick; Evaporator tilt; Numerical simulation

1. Introduction

When the LHP is applied on the spacecraft under microgravity conditions, the vapor-liquid distribution state of the evaporator core and the working fluid in the CC is random, unlike that in the ground, there will be obvious vapor-liquid interface. Once the evaporator core in the primary wick produces vapor to cause the accumulation and blockage, the working fluid in the CC will not be able to effectively supply to the primary wick, and the evaporator will have the phenomenon of high operating temperature or burning dry under small heat load[1]. Reasonable organization of the flow and heat transfer of the working fluid inside the evaporator is one of the ways to improve the heat transfer performance of the evaporator[2]. Therefore, a secondary wick is usually installed between the CC and the evaporator core to ensure the normal operation of the LHP in space applications[3, 4].

A few researches have suggested operation principle, performance and analysis of secondary wick in the cylindrical evaporator. Van et al.[5] investigated the influence of different connection modes between evaporator and CC, and concluded that the way to achieve the best performance of LHP is to conduct thermal separation and mass transfer coupling between evaporator and CC through a secondary wick and a bayonet, especially in microgravity and tilt attitude. Hoang[6] discussed the numerical method and prediction of the secondary wick transport requirements, and given theoretical aspects of heat transfer and fluid dynamics in the secondary wick with the model assumptions and simplifications. These studies on the secondary wick are analyzed from the theoretical and qualitative perspectives, and lack of experimental research.

In the ground environment, the force of gravity has an effect on the flowing situation of working fluid and on the initial vapor-liquid distribution, causing the relative position between evaporator and CC to influence the performance of LHP. In the past, some literature concerning the effect of evaporator tilt on LHP performance have reported. Bai et al.[7] experimentally found the operating temperature was much higher when the evaporator was a little higher than the CC at a tilt angle of 1.8°without a secondary wick. The experimental analysis indicated that the cooling effect of the returning liquid on the vapor region in the CC or evaporator core was crucial. Shen et al.[8] investigated the coupling effect of non-condensable vapor and evaporator tilts on the steady state operation of a LHP. The noteworthy phenomenon was that the increase of evaporator temperature was only about 7°C at an adverse tilt angle of 15°, which was much lower than that in Ref.[7] (about 15-30°C). This might be related to whether the secondary wick is installed in evaporator core and CC[8]. However, there was no specific study on the single variable of secondary wick in the LHP system.

As briefly reviewed above, few studies have reported the coupling effect of secondary wick and evaporator tilt in the LHP. In this paper, the effects of secondary wicks on the performance of LHP were investigated under different evaporator tilts, and the corresponding physical mechanism was analyzed theoretically based on the results of the experiments and simulations.

2. Numerical simulation

In this paper, a LHP with or without a secondary wick was taken as the research object to study the steady state inside the LHP and validate the effectiveness of proposed improvements through CFD numerical simulations. A 3D model of the whole LHP was built and numerical simulations of steady state operation were conducted by ANSYS software.

2.1. The LHP geometry

Figure.1 illustrates the LHP geometry studied in this work. The 3D model has the same structural parameters as the real LHP, which consists of the evaporator (include wicks), the compensation chamber (CC), and the condenser. In order to make the model compact, the vapor and liquid lines are slightly shorter than that in the experiment. Heat loads are applied on the edge of the evaporator of the LHP. Gravity was heavily considered in this work, which is the advantage of the 3D model.

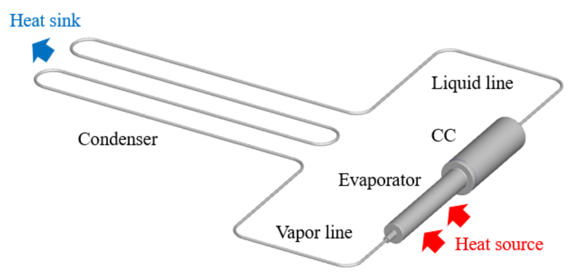

Figure 1. The LHP geometry

2.2. Capillary force model

The capillary force drives the condensed liquid back to the evaporator through the bayonet tube. The capillary force plays a significant role in the LHP circulation. In this work, the wick is assumed as an isotropic porous zone. The capillary force is described as a momentum source term added to the momentum equation, and the momentum source term is only applied to the liquid-vapor interface in the porous zone by UDFs. The capillary force, though appearing as a body force in the momentum equation, is a surface force perpendicular to the vapor-liquid interface. The magnitude of the capillary force is determined by the Young Laplace equation (1):

$$p_c = \frac{2\sigma cos\theta}{R} \qquad (1)$$

where p_c is the capillary force, σ is the surface energy of the liquid and θ is the contact angle of liquid at the solid– liquid interface, and R refers to the capillary radius in the capillary.

There are two main ways to apply the capillary force to porous media: one is to directly apply the capillary force to the vapor-liquid interface of the working fluid in the wick. Generally, the equivalent surface with a vapor phase volume fraction of 0.5 in the vapor-liquid two-phase transition zone of the working fluid is used as the vapor-liquid interface. This method is easy to accurately apply the capillary force at the vapor-liquid interface, and the operation is relatively simple, but it cannot reflect the difference of the capillary force caused by the different volume fraction of each phase in the two-phase region. At the same time, in the finite element calculation, the vapor volume fraction may not be a continuous surface, so it is difficult to define the normal vector of the surface to determine the direction of the capillary force. Another method is to obtain the iso-enthalpy line in the two-phase region according to the enthalpy value, apply the capillary force on the iso-enthalpy line, and take the normal direction of the iso-enthalpy line of the working fluid as the direction of applying the capillary force. Because the endothermic enthalpy of the working fluid will increase, but the phase transition does not necessarily occur, this method is also different from the real physical process.

In this paper, another method of applying capillary force is proposed, which can not only accurately apply the capillary force to the vapor-liquid interface transition region of the working fluid, but also distribute the capillary force according to the gradient of the phase fraction of the working fluid, which is more consistent with the real physical process. The specific methods are as follows:

$$S_c = p_c \nabla\alpha \qquad (2)$$

$\nabla\alpha_v$ represents the vapor phase volume fraction gradient of the working fluid in the vapor-liquid interface transition zone inside the wick. After the vapor volume fraction distribution field of the working fluid in the wick is obtained by the user-defined scalar (UDM), the vapor volume fraction gradient of the working fluid in the wick is obtained, and then the capillary force is applied to the vapor-liquid interface transition zone of the wick in the form of vapor gradient by the source macro, and finally the capillary wicking process of the wick is realized.

2.3. Boundary conditions

Similar to the role of film heating and water cooling in the experiment, the part of evaporator wall is set to Neumann boundary condition (constant heat flux) to represent the heat load, while the part of condenser wall is set as the Dirichlet boundary condition (constant temperature), which represents the heat taken away from the LHP by the water cooler.

3. Experimental system

In order to facilitate the installation or disassembly of the secondary wick, the conventional cylindrical CC construction was sectioned and a flange connection was used. Figure 2 displays the general design and method of construction for the removable structure. The special flanges had square grooves in which PTFE gaskets were placed. Hexagon socket bolts sealed the flanges, preventing the working fluid in the LHP from coming into contact with the outside environment. To lessen axial heat leakage and guarantee mechanical strength, stainless steel was used as the evaporator and CC's casing material.

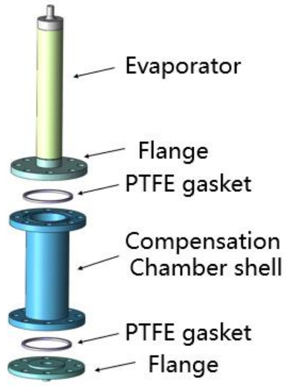

Figure 2. Scheme of the detachable experimental structure

Stainless steel wire mesh, which is cheap and readily available, is used to make the secondary wick in this research. Compared with the primary wick made of sintered metal powder, the increase in manufacturing cost and complexity of the secondary wick is very small and almost negligible. The secondary wick is utilized to link the evaporator and CC for mass transfer. The inner wall of the secondary wick has a gap with the outer surface of the bayonet, which allows the vapor in the evaporator core to return to the CC. The outer wall of the secondary wick, which is located in the evaporator core, and the inner wall of the primary wick need to be closely fitted. The secondary wick acts as compensation to ensure that the primary wick is always wet. Figure 3 displays the detailed structure of the processed primary wick as well as a SEM image of porous wicks. Nickel powder was used to sinter the primary wick. The working fluid used for the experiment was ammonia because of its strict and complex conditions.

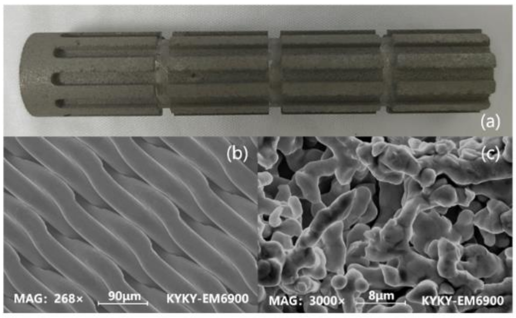

Figure 3. (a) The processed primary wick structure (b) SEM image of secondary wick (c) SEM image of primary wick

In addition, all of the LHP's transport lines, including the bayonet tube, vapor lines, condenser lines, and liquid lines, were made of stainless-steel pipes having an outside diameter of 3 mm and an inner diameter of 2 mm. Condenser lines were attached to four aluminum cold plate channels and maintained at 293 K with a water cooler. To provide a better liquid supply and cooling for the porous wick, one end of the bayonet tube was linked to the liquid line and the other end was pierced into the center of the evaporator core. The overall design and assembly scheme of the whole LHP structure are shown in Figure 4, which also depicts how the measure points are arranged in the LHP system. Three on the CC (T1-T3), two on the evaporator (T4-T5), two on the vapor line (T6-T7), one on the liquid line (T8), and two on the condenser (T9-T10) comprised the ten temperature measurement locations in total. A personal computer and a Keithley-2700 data gathering system made up the data acquisition system. Every second, the measured temperature data was captured and saved.

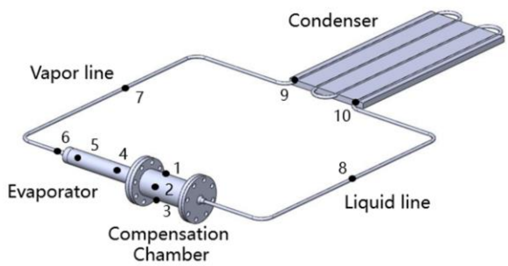

Figure 4. Scheme of the whole LHP structure

As shown in Figure 5, the heat transfer

performance of the LHP with or without secondary wick was explained at six different evaporator tilts (-15°, 0°, 15°, 30°, 45°, 90°). The applied heat load varied from 10 W to 80 W with a step of 10 W.

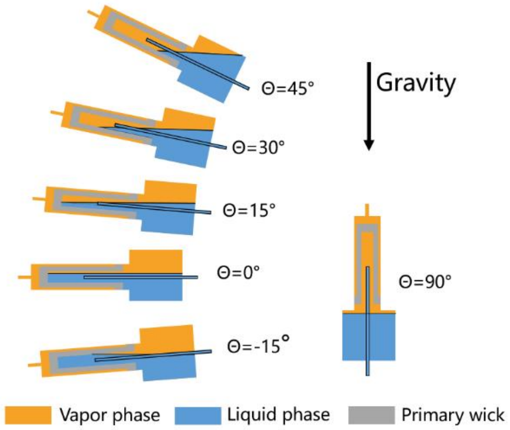

Figure 5. Schematic of the evaporator tilt θ in the gravity environment

4. Results and discussions

Table 1 displayed summary of the tested LHP operation results in forward motion (step increase of heat load) under different evaporator tilts with or without secondary wick, where √ meant that the LHP could start up at heat load of 10W, and operated normally at heat load of 20W-80W, × meant that the LHP cannot start-up normally at heat load of 5W/10W/20W. When it was θ=30° without secondary wick, the tested LHP operated normally at heat load of 10W-50W, and would dry out when the heat load was increased to 60W. The reasons for the changes would be analyzed and discussed in detail later.

Table 1. Summary of LHP operation results without or with a secondary wick

Secondary wick\θ	-15°	0°	15°	30°	45°	90°
with	√	√	√	√	√	√
without	√	√	√	o	×	×

The LHP performance under various evaporator tilts in the cases with and without a secondary wick is displayed in Figure 6. When there is no secondary wick, the adverse tilt-induced temperature increase rises noticeably as the heat load increases. This is especially true when θ = 30°, at which point the LHP dries out at 60 W. The tested LHP does not start up at a heat load of 10W when θ = 45°or 90°, so there is no valid data in in Figure 6. Nevertheless, the addition of a secondary wick reduces the temperature variations brought on by adverse tilt. As the heat load increases, the increment of temperature caused by adverse tilt declines. When θ >= 45°, both evaporator temperature and thermal resistance are almost unaffected by the variation of adverse tilt in the fixed thermal conductivity zone. When θ = 30°, the adverse tilt-induced temperature increase is only about 1.2K with a secondary wick at a heat load of 50W, which is much lower than that (about 15.5K) in the case without a secondary wick.

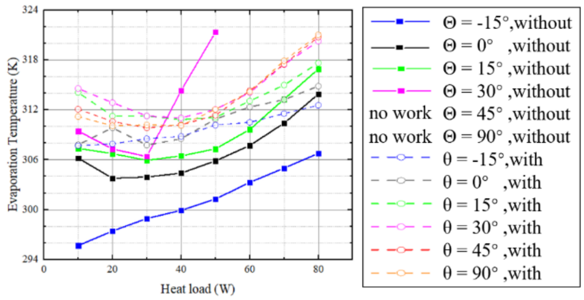

Figure 6. Evaporation temperature under different evaporator tilts

Evaporator tilts change the location of the liquid-vapor contact within the evaporator core, which is primarily responsible for the LHP's dependable performance. As shown in Figure 7, the larger the evaporator tilts, the smaller the direct contact area between the primary wick and the liquid in the evaporator core. And it is more difficult to replenish the liquid to keep the primary wick wet. This is why the LHP performance is worse with a larger evaporator tilt. In addition, the evaporation rate rose in tandem with the rise in heat load. If the amount of liquid replenished does not keep up with the mass reduction due to evaporation, it will lead to a thicker vapor blanket or even dry out in the primary wick. As a result, the adverse tilt-induced temperature increase rises significantly as the heat load increases. This is particularly true when θ = 30°, at which point the LHP dries out at 60W.

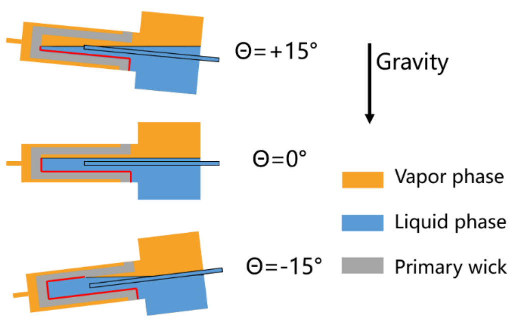

Figure 7. The contact area between the primary wick and liquid under various evaporator tilts

As shown in Figure 8, the LHP only runs stably for a few minutes at an adverse tilt angle of 45, and then there will be increasing temperature oscillation until it exceeds the safe operating temperature and is forcibly shut down. For the orientation "evaporator above CC", the primary wick has no direct contact with the liquid in the CC. Supplying liquid to the evaporator is the hardest at this time, since it tends to stay in the CC due to buoyancy and gravity forces. The heat leakage of the evaporator cannot be balanced by the reflux subcooling liquid, and the tested LHP does not work. However, after adding the secondary wick, as shown in Figure 9, the tested LHP operates smoothly under the same condition.

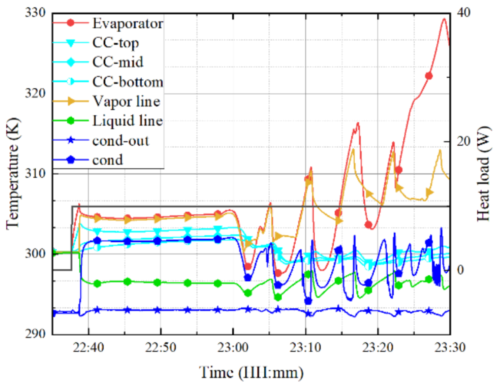

Figure 8. Temperature characteristics (θ = 45°) without secondary wick

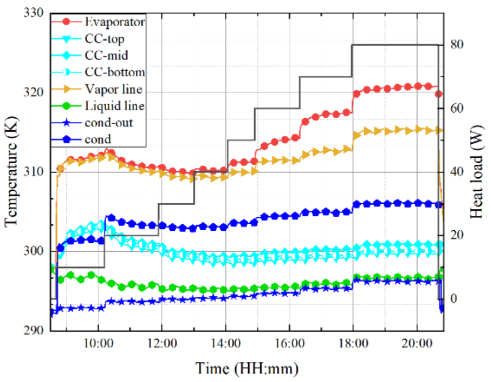

Figure 9. Temperature characteristics (θ = 45°) with secondary wick

To understand reason of the failure, a contrast simulation was conducted under the same operate condition as the feasibility experiment. Figure 10 and Figure 11 are contour diagrams of temperature and ammonia volume fraction (θ = 45°) without secondary wick on the symmetry plane, respectively. Based on Figure 10, temperature in the bayonet and evaporator inlet raises to a large value under the heat power of 20W. According to Figure 11, almost all the fluid in the evaporator, bayonet and wick is vapor. The large vapor pressure hinders liquid from returning back to the evaporator, which makes the LHP lose efficacy. The evaporator exceeds the safe temperature after iterating for about 1800 steps.

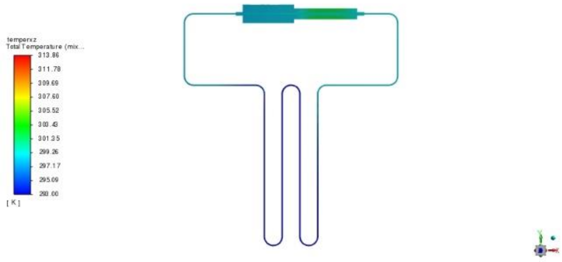

Figure 10. Contour diagram of temperature (θ = 45°) without secondary wick on the symmetry plane

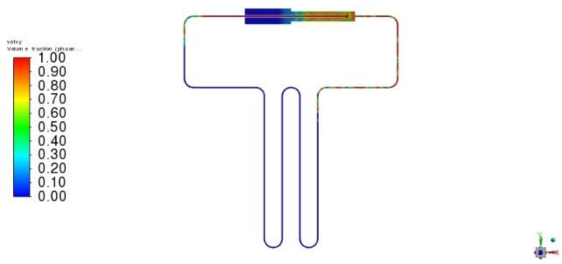

Figure 11. Contour diagram of ammonia volume fraction (θ = 45°) without secondary wick on the symmetry plane

In the case with secondary wick, temperature distribution (θ = 45°) with secondary wick on the symmetry plane of the LHP is shown in Figure 12. In the evaporator and CC, temperature increased along the flow direction, and then dropped a little because of the thermal conduction through bayonet. After condensing into liquid in the condensing tube by enhanced heat transfer with 293 K cooling plate, the fluid returned to the evaporator and completed a heat exchange circulation.

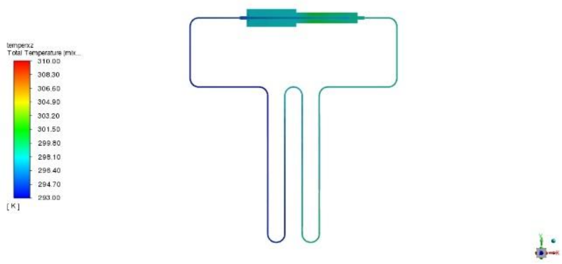

Figure 12. Contour diagram of temperature (θ = 45°) with secondary wick on the symmetry plane

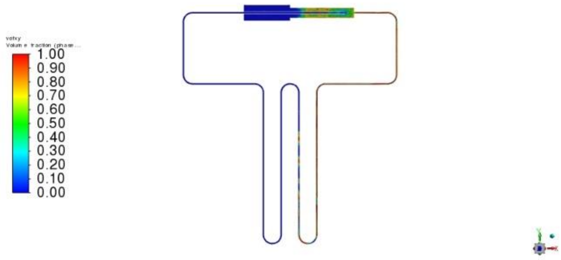

Figure 13. Contour diagram of ammonia volume fraction (θ = 45°) with secondary wick on the symmetry plane

Figure 14 illustrates the difference in liquid supply mode without or with secondary wick respectively. In the case without secondary wick, as shown in Figure 14(a), the liquid does not stay in the evaporator core, but flows straight along the bayonet's outer wall to the CC due to gravity and surface adhesion force. The primary wick will dry out without a liquid supply when θ = 45°/90° because there is no direct contact area between it and the liquid in the CC. After adding the secondary wick, as shown in Figure 14(b), the primary wick and the liquid in the evaporation core and CC are hydraulically and thermally associated with a capillary link.

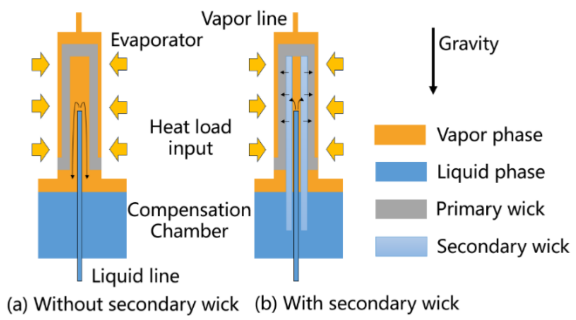

Figure 14. Different liquid supply modes without and with secondary wick

For one thing, the secondary wick improves the path of the reflux liquid from the bayonet to the primary wick and has the function of saving the return liquid in the evaporation core at any angle. For another, it can play a role in pumping the liquid from the CC to the evaporator, and insuring a wetted primary wick during start-up and power/sink temperature transient conditions, which result in an imbalance between the liquid taken away by evaporation from the primary wick and the liquid returning from the condenser. When θ>=45°, there is almost no contact between the primary wick and the liquid in the CC, and the liquid used for evaporation in the primary wick only comes from the secondary wick. Therefore, when θ>=45°, both evaporator temperature and thermal resistance are almost unaffected by the variation of adverse tilt in the fixed thermal conductivity zone.

5. Conclusion

The LHP without secondary wick was very sensitive to evaporator tilts. Adding a secondary wick could adapt to a wider range of evaporator tilts and operate normally when the evaporator was above the CC. The numerical and experimental results showed that the secondary wick could play a role in stabilizing the return flow of the working fluid, improving working fluid redistributions and making the LHP system operate more stably. This research of the secondary wick in LHP not only provides more support and reliability for space applications, but also helps LHPs adapt to various attitudes in gravity applications.

References

[1] T. Kaya, J. Ku, T.T. Hoang, M.K. Cheung, Investigation of low power start-up characteristics of a loop heat pipe, in: AIP Conference Proceedings, 1999, pp. 799-804.
[2] Y. Zhao, S. Chang, W. Zhang, B. Yang, Experimental research on thermal characteristics of loop heat pipe with liquid guiding holes, Applied Thermal Engineering, 101 (2016) 231-238.
[3] P.M. Dussinger, D.B. Sarraf, W.G. Anderson, Loop Heat Pipe for TacSat-4, Space, Propulsion & Energy Sciences International Forum Spesif-2009, 1103 (2009) 91-100.
[4] W.G. Anderson, P.M. Dussinger, S.D. Garner, J.R. Hartenstine, D.B. Sarraf, Loop Heat Pipe Design, Manufacturing, and Testing - an Industrial Perspective, Ht2009: Proceedings of the Asme Summer Heat Transfer, Vol 3, (2009) 497-503.
[5] S. Van Oost, B. Mullender, G. Bekaert, J.C. Legros, Secondary wick operation principle and performance mapping in LHP and FLHP evaporators, in: AIP Conference Proceedings, 2002, pp. 94-103.
[6] Hoang, Mathematical Modeling of Loop Heat Pipes Part Secondary Wick Analysis, International Energy Conversion Engineering Conference and Exhibit 5th (2007).
[7] L.Z. Bai, G.P. Lin, H.X. Zhang, D.S. Wen, Effect of evaporator tilt on the operating temperature of a loop heat pipe without a secondary wick, International Journal of Heat and Mass Transfer, 77 (2014) 600-603.
[8] H.F. Wang, G.P. Lin, X.B. Shen, L.Z. Bai, D.S. Wen, Effect of evaporator tilt on a loop heat pipe with non-condensable gas, International Journal of Heat and Mass Transfer, 128 (2019) 1072-1080.

Paper ID 041(S1)

Effect of evaporation and orientation on surface tension-induced liquid penetration in a porous medium

Rampally Srirama Chandra Murthy[1*] and Navneet Kumar[1]

[1] *Dept. of Mechanical Engineering, Indian Institute of Technology, Jammu, Jammu & Kashmir, 181221*

**Corresponding author email address: rampallysriram@gmail.com*

Abstract

Wicking is a well-studied process in both natural and industrial applications, with a notable example being the evaporation of liquids in heat pipes for temperature regulation. This study focuses on a simplified scenario where ethanol spreads horizontally across thin filter papers followed by subsequent evaporation. Three types of filter paper, each with different permeability, were used, and data were collected through optical and thermal imaging. The results for horizontal-oriented filter papers revealed that the steady-state spreading length (L_c) was much shorter than that obtained by following Jurin's law, indicating that evaporation is the limiting factor in such processes. However, these values were higher than the vertical counterparts by ~30% and this increase reflects the non-negligible contribution by the gravitational forces in the vertical cases. Thermal imaging revealed an uneven temperature profile, with an inversion near the middle of the wicked liquid length. We use this non-linear temperature distribution to assume a power-law relation of the evaporation rate as a function of the wicked length (local) and improve the existing *Constant Evaporation Model* (CEM) that assumes a constant evaporation rate throughout the wicked liquid length. This model is termed the *Non-Constant Evaporation Model* (NCEM). The NCEM yields $h - t$ curves that agree quite well with the experimental data. We further proposed two new dimensionless numbers that suitably collapsed various $h - t$ curves into a single master curve. The results provided new insights into wicking behavior, with important implications for thermal management systems, including wicks and heat pipes.

Keywords: Wicking; Evaporation; Volatile liquids; NCEM

1. Introduction

Capillary movement of liquids through porous materials is an important process in many fields, such as microfluidic devices [1], [2], paper-based fuel cells [3], [4], textile engineering [5], [6], oil recovery [7], medical testing [8], inkjet printing [9], and fluid flow in biological tissues [10]. Additionally, dynamic wicking can help to measure key properties of porous materials, like capillary radius (R_c) and permeability (K) [11], [12], [13]. Capillary flow in porous materials behaves similarly to how liquids move through narrow tubes, driven by capillary force. Porous materials can often be modeled as hollow tubes with an effective capillary radius.

Over a century ago, Lucas [14] and Washburn [15] described how liquids move through capillary tubes. They proposed that the distance a liquid spread (h) and the time (t) it takes follows a diffusion-like relationship: $h = (Dt)^{0.5}$, where D is a diffusion coefficient that depends on the size of the tube and the properties of the liquid. This relationship applies to both horizontal spread [16], [17], [18], [19] and vertical penetration [20], [21], [22], ignoring gravity. Similar results have been found for capillary flow in porous materials, whether the flow is unidirectional or radial, even in cases where the pores are not uniform in size [23], [24], [25], [26], [27].

However, in real-world situations, evaporation plays a key role during capillary penetration, especially when dealing with volatile liquids. As the liquid evaporates from the surface of the porous material, the speed at which the liquid front advances slows down [28]. As a result, the penetration process is limited to a certain region [28], [29], [30]. This evaporation effect is particularly important in applications like vertical capillary penetration, where gravity also plays a role [31], [32], [33].

Fries and his team studied how volatile liquids affect capillary dynamics. They used a liquid commonly found in the printing industry [34] and a metallic weave as the porous medium. By extending the Lucas-Washburn law, they added an evaporation term, which they linked to the total viscous resistance through what they called the "refill velocity" (discussed further in Section 5). Their key finding was that the capillary rise was limited by evaporation. However, their theoretical model overestimated experimental results by about 35%.

This difference might be due to factors like assuming a constant evaporation rate, using a simplified Lucas-Washburn model, treating the medium as homogeneous, and applying a one-dimensional analysis [28]. Recently, the effect of evaporation has gained attention in paper-based sensors and diagnostics [35], [36], where it can affect how far the detecting liquid can travel.

While most studies have focused on evaporation during vertical penetration, fewer have looked at its effects on horizontal flow, which is important for applications like printing, microfluidic devices, and textiles. Understanding how evaporation affects horizontal capillary penetration can help improve the design of porous structures in engineering applications.

In this study, we apply two simultaneous diagnostic methods – surface temperature measurements and optical imaging – to gain a deeper understanding of the dynamics of horizontal wicking of volatile liquids on thin porous media. Surface temperature data is used to construct the surface energy budget (SEB) in the steady state, helping to determine the evaporation rate based on measured parameters such as surface and ambient temperatures. By incorporating the energy equation into the momentum equation, we derive the height-time relationship, $h(t)$. The *Non-Constant Evaporation Model (NCEM)* [37] is employed to account for the length-wise variation of the evaporation rate, capturing the non-linear trend in surface temperature data more accurately. We demonstrate that these modifications improve the existing theoretical framework by better modeling the wicking behavior, particularly when phase change is involved. A comprehensive set of experiments was conducted to test and validate the proposed *NCEM* framework for horizontal orientations.

The article is organized as follows. Section 2 covers the materials and methods used in this study, followed by a discussion on the limitations of the existing theory in capturing the evaporation effects during horizontal liquid wicking. In the following sections, we present an improved mathematical model in Section 5 that accounts for height-wise evaporation variations in horizontal wicking. Results and discussions are provided in Sections 3, 4, and 6, with conclusions in Section 7.

Symbols

a_0, a_1	Evaporation rate constant ($kgm^{-2}s^{-1}$)
FP	Filter paper
A_b	The cross-sectional area of the FP (m^2)
z	Coordinate along paper length (m)
h	Location of liquid front at time ‘t’ (m)
$\bar{h}$	Average convective heat transfer coefficient ($Wm^{-2}K^{-1}$)
h_{fg}	Latent heat of vaporization (Jkg^{-1})
K	Permeability (m^2)
k	Thermal conductivity ($Wm^{-1}K^{-1}$)
L_c	Steady state length (m)
$\dot{M}_e$	Total evaporation mass flow (kgs^{-1})
$\dot{m}_e$	Evaporated mass ($kgm^{-2}s^{-1}$)
$\dot{M}_h$	Mass flow of the liquid front (kgs^{-1})
$\overline{Nu}$	Average Nusselt number
p_c	Capillary pressure (Nm^{-2})
$\dot{p}_{\dot{h}}$	Viscous pressure loss due to liquid front velocity (Nm^{-2})
Pr	Prandtl number
p_r	Viscous pressure loss due to refill velocity (Nm^{-2})
Ra	Rayleigh number
R_c	Capillary radius (m)
T_∞	Ambient temperature (K)
T_s	Surface temperature (K)
U	Uncertainty
t	Time (s)
t_p	Thickness of the FP (m)
v	Liquid front velocity (ms^{-1})
v_r	Refill velocity (ms^{-1})
W	Width of the filter paper (m)

Greek letters

λ	Fitting parameter
ϕ	Porosity
ρ_l	Liquid density (kgm^{-3})
σ	Interfacial Surface tension (Nm^{-1})
σ_s	Stefan-Boltzmann constant ($Wm^{-2}K^{-4}$)
θ	Contact angle (°)
ϵ	Emissivity

2. Methods & Methodology

We used a specially designed experimental setup and Whatman filter papers to study liquid spread on horizontal thin rectangular paper strips, essentially a 2D porous medium.

2.1 Experimental procedure:

We use Whatman filter paper (FP) of Grades 1, 4, and 5 (commonly referred to as 1001FP, 1004FP, and 1005FP). The filter papers were cut, precisely using a laser cutter, into a rectangular shape of 8.5cm × 2.5cm. Porosity and thickness values were taken from the manufacturer, and the same are seen in Table 1.

Table 1 Filter paper properties [38].

Grade	Paper Thickness t_p (m)	Porosity ϕ
1001 FP	180 x 10^{-6}	0.48
1004 FP	205 x 10^{-6}	0.76
1005 FP	200 x 10^{-6}	0.54

The experiments were conducted in controlled laboratory conditions (temperature of 28 ± 0.5 ˚C and relative humidity of $52 \pm 2\%$). Figure 1a shows the sketch of the experimental setup. A liquid reservoir (R1, 10cm x 10cm x 10cm) is seen at the right and an empty reservoir (R2, 10cm x 10cm x 10cm) seen on the left side of Figure 1a; both the reservoirs were made up of polymethyl methacrylate, PMMA and are separated by a divider (AA). Provisions are made such that the FP remains horizontal (and doubly exposed) and without buckling for a major portion with one end pasted on a horizontal platform (that is on top of R2, see Figure 1a) and the other end (~5mm from the top) is pasted on the right side of AA. This vertical 5mm long portion is dipped in the pool of ethanol inside R1. A top cover is placed over R1 to avoid unwanted mass loss from the liquid reservoir.

This top cover was initially a flat PMMA piece, which did allow more mass loss from the system, and that must be due to the circumferential gap between the lower surface of this plate and the top surface of R1. For this purpose, the top cover plate was specially designed as seen in Figure 1b. The rectangular slot (3cm x 0.5cm) at the top allows the FP to pass, while the other grooves allow efficient sliding (if needed) and stop unwanted evaporation. The assembled experimental setup can be seen in Figure 1c. A thermal (Fluke TiX580, sensitivity of 0.05K) and an optical camera (Nikon Z24) were used to track the temperature and liquid penetration with time as seen in Figure 1a. A small piece of graph paper was pasted on the horizontal platform for reference (Figure 1c) to measure capillary penetration over time. The optical images and films were then analyzed using *ImageJ* software for post-processing purposes. The thermal images were analyzed in *SmartView* software.

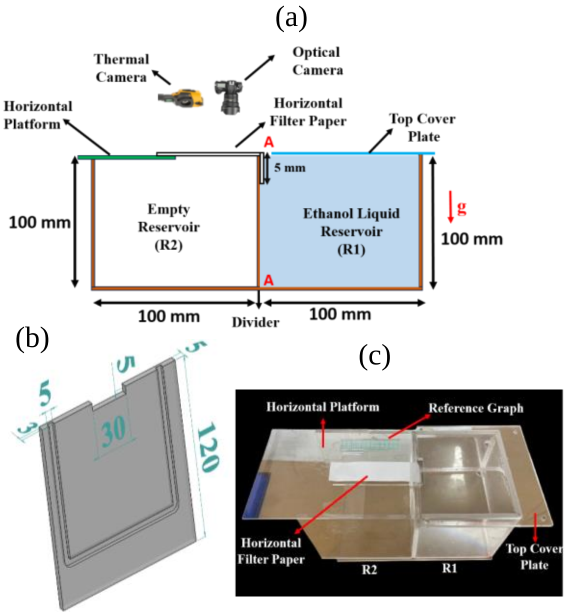

Figure 1. a) Schematic of the experimental setup, (b) top cover with slots for ethanol container (all dimensions are in mm), and (c) a sample photograph showing the experimental setup.

3. Results and Discussions

Liquid penetration on horizontal filter papers (HFP) is different than that on a vertical filter paper (VFP) [37] since the gravitational force is active in the latter case where the meniscus forms with a distinct capillary radius (R_c) that influences the height rise. We discuss the optical and thermal evolution of ethanol penetrating on FPs in both transient and steady states.

3.1 Optical analysis:

Figure 2 shows snapshots for the Whatman 1004FP case at notable instances. Time t = 0 corresponds to when the wicking front becomes visible in the camera mounted on the top. The transient wicking front growth is seen in Figure 2b-e. At t ~ 300 seconds (not shown), the wicking front stops growing and reaches a steady state (see Figure 3). The wicking front location was tracked along the line MM (see Figure 2d), and the distance penetrated was obtained against a graph paper serving as a calibrator. Note that the camera captured ~7.8cm length of the FP giving a pixilation error of ~0.20mm (U_{opt}).

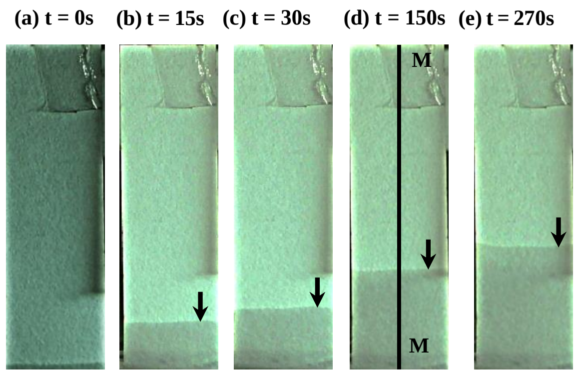

Figure 2. A series of snapshots captured at different time instants showing the location (marked by black arrows) of the wicking front on a horizontal 1004FP. The images are enhanced for clarity. The penetrated distance is measured along the mid line (marked MM in 'd').

Figure 3 shows the capillary penetration or wicking front location (h) for liquid ethanol on all the three FP cases. Initially, there is a rapid rise in h (~20 seconds), followed by a non-linear trend until a steady state (L_c) is reached: L_c values are ~32mm, ~20mm, and ~15mm for 1004, 1001, and 1005FP cases, respectively. The trends of highest and lowest steady-state lengths (L_c) are similar in the case of vertically oriented filter papers also [37]. The comparison is seen in Table 2.

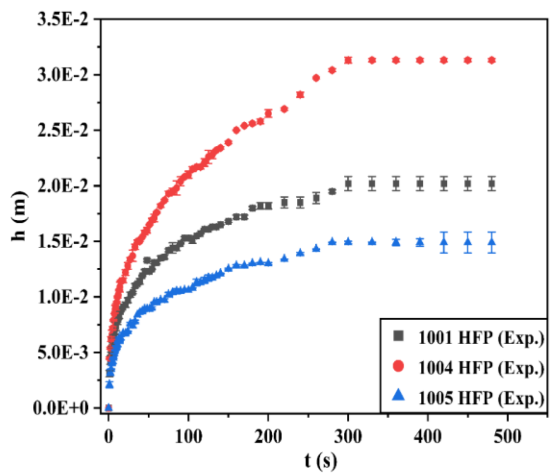

Figure 3. Temporal variation of capillary penetration for liquid ethanol in three different filter papers. The bar represents the experimental deviation across three experiments in each case.

The deviations across multiple experiments in each case for HFP are shown by bars in Figure 3. Note that without evaporation, the L-V meniscus would reach infinity (as per the Youngs-Laplace equation for the horizontal papers since surface tension force is unopposed in this orientation), which is much higher than L_c.

Table 2. Comparison of steady state lengths (L_c) in different orientations

Filter paper grade	Steady state length	
	VFP [37]	HFP
1001 FP	$\sim 15.1mm$	$\sim 20.2mm$
1004 FP	$\sim 26.4mm$	$\sim 31.3mm$
1005 FP	$\sim 12.4mm$	$\sim 14.9mm$

The data shows that the L_c, is consistently greater in the horizontal filter paper (HFP) compared to their vertical counterparts, across all cases studied here, suggesting that orientation does play some role in determining the L_c values in such processes. However, it remains to be seen as to how these observations would impact the scenarios in heat pipes (where gravity is important) and loop heat pipes (where gravity is not important) given the fact that the entire process is passive in nature.

3.2 Thermal analysis:

Ethanol's relatively high volatility leads to rapid evaporation that cools the surface leading to sub-ambient surface temperature values (at least when no external heating is done). We now discuss the surface temperature evolution.

Transient Analysis:

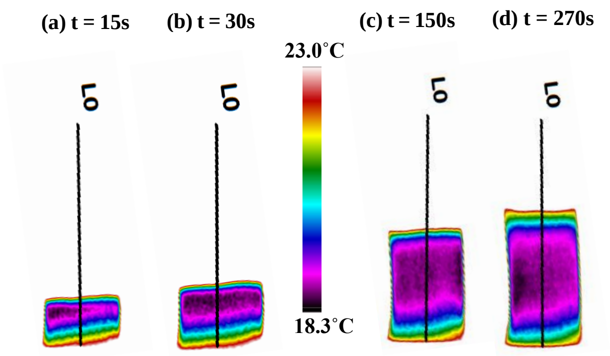

Figure 4. [Colour online] Time sequence of thermal images in local temperature scale (such that the hotter dry FP is not seen intentionally) for 1004FP at different time instants; the temperature value ranges between 18.3°**C** and 23°**C**.

Figure 4 shows thermal images at notable instances for 1004FP case. Magenta represents the lowest temperatures and red represents the highest. Higher temperature values are seen at the ethanol source (near the bottom) and near the liquid front. The temperature scale was chosen such that the dry FP zone is not seen in the thermal images.

Figure 5 shows the pixel-wise variation of the surface temperature along the centerline (L0) for 1004FP case. The surface temperature first decreases along L0, reaches a local minimum, and then rapidly increases when the dry FP region is approached; the temperature remains constant beyond this. The uncertainty in surface temperature, U_{T_s} [39], is ~0.10K.

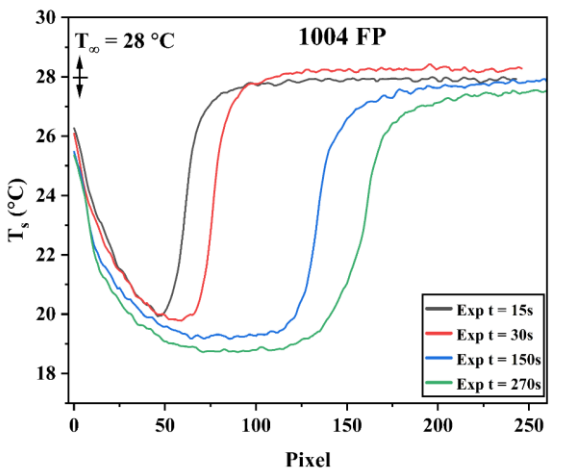

Figure 5. [Colour online] Height-wise variation of surface temperature along the centerline (L0) at four different time instants for 1004FP. A notable temperature jump is seen near the wicking liquid front when the dry FP region is approached. The double-headed arrow represents the fluctuations ($\pm\mathbf{0.5}$ °C) in the ambient temperature value throughout the experimental duration.

Steady-State Analysis:

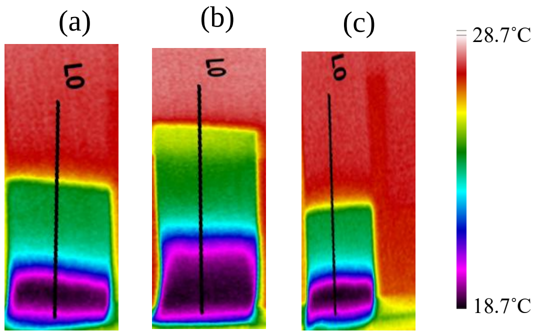

Figure 6. [Colour online] Thermal images in the steady state for (a) 1001FP, (b) 1004FP, and (c) 1005FP, shown in the global temperature scale. A sandwiched patch (warmer than the liquid ethanol and colder than the dry FP) representing the condensed water is also seen.

Figure 6 shows thermal images in steady states, highlighting a relatively "warmer" (seen in green color) zone, representing the condensed water, between the liquid ethanol region and the dry FP zone [40]. Condensation is unlikely to occur on the wicking liquid ethanol surface but can occur at the wicking front. However, since this front is moving in the transient state, condensation does not occur. All the conditions meet perfectly for the condensation to occur in the steady state.

Figure 7 shows surface temperature variation along L0 versus the liquid penetration length (h) for the three FPs. Paths 1-2-3 and 4-5 represent the liquid ethanol and the condensed water, respectively. Paths 3-4 and 5-6 indicate the ethanol-water and water-dry FP zone interfaces, respectively. These interfaces are diffusive in nature as far as temperature is concerned.

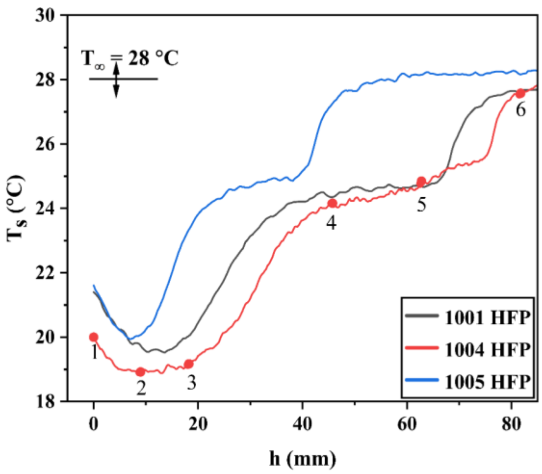

Figure 7. [Colour online] Surface temperature variation versus FP length along line L0 for 1001, 1004, and 1005FP in the steady state showing distinct temperature paths for liquid ethanol and condensed water zones. The double-headed arrow represents the temperature fluctuations ($\pm\mathbf{0.5}$°C).

4. Obtaining Permeability ($\boldsymbol{K}$) & Average Evaporated Mass ($\bar{\dot{m}}_e$)

In a non-evaporating horizontal system (in the initial time periods [28], [41]), the process of liquid spread on a porous surface is a competition of two forces (surface tension pulling the liquid while the viscous forces opposing it) leading to the dynamic motion of the liquid front. The dynamic pressure balance is given by,

$$\frac{2\sigma\cos\theta}{R_c} = \frac{\emptyset}{K}\mu_l h\frac{dh}{dt} \tag{1}$$

The terms in Eq. (1) can be rearranged to give,

$$\frac{a}{h} = \frac{dh}{dt} \tag{2}$$

where, $a = \left(\frac{2\sigma\cos\theta}{\emptyset\mu}\right)\frac{K}{R_c}$

With the known initial condition ($z = 0$ at $t = 0$), the solution to Eq. (2) is,

$$h^2 = \left[\frac{4\sigma \cos\theta K}{\phi \mu_l R_c}\right] t = [p]t \qquad (3)$$

where, p is the slope of the $h^2 - t$ experimental curve (see Figure 8), and we have incorporated capillary radius values as $59\mu m, 64\mu m, and\ 75\mu m$ for 1005FP, 1001FP, and 1004FP, respectively in Eq. (3) to obtain permeability. In fact, it is K/R value which is of significance (see Eq. 3) and the K value would depend on the choice of R, i.e., R_c (capillary radius) or R_s (nominal pore size quoted by the manufacturer) as used by a few others [42]. In both cases, the final outcomes remain unaltered.

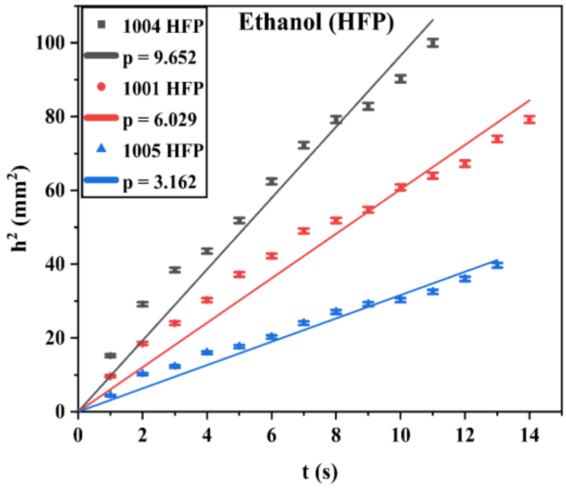

Figure 8. [Colour online] Variation of $\boldsymbol{h^2}$ versus time with linear fits for liquid ethanol wicking on the three FP cases studied here. Values of 'p' seen in the legend represent the slope of the linear fit in each case with units of $\boldsymbol{mm^2 s^{-1}}$. The error bars show the uncertainty $\left(\boldsymbol{U_{h_i^2}}\right)$ in each case.

The uncertainty $U_{h_i^2}$ [38] for the *i^th^* measurement of the height reached by the liquid front h_i^2 is evaluated using,

$$U_{h_i^2} = \sqrt{\left(2\, h_i\, U_{opt}\right)^2 + \left(\frac{U_d}{2\sqrt{3}}\right)^2} \qquad (4)$$

U_{opt} is the uncertainty contribution from the optical resolution as discussed in Section 3.1. The uncertainty U_d [43] (depth of dipping) is considered negligible and thus not included in this uncertainty calculation. Eq. 3 yields the permeability values, and its uncertainty (U_K) [38] was calculated as,

$$U_K = \sqrt{\left(\frac{\partial K}{\partial z} U_{opt}\right)^2 + \left(\frac{\partial K}{\partial \phi} U_\phi\right)^2 + \left(\frac{\partial K}{\partial R_c} U_{R_c}\right)^2} \qquad (5)$$

In obtaining U_K, we did not consider U_ϕ and U_{R_c}. The permeability and its uncertainty, hence calculated, are seen in Table 3.

Table 3. Permeability values for VFP and HFP cases, and their uncertainties based on Eq. 3 and 5.

Permeability, K (μm^2)			
	FP	**VFP** [37]	**HFP**
Ethanol	1001 FP	1.42 ± 0.03	2.26 ± 0.08
	1004 FP	4.86 ± 0.13	6.87 ± 0.03
	1005 FP	0.66 ± 0.05	1.23 ± 0.04

Data shows that permeability is consistently higher for HFP cases compared to the VFP, for all the three cases, suggesting the orientation to affect the fluid flow considerably.

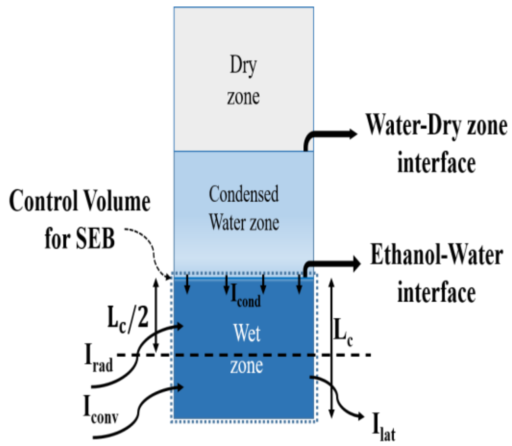

Figure 9 [Colour online] Schematic of the control volume in the steady state for the wet zone. SEB simplifies to energy balance terms between the surface and ambient, primarily through conduction, convection, and radiation.

Another critical factor influencing the wicking process is the evaporation rate, which plays a vital role in evaporating systems. We consider the wet zone (see Figure 9) as the control volume (CV) in the steady state and calculate the average evaporation rate, $\dot{m}_e$, using the surface energy budget (SEB) [44], [45], [46]. Rampally and Kumar [37] used SEB to calculate the average evaporated mass loss. In the steady state, the SEB is,

$$I_{gain} = I_{loss} \Rightarrow I_{cond} + I_{conv} + I_{rad} = I_{lat} \quad (6)$$

where, I_{gain} and I_{loss} are the heat fluxes received in the CV and lost by the CV, respectively. I_{lat}, I_{cond}, I_{conv}, and I_{rad} are the latent heat loss term due to evaporation from the FP, the heat conducted from the condensed water surface to wet zone, convective heat gain from the ambient, and net radiative heat gain from the ambient, respectively. The terms are expressed in Wm^{-2}. Eq. (6) can be finally written as,

$$\bar{\dot{m}}_e = \frac{\frac{k_L(T_{L-V}-\bar{T}_s)}{\frac{L_C}{2}} + \bar{h}(T_\infty-\bar{T}_s) + \sigma_s\epsilon(T_\infty^4-\bar{T}_s^4)}{h_{fg}} \quad (7)$$

where, the average convective heat transfer coefficient $\bar{h}$ is determined using a suitable Nusselt-Rayleigh (*Nu-Ra*) correlation for natural convection in horizontal configurations with both sides exposed. One such correlation proposed by Churchill and Chu [47] in case of the horizontal plates is,

$$\overline{Nu} = 0.96 + \left(Ra_{L_c}\right)^{1/6};\ Ra_{L_c} \le 10^3 \quad (8)$$

Rayleigh number is defined as $Ra_{L_c} = \frac{g\Delta\rho L^3}{\bar{\rho}\nu\alpha}$ [48]. Ra_{L_c} is determined by considering the overall change in density of the vapor phase, which is influenced by both the temperature and concentration differences between the evaporated vapors on a wet surface and the ambient, g is the gravitational acceleration, ν and α are the momentum and thermal diffusivities of air, respectively, and $\Delta\rho = \rho_s - \rho_\infty$. The density of ambient air is calculated using $\rho_\infty = \frac{p\,m}{k_B\,T}$, where p is absolute pressure (Pa) calculated at the elevated location of 327 meters (for Jammu, India), m is the molecular mass of dry air (~ 4.81 × 10^{-26}kg), k_B is the Boltzmann constant (~ 1.380649 × 10^{-23} J/K), and T is the absolute ambient temperature (K). The liquid-vapor mixture density is calculated using the correlation $ln(\rho_{v,l}) = \alpha_0 + \alpha_1\bar{T}_s + \alpha_2\bar{T}_s^{\,2} + \alpha_3\bar{T}_s^{\,3} + \alpha_4\bar{T}_s^{\,4} + \alpha_5\bar{T}_s^{\,5}$ [49], where $\bar{T}_s$ is surface temperature (°C) and air/vapor mixture densities at the liquid surface is, $\rho_s = \rho_{v,l} + \rho_\infty$.

With the measured average surface temperature of the wet zone and the ambient surface temperature, Ra_{L_c} is calculated, which in turn yields $\overline{Nu}$ from Eq. (8). Note that the experimental L_C value was used in the steady state for this purpose. The obtained $\overline{Nu}$ of the wet zone gives us $\bar{h}$, which is then used in Eq. (7) to estimate $\bar{\dot{m}}_e$.

Table 4. Comparison of calculated evaporation rates using SEB (Eq. 7) for both VFP and HFP.

Filter Paper Grade	$\bar{\dot{m}}_e(kg\ m^{-2}\ s^{-1})$ [VFP] [37]	$\bar{\dot{m}}_e(kg\ m^{-2}\ s^{-1})$ [HFP]
1001	2.67 ×10^{-04}	2.52 × 10^{-04}
1004	2.23 × 10^{-04}	2.43 × 10^{-04}
1005	2.67 × 10^{-04}	2.70 × 10^{-04}

The average evaporation rates, $\bar{\dot{m}}_e$ for both the VFP and HFP configurations are relatively close in magnitude for all the FPs (1001, 1004, and 1005). This suggests that the rate of evaporation is indeed determined as per the atmospheric demand and is weakly dependent either on the paper type or on the orientation.

5. Theoretical Framework:

Rampally and Kumar [37] developed an analytical framework (extension of the *CEM* [28]) for predicting the height of the wicking front in vertical systems with non-constant evaporation rate varying along the papers' height. The local evaporation rate ($\dot{m}_e$) was assumed to be a power function of 'z' only (not to vary across the FP width). In this study, we extended *NCEM* for horizontal systems by considering no gravity ($g = 0$) with two models as follows,

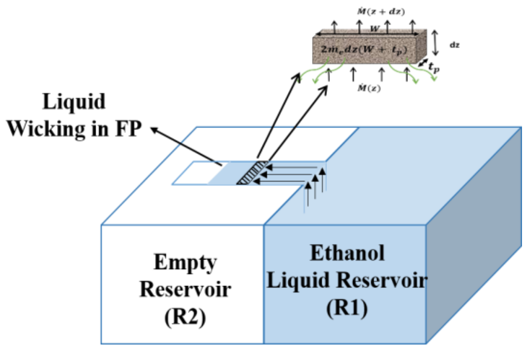

Figure 10. [Colour online] Integral and differential Mass Balance of the FP, showing the total mass inflow $\dot{\boldsymbol{M}}(\boldsymbol{z}=\boldsymbol{0})$ comprising mass flow for liquid front movement $\dot{\boldsymbol{M}}_{\boldsymbol{h}}$ and total evaporation mass flow $\dot{\boldsymbol{M}}_{\boldsymbol{e}}$.

$$\dot{m}_e = a_0\left(\frac{z}{h}\right)^{+\lambda};\quad [\ +\lambda \text{ model }] \quad (9)$$

$$\dot{m}_e = a_1\left(1-\frac{z}{h}\right)^{-\lambda};\quad [\ -\lambda \text{ model }] \quad (10)$$

where, λ is a fitting parameter that quantifies the non-uniformity of the evaporation flux, a_0 and a_1 are the corresponding proportionality constants. Note that $\lambda = 0$ in Eq. (9) returns to the CE model. To find the proportionality constant, say for 'a_0' in Eq. (9), we integrate the local evaporative mass loss $d\dot{M}(e)$, from an elemental FP strip of total perimeter $2(W+t_p)$, see Figure 10, and length 'dz' from 0 to h,

$$\int_0^h d\dot{M}(e) = \int_0^h -2\dot{m}_e(W+t_p)dz \quad (11)$$

Total evaporative mass flow from the entire FP is,

$$\dot{M}(e) = -2\bar{\dot{m}}_e h(W+t_p) \quad (12)$$

where, $\bar{\dot{m}}_e$ is the length-averaged evaporation rate, and is related to 'a_0' by,

$$\bar{\dot{m}}_e = \frac{a_0}{(1+\lambda)} \tag{13}$$

From Eq. (13) and Eq. (9), we get

$$\dot{m}_e = \bar{\dot{m}}_e(1+\lambda)\left(\frac{z}{h}\right)^{\lambda} \tag{14}$$

The overall mass inflow at $z = 0$, denoted as $\dot{M}(z = 0)$, can be separated into two parts: (i) the mass flow required to sustain the movement of the liquid front, $\dot{M}_{\dot{h}}$ and (ii) the total mass loss due to evaporation, $\dot{M}_e$. $\dot{M}_{\dot{h}}$ is given by,

$$\dot{M}_{\dot{h}} = \left(\frac{dh}{dt}\right)\rho_l W t_p \emptyset \tag{15}$$

The differential mass balance (see Figure 10) can be expressed as,

$$d\dot{M}(z) = \dot{M}(z+dz) - \dot{M}(z) = -2\dot{m}_e(W+t_p)dz \tag{16}$$

When integrating and using the boundary condition that the total mass inflow at $z = 0$ must be equal to $\dot{M}_{\dot{h}} + \dot{M}_e$, one obtains,

$$\dot{M}(z) = \dot{M}_{\dot{h}} + 2\bar{\dot{m}}_e(W+t_p)\left(1 - \frac{z^{\lambda+1}}{h^{\lambda+1}}\right)h \tag{17}$$

The local mass flow $\dot{M}(z)$ can be represented as a function of the flow velocity, which is used to calculate the viscous pressure loss. Additionally, the flow velocity within the filter paper (FP) can be broken down into two separate components. The first component corresponds to the velocity of the liquid front, represented by $\frac{dh}{dt}$. And, the second component is to replenish the lost liquid mass via evaporation, often termed refill velocity, v_r. It is evident that at $z = 0$, the velocity of the refill reaches its maximum value.

$$v_{r,0} = \frac{\dot{M}_e}{\rho_l A_b} = \frac{2\bar{\dot{m}}_e h(W+t_p)}{\rho_l W t_p \emptyset} \tag{18}$$

Evaporation rate varies with height and the refill velocity becomes,

$$v_r(z) = v_{r,0}\left[1 - \left(\frac{z}{h}\right)^{\lambda+1}\right] \tag{19}$$

It can be seen that v_r becomes zero at $z = h$ (for positive λ). In the *horizontal systems*, the surface tension pulls water along the solid surface while the evaporation and viscous forces act against this pull. The entire process is a competition of these forces leading to the dynamic motion of the liquid front eventually attaining an equilibrium condition given as,

$$p_c = p_{\dot{h}} + p_r \tag{20}$$

Where the individual terms refer to,
Capillary pressure, $p_c = \frac{2\sigma\cos\theta}{R_c}$
Viscous pressure loss due to $\frac{dh}{dt}$, $p_{\dot{h}}$
Viscous pressure loss due to $v_r(z)$, p_r
Viscous pressure loss can be calculated as,

$$p_{\dot{h}} = \left(\frac{\emptyset}{K}\mu\right)\int_0^h \dot{h}\,dz = \frac{\emptyset}{K}\mu h\frac{dh}{dt} \tag{21}$$

$$p_r = \frac{\emptyset}{K}\mu\int_0^h v_r(z)\,dz = \frac{\emptyset}{K}\mu v_{r,0}h\left(\frac{\lambda+1}{\lambda+2}\right)$$
[$+\lambda$ model] (22a)

$$p_r = \frac{\emptyset}{K}\mu\int_0^h v_r(z)\,dz = \frac{\emptyset}{K}\mu v_{r,0}h\left(\frac{1}{2-\lambda}\right)$$
[$-\lambda$ model] (22b)

All these terms are substituted in Eq. (20) to get,

$$\frac{2\sigma\cos\theta}{R} = \frac{\emptyset}{K}\mu h\frac{dh}{dt} + \frac{\emptyset}{K}\mu\left[\frac{2\bar{\dot{m}}_e(W+t_p)}{\rho_l W t_p \emptyset}\right]\left(\frac{\lambda+1}{\lambda+2}\right)h^2\ ;$$
[$+\lambda$ model] (23a)

$$\frac{2\sigma\cos\theta}{R_c} = \frac{\emptyset}{K}\mu h\frac{dh}{dt} + \frac{\emptyset}{K}\mu\left[\frac{2\bar{\dot{m}}_e(W+t_p)}{\rho_l W t_p \emptyset}\right]\left(\frac{1}{2-\lambda}\right)h^2\ ;$$
[$-\lambda$ model] (23b)

This can be further simplified as,

$$\frac{a}{h} = \frac{dh}{dt} + ch \tag{24}$$

where, a and c are written as,

$$a = \frac{2\sigma\cos\theta}{\emptyset\mu}\left(\frac{K}{R}\right) \tag{25}$$

$$c = \frac{2\bar{\dot{m}}_e(W+t_p)}{\rho_l W t_p \emptyset}\left(\frac{\lambda+1}{\lambda+2}\right);\ [\ +\lambda \text{ model}\ ] \tag{26a}$$

$$c = \frac{2\bar{\dot{m}}_e(W+t_p)}{\rho_l W t_p \emptyset}\left(\frac{1}{2-\lambda}\right);\ [\ -\lambda \text{ model}\ ] \tag{26b}$$

Eq. (24) can be rewritten as,

$$\int \frac{h}{-ch^2+a}dh = \int 1dt \tag{27}$$

With the boundary condition of $z = 0$ at $t = 0$, the solution to Eq. (24) is given in the form of $h(t)$

$$h = \sqrt{\frac{a}{c}\left(1 - e^{-2ct}\right)} \tag{28}$$

Eq. (28) is the solution using the Non-Constant Evaporation Model (*NCEM)* for horizontal orientation ($g = 0$).

Now, we compare the outcomes from the current NCE model with that of the CE model for the experimental data in 1001FP, 1004FP, and 1005FP cases for horizontal (as well as vertical [37]) configurations. Figure 11 shows a comparison of VFP cases with HFP for all the cases; the CE model overestimated the experimentally observed $h - t$ curves.

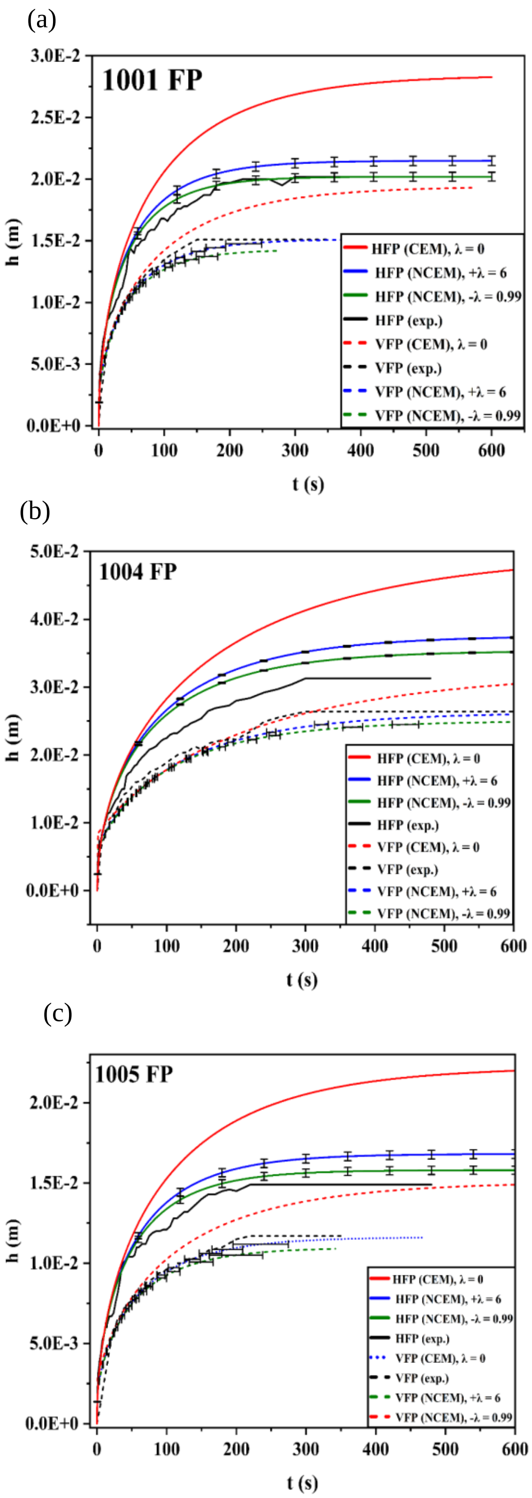

Figure 11. [Colour online] Comparison of the NCE and CE models with experimental data for (a) 1001FP, (b) 1004FP, and (c) 1005FP cases, showing the CE model overestimates while the NCE model agrees well with the experimental data when $\boldsymbol{+\lambda = 6}$, $\boldsymbol{-\lambda = 0.99}$ across all FP cases.

The predicted uptake curve has a similar shape as the experimental curve, with a maximum deviation of $\sim \pm 8\%$ at the end of the experiment. However, the proposed NCE model agrees reasonably well for 1001FP and 1005FP with the experiments when $\lambda = 6$ for $+\lambda$ model and $\lambda = 0.99$ for $-\lambda$ models in all the three cases studied here. Interestingly, these λ values are observed to be consistent across the three cases.

6. Time scales & Dimensional analysis

We have defined two dimensionless numbers previously [37] using the concept that the interplay is between the mass gain term (driven by surface tension) and the mass loss term (evaporation rate). This interplay yielded Evaporation Time Number (ETN) and Evaporation Height Number (EHN). These are given as,

$$\mathrm{EHN} = h\sqrt{\frac{c}{a}} = h\sqrt{\frac{\bar{\dot{m}}_e \mu R_c}{\sigma \rho_l K t_p}} \tag{37}$$

$$\mathrm{ETN} = ct = \frac{t\,\bar{\dot{m}}_e}{\rho_l t_p} \tag{38}$$

Note that ETN excludes the effect of the viscous and gravitational forces both while EHN excludes only the latter.

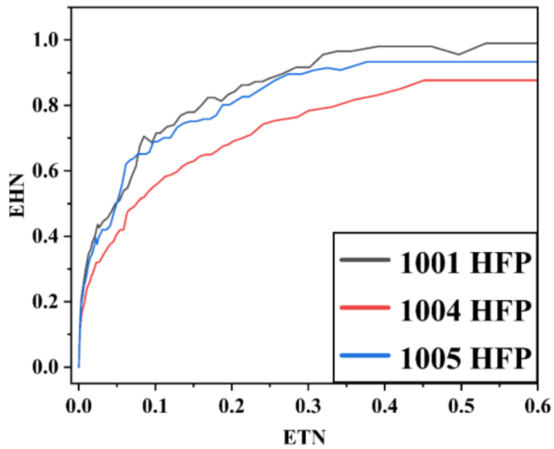

Figure 12. [Colour online] Variation of EHN versus ETN, indicating ETN as a potentially more suitable time scale in cases dominated by evaporation, with EHN values converging to $\sim\mathbf{1}$ in the steady state.

Figure 12 shows the variation of EHN versus ETN. These new numbers seem to collapse all three curves into a single master curve, thereby indicating the utility of these scales in such a system. Note that we used the average evaporation rate in the steady state for scaling; however, the temporal values of evaporation can also be used. Further, EHN-ETN curve also collapsed the completely different $h - t$ curves in the vertical cases as well [37].

7. Conclusions

We report findings from the investigation of the process of wicking liquid ethanol on horizontal thin rectangular filter papers exposed on both sides. The experiments were accordingly designed and were conducted under the controlled laboratory conditions on three different filter papers (FPs). The aim was to understand the importance of evaporation on the liquid penetration dynamics in horizontal configurations. Two diagnostic tools were used simultaneously: optical and thermal imaging.

As the liquid spreads across the horizontally oriented FPs, the wicking liquid front eventually reaches a finite steady-state position, marked by L_c. Possibly, without evaporation, the liquid front would reach infinity. Our findings indicate that evaporative mass loss plays a dominant role in limiting the liquid's spread, rather than capillary and viscous effects, which are usually considered in conventional wicking systems. The L_c values for the HFP are higher than the VFP cases indicating that the gravitational forces are non-negligible in the latter.

In this study, we adopted the *Non-Constant Evaporation Model (NCEM)* proposed by Rampally and Kumar [37], which assumes a power-law variation of the local evaporation rate. Here, we use *NCEM* by neglecting the gravitational effects ($g = 0$). The permeability values were obtained by $h^2 - t$ experimental curve in the initial ~15 seconds where its slope yields a ratio K/R; the choice of R is not of importance here and we chose to use $R = R_c$ where R_c were obtained for the three FPs in the vertical cases [37]. The Surface Energy Budget (SEB) equation was used to express the local evaporation rate as a function of the measured temperature, and this was integrated into the momentum equation to model the evolution of height versus time, $h(t)$ in the modified NCEM. The resulting model provided a close match with the experimental data (within $\pm 8\%$).

A key observation was the successful application of the non-dimensional numbers proposed by Rampally and Kumar [37]. When using ETH and ETN, we found an agreeable collapse of data across different experimental conditions. This indicates that these numbers effectively describe the wicking process in the presence of evaporation.

8. ACKNOWLEDGEMENTS

The authors greatly acknowledge the financial support provided under the SEED grant by IIT Jammu and SRG/2022/000680 by SERB, DST (GoI).

References

[1] X. Li, J. Tian, and W. Shen, Thread as a versatile material for low-cost microfluidic diagnostics, *ACS Appl Mater Interfaces*, 2010. 2(1): p. 1–6.

[2] T. L. Owens, J. Leisen, H. W. Beckham, and V. Breedveld, Control of microfluidic flow in amphiphilic fabrics, *ACS Appl Mater Interfaces*, 2011 3(10): p. 3796–3803.

[3] J. Ge, R. Schirhagl, and R. N. Zare, Glucose-driven fuel cell constructed from enzymes and filter paper, *J Chem Educ*, 2011, 88(9): pp. 1283–1286.

[4] C. W. N. Villarrubia *et al.*, Practical electricity generation from a paper based biofuel cell powered by glucose in ubiquitous liquids, *Electrochem commun*, 2014, 45: p. 44–47.

[5] E. Kim, Y. Xia, and G. M. Whitesides, Polymer microstructures formed by moulding in capillaries, *Nature*, 1995, 376(6541): p. 581–584.

[6] Y. Liu, J. H. Xin, and C.-H. Choi, Cotton fabrics with single-faced superhydrophobicity, 2012 *Langmuir*, 28(50), p. 17426–17434.

[7] N. R. Morrow and G. Mason, Recovery of oil by spontaneous imbibition, *Curr Opin Colloid Interface Sci*, 2001, 6(4): p. 321–337.

[8] A. W. Martinez, S. T. Phillips, and G. M. Whitesides, Three-dimensional microfluidic devices fabricated in layered paper and tape, *Proceedings of the National Academy of Sciences*, 2008, 105(50): p. 19606–19611.

[9] A. Clarke, T. D. Blake, K. Carruthers, and A. Woodward, Spreading and imbibition of liquid droplets on porous surfaces, *Langmuir*, 2002, 18(8): p. 2980–2984.

[10] K.Y. Jeong, J. S. Lee, D.-H. Paik, W.-K. Jung, and S.-W. Choi, Fabrication of cell-penetrable microfibrous matrices with a highly porous structure using a simple fluidic device for tissue engineering, *Mater Lett*, 2016, 168: p. 116–120.

[11] A. Marmur and R. D. Cohen, Characterization of porous media by the kinetics of liquid penetration: the vertical capillaries model, *J Colloid Interface Sci*, 1997, 189(2), p. 299–304.
[12] A. Marmur, Kinetics of penetration into uniform porous media: testing the equivalent-capillary concept, *Langmuir*, 2003, 19(14), p. 5956–5959.
[13] E. Fragiadaki, S. Harhalakis, and E. P. Kalogianni, Characterization of porous media by dynamic wicking combined with image analysis, *Colloids Surf A Physicochem Eng Asp*, 2012, 413: p. 50–57.
[14] R. Lucas, Ueber das Zeitgesetz des kapillaren Aufstiegs von Flüssigkeiten, *Kolloid-Zeitschrift*, 1918, 23(1), p. 15–22.
[15] E. W. Washburn, The dynamics of capillary flow, *Physical review*, 1921, 17(3): p. 273.
[16] A. Marmur, The radial capillary, *J Colloid Interface Sci*, 1988, 124(1): p. 301–308.
[17] A. Borhan and K. K. Rungta, On the radial spreading of liquids in thin porous substrates, *J Colloid Interface Sci*, 1992, 154(1), p. 295–297.
[18] D. Danino and A. Marmur, Radial capillary penetration into paper: limited and unlimited liquid reservoirs, *J Colloid Interface Sci*, 1994, 166(1), p. 245–250.
[19] M. Conrath, N. Fries, M. Zhang, and M. E. Dreyer, Radial capillary transport from an infinite reservoir *Transp Porous Media*, 2010, 84: p. 109–132.
[20] T. Delker, D. B. Pengra, and P. Wong, Interface pinning and the dynamics of capillary rise in porous media, *Phys Rev Lett*, 1996, 76(16), p. 2902.
[21] M. Lago and M. Araujo, Capillary rise in porous media, *J Colloid Interface Sci*, 2001, 234(1), pp. 35–43.
[22] S. F. Nia and K. Jessen, Theoretical analysis of capillary rise in porous media, *Transp Porous Media*, 2015, 110(1): p. 141–155.
[23] S. Mendez *et al.*, Imbibition in porous membranes of complex shape: quasi-stationary flow in thin rectangular segments, *Langmuir*, 2010, 26(2): p. 1380–1385.
[24] E. M. Benner and D. N. Petsev, Potential flow in the presence of a sudden expansion: Application to capillary driven transport in porous media, *Physical Review E—Statistical, Nonlinear, and Soft Matter Physics*, 2013, 87(3): p. 033008.
[25] D. Shou, L. Ye, J. Fan, and K. Fu, Optimal design of porous structures for the fastest liquid absorption, *Langmuir*, 2014, 30(1): p. 149–155.
[26] D. Shou *et al.*, Geometry-induced asymmetric capillary flow, *Langmuir*, 2014. 30(19): p. 5448–5454.
[27] D. Shou and J. Fan, Structural optimization of porous media for fast and controlled capillary flows, *Phys Rev E*, 2015, 91(5), p. 053021.
[28] N. Fries, K. Odic, M. Conrath, and M. Dreyer, The effect of evaporation on the wicking of liquids into a metallic weave, *J Colloid Interface Sci*, 2008, 321(1): p. 118–129.
[29] D. A. Lockington, J.-Y. Parlange, and M. Lenkopane, Capillary absorption in porous sheets and surfaces subject to evaporation, *Transp Porous Media*, 2007, 68: p. 29–36.
[30] S. Beyhaghi, S. Geoffroy, M. Prat, and K. M. Pillai, Wicking and evaporation of liquids in porous wicks: A simple analytical approach to optimization of wick design, *AIChE Journal*, 2014, 60(5): p. 1930–1940.
[31] N. Fries and M. Dreyer, An analytic solution of capillary rise restrained by gravity, *J Colloid Interface Sci*, 2008, vol. 320(1): p. 259–263.
[32] N. Fries and M. Dreyer, Dimensionless scaling methods for capillary rise, *J Colloid Interface Sci*, 2009, 338(2): p. 514–518.
[33] D. C. Standnes, Scaling group for spontaneous imbibition including gravity, *Energy & fuels*, 2010, 24(5): p. 2980–2984.
[34] T. Kawase, H. Sirringhaus, R. H. Friend, and T. Shimoda, Inkjet printed via-hole interconnections and resistors for all-polymer transistor circuits, *Advanced Materials*, 2001, 13(21): p. 1601–1605.
[35] S. Jahanshahi-Anbuhi *et al.*, based microfluidics with an erodible polymeric bridge giving controlled release and timed flow shutoff, *Lab Chip*, 2014, 14(1): p. 229–236.
[36] Z. Liu, J. Hu, Y. Zhao, Z. Qu, and F. Xu, Experimental and numerical studies on liquid wicking into filter papers for paper-based diagnostics, *Appl Therm Eng*, 2015, 88: p. 280–287.

[37] S. C. M. Rampally, A. Jain, and N. Kumar, Evaporation limited spreading of ethanol on rectangular porous strips: an experimental and theoretical investigation, *arXiv preprint arXiv:* 2407.20776, 2024.
[38] N. Koursari, O. Arjmandi-Tash, A. Trybala, and V. M. Starov, Drying of foam under microgravity conditions, *Microgravity Sci Technol*, 2019, 31: p. 589–601.
[39] R. J. Moffat, Describing the uncertainties in experimental results, *Exp Therm Fluid Sci*, 1988, 1(1): p. 3–17.
[40] S. C. M. Rampally, A. Jain, and N. Kumar, Capillary penetration of highly volatile liquids in a paper strip: an experimental study on wicking, evaporation, and condensation, *Int J Adv Eng Sci Appl Math*, 2023: p. 1–8.
[41] D. Quéré, Inertial capillarity, *Europhys Lett*, 1997, 39(5): p. 533.
[42] M. Conrath, N.Fries, M. Zhang, and M. E. Dreyer, Radial capillary transport from an infinite reservoir. *Transport in porous media*, 2010, 84: p. 109-132.
[43] M. Alberghini, S. V Boriskina, P. Asinari, and M. Fasano, Characterisation and modelling of water wicking and evaporation in capillary porous media for passive and energy-efficient applications, *Appl Therm Eng*, 2022, 208: p. 118159.
[44] M. Aminzadeh and D. Or, Pore-scale study of thermal fields during evaporation from drying porous surfaces, *Int J Heat Mass Transf*, 2017, 104: p. 1189–1201.
[45] N. Kumar and J. H. Arakeri, Evaporation from layered porous medium in the presence of infrared heating, *Water Resour Res*, 2018, 54(10): p. 7670–7687.
[46] M. Aminzadeh and D. Or, Temperature dynamics during nonisothermal evaporation from drying porous surfaces, *Water Resour Res*, 2013, 49(11): pp. 7339–7349.
[47] S. W. Churchill and H. H. S. Chu, Correlating equations for laminar and turbulent free convection from a vertical plate, *Int J Heat Mass Transf*, 1975, 18(11): p. 1323–1329.
[48] S. M. Bower and J. R. Saylor, A study of the Sherwood–Rayleigh relation for water undergoing natural convection-driven evaporation, *Int J Heat Mass Transf*, 2009, 52(13–14): p. 3055–3063.
[49] A. Faghri and Y. Zhang, *Transport phenomena in multiphase systems*. Elsevier, 2006.

Paper ID 044(S4)

Numerical and Experimental Investigation of a 10 kW Flat-Type LHP for Waste Heat Recovery

Shawn Somers-Neal[1], Tatsuki Tomita[1], Noriyuki Watanabe[1], Ai Ueno[1], Hosei Nagano[1*]

[1] *Nagoya University, Nagoya, Japan*
**Corresponding author email address: nagano@mech.nagoya-u.ac.jp*

Abstract

A flat-type loop heat pipe was designed to sustain power loads within the kilowatt scale for the use of waste heat recovery. The loop heat pipe used a stainless steel wick with a pore radius of 1.0 microns and a box-type wick design to reduce the pressure loss within the wick with water as the working fluid. Experimental testing was performed with the evaporator in an upright and flat orientation, with the condenser placed above the evaporator with a height difference of 0.3 m. For the experimental testing, passive cooling was used for the condenser. The loop heat pipe was able to sustain a 10 kW power load with the upright orientation and 8.5 kW with the flat orientation. The lowest thermal resistance value between the evaporator and the condenser was around 0.008 ℃/W for the upright orientation and 0.009 ℃/W for the flat orientation. To predict the performance of both orientations for the loop heat pipe a numerical model was developed. The average temperature difference between the numerical and experimental results was 10.2 ℃ for the upright orientation and 9.5 ℃ for the flat orientation.

Keywords: Loop heat pipe; Kilowatt power load; Numerical model; Waste heat recovery

1. Introduction

Due to the yearly increase in global emissions, improving the efficiency of certain applications can lead to a reduction in emissions. Industrial processing (IP) and internal combustion engines (ICEs) are a few examples of uses that could benefit from improving efficiencies through waste heat recovery [1-3]. A loop heat pipe (LHP) is a heat transfer device that can handle power loads found in these uses while providing waste heat recovery without using any additional energy.

An LHP consists of an evaporator, grooves, wick, vapor line (VL), condenser, liquid line (LL), and compensation chamber (CC). When heat is applied to the evaporator, the working fluid on the outer layer of the wick will heat up and turn to vapor. This vapor enters the grooves and moves to the VL and the condenser. In the condenser, the vapor will be cooled and will turn back to liquid while moving to the LL and then returning to the CC. The wick separates the CC and the evaporator, and the wick also draws the working fluid back to the outer layer of the wick to sustain the loop through capillary pressure. There are many uses for ICEs and IP that have power loads within the kW scale, and waste heat recovery can be used to help improve the overall efficiency.

Previous research on kW-class LHPs has been performed, but the research is still limited overall. The most recent work regarding kW-class LHPs includes research by Aono et al., which was performed with a flat-type LHP that was able to sustain a power load of up to 6.2 kW with a working fluid of water and a stainless steel wick that had a 1.2 µm pore radius [4]. More recent research performed by Wang et al. used a cylindrical-type LHP using an ammonia and nickel combination for working fluid and wick structure, which had a pore radius of 0.53 µm and sustained a power load of 1.03 kW [5]. Improving the maximum power load capabilities will increase the range of available uses for waste heat recovery.

A flat-type LHP was designed for higher power loads for the application of waste heat recovery. The wick was made of stainless steel and had a box-type design, and the condenser was cooled with passive cooling. Additionally, a numerical model was designed to estimate the temperatures and analyze the pressure loss throughout the LHP. Designing kW-class LHP helps expand the potential uses of waste heat recovery, leading to a reduction of emissions in uses such as IP and ICEs.

2.0. Experimental setup and testing

All of the dimensions for the LHP components can be found in Table 1, and the setup for the experiments and the wick can be seen in Figure 1. The wick was made of stainless steel, and its cores were used to help reduce pressure loss throughout the wick. The cores help lower the pressure loss because the flow path of the working fluid is reduced, and the length from the wick surface to the outside of the core is shorter than a wick without cores. Lastly, water was selected as the working fluid for the LHP because of the high heat of vaporization, boiling point, and low vapor pressure, which match well with the application of waste heat recovery.

Table 1. Dimension and properties of the LHP.

Section	Variable	Values
Wick	Pore size (μm)	2.0
	Porosity	0.4
	Permeability (m^2)	2.6×10^{-14}
	Number of cores	6
	Core diameter (mm)	18
	Overall (W/H/L) (mm)	143/22/145
Evaporator	Overall (W/H/L) (mm)	153/ 32/ 183
Grooves	Overall (W/H/L) (mm)	1.0/ 2.0/ 135
	Number of grooves	164
VL	Tube OD/ ID / L (mm)	19.1/ 16.6 / 2500
Condenser	Tube OD/ ID / L (mm)	12.7/ 10.7 / 5000
LL	Tube OD / ID / L (mm)	9.53/ 7.75 / 2200
CC	Overall (W/H/L) (mm)	105/ 135/ 160
Heater blocks	Overall (mm) (W/H/L)	143/ 16/ 115
Water	Volume (cm^3)	3300

2.1. Experimental testing

The VL, evaporator, CC, heater blocks, and LL were insulated during the testing, and the temperature of each section was measured using a total of 46 thermocouples. The thermocouple locations of each component can be seen in Figure 1, with Figure 1a showing the placement of the thermocouples for both the VL and LL, Figure 1b showing the locations for the condenser, and Figure 1c showing the CC and evaporator locations. For both experimental tests, the condenser was cooled using passive cooling, and the evaporator was located below the condenser by about 0.3 m. The upright orientation and flat orientation were both used for experimental testing, which can be seen in Figure 2. The gravity assist also helps performance because the height difference reduces pressure loss due to the hydrostatic pressure gain from the condenser being located above the evaporator. Step-up tests were performed with 0.5 kW steps and passive cooling, with water as the coolant. The experimental test was limited by the thermal paste as the damage occurs at the temperature of 320 °C or when the pressure of the CC reaches 0.6 MPa. The temperature, power, voltage, and time were recorded every 5 seconds using a data acquisition system for each test. Upon comprehending the experimental setup, the results of the experimental test will be discussed next.

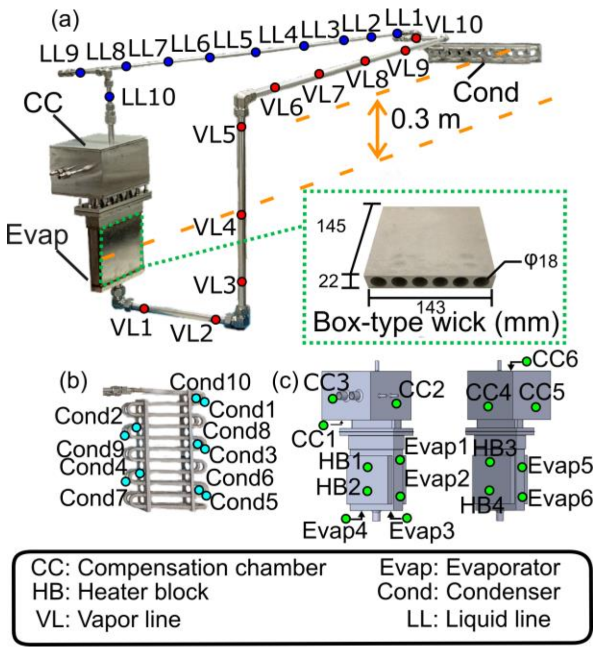

Figure 1. (a) A picture of the LHP with the thermocouple positions for the LL and VL and the dimensions of the box-type wick shown. (b) A photo of the condenser with the thermocouple positions is shown. (c) The CC and the evaporator are rendered in a 3D model with the positions of the thermocouples shown in the upright orientation.

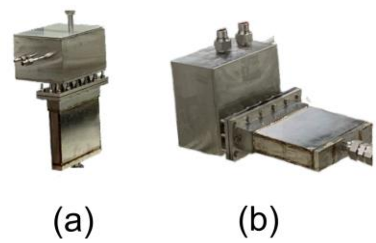

Figure 2. (a) A picture of the evaporator in the upright orientation. (b) A picture of the evaporator in the flat orientation.

2.2 Experimental results

Figures 3a and 3b show the results for upright and flat orientations, respectively. The results included temperature locations for the CC, evaporator, heater block, VL inlet, condenser inlet, LL inlet, and LL outlet. The highest power load achieved for the upright orientation was 10 kW, while for the flat orientation, the highest power load was 8.5 kW.

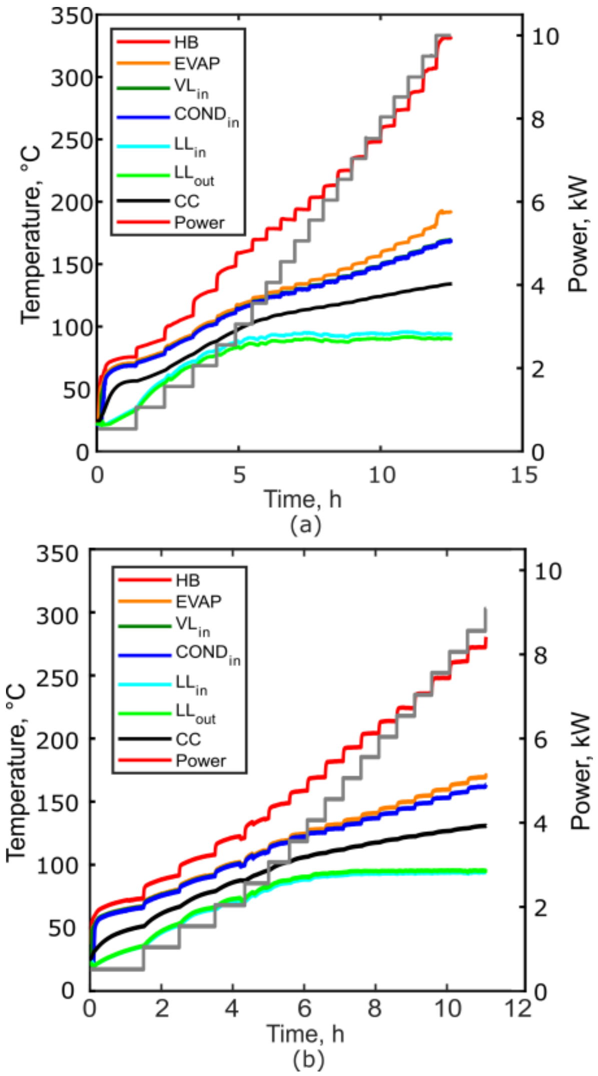

Figure 3. Experimental results for the temperature over time for the upright orientation. (b) Experimental results for the temperature over time for the flat orientation.

For the experimental testing, the upright orientation was stopped due to the maximum temperature being reached, and the flat orientation was stopped due to the pressure limit. The temperatures were similar between the two orientations for the lower power loads, but began to separate at higher power loads as the flat orientation began to become higher in temperature in most locations. This increase in temperature could be caused by the vapor layer that would form in the flat orientation, as the vapor in the core would become difficult to remove compared to the upright orientation. The thermal resistance between the heat source and the heat sink and the evaporative heat transfer coefficient can help demonstrate the efficiency of the LHP.

The thermal resistance calculation can be seen in Eq. 1:

$$R_{Evap-Cond} = \frac{T_{Evap,Max} - T_{Cond,Min}}{Q_{Load}} \quad (1)$$

where the $R_{Evap\text{-}Cond}$ is the thermal resistance between the heat source and heat sink, Q_{Load} denotes the power load, $T_{Evap,Max}$ refers to the maximum evaporator temperature, and $T_{Cond,Min}$ stands for the minimum condenser temperature. Based on previous research performed by Chernysheva and Maydanik, using the maximum temperature for the evaporator and minimum temperature for the condenser was found to be better for comparison for the thermal resistance [6]. The evaporative heat transfer coefficient was calculated using the average evaporator temperature, which can be seen in Eq. (2):

$$h_E = \frac{Q_{Load}}{(T_{Evap} - T_{VL})A} \quad (2)$$

where T_{VL} denotes the VL temperature, A stands for the area, T_{Evap} denotes the average evaporator temperature, and h_E signifies the evaporative heat transfer coefficient. The values for the thermal resistance and evaporative heat transfer coefficient for the upright and flat orientations can be seen in Figure 4 and Figure 5.

The values for the thermal resistance were lower for most power loads for the upright orientation compared to the flat orientation. The lowest value achieved for the upright orientation and flat orientation was about 0.008 °C/W for the upright orientation and about 0.009 °C/W for the flat orientation. For the evaporative heat transfer coefficient using the average temperature, the highest value was achieved at 4.5 kW with a value of about 92 kW/m^2/K for the upright orientation compared to the highest value for the flat orientation, which was at 2.5 kW with a value of about 80 kW/m^2/K. This difference shows that the orientation change affected the peak heat transfer coefficient as the peak occurred earlier in the flat orientation. Also, as expected, the heat transfer coefficient was higher in the upright orientation, but at the higher power loads, the heat transfer coefficient for the flat orientation was higher even though the temperatures were hotter than the upright orientation values. One reason for this difference could be that the connection quality was better for the flat evaporator. In a previous experimental test in the flat orientation, the heat transfer coefficient had a similar drop-off in the value at the higher power loads, but the results of the most recent test did not have the same issue and even performed better than the upright orientation at the higher power loads. On average, the heat transfer coefficient values were higher, and the thermal resistance values were lower for the upright orientation, suggesting that the upright orientation is better for operational performance. The upright orientation is ideal for performance compared to the flat orientation due to the vapor forming at the top of the core of the wick. The upright orientation allows any vapor that forms within the cores to escape to the CC due to buoyancy, which could not happen in the flat orientation. The upright orientation results could be further improved in the future using similar improvements made to the flat orientation for a better connection between the heater and the evaporator.

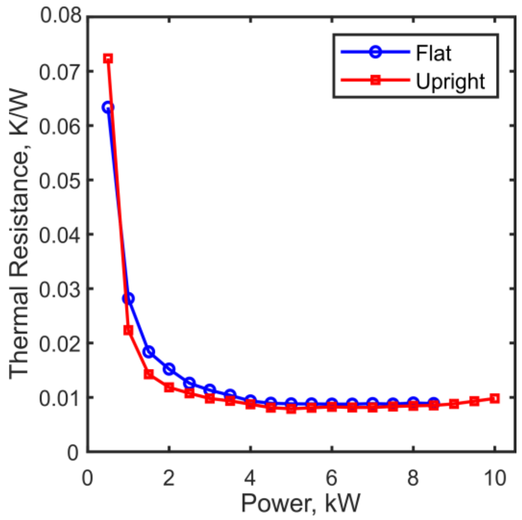

Figure 4. Thermal resistance values between the heat source and the heat sink at different power loads.

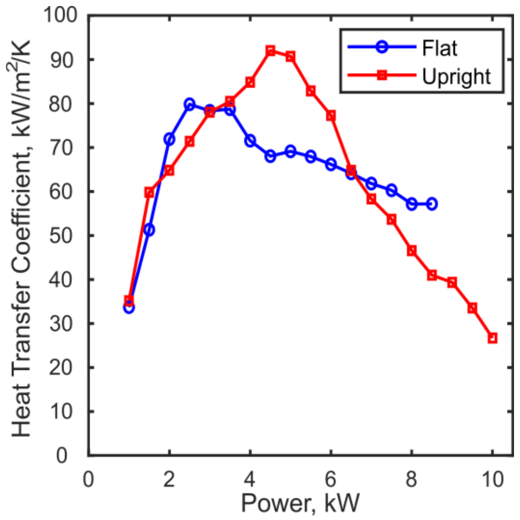

Figure 5. Evaporative heat transfer coefficient values for both orientations.

3. Numerical model

A steady-state numerical model was designed to predict the temperature performance and analyze the pressure loss throughout the LHP. The method used for modeling the LHP was inspired by a previous model developed by Jazebizadeh and Kaya [7].

3.1. Evaporator

The heat load for the model was broken into a few components, which can be seen in Eq. (3):

$$\dot{Q}_{Load} = \dot{Q}_{Amb} + \dot{Q}_E + \dot{Q}_S + \dot{Q}_{HL} \quad (3)$$

where $\dot{Q}$ denotes the heat transfer rate, subscript, *Amb* subscript stands for the ambient, *E* subscript signifies the evaporation, *S* subscript denotes the superheated, and *HL* subscript stands for the heat leak. The approach had to be updated for a flat-type evaporator, and the conduction through the walls of the evaporator case to the CC needed to be added since flat-type evaporators have thicker walls compared to cylindrical evaporators. The updated equation for the evaporator for a flat-type evaporator and the considered heat leak from the axial conduction can be seen in Eq. (4):

$$\dot{Q}_{HL} = \frac{1}{R_{HB\_CC}} \Delta T_{HB\_CC} + \frac{k_{eff} A_{wick}}{L_{wick}} \Delta T_{int\_CC} \quad (4)$$

where the ΔT_{HB_CC} stands for the temperature difference between the heater blocks and CC, ΔT_{int_CC} denotes the temperature difference between the surface interface of the wick and the CC, k_{eff} refers to the effective thermal conductivity, L signifies the length, R_{HB_CC} stands for the thermal resistance between the heat block and the CC, and the subscript *wick* signifies the wick.

3.2. Pressure loss

An approach for handling the pressure loss for a box-type wick was used to account for the effect of the flow path of the liquid from the core to the surface, which can be seen in Eq. (5)-(7):

$$P_{wick} = \frac{\dot{m} \mu t_{eff}}{W_{wick} L_{wick} K \rho} \quad (5)$$

$$t_{eff} = \frac{\sum t_i}{N} \quad (6)$$

$$t_i = \sqrt{x_i^2 + y_i^2} - r_c \quad (7)$$

where P_{wick} denotes the pressure loss within the wick, $\dot{m}$ stands for the mass flow rate, t signifies the thickness, w denotes the width, K signifies the permeability, r_c stands for the radius of the core and ρ denotes the density. Also, N signifies the number of nodes, x denotes the distance in the x-direction, y stands for the distance in the y-directions, i subscript denotes that value for an individual node. A breakdown of how the equations are applied to the wick can be seen in Figure 6. Determining the pressure loss is important due to the capillary limit within an LHP. The capillary limit is determined using properties which can be seen in Eq. (8):

$$P_{cap} = \frac{2\sigma cos\theta}{r_{pore}} \quad (8)$$

where P_{cap} stands for the capillary pressure, σ represents the surface tension, r_{pore} refers to the pore radius, and θ denotes the contact angle. The total pressure loss has to be less than the capillary pressure. The total pressure loss can be seen in Eq (9):

$$P_{total} = P_{wick} + P_{gr} + P_{TL} + P_G \quad (9)$$

where the subscript *total* stands for all of the pressure loss/gains of the entire LHP, *gr* subscript denotes the grooves, *TL* signifies the transport lines (VL, condenser, and LL), and *G* stands for gravity. The condition for the pressure loss can be seen in Eq. (10):

$$P_{total} < P_{cap} \quad (10)$$

The pressure loss had to be determined for every testing condition to ensure the capillary limit was not reached.

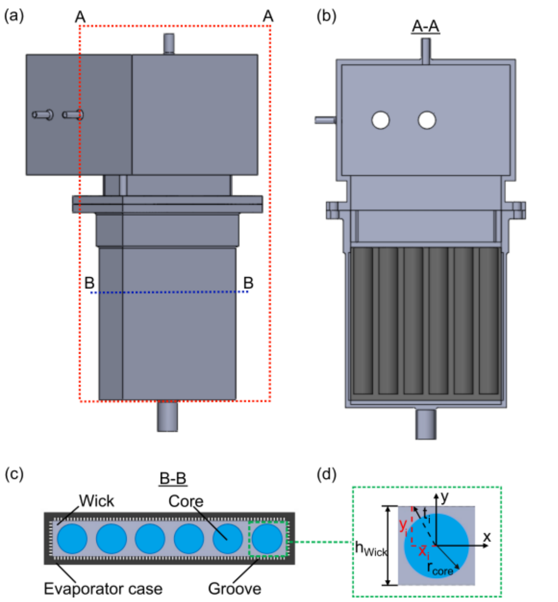

Figure 6. A 3D model of the CC and the evaporator showing two cuts for section AA and section BB. (b) Shows the internal structure of the LHP along the AA cut section. (c) The internal section of the evaporator with the wick and the grooves where the blue represents the working fluid. (d) The component breakdown for the effective wick thickness calculation.

3.3. Transportation lines

Temperature-dependent correlations were used to simulate the cooling for the transport lines. For passive cooling, two types of cooling were used: unsaturated and saturated boiling. Unsaturated cooling heat transfer coefficients were determined numerically to be 1 kW/m^2/K for the unsaturated cooling, and the saturated boiling cooling condition was determined using Eqs. (11)-(14) [8]:

$$\mathrm{Ra_D} = \frac{g\beta(T_{sf} - T_{Amb})D_o^3 \mathrm{Pr}}{\nu^2} \quad (11)$$

$$\mathrm{Nu} = \left\{6.0 + \frac{0.387\mathrm{Ra}_D^{1/6}}{\left[1 + (0.559/Pr)^{9/16}\right]^{8/27}}\right\}^2 \quad (12)$$

$$q = \mu_l h_{fg}\left[\frac{g(\rho_l - \rho_v)}{\sigma}\right]^{1/2}\left(\frac{C_p(T_{sf} - T_{sat})}{C_{sf}h_{fg}\mathrm{Pr}_l^n}\right)^3 \quad (13)$$

$$\mathrm{Nu} = \frac{hD}{k} \quad (14)$$

where $\mathrm{Ra_D}$ denotes the Rayleigh number, g signifies gravity, β is the coefficient of volume expansion, D indicates the diameter of the pipe, Pr is the Prandlt number, and ν is the kinematic viscosity. Also, Nu stands for the Nustel number, q is the heat flux, h represents the heat transfer coefficient, h_{fg} represents the enthalpy of vaporization, C_P denotes the specific heat, C_{sf} is an experimental constant based on the surface and fluid combination, n is an experimental constant based on the cooling fluid. Lastly, for subscripts, *sf* indicates the surface, *o* refers to the outside of the pipe, *sat* denotes saturated, *l* signifies liquid, and *v* indicates vapor. Before the numerical results were conducted, a sensitivity analysis was performed to ensure that the control volume size did not have an effect on the numerical results. Several control volume sizes were tested, and it was noticed that after increasing the number of control volumes from 150 to just under 300, the change in the CC temperature was less than 0.2 °C. With the small temperature changes based on the number of control volumes, a total of 150 volumes was used for numerical testing to help reduce calculation time. The lengths of each control volume for each section of the LHP are shown in Table 2. A comparison of the experimental results and the results from the model can be done to understand the accuracy of the numerical model.

Table 2. Length of control volumes for the model.

Section	Length (mm)	# of volumes
Grooves	12.3	11
VL	59.6	42
Condenser	63.7	80
LL	128	17

4. Results

The steady-state temperatures for the passive cooling experimental test compared with the model's results can be seen in Figure 7a for the upright orientation and Figure 7b for the flat orientation. The numerical model matched well with the experimental results, with the average temperature difference being 10.2 °C for the upright orientation and 9.5 °C for the flat orientation. The best-matched and worst-match components for both orientations were the same, as the CC was the best matched with a temperature difference of 7.3 °C for the upright orientation and 4.5 °C for the flat orientation. The worst-matched component was the evaporator, which had a temperature difference of 16.3 °C for the upright orientation and 14.1 °C for the flat orientation.

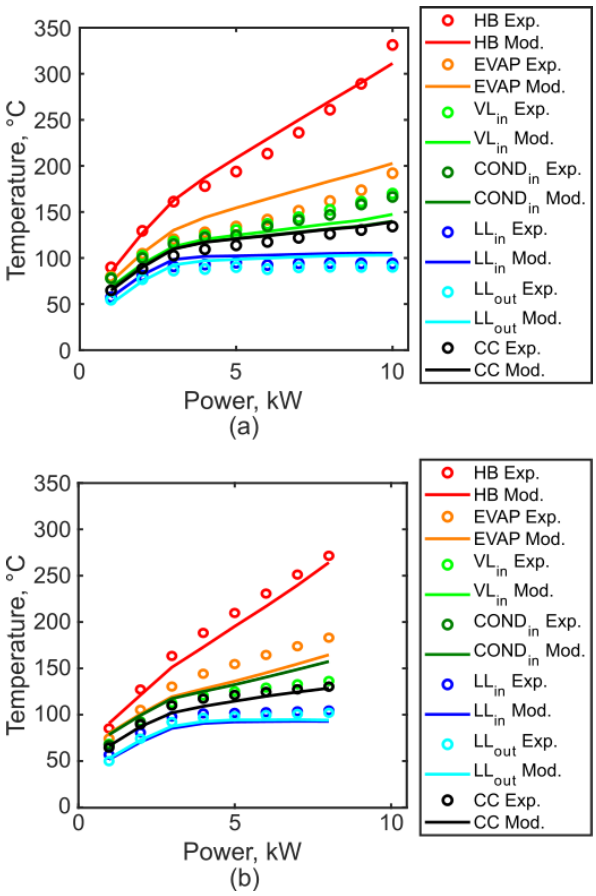

Figure 7. Model results vs. the steady-state temperatures for the upright orientation. (b) Model results vs. the steady-state temperatures for the flat orientation.

For the model, it seems that the model overpredicted the temperatures for the upright orientation; therefore, the benefit of the pressure gain and better fluid flow within the evaporator from the upright orientation was underpredicted. The flat orientation tended to underpredict the temperature, and this was most likely due to the vapor layer not being able to be simulated within the evaporator. This vapor layer would reduce performance, leading to higher temperatures, which was not accounted for within the model.

5. Conclusion

The LHP was able to handle power loads up to 10 kW with the upright orientation and 8.5 kW for the flat orientation. The lowest thermal resistance between the heat source and the heat sink was about 0.008 °C/W for the upright orientation and about 0.009 °C/W for the flat orientation. For the evaporative heat transfer coefficient, the highest value achieved was with the upright orientation, with a value of 92 kW/m^2/K and 80 kW/m^2/K for the flat orientation. The numerical model was able to predict the performance well, with the average temperature error being 10.2 °C and 9.5 °C for all power loads and locations for the upright and flat orientations, respectively. The increase in maximum power load in the LHP can help expand the potential uses for waste heat recovery in uses such as ICEs and IP.

References

[1] B. Orr, A. Akbarzadeh, M. Mochizuki, and R. Singh, A review of car waste heat recovery systems utilising thermoelectric generators and heat pipes. Applied Thermal Engineering, 2016. 101: p. 490.
[2] O. Farhat, J. Faraj, F. Hachem, C. Castelain, and M. Khaled, A recent review on waste heat recovery methodologies and uses: Comprehensive review, critical analysis and potential recommendations. Cleaner Engineering and Technology, 2022. 6: p. 100387.
[3] H. Jouhara, N. Khordehgah, S. Almahmoud, B. Delpech, A. Chauhan, and S. A. Tassou, Waste heat recovery technologies and uses. Thermal Science and Engineering Progress, 2018. 6: p. 268.
[4] Y. Aono, N. Watanabe, A. Ueno, and H. Nagano, Development of a loop heat pipe with kW-class heat transport capability. Applied Thermal Engineering, 2021. 183: p. 116169.
[5] H. Wang, G. Lin, H. Qin, R. Zhang, L. Bai, and Y. Guo, Design and experimental validation of a high capacity loop heat pipe for avionics cooling. Thermal Science and Engineering Progress, 2023. 45: p. 102139.
[6] M. A. Chernysheva and Y. F. Maydanik, Analysis of the thermal resistance of a loop heat pipe based on the P-T diagram of the working

fluid operating cycle. International Journal of Heat and Mass Transfer, 2023. 209: p. 124157.
[7] H. Jazebizadeh and T. Kaya, Numerical and experimental investigation of the steady-state performance characteristics of loop heat pipes. Applied Thermal Engineering, 2020. 181: p. 115577.
[8] Y. Çengel, Heat Transfer: A Practical Approach, 2nd ed., Boston: McGraw-Hill, 2003.

Paper ID 047(S7)

Numerical investigation of the hierarchical micro pore-channel composite evaporator for high-performance heat dissipation devices

Jiaxi Du[1], Jialin Liang[2], Binjian Ma[2], Huizhu Yang[2], Yue Yang[2], and Yonggang Zhu[2,3*]

[1] *School of Science, Harbin Institute of Technology (Shenzhen), Shenzhen, China*
[2] *School of Mechanical Engineering and Automation, Harbin Institute of Technology (Shenzhen), Shenzhen, China*
[3] *Shenzhen Fluentrop Technology, Shenzhen, China*
**Corresponding author email address: zhuyonggang@hit.edu.cn*

Abstract

With the increasing integration of portable electronic devices and the reduction of the available space inside them, the heat flux generated by high-power components increases dramatically, causing great difficulties in the thermal management of electronic devices. High-performance heat dissipation devices, such as ultra-thin flat heat pipes and vapor chambers, have attracted much attention due to their suitability for confined spaces and high heat transfer performance. The evaporator, as a key component of these ultra-thin heat transfer devices, where the intense phase change heat transfer process takes place inside the device, has a decisive influence on its thermal performance. In this study, we simulated the capillary-driven evaporation process in a hierarchical micro pore-channel composite evaporator using a dual-scale numerical model, analyzed the effect of microporous diameter, and predicted the overall thermal performance of the evaporators.

Keywords: Capillary-driven evaporation; Hierarchical microstructure evaporator; Numerical simulation; Heat dissipation.

1. Introduction

The effective thermal management of electronic components with ultra-high heat flux is crucial in advancing next-generation computation and communication technologies [1]. Conventional cooling technologies, such as air and liquid cooling, typically rely on highly complex equipment and external power supplies, and cannot solve the problem of heat dissipation in confined spaces [2]. Phase change heat transfer devices based on passive capillary wicking and thin-film evaporation processes, such as flat heat pipes and vapor chambers, have been widely researched and applied due to their better adaptability to this operating condition.

The performance of these phase change heat transfer devices is significantly affected by the evaporator design where intense phase change heat transfer occurs. Proper microstructure design can enhance capillary flow and phase change heat transfer of the working liquid in the evaporator of these devices and ultimately ensure that these electronic devices operate stably within a predetermined temperature range. Due to its significance, numerous evaporators with micro/ nano features have been proposed to improve the capillary-driven liquid film evaporation process of the phase-change heat transfer devices. Early research focused on investigating the amorphous microstructure evaporators made from conventional porous materials such as sintered powder, mesh, and metal foam. Besides, several evaporators with multi-pore size or composite structures were also proposed and investigated. However, due to the lack of artificial control over the internal structure, quantitative optimization of these evaporators is difficult, limiting further enhancement of their thermal performance. In recent years, well-defined structures have attracted more attention in this field. In order to improve the thermal performance of the evaporators, research on the capillary flow and evaporation process in micropillar arrays was first conducted. On this basis, experimental and numerical investigations of micropillar array evaporators were also conducted, in which the micropillars have various cross-section shapes such as circular, elliptical, and rectangular. An optimal evaporator necessitates the simultaneous fulfillment of three fundamental criteria: high capillary pressure, permeability, and a high heat transfer coefficient. The aforementioned evaporators, comprising arrays of microstructures with a single cross-sectional shape, are typically unable to balance the paradoxical relationship between capillary pressure and permeability. Hierarchical microstructural evaporators, particularly those comprising micro channel-pore composite structures, are regarded as pioneering designs poised to integrate these advantageous characteristics. Nevertheless, despite the completion of several laboratory studies on hierarchical microstructural evaporators, the majority of these devices possess a heated area of approximately 1 mm², which raises questions about their practical applicability at the device level.

In order to explore the potential of hierarchical microstructured evaporators for high heat dissipation devices, we developed a micro-macro dual-scale model to predict their heat transfer performance numerically.

2. Methodology

In this study, the heat transfer performance of the hierarchical composite evaporator with different pore diameter and total length is numerically predicted using a dual scale model. As shown in Figure 1, the hierarchical composite evaporator consists of a layer of microporous film with uniformly distributed micropores, rectangular microchannels arranged periodically along the y-axis, and a substrate. The capillary wicking and thin film evaporation characteristics of the evaporator are simulated sequentially at the cell and device levels. The micro-scale model is used to capture the interface shape dependent liquid flow and heat transfer characteristics in unit cells with different geometry and contact angle. And the macro-scale model is used to evaluate the overall thermal performance of the whole evaporator, including the dry-out heat flux and the effective heat transfer coefficient. The dual-scale model is solved numerically using rigorous grid-independent tests and is validated against two sets of heat transfer experiments on micropillar evaporators, which are widely used as benchmarks for validating relevant numerical models.

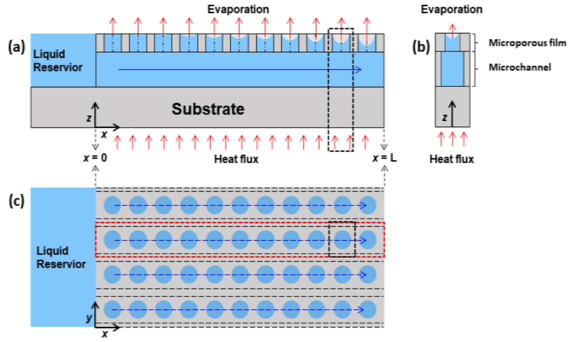

Figure 1. (a)Front view, (b)right view, and (c) top view schematics of the microporous film-microchannel composite evaporator.

2.1. Microscale model

Microscale simulations are performed in unit cells consisting of a minimal repetitive element of the composite microstructure and the liquid within it to investigate the effect of interface shape. For a unit cell with specific geometry, parametric studies of the interface shape have to be conducted first to build the liquid domains. Then, the microscale liquid flow and heat transfer simulations are conducted in the calculated liquid domain and predefined solid domain. Finally, the calculated permeability and heat transfer coefficient are constructed as functions of the interface shape and are passed to the macroscale models [3].

For a unit cell with specific geometry, the interface shape is a function of the local capillary pressure, which is the difference between liquid and vapor pressures. Gravity and inertia are ignored due to the small Bond number ($Bo \ll 1$) and Weber number ($We \ll 1$). Vapor pressure is assumed constant throughout the evaporator. Sufficient liquid supply allows the liquid to fill the microchannel and keep the interface pinned at the top of the hydrophilic micropore before dry-out. According to the Young-Laplace equation, the relationship between capillary pressure and local interface height (f) is:

$$\nabla \cdot \left(\frac{\nabla f - 1}{\sqrt{1 + |\nabla f|^2}} \right) = \frac{p_c}{\sigma} \quad (1)$$

where σ is the surface tension. Parametric studies were conducted to calculate the interface shape at different capillary pressures by solving Eq. (1). With the decrease of liquid pressure from the entrance to the center of the evaporators caused by the viscous liquid flow, the interface shape changes from flat to concave. When the contact angle decreases to the receding contact angle, the depinning of three phase line will lead to a localized dry-out phenomenon. The interface shape with contact angles ranging from 90° to 0 are calculated and used to build the liquid domains for micro scale liquid flow and heat transfer models.

In the micro scale heat transfer model, conduction is considered the dominant heat transfer mode in the liquid domain, due to the small Peclet number ($Pe \ll 1$). A quarter of the combination of both liquid and solid domains is used as the calculation domain. The governing equation of the heat transfer model is:

$$\nabla \cdot (k \nabla T) = 0 \quad (2)$$

where k is the thermal conductivity and T is the temperature. The calculation domain and boundary conditions are shown in Figure 3(a). A uniform heat flux $q_t^{"}$ transferred from the heated substrate is applied at the bottom of the unit cell. And the interfacial evaporative heat flux ($q_{eva}^{"} = \dot{m}_{eva}''/h_{lv}$) characterizes the heat transfer between the unit cell and the saturated vapor environment (at T_{sat}). The lateral heat conduction between unit cells is neglected, due to the small lateral temperature gradient compared with the vertical one from substrate to the interface. Thermal convection at the top of the microporous film is neglected in the model because it has a thermal resistance that exceeds the phase change heat transfer by about three orders of magnitude. The approximate Schrage's equation is used to calculate the evaporative mass flux:

$$\dot{m}''_{eva} = \frac{2\hat{\sigma}}{2-\hat{\sigma}}\left(\frac{M}{2\pi R}\right)^{1/2}\left(\frac{p_{sat}|_{T_{lv}}}{T_{lv}^{1/2}} - \frac{p_v}{T_v^{1/2}}\right) \quad (3)$$

where $\hat{\sigma}$, M, R, $p_{sat}|_{T_{lv}}$, p_v, T_{lv}, T_v are the accommodation coefficient (0.052), the molar mass of the liquid, the universal gas constant, saturation pressure at the interface pressure, vapor pressure, interface temperature and vapor temperature, respectively.

In microscale liquid flow model, half of a liquid domain is used as the calculation domain. Navier-Stokes equations are the governing equations of the steady-state laminar flow ($Re \ll 1$):

$$\nabla \cdot (\rho u) = 0 \quad (4a)$$

$$\rho(u \cdot \nabla)u = -\nabla p + \nabla \cdot \left(\mu(\nabla u + (\nabla u)^T)\right) \quad (4b)$$

where, ρ, μ, and p are the density, dynamic viscosity and pressure of liquid, u is the velocity vector. The calculation domain and boundary conditions are shown in Figure 3(b) and set as follows: (a) periodic boundary condition with a pressure difference (Δp_l) between the inlet and outlet of the microchannel; (b) shear-free boundary condition on the liquid–vapor interface; (c) symmetry boundary condition at the mid-surface of the domain; (d) no-slip walls at the bottom surface and the side surface in contact with the microchannel wall.

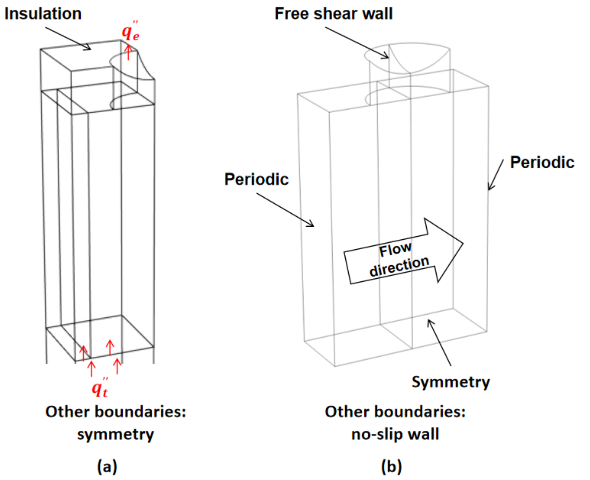

Figure 3. The schematic diagram of calculation domains and boundary conditions in micro scale (a) liquid flow and (b) heat transfer models.

A series of parametric studies of microscale heat transfer and liquid flow problems are solved in unit cells with various geometry. The calculated velocity and temperature fields are used to capture the microscale characteristic parameters, which are permeability κ and h_e, respectively. For a unit cell with specific geometry, κ is a function of interface shape only, and h_e is a function of interface shape and q''_t. The value of q''_t is set as equal to q''_{in} to reduce the complexity of the model here, considering the weak dependence of h_e on q''_t value.

The permeability κ calculated in microscale model is determined by Darcy's Law:

$$\bar{u} = -\frac{\kappa}{\mu}\nabla p \quad (5)$$

where $\bar{u}$ is the average velocity magnitude (along wicking direction) at the inlet (or outlet) of microchannel, and ∇p is the pressure gradient across a unit cell ($\nabla p = \Delta p/l$). And the heat transfer coefficient h_e under a given q''_t is defined as:

$$h_e = \frac{q''_t}{T_e - T_{sat}} \quad (6)$$

where T_e is the average temperature at the bottom surface of the unit cell.

2.2. Macroscale model

In the macroscale model, the coupled liquid flow and heat transfer phenomenon is studied in only one row of the evaporator due to the periodic arrangement (in y-direction). Macroscale liquid flow along the wicking direction, evaporative heat and mass transfer in the microstructures were mainly considered in this part. A nonlinear dual-dimensional and two-physics field-coupled model (one-dimensional fluid flow and two-dimensional heat conduction) is developed with reference to the iteratively solved device-level model in the study by Vaartstra et al [1]. The coupled liquid flow and heat transfer models and their coupling relationship are shown in Fig.4.

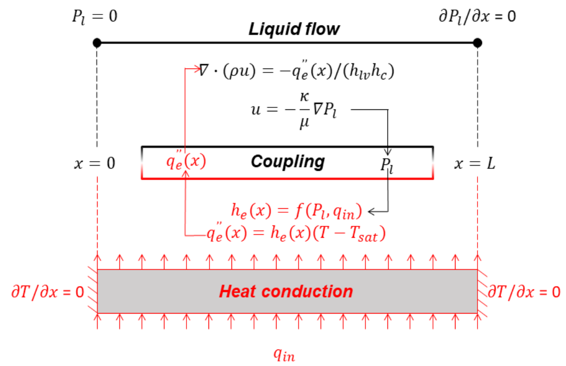

Figure 4. The schematic diagram of the macroscale model.

Liquid flow from the inlet ($x = 0$) to centerline ($x = L$) in the concerned row is simplified to a one-dimensional liquid flow problem in a continuous, porous media with variable permeability according to Darcy's Law to calculate the liquid pressure, where the local permeability is a function of liquid pressure itself (for a given microstructure). The mass transfer of evaporation is modeled as a volumetric mass loss in the continuity equation:

$$\nabla \cdot (\rho \dot{u}) = Q_{\mathrm{m}} \quad (7)$$

where, $Q_m = -q_{\mathrm{t}}''(x)/(h_{\mathrm{lv}} t_c)$, and $\dot{u}$ is the average velocity along wicking direction. Reference liquid pressure ($p_{\mathrm{l}} = p_{\mathrm{v}}$) at entrance and symmetry boundary condition at center line are set as boundary conditions of liquid flow model, respectively.

The heat transfer in the substrate is simplified to a two-dimensional heat conduction problem [4]. A uniform input heat flux q_{in}'' is applied at the bottom and dissipated by evaporative heat flux $q_{\mathrm{eva}}''(x)$ at the top of the substrate, where $q_{\mathrm{eva}}''(x) = h_{\mathrm{e}}(x)(T - T_{\mathrm{sat}})$ and T is the local temperature on the interface, and h_{e} is a function of q_{t}'' and p_{l}. Symmetry boundary conditions were set at both lateral boundaries of the substrate.

For each case of the evaporator with specific geometry parameters, various q_{in}'' are given from low to high value by a parametric sweep process to predict their heat transfer performance under different operating conditions. In each calculation, the temperature and flow fields are recorded until the p_{c} at centerline is equal to $p_{\mathrm{c,rec}}$. This extreme operating condition means that localized dry-out occurs at the centerline, which is the position most affected by the competing relationship between capillary pressure and flow resistance in the evaporator. The corresponding heat flux is called dry-out heat flux q_{dryout}''. In addition, the heat transfer coefficient of the entire evaporator $\overline{h_{\mathrm{e}}}$ is defined as the average value h_{e} at the top surface of the substrate under a specific operating condition.

3. Results and discussion

The dual-scale numerical model was validated by comparing two sets of calculated results ($\overline{h_{\mathrm{e}}}$ and q_{dryout}'') of cylindrical pillar array evaporators with experimental values in the literature which are widely used as benchmarks for model validation in the related numerical research. The predicted $\overline{h_e}$ was validated against the experiments conducted by Adera et al [5]. The evaporator was placed in a vacuum chamber at 3 kPa, and was surrounded by liquid water on all sides. The predicted and experimentally measured average superheats at different input heat fluxes are shown in Figure 5(a). The predicted q_{dryout}'' was validated by the experiments conducted by Zhu et al. [6], in which only one side of the evaporators was immersed in the water bath in an air ambient. The dry-out heat fluxes of two sets of evaporators with different wicking lengths were predicted by the model and compared with the experiment results, as shown in Figure 5(b). The high agreement between the predicted results and the experimental data demonstrates this dual-scale model's high accuracy in predicting evaporators' performance.

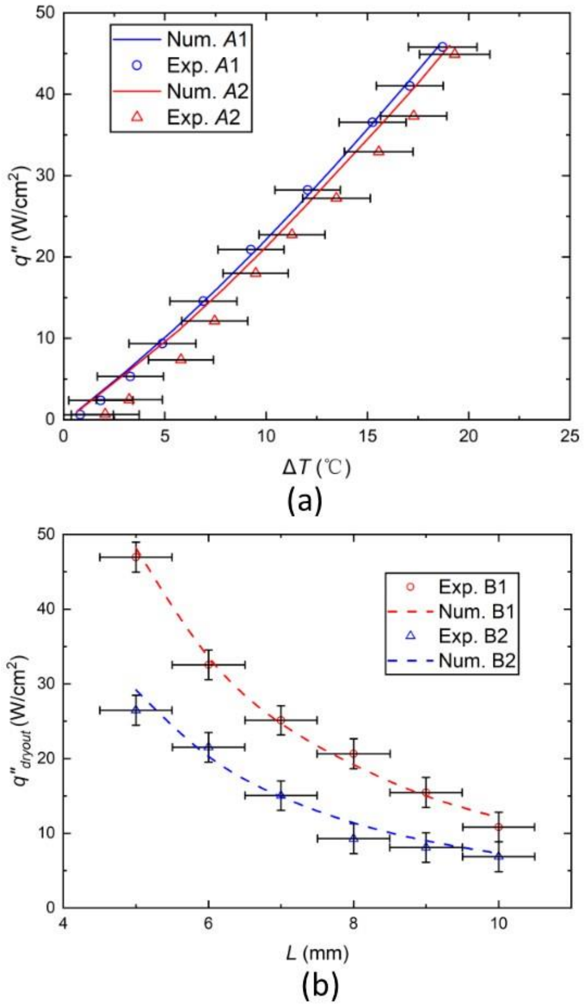

Figure 5. Comparison of the average evaporator superheat and dry out heat flux predictions of the proposed model and the experimental results.

Unlike normal micropillar evaporators, the hierarchical composite evaporator is considered as a special design that successfully balances the paradoxical dependence of capillary pressure and flow resistance on feature size. In particular, the capillary pressure and permeability of such hierarchical composite evaporator are no longer determined by the shape of the micropillar alone, but are decoupled to be determined by the characteristic size of the micropore and microchannel, respectively. In addition, the size of the micropore also has a great influence on the interface area and the length of the three-phase contact line, which affect the thin film evaporation characteristics. Therefore, for evaporators operating under high heat flux conditions, proper pore size design is an effective method of improving their thermal performance.

To assess the effect of pore size on the overall thermal performance of the evaporator, we first calculated the trend of capillary pressure versus contact angle for the working fluid (deionized water) in micropores of different diameters. As shown in Figure 6, as the diameter decreases from 15 to 2.5 μm, the capillary pressure shows a non-linear increase at all contact angles. Furthermore, the significant increase in decreasing capillary pressure will significantly increase the dry-out heat flux of evaporator.

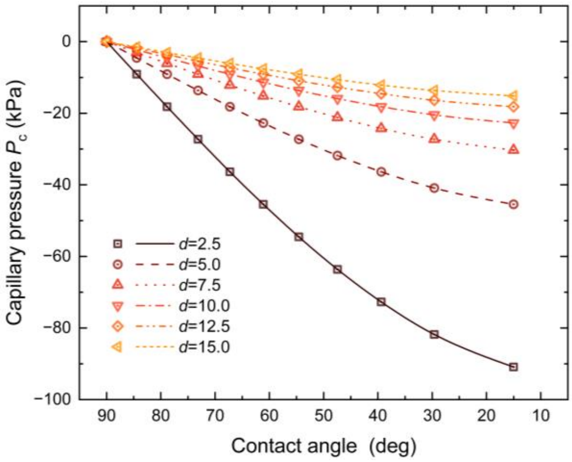

Figure 6. Capillary pressure versus contact angle for micropores with different diameter.

Figure 7 shows the calculated heat transfer coefficient of unit cells with different pore size, which are being heated with a uniform heat flux of 60 W/cm^2. The calculated evaporator has specific geometric parameters with microchannel width and height of 16 and 20 μm, and the thickness of the porous layer is 10 μm. The material of evaporator is silicon. As shown in the figure, the enlargement of the pore causes a significant increase in the heat transfer coefficient, which is dominated by the change in interfacial area. For the same reason, the effect of the contact angle on the heat transfer coefficient is more pronounced for larger diameter pores.

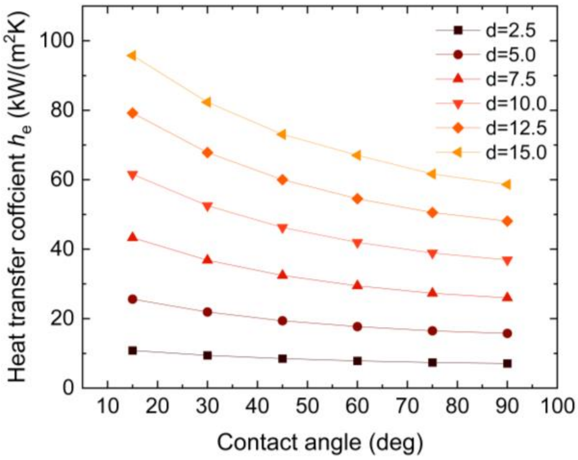

Figure 7. Heat transfer coefficient versus contact angle of unit cells with diameter.

Predictions of the thermal performance of evaporators with different pore sizes, including the dry-out heat flux and the efficient heat transfer coefficient at dry-out, are given in Table 1. From these results it can be seen that for a hierarchical composite evaporator with the same pore spacing design, the burnout heat flux (or critical heat flux density) increases with decreasing pore size. However, too small pore diameter will result in ultra-high heat flux density and low heat transfer coefficient, which is further manifested as ultra-high superheat at the wall. This problem will lead to the occurrence of boiling, which is considered to be an unstable heat transfer phenomenon in the field of heat dissipation in highly integrated electronic devices [7]. Increasing the heat transfer coefficient within the unit cell by reducing the pore spacing would be a viable way to further improve the thermal performance of the evaporator.

Table 1. Thermal performance of evaporators with different pore diameter.

Pore diameter	q''_{dryout}	$\overline{h_{\mathrm{e,dryout}}}$
μm	W/cm^2	kW/(m^{2}K)
7.5	251.9	42.017
10.0	189.6	51.418
12.5	151.5	64.269
15.0	92.3	67.718

4. Conclusions

In this study, we simulated the capillary-driven evaporation process in a hierarchical micro pore-channel composite evaporator using a dual-scale numerical model, analyzed the effect of microporous diameter, and predicted the integrated thermal performance of the evaporators. This work demonstrates the potential of the hierarchical micro pore-channel composite evaporator to operate at high heat flux conditions and provides theoretical guidance for further evaporator design.

5. ACKNOWLEDGEMENTS

This research was supported by the National Natural Science Fund of China, the Research Fund for International Scientists (No. 52250710157), and. Shenzhen Science and Technology Plan Project (No. KCXST20221021111216038). Jiaxi Du also acknowledges the sponsor of the International Academic Communication Fund for Postgraduate Students of Harbin Institute of Technology for participation in the Joint 22nd IHPC and 16th IHPS.

References

[1] G. Vaartstra, Z. Lu, and E. N. Wang, Simultaneous prediction of dryout heat flux and local temperature for thin film evaporation in micropillar wicks. International Journal of Heat and Mass Transfer, 2019. 136: p. 170.
[2] Z. Cui, L. Jia, Z. Wang, C. Dang, and L. Yin, Thermal performance of an ultra-thin flat heat pipe with striped super-hydrophilic wick structure. Applied Thermal Engineering, 2022. 208: p. 118249.
[3] G. Yuncu, Y. Akkus, and Z. Dursunkaya, Elliptical pillars for the thermal performance enhancement of micro-structured evaporators. International Communications in Heat and Mass Transfer, 2023. 148: p. 107036.
[4] A. S, and C.S. Sharma, Biomimetic micropillar wick for enhanced thin-film evaporation. Langmuir, 2023. 39: p. 6855.
[5] S. Adera, D. Antao, R Raj, and E. N. Wang Sharma, Design of micropillar wicks for thin-film evaporation. International journal of heat and mass transfer, 2016. 101: p. 280-294.
[6] Y. Zhu, D. S. Antao, Z. Lu, S. Somasundaram, T. Zhang and E. N. Wang, Prediction and characterization of dry-out heat flux in micropillar wick structures. Langmuir, 2016. 32: p. 1920.
[7] G. Yuncu, Y. Akkus, and Z.S. Dursunkaya, Elliptic micropillar wick evaporators for thermal management of high flux electronics. 2023 22nd IEEE Intersociety Conference on Thermal and Thermomechanical Phenomena in Electronic Systems (ITherm), 2023.

Paper ID 049(S2B)

Thermal Vacuum Testing of Loop Heat Pipe Controlled by Electrohydrodynamic Conduction Pump

Genki Seshimo[1*], Masahito Nishikawara[2], Takeshi Miyakita[3], Hiroshi Yokoyama[1]

[1] *Toyohashi Univ. of Tech., Aichi, Japan*
[2] *Nagoya Univ., Aichi, Japan*
[3] *Japan Aerospace Exploration Agency, Ibaraki, Japan*
**Corresponding author email address: seshimo.genki.rp@tut.jp*

Abstract

Loop Heat Pipes (LHPs) are two-phase heat transfer devices that can be used for spacecraft. In specific environments that have large ambient temperature variations, LHPs have risks of making equipped electric devices overcooled if they are used without temperature control. In this study, we developed a new temperature control technique using electrohydrodynamic (EHD) conduction pumps. An EHD conduction pump is installed to the liquid line of a LHP and generates pressure against the capillary force to impede heat transfer. This paper includes the experimental result of evaporator temperature control testing in a thermal vacuum environment. A feedback control algorithm for evaporator temperature with the EHD pump was newly developed for this test. The evaporator temperature was maintained near the constant temperature for 12 hours in a low-temperature environment. The power consumption of the EHD pump during the test was less than 27 mW. The detailed analysis confirmed two different LHP operation modes under control by EHD pump, restricting flow mode and switching flow direction mode. It is suggested that the EHD pump can control LHP with low power consumption and low-pressure drop in normal LHP operation, and that more accurate temperature control can be expected by improving the algorithm.

Keywords: EHD Conduction pump; Heat switch; Loop heat pipe; Lunar rover; Temperature control

1. Introduction

In space environments, Loop heat pipes (LHPs) are an effective option for dissipating heat of spacecraft electric equipment. They operate passively when the evaporator receives heat flux from the heat source, and the driving force of the working fluid is the capillary force of the wick. The evaporator temperature is mainly dependent on the temperature of the compensation chamber (CC), which is determined primarily from the heat load, the pressure drop of the entire system, and the ambient temperature [1].

In some cases, the evaporator temperature would be below the proper equipment temperature due to drastic decreases on ambient temperature, like the night in the lunar. Several techniques have been developed to control the CC temperature. Bypass valves were arranged in a branch pipe that short-circuits the vapor line (VL) and liquid line (LL) [2,3]. They operate passively based on the line pressure or working fluid temperature. As the LHP operation temperature decreases, the vapor flows into the blanch pipe and directly returns to the CC. As an active control technique, thermoelectric coolers (TECs) were installed on the CC [4,5]. They were also thermally connected to the evaporator to regulate the CC temperature using the heat flux from the evaporator.

Although these techniques have been verified to control the evaporator temperature, they would face some issues and requirements for spacecraft; that are less weight, less pressure drop during normal LHP operation, and less power consumption. We developed a new active technique using an electrohydrodynamic (EHD) conduction pump [6]. EHD conduction pumps are coulomb-force-driven pumps, and their advantages include no movable parts, adjustable flow resistance and pressure rise, and low power consumption. Figure 1 shows a conceptual diagram of the LHP controlled by the EHD conduction pump. An EHD conduction pump is installed in the LL, and the direction of the generated pressure is opposite to that of a flow driven by the capillary force.

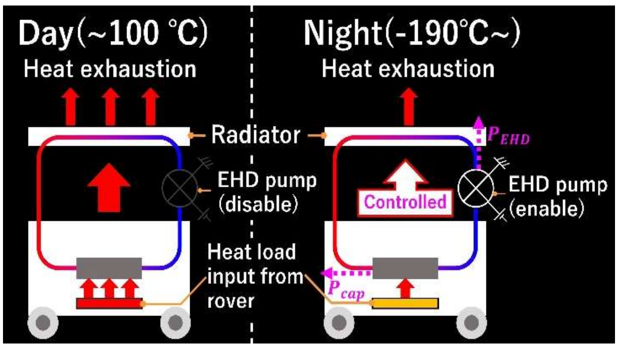

Figure 1. Conceptual diagram of LHP controlled by EHD conduction pump in lunar rover in day and cold night.

We previously developed a proper EHD conduction pump for the experimental LHP [7]. The developed EHD pump stopped the LHP heat transfer in a room temperature environment, and its power consumption was extremely small compared to other techniques. In this paper, we investigated the availability of a developed EHD pump for the evaporator temperature control, in which the development of a controller for evaporator temperature using an EHD pump and thermal vacuum testing of the evaporator temperature control were conducted.

2. EHD conduction pump

2.1 Requirement definition and construction of experimental EHD pump

According to the experimental LHP characteristics, some requirements were determined for the design of the experimental EHD pump. First, the working fluid was R134a, which can be used for LHPs and EHD pumps. Second, the generated pressure was set to 10 kPa to sufficiently overcome the capillary force of the wick.

An EHD pump that met requirements was designed through simulations using COMSOL Multiphysics® and the production of an EHD pump prototype. Figure 2 shows the structural diagram of the fabricated EHD pump. Ring-shaped electrodes made of stainless steel were embedded in the fluid path, and rod-shaped stainless steel electrodes were placed concentrically. 6-pairs of electrodes were constructed for gaining sufficient pressure generation. The rod used for the electrodes was covered with an insulation layer, except for the electrode section. Due to the high working fluid pressure, these structures were inserted into the manifold.

2.2 Evaluation of manufactured EHD pump

The manufactured EHD pump was evaluated in a preliminary experiment. Figure 3 shows the generated pressure and the power consumption characteristics against the applied voltage in no flowrate. Each point indicates the results of measuring for the steady state of constant applied voltage. Approximation curves drawn by dashed lines. Error bars indicate maximum and minimum values of each point except outside 3σ. The generated pressure was proportional to the square of the applied voltage, which agrees with the theoretical estimation [6]. The maximum generated pressure was approximately 10.8 kPa, and 170 mW was consumed at 11 kV. Approximately, the driving voltage of 6 kV and 30 mW of the power consumption was estimated to be necessary for sufficient generated pressure to overcome the capillary force, 3 kPa.

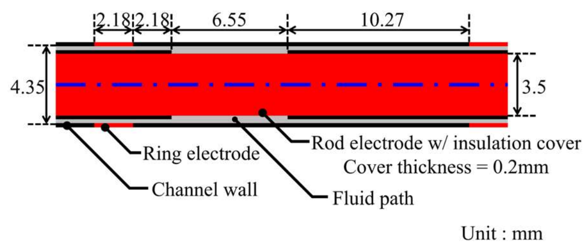

Figure 2. Structural diagram of EHD conduction pump. Rod electrode with cover and Ring electrodes are placed in concentric. There are 6 pairs of electrodes in manufactured EHD pump.

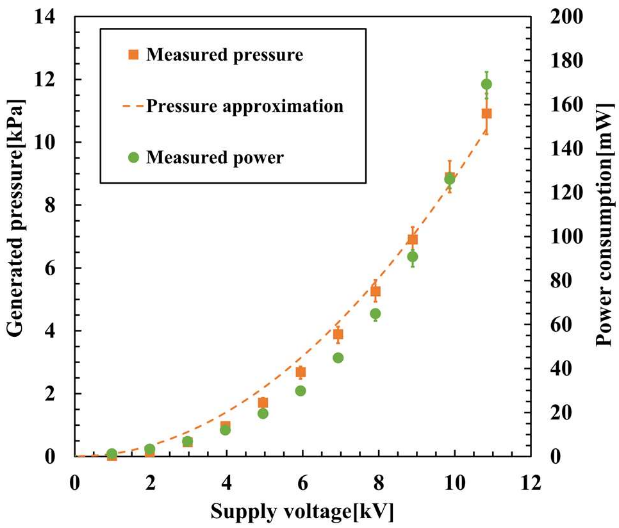

Figure 3. Characteristics of the developed EHD pump.

3. Thermal vacuum testing of LHP-EHD system

3.1 Thermal vacuum testing setup

The demonstration was conducted in a thermal vacuum environment. An overview of the experimental LHP equipped with an EHD pump is shown in Figure 4. Each point and legend indicate the thermocouple placement. The dimensions and materials of the LHP are summarized in Table 1. The experimental LHP had a cylindrical evaporator, and a disk-shaped black radiator as the condenser. The experimental LHP had a three-layer structure; with the upper layer being the radiator, the middle layer being the evaporator, CC, and vapor line, and the lower layer being the EHD pump and liquid line. The EHD pump was placed in the liquid line, and the distance between the EHD pump and the CC was 260 mm.

The experimental LHP equipped with the developed EHD pump was installed in the vacuum

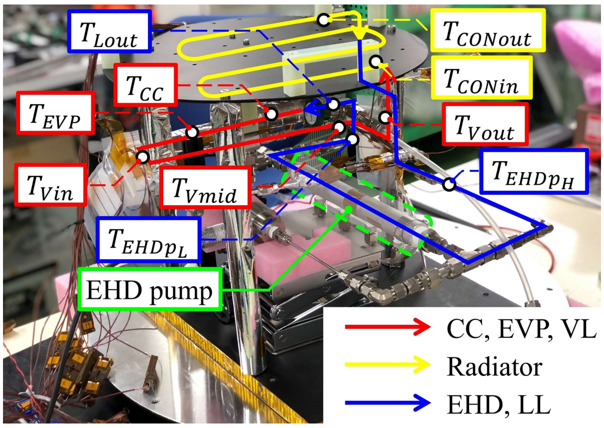

Figure 4. Overview of experimental LHP system with the EHD pump.

chamber. Only the equipped black radiator radiated heat into the black shroud in the vacuum chamber, and the other part was covered with multi-layer insulation (MLI). The evaporator is heated by a tape heater. Figure 5 presents an overview of measuring and control system. The temperature distribution and differential pressure of the EHD pump p_{EHD} were measured in the chamber, and the applied voltage V_{EHD} and current of the EHD pump I_{EHD} were measured in the power supply line.

3.2 EHD voltage control system

A LabVIEW-based applied voltage controller for the EHD pump was constructed for automatic evaporator temperature control. Figure 6 shows the structural diagram of the entire system. This system was based on proportional feedback control with the function for voltage raises rate limit. This function limits the slope when the input slope overcomes the setting value, and the function is valid when the following conditions are met:

$$\Delta V_i = \frac{V_i - V_{i-1}}{dT} > \Delta V_L \quad (1)$$

Table 1. Dimensions and materials of the LHP.

parameter	value
Evaporator size	φ18.6 mm × L76.5 mm
Wick size	φ12.6 mm × φ6 mm × L60 mm
Wick material	SUS304
pore diameter	2.8μm
porosity	40%
CC dimensions	Φ34 mm × 100 mm
VL length	700 mm
Condenser length	1500 mm
LL length	1300 mm
EHD pump length (in LL)	200 mm
VL tube diameter	φ3/16"
RAD/LL tube diameter	φ1/8"

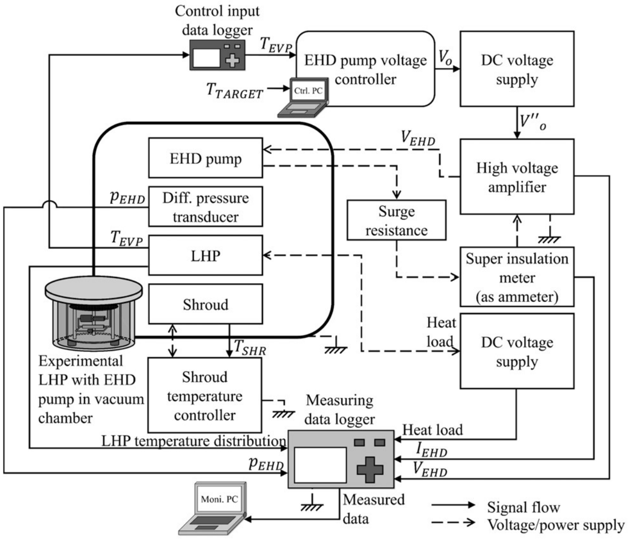

Figure 5. Overview of entire measuring and control system.

Here, V_i is the current input value, dT is time span, and ΔV_L is the slope limit. To smoothly change its operation, the restriction continues until the slope and current value from the input are below the slope limit and last output value, respectively. The current value comparison is described as follows:

$$V_i > V'_{o-1} \quad (2)$$

Here, V'_{o-1} is the last output. The output value is overridden if any comparison is met. V_i is used for the output only if both terms are not met. The override value calculate as follows:

$$V'_{o-1} + \Delta V_L \times dT \quad (3)$$

The output value is set to V'_o for the next time step calculation.

In thermal vacuum testing, the target and feedback values were the evaporator temperature.

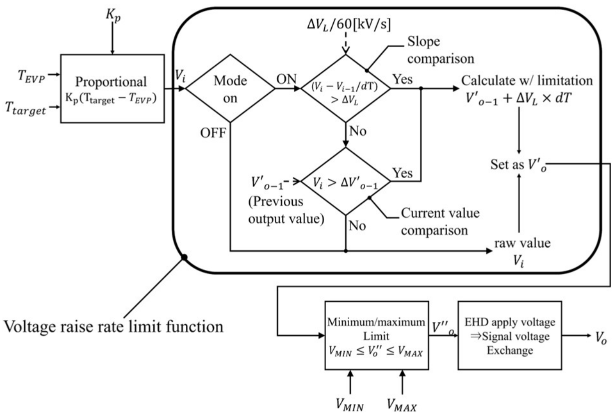

Figure 6. The structural diagram of voltage control system. In this paper, the first node of voltage raise rate limit function was fixed to ‘on’.

3.3 Procedures and conditions of the experiment

The experiment was carried out in the following order. First, it was confirmed that the LHP was operating stably with the shroud temperature $T_{SHR} =$ 27 °C. Then, the EHD pump controller was started. T_{SHR} had been changed with sequences, at first descent from 27 °C to −5 °C in 3 hours and held at −5 °C in 19 hours, then raised to 27 °C in 10 hours. The EHD controller was turned off after the stable operation of the LHP without control was confirmed. The heat load was almost constant at 4.6 W throughout the test. The target temperature in this experiment T_{TARGET} set for 35°C. For the input of the control system, the proportional gain $K_P =$ 10, minimum and maximum voltage limit set for $V_{MIN} = 0$ kV and $V_{MAX} = 9$ kV, respectively. The limitation of voltage raise rate ΔV_L set for 50 kV/min.

4. Results and discussion

The time series results of the test are shown in Figure 7. The T_{SHR} setting changed from 27 °C to −5 °C at EV1. It had started to apply a voltage to the EHD pump automatically after the T_{EVP} reached the T_{TARGET} at EV2. Between EV2 and EV3, T_{EVP} was almost constant at 33.6 °C, which was owing to restricting heat transfer under forward LHP fluid flows. EV3 shows the time when the LHP operation stopped for the first time. Between EV3 and EV5, T_{EVP} vibrated between 32.0 °C and 34.8 °C. These phenomena are discussed later. T_{SHR} was changed from −5 °C to 27 °C at EV4. At EV5, the vibration of T_{EVP} decreased. T_{EVP} exceeded the target value after EV6, and then the EHD pump automatically shut down.

The behavior of T_{EVP} changed at EV3 and EV5, indiating that there are two different LHP operation states. Here, we name these as “flow restriction mode” for EV2-EV3 and EV5-EV6, and “switching flow direction mode” for EV3-EV5, respectively. Figure 8 shows each typical behavior. In the switching flow direction mode shown in Figure 8 (I), it can be observed that there are 3 drastic changes from (a) to (c). Through the point of (a), the temperature at the outlet of the liquid line T_{Lout} drastically increases, which means that p_{EHD} overcomes capillary limit and backflow occur in the LHP by the EHD pump. Then, p_{EHD} is controlled to decrease as T_{EVP} increases. After (b), the fluid flow turned to forward direction and T_{Lout} decreases rapidly. T_{EVP} continues to increase due to the heat retention effect by stopping heat transfer to the vapor line or receiving warm liquid from the liquid line between (a) and (c). T_{EVP} decreases between (c) and (a’) due to normal heat transfer. The backflow occured again at (a'). These heat retention effects involved the LHP backflow, which caused the T_{EVP} to vibrate. In flow restriction mode shown in Figure 8 (II), there is no drastic transition in the T_{Lout}, which means that there is no backflow of LHP. T_{EVP} was maintained by the increased heat leak to CC involving an increased pressure drop by the EHD pump within the capillary force. As the T_{SHR} decreased and the V_{EHD} increased, the pressure drop exceeded the maximum capillary force for the first time at EV3.

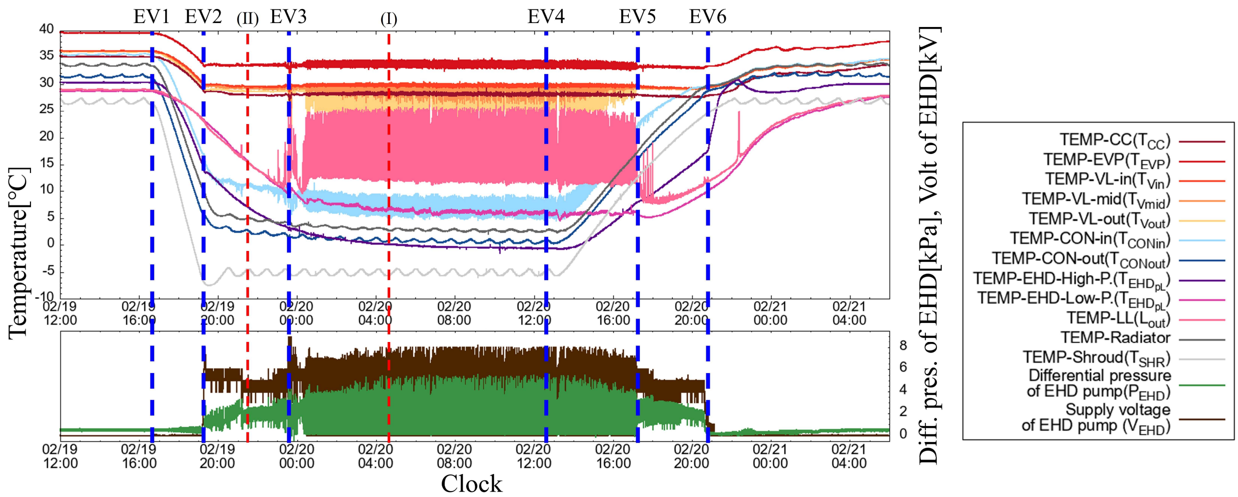

Figure 7. Time series result of the experiment with events (EVs). T_{SHR} setting changed from 27°C to -5°C at EV1. At EV2, the voltage started to be applied to the EHD pump. T_{EVP} started to vibrate at EV3. T_{SHR} setting changed from -5°C to 27°C at EV4. No longer vibrate of T_{EVP} observed after EV5. The applied voltage of EHD pump cut off at EV6.

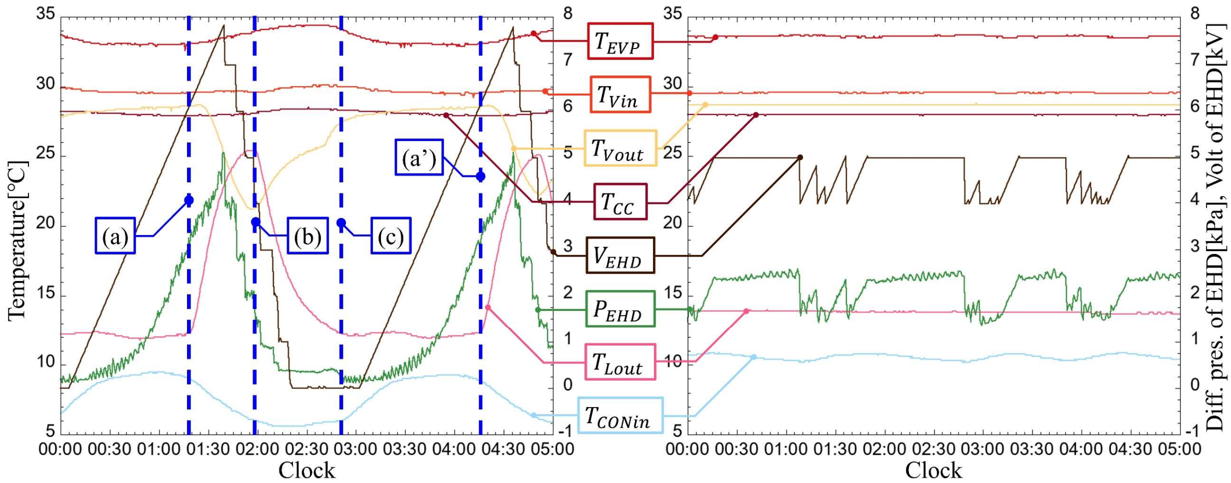

(I) switching flow direction mode (II) flow restriction mode

Figure 8. Typical behaviors between EVs, (I) EV2 and EV3, (II) EV3 and EV5.

As mentioned above, there was a temperature swing between 32.0 °C and 34.8 °C for T_{EVP}, and the average temperature was below the T_{TARGET}, 33.5 °C. There are some reasons considable for this results. First, some time lags between the control output and T_{EVP} may degrade the control performance and cause oscillations. In the peek-to-peek analysis, a 50 seconds average lag was observed between them. This time lag occurred in the backflow mode and led to an increase in temperature swings. This problem can be improved by developing more sophisticated controls that consider the time lag. It is also considered 2 reasons for average temperature offset: a control-derived offset and standing error of the thermocouples. According to the gain of proportional control $K_P = 10$ and Figure 8 (II), there is a standing offset of 0.5°C by the control method. There is 1.0°C of standing error between the measured T_{EVP} and the control input due to the temperature accuracy of the T-type thermocouples. These problems can be addressed by improving the control methods and measuring apparatus.

Throughout the test, the average power consumption was approximately 27 mW, which is approximately 0.6% of the heat load. This shows that the EHD conduction pump can be added to the heat switch function with sufficiently low power consumption.

5. Conclutions

In this paper, we demonstrate the temperature control of the LHP using the developed EHD pump. The developed EHD pump generated 11 kPa at the maximum applied voltage and can sufficiently overcome the capillary force. After evaluating the EHD pump, the thermal vacuum experiment was performed. The evaporator temperature was maintained at almost the target value over 12 hours in a low-temperature environment. There were two different LHP operation states observed in the result; the flow-direction-reversed state and flow-restricted state. The offset and vibration of the evaporator temperature may be alleviated by improving the experimental equipment or algorithms. The power consumption of the EHD pump was 27 mW, and it's sufficiently smaller than the heat load.

References

[1] Yu. F. Maydanik, Loop Heat Pipes, Applied Thermal Engineering, 2005, Vol. 25, Issues 5-6.

[2] J. Hartenstine, W. Anderson, K. Walker, M. Brown, Loop Heat Pipe with Thermal Control Valve for Variable Thermal Conductance Link of Lunar Landers and Rovers, 2011, 49th AIAA Aerospace Sciences Meeting including the New Horizons Forum and Aerospace Exposition.

[3] K. A. Gongharov, A. Yu. Kochetkov, V. N. Buz, Development of Loop Heat Pipe with Pressure Regulator, 2006, International Conference On Environmental Systems.

[4] J. Ku, L. Ottenstein, Thermoelectric Converters for Loop Heat Pipe Temperature Control: Experience and Lessons Learned, 2010, 40th International Conference on Environmental Systems.

[5] V.G. Pastukhov, Yu.F. Maydanik, Temperature control of a heat source using a loop heat pipe integrated with a thermoelectric converter, 2023, International Journal of Thermal Sciences, Vol. 184.

[6] Y. Feng, J. Seyed-Yagoobi, Understanding of electrohydrodynamic conduction pumping phenomenon, 2004, Physics of Fluids, Vol.16, No. 7.

[7] M. Nishikawara, T. Miyakita, G. Seshimo, H. Yokoyama, H. Yanada, Demonstration of heat switch function of loop heat pipe controlled by electrohydrodynamic conduction pump, 2024, Applied Thermal Engineering, Vol. 249.

Paper ID 050

Evaluation of Heat Transfer Characteristics in Pulsating Heat Pipes under Ultralow Filling Ratios: Effect of the Working Fluid Type

Atsushi Shiokawa[1*], Asami Hatamoto[1], Koji Fumoto[1]

[1] *Aoyama Gakuin University, Kanagawa, Japan*
c5623177@aoyama.jp

Abstract

In this study, the highly efficient heat-transfer phenomenon observed when the working fluid filling ratio in a pulsating heat pipe (PHP) is extremely low was investigated. The authors previously proposed this phenomenon as a new type of heat pipe called an ultralow-fill-rate heat pipe (ULFR-HP). The device consisted of a flat aluminum tube with a total length of 400 mm, featuring 28 straight channels, each with a square cross-section measuring 1.26 mm on each side. In this study, the heat transfer characteristics of the heating and cooling sections were evaluated to understand this unique phenomenon. Additionally, experiments were conducted using working fluids other than water, including alcohol-based fluids and refrigerants, to investigate the effects of different working fluids on device performance. The results confirmed that the ULFR-HP operated effectively with these alternative fluids, achieving a minimum thermal resistance of 0.041 K/W in the 400-mm device.

Keywords: Pulsating heat pipe; Aluminum flat plate; Filling ratio; Surface tension; Thermal transfer performance

1. Introduction

Recently, the miniaturization and performance enhancement of electronic devices have led to an increase in the heat generation density of electronic components. Particularly, the semiconductor components of electronic devices have low heat resistance and cannot maintain their performance once they exceed a certain temperature. Various heat pipe types utilizing the phase change of an internally sealed working fluid to transfer heat have been widely studied as cooling technologies to address this issue [1–5]. However, heat pipes face constraints such as capillary, sonic, entrainment, and boiling limits [6]. These limitations are particularly problematic when heat pipes are used to cool miniaturized electronic devices. Additionally, heat pipes are susceptible to the effects of gravity and heating orientation. To overcome these challenges, Akachi [7] invented the pulsating heat pipe (PHP) in 1990. A PHP consists of a single narrow tube that repeatedly loops between an evaporator and a condenser, with a certain amount of working fluid sealed inside. The PHP channel does not have a wick structure, and because the channel diameter is small (on the order of millimeters), the working fluid seals the channel cross-section via surface tension, and liquid slugs and vapor plugs alternate along the tube axis. As the working fluid continuously evaporates in the evaporator and condenses in the condenser, it enables latent heat transfer through a phase change and sensible heat transfer through self-excited working fluid oscillations. The heat transfer performance of a PHP is determined by several parameters, one of which is the working fluid fill rate. Rudresha et al. [8] clarified that the working fluid fill rate affects the heat transfer performance using a copper tube PHP and reported that the optimal fill rate was 55 vol.% of the channel volume. A review by Ayel et al. [9] suggested that the optimal PHP filling ratio lies within 50%–60%. Additionally, Yang et al. [10] reported that when the fill rate dropped below 20%, the liquid phase was not sufficiently supplied to the evaporator, leading to dry-out, which is the operational limit of a PHP.

This study focused on a new type of heat pipe with a unique operating principle, the ultralow-fill-rate heat pipe (ULFR-HP), which we previously devised [11]. Its appearance and experimental overview are almost identical to those of conventional PHPs. However, the ULFR-HP employs an extremely low fill rate (below 10 vol.%), which has traditionally led to dry-out. We reported that the ULFR-HP achieved highly efficient heat transfer compared with the conventional PHP (50 vol. %) and exhibits superior effective thermal conductivity and minimum thermal resistance. However, in our previous work, we only demonstrated the heat transfer performance when using water as the working fluid. To date, there are no reports on using fluids other than water in the ULFR-HP.

Therefore, this study aimed to clarify the impact of different working fluids on the heat transfer performance of a ULFR-HP. In this study, the effects of the surface tension and kinematic viscosity of different working fluids on the heat transfer performance using aqueous solutions with surfactants as working fluids were investigated. Additionally, experiments were conducted using single-component alcohol-based fluids (acetone and ethanol) and a fluorinated inert liquid (FC-72) as the working fluids to explore the possibility of using fluids other than water in the ULFR-HP.

2. Experimental setup and methods

2.1. Experimental setup

Figure 1 shows a schematic of the experimental setup. The experimental procedure followed the conventional PHP method. The ULFR-HP was arranged vertically. The upper part of the channel served as the cooling section, while the lower part served as the heating section. The experimental setup consisted of a heating system, vacuum pump system, measurement system, and syringe for the working fluid. The heating system included a cartridge heater and a transformer. The vacuum pump system was equipped with a digital vacuum gauge, and the measurement system featured thermocouples (K-type, eight points) attached to the ULFR-HP. Heat was supplied to the heating section using a heater block. The heating load from the heater was varied by adjusting the voltage. To reduce the thermal contact resistance, thermal grease was applied to the contact surface between the ULFR-HP and heater. The cooling section was open to the atmosphere, and heat was dissipated via natural cooling. Except for the ULFR-HP's cooling section, the system was covered with an insulation material to prevent heat loss.

Figure 2 shows a schematic of the test section and a detailed view of the channel cross section. The main component was aluminum with a total length of 400 mm, width of 48 mm, and thickness of 2 mm. The flow path comprised 28 parallel channels, each with a square cross-section measuring 1.26 mm on each side. The flow passage surfaces were anodized to suppress non-condensable gas generation. The serpentine channel structure has an open-loop configuration. The area ratios of the heating and cooling sections were set to either 20% and 50%, or 30% and 30%, respectively. The working fluids included water, aqueous solutions with added surfactants, acetone, ethanol, and FC-72. Tween 80 was used as a surfactant. The working fluid was thoroughly degassed using a vacuum pump.

Figure 3 shows a schematic of the experimental setup used to measure the droplet contact angle. This setup included a light source, high-speed camera, anodized aluminum sample, and stage. The liquid consisted of an aqueous solution with a specified amount of Tween 80 added, and 30 μL was dropped using a micropipette. The solid surface of the anodized Al sample was thoroughly cleaned using acetone and pure water. A light source illuminated the droplet from behind and a high-speed camera captured the droplet images. The droplet contact angles on the solid surface were measured using these images.

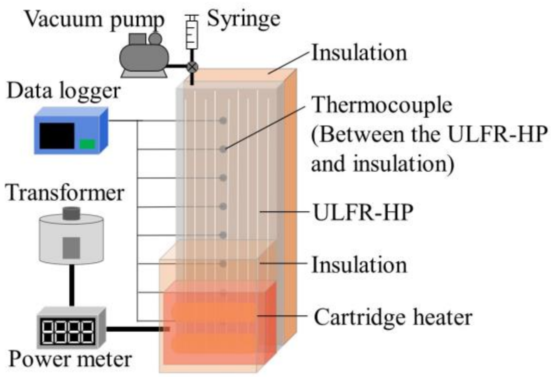

Figure 1. Schematic of the experimental setup.

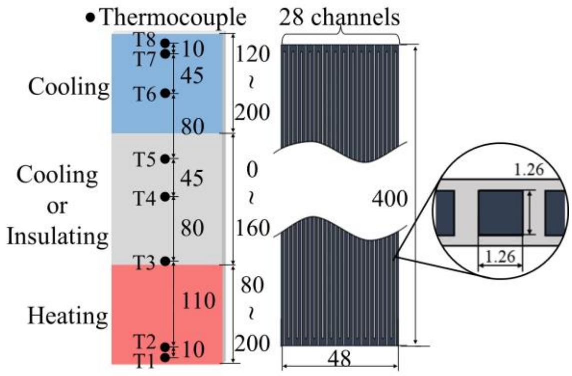

Figure 2. Testing part details (ULFR-HP).

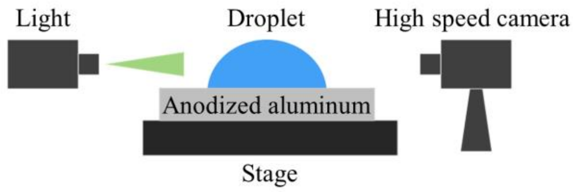

Figure 3. Schematic of the contact angle measurement method.

2.2. Experimental methods

The experimental parameters are listed in Table 1. In this experiment, the ULFR-HP was set up either vertically or horizontally with the type of working fluid as a variable parameter. The heating section area ratios were set to 20% or 30%.

The ULFR-HP was evacuated using a vacuum pump to a gauge pressure of -0.099 MPa or less, and the vacuum in the ULFR-HP was maintained by closing the attached valve. The working fluid was then injected using a syringe. Because dissolved air in the working fluid could adversely affect the ULFR-HP operation, the working fluid was degassed in advance using a vacuum pump. The working fluid filling ratio (FR) is defined as

$$FR=\frac{V_{fluid}}{V_{HP}}\times 100 \ \ [\text{vol.\%}] \tag{1}$$

where V_{fluid} is the working fluid volume at room temperature and atmospheric pressure and V_{HP} is the ULFR-HP channel volume. In this experiment, the filling ratio was zero (without working fluid), 10, and 50 vol.%. The 50 vol.% value was used for comparison with the conventional PHP. After the working fluid was filled, power was supplied to the cartridge heater via a transformer. The applied voltage was increased after confirming that the temperature measured by the thermocouples attached to the ULFR-HP reached a steady state. Steady state was defined as the condition where the temperature variation in the heating section over 5 min was within 1 K. For safety, the experiment was ended when the temperature in the heating section approached 100 °C.

Table 1. Experimental parameters.

Heating section area	Cooling section area	Working fluid
20%	50%	Surfactant solution
30%	30%	Water
		Acetone
		Ethanol
		FC-72

2.3. Evaluation methods

The net input heat Q_{net} supplied by the heater to the ULFR-HP was obtained by subtracting the ambient air heat loss Q_{loss} from the heater-provided heating amount Q_H. Assuming that Q_{loss} varies with the temperature difference between the heating section and the ambient air, a preliminary experiment was conducted to understand this correlation. Specifically, the experiment involved replacing the ULFR-HP with a solid aluminum plate of the same dimensions and known thermal conductivity $k_{AL} = 222$ [W/m · K] in the experimental apparatus shown in Figure 1. Figure 4 shows the details of the solid aluminum plate used in the preliminary experiment. The lengths of the heating, insulating, and cooling sections were 120, 160, and 120 mm, respectively. The net input heat Q_{net} and heat loss Q_{loss} in the preliminary experiment were respectively calculated as follows:

$$Q_{net} = k_{AL} \cdot \frac{A}{L_{BC}} \cdot (T_B - T_C) \ [\text{W}] \tag{2}$$

$$Q_{loss} = Q_H - Q_{net} \ [\text{W}] \tag{3}$$

where A is the cross-sectional area of the solid aluminum plate (equal to that of the ULFR-HP) and L_{BC} is the distance between measurement points B and C (0.03 m). T_B is the average temperature of the three points at measurement point B and T_C is the average temperature of the three points at measurement point C. The average temperature of the three points at measurement point A was taken as the heating section temperature T_H, and the temperature difference between T_H and the ambient air temperature T_a was correlated with Q_{loss}, as calculated using Eq. (3) and shown in Figure 5. The figure shows the results for the heating section with 30% coverage as a representative case. Similar experiments were conducted for the other heating section areas (20%). As can be seen in the figure, Q_{loss} is proportional to $T_H - T_a$. T_a and can be determined as follows:

$$Q_{loss} = 0.099(T_H - T_a) \ [\text{W}] \tag{4}$$

As a result, the net input heat Q_{net} was defined by combining Eqs. (3) and (4) as

$$Q_{net} = \ Q_H - 0.099(T_H - T_a) \ [\text{W}] \tag{5}$$

The thermal resistance R, which indicates the heat transfer performance of the ULFR-HP, is given by:

$$R= (T_{heat} - T_{cool})/Q_{net} \ \ [\text{K/W}] \tag{6}$$

where Q_{net} is calculated using Eq. (5). T_{heat} is the average value of T_1 and T_2, and T_{cool} is the average value of T_7 and T_8 at the positions shown in Figure 2.

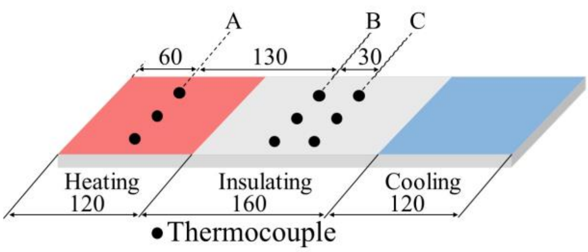

Figure 4. Details of the solid aluminum plate used in the preliminary experiment.

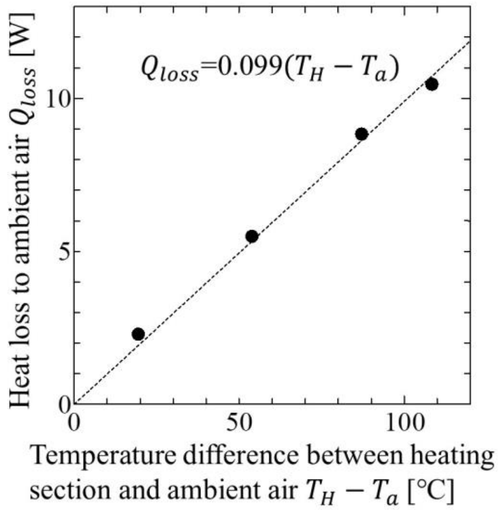

Figure 5. Heat loss to ambient air.

2.4. Preliminary experiment to verify reproducibility

Figure 6 shows the thermal resistance values obtained from the three tests conducted in the vertical position to demonstrate the ULFR-HP reproducibility. The horizontal axis represents Q_{net}. The heating section area ratio was 30%, and the cooling section area ratio was 30%. The filling ratio was set at 10 vol.%. The figure shows some variation in heat resistance at approximately $Q_{net} = 1$ W; however, as Q_{net} increased, the difference in heat resistance between each operation decreased. This indicates that the reproducibility improved with increasing input heat.

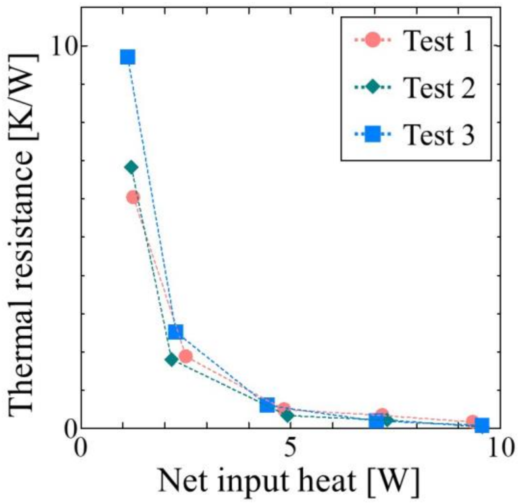

Figure 6. Experimental results to clarify data reproducibility. The experiments were conducted under the same conditions.

3. Results and discussions

3.1. Comparison between the ULFR-HP and the conventional PHP

In this section, the heat transfer characteristics of the conventional PHP and ULFR-HP are compared. The working fluid filling ratio was 50 vol.% for the conventional PHP and 10 vol.% for the ULFR-HP. Both devices have identical external shapes and channel dimensions, with the heating and cooling section areas each occupying 30%. The installation position was vertical, and the working fluid was water.

3.1.1. Temperature time history

Figure 7 shows the temperature time history of the conventional PHP (50 vol.%) and the ULFR-HP (10 vol.%). The figure also includes Q_{net}.

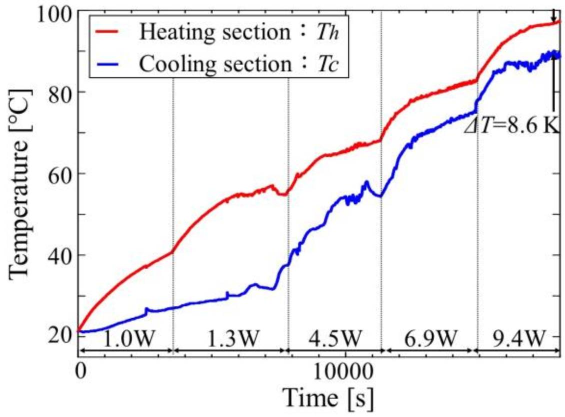

(a). PHP (50 vol.%).

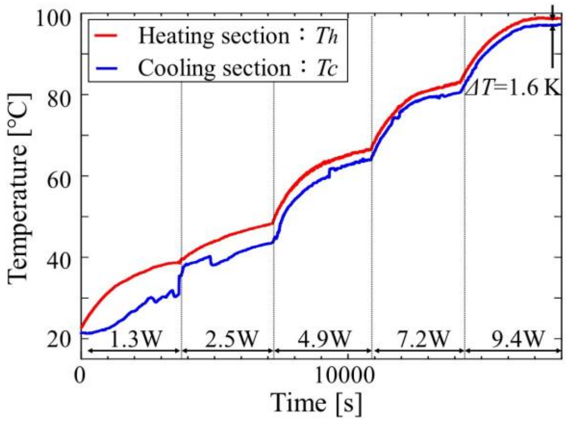

(b). ULFR-HP (10 vol.%).

Figure 7. Temperature time history of the conventional PHP and ULFR-HP.

From both figures, at all heat levels, the temperature difference between the heating and cooling sections in the ULFR-HP decreased compared to the conventional PHP, with the temperature difference for $Q_{net} = 9.4$ W being

1.6 K. Furthermore, focusing on the temperature behavior of each thermocouple, the ULFR-HP exhibited a smoother graph, indicating more stable heat transfer compared to the conventional PHP. This is attributed to the predominant latent heat transfer in the ULFR-HP, as discussed in Section 3.1.2.

Figure 8 shows the thermal resistance values of the conventional PHP (50 vol.%), the ULFR-HP (10 vol.%), and without working fluid (0 vol.%). The horizontal axis represents Q_{net}. As shown in the figure, the thermal resistance of the ULFR-HP is lower than that of the conventional PHP at all heat levels. The minimum thermal resistance of the ULFR-HP was 0.17 K/W for $Q_{net} = 9.4$ W, which is a reduction of approximately 81% compared to the conventional PHP (0.91 K/W).

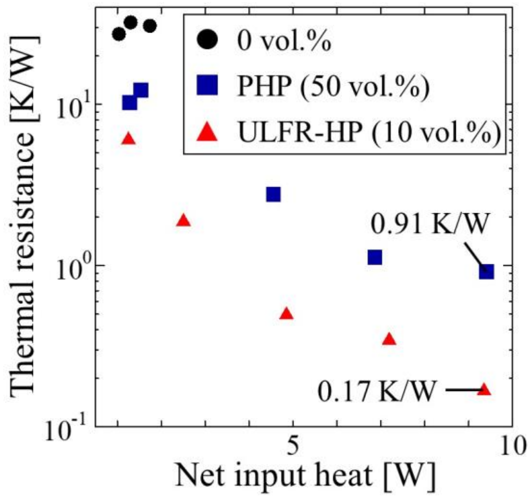

Figure 8. Thermal resistance of the conventional PHP and ULFR-HP.

3.1.2. Heat transfer characteristics in the heating and cooling sections

To gain a more detailed understanding of the heat transfer characteristics of the conventional PHP and ULFR-HP, the heat transfer performance was evaluated separately for the heating and cooling sections. The heat transfer coefficients for the heating and cooling sections (h_h and h_c, respectively) are defined as a heat transfer characteristic as follows:

$$h_h = q_h/\Delta T_h \ \ [\mathrm{W/m^2 \cdot K}] \quad (7)$$

$$h_c = q_c/\Delta T_c \ \ [\mathrm{W/m^2 \cdot K}] \quad (8)$$

Where $q_h\ (= Q_{net}/S_h)$ and $q_c\ (= Q_{net}/S_c)$ represent the heat fluxes in the heating and cooling sections, respectively, and S_h and S_c are the surface areas of each section. $\Delta T_h\ (= T_h - T_a)$ and $\Delta T_c\ (= T_a - T_c)$ refer to the temperature difference between the heating and insulating sections and between the insulating and cooling sections, respectively. $T_h, T_a,$ and T_c are the average wall temperatures of the heating, insulating, and cooling sections, respectively.

Figure 9 shows the heat transfer coefficients of the heating and cooling sections for both the conventional PHP and ULFR-HP. The horizontal axis represents the heat flux in the heating and cooling sections. As can be seen, the heat transfer coefficient of the heating section increases with the heat flux for both cases, ranging between 30–2200 $\mathrm{W/m^2 \cdot K}$, with both cases showing similar values. In contrast, the cooling section heat transfer coefficient for the PHP remained nearly constant around 270 $\mathrm{W/m^2 \cdot K}$ beyond a cooling section heat flux of 1200 W/m². For the ULFR-HP, the heat transfer coefficient increased linearly with the cooling section heat flux, ranging between 1000–2600 $\mathrm{W/m^2 \cdot K}$. Therefore, the significant difference in the ULFR-HP, as shown in Figure 8, is considered to stem from the improved cooling section heat transfer coefficient. Furthermore, the authors confirmed through neutron radiography experiments of the internal flow in the ULFR-HP that, unlike the conventional PHP, the ULFR-HP did not exhibit liquid slug oscillations. These liquid slugs tended to stagnate and were distributed in the heating and cooling sections, suggesting that latent heat was the primary heat transfer mode. The absence of pressure losses owing to liquid slug oscillations, as observed in conventional systems, and the reliance on the phase change of the working fluid for heat transfer are believed to contribute to the enhanced cooling section heat transfer coefficient.

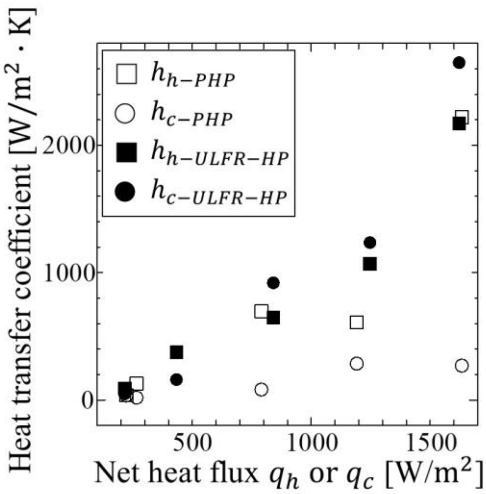

Figure 9. Heating and cooling section heat transfer coefficients for the conventional PHP and ULFR-HP.

3.2. Effect of surfactant concentration

3.2.1. Surface tension of the working fluid with surfactant addition

Figure 10 shows the relationship between the Tween 80 concentration in an aqueous solution, used as a surfactant, and the droplet contact angle on an anodized surface. The horizontal axis represents the Tween 80 concentration in the aqueous solution and the vertical axis represents the contact angle.

A surfactant molecule has a structure with two opposing properties: hydrophilicity and hydrophobicity. As the concentration of the surfactant increases beyond the saturation concentration for molecular dispersion, the surfactant molecules in the aqueous solution form aggregates (micelles), where the hydrophilic heads face the continuous water phase [12]. The critical micelle concentration (CMC) is the concentration at which micelle formation begins. When the surfactant concentration exceeds the CMC, the water surface is covered by surfactant molecules and the surface tension remains nearly constant. After a concentration of 0.5 mM, the contact angle remained nearly constant even as the concentration increased, as shown in Figure 10. Therefore, the CMC is considered to exist between 0.2 and 0.5 mM. Beyond 0.5 mM, the surface tension did not change, and only the kinematic viscosity increased. By comparing the results obtained using this concentration as the working fluid, the effect of kinematic viscosity on the heat transfer performance of the ULFR-HP can be evaluated.

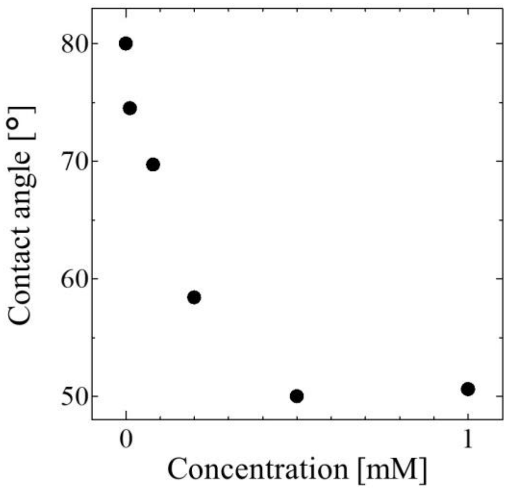

Figure 10. Relationship between surfactant concentration and contact angle.

3.2.2. Effect of surfactant concentration on the heat transfer characteristics

Table 2 lists the surfactant aqueous solution concentrations used in this experiment, and Figure 11 shows the relationship between the surfactant concentration and thermal resistance at a Q_{net} of approximately 15 W. The filling ratio was 10 vol.% for all cases, and the Q_{net} range was from 14.9 (0.5) to 15.8 W (0.2 mM). The area ratios are 20% and 50% for the heating and cooling sections, respectively. As can be seen, up to a concentration of 0.2 mM, the thermal resistance decreases as the surfactant concentration increases. The lowest thermal resistance within the scope of this experiment was 0.146 K/W at 0.08 mM, approximately 0.38 times that of 0 mM (0.384 K/W). This is considered to be due to the decrease in the surface tension of the working fluid. The reduction in surface tension increases the contact area between the liquid film remaining on the channel walls and walls themselves, while also reducing the liquid film thickness. As a result, the amount of evaporation from the liquid film increases as the liquid slug retreats from the heating to cooling section, which in turn reduces the liquid film thickness and leads to a decrease in thermal resistance. Therefore, it was previously considered that the ULFR-HP operated only with water due to wettability concerns; however, these results suggest that it can also operate with working fluids with a lower surface tension.

Meanwhile, after a concentration of 0.5 mM, increasing the surfactant concentration did not improve the heat transfer performance. This is considered to be due to the increase in the kinematic viscosity of the working fluid. Beyond 0.5 mM, the concentration reached the CMC, causing no further changes in surface tension while only increasing the viscosity. These results suggest that the liquid slug extension from the heating section to the adiabatic section and its movement towards the cooling section, as revealed by previous visualization experiments, were suppressed, leading to an increase in thermal resistance. The reason for this is as follows. This liquid slug flow is mainly observed in the low to high heat input ranges. It is considered a crucial flow characteristic for transitioning to the characteristic liquid slug distribution in the high heat input range, where the slug is almost stagnant in the heating and cooling sections, thus improving the thermal transport performance. Therefore, the increase in the working fluid dynamic viscosity likely inhibited the transition to the ULFR-HP-specific liquid slug distribution, resulting in increased thermal resistance.

Table 2. Surfactant addition concentration.

Surfactant	Addition concentration [mM]
Tween 80	0, 0.012, 0.08, 0.2, 0.5, 1.0

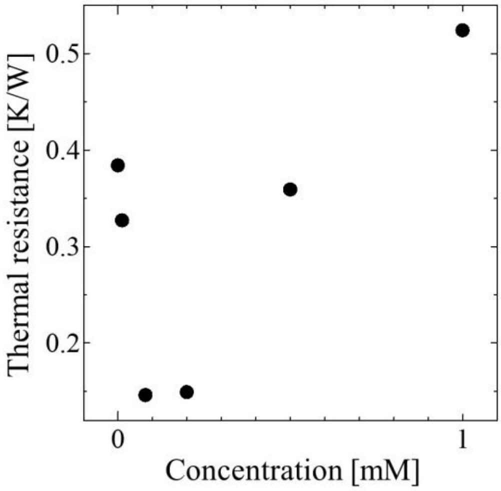

Figure 11. Relationship between concentration and thermal resistance at a net input heat of 15 W.

3.3. Effect of the type of working fluid on the heat transfer characteristics

Figure 12 shows the thermal resistance of the ULFR-HP filled with 10 vol.% of water, acetone, ethanol, and FC-72. The horizontal axis represents Q_{net}. Except for acetone at 8.8 W, the thermal resistance values for acetone and ethanol were lower than those for water at all heat loads. The minimum thermal resistance with ethanol was 0.041 K/W at 9.4 W, which is approximately 0.24 times that of water (0.17 K/W). This difference is likely because the surface tension of acetone and ethanol is approximately one-third that of water. Similar to the effect of surfactants, the reduction in surface tension promotes a phase change in the working fluid, thereby enhancing the heat transfer performance.

Furthermore, the kinematic viscosity of acetone (0.387 mm²/s) is approximately 0.4 times that of water (0.891 mm²/s), while the kinematic viscosity of ethanol (1.37 mm²/s) is approximately 1.5 times that of water [13]. Despite this, the thermal resistance of acetone and ethanol were lower than that of water. These findings suggest that the reduction in surface tension has a more dominant effect on the heat transfer performance of the ULFR-HP than the reduction in kinematic viscosity. Additionally, the thermal resistance of acetone increased at $Q_{net} = 8.8$ W. This increase is likely due to acetone's boiling point (56.6 °C), which is approximately half that of water, causing an excess of evaporation relative to condensation, leading to localized dry-out [13].

For all heat loads, the thermal resistance of FC-72 exceeded that of water. This is likely because the latent heat of evaporation (h_{fg}) for FC-72 (h_{fg} = 88 kJ/kg) is extremely low, approximately one-tenth that of ethanol (h_{fg} = 855 kJ/kg) and one-fifth that of water (h_{fg} = 2257 kJ/kg) [14]. Given the very low liquid-phase volume of 10 vol.%, FC-72 likely evaporates more actively even at low heat loads, reducing the liquid phase volume in the heating section and causing localized dry-out.

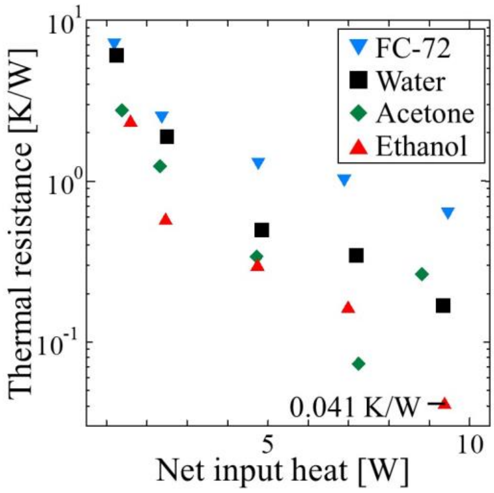

Figure 12. Thermal resistance for each working fluid.

4. Conclusion

In this study, the thermal transport characteristics of the conventional PHP and ULFR-HP were compared based on experimental results. Additionally, the impact of different working fluids on the thermal transport performance of different heat pipes were investigated. Based on the overall results, the main conclusions of this study can be summarized as follows:

(1) The significant difference in the thermal transport performance between the conventional PHP and ULFR-HP is attributed to the improved heat transfer rate in the cooling section of the ULFR-HP.
(2) A reduction in the surface tension of the working fluid decreased the thermal resistance of the ULFR-HP.
(3) The use of acetone and ethanol as working fluids reduced the thermal resistance

compared with that using water. This reduction likely results from the lower surface tension of the working fluids. Conversely, when using FC-72, the thermal resistance increased compared with that using water. This increase is likely due to the significantly lower latent heat of FC-72 compared with water.

5. ACKNOWLEDGEMENTS

This research was partially supported by JSPS KAKENHI (grant number 24K07362).

References

[1] X. Chen, H. Ye, X. Fan, T. Ren, G. Zhang, A review of small heat pipes for electronics, Applied Thermal Engineering, 2016, Vol. 96, pp. 1-17.
[2] V. G. Pastukhov, Y. F. Maidanik, C. V. Vershinin, M. A. Korukov, Miniature loop heat pipes for electronics cooling, Applied Thermal Engineering, 2002, Vol. 23, pp. 1125-1135.
[3] L. Vasiliev, D. Lossouarn, C. Romestant, A. Alexandre, Y. Bertin, Y. Piatsiushyk, V. Romancenkov, Loop heat pipe for cooling of high-power electronic components, International Journal of Heat and Mass Transfer, 2009, Vol. 52, pp. 301-308.
[4] L. L. Vasiliev, Micro and miniature heat pipes – Electronic component coolers, Applied Thermal Engineering, 2008, Vol. 28, pp. 266-273.
[5] W. Zhou, Y. Li, Z. Chen, L. Deng, Y. Gan, A novel ultra-thin flattened heat pipe with biporous spiral woven mesh wick for cooling electronic devices, Energy Conversion and Management, 2019, Vol. 180, pp. 769-783.
[6] Heat transfer engineering, The Japan Society of Mechanical Engineers (in Japanese), 2005, pp. 202-203.
[7] H. Akachi, Structure of a heat pipe, US Patent, 1990, 4, 921, 041.
[8] S. Rudresha, E. Babu, and R. Thejaraju, Experimental investigation and influence of filling ratio on heat transfer performance of a pulsating heat pipe, Thermal Science and Engineering Progress, 2023, Vol. 38, 101649.
[9] V. Ayel, M. Slobodeniuk, R. Bertossi, C. Romestant, Y. Bertin, Flat plate pulsating heat pipes: A review on the thermohydraulic principles, thermal performances and open issues, Applied Thermal Engineering, 2021, Vol. 197, 117200.
[10] H. Yang, S. Khandekar, M. Groll, Performance characteristics of pulsating heat pipes as integral thermal spreaders, International Journal of Thermal Sciences, 2009, Vol. 48, pp. 815-824.
[11] K. Fumoto, K. Ishii, Flat plate pulsating heat pipe operating at ultra-low filling ratio, Applied Thermal Engineering, 2023, Vol. 228, 120468.
[12] K. Hamano, Critical phenomena of surfactant micelle solutions, Journal of the Physical Society of Japan (in Japanese), 1993, Vol. 48, No. 9, pp. 718-721.
[13] New edition of handbook of thermophysical properties, The Thermophysical Society of Japan (in Japanese), 2008, pp42-47.
[14] M. Miura, T. Nagasaki, Y. Ito, Study on heat transport characteristics with liquid column oscillation in pulsating heat pipes (Effects of working fluids), Proceedings of the Heat Transfer Conference of the Japan Society of Mechanical Engineers (in Japanese), 2016, No. 16-33.

Paper ID 051(S4)

Optimal Heat Pipe Operation for Efficient Latent Energy Exchanger

Helen Skop*, Darrell Klammer

Smart Heat Corporation, Skokie, IL, USA
**Corresponding author email address: hskop@yahoo.com*

Abstract

Traditional methods for heat recovery rely predominantly on sensible heat transfer, which is unsuitable for effectively recuperating energy from the low-temperature wet exhaust emissions typical of many industrial processes. This paper explores the potential of heat pipes for latent heat transfer in waste heat recovery systems, particularly within the context of a novel technology referred to as a Latent Energy Exchanger (LEExchanger). The study examines the specific features of the LEExchanger in maintaining conditions for a stable, and therefore efficient, phase transition process, based on the mathematical similarity of process parameters and LEExchanger geometry. The impact of this similarity on the efficiency of heat pipes, which are integral to the energy transfer during phase transitions, is analyzed, along with the associated thermal resistances. Additionally, the paper presents the design and optimization of a LEExchanger, which utilizes heat pipes to facilitate energy transfer during phase transitions. Special attention is given to the internal and external surface arrangement of the heat pipe walls to ensure efficient condensation and evaporation processes. The study concludes that grooved surfaces on both sides of the heat pipe wall offer a cost-effective and efficient solution, capable of facilitating latent energy exchange, particularly for applications in waste heat recovery.

Keywords: Latent energy transfer; Low-temperature exhaust; Moist gas; Heat pipe; Heat and mass exchanger

1. Introduction

The decarbonization of processes in modern industry is crucial both for mitigating environmental impacts and improving energy efficiency. Traditionally, heat transfer technologies have been designed for the management of sensible heat. However, this approach is often unsuitable for effectively recuperating energy from the low-temperature wet exhausts common to many industrial processes. As these processes are modified to improve efficiency, significant challenges and substantial opportunities for innovation in energy recovery arise.

One of the most promising technologies in this context are heat pipes, which, despite traditional application in aerospace and electronics cooling, are increasingly being recognized for their potential in waste heat recovery systems. Heat pipes are noted for their high heat transfer capability and near-uniform temperature distribution. Yet employed in conventional sensible heat transfer applications, their heat transfer capacity is underutilized. The use of heat pipes in latent heat transfer processes, rather than traditional sensible energy transfer applications, has created a significant shift in focus from sensible heat transfer to latent heat transfer. Latent heat transfer is inherently more demanding than sensible heat transfer and presents unique technical challenges and opportunities.

The condensation of the vapor component in exhaust gases has become a process of special interest for enhancing energy efficiency across various sectors, including power generation, chemical engineering, distillation, and air conditioning. Moreover, the augmentation of Brayton cycle performance became possible through liquid addition to the gas flow before the turbine and after recuperation. This trend is further propelled by increasing urgency to address the water-energy nexus, which emphasizes the role of efficient heat transfer in condensing technology and encourages the development of novel approaches to manage latent heat.

2. Latent energy exchange approach

The Latent Energy Exchange (LEE) approach introduces a novel paradigm in heat transfer which employs a non-linear distribution of heat during condensation. This process alters the mass and dew point of a flow of a partially condensed mixture, requiring innovative techniques capable of managing these parametric changes effectively. Heat pipes play a crucial role in this process, facilitating the transfer of energy between phase change processes and enabling a balanced heat exchange with minimal temperature differences. The design of the Latent Energy Exchanger (LEExchanger) leverages a sequence of latent energy transfer processes—including condensation in the hot flow section, vaporization and condensation within heat pipes, and vaporization in the cold flow section—to achieve high-performance heat transfer (Figure 1).

As shown in Figure 2, the shape of the LEExchanger channel is formed by walls twisted in a logarithmic

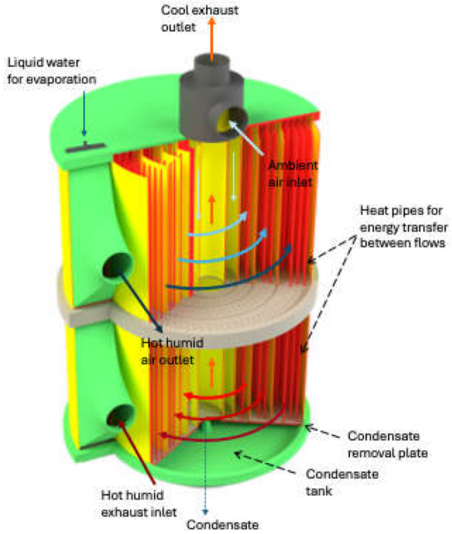

Figure 1. LEExchanger concept design.

spiral, resulting in an exponential change in the cross-sectional area of the channels:

$$\frac{W(1)}{W(2)} = e^{b(\theta 1-\theta 2)} \tag{1}$$

Latent energy may be transferred through the common interface surface (A_{if}) along the two logarithmic spiral channels in such a manner that in each section of the channels, the relationship between vapor saturation pressure and temperature may be determined by the Clausius-Clapeyron equation for air containing water vapor:

$$\frac{P_{v,sat}(1)}{P_{v,sat}(2)} = e^{\frac{L}{R_v}\left(\frac{1}{T_{sat}(2)}-\frac{1}{T_{sat}(1)}\right)} \tag{2}$$

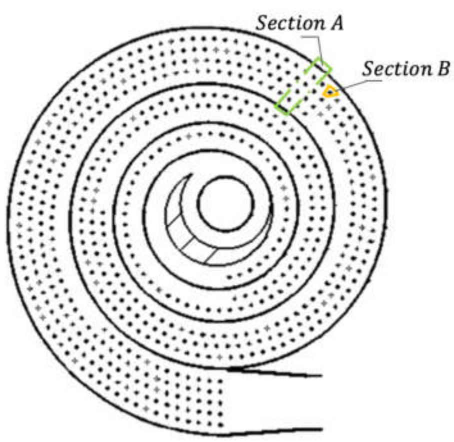

Figure 2. Logarithmic spiral channel of the LEExchanger.

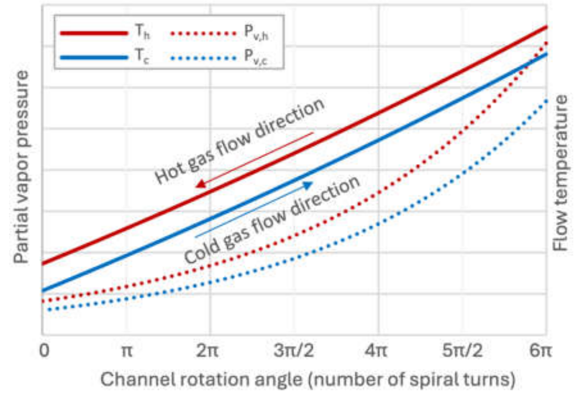

Figure 3. Flow temperature and vapor partial pressure distribution along LEExchanger flow paths.

The similarity of exponential changes in vapor saturation pressure and channel geometry maintains a state of flow saturation, ensuring stable LEE transition along the entire length of the channels and a constant minimum temperature difference between the flows. Figure 3 illustrates the parallel linear temperature distribution in the hot and cold flows along the logarithmic spiral channel, demonstrating the constant temperature difference between the flows. The change in partial vapor pressure in both LEExchanger channels is depicted by the similar exponential curves.

3. PCE transition around heat pipes

A computational model for a LEExchanger designed for heat recovery from an average commercial bakery oven was developed. The model, described in Table 1, balances the energy transferred from the hot flow to the cold flow via heat pipes:

$$Q_{h_{tot}} = Q_{hp_{lat}} = Q_{c_{tot}} \tag{3}$$

Table 1. LEExchanger pilot parameters.

Parameter Name	Value
Channel height	500 mm
Hot side inlet velocity	2 m s^{-1}
Channel temperature difference	10 K
Hot side outlet temperature	303 K
Cold side water inlet temperature	298 K
Atmospheric pressure	101,325 Pa
Hot side inlet mass flow rate	0.111 kg s^{-1}
Hot side inlet specific humidity	0.333 [-]

The process of condensation occurring on the exterior of the heat pipes, in the presence of non-condensable gases, contrasts with the evaporation inside the pipe, which occurs almost without impurities. Although these processes are similar, they are not identical. The contribution of sensible

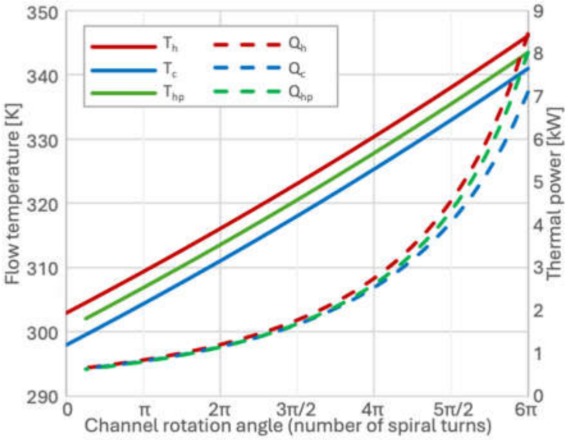

Figure 4. Temperature and energy transfer capacity of LEExchanger.

heat exchange from the dry components of the mixture on the outside results in a slight deviation of the heat transfer curve inside the heat pipe from the symmetry axis between the heat transfer lines in the hot and cold flows. This deviation is illustrated in Figure 4, highlighting the nuanced dynamics of heat transfer within the system.

4. Heat pipe distribution in channels

Control of latent energy transfer within the LEExchanger is tuned through strategic placement of heat transfer surfaces along the flow channels. This distribution is crucial, as the area of heat transfer (A_{ht}), must align proportionally to the change in mass flow resulting from ongoing phase transformation.

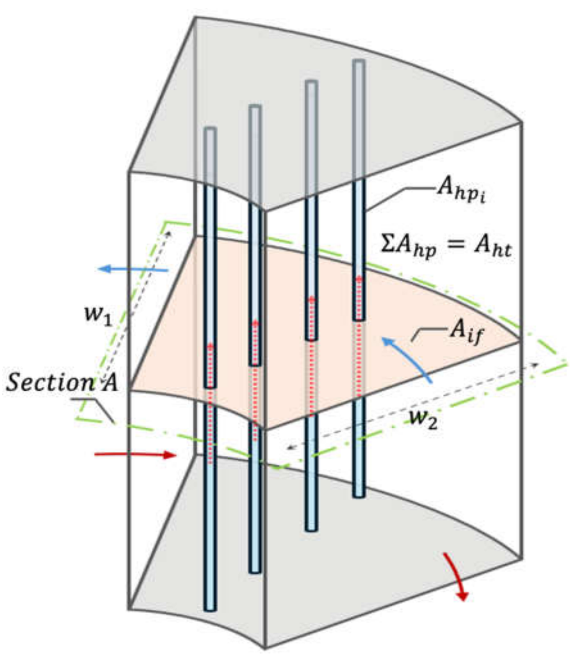

Figure 5. Heat pipes comprise the heat transfer area (A_{ht}) and interface surface (A_{if}) in hot and cold channels.

This relationship is described by the following equation:

$$\Delta\dot{Q}_{lat} = \dot{q} \times \Delta A_{ht} = L \times \Delta\dot{m}_v \quad (4)$$

The combined surface area of all heat pipes, positioned within the common interface surface, constitutes the total heat transfer surface (A_{hp}). To maintain stable phase transformation, the heat pipes must be strategically positioned along the interface surface (Figure 5) according to the distribution of condensation and evaporation processes, which are governed by the local partial vapor pressure:

$$\frac{\Delta A_{ht}}{\Delta A_{if}} = \frac{\Delta N_{hp} \times A_{hp}}{\Delta A_{if}} = C1 f(P_v) \quad (5)$$

The phase change mass transformation balance for the LEExchanger model was defined using Equations (3) and (4). The resulting condensate formation rate distribution for even distribution of phase transition along the channel is shown in Figure 6 and described by the following:

$$\frac{\Delta m_v}{\Delta A_{if}} = constant \quad (6)$$

It should be noted that the condensate formation rate inside the heat pipes exceeds the condensate formation rate outside of the heat pipes (in the hot channel). This is because the latent heat component of heat transfer inside the pipes surpasses the latent heat component outside of the pipes, where sensible heat transfer from non-condensable components also occurs.

Figure 6 also illustrates the deviation of the vapor formation rate inside the pipes from the average value vapor formation rate when assessing the formation processes within individual heat pipes.

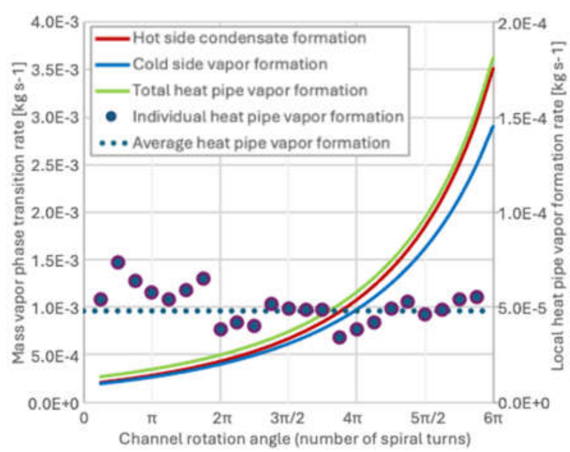

Figure 6. Mass rate of phase transition in channels and inside pipes with equal thermal power of pipes and in each pipe cross-section with a given design.

When using heat pipes with uniform thermal load and water-fill, such deviations can be compensated by adjusting the range of the circulating water mass fraction within the pipes and determining the minimum fluid fill volume of the pipes.

5. Mass transfer dynamics in and around heat pipes

Traditional criteria for evaluating the operation of heat pipes in sensible heat transfer focus on the heat transfer wall area and the thermal conduction capability. These factors are influenced by the wall's conductivity properties and the efficiency of phase change processes occurring inside the heat pipes. However, in a LEExchanger, heat pipes primarily facilitate LEE transitions between the outside and inside of the heat pipes. The efficiency of this heat transfer depends on maintaining the stable conditions that support these phase change processes. This requires providing and stabilizing the vapor pressures of both the hot and cold flow vapor outside the heat pipes, as well as the vapor inside the heat pipes, in accordance with the energy distribution throughout the LEExchanger (see Figure 7).

These phase transformations are accompanied by condensation of water on both the external and internal surfaces of the heat pipes, forming films which flow downward (Figure 8). The mass film formation rate of this condensate increases as more latent heat is transferred. However, this also creates additional resistance to thermal conductivity, which affects the temperatures of the flows outside and inside the heat pipe. Under these conditions, the optimal operation of the heat pipe depends on

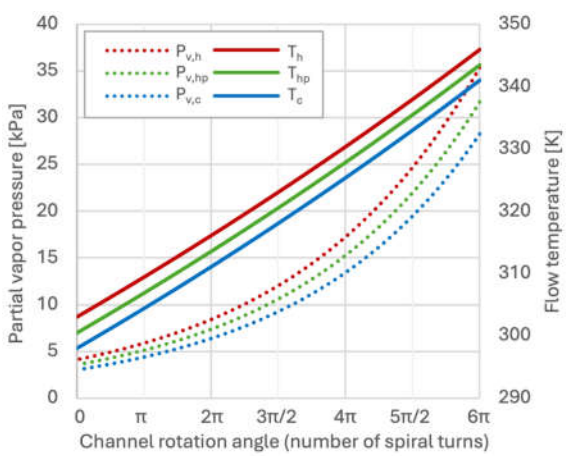

Figure 7. Vapor saturated partial pressure around and inside the heat pipes.

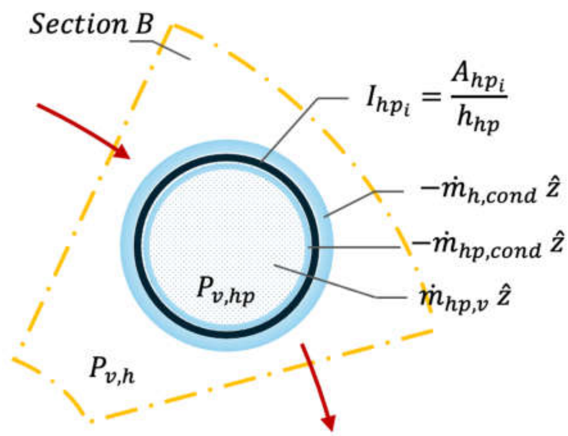

Figure 8. Condensate and vapor flow direction inside and outside of a heat pipe in the hot flow stream.

balancing the LEExchanger with the formation of corresponding resistances from the condensate films on the surfaces.

In order for heat pipes to operate efficiently within a LEExchanger, they must fulfill two critical conditions:

1. Effective Latent Heat Transfer: The heat pipes must efficiently transfer latent heat from the condensation occurring from the hot flow to the evaporation happening in the cold flow. This balance ensures that the heat flow from the hot side to the heat pipe is equal to the heat flow from the heat pipe to the cold side per Equation (3).

2. Stable Temperature Difference: A constant temperature difference between the hot and cold flows ($\Delta T_{h-c} = 5K$) must be maintained, which creates saturation conditions in the flow surrounding the heat pipe.

In this multi-stage system of phase transitions, the temperature difference between the hot and cold flows is distributed according to the thermal resistances present (Figure 9). The resistances include:

1. Hot Flow: Sensible cooling of the gas ($R_{h,sens}$), vapor condensation ($R_{h,cond}$), and cooling of the condensate film ($R_{h,f}$).

2. Heat Pipe: Conduction through the wall in the hot channel ($R_{hp,wh}$), evaporation from the condensate film ($R_{hp,f,evap}$), vapor transport along the central vertical heat pipe axis ($R_{hp,v}$), vapor condensation ($R_{hp,f,cond}$), and conduction through the wall to the cold channel ($R_{hp,w,c}$). Additionally, there is conduction along the heat pipe wall parallel to the central axis ($R_{c,f}$).

3. Cold Flow: Conduction through the water film ($R_{c,f}$), evaporation into the flow ($R_{c,evap}$), and limited sensible heating of the gas ($R_{c,sens}$).

As illustrated in Figure 9, the system of thermal resistances in the LEExchanger, represented by an electrical analog circuit, exhibits symmetry along an axis passing through the geometric center of the heat pipe. From this symmetry, it follows that the temperature drops between the external flows and inside of the heat pipe must be equal ($i.e., T_h - T_{hp} = T_{hp} - T_c$) to ensure saturation conditions at all stages of phase transition. For this to occur, all symmetric resistances within the system must be equal.

The most challenging resistances to balance are those associated with the condensate film in the hot flow, the water in the cold flow, and the condensate inside the pipe. These resistances must be equal to maintain proper thermal balance:

$$R_{h,f} = R_{hp,f,evap} = R_{hp,f,cond} = R_{c,f} \quad (8)$$

The mass rate of condensate film formation and the rate of water evaporation in the cold flow are practically equal due to the equal heat flow associated with these phase transitions. For instance, in the design under consideration, the rate of condensate formation in the hot flow is $0.00572\ mm\ s^{-1}$, while the rate of condensate film formation inside the pipe is $0.00612\ mm\ s^{-1}$.

However, the thickness of the film depends on the relationship between the processes of formation and transport along the pipe, calculated as follows:

$$\sigma = \frac{\dot{m}_{cond} - \dot{m}_{transport}}{\rho \times A_{hp}} \quad (9)$$

The rate of film transport, in turn, depends on the surface arrangement. Therefore, to achieve complete heat transfer balance and maintain saturation conditions, and thus stable operation of the heat pipes in the heat exchanger, the external and internal heat pipe wall should receive similar surface treatment, creating near-identical conditions for film mass transfer during the phase transition.

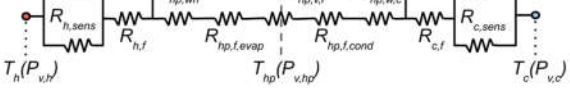

Figure 9. Electrical circuit analogy of thermal resistances in LEExchanger between the hot flow (red), heat pipe, and cold flow (blue).

6. Surface arrangement strategies for optimal heat pipe operation

In traditional approaches to optimizing heat pipe operation, the focus is primarily on extending the external surface area, often through the addition of fins or similar enhancements, to improve heat transfer efficiency. While this method is effective in many cases, it primarily addresses sensible heat transfer and does not fully account for the specific requirements of LEExchanger. As discussed in the previous sections, the optimal operation of heat pipes in LEExchangers necessitates a more holistic design approach, where both the external and internal surfaces of the heat pipe wall are carefully selected to facilitate simultaneous condensation and evaporation processes.

Over the past decade, significant research has been dedicated to enhancing heat transfer through the strategic arrangement of condensation surfaces. This research has largely focused on the condensing side of the wall, where various innovations, such as the use of hydrophobic and hydrophilic surface treatments, have been explored. These solutions, while effective in certain contexts, have not yet been fully developed for specific technological applications and often remain prohibitively expensive. This makes them unsuitable for cost-sensitive systems like the LEExchanger, whose primary application is in waste heat recovery—a field where cost efficiency is crucial.

A particularly promising solution involves the use of grooved surfaces. This approach has been proven effective on both external and internal walls of heat pipe, facilitating both condensation and evaporation processes. The analysis procedure for the coupled condensing/evaporating films flowing down along the outer and inner walls of a vertical grooved tube has shown the effectiveness of this method, as performed by researchers in [3]. In traditional heat pipe research, the use of a grooved inner surface has been shown to efficiently transport condensed liquid back to the evaporator section, ensuring continuous and optimal operation. The primary advantage of grooved wick structures lies in their cost-effectiveness, as the grooves can be formed as part of the extrusion process, making them a practical choice for gravity-neutral or gravity-aided applications.

7. Conclusion

This study has demonstrated the critical role of heat pipes in optimizing the performance of Latent Energy Exchangers (LEExchangers) for waste heat recovery. Unlike traditional heat transfer methods that focus on extending external surface areas through fins and other enhancements, the LEExchanger requires a more comprehensive design approach. The research highlights the importance of carefully arranging both the internal and external surfaces of heat pipe walls to support efficient phase transitions, particularly condensation and evaporation. Among various surface arrangement strategies, the use of grooved surfaces on both sides of the heat pipe wall has proven to be highly effective. This solution, which has been validated in [3], not only optimizes heat transfer but also aligns with the cost-sensitive nature of waste heat recovery applications. The dual-sided grooved design offers balanced, stable operation by enhancing the management of condensing and evaporating films within the heat pipe, ultimately contributing to the overall efficiency of the LEExchanger system.

8. ACKNOWLEDGEMENTS

The authors are grateful to the U.S. Department of Energy (DOE) for their generous support. This material is based upon work supported by the DOE under DE-EE0011218.

References

[1] H. Skop, D. Klammer, and D. Brega, Heat-mass exchanger with equilibrium transfer of latent energy via heat pipes. in Joint 21st International Heat Pipe Conference (IHPC) and 15th International Heat Pipe Symposium (IHPS), 2023. Melbourne, Australia.

[2] H. Skop, Patent No. 11,703,285: Apparatus and Method for Latent Energy Exchange. United States Patent, 2023.

[3] I.S. Park and D.H. Choi, Heat- and mass-transfer analysis for the condensing film flow along a vertical grooved tube. International Journal of Heat and Mass Transfer, 2001. 44(22): p. 4277.

Paper ID 055

Spreading Thermal Resistance of Boiling-driven Heat Spreader

Jung Chan Moc[1], Su Yoon Doh[1] and Jungho Lee[1*]

[1] *Department of Mechanical Engineering, Ajou University,*
206 Worldcup-ro, Yeongtong-gu, Suwon, Gyeonggi-do 16499, Republic of Korea
**Corresponding author's email address: jungholee@ajou.ac.kr*

Abstract

As the heat generation in electronic devices increases while their size decreases, the challenge of effective thermal management is becoming more significant. Boiling-driven heat spreaders, which operate through boiling rather than evaporation and do not require wick structures, offer a novel approach with higher operational limits. Despite the potential advantages, existing research on boiling-driven heat spreaders has focused primarily on their axial thermal performance, with less attention given to their heat spreading capabilities. However, in evaluating heat spreaders' thermal performance, axial heat transfer and heat spreading are crucial factors. In this study, we fabricated a boiling-driven heat spreader and quantified its heat spreading performance by measuring spreading thermal resistance and temperature uniformity. The fabricated boiling-driven heat spreader achieved a remarkably low spreading thermal resistance of 0.1 K/W at high heat fluxes of 300 W/cm². Additionally, the temperature uniformity of the condenser section showed significant improvement compared to a copper plate of the same dimensions across all heat flux ranges. These results confirm that the boiling-driven heat spreader has excellent heat transfer capabilities and effectively spreads heat evenly across the cold side, indicating that it is a highly efficient heat spreader overall.

Keywords: Spreading Thermal Resistance; Boiling-driven Heat Spreader; Thermal Performance; Electronics Cooling

1. Introduction

As the heat generation in electronic devices increases while they become more compact, the heat flux within these devices is rapidly rising. Effective thermal management is essential to address this issue. A heat spreader, which efficiently spreads high heat flux to a heat sink, plays a crucial role in this process. A common example of such a device is the vapor chamber, widely used for cooling electronic equipment. The vapor chamber comprises a container, a wick structure, and a working fluid. It operates by evaporating the working fluid at the hot side and condensing it at the cold side, with the fluid circulating back through the wick structure. However, the wick structure relies on capillary action to circulate the working fluid, which can lead to dry-out at heat fluxes exceeding 150 W/cm². This dry-out phenomenon hinders fluid circulation, drastically reducing thermal management performance and potentially leading to failure. Additionally, the capillary action is affected by gravity, causing performance variations depending on the orientation of the vapor chamber.

To overcome these challenges, boiling-driven heat spreaders, which do not require a wick structure, have recently gained attention. These heat spreaders operate through boiling and utilize the bubble pumping effect to circulate the working fluid effectively. Unlike vapor chambers, this mechanism allows boiling-driven heat spreaders to maintain low thermal resistance without dry-out, even at high heat fluxes. Moon et al. [1] evaluated the thermal performance of boiling-driven heat spreaders under various filling ratios, operating orientations, and temperatures. Wang et al. [2] investigated the impact of heat spreader thickness on thermal performance. Lim et al. [3] explained the operating mechanism of boiling-driven heat spreaders through flow visualization.

However, existing studies have not sufficiently evaluated the spreading thermal resistance and temperature uniformity index (TUI) of the condenser section in boiling-driven heat spreaders. Spreading thermal resistance is a crucial metric for assessing the performance of a heat spreader, indicating how effectively heat is spread and dissipated. The temperature uniformity index (TUI) of the condenser section measures how evenly heat is spread across the heat sink, with higher uniformity leading to more efficient heat dissipation. Vapor chambers have traditionally been evaluated using these metrics to assess their thermal management performance. As a new concept in heat spreaders, boiling-driven heat spreaders require a thorough evaluation of their operating characteristics and thermal performance. In this study, we quantitatively evaluated the thermal management and heat spreading performance of boiling-driven heat spreaders using the metrics of spreading thermal resistance and temperature uniformity index (TUI), which have been applied in previous heat spreader performance assessments.

2. Fabrication and Apparatus

2.1. Boiling-driven heat spreader

Figure 1. Boiling-driven heat spreader.

Figure 1 shows the boiling-driven heat spreader used in this study. It is a rectangular structure composed of two copper plates with dimensions of 90 mm × 90 mm × 2 mm. The boiling section covers the condenser section and is sealed by welding. A 25 mm × 25 mm boiling enhancement coating was applied to the center of the boiling section to enhance boiling performance. Degassed water was used as the working fluid, and 4.1g was injected.

2.2. Test setup

A heater assembly was attached to the boiling section to apply heat to the boiling-driven heat spreader. This assembly consisted of a 10 mm × 10 mm × 3 mm copper block and a 10 mm × 10 mm ceramic heater, with a T-type thermocouple inserted into the center of the copper block to measure the junction temperature. The heater assembly was soldered to the center of the outer wall of the boiling section and insulated with epoxy to minimize heat loss. The test setup is shown in Figure 2(a). The condenser section of the boiling-driven heat spreader was attached to an aluminum cold plate using thermal grease, and 40°C water was circulated through the cold plate using a thermostatic bath. Nine T-type thermocouples were inserted into the cold plate to measure the temperature of the condenser section. performance test setup

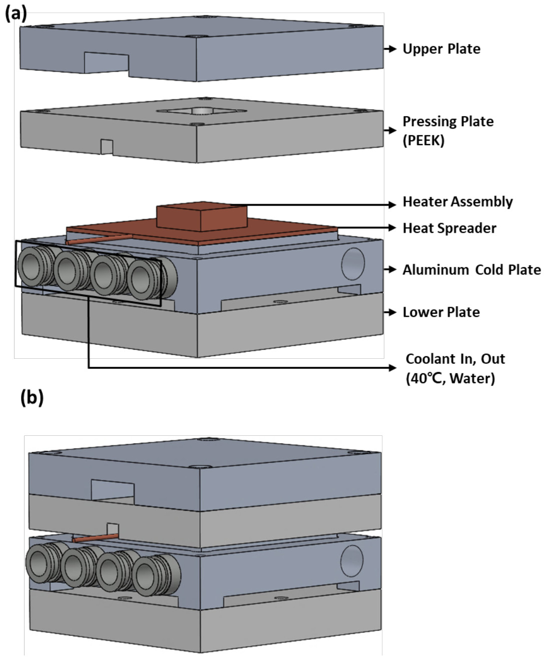

Figure 2. Boiling-driven heat spreader thermal performance test setup. (a) Exploded view. (b) Assembled view.

Additionally, the surrounding area of the boiling-driven heat spreader was insulated with a PEEK housing to minimize heat loss.

2.3. Thermal performance test

The experiment was conducted by assembling the test setup, as shown in Figure 2(b). Power was supplied to the ceramic heater via a power supply, and temperature data was collected using 10 thermocouples. The experiment gradually increased the heat flux from 2 W/cm² to 300 W/cm². The steady-state was confirmed when the temperature difference over 50 seconds, measured by the thermocouple inserted into the copper block, was less than 0.1°C between the initial and final 25 seconds. The experiment continued with further increases in heat flux. The experiment was conducted in four different orientations: when the boiling-driven heat spreader was positioned horizontally with the boiling section facing up ("horizontal face up"), horizontally with the boiling section facing down ("horizontal face down"), vertically with the inlet aligned parallel to the ground ("vertical right"), and vertically with the inlet perpendicular to the ground ("vertical up"). To ensure repeatability, each orientation was tested twice, resulting in eight experiments.

3. Experimental results

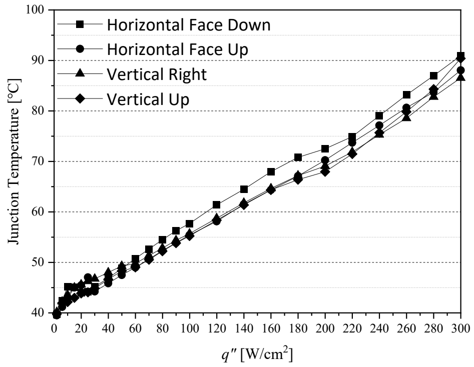

Figure 3. Junction temperature of the Boiling-Driven Heat Spreader by operating orientation.

The junction temperature of the boiling-driven heat spreader is shown in Figure 3. with the average values obtained from two repeated experiments for each operating orientation. The junction temperature increased as the heat flux increased, reaching a maximum of 91°C at 300 W/cm² in the horizontal face-down orientation. In contrast, the vertical right orientation recorded the lowest junction temperature at 86.5°C under the same heat flux, showing a difference of about 4.5°C between the two orientations, indicating minimal variation in junction temperature based on orientation. In all orientations, the junction temperature remained below 79°C at a heat flux of 240 W/cm², which is lower than the allowable temperature range for CPUs and GPUs (80–85°C). This suggests that the boiling-driven heat spreader can be effectively used for cooling high-heat-flux electronic devices.

The spreading thermal resistance of the boiling-driven heat spreader is presented in Figure 4. The results for each orientation are shown in Figure 4(a). The working fluid within the boiling-driven heat spreader operates in a very constrained environment with a gap of 0.8 mm. Due to this limited space, the wall superheat required for boiling increases. This leads to the spreader operating primarily through micro-convection and evaporation at low heat fluxes, resulting in relatively high axial thermal resistance. However, as nucleate boiling initiates, thermal resistance decreases, and at heat fluxes above 40 W/cm², the spreading thermal resistance drops below 0.2 K/W for all orientations. In particular, the vertical up orientation recorded a very low spreading thermal resistance of 0.088 K/W at a heat flux of 200 W/cm². The standard deviation of thermal resistance across all orientations was 0.006 K/W, indicating consistent performance regardless of orientation.

Figure 4(b). compares the performance of the boiling-driven heat spreader with that of a copper plate of the same dimensions under identical test conditions. The results demonstrate that the boiling-driven heat spreader exhibits lower thermal resistance at heat fluxes above 30 W/cm², with approximately 43% lower spreading thermal resistance than the copper plate, indicating superior heat dissipation performance. The Temperature Uniformity Index (TUI) is shown in Figure 5. The TUI of the boiling-driven heat spreader was lower than that of the copper plate at all heat fluxes except 2 W/cm², indicating a more uniform temperature distribution in the condenser section of the boiling-driven heat spreader compared to the copper plate. Particularly in the range above 200 W/cm², the TUI remained stable without significant changes. This stability is attributed to the bubble pumping phenomenon, where vapor bubbles escape the boiling surface, immediately displacing the limited volume of working fluid and supplying new liquid to the boiling enhancement surface.

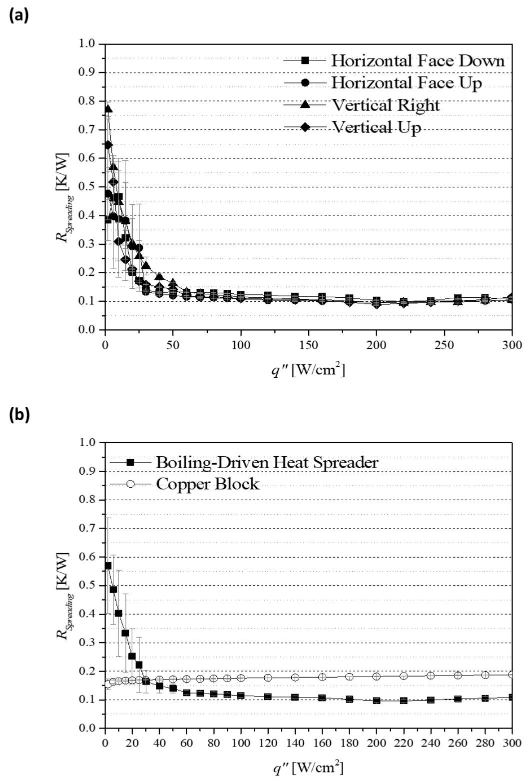

Figure 4. Spreading thermal resistance of the Boiling-Driven Heat Spreader. (a) Different orientations. (b) Comparison between the boiling-driven heat spreader and copper block.

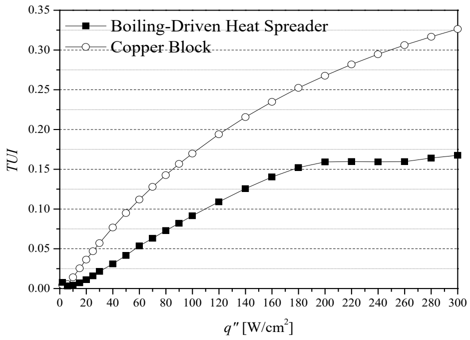

Figure 5. Temperature uniformity index comparison between the boiling-driven heat spreader and copper block.

As a result, the boiling-driven heat spreader not only maintains low thermal resistance at high heat fluxes but also ensures uniform temperature distribution in the condenser section, making it ideal for high-performance thermal management.

4. Conclusions

In this study, a boiling-driven heat spreader was fabricated, and an analysis of spreading thermal resistance and temperature uniformity index (TUI) was conducted, focusing on aspects that had not been previously evaluated. The spreading thermal resistance achieved a low value of approximately 0.1 K/W at high heat fluxes above 100 W/cm², regardless of the operating orientation. The TUI was also found to be lower than that of a copper plate with the same dimensions across all heat fluxes above 6 W/cm², and it remained stable with almost no change at high heat fluxes exceeding 200 W/cm² due to the active circulation of the working fluid. Consequently, this study confirmed that the boiling-driven heat spreader maintains low thermal resistance and evenly distributes heat to the heat sink even at high heat fluxes. Therefore, the boiling-driven heat spreader is expected to be effectively applied to thermal management in electronic devices with heat fluxes exceeding 200 W/cm².

5. ACKNOWLEDGEMENTS

This work was supported by a National Research Foundation of Korea (NRF) grant funded by the Ministry of Science and ICT, Korea (No. NRF-2020R1A2C3008689).

References

[1] Moon. J. H, Fadda. D, Shin. D. H, Kim. J. S, Lee. J, You. S. M, Boiling-driven, wickless, and orientation-independent thermal ground plane. International Journal of Heat and Mass Transfer, Vol. 167, 120817.

[2] Wang. X, Moon. J. H, Fadda. D, Shin. D. H, Lee. J, You. S. M, Boiling-driven, wickless, and orientation-independent thermal ground plane. International Journal of Heat and Mass Transfer, 167, 120817.

[3] Lim. H, Doh. S. Y, Shin. D. H, You. S. M, Lee. J, Thermal performance of a boiling-driven heat spreader using passive flow control. Case Studies in Thermal Engineering, 41, 102604

Paper ID 058(S8)

The aluminum boiling-driven heat spreader

Su-Yoon Doh[1], Junyoung Choi[1], Seung M. You[2] and Jungho Lee[1*]

[1] *Department of Mechanical Engineering, Ajou University, Suwon 16499, Republic of Korea*
[2] *Department of Mechanical Engineering, The University of Texas at Dallas, TX 75080, USA*
[*] *Corresponding author email address: jungholee@ajou.ac.kr*

Abstract

This study explores the development and performance of an aluminum boiling-driven heat spreader (Al-BDHS) that offers enhanced capability for high-heat-flux applications compared to typical aluminum heat spreaders in electronic device cooling. The Al-BDHS, lighter and more cost-effective than its copper counterpart, integrates easily with aluminum heat sinks and operates through a bubble pumping mechanism on a microporous-coated surface, eliminating the need for a wick and maintaining performance regardless of orientation. Using acetone as the working fluid, tests demonstrated that optimal boiling heat transfer is achieved when the coating thickness is approximately four times the diameter of the aluminum powder used. The Al-BDHS maintained consistent thermal performance, even at heat fluxes as high as 150 W/cm², without the risk of dryout. This study provides valuable insights into advanced thermal management strategies for high-performance electronic devices.

Keywords: boiling-driven; aluminum; heat spreader; Thermal performance

1. Introduction

The increasing power demands of high-performance electronic devices necessitate advanced thermal management strategies [1]. Among these, the boiling-driven heat spreader (BDHS) has emerged as a promising solution, capable of operating at higher heat fluxes than conventional evaporation-driven heat spreaders [2]. Unlike traditional systems, the BDHS maintains consistent performance regardless of orientation, thanks to a bubble pumping mechanism facilitated by boiling on a microporous-coated surface. Notably, this device does not require a wick, as the bubble pumping ensures continuous delivery of the working fluid under high heat flux conditions, effectively preventing dryout.

Previous studies have focused on developing a BDHS using copper (Cu-BDHS); however, this study introduces an aluminum version (Al-BDHS). Aluminum offers significant advantages over copper, being lighter, more cost-effective, and easily integrated with widely used aluminum heat sinks.

In this study, we investigate the boiling heat transfer performance of the microporous coating, a critical component of the aluminum boiling-driven heat spreader (Al-BDHS), using acetone as the working fluid. The fabricated Al-BDHS, with an optimized coating, demonstrates enhanced heat-spreading performance and orientation-independent operation. These findings provide valuable insights into advanced thermal management solutions for high-heat-flux applications in electronic device cooling.

2. Boiling-driven Heat Spreader

Figure 1 illustrates the operational mechanism of the boiling-driven heat spreader, which consists of a flat container with a microporous coating on the heating surface. When the surface is heated, boiling initiates, leading to an increase in bubble pressure that expels the working fluid to the sides. This continuous boiling process generates a bubble pumping effect, allowing the condensed working fluid from the sides to be replenished on the heating surface during operation [3].

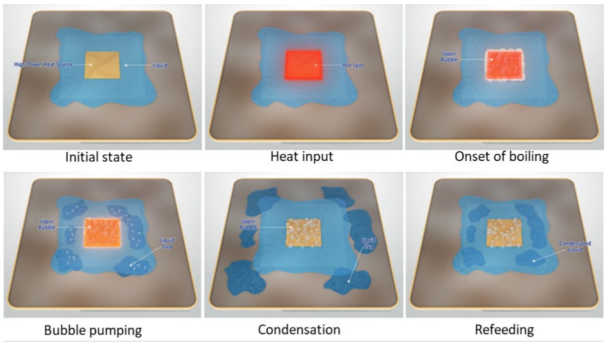

Figure 1. Schematic diagram of the working mechanism of the boiling-driven heat spreader

Figure 2 compares the thermal performance of the vapor chamber and the boiling-driven heat spreader. The vapor chamber relies on evaporative heat transfer and functions optimally at lower heat fluxes. However, it suffers from performance variability due to its wick-based fluid circulation system and is prone to dryout at higher heat fluxes.

In contrast, the boiling-driven heat spreader, which has a wickless design and is engineered for efficient operation around 20 W/cm², maintains consistent performance even at high heat fluxes. Its simpler structure and the proper filling ratio of the working fluid effectively eliminate the risk of dryout.

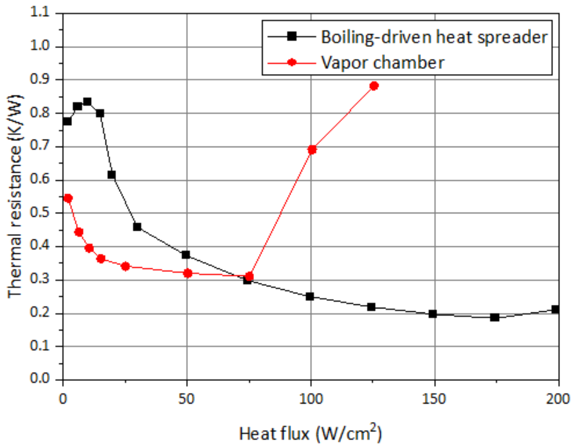

Figure 2. Thermal resistance of the boiling-driven heat spreader and typical heat spreader (vapor chamber)

3. Aluminum Microporous Coating

Enhancing boiling heat transfer in the boiling-driven heat spreader is crucial. To achieve this, a microporous coating was fabricated using brazed aluminum powder. The brazing process for the microporous coating was carried out using equipment that shown in Figure 3. The coating height was precisely controlled by combining a precision height gauge with a minimum scale of 10 µm and a machined scraper. The coating was then formed by heating it to approximately 600°C in a vacuum furnace.

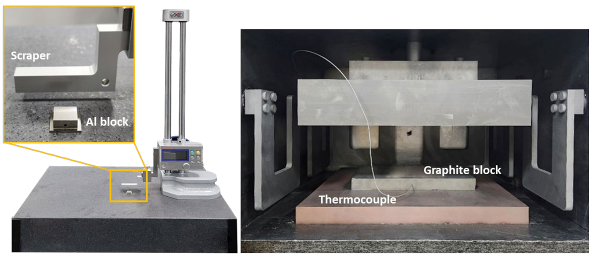

Figure 3. Coating fabrication equipment and high vacuum furnace

The detailed morphology of the microporous coating, made from 60 µm diameter aluminum particles, was captured using a scanning electron microscope (SEM). The pore diameter is approximately 50 µm, and the porous structure facilitates the efficient supply of the working fluid to the heated surface through strong capillary action, as shown in Figure 4. Additionally, the numerous microscale cavities where boiling occurs significantly enhance boiling heat transfer.

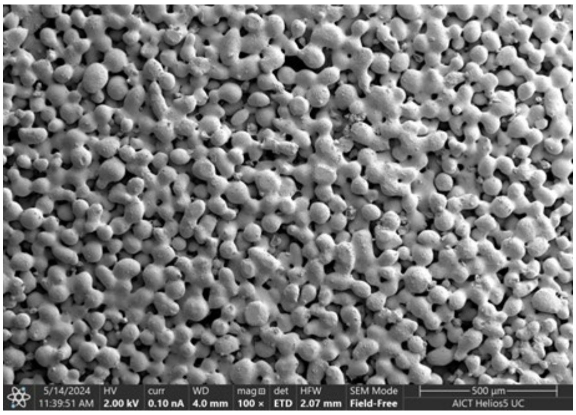

Figure 4. SEM Image of the coating with brazed aluminum particles

Pool boiling tests were conducted using acetone as the working fluid to determine the optimal coating thickness by comparing boiling heat transfer performance based on the powder's diameter and the coating's thickness. Acetone was selected for its excellent chemical compatibility with aluminum [4]. The test results confirmed that optimal performance is achieved when the coating thickness is approximately four times the diameter of the powder. Specifically, the tests indicated that a coating thickness of 240 µm provided the best boiling heat transfer performance. As shown in Figure 5, using the 240 µm coating reduces wall superheat by more than 10°C compared to a plain surface at the same heat flux, and increases the critical heat flux (CHF) from 48 W/cm² to 62 W/cm². These results align with previous studies, which found that the pool boiling performance of microporous structures made from particles is optimal when the coating thickness is approximately 3 to 5 times the particle diameter [5].

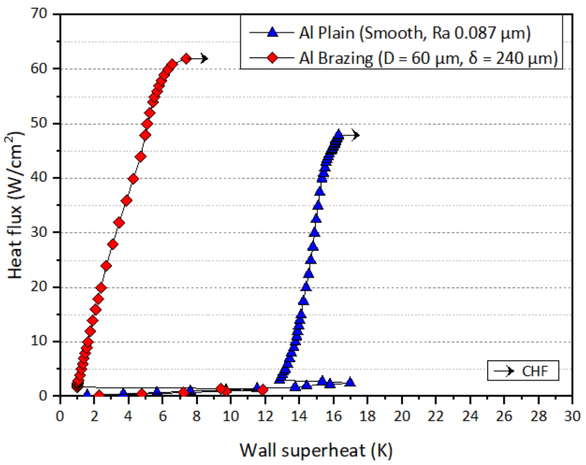

Figure 5. Pool boiling test results for aluminum plain and brazing surface

4. Aluminum boiling-driven heat spreader

As depicted in Figure 6, the test sample was machined from aluminum, with an area of 90 mm² and a thickness of 3 mm. An aluminum plate with a 240 μm thick coating, optimized for the best boiling heat transfer performance (boiling side), was diffusion bonded to a plate with machined ribs (condensation side).

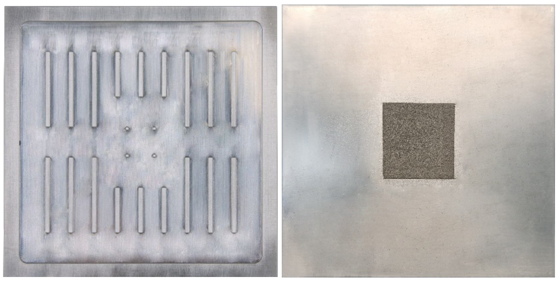

Figure 6. Typical picture of the aluminum boiling-driven heat spreader before diffusion bonding

The container was maintained at a vacuum of 10^{-3} hectopascals using a rotary pump and a turbo pump, and acetone, from which non-condensable gases (NCGs) had been removed by heating for one hour, was injected. For the heat transfer performance test of the Al-BDHS, a 10 x 10 mm² ceramic heater and an aluminum block were soldered to the boiling side, and the hot side temperature (T_h) was obtained by measuring the center temperature of the aluminum block.

5. Results

The test specimen was attached to the water-cooled aluminum cooling plate of the thermal performance test apparatus using thermal grease to minimize contact thermal resistance, and the cold side temperature (T_c) was obtained by measuring the temperature of the aluminum cooling plate.

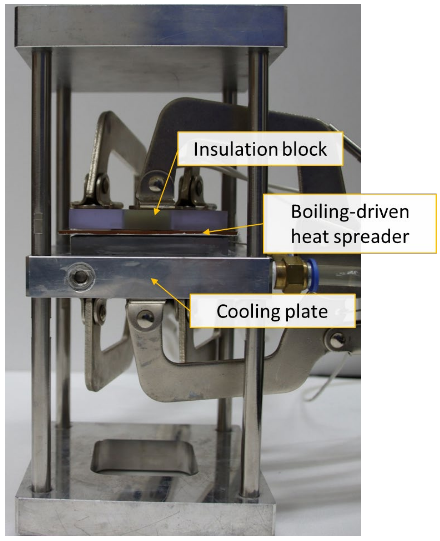

Figure 7. Thermal performance test apparatus

The thermal resistance of Al-BDHS was calculated using the hot surface temperature and the cold surface temperature as described in Equation 1.

$$T_{\mathrm{h.s}} = T_{\mathrm{h}} - \frac{t_{al}}{k_{\mathrm{al}} A_{al}} \times Q - \frac{t_{solder}}{k_{solder} A_{solder}} \times Q$$

$$T_{\mathrm{c.s}} = T_{\mathrm{h}} - \frac{t_{al}}{k_{\mathrm{al}} A_{al}} \times Q - \frac{t_{grease}}{k_{grease} A_{grease}} \times Q$$

$$R_{BDHS} = \frac{T_{\mathrm{h.s}} - T_{\mathrm{c.s}}}{Q} \tag{1}$$

The test results are shown in Figure 8, where it can be seen that the thermal resistance significantly decreased after starting operation at 10 W/cm². According to the pool boiling test on the coating shown in Figure 5, it was observed that the initiation of boiling was difficult due to the characteristics of acetone, which has a small contact angle. However, in the case of Al-BDHS, the sufficient removal of NCGs and the injection under high vacuum conditions allowed for easier initiation of boiling.
As the heat flux increased, the thermal resistance gradually rose. This increase is attributed to the low surface tension of acetone, which reduces capillary forces and makes it difficult to supply acetone to the heated surface. Finally, dryout occurred at 100 W/cm².

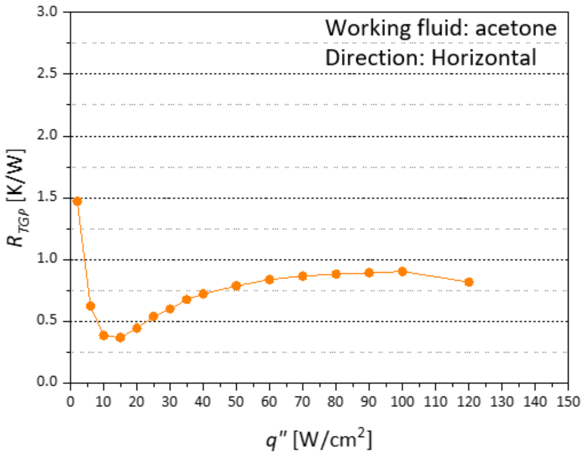

Figure 8. Thermal performance of Al-BDHS

6. Conclusions

This study explored the thermal performance of an aluminum boiling-driven heat spreader (Al-BDHS) optimized for high-heat-flux electronic cooling. The Al-BDHS, featuring a 240 µm thick microporous coating, demonstrated improved boiling heat transfer, reducing wall superheat and increasing critical heat flux (CHF). Tests showed that the device maintained low thermal resistance at heat fluxes starting from 10 W/cm², with easier boiling initiation due to effective NCG removal and high vacuum conditions. However, thermal resistance gradually increased at higher heat fluxes, leading to dryout at 100 W/cm², primarily due to acetone's low surface tension and latent heat.

If further studies are conducted on coatings with higher permeability or fluids with higher latent heat, the performance of the Al-BDHS could be further enhanced. The Al-BDHS presents a promising solution for advanced thermal management in high-power electronics.

7. ACKNOWLEDGEMENTS

This work was supported by the Innovative Energy Efficiency R&D Program of the Korea Institute of Energy Technology Evaluation and Planning (KETEP), grant funded by the Ministry of Trade, Industry & Energy, Korea. (Grant No. 20212020800270).

References

[1] Bar-Cohen, A., & Wang, P. (2012). Thermal management of on-chip hot spot.

[2] Moon, J. H., Fadda, D., Shin, D. H., Kim, J. S., Lee, J., & You, S. M. (2021). Boiling-driven, wickless, and orientation-independent thermal ground plane. International Journal of Heat and Mass Transfer, 167, 120817.

[3] Wang, X., Moon, J. H., Fadda, D., Shin, D. H., Lee, J., & You, S. M. (2022). Experimental investigation of heat spreading in a wickless and ultrathin thermal ground plane. Case Studies in Thermal Engineering, 31, 101799.

[4] Wallin, P. (2012). Heat Pipe, selection of working fluid. *Heat and Mass Transfer Project Report*, 1-7.

[5] Sarangi, S., Weibel, J. A., & Garimella, S. V. (2015). Effect of particle size on surface-coating enhancement of pool boiling heat transfer. *International Journal of Heat and Mass Transfer*, *81*, 103-113.

Paper ID 061(S6)

Thermal performance of the geothermal thermosyphon for snow melting on paved roads

Hyunmuk Lim, Seokjin Lee, Sukkyung Kang, and Jungho Lee*

Department of Mechanical Engineering, Ajou University, Suwon, Republic of Korea
**Corresponding author email address: jungholee@ajou.ac.kr*

Abstract

This study suggests a geothermal thermosyphon using a stainless-steel container and acetone. A thermosyphon experimental setup was designed to demonstrate the thermal resistance of geothermal thermosyphon at the underground temperature of 15°C. The thermal resistance of the experimental result is 0.08 K/W. The geothermal thermosyphon was numerically evaluated for its snow removal performance. The numerical simulations are performed on installation parameters of a full-scale geothermal thermosyphon. The numerical results show the thermal performance in heat release and heat flux on the road surface. These results indicated the trends in thermal performance for snow removal. The optimal installation design could be achieved when thermosyphons are installed close to the pavement surface, with narrow spacing between pipes and proper insulation to minimize heat loss. This paper provides valuable guidelines for designing and implementing geothermal thermosyphon for snow melting infrastructure, contributing to environmentally friendly and efficient snow management practices.

Keywords: Snow removal; Road pavement; Geothermal energy; Thermosyphon

1. Introduction

Snow melting on paved roads is essential from an economic, social, and industrial perspective. Chemical snow melting methods are widely used, but those have problems such as environmental pollution and accelerated corrosion of roads and vehicles. In addition, electric heating methods have the disadvantages of high energy consumption and difficulties in application outside of cities. So, this research introduces a thermosyphon technology for melting snow by utilizing subterranean heat [1]. Experimental and numerical methods were used to verify the performance of snow melting using geothermal energy. Experiments were conducted to demonstrate a lab-scale geothermal thermosyphon. The experimental results determined the geothermal thermosyphon's thermal resistance and effective thermal conductivity. Numerical studies were conducted to evaluate realistic installation conditions for the geothermal thermosyphon's spacing, depth, and insulation [2]. As a result, this study shows the maximum heat flux that can heat a paved road with underground heat and the difference in performance based on installation conditions. The results of this study could predict the performance of snow-melting devices that can operate independently of geographical location, providing new ideas for the commercialization of thermosyphon technology utilizing renewable energy.

2. Geothermal snow removal thermosyphon

The thermosyphon was designed with stainless steel (ASTM S30400), which is highly corrosion resistant; acetone, chemically compatible with stainless steel, was chosen as the working fluid [3]. Ammonia is the commonly used working fluid for geothermal thermosyphons, but in case of leakage, it can cause severe toxicity to humans [4]. Acetone, which was used in this study, is a promising alternative as a working fluid for geothermal thermosyphons.

2.1. Experimental approach

Experimental studies were performed to demonstrate the feasibility and thermal performance of the thermosyphon. An experimental test rig was made, as shown in Figure 1. The experimental conditions considered the seasonal and geothermal temperatures in Suwon, Republic of Korea. The temperature in the basement is always 15 degrees, regardless of outside weather factors, from a depth of 5 m to 200 m. So, the amount of heat supplied through the band heater was increased until the temperature of the evaporator section reached 15°C. The temperature of the condenser section was kept constant temperature at 0°C through a water bath. The whole experimental setup was well insulated, and the energy balance in the experiment was at least 99%.

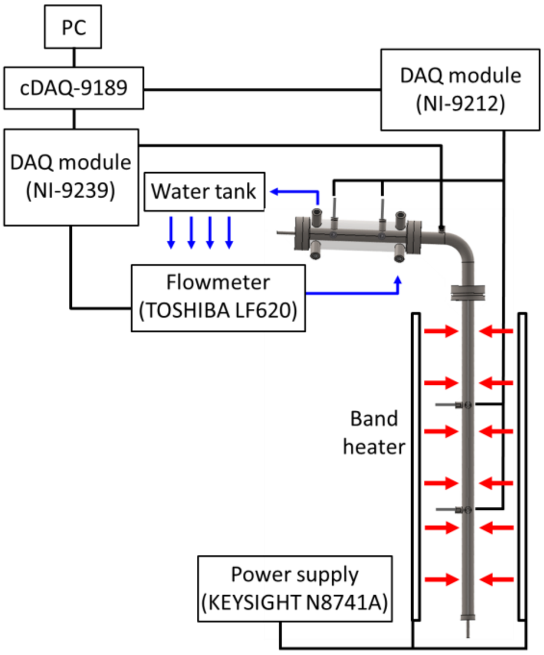

Figure 1. Schematics of the lab-scale experimental setup for geothermal thermosyphon

2.2. Numerical approach

As shown in Figure 2, the thermosyphon region was modeled with a condensation section of 3 meters and an evaporation section of 15 meters. Three thermosyphons are installed at the borehole in the center of the computational model. The temperature for the wall condition is a depth-dependent temperature change. The roads' surface is assumed to be convection heat transfer with -2°C of the air temperature and 50 W/m^2·K of the heat transfer coefficient. The computational grids are generated with hexahedral conformal grids, as shown in Figure 2(b). The grids were determined to be about 2,300,000 by the grid-independent test.

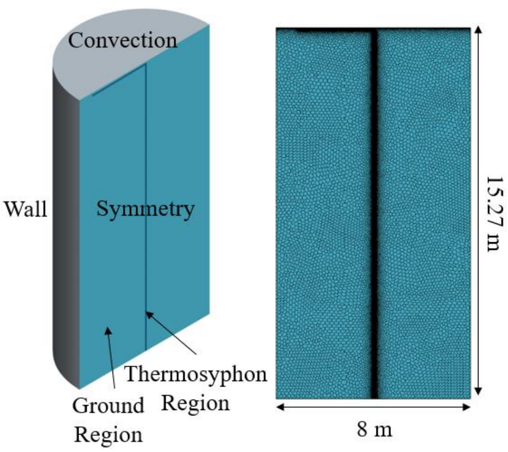

(a) (b)

Figure 2. (a) Boundary conditions of the numerical geometry, (b) Grid of the numerical model for geothermal thermosyphon

The parameters of geothermal thermosyphon devices were the burial depth from the pavement surface, burial spacing within the pavement, and thermosyphon distance within the borehole. Table 1 summarizes the specifications of the numerical studies conducted.

Table 1. Specifications of the geometrical parameters of the geothermal thermosyphons

No.	Depth (mm)	Spacing (mm)	Distance (mm)
1			50
2		100	150
3			250
4			50
5	70	200	150
6			250
7			50
8		400	150
9			250

3. Data reduction

The heat transfer performance can be expressed as Equation 1 with the wall temperature difference of the temperature at the evaporator and condenser and the input power [5].

$$R_{GT} = \frac{T_H - T_L}{Q} = \frac{T_H - T_L}{IV} \qquad (1)$$

Thermal resistance, obtained from the temperature difference and the amount of heat applied, allows us to evaluate how easily the heat is transferred. Temperature was measured until the average temperature difference over 10 minutes converged to within 0.2°C. The heat can be calculated by the voltage and current applied to the band heater, and the energy balance was calculated with the heat output through the cooling jacket. Specifically, the measurement error of temperature using T-type thermocouples is 0.4%, and the voltage and current accuracy are 0.2% and 0.1%, respectively. The experimental uncertainties could be calculated with equation 2 [6]. The uncertainty analysis of this study was performed on the thermal resistance. The maximum expanded relative uncertainty of the thermal resistance is 6.9%.

$$\delta R = \sqrt{\sum_{i=1}^{n} \left(\frac{\partial R_i}{\partial x_i} \delta x_i \right)^2} \qquad (2)$$

4. Results and discussions

The thermal performance of the newly designed stainless steel-acetone thermosyphon was experimentally verified over a geothermal temperature range. The thermal performance was tested by maintaining the condenser temperature through cooling water at 0°C. The temperatures of the condenser, evaporator, and condenser sections were verified by increasing the heat applied to the band heater. The experiments were performed until the evaporator temperature exceeded 15°C, and the experimental results are shown in Figure 3. According to the input power, the evaporator and condenser temperatures indicate that the thermosyphon can operate stably in the temperature range of 0°C to 15°C. In particular, the acetone inside the thermosyphon can transfer heat from the high-temperature section to the low-temperature section through repeated evaporation and condensation, and its performance was verified.

Numerical analysis predicted the snow removal device's performance according to the thermosyphon's installation configuration. A snow removal equipment using thermosyphons absorbs heat from the ground. The snow removal equipment using thermosyphons absorbs heat from the ground by installing multiple thermosyphons within a single borehole. Therefore, the distance between each thermosyphon inside the borehole affects the surrounding ground and the thermosyphon's temperature.

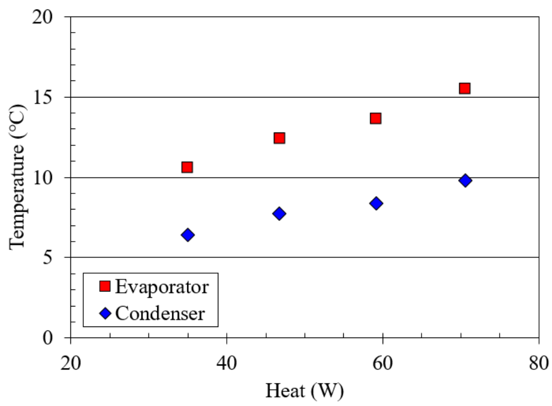

Figure 3. Experimental results of the geothermal thermosyphon

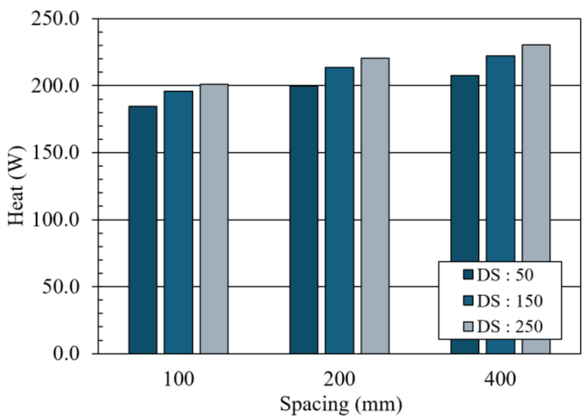

Figure 4. Numerical results on the heat transmission of the geothermal thermosyphon

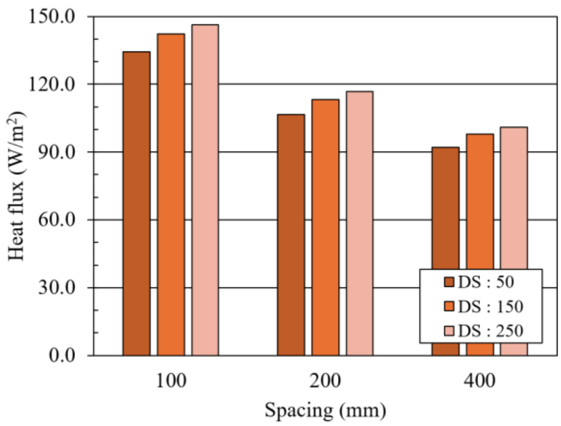

Figure 5. Numerical results on the maximum heat flux of geothermal thermosyphon

Figure 4 and Figure 5 show all the numerical results regarding the spacing of thermosyphons inside the borehole. As evident from the analysis results, in all conditions, the heat transmission and maximum surface heat flux tend to increase as the spacing of the heat thermosyphon increases. For example, under the condition where the burial depth in the road pavement is 70 mm, and the burial spacing is 100 mm, increasing the installation distance of thermosyphons inside the borehole from 50 mm to 250 mm results in an increase in heat supply capacity from 184.6 W to 201.1 W. The maximum heat flux increases from 134.3 W/m² to 146.2 W/m².

5. Conclusions

A thermosyphon's design and thermal performance utilizing underground heat have been studied experimentally and numerically. The stainless steel-acetone thermosyphon was verified to operate in the lower temperature range of geothermal environments, and the amount of heat that could be transferred to the ground surface was predicted by numerical methods. Based on the subsurface temperature distribution in Suwon, South Korea, installation conditions were identified for achieving heat fluxes of up to 146.2 W/m^2. Thus, the stainless steel-acetone geothermal thermosyphon presented in this study has shown promise as a future snow-melting method for paved roads.

Acknowledgment

This work was supported by the Innovative Energy Efficiency R&D Program of the Korea Institute of Energy Technology Evaluation and Planning (KETEP) grant funded by the Ministry of Trade, Industry & Energy, Korea. (Grant No. 20212020800270), and a National Research Foundation of Korea (NRF) grant funded by the Korean government (MSIT) (Grant No. 2022R1C1C2006156).

References

[1] H. Liu, P. Maghoul, A. Bahari and M. Kavgic, Feasibility study of snow melting system for bridge decks using geothermal energy piles integrated with heat pump in Canada, Renewable Energy, 2019, 136: p. 1266-1280.
[2] Z. Chi, T. Yiqiu, C. Fengchen, Y. Qing, and X. Huining, Long-term thermal analysis of an airfield-runway snow-melting system utilizing heat-pipe technology, Energy Conversion and Management, 2019, 186: p. 473-486.
[3] H. Lim and J. Lee, Flat plate two-phase heat spreader on the thermal management of high-power electronics: a review. Journal of Mechanical Science and Technology, 2021, 35: p. 4801-4814.
[4] N. N. Babu and H. C. Kamath, Materials used in heat pipe. Materials Today: Proceedings, 2015, 2(4-5): p. 1469-1478.
[5] J. Seo, S. Kang, K. Kim, and J. Lee, Compact heat pipe heat exchanger for waste heat recovery within a low-temperature range. International Communications in Heat and Mass Transfer, 2024, 155: p. 107550.
[6] R. J. Moffat, Describing the uncertainties in experimental results. Experimental Thermal and Fluid Science, 1988, 1(1): p. 3–17.

Paper ID 062

Thermal Performance of Surface Characterization for Two-phase Immersion Cooling using HFE-7200

Sanghyeon Shin[1] and Jungho Lee[1*]

[1] *Department of Mechanical Engineering, Ajou University,*
206 Worldcup-ro, Yeongtong-gu, Suwon, Gyeonggi-do 16499, Republic of Korea
**Corresponding author's email address: jungholee@ajou.ac.kr*

Abstract

The recent advancements in AI have led to increased heat generation in CPUs and GPUs, consequently driving the expansion of data centers. Traditional air-cooling methods used in existing data centers are becoming increasingly inadequate to effectively manage the rising heat loads, prompting extensive research into immersion cooling. While numerous studies have explored thermal performance enhancement through surface modification in two-phase immersion cooling, this research has largely been confined to pool boiling chambers, which do not accurately reflect actual server environments. In this study, we fabricated surface-modified samples using copper foam and sintered copper microporous coating (MPC) with varying thicknesses and evaluated thermal performance within a chamber designed to simulate real server immersion cooling conditions. The results showed that both surface modification methods significantly reduced the maximum superheat by more than 15K and increased the critical heat flux (CHF) compared to smooth surfaces. The copper foam demonstrated the highest convective heat transfer coefficient at 300 µm, while the sintered copper MPC exhibited the highest at 200 µm. Both surface modification methods showed an increasing trend in CHF with increasing thickness, although the changes in CHF for sintered copper MPC were minimal compared to the more pronounced improvements observed with copper foam. This study contributes insights into the most effective surface modification techniques and optimal thicknesses for practical application in immersion cooling environments.

Keywords: Immersion cooling; Surface modification; Dielectric liquid, Critical heat flux

1. Introduction

Recently, as interest in AI has increased, the performance improvements in CPUs and GPUs have led to an increase in Thermal Design Power (TDP) and the expansion of hyperscale data centers. Electronic equipment must be maintained at a temperature below 85 ℃ to ensure stable server operation [1]. However, the air-cooling methods used in conventional data centers are limited in effectively dissipating the increasing heat load. Consequently, research on immersion cooling, where server boards are directly immersed in dielectric liquid for cooling, has been actively researched.

Immersion cooling includes single-phase cooling using sensible heat and two-phase cooling using latent heat. With boiling heat transfer, two-phase immersion cooling possesses a convective heat transfer coefficient that is an order of magnitude higher than single-phase immersion cooling [2]. Therefore, two-phase immersion cooling more effectively addresses the increasing heat dissipation challenges.

Two-phase immersion cooling uses dielectric liquid, which has high wettability and low thermal-physical properties compared to water. When surface modification is applied, the heat transfer coefficient and Critical Heat Flux (CHF) can be increased compared to a smooth surface [3]. Therefore, surface modification is a promising option for enhancing the heat transfer performance of dielectric liquids. Extensive research has been conducted to enhance thermal performance through surface modifications in pool boiling using dielectric liquids to apply immersion cooling. However, most of this research has been conducted in pool boiling chambers, where the heat source is small, and experiments are conducted horizontally, which is not representative of the actual immersion cooling environment in servers. Therefore, it is crucial to identify the most effective surface modification method when applied to actual application environments.

In this study, experiments were conducted in a chamber that simulated a server's actual immersion cooling environment. Additionally, we performed surface modification using copper foam and sintered copper MPC and evaluated the thermal performance based on coating thickness. The goal is to propose the most effective surface modification method and optimal thickness for application to actual server boards.

2. Fabrication and experiment

2.1. Sample fabrication

The surface modification was performed using copper foam and sintered copper microporous coating. First, the copper foam samples were fabricated as follows. Copper foam with 200, 300, and 500 µm / 130 ppi was placed on a copper block, and then a graphite block weighing approximately 200 g was placed on top to apply pressure. And sintering in a vacuum furnace (1040℃, 1 hour heated, 30 minutes maintained) to attach each other. For the sintered copper MPC samples, copper powder with a particle size of 62 µm was used. A mixture of thinner and copper powder was evenly spread over the copper block, and the sintering was done under the same conditions as the copper foam samples. After sintering, the thickness of the samples was measured to be approximately 200, 300, and 500 µm.

The fabricated copper blocks, each measuring 25.4 × 25.4 mm^2, were soldered to ceramic heaters of the same size. A wire thermocouple (TC) was inserted into the center of the copper block to measure the junction temperature of the copper block. Subsequently, the samples were placed in PEEK molds and attached with epoxy, as shown in Figure 1(a). The completed samples were then fixed at the center of a 5 mm thick polycarbonate board to simulate a server board, as shown in Figure 1(b).

(a)

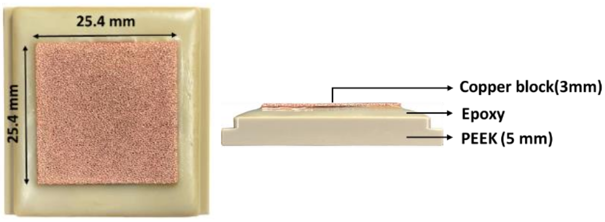

(b)

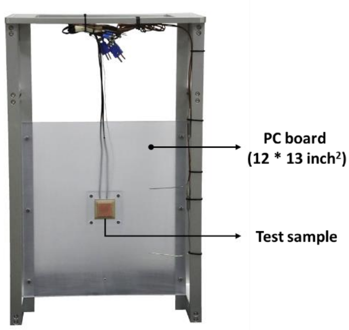

Figure 1. Two-phase immersion cooling test sample. (a) Test sample (b) Test sample and PC board assembly

2.2. Experimental setup

The equipment used in the experiment is shown in Figure 2. The chamber was designed to accommodate an E-ATX standard server board (12 × 13 inch^2), the size of a commercially available board. The working fluid used was 3M Novec HFE-7200, with a boiling point of 76°C. Three thermocouples were inserted inside the chamber to measure the temperature of the liquid top, bottom, and vapor. The saturation condition was considered the point at which the three TC readings equalized. During the experiments, a cartridge heater and condenser were used to maintain the chamber in a saturated state. A pressure transducer was installed at the top of the chamber to maintain the internal pressure at 1 atm. Additionally, a high-speed camera was used to visualize the bubbles' behavior.

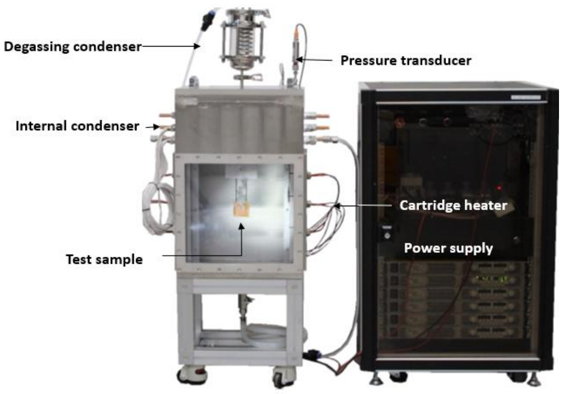

Figure 2. Experimental setup of two-phase immersion cooling

2.3. Data reduction

The following methodology was employed to calculate the wall superheat (ΔT_{sat}) and heat transfer coefficient (h). First, it was assumed that the problem could be treated as a one-dimensional heat conduction issue because the heating area was identical to the area of the heater, and insulation was provided using PEEK and epoxy. Using Eq (1), the thermal resistance of the copper block was calculated, which allowed for the determination of the wall temperature.

$$T_w = T_h - q\frac{d}{kA} \tag{1}$$

Using Eq (2), the wall superheat was determined from the previously calculated wall temperature and the measured liquid temperature.

$$\Delta T_{sat} = T_w - T_{sat} \tag{2}$$

Finally, heat transfer coefficient was calculated with Newton's cooling law Eq (3).

$$h = \frac{q''}{T_w - T_{sat}} \tag{3}$$

3. Test result and discussion

Experiments were conducted under identical conditions to investigate the effects of surface modification methods and thickness. To compare the thermal performance improvements through surface modification, the experiments were first performed on a smooth surface. Both surface modification methods resulted in a reduction in maximum wall superheat and an enhancement in CHF compared to the smooth surface. At the same heat flux of 15 W/cm², all surface modification methods exhibited a reduction in superheat of more than 15 K compared to the smooth surface, and CHF was also improved in all cases.

Surface modification was performed using two methods: copper foam and sintered copper MPC. To compare the effects of thickness, samples were fabricated with thicknesses of approximately 200, 300, and 500 µm, and experiments were conducted accordingly. The experimental results for each surface modification method according to thickness can be seen in Figure 3. For the sintered copper MPC samples, the highest heat transfer coefficient was observed at a thickness of 200 µm, while the highest CHF was recorded at 23 W/cm² with a thickness of 500 µm. In the case of copper foam, the highest heat transfer coefficient was observed at a thickness of 300 µm, and the highest CHF of 31 W/cm² was recorded at 500 µm. Although the copper foam at 500 µm exhibited the highest CHF, it also showed an increase in maximum superheat to 17.8 K, which is more than 7 K higher compared to other surface modification samples. For CHF, both surface modification methods exhibited an increasing trend with increasing thickness. While the change was minimal for the sintered copper MPC samples, the copper foam showed significant improvements with increasing thickness.

The sintered copper MPC samples exhibit a higher heat transfer coefficient compared to the copper foam as shown in Figure 4(a). This is attributed to the smaller pore size and the greater number of nucleation sites in the sintered copper MPC. Due to

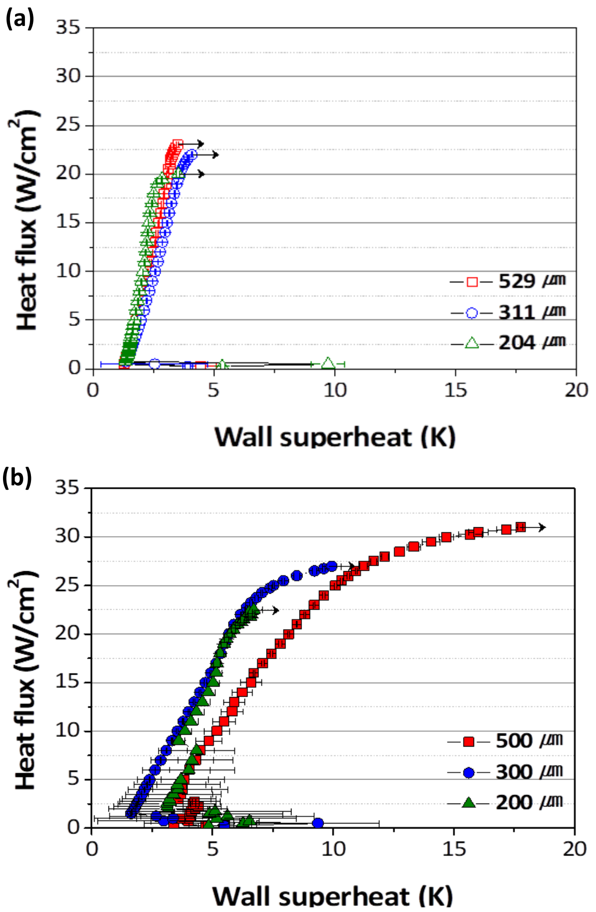

Figure 3. Pool boiling curve of surface modification methods (a) Sintered copper MPC, (b) Copper foam

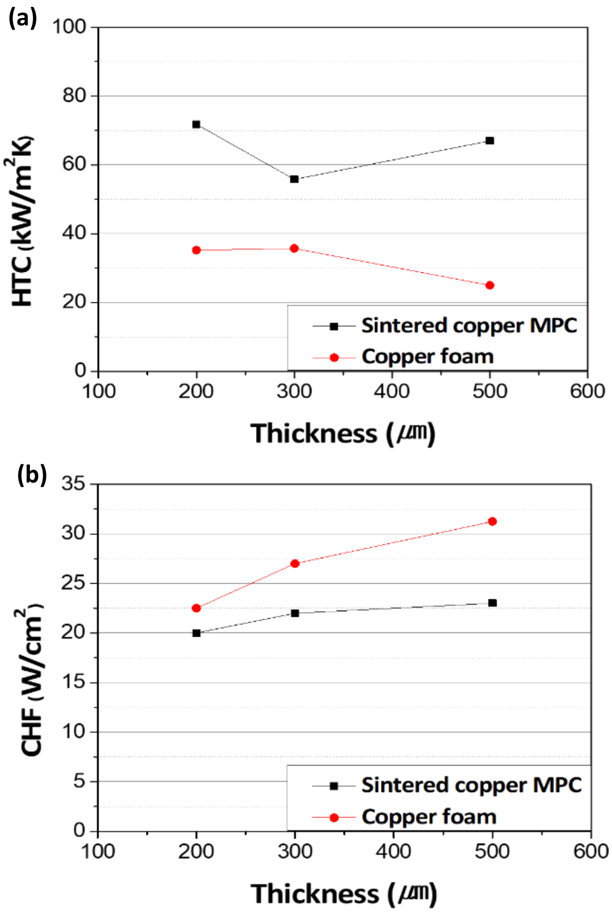

Figure 4. Comparison of immersion cooling performance based on thickness (a) Heat transfer coefficient (b) Critical heat flux

the low surface tension of dielectric liquids, larger cavities may fail to retain vapor embryos effectively. Therefore, the smaller and more densely distributed pores in the sintered copper MPC samples are believed to result in a lower maximum superheat. Additionally, while the CHF improvement is significant with increasing thickness in the copper foam, the increase in CHF for the sintered copper MPC is relatively minor as shown in Figure 4(b). This can be attributed to the larger pore size in the copper foam, which facilitates easier bubble departure and consequently better liquid supply.

4. Conclusions

In this study, a chamber simulating an actual server environment was fabricated, and surface modification was carried out using copper foam and sintered MPC. To analyze the effects of thickness, experiments were conducted on samples fabricated at three different thicknesses: 200, 300, and 500 µm.

1. Both surface modification methods showed improvements in maximum superheat and CHF compared to a smooth surface, with a reduction in maximum superheat of over 15 K at a heat flux of 15 W/cm².
2. For the sintered copper MPC, the highest heat transfer coefficient was observed at 200 µm, while the CHF of 23 W/cm² was the highest recorded at 500 µm.
3. For the copper foam, the highest heat transfer coefficient was observed at 300 µm, and the CHF of 31 W/cm² was the highest recorded at 500 µm.
4. The sintered copper MPC showed a reduction in maximum wall superheat by more than 2 K compared to the copper foam. This is due to the smaller pore size and the greater number of nucleation sites compared to the copper foam.
5. The CHF improvement with increasing thickness is more pronounced in copper foam compared to MPC samples. This is likely because the larger pore size in the copper foam allows for easier bubble departure, leading to more efficient liquid supply.

5. ACKNOWLEDGEMENTS

This work was supported by a National Research Foundation of Korea (NRF) grant funded by the Ministry of Science and ICT, Korea (No. NRF-2020R1A2C3008689).

References

[1] Murshed, S. S., & De Castro, C. N. (2017). A critical review of traditional and emerging techniques and fluids for electronics cooling. Renewable and Sustainable Energy Reviews, 78, 821-833.

[2] Mudawar, I. (2001). Assessment of high-heat-flux thermal management schemes. IEEE transactions on components and packaging technologies, 24(2), 122-141.

[3] Sajjad, U., Sadeghianjahromi, A., Ali, H. M., & Wang, C. C. (2021). Enhanced pool boiling of dielectric and highly wetting liquids–A review on surface engineering. Applied Thermal Engineering, 195, 117074.

Paper ID 067(S2C)

Visualization Experiments and Numerical Analyses of Ultra-thin Heat Pipes Using a Wick Structure with Non-uniform Shape

Yasushi Koito*, Junichi Akiyama, and Hiroto Ueno

Kumamoto University, Kumamoto, Japan
** Corresponding author email address: koito@gpo.kumamoto-u.ac.jp*

Abstract

A wick structure with a constriction shape was proposed to improve the thermal performance of ultra-thin heat pipes. Visualization experiments and numerical analyses were conducted with two types of wick structures with and without a constriction shape. In the experiments, fluid-flow and phase-change phenomena in the heat pipe were captured with a video camera, and temporal changes in temperatures were measured with thermocouples. In the numerical analyses, velocity and temperature distributions in the heat pipe were obtained. The experimental results confirmed that the constriction shape prevented the liquid slug formation in the vapor-flow channels and thus improved the thermal performance of the heat pipe. The numerical results clarified that the constriction shape increased a condensation area not only in the constriction direction but also in the vapor-flow direction in the vapor-flow channels. Thus, it was explained that the condensation-area increase in the two directions improved the thermal performance of the heat pipe.

Keywords: Ultra-thin heat pipe; Centered wick structure; Striped wick structure; Condensation; Liquid slug

1. Introduction

Ultra-thin heat pipes have been developed for the enhancement of heat removal within a thin electronic device like a smartphone. Since the overall thickness is less than 1 mm, ultra-thin heat pipes cannot be fabricated with a traditional design of a wick structure, that is, a wick structure cannot be attached to the inner wall of a heat pipe container. Thus, centered [1–3] or striped [4–6] wick structures have been proposed to leave vapor-flow channels within the heat pipe. In the heat pipe with a centered wick structure, vapor-flow channels are left on both sides of the wick structure. In the heat pipe with a striped wick structure, wick structures and vapor-flow channels are arranged alternately.

The centered and striped wick structures are effective to leave vapor-flow channels within an ultra-thin heat pipe. The height of the vapor-flow channels is the same as the thickness of the wick structures. However, at a condenser section of the heat pipe, vapor is directly cooled by the inner wall of a heat pipe container, which essentially differs from heat pipes with a traditional wick structure. Because of this, condensate droplets were observed in the vapor-flow channels, and in some cases, the droplets coalesced to form a liquid slug [7, 8].

The liquid slug hinders vapor flow in the vapor-flow channels. Thus, it is expected that the thermal performance of ultra-thin heat pipes with a centered or a striped wick structure would be increased when the liquid slug is eliminated in the vapor-flow channels. In the present study, therefore, a non-uniform wick structure, that is, a wick structure with a constriction shape was proposed. This wick structure was intended to prevent liquid slug formation by partially increasing the width of the vapor-flow channels. Visualization experiments and numerical analyses were conducted with two types of wick structures with and without a constriction shape. Based on the experimental and numerical results, discussion was conducted on the effectiveness of the constriction shape.

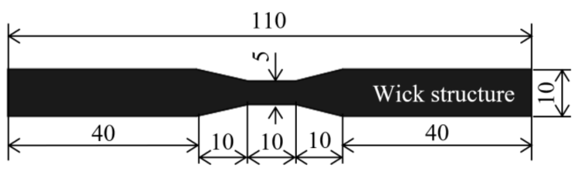

Figure 1. Dimensions of the wick structure with a constriction shape.

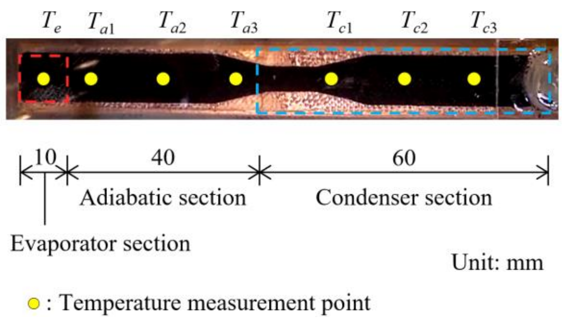

Figure 2. Wick structure with a constriction shape in a semi-transparent heat pipe.

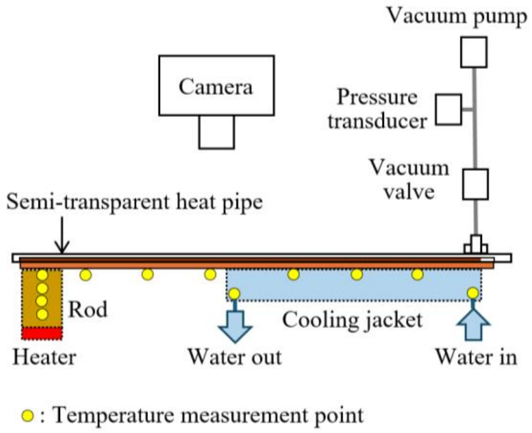

Figure 3. Experimental apparatus.

2. Experimental method

Figure 1 shows the design of a constriction-shaped wick structure. The wick structure was 110 mm long, and the constriction shape was made at the middle, where the width was constricted from 10 mm to 5 mm. A semi-transparent heat pipe developed in the previous study [7] was used, and the wick structure was placed as shown in Figure 2. The wick structure was made by sintering copper powders. The thickness of the wick structure was 0.5 mm, which was equal to the height of the vapor-flow channels. An evaporator, adiabatic, and condenser sections of the heat pipe were 10 mm, 40 mm, and 60 mm long, respectively. Water was used as a working fluid.

Figure 3 shows an experimental apparatus. The heat pipe was placed horizontally. A heater and a cooling jacket were mounted on the evaporator and condenser sections of the heat pipe, respectively. In experiment, the evaporator section was heated and the condenser section was water-cooled. Fluid-flow and phase-change phenomena in the heat pipe were captured with a video camera, and temporal changes in temperatures were measured with thermocouples. Temperature measurement points are also shown in Figures 2 and 3. The temperature and flow rate of the cooling water were 15°C and 50 mL/min, respectively. The heating was started under the condition that the electrical power (P) to the heater was 4 W, and then P was increased stepwise when the temperature changes reached a steady state. The experiment was terminated when the evaporator temperature (T_e) reached 90°C. For comparison, the experiments were also conducted when the wick structure without a constriction shape was placed in the heat pipe. The width of the wick structure was constant at 10 mm. The wick length and wick thickness were the same as those of the constriction-shaped wick structure. From temperature gradient in a rod between the heat pipe and the heater, the heat transfer rate (Q) was evaluated by using Fourier's law.

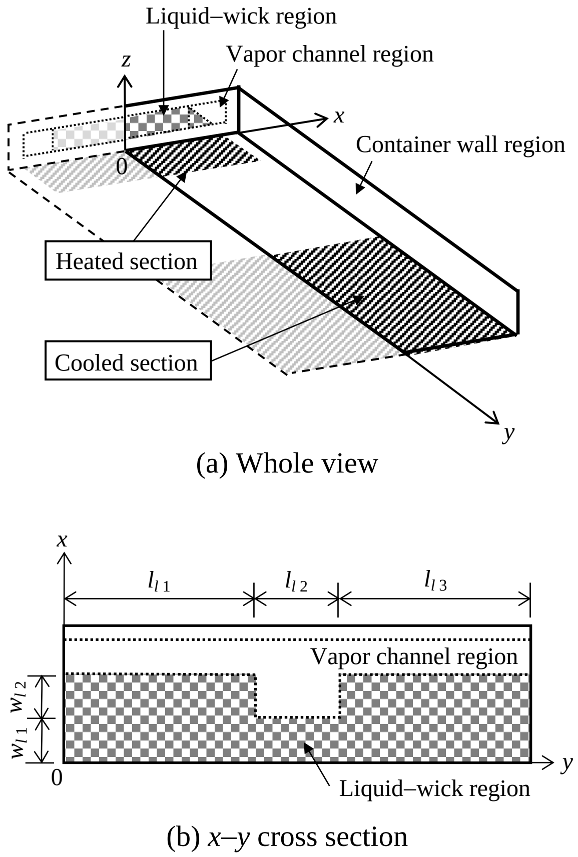

Figure 4. Mathematical model of the heat pipe.

3. Numerical method

Figure 4 shows a mathematical model of the ultra-thin heat pipe with a constriction-shaped wick structure. Because the wick structure was placed at the center of the heat pipe, numerical analyses were conducted for the half domain of the heat pipe. As shown in Figure 4 (a), the model comprised three regions: a vapor channel, liquid–wick, and container wall regions in the x-y-z coordinate system. These three regions were the same in length (l_l). Heated and cooled sections were on the bottom of the model. Except for these two sections, the rest of the outer surface of the model was insulated. Figure 4 (b) shows the $x-y$ cross section of the model at the center of the vapor channel region in the z direction. For simplicity, the constricted part of the wick structure was considered to be rectangular in shape.

The same governing equations and boundary conditions as those in the previous paper [9] were applied to the present model. As the governing equations, the conservation equations of mass, momentum, and energy were given for the vapor channel and liquid-wick regions. Only the conservation equation of energy was used for the container wall region. The boundary conditions were applied to the solid-liquid, solid-vapor, and liquid-vapor interfaces as well as the heated, cooled, and adiabatic sections of the model. The governing equations were discretized by using the control volume method, and calculations were conducted based on the SIMPLE algorithm. Non-uniform mesh was used in a computational domain.

As mentioned earlier, the vapor flow is hindered by a liquid slug in the vapor-flow channels. Thus, it was assumed that condensation of vapor occurs only in the vapor-flow channel upstream of the liquid slug. Based on this assumption, the vapor-liquid interface was separated into condensation and non-condensation interfaces, and thermal boundary conditions were applied as follows:

Condensation interface ($0 \le y \le l_{LS}$) :

$$T_v = T_l = \left(\frac{1}{T_{ref}} - \frac{R_g}{h_{fg}} \ln \frac{p_v}{p_{ref}}\right)^{-1} - 273.15 \tag{1}$$

Non-condensation interface ($l_{LS} < y \le l_t$) :

$$\lambda_v \frac{\partial T_v}{\partial x} = \lambda_{eff} \frac{\partial T_l}{\partial x} \tag{2}$$

where T_v is the vapor temperature, T_l is the liquid-wick temperature, T_{ref} is the reference temperature, p_v is the vapor pressure, and p_{ref} is the reference pressure. Moreover, h_{fg} is the latent heat, R_g is the gas constant, λ_v is the thermal conductivity of the vapor channel region, and λ_{eff} is the effective thermal conductivity of the liquid-wick region. $y = l_{LS}$ is the boundary between the condensation and non-condensation interfaces, which implies a condensation end point.

Numerical conditions were given according to the heat pipe and wick structure used in the experiments. Regarding the wick structure with a constriction shape, the dimensions were given as $l_{l\,1} = l_{l\,3} = 45$ mm, $l_{l\,2} = 20$ mm, and $w_{l\,1} = w_{l\,2} = 2.5$ mm. For comparison, the numerical analyses were also conducted when the wick structure without a constriction shape was placed in the model.

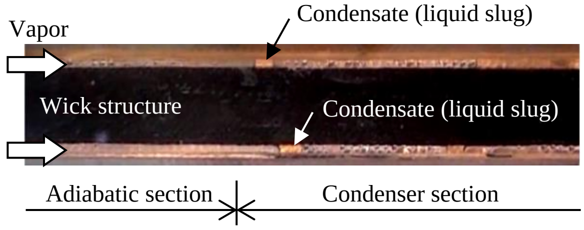

(a) Without a constriction shape

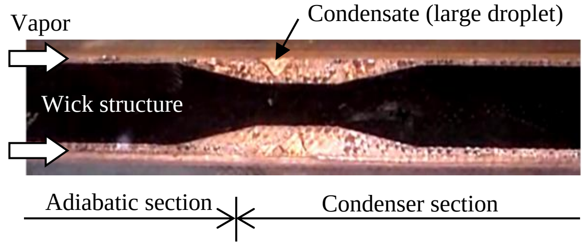

(b) With a constriction shape

Figure 5. Images in the heat pipe (P = 18 W).

4. Results and discussion

4.1. Experimental results

Figure 5 shows images in the semi-transparent heat pipe at P = 18 W for the wick structures (a) without and (b) with a constriction shape. The vapor-flow channels and wick structure at the adiabatic and condenser sections are shown. The evaporator section is located to the left of the image. Liquid evaporates at the evaporator section, and vapor flows toward the condenser section. In each image as indicated by arrows, the vapor was flowing to the right in the vapor-flow channels. For the wick structure without a constriction shape, because the width of the vapor-flow channel was entirely very small, condensate droplets coalesced to form a liquid slug, which was observed in both of the vapor-flow channels as shown in Figure 5 (a). The liquid slug was pushed by the vapor flow, and then absorbed into the wick structure. However, the generation and absorption of the liquid slugs were repeated, which would hinder the vapor flow in the vapor-flow channels. The generation and absorption of the liquid slugs were observed around y = 55 mm at P = 18 W.

The coalescence of condensate droplets was also observed in the case of the wick structure with a constriction shape. However, no liquid slugs were observed in this case. The liquid slug formation was prevented by the constriction shape, that is, an increase in the width of the vapor-flow channels where condensation occurred. Instead of the liquid slug, a large liquid droplet was observed in the constricted region as shown in Figure 5 (b). The liquid droplets grew larger over time, and was absorbed when it came into contact with the wick structure.

The thermal resistance (R) of the heat pipe was evaluated by

$$R = \frac{T_e - (T_{c1} + T_{c2} + T_{c3})/3}{Q} \tag{3}$$

where Q is the heat transfer rate of the heat pipe. Moreover, the Q value when T_e = 90°C was defined as the maximum heat transfer rate (Q_{max}).

Figure 6 compares the R values for the wick structures with and without a constriction shape. The comparison indicates that the R value with a constriction shape was entirely lower than that without a constriction shape. Besides, the Q_{max} value with a constriction shape was 27.4 W, which was 21.2% larger than that without a constriction shape. These experimental results confirmed that the constriction shape improved the thermal performance of the heat pipe.

4.2. Numerical results

For the wick structure without a constriction shape, experimental and numerical results are compared in Figure 7 (a) regarding the temperature distribution of the heat pipe at P = 18 W. The numerical result was obtained with l_{LS} = 65 mm. The numerical result depends on the l_{LS} value, and fairly good agreement between the experimental and numerical results was obtained when l_{LS} = 65 mm. In the present experiments, the generation and absorption of the liquid slugs were observed around y = 55 mm in the vapor-flow channels. Thus, the setting l_{LS} = 65 mm was acceptable in this calculation.

Experimental and numerical results are also compared in Figure 7 (b) for the wick structure with a constriction shape. The numerical results were obtained for the two cases of l_{LS} = 65 mm and 80 mm. l_{LS} = 80 mm implies that l_{LS} located at the center of the condenser section in the y direction. Regarding the temperature difference between the evaporator and condenser sections, the numerical result with l_{LS} = 65 mm was larger than the experimental result. Although the constriction of the wick structure was considered in the calculation, a difference was found between the experimental and numerical results when l_{LS} = 65 mm. Fairly good agreement was obtained when l_{LS} = 80 mm. The present experimental results

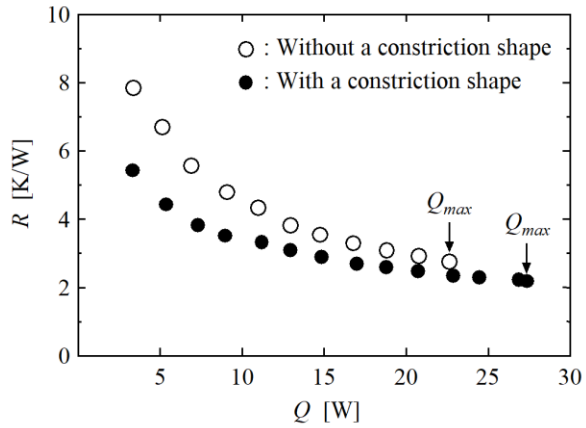

Figure 6. Thermal resistance of the heat pipe.

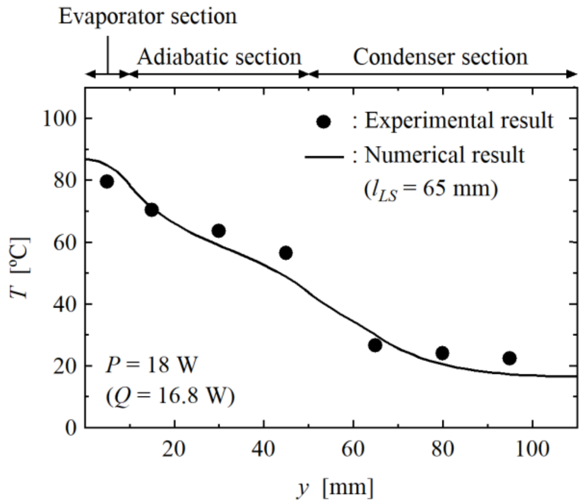

(a) Without a constriction shape

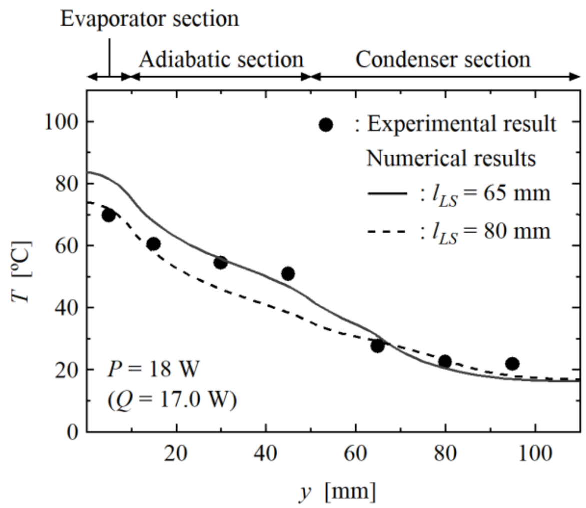

(b) With a constriction shape

Figure 7. Comparison between experimental and numerical results.

confirmed that the constriction shape of the wick structure prevented the liquid slug formation. This prevention increased the condensation interface in the vapor-flow direction, and thus the fairly good agreement was obtained when l_{LS} was increased from 65 mm to 80 mm. The constriction shape of the wick structure increased the condensation area not only in the constriction direction but also in the vapor-flow direction in the vapor-flow channels.

Together with the temperature distributions shown in Figure 7, the numerical results of vapor velocity distributions were also obtained in the above calculations. These vapor velocity distributions are shown in Figure 8 for the wick structures (a) without and (b) with a constriction shape. The distributions on the *x*–*y* cross section at the center of the vapor channel region in the *z* direction are shown here. In Figure 8 (a), because of l_{LS} = 65 mm, no vapor flow was found in the vapor-flow channel downstream of y = 65 mm. In Figure 8 (b), since the vapor velocity distribution was obtained with l_{LS} = 80 mm, the vapor flow further downstream within the vapor-flow channel was demonstrated. The inflow of vapor into the constriction region (2.5 mm ≤ x ≤ 5.0 mm and 45 mm ≤ y ≤ 65 mm) was confirmed. The vapor flow downstream of the constriction region was also confirmed. These vapor flows explained the thermal performance improvement of the heat pipe. Since the non-condensation interface was still found in Figure 8 (b), the thermal performance of the present heat pipe would be further improved by increasing the condensation interface within the vapor-flow channels.

5. Conclusions

A constriction-shaped wick structure was proposed for ultra-thin heat pipes. The experimental results confirmed that the constriction shape prevented the liquid slug formation in the vapor-flow channels. It was also confirmed that the constriction shape decreased the thermal resistance and increased the maximum heat transfer rate of the heat pipe. The numerical results clarified that the constriction shape increased a condensation area not only in the constriction direction but also in the vapor-flow direction in the vapor-flow channels. The condensation-area increase in the two directions explained the thermal performance improvement of the heat pipe.

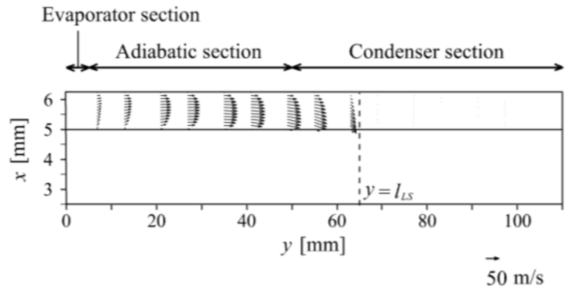

(a) Without a constriction shape

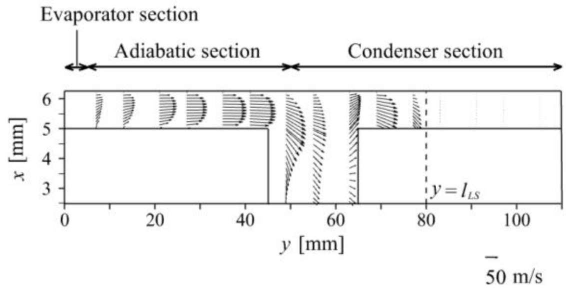

(b) With a constriction shape

Figure 8. Vapor velocity distributions.

References

[1] M. S. Ahamed, Y. Saito, K. Mashiko, and M. Mochizuki, Characterization of a high performance ultra-thin heat pipe cooling module for mobile hand held electronic devices. Heat and Mass Transfer, 2017. 53: p. 3241.
[2] H. Tang, Y. Xie, Y. Tang, X. Wu, C. Wu, and Y. Sun, Stress analysis and thermal performance of ultra-thin heat pipes for compact electronics. International Communications in Heat and Mass Transfer, 2022. 139: 106484.
[3] F. Yi, Y. Gan, Z. Xin, Y. Li, and H. Chen, Analysis of thermal characteristics of the heat pipes with segmented composite wicks. International Journal of Thermal Sciences, 2023. 191: 108341.
[4] Z. Cui, L. Jia, Z. Wang, C. Dang, and L. Yin, Thermal performance of an ultra-thin flat heat pipe with striped super-hydrophilic wick structure. Applied Thermal Engineering, 2022. 208: 118249.
[5] S. Chai, X. Mei, F. Gao, Y. Xie, and L. Lu, Comprehensive optimization design of ultra-thin flat heat pipe based on pressure-bearing and heat transfer performance. Case Studies in Thermal Engineering, 2023. 49: 103302.
[6] G. Chen, C. Yan, S. Yin, Y. Tang, W. Yuan, and S. Zhang, Vapor-liquid coplanar structure enables high thermal conductive and extremely ultrathin vapor chamber. Energy, 2024. 301: 131689.
[7] C. Chen, R. Kakizoe, and Y. Koito, Visualization experiments on operational characteristics of a centered-wick heat pipe (Effect of liquid volume). Multiphase Science and Technology, 2021. 33(4): p. 45.

[8] Y. Koito, C. Chen, R. Kakizoe, and A. Fukushima, Fluid flow and heat transfer characteristics of a centered-wick heat pipe with additional working fluid: Experimental study with visualization. Multiphase Science and Technology, 2023. 35(2): p. 43.

[9] Y. Koito and C. Chen, Thermal and hydrodynamic characteristics of an ultra-thin flattened centered-wick heat pipe: Experiments and numerical analyses. Applied Thermal Engineering, 2024. 239: 122064.

Paper ID 069(S3)

Experimental study of pulsating heat pipes for cooling the stator of an electrical machine

Halima Aziza[1*], Riadh Boubaker[1,2], Safouene Ouenzerfi[1,2], Naoko Iwata[3], Vincent Dupont[3], Souad Harmand[1]

[1] *Univ. Polytechnique Hauts-de-France, CNRS, UMR 8201- LAMIH - Laboratoire d'Automatique de Mécanique et d'Informatique Industrielles et Humaines, F-59313 Valenciennes, France*

[2] *Innov cool Tech, UPHF, F-59313 Valenciennes, France*

[3] *Calyos, 4ième Rue 20,6040, Charleroi, Belgium*

**Corresponding author email address: halimaaziza65@gmail.com*

Abstract

As the electrification of transport systems expand, the development of high-power high-efficiency electric motors is becoming essential. In order to ensure the integrity and the safety of E-vehicles, a rigorous thermal management is required. The subject of this study is to determine the thermal performances of a novel design pulsating heat pipes (PHP) designed to cool the stator of an e-motor. The device is partially filled up (38 %) with R1233Zd and is made of copper tubes. The novel design has 10 segments; each is composed of 3 sections evaporator, adiabatic and condenser regions and had two different cross section (rectangular and circular). The critical inner diameter (ID) was used in the evaporator (1,75 mm), and a significantly larger ID in the other regions, with two types of inner surfaces (grooved and smooth). The device was tested at different heat inputs (200 to 1000 W) and in various volumetric airflows. The study demonstrated the capacity of the PHP to dissipate high heat powers up to 1000 W while maintaining a thermal resistance lower than 70 K/kW and a temperature under 90 °C.

Keywords: Pulsating Heat Pipe; E-motor; Heat transfer; Thermal management

1. Introduction

Global rush to reduce greenhouse gas emissions, improve air quality and decrease dependency on fossil fuels, shifted the transportation industry towards electrification. The shift toward more compact and powerful electric motors presents significant challenges in managing heat losses. As these motors become more integral to modern technology, particularly in electric vehicles, the importance of effective thermal management cannot be overstated. Pulsating heat pipes (PHP or OHP) have gained considerable interest in recent years due to their exceptional efficiency and eco-friendly nature as heat transfer systems. They provide viable solutions for cooling e-motors.

Several studies have investigated the performance of pulsating heat pipes to assess their efficacy and improve the understanding of their behavior. Some of these studies investigated the performance of the PHP in cooling powertrain components such as batteries, a study by Chi et al. [1] used a pulsating heat pipes made out of copper and had an internal diameter of 1 mm, where several parameters were inspected to verify the potential of using the PHP as cooling module. The thermal performance was primarily dependent on the quantity of working fluid charged. The system functioned correctly with a filling ratio (FR) that was around 10% of the total. The variation in the FR amount ranged from 10% to 26% as the heat input increased. The thermal resistance of the OHP system was only little affected by the inclination angles at high heat input. The heater surface temperature was consistently maintained at around 60 °C for heat fluxes below Q = 20 W [1]. In a similar study Chen and Li [2] investigated the thermal management of a 68 Ah square lithium iron phosphate battery using an aqueous TiO_2-based PHP. Heat dissipation tests were conducted under various vehicle workloads and ambient temperatures. The TiO_2-based PHP was found to optimize heat dissipation performance maintaining maximum temperature and temperature gradient within 35.86 ºC and 1.15 ºC. The PHP also improved uniformity in temperature at the battery surface by up to 60% under different operating conditions. As operating conditions changed, battery heat generation increased, leading to a gradual increase in temperature difference between the evaporation and condensation ends of TiO_2-PHP, accelerating the start of the PHP. The PHP operated efficiently and achieved effective heat transfer and dissipation under environmental temperature and battery heat generation.

However, there is lack of research on the utilization of PHP for cooling the electric motors. Zhu et al. [3] proposed a novel cooling solution based on a 3D rotational oscillating heat pipes (ROHP), designed for cooling the rotor part of the motor, for urban electric vehicles, which depends on the gravity, centrifugal force and cooling air generated by motor rotation. The experimental study consisted of two stages: theoretical study and application feasibility study. The theoretical study revealed the influence mechanism of rotation on ROHP performance, while the application feasibility study verified the heat dissipation capacity of the ROHP under real driving cycles. It was concluded that ROHP can be used to dissipate heat and maintain the temperature of the permanent magnet in an in-wheel motor under different heating powers and rotation speeds. In a similar study, Czajkowki et al. [4] focused on flower shaped oscillating heat pipes (FSOHP). The experimental set-up consisted of 8 horizontal bends on the bottom (evaporator) and the top (condenser) connected by a 1.1 m long vertical quasi-adiabatic section of capillaries filled with deionized water. The study examined various rotational speeds and heat loads, with different filling ratios. The results showed that a higher temperature amplitude in rotary system associated with obtaining the appropriate level of pressure required to cause the slug-plug internal displacement flow, directly affecting the increase in flow rate of the working fluid and the heat transport capabilities of the FSOHP improved as the centrifugal acceleration increased. Other studies focused on the cooling of the stator, A Prianingsih et al. [5] investigated the thermal performance of pulsating heat pipes cooling the stator of an e-motor. The pulsating heat pipes were made of a copper capillary tube, using acetone as a working fluid with a filling ratio of 0.5 and were able to decrease the temperature of the outer surface of the e-motor by 84.05 K. The thermal resistance was 0.21 K/W when subjected to a heat load of 120 W. J.F. Bonnenfant [6] conducted an experimental study to assess the efficiency of a pulsating heat pipes in cooling the stator of a motorized turbomachine. The PHP consisted of 24 branches with an internal diameter of 2.4 mm. Acetone, ethanol and N-pentane were used as working fluids at varying filling ratios, in three different inclinations. It was demonstrated that the thermal conductance rose by six times more compared to the conductive ones, also that the presence of the PHP increases by a factor of 20 to 25 the pure diffusive situation.

Previous research demonstrated the ability of the PHP in cooling e-motors. The present study focuses on the evaluating of the thermal performances of a novel design pulsating heat pipes developed by Calyos S.A., initially for the cooling of a stator of an unmoving industrial device in horizontal position.

2. Experimental apparatus and procedure

The pulsating heat pipe, investigated in this study, was made out of ten individual sections, each considered on its own a PHP, and is composed from an evaporator, an adiabatic and condenser segments, as illustrated in Figure 1, which were then assembled into a cohesive cylindrical structure, designed specifically to fit seamlessly with the stator design, and were connected to ensure the flow of the working fluid. Figure 2 represents the final configuration of the PHP after the assembly of its sections.

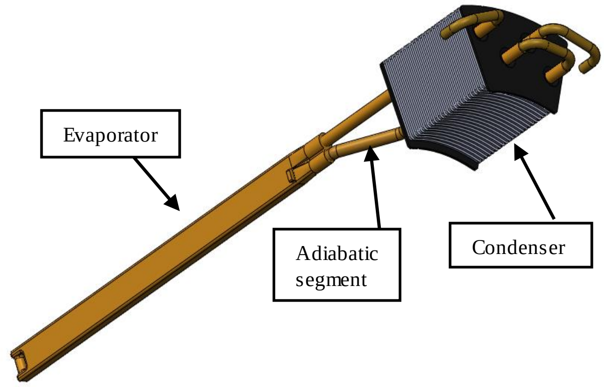

Figure 1. Schematic of the sections of the PHP.

Figure 2. Final configuration of the PHP after the assembly of ten sections.

The tube of the PHP is made out of copper and is partially filled (38 % FR) with R1233zd(E). The selection of this refrigerant as the working fluid is based on its dielectric properties, low boiling point of 18.3 °C, and decreased latent heat. These characteristics make it an ideal choice for cooling e-motors. Due to its low Global Warming Potential (GWP=1) and Ozone Depletion Potential (ODP=1), it is a highly favorable option in terms of ecological and environmental friendliness.

The evaporator tube was 3D printed in a rectangular cross section shape with smooth inner surface, and is divided into four channels each have a hydraulic diameter of 1.75 mm, which was selected to not exceed the critical diameter. Each evaporator span a length of 185.30 mm and a width of 11 mm. The adiabatic and condenser segment both features a circular cross section and are composed from two types of tubes, one with inner smooth surface with a 4 mm inner diameter, the other with grooved inner surface and a diameter of 4.58 mm. The tube at the condenser are equipped with twenty five cooling fins and were made out of aluminum, with a thickness of a 1 mm and the spacing between is 1.2 mm.

To simulate the heat losses from the stator, ten cartridge heaters were utilized to heat up the evaporator. A fan capable of delivering six different air velocities is connected to the condenser through an air duct measuring 175 cm in length and 9.8 cm in diameter. A flow straightener is incorporated to ensure uniform air distribution. The experimental test bench is illustrated in the Figure 3 below.

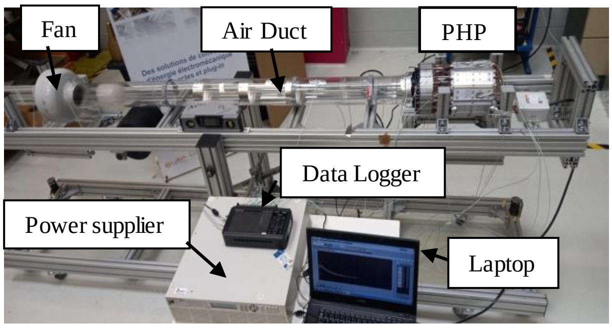

Figure 3. Experimental test-bench.

The thermal performance of the PHP is determined with thermocouples located on the three sections. Six thermocouples are utilized on the evaporator segment, and are positioned on an alternating basis among the other segments. On the adiabatic and condenser segment, five thermocouples were positioned in the same way as the evaporator, with the addition of three thermocouples on the condenser, two on the back and front fins and one was added on the turns of the condenser. Figure 4 represents the positioning of the thermocouples on the three segments of the PHP.

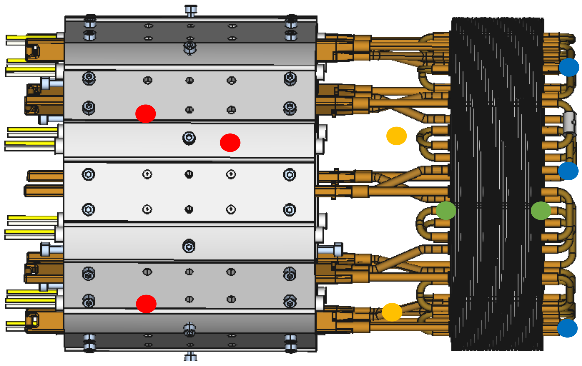

Figure 4. Thermocouples position, red (evaporator), orange (adiabatic section), blue (condenser), green (fins).

Monitoring the evolution of the overall thermal resistance Rth_{Tot} of the system, the thermal resistance of the evaporator Rth_{Ev} and the condenser Rth_{Cond}, are calculated as follows:

$$Rth_{Tot} = \frac{\bar{T}_{Ev} - T_{air}}{Heat\ Power} \quad (1)$$

$$Rth_{Ev} = \frac{\bar{T}_{Ev} - \bar{T}_{Ad}}{Heat\ Power} \quad (2)$$

$$Rth_{Cond} = \frac{\bar{T}_{Ad} - T_{air}}{Heat\ Power} \quad (3)$$

Where the $\bar{T}_{Ev}, \bar{T}_{Ad}$ represent the average temperature at the evaporator and the adiabatic segment, respectively.

3. Results and discussion

A series of tests were conducted to examine the parameters affecting the performance and efficiency of the PHP under varied operating conditions, with a fixed inclination of 0° (horizontal). These elements include heat input and varying airflow.

3.1. Influence of heat input

The objective of this set of tests was to analyze the temperature profiles and performances of the PHP under a constant airflow rate while varying the heat input. The heat input was varied incrementally from the value of 200 W to the value of 1000 W and vice versa.

Figure 5 represents the temperature profile of the PHP at different heat power input and volumetric airflow of 55.8 dm^3/s. The evaporator temperature reached a steady-state value at each heat input level, except for 800 W. The oscillations began at the lowest heat input and increased as the heat input rose, becoming stabilized in the steady state regime and achieving a stable operating mode. At 800 W, a partial dry-out occurred, indicated by a noticeable change in the temperature profile and more pronounced oscillation amplitudes, likely due to the presence of more bubbles in the evaporator section, which increased the temperature difference between the evaporator and condenser. The presence of oscillations from the lowest heat input level and their increasing amplitude with higher heat inputs demonstrate the dynamic nature of the PHP and its response to varying thermal loads. The steady state temperatures further indicate the stability of the PHP and reflects its effectiveness in maintaining the motor at a stable operating temperature, which is crucial for preventing overheating and ensuring performance and longevity of the motor. This can be shown by the observation that the temperature in the evaporator section remained below 88 °C, even under the highest power conditions. The temperature over the whole evaporator portion was consistent, as indicated by the readings from all the thermocouples. The thermal uniformity observed indicates the absence of any hotspots, thereby verifying the efficient connection and effective dissipation of heat throughout all segments of the PHP.

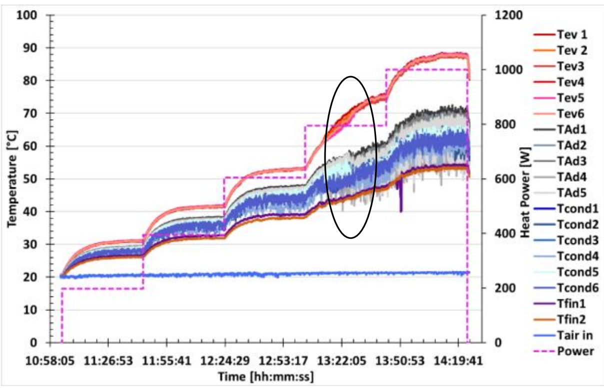

Figure 5. Temperature profile of the PHP at different heat input for a volumetric air flow of 55.8 dm³/s.

Thermal resistance was shown in Figure 6; it remained almost stable as the heat power increased up to 800 W. Beyond this point, a sudden increase in the thermal resistance of the evaporator was observed, leading to an overall increase in the total thermal resistance. This abrupt rise is attributed to the partial dry-out occurring at the 800 W heat input, which disrupts the efficient heat transfer process. Despite this, the overall thermal resistance remained under 70 K/kW. This low thermal resistance also highlights the system overall energy efficiency.

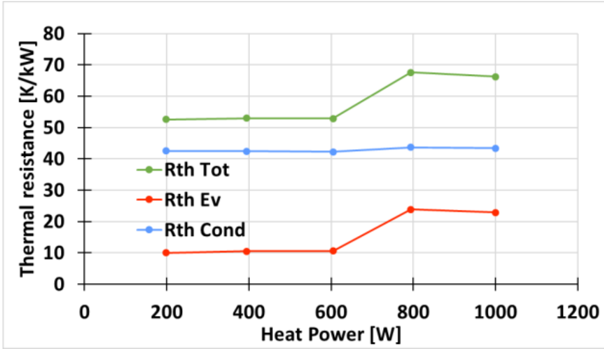

Figure 6. Thermal Resistance vs. Heat Input at a constant volumetric airflow of 55.8 dm³/s.

3.2. Influence of airflow rate

To investigate the influence of the airflow rate on the PHP performance, we conducted a test where the heat power was fixed at 800 W, while varying the airflow rate from highest to lowest (55.8 dm³/s to 23.3 dm³/s). As we reduced the air velocity, there was a slight increase in the evaporator temperature as illustrated in Figure 7, and the oscillation amplitudes became more pronounced. At volumetric flow rate 23.3 dm³ /s, complete dry-out occurred, and the oscillations ceased, marking a limit in the performance of the PHP at low airflow rate. The temperature of the evaporator in the volumetric airflow of 55.8 m³/s, 48.2 dm³/s and 38.4 dm³/s exhibited few fluctuations and remained nearly constant and didn't surpass the 85 °C. This suggests that the device has the ability to efficiently cool a maximum of 800 W, even when the airflow is at a moderate level. It is capable of achieving this without experiencing overheating or the development of localized areas of high temperature on the evaporator part.

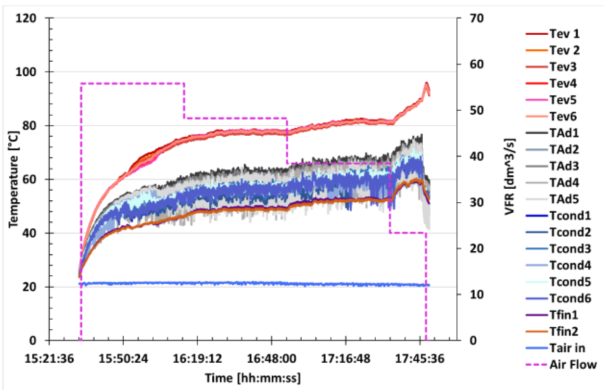

Figure 7. Temperature profiles at 800W heat power and varying volumetric flow.

The thermal resistance observed in Figure 8, aligns consistently with the temperature profile observed earlier. A notable pattern emerged where higher volumetric airflow corresponded to lower total thermal resistance, correlating directly with improved PHP performance. As the airflow increases, the PHP ability to dissipate heat improves. This improvement is related to the fact that increasing airflow enhances the heat transfer exchange between the air and the fins in the condenser section.

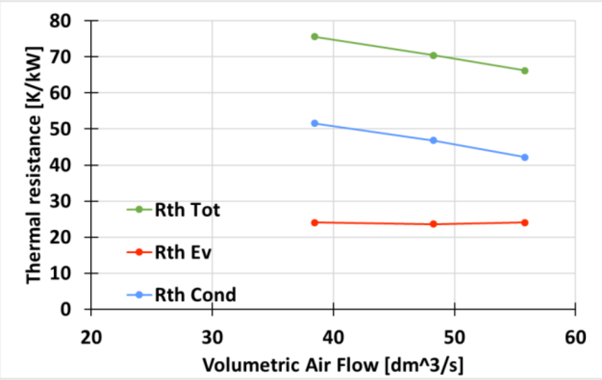

Figure 8. Thermal Resistance vs. Volumetric airflow.

4. Conclusion

The tests conducted at horizontal inclination with varying heat inputs from 200W to 1000W revealed key insights into the PHP's temperature profiles and thermal resistance. Oscillations initiated at the lowest heat input of 200 W. Thermal resistance analysis corroborated these findings, with the total thermal resistance of the systems being under 70 K/kW even under high heat power and the occurrence of a partial dry-out.

Tests conducted at different air velocities while maintaining a constant heat input of 800 W demonstrated the significant impact of air velocity on PHP performance. Higher air velocities resulted in lower total thermal resistance, enhancing cooling efficiency, confirming better performance at higher flow rates.

Even under harsh operating conditions, high heat and moderate airflow, the device eliminated the formation of local hotspots at the evaporator and withheld its uniform temperature throughout the tests.

The PHP has proven its ability to efficiently disperse heat under different situations, thereby validating its potential as a cooling medium for electric motors in electric vehicles. In the future, our work will prioritize evaluating the device's performance at different inclinations to understand how gravity affects its overall performances.

5. Acknowledgements

This work has been achieved within the framework of EE4.0 project. EE4.0 is co-financed by European Union with the financial support of European Regional Development Fund (ERDF), French State and the French Region of Hauts-de-France

References

[1] R.-G. Chi, W.-S. Chung and S.-H. Rhi, "Thermal characteristics of an oscillating heat pipe cooling system for electric vehicle Li-Ion batteries," Energies, 2018.

[2] M. Chen and J. Li, "Nanofluid-based pulsating heat pipes for thermal management of lithium-ion batteries," Journal of Energy Storage , vol. 32, p. 101715, 2020.

[3] L. Zhu, L. Zhu and S. Wang, "Experimental investigation on rotational oscillating heat pipe for in-wheel motor cooling of urban electric vehicle," International Communications in Heat and Mass Transfert, vol. 151, p. 107209, 2024.

[4] C. Czajkowski, A. I.Nowak and S. Pietrowicz, "Flower Shape Oscillating Heat Pipe – A novel type of oscillating heat pipe in a rotary system of coordinates – An experimental investigation," Applied Thermal Engineering, vol. 179, p. 115702, 2020.

[5] N. A Prianingsih, A. Winarta, A. Bambang and N. Putra, "Thermal performance of Pulsating heat pipes on Electric Motor as Cooling Application," in The 3rd International Tropical Renewable Energy Conference “Sustainable Development of Tropical Renewable Energy”, 2018.

[6] J.-F. Bonnenfant, "Experimental analysis and modeling of oscillating heat pipes in an aeronautical context," doctoral thesis of ISAE-ENSMA Ecole Nationale Supérieure de Mécanique et d’Aérotechique Poitiers, France, 2013.

Paper ID 070(S4)

Heat pipe assisted combined power generation and water desalination

Oranit Traisak[1*], Aliakbar Akbarzadeh[1], Abhijit Date[1]

[1] *School of Engineering, RMIT University, Melbourne, Australia*
**Corresponding author email address:S3907595@student.rmit.edu.au, abhijit.date@rmit.edu.au*

Abstract

This study presents a heat pipe-assisted system for combined power generation and water desalination, focusing on finding a solution to the global energy and water crisis. The proposed system is capable of utilizing industrial waste heat, with help of heat pipes, thermoelectric generators (TEG), and a direct contact membrane distillation (DCMD) unit to produce freshwater and power. Waste heat is transferred to the hot side of the TEG, while the cold side of TEG is cooled by saline water. Water vapour from the saline water passes through the hydrophobic membrane producing freshwater. Mathematical modeling and experimental validation confirm the system's ability to utilize low temperature waste heat and produce freshwater and power. Initial results indicate a stable freshwater yield, with electrical power generation of 6.8W and a freshwater mass flux of 1.7 kg/m²·h. This integrated approach demonstrates the potential of low-grade heat sources for sustainable desalination and power generation, contributing to the dual challenge of energy and water scarcity.

Keywords: Thermoelectric generator; Membrane distillation; Combined power generation; Water desalination technology

1. Introduction

Around the world, communities grapple with the intertwined challenges of water scarcity and energy access [1, 2]. With the global population steadily rising, demand for water and energy has reached unprecedented levels, straining already limited resources. Despite Earth's abundant water coverage, only a small fraction is drinkable, primarily due to the prevalence of saline sources and inaccessible frozen reserves. Compounding this issue, traditional energy sources, crucial for processes like desalination, are depleting rapidly [2]. Water scarcity affects billions globally, with projections indicating worsening conditions in the coming years. Desalination presents a promising solution, tapping into the vast reserves of seawater. However, current methods face obstacles such as rising costs and environmental concerns, necessitating the exploration of more sustainable alternatives. Simultaneously, the energy crisis looms large, with millions lacking access to reliable electricity sources. Energy-intensive processes like desalination further exacerbate this issue, highlighting the interconnectedness of water and energy challenges.

Substantial amount of industrial waste heat is generated worldwide [3]. This waste heat represents a largely untapped resource with great potential for addressing energy needs [4]. Our proposed system capitalizes on this availability of industrial waste heat, leveraging it for evaporative desalination processes. By harnessing this waste heat, our system not only mitigates environmental impact but also provides a sustainable energy source for desalination [5, 6]. Additionally, the generation of electricity through thermoelectric cells further maximizes the utilization of this abundant heat resource. Our proposed system addresses these dual challenges by utilizing industrial waste heat for membrane distillation while generating electricity through thermoelectric cells [7, 8]. The industrial waste heat is effectively captured and transported to the thermoelectric generators with the help of heat pipes.

2. Methodology and result

The proposed system combines power generation and water desalination. The system consists of 3 main components. Heat pipe heat exchanger, Thermoelectric generator (TEG) and Membrane Distillation (MD). Waste heat is captured and transferred to the hot side of thermoelectric generators with heat pipe. Cold side of the thermoelectric generators are cooled by saline water that needs to be treated. MD utilizes hydrophobic membrane that allows only water vapors to transfer to the permeate side. Freshwater can be produced by temperature and pressure difference.

2.1. Method

This research designs, creates and builds the proposed system. Computational modeling predicts power that can be generated and freshwater production.

62 Fins and 4 heat pipes collect waste heat. Heat will transfer to TEG and Direct Contact Membrane Distillation (DCMD) configuration, as in Figure 1.

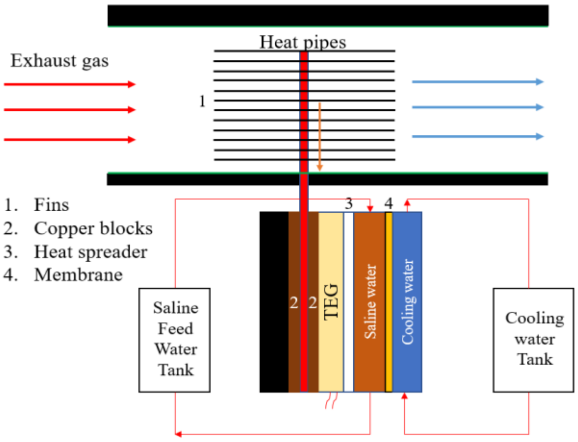

Figure 1. Schematic of design system.

Thermal resistance of the system, as Figure 2. Also, assumptions are applied in computational modelling. For instance, heat transfer in one dimension, well insulated and no heat loss to surrounding, uniform temperature of each component and contact resistance is negligible.

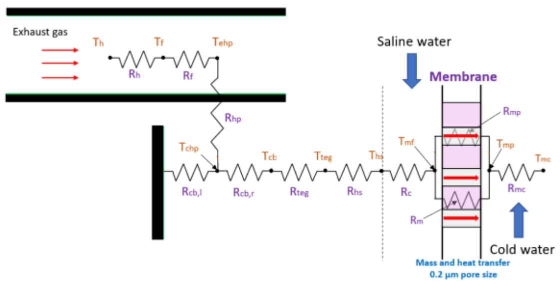

Figure 2. Thermal resistance of proposed system.

The implicit finite-difference method to determine temperatures and node equation can be derived from energy balance [4] as following equation.

$$\dot{E}_{in} + \dot{E}_{out} = \dot{E}_{st} \tag{1}$$

Also, resistance of each component can be calculated by conductive and convective resistance equations except resistance of heat pipes.

Resistance of each heat pipe composes of four thermal resistances as following equations [11].

$$R_{hp} = \frac{1}{N_{hp}} \cdot (R_{p,e} + R_{w,e} + R_{w,c} + R_{p,c}) \tag{2}$$

$$R_{p,e} = \frac{ln\left(\frac{d_o}{d_i}\right)}{2\pi L_{e,c} k_{hp}} \tag{3}$$

where N_{hp} is number of heat pipes, d_o is outside diameter of heat pipe, d_i is inside diameter, $L_{e,c}$ is length of both evaporator and condenser and k_{hp} is thermal conductivity of heat pipe.

$$R_{w,e} = \frac{ln\left(\frac{d_i}{d_v}\right)}{2\pi L_{e,c} k_{eff}} \tag{4}$$

where d_v is vapour spacing and effective thermal conductivity $k_{eff} = \varepsilon k_l + k_w(1-\varepsilon)$, k_l is water conductivity and k_w is wick conductivity. Wick porosity may be calculated as following equation.

$$\varepsilon = 1 - \frac{1}{4}(1.05)\pi N_w d_w \tag{5}$$

where N_w is the number of mesh and d_w is wire diameter.

In terms of TEG performance, temperatures are utilized to predict TEG efficiency which can be expressed by Equation (6).

$$\eta_{TEmax} = \frac{W_{elec}}{Q_h} = \frac{(T_h - T_c)}{T_h} \frac{\sqrt{1+ZT}-1}{\sqrt{1+ZT}+\frac{T_c}{T_h}} \tag{6}$$

where ZT is figure of merit which can illustrate relationship between performance of TEG materials and temperature difference across TEG. The ZT can be calculated by Eq. (7).

$$ZT = \left[\frac{(\alpha_p - \alpha_n)^2}{\left((\lambda_p \rho_p)^{1/2} + (\lambda_n \rho_n)^{1/2}\right)^2}\right]\left[\frac{T_h - T_c}{2}\right] \tag{7}$$

where α_p and α_n are Seebeck coefficients of P and N-type semiconductors. λ_p and λ_n are thermal conductivities of P and N-type semiconductors. ρ_p and ρ_n are electrical resistivities of P and N-type semiconductors. T_h and T_c are temperature of hot and cold side.

For Direct Contact Membrane distillation (DCMD). Heat transfer and mass transfer occur concurrently as shown in Figure 3. Also, temperature gradient decreases due to boundary layer resistance, membrane resistance and resistance of membrane pores.

For modelling, it assumes that heat transfer rate at feed side ($\dot{Q}_f$), across membrane ($\dot{Q}_m$) and at permeate side ($\dot{Q}_p$) are equal.

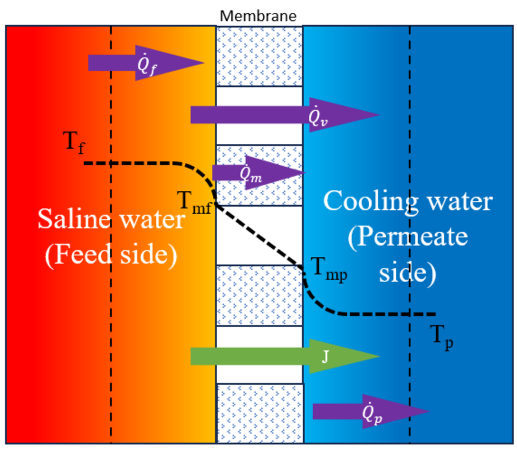

Figure 3. Temperature gradient, mass and heat transfer of DCMD configuration.

Heat transfer rate of feed and permeate solution can be calculated by following equation.

$$\dot{Q}_f = Ah_f(T_f - T_{mf}) \quad (8)$$

$$\dot{Q}_p = Ah_p(T_{mp} - T_p) \quad (9)$$

where h_f and h_p are convective heat transfer coefficient of feed and permeate solution. A is area of heat transfer. T_f and T_p are bulk feed and permeate temperature. T_{mf} and T_{mp} are membrane feed and permeate temperature.

In addition, heat transfer rate of membrane can be expressed by Eq. (10).

$$\dot{Q}_m = \dot{Q}_{cm} + \dot{Q}_v = Ak_{mt}\left(\frac{T_{mf}-T_{mp}}{\delta_m}\right) + AJ\Delta H_{v,w} \quad (10)$$

where k_{mt} is thermal conductivity of membrane, δ_m is thickness of membrane. J and $\Delta H_{v,w}$ are mass flux and vapor enthalpy of water which can be described by Eq. (11) and Eq. (12), respectively.

$$\Delta H_{v,w} = 1.7535T_{mf} + 2024.3 \quad (11)$$

$$J = C_m(P_{v,sw} - P_{v,w}) \quad (12)$$

where $P_{v,w}$ and $P_{v,sw}$ are vapor pressure of water and seawater, which can be estimated by Eq. (13) and Eq. (14) [10], respectively. C_m is mass transfer coefficient.

$$P_{v,w} = exp\left(\frac{a_1}{T_{mp}} + a_2 + a_3T_{mp} + a_4T_{mp}^2 + a_5T_{mp}^3 + a_6 \times ln(T_{mp})\right) \quad (13)$$

$$P_{v,sw} = P_{v,w} \times exp(-4.5818 \times 10^{-4}S - 2.04431 \times 10^{-6}S^2) \quad (14)$$

where S is salinity $(0 - 160\ g/kg)$.
$a_1 = -5800, a_2 = 1.3915, a_3 = -4.8640 \times 10^{-2}, a_4 = 4.1765 \times 10^{-5}, a_5 = -1.4452 \times 10^{-8}, a_6 = 6.5460$

There are three mass transfer coefficients can be selected which depending on membrane pore diameter and Knudsen number (Kn) that is the ratio of the gas mean free path (λ) to the membrane pore diameter [9]. The coefficient equations compose of Knudsen diffusion equation, molecular diffusion equation and Knudsen-molecular diffusion equation.

However, in this study, mass transfer coefficient is determined by Eq. (15) which is molecular diffusion equation.

$$C_m = \frac{\varepsilon_m}{\delta_m\tau}\frac{P_tD_{w-a}}{P_a}\frac{M}{RT} \quad (15)$$

where $\varepsilon_m, \delta_m, R, M, \tau$ and r are membrane porosity, membrane thickness, gas constant, water molecular weight, membrane tortuosity, mean pore size radius, entrapped air pressure, respectively. $P_tD_{w-a} = 1.895 \times 10^{-5}T^{2.072}$

Membrane feed and permeate temperature can be predicted as follows:

$$T_{mf} = \frac{h_m\left(T_p+\frac{h_f}{h_p}T_f\right)+h_fT_f-J\Delta H_{v,w}}{h_m+h_f\left(1+\frac{h_m}{h_p}\right)} \quad (16)$$

$$T_{mp} = \frac{h_m\left(T_f+\frac{h_p}{h_f}T_p\right)+h_pT_p+J\Delta H_{v,w}}{h_m+h_p\left(1+\frac{h_m}{h_f}\right)} \quad (17)$$

where $h_m = \frac{k_m}{\delta_m}$

Initial setting of the modelling, as shown in Table 1.

Table 1. Initial temperatures of exhaust gas and water.

Exhaust temperature	140 °C
Saline water	20 °C
Cooling water	20 °C

2.2. Result and discussion

The effect of velocity of the flue gas (hot air) on the rate of heat transfer was examined and is presented in Figure 4. The modelling results show that for flue gas velocity of 0.5m/s to 1.5m/s the rate of heat transfer increased from 530W to 760W and the power output from the TEG varied from 4.5W to around 6.8W. It was observed that for the proposed system the effect of flue gas velocity on the heat transfer rate and hence the TEG power starts to diminish beyond 1.5m/s.

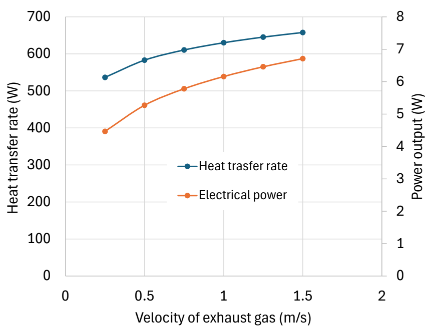

Figure 4. Effect of flue gas velocity on heat transfer rate and TEG power output

Hence further detailed modelling analysis was conducted under 1.5m/s flue gas velocity. Figure 5 shows that for flue gas (modelled as hot air) temperature of 140°C and velocity of 1.5m/s, the steady state was achieved in around 35 to 40min. At this steady state the hot side temperature of the TEG was predicted to be reach around 75 °C and saline water temperature of around 24 °C. With the available temperature difference the model predicts electrical power output of around 6.8W and permeate flux of around 2 kg/m^{2}h.

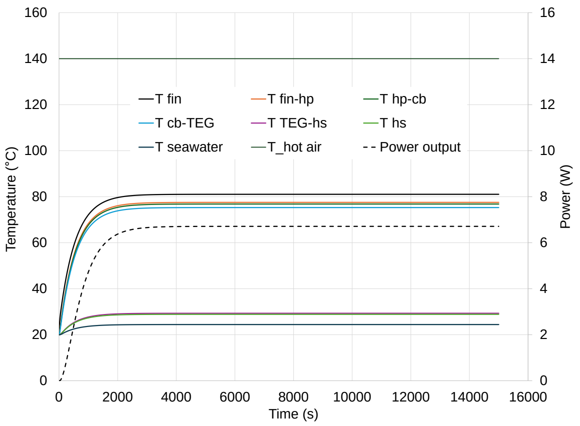

Figure 5. Thermal performance prediction of HP-TEG-MD system

Experiments were conducted on a bench scale prototype. For a thermal energy input rate of around 400W, at steady state condition the hot side of the TEG reached a temperature of around 133 °C and the saline water temperature was around 30 °C similar to the model, except that the TEG hot side in the experiments was much hotter than the model. Figure 6 shows how the system behaves from start of the test to the steady state condition with feedwater salinity of around 1% (10000ppm) of mixed salt (similar to sea salt). The steady state condition is achieved in around 25min compared to around 40min as predicted by the model.

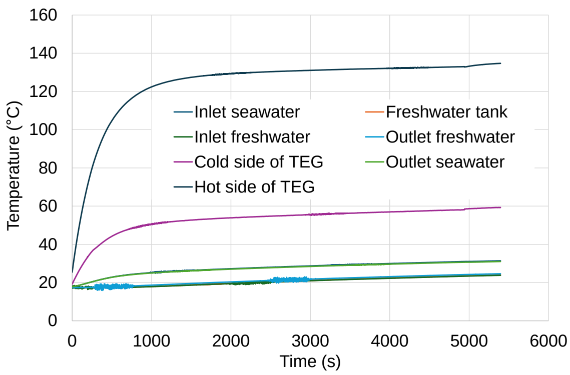

Figure 6. Experimental thermal behavior of the system

Through experiments it was established that under around 400W of heat flow rate and with feed water salinity of around 1% the system can produce around 1.7kg/m^2.h of fresh water, which is similar to what was predicted. But further research is needed to refine the mathematical model and also to conduct further testing to improve confidence on the experimental results.

3. Conclusion

An innovative combined desalination and power generation system with heat pipes has been discussed in this paper that can utilize low-grade heat source. The proposed system has modelled in Matlab and the modelling shows promising results with high freshwater yield. Experimental set-up has been developed to validate the model and preliminary experiments have confirmed high freshwater yield. Further experimental results indicate that with a source temperature of around 140 °C the feed water only reaches up to 30 °C, and it takes around 1 hour to reach the steady state condition. Further the experimental results and modelling show that with reduced temperature of permeate side the freshwater yield increases. The TEG cold side temperature is also very sensitive to the permeate side temperature and has potential to produce more power from TEG’s.

References

[1] Van Vliet, M.T.H., et al., Global water scarcity including surface water quality and expansions of clean water technologies. Environmental research letters, 2021. 16(2): p. 24020.
[2] Turiel, A., The energy crisis in the world today: analysis of the World Energy Outlook 2021. 2022.
[3] Waste Heat Recovery: Technology and Opportunities in U.S Industry. 2008.
[4] Duke, M., Industrial waste heat powers desalination. Membrane Technology, 2012. 2012(5): p. 9.
[5] Fierro, J.J., et al., Evaluation of waste heat recovery technologies for the cement industry. International Journal of Thermofluids, 2020. 7-8: p. 100040.
[6] Ghaffar, A., et al., Simultaneous solar water desalination and energy generation by high efficient graphene oxide-melanin photothermal membrane. Journal of Environmental Chemical Engineering, 2022. 10(5): p. 108424.
[7] Date, A., et al., Theoretical and experimental study on heat pipe cooled thermoelectric generators with water heating using concentrated solar thermal energy. Solar Energy, 2014. 105: p. 656-668.
[8] Date, A., et al., Performance review of a novel combined thermoelectric power generation and

water desalination system. Renewable Energy, 2015. 83: p. 256-269.
[9] J. Phattaranawik, R. Jiraratananon, and A. G. Fane, "Effect of pore size distribution and air flux on mass transport in direct contact membrane distillation," *Journal of Membrane Science,* vol. 215, no. 1, pp. 75-85, 2003/04/15/ 2003, doi: https://doi.org/10.1016/S0376-7388(02)00603-8.
[10] K. G. Nayar, M. H. Sharqawy, L. D. Banchik, and J. H. L. V, "Thermophysical properties of seawater: A review and new correlations that include pressure dependence," *Desalination,* vol. 390, pp. 1-24, 2016.
[11] M. F. B. Remeli, "Simultaneous Industrial Waste Heat Recovery and Power Generation Using Heat Pipe Assisted
Thermoelectric Generator," Doctor of Philosophy, School of Aerospace Mechanical and Manufacturing Engineering, RMIT University, 2015.

Paper ID 071(S8)

Low Pressure Drop Biomimetic Manifold Microchannels for Cooling Electronic Devices

Keyi Huang[1], Guiping Lin[2,1], Kai Tang[1], and Yuandong Guo[1,3*]

[1] *School of Aeronautic Science and Engineering, Beihang University, Beijing, China*
[2] *Hangzhou International Innovation Institute, Beihang University, Hangzhou, China*
[3] *Ningbo Institute of Technology, Beihang University, Ningbo, China*
[*] *Corresponding author email address: guoyd@buaa.edu.cn*

Abstract

The increasing integration of electronic devices has resulted in the development of more compact chips, leading to higher heat flux and restricted heat dissipation paths. This has necessitated the creation of compact cold plates to facilitate the heat dissipation of multiple chips. In this study, a multi-chip cold plate that incorporates leaf vein inspired manifold microchannel (MMC) heat sinks with a fractal flow distributor is proposed. The thermal-hydraulic performance of a single MMC heat sink and the overall cold plate is evaluated through a pumped two-phase fluid loop. The single heat sink was observed to be capable of dissipating 94 W/cm^2 with a low pressure drop of no more than 9 kPa. For the multi-chip cold plate, stable operation can be ensured when the outlet dryness is below 0.16 and the base temperature does not exceed 60 °C under 30 W/cm^2, with temperature uniformity better than 10 °C. This multi-chip cold plate represents a novel approach to the cooling of integrated electronic devices.

Keywords: Multi-chip; Manifold microchannel; Low pressure drop; Flow boiling; Biomimetic structure.

1. Introduction

The continuous upgrading of electronic devices is driving the accelerated development of sophisticated technologies, including 5G communications, artificial intelligence, and aerospace. In recent years, the limitation of single-chip capability has prompted the evolution of electronic devices towards multi-chip integration. This includes the development of large-scale integrated circuits [1,2], insulated gate bipolar transistor (IGBT) modules [3], active phased array antennas (APAA) [4,5], and light-emitting diode (LED) arrays [6]. The compact configuration of these microchips gives rise to a considerable power density, augmented self-heating, and constrained heat transfer pathways [7]. When the temperature of an electronic device exceeds a certain threshold, several adverse effects can occur, including performance degradation and abnormal functionality. Fluctuations in junction temperature resulting from waste heat can lead to bond wire detachment due to shear stress in IGBT modules [8]. Additionally, the electromagnetic performance of APAA can be compromised by overheating or non-uniform temperature distributions, resulting in significant phase errors exceeding 3° [9]. Similarly, in LED arrays, approximately 70-85% of the input power is converted to heat [10]. An elevated junction temperature have adverse effects on the wavelength stability, luminous efficiency, and lifetime of the device [11]. Therefore, the thermal management of integrated chips has become a significant research topic.

Considering the markedly high heat flux exhibited by multi-chip electronic devices, it is evident that traditional forced air cooling techniques are no longer applicable. In recent years, there has been a growing interest in microchannel liquid cooling due to its superior heat transfer performance. The concept of microchannel heat sink (MCHS) was initially proposed by Tuckerman and Pease during their research on liquid cooling of very-large-scale integrated circuits [12]. Subsequently, a number of studies focused on the microchannel cooling of multi-chip devices. These studies investigated the impact of microchannel dimensions [13,14], pin-rib layouts [15] and flow distribution structures [16,17] on the thermal-hydraulic performance of MCHS under varying heat loads.

Among the numerous optimized microchannel structures, manifold microchannels (MMCs) emerged as a highly effective solution for the thermal management of integrated chips and power electronics. The MMC is characterized by additional manifold structures that divide the overall heat sink into an array of U-shaped subchannels, thereby significantly reducing the flow distance [18]. In the experiments conducted by Erp et al. [19], a manifold comprising 10 inlet and outlet channels, together with parallel embedded microchannels, was demonstrated to be an effective means of controlling the single-chip temperature rise below 60 K at a heat flux of 1723 W/cm^2. Furthermore, Erp et al. [20,21] designed a larger MMC heat sink for the simultaneous cooling of 20 active devices of a power electronic converter. A flow rate of 1 mL/s enables the heat dissipation of 600 W while maintaining a maximum junction temperature rise below 60 K. However, a notable temperature non-uniformity of over 15 K exists between the transistors, and the total pressure drop was 50 kPa. Yang et al. [22] proposed double H-type MMCs for large-area chip cooling. When subjected to a heat load of 417 W, the average and maximum chip temperature rise were observed to be 22.2 K and 34.7 K, respectively, with a pump pressure of 35 kPa. Drummond et al. [23] processed a 3×3 MMC heat sink array for embedded two-phase cooling. When a uniform heat flux of 1020 W/cm^2 was applied, the chip temperature rise relative to the fluid inlet was less than 69 °C, and the pressure drop was approximately 120 kPa. Although the heat transfer in MMCs has been observed to be enhanced, the flow resistance remains considerable. This is due to the fact that the increase in pressure drop resulting from the narrow contractions and bends in the flow path counterbalanced the reduction in flow path length [19]. Furthermore, in two-phase cooling, the accumulation of bubbles causes more pronounced increase in pressure drop, leading to a considerable consumption of pumping power, which limits the potential application of MMCs.

In contrast, natural flow structures, such as tree branches, leaf veins, rivers and blood vessels, have evolved over an extended period to form distinctive features that exhibit minimal flow resistance. In the studies conducted by Ma et al. [24] and Ji et al. [25], the performance of bio-inspired fractal microchannels was compared with that of traditional microchannels. It was found that the pressure drop was reduced by 46% and 92%, respectively, accompanied by an enhancement in heat transfer coefficient. In addition, Zhao et al. [26] fabricated a leaf vein-inspired three-tiered open microchannel and carried out flow boiling experiments. The pressure drop was maintained below 10 kPa, as the heat dissipation exceeded 100 W/cm^2. These investigations demonstrate that the biomimetic microchannel designs exhibit a notable reduction in flow resistance, which is beneficial for energy conservation of the cooling system.

In this study, a compact multi-chip cold plate combining the MMC with biomimetic structures was proposed. This cold plate consists of leaf vein inspired MMC heat sinks and a fractal flow distributor. The thermal-hydraulic performance of a single leaf vein inspired MMC heat sink was investigated through visualization experiments at different flow rates. Additionally, the temperature uniformity and two-phase instability of the overall cold plate were evaluated and compared with the single-chip results. When situated within an appropriate outlet dryness range, the biomimetic MMC cold plate is capable of cooling multiple hotspots simultaneously with a low pressure drop. This represents a promising solution for the integrated cooling of electronic devices.

2. Experimental Setup and Methods

2.1. Test Section Design and Assembly

Figure 1(a) illustrates the water distribution function of a plant, whereby the water transported from the stems is evenly distributed to each leaf. Subsequently, the leaf veins facilitate the distribution of water to each cell, thereby supporting the process of photosynthesis within the cells. Inspired by the leaf water transport mechanism, a compact multi-chip cold plate was designed. The cold plate incorporates eight leaf vein inspired MMCs. In each MMC, the working fluid is distributed through the manifold channels and flows into the underlying microchannels where it undergoes an evaporation process due to heat absorption. This flow distribution structure is based on the structure of a leaf vein, as illustrated in Figure 1(b). Figure 1(c) depicts the configuration of the overall cold plate. The upper layer of the cold plate features a fractal flow distributor, which ensures uniform distribution of the working fluid to the eight MMC heat sinks. Subsequently, the two-phase fluid is released through the fractal flow distributor. This biomimetic cold plate design allows for the implementation of multi-chip cooling functionality within a restricted space.

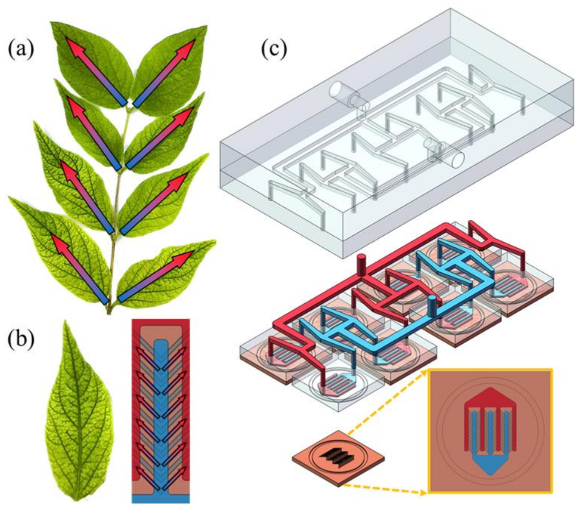

Figure 1. (a) Water transport structure of plant leaves. (b) Design of leaf vein inspired MMC heat sink. (c) Design of the biomimetic cold plate.

In order to evaluate the fundamental thermal-hydraulic performance of a single leaf vein inspired MMC heat sink, a test section was constructed in accordance with the configuration shown in Figure 2(a). The test section is comprised primarily of a visualization fluid supply plate, a manifold plate, a leaf vein microchannel plate, a ceramic heater, insulation material, and a retaining plate.

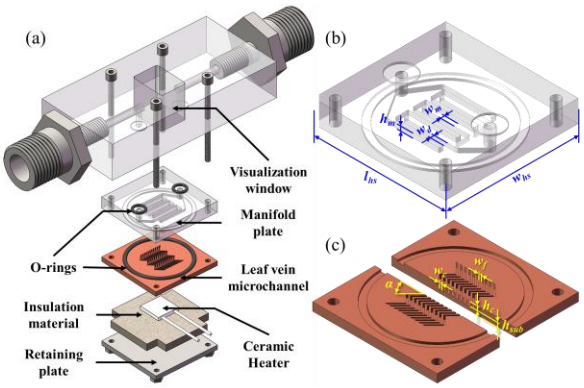

Figure 2. (a) Assembly of the single heat sink test section. (b) Parameters of the PC manifold plate. (c) Parameters of the copper microchannel plate.

The manifold plate and the microchannel plate are of particular significance with regard to flow and heat transfer. The manifold layer was etched onto a polycarbonate (PC) plate, while the microchannels were etched with great precision onto an oxygen-free copper plate. The geometric parameters of the PC manifold plate and the copper microchannel plate are illustrated in Figure 2(b) and (c), respectively. The specific values for these parameters are presented in Table 1 for reference.

Table 1. Dimensions of the designed MMC.

Variable	Parameter	Value
l_{hs}	Heat sink length	30 mm
w_{hs}	Heat sink width	30 mm
h_m	Manifold channel height	0.5 mm
w_m	Manifold channel width	1 mm
w_d	Divider width	1 mm
w_c	Microchannel width	0.3 mm
h_c	Microchannel height	0.5 mm
w_f	Fin width	0.3 mm
h_{sub}	Substrate height	1.5 mm
α	Incidence angle	45°

To prevent leakage of the working fluid, circular grooves were etched and O-rings were placed between the manifold plate and the microchannel plate, as well as between the manifold plate and the visualization fluid supply plate. A 10 mm×10 mm ceramic heating pad with a resistance of approximately 6Ω was placed under the MMC for heating. In order to minimize heat exchange between the test section and the environment, insulation material is wrapped beneath the ceramic heater and around the test section. The test section is assembled and affixed by means of screws.

Figure 3 illustrates the assembly of the multi-chip cold plate test section. The cold plate comprises a Fluid supply plate, a fractal flow distributor, and 8 leaf vein inspired MMC heat sinks. Additionally, the test section is assembled and fixed by screws. During the test, 8 ceramic heating pads were supplied by 8 DC power supplies to investigate the flow boiling heat transfer performance of the two-phase cold plate.

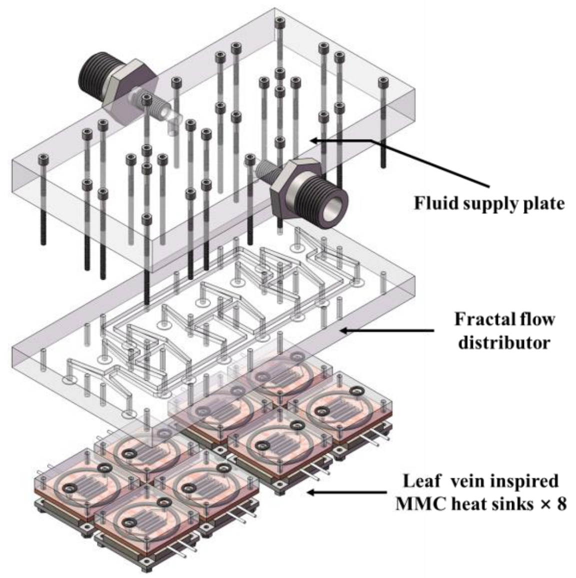

Figure 3. Assembly of the multi-chip cold plate test section.

2.2. Two phase Fluid loop

A mechanically pumped two-phase fluid loop was utilized to assess the flow and heat transfer characteristics of the biomimetic cold plate at specified mass flow rates, as illustrated in Figure 4(a). The micropump GB-P23 was utilized for the purpose of propelling the working fluid through the loop. A volumetric flow meter (CX-M5.2-AL) was utilized to ascertain the real-time flow of the working fluid within the loop, while a pressure transmitter (Omega PX409) was employed to monitor the pressure within the reservoir. The heat transfer characteristics were quantified by measuring the base temperature of the heat sink with K-type thermocouples. The flow characteristics were evaluated based on the pressure drop across the test section. The output voltage and current displayed by the heating power supply (IVYTECH, 6005) were recorded and the heating power was

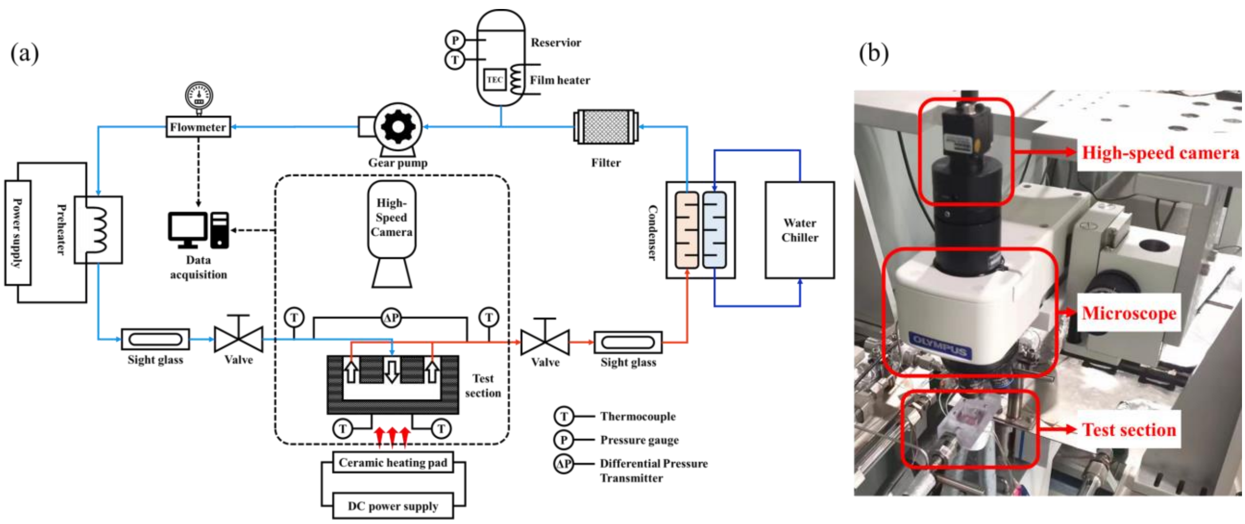

Figure 4. (a) Schematic diagram of the mechanically pumped two-phase fluid loop. (b) Concrete image of the high-speed camera system.

calculated. This was then converted to effective heat flux by subtracting the heat leakage measured in the experiment. A sight glass is provided at both the front and back of the test section, allowing for observation of the phases of the working fluid. An external water chiller serves as the primary cooling source for the entire loop, maintaining a continuous supply of low-temperature water to the serpentine condenser. This configuration ensures that the working fluid leaves the condenser in its liquid phase.

A microscope (Olympus, U-TLU) equipped with a high-speed camera (YVSION, OSG030-790UM) was employed to observe the bubble movement and flow patterns in the manifold channels and microchannels, with the aim of elucidating the enhanced heat transfer mechanism, as illustrated in Figure 4(b).

As a low-boiling point e-fluoride fluid, HFE-7000 was selected as the working fluid with a saturation temperature of 40°C and an inlet subcooling of 15°C. The fundamental thermophysical characteristics of HFE-7000 are presented in Table 2.

Table 2. Fundamental thermophysical characteristics of HFE-7000 [27].

Variable	Parameter	Copper
T_{sat}	Saturation temperature	40 °C
P_{sat}	Saturation pressure	122.8 kPa
ρ_l	Liquid density	1362 kg/m^3
ρ_v	Vapor density	10 kg/m^3
c_p	Liquid specific heat	1.28 kJ/(kg·K)
h_l	Liquid enthalpy	250.8 kJ/kg
h_v	Vapor enthalpy	384.9 kJ/kg
σ	Surface tension	10.23 kN/m

2.3. Data reduction and uncertainties

The heat flux can be calculated by multiplying the voltage and current output from the DC power supply, subtracting the heat leakage from the test section, and dividing by the area of the heat source.

$$q = \frac{U \cdot I - Q_{\text{leak}}}{A} \tag{1}$$

The working fluid in the test section was drained, and the test section was heated at a lower power in order to measure the amount of heat leakage corresponding to different base temperatures. The heat leakage data were fitted as shown in Figure 5.

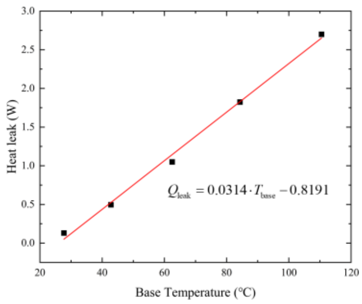

Figure 5. Fitted curve of test section heat leakage.

Base temperature is averaged from two thermocouple readings attached to the copper surface.

$$T_{\text{base}} = \left(T_{\text{TC-1}} + T_{\text{TC-2}}\right)/2 \tag{2}$$

The exit vapor quality is calculated as:

$$x = \frac{U \cdot I - Q_{\text{leak}} - \dot{m}c_p\left(T_{\text{out}} - T_{\text{in}}\right)}{\dot{m}\left(h_v - h_l\right)} \tag{3}$$

The mass flow rate is calculated as:

$$\dot{m} = \rho_l \cdot \dot{V} \tag{4}$$

The uncertainties of the main measurement parameters, based on the accuracy of the relevant equipment, are summarized in Table 3. The uncertainties of the non-directly measured parameters are obtained using classic error transmission theory.

Table 3. Uncertainties of the measured parameters.

Parameter	Uncertainty
Power supply voltage	0.1%
Power supply current	0.1%
Temperature	0.5%
Pressure drop	±0.1%FS
Volumetric flow rate	±0.1%FS
Heat flux	±4%

3. Results and discussion

3.1. Thermal-hydraulic performance of the MMC heat sink

The thermal-hydraulic performance of the MMC heat sink was initially evaluated at a relatively low flow rate of 2000 mL/h, as illustrated in Figure 6. Single-phase flow was observed when the heat flux was less than 10 W/cm^2. As the heat flux increases, the base temperature rises rapidly, while the pressure drop remains constant. Upon exceeding a heat flux of 10 W/cm^2, the generation of bubbles can be observed through the visualization window. In such cases, the utilization of the latent heat of phase change results in a deceleration of the temperature increase with respect to heat flux. When the heat flux is less than 30 W/cm^2, the flow resistance remains relatively low.

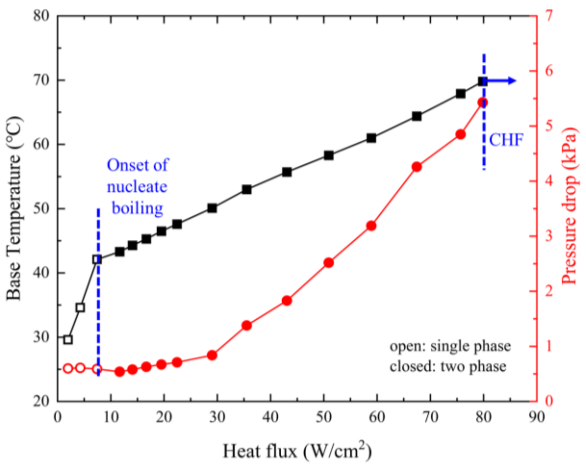

Figure 6. Thermal-hydraulic performance of single heat sink at 2000 mL/h.

As the heat flux continues to increase, the pressure drop of the test section rises significantly. The critical heat flux (CHF) is 79.8 W/cm², at which the MMC base temperature is approximately 70 °C and the pressure drop is 5.43 kPa.

Furthermore, the base temperature and pressure drop of the MMC heat sink at varying heat fluxes were evaluated at three higher flow rates and compared with the data presented by Dang et al. [28], as shown in Figure 7 and Figure 8, respectively. The trends of base superheat (ΔT refers to base temperature minus inlet temperature) with heat flux are consistent across the three different flow rates. The steeper slope of the curve in the two-phase region indicates that the MMC heat sink exhibits a higher heat transfer coefficient (HTC) in the flow boiling condition. As the flow rate increases, the base superheat decreases and the onset of boiling is delayed.

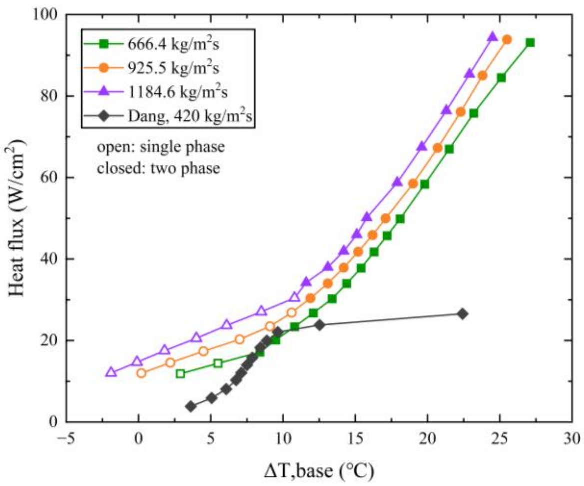

Figure 7. Heat transfer performance of single heat sink at three different flow rates compared with Dang et al.

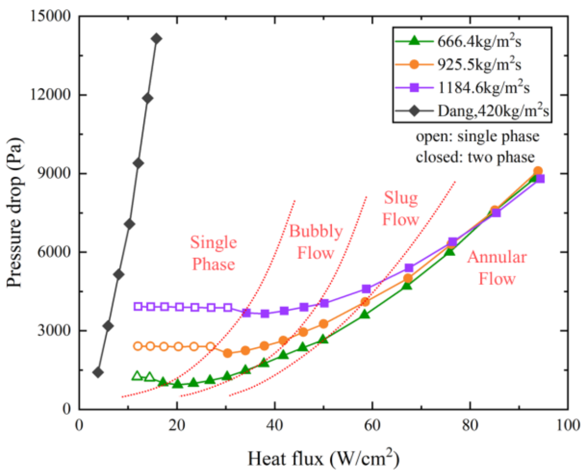

Figure 8. Pressure drop of single heat sink at three different flow rates compared with Dang et al.

In comparison to the experiments conducted by Dang et al., the leaf vein inspired MMC heat sink exhibited superior heat dissipation capabilities, demonstrating the potential to adapt to higher heat fluxes without reaching the CHF in all three sets of tests.

With regard to flow resistance, the pressure drop remains essentially constant within the single-phase region, as shown in Figure 8. However, a notable increase is observed within the two-phase region, proportional to the heat flux. As the flow rate increases, the pressure drop increases in the lower heat flux region, but tends to be uniform in the higher heat flux region. This is due to the fact that an increase in flow rate suppresses the liquid-vapor phase change, which in turn reduces the increase in pressure drop due to bubble expansion and accumulation. In contrast with the pressure drop data presented by Dang et al., the leaf vein inspired MMC heat sink exhibits a significantly lower pressure drop, due to the noticeably shortened flow path. Moreover, the pressure drop remains below 9 kPa when the heat flux reaches 94 W/cm^2.

3.2. Flow patterns of the MMC heat sink

In the single heat sink experiments, a high-speed camera was employed to document the flow patterns at varying heat flow densities, thereby elucidating the flow and heat transfer mechanism of the leaf vein inspired MMC. Two photographic locations were selected in proximity to the manifold inlet channel and manifold outlet channel, respectively, as illustrated in Figure 9.

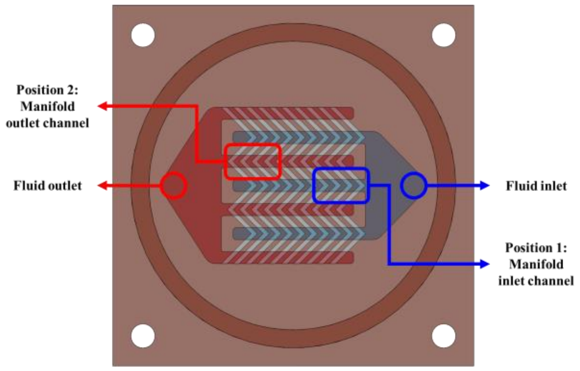

Figure 9. High-speed camera photo positions.

The flow patterns at the manifold inlet and outlet channels corresponding to several typical heat fluxes were recorded at a volume flow rate of 2000 mL/h, as illustrated in Figure 10. Upon reaching a heat flux of 11.7 W/cm^2, the MMC heat sink entered the initial boiling stage. At this juncture, tiny, circular bubbles emerged within the microchannel and subsequently discharged the heat sink via the manifold outlet channel. The corresponding outlet dryness (x) was determined to be 0.024. As the heat flux was increased to 19.5 W/cm^2, the outlet dryness was 0.07, and backflow bubbles were observed in the manifold inlet channels. Concurrently, a typical slug flow was formed in the microchannels and the manifold outlet channels. Upon further increasing the heat flux to 29 W/cm^2, a slug flow was also observed in the manifold inlet channel. Additionally, bubbles in the manifold outlet channel merged to form an annular flow, corresponding to an x value of 0.16. At a heat flux of 43.1 W/cm^2, stable annular flow was observed in all channels throughout the

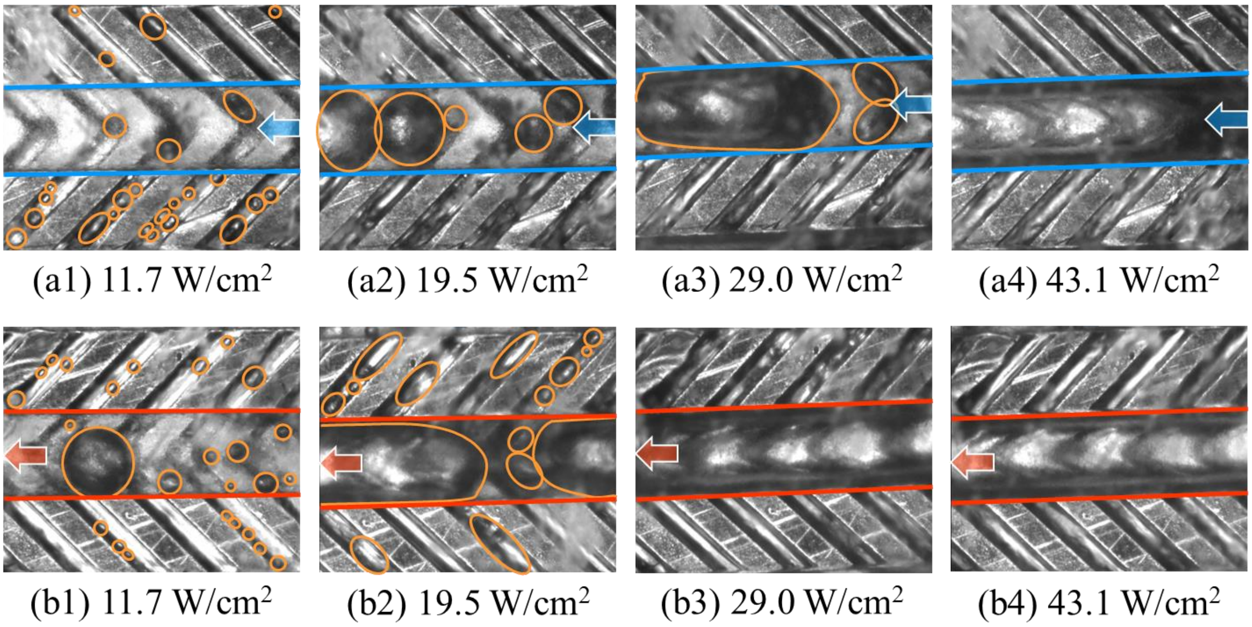

Figure 10. Variation of flow patterns with heat fluxes of MMC heat sink (a) position 1 and (b) position 2 at 2000 mL/h.

MMC heat sink, and no isolated bubbles could be identified. At this condition, the outlet dryness was x = 0.3.

A comparison of the present result with that of Figure 6 reveals that when all the channels of the MMC heat sink are filled with annular flow, it represents the inflection point at which the pressure drop curve increases significantly. The findings indicate that when the outlet dryness is maintained at approximately 0.16, the pressure drop associated with two-phase flow boiling is comparable to that of single-phase flow, yet there is a notable enhancement in the heat transfer coefficient. As the outlet dryness increases, the expansion space of the bubbles is compressed, resulting in backflow of the bubbles into the inlet manifold. This phenomenon is the primary cause of the observed increase in pressure drop.

3.3. Cooling performance of multi-chip cold plate

Eight MMC heat sinks were integrated into a multi-chip cold plate and their cooling performance was evaluated. To ensure that each heat sink was subjected to the same heat flux, the ceramic heating pad of each heat sink was powered by an independent DC power supply. The impact of varying heat fluxes (5 W/cm^2 to 30 W/cm^2) on the base temperatures of eight MMC heat sinks was investigated through flow boiling experiments. In the experiments, the volume flow rate was maintained at 16000 mL/h, with an average volume flow rate of 2000 mL/h for each single MMC heat sink. The results are presented in Figure 11.

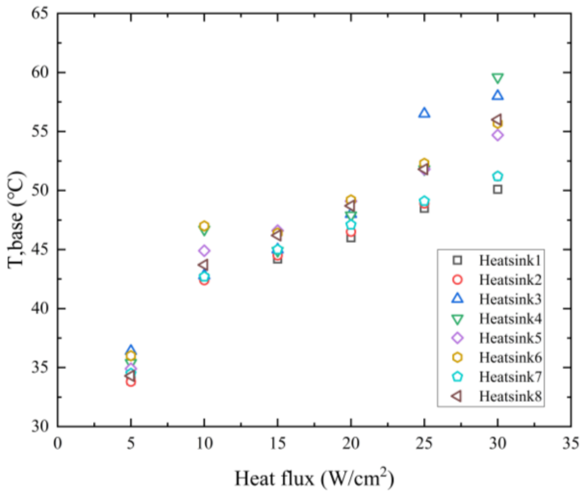

Figure 11. Base temperatures of eight individual heat sink of multi-chip cold plates at different heat fluxes (16000 mL/h).

At a heat flux of 5 W/cm^2, the working fluid within the cold plate was observed to be in a state of single-phase flow. Upon elevating the heat flux to values exceeding 10 W/cm^2, the eight heat sinks were observed to be in a state of flow boiling. As the heat flux continues to increase, a gradual temperature difference emerges between the heat sinks. At a heat flux of 30 W/cm^2, the maximum and minimum base temperatures of the eight heat sinks exhibited a difference of approximately 10°C.

Furthermore, the flow and heat transfer characteristics of the multi-chip cold plate were compared with those of a single MMC heat sink, as illustrated in Figure 12. In consideration of the temperature curves, the trend of base temperature averages for heat sinks in the multi-chip cold plate with heat flux was found to be essentially identical to that of the individual MMC heat sink. However, when the heat flux is increased, the average base temperature of the multi-chip cold plate is observed to be higher, whereas the base temperature of the single MMC heat sink is approximately equal to that of the lowest temperature among the eight heat sinks in the multi-chip cold plate. This finding indicates that for two-phase flow boiling, the combination of multiple heat sinks has a slight detrimental impact on the heat transfer performance of the individual heat sinks, with an increase in the average base temperature of approximately 5°C at a heat flux of 30 W/cm^2.

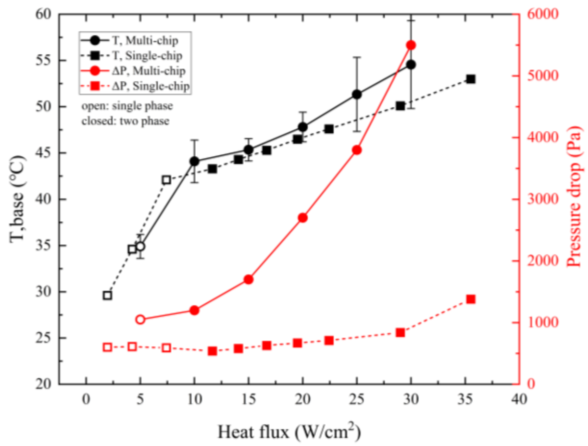

Figure 12. Comparison of flow and heat transfer characteristics of multi-chip cold plate and single MMC heat sink.

In terms of flow resistance, the pressure drop of the multi-chip cold plate is markedly higher than that of the single MMC heat sink. This phenomenon can be attributed to the necessity for the two-phase working fluid to flow through the fractal flow distributor of the cold plate, which significantly increases the length of the flow path. As a result, the overall pressure drop of the multichip cold plate is 5.5 kPa at 30 W/cm², whereas at the same heat flux, the pressure drop of the single MMC heat sink is less than 1 kPa.

Figure 13 illustrates the specific temperature distribution of the eight MMC heat sinks at a heat flux of 30 W/cm². Despite the overall cold plate exhibiting a temperature difference of no more than 10°C, there is considerable scope for enhancement in terms of temperature uniformity.

As shown in Figure 13, despite HS-1 and HS-3, in addition to HS-2 and HS-4, occupying the same side of the working fluid distribution channel, the temperature discrepancy between them is the most pronounced. One potential reason for this phenomenon is that as HS-3 generates a greater number of bubbles due to the temperature increase, it consequently increases its own flow resistance, thereby necessitating an increased flow of working fluid to its neighboring HS-1.

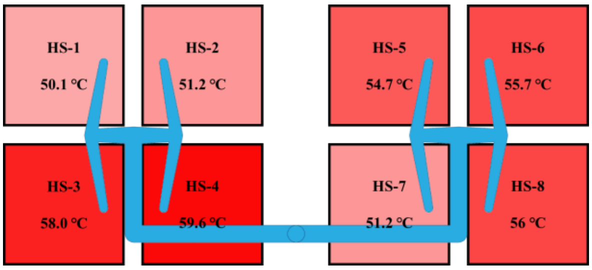

Figure 13. Comparison of flow and heat transfer characteristics of multi-chip cold plate and single MMC heat sink.

Furthermore, in order to guarantee the normal function of the multi-chip cold plate, it is advised to regulate the outlet dryness of the multi-chip cold plate by adjusting the inlet subcooling, with a value of less than 0.16. When the outlet dryness is excessive, as discussed in section 3.2, it may result in bubble accumulation and backflow, which markedly impacts the flow distribution within the multi-chip cold plate and gives rise to a considerable temperature disparity.

Moreover, to further enhance the flow and heat transfer performance of the multi-chip cold plate, it is recommended that the cross-sectional area of the outlet channels of the heat sinks and cold plate be expanded in subsequent work. This would provide more space for the expansion and accelerated discharging of the bubbles.

4. Conclusion

In this study, a multi-chip cold plate combining the leaf vein inspired MMC heat sinks with a fractal flow distributor was proposed and experimentally tested. The flow and heat transfer characteristics were investigated for a single heat sink and an overall multi-chip cold plate, respectively. Furthermore, the heat transfer mechanism of the MMC heat sink was analyzed with the aid of visualization images, and the following conclusions were obtained:

(1) The base temperature and pressure drop variations of a single leaf vein inspired MMC heat sink were tested at varying flow rates and heat fluxes. The results demonstrated that the structure exhibited favorable flow and heat transfer characteristics, capable of dissipating 94 W/cm² through a pressure drop of no more than 9 kPa without reaching its CHF.

(2) Images captured by a high-speed camera of a single MMC heat sink revealed the transition in flow patterns within the manifold inlet and outlet channels, which corresponded to different heat fluxes at a rate of 2000 mL/h. It was determined that upon reaching an outlet dryness of 0.16, the MMC is filled with annular flow. Furthermore, the accumulation of bubbles is identified as a significant contributing factor to the increased pressure drop.

(3) The average base temperature of the multi-chip cold plate is slightly higher than that of the single heat sink under identical operational conditions. Furthermore, the pressure drop is markedly greater due to the augmented flow path. The temperature differential between the heat sinks does not exceed 10°C, and the pressure drop is 5.5 kPa at 30 W/cm².

The biomimetic design of the two-phase multi-chip cold plate exhibits enhanced stability and heat dissipation relative to a single-phase cold plate under specific outlet dryness conditions. This innovative design offers promising potential for broad application in cooling electronic devices.

5. ACKNOWLEDGEMENTS

This work is supported by Young Elite Scientists Sponsorship Program by CAST (No. 2023QNRC001).

References

[1] S.G. Kandlikar, Review and Projections of Integrated Cooling Systems for Three-Dimensional Integrated Circuits, J. Electron. Packag. 136 (2014) 024001.

[2] H. Lee, Y. Jeong, J. Shin, J. Baek, M. Kang, K. Chun, Package embedded heat exchanger for stacked multi-chip module, Sens. Actuators Phys. 114 (2004) 204–211.

[3] W. Lai, Z. Xing, R. Yao, X. Ding, J. Shi, Y. Min, H. Li, C. Yang, W. Han, Y. Yuan, Study on Condition Monitoring Method Based on Magnetic Flux Density for Multi-Chips Parallel IGBT

Modules, IEEE Trans. Ind. Appl. 60 (2024) 6499–6511.
[4] Yu.E. Nikolaenko, D.V. Pekur, V.Yu. Kravets, V.M. Sorokin, D.V. Kozak, R.S. Melnyk, L.V. Lipnitskyi, A.S. Solomakha, Thermal performance of low-cost cooling systems for transmit/receive modules of phased array antennas with and without gravity heat pipes, Front. Heat Mass Transf. 18 (2022).
[5] H.-I. Kim, A. Wilcher, W. Lee, J.M. Jaime, D. Otts, S. Nelson, Y.-K. Yoon, Metaconductor-Based Integrated Array Antenna for High-Efficiency Millimeter-Wave Wireless Communications and Radar Applications, IEEE Trans. Compon. Packag. Manuf. Technol. 14 (2024) 1134–1137.
[6] S. Liang, R. Hao, D. Fan, B. Li, J. Huang, Y. Zhang, J. Wu, Y. Li, J. Mo, Structural optimization and numerical thermal analysis of ultraviolet light-emitting diodes with high-power multi-chip arrays, Optik 222 (2020) 165333.
[7] S.V. Garimella, A.S. Fleischer, J.Y. Murthy, A. Keshavarzi, R. Prasher, C. Patel, S.H. Bhavnani, R. Venkatasubramanian, R. Mahajan, Y. Joshi, B. Sammakia, B.A. Myers, L. Chorosinski, M. Baelmans, P. Sathyamurthy, P.E. Raad, Thermal Challenges in Next-Generation Electronic Systems, IEEE Trans. Compon. Packag. Technol. 31 (2008) 801–815.
[8] C. Wang, Y. He, C. Wang, L. Li, X. Wu, Multi-Chip IGBT Module Failure Monitoring Based on Module Transconductance with Temperature Calibration, Electronics 9 (2020) 1559. https://doi.org/10.3390/electronics9101559.
[9] Y. Wang, C. Wang, P. Lian, S. Xue, J. Liu, W. Gao, Y. Shi, Z. Wang, K. Yu, X. Peng, B. Du, S. Xiao, Effect of Temperature on Electromagnetic Performance of Active Phased Array Antenna, Electronics 9 (2020) 1211.
[10] K. Ben Abdelmlek, Z. Araoud, K. Charrada, G. Zissis, Optimization of the thermal distribution of multi-chip LED package, Appl. Therm. Eng. 126 (2017) 653–660.
[11] H.-H. Wu, K.-H. Lin, S.-T. Lin, A study on the heat dissipation of high power multi-chip COB LEDs, Microelectron. J. 43 (2012) 280–287.
[12] D.B. Tuckerman, R.F.W. Pease, High-performance heat sinking for VLSI, IEEE Electron Device Lett. 2 (1981) 126–129.
[13] Z. Wang, S. Zheng, S. Xu, Y. Dai, Investigation on the thermal and hydrodynamic performances of a micro-pin fin array heat sink for cooling a multi-chip printed circuit board, Appl. Therm. Eng. 239 (2024) 122178.
[14] D. Ansari, J.H. Jeong, A novel variable-height-pinfin isothermal heat sink for densely-packed concentrated photovoltaic systems, Energy Convers. Manag. 258 (2022) 115519.
[15] J. Zhang, W. Guo, Z. Xie, X. Guan, X. Qu, Y. Ge, Optimization of fin layout in liquid-cooled microchannels for multi-core chips, Case Stud. Therm. Eng. 41 (2023) 102615.
[16] N. Zhang, Embedded cooling method with configurability and replaceability for multi-chip electronic devices, Energy Convers. Manag. (2022).
[17] T. Wei, H. Huang, Y. Ma, J. Qian, Design and Fabrication of Multi-Layer Silicone Microchannel Cooler for High-Power Chip Array, in: 2021 22nd Int. Conf. Electron. Packag. Technol. ICEPT, IEEE, Xiamen, China, 2021.
[18] X. Pu, Z. Zhao, M. Sun, Y. Huang, Numerical study on temperature distribution uniformity and cooling performance of manifold microchannel heat sink, Appl. Therm. Eng. 237 (2024) 121779.
[19] R. van Erp, R. Soleimanzadeh, L. Nela, G. Kampitsis, E. Matioli, Co-designing electronics with microfluidics for more sustainable cooling, Nature 585 (2020) 211–216.
[20] R.V. Erp, G. Kampitsis, E. Matioli, A manifold microchannel heat sink for ultra-high power density liquid-cooled converters, in: 2019 IEEE Appl. Power Electron. Conf. Expo. APEC, IEEE, Anaheim, CA, USA, 2019: pp. 1383–1389.
[21] R. van Erp, E. Matioli, Efficient Microchannel Cooling of Multiple Power Devices With Compact Flow Distribution for High Power-Density Converters, IEEE Trans. POWER Electron. 35 (2020).
[22] Y. Yang, J. Du, M. Li, W. Li, Q. Wang, B. Wen, C. Zhang, Y. Jin, W. Wang, Embedded microfluidic cooling with compact double H type manifold microchannels for large-area high-power chips, Int. J. Heat Mass Transf. 197 (2022) 123340.
[23] K.P. Drummond, D. Back, M.D. Sinanis, D.B. Janes, D. Peroulis, J.A. Weibel, S.V. Garimella, Characterization of hierarchical manifold microchannel heat sink arrays under simultaneous background and hotspot heating conditions, Int. J. Heat Mass Transf. 126 (2018) 1289–1301.
[24] C. Ma, Y. Sun, Y. Wu, Q. Zhang, Y. Wang, G. Ding, A bio-inspired fractal microchannel heat sink with secondary modified structure and sub-total-sub fluid transmission mode for high heat flux and energy-saving heat dissipation, Int. J. Heat Mass Transf. 202 (2023) 123717.
[25] X. Ji, X. Yang, Y. Zhang, Y. Zhang, J. Wei, Experimental study of ultralow flow resistance fractal microchannel heat sinks for electronics cooling, Int. J. Therm. Sci. 179 (2022) 107723.
[26] Q. Zhao, J. Zhou, M. Lu, X. Chen, Multi-tiered configurations improved flow boiling performance:

Comparation investigation of leaf vein inspired two-tiered and three-tiered open microchannels, Int. J. Therm. Sci. 201 (2024) 109021.
[27] B. Jakubowska, D. Mikielewicz, M. Klugmann, Experimental study and comparison with predictive methods for flow boiling heat transfer coefficient of HFE7000, Int. J. Heat Mass Transf. 142 (2019) 118307.
[28] C. Dang, L. Jia, Q. Peng, L. Yin, Z. Qi, Comparative study of flow boiling heat transfer and pressure drop of HFE-7000 in continuous and segmented microchannels, Int. J. Heat Mass Transf. 148 (2020) 119038.

Paper ID 073(S5)

Experimental Study on thermal performance of a 3D printed Titanium-Water Heat Pipe

Shuaiting Lu[1], Huizhi Wang[2], Yuandong Guo[1*], Jinyin Huang[2], Jianyin Miao[2], Guiping Lin[3,1]

[1] Laboratory of Fundamental Science on Ergonomics and Environmental Control, School of Aeronautic Science and Engineering, Beihang University, Beijing 100191, PR China

[2] National Key Laboratory of Spacecraft Thermal Control, Beijing Institute of Spacecraft System Engineering, Beijing 100094, PR China

[3] Hangzhou International Innovation Institute, Beihang University, Hangzhou 311115, PR China

**Corresponding author email address: guoyd@buaa.edu.cn*

Abstract

With the continuous increase in energy demand for spacecraft, the demand for waste heat dissipation is also increasing, leading to a demand for large-area radiators. Current radiator design shows an increasing dependence on heat pipes. For future space transportation and planetary exploration mission power applications, space nuclear systems require large area radiators to reject the unconverted heat to space at high temperature. Titanium-water heat pipes with high thermal conductivity at high temperature can efficiently transfer heat and minimize the area of radiators. This paper conduct experimental research based on a 3D printed titanium-water heat pipe, by applying different heating powers to the heat pipe in the working temperature range of 100-225 °C to study the heat transfer ability of the titanium-water heat pipe. Results indicate that: the MHTTD of the heat pipe increases with the increase of heating power; when the working temperature is below 200 °C, the heat transfer resistance of the titanium-water heat pipe remains almost unchanged, while when the working temperature is above 200 °C, the heat transfer resistance of the titanium-water heat pipe increases; the MHTP of the titanium-water heat pipe at the temperature of 200 °C is 893.9W.

Keywords: Titanium-water heat pipe; 3D print; Thermal management; High temperature heat transfer

1. Introduction

With the continuous increase in energy demand for spacecraft, new energy driven spacecraft has become the future development trend, such as nuclear powered spacecraft. The demand for waste heat dissipation is also increasing, leading to a demand for large-area radiators. Current radiator design shows an increasing dependence on heat pipes [1]. For future space transportation and planetary exploration mission power applications [2-3], space nuclear systems require large area radiators to reject the unconverted heat to space at high temperature. Heat pipes with high thermal conductivity can efficiently transfer heat and minimize the area of radiators.

Generally, space nuclear systems with a large amount of waste heat cause radiators work at high temperature in the 400 K to 550 K [4-5]. Axially-grooved ammonia heat pipes are widely used in satellites for temperature homogenization in structural panels [6], which however cannot operate at the required high temperature.

NASA has improved the technology capability of titanium-water heat pipes for operation in the 310 K to 530 K temperature range, whose transport capability at 500K ranged from 800W to +900W [7]. Previous study has shown that water heat pipe with a 15-3 beta-titanium alloy tube wall can operate at 280 °C over 30000 hours. 15-3 beta-titanium alloy provides a high strength to mass ratio, so it remains a leading candidate for high-temperature water heat pipe radiators for aerospace applications [8].

It is meaningful to study the maximum heat transfer power of titanium-water heat pipes, as this relates to the space between the heat pipes arranged on the radiator. For heat pipes with sufficient heat transfer capacity, the number of heat pipes used for radiators can be reduced, thereby reducing weight. A hybrid screen-groove heat pipe carried 390 W before partial dryout, and 450 W with partial dryout, during the against gravity test [9]. However, in order to achieve application on next-generation spacecraft, the maximum heat transfer power of titanium-water heat pipes needs further research and improvement.

This paper selects a 3D printed titanium-water heat pipe as the research object, builds a high-temperature titanium-water heat pipe thermal performance experimental setup, and applies different heating powers to the heat pipe in the working temperature range of 100-225 ℃ to study the heat transfer ability of the titanium-water heat pipe.

2. Experimental setup

The experimental setup shown in Figure 1 consists of a titanium-water heat pipe, a heating system, a condensing system, and a temperature measuring system.

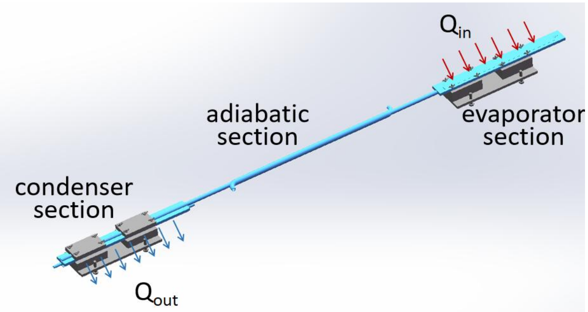

Figure 1. Schematic diagram of experimental setup.

2.1. Titanium-water heat pipe

The appearance of titanium-water heat pipe is a slender circular tube with multiple Ω-shaped microchannels inside, aimed at increasing the heat transfer area of water. The cross section of the titanium-water heat pipe is shown in Figure 2. Due to the low thermal conductivity of titanium, which is only 22 W/(m*K), the thickness of the titanium tube wall is reduced to 1.00-2.58 mm in order to minimize the thermal resistance of the hot pipe diameter and to have a more uniform temperature distribution across the entire radiator [10].

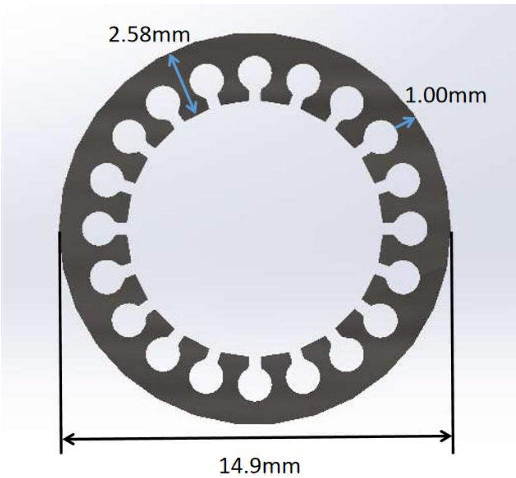

Figure 2. Cross section of the titanium-water heat pipe.

Since titanium cannot be extruded in the same way as aluminum to form grooved heat pipes for space radiators [11], 3D printing is used to process this type of titanium-water heat pipe.

2.2. Heating system

The heating system consists of 5 identical ceramic heating plates, each with a size of 90mm × 30mm, evenly distributed in the evaporator section of the heat pipe. The length of the evaporator section is 500mm. The ceramic heating plates are attached to the heating plate above the heat pipe evaporator section. Each ceramic heating element is connected to an independent power supply, with a current limit of 4A and a voltage limit of 120V.

The outside of the heat pipe is covered with insulation asbestos, but it still cannot prevent the heat leaking into the air. Therefore, it is necessary to calculate the system's heat leakage power, and subtract the heat leakage power from the electric heating power to obtain the actual heating power of the heat pipe.

Three temperature measurement points are arranged outside of the insulation asbestos to obtain the average temperature. The outside of the insulation asbestos is considered as a cylindrical surface with an area of 0.012 m^2. The natural convective heat transfer coefficient between insulation asbestos and air is taken as 20 W/(m^2*K). The leakage heat power of the system can be calculated, as shown in Equation 1.

$$Q_{leak} = h_a A_{oa} (T_{oa} - T_a) \tag{1}$$

where, A_a is the heat transfer area, m^2; h_a is the heat transfer coefficient between insulation asbestos and air, W/(m^2*K), T_a is the air temperature, K; T_{oa} is the average temperature of insulation asbestos, K.

The electric heating power is calculated based on the voltage and current of 5 heating circuits [12], as shown in Equation 2.

$$Q_{electric} = \sum_{j=1}^{5} U_j I_j \tag{2}$$

where, U_j is the voltage of the heating circuit j; V; I_j is the current of the heating circuit j, A.

The actual heating power is calculated using Equation 3.

$$Q = Q_{electric} - Q_{leak} \tag{3}$$

2.3. Condensing system

The condensing system consists of a cold plate and a condensation circuit passing through the cold plate. The low-temperature working fluid in the condensation circuit is silicone oil, which can provide a cooling temperature of 5-70 °C for the heat pipe.

At times, in order to operate the heat pipe at high temperatures up to 200 °C, it is necessary to place 1-6 layers of polyimide film between the cold plate and the heat pipe, with a single layer thickness of 0.1mm. The purpose is to increase the heat transfer resistance between the cold plate and the heat pipe, thereby increasing the heat transfer temperature difference and achieving the goal of improving the heat pipe's operating temperature.

2.4. Temperature measuring system

Sixteen temperature measurement points are arranged on the surface of the heat pipe, including the evaporator section T_1-T_6, the adiabatic section T_7-T_{10}, and the condenser section T_{11}-T_{16}. Their positions are shown in Figure 3.

Figure 3. Diagram of temperature measurement points distribution on the surface of heat pipe.

There are a total of 6 measuring points (T_1-T_6) in the evaporator section: 10mm, 20mm, 30mm, 150mm, 300mm, and 450mm from the hot end of the heat pipe, respectively. There are also a total of 6 measuring points (T_{11}-T_{16}) in the condenser section: 450mm, 300mm, 150mm, 30mm, 20mm, and 10mm from the cold end of the heat pipe, respectively. Especially, the distances between the hot end and T_1,T_1 and T_2, and T_2 and T_3 are all 10mm. They are used to determine whether there is a drying phenomenon in the evaporator section. Similarly, the distances between T_{14} and T_{15}, T_{15} and T_{16}, and T_{16} and the cold end are also all 10mm, used to determine whether there is a liquid blockage phenomenon in the condenser section.

2.5. Experimental setup posture

The experimental setup is placed as unfavorable gravity posture. The unfavorable gravity condition is that the ceramic heating plate in the evaporator section is located above the heat pipe, while the cold plate in the condenser section is located below the heat pipe. In this posture, the bubbles generated in the evaporator section gather near the heating surface, while the condensate generated in the condenser section gathers near the cooling surface, which is not conducive to heat transfer. The maximum heat transfer capacity of the heat pipe obtained under this condition is relatively conservative.

3. Experimental results

The experimental strategy is to achieve equilibrium in the titanium water heat pipe by adjusting the temperature of the cooling working fluid at a determined experimental temperature, given different heating powers.

The temperature adjustment range of the cooling working fluid is 5-70 °C which causes practical problem. This leads to the inability to reach equilibrium at higher power levels at lower experimental temperatures, as the lowest cooling fluid temperature is 5 °C, before reaching the maximum heat transfer capacity of the titanium water heat pipe. At higher experimental temperatures, due to the maximum cooling working fluid temperature of 70 °C, equilibrium cannot be achieved at higher target temperatures at power below the maximum heat transfer capacity. By placing multiple layers of polyimide film with poor thermal conductivity between the heat pipe and the cold plate in the condensation section, the titanium-water heat pipe can achieve equilibrium at higher operating temperatures and lower heating power conditions.

When the adiabatic section temperature is 100 °C, 125 °C, 150 °C, 175 °C, 200 °C, and 225 °C, experiments are conducted at different heating powers, as shown in Table 1.

Table 1. Table of experimental conditions.

Adiabatic section temperature (°C)	Heating power (W)
100	200/300/400/500
125	300/400/500/600
150	500/600/700/800
175	700/800/900
200	850/900
225	700/800/850

Conduct experiments at different temperatures and heating powers. When the temperature measured by each temperature measuring point change by less than 1 °C within 2 minutes, it is considered that the titanium-water heat pipe has reached a heat transfer equilibrium state. In thermodynamic equilibrium, the difference between the maximum temperature of the evaporator section and the minimum temperature of the condenser section ΔT_{max} (i.e. MHTTD: the maximum heat transfer temperature difference) of the titanium-water heat pipe is shown in Figure 4.

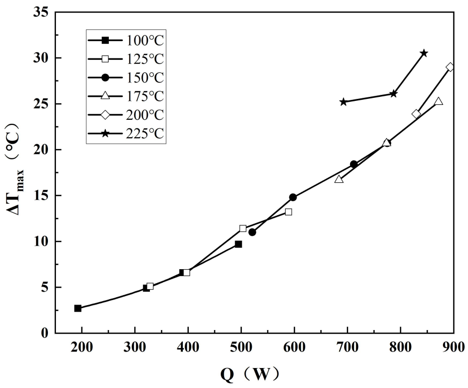

Figure 4. The maximum heat transfer temperature difference ΔT_{max} of titanium-water heat pipe varies with actual heating power Q at different temperatures.

At all temperatures, the MHTTD increases with the increase of actual heating power. Moreover, when the temperature is below 200 ℃, applying similar actual heating power to the titanium-water heat pipe at different operating temperatures results in similar MHTTD for the heat pipe. This can be understood as below 200 ℃, the heat transfer resistance of titanium-water heat pipes is constant, and the MHTTD is only affected by the heat transfer power. It is worth noting that when the working temperature of the titanium-water heat pipe reaches 225 ℃, the MHTTD under the same actual heating power is significantly higher than other temperatures, indicating an increase in the heat transfer resistance of the heat pipe at this time.

Specifically, when the working temperature of the titanium-water heat pipe is 200 ℃ and the actual heating power is 893.9W, the heat pipe can reach thermodynamic equilibrium. If the heating power continues to increase at this time, there will be a significant drying phenomenon in the evaporator section, as the T_2 suddenly increases by more than 20 ℃ within 5 seconds, and the heat pipe cannot reach thermodynamic equilibrium. Therefore, it can be inferred that the maximum heat transfer power (MHTP) of the titanium-water heat pipe at the temperature of 200 ℃ is 893.9W.

4. Conclusions

This article investigates the heat transfer performance of a 3D printed titanium-water heat pipe. We design and assemble a titanium-water heat pipe experimental setup, and conduct heat transfer performance experiments on the titanium-water heat pipe at different working temperatures and heating powers. The results showed that:

(1) At different working temperatures, the MHTTD of the titanium-water heat pipe increases with the increase of heating power;

(2) When the working temperature is below 200 ℃, applying similar heating power to the titanium-water heat pipe at different temperatures results in similar MHTTD for the heat pipe;

(3) When the working temperature is below 200 ℃, the heat transfer resistance of the titanium-water heat pipe remains almost unchanged, while when the working temperature is above 200 ℃, the heat transfer resistance of the titanium-water heat pipes increases.

(4) The MHTP of the titanium-water heat pipe at the temperature of 200 ℃ is 893.9W.

5. ACKNOWLEDGEMENTS

This work is supported by Young Elite Scientists Sponsorship Program by CAST (No. 2023QNRC001).

References

[1] Hainley D C .User's manual for the Heat Pipe Space Radiator design and analysis Code (HEPSPARC). 1991.
[2] Lee, Kuan-Lin, William G. Anderson and Calin Tarau. Titanium-Water Heat Pipe Radiators for Kilopower System Cooling Applications. in International Energy Conversion Engineering Conference, 2018.
[3] Lee, Kuan-Lin, Calin Tarau and William G. Anderson. Titanium Water Heat Pipe Radiators for Space Fission System Thermal Management. 2018.
[4] Anderson, William G., Richard Bonner, John R. Hartenstine and Jim Barth. High Temperature Titanium-Water Heat Pipe Radiator. 2006.
[5] Anderson, William G., David B. Sarraf, Peter M. Dussinger, Theodore Garry Stern and Jim Barth. Development of a High Temperature Water Heat Pipe Radiator. 2005.
[6] Enke J V V .Transient response of an axially-grooved aluminum-ammonia heat pipe with the presence of non-condensable gas. Applied thermal engineering: Design, processes, equipment, economics, 2021, 183(Pta1).
[7] Rosenfeld, John H. and Nelson J. Gernert. Advances in High Temperature Titanium-Water Heat Pipe Technology. 2007.
[8] Rosenfeld, John H. and Nelson J. Gernert. Life Test Results for Water Heat Pipes Operating at 200 °C to 300 °C. 2008.
[9] Beard, D., Anderson, W. G., Tarau, C., Ababneh, M., Schwartz, B., & Lee, K. L. (2017). High temperature water heat pipes for Kilopower

system. In 15th International Energy Conversion Engineering Conference (p. 4698).

[10] Lee, Kuan-Lin, Jaikrishnan R. Kadambi, and Yasuhiro Kamotani. "The influence of non-condensable gas on an integral planar heat pipe radiators for space applications." International Journal of Heat and Mass Transfer 110 (2017): 496-505.

[11] Anderson, William G., Peter M. Dussinger, Richard Bonner and David B. Sarraf. High Temperature Titanium-Water and Monel-Water Heat Pipes. 2006.

[12] Fleming A J, Thomas S K, Yerkes K L. Titanium-water loop heat pipe operating characteristics under standard and elevated acceleration fields. Journal of Thermophysics and Heat Transfer, 2010, 24(1): 184-198.

Paper ID 078

Thermal Performance Enhancement of Two-Phase Closed Thermosyphon by Thread Tapping inside the Evaporator

Sukkyung Kang[1], Seokjin Lee[1], and Jungho Lee[1*]

[1] *Department of Mechanical Engineering, Ajou University,*
206 Worldcup-ro, Yeongtong-gu, Suwon, Gyeonggi-do 16499, Republic of Korea
**Corresponding author's email address: jungholee@ajou.ac.kr*

Abstract

To enhance the thermal performance of a two-phase closed thermosyphon (TPCT), numerous surface modification methods, including microporous coating and wet etching, have been applied to the inner surface of TPCT. However, the previously considered methods have limited durability, productivity, and scalability for industrial applications such as heat pipe heat exchangers for waste heat recovery. The present study experimentally explored the performance improvement of TPCT by thread tapping, which is a very simple, highly productive, and long-lasting surface modification method. We used a copper TPCT with an inner diameter of 26.04 mm and a total length of 500 mm (300, 75, and 125 mm for the evaporator, adiabatic, and condenser sections, respectively) and used water as the working fluid. A threading tap with a height and pitch of 0.3 and 0.5 mm, respectively, was used to create a threaded structure on the inner surface of the evaporator, and the average arithmetic roughness (R_a) of the modified surface was 69 µm. The results showed that the thermal resistance of the thermosyphon with threaded evaporator was reduced by up to 42.1% compared to the bare one, due to the increase in both nucleation sites and heat transfer area in the evaporator section.

Keywords: Two-phase closed thermosyphon; Surface modification; Performance enhancement; Thread tapping

1. Introduction

A two-phase closed thermosyphon (TPCT) is an effective heat transfer device that can transfer much heat by utilizing latent heat, also known as a wickless heat pipe [1]. As shown in Figure 1, it consists of an evaporator, adiabatic, and condenser sections. The liquid changes into a vapor through pool boiling and/or film evaporation by absorbing heat from a heat source in the evaporator. The generated vapor rises to the condenser by pressure difference, and the heat is released to the heat sink as the vapor condenses on the condenser surface. The liquid condensate is returned to the evaporator by gravity. Because of its high manufacturability, reliability, and thermal performance, TPCT is utilized in various thermal applications, including waste heat recovery, HVAC systems, data center cooling, and solar applications.

Surface modification is widely utilized in many thermal applications to enhance boiling and evaporation heat transfer. In several studies, surface modification methods such as SiO_2 coating, oxide porous coating, metallic porous coating, graphene-nanoplatelets (GNPs) coating, and microporous structure have been applied to evaporators where boiling and evaporation are the main operating principles for improving TPCT performance [2–9]. Their findings confirm that surface modifications of the evaporator that increase the number of nucleation sites or make the surface more hydrophilic can effectively enhance the thermal performance of TPCT.

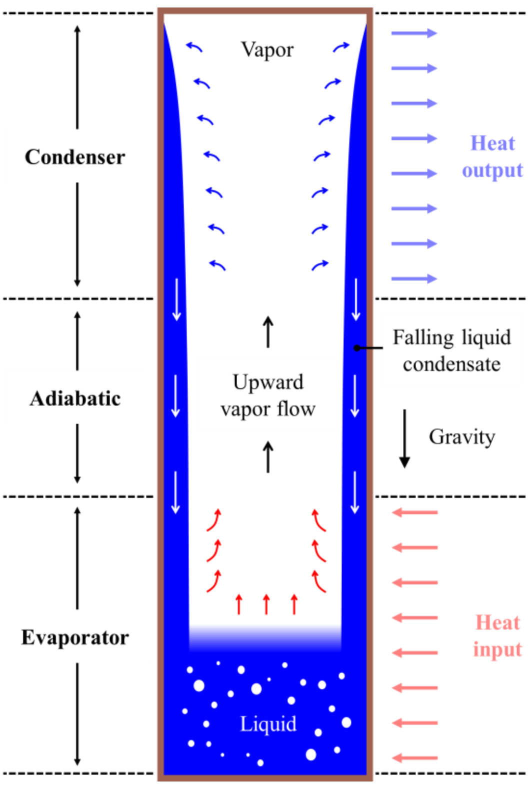

Figure 1. Structure and working principle of two-phase closed thermosyphon (TPCT).

The previously reviewed surface modification methods are sufficient for lab-scale sample production but have limitations when applied on an industrial scale, such as high equipment cost and low productivity. For example, electrodeposition requires expensive, high-current power supplies, and sintering requires large, high-temperature vacuum furnaces that can accommodate a TPCT, requiring significant time. Furthermore, the durability of the modified surface must also be considered in industrial applications, but SiO_2 coatings and chemical etching are limited in their durability.

Tapping is the process of creating threaded holes to accept screws, bolts, or other threaded fasteners and attachments. The threaded surface of the TPCT evaporator not only increases the effective heat transfer area but makes the surface more hydrophilic. Furthermore, its high productivity, low cost of surface modification, and absence of durability problems make it more suitable for industrial applications than surface modification methods reviewed in the literature. In the present work, thread tapping was applied to the TPCT evaporator. The thermal performance (heat transfer coefficient at each evaporator and condenser, overall thermal resistance) of TPCT with threaded and bare surfaces was measured, and the effect of thread tapping on TPCT performance was discussed in detail.

2. Fabrication of evaporator with threaded surface

This study used a lathe to create a threaded surface inside the pipe. After fixing a threaded tap with a pitch of 0.5 mm and a height of 0.3 mm, a copper pipe with an outer diameter of 28.06 mm, an inner diameter of 26.04 mm, and a length of 300 mm was rotated and slowly moved towards the threaded tap. Figure 2 shows photographs and micrographs of the threaded surface of the evaporator. The fabricated threaded surface had an arithmetic average roughness (R_a) of 69 µm and increased the effective heat transfer area by about 1.58 times compared to the bare surface.

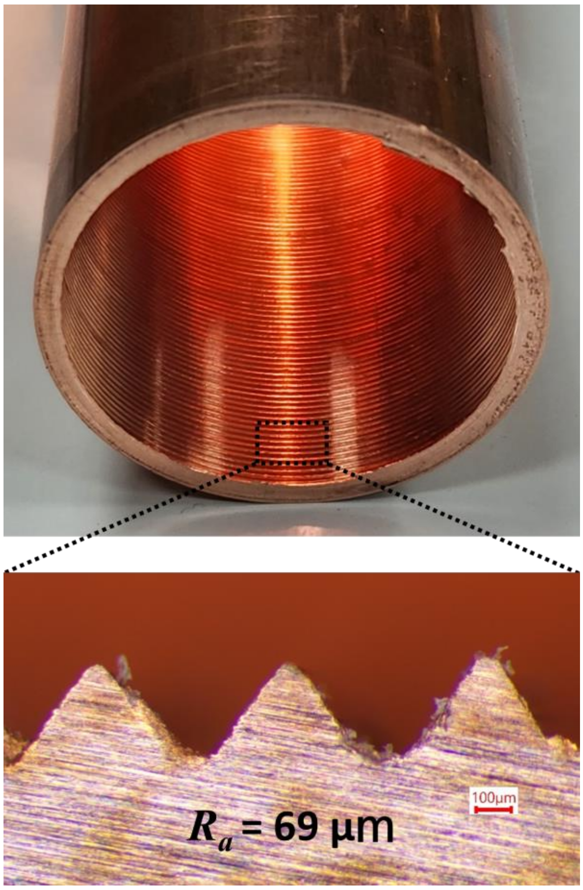

Figure 2. Photographs and micrographs of the threaded surface of the evaporator.

3. Experimental method

3.1. Experimental device and conditions

Figure 3 shows a schematic diagram of the TPCT test device. It has an inner diameter of 26.04 mm and a total length of 500 mm, with 300, 75, and 125 mm lengths for the evaporator, adiabatic, and condenser sections, respectively. The evaporator and condenser are made of copper, and the adiabatic section is made of stainless steel. The three sections are separated to allow replacement of the evaporator. Eight cartridge heaters are installed in the evaporator, and the DC power supply (Keysight N8928A) is used to apply heat. There is a water jacket in the condenser, and heat is rejected by flowing coolant with a temperature of 20°C from the constant temperature water tank at a mass flow rate of 0.145 kg/s. The flow rate of the coolant was measured using an electronic flowmeter (TOSHIBA LF620). The adiabatic section measured the internal working fluid temperature and TPCT working pressure using a T-type thermocouple and pressure transducer, respectively. In the evaporator and condenser, the wall temperature is measured using T-type thermocouples (3 points in the evaporator and 2 points in the condenser). The wall and working fluid temperature, TPCT pressure, and coolant flow rate were acquired using a data acquisition system (VTI EX1032A). The filling ratio, the volume of the working fluid to the evaporator, was 25%. The heat flux conditions and inclination angle were chosen as 5 to 100 kW/m^2 and 90 degrees, respectively.

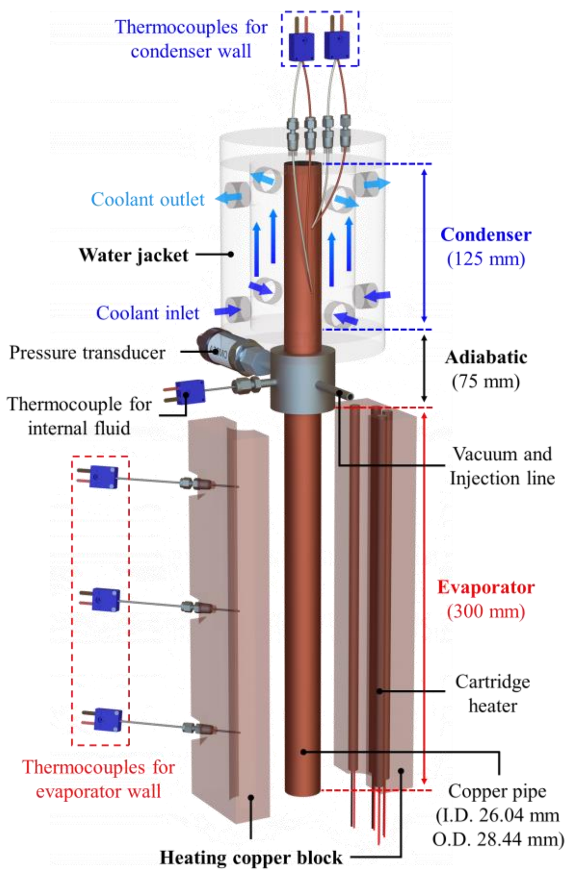

Figure 3. Schematic diagram of the TPCT test device.

3.2. Experimental procedure

Before the experiment, we remove the oxide film and organic compounds from the inner surface of the TPCT using acetone and acetic acid, respectively. After that, we used a vacuum pump to reduce the internal pressure of the TPCT to no more than 3 mTorr and confirmed that the vacuum inside the TPCT was maintained. After the cleaning and vacuum process, water was boiled at 1 atm for 2 hours to remove dissolved non-condensable gases (NCGs) such as nitrogen. The degassed working fluid was injected into the TPCT device using an injection chamber equal to the target volume.

3.3. Data reduction

In the data reduction process, all measured data, including temperature and pressure, were averaged over 5 minutes under steady-state conditions. The heat transfer coefficient at the evaporator section (h_{eva}) is calculated by the following equation:

$$h_{eva} = \frac{Q_{eva}}{A_{eva}\left(T_{w,eva} - T_{sat}\right)} \quad (1)$$

where Q_{eva}, A_{eva}, $T_{w,eva}$, T_{sat} are the heat transfer rate at the evaporator, the surface area of the evaporator, the average wall temperature of the evaporator, and the saturation temperature inside the TPCT, respectively. The overall thermal resistance of the TPCT (R_{th}) can be obtained by following Equation (3).

$$R_{th} = \frac{T_{w,eva} - T_{w,cond}}{Q_{eva}} \quad (3)$$

where $T_{w,cond}$ is the average inner wall temperature of the condenser.

4. Results and discussions

The evaporator heat transfer coefficient of TPCT with bare and threaded evaporators are shown in Figure 4 (a). The heat transfer coefficient of the threaded evaporator was higher than that of the bare evaporator for all heat flux conditions. The heat transfer coefficient at the evaporator increased by a minimum of 180.1% and a maximum of 231.8% due to the thread tapping. This performance improvement is due to the relatively large effective heat transfer area of the threaded surface compared to the bare surface and the slight increase in nucleation sites due to the surface nicks and scratches created during the tapping process.

Figure 5 compares the overall thermal resistance of TPCT with bare and threaded evaporators. The evaporator heat transfer coefficient significantly increased (minimum 180.1%) due to the evaporator's threaded structure, while the condenser heat transfer coefficient slightly decreased (maximum 26.1%) as the liquid film thickness increased due to higher vapor production. As a result, the overall thermal resistance of TPCT is

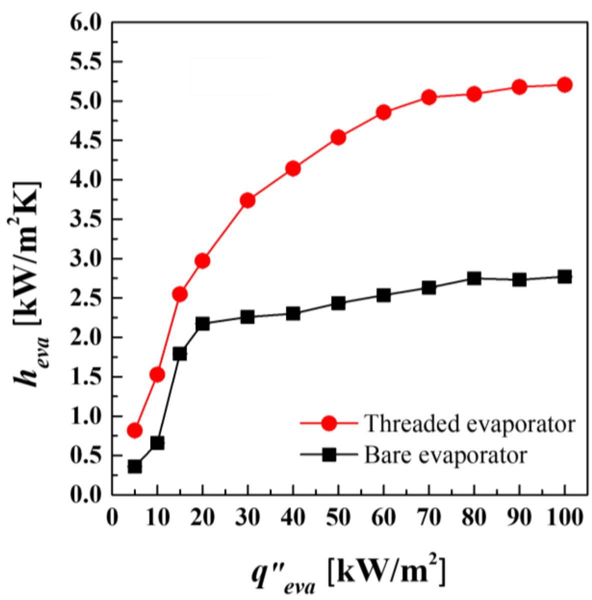

Figure 4. The evaporator heat transfer coefficient of TPCT with bare and threaded evaporator

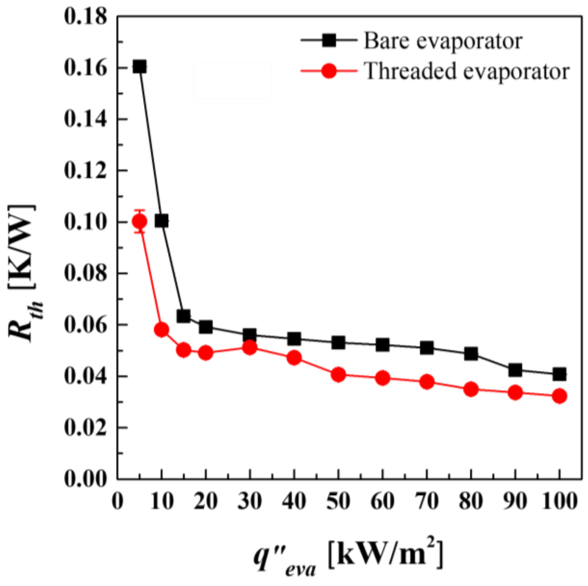

Figure 5. The thermal resistance of TPCT with bare and threaded evaporator

reduced by a maximum of 42.1% and a minimum of 8.6% due to the evaporator threaded structure as shown in Figure 5.

5. Conclusions

In this work, thread tapping, a very simple, highly productive, and long-lasting surface modification method, was applied to the evaporator section of TPCT, and its performance improvement was experimentally investigated. It was found that the threaded structure in the evaporator increased the evaporator heat transfer coefficient by up to 231.8% and reduced the overall thermal resistance of TPCT by up to 42.1%.

6. ACKNOWLEDGEMENTS

This work was supported by the Innovative Energy Efficiency R&D Program of the Korea Institute of Energy Technology Evaluation and Planning (KETEP) grant funded by the Ministry of Trade, Industry & Energy, Korea. (Grant No. 20212020800270), and a National Research Foundation of Korea (NRF) grant funded by the Ministry of Science and ICT, Korea (No. NRF-2020R1A2C3008689).

References

[1] Kang S, Seo JH, Lee J. Effect of inner diameter on the confinement of two-phase closed thermosyphon. International Communications in Heat and Mass Transfer 2023;147:106997.
[2] Rahimi M, Asgary K, Jesri S. Thermal characteristics of a resurfaced condenser and evaporator closed two-phase thermosyphon. International Communications in Heat and Mass Transfer 2010;37:703–10.
[3] Solomon AB, Roshan R, Vincent W, Karthikeyan VK, Asirvatham LG. Heat transfer performance of an anodized two-phase closed thermosyphon with refrigerant as working fluid. Int J Heat Mass Transf 2015;82:521–9.
[4] Brusly Solomon A, Arul Daniel V, Ramachandran K, Pillai BC, Renjith Singh R, Sharifpur M, et al. Performance enhancement of a two-phase closed thermosiphon with a thin porous copper coating. International Communications in Heat and Mass Transfer 2017;82:9–19.
[5] Alammar AA, Al-Mousawi FN, Al-Dadah RK, Mahmoud SM, Hood R. Enhancing thermal performance of a two-phase closed thermosyphon with an internal surface roughness. J Clean Prod 2018;185:128–36.
[6] Zhao Z, Jiang P, Zhou Y, Zhang Y, Zhang Y. Heat transfer characteristics of two-phase closed thermosyphons modified with inner surfaces of various wettabilities. International Communications in Heat and Mass Transfer 2019;103:100–9.
[7] Kim Y, Shin DH, Kim JS, You SM, Lee J. Effect of sintered microporous coating at the evaporator on the thermal performance of a two-phase closed thermosyphon. Int J Heat Mass Transf 2019;131:1064–74.
[8] Kim Y, Kim JS, Shin DH, You SM, Lee J. Enhanced thermal performance of a thermosyphon for waste heat recovery: Microporous coating at evaporator and hydrophobic coating at condenser. Appl Therm Eng 2020;175:115332.
[9] Ng VO, Yu H, Wu HA, Hung YM. Thermal performance enhancement and optimization of two-phase closed thermosyphon with graphene-nanoplatelets coatings. Energy Convers Manag 2021;236:114039.

Paper ID 079

Experimental Study on Oscillating Heat Spreader with Topology Optimization Channels for the Cooling of Multiple Heat Source Electronics

Ziang Li, Guoqing Zhou, Jian Qu*

School of Energy and Power Engineering, Jiangsu University, Zhenjiang 212013, China
**Corresponding author email address: rjqu@ujs.edu.cn*

Abstract

For the cooling of multiple heat source electronics, this paper developed an aluminum-based oscillating heat spreader (OHS) characterized by topology optimization channels. The startup and heat transfer performance of the OHS heated by four identical heat sources were experimentally studied. R134a was used as the working fluid at filling ratios of 55%, 65%, and 75%. The results indicate that the startup performance of the OHS was minimally affected by the filling ratio. At a cooling water flow rate of 1.04 L/min (LPM), the similar startup temperature of approximately 32.2 ℃ and the same startup heat power of 100 W were obtained for different filling ratios. Excessively low or high flow rate of cooling water degraded startup performance. Increasing the flow rate reduced the temperature of heating areas, while a further increase may compromise the temperature uniformity under high heat powers. At a flow rate of 1.04 LPM and a heat power of 700 W (175 W for each heat source), the thermal resistance of the OHS is 0.074 ℃/W at the filling ratio of 65%, and the average temperature of heating areas is 76.7 ℃, 13.8 ℃ lower than that of an aluminum plate of a same size. The temperature differences between the heating area and the non-heating central and peripheral areas are 17.9 ℃ and 28.6 ℃, respectively, representing reductions of 8.7 ℃ and 16.1 ℃ compared to an aluminum plate. This study indicates that the OHS could effectively control temperatures of multiple heating areas and therefore greatly enhancing the overall temperature uniformity.

Keywords: oscillating heat pipe; heat spreader; thermal resistance; topology optimization channel; multiple heat sources

1. Introduction

The rapid development of electronic devices, such as multiple-chip modules (MCMs) and arrays of multiple AC/DC converters, has made heat dissipation issues increasingly prominent [1]. For thermal management scenarios featured by multiple-chips induced heat sources, as opposed to the uniform heating by only a solitary heat source, the presence of multiple heat sources can readily engender multi-peak heat flux phenomena [2]. Additionally, the existence of localized hotspots due to non-uniform heating may instigate thermal stress deformation or even electronic device failure [3]. Consequently, the thermal management challenge related to multiple heat sources has emerged as a pivotal and formidable undertaking. In recent years, oscillating heat pipes (OHPs) have received considerable attention because of their distinctive ‘self-excited’ thermally-driven oscillation and circulating motions of slugs/plugs [4]. Flat-plate OHPs (FPOHPs) are predominantly employed in the axial heat transfer mode of a uniform heat source, while their utilization as heat spreaders for multiple heat sources is hardly reported [5].

Li and Li [6] proposed an aluminum-based FPOHP with many parallel channels, featured by bottom central heating at one side and top entirely cooling at the opposite side. At an optimal filling ratio (FR) of 75%-80%, a minimum thermal resistance of 0.225 ℃/W was achieved using acetone as the working fluid. This FPOHP exhibited the capability of local temperature control and heat dissipation, while it is imperative to maintain persistent improvement to meet heat sources having small areas and high heat powers. The concept of heat-targeting channel was first proposed by Lu et al. [7] to address the issue of thermal shorting of FPOHP at a high flow rate of cooling water, and it emphasized the design strategy of gathered channels around a small heat source area, namely the footprint of the heat source could cover more U-turns or channels. With the aid of heat-targeting channel design, the FPOHP can reduce the startup power, and produce oscillating fluid motions in a thermal spreading pattern. To dissipate the heat of high-power electronic chips in the anti-gravity pattern, Li et al. [8] proposed a two-layer aluminum-based flat-plate oscillating heat spreader (FPOHS) with an integrated heat-targeting channel design. Under the heat power of 600 W, the heat transfer performance is almost unaffected by the gravity direction.

The channel layout within an FPOHP assumes a paramount significance in governing the fluid flow and heat transport inside. Based on the principles of the topology optimization method, capable of directly influencing the spatial arrangement of materials and interconnectivity within a design domain [9], this study endeavors to establish an oscillating heat spreader (OHS) catering to multiple heat sources. By prioritizing minimal thermal compliance as a primary design objective, the OHS characterized with topological channel layouts was proposed to satisfy the demand for electronics cooling with multiple heat sources. The study validated the efficacy of the OHS and shed light on a novel thermal control path amidst multiple heat sources scenarios.

2. Channel layout design through topology optimization method

Utilizing the variable density model in topology optimization, the two-phase flow channel region could be approximately featured by a material characterized by a much higher thermal conductivity than that of the solid substrate region. Four heat sources with each measuring an area of 15 mm × 15 mm are evenly distributed within a design domain of 80 mm × 80 mm. Employing the minimum thermal compliance as the objective, the topological channel structure comparable to the four-heat source configuration was generated as displayed in Fig. 1.

Subsequently, a multiple-heat source OHS having an overall dimension of 100 mm × 100 mm × 2 mm was developed with the aid of the topology optimization method (see Fig. 2). Noted that four couples of Tesla valves were adopted to facilitate the circulation flow inside the device.

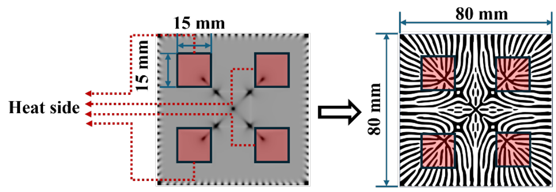

(a)

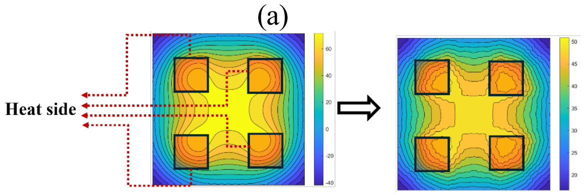

(b)

Fig. 1. Topology optimization for four heat sources: (a) relative density field, and (b) relative temperature field

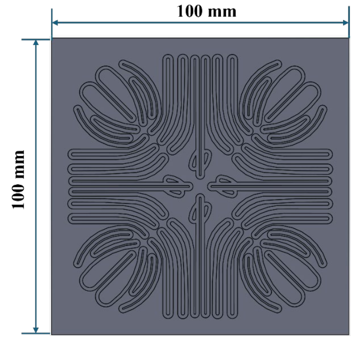

Fig. 2. OHS with topology optimization channel design suitable for four heat source cooling

3. Experimental setup

Fig. 3 depicts the schematic diagram of the experimental setup and thermocouple arrangement. The experimental setup mainly consists of an aluminum-based OHS, an electrical heating module, a water-cooling module, and a data measurement and acquisition module.

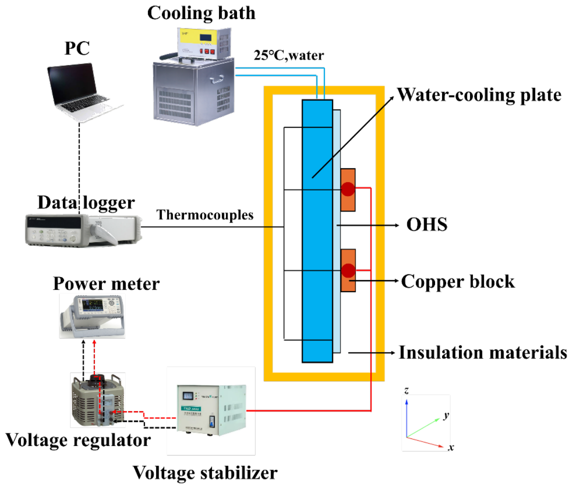

(a)

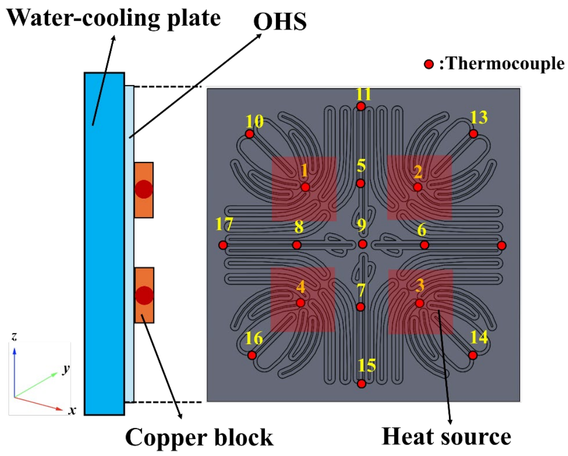

(b)

Fig. 3. Experimental setup (a) and thermocouple arrangement (b)

4. Data reduction

The system thermal resistance is an important indicator for evaluating the heat dissipation performance of the OHS, which can be expressed as

$$R_{sys}=\frac{T_h-T_{water\text{-}in}}{Q_{water}} \quad (1)$$

where Q_{water} is the heat removed by the cooling water as calculated by Eq. (2); T_h and $T_{water\text{-}in}$ represent the average temperature of four heating areas (expressed as Eqs. (3)) and the temperature of cooling water at the inlet (maintain at 25 °C), respectively.

$$Q_{water}=\dot{m}c_p\left(T_{water\text{-}out}-T_{water\text{-}in}\right) \quad (2)$$

$$T_h=\sum_{i=1}^{4}T_i/4 \quad (3)$$

where $\dot{m}$ denotes the mass flow rate of the cooling water. By comparing the value of Q_{water} and the heat power input, the maximum heat loss rate was estimated to be about 4.5%.

The temperature uniformity can be primarily assessed by the temperature difference between the heating area and the non-heating central area, as well as between the heating area and the non-heating peripheral area as illustrated in Fig. 3 (b). Their calculation could be respectively expressed as

$$\Delta T_{in}=T_h-\sum_{i=5}^{9}T_i/5 \quad (4)$$

$$\Delta T_{out}=T_h-\sum_{i=10}^{17}T_i/8 \quad (5)$$

5. Results and discussion

To understand the performance characteristics of the OHS utilized for cooling multi-heat sources, the effects of filling ratio and flow rate of cooling water on the heat transfer performance of the OHS and the temperature uniformity will be compared and analyzed in this section.

5.1. Effect of filling ratio

Fig. 4 shows the wall temperature variation of the OHS at different filling ratios when the flow rate of cooling water (q) is 1.04 L/min (LPM). As a total heat power of 100 W (25 W for each heat source) was applied, obvious temperature oscillations appeared at the heated area for each filling ratio, indicating that it was started up smoothly, and the startup temperature was about 32.2 °C. As the heat power was increased to 500 W, the oscillation amplitude and frequency of temperature increased slightly, and the temperature difference among these four heat sources became distinguished, indicating that the working fluid entered a global unidirectional circulation mode in the channel loop. It is worth noting that, the oscillation amplitude of the wall temperature in the heating area is lower at FR=65% than that at other filling ratios. The small temperature fluctuation is beneficial to reducing the plate deformation caused by thermal stress. When the heat power reaches 700 W, the wall temperature is lower than 85 °C at all filling ratios, without stagnation or dry-out of the OHS, ensuring the safe operation of the chip.

The initialization of OHS could be triggered at each filling ratio when the heat power reaches 100 W, suggesting its insignificant role on the startup performance. It may be attributed to the shorter path of the fluid movement from the condenser section to the evaporator section, and thus a smaller pressure difference is required to overcome the flow resistance and drive the liquid-slug/vapor-plug movement inside.

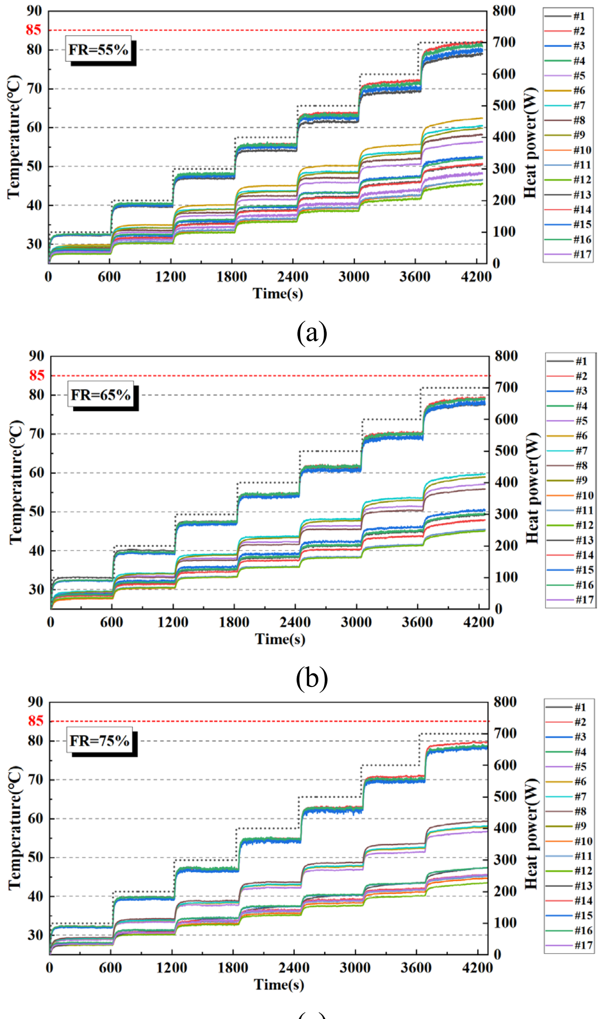

(a)

(b)

(c)

Fig. 4. Temperature profiles of the OHS under different filling ratios (q=1.04 LPM): (a) FR=55%; (b) FR=65%; (c) FR=75%

Fig. 5 shows the average temperature of four heating areas and the system thermal resistance of the OHS versus the heat power at a cooling water flow rate of 1.04 LPM. As shown in Fig. 5(a), at a heat power of 100 W, the lowest average temperature was obtained at FR=65%. As the heat power increased, the temperature difference between the OHS and the aluminum plate became more evident as shown in Fig. 5 (a). At a heat power of 700 W, the average temperature was 76.7 ℃ at FR=65%, slightly lower than that at other filling ratios, while it was 13.8 ℃ lower than that of the aluminum plate. Simultaneously, the system thermal resistance remained relatively stable with the increase in heat power, as shown in Fig. 5(b). At FR=65%, the OHS yielded a lowest system thermal resistance of 0.074 ℃/W at a heat power of 700 W. The corresponding surface temperature measurement points were interpolated to generate temperature contour maps as displayed in Fig. 6. According to the temperature contour map, it is clear that the OHS could significantly reduce the temperature of heated areas and enhance the overall temperature uniformity compared to the aluminum plate. The unidirectional circulation of the working fluid inside the OHS could greatly intensify the heat transport among these heating areas, enhancing the temperature uniformity across these four areas.

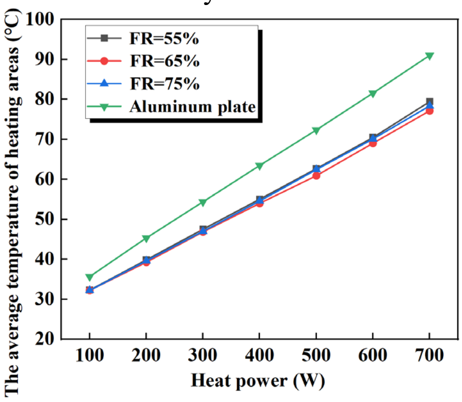

(a)

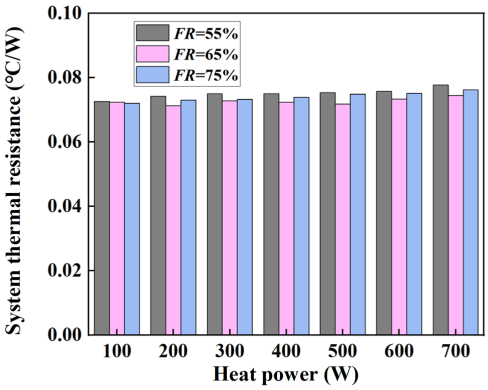

(b)

Fig. 5. Temperature control capability of the heating areas (q=1.04 LPM): (a) the average temperature of heating areas; (b) system thermal resistance

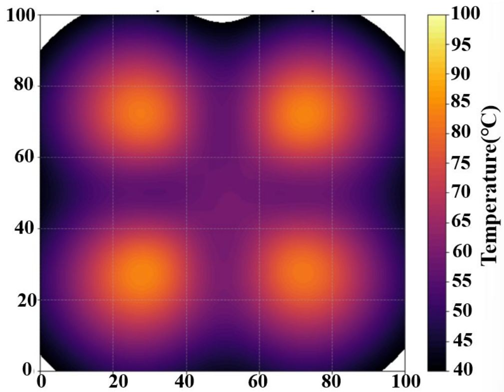

(a)

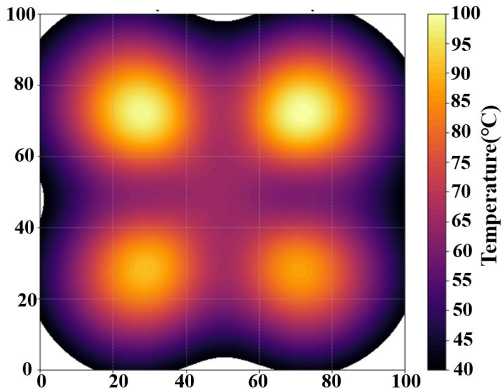

(b)

Fig. 6. Comparison of temperature contour maps at a heat power of 700 W: (a) OHS (FR=65%, q=1.04 LPM); (b) aluminum plate

Fig. 7 shows the temperature difference between these heating areas and other regions at a cooling water flow rate of 1.04 LPM. Normally, a smaller temperature difference indicates better temperature uniformity. Obviously, a significant reduction of temperature difference was achieved for the OHS as compared with the aluminum plate. Besides, the OHS at the filling ratio of 65% exhibits smaller temperature differences than that of 55% or 75% filling ratio. At a heat power of 700 W, the temperature differences of ΔT_{in} and ΔT_{out} were 17.9 and 28.6 °C, respectively, at the filling ratio of 65%. The corresponding temperature differences were 8.7 and 16.1 °C lower than that of the aluminum plate, representing reductions of 32.7% and 36.0%, respectively.

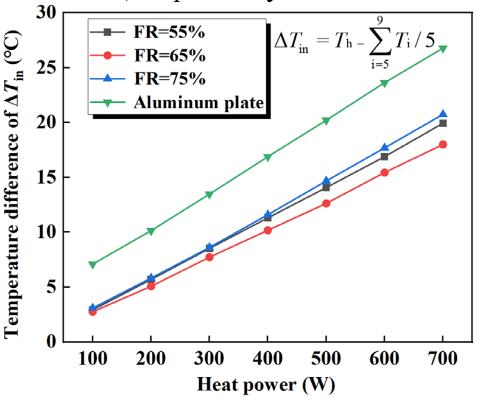

(a)

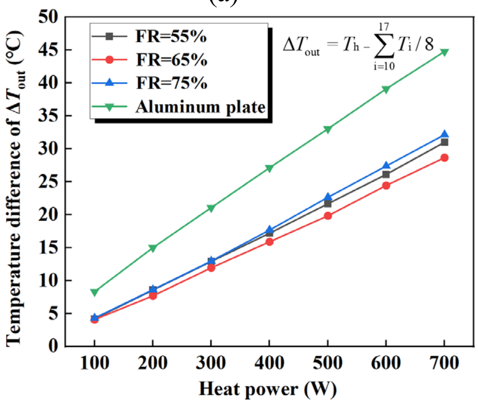

(b)

Fig. 7. Comparison of temperature differences versus heat power for the OHS at different filling ratios and aluminum plate (q=1.04 LPM): (a)ΔT_{in}; (b) ΔT_{out}

5.2. Effect of flow rate of cooling water

As shown in Fig. 8 (a), at a cooling water flow rate of 0.4 LPM, no temperature oscillation was observed under heat powers of 100 and 200 W, indicating that the fluid medium remained stagnant. During this stage, the heat transport primarily depends on conduction through the aluminum shell. When the heat power reached 300 W, temperature oscillations appeared, indicating that slugs/plugs began to oscillate and the OHS successfully started up, with a startup temperature of approximately 45 °C. At a heat power of 500 W, the working fluid entered the state of global pulsation or unidirectional circulation. Owing to thermal inertia and heat accumulation, slugs and plugs overcome flow resistance, contributing to high-frequency, low-amplitude temperature oscillations. As the heat power was increased from 600 W to 700 W, the temperature profiles both at positions of #2 and #3 thermocouples exhibited a sawtooth pattern, indicating the occurrence of secondary startup. After reaching a quasi-steady state, the temperature oscillations became weaker, accompanied with intermittent temperature drops. In Fig. 8 (b), at a flow rate of 0.64 LPM, the temperature variation was similar to that at 0.4 LPM. When the heat power reached 700 W, the temperature of the heating area exceeded 85 °C.

At flow rates of 0.88 and 1.04 LPM, the OHS initialized at 100 W with a startup temperature of approximately 33 °C (see Fig. 8 (c) and Fig. 8 (d)). After startup, it maintained stable global pulsation or directional circulation at all heat powers. Compared to lower flow rates, both the startup power and startup temperature were significantly reduced, indicating that the improvement of startup performance after increasing the cooling water flow rate.

When the cooling water flow rate reached 1.20 LPM, temperature oscillations initially appeared at the heat power of 100 W (see Fig. 8 (e)), however they disappeared rapidly, returned to stagnation. Successful startup only occurred as the heat power was increased to 200 W. It can be explained that excessive cooling would remove heat rapidly from the heat source by the OHS, which hampered the heat absorption by liquid medium and as well as bubble nucleation and generation within the heating area. As a result, the pressure difference accumulated in the channel would be insufficient to drive the working fluid properly. Therefore, the increase of the cooling water flow rate cannot definitely enhance the startup performance, and an optimal flow rate range of 0.88-1.04 LPM was evidenced to improve the startup performance.

In summary, there is an optimal cooling condition that enables the OHS to achieve a better startup performance. A recent work by Abela et al. [10] demonstrated that the cooling boundary influences the initial distribution of slugs/plugs inside OHP channels. At a low flow rate of cooling water, short liquid slugs tend to accumulate in the condenser section rather than in the evaporator section. Conversely, a quite high flow rate will cause the occurrence of thermal shorting [7], making startup failure at low heat powers.

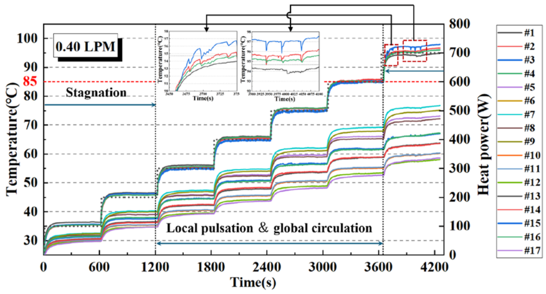

(a)

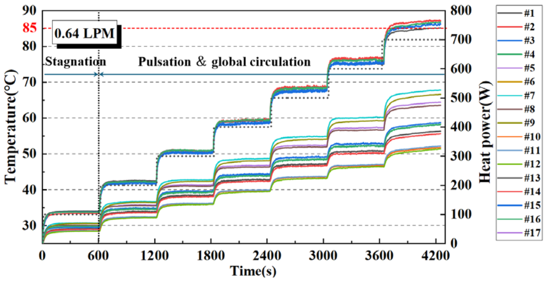

(b)

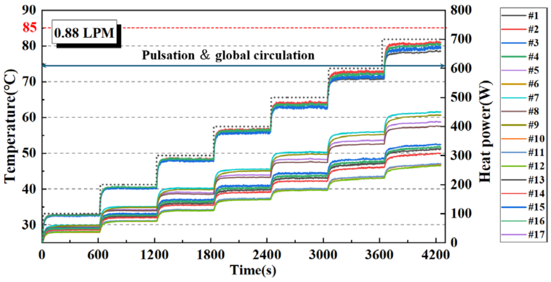

(c)

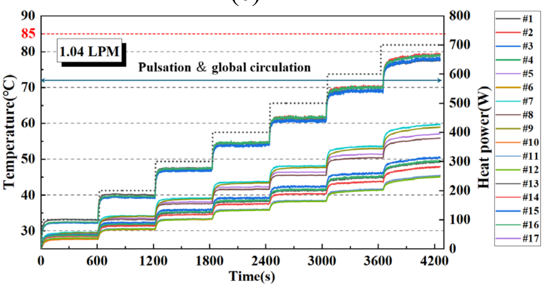

(d)

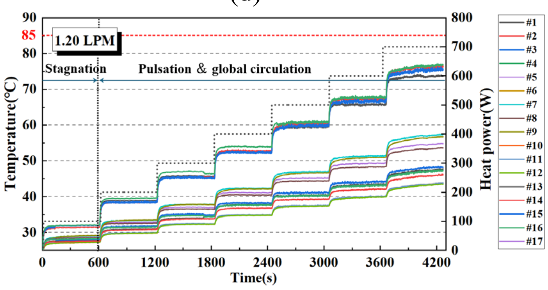

(e)

Fig. 8. Temperature profiles of the OHS at different flow rates of cooling water (FR=65%): (a) $q = 0.40$ LPM; (b) $q = 0.64$ LPM; (c) $q = 0.88$ LPM; (d) $q = 1.04$ LPM; (e) $q = 1.20$ LPM

In Fig. 9, as the flow rate of cooling water increases, both the average temperature of the heating areas and the system thermal resistance decrease. At a heat power of 700 W, it was able to maintain the average temperature below 85 °C at a flow rate greater than 0.4 LPM. However, the effect of flow rate on the reduction of the average temperature and system thermal resistance gradually diminished as the heat power was increased. For example, at a heat power of 700 W, when the flow rate rose from 0.40 LPM to 1.20 LPM at an increment of approximately 0.20 LPM, the average temperature decreased by 9.6 °C, 6.0 °C, 1.8 °C, and 1.9 °C, with respective reduction rates of 10.1%, 7.1%, 2.3%, and 2.5%. This indicated a diminishing marginal effect on the performance improvement.

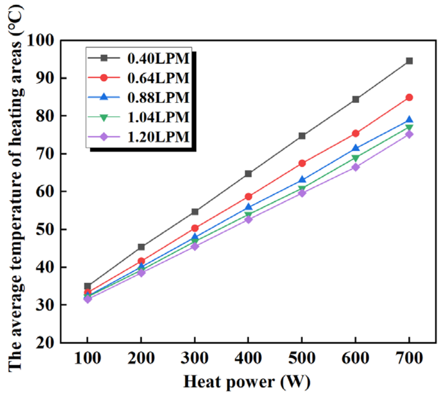

(a)

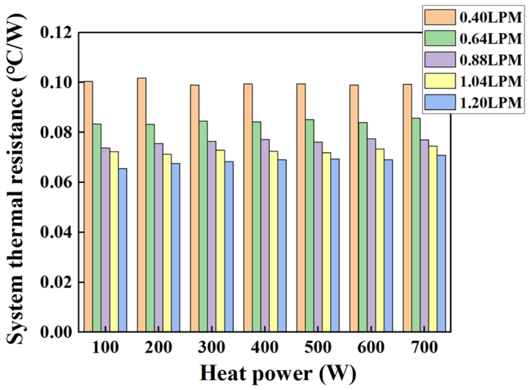

(b)

Fig. 9. Temperature control capability of the OHS at different flow rates of cooling water (FR=65%): (a) average temperature of the heating areas; (b) system thermal resistance

Within the heat power range of 100-600 W, both ΔT_{in} and ΔT_{out} decreased slightly as the flow rate of cooling water increased (see Fig. 10), and the best temperature uniformity of the OHS appeared at the flow rate of 1.20 LPM. However, at the highest heat power of 700 W, both above temperature differences initially slightly decreased with increasing the flow rate, and then they increased. At the flow rate of 0.88 LPM, the OHS exhibited the best temperature uniformity. Therefore, at a higher heat power, increasing the flow rate of cooling water may degrade the temperature uniformity.

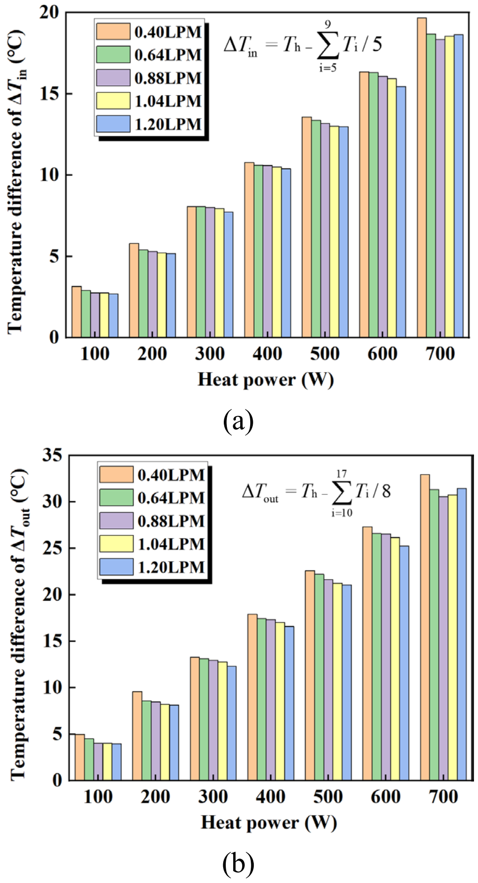

Fig. 10. Temperature differences at different flow rates of cooling water (FR=65%) between the heating area and the non-heating central area (a) and between the heating area and the non-heating peripheral area (b)

6. Conclusion

To address the thermal challenge for cooling multiple heat source electronics, an OHS with topology optimization channels was developed in this study. The effects of filling ratio and flow rate of cooling water on the heat transfer performance of the OHS and the temperature uniformity were experimentally investigated and compared. The main conclusions are summarized as follows:

(1) The filling ratio has a small impact on the startup performance of the OHS, but there existed an optimal value of about 65%, corresponding to both the lowest temperature of the heating area and the lowest system thermal resistance.

(2) There is an optimal flow rate of cooling water range from 0.88-1.04 LPM with respect to the lower startup temperature and startup heat power. A lower flow rate of cooling water affects the initial distribution of liquid-slugs and vapor-plugs, while an excessive flow rate may cause thermal shorting, both of which degrade the startup performance at low heat powers.

(3) Although increasing the flow rate of cooling water reduced the temperatures of heating areas, the improvement diminished at higher flow rates. Moreover, at higher heat powers, the increase of the flow rate may reduce temperature uniformity.

(4) The OHS can achieve effective temperature control of multiple heating areas, thereby greatly enhancing the overall temperature uniformity. At a flow rate of 1.04 LPM and a heat power of 700 W (175 W for each heat source), the average temperature of heating areas was 76.7 °C, 13.8 °C lower than that of an aluminum plate. The temperature differences between the heating area and the non-heating central and peripheral areas were 17.9 °C and 28.6 °C, respectively.

References

[1] R.V. Erp, R. Soleimanzadeh, L. Nela, G. Kampitsis, E. Matioli, Co-designing electronics with microfluidics for more sustainable cooling, Nature 585 (2020) 211-216.
[2] Y. Hadad, B. Ramakrishnan, R. Pejman, S. Rangarajan, P.R. Chiarot, A. Pattamatta, B. Sammakia, Three-objective shape optimization and parametric study of a micro-channel heat sink with discrete non-uniform heat flux boundary conditions, Appl. Therm. Eng. 150 (2019) 720–737.
[3] Y.J. Li, S. Roux, C. Castelain, Y.L. Fan, L.G. Luo, Design and Optimization of Heat Sinks for the Liquid Cooling of Electronics with Multiple Heat Sources: A Literature Review, Energies 16 (2023) 7468.
[4] W.Y. Kim, S.J. Kim, Fundamental Issues and Technical Problems About Pulsating Heat Pipes, J. Heat Transf. 143 (2021) 100803.
[5] V. Ayel, M. Slobodeniuk, R. Bertossi, C. Romestant, Y. Bertin, Flat plate pulsating heat pipes: A review on the thermohydraulic principles, thermal performances and open issues, Appl. Therm. Eng. 197 (2021) 117200.
[6] C.X. Li, J. Li, Thermal characteristics of a flat plate pulsating heat pipe module for onsite cooling of high power server CPUs, Therm. Sci. Eng. Prog. 37 (2023) 101542.
[7] H. Lu, S.M. Thompson, F.F. Laun, H.B. Ma, Effect of cooling rate on thermal performance of an oscillating heat spreader, J. Thermophys. Heat Transf. 30 (2016) 461–465.
[8] Z.A. Li, G.Q. Zhou, P. Cheng, J. Qu, Heat transfer performance of novel 3D flat-plate oscillating heat spreader under gravity-assisted and anti-gravity conditions for high-density power

electronics cooling, Appl. Therm. Eng. 252 (2024) 123726.
[9] J.H. Lim, S.J. Kim, A channel layout of a micro pulsating heat pipe for an excessively localized heating condition, Appl. Therm. Eng. 196 (2021) 117266.
[10] M. Abela, M. Mameli, S. Filippeschi, B.S. Taft, Innovative experimental approach for the dynamic multi-variable investigation of pulsating heat pipes. Appl. Therm. Eng. 236 (2024) 121910.

Paper ID 080(S2A)

Heat Transfer Characteristics of Oscillating Heat Spreader with Petal-shaped Topological Channel Layout

Guoqing Zhou, Ziang Li, Jian Qu*

School of Energy and Power Engineering, Jiangsu University, Zhenjiang 212013, China
**Corresponding author email address: rjqu@ujs.edu.cn*

Abstract

For the cooling of high-power and compact electronic devices, this paper developed a novel aluminum-based oscillating heat spreader (OHS) characterized by petal-shaped topological channel layout. The experimental study was conducted to investigate the heat transfer performance and temperature uniformity using R1233zd (E) as the working fluid at filling ratios of 40%-70%. To reduce the gravity dependence, a design of variable cross-section channels was adopted. Experimental results demonstrate that an optimal filling ratio of 70% was evidenced with respect to minimum thermal resistances of 0.184 and 0.180 W/(m·K), in horizontal and vertical orientations, respectively, with reductions of 25.1% and 26.7% compared to an aluminum plate of a same size. Furthermore, the OHS could dissipate heat up to 300 W (133 W/cm²) while maintaining the surface temperature below 100 °C, and the average temperature difference between the center and boundary was reduced by 17.7°C compared to the aluminum plate. This study highlights the potential of the OHS for effective cooling of high-power electronic devices.

Keywords: Oscillating heat spreader; Topology optimization; Heat transfer performance; Thermal resistance; Temperature uniformity

1. Introduction

Nowadays, the trend towards miniaturization, high performance, and multi-functionality boosts the wide applications of high-power electronic chips, accompanied by a growing increase in heat generation and temperature non-uniformity [1,2]. Hence, the development of high-efficiency heat dissipation strategy become a key issue to ensure the reliability and safety of electronic devices. Conventional heat pipes, worked as two-phase heat transfer devices, have been widely used for electronic cooling due to their high thermal conductivities and passive nature. However, the required capillary structures and relatively low heat transfer limitations largely restrict their applications for high-power and compact electronic devices [3].

Owing to the simple structure, high heat transport capability, and strong environmental adaptability, flat plate oscillating heat pipes (FPOHPs), also called pulsating heat pipes, have become a promising candidate for high-power electronics cooling [4,5]. As a wickless heat pipe technology, the FPOHP normally work as a one-dimensional heat transfer device, with one end being heated and the other end for condensation. Sometimes, the central part becomes the heated region, and the two ends are used for condensation [6]. For many practical applications, however, the FPOHP needs to act as a heat spreader and absorb heat from the central part of one side, and then dissipate it to the entire area of the other side. In recent years, some innovative radial channel structures have been proposed to enable FPOHPs to work like high-efficiency heat spreaders. Laun et al. [7] developed a radial FPOHP with Tesla valves, and it could achieve a cooling capacity for 525 W within an area of 100 mm × 100 mm. Kelly et al. [8] proposed an FPOHP having tree-like radial channel structures, expanding the fluid flow area and reducing the junction temperature by 23°C under the heat input of 30 W, in despite of significant temperature differences and higher flow resistances. Schwarz et al. [9] developed floral and star-shaped radial FPOHPs, and the experimental comparison demonstrated that heat transfer performance could be improved when the fill ratio exceeded 70%. Jang et al. [10] conducted experimental studies on radial FPOHPs with variable-diameter channels, showing a reduction in thermal resistance by up to 11.7% compared to constant-diameter channels, and an increase in heat transfer capacity of up to 37.5% was achieved. To dissipate heat of high-power electronic chips in the anti-gravity condition, a novel two-layer aluminum radial FPOHP with an integrated heat-targeting channel design was recently developed by Li et al. [11]. Under the heat power of 600 W, the heat transfer performance is almost unaffected by the gravity orientation.

The aforementioned works exhibit the application prospect of FPOHPs as heat spreaders for heat dissipation and temperature control. However, the radial FPOHPs usually require complicated channel designs due to the compact central heating area. To investigate the impact of channel layout on FPOHP heat transfer performance, Lim and Kim [12] introduced the concept of effective dissimilarity to quantify its effect on a flat micro-pulsating heat pipe (MPHP) under localized heating conditions. It was confirmed that the thermal performance of the MPHP could be largely improved by maximizing the effective dissimilarity with respect to the channel arrangement. Inspired by the topology optimization method, normally used for heat exchanger design [13], Lim and Kim [14] proposed a channel layout for cooling the local heat source using the topology optimization design, and a significant improvement in heat transfer performance was achieved as compared with conventional channel layouts. Although these MPHPs still functioned at a traditional mode, it offers a valuable insight for the channel design of radial FPOHPs. Based on topology optimization algorithms, the novel channel design provides the possibility to identify optimal paths that improve fluid motion and heat transfer efficiency.

In this study, we pursue the design goal to match with the cooling requirement of high-power electronic devices having small surface areas. The radial FPOHP is termed as oscillating heat spreader (OHS), and a petal-shaped channel structure was developed using the design strategy of topology optimization methods. Experimental studies and comparisons demonstrated the design effectiveness on heat transfer performance enhancement and high-efficiency heat dissipation, providing a promising alternative for cooling high-power chips.

2. Channel layout design via topology optimization method

In this study, a topology optimization model was employed to assist the channel design of OHS. The model is originated from heat conduction and the two-phase flow channels approximated as a material with high thermal conductivity. Additionally, the variable density model is utilized for characterizing the topological structure. In the design domain, the relative density (ρ_i) represents the distribution of channels (ρ_i=0) and solid walls (ρ_i=1), which is a continuous variable ranging from 0 to 1. The relationship between relative density and thermal conductivity was established with the aid of the interpolation model of solid isotropic material with penalization (SIMP) [15] described as

$$\lambda(\rho_i) = (\lambda_{eff} - \lambda_s)(1-\rho_i)^p + \lambda_s \tag{1}$$

where, λ, λ_{eff} and λ_s represent the thermal conductivity at discrete node i, the effective thermal conductivity of FPOHP channels, and the thermal conductivity of the solid wall material, respectively. ρ_i denotes the relative density at the discrete node, and p is the penalization factor.

The finite element method is used to solve the steady-state temperature field under the current relative density distribution. The subsequent topology optimization model iterates the relative density in light of the temperature field. Topology optimization is essentially a mathematical programming method that consists of an objective function and constraints. The corresponding mathematical model for topology optimization is given as follows:

$$\text{Min: } c = \sum_{i\in\Omega} T_i q_i = Q_{in}(T_{heat} - T_{cond}) \tag{2}$$

$$\text{Subject to: } 0 < \rho_{min} \le \rho_i \le 1, i \in \Omega \tag{3}$$

$$\frac{\sum_{i\in\Omega}\rho_i}{V_\Omega} \ge \rho_0 \tag{4}$$

$$\left(\frac{\partial c}{\partial \rho_i}\right)^* = \frac{n_m}{\sum_{j=1}^{n_m}\left((1-\rho_j)\frac{\partial c}{\partial \rho_j}\right)}\frac{\partial c}{\partial \rho_i},\ \mathrm{dist}(i,j) \le (L_{max}/2) \tag{5}$$

$$\Delta\varepsilon_i = \varepsilon_0 - \frac{\sum_{j=1}^{n_l}\rho_j}{n_l} \le 0 \tag{6}$$

where, c represents the thermal compliance, Q_{in} is the total input heat, and T_{heat} and T_{cond} are the average temperatures at the heat source and cooling boundaries, respectively. ρ_0 is the initial relative density, and V_Ω is the total volume of the topology domain. L_{max} represents the maximum channel size. $\Delta\varepsilon_i$ is the constraint on the local minimum solid volume fraction in local regions. According to Eq. 2, the minimization of thermal compliance was selected as the objective function, representing the smallest temperature difference between the heat source and the cooling boundary under a given heat input. Additionally, the channel size of the oscillating heat pipe must be limited to ensure stable slug-plug formation. Hence, a maximum size constraint (see Eq. 5) [14,16] restricts the channel dimension and a minimum volume constraint (see Eq. 6) [14] prevents excessive branching are implement.

By solving the topology optimization model using the method of moving asymptotes, Fig. 1 displays the iterative history of the objective function (also thermal compliance), the topological channel morphology, and the average temperature difference between the heating region and the cooling boundary. Eventually, a topology channel structure could be obtained that minimizes the temperature difference between the heat source and the cooling boundary after over 500 iterations. Based on the optimized channel layout as shown in Fig. 2, a novel OHS was developed, featured by a petal-shaped channel structure having variable-diameter channels.

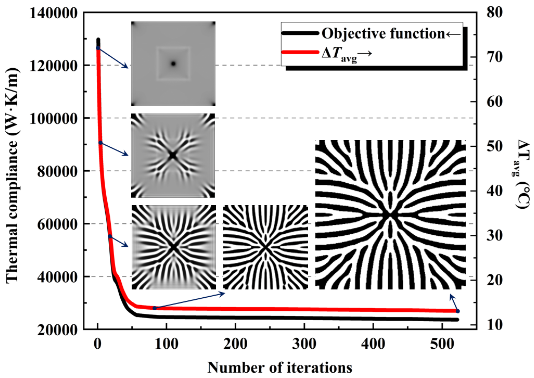

Figure 1. The iterative history of topological channel morphology.

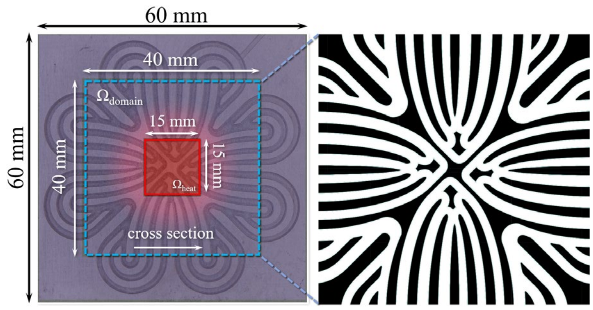

Figure 2. The OHS with topological channel structures (left) and an enlarged view of its design domain (right).

3. Fabrication of OHS and experimental setup

3.1 Fabrication of OHS

According to above channel design, an OHS with a radial topology channel layout was fabricated using 3003 aluminum alloy. As illustrated in Fig. 2 (left), the OHS has an overall size of 60 mm × 60 mm. Additionally, the thicknesses of substrate and cover plate are 2 mm and 0.25 mm, respectively (see Fig. 3). On the substrate, channels characterized by alternating widths of 1.5 mm and 1.1 mm, and a depth of 1.5 mm were fabricated using a CNC milling machine. The substrate and cover plate were then brazed together to form a total thickness of about 2.25 mm. R1233zd (E) was selected as the working fluid due to its low global warming potential (GWP) and favorable thermophysical properties [17].

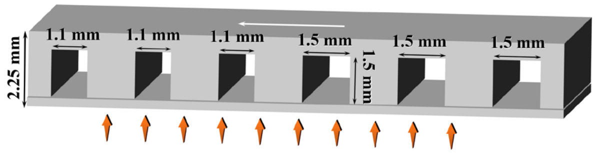

Figure 3. Schematic diagram of the channel cross section of the OHS.

3.2 Experimental setup

Fig. 4 illustrates the experimental setup of the OHS, consisting of four main components: the OHS itself, a heating module, a liquid cooling module, and a data measurement and acquisition module. In this study, a copper block with embedded electric heating elements was used to simulate the heat generation of a high-power electronic chip. The copper block, containing two electric heating rods inside, has a heating surface of 15 mm × 15 mm in direct contact with one side of the OHS. To accurately measure the maximum temperature on the simulated chip surface, a rectangular groove was machined into the centre of the copper block to securely house a T-type thermocouple (OMEGA, ±0.2 °C in accuracy). All temperature data were collected and recorded using a data logger (Agilent 34970A), with thermocouple measurement points detailed in Fig. 5. The inlet temperature of cooling water is 25 °C and the flow rate is 1.2 L/min. Additionally, a 1.0 mm thick copper spacer with a centre hole was placed between the OHS and cooling block to prevent excessive heat conduction from the evaporator directly to the condenser, or ‘thermal shorting’ [18].

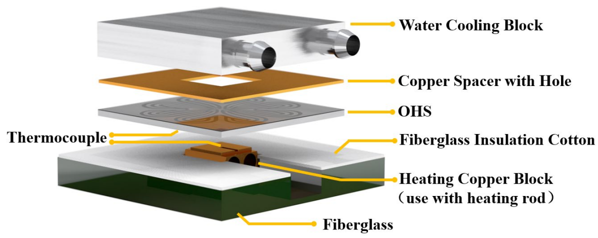

Figure 4. Schematic diagram of the experimental setup for OHS.

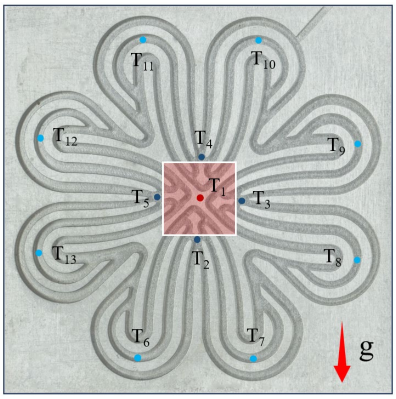

Figure 5. Arrangement of thermocouple measurement points on the OHS.

To understand the effect of inclination angle on the heat transfer performance of the OHS, the experimental test was conducted at both horizontal and vertical orientations for the OHS as illustrated in Fig. 6. Obviously, at the vertical orientation condition, the upper part of the OHS works approximately at the bottom heat mode, while the other half functions approximately at the top heat mode, namely anti-gravity condition. In addition, a solid 3003 aluminum plate was also prepared to establish reference benchmarks to assess the OHS performance having topology optimization channels.

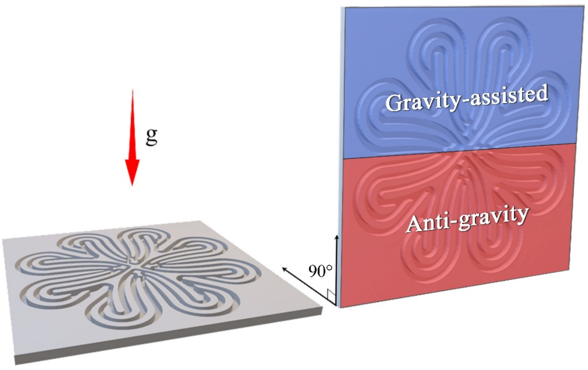

Figure 6. Schematic diagram of the OHS at horizontal and vertical orientations.

4. Data reduction and uncertainty analysis

Thermal resistance is a crucial parameter for evaluating the heat transfer performance of an FPOHP, which can be expressed as

$$R = \frac{T_h - T_c}{(1-\varphi)Q_{in}} \tag{7}$$

where Q_{in} represents the input heat power, which is directly measured by a power meter. φ is the heat loss from the test section to the ambience. According to a set of thermal balance test with respect to heat loss, a mean value of 0.068 was adopted. T_h and T_c are the average temperatures of heating and cooling surfaces, respectively, under steady-state conditions, respectively given by

$$T_h = \overline{T}_1 \tag{8}$$

$$T_c = \sum_{i=6}^{13} T_i / 8 \tag{9}$$

Based on the Holman's analysis method, the maximum uncertainty of thermal resistance is approximately 5.7%.

5. Results and discussion

5.1. Heat transfer performance

Fig. 7 compares the temperature profiles (T_1) of heating surface at the horizontal and vertical OHS at different filling ratios ranging from 40%-70%, and the aluminum plate was also used as a benchmark. Compared to the aluminum plate, significant reductions in the temperature of heating surface were achieved for the OHS at filling ratios ranging from 50%-70%. However, the temperature at the 40% filling ratio was even higher than that of the aluminum plate, implying the startup failure of this device. At the stagnation condition of fluid medium inside of the OHS, the heat transport largely dependent on heat conduction, and thus the device was featured by lower thermal conductivity that that of the pure aluminum plate.

For the horizontally oriented OHS, at the relatively high heat powers of 200 W, 250 W, and 300 W, the surface temperature of the heat source (T1) was approximately reduced by 13.6 °C, 14.9 °C and 13.8 °C, respectively, compared to the aluminum plate at the filling ratio of 70%. The power reduction experiment can assess the capability of the slug-plug system to maintain thermal inertia. If slugs/plugs inside the OHS stagnate early, it indicates that the system cannot generate a driving force greater than the flow resistance at that heating power. Specifically, at a filling ratio of 60 or 70%, the OHS maintains high heat transfer performance at the lower heating power of 100 W in both horizontal and vertical orientations, with temperature reductions of 6.7 °C and 6.9 °C, respectively, compared to the aluminum plate. This indicates that the OHS with topological channels can effectively maintain the thermal inertia of the slug-plug system in both orientations. More importantly, this OHS exhibited the heat dissipation capability of a heat power of 300 W (133 W/cm²) without exceeding a maximum surface temperature of 100 °C.

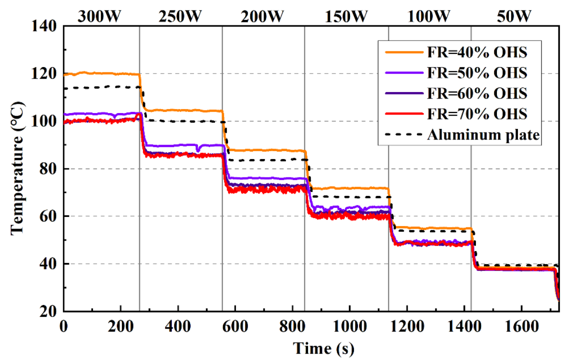

(a)

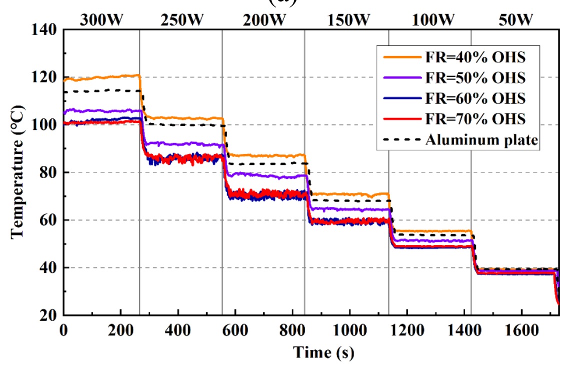

(b)

Figure 7. Comparison of temperature profiles (T_1) of the OHS at different filling ratios and aluminum plate in horizontal orientation (a) and vertical orientation (b) during the heat power reduction experiment.

Fig. 8 display the variations of thermal resistance of the OHS at different filling ratios in both horizontal and vertical orientations. Notably, the thermal resistance of the OHS at a filling ratio ranging from 50%-70% rapidly decreased as the heat power increased from 50 W to 100 W, indicating the startup of this device. On the contrary, the thermal resistance of the OHS was even higher than that of the aluminum plate due to the startup failure as mentioned above. At the heat power of 100-200 W, the thermal resistance of the OHS decreased further at a filling ratio of 60% or 70%. Specifically, at the filling ratio of 70%, minimum thermal resistances of 0.184 and 0.180 W/(m·K) were achieved in the horizontal and vertical orientations, respectively, representing a reduction of about 25.1% and 26.7% compared to the aluminum plate. With the further increase of heat power, however, the thermal resistance increased with the heat power. At the filling ratio of 50%, the OHS shows earlier performance degradation and the smallest thermal resistance appeared at the heat power of 100 W. Finally, compared to the horizontal orientation, the vertically oriented OHS at a filling ratio of 60-70% demonstrates better heat transfer performance in the heat power range of 100-200 W, and the OHS at 70% filling ratio was less affected by the orientation.

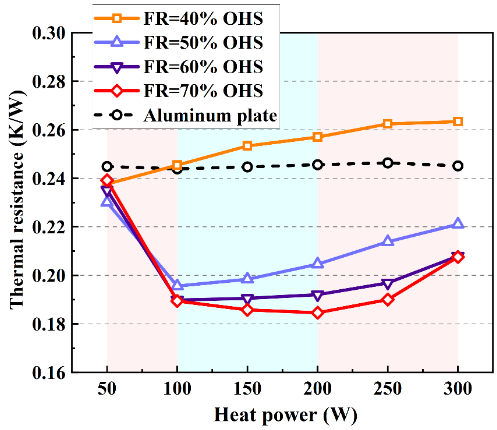

(a)

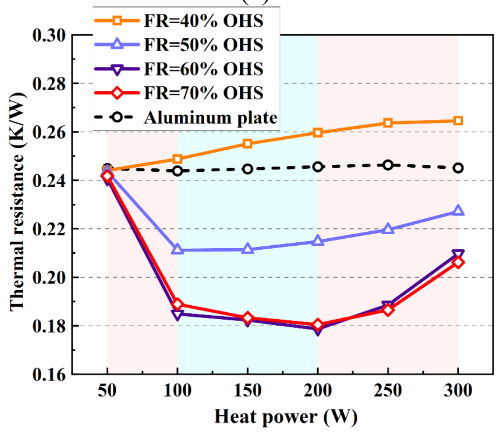

(b)

Figure 8. Thermal resistance versus heat power for OHS at different filling ratios: (a) horizontal orientation; (b) vertical orientation

5.2. Temperature uniformity

Based on the radial basis function method, we can obtain the temperature field of the OHS derived from the measurement of 13 thermocouples and interpolation processing. Fig. 9 displays the temperature distributions of the OHS (FR=60%) and aluminum plate under the heat power of 200 W at the quasi-steady state. It is evident that the OHS in both horizontal and vertical orientations showed better temperature uniformity compared to the aluminum plate. This is further validated by the temperature profile along the central cross-section of the device or plate as shown in Fig. 10. It can be found that the OHS maintained both a lower center temperature and a higher cooling boundary temperature, with the average temperature difference between the center surface and the boundary reduced by 17.7 °C compared to that of the aluminum plate, suggesting that the OHS effectively dissipated the localized heat at the center.

In addition, when comparing the vertical and horizontal orientations, the isotherm of the vertical OHS in Fig. 9(b) demonstrate a more uniform temperature distribution in the gravity-assisted region, while the anti-gravity region shows a more pronounced temperature difference. It indicates that the presence of gravity enhanced the temperature uniformity in the certain region of the vertical OHS, whereas the non-uniformity is more prominent in regions where gravity hinder the heat transport.

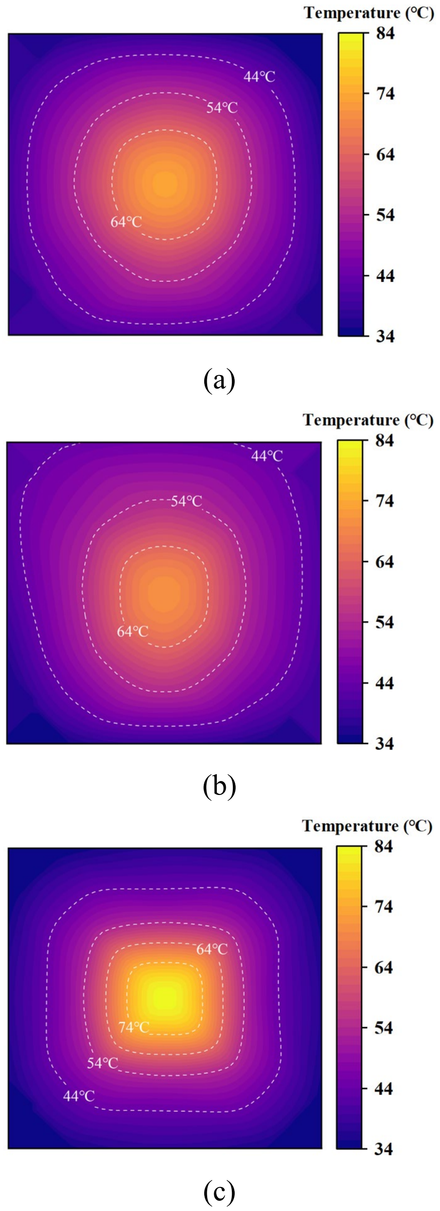

Figure 9. Temperature distributions of the OHS (horizontal orientation (a) and vertical orientation (b)) and solid aluminum plate (c) under the heat power of 200 W (FR=60%).

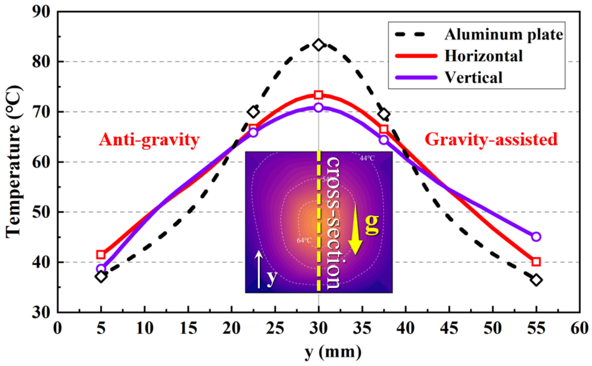

Figure 10. Interpolation temperature profile along the central cross-section of OHS in both horizontal, vertical orientations and the solid aluminum plate under the heat power of 200 W (FR=60%).

6. Conclusions

For the cooling of high-power electronic devices, a novel petal-shaped oscillating heat spreader (OHS) was developed through a topology optimization method on the basis of the variable density model. Additionally, a variable cross-section design was used to improve the operational reliability of OHS in various orientations. The effects of filling ratio and orientation on the heat transfer performance of the OHS and the temperature uniformity were experimentally investigated and compared. The main conclusions are summarized as follows:

(1) There existed an optimal filling ratio of 70% with respect to the lowest temperature of heating surface and the minimum thermal resistance of the OHS. Correspondingly, the minimum thermal resistance of 0.184 and 0.180 W/(m·K) were achieved in the horizontal and vertical orientations, respectively, which were reduced by about 25.1% and 26.7% as compared with the aluminum plate.

(2) The OHS exhibited the heat dissipation capability of 300 W (133 W/cm²) without exceeding a maximum surface temperature of 100 °C.

(3) The average temperature difference of the OHS between the center of the heated surface and the boundary was reduced by 17.7°C compared to the aluminum plate, demonstrating a significant improvement in temperature uniformity.

7. ACKNOWLEDGEMENTS

The financial grant from the National Natural Science Foundation of China (No. 52276067) is gratefully acknowledged.

References

[1] D.F. Hanks, Z.M. Lu, Sircar, J. Sircar, T.R. Salamon, D.S. Antao, K.R. Bagnall, B. Barabadi,

E.N. Wang, Nanoporous membrane device for ultra high heat flux thermal management, Microsystems & nanoengineering, 2018. 4 (1): p.1.
[2] J. Mathew, S. Krishnan, A Review on Transient Thermal Management of Electronic Devices, J. Electron. Packag, 2022. 144(1): p.010801.
[3] X.P. Chen, H.Y. Ye, X.J. Fan, T.L. Ren, G.Q. Zhang, A review of small heat pipes for electronics, Applied Thermal Engineering, 2016. 96: p.1-17.
[4] V. Ayel, M. Slobodeniuk, R. Bertossi, C. Romestant, Y. Bertin, Flat plate pulsating heat pipes: A review on the thermohydraulic principles, thermal performances and open issues, Appl. Therm. Eng, 2021.197: p.117200.
[5] W. Kim, S.J. Kim, Fundamental Issues and Technical Problems About Pulsating Heat Pipes, J. Heat Transf, 2021. 143: p.100803.
[6] Z.A. Li, G.Q. Zhou, P. Cheng, J. Qu, Heat transfer performance of novel 3D flat-plate oscillating heat spreader under gravity-assisted and anti-gravity conditions for high-density power electronics cooling. Applied Thermal Engineering, 2024. 252: p.123726.
[7] F.F. Laun, H. Lu, H.B. Ma, An experimental investigation of an oscillating heat pipe heat spreader, Journal of Thermal Science and Engineering Applications, 2015. 7(2): p.021005.
[8] B. Kelly, Y. Hayashi, Y.J. Kim, Novel radial pulsating heat-pipe for high heat-flux thermal spreading, International Journal of Heat and Mass Transfer, 2018. 121: p.97-106.
[9] F. Schwarz, P. Messmer, A Lodermeyer, V Danov, C Fleßner, S Becker, R Hellinger, Analysis of improved pulsating heat pipe designs for hot spot applications, International Journal of Heat and Mass Transfer, 2022. 196: p.123294.
[10] D. S. Jang, W. Cho, S.H. Ham, Y. Kim, Thermal spreading characteristics of novel radial pulsating heat pipes with diverging nonuniform channels, International Journal of Heat and Mass Transfer, 2022. 199: p.123488.
[11] C.X. Li, J. Li, A dumbbell-shaped 3D flat plate pulsating heat pipe module augmented by capillarity gradient for high-power server CPU onsite cooling, Energy Conversion and Management, 2023. 292: p.117384.
[12] J. Lim, S.J. Kim, Effect of a channel layout on the thermal performance of a flat plate micro pulsating heat pipe under the local heating condition, International Journal of Heat and Mass Transfer, 2019. 137: p.1232-1240.
[13] A. Fawaz, Y. Hua, S.L. Corre, Y. Fan, L. Luo, Topology optimization of heat exchangers: A review, Energy, 2022. 252: p.124053.
[14] J. Lim, S.J. Kim, A channel layout of a micro pulsating heat pipe for an excessively localized heating condition, Applied Thermal Engineering, 2021. 196: p.117266.
[15] E. Andreassen, A. Clausen, M. Schevenels, B.S. Lazarov, O Sigmund, Efficient topology optimization in MATLAB using 88 lines of code, Structural and Multidisciplinary Optimization, 2011. 43: p.1-16.
[16] E. Fernández, M. Collet, P. Alarcón, S. Bauduin, P. Duysinx, An aggregation strategy of maximum size constraints in density-based topology optimization, Structural and Multidisciplinary Optimization, 2019. 60: p.2113-2130.
[17] T. Wang, X. Liu, M. He, Y. Zhang, Molecular dynamics simulation of thermophysical properties and condensation process of R1233zd (E), International Journal of Refrigeration, 2020. 112: p.341-347.
[18] H. Lu, S. M. Thompson, F. F. Laun, H. B. Ma, Effect of cooling rate on thermal performance of an oscillating heat spreader, Journal of Thermophysics and Heat Transfer, 2016. 30(2): p. 461-465.

Paper ID 081(S2B)

Measurement of Impact Force of Geyser Boiling in Two-Phase Closed Thermosyphon

JinHyeuk Seo[1], and Jungho Lee[1*]

[1] *Department of Mechanical Engineering, Ajou University, Suwon, Republic of Korea*
**Corresponding author's email address: junghole@ajou.ac.kr*

Abstract

A two-phase closed thermosyphon (TPCT) has been widely attracting attention as a heat transfer device. Research on improving the thermal performance and durability of TPCT is needed for it to be continuously used in practical fields. However, most of the research mainly has been limited to studies that improve the thermal performance of TPCT. Therefore, in this study, we tried to research the geyser boiling phenomena (GBP) that affect the durability of TPCT. To measure the impact force generated from GBP, a TPCT with a load cell was installed, and the condenser and the adiabatic section were made possible to visualize. In addition, water and ethanol were used as working fluids to confirm the effects of thermal properties. The experiment resulted in ethanol showing higher thermal performance and lower impact force at a low heat flux and water having better operating conditions as the heat flux increased.

Keywords: Geyser Boiling; Two-Phase Closed Thermosyphon; Impact Force; Visualization

1. Introduction

A TPCT is a device for transporting a large amount of heat because it uses latent heat energy [1–4]. Generally, TPCT consists of three parts: evaporator, adiabatic section, and condenser. The vapor created at the evaporator is condensed at the condenser, and the condensate returns to the evaporator by gravitational force, as shown in Figure 1.

Due to its advantages, such as its simple structure and easy maintenance, the TPCT has received attention in the field of heat exchangers [5–7]. The TPCT has two primary limits because an individual TPCT operates in low heat flux due to the increase in the number of TPCTs: the first is low thermal performance, and the other is GBP.

Various researchers have covered the enhancement of thermal performance in the TPCT [1–4,8,9]. However, GBP has not been investigated despite the risk of fatigue failure.

GBP is a chaotic flow that occurs in the TPCT. When heat is supplied to the evaporator, the liquid stores internal energy. This energy is utilized to make the bubble (Figure 2. (a)) and its growth (Figure 2. (b)). The rapid growth of the bubble pushes up the liquid, which hits the cap of the TPCT (Figure 2. (c)). After that, the bubble and liquid were mixed and fell to the evaporator (Figure 2. (d)). GBP can impact TPCT and be hazardous. Hence, GBP is a phenomenon that should be avoided when operating the TPCT [10–12].

The GBP studied so far was determined based on the temperature or pressure variation in the TPCT

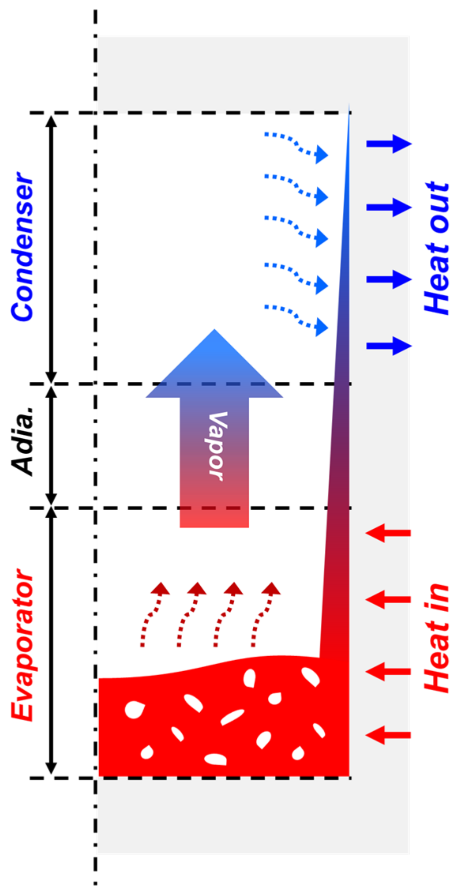

Figure 1. Principle of TPCT operation

[10,12]. This method for measuring GBP is not precise because the internal flow behavior only depends on temperatures and pressures due to an invisible experimental setup. Although the visualization studies for GBP also existed, the experimental setup, which totally consisted of

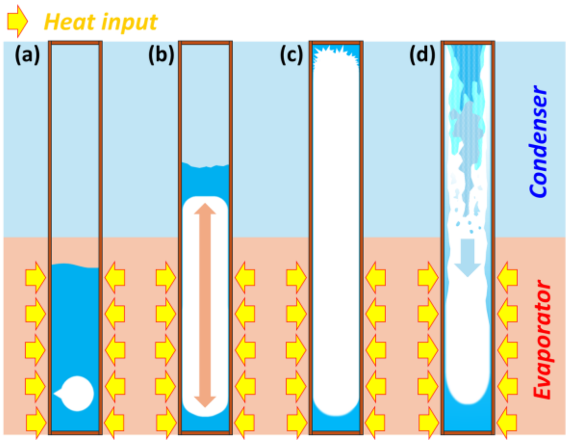

Figure 2. Sequence of GBP occurrence

transparent materials, could not guarantee the actual operating environment of the TPCT. Especially, the initial condition for GBP occurrence might be different such as a bubble embryo.

Hence, this study analyzed GBP by installing the load cell at the top of TPCT. Even the TPCT can provide the internal flow because the adiabatic section and the condenser were quartz, while the evaporator was copper. Additionally, the working fluid effect for GBP was analyzed by using water and ethanol. Based on the results from this study, the occurrence of GBP can be confirmed clearly, and the impact force exerted by GBP can be obtained. In addition, this study presented the working fluid that can provide the best conditions during TPCT operation in terms of thermal performance and impact force.

2. Experimental setup and procedure

The experimental setup image is shown in Figure 3. The TPCT consisted of the evaporator, the adiabatic section, and the condenser. Each part had a length of 150 mm and an inner diameter of 15 mm. The evaporator was made of copper and had eight cartridge heaters. The adiabatic section and the condenser were one body of cylindrical quartz used to visualize internal flow in the TPCT. The condenser was covered with a water jacket. The water jacket was kept in cold conditions by flowing coolant. The coolant is water, which was maintained at the targeted temperature. The water jacket is made of acrylic to avoid disturbing the visualization. The separation plate was used between the condenser and the adiabatic section to prevent the leak from the condenser. A load cell and pressure transducer were installed at the top of the condenser to measure the force and the pressure generated by the internal flow. A stainless-steel plate with a diameter of 14 mm was attached to the load cell. This plate helped the load cell measure all flow

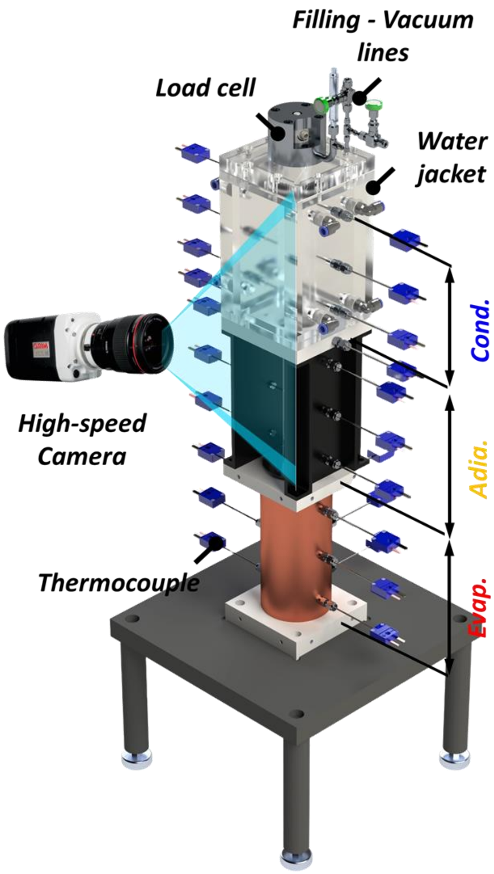

Figure 3. Experimental setup

behavior because the sensing area of the load cell had only half of the inner diameter. 25 T-type thermocouples measured the wall and the internal temperatures of each part. The measured force, pressure, and temperature had a sampling rate of 500 samples/sec and were stored on the desktop through the data acquisition system in real-time. A high-speed camera performed the visualization, and the recording speed was 500 frames/sec to compare

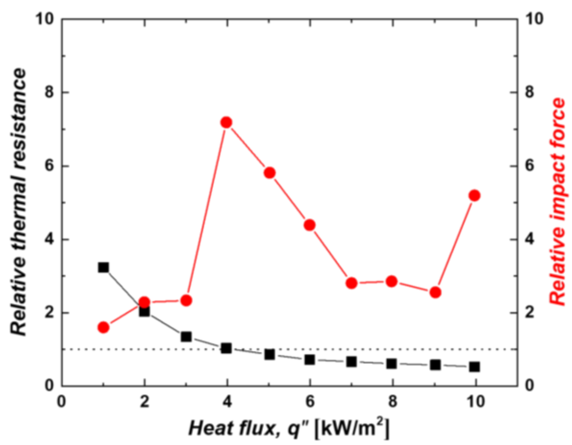

Figure 4. Relative thermal resistance and impact force according to heat flux

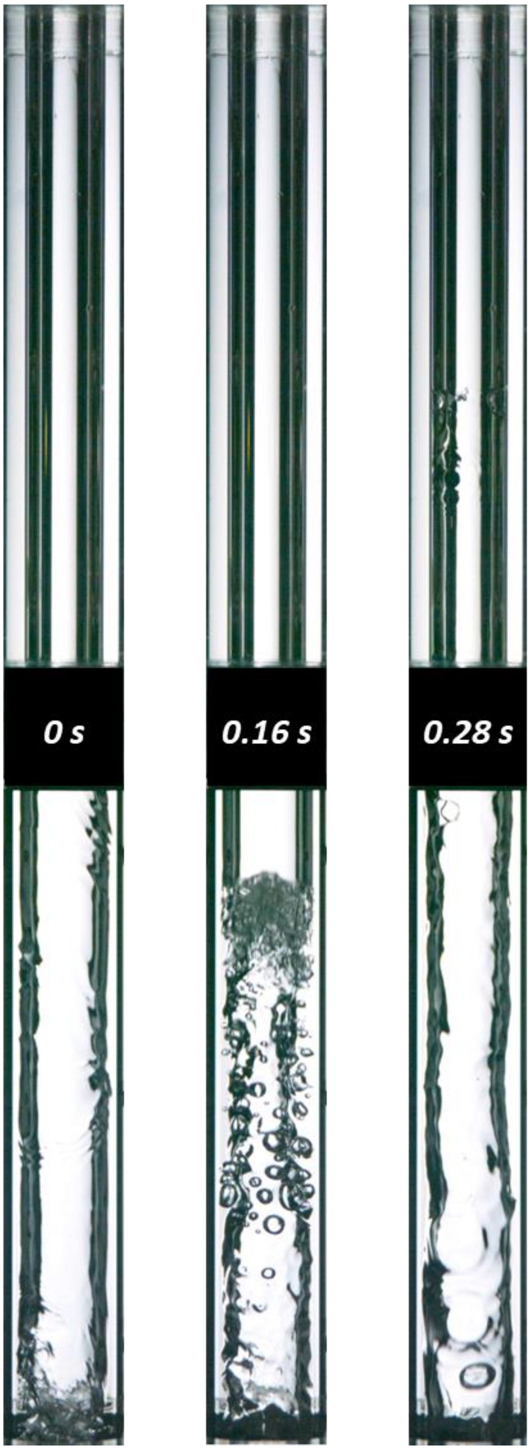

Figure 5. Visualization image of ethanol (q''=6 kW/m^2)

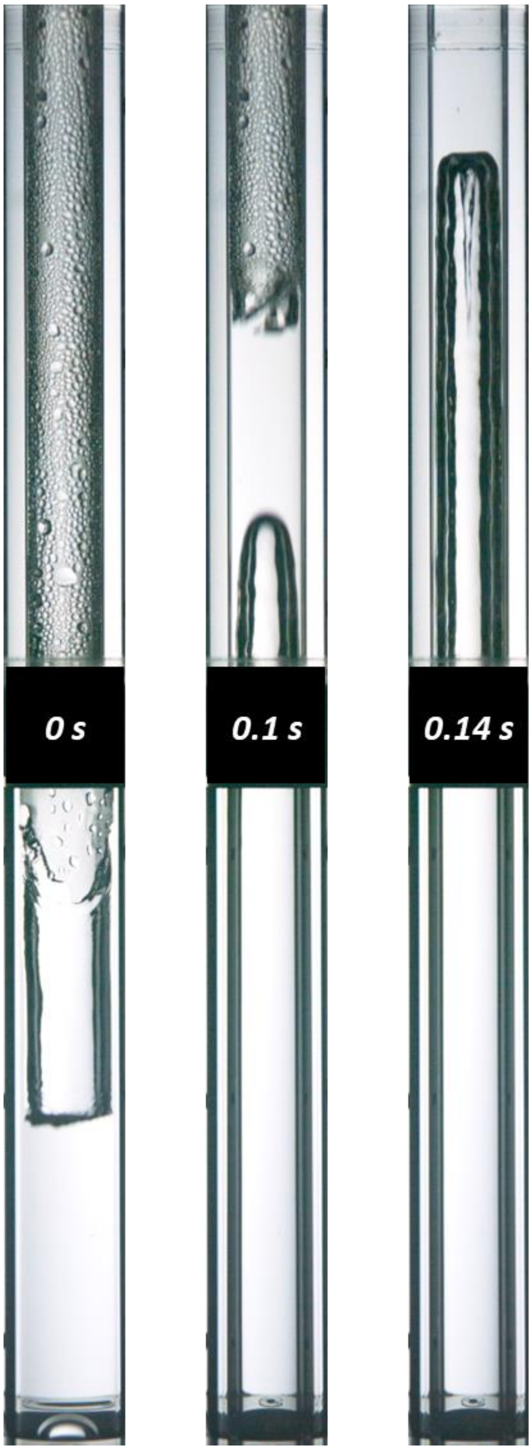

Figure 6. Visualization image of water (q''=6 kW/m^2)

with the measured data set easily. DI water and ethanol were selected as working fluids to compare their characteristics for GBP. The filling ratio (FR) was 100%, and the heat flux increased by 1 kW/m^2 from 1 kW/m^2 to 10 kW/m^2.

Before the experiments, the experimental setup was cleaned with chemicals appropriate to the material. The cleaned evaporator and quartz cylinder (condenser and adiabatic section) were vertically aligned and assembled. The assembled experimental setup was connected to the vacuum pump, but the vacuum was controlled, and when the target vacuum was reached, the working fluid was injected. The injected working fluid has undergone sufficient degassing before injection. The device's cartridge heater was connected to the power supply, and the heat source was supplied. The temperature, pressure, and force measurement data were connected to the data acquisition system so that data could be collected.

3. Data reduction

Data reduction was calculated using the average data collected for 10 minutes after reaching a steady state.

Thermal resistance was used as an indicator of thermal performance, and the equation is as follows:

$$R_{th} = \frac{T_{w,eva} - T_{w,cond}}{Q_{eva}} \quad (1)$$

where $T_{w,evap,}$ and $T_{w,cond}$ are the average inner wall temperature of the evaporator and the condenser, respectively.

The impact forces were simultaneously also measured. However, the load cell provided the force data without data reduction. Hence, the additional data reduction process was not needed for them. To easily compare the thermal performance and impact force of ethanol and water, additional data reduction was carried out by dividing the measured value of water by the measured value of ethanol, as shown in Eqs (2) and (3) below:

$$\text{Relative thermal resistance} = \frac{R_{th,Water}}{R_{th,Ethanol}} \quad (2)$$

$$\text{Relative impact force} = \frac{F_{Water}}{F_{Ethanol}} \quad (3)$$

where $R_{th,Water}$ and $R_{th,Ethanol}$ are the thermal resistances of water and ethanol. F_{water} and $F_{Ethanol}$ are the impact forces of water and ethanol.

4. Results and discussion

A graph of the relative thermal resistance and impact force of water versus ethanol is shown in Figure 4. When the relative thermal resistance is greater than 1, it means that the thermal performance of water is relatively low compared to that of ethanol. Ethanol's thermal performances were superior to those of water at initial low heat fluxes. However, it gradually deteriorated based on a 4 kW/m^2 heat flux. This is because ethanol, which has a relatively low boiling point and low latent heat of evaporation, facilitates boiling and evaporation (Table 1). As the heat flux increases, boiling occurs in the water, improving its thermal performance.

When the relative impact force is greater than 1, water's impact force is greater than that of ethanol. The relative impact force showed a different trend from the thermal performance. In all heat fluxes, water's impact forces were greater than those of ethanol, and in particular, the impact force of water at a heat flux of 4 to 6 kW/m^2 was up to about 8 times greater. This is because, as can be seen in Figures 5 and 6, GBP occurred in water based on the same heat flux but not in ethanol.

Table 1. Thermal properties of working fluids

Working fluid	T_{sat}	ρ_l	σ	h_{fg}
	(°C)	(kg/m^3)	(mN/m)	(kJ/kg)
Water	100	958	59	2257
Ethanol	78	757	17.3	960

5. Conclusions

In this study, TPCT thermal performance using water and ethanol was measured, and the impact force of GBP was compared using load cells installed simultaneously. The experiment found that using ethanol with relatively low impact force and high thermal performance at a low heat flow rate ($q'' \leq 6$ kW/m^2) is advantageous for TPCT operation. However, it was found that at a high heat flux ($q'' > 6$ kW/m^2), using water with relatively reduced impact force and improved thermal performance is helpful for TPCT operation.

6. ACKNOWLEDGEMENTS

This work was supported by the Innovative Energy Efficiency R&D Program of the Korea Institute of Energy Technology Evaluation and Planning (KETEP) grant funded by the Ministry of Trade, Industry & Energy, Korea. (Grant No. 20212020800270), and a National Research Foundation of Korea (NRF) grant funded by the Ministry of Science and ICT, Korea (No. NRF-2020R1A2C3008689).

References

[1] Y. Kim, J.S. Kim, D.H. Shin, S.M. You, J. Lee, Enhanced thermal performance of a thermosyphon for waste heat recovery: Microporous coating at evaporator and hydrophobic coating at condenser, Applied Thermal Engineering, 2020, 175: 115332.

[2] Y. Kim, D.H. Shin, J.S. Kim, S.M. You, J. Lee, Boiling and condensation heat transfer of inclined two-phase closed thermosyphon with various filling ratios, Applied Thermal Engineering, 2018, 145: p.328.

[3] Y. Kim, J.S. Kim, D.H. Shin, J.H. Seo, S.M. You, J. Lee, Effects of hydrophobic and superhydrophobic coatings of a condenser on the

thermal performance of a two-phase closed thermosyphon, International Journal of Heat Mass Transfer, 2019, 144: 118706.

[4] D. Seo, Y. Kim, J.H. Seo, D.H. Shin, Y. Nam, J. Lee, Modeling and optimization of hydrophobic surfaces for a two-phase closed thermosyphon, International Journal of Heat Mass Transfer, 2021 165: 120680.

[5] H. Jouhara, S. Almahmoud, D. Brough, V. Guichet, B. Delpech, A. Chauhan, L. Ahmad, N. Serey, Experimental and theoretical investigation of the performance of an air to water multi-pass heat pipe-based heat exchanger, Energy, 2021, 219: 119624.

[6] J. Ramos, A. Chong, H. Jouhara, Experimental and numerical investigation of a cross flow air-to-water heat pipe-based heat exchanger used in waste heat recovery, International Journal of Heat Mass Transfer, 2016, 102: p.1267.

[7] W. Srimuang, P. Amatachaya, A review of the applications of heat pipe heat exchangers for heat recovery, Renewable and Sustainable Energy Reviews, 2012, 16: p.4303.

[8] S. Kang, J.H. Seo, J. Lee, Effect of inner diameter on the confinement of two-phase closed thermosyphon, International Communications in Heat and Mass Transfer, 2023, 147: 106997.

[9] D. Seo, J. Shim, D.H. Shin, Y. Nam, J. Lee, Dropwise condensation of acetone and ethanol for a high-performance lubricant-impregnated thermosyphon, International Journal of Heat Mass Transfer, 2021, 181: 121871.

[10] L.H.R. Cisterna, F.H. Milanez, M.B.H. Mantelli, Prediction of geyser boiling limit for high temperature two-phase thermosyphons, International Journal of Heat Mass Transfer, 2021, 165: 120656.

[11] M.R.S. Emami, S.H. Noie, M. Khoshnoodi, M.T.H. Mosavian, A. Kianifar, Investigation of geyser boiling phenomenon in a two-phase closed thermosyphon, Heat Transfer Engineering, 2009, 30: p.408.

[12] N.Y. Londoño Pabón, J.P. Florez Mera, G. Serafin Couto Vieira, M. Barbosa Henriques Mantelli, Visualization and experimental analysis of Geyser boiling phenomena in two-phase thermosyphons, International Journal of Heat Mass Transfer, 2019, 141: p.876.

Paper ID 083(S2A)

Novel Pulsating Heat Pipe Composed of Wire-Plate Grooves

Larissa Krambeck*, Kelvin Guessi Domiciano, Kênia Warmling Milanez, Marcia Barbosa Henriques Mantelli

Heat Pipe Laboratory, Federal University of Santa Catarina, Florianopolis/SC, Brazil
* *larissa.krambeck@labtucal.ufsc.br*

Abstract

The present work proposes a novel pulsating heat pipe, composed of flat plates and solid wires, forming a new channel geometry in a closed-loop arrangement, manufactured by diffusion bonding. The proposed channel has four sharp grooves in the corners, resulting from the contact line between the solid copper wires and plates. This wire-plate pulsating heat pipe was experimentally investigated. The data showed that, depending on the operation parameters, the device could work as a heat pipe or a pulsating heat pipe, for lower and higher power input levels, respectively. Besides, the proposed device was able to start at low heat loads and at reduced evaporator temperature when in a pulsating heat pipe mode, which is a great advantage when compared to ordinary ones. The main novelty of the present research is the new channel profile for a pulsating heat pipe, which was shown to improve the heat transfer capacity during the startup, extending the thermal load range applications of these devices.

Keywords: Pulsating heat pipe; Wire-plate grooves; Channel geometry; Diffusion bonding; Thermal Performance.

1. Introduction

Flat plate pulsating heat pipes (PHPs) may be feasible solutions for the thermal management of microelectronic components that integrate printed circuit boards and multi-chip modules in electronic equipment, including those for space applications. Operating due to the oscillations of a working fluid slug flow in confined channels, they are efficient passive heat transfer devices, especially for high and concentrated heat fluxes [1,2].

The channel geometry is the dominant parameter that influences the flow regime and the working fluid distribution, directly impacting the thermal behavior of the PHP [3,4]. Although many studies on channel shapes can be found, most researchers worldwide still deal with traditional channels due to the ease of fabrication. Rectangular and circular cross-sections are considered the standard ones for the flat PHPs. Several authors [5–9] agree that PHPs with square/rectangular cross-section channels show lower thermal resistances and evaporator temperatures (principally in horizontal position) and can transfer higher heat loads when compared with circular profiles. However, they show later startups, caused by a delay at the beginning of oscillation. As highlighted by Ayel et al. [4], due to capillary forces, the liquid tends to accumulate in the edges, resulting in reduced menisci curvature radii. Therefore, sharp corners act as capillary structures, keeping the evaporator edges wet. As a result, the liquid flows in the corners from the condenser to the evaporator, not blocking the vapor flow [10].

Furthermore, channel geometries affect the flow patterns. The sharp angles can reduce the Kelvin-Helmholtz and other dynamic instabilities that favor the transition from slug flow to annular flow, achieving higher heat transfer capacity and lower overall thermal resistances [11].

Some new cross-section proposals emerged to improve liquid pumping and thermal efficiency and decrease the dependency on gravity [1]. Qu et al. [12] verified that the PHPs with a triangular channel shape have better thermal performance than the rectangular ones. The sharper angles improve the capillary forces and the bubble formation, consequently improving the working fluid phase change. Wang et al. [13] studied corrugated geometries at different positions in tubular PHP made of glass. They achieved a better thermal performance using a corrugated configuration in the evaporator section. Cai et al. (2006) produced a PHP with a flat surface from a tubular device by compressing of a copper tube inside a flat plate and a mold with a dual-radius shape. Two microgrooves were formed at the interface of the two profiles, which worked as a wick structure, keeping the evaporator wet. Besides, Qu et al. (2017) investigated tubular OHP with internal helical microgrooves. The helical structure enhanced the effective thermal conductivity, standing for higher heat inputs at both horizontal and vertical orientations due to the intensification of the phase change.

Novel channel geometries for flat plate PHPs to enhance the boiling phenomenon have also been researched. Kim and Kim [16] explored a micro flat plate PHP with different dimensions of reentrant cavities fabricated onto a silicon wafer. However, it was not able to improve the cold liquid circulation from the condenser, as the cavities were perpendicular to the channel. The startup happened at lower power inputs as the cavities helped decrease the wall superheating and increase the bubble production.

Krambeck et al. [17] investigated two diffusion-bonded PHPs, one with a simple round cross-section channel and another with a round cross-section and ultra-sharp lateral grooves, in the evaporator section. The application was for the thermal management of large-scale electronic gadgets in a wide range of applied heat loads. Their main conclusion is that grooved PHP presented higher thermal performance than round one for most applied heat loads and operation orientations, resulting in a difference in the average temperatures between the evaporator's round and grooved PHP of 2.1 °C. Besides, Krambeck et al. [17] showed that the diffusion bonding process was capable of manufacturing high-quality flat PHPs with different internal channels, being a promising technology for such applications. Using the same fabrication process, Paiva et al. [18] developed wire-plate heat pipes (HPs) composed of a sandwich of copper flat plates and solid wires by diffusion bonding. The contact between the wire and plates creates four very sharp grooves in each channel, as shown in Figure 1, with an excellent pumping capacity.

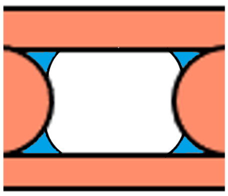

Figure 1. Wire-plate channel profile and four sharp grooves.

Despite the huge capacity for transferring heat, PHPs have a strong drawback, as they require high heat loads and elevate temperature differences for the startup in the oscillating slug flow mode. This fact reduces their applicability in many equipment where high temperatures are not allowed or when the heat load range is wide [19].

The PHP thermal performance can be enhanced by the proposal of a new shape of channels using grooves once they work as artificial nucleation sites, which may help in the bubble formation and, as a wick structure, in the spreading of the liquid along the evaporator.

In this context, the present work proposes a novel PHP, composed of flat plates and solid wires, forming a new channel geometry in a closed-loop arrangement, manufactured by diffusion bonding. The proposed channel has four sharp grooves in the corners, made by the contact line of solid copper wires and plates. The wire-plate PHP was experimentally investigated to assess the improvements in the thermal performance of PHPs.

2. Methodology

The manufacturing of the proposed PHP, the setup used for the experiments, the experimental procedure and the thermal analysis method employed are described in this section.

2.1 Fabrication of the wire-plate PHP

A mini wire-plate pulsating heat pipe with 100 x 55 mm^2 was designed to have 16 parallel interconnected parallel channels in a closed-loop arrangement, made of solid copper wires. The geometry details of the new channel and the PHP design are shown in Figure 2.

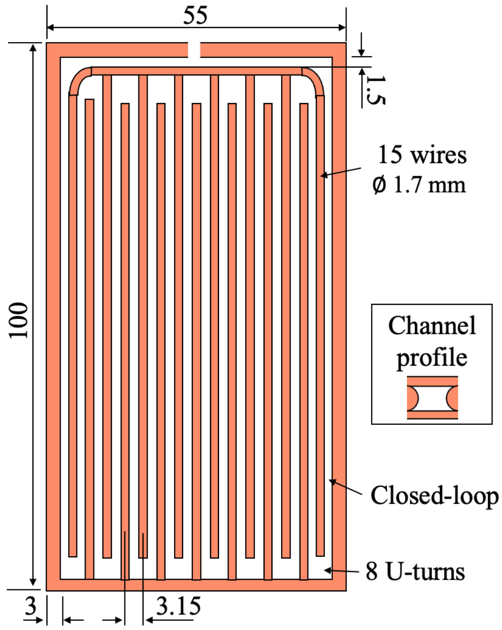

Figure 2. Wire-plate PHP design.

To fabricate the proposed device, closing copper sheets (0.5 mm thick) were used to form a sandwich with a copper hollow frame (1.5 mm thick) and fifteen solid copper wires with a diameter of 1.7 mm. The flat plates were cut in the water jet machine. Spot welding was used to fix the wires and plates to the desired positions, as seen in Figure 3 (both end sides of each wire are flat).

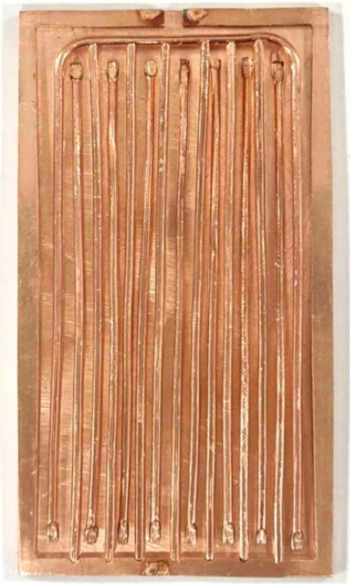

Figure 3. Internal view of the wire-plate PHP before closing.

In the sequence, the stacked set was diffusion bonded. The diffusion bonding cycle was the same one used by [20], in which the pilled plates remained for one hour at 875 °C, after heating at 10 °C/min, inside a furnace (*Jung*™) with an inert atmosphere of 95 % argon and 5 % hydrogen. Due to the difference in thickness between the hollow frame and the solid wires, two thermal cycles were performed, one to diffusion bond the wires to the closing plates and another to seal the borders. Because both cycles were applied in the same manufacturing procedure, the frame has a lower thickness compared to the rest of the wire-plate PHP, which can be noticed in Figure 4a. The resulting grooves of the channel and the wire oval shape, a small deformation due to the pressure applied during the fabrication process, can be seen in Figure 4b.

Therefore, the fabricated PHP had a final thickness of 2.80 mm, a mass of 99.86 g, and a total internal void volume of 4.12 ml. Degassed distilled water was used as the working fluid. The spacing between the wires worked as channels with four sharp grooves, through which water flowed in confined conditions (critical diameter smaller than 4 mm, according to the Bond number [21]), resulting in a slug-plug flow.

Preliminary experimental work showed that the wire plate PHP was capable of working as a conventional heat pipe (no oscillations) or as an ordinary PHP, depending on the filling ratio (FR), which is defined as the ratio between the volume of the working fluid and the total void volume (V_l/V_t) of the device. In this way, after testing several amounts of working fluid inside the wire-plate PHP, two of the tested FRs were selected as presenting the best thermal performance for operation as a conventional HP or a PHP, of 19% (0.78 ml) and 67% (2.76 ml), respectively.

a) External view

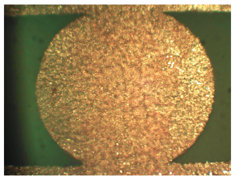

b) Grooves' view (OM image)

Figure 4. Resulting wire-plate PHP after the diffusion bonding.

2.2 Experimental Setup

Figure 5 shows a schematic of the setup developed for the thermal tests. The length of the PHP was divided into: evaporator (14 mm), adiabatic (71 mm), and condenser (15 mm) sections. In the evaporation section, a heater composed of a cartridge resistor inside a copper block (14 x 55 x 14 mm³), fed by a programmable power supply unit (*TDK-Lambda*™ GEN300-17), simulated the heat dissipation of multi-chip modules. Cooling water from a thermal bath (*Lauda Ecoline*™ RE212) flew through a metallic block (15 x 55 x 22 mm³) in a small heat exchanger, removing heat from the condenser. The cooling water temperature was kept at 20 °C with a constant flow rate of 4.1 l/min. For both evaporator and condenser blocks, the contact resistance was reduced with the use of thermal grease. The entire setup was insulated by a 30 mm thick blanket from *Isoglas*®, with a thermal conductivity of 0.045 W/mK.

Three T-type (*Omega Engineering*™) thermocouples in each section recorded the temperature measurements, which were attached to the outer surface of the wire-plate PHP using *Kapton*® tapes. Figure 5 shows, on the right side, the thermocouples distribution along the proposed device. Also, one thermocouple measured the environment temperature. A data acquisition system (*DAQ-NI*™ SCXI-1000) acquired the temperature readings, which were stored in a computer.

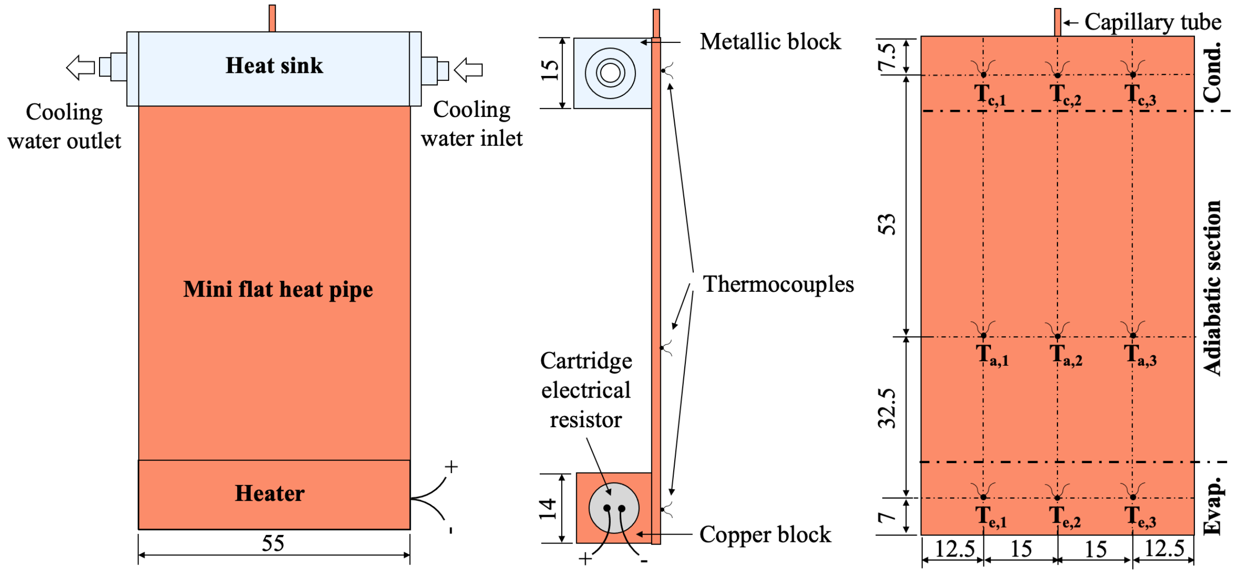

Figure 5. Experimental setup.

2.3 Experimental Procedure

For all tests of the novel PHP, the first procedure was to evacuate the device and charge it with the desired amount of working fluid. A turbomolecular pumping station, *Edwards*™ T-Station 85, was used to achieve a high vacuum of 4×10^{-5} mbar inside the wired PHP. Then, using special vacuum tubes (*Tygon*®) and forceps, degassed distilled water was inserted into the device. In the sequence, a purging process was performed to eliminate any possible non-condensable gases, which could jeopardize the thermal performance. For each thermal test, a new filling process was accomplished with the desired FR, repeating all these steps.

The thermal tests were performed in the horizontal orientation (evaporator at the same level as the condenser). Heat transfer rates from 10 to 160 W (corresponding to a heat flux from 1.3 to 20.8 W/cm^2) were applied in the evaporator during 600 s, to guarantee steady-state conditions, considered reached when the evaporator temperature variation was lower than 1 °C/min. The experiment was turned off when the evaporator temperature reached 100 °C, an adopted limit temperature, considering the possible application of the device for the thermal control of electronics. The heat flux was expressed by the dissipated thermal load divided by the heater contact area of 770 mm^2.

2.4 Thermal Evaluation

The overall thermal resistances are usually employed to estimate the thermal performance of such devices, defined as the ratio between the temperature difference of the evaporator and condenser regions and the heat load, i.e.:

$$R = \frac{\bar{T}_e - \bar{T}_c}{q} = \frac{\bar{T}_e - \bar{T}_c}{U \cdot I} \tag{1}$$

where $\bar{T}_e$, and $\bar{T}_c$ are the average temperature of the evaporator and condenser, respectively. The heat load, q, is determined by the voltage (U) and the electric current (I) applied to the cartridge electrical resistor.

The average temperatures, $\bar{T}$, for the evaporator and condenser sections, are calculated by:

$$\bar{T} = \frac{\sum_{j=1}^{M} \frac{1}{N} \sum_{i=1}^{N} T_i}{M} \tag{2}$$

where T_i are the thermocouple temperature readings at steady-state conditions, N is the number of samples, and M is the number of thermocouples in each section. In the present work, the number of temperature measurements is 50, which corresponds to the data recorded at the last 50 seconds for each heat load, after the steady state conditions were reached.

The thermal resistance uncertainty, $\delta(R)$, was calculated using the error propagation method proposed by Holman et al. [22] with the following expression:

$$\delta(R)^2 = \sum_{i=1}^{n}\left[\frac{\partial f}{\partial x_i}\delta(x_i)\right]^2 \qquad (1)$$

where $\delta(x_i)$ is the measurement uncertainties of temperatures, voltage, and current. f is given by Eq. (2). After calibrating the experimental setup, a temperature uncertainty of ± 0.13 °C was found. According to the power unit manufacturer, the voltage and current uncertainties were 0.03 V and 0.0085 A, respectively.

3. Results and Discussion

The experimental results regarding the thermal performance of the new wired PHP and its comparison with other technologies in the horizontal orientation are presented in this section.

As mentioned before, the wire-plate PHP may present two distinct performances that depend on the filling ratio: operation as a heat pipe or as a PHP. To help the analysis, the thermal behavior of these two technologies in the horizontal position, which were studied in Krambeck et al. [23], are characterized. The first technology is the wire-plate flat HP, very similar to the one described in Figures 2 and 3 but without the confined channel in a closed-loop fashion, only allocated in the length of the HP to bring the liquid from the condenser to the evaporator, as the schematized design presented in Figure 6a. The second device is an ordinary flat plate PHP, Figure 6b, with 16 interconnected channels with a square cross-section. Both were fabricated by diffusion bonding with equal external dimensions and tested under exactly the same conditions. Their main characteristics are presented in Table 1.

Table 1. Principal characteristics of heat pipe technologies for comparison.

Features	Wire-plate HP	Ordinary PHP
Mass [g]	94.86	105.36
Container	Copper	
Length [mm]	100	
Width [mm]	55	
Thickness [mm]	2.79	2.65
Internal structure	12 solid copper wires	16 square channels 1.5 x 1.5 mm^2
Internal channel arrangement	Parallel	Interconnected in a closed loop
Void volume [ml]	4.60	2.85
Working fluid	Deionized distilled water	
Best filling ratio [%]	17	65

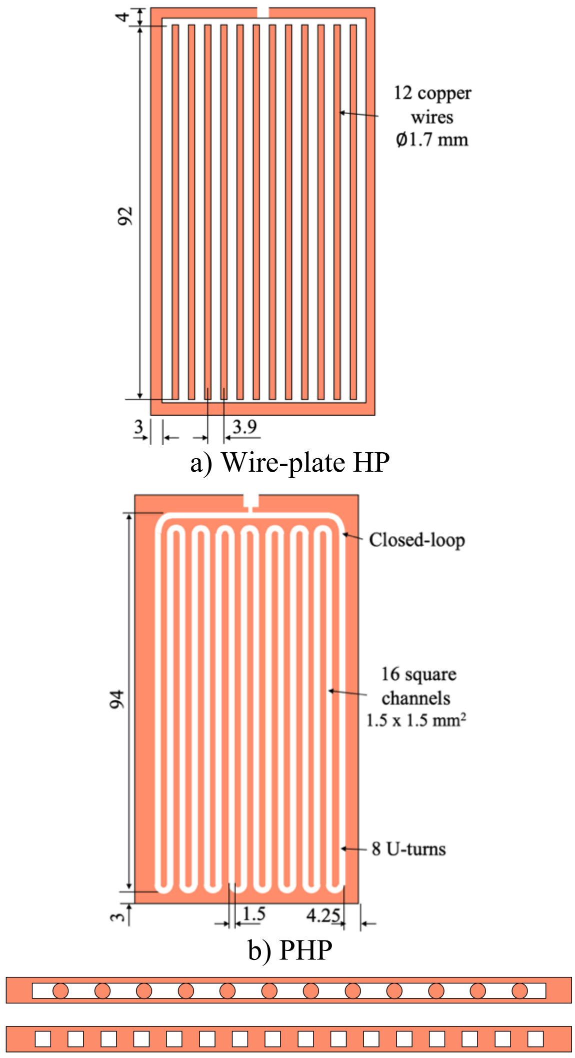

a) Wire-plate HP

b) PHP

c) Cross-sections

Figure 6. Heat pipe technologies for comparison: wire-plate HP and ordinary PHP [23].

Only the best filling ratio for each device, for operation in the horizontal position, is used for comparison. The slight difference in thickness is related to the internal structure.

3.1 HP Standard Thermal Behavior

Figure 7 shows the temperature transient of an HP with wire-plate grooves with FR of 17% for all the tested heat loads until the evaporator reached 100 °C. As a typical behavior of a conventional heat pipe, all the temperatures ascended for each increased heat load, reaching a steady-state condition. The device started operating from the first thermal loads, with the evaporator showing the onset of a dry-out (sudden evaporator temperature increase) at 50 W (6.5 W/cm^2), which, however, did not avoid the device operation until 130 W (16.9 W/cm^2), when the evaporator reached 100 °C and the experiment was shut down.

3.2 PHP Standard Thermal Behavior

The PHP starts its operation gradually. As large bubbles in the evaporator are generated, they push the hot fluid slugs from the evaporator to the condenser section, forming a slug-plug flow that transfers heat mainly by convection. In the beginning, the temperature oscillations are high, but they tend to stabilize over time. Therefore, the startup of a PHP operation is characterized by the drop in the evaporator temperature, which approaches that of the adiabatic section temperature, with a concomitant increase in the condenser temperature. After that, the device reaches the typical stable circulation operation regime.

The temperature transient behaviors for the flat conventional PHP studied, under several heat loads, are presented in Figure 8. It can be observed that the PHP reached a steady-state condition for each heat load applied. Exceptionally, during the startup of the PHP, a surpass of this maximum evaporator temperature was tolerated for the PHP to create the necessary PHP activation conditions, as noticed in previous tests. After that, the same 100 °C temperature limit was respected.

The PHP startup occurred at 60 W (7.8 W/cm^2), with the evaporator reaching the temperature of approximately 115 °C (which overpassed the limit for actual applications). After that, the temperature levels decreased, and the oscillations continued until 110 W (14.3 W/cm^2). At around 120 W (15.6 W/cm^2), a more stable operation was reached with smaller temperature amplitudes. This condition was observed up to 170 W (22.1 W/cm^2), the maximum power supported considering the evaporator temperature of 100 °C.

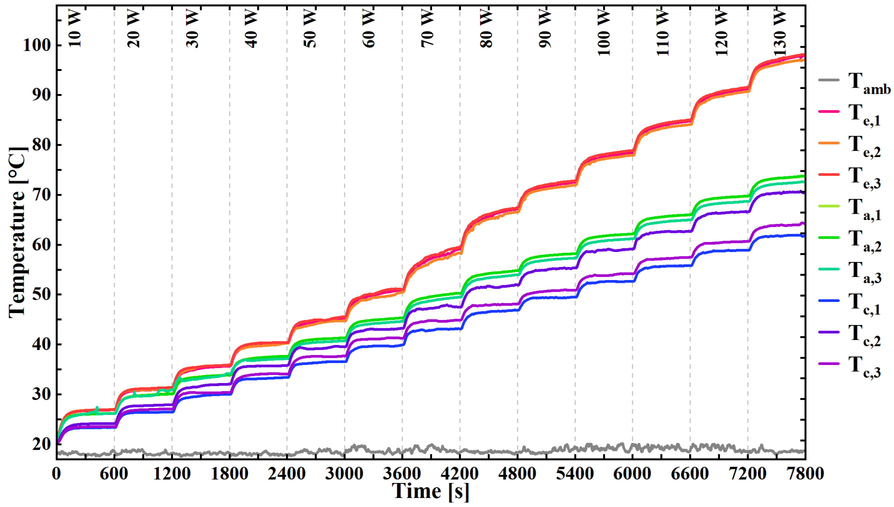

Figure 7. Transient of temperatures of the flat HP with wire-plate grooves.

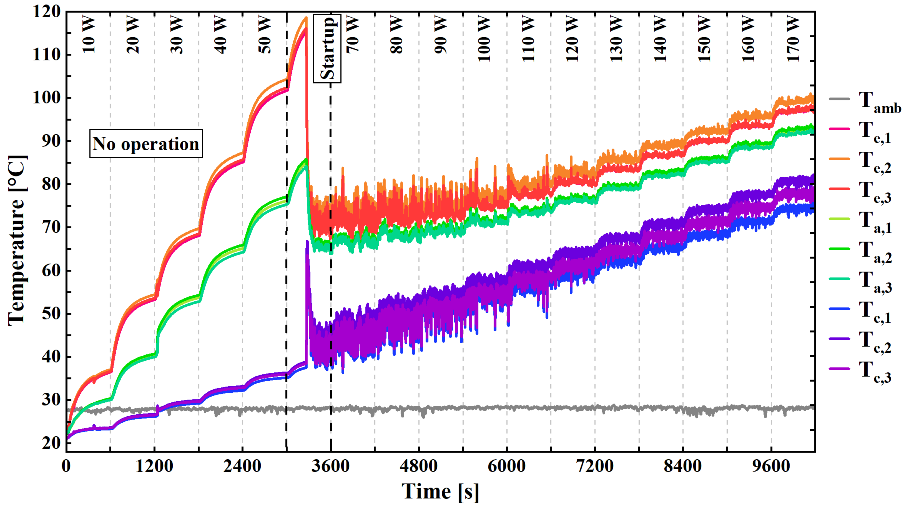

Figure 8. Transient of temperatures of the flat PHP with square channels.

3.3 Thermal Behavior of the Wire-plate PHP

Figure 9 shows the temperature transient for all applied heat loads of the wire-plate PHP, with FR 67 %, operating in the horizontal orientation. This high FR provides a typical behavior in slug-plug flow, i.e., in an oscillating cycle, typical of PHPs. For every heat load, all the temperatures increased until they reached steady-state conditions.

According to Figure 9, the wire-plate grooves aided the PHP startup process, as the PHP worked with smaller temperature differences among regions when compared to a conventional PHP in the horizontal position. The temperature oscillations, typical for a PHP operation, started at 60 W (7.8 W/cm^2) with an evaporator temperature lower than 90 °C. After that, slug-plug flow was sustained until 160 W (20.8 W/cm^2). No dry-out was noticed.

A completely different operation was performed by the wired PHP with a FR of 19 %, as observed in the temperature transient for all tested heat loads in Figure 10. With this volume of working fluid, the novel wire-plate PHP worked similarly to a conventional grooved heat pipe, in which the temperatures of three sections rose for each increased heat load, reaching a steady-state condition.

Therefore, the wire-plate PHP started its operation since the first thermal load, 10 W (1.3 W/cm^2), once the evaporator and condenser temperatures were very close to each other, up to 60 W (7.8 W/cm^2) when the evaporator dry-out onset was observed, characterized by the sudden evaporator temperature increase. Despite the dry-out onset, the device continued transporting heat until 110 W (14.3 W/cm^2), when the evaporator reached 100 °C.

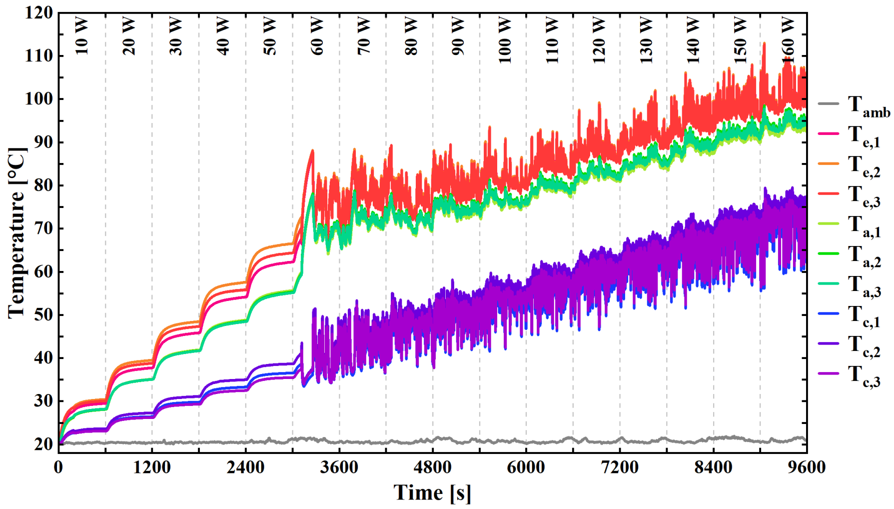

Figure 9. Transient of temperatures of the wire-plate PHP with a FR of 67 %.

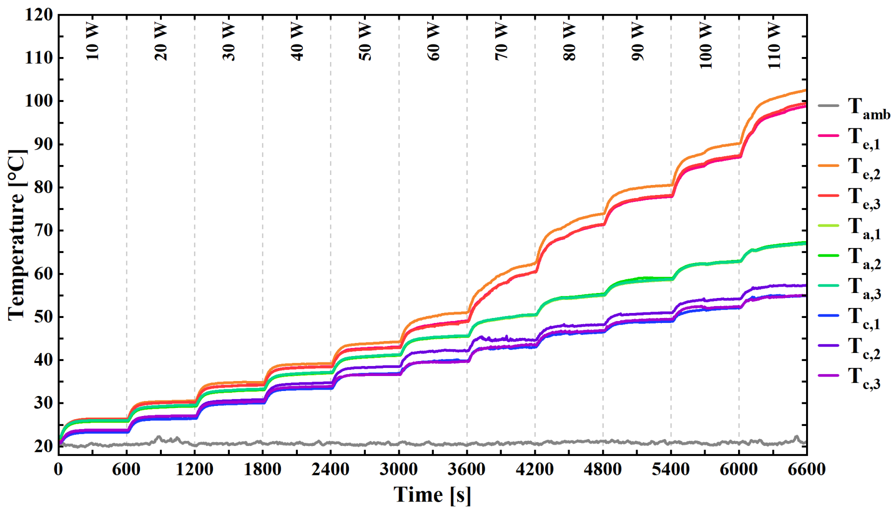

Figure 10. Transient of temperatures of the wire-plate PHP with a FR of 19 %.

3.4 Thermal Performance Comparison

In Figure 11, curves of the thermal resistance as a function of the heat load for the novel wire-plate PHP, the traditional PHP (square channels) and the HP with wire-plate grooves are compared for the horizontal position. The measurement uncertainties are shown in vertical bars over the data points. Curves for three devices transferring heat only by conduction (without working fluid) are also presented.

The HP with wire-plate grooves (light blue line) showed excellent thermal performance, presenting a smaller thermal resistance value of 0.15 ± 0.02 °C/W at 50 W (6.5 W/cm^2), which was extremely lower than the empty (only conduction) thermal resistance of 1.54 ± 0.34 °C/W (blue line). After that, the HP faced an onset of dry-out on the evaporator, which did not interfere with the tube's functioning, but slightly increased the thermal resistance up to 0.26 ± 0.02 °C/W at the maximum heat power, 130 W (16.9 W/cm^2).

The square channel PHP with FR 65% (light pink line) presented a thermal resistance at the same level as observed for the pure conduction resistance for the empty PHP (1.37 ± 0.41°C/W - pink line), up to 50 W (6.5 W/cm^2), when the PHP started up. The pulsating mode started at 60 W (7.8 W/cm^2), when the thermal resistance suddenly reduced with the power input increase, reaching a minimum value of 0.12 ± 0.01 °C/W at 170 W.

The novel wire-plate PHP with FR of 19% (light purple line) performed exactly as the wire-plate HP, considering the uncertainties, from 10 to 60 W. After that, the evaporator dry-out occurred, supporting a maximum heat load of 110 W (14.3 W/cm^2). The lowest thermal resistance achieved was 0.12 ± 0.04 °C/W at 50 W (6.5 W/cm^2).

The wired PHP with FR 67% (purple line) worked as a typical heat pipe with satisfactory thermal behavior up to 60 W (7.8 W/cm^2) with thermal resistances of about 0.5 °C/W, which represented a reduction of approximately 65% to the only conduction operation (1.46 ± 0.32 °C/W - dark blue line). Subsequently, the slug-plug flow (pulsating mode) took over as the dominant method of working fluid motion, decreasing the thermal resistance steadily up to 0.19 ± 0.02 °C/W at 160 W, the maximum dissipated power until the evaporator reached 100 °C. It corresponds to a thermal resistance reduction of 86 % compared to the empty wired PHP (1.46 ± 0.32 °C/W - dark blue line).

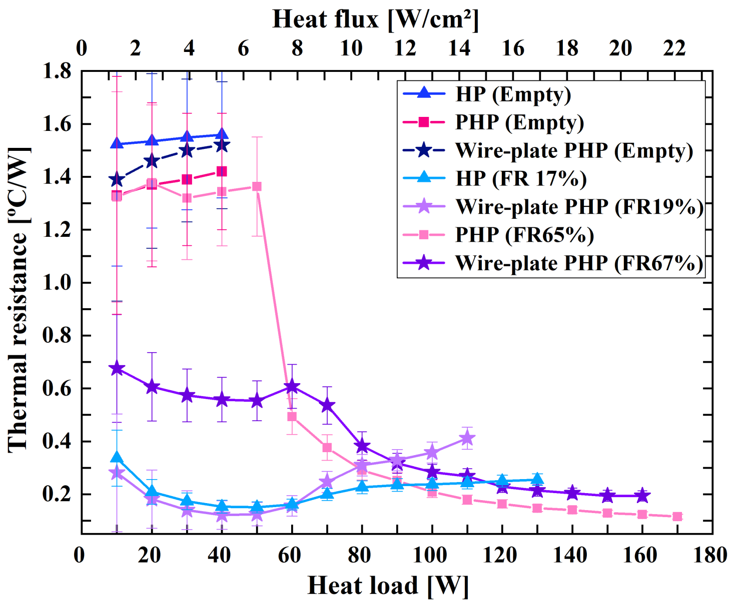

Figure 11. Thermal resistance comparison.

Table 2 presents the main thermal characteristics of the wired PHP compared to the grooved HP and conventional PHP, at the horizontal position, for a better understanding of the new channel impact on the thermal performance of the device, where q_{max} is the maximum power input carried out before the evaporator reaches an average temperature of 100 °C, R_{min} is, from all test conditions, the minimum thermal resistance reached, $q_{startup}$ represents the heat load in which that device began to operate effectively, $\overline{T}_{evap,startup}$ is the average evaporator temperature during the startup and $q_{dry\ out}$ is the power input where the onset of the evaporator dry-out is observed. In general, the HP with wire-plate grooves operates efficiently. The major issues regarding the conventional PHP are the high heat loads and the average evaporator temperatures required for the device to start.

The FR of 17% provided a typical HP performance to the wire-plate PHP, with low thermal resistances, even lower than the traditional HP, and the same heat load for the dry-out onset.

Table 2. Thermal performance comparison between wire-plate HP, conventional PHP and wire-plate PHP.

Characteristics	Wire-plate HP	Ordinary PHP	Wire-plate PHP	
			As HP (FR 17%)	As PHP (FR 67%)
q_{max} [W]	130	170	110	160
R_{min} [°C/W]	0.15	0.12	0.12	0.194
$q_{startup}$ [W]	10	60	10	10
$\overline{T}_{evap,\ startup}$ [°C]	27.0	116.7	26.3	30.1
$q_{dry\text{-}out\ onset}$ [W]	70	No dry-out	70	No dry-out

The wired PHP with a high FR of 67% could start from the first heat loads (10 W) with a low evaporator temperature, eliminating the main startup problem of the conventional PHP. Besides that, the device could maintain the operation in high heat loads with low thermal resistances, also improving the grooved HP performance.

To sum up, the new channel design for PHPs produced two different performances. Despite the low FR providing an interesting and similar behavior to an HP, the most highlighted improvements of the wire-plate channels were achieved in the PHP operation, i.e., with high FR. The groove's enhancements to the PHP are related to an early startup at low evaporator temperatures, even under low heat loads, at the horizontal position.

The main novelty of the present research is the use of a new channel profile in a pulsating heat pipe, never used before in the literature, which improves the heat transfer capacity during the startup, extending the thermal load range applications.

4. Conclusions

In this research, a novel pulsating heat pipe composed of wire-plate grooves was proposed and thermally tested. The pulsating heat pipe was manufactured by diffusion bonding of flat plates and internal solid wires, which were disposed of in a closed-loop fashion, forming a new channel geometry for pulsating heat pipes. Its thermal performance was characterized under two different operations, an HP and a PHP.

The proposed PHP channels with sharp corners improved the startup for low power inputs, in which they worked as capillary structures, keeping liquid along the channel. As a result, before working in the oscillating mode, this device can operate as a heat pipe starting from the first power inputs, which extends the heat load range.

The main novelty of the present research is the use of a new channel profile in a pulsating heat pipe, never used before in the literature, which improves the heat transfer capacity during the startup, extending the thermal load range applications and reducing the evaporator temperature required for the device startup.

5. Acknowledgements

Acknowledgments are provided to the National Council for Scientific and Technological Development (CNPq), National Fund for Scientific and Technological Development (FNDCT), and Ministry of Science, Technology, and Innovations (MCTI) for the project fundings 441678/2023-8, 405784/2022-8 and 406451/2021-4, and scholarship under grant number 381267/2023-7. The authors also acknowledge the Foundation for Research Support of Santa Catarina (FAPESC) for providing a scholarship under grant number 3003/2021.

References

[1] H. Yang, S. Khandekar, M. Groll, Performance characteristics of pulsating heat pipes as integral thermal spreaders, Int. J. Therm. Sci., 48 (2009) 815–824.

[2] S. Khandekar, M. Schneider, P. Schäfer, R. Kulenovic, Thermofluid Dynamic Study of Flat-plate Closed-loop Pulsating Heat Pipes, Microscale Thermophys. Eng., 6 (2002) 303–317.

[3] D. Zhang, Z. He, E. Jiang, C. Shen, J. Zhou, A review on start-up characteristics of the pulsating heat pipe, Heat Mass Transf. Und Stoffuebertragung, 57 (2021) 723–735.

[4] V. Ayel, M. Slobodeniuk, R. Bertossi, C. Romestant, Y. Bertin, Flat plate pulsating heat pipes: a review on the

thermohydraulic principles, thermal performances and open issues, Appl. Therm. Eng., 197 (2021).
[5] S. Khandekar, M. Schneider, P. Schäfer, R. Kulenovic, Thermofluid dynamic study of flat plate closed loop pulsating heat pipes, Microscale Thermophys. Eng., 6 (2003) 303–317.
[6] C. Hua, X. Wang, X. Gao, H. Zheng, X. Han, G. Chen, Experimental research on the start-up characteristics and heat transfer performance of pulsating heat pipes with rectangular channels, Appl. Therm. Eng., 126 (2017) 1058–1062.
[7] A. Facin, L. Betancur, M. Mantelli, J.P. Florez, B.H. Coutinho, Influence of channel geometry on diffusion bonded flat plate pulsating heat pipes, in: 19th Int. Heat Pipe Conf. 13th Int. Heat Pipe Symp., Pisa, Italy, 2018: pp. 4–5.
[8] J. Lee, S.J. Kim, Effect of channel geometry on the operating limit of micro pulsating heat pipes, Int. J. Heat Mass Transf., 107 (2017) 204–212.
[9] K. Mehta, N. Mehta, V. Patel, Influence of the channel profile on the thermal resistance of closed-loop flat-plate oscillating heat pipe, J. Brazilian Soc. Mech. Sci. Eng., 42 (2020) 1–12.
[10] V.P. Carey, Liquid-vapor phase-change phenomena : an introduction to the thermophysics of vaporization and condensation processes in heat transfer equipment, 2nd ed, Taylor & Francis, New York, 2008.
[11] S. Khandekar, P. Charoensawan, M. Groll, P. Terdtoon, Closed loop pulsating heat pipes - Part B: Visualization and semi-empirical modeling, Appl. Therm. Eng., 23 (2003) 2021–2033.
[12] W. Qu, Y. Zhou, Y. Li, T. Ma, Experimental study on mini pulsating heat pipes with square and regular triangle capillaries, in: 14th Int. Heat Pipe Conf., Florianopolis, Brazil, 2007.
[13] J. Wang, H. Ma, Q. Zhu, Y. Dong, K. Yue, Numerical and experimental investigation of pulsating heat pipes with corrugated configuration, Appl. Therm. Eng., 102 (2016) 158–166.
[14] C. Qingjun, C. Chung-Lung, J.F. Asfia, Heat transfer enhancement of planar pulsating heat pipe device, in: Proc. 2006 ASME Int. Mech. Eng. Congr. Expo. IMECE2006 - Heat Transf., American Society of Mechanical Engineers (ASME), Chicago, IL, United States, Illinois, USA, 2006: pp. 153–158.
[15] J. Qu, X. Li, Q. Xu, Q. Wang, Thermal performance comparison of oscillating heat pipes with and without helical micro-grooves, Heat Mass Transf. Und Stoffuebertragung, 53 (2017) 3383–3390.
[16] W. Kim, S.J. Kim, Effect of reentrant cavities on the thermal performance of a pulsating heat pipe, Appl. Therm. Eng., 133 (2018) 61–69.
[17] L. Krambeck, K.G. Domiciano, L.A. Betancur-arboleda, M.B.H. Mantelli, Novel flat plate pulsating heat pipe with ultra sharp grooves, Appl. Therm. Eng., 211 (2022).
[18] K. V. Paiva, M.B.H. Mantelli, Wire-plate and sintered hybrid heat pipes: Model and experiments, Int. J. Therm. Sci., 93 (2015) 36–51.
[19] L.A. Betancur-Arboleda, Flat Plate Pulsating Heat Pipes: New Fabrication Technologies, Experiments and Modeling, Universidade Federal de Santa Catarina, 2020.
[20] L. Krambeck, K.G. Domiciano, M.B.H. Mantelli, A new flat electronics cooling device composed of internal parallel loop heat pipes, Exp. Comput. Multiph. Flow, 1 (2024) 1–10.
[21] L. Krambeck, Flat mini heat pipe technologies for the thermal management of electronics, Federal University of Santa Catarina, 2024.
[22] J.P. Holman, Experimental methods for engineers, 8th ed., New York, USA, 2011.
[23] L. Krambeck, K.G. Domiciano, M. Mameli, S. Filippeschi, M.B.H. Mantelli, Comparison of the thermal performance of a wire-plate and a pulsating heat pipe, in: Proc. 41st UIT Int. Heat Transf. Conf., Napoli, Italy, 2024.

Paper ID 084(S3)

Electric Vehicle Battery Cooling via Loop Heat Pipes coupled with Underbody Aerodynamics

Marco Bernagozzi[1*], Marco Marengo[2], and Anastasios Georgoulas[1]

[1] *School of Architecture, Technology and Engineering, University of Brighton, Brighton, United Kingdom*
[2] *Department of Civil Engineering and Architecture, University of Pavia, Pavia, Italy*
**Corresponding author email address: m.bernagozzi3@brighton.ac.uk*

Abstract

This paper presents a feasibility study on a fully passive cooling system for electric vehicles using Loop Heat Pipes (LHP) to transfer the batteries excess heat to the underbody of the vehicle. Multiple LHPs are in contact with a battery module, on the evaporator side, while their condensers are embedded in the underbody of the vehicle, cooled via aerodynamic cooling. The study is conducted numerically, by means of a previously validated transient 1-D Lumped Parameter Model (LPM) able to simulate the thermos-fluidic behavior of the LHP, and aerodynamic CFD simulations coupled with heat transfer. The CFD results provide the convection heat transfer coefficient at the condenser wall, which is inputted into the 1-D LPM to design the condenser in order to achieve successful operation of the cooling system, and to evaluate the temperature evolution of the cells. The performance of the proposed cooling system was evaluated over 1C, 2C, 3C charging cycles followed by a 30 minutes 1C driving section. The proposed cooling system was able to contain the cell temperature inside the acceptable limits, even at challenging conditions such as 3C charging, with maximum temperature being 51.6 °C for 3C, 39.3 °C for 2C and 27.5 °C for 1C. All without using any additional energy.

Keywords: Loop Heat Pipe; Electric Vehicle; Aerodynamic Cooling.

1. Introduction

Growing demand for cleaner air and sustainable future, together with a global effort to reduce GreenHouse Gas (GHG) emissions, have pushed the development and adoption of Electric Vehicles (EVs) as the selected choice for passenger transport. EVs numbers are in constant growth, albeit far from the ambitious targets set by several governments worldwide [1]. Reasons are to be found in perceived lack of range, lack of infrastructure, high cost and charging times, amongst others [2].

In order to improve on this limited numbers situation, appropriate thermal management can help tackling problems such as slow charging, lack of range and high cost, as temperature play a critical role on the operation of the batteries. In fact, Li-Ion batteries (the go-to choice for EVs nowadays) desire to be in the narrow range of 25 °C – 40 °C, even if up to 50°C is considered acceptable [3], and to be outside of this range would lead to a reduction in power output and operational life, as well as safety risks, e.g. thermal runaway[4]. In fact, a safety threshold has been set at 60 °C, to avoid the onset of disruptive failure scenarios.

Currently, the most common Battery Thermal Management Systems (BTMS) utilise air or liquid convection. Air convection is preferred when cost and weight are to be minimized, at the expense of performance (e.g. Nissan Leaf, Renault Zoe). This BTMS is simple and cheap but inefficient due to the poor thermal properties of air, and as such it does not allow fast charging. Moreover, it consumes high parasitic power due to the frequent presence of fans [5]. Liquid BTMS, on the other hand, is very efficient and allows for fast charging. It often uses a cold plate at the bottom of the battery pack, or meandering pipes (Tesla), where liquid is moved by a pump [6]. This solution, albeit efficient, is expensive, complex and costly in terms of money and parasitic power.

Research have suggested the use of passive cooling methods, in the forms of PCM, heat pipes and immersion cooling, all with their relative pros and cons. The Authors proposed an innovative BTMS using Loop Heat Pipes and graphite sheets [7], which proved to be successful and allowing better performance than an analogue BTMS relying on active cold plate. In fact, the LHP BTMS was able to reduce the maximum temperature of the cells, compared to the active cold plate BTMS, by 3.6 °C during 10-minutes fast charge at 4C. The LHPs were placed at the bottom of the battery module, acting as thermal vectors between the pack and the HVAC chiller already included in the vehicle, hence reducing the required complexity of the system. More importantly, heat was transferred without the need of parasitic power for the pump. In this scenario, the condenser of the LHP was foreseen to be embedded in the heat exchanger of the HVAC system of the car, hence actively cooled.

In the present work, the Authors propose a variation on the previously developed and tested LHP BTMS, where the condenser is placed on the underbody of the vehicle (as illustrated in Figure 1), cooled by the external ambient air, thus further reducing the parasitic power needed. In this way, aerodynamic cooling of the battery cells is achieved without reducing the aerodynamic performances by increasing the drag (by creating any openings on the exterior of the car).

Figure 1. Idea of the proposed BTMS, where the condenser of the LHP is cooled by aerodynamic forced convection (image modified from ImageFX).

The feasibility of this design is studied numerically, with an experimentally validated 1-D Lumped Parameter Model (LPM) developed by the Authors [8]. This 1-D code is used to calculate the battery cells and LHP evaporator and condenser temperature trends in response to different usage conditions of the batteries (i.e., different driving speeds). In turn, via CFD simulations of the entire vehicle in OpenFOAM CFD Toolbox, a precise estimation of the air temperatures in the vicinity of the vehicle underbody is conducted, leading to the appropriate valued of Heat Transfer Coefficient (HTC) to feed back to the 1-D LPM for the design and evaluation of the condenser feasibility, as well as the prediction of the cells temperature at different charging cycles.

2. Method

The present work utilities two numerical simulations on open-source software coupled together. Firstly, CFD simulations running on OpenFOAM are employed to calculate the heat transfer coefficient (HTC) at the boundary region of the underbody of the car, where the LHP condenser is placed and is rejecting heat to the environment. Secondly, these HTC values are fed back to the 1-D LPM running on Octave, which simulates the excess heat from the cell absorbed by the LHPs, returning the temperature trends of the battery cells. With this method, it is possible to evaluate the effect of different airstream velocities on the thermal performance of the cooling system and design an adequate condenser for different conditions.

2.1. Lumped Parameter Model

In this model, graphite sheets are sandwiched between the battery cells, to improve the heat transfer in the vertical direction, and isolating the cells from one another, ultimately delaying the spreading of an adverse thermal event (e.g., thermal runaway), as shown in Figure 2. The LHP is a flat LHP made out of copper, more details on its geometry can be found on [7]. The working fluid used for the LHP in this case is ethanol.

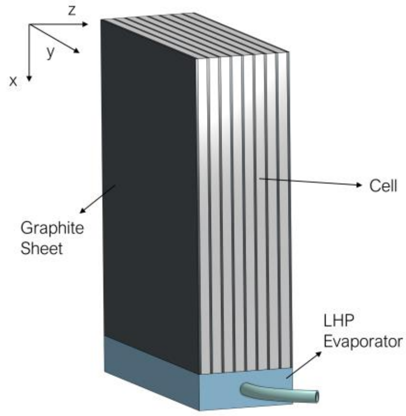

Figure 2. Schematic of the LHP-BTMS with graphite sheets [8].

The proposed Battery Thermal Management Systems uses series of LHPs at the bottom of battery modules. Previous research from the Authors [8] have suggested that a number of LHP evaporators from 2 to 6 can suffice to meet industry requirements, albeit to different standard commiserated with the increased annexed weight. In order to model the thermal behavior of the cell and battery assembly, the thermal network depicted in Figure 3 is used.

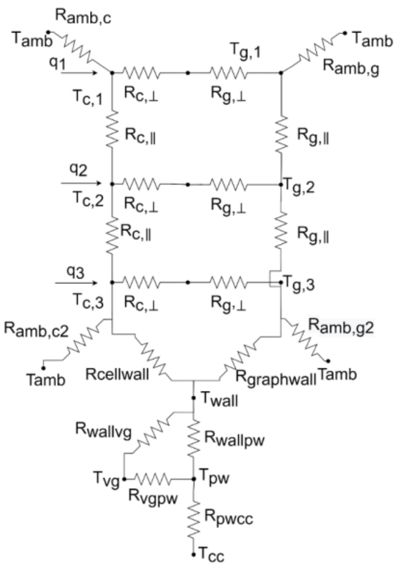

Figure 3. Thermal network used to model the cell, graphite and evaporator assembly.

In this work, the thermal network proposed in Figure 3 is not altered, and its equations and assumptions can be found in previous works of the Authors [8]. Instead, from the previous version of this code, the condenser model was changed to accommodate air convection thermal resistance R_{free}, as shown below:

$$T_{cond,i} = f_{sat}\left(P_{cond,i}\right) \quad (1)$$

$$\dot{Q}_{cond,i} = \frac{T_{air} - T_{cond,i}}{R_{air} + R_P + R_{cond}} = \dot{m}(h_{i+1} - h_i) \quad (2)$$

$$h_{i+1} = \frac{\dot{Q}_{cond,i}}{\dot{m}} + h_i \quad (3)$$

$$h_{v,l} = f_{sat}(T_{cond,i}) \quad (4)$$

$$x_{i+1} = f_{sat}(h_{i+1}) = \frac{h_{i+1} - h_l}{h_v - h_l} \quad (5)$$

Eq (1) calculates the internal two-phase fluid temperature, from the assumption of saturated fluid. Eq. (2) calculates the heat lost from the fluid to the air at the i-th node of the condenser, considering three resistances connected in series, i.e., external air convection (heat transfer coefficient h_{air} calculated via CFD simulations), conduction through the pipe and two-phase convection inside the pipe (heat transfer coefficient h_{2p} calculated thanks to Shah correlation).

R_{air}	R_{cond}	R_p
$\frac{1}{h_{air}A_{free}}$	$\frac{1}{h_{2p}A_{cond}}$	$\frac{ln\left(\frac{r_{cond,e}}{r_{cond,i}}\right)}{2\pi k_c L_x}$

Eq (3) calculates the variation in enthalpy due to the loss of power, which then, thanks to the estimation of the vapour enthalpy (eq. 4) from saturation tables, allows to calculate the vapour quality variation (eq 5). Hence, with this algorithm the length of condenser pipe is calculated and checked that it is sufficient to dissipate the amount of heat absorbed at the evaporator, by fully condensing the vapour. A non-complete condensation phenomenon, in the long run, will offset the evaporator-condensation fluid charge balance of the LHP device and eventually lead to dry-out.

This model has been validated for different geometries (cylindrical and flat evaporator) and for different working fluids (water, ethanol, acetone and Novec649) [8].

2.2. CFD Model

For the CFD simulations the open source CFD Toolbox OpenFOAM v. 8.0 was utilised to compute the aerodynamics and the resulting heat transfer distribution in the underbody of the car so that an accurate estimation of the local HTCs could be obtained. In more detail, the buoyantSimpleFoam solver was employed for this purpose.

The mass, momentum, and energy conservation equations govern the fluid movement and interactions. In the considered steady-state turbulent flows, the first two equations, respectively, can be written as follows:

$$\nabla \cdot (\rho u) = 0 \quad (6)$$

$$\frac{\partial(\rho u)}{\partial t} + \nabla \cdot (\rho u u) = -\nabla p + \rho g + \nabla \cdot \left(2\mu_{eff} D(u)\right) - \nabla\left(\frac{2}{3}\mu_{eff}(\nabla \cdot u)\right) \quad (7)$$

Where $\boldsymbol{u}$ is the velocity field, ρ is the density, p is the static pressure, and $\boldsymbol{g}$ is the gravitational acceleration. The effective viscosity μ_{eff} is the sum of turbulent μ_t and dynamic viscosity μ, and $D(\boldsymbol{u})$ is the rate of deformation tensor, defined as:

$$D(u) = \frac{1}{2}(\nabla u + (\nabla u)^T) \quad (8)$$

OpenFOAM determines the pressure gradient and gravity force terms in Equation (7) utilising equation (9) below:

$$-\nabla p + \rho g = -\nabla\left(p_{rgh} + \rho g \cdot r\right) + \rho g = -\nabla p_{rgh} - (g \cdot r)\nabla\rho - \rho g + \rho g = -\nabla p_{rgh} - (g \cdot r)\nabla\rho \quad (9)$$

where p_{rgh} is the hydrostatic pressure, $p_{rgh} = p - \rho \boldsymbol{g} \cdot \boldsymbol{r}$, and $\boldsymbol{r}$ is the position vector.

Simulation of heat transfer is performed by solving the energy equation and particularly utilising the sensible enthalpy model of the proposed solver, which solves the following equation (10):

$$\nabla \cdot (\rho u h) + \frac{\partial(\rho K)}{\partial t} + \nabla \cdot (\rho u K) - \frac{dp}{dt} = \nabla \cdot \left(2a_{eff}\nabla h\right) + \rho u \cdot g \quad (10)$$

The enthalpy per unit mass h is the sum of energy per unit mass e and kinematic pressure, $h = e + p/\rho$. $K \equiv |\boldsymbol{u}|^2/2$ is the kinetic energy per unit mass, and α_{eff}/ρ is the effective thermal diffusivity. For turbulence the standard K-ε model is employed.

3. Results

3.1. CFD Results for HTC estimation

3D symmetric Reynolds Averaged Navier Stokes (RANS) simulations were performed for the purposes of the present investigation. The computational domain and applied boundary conditions are depicted as well as some details of the Computational Mesh are shown in Figure 4.

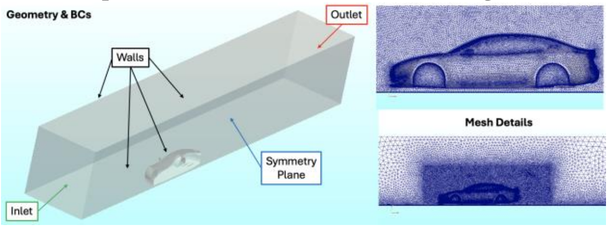

Figure 4. Computational domain, applied boundary conditions and computational mesh details.

As it can be seen from Figure 4, a hybrid, unstructured computational mesh was utilised, consisting of a combination of 8,096,459 tetrahedral and 984,614 prismatic cells. Two types of wall boundaries are employed in the underbody section: a heated wall with a constant temperature condition, which corresponds to a dedicated condenser area for the LHPs; and an adiabatic wall, which corresponds to the remaining outer surface of the considered vehicle underbody. A ~1 m^2 wide surface representing the area occupied by the LHP condenser was superimposed at the underbody of the vehicle and fixed at 40 °C, representing a worse case scenario.

Figure 5 shows the spatial distribution of pressure, velocity and temperature in the vicinity of the vehicle for a speed of 7 m/s (~ 25 km/h). it is evident how the temperature increases towards the end of the area occupied by the condenser, due to the heat received Moreover, top left part of Figure 5 illustrates the sampling plane and line (both located 1 cm below the underbody surface) together with the computed temperature distribution. It is evident how the air temperature increases towards the end of the area occupied by the condenser, due to the heat received by the hot surface. From the top right image of Figure 5 it is evident however how thin is the thermal boundary layer developed by placing the condenser at the underbody.

The horizontal plane positioned 1 cm below the underbody surface helps to visualise the temperature distribution and a sampling line running along the same plane and corresponding to the middle longitudinal axis of the condenser area is used to estimate the local HTCs. The resulting HTCs along the proposed sampling line for the different simulated vehicle speeds, with a total heat emitted from the battery pack of 480 W, are plotted in Figure 6.

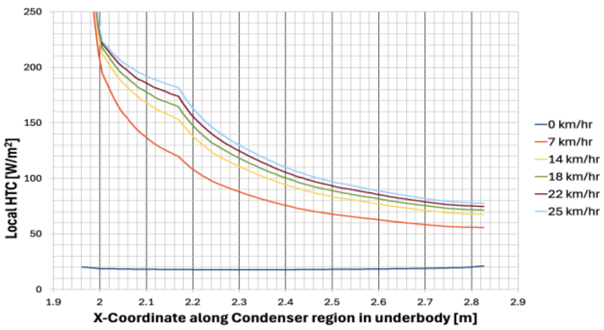

Figure 6. CFD predicted local HTC values versus vehicle moving speed, along the LHP condenser region in the considered vehicle underbody.

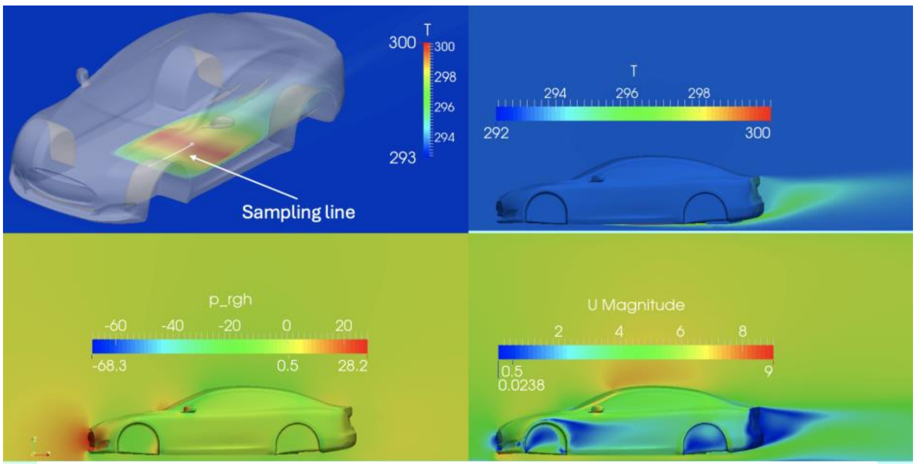

Figure 5. Temperature, pressure and velocity distribution in the vicinity of considered vehicle and sampling line locations for local HTC estimation.

3.2. LPM Results on Cell Temperature

Thanks to the CFD results, now different HTC values are available to be fed back to the LPM code, in order to evaluate the performance of the proposed BTMS, using LHPs, graphite sheets and aerodynamic forced convection at the LHP condenser.

In order to replicate scenarios representative of a real situation, it was chosen to simulate a charging break undertaken by the vehicle, followed by a 30-minute period of driving at 25 km/h (7 m/s). The C-Rate selected were 1C, 2C and 3C, with the last one representing the state of the art in terms of fast charging. The C-Rate is a measure of the rate at which a battery is discharged or charged, relative to its maximum capacity; in fact, it is defined as the discharging/charging current divided by the battery capacity, e.g., 1C means full charge in one hour, 0.5C full charge in 2 hours and so on. Charging the batteries from 20% to 80% capacity at these currents would take 36, 18 and 12 minutes, respectively.

Figure 7 shows the trends of the heating power emitted by a single cell during these three scenarios. The time average values for these cycles are 3 W for 1C, 12 W for 2C and 27 W for 3C. The assumed pack architecture is composed by 8 modules made by 12 cells each, hence the heating powers released by the pack in the three cases are 288 W for 1C, 1152 W for 2C and 2592 W for 3C. It is evident how there is significant difference between different usages, which makes the design of these systems quite challenging.

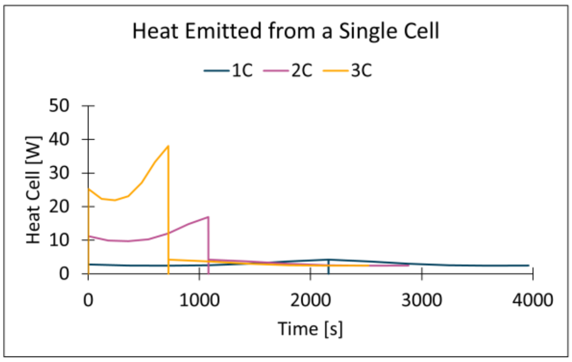

Figure 7. Plot showing the different trends of heat release by a single cell during the different cycles.

A notable aspect of these cycles is that they extend beyond the charging phase, which is often the sole focus in the literature. Instead, they encompass the post-charging period, evaluating the BTMS ability to maintain cells temperatures within acceptable parameters.

Using the temperature values resulting from the CFD simulations, it is possible to estimate the HTC at different velocities. In this case it is of interest to look at the values for 0 and 7 m/s. Because in the CFD model it was assume a worst-case scenario of constant condenser temperature of 40 °C, by changing the heat released at the underbody one can calculate the HTC related to the different charging phases, as shown in Table 1.

Table 1. HTC (in W/m^{2}K) at different charging phases and different speeds (in m/s) calculated from the temperature variations obtained by the CFD simulations.

Speed (m/s)	1C	2C	3C
0	11	44	99
2	59	237	534
4	71	285	641
5	75	300	675
6	78	313	703
7	81	323	727

As previously mentioned, in this paper only the velocity of 0 m/s (charging phase, stationary vehicle) and 7 m/s (urban driving vehicle) are considered. Higher velocities will be considered in future stages of this work.

After several iterations, a solution was found that would ensure full condensation of the working fluid inside the LHP condenser. As a result, suitable geometrical parameters were selected, presented in Table 2.

Table 2. Selected geometrical parameters for LHP condenser design.

#LHP	4	
L cond	2.5	m
ID/OD	6/6.5	mm

Furthermore, simulations results indicated that 4 LHPs (Figure 8) applied to the battery module provide superior performance compared to 2 LHPs, as proved by the results of the average cell temperature shown in Figure 9, where for 2 LHPs the safety threshold of 60 °C is exceeded.

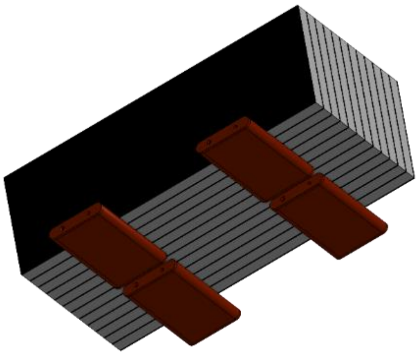

Figure 8. 12-cell module cooled down by 4 LHP evaporators. Piping coming in and out of the evaporator were omitted from the image for clarity.

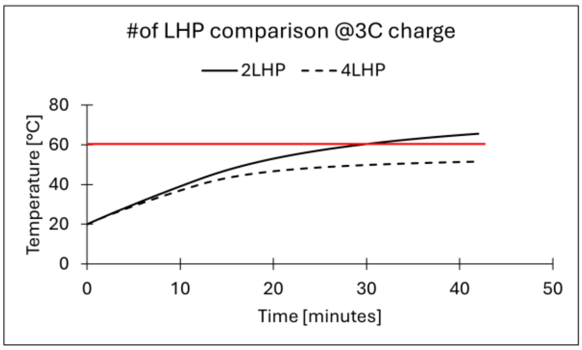

Figure 9. Comparison of the module cells average temperature during 3C charge followed by 1C cooldown when cooled by 2 or 4 LHPs.

LHP Temperature Results

Looking firstly at the LHP results presented in Figure 10, one can notice that indeed the condenser achieves full condensation, as the yellow line which represents the outlet temperature of the condenser, is in equilibrium with the ambient temperature in the 2C and 3C case (20 °C). In the 1C case, this happens only after the end of the charging phase, with the increased HTC given by the movement of the car. However, the condenser is properly sized as the final vapour quality if 0.07.

From Figure 10 however it is clear that despite the lower heating power of the 1C phase, the cell temperature keeps on increasing, without temperature drop. This does not pose a serious issue due to the timeframe of the phenomenon. However if several of these fast-charging followed by 1C driving cycles are happening one after the other in rapid succession, results indicate that the temperature would reach unwanted values. This suggests that the design following this feasibility study could be improved and optimized.

Cells Temperature Results

The cells temperature results shows that the proposed passive BTMS idea is feasible, as the temperature values are satisfactory. In more detail, the comparison graphs of Figure 11, demonstrates that the cell temperatures never reach the safety threshold of 60 °C, even after 3C fast charging (12 minutes). In fact, after the 3C fast charge and cooldown cycle, the maximum average cell temperature of the module is 51.6 °C, which is slightly above the acceptable threshold. However, it is important to point out that 3C fast charge is the state of the art, represented by the Porsche Taycan, which offers fast charge in 19 minutes; thus, this scenario would represent an improvement to the current EV charging situation.

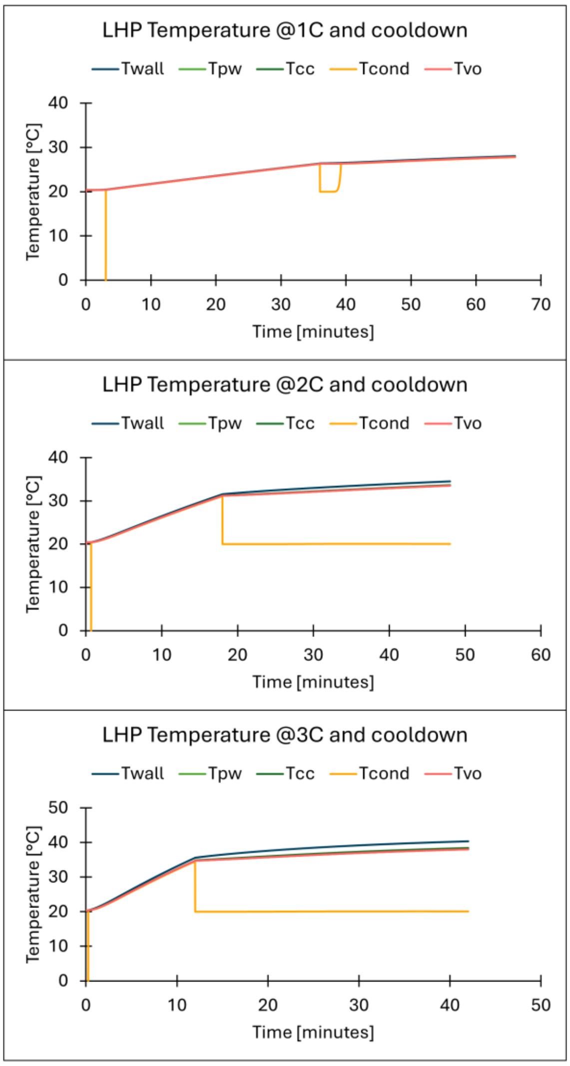

Figure 10. LHP nodes temperatures trends for 1C, 2C and 3C, showing full condensation at the condenser. Twall, Tpw, Tcc, Tcond and Tvo are the temperature of the wall, primary wick,

compensation chamber, condenser outlet and evaporator outlet, respectively.

Analyzing the 2C results, which correspond to an 18-minute fast charging scenario, reveals that cell temperatures consistently remain below the optimal threshold of 40°C, with a peak temperature of 39.3°C. This performance suggests the BTMS is well-suited for vehicle applications where charging times under 10 minutes are not essential (standard city cars, delivery vehicles, taxis).

Finally, for 1C, the maximum temperature reached by the cells was 27.5 °C, suggesting that a cooling system may be unnecessary under these conditions.

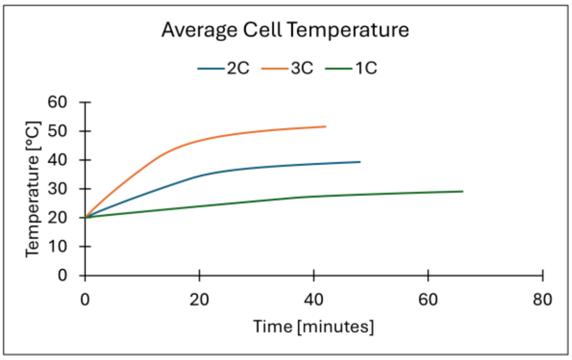

Figure 11. Average cell module temperature evolution at different fast charge cycles and cooldowns.

4. Conclusions

This work presents a feasibility study of a fully passive Battery Thermal Management System (BTMS) for Electric Vehicles (EV), utilizing Loop Heat Pipes (LHP) as a thermal vector, connecting the bottom of the battery pack with the underbody of the vehicle. In this way, aerodynamic cooling can be applied to the battery cells without spoiling the aerodynamic performance by introducing additional drag.

A two-tier open-source simulation procedure has been employed: firstly, utilizing CFD simulations on OpenFOAM to calculate the Heat Transfer Coefficient (HTC) at the underbody, due to the forced air convection created by the moving vehicle; secondly, an in-house generated and validated 1-D Lumper Parameter Model (LPM) predicted the thermal behavior of the cell and LHP assembly and helped to calculate the cell temperature evolution. Particular care was taken in ensuring that the condenser geometry would be suitable to achieve full condensation, at given HTCs.

The performance of this fully passive BTMS was evaluated over 1C, 2C, 3C charging cycles followed by a 30 minutes 1C driving section. The results can be summarized as follows:

- 2 LHPs are not able to maintain a 12-cell module under the 60 °C safety threshold, while with 4 LHPs the temperature requirements are met.
- The condenser was properly sized to achieve full condensation at the three charging cases.
- The proposed BTMS was able to contain the cell temperature inside the acceptable limits, even at challenging conditions such as 3C charging, with maximum temperature being 51.6 °C for 3C, 39.3 °C for 2C and 27.5 °C for 1C.

This work proved that this fully passive BTMS using LHPs and aerodynamic cooling is feasible and able to contain the battery cell temperatures in acceptable ranges.

5. Future Work

The next steps of this investigation revolve around expanding the simulated dataset, by including:

i) different driving cycles and C-rates;
ii) different working fluids;
iii) different LHP configurations;
iv) higher speeds and different ambient temperatures.

Following, the Authors will investigate the benefit of tailoring the LHP condenser design to the available HTCs, exploiting the fact that is higher towards the front of the vehicle.

The ultimate goal of this project would be to have coupled conjugated heat transfer simulations of a scenario where the LHP is physically embedded in the vehicle underbody and two-phase convection, conduction through solid and forced convection heat transfer mechanisms are all considered. With this in mind, the LPM model describing the cell-LHP thermal behaviour will be inserted into the OpenFOAM solver code to directly solve transient problems.

6. ACKNOWLEDGEMENTS

The Authors would like to thank the School of Architecture, Technology and Engineering at the University of Brighton for the financial support to attend this conference.

References

[1] International Energy Agency (IEA), Global EV Outlook 2020. , Paris, 2020.

[2] L. Noel, G. Zarazua de Rubens, B.K. Sovacool, and J. Kester, “Fear and loathing of electric vehicles: The reactionary rhetoric of range anxiety.,” Energy Research and Social Science. vol. 48, no. April 2018, pp. 96–107, 2019.

[3] P. Qin, M. Liao, D. Zhang, Y. Liu, J. Sun, and Q. Wang, “Experimental and numerical study on a novel hybrid battery thermal management system integrated forced-air convection and phase change material.,” Energy Conversion and Management. vol. 195, no. March, pp. 1371–1381, 2019.

[4] Q. Wang, P. Ping, X. Zhao, G. Chu, J. Sun, and C. Chen, “Thermal runaway caused fire and explosion of lithium ion battery.,” Journal of Power Sources. vol. 208, pp. 210–224, 2012.

[5] G. Zhao, X. Wang, M. Negnevitsky, and H. Zhang, “A review of air-cooling battery thermal management systems for electric and hybrid electric vehicles.,” Journal of Power Sources. vol. 501, no. April, p. 230001, 2021.

[6] A. Maiorino, C. Cilenti, F. Petruzziello, and C. Aprea, “A review on thermal management of battery packs for electric vehicles.,” Applied Thermal Engineering. vol. 238, p. 122035, 2024.

[7] M. Bernagozzi, A. Georgoulas, N. Miché, C. Rouaud, and M. Marengo, “Novel battery thermal management system for electric vehicles with a loop heat pipe and graphite sheet inserts.,” Applied Thermal Engineering. vol. 194, no. May, p. 2021.

[8] M. Bernagozzi, “Development and Characterisation of an Innovative Battery Thermal Management System for Electric Vehicles with Loop Heat Pipes and Graphite Sheets,” (2022).

Paper ID 085(S2B)

Modeling Ultra-Thin Flat Loop Heat Pipes using a 1-D Lumped Parameter Approach

Marco Bernagozzi[1*], Kelvin Guessi Domiciano[2], Larissa Krambeck[2], Marcia B. H. Mantelli[2], and Marco Marengo[3]

[1] *School of Architecture, Technology and Engineering, University of Brighton, Brighton, UK*
[2] *Heat Pipe Laboratory, Federal University of Santa Catarina, Florianopolis, Brazil*
[3] *University of Pavia, Pavia, Italy*
* *M.Bernagozzi3@brighton.ac.uk*

Abstract

In the present study, the transient behavior of a diffusion-bonded ultra-thin LHP, specifically designed for the thermal management of smartphones, is predicted by means of a 1-D Lumped Parameter Model (LPM). The LPM approach was previously validated for larger LHPs with different working fluids and is one of the few highly reliable transient models available in literature. The main novelty of this work is the extension of the application range of the LPM model to ultra-thin LHPs, where various parameters may affect the operation of these devices, such as heat leakage by conduction through the case material. The proposed LPM consists of a thermal network describing the thermo-fluidic behavior of the evaporator, connected to a series of mass, momentum, and energy conservation, solved iteratively to predict the device temperatures, heat transfer rates, and thermal resistances. The LPM model successfully predicted the transient temperature of the LHP with the highest and lowest average difference of 0.99 °C and 1.65 °C, respectively. Also, this approach estimated the steady-state thermal resistance with an average discrepancy of 28%. Therefore, the LPM showed to be a powerful design tool to predict and simulate the operation conditions of heat pipes, from ultra-thin to larger ones.

Keywords: Flat Loop Heat Pipe; Lumped Parameter Model; Transient Modelling; Diffusion Bonding; Thermal performance.

1. Introduction

Lightweight, compactness and high performance are the requirements for thermal management of electronic gadgets. Flat Loop Heat Pipes (LHPs) are suitable passive cooling solutions as they can separate the evaporator from the condenser section, optimizing the integration to the electronic devices. Moreover, the LHPs can be miniaturized, reducing the final thickness of electronics [1].

Investigation on novel manufacturing method for LHP have been object of interesting research over the last few years, and amongst those diffusion bonding has been proven to be an extremely effective manufacturing technique for producing flat heat pipes [2, 3]. Domiciano et al. [3] developed a diffusion-bonded ultra-thin LHP for small electronic gadgets, like smartphones and tablets, which validated the fabricating method and resulted in a device with excellent thermal performance under natural convection as a heat sink.

Despite the recent technical progress in heat pipe manufacturing, their adoption from industry is still limited, mainly due to the uncertainty on predicting their behaviour and the lack of a design tool. This is where numerical simulations methods offering accurate results in short computational time become greatly appealing. Prime example of this is the Lumped Parameter Modelling, where continuous complex geometries are broken down and assigned into discrete components, called nodes.

Applying this approach to a LHP means dividing it into discrete components like the evaporator, condenser, vapor, and liquid lines. The governing equations based on mass, momentum, and energy conservation are solved iteratively to predict key performance parameters like operating temperatures, heat transfer rates, and thermal resistances.

In the present work, a previously validated 1-D Lumped Parameter Model (LPM) for thermodynamic simulation of large-scale LHPs is used to predict the thermal performance of an ultra-thin flat LHP, designed for electronics cooling applications, especially smartphones. As the compactness of these two-phase devices affects the heat conduction by the wick structure and case material, this heat leakage became crucial for modeling ultra-thin LHPs. The proposed model is used to replicate the experimental results reported by Domiciano et al. [3]. Therefore, the main aim of this research is to understand if the envelope of this LPM can be pushed to successfully simulate and predict the thermal performance of ultra-thin LHPs.

2. Studied LHP

The studied LHP was manufactured by diffusion bonding of three copper sheets. The total thickness of this device is 1.56 mm, given by two external sheets of 0.3 mm and one internal structure 1.0 mm thick. The flat LHP container was divided into four sections, as shown in Figure 1, which are the evaporator, vapor line, condenser, and vapor line. Due to the compactness requirements of the proposed device, the compensation chamber was suppressed.

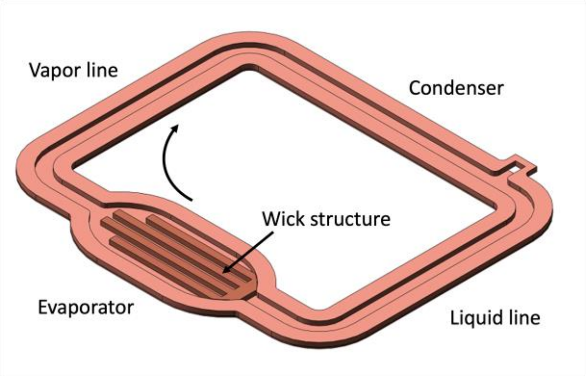

Figure 1. Design of the ultra-thin LHP.

The evaporator contains a wick structure made by the sintering process of a copper powder. Its geometry improves the evaporation of the working fluid and guarantees a single direction of the loop, given by a vapor barrier on the liquid line side. The main properties of the sintered copper powder is shown in Table 1.

The diffusion bonding consisted of submitting the pilled copper sheets, with the sintered powder wick, into a pressure system made by screws and a matrix, followed by a thermal process in a furnace (Jung® LT1513) at 875 °C for one hour. An atmosphere of argon (95%) and hydrogen (5%) inside the furnace reduced corrosion effects. More details about the applied diffusion bonding procedure can be found in Domiciano et al. [3]. The sintering powder process was the same as the diffusion bonding, without the pressure application. In the end, a capillary tube was brazed to the container, and a leakage test was performed.

Ethanol was selected as the working fluid with the filling ratio (FR) that provided the best thermal performance, which corresponds to an FR of 30 %, according to previous tests [3]. FR is defined as the total volume of working fluid divided by the total internal void volume. Table 1 presents the main features of the resulting LHP.

Table 1. Main characteristics of developed LHP.

Component	Characteristic
Total dimensions [mm^3]	76 x 60 x 1.56
Evaporator area [mm^2]	37.5 x 20
Evaporator active area [mm^2]	10 x 10
Evaporator wick area [mm^2]	29 x 1.5
Vapor grooves area [mm^2]	23.5 x 1.3
Vapor line channel area [mm^2]	79.17 x 3
Liquid line channel area [mm^2]	79.17 x 3
Condenser area [mm^2]	46 x 3
Working fluid	Ethanol
Filling ratio [%]	30
Volume [ml]	0.26
Particle average diameter [μm]	49.72 [4]
Porosity [%]	53.46 ± 3.87 [4]
Permeability [10^{-12} m^2]	1.99 ± 1.02 [5]
Effective porous radius [μm]	21.04 ± 2.2 [6]

For the experimental test, a workbench, schematized in Figure 2, mimicked the power input of a typical electronic chip, using a cartridge electrical resistor. The resistor was embedded in a copper block (1 cm^2 of contact area) and attached to the outer surface of the evaporator, supplied by a power energy system (TDK-Lambda® GEN300-5). The contact resistance was reduced by thermal grease. Natural convection removed the excess heat in the condenser section, in which the environment was kept at 24 ± 1 °C. Also, the evaporator was insulated with PTFE polymer (Polytetrafluoroethylene), minimizing the heat loss to the environment.

A data acquisition system (DAQ-NI® SCXI-1000), a laptop (Dell®), and T-type thermocouples (Omega Engineering®) acquired temperature measurements. Six thermocouples were fixed at the external surface, according to the positions presented in Figure 2, using thermosensitive adhesive strip Kapton®. Also, the environment temperature was measured during the test.

The LHP was tested in gravity-assisted orientation, meaning the evaporator was below the condenser. Heat loads were applied from 0.5 to 8 W for 1200 seconds each, guaranteeing steady-state conditions (temperature variation lower than 0.1 °C/min). Data was acquired every one second.

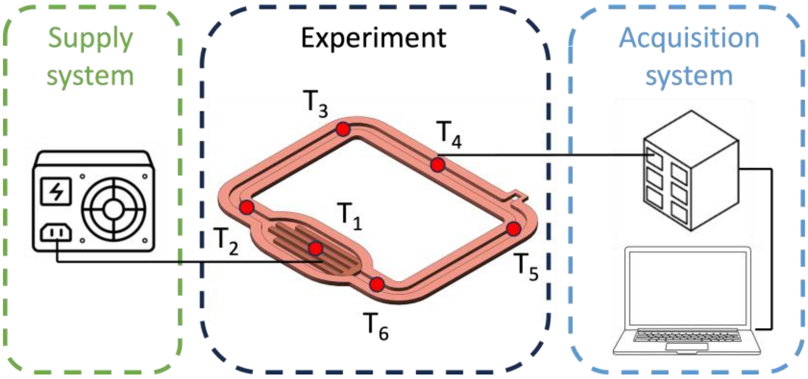

Figure 2. Experimental apparatus.

The LHP thermal performance was evaluated by the overall thermal resistance, R_{exp}, estimated by:

$$R_{\exp} = \frac{T_1 - T_4}{q} \tag{1}$$

where T_1 is the evaporator temperature, T_4 is the temperature measurement in the middle of the condenser, and q is the heat load, given by the current times the voltage.

A calibration procedure was performed in the entire experimental workbench to reduce the errors related to the temperature measurements. The overall thermal resistance uncertainty, δR_{exp}, was calculated by:

$$\delta(R_{\exp})^2 = \left[\frac{\partial R}{\partial T_1}\delta T_1\right]^2 + \left[\frac{\partial R}{\partial T_4}\delta T_4\right]^2 + \left[\frac{\partial R}{\partial q}\delta q\right]^2 \tag{2}$$

where this expression includes the uncertainties of the thermocouples, data acquisition system, and power supply unit, determined by the error propagation technique according to Holman [7]. After the calibration, the maximum temperature uncertainty was 0.21 °C.

3. Lumped Parameter Model

The LPM model used in this work is taken from the validated works by Bernagozzi et al. [8] [9], which have been successfully validated with different LHP layout (flat plate and cylindrical) and different working fluids (R123, ammonia, water, ethanol and Novec 649©).

The principal modifications of the LPM for the present ultra-thin device are the absence of the compensation chamber and the working fluid confinement, induced by the thickness reduction, increasing the heat leak from the evaporator to the liquid line.

A schematic design of the thermal network, which was modified for the proposed ultra-thin LHP, can be seen in **Error! Reference source not found.**a. Compared to previous works [8] and [9], the compensation chamber was removed from the thermal network. Experimental data from [3] were used: the average heat transfer coefficient by natural air convection in the condenser (30.4 W/m^{2}K), the working fluid mass flow rates, and the average experimental heat leakage from the evaporator to the environment through the insulation (15.46%).

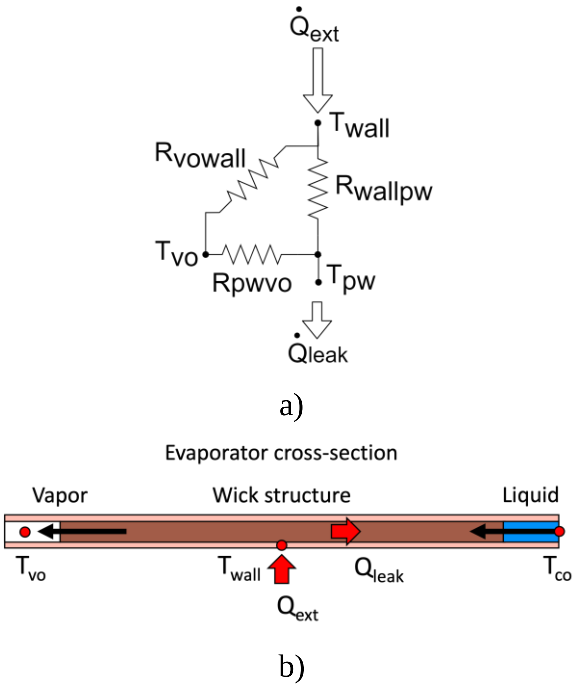

Figure 3. Flat Plate LHP evaporator a) thermal network and b) schematic for reference. wall: evaporator wall; vo: vapour outlet – exiting the

evaporator; co – condenser outlet – all the condenser section and liquid line are subjected to the same external heat transfer coefficient hence considered as condenser.

Error! Reference source not found.b shows the actual location of the temperature estimations from the proposed model. As mentioned, heat is applied in the external surface (Q_{ext}) of the evaporator, where the temperature of this region is given by T_{wall}. In the sequence, heat is transferred to the working fluid, resulting in its evaporation and leaving the evaporator with T_{vo}. However, due to the wall and wick structure material, a fraction of the total heat leaks the liquid line section, which does not contribute to the evaporation of the working fluid (Q_{leak}). Vapor starts to condense while flows in the condenser section. The condensed liquid exits the condenser with T_{co}, flowing back to the evaporator from the condenser through the liquid line, closing the loop. It is worth to mention that, since both the condenser and the liquid line are subjected to the same external heat transfer conditions, they are both treated as condenser in the model.

Error! Reference source not found.a displays the thermal network associated to the evaporator which instructed the writing of the main ODE system, presented in Eqs. (3-5). The first one, the evaporator wall node, is expressed as follows:

$$\dot{m}_{wall} c_{p,wall} \frac{dT_{wall}}{dt} = \frac{T_{vo} - T_{wall}}{R_{vowall}} + \frac{T_{co} - T_{wall}}{R_{wallco}} + \dot{Q}_{ext} \quad (3)$$

where $\dot{m}_{wall}$ is the mass flow rate in this node, $c_{p,wall}$ is the specific heat of the evaporator wall and R_{vowall} and R_{wallco} are the thermal resistance between T_{wall} and T_{co}, and between T_{wall} and T_{co}, respectively.

The second node is in the vapor channels, where vapor leaves from the evaporator. The governing equation of this element is:

$$\dot{m}_{vo} c_{p,v} \frac{dT_{vo}}{dt} = \frac{T_{co} - T_{vo}}{R_{covo}} + \frac{T_{wall} - T_{vo}}{R_{vowall}} + \dot{m} c_{p,v} (T_{sat} - T_{vo}) \quad (4)$$

where $\dot{m}_{vo}$ is the vapour mass flow rate generated by boiling, $c_{p,v}$ is the specific heat of the vapor phase and R_{covo} and R_{vowall} are the thermal resistance between T_{co}, and T_{vo} and between T_{vo} and T_{wall}, respectively. The last element of Eq. (4) accounts for the vapour superheat.

The last node is in the end of the condensing section, where vapor enters the inlet section and leaves as a liquid. Therefore, the following equation expresses the transient behavior in this node:

$$\dot{m}_{co} c_{p,co} \frac{dT_{co}}{dt} = \frac{T_{vo} - T_{co}}{R_{covo}} + \frac{T_{wall} - T_{vo}}{R_{vowall}} - \dot{m} c_{p,l} (T_{co} - T_{ll}) - \dot{Q}_{leak} \quad (5)$$

where $\dot{m}_{co}$ is the liquid mass flow rate returning to the evaporator and $c_{p,l}$ is the specific heat of the liquid phase. The second to last element of Eq. (5) accounts for the subcooling coming from the liquid line.

Besides these expressions, another governing equation related to the heat leakage from the evaporator to the liquid line due to the temperature difference between these two regions is used, which is crucial for the operating of compact two-phase devices. Thus, there is an increase in the temperature of the liquid line given by this heat leakage ($\dot{Q}_{leak}$), which can be assessed with the following expression:

$$T_{co} = T_{ll} + \frac{\dot{Q}_{leak}}{\dot{m} c_{p,l}} \quad (6)$$

where T_{ll} is the last node of the liquid line.

Lastly, the LPM model can evaluate the steady-state thermal resistance (R_{num}) with the following expression:

$$R_{num} = \frac{T_e - T_c}{q} \quad (7)$$

where T_e is the evaporator temperature given by T_{wall} and T_c is the condenser temperature that can be assessed by the average temperature between T_{vo} and T_{co}.

4. Results and discussion

4.1. Experimental results

In order for the ultra-thin LHP to start its operation as a two-phase device, a pressure difference between the evaporator and the condenser must exist, given by the temperature variation in these regions. Therefore, with the wick structure of the LHP fully saturated with liquid, when heat is applied to the outer surface of the evaporator, its temperature increases, generating vapor. The resulting vapor flows in the direction of the condenser, condensing it up to some fraction of the condenser. Assisted by the capillary and vapor pressure, the condensate returns to the evaporator. Thus, in this paper, the startup can be considered when vapor reaches the condenser section, increasing its temperature (T_4 in Figure 2).

Figure 4 shows the temperature distribution of the ultra-thin flat LHP operating in the gravity-assisted orientation under several heat loads. With the increase of the power input, the steady-state temperature of each power level increased. The startup of LHP occurred at 2 W, when the condenser temperature (T_4) increased and overlapped the inlet evaporator temperature (T_6). For the LHP startup, an evaporator temperature of 43.36 °C and a temperature difference between the evaporator and condenser of 1.63 °C was necessary.

From Figure 4, above 4 W, all temperatures of the condenser section (T_3, T_4 and T_5) were kept at almost the same level, meaning that at this heat load, the entire condenser area was being used for the condensation of the working fluid.

The maximum heat flux dissipated by the LHP, without reaching the established limit temperature of 100 °C, was 8 W, with an evaporator temperature of 90.6 °C. No dry-out condition was observed, which means that the LHP could transfer higher heat fluxes; however, with a higher evaporator temperature.

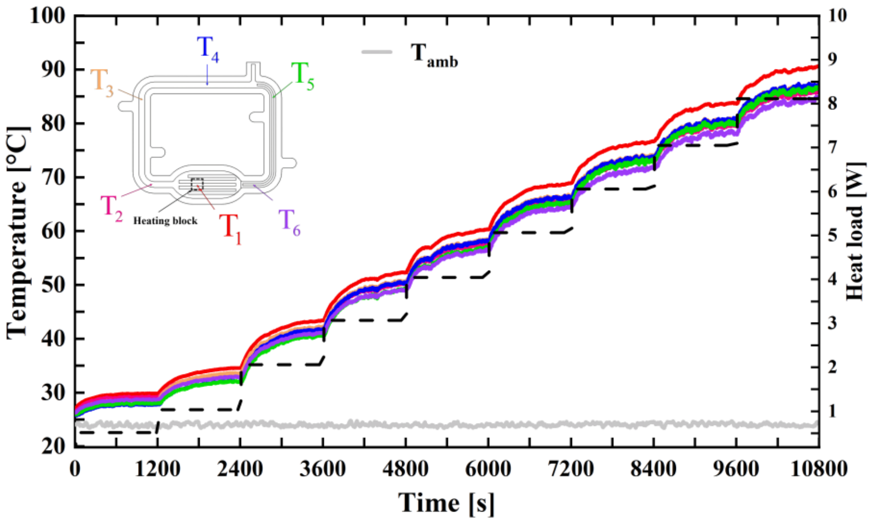

Figure 4. Temperature distribution of ultra-thin flat LHP operating in the gravity-assisted orientation [3].

4.1. Numerical results

Figure 5 presents the transient temperatures along the LHP given by the experimental data and numerical results. The dashed grey line shows the experimental results from [3], while the solid black line illustrates the numerical data obtained with the present LPM. In Figure 5a, T_{wall} is the evaporator temperature measured by T_1. In Figure 5b, T_{vo} is the evaporator outlet temperature obtained by T_2. In Figure 5c, T_{co} is the condenser exit temperature provided by T_5.

In Figure 5a, from 0.5 to 2 W, both numerical and experimental lines present an excellent match, both in terms of steady state values and trends. Above 2 W, a discrepancy at the end of the steady state section starts to appear, with the numerical model underpredicting the experimental data. However, both data still show satisfactory agreement, with an average difference between the evaporator temperature (T_1) and the numerical evaporator temperature ($T_{wall,num}$) of 0.99 °C.

For the evaporator outlet temperature, Figure 5b shows good agreement between the numerical and experimental data for all applied heat loads, with the exception of 8 W. In this case, the average difference between both temperatures (experimental and numerical) was 1.20 °C.

The last comparison presented is the condenser outlet temperature. From Figure 5c, some minor differences can be seen in all heat loads, in which the numerical data presents lower temperatures up to 2 W and higher from 5 W to 8 W. The comparison of this case showed the highest discrepancy between the numerical and experimental temperatures, 1.65 °C.

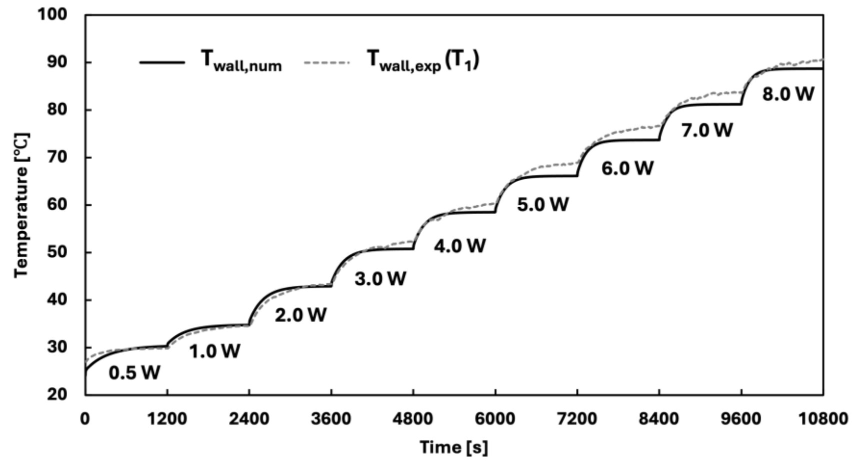

(a)

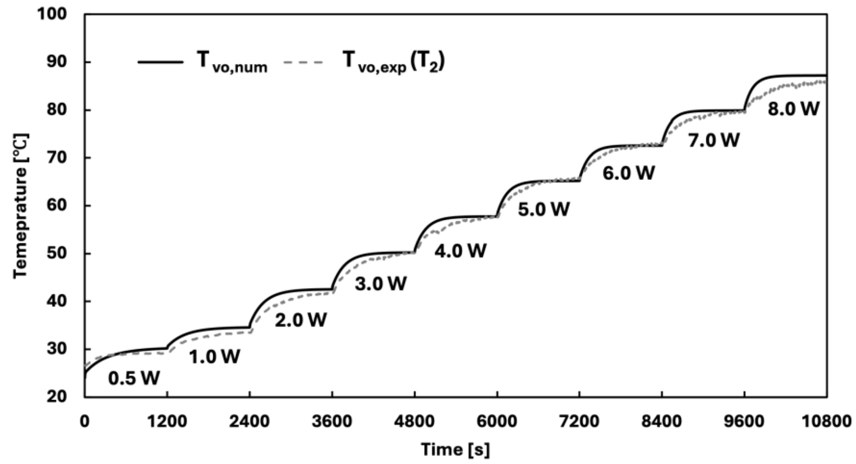

(b)

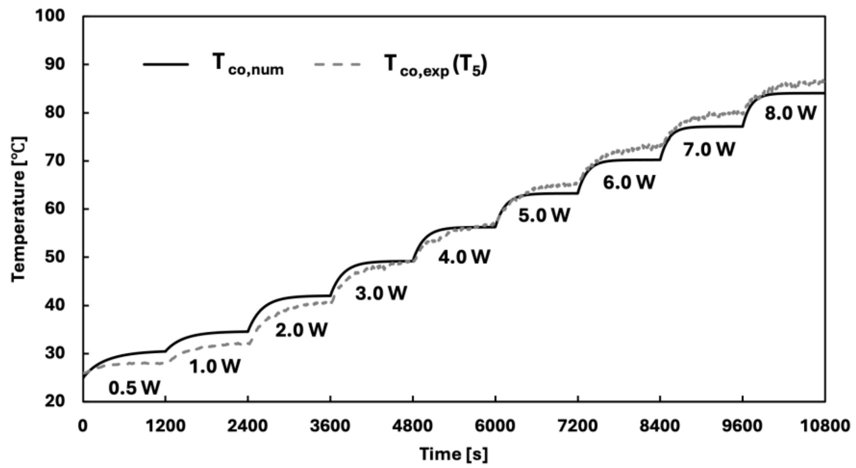

(c)

Figure 5. Comparison of the experimental and numerical transient temperatures along the LHP (a) evaporator wall, (b) evaporator exit, and (c) condenser outlet.

Figure 6 shows the comparison between the experimental (black round dots) thermal resistance, given by Eq. (1), and the numerical (grey line) thermal resistance obtained by Eq. (7). The thermal resistance of the proposed LHP without working fluid inside, i.e., transferring heat only by heat conduction, was 3.33 ± 0.43 °C/W. From Figure 6, it is clear that the LHP startup at 2 W, as mentioned in Figure 4, with an abrupt decrease in its thermal resistance. Above 2 W, the thermal resistance remained at an almost constant level, reaching the minimum value of 0.4 °C/W at 7 W.

Since the proposed LPM model only considers the LHP operating as a two-phase device, the comparison of the numerical and experimental results accounts only heat loads from 2 W to 8 W, where the LHP properly operates. Considering this range of operation, the numerical model could successfully predict the thermal resistance of the proposed LHP, presenting an average discrepancy of 28%.

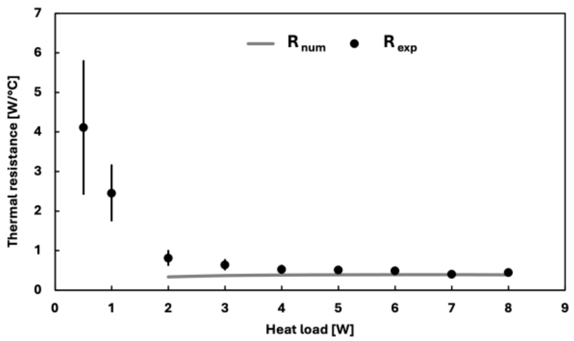

Figure 6. Comparison between the numerical and the experimental thermal resistance.

From the presented results, the proposed LPM model could successfully simulate and predict the transient temperature of the LHP for all applied heat loads, including those where the LHP was not operating as a two-phase device. Considering the thermal resistance, the LPM model reasonably estimated it, but improvements can be made, especially in simulating the condenser section temperature; however, only for the heat loads where the LHP was operating in two-phase mode.

In this context, in general, the proposed LPM showed to be a successful tool for the transient thermal performance prediction of an ultra-thin LHP.

5. Conclusions

In the present work, a previously studied 1-D lumped parameter model, already validated for larger LHPs and different working fluids, is proposed for predicting the transient thermal behavior of an ultra-thin LHP specially designed for smartphones. The main goal of this research was to understand the applicability of the 1-D LPM for ultra-thin two-phase devices. The results have shown that:

a. The proposed LHP properly operated in the gravity-assisted mode, starting at 2 W up to 8 W with a minimum thermal resistance of 0.4 °C/W at 7 W.
b. The proposed 1-D LPM can successfully simulate and predict the transient temperature and thermal resistance of a ultra-thin LHP of 1.56 mm of total thickness if the heat leakage from the evaporator to the liquid line is considered.
c. The transient behavior of the LHP can be predicted by estimating three temperatures along the LHP: the evaporator, the outlet evaporator, and the condenser exit. Comparing these results with the experimental data, an average temperature difference between these results of 0.99 °C, 1.20 °C, and 1.65 °C, respectively, were obtained.
d. The 1-D LPM model predicted the steady-state thermal resistance with an average discrepancy of 28% for the heat loads in which the LHP was able to operate as a two-phase device.

Finally, the present research showed the possibility of using the 1-D LPM for ultra-thin LHPs operating in the gravity-assisted mode with ethanol as the working fluid. In future works, new operation conditions and different working fluids must be accomplished in order to improve the proposed model as design tool for new ultra-thin two-phase devices. Furthermore, this model can be used to compute the combined effect of thermal resistance, density of the device and its thickness, which is one of the most important parameters for the thermal management of smartphones or microelectronics, to compare it with other standard technologies.

6. Acknowledgements

The authors acknowledge the National Council for Scientific and Technological Development (CNPq), National Fund for Scientific and Technological Development (FNDCT), and Ministry of Science, Technology, and Innovations (MCTI) for funding the projects: 405784/2022-8 and 406451/2021-4, and the scholarship of the second author, under grant number 381267/2023-7. The authors also acknowledge the Foundation for Research Support of Santa Catarina (FAPESC) for providing a scholarship for the first author under grant number 3003/2021. Also, acknowledgments are offered to the Graduate Program in Mechanical Engineering of UFSC, which funded the congress participation of the research team. Finally, the Authors would like to thank the School of

Architecture, Technology and Engineering at the University of Brighton for the economic support.

References

[1] H. Tang, Y. Tang, Z. Wan, et al., Review of applications and developments of ultra-thin micro heat pipes for electronic cooling, Applied Energy. 2018, 223 (April): pp. 383–400.

[2] K.G. Domiciano, L. Krambeck, J.P.F. Mera, and M.B.H. Mantelli, Study of a new thin flat loop heat pipe for electronics, Heat and Mass Transfer/Waerme- und Stoffuebertragung. 2023, (0123456789): p.

[3] K.G. Domiciano, L. Krambeck, J.P.M. Floréz, and M.B.H. Mantelli, Thin diffusion bonded flat loop heat pipes for electronics : Fabrication , modelling and testing, Energy Conversion and Management. 2022, 255 (November 2021): p.

[4] J.P.M. Florez, M.B.H. Mantelli, G.G.V. Nuernberg, and F.H. Milanez, Powder Geometry based models for sintered media porosity and effective thermal conductivity, Journal of Thermophysics and Heat Transfer. 2014, 28 (3): pp. 507–517.

[5] J.P. Flórez Mera, M.E. Chiamulera, and M.B.H. Mantelli, Permeability model of sintered porous media: analysis and experiments, Heat and Mass Transfer/Waerme- und Stoffuebertragung. 2017, 53 (11): pp. 3277–3285.

[6] J.P.F. Mera, Heat and Mass Transfer Analysis of a Copper Loop, (2016).

[7] J.P. Holman, Experimental methods for engineers. , New York, USA, 2011.

[8] M. Bernagozzi, A. Georgoulas, N. Miché, C. Rouaud, and M. Marengo, Novel battery thermal management system for electric vehicles with a loop heat pipe and graphite sheet inserts, Applied Thermal Engineering. 2021, 194 p.

[9] M. Bernagozzi, S. Charmer, A. Georgoulas, I. Malavasi, N. Michè, and M. Marengo, Lumped parameter network simulation of a Loop Heat Pipe for energy management systems in full electric vehicles, Applied Thermal Engineering. 2018, 141 pp. 617–629.

Paper ID 087(S8)

Thermal Characteristics of Concentric Annular Thermosyphon with Phase Change Material

Weeranut Intagun, Paisan Comsawang, Nattawut Tharawadee and Nat Thuchayapong*

Department of Mechanical Engineering, Faculty of Engineering and Industrial Technology,
Silpakorn University, Thailand
**Corresponding author email address: thuchayapong_n@su.ac.th*

Abstract

This research investigates the thermal performance of a concentric annular thermosyphon with phase change material (PCM). The PCM is designed to be inside the thermosyphon to absorb heat during its operation, store heat when it is not in operation, and release the stored heat when it resumes operation. Experimental studies were conducted to evaluate the thermal resistance and temperature distribution of the thermosyphon using paraffin wax as the PCM. Distilled water was used as the working fluid with the filling ratio of 60 %. The thermosyphon was constructed from a steel tube with an outer diameter of 76.6 mm and a total length of 1000 mm. The lengths of the evaporator, adiabatic, and condenser sections were 300 mm, 300 mm, and 400 mm, respectively. The evaporator was heated by a band heater with variable heat inputs of 1700 W, 1900 W, and 2100 W. Cooling water circulated through a cooling jacket at a mass flow rate of 60 L/min to transfer heat in the condenser section. The results showed that the thermosyphon with PCM had low thermal resistance (0.012-0.014 K/W). The phase change behavior of the PCM is investigated and reported.

Keywords: Heat Storage; Phase Change Material; Thermal Resistance; Thermosyphon

1. Introduction

A thermosyphon or wickless heat pipe is a heat-transfer device which transfers heat from a source to a sink. The heat transfer mechanism of thermosyphon employs a method of passive heat exchange based on the internal phase change of vapor/liquid, which is the continuous circulation of two-phase flow without the wick. It has been widely employed in various areas, such as industrial heat recovery, solar applications, thermal storage, geothermal applications, and flue gas heat recovery [1-5]. Thermal energy storage (TES) is one of the interesting methods for storing thermal energy, which can be used directly without being converted to another form. The TES can be categorized into two forms: Physical Storage (and Thermochemical heat storage. Moreover, physical storage can be classified into sensible heat storage devices and latent heat storage devices. Phase Change Material (PMC) is a material that a phase transformation between the solid and liquid phases, which absorbing or releasing a high amount of energy. The utilization of the PCM is the most common application in both renewable and fossil energy systems [6-10]. Paraffin wax is the organic PCM, as well as paraffin-based PCM, which is the most widely used substance for storing thermal energy. Due to this, it has good thermal and energy storage properties with a transition temperature of 50–59 ◦C. In addition, the paraffin is nontoxic, has chemical stability, negligible supercooling, a high enthalpy of melting/crystallization, and is a relatively low priced [11-12]. Thus, the aim of this research is to investigate the thermal performance of a concentric annular thermosyphon with phase change material (PCM).

2. Concept Design

In this research, the concentric annular thermosyphon with PCM was designed and tested, as shown in Figure 1. The objective was to store heat within the PCM inside the thermosyphon when it is not in operation and to release the stored heat once it resumes operation. This helps the heat pipe reach a steady state more quickly and begin functioning faster. It can be divided into three heating modes, as shown in Figure 1.

Mode 1, as shown in Figure 1(a), occurs when the thermosyphon with PCM starts operating. Heat is absorbed into the PCM, and as the PCM undergoes a phase change, a significant amount of heat is stored within it.

Mode 2, as shown in Figure 1(b), occurs when the heat supply to the thermosyphon heat pipe is stopped. A vacuum forms inside the pipe because no working fluid is available to transfer heat to the condenser section. The insulated section of the thermosyphon acts as a thermal barrier, allowing the heat to remain stored in PCM.

Mode 3, as shown in Figure 1(c), occurs when heat is applied to the thermosyphon with PCM again. The working fluid evaporates and absorbs heat from the PCM, causing the temperature of the heat pipe to rise more quickly, as it receives additional heat from the PCM.

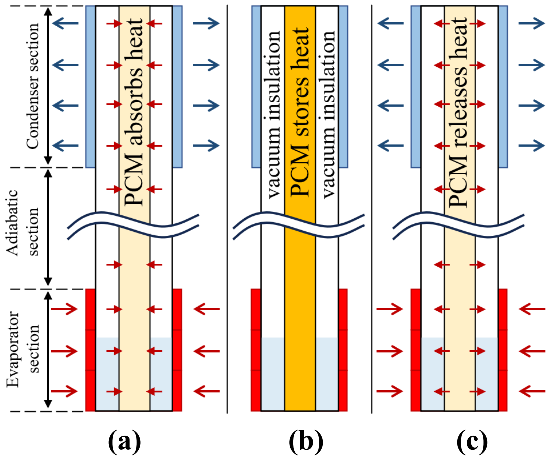

Figure 1. The heating mode of thermosyphon with PCM

From the design concept discussed above, this type of heat pipe will maintain a more consistent temperature and can operate more quickly when reheated.

3. Experimental Setup

The present work experimentally investigates the thermal characteristics of concentric annular thermosyphon with phase change material. The total length of the concentric annular thermosyphon was 1 m. The internal diameter (D_i) is 40.2 mm with the thickness of 1.8 mm. The internal diameter (D_o) is 76.2 mm with the thickness of 2.2 mm. as shown in Figure 2. The working fluid is deionized water with the filling ratio is 60 %. Vacuum was established in the thermosyphon by using a vacuum pump. The PCM in this study is paraffins wax Grade 58 which has a melting temperature of 58 °C. Due to the paraffin is widely available from various manufacturers, relatively inexpensive, and has a melting temperature suitable for a wide range of applications. The paraffins wax was filled of 850 g.

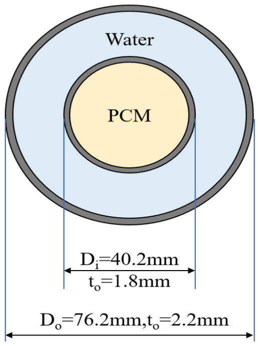

Figure 2. The cross-sectional view of the concentric annular thermosyphon with PCM

A schematic diagram of the experimental setup is shown in Figure 3. The experimental setup consists of the concentric annular thermosyphon with PCM, a heater, a wattmeter, a rotameter, datalogger and thermocouples. For the concentric annular thermosyphon with PCM, the evaporator, adiabatic and condenser length are 300 mm, 300 mm and 400 mm, respectively. The evaporator section is heated by the band heater. Cooling water is passed into the cooling water jacket to exchange heat with the condensation section of the concentric annular thermosyphon with PCM. The thermocouples were placed on the evaporator section, adiabatic section, condenser section, PCM section, the ambient, and the inlet and outlet of the cooling water jacket, respectively.

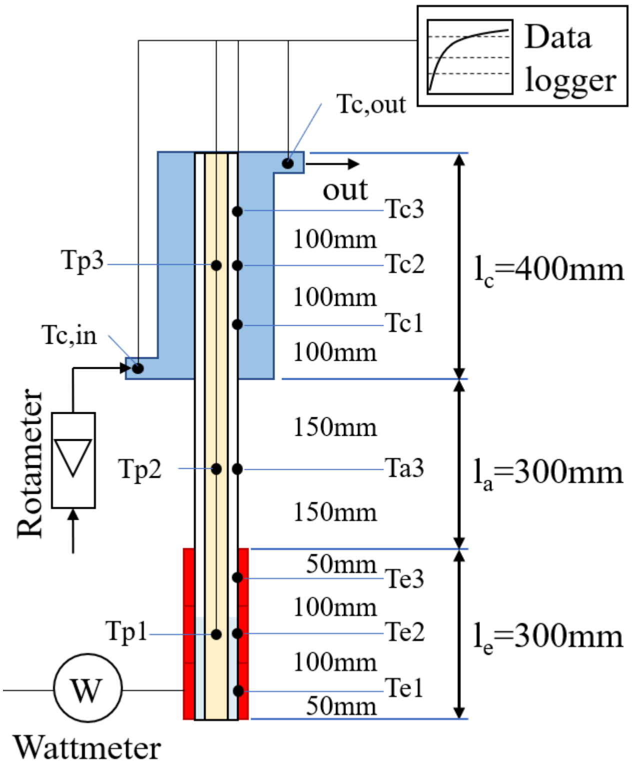

Figure 3. The schematic of the experimental setup.

In this research, the mass flow rate in the condenser section is 60 L/min. The first step, the evaporator section is heated according to the specified value, and the heat input values vary between 1700 W, 1900 W, and 2100 W, respectively. The temperature was collected until the study state of 60 min. After that in the second step, the heater worked in the off mode for 30 min. Next, the heater worked in the on mode until the study state again for 60 min. The temperature data were collected at 1-second intervals.

The thermal resistance of thermosyphon with PCM was calculated from Eq 1.

$$Z = \frac{(Te,avg.-Tc,avg.)}{Q}. \qquad (1)$$

Where Z is thermal resistance, $Te,avg.$ is the average temperature in evaporation section, $Tc,avg.$ is average temperature in condenser section, and Q is heat throughput in condenser section

The heat throughput in condenser section was calculated from Eq 2.

$$Q = \dot{m}c_p(Tc,out - Tc,in). \qquad (2)$$

Where $\dot{m}$ is the water mass flow rate, c_p is the specific heat capacity of water, Tc,out and Tc,in are the inlet and outlet temperatures of the water flowing through the water jacket

4. Results and discussion

4.1. The thermal resistance and temperature distribution of the thermosyphon with PCM

From the experiment, heat input between 1700 and 2100 was applied to the evaporator section to investigate the thermal performance. It was found that the temperature distribution of thermosyphon with PCM was shown in Figure 4. The average temperature difference between evaporator section and condenser section ($T_{e,avg.}$-$T_{c,avg.}$) is between 19.7-23.6 °C. This shown that the thermosyphon with PCM can transfer heat with low temperature distribution.

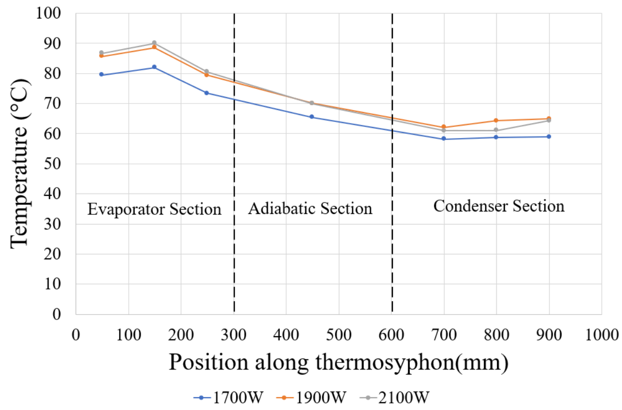

Figure 4. Temperature distribution of thermosyphon with PCM

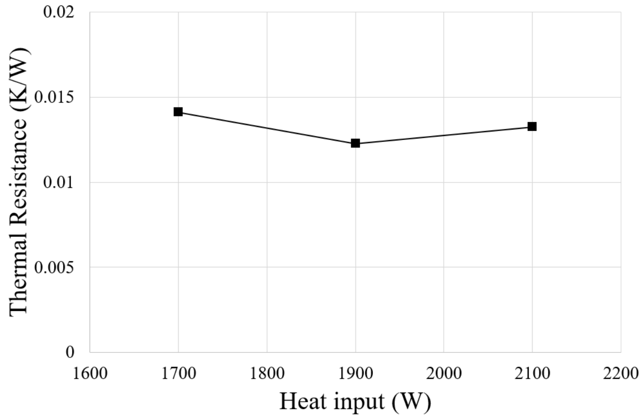

Figure 5. Thermal resistance of thermosyphon with PCM

From Figure 5, it can be seen that the thermal resistance of thermosyphon with PCM is between 0.012 to 0.014 K/W. This shown that the thermosyphon with PCM has low thermal resistance at heat inputs ranging from 1700 to 2100 W.

4.2. Heat transfer characteristics of thermosyphon with PCM

The temperature characteristics of the thermal characteristics of the thermosyphon with PCM at 2100 W shown in Figure 6. From the results, the temperature distribution for one hour until to the steady state. The average temperature was higher than the melting point of PCM which the heat energy was absorbed and storage in the PCM with the latent and sensible heat. After that in the second step, the temperatures of thermosyphon were decease due to the cooling system.

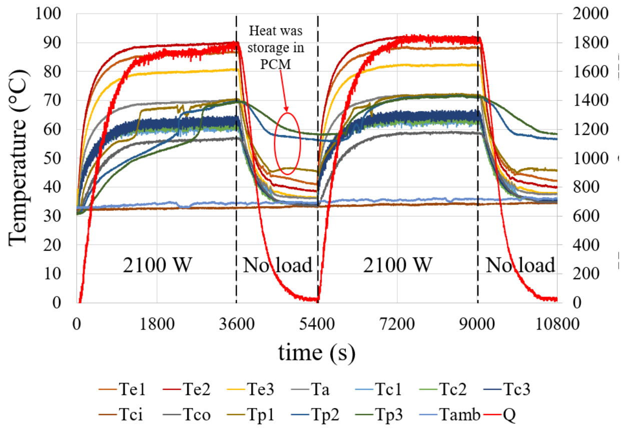

Figure 6. Heat transfer characteristics of thermosyphon with PCM

Figure 7 shows the phase change behavior of the PCM in the thermosyphon heat pipe. As the thermosyphon with PCM begins to operate, the temperature of the PCM rises to 58°C, at which point it undergoes a phase change from solid to liquid. It can be observed that the temperature of the PCM in the evaporator section (Tp1) undergoes a phase change first due to the heat transferred from the working fluid in the evaporator. The PCM then gradually melts, progressing from the evaporator section to the PCM in the adiabatic section (Tp2) and the condenser section (Tp3), respectively.

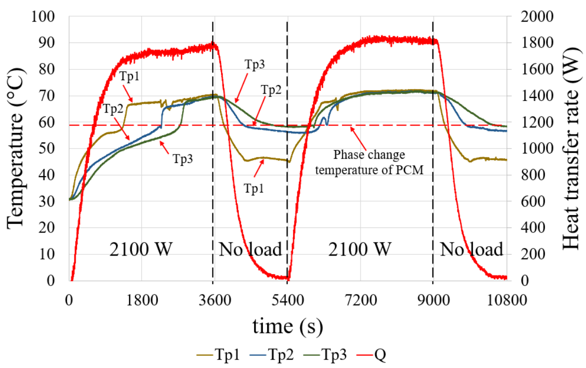

Figure 7. Heat transfer characteristics of PCM

When the heat supply is stopped, it can be observed that, although the temperature of the thermosyphon drops rapidly as shown in Figure 6, the temperature of the PCM decreases only slightly. However, the temperature of the PCM in the evaporator section decreases more significantly because the working fluid in this section extracts heat from the PCM. This causes a noticeable temperature drop in the PCM shortly after the heat supply is stopped, as the heat transfer continues for a short period. Once the heat pipe stops operating, the temperature of the PCM stabilizes. This is due to the vacuum conditions inside the heat pipe, which help trap the heat within the PCM.

When heat is reapplied to the thermosyphon, the stored heat is released back into the thermosyphon, allowing it to resume operation more quickly. However, due to the relatively small amount of PCM used in this study and the PCM in the evaporator section not storing heat effectively, the overall heat storage capacity of the PCM was insufficient. As a result, no significant temperature increase was observed when heat was reapplied to the thermosyphon. However, the PCM in the adiabatic and condenser sections was found to store heat effectively. Therefore, future research should focus on designing a heat pipe with an increased amount of PCM in these sections to improve overall performance and efficiency.

5. Conclusions

This research investigates the thermal Characteristics of a concentric annular thermosyphon with PCM to enable the thermosyphon to store heat and maintain a stable operating temperature. The PCM also helps release heat to enhance the efficiency of the heat pipe when it resumes operation after reheating. The experimental results showed that the PCM in the adiabatic and condenser sections was able to effectively store heat, whereas the PCM in the evaporator section had relatively low heat storage efficiency. Consequently, the overall heat storage capacity was insufficient, and no significant temperature increase was observed when the heat was reapplied. The study concludes that future designs should increase the amount of PCM in the adiabatic and condenser sections to improve the system's performance and heat storage capacity.

6. ACKNOWLEDGEMENTS

This research is financially supported by the Silpakorn University Research, Innovation and Creative Fund and Department of Mechanical Engineering, Faculty of Engineering and Industrial Technology, Silpakorn University, Thailand. The authors would like to express appreciation to the Laboratory of Innovation Fuels and Energy, Department of Mechanical

Engineering, Faculty of Engi- neering and Industrial Technology, Silpakorn University.

References

[1] Wang, X., Liu, H., Xue, Y., Wu, N., Gan, W., & Zhu, Y. (2024). Experimental and CFD investigation on the thermal performance of two phase closed thermosyphons: Effect of corrugated evaporator. Applied Thermal Engineering, 124494.

[2] Srivastava, A., Kumar, P., Ambirajan, A., Dutta, P., Varghese, Z., Rohith, B. L., & Subrahmanya, P. (2024). Experimental investigation of thermosyphons with horizontal evaporator for low heat flux applications. *Applied Thermal Engineering*, *257*, 124249.

[3] Battisti, R., Milanez, K. W., Mantelli, M. B., dos Santos, M. C., Medina, L. C., Marangoni, C., & Machado, R. A. (2020). Energy conditions assessment of a two-phase annular thermosyphon used as heat supplier for a new pilot-scale falling film distillation unit. *Thermal Science and Engineering Progress*, *19*, 100648.

[4] Zhao, Z., Jiang, P., Zhou, Y., Zhang, Y., & Zhang, Y. (2019). Heat transfer characteristics of two-phase closed thermosyphons modified with inner surfaces of various wettabilities. *International Communications in Heat and Mass Transfer*, *103*, 100-109.

[5] Hee Lee, C., Seo, S. W., Park, D. K., & Lee, K. Y. (2023). Influence of cellulose nanofiber fluid on flow instability and heat transfer of two-phase closed thermosyphon. *Heliyon*, *9*(10).

[6] Wu, W., Yang, X., Zhang, G., Chen, K., & Wang, S. (2017). Experimental investigation on the thermal performance of heat pipe-assisted phase change material based battery thermal management system. *Energy Conversion and Management*, *138*, 486-492.

[7] Ahmed, M. A., Rofaiel, I. Y., & Essa, M. A. (2020). Experimental study for the performance of an integrated solar collector water heater based on helical fins heat pipes using phase changing material. *The Egyptian International Journal of Engineering Sciences and Technology*, *30*(Mechanical Engineering), 22-38.

[8] Zhong, W., & Ji, W. (2021). Applications of coupling thermosyphons with phase change materials: a review. *Energy and Buildings*, *233*, 110690.

[9] Li, B., Song, S., Tian, J., Ren, B., Yu, J., & Wang, Y. (2024). Thermal performance of a novel composite phase change material for solar-assisted air source heat pump packed bed thermal energy storage application. *Applied Thermal Engineering*, 124582.

[10] Zhao, J., Lv, P., & Rao, Z. (2017). Experimental study on the thermal management performance of phase change material coupled with heat pipe for cylindrical power battery pack. *Experimental Thermal and Fluid Science*, *82*, 182-188.

[11] Bharathiraja, R., Ramkumar, T., & Selvakumar, M. (2023). Studies on the thermal characteristics of nano-enhanced paraffin wax phase change material (PCM) for thermal storage applications. *Journal of Energy Storage*, *73*, 109216.

[12] Al-Gunaid, T., Sobolčiak, P., Chriaa, I., Karkri, M., Mrlik, M., Ilčíková, M., ... & Krupa, I. (2023). Phase change materials designed from Tetra Pak waste and paraffin wax as unique thermal energy storage systems. *Journal of Energy Storage*, *64*, 107173.

Paper ID 088(S2C)

An Experimental Investigation of Aluminum/Ammonia Heat Pipe with Rectangular Smooth Edge Axial Groove Wick

Amawasee Rukruang[1,2], Sajad Mishkhas[1], Meng-Hao Chen[3], Tzu-Hui Yu[3], Yen-Ting Chen[3], Jong-Shinn Wu[3], Piyatida Trinurak[4], Somchai Wongwises[5], and Chi-Chuan Wang[1,*]

[1] *Department of Mechanical Engineering, National Yang Ming Chiao Tung University, Hsinchu, Taiwan*
[2] *Logistics Engineering Program, Faculty of Engineering, Thaksin University, Phatthalung, Thailand*
[3] *Taiwan Space Agency, Hsinchu, Taiwan*
[4] *Department of Mechanical Engineering, Faculty of Engineering, King Mongkut's University of Technology Thonburi (KMUTT), Bangmod, Bangkok 10140, Thailand*
[5] *Fluid Mechanics, Thermal Engineering and Multiphase Flow Research Lab. (FUTURE), Department of Mechanical Engineering, Faculty of Engineering, King Mongkut's University of Technology Thonburi (KMUTT), Bangmod, Bangkok 10140, Thailand*
**Corresponding author email address: ccwang@nycu.edu.tw*

Abstract

The aluminum/ammonia heat pipe is commonly used in aerospace applications because it is lightweight and highly effective for thermal management. This heat pipe is accompanied by a rectangular smooth edge axial groove wick. The heat pipe is 1 m long, consisting of a 250 mm evaporator, 500 mm adiabatic section, and 250 mm condenser. The test was conducted under a heat load of 50 – 450 W, a cooling water temperature of 15 – 30 °C, and a water flow rate of 1 LPM. The heat pipe was horizontally placed for all test conditions. This study examined the effects of heat load and cooling water temperature to determine the heat pipe performance through the overall thermal resistance. The optimal test conditions were a heat load of 250 W and a cooling water temperature of 30°C, resulting in a minimum overall thermal resistance of about 0.0823 °C/W. Furthermore, axial and circumferential temperature distributions along the heat pipe were investigated. However, it can be concluded that various parameters and heat transfer processes influence the heat pipe performance and that a single parameter may not fully capture its outstanding performance.

Keywords: Aerospace application, Cooling capacity, Electronic cooling, Temperature gradient, Thermal performance

1. Introduction

Heat pipes are highly effective devices for thermal heat transfer. Gaugler [1] pioneered the heat pipe principle and issued its first US patent in 1944. Then, Trefethen [2] suggested the idea of the heat pipe again in 1962, and it was issued as a patent in 1963 by Wyatt [3]. In 1964, "Heat pipe" was formally named by Grover et al. [4] as a simplistic heat transmission device. The most prominent advantages are their isothermal properties, high thermal conductivity, ability to transfer heat through long-distance, works against gravity, and many more. Due to their benefits, heat pipes have been widely used in many applications, such as electronic cooling, military, and aerospace industries. The device operates by making phase phenomenon, facilitating liquid-vapor circulation between the evaporator and condenser sections. The condensate liquid flows back to the evaporator from the condenser with the help of capillary force, which is often made available from the wick structure [5].

Copper/Water is the most common combination upon heat pipe application especially in typical electronics cooling. However, aluminum material is much preferred for heat pipes extensively in aerospace applications due to their lightweight requirement. To ensure the compatibility of working fluids and the material. Ammonia is regarded as the best working fluid as far as aluminum heat pipe is concerned for its superior merit numbers [6]. An axial groove wick also performs well when it does not operate under gravity, which is the case in aerospace applications. Several researchers have investigated the performance of heat pipes regarding the wick structures, working fluid, thermal behavior, and so on. Both experimental and numerical studies had been reported in the literature.

Stephan and Busse [7] proposed a 2D model in the grooved aluminum/ammonia heat pipe. They reported that assuming an interface temperature equal to the saturation temperature leads to a significant overprediction of the radial heat transfer coefficient. El-Genk and Huang [8] examined a grooved copper/water heat pipe under transient response operation. This study focused on analyzing the axial temperature distribution along the heat pipe. Furthermore, the effects of coolant flow rate and step change in power on the heat pipe were investigated. Desai et al. [9] conducted a simulation on a trapezoidal grooved aluminum/ammonia heat pipe. The results suggested that the total thermal resistance increases with higher groove height and decreases with increased groove number and groove inclination angles. Wei et al. [10] numerically examined the heat transfer and flow characteristics through CFD simulation for an omega wick heat pipe. Enke et al. [11] numerically investigated the effect of non-condensable gas in the heat pipe to monitor the axial wall temperatures. Huang et al. [12] introduced a partially-hybrid mesh-groove wick to improve the L-shaped copper-ethanol heat pipe. They reported that the thermal resistance could be reduced by about 57.4% when using the partially-hybrid wick. Wong et al. [13] presented the axial wall temperature distribution on composite mesh-groove heat pipe. They reported that the partial dry-out can be observed at a heat load of 6 W and an inclination angle of 15°. Gomaa et al. [14] tested grooved heat pipes with various groove ratios and working fluids. The experimental results revealed that the grooved heat pipes performed better than that of the smooth heat pipe by about 50.6%.

Based on the literature mentioned above, several key parameters influence the thermal performance of heat pipes, including the wick structure, heat load, orientation, working fluid, and cooling capacity. However, limited information is available regarding the impact of cooling temperature on the condenser. Therefore, the objective of this study aims to provide more insights into the effect of cooling water temperatures on the performance of heat pipes. Additionally, an analysis of the axial and circumferential temperature distribution along the heat pipe is examined accordingly.

2. Research method

2.1. Aluminum heat pipe design

The heat pipe was made from aluminum alloy (AA6063, T66) with outer and inner diameters of 17.86 and 15.44 mm, respectively. The rectangular with a smooth edge was fabricated as an axial groove along the total length. The cross-section and dimensions of the heat pipe were reported by Sajad et al. [15]. The total length of the heat pipe is 1000 mm, in which the evaporator and condenser lengths are 250 mm, and the adiabatic section length is 500 mm.

2.2. Experimental apparatus and method

The experimental apparatus and setup are presented in Figure 1. The evaporator section was powered by an AC power supply, which provided the necessary heat source. The evaporator section comprised fifteen heating cartridges and five aluminum alloy 6601 blocks. All blocks were housed in Bakelite to ensure well-insulation. Each block contained two thermocouples, and a 0.5 mm air gap was maintained between blocks to minimize axial heat conduction. This setup ensured that heat conduction remained one-dimensional through the heating block. The condenser section was fitted with an aluminum alloy 1050 block that used water cooling to remove heat. Seven axial wall temperatures were attached alongside the condenser length. Five thermocouples were directly attached to the wall in the adiabatic section.

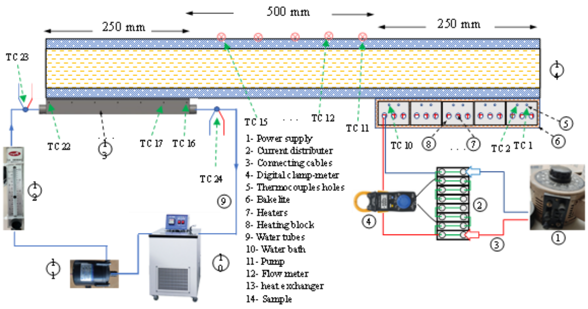

Figure 1. Experiment facility.

T-type thermocouples were well-calibrated at a controllable temperature in the water basin with RTD standard. All data were acquired using MX100 from Yokogawa, which was recorded when reaching a steady state for 20 mins. The test conditions are presented in Table 1.

Additionally, twenty-five thermocouples in five axial locations have been used to measure circumferential temperature, as specified in Figure 2.

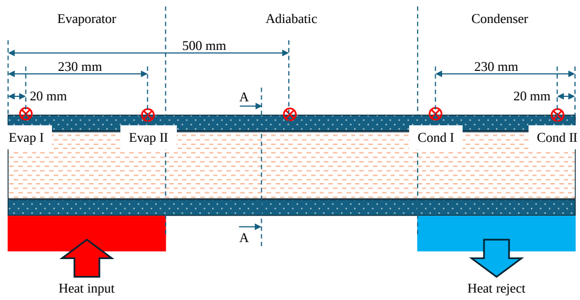

(a)

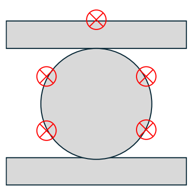

(b)

Figure 2. The circumferential measured temperature on heat pipe: (a) specify locations and (b) section A-A.

Table 1. Test conditions

Parameter	Condition
Heat load (W)	50 – 450
Water flow rate (LPM)	1
Water temperature (°C)	15 – 30
Heat pipe orientation	Horizontal
Working fluid	Ammonia

2.3. Data reduction

Heat was supplied by an AC power supply through the heating cartridges on the evaporator section. The voltage was measured using a power meter. Thus, the input power (P) can be computed from

$$P=IV \tag{1}$$

where V is the voltage (V), and I is the electrical current (A).

The heat transfer rate at the condenser section (Q_c) can be imposed as

$$Q_c = m_w C_{p,w}\left(T_{w,o} - T_{w,i}\right) \tag{2}$$

where m_w is the mass flow rate of the water (kg/s), $C_{p,w}$ is the specific heat capacity (J/kg·K), and T_w is the temperature of the water. The subscriptions, *i* and *o* denote the inlet and outlet of waterflow, respectively.

The overall thermal resistance of the heat pipe (R_{th}) can be determined based on the wall temperature difference between the evaporator and condenser sections to the heat input, as follows.

$$R_{th} = \frac{T_{evap} - T_{cond}}{P} \tag{3}$$

where T_{evap} and T_{cond} are the wall temperatures at the evaporator and condenser sections, respectively.

The inner wall temperature at the evaporator and condenser can be determined by reduction from the thermal resistance network. That is

$$T_{evap} = T_{TC,i} - \left(R_{hb} + R_c + R_p\right)P \tag{4}$$

where $T_{TC,i}$ is the axial measured temperature at a specific location, R_{hb} is the heating block resistance due to conduction, R_c is the contact resistance, and R_p is the resistance due to conduction through the pipe.

The same procedure is applied to compute the inner wall temperature at the condenser.

$$T_{cond} = T_{TC,i} + \left(R_{HX} + R_c + R_p\right)P \tag{5}$$

where R_{HX} is the resistance due to conduction in the cooling water heat exchanger.

3. Results and discussion

The current work experimentally examined the thermal performance of an aluminum/ammonia heat pipe with a rectangular smooth edge axial groove wick. The study investigates the key factors (heat load and cooling water temperature) that influence the performance of the heat pipe. Additionally, axial and circumferential temperature distributions along the heat pipe are evaluated and discussed in this section.

The validation and integrity of the experimental setup are represented using an energy balance between heat input and cooling water capacity. Our study revealed that the average deviation of the heat source and heat sink is approximately 6.42%, as shown in Figure 3. Hence, we can conclude that the experimental apparatus and setup are ready for testing.

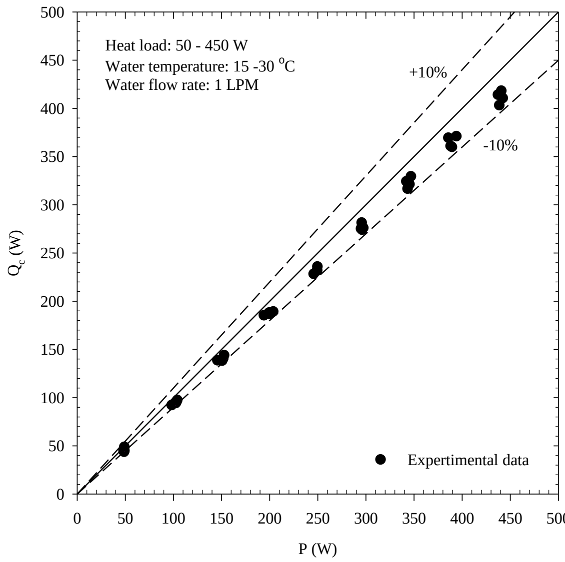

Figure 3. Energy balance between heat load and water cooling of the aluminum/ammonia heat pipe study.

3.1. Effect of heat load on overall thermal resistance

The variation of overall thermal resistance versus heat load with various water temperatures is presented in Figure 4(a). The figure shows that the overall thermal resistance (R_{th}) decreases with increasing heat load, irrespective of changes in water temperature. However, the thermal resistance will reduce until reaching a certain point; then, it faces a reversed trend. This study found that the thermal resistance is comparatively higher at a heat load (P) of 50 – 150 W but the thermal resistance reveals a considerable drop with the rise of thermal power. Note that the total thermal resistance of the heat pipe comprises evaporator part and condenser part. In the low heat flux regime, the evaporator resistance is larger due to evaporation is the main heat transfer mode. Subsequently, a further rise of supplied power leads to initialization of nucleate boiling and a more pronounced increase of heat transfer coefficient and an appreciable drop of total thermal resistance upon rising power. This can be made clear from the evaporator resistance from Fig. 5(b). Note that at a lower water temperature like 15 °C, the corresponding saturation temperature inside the heat pipe is lower, which impedes both evaporation and nucleate boiling. As a result, the total resistance and the resistance in evaporator is only slightly reduced with the supplied power (when P is less than 150 W). Note that a sharp decline of either thermal resistance or evaporator resistance occurs when the supplied power exceeds 150 W for T_{water} = 15 °C. This phenomenon is associated with the onset of nucleate boiling (ONB) where a sharp drop of wall superheat might occur near the ONB, thereby leading to a drop of thermal resistance at this supplied power. The phenomenon of sharp decline of thermal resistance at this supplied power becomes less pronounced when the water temperature is increased. This is because the boiling performance is improved, and the required wall superheat is thus reduced. Yet some of the existing correlations had clearly outlined that the wall superheat at ONB is reduced when the saturation temperature (pressure) is increased. For example, the correlation of Sato and Matsumura (1963) [16]

$$\Delta T_{w,ONB} = \left(T_w - T_{sat}\right)_{ONB} = \frac{8\sigma T_{sat} q_{ONB}}{k_l h_{lg} \rho_g} \qquad (6)$$

and the correlation of Kandlikar et al. (1997) [17]

$$\Delta T_{w,ONB} = \frac{8.8\sigma T_{sat} q_{ONB}}{k_l h_{lg} \rho_g} \qquad (7)$$

As a result, the ONB is lowered when the water temperature is raised, and the sharp decline phenomenon of thermal resistance is eased.

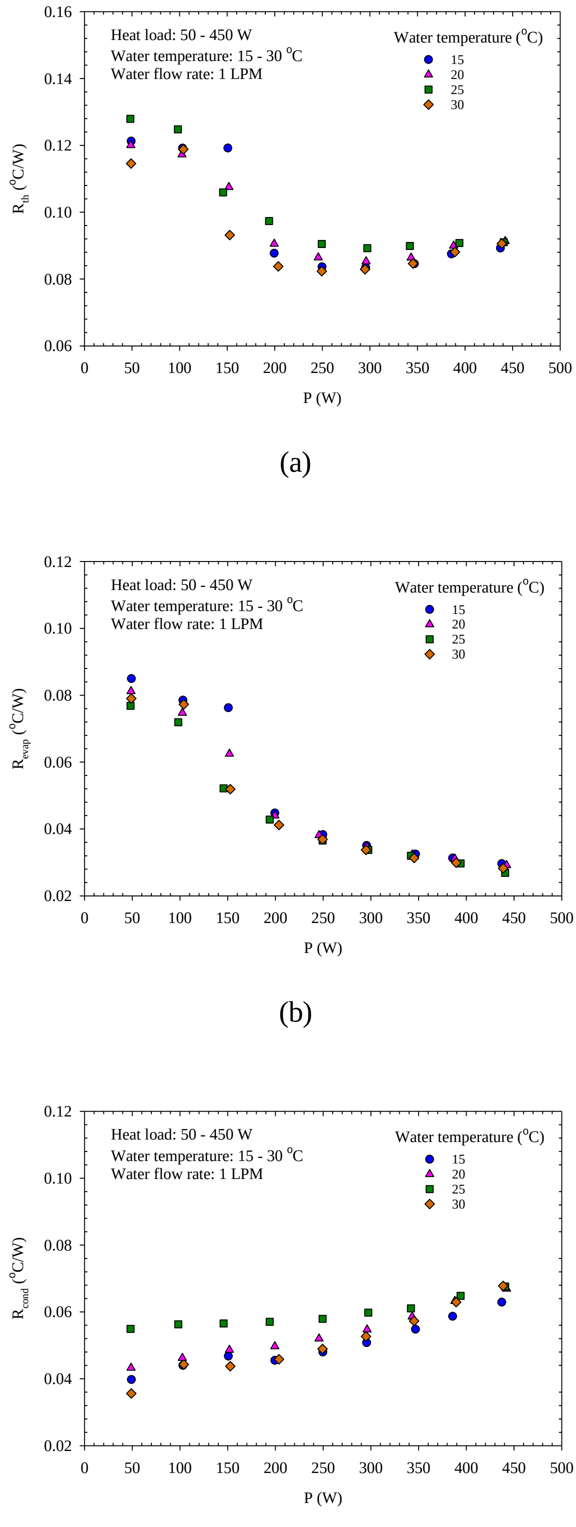

Figure 4. Variation of overall thermal resistance with various cooling water temperatures for (a) total thermal resistance; (b) evaporator resistance; and (c) condenser resistance.

However, it should be mentioned that the condenser heat transfer coefficient deteriorated with the rise in thermal power because a higher pressure occurs. This can be made clear from Fig. 5(c) where a consistent rise of condensation thermal resistance irrespective of water temperature. Also, the higher the water temperature is, the higher the thermal resistance becomes. The results are in line with general understanding of condensation process where high pressure impairs the condensation HTC. Yet, there is no sharp rise of condensation resistance. This is associated with the nature of condensation. This also helps to explain a threshold (minimum) thermal resistance prevails at a certain supplied power. It is found that the highest water temperature (30°) results in the lowest thermal resistance. At a higher pressure, a higher boiling HTC prevails. Again, the influence of water temperature on thermal resistance is less pronounced with further rise of supplied power due to the competing effects amid evaporator and condenser.

The minimum thermal resistance is obtained at a heat load near 250 W; however, the thermal resistance slightly increases after this point. Therefore, it can be identified that the heat pipe operates most efficiently at P = 250 W with an overall thermal resistance of 0.0823 °C/W. With the rise of heat load beyond this optimal range (P > 250 W). Yet, as depicted in Fig. 5(b) and 5(c), the rise in condensation resistance offset the decline of evaporator resistance, hence the overall thermal resistance is slightly rise after P > 250 W. It is also interesting to know that the effect of water temperature on the thermal resistance becomes less pronounced when the power is increased. Note that the pressure rise inside the heat pipe arises from the rise of input power and the rise of coolant water temperature. Apparently, the effect of input power far exceeds that of increase of water temperature, thereby no detectable difference in thermal resistance subject to water temperature.

3.2. Effect of cooling water temperature on overall thermal resistance

Typically, the cooling temperature at the condenser section significantly impacts the overall thermal resistance. Figure 5a exhibits a variation in the temperature difference between the evaporator and adiabatic sections. The plots show that the temperature difference between the evaporator and the adiabatic sections generally increases with increasing heat load. This is because as more heat is applied to the evaporator, the evaporator temperature rises, while the adiabatic section (which should experience minimal heat input) maintains a relatively lower temperature. At lower cooling water temperatures (15 °C and 20 °C), the evaporator needs to operate at a higher temperature to maintain efficient heat transfer, resulting in a larger temperature difference between the evaporator and the adiabatic sections. This is especially pronounced at higher heat loads, where thermal resistance is higher. At higher cooling water temperatures (25 °C and 30 °C), the temperature difference between the evaporator and adiabatic sections is generally lower because the system operates with a smaller overall temperature gradient and lower thermal resistance. The heat pipe appears to operate more efficiently in this range, resulting in more uniform temperatures across the system.

Figure 5b plots a variation in the temperature difference between the adiabatic and condenser sections. At a lower cooling temperature, the temperature difference between the vapor in the heat pipe and the cooling water increases. This larger temperature difference enhances the heat transfer rate from the vapor to the cooling water, promoting more efficient condensation. Efficient condensation reduces thermal resistance by allowing more heat to be rejected from the system with less resistance. On the contrary, if the cooling water temperature at the condenser is higher, the temperature difference between the vapor and the cooling water decreases. This reduced temperature gradient slows condensation, leading to less efficient heat transfer. As a result, the overall thermal resistance increases because the heat pipe becomes less effective at rejecting heat at the condenser. Both behaviors are represented in the plotted cooling water temperatures of 15 °C and 20 °C.

However, it is noteworthy that the lowest overall thermal resistance occurs at a cooling water temperature of 30 °C, while the highest one is obtained at 25 °C, as illustrated in Figure 4. The thermal resistance behaviors may be associated with the vapor pressure inside the heat pipe which is higher at a cooling water of 30 °C. This could enhance the evaporation process because of higher vapor pressure that promotes nucleate boiling process. The reduced surface tension and viscosity at higher temperatures might also improve the liquid return through the wick structure, reducing the possible dry-out and ensuring continuous operation. This improved liquidity and yielded a lower thermal resistance. Conversely, at 25 °C cooling water temperature, the boiling heat transfer is inferior and might be less favorable, leading to a less efficient heat transfer performance. The fact that thermal resistance depends on the balance of the various heat transfer processes (evaporation, condensation, and liquid return) in various operating conditions helps to explain the aforementioned result.

In the overview, the comparison results indicate that the overall thermal resistance at a cooling water temperature of 30 °C is lower than 0.29 – 27.95% (for T_w = 15 °C), 0.79 – 15.41% (for T_w = 20 °C), and 0.44 – 16.19% (for T_w = 25 °C).

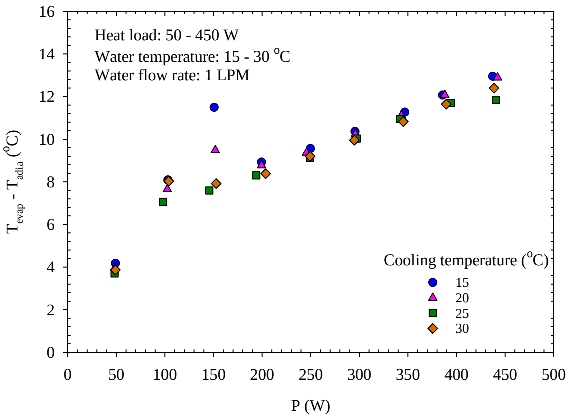

(a)

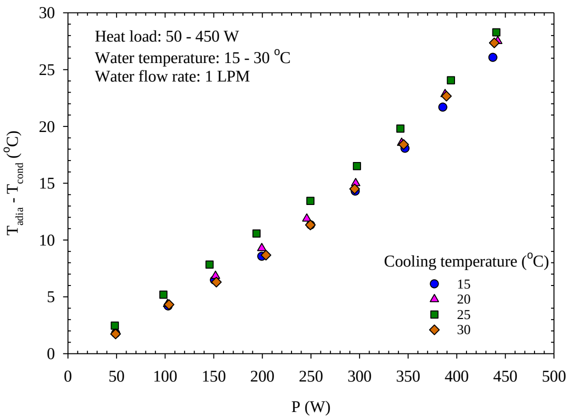

(b)

Figure 5. Variation of temperature difference at (a) evaporator and (b) condenser.

3.3. Axial temperature distribution

The cooling water temperature at the condenser section of the heat pipe directly influences the temperature at the evaporator section. The axial temperature distribution along the heat pipe is depicted in Figure 6. The results indicate that the temperature varies subject to the cooling water temperature; that is, the rise of the cooling water temperature elevates the temperature alongside the heat pipe. However, the temperature difference between the evaporator and condenser sections creates a driving force for heat transfer within the heat pipe. When the cooling water temperature at the condenser is low, the temperature difference between the evaporator and condenser is increased which implies a lower effective thermal conductivity and an inferior heat transfer performance. Conversely, the temperature difference between the evaporator and condenser decreases when the cooling water temperature is higher. This implicates a higher effective thermal conductivity and a better heat transport efficiency.

With a lower cooling water temperature, the vapor in the heat pipe condenses more effectively in the condenser section. Efficient condensation reduces the vapor pressure in the condenser, promoting better vapor flow from the evaporator to the condenser. This efficient vapor flow can lower the evaporator temperature as the heat is removed more effectively. As heat is more effectively rejected in the condenser, the evaporator section can maintain a lower temperature for a given heat input, leading to more efficient operation. When the cooling water temperature increases, the vapor in the condenser section might not condense as efficiently. This can lead to higher vapor pressure in the condenser, which reduces the pressure differential between the evaporator and condenser. As a result, the vapor flow from the evaporator to the condenser becomes less efficient. Due to less efficient heat rejection, the evaporator section might have to operate at a higher temperature to maintain the same heat load. The higher evaporator temperature compensates for the reduced temperature gradient and less efficient condensation process. Moreover, lower cooling water temperatures ensure more effective condensation and, thus, more effective liquid return, keeping the evaporator temperature lower. If the cooling water temperature is too high, the liquid return to the evaporator might be insufficient, leading to dry-out conditions in the evaporator. This lack of liquid can cause the evaporator temperature to rise sharply, further increasing the temperature and thermal resistance. However, maintaining an appropriate cooling water temperature at the condenser is crucial for controlling the evaporator temperature and ensuring the efficient operation of a heat pipe system.

As demonstrated in Figure 7, one interesting observation is the minimum temperature difference between the evaporator and condenser sections at a cooling water temperature of 30 °C. In contrast, the maximum temperature difference in evaporator and condenser yields at a water temperature of 25 °C. Again, this can also be clarified from the previous discussion according to overall thermal resistance. The overall thermal resistance is lower at 30 °C. This lower thermal resistance correlates with the lower temperature difference because less resistance in the system means heat is transferred more effectively from the evaporator to the condenser, resulting in a smaller temperature difference. Furthermore, the working fluid properties (such as viscosity and surface tension) might be optimal for the wick structure's capillary action. This ensures efficient liquid return and helps maintain a more uniform temperature distribution between the evaporator and condenser, contributing to a lower temperature difference. The heat pipe is probably designed to operate most efficiently within a certain temperature range. It can be implied that the cooling water temperature of 30 °C is within or near the optimal operating range for this heat pipe, where the evaporation and condensation processes are balanced to minimize temperature differences.

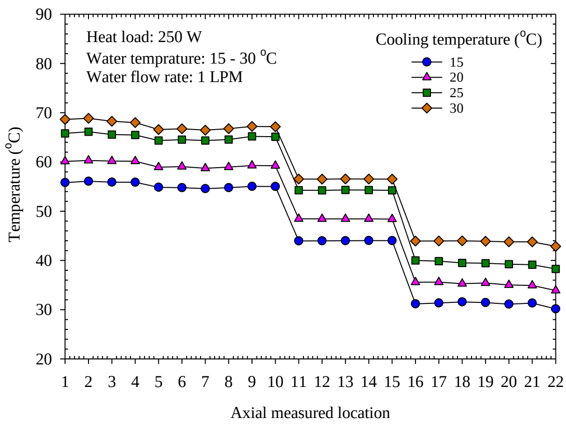

Figure 6. Temperature distribution along an aluminum/ammonia heat pipe axis.

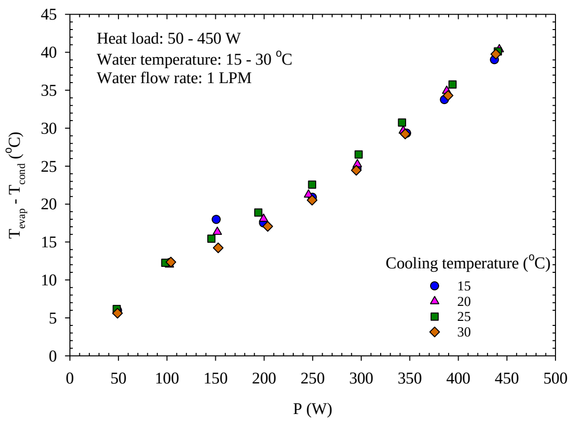

Figure 7. Variation of the temperature difference between evaporator and condenser sections.

Furthermore, the deviation in temperature differences between the evaporator and condenser sections accounts for 0.33 – 26.30% (for T_w = 15 °C), 1.46 – 14.76% (for T_w = 20 °C), and 0.92 – 10.64% (for T_w = 25 °C) higher than a cooling water temperature of 30 °C.

3.4. Circumferential temperature distribution

Results show that while the circumferential temperature drops slightly to the top of the heat pipe in the evaporator (see Figure 8a), yet it increases more appreciably in the condenser. Since the heat source location is at the bottom of the heat pipe, the former might be due to the heater location; otherwise, the circumferential temperature is almost uniform. This result is in accordance with Faghri [18], who proved that either circumferential heating or applying a heat block does not affect the axial temperature. The interesting finding in this work is that although the wick structure is grooved—so liquid tends to accumulate at the bottom due to gravity—the circumferential temperature is almost uniform. This might be explained since a large portion of the evaporator cross-section is occupied by vapor.

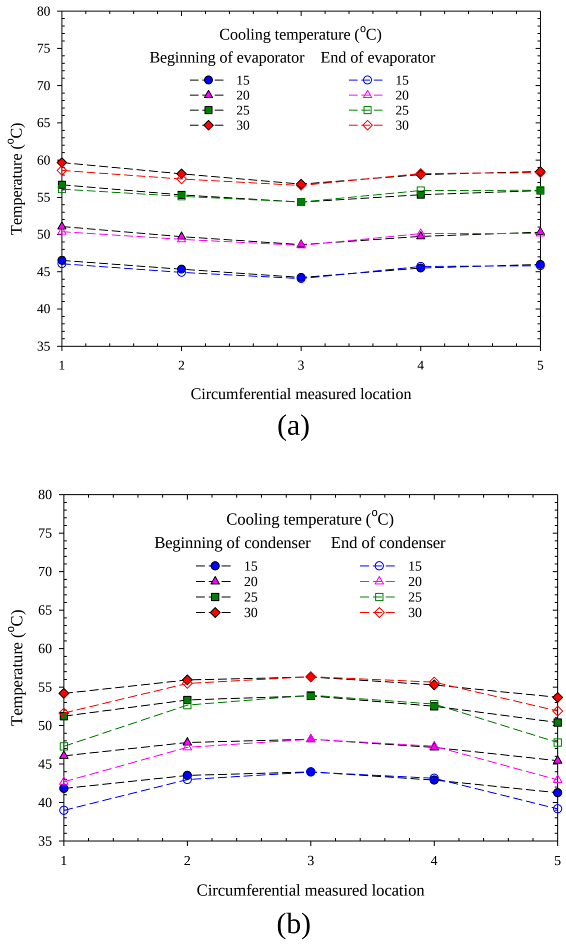

Figure 8. Circumferential temperature change in (a) evaporator and (b) condenser.

For the condenser (see Figure 8b), the thermocouple at the top shows a higher temperature compared to the side thermocouples. This is due to the flow pattern of stratified flow prevails in the condenser regime.

Conclusions

The experimental study focused on an aluminum/ammonia heat pipe with an axial groove wick. The heat pipe was made from an aluminum alloy with outer and inner diameters of 17.86 mm and 15.44 mm, respectively. It consisted of an evaporator and condenser with lengths of 250 mm each and an adiabatic section of 500 mm. The study investigated test conditions under a heat load ranging from 50 W to 450 W, a cooling water temperature from 15 °C to 30°C, and a water flow rate of 1 LPM. The heat pipe was placed horizontally for all test conditions. Ammonia was used as the working fluid with a fixed filling ratio of around 27%. The study examined the effects of heat load and cooling water temperature and investigated the axial and circumferential temperature distributions along the heat pipe. The significant findings from the tests are summarized as follows:

1. The overall thermal resistance decreases with increasing heat load, regardless of changes in water temperature. The minimum overall thermal resistance is obtained from a heat load of 250 W and a cooling water temperature of 30 °C. This can be considered the optimal point in the test, resulting in an overall thermal resistance of 0.0823 °C/W.
2. At various cooling water temperatures, the overall thermal resistance at a cooling water temperature of 30°C is lower by 0.29 – 27.95% (for T_w = 15 °C), 0.79 – 15.41% (for T_w = 20 °C), and 0.44 – 16.19% (for T_w = 25 °C) compared to the baseline.
3. The temperature along the axis of the heat pipe changes based on the cooling water temperature. Specifically, an increase in the cooling water temperature results in a rise in the temperature along the heat pipe. The difference in temperature between the evaporator and condenser sections ranges from 0.33 – 26.30% (at T_w = 15 °C), 1.46 – 14.76% (at T_w = 20 °C), and 0.92 – 10.64% (at T_w = 25 °C) higher than those of the 30 °C cooling water temperature.
4. The circumferential temperature drops slightly to the top of the heat pipe in the evaporator. It has been proven that heating around the outside or a heat block does not affect the axial temperature.
5. The circumferential temperature on the top of the condenser is higher than the side measuring. This is because of the stratified condensing regime. Based on the temperature gradient, it can be inferred that a considerable portion of the condenser cross-section is filled with liquid.

ACKNOWLEDGEMENTS

The authors thank the Taiwan Space Agency, the National Science and Technology Council of Taiwan under the contract of 111-2221-E-A49-090-MY3 for providing financial support. The last author acknowledges KMUTT for providing a Distinguished Visiting Professorship during a short visit at Mechanical Engineering Department, KMUTT.

References

[1] R.S. Gaugler, Heat transfer device, U.S. Patent 2350348, 1944.
[2] L. Trefethen, On the surface tension pumping of liquids or a possible role of the candlewick in space exploration, G. E. Tech., Ser. No. 615 D114, 1962.
[3] T. Wyatt, Satellite temperature stabilization system. Early development of spacecraft heat pipes for temperature stabilization, U.S. Patent 3152774, 1963.
[4] G.M. Grover, T.P. Cotter, G.F. Erickson, Structures of Very High Thermal Conductance. Journal of Applied Physics, (1964). 35: p. 1990–1991.
[5] M.B.H. Mantelli, Thermosyphons and heat pipes: Theory and applications. Springer, 2021.
[6] C.-C. Wang, Heat transfer design, 2007.
[7] P.C. Stephan, C.A. Busse, Analysis of the heat transfer coefficient of grooved heat pipe evaporator walls. International Journal of Heat and Mass Transfer, 1992. 35: p. 383–391.
[8] M.S. El-Genk, H. Lianmin, An experimental investigation of the transient response of a water heat pipe. International Journal of Heat and Mass Transfer, 1993. 36: p. 3823–3830.
[9] A. Wei, X. Ren, S. Lin, X. Zhang, CFD analysis on flow and heat transfer mechanism of a microchannel Ω-shape heat pipe under zero gravity condition.

International Journal of Heat and Mass Transfer, 2020. 163: p. 120448.

[10] A.N. Desai, V.K. Singh, R.N. Patel, Effect of Geometrical Parameters on the Thermal Performance of Ammonia-Based Trapezoidal-Shaped Axial Grooved Heat Pipe. Journal of Heat Transfer, 2019. 141.

[11] C. Enke, J. Bertoldo Júnior, V. Vlassov, Transient response of an axially-grooved aluminum-ammonia heat pipe with the presence of non-condensable gas. Applied Thermal Engineering, 2021. 183: p. 116135.

[12] G. Huang, W. Li, G. Zhong, A.A. Abdulshaheed, C. Li, Optimizing L-shaped heat pipes with partially-hybrid mesh-groove wicking structures. International Journal of Heat and Mass Transfer, 2021. 170: p. 120926.

[13] S.-C. Wong, M.-S. Deng, M.-C. Liu, Characterization of composite mesh-groove wick and its performance in a visualizable flat-plate heat pipe. International Journal of Heat and Mass Transfer, 2022. 184: p. 122259.

[14] A. Gomaa, W. Ahmed Rady, A.Z. Youssef, A.M. Elsaid, Thermal performance of heat pipe at different internal groove ratios and working fluids: An experimental investigation. Thermal Science and Engineering Progress, 2023. 41: p. 101827.

[15] S. Mishkhas, M.-H. Chen, T.-H. Yu, Y.-T. Chen, J.-S. Wu, C.-C. Wang, An Experimental Study of a Grooved Aluminum-Ammonia Heat Pipe: The Effect of Tilting and Non-uniform Heat Transfer on Thermal Behavior, Applied Thermal Engineering 252 (2024) 123714.

[16] T. Sato, H. Matsumura, On the Conditions of Incipient Subcooled-Boiling with Forced Convection, Bulletin of JSME 7 (1964) 392–398.

[17] S.G. Kandlikar, V. Mizo, M. Cartwright, E. Ikenze, Bubble nucleation and growth characteristics in subcooled flow boiling of water, in: 1997.

[18] A. Faghri, Heat pipe science and technology, Taylor & Francis, 1995.

Paper ID 090(S2B)

Fabrication Procedures and Experimental Study of a Sodium Rod-Plate Heat Pipe

Elvis Falcão de Araújo[1,2*], Alice Toledo de Castro[1], Juan Pablo Flórez Mera[1,2], Luis H.R. Cisterna[3] and Marcia Barbosa Henriques Mantelli[1]

[1]*Heat Pipe Laboratory, Federal University of Santa Catarina, Florianópolis, Brazil*
[2]*Institute for Advanced Studies, Department of Aerospace Science and Technology, São José dos Campos, Brazil*
[3] *School of Mechanical Engineering, Industrial University of Santander, Bucaramanga, Colombia*
[4]*University of Tarapacá, Arica, Chile*
**Corresponding author email address: elvis.araujo@labtucal.ufsc.br*

Abstract

Heat pipe-cooled micro reactors are currently one of the best alternatives for power and propulsion supply in deep space missions and interplanetary outposts. The core of a micro reactor operates in the range between 800 K and 1400 K, so liquid metals are a feasible choice for heat pipe working fluid. The rod-plate technology is a concept inspired in wire-plate heat pipes, where an array of individual heat pipes is formed by sandwiching a set of parallel-disposed bars between flat plates. This work is a complete report on the design, fabrication and testing of rod-plate AISI 316L/sodium heat pipes developed for space applications. An on-site developed charging system was used to fill the heat pipe with sodium. The device was tested in a horizontal orientation. Heat was applied to the evaporator by an induction furnace and was released from the condenser by radiation and natural convection, as this section remained exposed to the environment. Although with a lower temperature gradient in the central channel, the device could successfully reach startup at 666 °C vapor temperature. At maximum heat input conditions, the device reached a 1037 W heat transfer rate and a 0.112 K/W thermal resistance.

Keywords: Micro reactors; sodium; rod-plate; induction; radiation; natural convection; thermal performance.

1. Introduction

Space exploration is a critical matter for human development in the third millennium. There are many reasons for investing in space technology, such as the limited resources of planet Earth and the possibility of its collision with space bodies. It is paramount for humanity to overcome planetary restrictions and to be able to establish extraterrestrial occupations. Therefore, space agencies and governments are constantly conducting research on deep space missions, asteroid mining, deflection of threatening space objects, and manned bases on Mars and the Moon. Science missions are also continuously being deployed to increase mankind's knowledge about space [1].

One of the major cornerstones for the development of space technology is the availability for compact, abundant and reliable energy sources for power and propulsion. Among plausible options are chemical, solar, radioisotope, and nuclear reactors. However, the latter stands out due to the compact size and the high-power levels attainable for long lifetimes, with high reliability, low maintenance cost and independence of distance from the Sun.

Heat pipe-cooled reactors excel among nuclear designs due to several advantages, e.g., strong negative reactivity feedback, robustness and passive heat removal, with the absence of a pumped primary cooling loop, tubing, pipe valves, etc., decreasing the overall system weight and size [2]. As usually several heat pipes are used in parallel, the system is also inherently redundant, which is crucial for space applications. If a certain number of heat pipes fail, the adjacent ones compensate for it and transport the remnant heat.

According to Bejan & Kraus [3], heat pipe operation is feasible at temperatures between the triple and the critical points of the utilized working fluid. As the temperature inside the reactor vessel ranges between 800 K and 1400 K, liquid metals are the best working fluid choice. Various theoretical and experimental studies have been devoted to the development of liquid metal heat pipes and to the understanding of the physics involved [4]-[6]. Most of the literature studies are regarded to the "traditional" cylindrical containers with machined grooves or porous media, which are usually attached to the device's inner walls. Therefore, research regarding the development of heat pipes for non-conventional applications is mostly welcome.

Araújo et al. [7] introduced the rod-plate heat pipe concept, i.e., a flat device composed by an arrangement of bars sandwiched between flat plates. Both bars and plates were made of stainless steel (AISI) 316-L. The sharp corners between plates and bars formed channels that worked as artery porous media, accommodating the liquid phase of the working fluid. Due to fluid-solid surface tension property, the liquid tended to accrue in these sharp corners. Consequently, the working fluid was pumped from the condenser to the evaporator due to the difference between the meniscus radii in these sections. Araújo et al. [7] explored the concept of mini heat pipes [8]-[10], which usually operates in intermediate temperatures, to larger devices, 500 mm long. Figure 1 sketches the rod-plate heat pipe, while Figure 2 and Figure 3 show section views with relevant dimensions.

The studied heat pipe was comprised of two 2-mm thick cap plates, two 7.94-mm diameter rods, four 2-mm thick intermediate plates (or lateral frames), three layers of #70 screen mesh, which were spot-welded to both cap plates, and a filling umbilical tube. Screen meshes were installed between the internal wall and the bar tips in the evaporator region, covering the internal surfaces of a chamber (see Figure 1). By capillarity, working fluid was distributed to all the channels. The filling umbilical tube was located by the evaporator close to the mesh, to ensure that the working fluid would wet the screen before being spread to the channels. There were eight grooves formed by sharp corners (see Figure 3): four in the central channel (between bars) and two in each lateral channel (between bar and lateral frame).

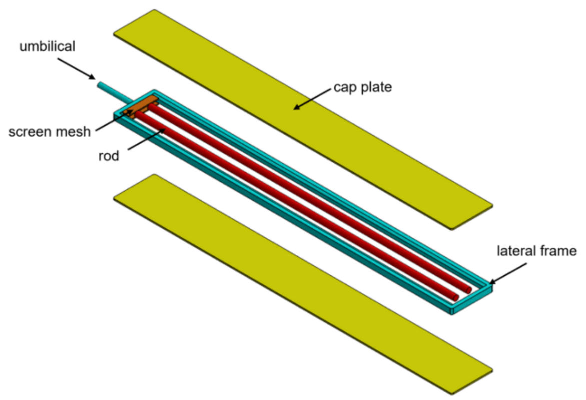

Figure 1. Rod-plate heat pipe assembly layout.

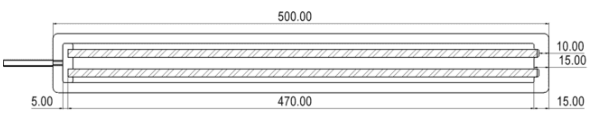

Figure 2. Rod-plate heat pipe top view with dimension in millimeters.

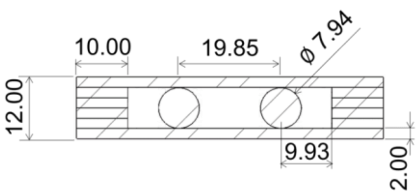

Figure 3. Rod-plate heat pipe cross-section view with dimension in millimeters.

The device developed by Araújo et al. [7] was modelled, built and tested for deionized water as the working fluid. It presented a minimum thermal resistance of 0.123 K/W, for 171.57 W of transported heat, for a controlled temperature thermal bath that removed heat from the condenser. They showed that the maximum heat transfer per groove was of 22.18 W, proving the feasibility of the rod-plate technology for moderate-temperature applications (20 – 200 ºC).

This paper is a follow-up of the experimental study of Araújo et al. [7] where, instead of water, molten sodium (Na) was the working fluid, to operate in the high temperature range of 800 K to 1400 K. This manuscript aims to assess the operation of a sodium rod-plate heat pipe at transient conditions and evaluate its main steady-state performance parameters, such as thermal resistance and heat transfer rate. The device was tested in horizontal orientation, which better represents space operation conditions in laboratory. The evaporator was heated by an induction furnace, while the condenser remained exposed to the environment, rejecting heat by radiation and natural convection.

2. Methodology

2.1. Heat Pipe Production

Details of manufacturing procedures can be found in Araújo et al. [7], so the present paper focuses on the charging process for liquid metal working fluids. Sodium reacts violently with water, either pure or mixed in atmospheric air. This exothermic reaction can cause explosions and compromise operator safety. Moreover, it produces sodium hydroxide (NaOH), which is deposited on the surface of metallic sodium. As shown in Table 1, the melting and boiling temperatures of sodium hydroxide are roughly 1.6 and 3.3 times that of metallic sodium. Hence, the presence of the former in the device might cause evaporation overheating during heat pipe startup. Moreover, during tests, working fluid impurities or non-condensable gases are gradually pushed to the condenser end, partially blocking the condenser, and so a poor heat exchange region (cold tip) is formed, increasing the temperature gradient and deteriorating thermal performance.

Table 1. Melting and boiling temperatures of Na and NaOH, considering atmospheric pressure.

Substance	$T_{melting}$ [K]	$T_{boiling}$ [K]
Na	370.95	1155.95
NaOH	591.15	1661.15

For the aforementioned reasons, the exposure of sodium direct to the environment must be minimized during the charging process. A special charging apparatus was designed inspired in the one developed by Cisterna et al. [11], with features that favored crew safety and working fluid purity. It was formerly used by Castro [12] to charge loop-type sodium thermosyphons. Figure 4 shows a picture of the charging system. Most of the components were contained within a 1975 mm x 750 mm x 800 mm showcase, namely, the charging bench. The parts inside it are referred to as the fundamental components. Composed the setup: a CR1000 Datalogger Campbell® Scientific data acquisition system (DAS) with OMEGA® K-type thermocouples, a computer, Proportional-Integral-Derivate (PID) controllers, an Edwards nXDS15iC dry scroll pump, an argon tank with an analog pressure regulator, and silicone hose connections. The charging bench served both to hold the fundamental components in place and to protect the crew from direct contact with them. Its front cover could be opened and was partially made of acrylic, allowing one to visualize the system from outside. It included a grooved hole that was used to indirectly manipulate a ball valve, one of the fundamental components, utilizing a valve handle extender.

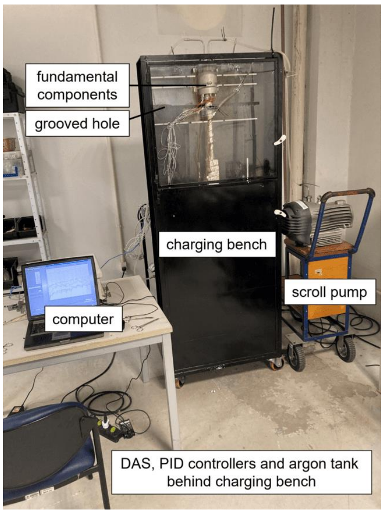

Figure 4. Fully assembled charging system.

Figure 5 sketches the utilized connections made with silicone hoses. All metallic parts represented in this figure were made of stainless steel. Solid sodium was inserted into a reservoir, which had a top cap with two curved tubes, one connected to the pump and the other the argon tank. The reservoir remained sealed by a flange and a Teflon O-ring. Inside it, the sodium stones stayed over a grid, with a filter just below it. Both components were used to retain sodium hydroxide and prevent it from entering the heat pipe. An upside-down Y-tube was used with the upper end linked to the reservoir by a Swagelok® SS-43GS8 ball valve, while the second and third ends were coupled to the scroll pump and the heat pipe, respectively.

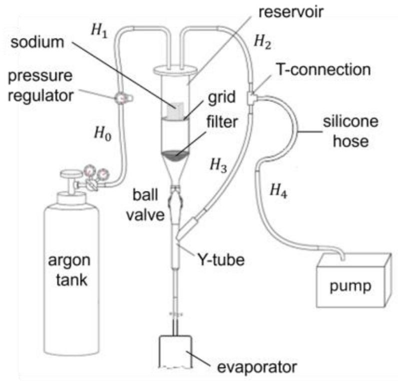

Figure 5. Charging system connections schematic.

Sodium was melted by a special heating system before entering the heat pipe. Figure 6 shows the fundamental components of this heating setup, where part of the components of Figure 5 were inserted. The reservoir was surrounded by two half-cylinder-shaped aluminum blocks with embedded 440 W - 220 V cartridge resistances. This arrangement was responsible for melting the sodium pieces inside the reservoir. A 1040 W OMEGALUX FGH102-100 strip resistance was wound around the end of the reservoir, ball valve, Y-tube, fill stem and heat pipe evaporator, to prevent sodium from refreezing during the charging process. All the fundamental components were fixed on the back of the charging bench with threaded bolts, nuts and washers. Support plates were used to hold the heat pipe in position. To ensure leak tightness, the heat pipe umbilical was placed in direct contact with Y-tube's bottom end, and metal clampers were applied at the silicone connections.

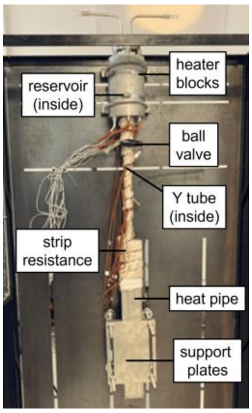

Figure 6. Fundamental components.

Temperature was controlled and monitored all along the sodium flow path by OMEGA® K-type thermocouples. Figure 7 shows temperature measurement locations along the fundamental components, where TC represents control thermocouples and T stands for monitoring thermocouples. Five temperature sensors were coupled to the PID controllers that regulated the power applied to the resistances, located at the reservoir, valve, Y-tube, beginning of fill stem and heat pipe evaporator, and were used to maintain these temperatures between 415 K and 495 K. Another fifteen thermocouples were attached to the charging components and coupled to the data acquisition system. They were employed to monitor the temperature distribution.

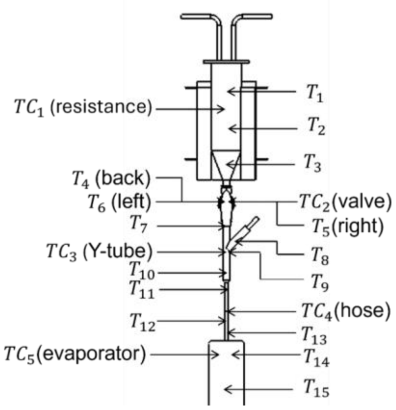

Figure 7. Thermocouple positions in charging system.

All the weight measurements were performed on a Marte® AS550C precision balance. The empty heat pipe was weighted ten times, and the value of 2308.73 ± 0.24 g was obtained. It was then fixed on the charging bench and coupled to the Y-tube. To remove humidity, with the valve opened, the system was simultaneously evacuated and heated to > 100 °C by turning the pump and controllers on. After 30 minutes, they were turned off and the system was pressurized with 1 atm of argon to facilitate the opening of the reservoir. The sodium stones were removed from a pot with kerosene, an inert substance that prevents sodium-water reaction. They were then cleaned, and the external layer of NaOH was cut with a hand knife. The pure sodium pieces were then weighted. After the desired mass was obtained, they were introduced into the reservoir.

Two sequential argon pressurizations followed by evacuations were performed to create a controlled environment with < 10 ppm air concentration inside the charger. With the ball valve closed, the reservoir was subsequently pressurized with 1 bar of argon, while vacuum was created in the Y-tube and heat pipe, generating a pressure difference between these two chambers. With hoses H_1, H_2 and H_4 closed (see Figure 5), the resistances were turned on, causing the sodium to melt. After 20 minutes, when the sodium was entirely liquid, the ball valve was opened. The sodium flew to the heat pipe due to the gravity action and the pressure difference between the reservoir and the Y-tube. The desired charging mass was defined based on the theoretical model presented by Araújo et al. [7] for 1 kW heat transfer rate, 1000 K operation temperature and no heat losses. The obtained optimum charging mass was 12.59 g. However, 23.38 ± 0.03 g was inserted into the charger, based on former experiments [12], with only 10.62 ± 0.30 g entering in the device.

The resistances were then turned off. After the system cooled down to room temperature, the heat pipe was detached from the charger, with a Kelly clamp closing its hose, and linked to the scroll pump to purge argon and sodium vapor. A filter with a steel sponge was applied between the heat pipe and the pump to prevent sodium vapor and solid particles from entering the latter and damaging it. At this stage, a vacuum level of 5.0 × 10^{-2} was attained. To seal the device, the closure methodology devised by Cisterna [11] was applied. Figure 8 shows the resulting heat pipe.

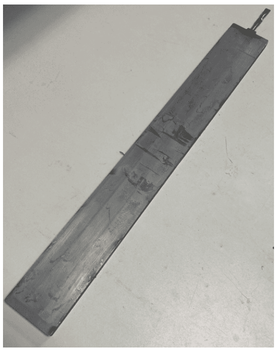

Figure 8. Produced rod-plate heat pipe.

2.2. Test Bench

Figure 9 shows the test bench used for sodium rod-plate heat pipe investigation, featuring the following main components: a Eutothermo® induction furnace EURO 25 kW, coupled to a copper coil, the heat pipe itself in horizontal orientation, a layer of fiberglass blanket, twenty-five OMEGA® K-type thermocouples with silica fiber insulation, connected to a CR1000 Datalogger Campbell Scientific data acquisition system, and a S65 FLIR® thermographic camera. The evaporator remained inside the coil with an imposed electrical current, with a plastic mold applied between the two, for electrical insulation. The fiberglass blanket cover was 10 cm thick and thermally insulated the evaporator and the adiabatic section of the heat pipe. The condenser was kept exposed to the environment to reject heat by natural convection and radiation. The lengths of the evaporator, adiabatic section and condenser were, respectively, 100, 300 and 100 mm.

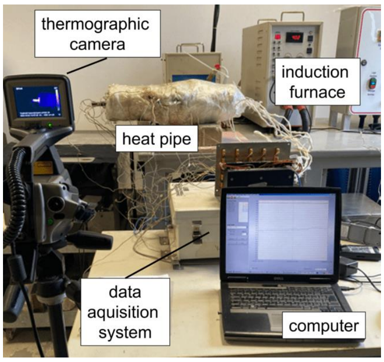

Figure 9. Experimental test bench.

Twenty-one (T_1 to T_{21}) thermocouples were spot-welded to the centerlines of the top, lateral and bottom surfaces of the heat pipe. This setup allows the assessments regarding the effect of gravity and channel geometry on thermal performance. Figure 10 shows the temperature measurement positions along the heat pipe.

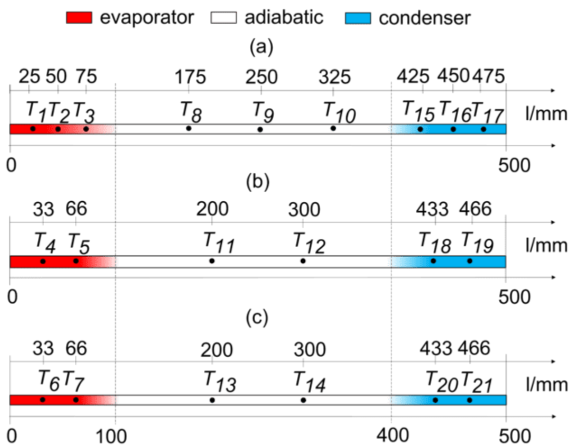

Figure 10. Heat pipe temperature measurement points. (a) Top face. (b) Lateral face. (c) Bottom face.

Thermocouple T_{22} was installed at the lateral wall opposite to that of thermocouples T_{18} and T_{19} and in the middle of the condenser (x = 450 mm). The infrared (IR) thermographic camera was placed at approximately 1 m from the test bench, to avoid damages ensued by the high experimental temperatures, and pointed to thermocouple T_{22}. For each experimental testing in steady-state conditions, the emissivity assumed by the camera was calibrated, so the temperatures indicated by the IR camera and thermocouple T_{22} were as close as possible. Thermocouples T_{23} and T_{24} were used to estimate the heat losses and were installed at the inner and outer walls of the thermal insulation, in the middle of the adiabatic section (x = 250 mm). Thermocouple T_{25} measured the environment temperature.

2.3. Experimental Procedure

A test utilizing a heat pipe with no working fluid, labeled as test E_0, was performed before charging the device. The results of this experiment can be confronted with the ones for a charged heat pipe to evaluate the performance improvement as it transitions from a hollow container, that transfers heat only by conduction, to a superconductor. To avoid excessive thermal stresses to the container, a lower heat load, of 24.85 W, was applied to the evaporator utilizing aluminum blocks with embedded cartridges resistances, which were fed by a Heinziger® PTN 125-10 power source.

The experiments with sodium heat pipes began by setting inductor current to a minimum level. As the startup proceeded, temperatures gradually increased up to a point where they didn't vary more than 10 °C within a 10 min period, when the experiment was assumed to be at a steady state. Inductor current was then increased, and the process repeated until the maximum current level was reached. The used current levels were 260 A, 400 A, 600 A, 800 A and 1000 A. Table 2 compiles the test matrix for the present study.

Table 2. Heat pipe experimental test matrix.

Test	I [A]
E_1	260
E_2	400
E_3	600
E_4	800
E_5	1000

2.4. Data Reduction

In liquid-metal heat pipes, a cold tip can result from either non-condensable gas pushed to the condenser end or from free molecular vapor flow, when the condenser vapor is rarefied, and the continuum hypothesis fails. Tournier and El-Genk [13] defines three flow regimes based on molecular mean free path λ_p: free molecular flow for Kn > 1.00, transition flow for 0.01 < Kn < 1.00 and continuum or viscous flow for Kn < 0.01, where Kn is the Knudsen number, expressed as:

$$Kn = \frac{\lambda_p}{D_v} \quad (1)$$

with D_v the diameter of the vapor passage. According to Cao and Faghri [14], the following equation can be used to determine the transition temperature T_t for a given Kundsen number:

$$\ln\left(\frac{T_t \rho_v \bar{R}}{P_0}\right) + \frac{h_{fg}}{\bar{R}}\left(\frac{1}{T_t} - \frac{1}{T_0}\right) \quad (2)$$

where ρ_v is the vapor density, T_0 and P_0 are, respectively, reference temperature and pressure values, $\bar{R}$ is the mass-specific gas constant and h_{fg} is the latent heat of vaporization. The vapor density, in terms of the Knudsen number, is:

$$\rho_v = \frac{1.051\kappa}{\sqrt{2}\pi\sigma_d^2 \bar{R} D_v Kn} \quad (3)$$

with κ the Boltzamnn constant and σ_d the collision distance between molecules which, for sodium, can be assumed 2.38×10^{-10} m [15]. The vapor diameter of 8.32 mm was obtained through the meniscus geometry model devised by Araújo et al. [7], assuming an average radius-of-meniscus between the maximum and minimum values: $R/(\cos\alpha - \sin\alpha)$ and 0.01 mm, respectively, with R = 3.97 mm as the rod radius and α = 10° the contact angle. The transition temperatures, determined by equation (2), are 295 °C and 464 °C for Knudsen numbers of 1.00 and 0.01, respectively.

Emissivity and temperature measurements were used to evaluate evaporator heat intake Q_e, evaporator heat flux q_e'', heat rejected by condenser Q_c, heat loss through insulation at the adiabatic section Q_a, and thermal resistance R_t. The temperature of a given heat pipe zone was the average of the measured values of all thermocouples inside it. The steady-state values were the average of the last 300 measurements. The heat loss Q_a was the parcel of the input heat Q_e that did not reach the condenser:

$$Q_e = Q_a + Q_c \quad (4)$$

The thermal resistance R_t was given by:

$$R_t = \frac{\bar{T}_e - \bar{T}_c}{Q_c} \quad (5)$$

where $\bar{T}_e$ and $\bar{T}_c$ were the evaporator and condenser temperatures, respectively. The adiabatic section temperature $\bar{T}_a$ is estimated as the vapor temperature at a given experimental condition.

Figure 11 shows dimensions used for condenser heat transfer calculation, which assumed the values: H = 12 mm, W = 59.7 mm, L_c = 100 mm, w_c = 19.85 mm and w_{tl} = 9.93 mm. The condenser area was divided into subregions for the calculation of the radiative Q_{rad} and natural convection Q_{nc} heat transfer rates. For the radiative losses, the condenser surface was split into top-central, lateral, bottom-central and tip regions, with dimensions of, respectively, $L_c \times w_c$, $L_c \times (2w_c + H)$, $L_c \times w_c$ and $W \times H$.

The top and bottom-central regions were equivalent to the areas of the condenser top and bottom faces comprehended between the rods. The lateral region included the remainder of the top and bottom faces, i.e., the fraction of the condenser surface under direct influence of the lateral channel. In the top-central, bottom-central and lateral subregions, the faces were discretized into 5 mm-long elemental areas. The tip surface was subdivided into elemental areas under effect of the central and lateral channels, with dimensions of, respectively, $w_c \times H$ and $w_{tl} \times H$. For the natural convection calculations, the condenser was solely subdivided into top, lateral, bottom and tip faces, with dimensions of, respectively, $L_c \times W$, $L_c \times H$, $L_c \times W$ and $W \times H$.

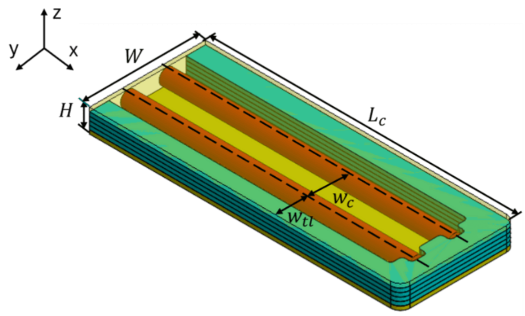

Figure 11. Dimensions utilized for condenser heat transfer calculation.

To obtain temperature values for each elemental area, profiles were created from the interpolation or extrapolation of data points. Parabolas were utilized with the following conditions: dT/dx = 0 (null heat flux) in the adiabatic section and at the condenser tip, and dT/dx is continuous in a given point if the next one is in the same vapor conditions. The central $T_{tip,c}$ and lateral $T_{tip,l}$ tip temperatures T_{tip} were evaluated as:

$$T_{tip,c} = [T_t(L) + T_b(L)]/2 \quad (6)$$

$$T_{tip,l} = T_l(L) \quad (7)$$

where L = 500 mm was the heat pipe length, and $T_t(x)$, $T_b(x)$ and $T_l(x)$ were, respectively, the top, bottom and lateral temperature profiles.

The following expression was obtained for surface emissivity through the methodology described in the previous subsection:

$$\varepsilon = 0.00015\,T + 0.63264 \pm 0.02249 \quad (8)$$

For each subregion j, the total radiative heat transfer rate can be expressed as:

$$Q_{rad,j} = \sum_{i=1}^{n} \sigma \varepsilon_i A_{i,j} \left[T_{i,j}^4 - T_0^4\right] \quad (9)$$

where i stood for elemental region, A was the area and T_0 was the environment temperature measured by thermocouple T_{25}. The total radiation heat transfer Q_{rad} could be obtained by summing the contributions from all subregions.

To compute natural convection heat transfer, a mean surface temperature $\overline{T_s}$ was evaluated from the area weighted average of the temperatures of the elemental zones. Since the room temperature variation was small in the tests, the properties of the surrounding buoyant fluid, which is air, were evaluated at a temperature of 25 ºC, where the Prandtl number Pr was approximately 0.73. The Rayleigh number Ra associated with natural convection adjacent to a surface could be written as:

$$Ra = \frac{g\beta(\overline{T_s} - T_0)L^3}{\nu\alpha} \quad (10)$$

where g was gravity, β the thermal expansion coefficient, ν the momentum diffusivity, α the thermal diffusivity, and L the characteristic length, which, for vertical plates, is the plate length itself and, for horizontal plates, can be cast as [16]:

$$L = A_s/p_s \quad (11)$$

with A_s and p_s the plate surface area and perimeter, respectively. In all experiments and for all heat pipe faces, the Rayleigh number remained between 10^4 and 10^7. The condenser top and bottom faces could be considered as horizontal hot plates facing, respectively, upwards and downwards. The lateral and tip faces could be assumed as hot vertical plates. For $Pr > 0.7$, the top face Nusselt number was expressed as [16]:

$$Nu = 0.54Ra^{1/4}, 10^4 \leq Ra \leq 10^7 \quad (12)$$

$$Nu = 0.15Ra^{1/3}, 10^7 \leq Ra \leq 10^{11} \quad (13)$$

For $10^4 < Ra < 10^9$ and $Pr > 0.7$, the Nusselt number Nu for the condenser bottom face was written as [17]:

$$Nu = 0.52Ra^{1/5} \quad (14)$$

For natural convection next to a vertical plate with $Ra < 10^9$, which was the case for the condenser lateral and tip faces, the Nusselt number could be obtained, with good accuracy, by using [18]:

$$Nu = 0.68 + \frac{0.670Ra^{1/4}}{\left[1 + \left(\frac{0.492}{Pr}\right)^{9/16}\right]^{4/9}} \quad (15)$$

The heat transfer coefficient h was evaluated for each condenser face by:

$$h = k_f \frac{Nu}{L} \quad (16)$$

with k_f the thermal conductivity of the buoyant fluid. For a single face j, the natural convection heat transfer rate $Q_{nc,j}$ was expressed as:

$$Q_{nc,j} = h_j A_j (\overline{T}_{s,j} - T_0) \quad (17)$$

The total condenser heat release by natural convection Q_{nc} was computed from the sum of the values for all surfaces, and the total heat rejection Q_c was given by:

$$Q_c = Q_{rad} + Q_{nc} \quad (18)$$

The heat loss through the insulation Q_a was calculated from the conduction heat transfer across the glass fiber blanket along the adiabatic section span. The geometry was approximated to a hollow cylinder, so the heat loss expression was:

$$Q_a = \frac{T_{23} - T_{24}}{2\pi k_{gf} \ln \frac{D_{out}}{D_{in}}} \quad (19)$$

$$D_{in} = \frac{4WH}{2W + 2H} \quad (20)$$

where k_{gf} was the thermal conductivity of the glass fiber blanket, D_{out} = 210 mm was the insulation outer diameter and D_{in} = 20 mm was the external hydraulic diameter of the heat pipe involucre. The evaporator heat flux q_e'' was evaluated assuming that heat input was uniformly distributed along the evaporator area inside the inductor:

$$q_e'' = \frac{Q_e}{2L_e(W + H)} \quad (21)$$

with L_e = 100 mm the evaporator length.

2.5. Uncertainty Analysis

As mentioned, temperature values used in this work were an average of 300 data points. The temperature A-type uncertainty, $U_{T,A}$ [19] was evaluated using:

$$U_{T,A} = \sqrt{\frac{\sum_{i=I}^{\vartheta+I}(T_i - \overline{T})^2}{\vartheta}} \quad (22)$$

where ϑ = 299 was the number of degrees of freedom, T_i was the i-th temperature value, and $\overline{T}$ was the average value. Temperature B-type uncertainty was based on manufacturer information [20], which quoted a highest standard error range between 2.2 °C and 0.75% of the measured value. Assuming a rectangular error probability distribution, the standard uncertainty $U_{T,B}$ is expressed as:

$$U_{T,B} = a_T/2\sqrt{3} \quad (23)$$

with a_T the quoted error limit. For aerospace applications, the expanded temperature uncertainty U_T formula shown below is the most recommended [19]:

$$U_T = t_{95}U_{T,A} + U_{T,B} \tag{24}$$

with t_{95} the t-Student factor for a 95 % confidence level. To compute length standard uncertainty U_L, the ruler resolution, 1 mm, was assumed as the quoted limit of error. The emissivity standard uncertainty U_ε was evaluated by:

$$S_{TT} = \sum_{i=1}^{n}(T_i - \bar{T})^2 \tag{25}$$

$$S_{T\varepsilon} = \sum_{i=1}^{n}(T_i - \bar{T})(\varepsilon_i - \bar{\varepsilon}) \tag{26}$$

$$S_{\varepsilon\varepsilon} = \sum_{i=1}^{n}(\varepsilon_i - \bar{\varepsilon})^2 \tag{27}$$

$$S_e = \frac{S_{\varepsilon\varepsilon} - (S_{T\varepsilon})^2/S_{TT}}{n-2} \tag{28}$$

$$U_\varepsilon = t_{95}S_e\sqrt{\frac{1}{n} + \frac{(T_0 - \bar{T})^2}{S_{TT}}} \tag{29}$$

where n = 74 was the number of emissivity data points, ε_i was the i-th emissivity value, $\bar{\varepsilon}$ was the average emissivity, and T_0 was a reference temperature.

In this work, all variables were considered independent error sources. Therefore, the uncertainties associated with results obtained from data reduction were obtained through the following uncertainty propagation approach. If R is a continuous function of variables V_1, V_2, …, V_N, its standard uncertainty U_R can be cast as:

$$(U_R)^2 = \sum_{i=1}^{N}\left[\left(\frac{\partial R}{\partial V_i}\right)^2 (U_i)^2\right] \tag{30}$$

3. Results

3.1. Transient Operation

In the analysis of the heat pipe's transient operation, only the temperature distribution at the top face was assessed, as the temperature-time dependence trends were similar for the other surfaces. Figure 12 shows the variation of temperature with time throughout the experiment. In the evaporator and adiabatic zones, the thermocouples presented close values within a given section, so average values are presented for the sake of simplicity. In the condenser, temperatures for the beginning (T_{15}) and end (T_{17}) of the zone are presented to capture the advance of the vapor front with heat load and time increase. The heat pipe reached startup when the temperature at the first condenser thermocouple location (T_{15}) achieved the continuum limit (Kn = 0.01, T_t = 464 °C). The heat pipe was assumed at a full continuum regime when the last condenser temperature (T_{17}) achieved this mark. The vapor temperatures at these points were the heat pipe's startup and continuum temperatures.

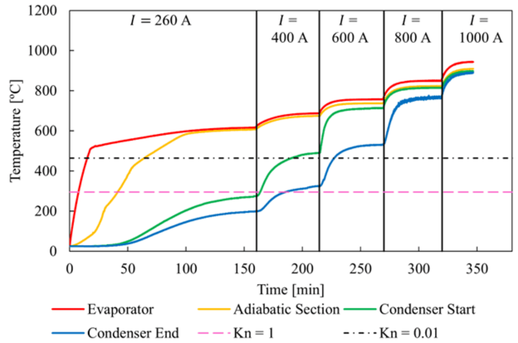

Figure 12. Top face transient temperature results.

In the first power input level, the evaporator vapor pressure was too low to induce an appreciable vapor flow into the condenser. Therefore, the vapor remained in the molecular regime. In this condition, the condenser transferred heat mostly by conduction. With the heat load increase, the condenser temperature increased, and the temperature drop decreased, indicating a rise of the condenser vapor. The startup temperature and time were, respectively, 666 °C and 190 min, while those for continuum regime were 724 °C and 227 min, respectively. A high temperature increase was observed in T_{15} and T_{17} relatively to the other heat pipe locations in, respectively, tests E_3 and E_4 as an outcome of vapor front advance.

3.2. Steady-State Operation

Figure 13 shows axial steady-state temperature distributions as a function of the heat pipe length, for tests E_1 and E_5 (see Table 2). For the lowest power inputs (lowest inductor current), condenser temperatures were in the transition zone, between Kn = 1 and Kn = 0.01. Since startup was not reached in this condition, the condenser main heat transfer mechanism was conduction through the container material, thus the temperature gradients did not vary with the evaluated surface. In test E_5, temperature profiles were roughly similar for the top and bottom faces, which indicated that capillary was dominant over gravity as the governing force on liquid distribution. The lateral condenser surface presented a cold tip, because the lateral channel of the heat pipe had only two grooves, while the central one had four, with therefore, a higher capillary force.

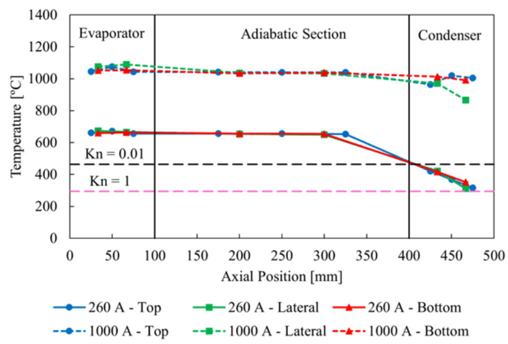

Figure 13. Axial steady-state temperature distributions for different heat pipe faces.

Figure 14 displays the axial steady-state temperature profiles for the top face. The dashed grey lines represent the interpolation and extrapolation curves. The heat transfer capacity increased with heat load due to the rise of the heat pipe's operation temperature and the advance of the vapor front, this latter evidenced by the reduction of the overall temperature drop. In test E_5 (I = 1000 A), there was a slight temperature rise from T_{16} to T_{17}, as, in this condition, the condenser vapor was in full continuum regime all along the heat pipe, and temperature was mainly governed by the surface cooling rate, which was higher close to the middle of the condenser than in the surroundings of its tip.

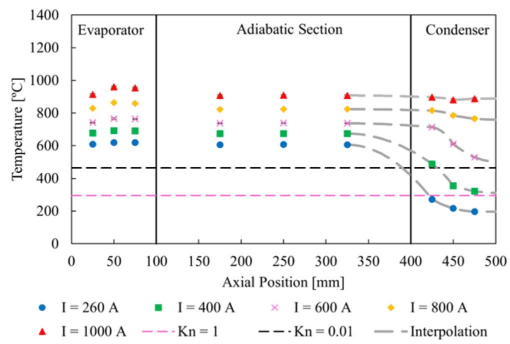

Figure 14. Top face axial steady-state temperature distributions.

Figure 15 shows the variation of the heat transfer rate with vapor temperature for the various tested conditions. The transferred heat increased linearly with vapor temperature, with values ranging between 87 W and 1037 W. The maximum value validates the heat pipe as a feasible technology for space micro reactors.

Figure 16 displays the thermal resistance as a function of the vapor temperature, which decreases with the increasing heat load, due to the advance of the vapor front, reaching a minimum value of 0.112 K/W.

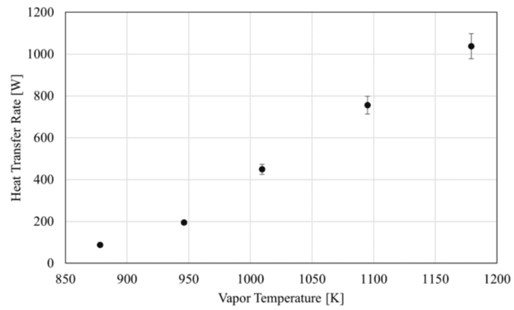

Figure 15. Heat transfer rate as a function of vapor temperature.

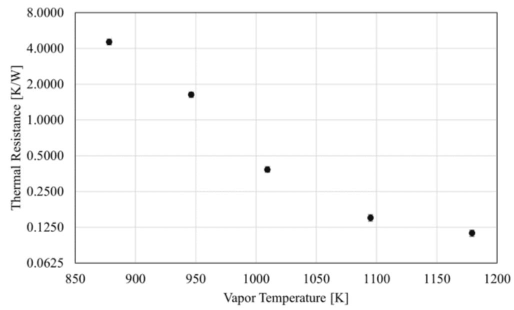

Figure 16. Thermal resistance as a function of vapor temperature.

Comparing with the empty container, which resistance was of 3.643 ± 0.034 K/W, it can be noticed that the device operated as a thermal superconductor. The large resistances in the early startup stages were due to the rarified vapor condition observed in a considerable portion of the condenser. With the vapor temperature (and pressure) increase, the vapor changed to continuum state, filling gradually the whole condenser, and so decreasing the thermal resistance decrease rate. However, a horizontal asymptote was not reached, showing that the device did not achieve any operational limit.

Figure 17 presents the heat fluxes as a function of the vapor temperature. A close to linear curve is observed, with a maximum of 7.36 W/cm^2, which can be considered a high heat flux.

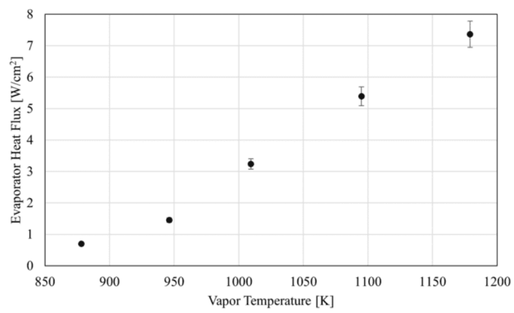

Figure 17. Evaporator heat flux as a function of vapor temperature.

Conclusions

This paper describes the procedures used for fabrication and testing of a sodium rod-plate heat pipe operating horizontally. The innovative charging system provided safety for the operator and high quality for the produced sodium heat pipes. A mass of 10.62 g of sodium was introduced into the heat pipe. Through the data analysis, it was possible to identify the advance of the vapor front in a continuous state by the monotonical increase of the condenser temperatures with time, compared to that of the other regions. The device transferred up to 1037 W (heat flux of 7.36 W/cm^2), with a thermal resistance of 0.112 K/W. These results show that the device is suitable for space micro reactor heat transport applications.

References

[1] M. A. Gibson et al., "Development of NASA's small fission power system for science and human exploration," 12th Int. Energy Convers. Eng. Conf. IECEC 2014, no. July, 2014.

[2] A. C. Kadak, "A comparison of advanced nuclear technologies." Columbia University in the City of New York, 2017.

[3] A. Bejan and A. D. Kraus, Heat Transfer Handbook- Heat Exchangers, no. v. 1. 2003.

[4] J. H. Boo, S. M. Kim, and Y. H. Kang, "An Experimental Study on a Sodium Loop-type Heat Pipe for Thermal Transport from a High-temperature Solar Receiver," Energy, vol. 69, pp. 608–617, 2015.

[5] C. Wang, D. Zhang, S. Qiu, W. Tian, Y. Wu, and G. Su, "Study on the characteristics of the sodium heat pipe in passive residual heat removal system of molten salt reactor," Nucl. Eng. Des., vol. 265, pp. 691–700, 2013.

[6] W. Teng, X. Wang, and Y. Zhu, "Experimental investigations on start-up and thermal performance of sodium heat pipe under swing conditions," Int. J. Heat Mass Transf., vol. 152, p. 119505, 2020.

[7] E. F. de Araújo, J. P. F. Mera, L. H. R. Cisterna, and M. B. H. Mantelli, "New water-stainless steel rod-plate heat pipe: model and experiments," Heat Mass Transfer, vol. 60, pp. 1073-1074, 2024.

[8] Y. X. Wang and G. P. Peterson, "Analysis of Wire-Bonded Micro Heat Pipe Arrays," J. Thermophys. Heat Transf., vol. 16, no. 3, 2002.

[9] K. Vieira De Paiva, M. Barbosa Henriques Mantelli, and L. Kessler Slongo, "Thermal behavior analysis of wire mini heat pipe," J. Heat Transfer, vol. 133, no. 12, pp. 1–9, 2011.

[10] M. B. H. Mantelli, J. V. C. Batista, and J. P. F. Mera, "Experimental study of multidimensional wire-plate/sintered hybrid mini heat pipes for electronics," Heat Mass Transfer, vol. 60, no. 4, pp. 725–750, 2024.

[11] L. H. R. Cisterna, G. Vitto, M. C. K. Cardoso, E. L. Fronza, M. B. H. Mantelli, and F. H. Milanez, "Charging procedures: effects on high temperature sodium thermosyphon performance," J. Brazilian Soc. Mech. Sci. Eng., vol. 42, no. 8, pp. 1–11, 2020.

[12] A. T. De Castro, "Desenvolvimento de um Termossifão Bifásico de Sódio em Circuito (Master's Thesis)," Federal Unversity of Santa Catarina, 2023.

[13] J. M. Tournier and M. S. El-Genk, "A vapor flow model for analysis of liquid-metal heat pipe startup from a frozen state," Int. J. Heat Mass Transf., 1996.

[14] Y. Cao and A. Faghri, "Simulation of the early startup period of high-temperature heat pipes from the frozen state by a rarefied vapor self-diffusion model," J. Heat Transfer, 1993.

[15] M. S. El-Genk and J.-M. P. Tournier, "Uses of Liquid-Metal and Water Heat Pipes in Space Reactor Power Systems," Front. Heat Pipes, vol. 2, no. 1, 2011.

[16] J. r. Lloyd and W. R. Moran, "Natural convection adjacent to horizontal surface of various planforms," ASME J. Heat Transf., vol. 96(4), pp. 443–447, 1974.

[17] E. Radziemska and W. M. Lewandowski, "Heat transfer by natural convection from an isothermal downward-facing round plate in unlimited space," Appl. Energy, vol. 68, no. 4, pp. 347–366, 2001.

[18] S. W. Churchill and H. H. S. Chu, "Correlating equations for laminar and turbulent free convection from a vertical plate," Int. J. Heat Mass Transf., vol. 18, no. 11, pp. 1323–1329, 1975.

[19] Ronald H. Dieck, Measurement uncertainty: methods and applications, 2nd ed. Durham, 1997.

[20] OMEGA Engineering, "Thermocouple types," 2023. https://www.omega.com/en-us/resources/thermocouple-types.

Paper ID 092(S7)

Experimental studies and analytical mathematical modeling of the evaporation rate of the sintered-grooved wick

Wanchai Pileug1*, Pradit Terdtoon 1, Niti Kammuang-lue 1 and Phrut Sakulchangsatjatai 1
[1] *Chiang Mai University, Chiang Mai, Thailand*
**Corresponding author email address: wanchai.pileug@gmail.com*

Abstract

This study investigates the evaporation rate from a sintered-grooved wick through experimental studies and analytical mathematical modeling. Heat pipes, integrating devices employing heat conduction and phase change principles, are crucial for effective heat transfer in various applications, including cooling electronic circuit. Mathematical modeling, employing both numerical and analytical methods, is widely used to simulate heat pipe behavior, considering governing equations and boundary conditions across different domains. Experimental studies explore the impact of parameters like particle size, porosity, and thickness on heat transfer coefficients. Mathematical modeling aims to predict thermal properties and evaporation rates, considering factors like capillarity, gravity, and porosity. Experimental results indicate that increased heat input and porosity lead to higher evaporation rates. Comparison with previous research shows variations in evaporation rates due to differences in porous material sizes and structures. The model can predict the evaporation rate with STD 44.9% when porosity changes. This study contributes understanding and prediction of evaporation rates in sintered-grooved wicks for improved thermal modeling accuracy.

Keywords: Heat pipe, evaporation rate, sintered-grooved wick, mathematical modeling, experimental studies

1. Introduction

The heat pipe is a heat transfer device that integrates the principles of both heat conduction and phase change from evaporation and condensation to manage heat transfer between two environments effectively. The heat pipe was introduced inside a portable computer to cool the electronic circuitry, which contains CPU chips and GPUs. The heat pipe consists of a container, wick, and a vapor core.

There have been numerous research studies on the operation of heat pipes, both experimental and mathematical modeling. Mathematical modeling is employed to simulate the behavior of heat pipes using both numerical and analytical methods. Governing equations and boundary conditions are utilized in mathematical models and refined to predict the heat transfer characteristics of heat pipes. Heat pipes consist of three domains: the vapor core, the wick structure, and the pipe wall as shown in Figure 1. The most important boundary condition is between the liquid and vapor.

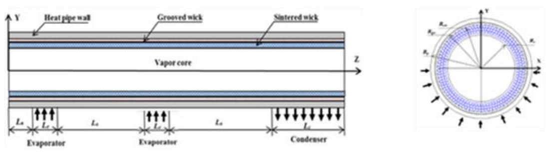

Figure 1 Components of the heat pipe.

This describes the evaporation from the wick structure evaporation section and the condensation of the working fluid in the condensation section into the wick structure to draw the liquid back to the evaporation section. The wick structure, depicted in Figure 1, comes in various forms, which affect the rate of evaporation and the density of the working fluid within the wick structure. This variation in structure impacts both the numerical and analytical modeling of heat pipes.

Previous research has investigated mathematical models in both 2D and 3D, employing both numerical and analytical methods [3, 4]. It was found that prior mathematical modeling research utilized free surface evaporation equations as boundary conditions for evaporation and condensation, yielding predictions consistent with experimental results. However, this approach involved assuming free surface evaporation conditions in the boundary conditions for calculations. In reality, evaporation from various porous material structures may differ from free surface evaporation. Previous mathematical modeling studies have not extensively explored the evaporation rate data from porous material structures, which could lead to more comprehensive and realistic mathematical models.

There have been numerous experimental and mathematical modeling studies examining the impact of parameters on heat transfer from evaporation in porous material structures. Hanlon and Ma (2003) found that particle size, porosity, and thickness of the porous material structure affect the heat transfer coefficient of evaporation. Additionally, experimental studies on evaporation rates from porous media with closely packed cylindrical vertical rods by Kumar and Arakeri (2011) revealed a gradual decrease in evaporation rate, drastically reducing after 22 hours of operation.

Furthermore, reports on the evaporation characteristics with different porosities of porous material structures by Yeu and Vakhguelt (2018) demonstrated that the evaporation rate can vary with changes in particle size and porosity, and a decrease in structure thickness leads to an increase in evaporation rate and may induce easier drying out due to enhanced evaporation resulting from thinner porous structures. However, subsequent studies by Li and Peterson (2006) and Sudhakar et al. (2011) reported that when heat is applied to water-saturated porous material structures, it can cause the working fluid in the porous material to retreat from the structure due to liquid loss through evaporation. Excessive heat can render the fluid evaporation insufficient, leading to dry-out of the wick structure.

In constructing mathematical models to predict the heat performance of any miniature heat pipe, a set of equations regarding the evaporation rate is essential. These equations must encompass both free surface and under varying pressure conditions to calculate the evaporation rate of the working fluid at boundary conditions. However, previous studies have been scarce in attempting to find evaporation rates and validating assumptions from the theory of free surface evaporation in mathematical models of heat pipe systems.

This research aims to investigate the evaporation rate of working fluids from widely used sintered-groove porous material structures in heat pipes and derive equations for evaporation to be integrated into mathematical models for enhanced accuracy and alignment with reality.

2. Materials and Methods

2.1 Experimental studies

The installation of the experiments and the experimental procedures are explained in this section. These are outlined in the following two subsections: the first subsection covers the experimental setup, while the second subsection details the experimental procedures.

2.1. 1Experimental setup

An experiment to study the effect of heat feed on the evaporation rate in a porous material structure on a square curved plate, as shown in Figure 2.

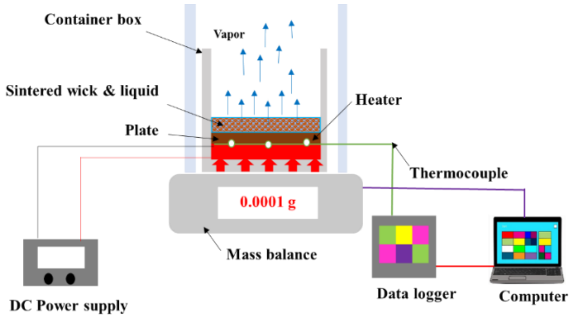

Figure 2 The schematic diagram of evaporation rate experimental setup

In this experiment, we inferred that evaporation from the cylindrical heat pipe has been condensed into rectangular sheets for easy observation using a high-precision electronic balance (±0.0001g). The test setup includes insulation, electronic heating apparatus, grooved copper plates, K-type thermocouples for temperature measurement (with uncertainty of ±1oC), a data logger (BrainChild VR18), a power supply (GW Instek GPR-7550D) (±0.5% of rdg), and a computer. The sintered-groove copper plate, measuring 30×30 mm, serves as the substrate for the porous material structure. The porous material structure is a composite of sintered-groove powder and is homogenous, made from sintered-groove powder adhered to the grooved surface of the copper plate to conform to the interior of the heat pipe. The thickness of the porous material structure is 0.6 mm with a porosity of 0.61-1.00. The heater source is positioned beneath the sintered-groove plate, measuring 35×35 mm, to avoid heat loss from the packaging box. Insulation wraps all exterior walls to prevent heat loss and ensure compatibility with the electronic balance. Additionally, the insulation aids in preventing heat transfer to the electronic balance. The sintered-groove plate receives heat from the DC power supply (GW Instek GPS 3030D). The working fluid is water due to its higher latent heat and compatibility with copper [1]. Details of the sintered-groove plate are provided in Table 1.

Table 1 Experimental specifications of sintered-grooved plate

Parameter	Value	Unit
Material	Copper	-
Grooved plate size	30×30	mm2
Grooved depth	0.2	mm
Number of grooves	65	-
Spherical powder size	150-280	µm
Wick thickness	0.6	mm
Porosity	0.61, 0.67, 0.71 and 1.00	-
Working fluid	Water	-

2.1.2 Experimental procedure

The experimental process was carried out to study the evaporation rate of the working fluid inside the sintered-grooved wick plate. It is filled with a working fluid of water by a vacuum pump system. Then, a sintered-grooved wick plate is placed on a heater inside the packing box. The contact surface between the heater and the sintered-grooved wick plate is connected using a thermal grease and tightly held by bolts to reduce the thermal contact resistance between the two surfaces. The 5 W heat input is inserted into the center-shape sheet at an atmospheric pressure of atm, a relative humidity of 50–60%, and a test room temperature of 25±1 °C. The heat input test at 5 W to determine the evaporation by equation)1:(

$$\frac{dh}{dt} = \frac{\Delta m_{loss} \times A_s \times \rho_{wf}}{\Delta t_{evap.}} \quad (1)$$

By dh/dt, the evaporation rate (mm/s) is the change in the total mass of the active substance (water) for the initial and final absence of liquid in the permeable material (g). The heating area of the centrifugal plate is the density of the working substance and is the total time of evacuation (s).

2.2 Mathematical model

For a mathematical model, this article focuses on developing an analytical model to predict evaporation in a porous material by simulating the state with a two-dimensional model since it is a single-directional evacuation. Figure 3 shows a diagram for using the mathematical model analysis of evaporations in wick structure.

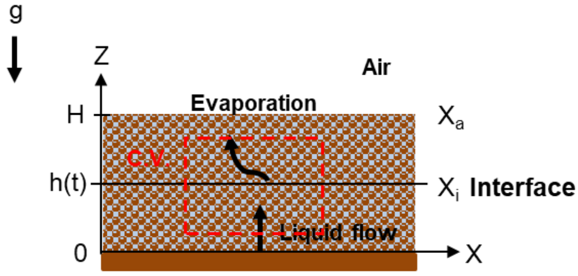

Figure 3 Schematic diagram of porous medium system

2.2.1 Equation liquid evaporation position

For the mathematical model construction for this study, it relies on the following assumptions:

- Assume heat transfer and fluid flow are in a steady state, with laminar flow and incompressible fluid flow.

- Isothermal properties for the working substance and constant properties for the walls.

- Gravitational forces are considered due to atmospheric conditions.

The relevant governing equations for analysis to find the evaporation rate are given as follows: Equation (2(represents the diffusion-controlled propagation according to Fick's law, and for the evaporation within the porous material structure, an equation describing the evaporation in the porous material structure and its associated gravitational forces is necessary, as shown in Equation (3(, to find the position of the fluid inside the porous material. Then, combining Equations (2(and (3(using Boundary conditions, as shown in Equation (4(.

$$\frac{dh}{dt} = -\frac{c_g D_{va}}{c_l \tau} \frac{1}{H-h} \ln\left(\frac{1-X_a}{1-X_i}\right) \quad (2)$$

$$\frac{dh}{dt} = \frac{v}{\varepsilon} = \frac{K}{\mu_l \varepsilon} \frac{P_c - \rho_l g h}{h} \quad (3)$$

After that, combine the results of equations (2(and (3(using boundary conditions as in equation (4(.

$$X(z=h) = X_i$$
$$X(z=H) = X_a \quad (4)$$

2.2.2 Liquid evaporation with capillary and gravity

Liquid evaporation with capillary and gravity is described by Equation (5(

$$\frac{dh}{dt}=\frac{K}{\mu_l\varepsilon}\frac{P_c-\rho_l gh}{h}-\frac{c_g D_{va}}{c_l\tau}\frac{1}{H-h}\ln\left(\frac{1-X_a}{1-X_i}\right) \quad (5)$$

when $K=\frac{4}{180}\frac{\varepsilon^3 r^2}{(1-\varepsilon)^2}$ shows the permeability, $P_c=3\times\left(\frac{1-\varepsilon}{\varepsilon}\frac{\sigma\cos\theta}{r}\right)$ capillary pressure, $\tau=1+0.41\ln\left(\frac{1}{\varepsilon}\right)$ tortousity and $X_i=\exp\left(-\frac{\zeta}{\hat{R}}\left(\frac{1}{T_g}-\frac{1}{T_{sat}}\right)\right)$ the Clausius-Clapeyron

Therefore, Equation (5) can describe the evaporation phenomenon analytically to predict the evaporation rate and serve as Boundary conditions for the mathematical model of the heat pipe.

3. Results and Discussion

The results obtained from experiments and mathematical modeling will be compared for the evaporation within the porous material structure under normal conditions.

3.1 Effect of heat input on evaporation rate

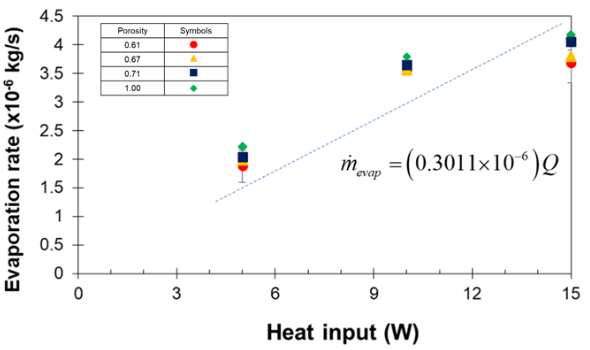

Figure 4 Effect of heat input on evaporation rate

From Figure 4, the experimental results show that when heat input increases from 5to 15 watts, or by 200%, the fluid within the porous material structure evaporates faster, with a significant increase in the evaporation rate of 98.5%. This is because higher heat to the wick-groove plate leads to faster evaporation, as evidenced by the significant increase in evaporation rate. An evaporation equation can be derived from increased heat input resulting in increased evaporation, referencing the trend of evaporation from the free surface, as shown in Equation (6(.

$$\dot{m}_{evap}=\left(0.3011\times10^{-6}\right)Q \quad (6)$$

Furthermore, the graph also demonstrates the effect of porosity on the evaporation rate, which will be presented in the next section. Thus, increased heat input leads to an increase in the evaporation rate.

3.2 Effect of porosity on evaporation rate

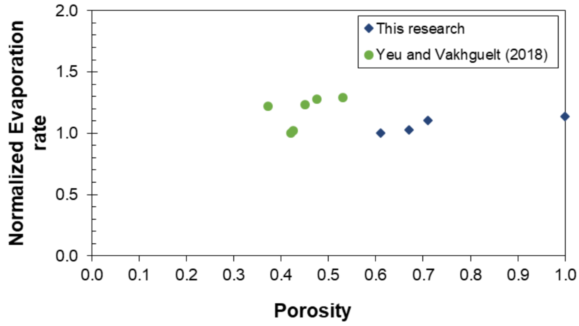

Figure 5 Effect of porosity on evaporation rate

From Figure 5, the experimental results show that when porosity increases from 0.61to 1.00, or by 63.9%, the fluid within the porous material structure evaporates faster, with a significant increase in the evaporation rate of 13.6%. This is because increasing porosity enlarges the pore size, increasing the contact area for heat transfer, resulting in an increased evaporation rate. However, lower porosity makes the wick pores smaller, reducing the contact area for heat transfer with the fluid, making evaporation more difficult. Hence, increasing porosity results in an increase in the evaporation rate by 13.6%.

In addition, Yeu and Vakhguelt (2018(research investigated the effect of porosity on the evaporation rate of porous ball metal materials ranging in size from 5 to 10 mm. The research results depicted in Figure 5 revealed that as the porosity increased from 0.42 to 0.53 (26.2%), there was a significant 29.2% increase in the evaporation rate of the aqueous working fluid.

It can be observed that the evaporation rate results obtained by Yeu and Vakhguelt (2018) are higher than those of this research, likely due to differences in the sizes of the porous materials, resulting in varying porosities. Despite this study having a higher porosity compared to the experiment conducted by Yeu and Vakhguelt (2018), it resulted in much smaller pores. Consequently, the resulting evaporation rate is lower than that observed in the previous research. But the evaporation rate trend was agreed upon when the porosity changed.

3.3 Validation results of experimental data with mathematical model of evaporation rate

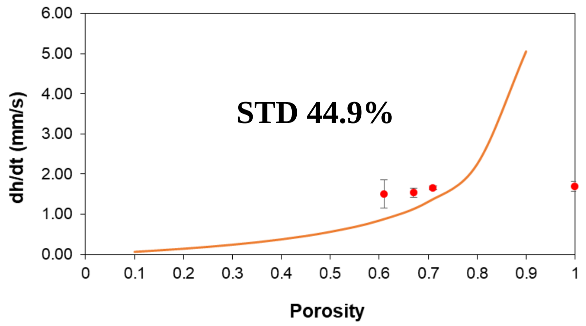

Figure 6 Validation of the effect of porosity on evaporation rate

From Figure 6, the experimental results of porosity are compared with the mathematical model. It is found that the model can predict the evaporation rate with STD 44.9% when porosity changes. The trend follows the logarithmic function, and as porosity approaches 1.00, evaporation increases. As porosity increases, the evaporation rate increases dramatically. This differs from free surface evaporation, which has a linear relationship. This difference arises from variations in porosity, leading to differing rates of evaporation. However, the model developed includes the effects of capillarity, gravitational forces, and porosity of the porous material, making it unsuitable for predicting evaporation from the free surface, as observed from the discrepancy in results at porosity equal to 1.00.

3. Conclusion

- When heat input increases by 200%, the evaporation rate increases by 98.5%.

-When porosity increases by 63.9%, the evaporation rate increases by 13.6%.

- The obtained evaporation rate equation can predict the results with a standard deviation of 44.9% within the range of porous wick, but it cannot accurately predict in the absence of a porous wick or when porosity equals 1.00.

This body-text paragraph has been pre-formatted with one-line spacing. There is no space or blank lines between the paragraphs. There is a first line indent of 3 mm. All paragraphs should be fully justified. The paper size selected for this template is A4 (210mm x 297mm). The font size is Times New Roman 11 pt. The paper margins are 20 mm on left and right side of the page and 25 mm on the bottom and the top sides, respectively. Please do not include any page numbers on this document. The figures should be good quality JPG/TIFF format. Leave one blank line (or equivalent spacing) above and below the figures and tables [1].

Place figures centered on the width of the text column and either at the top or bottom of the page as close as possible to their first mentioned in the text.

3. ACKNOWLEDGEMENTS

The presented work was financially supported by Fundamental Fund 2023, Chinag Mai University, The Thailand Research Fund (TRF), Reseach and Researcher for Industries (RRI) (Contract no. PHD60I0092) and Fujikura Electronics (Thailand) Ltd.

References

[1] Faghri, A. (1995). Heat Pipe Science and Technology. Washington, D.C.: Taylor and Francis.
[2] Reay, D. (2006). Heat Pipe, 5th edition. Oxford: Elsevier.
[2] Intagun, W., Terdtoon, P. and Sakulchangsatjatai, P. (2013). Flattening Effect on Heat Transfer Characteristics of Sintered-Wick Heat Pipe, American Journal of Applied Sciences, vol. 10(7), p. 760-766.
[3] Tharawadee, N., Terdtoon, P. and Kammuang-lue, N. (2013). An Investigation of Thermal Characteristics of a sintered-wick Heat Pipe with Double Heat Sources, American Journal of Applied Science, vol. 10(9), pp. 1077-1089.
[4] Hanlon, A.M. and Ma, B.H. (2003). Evaporation heat transfer in sintered porous media, ASME Journal of heat transfer, vol. 125, p. 644-652.
[5] Kumar, N. and Arakeri, H.J. (2018). Sustained high evaporation rate from porous media consisting of packed circular rods, International Journal of Thermal Sciences, vol. 133, August 2018, p. 299-306.
[6] Kumar, N. and Arakeri, H.J. (2018). Sustained high evaporation rate from porous media consisting of packed circular rods, International Journal of Thermal Sciences, vol. 133, August 2018, p. 299-306.
[7] C. Li, G.P. Peterson, Evaporation/Boiling in Thin Capillary Wicks (II)-Effects of Volumetric Porosity and Mesh Size, Journal Heat Transfer 2006; 128 (12):1320–1328.
[8] H. Shabgard, A. Faghri, Performance characteristics of cylindrical heat pipes with

multiple heat sources, Applied Thermal Engineering 2011; 31(16), 3410–3419.
[9] Yeu, L.Y. and Vakhguelt, A (2011). An Experimental Study in the Fundamentals of Evaporation from Porous Structure, paper presented in the 10th International Heat Pipe Symposium, Taipei, Taiwan.

Paper ID 093(S2B)

Experimental studies on startup behavior of cylindrical evaporator nickel bi-porous wicked miniature loop heat pipe

Toni Kumari[1]*, Chandan Nashine[1], and Manmohan Pandey[1*]

[1] *Indian Institute of Technology, Guwahati, India*
**Corresponding author email address: ktoni@iitg.ac.in, manmohan@iitg.ac.in*

Abstract

In the current work, a nickel bi-porous wicked cylindrical evaporator miniature loop heat pipe was developed and tested using pentane as the working fluid. The thermal behavior of the device was investigated, focusing on its startup characteristics under varying heat loads and sink temperatures. The device was subjected to a range of heat loads (5 W, 15 W, 25 W, 20W, 30 W, 35 W, and 45 W) while maintaining a constant sink temperature, followed by tests at different sink temperatures (5°C, 10°C, 15°C, and 20°C) with fixed heat loads. It was found that the startup time initially decreases with increasing heat load due to enhanced vaporization of the working fluid, leading to quicker establishment of vapor pressure. However, beyond a certain limit, increased heat loads result in longer startup times due to heat leakage in the compensation chamber and two-phase flow instabilities. Additionally, higher sink temperatures were found to increase the evaporator temperatures, contributing to longer startup times to reduced temperature gradients. The findings provide insights into optimizing the loop heat pipe's performance for effective thermal management of electronic systems.

Keywords: Miniature loop heat pipe; Startup; Temperature overshoot; Cylindrical evaporator; Bi-porous wick

1. Introduction

Modern compact electronic devices require high heat dissipation from the heat generating area for their proper functioning. A loop heat pipe (LHP) is a passive two-phase heat transfer device [1] that has the potential to overcome ongoing and future heating issues [2]. The device has a wick structure [3, 4] that utilizes the capillary action [5] to circulate the fluid inside the loop, thus obviating the need for an external power source. Therefore, LHP is very suitable for space and remote applications [6, 7]. Miniaturization of modern electronic devices has necessitated small-size LHPs, namely, miniature loop heat pipes (mLHPs) and micro loop heat pipes.

Various equipment, which are very sensitive to temperature need precise control of this. There are several literatures available that has observed temperature overshoot in the startup of the device [8-11] Therefore, studies of the startup of the device become very important. Vershinin, S. V., and Maydanik, Y. F [12], studied the pulsation in evaporator temperature at different conditions and found distribution of working fluid plays a major role in the pulsation of evaporator temperature. Feng et al. [13] experimentally studied the instability of a dual compensation chamber loop heat pipe. They focused on temperature oscillation, temperature hysteresis, and flow reversal and found low heat load startup: temperature hysteresis and reverse flow appear. At low heat load startups, temperature oscillation was also observed. Celata et al. [14] compared the favorable position (the compensation chamber above the evaporator) of the device with the unfavorable position (the compensation chamber below the evaporator) during the startup test. For both positions, startup had taken a longer time. At the heat load of 20 W, the device took 50 min for the startup, and at 50 W it took 20 min. Starting up the device required a heat load of at least 20W. Qu et al. [15] designed a dual evaporator loop heat pipe to study the startup behavior of the device at different conditions. They found liquid-vapour distribution in the evaporator core and vapour grove had a significant role in startup and the best distribution was when there was liquid inside the evaporator core and vapour inside the vapour grooves. Visual experiments were carried out by Du et al. [16] to understand the behaviour of temperature oscillation in the LHP device. They also studied the nature of temperature oscillation under different heat loads and filling ratios. It was found that by increasing the filling ratio temperature oscillation was delay and at higher heat load startup time decreased and oscillation frequency increased due to increase in evaporation rate. To control the temperature overshoot at high heat loads of 180 W to 270 W Kwon et al. [17] successfully implemented a bypass line between the evaporator and compensation chamber to avoid overheating. Bai et al. [18] and Fu et al. [19] successfully implemented dual compensation chamber LHP (DCCLHP) to focus on the issue related to the orientation and improve the low heat startup performance. The DCCLHP also lowered the evaporator temperature and worked properly at low inventory, compared to the conventional LHP.

2. Methodology

The current fabricated miniature loop heat pipe (mLHP) has a bi-porous nickel wick cylindrical evaporator, as shown in Figure 1. For the bi-porous wick, 30 % salt (NaCl) by volume was used as a pore former and well mixed with nickel powder. The powder was compacted and sintered inside the evaporator tube to avoid the fitting problem and thermal contact resistance between the wick and the evaporator wall. The tubing of the liquid line (LL) and vapor line (VL) were made of stainless steel and had an inner diameter of 4 mm. The length of the liquid and vapor lines were 500 mm and 350 mm, respectively.

2.1. Experimental setup

For the final setup, the device first went for a leakage test. After successful leak testing of the mLHP, the device was charged with pentane working fluid at a charging ratio of 50%, and other details are listed in Table 1. The temperature at different locations of the device was recorded with the help of a fine wire T-type thermocouple and data acquisition system, as shown in Figure 2. A flat cartridge heater of dimension 3 mm x 10 mm x 50 mm was used to mimic the heat source for the evaporator. An aluminum saddle was used to transfer heat from the ceramic heater's flat surface to the evaporator's cylindrical surface. A copper-finned heat exchanger, dimension 150 mm x 200 mm was used as a heat sink. A Recirculating chiller maintained the heat sink temperature at the desired value.

Table 1. Description of the device

Evaporator material	Stainless steel
Tubing material	Stainless steel
Condenser	Copper fined
Wick	Nickel
Pore former	NaCl
Working fluid	Pentane
Evaporator inner diameter	10 mm
Tube diameter	4 mm
Evaporator diameter	10 mm
Liquid line length	500 mm
Vapour line length	300 mm

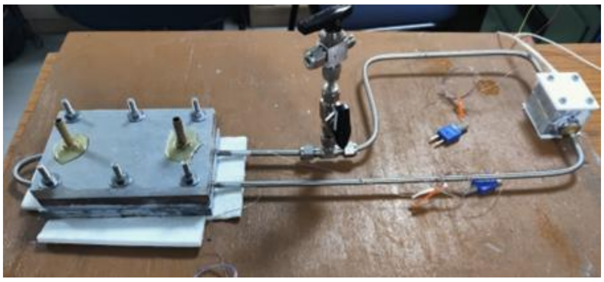

Figure 1. The fabricated miniature loop heat pipe

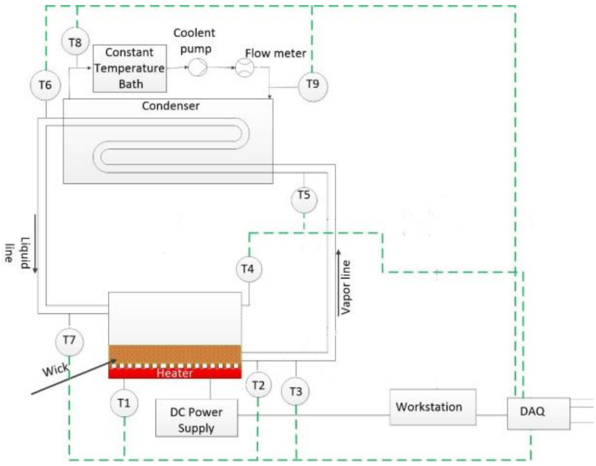

Figure 2. Schematic of experimental setup

3. Result and discussion

The temperatures at different device locations were recorded with time, which helped to study the thermal behavior of the device. The startup characteristic of the mLHP device was observed under various working conditions, such as different sink temperatures and heat loads. First, the device was tested under different heat loads such as 5 W, 15 W, 20 W, 25 W, 30 W, 35 W, and 45 W while keeping the sink temperature constant. Then, the sink temperature was varied one by one, such as 5°C, 10°C, 15°C, and 20°C, while the heat load was fixed.

3.1. Startup of mLHP 20°C sink temperature

To study the startup behavior of the device, the temperature at different locations, such as evaporator (Evap), vapour line (VL), condenser inlet (Cin), condenser outlet (Cout), liquid line (LL), and compensation chamber (CC) were recorded with respect to time at a sink temperature of 20°C. The device has a zigzag startup at 5 W, and the startup time was about 2000 seconds, as shown in Figure 3. At 20 W, the heat leak in the compensation chamber (CC) was dominated, and the device showed a zigzag startup at about 1500 seconds, as shown in Figure 4.

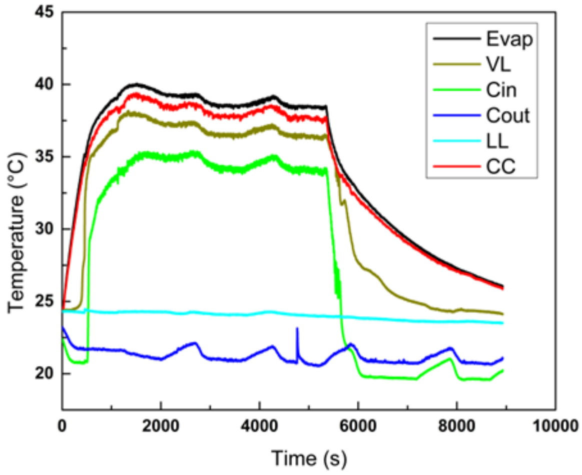

Figure 3. Startup behavior of mLHP at 5 W.

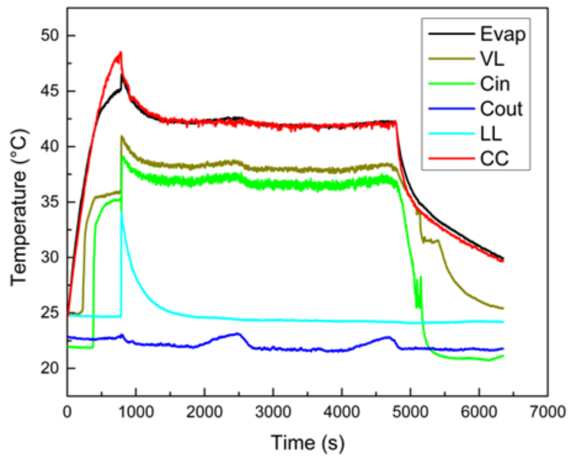

Figure 4. Startup behavior of mLHP at 20 W.

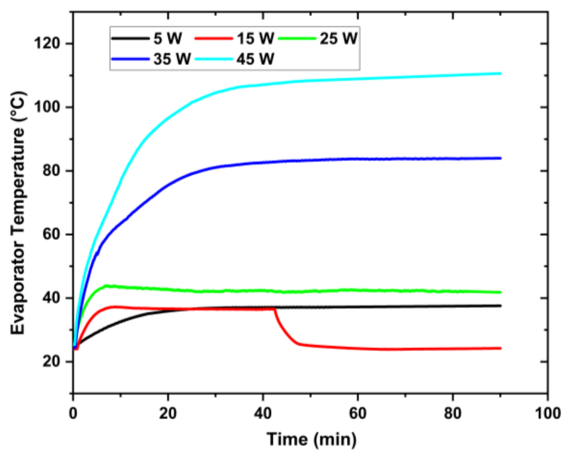

Figure 5. Startup comparison of the device at different heat loads with 5°C sink temperature.

3.2. Effect of heat load on the startup of mLHP

The mLHP device was tested under various operating conditions to thoroughly understand its startup characteristics. As shown in Figure 5, the startup of the mLHP device under different heat loads such as 5 W, 15 W, 25 W, 35 W, and 45 W for a sink temperature of 5°C. The steady-state temperature at 5 W heat load was about 37.2°C, and the startup time was approximately 21 minutes. At a heat load value of 15 W, it seemed that the device had reached a steady state with a temperature of 36.5°C, but as 42.5 minutes passed, the temperature suddenly started to decrease. After approximately 10 minutes, it settled at a comparatively lower final steady-state temperature of 24°C. At 25 W heat load, the device's startup time was comparatively very low, about 3.9 minutes, and the steady state temperature was 42°C. As further heat load value increased from 35 W to 45 W, startup time and steady-state temperature were also increased from 29.6 minutes to 32.95 minutes and 83.5°C to 109°C, respectively.

The temperature of the heat sink increased to 10°C while maintaining the same heat load values of 5 W, 15 W, 25 W, 35 W, and 45 W. At a heat load of 25 W, the device experienced a minor overshoot. The overshoot and steady-state temperature at 25 W heat load were 57.5°C and 50.25°C, as illustrated in Figure 6. Although the startup trend at 10°C and 5°C sink temperatures for the remaining heat loads (4 W, 15 W, 35 W, and 45 W) was similar, the startup time and steady-state temperature differed. Increasing the sink temperature resulted in an increase in the evaporator temperature.

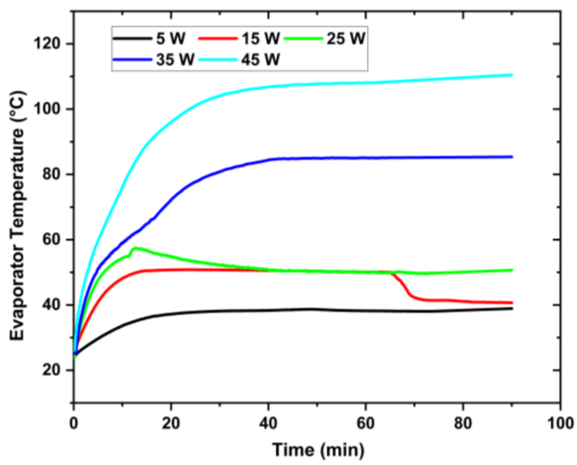

Figure 6. Startup comparison of the device at different heat loads with 10°C sink temperature.

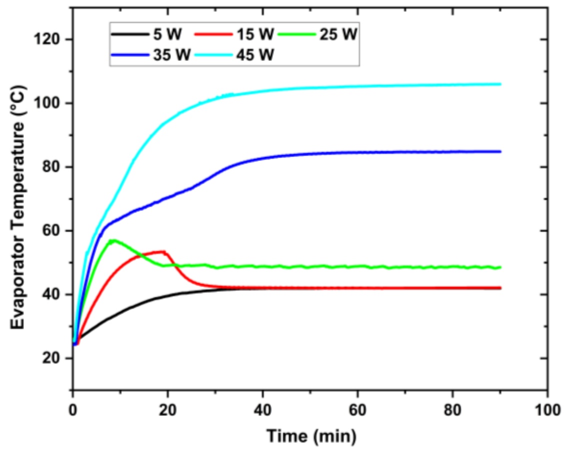

Figure 7. Startup comparison of the device at different heat loads with 15°C sink temperature.

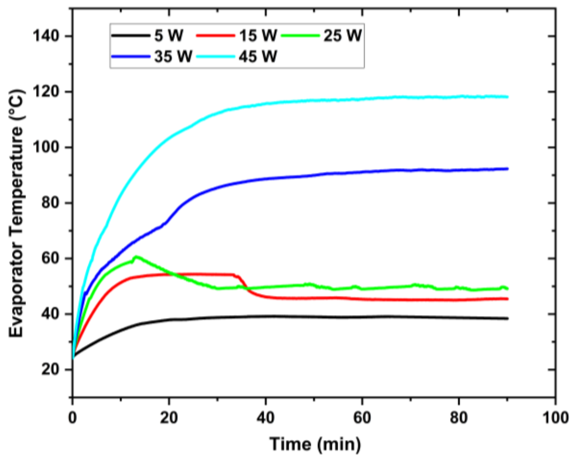

Figure 8. Startup comparison of the device at different heat loads with 20°C sink temperature.

Figure 7 and Figure 8 showed the evaporator temperature of the device with respect to time at sink temperatures of 15 °C and 20 °C, respectively. In Figure 7, temperature overshoot for 15 W and 25 W heat loads values were observed, and the corresponding overshoot temperatures were 53.4°C and 56.87°C, and steady-state temperatures were 42°C and 48.5°C, respectively.

The startup time of the mLHP initially decreases with an increase in heat load but then starts to increase again. Higher heat loads can lead to more rapid vaporization of the working fluid in the evaporator. This can quickly create sufficient vapor pressure to drive the fluid through the loop, which results in a decrease in startup time. On further increasing the heat load, the heat leakage (evaporator to Compensation chamber) also increases, which can trigger two-phase flow instabilities, such as boiling crises or liquid slugs. These instabilities can disrupt the regular operation of the mLHP and delay startup. Also, as the heat load continues to increase, the evaporator may reach saturation, where the liquid cannot absorb any more heat without vaporizing. This can lead to a decrease in the temperature difference and a slower startup process.

3.3. Effect of sink temperature on the startup of mLHP

The thermal performance of the mLHP device was compared under different sink temperatures such as 5°C, 10°C, 15°C, and 20°C while keeping the heat load constant. The Figure 9 shows the startup behavior of the device at a low heat load, which was 5 W. The startup time for all sink temperatures was nearly 20 minutes except for the 15 °C sink temperature, which was about 24.75 minutes. The device's behavior was quite different at 15 W as shown Figure 10. The graphs showed that the device had maintained a constant evaporator temperature for a long time but was still not in a steady state. After some time, the evaporator temperature started to decrease and settled for a lower steady-state temperature. At 25 W heat load, all sink temperatures startup were overshoot zigzag as shown in Figure 11. The startup was smooth for a heat load value of 45 W, as shown in Figure 12.

The start-up time and evaporator temperature have a clear relationship with the sink temperature. A smaller temperature gradient between the evaporator and the sink means less driving force for heat transfer. This can lead to a slower rate of heat transfer from the evaporator to the condenser, which leads to a rise in evaporator

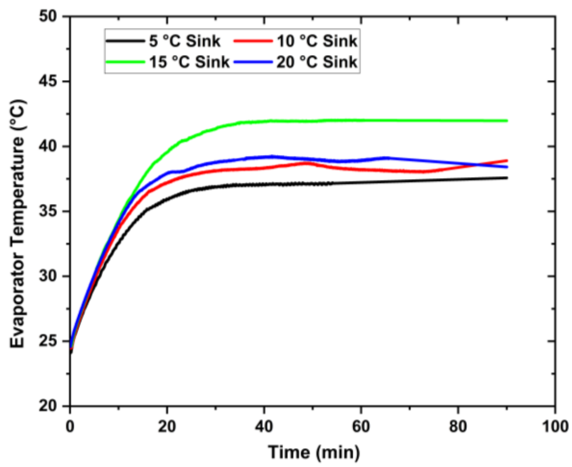

Figure 9. Effect of heat sink temperature on the startup behavior of the device at heat load 5 W

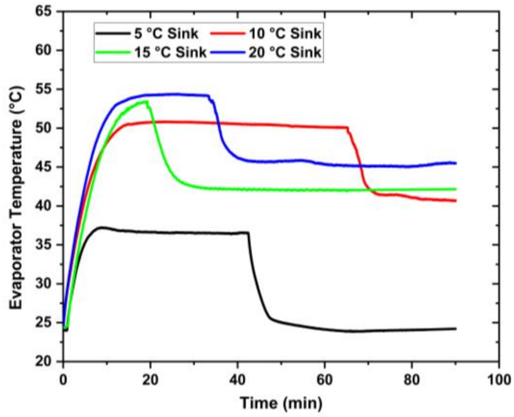

Figure 10. Effect of heat sink temperature on the startup behavior of the device at heat load 15 W

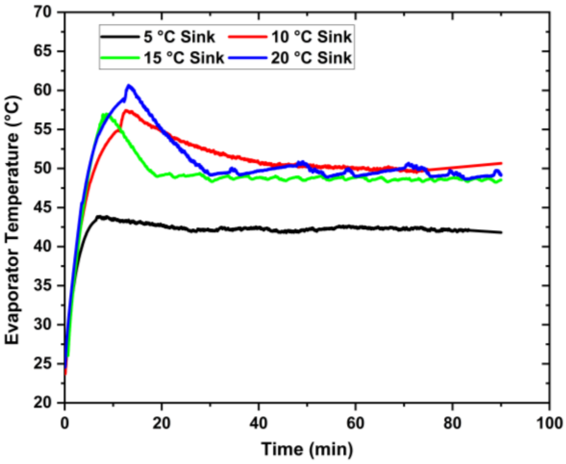

Figure 11. Effect of heat sink temperature on the startup behavior of the device at heat load 25 W

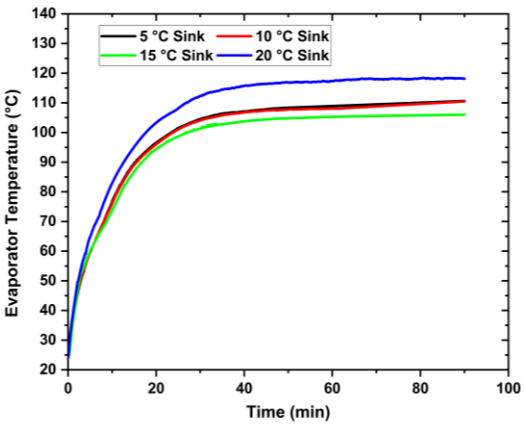

Figure 12. Effect of heat sink temperature on the startup behavior of the device at heat load 45 W.

temperature at higher sink temperatures. A higher sink temperature can increase the vapor pressure in the condenser. This can reduce the pressure difference between the evaporator and the condenser, which is crucial for driving the vapour flow through the loop, which leads to increase in startup time.

4. Conclusions

A nickel bi-porous wicked cylindrical evaporator mLHP was successfully fabricated and tested under various operating conditions. The device was charged (50%) with pentane as the working fluid. Temperature overshoots were observed at 15 W and 25 W heat load for all sink temperatures except 5°C. The relationship between heat load and startup time demonstrates that, while moderate increases in heat load facilitate quicker startups through enhanced vaporization, excessive loads can disrupt the normal operation due to instabilities and heat leakage. Furthermore, variations in sink temperature significantly affect both the device's startup dynamics and steady-state temperatures. These results highlight the significance of maintaining a balance between heat load and sink temperature in order to optimize the efficiency of mLHP systems in practical applications. Future work should focus on further refining these parameters and exploring advanced materials or designs that could enhance the efficiency and reliability of mLHPs in diverse thermal management scenarios.

5. ACKNOWLEDGEMENTS

This work was partially funded through Grant No. CRG/2020/006333 of SERB, DST, Govt. of India.

References

[1] Nashine, Chandan, and Manmohan Pandey. "Thermo-hydraulic modelling of miniature loop heat pipes." In Proceedings of the 26thNational and 4th International ISHMT-ASTFE Heat and Mass Transfer Conference December 17-20, 2021, IIT Madras, Chennai-600036, Tamil Nadu, India. Begel House Inc., 2021.

[2] Maydanik, Yu F. "Loop heat pipes." Applied thermal engineering 25, no. 5-6 (2005): 635-657.

[3] Kumari, Toni, Chandan Nashine, and Manmohan Pandey. "Fabrication of a cost-effective bi-porous composite wick for loop heat pipes." In North-East Research Conclave, pp. 117-124. Singapore: Springer Nature Singapore, 2022.

[4] Kumari, Toni, and Manmohan Pandey. "Study of Physical Characteristics of a Bi-porous Composite Capillary Wick for a Flat Miniature Loop Heat Pipe." In Conference on Fluid

Mechanics and Fluid Power, pp. 211-221. Singapore: Springer Nature Singapore, 2022.
[5] Kumari, T., Nashine, C., and Pandey, M. (2023). Experimental Investigation of Sintered Bi-porous Capillary Wicks for Miniature Loop Heat Pipes. In 10th International and 50th National Conference on Fluid Mechanics and Fluid Power, IIT Jodhpur, 2023.
[6] Launay, Stéphane, Valérie Sartre, and Jocelyn Bonjour. "Parametric analysis of loop heat pipe operation: a literature review." International Journal of Thermal Sciences 46, no. 7 (2007): 621-636.
[7] Ahmed, Shahnawaz, Manmohan Pandey, and Masahiro Kawaji. "Loop heat pipe design: an evaluation of recent research on the selection of evaporator, wick, and working fluid." Journal of Thermal Science and Engineering Applications 14, no. 7 (2022): 070801.
[8] Jung, Eui Guk, and Joon Hong Boo. "Overshoot elimination of the evaporator wall temperature of a loop heat pipe through a bypass line." Applied Thermal Engineering 165 (2020): 114594.
[9] Wu, Tong, Tingting Wang, Zhengyuan Ma, Zikang Zhang, Wei Liu, and Zhichun Liu. "Experimental investigation on the start-up performance of a loop heat pipe with three flat disk evaporators combined." Applied Thermal Engineering 216 (2022): 119128.
[10] Vershinin, S. V., and Yu F. Maydanik. "Investigation of pulsations of the operating temperature in a miniature loop heat pipe." International Journal of Heat and Mass Transfer 50, no. 25-26 (2007): 5232-5240.
[11] Nashine, C., Pandey, M., and Baraya, K. “Start-up and transient characteristics of MLHP.” In 10th International and 50th National Conference on Fluid Mechanics and Fluid Power, IIT Jodhpur, 2023.
[12] Vershinin, S. V., & Maydanik, Y. F. (2007). Hysteresis phenomena in loop heat pipes. Applied Thermal Engineering, 27(5-6), 962-968.
[13] Feng, J., Lin, G., & Bai, L. (2009). Experimental investigation on operating instability of a dual compensation chamber loop heat pipe. Science in China Series E: Technological Sciences, 52(8), 2316-2322
[14] Celata, G. P., Cumo, M., & Furrer, M. (2010). Experimental tests of a stainless steel loop heat pipe with flat evaporator. Experimental Thermal and Fluid Science, 34(7), 866-878.
[15] Qu, Y., D. Zhou, S. Qiao, K. Zhou, and Y. Tian. "Experimental study on the startup performance of dual-evaporator loop heat pipes." International Journal of Thermal Sciences 170 (2021): 107168.
[16] Du, Sheng, Quan Zhang, Li Ling, Sikai Zou, Lijun Liu, and Fanxi Meng. "Visualization investigation on temperature oscillation and two-phase behaviors of a flat loop heat pipe." Journal of Thermal Science 32, no. 4 (2023): 1536-1546.
[17] Kwon, Cheong Hoon, and Eui Guk Jung. "Overshoot temperature control on evaporator wall of loop heat pipe for space vehicle thermal control through bypass line under high thermal load." Applied Thermal Engineering 219 (2023): 119446.
[18] Bai, Lizhan, Guiping Lin, Dongsheng Wen, and Jianting Feng. "Experimental investigation of startup behaviors of a dual compensation chamber loop heat pipe with insufficient fluid inventory." Applied Thermal Engineering 29, no. 8-9 (2009): 1447-1456.
[19] Fu, Jingwei, Lizhan Bai, Yunfei Zhang, Huanfa Wang, and Guiping Lin. "Improved startup performance of a dual compensation chamber loop heat pipe by sequential cooling to the compensation chambers." International Journal of Heat and Mass Transfer 233 (2024): 126046.

Paper ID 095(S5)

Heat Transfer Performance of a Six-turn Pulsating Heat Pipe for Aeronautical Application under Vibration Environment

Naoko Iwata[1*], Vincent Dupont[1], and Antoine de Ryckel[1]

[1] *Calyos S.A., Charleroi, Belgium*
**naoko.iwata@calyos-tm.com*

Abstract

Pulsating heat pipes (PHP) have attracted industry attention as a promising heat transfer device for automobiles and aeronautics. In these applications, PHP might be exposed to a vibration environment. However, only a few studies have investigated the impact of vibration. The present study reports vibration test results by changing the PHP orientations and vibration directions, aiming to provide a complete view of the vibration impact on PHP performance under low to high frequencies (5-2000 Hz) typically applied for aeronautical applications. Moreover, a random vibration test was also performed to see the influence of actual vibration. The PHP was designed for electronics mounted on aeronautical vehicles. Although the number of turns was limited to six due to the envelope constraints, thanks to three different cross-sectional geometries, the PHP operated in a horizontal orientation as well as in bottom-heated mode. The results of the sine-sweep and sine-dwell tests showed PHP performance was affected by the vibration from 20 to 70 Hz that gave the maximum acceleration of 7g: in most cases, the performance degraded except for a couple of cases in which the vibration direction was perpendicular to the fluid oscillation. The random vibration generally had less impact than the other tests.

Keywords: Pulsating heat pipe; Vibration test; Sine-sweep; Random; Orientation; Tube cross-section

1. Introduction

In recent years, pulsating heat pipes (PHPs) [1, 2] , also called oscillating heat pipes, have attracted industry attention as a promising heat transfer device. Proposed applications for PHP include electronics [3, 4], automobiles [5, 6], and satellites [7, 8].

PHP might be exposed to a vibration environment in some applications such as automobiles and aeronautics. Since heat transfer in PHP is due to fluid oscillation, external mechanical vibration can affect its performance. However, only a few studies have investigated the impact of vibration. Alaei et al. [9] added low-frequency vibrations (10-30 Hz) to a bottom-heated PHP perpendicular to the fluid flow direction and found the vibration reduced the thermal resistance. Chen et al. [10] conducted an experiment in which a transparent PHP was subjected to local vibration (200-300 Hz) and reported that the vibration reduced the startup temperature.

The proposed study reports vibration test results with changing PHP orientations and vibration directions, aiming to provide a complete view of the vibration impact on PHP performance under low to high frequencies (5-2000 Hz) typically applied for terrestrial and aeronautical applications. Moreover, a random vibration test was also performed to see the influence of actual vibration. The PHP was designed for electronics mounted on aeronautical vehicles. Although the number of turns was limited to six due to the envelope constraints, thanks to three different cross-sectional geometries, the PHP operated in a horizontal orientation as well as in bottom-heated mode. The vibration tests were conducted in three different PHP orientations.

2. Experimental setup

2.1. Pulsating heat pipe

A six-turn PHP with a stainless steel (SS316L) seamless pipe was designed and fabricated by Calyos S.A. Both pipe ends were interconnected with a T-junction, which realized a closed-loop PHP, as shown in Figure 1. The inner and outer diameters of the pipe are 2.5 mm and 2.0 mm, respectively. A part of the circular tubes mounted on the evaporator and condenser was deformed to a triangular cross-section to increase the heat transfer area in direct contact with the active surface and allow capillary effect and storage of the liquid in the corners. This led to the improvement of the heat transfer from the heater to the fluid and promotes vapor generation, which contributes to stable fluid oscillation [11]. The tubes between the evaporator and condenser on one side of the PHP were flattened to keep the device thickness below 4mm. Two copper plate saddles are brazed to the pipe: an L 25 x W 25 x T 0.5 mm³ and L 50 x W 65 x T 0.5 mm³, respectively, at the evaporator and condenser levels. Generally, PHP has a 180° bend part on both ends, while the radius of curvature of the proposed PHP is 90°.

Instead, the PHP has a concentric configuration so that each pipe can be contacted with the plates of the evaporator and the condenser. A HFO refrigerant R1233zd(E) was charged with a filling ratio of 50 % as a working fluid. The PHP was pinched and welded so that a charging valve was detached from the PHP to avoid mechanical issues on the shaker.

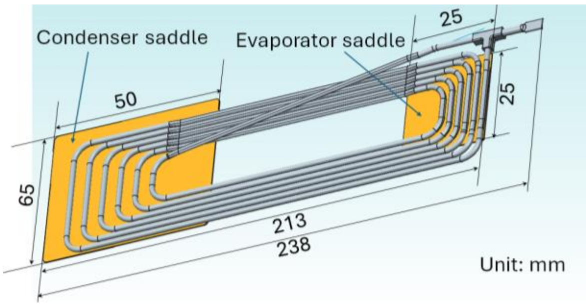

Figure 1. Schematics of PHP.

Twenty-six thermocouples were attached to the PHP; one on the heater, five on the evaporator saddle, six on the condenser saddle, and 14 on the tube surface of the adiabatic section, as shown in Figure 2. The thermocouples were attached using aluminum tape covered with Kapton tape or glued with Duralco 132, a high thermal conductivity epoxy.

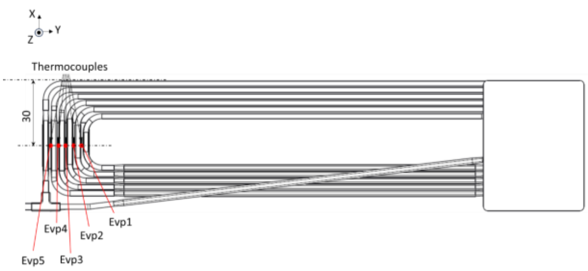

(a)

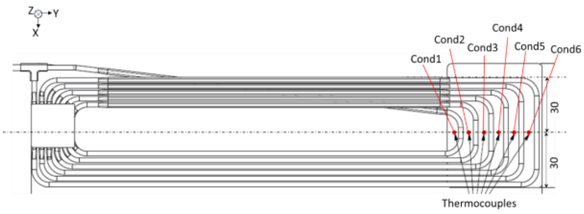

(b)

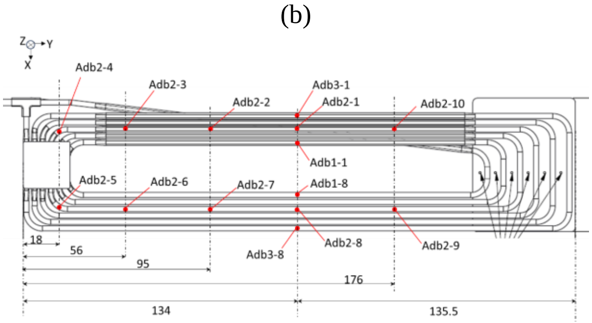

(c)

Figure 2. Thermocouple locations. (a) evaporator, (b) condenser, and (c) adiabatic section.

The temperatures measured by the thermocouples Evp3, Cond1, and Adb1-8 in Figure 2 are shown as the temperatures of the evaporator, condenser, and adiabatic section, respectively, in Figures from Figure **5** to Figure **18**.

2.2. Vibration test setup

The PHP's evaporator and adiabatic section were fixed between aluminum and stainless steel plates via thermal insulation sheets (Depron foam). An aluminum plate with four holes was mounted on the condenser saddle to fix the condenser on the shaker. A fan (RS PRO axial fan) was installed 30 mm away from the condenser saddle, providing an average airflow of 1 m/s. The holes of the aluminum plate allowed the condenser saddle to be cooled by the forced air convection. The fan was supported by aluminum jigs that was mounted on a table outside of the shaker so that the vibrations were not applied to the fan to avoid a damage caused by the vibration. A polyimide sheet heater (MINCO HAP6497) was glued on the flat surface of the evaporator saddle. A constant power was applied to the heater by a power supply unit (AGILENT N8762A). The power to the heater and temperatures were acquired and recorded by a data acquisition system (KEYSIGHT 34980A). The PHP was set on the shaker in three orientations: vertical bottom-heated mode (BHM), side, and horizontal, and vibration was applied in three directions in each PHP orientation as shown in Figure 3. As a representative example, Figure 4 shows the test setup with the vertical bottom-heated mode (BHM) PHP on the shaker.

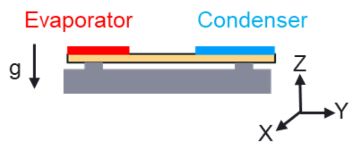

(a)

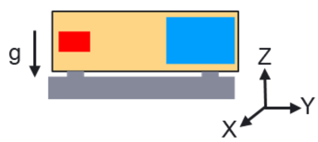

(b)

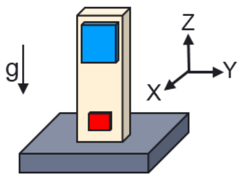

(c)

Figure 3. Test setup configuration and vibration direction. (a) horizontal PHP, (b) side PHP, and (c) BHM PHP. The arrow with "g" shows the gravitational direction.

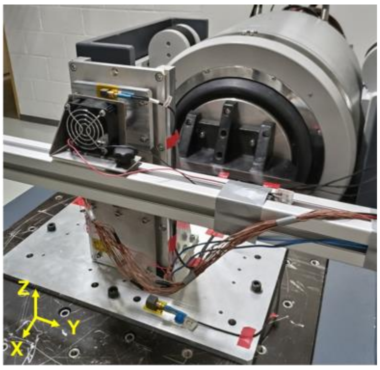

Figure 4. Test setup on the shaker (x-axis, BHM PHP).

2.3. Test sequence

Table 1 lists the test conditions with the frequency for the sine-sweep and sine-dwell tests, the acceleration level for sine-dwell tests, and the test duration and heater power for all tests. For each PHP orientation and vibration direction condition, the sine-sweep vibration from 5Hz to 2000Hz and then back to 5Hz was first performed for 17 minutes to detect the frequency with the greatest impact on PHP performance. The acceleration levels were varied from 0.13g to 7g along an acceleration curve with respect to the frequency defined for aeronautical applications. Next, a random vibration test was carried out to verify the behavior of PHPs similar to a more representative vibration environment. Lastly, the sine-dwell test was done at the most impactful frequency based on the sine-sweep test. Up to three frequencies were chosen at which the temperature change began. The frequency for the sine-dwell test varied depending on the PHP orientations and vibration directions. The acceleration of the sine-dwell test was determined by the above-mentioned curve, but the notching was considered. Only in the Y-direction sine-dwell test of the side PHP, the acceleration was increased from 1g to 7g every two minutes while the frequency was fixed at 35Hz to evaluate the impact of the acceleration on the PHP behavior. The Z-direction sine-dwell test of the BHM PHP was not conducted due to the limitation of testing time.

The nominal durations of the random and sine-dwell tests were five minutes and ten minutes, respectively in line with the system thermal time constant. The duration was extended when the temperature kept increasing or dropping during the vibration.

Before the first test (i.e., sine-sweep test), a low-level sine sweep was performed to obtain mechanical response data of the setup and to set up notching if necessary, with the acceleration level of 0.1g. The acceleration level above 1000Hz in most sine-sweep tests was reduced from the planned 7g to 1.7g because resonance was generally observed at higher frequencies than a several hundred hertz. This did not affect the sine-dwell tests because the major temperature change was typically found at the low frequency below 100Hz and therefore the dwell tests were conducted at the low frequencies, as described in section 3.1. All the vibration tests were conducted after the PHP reached a thermally steady state.

The heater power (Q) was fixed at 5W for the horizontal and side PHPs as it was the maximum power for them, while 7.5W and 30W were applied to the BHM PHP because it was able to transfer more than 30W.

Table 1. Test conditions. X, Y, and Z show the vibration directions according to Figure 3.

Orientation		Horizontal PHP	Side PHP	BHM PHP	
Heater power [W]		5	5	7.5	30
X	Sine-sweep	5 Hz - 2000 Hz - 5 Hz, 17 min.	5 Hz - 2000 Hz - 5 Hz, 17 min.	5 Hz - 2000 Hz - 5 Hz, 17 min.	5 Hz - 2000 Hz - 5 Hz, 17 min.
	Dwell	15 Hz 1.2 g, 11 min. 50 Hz 7 g, 10 min.	50 Hz 7 g, 10 min. 1850 Hz 4 g, 10 min.	N/A	35 Hz 7 g, 10 min. 225 Hz 1.7 g, 10 min. 260 Hz 1.7 g, 10 min.
	Random	5 min.	5 min.	5 min.	5 min.
Y	Sine-sweep	5 Hz - 2000 Hz - 5 Hz, 17 min.	5 Hz - 2000 Hz - 5 Hz, 17 min.	5 Hz - 2000 Hz - 5 Hz, 17 min.	5 Hz - 2000 Hz - 5 Hz, 17 min.
	Dwell	50 Hz 7 g, 10 min.	35 Hz 7 g, 10 min. 35 Hz 1 - 7 g (2 min. each)	35 Hz 7 g, 10 min.	35 Hz 7 g, 10 min.
	Random	5 min.	5 min.	5 min.	5 min.
Z	Sine-sweep	5 Hz - 2000 Hz - 5 Hz, 17 min.	5 Hz - 2000 Hz - 5 Hz, 17 min.	5 Hz - 2000 Hz - 5 Hz, 17 min.	5 Hz - 2000 Hz - 5 Hz, 17 min.
	Dwell	30 Hz 4.19 g, 20 min. 50 Hz 7 g, 20 min.	60 Hz 7 g	N/A	N/A
	Random	5 min.	5 min.	5 min.	6 min.(1st) 5 min. (2nd)

3. Results

3.1 Sine-sweep and sine-dwell vibrations parallel to fluid oscillation

During the sine-sweep, the change in the PHP temperatures was mainly observed at a low frequency range from 20 to 70Hz, regardless of the PHP orientations and vibration directions. Figure 5, Figure **6** and Figure **7** are representative examples of the temperature evolution during the sine-sweep tests. At the low frequency mentioned above, the evaporator temperatures increased, and condensers dropped, but then each returned to its original temperature or even lower in a few minutes before the frequency reached 100Hz. The same behavior was seen during the down-sweep vibration around the same frequency as the up-sweep. The vibration direction was parallel to the fluid oscillation in all three cases, whereas the BHM PHP (Figure 7) showed less influence of the vibration on the PHP performance than the horizontal (Figure 5) and side PHP (Figure 6).

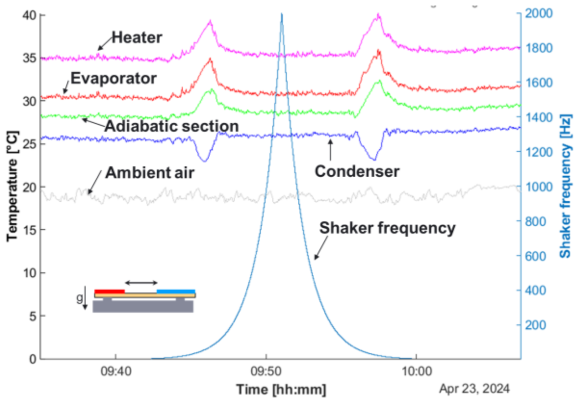

Figure 5. Sine-sweep (Y-direction) test result of horizontal PHP.

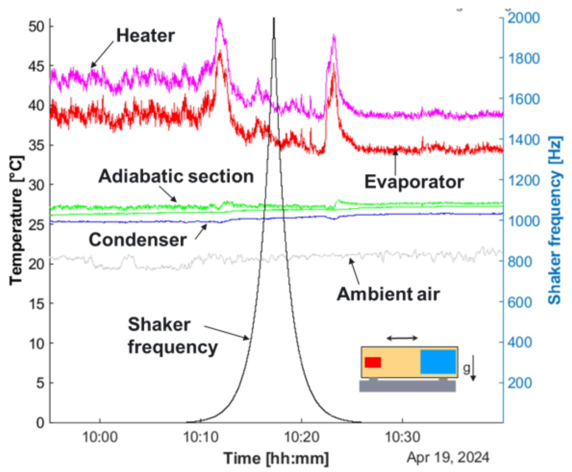

Figure 6. Sine-sweep (Y-direction) test result of Side PHP.

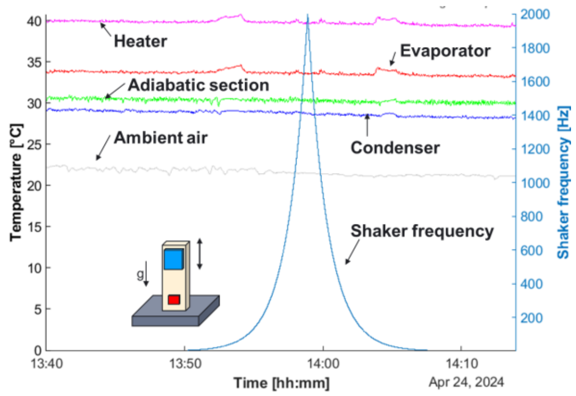

Figure 7. Sine-sweep test (Z-direction) result of BHM PHP (Q = 7.5 W).

For sine-dwell tests of the horizontal and side PHPs, 50Hz and 35Hz were chosen, respectively, at which the evaporator temperature started rising and the condenser temperature dropped. Figure 8 shows the temperature evolution of the horizontal PHP. The temperatures showed a reaction, i.e., increasing or decreasing, in a few seconds after the vibration started. Same as the sine-sweep test, the PHP showed a partial dry-out, i.e., the evaporator temperature rose, and the condenser dropped. On the other hand, however, the temperatures did not return to their original level but remained higher or lower than those before the vibration. Yet the PHP did not completely lose its function, since the evaporator temperature was 50 °C lower than that of the empty PHP with the same power input to the heater. It should be noted that the temperatures returned to the original level immediately after the vibration stopped.

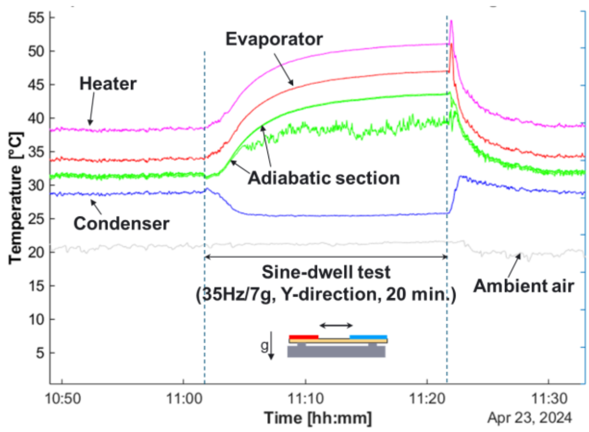

Figure 8. Sine-dwell test (50Hz / 7g, Y-direction) result of horizontal PHP.

Figure 9 shows the temperature evolution of the side PHP during the Y-direction sine-dwell test at 35Hz / 7g. The PHP performance was degraded by the vibration same as seen in Figure 7. Moreover, the temperature fluctuation was induced in the evaporator, which disappeared once the vibration terminated.

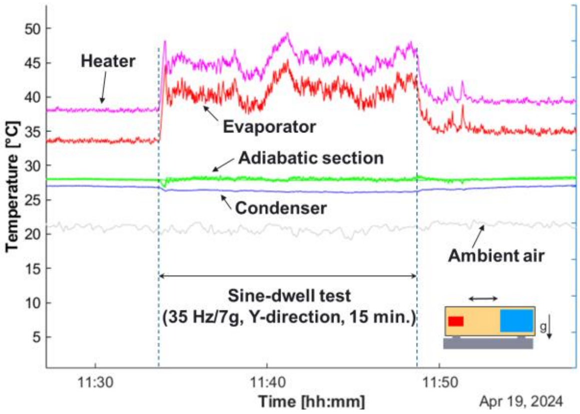

Figure 9. Sine-dwell test (35Hz / 7g, Y-direction) result of Side PHP.

After the test of Figure 9, the acceleration was changed from 1g to 7g by fixing the frequency at 35Hz. The temperature evolution is shown in Figure 10. The vibration effect began to be seen around 2-3 g by the spikes and the drift of the evaporator temperature. This grew to the periodic fluctuation around 4-5g, and eventually the oscillation that was similar to the one in Figure 9 appeared at 6-7g. The result demonstrated the largest acceleration (i.e., 7 g) in the low frequency between 35Hz to 60Hz could cause the temporal performance degradation of the PHP during the sine-sweep tests.

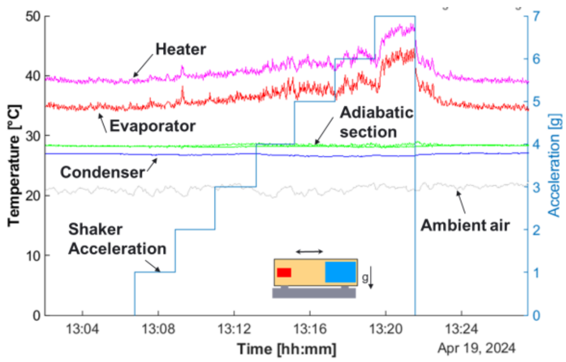

Figure 10. Sine-dwell test (35Hz / 1-7g, Y-direction) result of Side PHP.

3.2 Sine-sweep and sine-dwell vibrations perpendicular to fluid oscillation

Compared to the vibration parallel to the fluid oscillation, the vibration perpendicular to it had a different or less impact on degrading the PHP behavior. Figure 11 shows the temperature evolution during the Z-direction sine-dwell test of the side PHP. The intermittent spikes appeared in the evaporator temperature during the vibration, which indicated a stop-over of the fluid oscillation i.e. a drying-rewetting aperiodic mode at evapator level. Apart from this, the temperature stayed the same level as before the vibration.

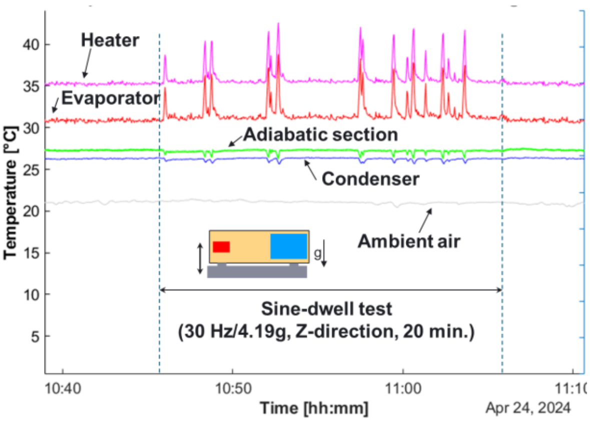

Figure 11. Sine-dwell test (30 Hz / 4.19g, Z-direction) result of Side PHP.

The vibration influence was smaller on the horizontal PHP than on the side PHP in some cases. Figure 12 shows the result of the sine-dwell test at 15Hz. The PHP performance was not influenced as much as other test results shown before, though temperature fluctuations appeared slightly more intense than before the vibration. The temperature change appeared around 15Hz in the sine-sweep test as shown in Figure 13, there was the possibility that the low acceleration level of 1.4g mitigated the impact during the sine-dwell test.

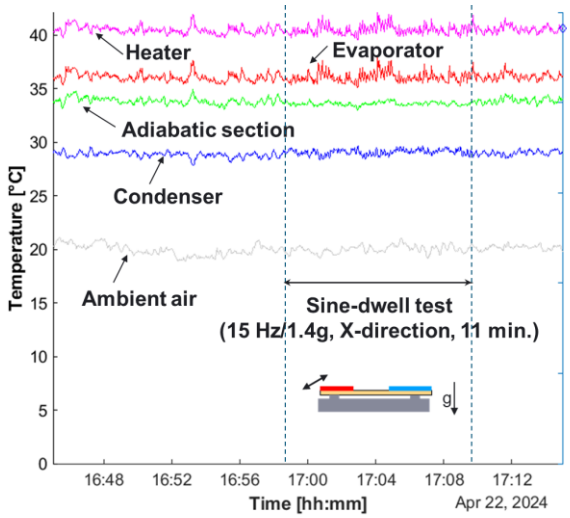

Figure 12. Sine-dwell test (15Hz / 1.4g, X-direction) result of horizontal PHP.

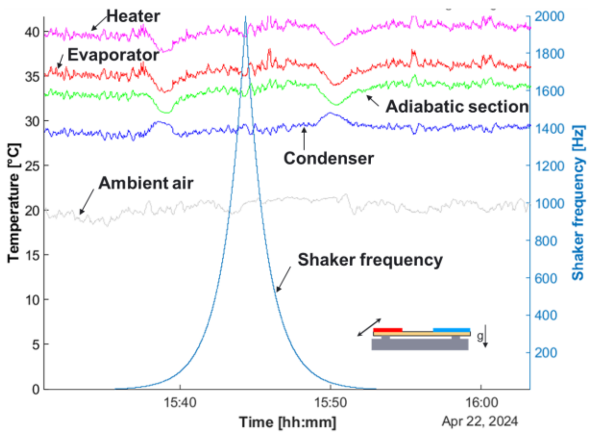

Figure 13. Sine-sweep test (X-direction) result of horizontal PHP.

Among all the sine-dwell vibration tests, there were only two cases in which the PHP performance was improved by the vibration. One was conducted at the frequency of 50Hz in the X direction for the horizontal PHP, as shown in Figure 14. The temperature oscillation that was seen before the vibration was relaxed and the evaporator temperature decreased 3-4 °C. This suggested that the vibration changed the flow regime inside the PHP, though a detailed interpretation was difficult without a visualization of the flow. The other case of performance improvement was the side PHP in X-direction vibration at 50Hz / 7g, which is discussed in section 4.

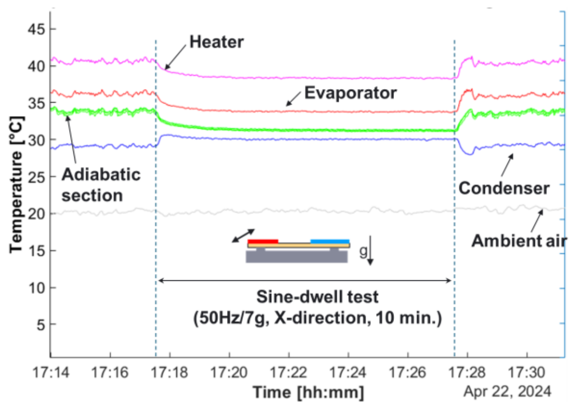

Figure 14. Sine-dwell test (50Hz / 7g, X-direction) result of horizontal PHP.

The BHM PHP also had less impact on its performance compared to the parallel vibration, as shown in Figure 15. No obvious impact on the temperature was found apart from the 1K decrease in the evaporator temperatures after the vibration. On the other hand, when there was a heat input of 30W instead of 7.5W, the PHP performance was degraded more obviously, as shown in Figure 16. This suggested that the fluid oscillation that was close to its operational limit was more affected by the vibration.

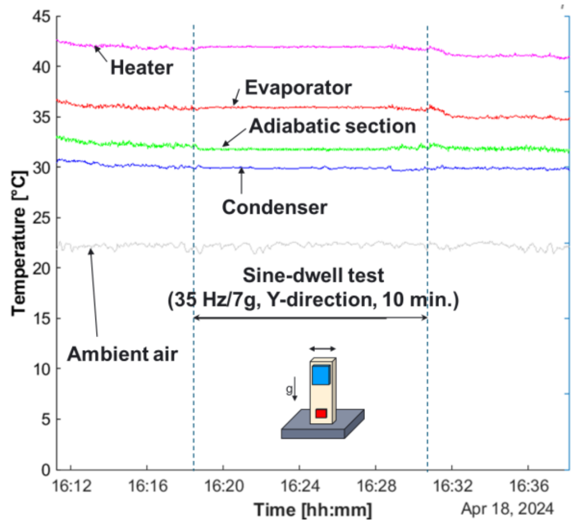

Figure 15. Sine-dwell test (35Hz / 7g, Y-direction) result of BHM PHP (Q = 7.5W).

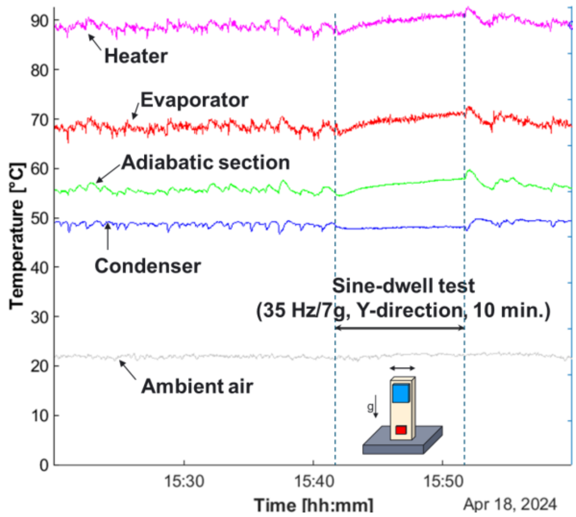

Figure 16. Sine-dwell test (35Hz / 7g, Y-direction) result of BHM PHP (Q = 30W).

Whereas most of the sine-dwell tests were conducted with a frequency less than 100Hz without considering the mechanical resonance of the PHP, the BHM PHP was tested at its resonance frequency of 260Hz. The temperature evolution is shown in Figure 17. No significant change was seen in the temperatures, which indicated that the mechanical resonance did not impact the hydraulic and thermal behavior.

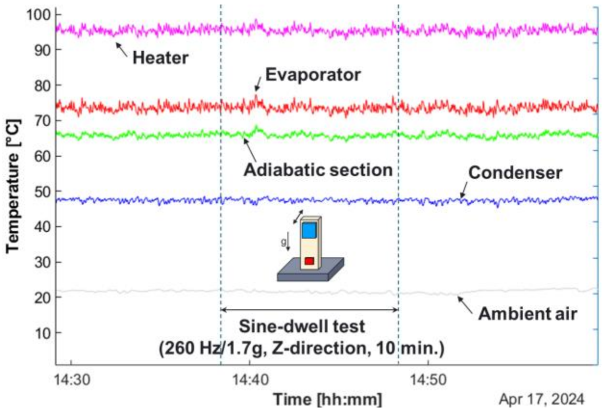

Figure 17. Sine-dwell test (260Hz / 1.7g, X-direction) result of BHM PHP (Q = 7.5W).

3.3 Random vibration effects

Compared to the sine-dwell vibration, the random vibration had less impact on the PHP performance in general. As one of the most affected results, Figure 18 shows the temperature evolution of the side PHP at the Y-direction vibration, i.e., parallel to the fluid oscillation. The evaporator temperature increased by about 1K during the vibration and decreased by 2K after it, which led lower temperature than that before the vibration.

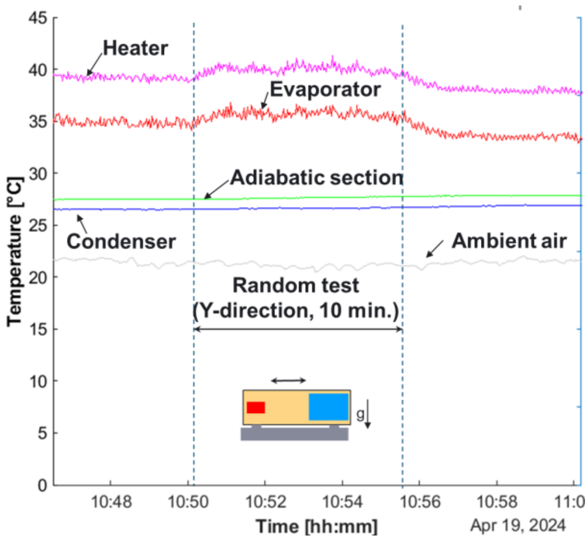

Figure 18. Random test (Y-direction) result of side PHP.

A significant change was seen in the temperatures of the BHM PHP (Q = 30 W) during the Z-direction random cycle, as shown in Figure 19. The temperature oscillation suddenly disappeared in the middle of the vibration and did not appear again even after the vibration stopped. The random vibration was loaded to the PHP again with the same conditions, but the temperature oscillation did not come back except for a fluctuation shown in Figure 20.

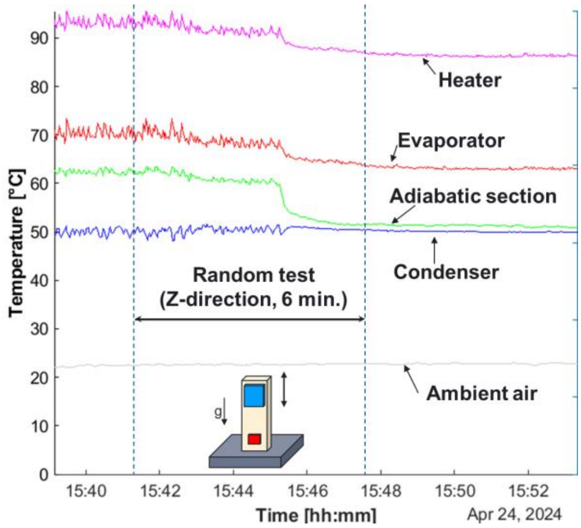

Figure 19. First random test (Z-direction) result of BHM PHP (Q = 30W).

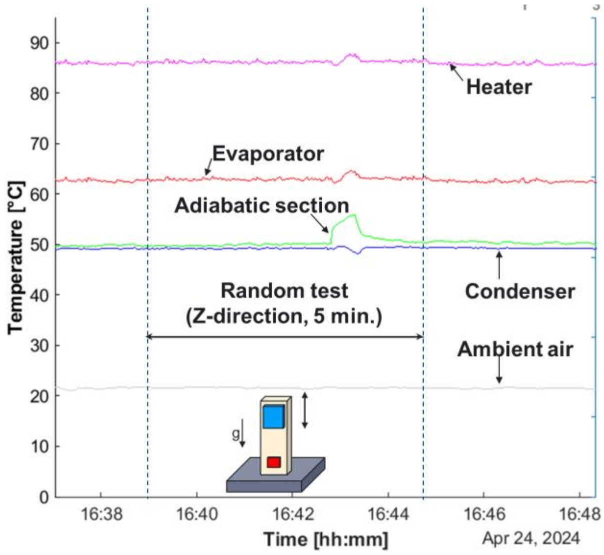

Figure 20. Second random test (Z-direction) result of BHM PHP (Q = 30W).

4. Discussion

In sine-sweep tests, generally, no significant change in temperature was found at the high frequency above 300Hz. On the other hand, the evaporator temperature decreased, and the condenser increased at low frequency i.e. around 20 to 40Hz. Then, the temperature returned to the original temperature level at about 60Hz. It is important to notice that the frequency that influenced the fluid oscillation could be slightly different from the above identified frequencies as any change in hydraulic behavior take time to induce a measurable effect of temperature evolution.

The sine-dwell tests showed different results depending on the PHP orientation and vibration frequencies as summarized in Table 2. The influence on the PHP was grouped into seven categories as shown in the color map. In most of the cases, the PHP performance degraded, i.e., the thermal resistance between the evaporator and the condenser, R_{th}, increased during the vibration. The worst case was that the fluid oscillation stopped, and the evaporator temperature increased (color; yellow). In other cases, the temperature oscillation continued such as in Figure 9, or the stop-over was observed like Figure 11. Importantly, however, as soon as the vibration stopped, this behavior disappeared and the R_{th} returned to the level before the vibration. It can be said that the changes caused by sine-dwell and sine-sweep vibrations were not irreversible.

The vibration affected the PHP performance more when it was parallel to the fluid oscillation than when it was perpendicular to it, though the latter also caused the R_{th} increase. The improvement in R_{th} (color: green) was only observed in the horizontal and side PHP when the perpendicular vibration (X-direction) was loaded. Interestingly, this occurred at the same frequency of 50Hz. In both cases, the temperature oscillations disappeared during the vibrations. There were no sine-dwell tests where R_{th} decreased during the presence of temperature oscillations.

Table 2. Synthesis of the sine-dwell test results. See the color map below for the colors in the "temp. reaction" column.

PHP orientation	Vibration direction	Heater power [W]	frequency [Hz]	acceleration level [g]	temp. reaction
Horizontal	X	5	15	1.2	W
	X	5	50	7	G
	Y	5	50	7	Y
	Z	5	30	4.19	O
	Z	5	50	7	Y
Side	X	5	50	7	O
	X	5	50	7	G
	X	5	1850	4	Y
	Y	5	35	7	O
	Y	5	35	1	O
	Y	5	35	2	O
	Y	5	35	3	O
	Y	5	35	4	O
	Y	5	35	5	O
	Y	5	35	6	O
	Y	5	35	7	O
	Z	5	30	4.19	P
	Z	5	60	7	P
BHM	X	30	35	7	Y
	X	30	225	1.7	Y
	X	30	260	1.7	W
	Y	30	35	7	Y
	Y	7.5	35	7	O

Color map for the temperature reaction

	with temp. oscillation	w/o oscillation	periodic dry-out	No change
Rth ↑				
Rth ↓	not observed		not observed	

5. Conclusions

A PHP was designed, and a prototype was fabricated for electronics mounted on aeronautical vehicles where the PHP will be exposed to a vibration. Since heat transfer in PHP is due to fluid oscillation, external mechanical vibration can affect its performance. The PHP was tested under the sine-sweep, sine-dwell, and random vibration, aiming to provide a complete view of the vibration impact on PHP performance under low to high frequencies (5-2000Hz) typically applied for aeronautical applications in the development process. The PHP consisted of six-turns stainless steel tubes with different cross-sectional geometries so that the PHP operated in a horizontal orientation as well as in bottom-heated mode. The main outcomes of the vibration tests were as follows:

- The temperature measuring the tube surface reacted in a few seconds after the vibration started in the sine-dwell tests.
- The results of the sine-sweep and sine-dwell tests showed PHP performance was affected

by the vibration from 20 to 70Hz that gave the maximum acceleration of 7g.

- The behavior observed during the vibration tests such as partial dry-out or stop-over disappeared immediately after the vibration stopped.
- Generally, no significant impact was seen at a frequency higher than 100Hz.
- In most test cases, the performance degraded except for a couple of cases in which the vibration direction was perpendicular to the fluid oscillation and the PHP orientation was side or horizontal.
- The vertical bottom-heated PHP was less influenced by the vibration than the horizontal and side PHP.
- The random vibration generally had less impact than the other tests.

PHPs are increasingly attracting industry attention as innovative heat transfer devices. What this study reports will provide useful data for the use of PHP in environments where mechanical vibrations are applied, such as aircraft and automobiles.

6. ACKNOWLEDGEMENTS

The present work has received funding from the Wallon Region Skywin Eloise project under grant agreement No 8524 The authors thank V2i S.A. for their support and expertise regarding vibration testing.

References

[1] H. Akachi, Structure of a heat pipe. U.S. Patent: No. 4921041, 1990.

[2] H. Akachi, Structure of a micro-heat pipe. U.S. Patent: No. 5219020, 1993.

[3] S. K. Hota, K.-L. Lee, B. Leitherer, G. Elias, G. Hoeschele and S. Rokkam, Pulsating heat pipe and embedded heat pipe heat spreaders for modular electronics cooling. Case Studies in Thermal Engineering, 2023. 49: p. 103256.

[4] H. Constantinou, S. Lani, G. Rouaze and J. R. Thome, High Performance Pulsating Heat Pipe for Electronics Cooling. IEEE, 2022. San Diego, U.S.A.

[5] M. Chen and J. Li, Nanofluid-based pulsating heat pipe for thermal management of lithium-ion batteries for electric vehicles. Journal of Energy Storage, 2020. 32: p. 101715.

[6] J.-S. Lee, S.-J. Kim, W.-S. Han and S.-H. Rhi, Anti-Gravity 3D Pulsating Heat Pipe for Cooling Electric Vehicle Batteries. energies, 2024. 17(10): p. 2283.

[7] B. S. Taft and K. W. Irick, ASETS-II oscillating heat pipe space flight experiment: the first six months on orbit. Frontiers in Heat and Mass Transfer, 2019. 12: p.1.

[8] M. Ando, A. Okamoto, K. Tanaka, M. Maeda and H. Sugita, On-orbit demonstration of oscillating heat pipe with check valves for space application. Applied Thermal Engineering, 2019. 130: p. 552.

[9] Alaei and M. H. Kafshgari, Low-frequency vibrations on the thermal performance of an oscillating heat pipe. Industrial & Engineering Chemistry Research, 2014. 53: p. 12179.

[10] J. Chen, J. Dong, and Y. Yao, Experimental study on the starting-up and heat transfer characteristics of a pulsating heat pipe under local low-frequency vibrations. Energies, 2021. 14: p. 6310.

[11] Q. Cai, C. L. Chen, and J. F. Asfia, Heat transfer enhancement of planar pulsating heat pipe device. The American Society of Mechanical Engineers International Mechanical Engineering Congress and Exposition – ASME IMECE, 2006. Illinois, U.S.A.

Paper ID 096(S8)

Experimental investigation of the effect of the vibration on the operation of the direct contact condensation "box" component of a Capillary Jet Loop

V. Dupont[1*] , C. Popper[1], M. Bertha[2] , S. Hoffait[2], and A. de Ryckel[1]
[1] *Calyos S.A., Charleroi, Belgium*
[2]*V2i S.A., Liège, Belgium*
**vincent.dupont@calyos-tm.com:*

Abstract

In this experimental study the "-dcc box" component of a Capillary Jet Loop architecture (CJL-dcc) is submitted to vibration on a shaker first in the z-axis direction i.e. the direction of the "-dcc tube" and second in the transverse x-axis direction. The two-phase ring (TPR) provides the liquid to the capillary structure and the capillary evaporator induces vapor jets thanks to four injector elements in parallel. The momentum exchange between the high velocity acetone vapor flows and the low velocity of the subcooled liquid ensures both transport and condensation functions before the connecting lines. This paper discusses the design, material and experimental performances of this specific demonstrator able to transfer 1.57 kW from a 90 x 90 mm² footprint heater. The two type of vibrations cycles are investigated: random and sine sweep. Based on the thermal reaction of the CJL during the sine sweeps, several spot frequencies are selected on both z-axis and x-axis to perform spot frequency vibration during a period long enough to reach the system thermal steady state.

Keywords: Direct Contact Condensation; Injector; Ejector; Capillary Thermosyphon; Capillary Jet Loop; Vapor Driven Pump.

1. Introduction

Passive two-phase capillary heat transport technologies can be used for thermal management in aircraft (sub) systems and/or components. In particular, Loop Heat Pipe has been proposed and successfully tested on several projects but suffers several limitations. The first one is due to the presence of vapor and liquid in the transport lines that makes the system sensitive to the acceleration forces and limits the transport distance and/or the use of ammonia as a working fluid. Moreover, if for any reason the design acceleration is exceeded, the capillary evaporator deprimes and the hot source must be cut off before any new heat application, therefore limiting the operability of the aircraft. The second key point is to ensure uniform heat distribution regardless of the combination of aircraft attitude, available power, and local acceleration. With parallel connections inside the condenser, additional pressure drops are necessary to successfully distribute the flow and both the vapor quality and the hydrostatic head between channels make condenser sizing difficult. To overcome these difficulties, the Capillary Jet loop operating in direct condensation mode (CJL-dcc) transforms a two-phase flow into a single-phase system [1-4].

2. Direct contact condensation with a Capillary Jet Loop (CJL-dcc)

The working principle of the CJL-dcc is presented in detail in [2], it is a combination of a jet pump driven by the vapor flow generated by one or more capillary evaporators. The momentum exchange between the high velocity vapor and the so-called two-phase ring (TPR) flow induces the fluid motion thanks to the injector elements. The key point of the design in direct condensation mode is to ensure complete condensation before reaching the transport line to lower the acceleration effect. In comparison to "LHP vapor driven system" [5-6], the CJL is more a "CPL vapor driven system" because it is possible to operate several evaporator in parallel without conflict between the different compensation chambers. In case of reservoir function need, it shall be located at the outlet of the -dcc tube. Today the LHP vapor driven [5-6] have only been operated with steam and water is an issue in terms of chemical compatibility (with usual material except titanium,) and operation during freezing conditions in particular cold startup, typically at -55°C for aeronautical devices. CJL architecture allows to use acetone [2, 4] for better performances or R1233zd(E) [3] working fluid for safety reasons.

The refrigerant CJL [3] was equipped with a single injector and the condensation performed in the TPR itself i.e. the vapor was potentially able to reach the subcooler. To transfer higher heat load (HL), it is convenient to use several injectors in parallel, creating a new component so-called "-dcc box", from where, by design, the vapor is unable to escape [4]. Such architecture has been successfully tested, on ground condition, to transport heat from a hot oil flow as heat source to a composite material as coolant surface that is part of the nacelle in a turboprop transport aircraft [4]. It performs both ice protection and oil cooling. This *Bisance demonstrator* was tested with a single capillary loop and four injectors "-dcc box" component with acetone for better performance. A strong coupling between the condensation performance and the entrainment ratio has been clearly identified.

LHP operation under vibrations have been extensively tested in the past, leading to the conclusion that capillary evaporator is insensitive to the standard level encountered during aeronautical most severe qualification cycles. A good example is an ammonia LHP given in [7]. At the pore scale the acceleration effects on the liquid/vapor interface are completely damped by the viscosity forces. A method to predict such a resonance capillary tubes is discussed in §8.1.

Because vibrations can strongly deform the liquid/vapor interface (vapor jet and/or bubbles) inside macroscale tubes, they might impact both thermal and hydraulic performances of the CJL operating in -dcc mode. Thus, the present work focus on the vibrations impact of this specific element of the thermal architecture i.e. the "-dcc box" component with limited change on the other elements.

2.1 Eloise CJL demonstrator

The Eloise demonstrator, presented in 'Figure 1', is an upgraded variation of the previous *Bisance RS-0/1 demonstrator* [4].

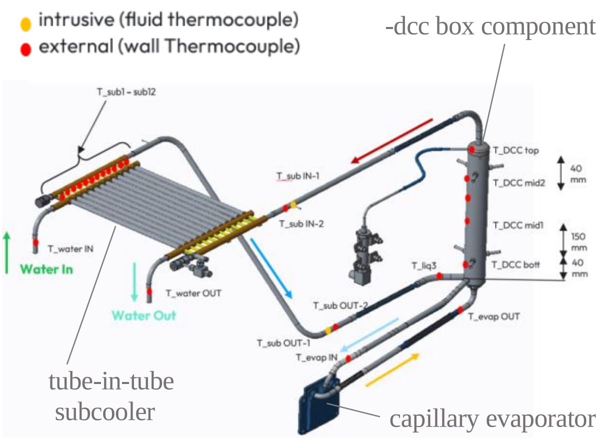

Figure 1. main components and thermocouple's locations of the *Eloise CJL demonstrator*.

The working fluid remains acetone. The single evaporator thermal performances are evaluated from the temperature of 2 thermocouples - bonded inside a 1.2 mm width groove inside the 5 mm thickness wall – and averaged to determine $T_{Ev\ wall}$ with an uncertainty of +/-0.3K. The other thermocouples are located outside the tube of the system except the subcooler inlet and outlet that are intrusive. The absolute system pressure is measured at the top of the "-dcc box" (cf 'Figure 1') with an absolute pressure transducer Keller PAA-33X, 0-10 bars pressure transducer with an accuracy of 0.10% EM i.e. +/-10 mbar, on the measurement range This pressure is used to determine the saturation temperature $T_{sat}(P_{loop})$ from the NIST Refprop data for acetone. After the breaking of the flexible line the transducer has been located at subcooler level (cf. 'Table 1'). The heating element is an aluminum block equipped with two heating cartridges. The contact area (thermal grease) is 90 x 90 mm² i.e. 1'570 W gives 19.4W/cm².

The cold source is a tube-in-tube subcooler exchanger connected with an ethylene-glycol water coolant loop. The subcooler is based on twelve 7x0.25mm copper inner grooved tube (IGT) with a pitch of 22mm The IGT active length is 360mm and the 14.0mm internal diameter stainless steel manifold (distributor or collector) include a 19.0mm extra length before Swagelok union. A 0.5mm thick annular counterflow is created around each IGT with mass flow set to 5LPM (Water93%-EG7%) at +20°C for any test. Several type-T thermocouples and one absolute pressure transducer permit to estimate the various thermal resistances along the thermal chain and the entrainment ratio of the TPR [4] as presented in §4.2.

The data acquisition device is a standard Agilent 3472A connected to a PC via an Ethernet connection and a LabVIEW interface.

2.2 Specific "-dcc box" design for shaker operation

The original aluminum "-dcc box" component [4] is modified with flexibles stainless steel lines and is a full stainless steel assembly vertically oriented (cf. 'Figure 2'). This orientation led to a positive effect of the acceleration of the gravity. The internal design keeps the original internal components with four 344mm long 12mm internal diameter and straight "-dcc tubes" coaxial to the 3.1mm injector.

An overview of the "-dcc box" component bolted to the shaker is presented in 'Figure 3'. Some calculations performed by V2i lead to a specific mechanical design for the exit tube in the center that shall be maintained with some reinforcement. The resonance frequency of the "-dcc tubes were supposed to be over 534Hz. In fact a rattling noise during the first x-axis shaking campaign tentative led to a modification of the internal design with several welding point to better maintain the -dcc tubes together (*Ib* in 'Table 1') solved this problem.

A robust aluminum structure maintains the "-dcc box" component on the shaker base plate. This hardware version allows us to limit the effect of the vibrations cycle to the physics of the vapor injection inside a confined subcooled flow.

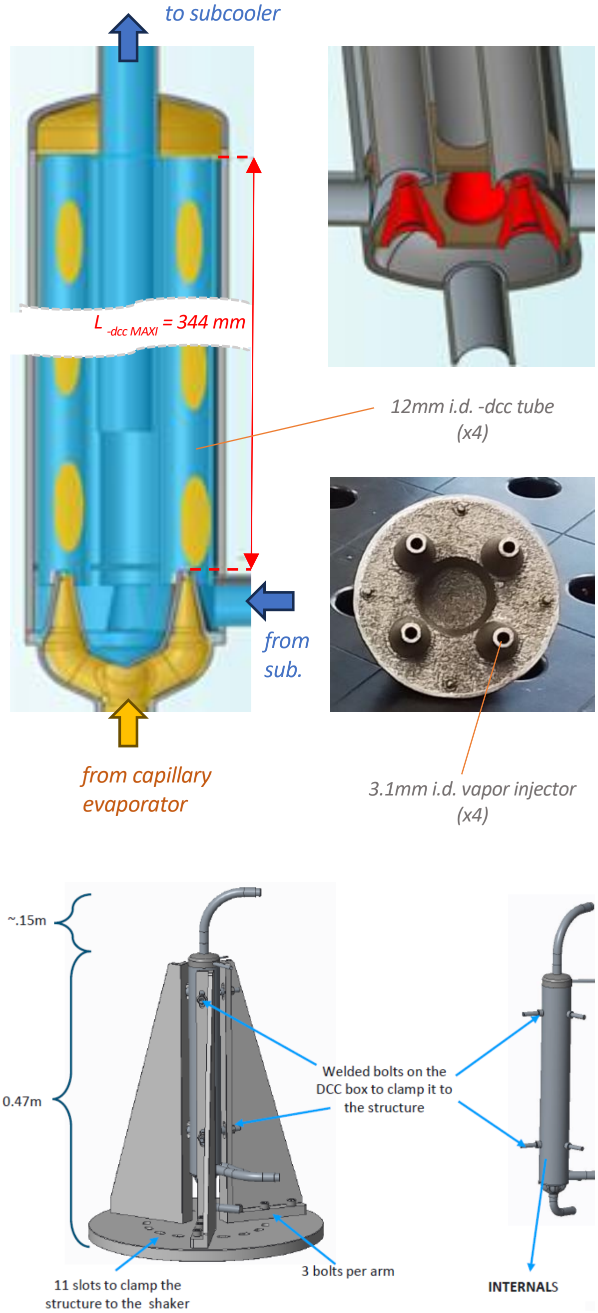

Figure 2. vertical "-dcc box" component design of the Eloise CJL demonstrator with 3D printed injector part and the aluminum external structure.

3. Vibration tests campaign

The demonstration is tested in the V2i facility with a Dongling BT600M shaker capable of a maximum acceleration of 43.7g, a maximum displacement of 76mm, a maximum usable frequency of 2'000Hz with an effective moving mass of 80kg. The size of the slip plate is 0.6x0.6m².

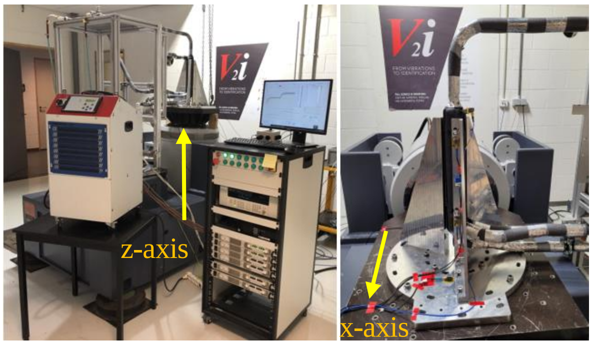

Figure 3. Eloise CJL demonstrator with the "-dcc box" component bolted on the shaker for z-axis test (left) and (x-axis) tests.

'Table 1' gives the tests conditions corresponding to each test number used here after in the legend of the graphs or in the text. Only some representative CJL parameter evolution graphs are given in the present publication but synthesis figures are based on the whole database.

Table 1. definition of the test campaign.

#	vibration test cycle			HL	-dcc	Pres.	In.
	none	z-axis	x-axis	cycle	box	loc.	?
1	x	-	-	Q max	Ia	-dcc	n
2	x	-	-	2 steps	Ia	-dcc	n
3	x	-	-	Q max	Ia	-dcc	y
4	x	-	-	Q max	Ia	-dcc	y
5	x	-	-	2 steps	Ia	-dcc	y
6	x	-	-	Q max	Ia	-dcc	y
8	-	S. sweep	-	Q max	Ia	-dcc	y
9	-	S. sweep	-	Q cte	Ia	-dcc	y
10	-	S. sweep	-	Q cte	Ia	-dcc	y
11	-	S. sweep	-	Q cte	Ia	-dcc	y
12	-	Spot	-	Q cte	Ia	-dcc	y
13	-	Random	-	2 steps	Ia	sub.	y
14	-	Random	-	3 steps	Ia	sub.	y
15	x	-		2 steps	Ia	sub.	y
17	-	-	S. sweep	Q cte	Ia	sub.	y
18	x	-	-	Q max	Ib	sub.	y
20	x	-	-	2 steps	Ib	sub.	y
21	-	-	S. sweep	Q max	Ib	sub.	y
22	-	-	Random	Q max	Ib	sub.	y
23	-	-	S. sweep	Q cte	Ib	sub.	y
24	-	-	Spot	Q cte	Ib	sub.	y

4. Data reduction

4.1 Saturation temperature measurement

An accurate evaluation of the saturation condition inside the loop is necessary to correctly evaluate the part of the vaporized heat load and the enthalpy balance at both subcooler and capillary evaporator. 'Figure 4' shows the comparison of the saturation temperature calculated from the signal given by the pressure transducer located at the top of the "-dcc box" to the external temperature of the vapor tube at the inlet of the manifold of the four injectors. The match is very good. As discussed, during the campaign the location of the pressure transducer has been moved after test #12 from the top of the -dcc box (breaking of the connecting flexible line and strong signal reaction during the x-axis shaker solicitations). Thus, *T Ev OUT* value is chosen as saturation temperature to perform the analysis.

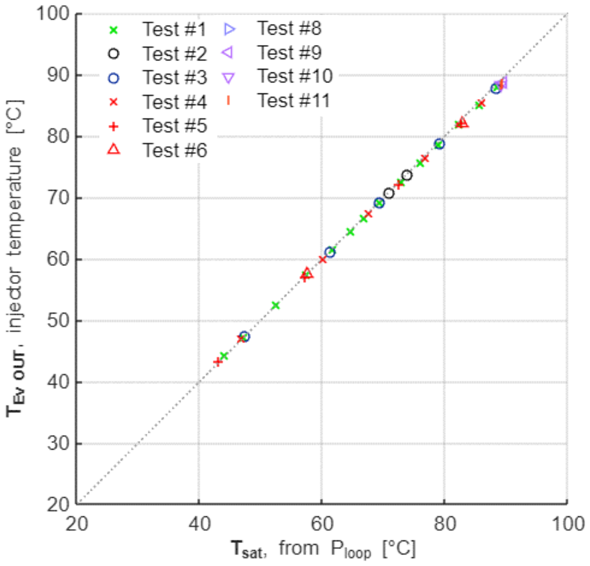

Figure 4. external vapor tube temperature versus acetone saturation temperature calculated from the pressure at the top of the -dcc box.

4.2 CJL γ entrainment factor

The two-phase ring entrainment ratio γ is arbitrary defined by:

$$\dot{m}_{TPR} = \gamma_{-dcc\,min}\,\dot{m}_{vap} \qquad (1)$$

where the vaporized heat load is given by the following enthalpy balance:

$$\dot{m}_{vap} = \Delta h_{LV} + Cp_L(T_{Ev\,OUT} - T_{sub\,OUT\,1}) \qquad (2)$$

The acetone mass flow rate inside the TPR is not directly measured. Thus, this calculation only gives a minimum value because, by "-dcc box" component design, fully condensation is achieved to reach a steady state and the heat shall be released at subcooler level (in single phase liquid condition) to reach steady state leading to the following relation:

$$\gamma_{-dcc\,min} = \frac{\Delta h_{LV} + Cp_L(T_{Ev\,OUT} - T_{sub\,OUT\,1})}{Cp_L(T_{sub\,IN\,1} - T_{sub\,OUT\,1})} \qquad (3)$$

In summary, it is possible to determine the $\gamma_{\text{-dcc min}}$ factor with only three thermocouples; one on the external part of the vapor tube (pt '2') and the two intrusive one's located in the middle of liquid flow at the inlet and the outlet of the subcooler (pt. '6' and '7') on the CJL circuit of Figure 5. The higher is $\gamma_{\text{-dcc min}}$ the better is the hydraulic performance and, also, the global thermal performance (because of the temperature gradient at subcooler level). More details are available on [4].

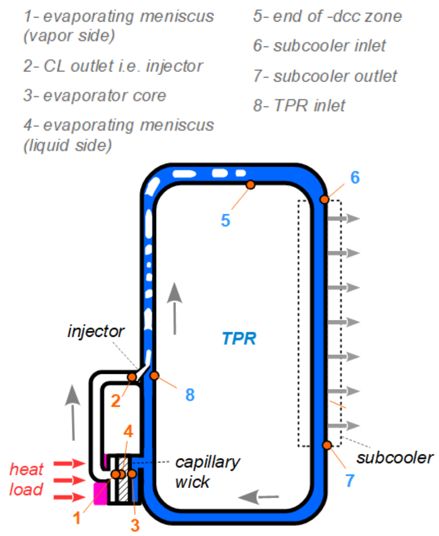

Figure 5. schematic view of the CJL circuits

4.3 CJL global thermal resistance

The global thermal resistance of the system is based on the total thermal gradient in the system, including the liquid cooling exchanger side. The lower is Rth_{global} the better is the CJL performance. It is given by the following equation:

$$Rth_{global} = \frac{0.5(T_{Ev\,wall\,1} + T_{Ev\,wall\,2}) - T_{water\,IN}}{Q_{HL}} \qquad (4)$$

5. CJL performances without vibrations

'Figure 6' shows both global thermal resistance and γ entrainment ratio, versus the heat load (HL), determined with, respectively, equations (4) and (3) and after the modification of the internal part of the "-dcc box". This test #8 is performed, before truck transportation without vibrations. The parameters evolutions are smooth, and the test duration is 3h30 with a maximum heat transport of 1'570W.

'Figure 7' gives the metrics for the whole databases showing a decrease of both Rth_{global} and γ with the heat load. This trend and the performances are inline, a bit better, with the performances measured with the *Bisance CJL* *demonstrator* before the design adaptation of the "-dcc box" component to the shaker [4]. Performances are independent of the various test conditions but, between 500W and 900W, two set of points, corresponding to test #1 and test #8 curve are separated. Today, no clear explanation is found, and the two curves are used as reference in the paper.

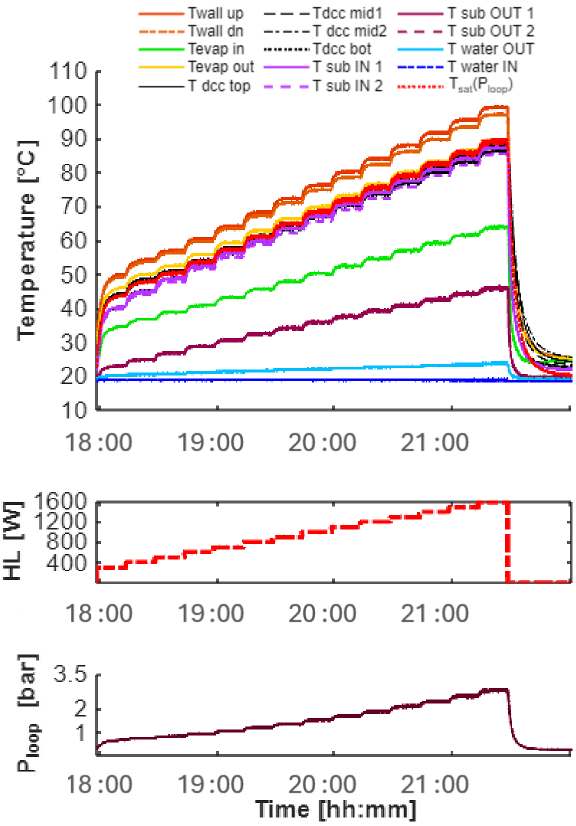

Figure 6. evolution of the CJL parameters versus the heat load w/o vibration during the test #18.

6. CJL operation under random frequency

The vibration cycle imposed to the "-dcc box" component by the shaker is a usual cycle for a component located inside an engine environment. 'Figure 8' shows a typical recording of the accelerometer bonded on the baseplate of the component, the acceleration power spectral density curve, applied on both x-axis and z-axis, versus the frequency is ranging from 5 to 2'000Hz.

The applied random cycles are nominal without need to decrease the level and/or to notch the frequency. 'Figure 9' and 'figure 10' shows the parameter evolutions during the random cycles on, respectively, the z-axis and x-axis direction as defined in 'Figure 3'. During z-axis testing, at 500W heat load, the vibration is started in the middle of the power step leading to a clear but limited increase of the temperatures of the evaporator and a decrease of the subcooler outlet temperature.

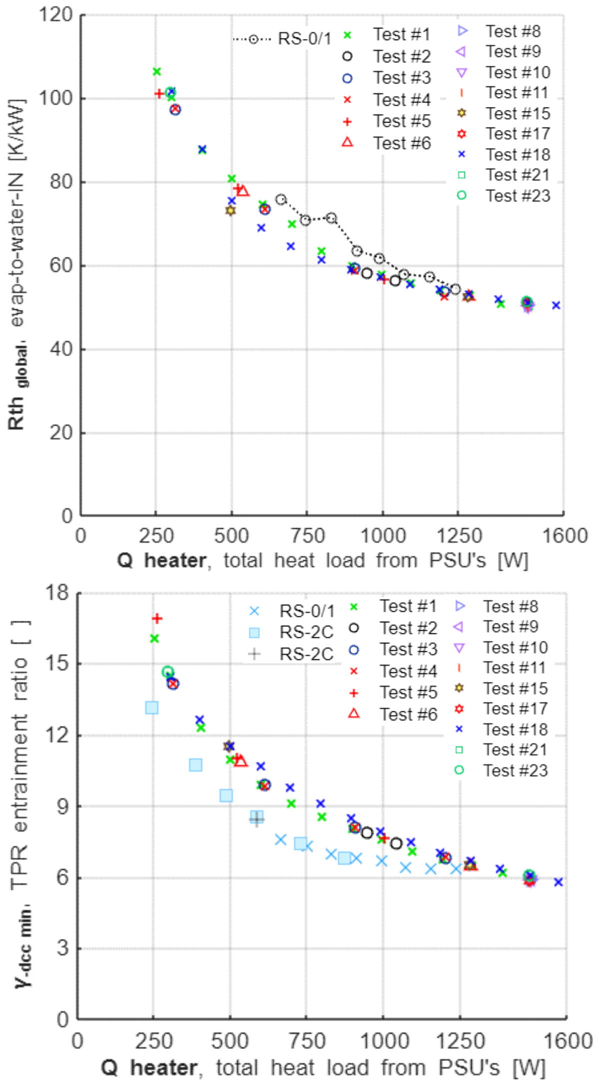

Figure 7. database global thermal resistance and γ entrainment ratio versus the heat load and comparison with the RS0/1demonstrator results [4].

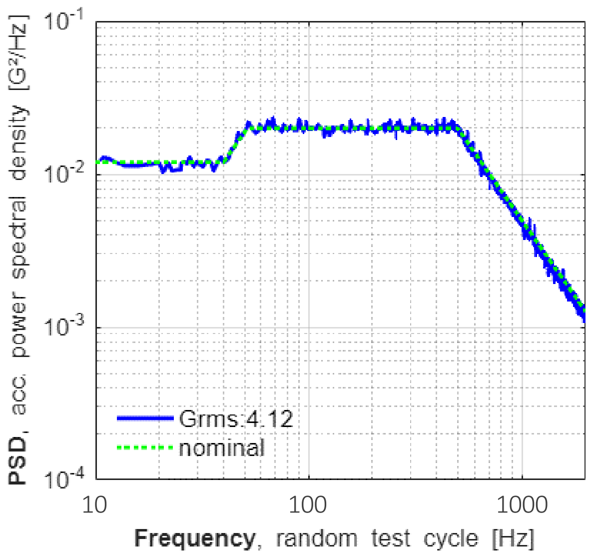

Figure 8. typical PSD cycle versus shaker frequency applied on both x-axis and z-axis.

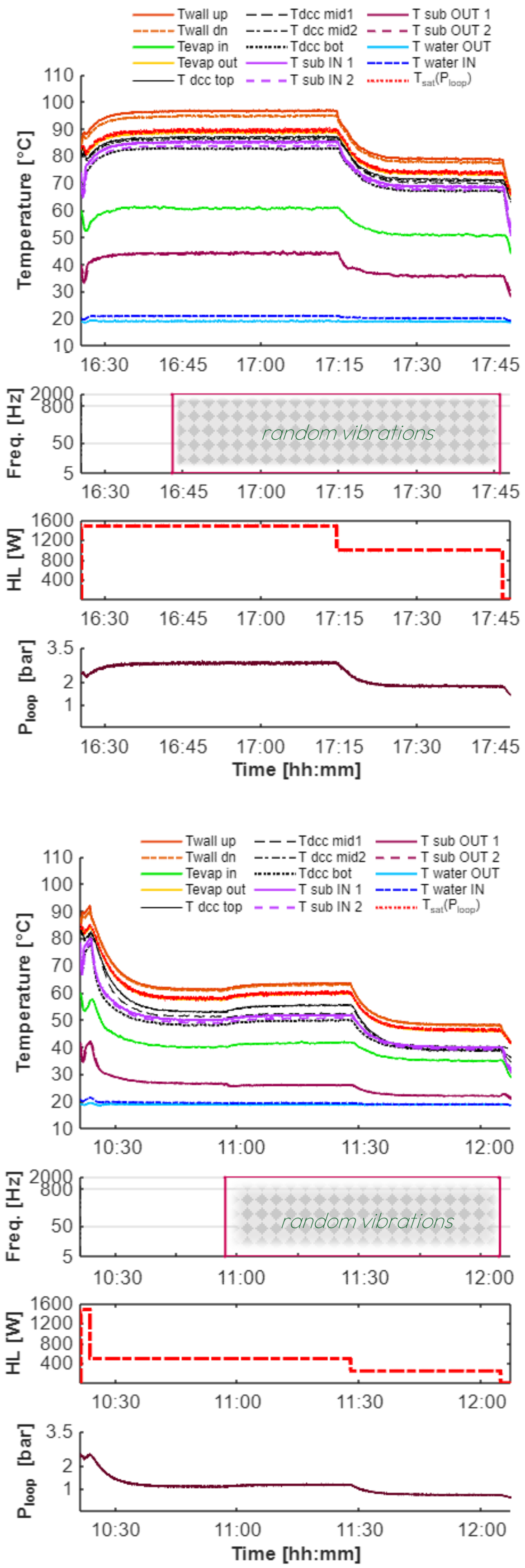

Figure 9. evolution of the CJL parameters during the random vibration cycle in z-axis direction during test #14 (top) and test #15 (bottom).

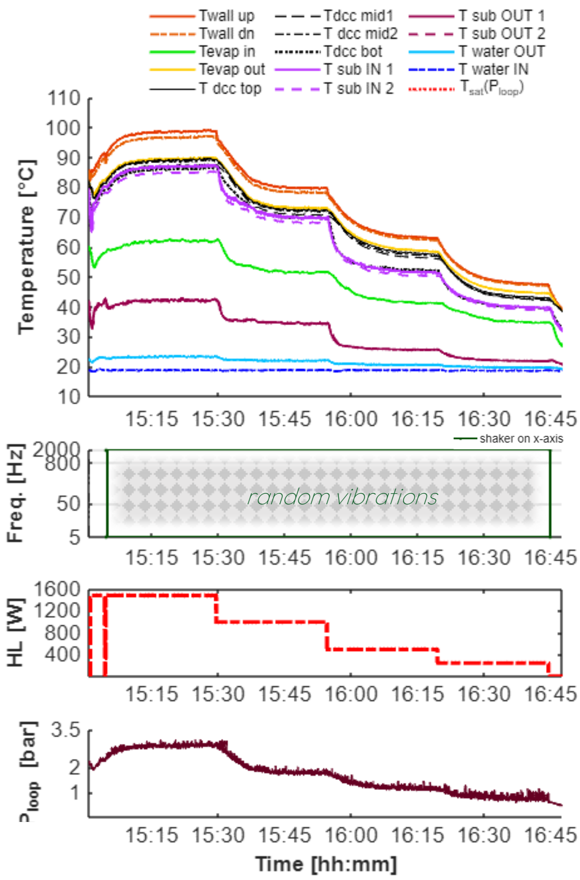

Figure 10. evolution of the CJL parameters during the random vibration cycle in x-axis direction #24.

'Figure 11' shows the global thermal resistance and γ entrainment ratio during random vibration tests versus the heat load and the comparison with the two reference tests without vibrations. The impact is less than 7.8%, on the total thermal resistance at low heat load (250W) and is negligeable above 1kW during random cycle conditions. The increase of the thermal resistance is clearly related to a decrease of entrainment ratio γ (this observation seems obvious from equation 3). The orientations of the vibrations (z-axis or x-axis) seems to have no impact on the performances.

The clear dependency of the vibrations impact with the heat load suggests that the origin of the degradation is more hydraulic than mechanical as discussed in §8.

7. Performances sine dwell spot frequency

The test method is as follow. A close to maximum heat load is applied on the evaporator and after stabilization, ten sine shaped sweep cycles, from 5 to 2'000Hz and back to 5 Hz, are applied with the shaker on z-axis or x-axis. The sweeping rate is 1 octave per minute (log scale on gives a linear curve).

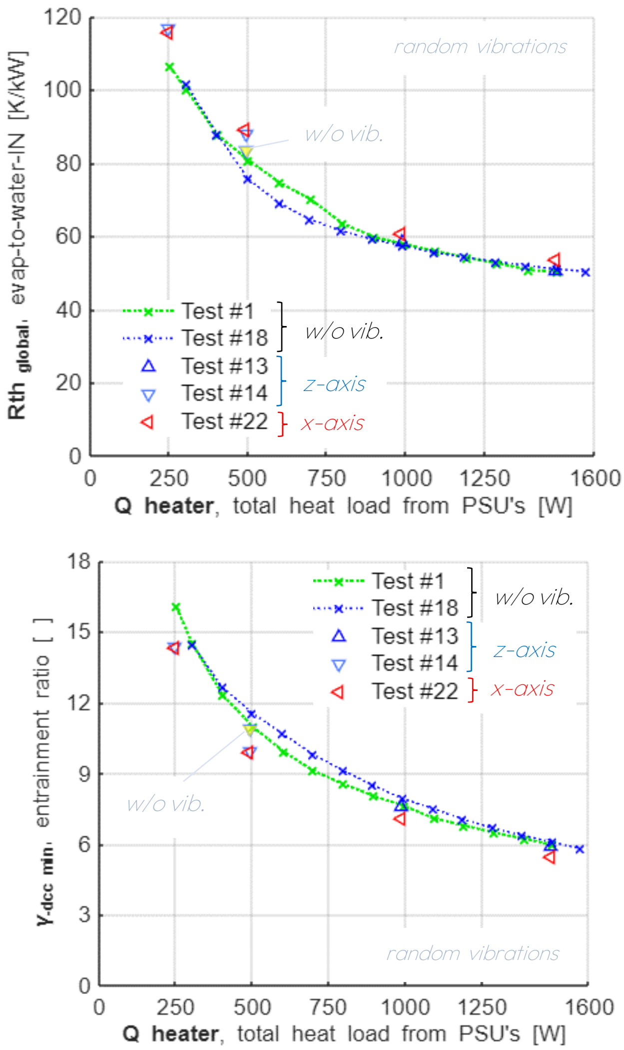

Figure 11. CJL -dcc global thermal resistance and γ minimum entrainment ratio during random vibration tests versus the heat load and comparison with the two references w/o vibrations.

The total duration of each power step is then close to 18 minutes (2 sweeps) i.e. enough to reach a thermal steady state. As a representative example, ‘Figure 13’ shows the temperatures and shaker z-axis frequency on the same graph. At 1.45kW the global thermal resistance - evaporator wall to water inlet - is 53.6 K/kW and a 3.3K (+4.2%) increase can be evaluated on the last sweep.

The shaker data are “manually” synchronized to the thermocouple’s evolutions assuming the same effect of uprising frequency with the down rising part of the cycle. This method is a simple way to consider the thermal response of the wall material but is a bit artificial. The “best” spot frequencies selected are summarized in ‘Table 2’ and applied during a stabilized power step of 1.5kW (cf. ‘Figure 14’) and 1.3kW, respectively in z-axis and in x-axis (cf. ‘Figure 15’). Clearly the mechanical solicitations along the x-axis were more critical for the component structure leading to a clear reduction of the acceleration level in comparison to the z-axis as indicated in ‘Table 2’. Despite these precautions, during the last planned test (test #24), the stainless steel flexible that connect the outlet of the TPR to the inlet of the ‘-dcc box’ components break due to fatigue leading to the end of the tests campaign. Thus, for the 269Hz spot frequency step, in ‘Figure 15’, the average is calculated before the sharp increase of the temperature assuming this behavior is related to the acetone circuit leakage.

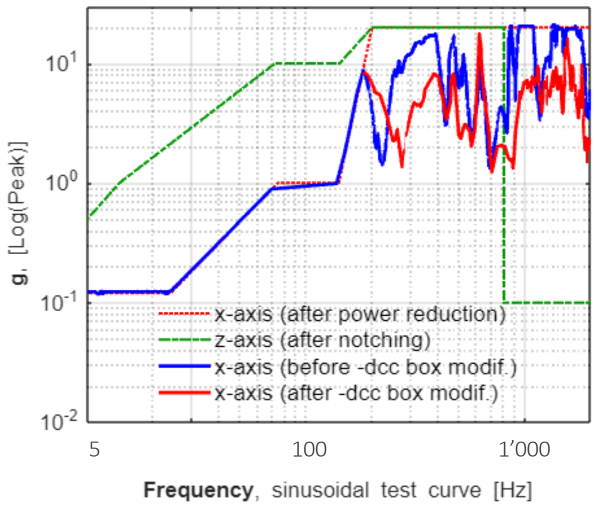

Figure 12. shaker control on x-axis with active notching at 30g – before (blue line) and after (red line) the modification of the internal structure of the “-dcc box” component.

Table 2. acceleration applied during the spot frequency tests.

#	HL [kW]	acc. [g]	spot freq. (time avg) [Hz] z-axis	x-axis
12	1.5	6	60	-
		10	80/100/120	-
		13.7	160	-
		20	330	-
24	1.3	0.93	-	67.5
		1.1	-	130
		2.0	-	269

‘Figure 16’ shows that during spot sine test the performance can decrease of 13% at 100Hz on z-axis. An identification of the “thermal resonance” frequencies seems necessary when the “-dcc box” is in the vicinity of a turning shaft (propeller, gear box, etc.). When the vibrations stop the CJL recovers its full thermal performance. X-axis reactions are lower than the z-axis one but the acceleration level are also lower because of the mechanical limitations.

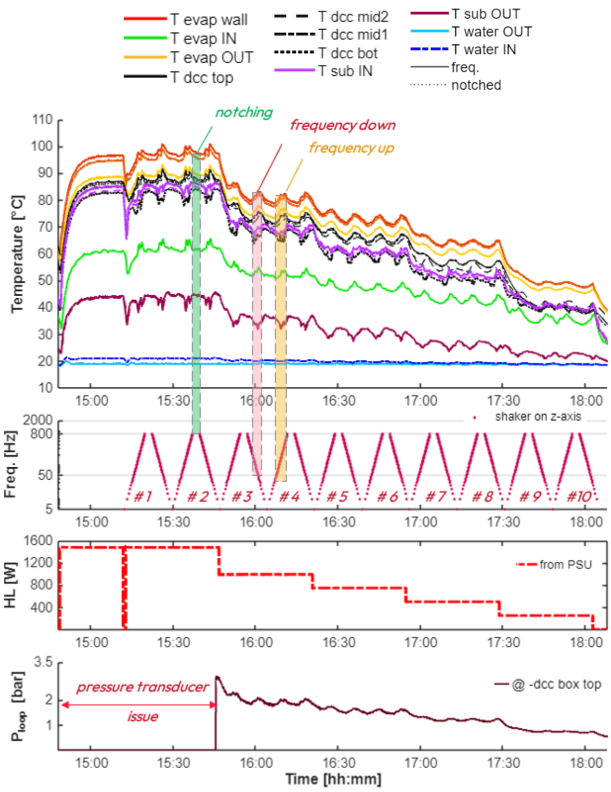

Figure 13. Test #8 Q max under z-axis 5Hz-2kHz frequency sweep cycles (below: print screen of the Labview I/F)., 1.45 to 0.25kW.

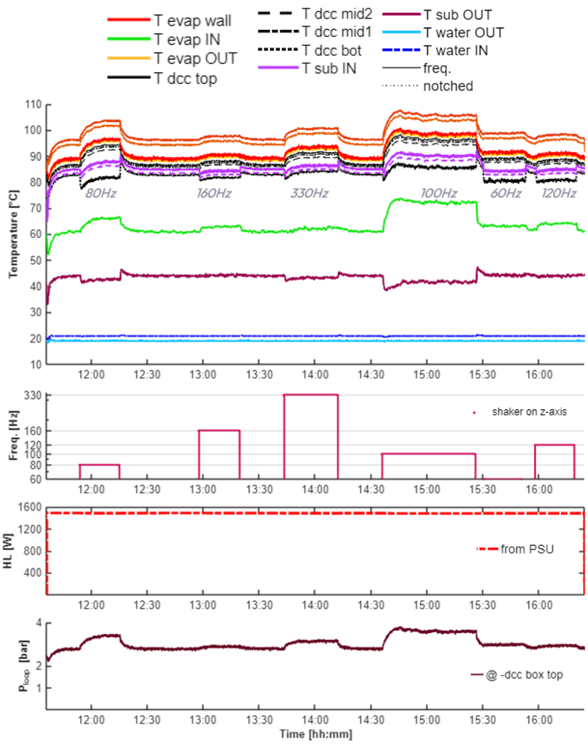

Figure 14. Test #12 (V2i), x-axis spot frequencies at 1'500W.

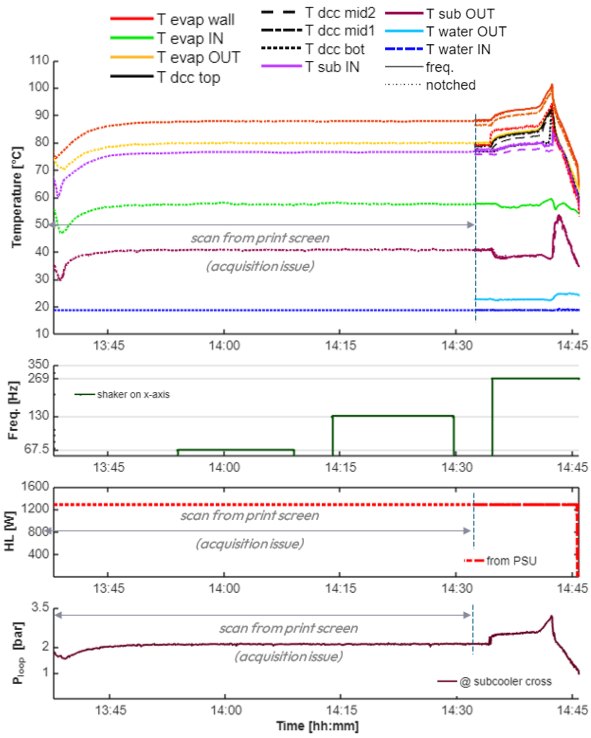

Figure 15. Test#24 x-axis spot frequencies at 1'300W.

8. Analysis and discussion

Several assumptions are proposed hereafter to give discuss the causes of the performance decreases with vibrations.

8.1 Frequency effect on the free surface at bubble size level

The injection of vapor inside each "-dcc tube" induces a two-phase flow with different dimensions of the vapor bubbles. As reminder CFD calculations have been performed [8] considering the real two-phase condensing flow at the outlet of the injector. It is nevertheless interesting to evaluate the resonance frequency of a free interface inside a capillary tube [9]:

$$f_0 = \frac{1}{\pi}\sqrt{\frac{g_{acc}}{R_{tube}}} \tag{6}$$

$$R_{tube} = F_{contraction}\, R_{injector} \tag{7}$$

According to [10] the contraction of the vapor jet is 0.606 at vena contracta. The resonance frequency calculated from equation 7 are given in 'Figure 18' leading to order of magnitude in line with the observation during the frequency sweep summarize in 'Table 2' for z-axis vibrations.

The hydrodynamic origin of the vibrations is likely to increase the shear stress during the condensation and to slow down the TPR flow. A transparent "-dcc box" external wall and transparent

"-dcc tubes" might be a convenient way to confirm this assumption and to better understand the behavior under vibrations.

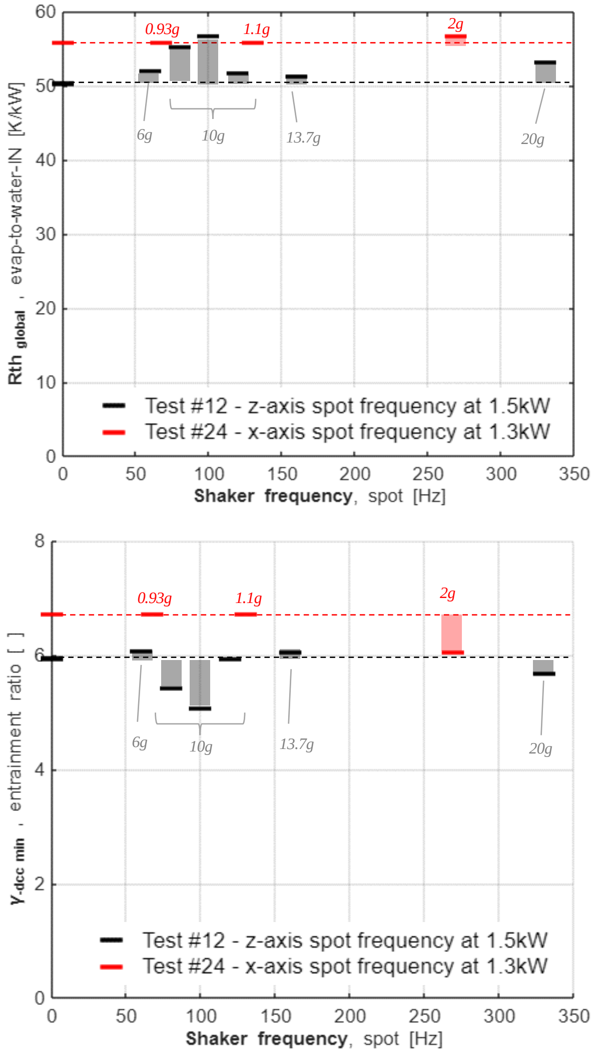

Figure 16. CJL -dcc global thermal resistance and γ entrainment ratio versus sine spot frequency value.

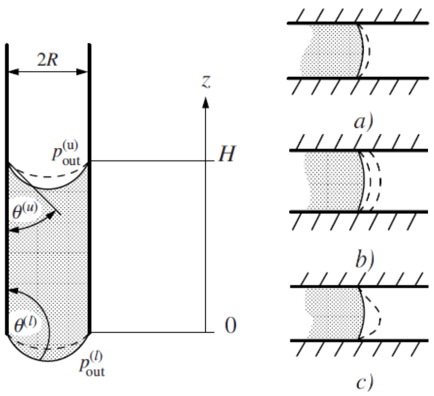

Figure 17. Geometry of a liquid column in a capillary tube excited by an oscillatory pressure gradient. The lower meniscus is fixed at the lower end of the capillary tube due to the gravitational force. Dashed lines: actual positions of menisci. Solid lines: equilibrium positions. [9].

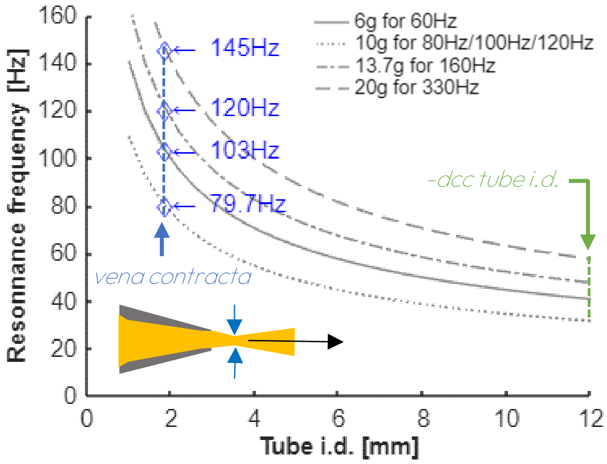

Figure 18. z-axis resonance frequencies corresponding the vena contracta of the vapor jet based on equations 6 and 7.

8.2 Tube deformation

In 'figure 19' the dynamic simulations of the '-dcc tubes' under the nominal x-axis sinusoidal curve gives a maximum displacement of 1.24mm above 534Hz (before component). Thus the movement of the tube should not explain the vibration impact.

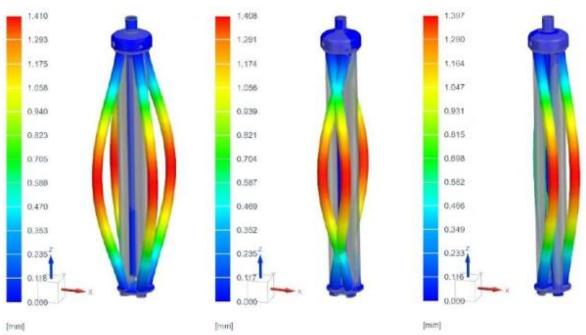

Figure 19. Three first oscillation mode identified by dynamic simulations of the '-dcc tubes' under the nominal sinusoidal cycle (RTCA/DO-160F Fig. 8-2 curve-w) along the x-axis.

8.3 Sloshing motion inside the reservoir

Because the internal volume between the -dcc box component and the four dcc tube acts as a reservoir both solicitations on x-axis and z-axis might generate sloshing waves. Both regular and irregular non-periodic, frequencies appear in simple cylindrical reservoir [11]. More work is needed to apply this complex theory to the present design where the internal tubes create a damping effect. The waves should mix the hotter liquid on the top to the cold one in the bottom, leading to a cold shock i.e. a sudden drop of the saturation pressure in the loop. But the tests show that every time the vibrations the saturation increases. Thus, the slogging is not an issue in the test's conditions.

9. Conclusions and perspectives

Capillary Jet Loop (CJL) appears to be a promising passive two-phase technology for aeronautics. The main advantages are a better resistance to accelerations and easier distribution of the hot liquid flow on a complex volumetric heat exchanger like a turbomachine air intake. The CJL can operate several capillary evaporator in parallel with acetone, a working fluid suitable for -55°C startup conditions.

In the present study the former CJL reduced scale demonstrator previously developed for anti-icing purpose is modified with a novel cylindrical vertical version of the "-dcc box" component that can be mounted on a shaker to perform vibration test representative of an aircraft engine environment. The condensation still takes place inside 344 mm long "-dcc tubes" located directly after the 4 injectors. By design of the "-dcc box" exit the vapor cannot flow to the subcooler. The gravity has a positive effect and contribution, with the momentum exchange at injection level to transfer the heat to the tube-in-tube subcooler. The heat load ranges from 0.25 1.57kW with 5LPM water glycol at +20°C.

Three type of test vibration cycle are performed: random, sine shaped sweep and spot frequency for both x-axis and z-axis. Despite some mechanical issue and design reinforcement the campaign demonstrates that the impact is less than 7.8%, on the total thermal resistance at low heat load (250W) and is totally negligeable above 1kW during random cycle. This effect is very likely due to a destruction of the large bubbles by the vibrations that lead to an increase of the friction shear stress and a decrease in the entrainment factor γ ratio in the two-phase ring. During spot sine test the performance can decrease of 13% at 100Hz on z-axis. An identification of the "thermal resonance" frequencies seems necessary when the "-dcc box" is in the vicinity of a turning shaft (propeller, gear box, etc.). When the vibrations stop the CJL recovers its full thermal performance.

TRL 5 level is reached for the "-dcc box" components and the risk can be considered reduced to an acceptable level for further developments of the technology like convergent-divergent "-dcc tubes", and/or alternative fluids to acetone to improve the ejector efficiency. Variable section injectors, temperature dependent, and CJL assisted by tiny mechanical pumps located after the subcooler also under investigation to increase the scope of use despite the loss of mechanical passivity.

10. Acknowledgements

The present work has received funding from the Wallon Region Skywin *Eloise project* under grant agreement No 8524 and, from HORIZON JU Clean Aviation 2022 *TheMa4HERA project* under grant agreement No 101102008. The present publication reflects only the author's views, and the JU is not responsible for any use that may be made of the information it contains.

References

[1] V. Dupont, EP3250870A1 patent, 2015.

[2] V. Dupont, B. Paran, S. Van Oost, and C. Billet C., Capillary Jet Loop, Proc. of 19th International Heat Pipe Conference, Pisa, Italy, June 10-14, 2018.

[3] R. Clavenna, L. Araneo, V. Dupont, R. Boubaker, Capillary Jet Loop performance in parabolic flight, Applied Thermal Engineering, 2022.

[4] V. Dupont, F. Accorinti, M. Henno, P. S. Serrano Perez, and F. Redondo Carracedo, Capillary Jet Loop in direct contact condensation mode used to perform ice protection function of a turboprop composite nacelle intake. Joint 21st IHPC and 15th IHPS, Melbourne, Australia, 2023.

[5] V. Kiseev, and O. Sazhin, experimental study of loop heat pipes with steam jet pump. IJHMT (115) p. 137, 2017

[6] L. Liu, B., Yuan, C., Cui, X. Yang and J. Wei, Investigation of a loop heat pipe to achieve high heat flux by incorporating flow boiling. International Journal of Heat and Mass Transfer (195), 2022

[7] A. Phillips, J. Fale, N. Gernert, D. Sarraf and W. Bienert, Loop heat pipe qualification for high vibration and high-g environments, 36th AIAA Aerospace Sciences Meeting and Exhibit, 1998.

[8] C. Braga Vieira, T. Nicolle, F. Accorinti, O. de Ghelin, C. Goffaux and V. Dupont. Computational simulation of a vapor jet into a subcooled flow inside a capillary jet loop system operating in direct condensation mode in Joint 21st IHPC and 15th IHPS. 2023. Melbourne, Australia

[9] M. Hilpert, D. Stopper and G. H. Jirka, resonance of a liquid column in a capillary tube, Z. angew. Math. Phys. (48) p. 424, 1997.

[10] A. R., Ghalati, S. Croquer, H. Nesreddine, S. Poncet, and J. Lacey, 1d modelling of the liquid-gas jet pump performance. Proc. of the CSME Int. Congress, CFD Canada, May 28-31, Sherbrooke QC, Canada, 2023.

[11] Z. Wang, L. Zou and Z. Zong, three dimensional sloshing of stratified liquid in a cylindrical tank, Ocean Engineering (119) p. 58, 2016.

Paper ID 097(S2A)

Experimental study of low cost extruded aluminum profiles as pulsating heat pipes for long distance heat transfer

Claus Brede[1,2*], Stefan Becker[2] and Florian Schwarz[1]

[1] *Innovation Center of applied Power Electronics, Siemens AG, Erlangen, 92056, Germany*
[2] *Insitute of Fluid Mechanics, Friedrich-Alexander University Erlangen-Nuremberg, Erlangen, 91058, Germany*
**Corresponding author email address: claus.brede@siemens.com*

Abstract

To meet increasing cooling challenges in power electronics, pulsating heat pipes (PHPs) are a viable option. PHPs use a two-phase flow of a fluid inside a sealed container for heat transfer which surpasses thermal conduction. In this work we present the usage of low cost extruded aluminum profiles as the container for PHPs thereby establishing a cost-efficient production method. We compare profile lengths of 250 mm up to 1000 mm filled with water and ethanol as working fluids in the vertical and horizontal orientation. The highest heat loads are achieved with 40% water filled profiles, which can transport up to 200 W/cm^2 over the cross section of the PHP. In general, independent of the system length, a filling ratio of 40% leads to lower thermal resistances than filling ratios of 60%. Horizontal operation is only possible to a limited extent. We found out that aluminum profiles which are used as PHPs show a massive potential in heat transport. The gravity dependence of such a system is presenting a current challenge and must be improved in further investigations.

Keywords: Oscillating Heat Pipe (OHP); Pulsating Heat Pipe (PHP); Power Electronics; Thermal Management; Thermosyphon; Cost efficient heat transfer; Aluminum profile

1. Introduction

In power electronics waste heat densities are increasing rapidly [1]. Therefore, new cooling concepts must be developed to reach a sufficiently low enough device temperature. In addition, a well-designed cooling concept leads to lower operating temperatures, thereby contributing to an extended lifespan of electronic components [2]. Furthermore, electronic chips at a lower temperature are more efficient [3]. Better cooling systems also allow smaller cooling devices which results in less material consumption and therefore more sustainable devices.

A method to reach these specifications is using pulsating heat pipes (PHPs) investigated in this paper. PHPs are a passive two-phase system for heat spreading. They operate reliably if there is a continuous oscillating plug flow inside the meandering channel structure. This formation depends on the surface tension. The smaller the diameter, the more dominates the surface tension, and the gravitational force which also influences the fluid can be neglected. The maximum diameter D_{max} is defined by equation (1) [4].

$$D_{max} = 2 * \sqrt{\frac{\sigma * Bo}{g*(\rho_l - \rho_v)}} \quad (1)$$

Hereby g is the gravitational force, σ represents the surface tension, ρ_l is the liquid density and ρ_v the vapor density. The dimensionless Bond number Bo describes the ratio of hydrostatic and capillary pressure. Taft and Williams [5] set a Bo number of 0.85 for the maximum radius. For too small diameters viscose effects are dominant which lead to a reduced ability of the system to form proper oscillation [6, 7]. Therefore, the optimal diameter lies close to D_{max} but below this value [8]. The general trend is that with rising temperature the maximum diameter decreases [9].

In the field of PHPs, the filling ratio

$$\phi = \frac{liquid\ volume}{total\ volume} = \frac{V_l}{V_t} \quad (2)$$

is defined as the ratio of the liquid volume V_l to the total volume V_t and is given by equation (2). In the current study filling ratios of 40 % and 60 % for fluids of water and ethanol are chosen. The orientation of the PHP system influences the working mechanism of the PHP. In vertical orientation, with the evaporator located at the bottom, gravity supports the functional principle of the PHP. Since the vapor bubbles flow towards the condenser due to buoyancy force, while the liquid plugs flow back to the evaporator due to gravity. This supports the pressure forces responsible for oscillation and thus ensures more effective operation [10]. Vertical orientation refers to the gravity-assisted operation mode with the evaporator at the bottom and the condenser at the top. Ji et al. [11] have conducted studies regarding a dynamic critical diameter of pulsating heat pipes in vertical operation. Thereby finding relations to make the critical diameter of the PHP not only dependent on the fluid parameters at specific temperatures like equation (1). They come to the result that although for diameters which are larger than D_{max} the PHP in the nonheated scenario has no separation of liquid and vaper plugs this can change with the application of specific heat loads thereby making a PHP operation in the vertical orientation possible. This characteristic is dependent on the applied heat flux, temperature at the condenser and filling ratio. In addition, there are two main working principles in the gravity assisted orientation in terms of flow characteristic. For PHP diameters larger than the critical diameter, the system cannot establish a stable oscillation since the capillary force is not strong enough. Hence a different two-phase heat transport is developed. In this operation the system acts as several interconnected thermosyphons. This means that in every tube vapor flow is orientated from the evaporator to the condenser. In the same channel a counter current flow of liquid takes place. This means the two phases are in direct contact and the heat transport is based on latent heat transport [12]. This flow characteristic is not only dependent on the diameter but also on the fluid-filling-ratio [13, 14, 15]. Due to the capillary force at low filling ratio most of the fluid accumulates in the sharp angled corners. This hinders the establishment of a slug train [15]. Another influence parameter on the performance is the shape of the cross section of the several channels in the PHP. The hydraulic diameter for non-circular cross sections is given by equation (3). This equation sets the area A and the circumference C in relation thereby not considering that by this correlation if the hydraulic diameter of a round cross section is the same as the one of a rectangular the overall volume is a different one [13].

$$D_h = 4 * \frac{A}{C} \tag{3}$$

Furthermore, the corners of the non-round capillary influence the flow pattern in PHPs. In vertical orientation, the corners assist the flow of fluid from the condenser back to the evaporator due to their capillary force. Thereby higher heat fluxes can be reached with squared corners than with round corners at same hydraulic diameters [13, 16]. For non-round cross section also the contact area of fluid and inner container wall is larger thereby leading to higher heat flux at same heat densities transported over the inner container wall, which results in more evaporation of fluid [17]. Channels with rectangular cross sections led to an easier dry out at the evaporator in horizontal orientation [18]. There are different methods of production for PHPs. To form a flat PHP into an existing surface the meandering structure is milled or etched into a metal plate. Afterwords this plate is closed by soldering or bonding a cover plate [10, 13, 19, 20]. This method has the disadvantage that it is connected to some complex production steps which make the production very costly [21]. PHPs of this kind are so called flat plate pulsating heat pipes (FPPHP). Another common method is to bend a pipe to a meandering structure to form the PHP channel structure [22]. This method is easier in production, but it proposes the disadvantage of higher absolute thermal resistance [18]. Furthermore, the bending angel of the tubes which is limited by the tube material is a parameter that influences the packing density of the tubes themselves. Generally, the channel inside of FPPHPs have a rectangular shape whereas the diameter of bended tubes is circular [18]. These two most common production methods differ in their areas of application [23]. Other less common manufacturing methods include additive manufacturing or flexible PHPs out of different layers of polymer components [18]. In this study by using an extrusion process a different approach is chosen with the goal of establishing a more cost-efficient production of PHPs. The channels for the FPPHP are extruded into an aluminum body. This production method is defined by pressing of aluminum through a predefined opening of the extrusion mold thereby making it a very simple production method for linear structures based on plastic deformation [24]. This way of shaping materials is established in various forms in the industry. After this process inside the profile there are parallel channels which need to be connected and sealed to form the container structure of the PHP.

2. Experimental setup

In this study we investigate the usage of extruded aluminum profiles as PHPs. The extruded profiles are made of aluminum 6061, with a height of 5 mm and a width of 124 mm. They consist of 21 continuous channels, each with a width of 4,7 mm and a height of 2,5 mm. As the profiles cannot be used for experiments in their raw state, they are further processed. Every second web between the channels on the front side is shortened using countersinking erosion, allowing two adjacent channels to be connected. The same procedure is applied on the opposite side, offset by one channel,

Figure 1. Photographic image of the front side of the altered aluminum profile.

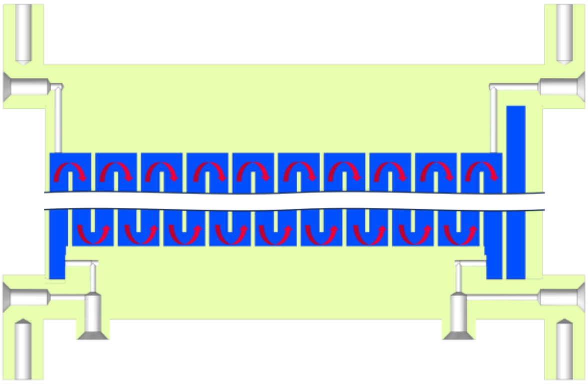

Figure 2. Channel structure of the aluminum profile after it is sealed by the end caps.

to create one continuous channel from the 20 individual ones. Due to the odd number, the 21st channel is sealed and not part of the PHP channel structure. The front side of such a profile is shown in figure 1. The entire channel layout is depicted in figure 2. For both ends of the profile, caps are made to seal the system from the surroundings. These also serve as access points to the interior of the PHP for loading and unloading with fluid.

The structure of the channels inside the profile is determined by the manufacturing process and does not correspond to a perfect rectangle. The exact layout is shown in figure 3. The hydraulic diameter D_h for a non-circular diameter is calculated using equation 3. Therefore, the dimensions of the individual channels used results in a hydraulic diameter of 2,95 mm. This value lies below the critical diameter values for water of 4,5 mm for 120°C but above the critical value for ethanol of 2,6 mm for 120°C. Therefore, operation, especially in a horizontal orientation, is questionable. The heat source of the PHP is located at one end of the extruded profile and has a length of 65 mm. The

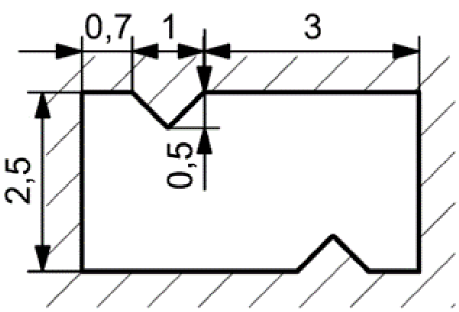

Figure 3. Cross section of one channel of the aluminum profile.

cooling section is on the opposite side with a length of 125 mm. Both sections transfer heat from the top and from the bottom of the profile. The heaters on the evaporation side are mounted on copper plates, which has a thickness of 10 mm. The copper plates serve for easier attachment of the heaters and better heat distribution. During operation, the heater section as well as the adiabatic section are fully insulated with multiple layers of insulation mats to minimize heat losses. The adiabatic section is between the heater side and the cooling side. In the experiments, profiles with different lengths of 250 mm, 500 mm and 1000 mm are tested. Since the setup of the heater side and cooling side remains the same for all experiments, the only change with the length of the profile is the length of the adiabatic section. At the condenser section where heat is transported from the profile to a heatsink. In this section cooling fins are mounted on the surfaces of the PHP. These fins are in a chamber which is blown through with air powered by a suction-side fan with a volume flow of 850 m^3/h. Figure 4 shows the entire test rig with insulation. The entire profile without insulation for the 500 mm profile is shown in figure 5. During all measurements, the ambient lab temperature is held between 21°C and 23,5°C. The power input P_{el} to the heaters is calculated by multiplying the voltage U and current I according to equation 5.

$$P_{el} = U * I \tag{5}$$

Each of the three profiles is tested empty and filled with water and ethanol. The filling-ratio is

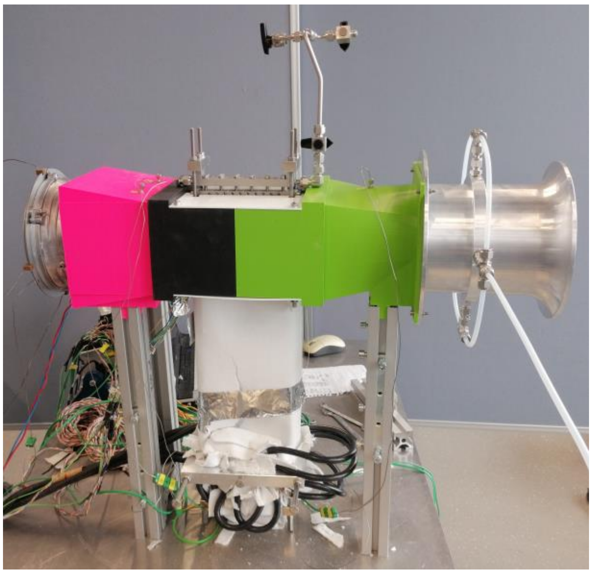

Figure 4. Photographic presentation of the testing rig for the 500 mm profile, with insulation in vertical condition.

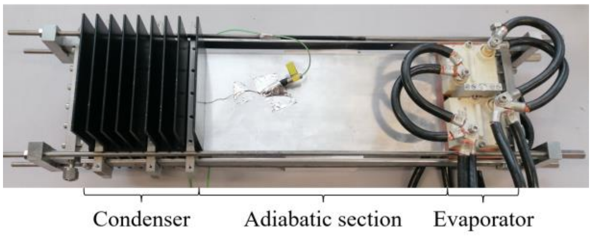

Figure 5. Photographic presentation of the aluminum profile with mounted heaters and cooling fins for the 500 mm profile.

set at 40% and 60% respectively. Additionally, measurements are performed in both horizontal and vertical orientation. Prior to the measurement, the profiles are evacuated to an absolute pressure of less than 4 × 10−4 mbar.

3. Results of the air-cooled PHP in vertical orientation

First the measurement results in the vertical orientation are presented.

3.1. Characteristic behavior for different fluid and filling ratios

Figure 6 presents the evaporator temperature for different power levels in all vertical measurements for the 500 mm profile. The temperature of the empty measurement increases linearly with increasing power. Both 60 % filled profiles with water and ethanol exhibit higher temperature levels throughout the whole measurement compared to the 40% filled profiles with the same fluid. The ethanol measurements exhibit lower temperatures than the water measurements at low power levels. This occurs due to the lower evaporation temperature of ethanol in comparison to water. Additionally, the ethanol curves show a steeper increase along the power ramp since the evaporation enthalpy of

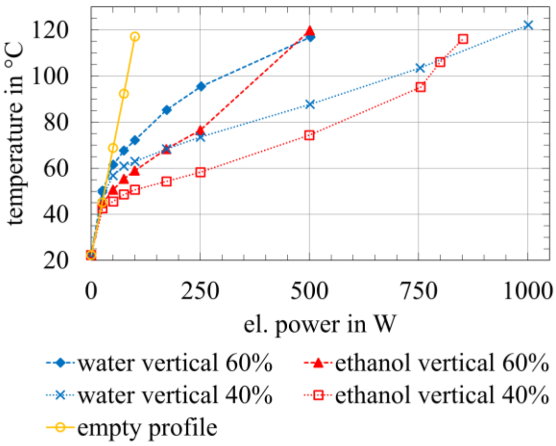

Figure 6. The evaporator temperature of the 500 mm profile with increasing power for different fluids and fill-ratios in vertical position.

ethanol is lower than for water. Thus, the highest power of 1000 W can be achieved with the 40% filled water configuration. This corresponds to a heat flux density of 160 W/cm^2 at the cross section of the PHP. Both ethanol configurations show a bend in the curve indicating a change in flow behavior inside the PHP. The 60% filled profile exhibits this bend at 250 W and 76°C, while the 40% filled profile shows it at 750 W and 92°C. This bend suggests less efficient heat transfer and, consequently, an increase in evaporator temperature. The measurements for the other two profile lengths show a similar behavioral characteristic.

3.2 Analysis of the thermal resistance

The thermal resistance R_{th} is calculated by

$$R_{th} = \frac{T_{evap} - T_{amb}}{P_{el}} . \tag{6}$$

Whereas T_{evap} is the temperature at the mean temperature at the evaporator, T_{amb} the ambient temperature and P_{el} the electrical power.

For the measurements of the 500 mm profile the R_{th} for different power levels is shown in Figure 7. The thermal resistance for the empty measurement is constant at a high value of over 0.9 K/W since for a heat transfer based only on conductivity the thermal resistance is independent of the supplied power. Initially for low power and temperature, for all PHP measurements, the R_{th} is located near the value of the empty profile as there is no improvement in the thermal properties of the profile due to flow effects inside. Subsequently for increasing powers, the R_{th} rapidly decreases for all PHP configurations. The minimum value for the measurements with 60% filling is 0.2 K/W, for the measurements with 40% filling, the value decreases to 0.1 K/W.

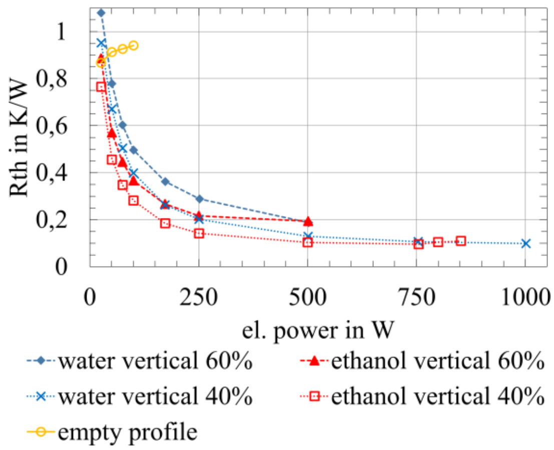

Figure 7. Thermal resistance of the 500 mm profile with increasing power for different media and filling-ratios, in vertical orientation.

3.3 Temperature behavior along the PHP

The temperature distribution along the profile provides information about the effectiveness of heat transfer at the respective power levels. If there is a uniform temperature along the adiabatic section, it indicates a low thermal resistance along that section and thereby an efficient heat transfer. Along the profiles, there are five temperature measurement points attached to the profile's surface. The first measurement point (T_{Heater}) is located at the center of the heating surfaces. 20 mm after the start of the adiabatic section, there is the next measurement point ($T_{adiabatic,1}$), followed by a measurement point at the center of the adiabatic section ($T_{adiabatic,2}$), and another one 20 mm before the cooling fins begin ($T_{adiabatic,3}$). The last measurement point is located at the center of the cooling fins (T_{Cooler}). Figure 8 illustrates the temperature along the profile for different PHPs with a length of 500 mm at their maximum power levels and the empty profile. In all PHP configurations, there is a small temperature difference between the start of the profile at the evaporator and the middle of the profile. This temperature difference is smaller than the temperature difference between the middle of the profile and the end of the adiabatic section at the condenser. For the profiles filled with 60%, the temperature gradient is greater than 30 K, whereas for the profiles filled with 40%, it is 10.8 K for water and 6.4 K for ethanol. The temperatures at the condenser are also higher for the profiles filled with 40%, which is attributed to the higher transferred heat. It can be concluded that ethanol at a filling ratio of 40% shows the best thermal behavior along the adiabatic section. This indicates a thermosyphon characteristic. Since for a thermosyphon the adiabatic section shows the most uniform temperature [25]. Furthermore, a thermosyphon which in this case is supported by the capillary effect of the corners of the channels can perform at lower thermal resistances than a PHP [25].

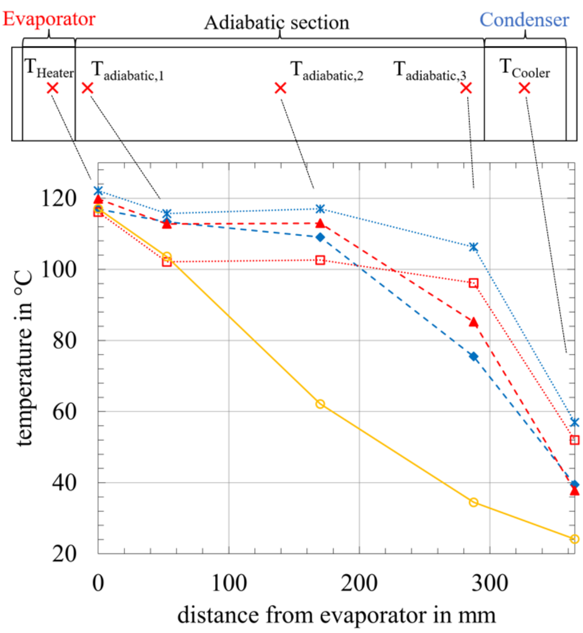

Figure 8. Schematic representation of temperature measurement points along the profile, and results for the 500 mm profile at different fluid-filling ratios.

3.4 Comparison of the thermal behavior of profiles with different lengths

By varying the length of the adiabatic section, the aim is to test to which extent the length of the system has an influence on the operation. In figure 9, the evaporator temperatures are shown for the profiles filled with 40% water and different system length, with increasing power. All three profiles are capable of transferring power over at least 750 W. However, with increasing length, each profile operates at a higher temperature for the same power, resulting in a decrease in maximum power as well. Nevertheless, it can be observed that even with the longest configuration of 1000 mm, the temperature trend still follows that of the 250 mm profile, with only a shift of temperatures towards higher values. This trend is similar for all fluid-filling-ratios. Thereby proving that an increase in length leads to a decline of heat transfer. The overall function principle is still observed, showing that the given profiles can transport heat over at least 1000 mm.

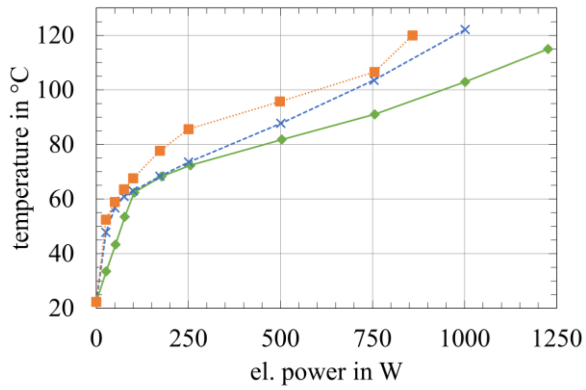

Figure 9. Evaporator temperatures of profiles filled with 40% water.

4. Operation characteristic at horizontal orientation

In addition to the vertical orientation, the profiles are also tested horizontally. In configurations with 40% filling, there is no change in behavior compared to the empty measurement, neither with water nor with ethanol. Therefore, there is no internal PHP behavior in these cases.

The temperature profile of the 250 mm profile, filled with 60% water and horizontally oriented, is shown in figure 10. Initially there is no significant change in behavior compared to the empty measurement, up to a power of 175 W. However, at the next power increase, the temperature suddenly drops from 90.3°C and stabilizes at a lower temperature of about 80°C. Additionally, there is a strong temperature fluctuation at all measurement points. Therefore, a pulsation in the system occurs starting from a power of 250 W. This behavior remains unchanged at higher temperature levels. A maximum power of 1000 W can be reached, corresponding to a power density over the profile cross-section of 160 W/cm^2. The temperature pulsations are observed at temperature measurement points, up to a power of 1000 W. Ethanol shows a similar behavior at 60% filling-ratio and horizontal orientation. Whereas at a temperature of 88.4°C the temperature drop occurs reaching a temperature of about 70°C. This drop occurs at 175 W. The measurements in the horizontal orientation deviate from the values of the empty measurement much later than in the vertical orientation. This proofs that in the lower power range, a thermosyphon characteristic without oscillation is initially established in the vertical orientation. This operation is not possible in the horizontal orientation, as gravity support is required to transport the condensed fluid from the condenser back to the evaporator. Only at higher powers and temperatures does oscillation occur in both vertical and horizontal orientations. However, this oscillation is not pronounced throughout the entire system, but only in certain areas. For both water and ethanol, the temperatures are only slightly higher than those of the respective vertical measurements from a power of 250 W onwards. In fact, the temperature measurement with ethanol at powers above 750 W is even lower than the result of the vertical measurement. The horizontal operation was not possible for the profile length of 500 mm and 1000 mm. This dependency on length is also a result of the too large diameter of the channels therefore more detailed investigations of the performance of such extruded profiles with smaller diameter have to be conducted. Furthermore, this matches with results from Lin et. al. how showed that for increasing length PHPs with different diameters failed to start up [6].

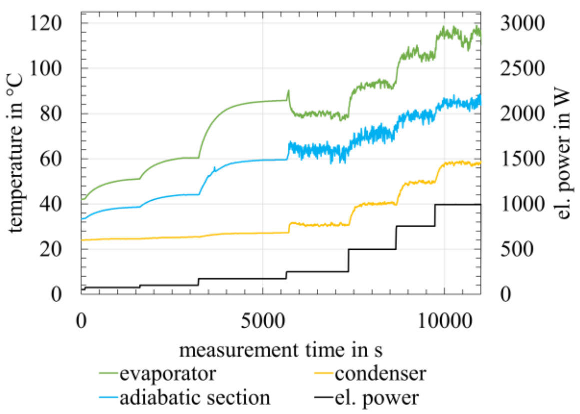

Figure 10. Temperature behavior of the 250 mm profile filled with 60% water in horizontal position.

5. Conclusions

Our study shows that extruded aluminum profiles can transport heat as a PHP over distances of at least 1000 mm. Different length of profile were tested with fluids ethanol and water at 40% and 60% filling-ratio. The experiments were conducted in vertical and horizontal orientation. The main conclusions of the study are the following:

• It has been shown that extruded aluminum profiles are very well suited for use as pulsating heat pipes. The heat transfer performance has achieved power levels of up to 1250 W.

• For a filling with water and ethanol at 40% and 60%, respectively, a minimum fourfold increase in the transferable power compared to empty measurements can be achieved in the vertical orientation.

• Due to its lower boiling point, ethanol always exhibits an earlier onset of flow behavior at lower temperatures and power levels compared to water.

• The starting temperature and the overall temperature level during the entire measurements are consistently lower for profiles filled to 40% compared to those filled to 60%.

• For profiles filled with water, the onset of pulsating flow occurs earlier due to higher surface tensions. Subsequently, the temperature increase with increasing power is lower than for profiles filled with ethanol.

• Stable operation in the horizontal orientation is only possible for the shortest profile with a length of 250 mm and a filling of 60%.

• Increasing the profile length results in lower heat transfer.

• Due to the large channel cross-section, PHP

operation in the gravity assisted orientation is only possible with increasing power. For low powers, a thermosyphon characteristic occurs in the channels, which brings about a homogeneous behavior in the adiabatic zone.
The channels with a width of 4.7 mm have a large hydraulic diameter. By using profiles with reduced channel dimensions, capillary forces have a stronger effect, allowing for horizontal operation and operation against gravity, unlike the case studied here. Achieving orientation-independent heat transfer is desirable to have more design flexibility for cooling applications. Furthermore, the profile is designed as an open-loop pulsating heat pipe (OLPHP). By connecting the last two channels, a closed-loop channel structure, known as a closed-loop pulsating heat pipe (CLPHP), could be achieved. This optimization would reduce edge effects and allow for a circulating flow. This possibility should be investigated in future studies to determine if this operating mode can achieve a more uniform temperature across the entire width of the profile, thereby further increasing the transferable power.

References

[1] J. Calame, R. Myers, S. Binari, F. Wood, M. Garven, Experimental investigation of microchannel coolers for the high heat flux thermal management of gan-on-sic semiconductor devices, International Journal of Heat and Mass Transfer 50 (23) (2007) 4767 – 4779.
[2] IKONEN, Mika, et al. Power cycling lifetime estimation of IGBT power modules based on chip temperature modeling. 201Applied Catalysis A: General, (2001) 207(1) 355.
[3] B. Yang, P. Wang and A. Bar-Cohen, Mini-Contact Enhanced Thermoelectric Cooling of Hot Spots in High Power Devices, IEEE Transactions on Components and Packaging Technologies (30), (2007), 432-438.
[4] C. B. Tibiri¸c´a, G. Ribatski, Flow boiling phenomenological differences between micro- and macroscale channels, Heat Transfer Engineering 36 (11) (2015) 937–942.
[5] B. Taft, A. Williams, Review of pulsating heat pipe working fluid selection, Journal of Thermophysics and Heat Transfer 26 (4) (2012) 651–656.
[6] Z. Lin, S. Wang, J. Chen, J. Huo, Y. Hu, W. Zhang, Experimental study on effective range of miniature oscillating heat pipes, Applied Thermal Engineering 31 (5) (2011) 880–886, mNF 2009 Special Issue.
[7] X. Liu, Q. Sun, C. Zhang, L. Wu, High-speed visual analysis of fluid flow and heat transfer in oscillating heat pipes with different diameters, Applied Sciences 6 (11) (2016).
[8] F. Islam, F. Akhter, S. Haider, M. Ali, Effect of inner diameter on the thermal performance of closed loop pulsating heat pipe, International Journal of Mechanical and Production Engineering 5 (7) (2017) 69–72.
[9] F. Schwarz, Optimierte Pulsierende Heatpipe Designs zur Kühlung von Leistungselektronik, FAU University Press, 2022.
[10] S. A. Jahan, M. Ali, M. Islam, Effect of inclination angles on heat transfer characteristics of a closed loop pulsating heat pipe (clphp), Procedia Engineering 56 (2013) 82–87, 5th BSME International Conference on Thermal Engineering.
[11] Y. Ji, L. Chu, H. Ma, Y. Shen, X. Zhu, C. Yu, Z. Liu, Dynamic critical diameter of an oscillating heat pipe in vertical orientation, International Communications in Heat and Mass Transfer 150 (2024) 107–178.
[12] S. Khandekar, Thermo-hydrodynamics of closed loop pulsating heat pipes (2004).
[13] H. Yang, S. Khandekar, M. Groll, Performance characteristics of pulsating heat pipes as integral thermal spreaders, International Journal of Thermal Sciences 48 (4) (2009) 815–824.
[14] B. Markal, K. Aksoy, The combined effects of filling ratio and inclination angle on thermal performance of a closed loop pulsating heat pipe, Heat and Mass Transfer 57 (2021) 751–763.
[15] J. Qu, H. Wu, P. Cheng, Start-up, heat transfer and flow characteristics of silicon-based micro pulsating heat pipes, International Journal of Heat and Mass Transfer 55 (21-22) (2012) 6109–6120.
[16] J. Lee, S. J. Kim, Effect of channel geometry on the operating limit of micro pulsating heat pipes, International Journal of Heat and Mass Transfer 107 (2017) 204–212.
[17] A. Facin, L. Betancur, M. Mantelli, J. P. Florez, B. H. Coutinho, Influence of channel geometry on diffusion bonded flat plat pulsating heat 33 pipes, in: 19th International Heat Pipe Conference and 13th International Heat Pipe Symposium, Pisa, Italy, 2018.
[18] V. Ayel, M. Slobodeniuk, R. Bertossi, C. Romestant, Y. Bertin, Flat plate pulsating heat pipes: A review on the thermohydraulic principles, thermal performances and open issues, Applied Thermal Engineering 197 (2021).
[19] R. Dreiling, S. Zimmermann, T. Nguyen-Xuan, P. Schreivogel, F. di Mare, Thermal resistance modeling of flat plate pulsating heat pipes,

International Journal of Heat and Mass Transfer 189 (2022).
[20] J. Kim, S. J. Kim, Experimental investigation on the effect of the condenser length on the thermal performance of a micro pulsating heat pipe, Applied Thermal Engineering 130 (2018) 439–448.
[21] D. Bastakoti, H. Zhang, D. Li, W. Cai, F. Li, An overview on the developing trend of pulsating heat pipe and its performance, Applied Thermal Engineering 141 (2018) 305–332.
[22] C. Czajkowski, A. I. Nowak, S. Pietrowicz, Flower shape oscillating heat pipe – a novel type of oscillating heat pipe in a rotary system of coordinates – an experimental investigation, Applied Thermal Engineering 179 (2020).
[23] A. Takawale, S. Abraham, A. Sielaff, P. S. Mahapatra, A. Pattamatta, P. Stephan, A comparative study of flow regimes and thermal performance between flat plate pulsating heat pipe and capillary tube pulsating heat pipe, Applied Thermal Engineering 149 (2019) 613–624.
[24] P. K. Saha, Aluminum extrusion technology, Asm International, 2000.
[25] S. Khandekar, Thermofluid dynamic study of flat-plate closed-loop pulsating heat pipes, Microscale Thermophysical Engineering 6 (4) (2003) 303–317.

Paper ID 099(S7)

Accommodating Thermal Stress in High-temperature Heat Pipes

Longfei Hu[1*], Bo Li[1], Wei Qu[1], Xiaoguang Luo[1,2], Jijun Yu[1,2], Bangcheng Ai[1,2], and Mohan zhang[3]

[1] *China Academy of Aerospace Aerodynamics, Beijing, China*
[2] *Laboratory of Aero-thermal Protection Technology for Aerospace Vehicles, Beijing, China*
[3] *Jiangsu Vilory Advanced Materials Technology Co. Ltd, Xuzhou, China*
**Corresponding author email address:* lfhu2010@hotmail.com

Abstract

In this study, sodium/Inconel 718 heat pipes incorporating topological wicks and traditional wicks were designed and fabricated. Then their thermal properties were initial investigated by radiant heat tests. It was found that the presence of topological wicks did not affect thermal behaviors of sodium/Inconel 718 heat pipes. All heat pipes startup successfully and exhibited a consistent startup temperature of 420°C. Severe temperature gradients were produced during radiant heat tests, resulting in thermal stress concentration in the heat pipes. A subsequent thermal stress simulation demonstrated that topological wicks could accommodate thermal stresses in sodium/Inconel 718 heat pipes. With incorporating topological wicks, maximum thermal stresses in the heat pipes was reduced by approximately 21%. This finding provided valuable insights for mitigating undesired deformation in high-temperature heat pipes, offering practical guidance for engineering applications.

Keywords: Sodium; Inconel 718; Heat pipes; Startup; Thermal stress

1. Introduction

Recently, high-temperature heat pipes had garnered increasing attention due to their exceptional conductivity, inherent safety, and self-actuating operation [1, 2]. They were well-suited for demanding thermal control applications, such as leading edge of hypersonic vehicles, large-scale heat ex-changers, heat radiator of space reactors and so on [3-5]. For these applications, alkali-metal heat pipes offered high redundancy at source temperatures of 600-1500°C [6].

Alkali-metal heat pipes have been systematically investigated by various researchers [7-9]. Steeves and his co-workers[10] proposed the utilization of sodium heat pipes and lithium heat pipes for leading edge cooling of hypersonic vehicles, and verified the feasibility theoretically. Subsequently, Lu et.al [11] and Ai et.al [12] fabricated sodium/GH4099 heat pipes and lithium/C-103 heat pipes, and verified the feasibility of leading edge cooling experimentally. Rosenfeld and his co-workers [13, 14] fabricated sodium/Inconel 718 heat pipes and tested them as heat ex-changers for 10 years. At 700°C isothermal operation, sodium/Inconel 718 heat pipes exhibited imperceptible degradation, providing compelling evidence for long-term engineering application. Hu et.al [15] designed and fabricated sodium/GH4099 heat pipes as heat radiators of a space reactor. They found that a highly adherent Al_2O_3 layer with $\varepsilon \geq 0.9$ was formed on the pre-oxidized heat pipe surface, radiating enough heat even in a micro-gravity environment [16, 17].

Thermal stress concentration in startup and shut down was identified as a potential source for heat pipe failures. Indeed, certain failure modes observed may be attributed to thermal stress concentration [18]. Therefore, it was of great use for accommodating thermal stress in high-temperature heat pipes. Metamaterials exhibited unusual properties, such as negative Poisson´s ratio, negative elasticity, negative bulk modulus and negative thermal expansion [19, 20]. These might reduce the maximum thermal strain and help accommodate thermal stress in high-temperature heat pipes.

In this study, metamaterials were used as topological wicks of high-temperature heat pipes. Sodium/Inconel 718 heat pipes incorporating topological wicks and traditional wicks were designed and fabricated in China Academy of Aerospace Aerodynamics (CAAA). Then their thermal properties were evaluated by radiant heat tests. Based on the experimental results, thermal stresses in sodium/Inconel 718 heat pipes were simulated. Capillary effects of topological wicks were analyzed.

2. Experimental

Heat pipes transferred heat efficiently from evaporator to condenser, which offered inherent redundancy for isothermal operation, seen in Figure 1 [21]. In Figure 1, heat was absorbed within the evaporator. The working fluid melted and evaporated to a gaseous state. A slight internal pressure differential was induced by this evaporation. As a result, the gaseous working fluid flowed from evaporator to condenser. Subsequently, the gaseous working fluid condensed into a liquid state and released heat in the condenser. Finally, the liquid working fluid returned to the evaporator through capillary action of a wick, completing the cycle of isothermal operation.

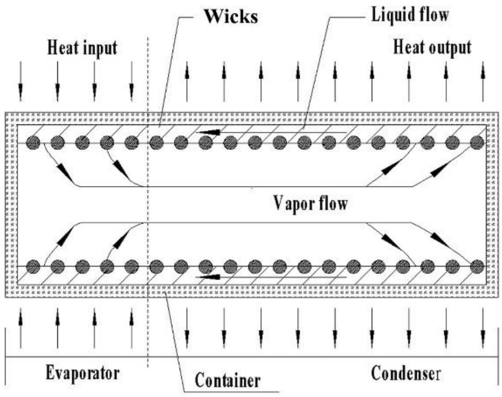

Figure 1. Illumination of a heat pipe operation showing heat pipe shell, working fluid, and wicks [21]

2.1. Design of sodium/Inconel 718 heat pipes

Sodium with a purity level of 99.9% was selected as working fluid. Inconel 718 alloy, which could be commercially obtained for additive manufacture, was selected as raw materials for heat pipe walls. Metamaterials and stainless steel wires were selected as topological wicks and traditional wicks, respectively. A pure nickel tube with an outer diameter of 6 mm and an inner diameter of 4 mm was used for sodium charging. Sodium/Inconel 718 heat pipes with dimensions of Φ25×400mm were designed for thermal property investigation.

Figure 2 showed schematic diagram of designed sodium/Inconel 718 heat pipes, including Inconel 718 heat pipe wall, two endcaps, wicks, a charging tube, and working fluid. Inconel 718 heat pipe wall and two endcaps had a thickness of 2.5 millimeters. Twenty annular gaps were evenly distributed on the inner surface of Inconel 718 heat pipe wall. Each of these gaps was 0.4 mm in width and 0.5 mm in height. The topological wicks featured a lattice structure composed of diamond unit cells with struts, creating metamaterials. Each diamond unit cell measured 0.7mm in length, 0.7 mm in width, and 0.7 mm in height. The struts had a diameter of 0.15 mm. The traditional wicks consisted of a sandwich structure comprising two layers of 300 mesh stainless steel wires and one layer of 100 mesh stainless steel wires. Furthermore, a pure nickel tube was integrated into the endcaps for the purpose of charging working fluid. The working fluid was absorbed within the annular gaps and the wicks.

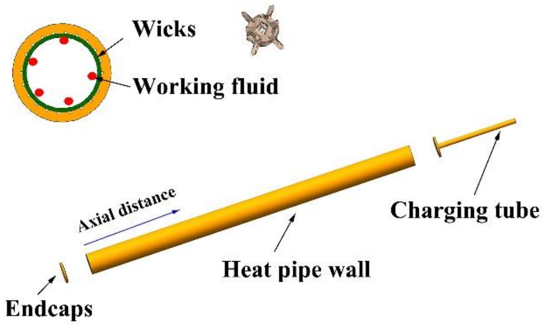

Figure 2. Schematic diagram of designed sodium/Inconel 718 heat pipes

2.2. Fabrication of sodium/Inconel 718 heat pipes

Sodium/Inconel 718 heat pipes were fabricated using the following processes: (1) Inconel 718 heat pipe walls and endcaps were additive manufactured through selective laser melting (Realizer SLM 125, Germany). Annular gaps were formed in situ on the heat pipe walls, seen in Figure 3. (2) The additive manufactured heat pipes walls and endcaps were heated at 1000°C oven for 2 hours, eliminating residual stresses caused by laser melting. (3) A sandwich structure, consisting of three layers of stainless steel wires, was welded on the inner surface of a heat pipe wall incorporating no wicks. (4) All the components were ultrasonically cleaned with acetone, ethanol, de-ionized water, then oven-dried at 70°C oven overnight. (5) The cleaned components were welded together with a pure nickel tube to obtain heat pipe shells for the purpose of sodium charging. (6) Certain amounts of sodium were charged into the heat pipe shells via an argon/vacuum facility. Details about sodium charging and the argon/vacuum facility were available elsewhere [11].

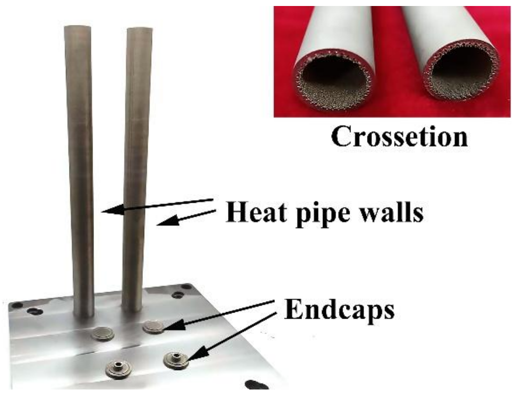

Figure 3. Additive manufactured heat pipe walls and endcaps.

Mass of sodium charged into a heat pipe shell was calculated using Equation (1):

$$M_{Na} = K \times \rho_{Na} \times V_{cap} \times P_{cap} \qquad (1)$$

Where M_{Na} represented the mass of sodium (g); K represented factor of safety (ranged from 1.2 to 3); ρ_{Na} represented density of sodium (g/cm³); V_{cap} represented volume of the wicks (cm³); P_{cap} represented porosity of the wicks. The calculated results implied that the mass of sodium charged into a heat pipe shell ranged from 7.9g to 19.8g. In this study, a charging mass of 12g was used for heat pipe fabrication.

Figure 4 showed photograph of fabricated sodium/Inconel 718 heat pipes. Three heat pipe models, were obtained. They were designated as HP1, HP2, and HP3, respectively. Among them, HP1 and HP2 utilized metamaterials as topological wicks, while HP3 employed stainless steel wires as traditional wicks [22]. For comparison, the inner diameter and outer diameter of HP1-3 were identical.

Table 1 presented detailed information of fabricated sodium/Inconel 718 heat pipes. From Table 1, we observed that the charged sodium in HP1-3 was in the range of 11.5g-13.4g, corresponding to charging ratios ranging from 9.6% to 11.2%. The average densities of HP1-3 were 2.38-2.70 g/cm³, which were comparable to those reported in previous studies [22, 23].

Figure 4. Photograph of fabricated sodium/Inconel 718 heat pipes.

Table 1. Detailed information of fabricated sodium/Inconel 718 heat pipes.

Models	Model weight (g)	Charged sodium (g)	Charging ratio (%)
HP1	467.1	12.9	10.7%
HP2	481.3	13.4	11.2%
HP3	530.6	11.5	9.6%

2.3. Characterization of sodium/Inconel 718 heat pipes

2.3.1 Radiant heat tests

Thermal properties of sodium/Inconel 718 heat pipes were investigated by radiant heat tests in a 30kW calorifier [15]. Figure 5a showed schematic diagram of radiant heat test setup. During radiant heat tests, all heat pipes were oriented horizontally, with lengths of 250mm for evaporator, length 50mm for adiabatic, and length 100mm for condenser. The evaporator absorbed heat input when inserted into the calorifier. The adiabatic was surrounded by porous Al_2O_3, preventing undesirable heat losses. The condenser dissipated heat directly into air environment.

Seven thermocouples (TCs) were spot-welded on the surface of HP1-3, checking temperature reading during radiant heat tests. The TCs' locations were shown in Figure 5b. In Figure 5b, TC1-4 and 7 were used to check axial temperature readings, while TC4-6 were used to check radial temperature readings. All TCs used for temperature reading were K type thermocouples, with a diameter of 250μm. Their accuracy was ±0.75% of the temperature reading (T).

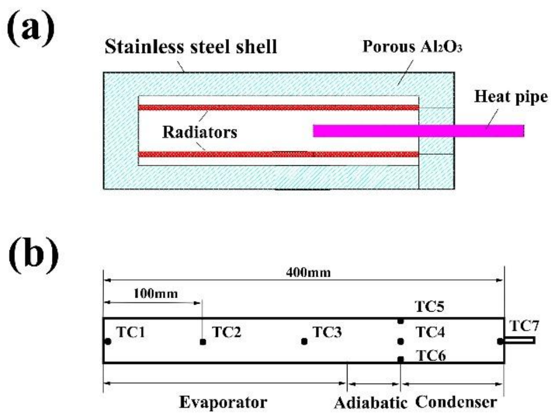

Figure 5. Schematic diagram of radiant heat test setup (a) and the thermocouples' location (b).

In this study, radiant heat tests were performed in two conditions: (1) evaporators of the heat pipes were inserted into the calorifier, then the calorifier was heated from room temperature to 850°C, 900°C, and 950°C, referred as test condition 1; (2) the calorifier was heated to 900°C, then evaporators of the heat pipes were inserted, referred as test condition 2.

2.3.2 Thermal response simulation and stress analysis

An in-house software, named Thermal Analysis of Heat Pipes (TAHP), was used for thermal response simulation of sodium/Inconel 718 heat pipes [20]. TAHP was based on a temperature-front model. Details about this model could be found elsewhere [24]. A brief description of this model was as below: In the process of calorifier heating, sodium in the heat pipes melted and evaporated to a gaseous state, producing a continuous flow area in the evaporator. The interface between this continuous flow area and discontinuous flow area was defined as temperature-front. Then different thermal properties were assigned to these two areas, thermal response were simulated with these properties. The temperature-front position and its movement were determined by location energy conservation theory.

To analyze thermal stress in sodium/Inconel 718 heat pipes, it was crucial to understand mechanical properties of topological wicks. The mechanical properties could be accurately determined by employing by Equation (2) and Equation (3) [25, 26]:

$$\frac{E_{cap}}{E_s}=\frac{\sqrt{6}\pi\left(\frac{3}{4}\right)^2\left(\frac{r}{l}\right)^4}{1+\frac{3}{2}\left(\frac{r}{l}\right)^2} \tag{2}$$

$$\frac{\sigma_{cap}}{\sigma_s}=\frac{9\pi}{4\sqrt{6}}\left(\frac{r}{l}\right)^3 \tag{3}$$

Where E_{cap} represented elastic modulus of topological wicks (MPa); E_s represented elastic modulus of Inconel 718 alloy (MPa); σ_{cap} represented yield stress of topological wicks (MPa); σ_s represented yield stress of Inconel 718 alloy (MPa); r represented radius of struts in topological wicks (m); l represented length of struts in topological wicks (m).

Table 2 presented parameters utilized for thermal response simulation. Test condition 2 was employed for thermal response simulation. In the process of thermal response simulation, both convection and radiation were considered for heat pipe cooling. Film coefficient of the condenser was assumed to be 20W/m²/°C. Emissivity of the condenser was assumed to be 0.9 (the emissivity of oxidized Inconel 718 alloy). To analyze thermal stress, one endcap of the heat pipes was fixed. Thermal stresses in HP2 and HP3 were analyzed, revealing effects of topological wicks.

Table 2. Parameters utilized for thermal response simulation.

Models	HP2/HP3	Calorifier temperature	900°C
Evaporator	250 mm	Heating time	780s
Adiabatic	50 mm	Emissivity	0.9
Condenser	100 mm	Film coefficient	20 W/m²/°C

3. Results

3.1. Test results

Figure 6 showed test results of HP1 heated from room temperature to 850°C, 900°C, and 950°C (test condition 1). In Figure 6a, HP1 experienced startup failure. The ultimate temperature difference of TC1-7 was 325°C, indicating the presence of asymmetric heating. In Figure 6b and Figure 6c, HP1 startup successfully, exhibiting uniform temperatures of 750°C and 800°C, respectively. With calorifier temperature increment, the ultimate temperature difference of TC1-7 reduced to 46°C, indicating the isothermal operation of HP1.

Figure 7 showed a typical image of operated HP1 (t=3000s, 900°C heating). In Figure 7, HP1 displayed a bright and uniform condenser. Heat absorbed within evaporator of HP1 was efficiently transferred to condenser, and then dissipated to the surrounding air environment. The isothermal operation of HP1 was confirmed once again [27].

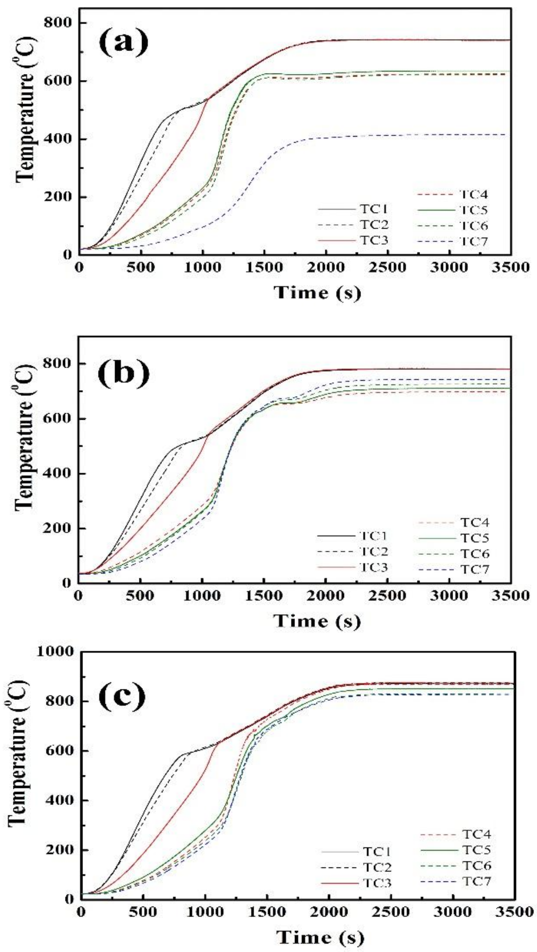

Figure 6. Startup results of HP1 heated from room temperature to: (a) 850°C, (b) 900°C, (c) 950°C.

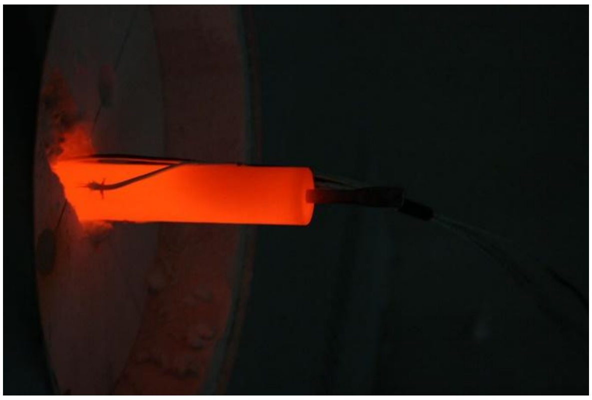

Figure 7. A typical image of HP1 heated room temperature to 900°C (t=3000s).

Figure 8 showed test results of HP1-3 heated at 900°C calorifier (test condition 2). In Figure 8, all heat pipes startup successfully and operated at an isothermal state. The startup processes consisted of three stages: heat transfer stage, startup stage, and operating stage. Each stage served a specific model and involved distinct operation mechanisms. During heat transfer stage from 0 to110 seconds, heat absorbed within HP1-3 was transferred solely through the heat pipe walls. Temperatures of TC1-7 increased linearly and reached 55-543°C. During startup stage from 110 to 230 seconds, heat transfer in HP1-3 was primarily driven by the working fluid rather than the heat pipe walls. As a result, temperatures of TC1-7 increased and reached an identical temperature of approximately 500°C. During operating stage from 230 to 780 seconds, HP1-3 operated in an isothermal manner. Temperatures of TC1-7 increased simultaneously and reached approximately 700°C. Moreover, it was noted that the startup time in Figure 8 was shorter than that in Figure 6. This was most probably caused by the high heat input in test condition 2 [20, 27].

Figure 9 showed optical images of tested sodium/Inconel 718 heat pipes. In Figure 9, the tested heat pipes still maintained their integrity. No sodium leakage or deformation was observed. As HP1 and HP2 displayed similar test results to that of HP3, it was reasonable to conclude that the presence of topological wicks did not affect thermal behavior of sodium/Inconel 718 heat pipes. To illuminate capillary effects of topological wicks, thermal response simulation and thermal stress analyses were carried out for HP2 and HP3.

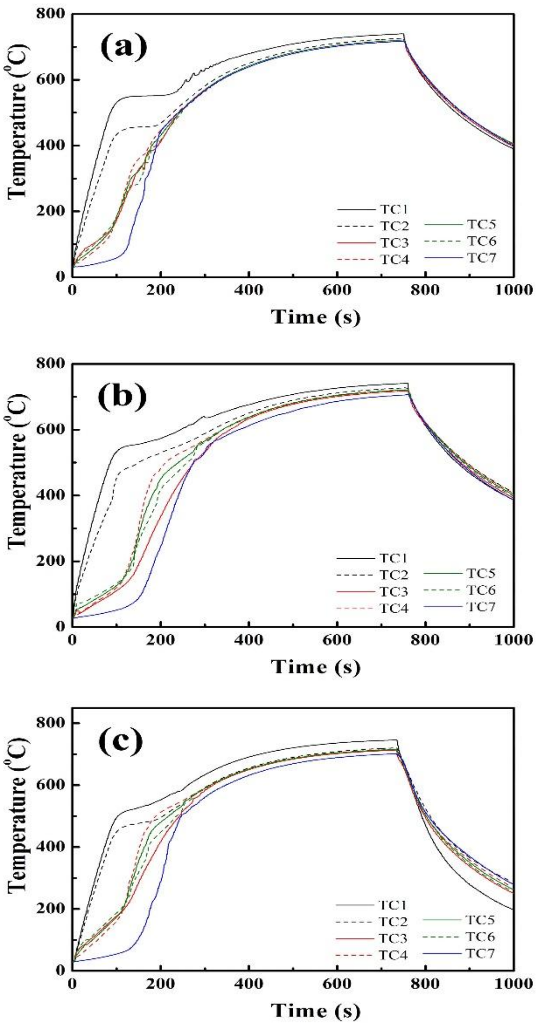

Figure 8. Startup results of HP1-3 heated at 900°C calorifier: (a) HP1, (b) HP2, (c) HP3.

Startup results of HP1-3 heated at 900°C calorifier: (a) HP1, (b) HP2, (c) HP3.

Figure 9. Optical images of tested sodium/Inconel 718 heat pipes.

3.2. Simulation results

Thermal response of HP2 and HP3 were simulated under test condition 2. The results revealed a remarkable similarity in their thermal behavior. This was in agreement with test results in section 3.1. Figure 10 showed the simulated temperature profiles of sodium/Inconel 718 heat pipes. This graph provided a visual representation of the thermal behaviors. At the heating times of 125s, 150s, and 175s, severe temperature gradients were observed in the sodium/Inconel 718 heat pipes. Consequently, thermal stresses in HP2 and HP3 were analyzed based on temperature profiles at these specific time points.

Figure 11 showed a visual representation of simulated thermal stresses within the heat pipes, specifically the hoop stresses. In the startup process, high stress areas were produced both in HP2 and HP3. With the elongation of time, these stress areas moved directly from adiabatic region to the nearby endcap. Compared to HP3, HP2 experienced relatively lower thermal stresses. This was most probably related to negative Poisson´s ratio of topological wicks, which could decrease maximum thermal strain and help accommodate thermal stresses in the heat pipes [20].

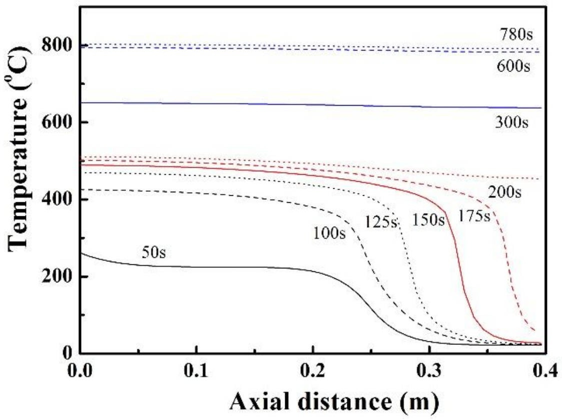

Figure 10. Simulated temperature profiles of sodium/Inconel 718 heat pipes (HP2/HP3).

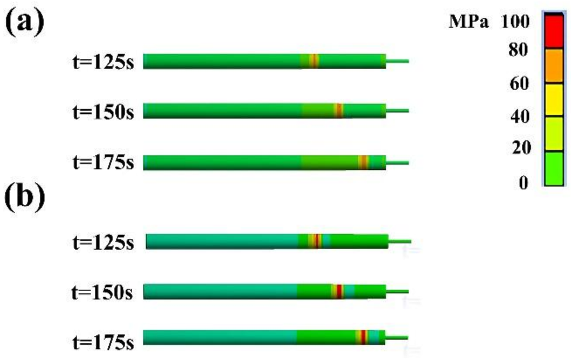

Figure 11. Simulated thermal stresses in sodium/Inconel 718 heat pipes: (a) HP2, (b) HP3.

The calculated thermal stress profiles in sodium/Inconel 718 heat pipes were shown in Figure 12. At heating times of 125s, 150s, and 175s, maximum thermal stresses in HP3 were 96.3MPa, 104.6MPa, and 108.8MPa, respectively, while those in HP2 were 75.4MPa, 83.4MPa, and 84.5MPa, respectively. With the incorporation of topological wicks, a reduction of about 21% maximum thermal stresses was obtained. Stress accommodation effects were confirmed once again. This finding provided valuable insights for mitigating undesired deformation in high-temperature heat pipes, offering practical guidance for engineering applications.

Table 3 presented yield strength of Inconel 718 alloy [28]. From Table 3, it was observed that the simulated stresses were lower than the yield strength of Inconel 718 alloy. Therefore, thermal deformation did not occur in both HP2 and HP3. This was consistent with the optical images in Figure 9.

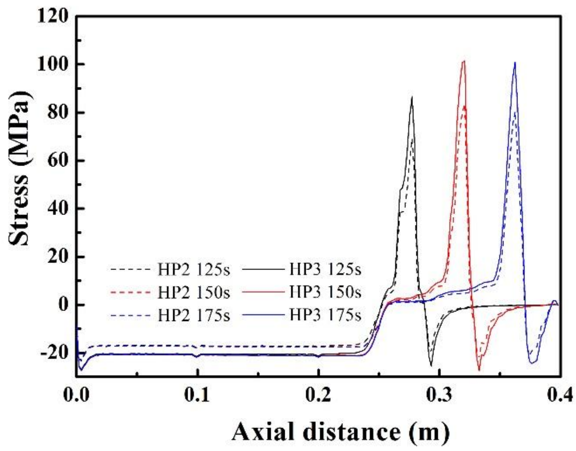

Figure 12. Thermal stress profiles in sodium/Inconel 718 heat pipes.

Table 3. Yield strength of Inconel 718 alloy [28].

Temperature (°C)	Strength (MPa)	Temperature (°C)	Strength (MPa)
20	1365	704	1006
315	1265	760	851
537	1192	815	723
648	1103	871	275

4. Discussion

4.1. Startup temperature

Based on previous reports [11, 30], startup of high-temperature heat pipes was found to be correlated with saturated pressure of the working fluid. Saturated pressure of sodium could be determined by Equation (4):

$$\lg P_s = A - \frac{B}{T} - C\lg T \qquad (4)$$

Where T represented operating temperature of the heat pipes (K), and the constants A, B, and C

were defined as 4.544579, 5242.1, and 0, respectively. At operating temperature of 750°C, the saturated pressure of sodium was calculated to be 26000Pa.

Startup temperature of sodium/Inconel 718 heat pipes was determined by Equation (5):

$$T^* = \frac{\sqrt{2}\pi D_0^2 Kn P_s d}{\kappa} \quad (5)$$

Where T^* represented startup temperature of heat pipes (K); D_0 represented characteristic diameter of sodium atoms (3.567×10^{-10} m); Kn represented Knudsen number (defined as 0.01); d represented inner diameter of heat pipes (1.8×10^{-2}m); κ represented Stefan Boltzmann constant (5.67×10^{-8} W m$^{-2}\cdot$ K^{-4}); P_s represented saturated pressure of sodium ($\times10^5$ Pa). The calculated startup temperature of sodium/Inconel 718 heat pipes was about 420°C, being lower than operating temperature in section 3.1. As a result, sodium/Inconel 718 heat pipes startup successfully in radiant heat tests.

4.2. Capillary effects

Capillary effects of various wicks were investigated, including annular gaps, stainless steel wires, stainless steel wires combined with annular gaps, and metamaterials combined with annular gaps (topological wicks). All wicks were fabricated on a strip surface with dimensions of 300mm×25mm×2mm (length×width×thickness). Then, one side of the strip was vertically immersed in ink, and the absorption results were shown in Figure 13. In Figure 13, it was evident that the absorption lengths of these wicks were 30mm, 52mm, 60mm, and 110mm, respectively. Topological wicks displayed the best capillary effects.

Figure 13. Capillary action of various wicks.

Compared with HP3, the topological wicks of HP1 and HP2 were chemically compatible with heat pipe walls, indicating that HP1 and HP2 could be utilized as flexible heat pipes. HP1 was bent and tested under anti-gravity conditions, as shown in Figure 14. In Figure 14, the bent HP1 still maintained exceptional conductivity and self-actuating operation, demonstrating the flexibility of topological wicks. This was instructive for developing flexible and anti-gravity heat pipes.

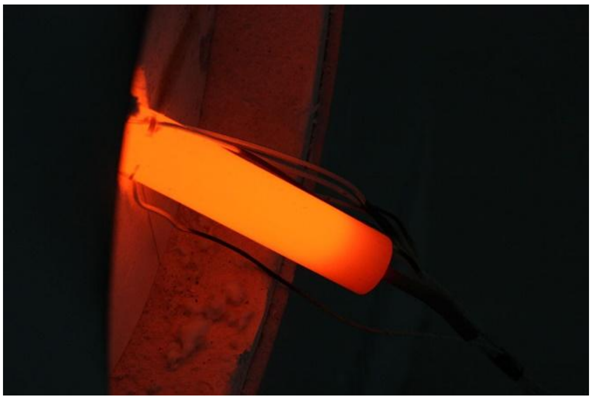

Figure 14. Optical images of bended sodium/Inconel 718 heat pipes in radiant heat tests.

4.3. Further works

Recently, metamaterals were utilized to accommodate thermal stress in heat pipe cooled nosecaps. Nosecap shaped heat pipes, incorporating topological wicks, were designed and fabricated. Then their thermal properties and thermal stresses were investigated via wind tunnel tests. Mitigating undesired deformation phenomenon was found. Details about this works would be reported later.

5. Conclusions

In this study, metamaterials were utilized to accommodate thermal stress in high-temperature heat pipes. Sodium/Inconel 718 heat pipes, incorporating topological wicks and traditional wicks, were designed and fabricated. Subsequently, their thermal properties were examined through radiant heat tests and thermal stress simulations. The analysis of experimental and simulation results led to the following conclusions:

(1) Startup temperature of the sodium/Inconel 718 heat pipes was about 420°C. As heated from room temperature to 900°C and 950°C, HP1 successfully startup, exhibiting uniform temperatures of 750°C and 800°C, respectively.

(2) HP1 and HP2 displayed similar test results to that of HP3, therefore it was concluded that the presence of topological wicks did not affect thermal behaviors of sodium/Inconel 718 heat pipes.

(3) Topological wicks could accommodate thermal stresses in sodium/Inconel 718 heat pipes. With incorporation of topological wicks, a reduction of about 21% maximum thermal stresses was obtained

(4) The bent HP1 still maintained exceptional

conductivity and self-actuating operation, demonstrating the compatibility and flexibility of topological wicks.

(5) This finding provided valuable insights for mitigating undesired deformation in high-temperature heat pipes, offering practical guidance for engineering applications.

Acknowledgements

The author would like to thank Professor Xuejun Zhang for useful discussions about thermal stress simulation.

Referencs:

[1] T.J. Dickinson , W.J. Bowman , and M. Stoyanof, Performance of liquid metal heat pipes during a space shuttle flight, J. Thermophys. Heat Transf., 1998 (12) 263–269.

[2] A. Faghri, Heat pipe science and technology, Second version, University of Connecticut, ISBN: 978-0-9842760-1-1, U.S.A. 2016.

[3] D.E. Glass, and C.J. Camarda, Fabrication and testing of a leading edge-shaped heat pipe, AIAA-99-4866. 1999. https://doi.org/10.2514/2.3515.

[4] M. Chu, Q. Lu, H.T. Han, L.F. Hu, J.J. Yu, and B.C. Ai , Fabrication of sodium/Inconel/718 heat pipes for combustor cooling, Microgra. Sci. Technol., 2019 (31) 783-791.

[5] M.S. El-Genk and J.T. Seo, Study of the SP-100 radiator heat pipes response to external thermal exposure", J. Propul. Power, 1990 (6) 69–77.

[6] J.M. Tournier and M.S. El-Genk, Startup of a horizontal lithium-molybdnum heat pipe from a frozen state, Int. J. Heat Mass Transf., 2003 (46) 671-685.

[7] Y. Cao, and A Faghri, A numerical analysis of high-temperature heat pipe startup from the frozen state, J. Heat Transf., 1993 (115) 247-254.

[8] D.E. Tilton, L.C. Chow, and E.T. Mahefkey, Transient response of a liquid metal heat pipe, J. Thermophys. Heat Transf, 1988 (2) 25-30.

[9] G.Y. Li, and J. Tu, Working fluid selection for high-temperature heat pipes, Energy Conserv. Technol., 2001 (19) 42-44. (In Chinese)

[10] C.A. Steeves, M.Y. He, S.D. Kasen, L. Valdevit, H.N.G. Wadley, and A.G. Evans, Feasibility of metallic structural heat pipes as sharp leading edges for hypersonic vehicles, J. Appl. Mechan., 2019 (76) 1-9.

[11] Q. Lu , H.T. Han, L.F. Hu, S.Y. Chen , J.J. Yu , and B.C. Ai , Preparation and testing of nickel-based superalloy/sodium heat pipes, Heat Mass Transf., 2017 (53) 3391-3397.

[12] B.C. Ai , J.J. Yu , S.Y. Chen , Q. Lu, H.T. Han, and L.F. Hu, Fabrication and testing of lithium/C-103 alloy heat pipe for sharp leading edge cooling, Heat Mass Transf., 2018 (54) 1359-1366.

[13] J.H. Rosenfeld, D.M. Ernst, J.E. Lindemuth et al., An overview of long duration sodium heat pipe tests [R], Lancaster, Pennsylvania: Thermacore International, Inc., 2004.

[14] J.H. Rosenfeld, K.G. Minnerly, and C.M. Dyson, Ten year operating test results and post-test analysis of a 1/10 segment stirling sodium heat pipe Phase III Final Report [R], Lancaster, Pennsylvania, Thermacore, Inc., 2012.

[15] L.F. Hu, Z. Chen , K.T. Shi , J.T. Shi, X.G. Luo, and C Liu., Sodium/GH4099 heat pipes for space reactor cooling, Microgra. Sci. Technol., 2021 (33) 60.

[16] M. El-Genk , and J.M. Tournier, Uses of liquid-metal and water heat pipes in space reactor power systems, Front. Heat Pipes, 2011 (2) 1-24.

[17] C.L. Wang, J. Chen, S.Z. Qiu, W.X. Tian, D.L. Zhang, and G.H. Su, Performance analysis of heat pipe radiator units for space nuclear power reactor, Ann. Nucl. Energy, 2017 (103) 74-84.

[18] S.Y. Chen, H.T. Han, J.T. Shi, Q. Lu, L.F. Hu, and B.C. Ai, Applications of sodium/GH4099 heat pipes for nosecap cooling", Microgra. Sci. Technol., 2019 (31) 417-424.

[19] R. Hedayati, A.M. Leeflang, and A.A. Zadpoor, Additively manufactured metallic pentamode meta-materials, Appl. Phys. Lett., 2017 (110) 091905.

[20] L.F. Hu, K.T., Shi, X.G. Luo, J.J. Yu, B.C. Ai, and C. Liu, Application of additively manufactured pentamode metamaterials in sodium/Inconel 718 heat pipes, Mater., 2021 (14) 3016.

[21] D.E. Glass, and C.J. Camarda, Fabrication and testing of a leading-edge-shaped heat pipe, AIAA-99-4866, 1999.

[22] V. Tolubinskii, E. Shevchuk, and V. Stambrovskii, Study of liquid-metal heat pipes characteristics at start-up and operation under gravitation", 3rd International Heat Pipe Conference, Vol. 1, pp. 274–282, 1978.

[23] H.T. Han, Z. Chen, L.F. Hu, S.Y. Chen, B.C. Ai, and W. Qu, High-temperature heat pipe enhanced thermal protection structure for scramjet combustion chamber, J. Aerospace Power, 2017 (32) 1043-1050. (In Chinese).

[24] D.Y. Deng, S.Y. Chen, B.C. Ai, W. Qu, and J.J. Yu, Calculation investigation of high-temperature heat pipe startup of sharp leading edge, Acta Aerodyn. Sin., 2016 (34) 646-651. (In Chinese)

[25] S. Ahmadi, G. Campoli , S.A. Yavari, B. Sajadi, R. Wauthle, J. Schrooten, H. Weinans, and

A. A. Zadpoor, Mechanical behavior of regular open-cell porous biomaterials made of diamond lattice unit cells, J. Mech. Behav. Biomed. Mater., 2014 (34) 106–115.
[26] A. A. Zadpoor and R. Hedayati, "Analytical relationships for prediction of the mechanical properties of additively manufactured porous biomaterials", J. Biomed. Mater. Res. Part A, 2016 (104) 3164–3174.
[27] S.D. Kasen, Thermal management of hypersonic leading edges, PH.D dissertation, The faculty of the School of Engineering and Applied Science, University of Virginia, USA, May 2013.
[28] M.G. Yan, B.C. Liu, J.G. Li, S.P. Wu, J. Hua, B.L. C.G. Xu, Li, F.C. Zeng, X.R . Wu, X.R. Zhou, et al. China Aeronautical Material Handbook, 2nd ed.; Published by China Standard Committee: Beijing, China, 2002; pp. 323-360. ISBN 7-5066-2439-7. (In Chinese)
[29] M. Murdock and M. Human, "Thermal stress distribution in a high temperature heat pipe", AIAA-00-2946, 2000.
[30] T.J. Dickinson, Performance analysis of a liquid metal heat pipe space shuttle experiment. Master's Thesis, The Graduate School of Engineering of the Air Force Institute of Technology, Wright-Patterson AFB, Montgomery County, OH, USA, December 1996.

Paper ID 102

Study of the Pool Boiling Heat Transfer Coefficient in a Thermosyphon

Souza, Fernando Gonçalves[1*], Ribeiro, Andreza Sousa[1], Pabon, Nelson Yurako Londoño[1] and Mantelli, Marcia Barbosa Henriques[1]

[1] *Federal University of Santa Catarina, Florianopolis, 88040-900, Brazil*
* *Corresponding author email address: fernando.souza@labtucal.ufsc.br*

Abstract
This work proposes a new correlation to predict the pool boiling heat transfer coefficient of a two-phase thermosyphon. To achieve this, the heat transfer characteristics of the two-phase thermosyphon were experimentally studied using two working fluids: water and ethanol, for three different power levels. The proposed correlation is based on the bubble formation process and uses the dimensionless bubble release number, together with the pool boiling heat transfer coefficient. Additionally, the proposed correlation was compared with other literature correlations, showing good agreement with the experimental data.

Keywords: Pool Boiling Heat Transfer Coefficient, Two-phase thermosyphon, Pool boiling

1. Introduction

Two-phase closed thermosyphon is a highly efficient passive heat transfer device. This device can be described as an evacuated tube, sealed at both extremities, within which a working fluid is introduced. This device is typically composed of three sections: evaporator, adiabatic section, and condenser. The adiabatic section may be omitted, depending on the particular requirements of the thermosyphon application. During operation, a heat flow is imposed to the evaporator, resulting in the evaporation of the working fluid contained within this section. The vapor generated is capable of reaching the condenser section, as a consequence of the increased pressure in this section. The heat is then rejected through the condensation of the working fluid in the condenser and the condensed liquid returns to the evaporator by the action of gravity, closing the phase change cycle. Due to this operating principle, two-phase thermosyphons are capable of transferring large heat flows, even with small temperature differences between the evaporator and the condenser.

The startup of closed two-phase thermosyphons is triggered by the promotion of the working fluid's evaporation within the evaporator section. In the case of thermosyphons, this evaporation can occur through either pool boiling or film boiling, mechanisms, depending on geometry of the evaporator and the amount of the working fluid (filling ratio – ratio between the fluid and evaporator volumes).

Both boiling and condensation heat transfer processes are convective, and so, they are associated with a heat transfer coefficient that characterizes them. The literature on two-phase thermosyphons presents several correlations for the estimation of the evaporator and condenser section heat transfer coefficients, resulted from the application of different methodologies.

Specifically for pool boiling, Table 1 shows some of the correlations studied by Jafari et al. [1] to estimate this parameter in two-phase thermosyphons.

Table 1. Pool boiling correlations.

Correlations			Authors
$h_{e,p} = 0.44 Pr_l^{0.35}\left(\frac{k_l}{L_b}\right)\left(\frac{\rho_l}{\rho_l-\rho_v}\cdot\frac{q\cdot P\times10^{-4}}{\rho_v g h_{fg}\mu_l}\right)^{0.7}$		(1)	Kutateladze [2]
$h_{e,p} = 0.075 q^{0.67}\left[1+10\left(\frac{\rho_l}{\rho_l-\rho_v}\right)^{0.67}\right]\left[\frac{k_l^2}{\nu\sigma T}\right]^{0.33}$		(2)	Labuntsov [3]
$h_{e,p} = 0.32\left(\frac{\rho_l^{0.65}k_l^{0.3}Cp_l^{0.7}g^{0.2}}{\rho_v^{0.25}h_{lv}^{0.4}\mu_l^{0.1}}\right)\left(\frac{P}{P_{atm}}\right)^{F} q^{0.4}$	whith ***F*** = 0.30	(3)	Imura et al. [4]
	whith ***F*** = 0.23	(4)	Shiraishi et al. [5]

*The subscripts **l** and **v** indicate the thermodynamic phase where the fluid property is estimated.*

In Tab. 1 Pr is the Prandtl number, g is the gravity acceleration, k is the thermal conductivity, ρ is the density, μ is the dynamic viscosity, υ is the kinematic viscosity, σ is the surface tension, Cp is the specific heat, h_{fg} is the latent heat of vaporization, q is the heat flux, P and T are the saturation pressure and temperature, respectively, P_{atm} is the atmospheric pressure and L_b is the bubble length given by $[\sigma/g(\rho_l - \rho_v)]^{1/2}$. Each of the fluid properties must be obtained in accordance with its phase, indicated by the subscript: l is the liquid phase and v is the vapor phase.

Equations 1 and 2 are correlations derived from studies of pool boiling in the absence of confinement and with the heater situated horizontally at the bottom of the pool. Equation 3 was developed by Imura et al. [4] with pool boiling data for thermosyphons specifically. Subsequently, Shiraishi et al. [5] recommended modifying the exponent of the pressure term from 0.3 to 0.23 when water, ethanol, or R113 refrigerant are employed as the working fluid of the thermosyphon, see Eq. 4.

In the study conducted by Jafari et al. [1], the authors sought to analyze the correlations presented in Table 1 in comparison with experimental data obtained from a thermosyphon. They observed discrepancies between the estimated values by each correlation. The correlations developed for unconfined pool boiling (Eqs. 1 and 2) yielded values for the heat transfer coefficient that were higher than those reported from the tested thermosyphon data. In contrast, the correlations developed with boiling data in thermosyphons (Eqs. 3 and 4) show an agreement of ±30% with the experimental results.

The discrepancy between the results may be attributed to the fact that the classical theory of pool boiling typically examines this phenomenon in horizontal heaters situated at the bottom of the liquid pool, a configuration that usually does not match with standard two-phase thermosyphon geometries. These devices typically have the evaporator oriented vertically, resulting in a vertically oriented heated tube wall. This geometry actually affects the balance of forces on the vapor bubble, as observed by Pabon et al. [6] in their study of geyser boiling in thermosyphons. Furthermore, the formation of the bubble may occur in a confined environment, depending on the internal diameter of the thermosyphon.

The objective of this article is to present a correlation for the heat transfer coefficient of pool boiling for thermosyphons as a function of common dimensionless numbers. The correlation was obtained based on experimental data of a closed two-phase thermosyphon loaded with water and ethanol.

2. Methodology

2.1. Experimental Setup

Figure 1a shows the thermosyphon used for the experimental study to obtain the evaporator boiling heat transfer coefficients. The thermosyphon used in this work was manufactured according to the methodology presented by Mantelli [7]. It consisted of a 500 mm stainless steel AISI 316 long tube, with inside and outside diameters of 22 mm and 25.4 mm, respectively. The evaporator, adiabatic and condenser sections were of 200 mm, 100 mm, and 200 mm, respectively. The tube was sealed and vacuumed.

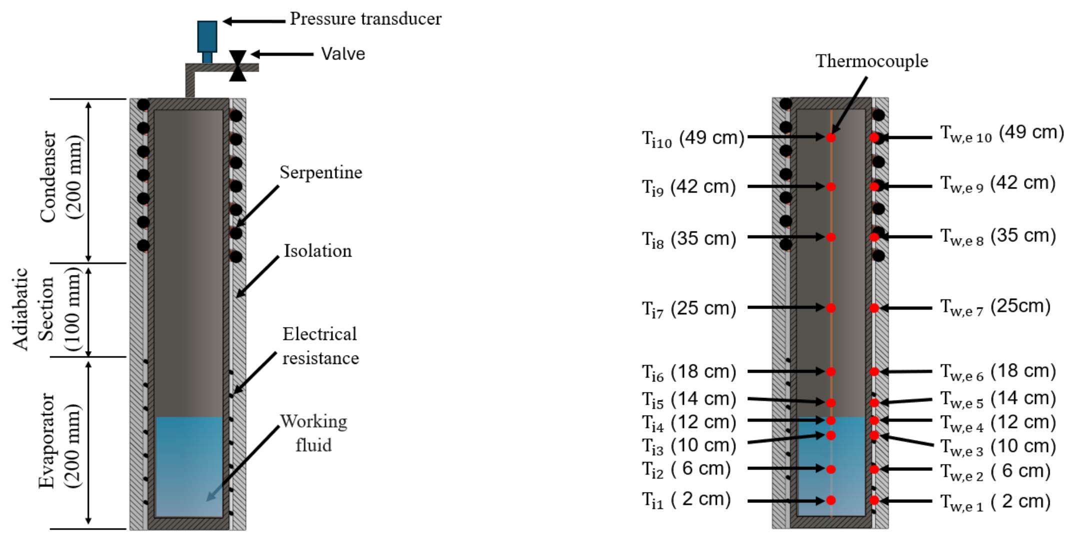

a) Some components of bench. b) Instrumentation.

Figure 1. Experimental bench.

The heat supply to the evaporator was provided by a 28 Ω electric resistance wire, evenly spaced and wrapped around the tube, to ensure uniform heat distribution along the evaporator. The resistance was connected to an Maisheng power supply, model MP15010D, capable of supplying a nominal power of up to 1500 W. To prevent heat losses, the evaporator, adiabatic and condenser sections were insulated with glass wool, with a thickness of 44 mm.

A copper serpentine with an outer diameter of 6.35 mm and a thickness of 1 mm was used for heat dissipation in the condenser. The total length of the coil was 200 mm, evenly distributed over 14 turns around the condenser. Water circulated inside the serpentine, with the inlet temperature controlled at 20°C using a thermal bath from the brand LAUDA, model LCK 2871. The mass flow rate was monitored by a rotameter from the brand Omega, model FL-1501A, maintaining a constant rate of 6.1 g/s.

The temperature distribution along the internal and external thermosyphon tube surfaces was measured using 20 thermocouples of type K (chromel-alumel). The distribution along the tube was as follows: 12 thermocouples in the evaporator section (6 internal and 6 external), 2 in the adiabatic section (1 internal and 1 external), and 6 in the condenser section (3 internal and 3 external). Additionally, three thermocouples were installed to measure the ambient temperature, as well as the inlet and outlet temperatures of the thermal bath. The locations of thermocouples are shown in Figure 1b.

An Omega pressure sensor, model PX409-015V5V, was installed on top of the condenser to record the internal pressure of the thermosyphon during operation. This device is of the piezoresistive type, with a response time of less than 1 ms. Its measuring range varies between 0 to 15 psi.

Data was collected using a Campbell Scientific data acquisition system consisting of a CR1000 module, AM25T multiplexer, and data acquisition code developed in the Logger Net program. The time interval was set at 2 s to allow the datalogger to record all temperatures.

Tests were carried out using two working fluids: water and ethanol, subjected to three heat rates: 20W, 40W, and 60W applied to the evaporator section. The filling ratio (FR) was 60% (45.6 ml), where the FR expresses the ratio between the volume of the working fluid and the volume of the evaporator.

In the experimental procedure, the mass flow rate of the thermal bath was first adjusted and then the temperature was set at 20°C. Once the condenser reached this target temperature, the power input in the evaporator section was set to 20 W. After reaching steady state conditions, the power was increased to 40 W and then to 60 W.

2.2. Data reduction

Radial heat transfer is used to determine the inner wall temperature of the tube, aiming for a more accurate heat transfer coefficient determination, during pool boiling. Actually, the wall temperature corresponds to the solid-liquid interface on the inner wall surface. This inside wall surface temperature is calculated from the outside temperature data, taking into account the wall thickness of the tube using Fourier's Law (Bergman et al. [8]):

$$Q = \frac{\bar{T}_{w,e} - \bar{T}_{w,i}}{\frac{\ln(D_{ext}/D_{in})}{2\pi k L_e}} \tag{5}$$

where Q is the electrical power that is applied to the evaporator section obtained by the multiplication of the voltage (V) and the current (I) of the electrical source; D_{ext} and D_{int} are the external and internal diameters, respectively; k is the thermal conductivity of stainless steel (tube material), and L_e is the evaporator section length. The evaporator wall surface temperature $\bar{T}_{we}$ is considered as the average of six temperatures measured at the evaporator section.

The evaporator heat transfer coefficient h_e is calculated as the ratio of applied heat flux in the evaporator to the temperature gradient between the evaporator wall internal and the temperature at the center of the pool, measured by the thermocouple in the position 6 centimeters from the bottom; It is calculated as follows:

$$h_{exp.} = \frac{Q}{A\left(T_{w,i\,2} - T_{i\,2}\right)} \tag{6}$$

where A is the outside surface area of the evaporator section.

2.3. Heat Transfer Coefficient Correlation

To develop a new correlation for the heat transfer coefficient in the evaporator section, the physical mechanisms of pool boiling associated with the growth of vapor bubble need to be known.

Carey [9] explains that the formation and growth of a vapor bubble occur in two consecutive stages. Initially, the bubble growth is controlled by inertia: the growth rate is governed by the interaction between the bubble and the surrounding liquid in movement. This mechanism persists until the bubble reaches a size such that the interfacial heat transfer between the vapor and the liquid becomes significant. In the second stage, the growth becomes controlled by the heat transfer, and the bubble expands more slowly, constrained by the heat supplied to the liquid-vapor interface.

Besides those mechanisms, Mantelli [7] highlights what the size of the bubble at the moment it detaches is primarily determined by the balance of interfacial tension and buoyancy forces. These forces influence the growth and size of a bubble on the metallic surface of the thermosyphon. Thus, an effective way to evaluate these mechanisms during the boiling process is through the use of dimensionless numbers. According to Bergman et al. [8], this approach enhances the understanding of related physical mechanisms and suggests simplified procedures for generalizing and representing heat transfer results.

In this context, some dimensionless numbers are frequently used to characterize pool boiling such as: Prandtl, Jakob, Bond and Grashof.

In a thermosyphon, there is a minimum heat flux necessary for the device to avoid operating in the Geyser Boiling regime, which is characterized by significant temperature and pressure oscillations. This condition can be represented by the dimensionless parameters mentioned above. Cisterna et al. [10] experimentally demonstrated that bubble formation is directly related to the wall superheating temperature and they proposed a dimensionless number, known as the bubble release number (φ), which quantifies the necessary wall superheat to form a bubble, at a given liquid pool saturation temperature, given by:

$$\varphi = \frac{\Delta T}{T_{sat}} = \frac{T_w - T_{sat}}{T_{sat}} \tag{7}$$

where T_w and T_{sat} represent wall temperature and liquid pool saturation temperature, respectively.

Furthermore, Jensel and Memmel (apud [9]) developed a correlation that takes into account the effects of bubble growth. This correlation considers the bubble departure diameter, buoyancy force, surface tension, inertia, thermophysical properties, and wall superheat temperature.

Cisterna et al. [10] showed that the correlation proposed by Jensel and Memmel (apud [9]) exhibits good agreement in representing bubble departure phenomena in thermosyphons and demonstrated that this equation can be associated with bubble release number (φ) and other dimensionless parameters, by the expression:

$$\varphi = a_1 \frac{Co^{1,5}}{Bo_c^{1,44}} \cdot \frac{\mathrm{Pr}_l \cdot Gr_c}{Ja_c} \tag{8}$$

where a_1 is a constant related to the fluid, Co is the confinement number, Pr_l is the Prandtl number, Gr_c is the corrected Grashoff number, Bo_c is the corrected Bond number, and Ja_c is the corrected Jakob number, all depending on the operating temperature, thermophysical properties of the working fluid, and internal diameter of the thermosyphon. These paraments are written as:

$$Co = \frac{d_b}{D_{int}} \tag{9}$$

$$Pr_l = \frac{c_{pl} \cdot \mu_l}{k_l} \tag{10}$$

$$Ja_c = \frac{\rho_l \cdot c_{pl} \cdot T_{sat}}{\rho_v \cdot h_{lv}} \tag{11}$$

$$Bo_c = \frac{\mathrm{g} \cdot (\rho_l - \rho_v) \cdot D_{int}^2}{\sigma} \tag{12}$$

$$Gr_c = \frac{\frac{\mathrm{g} \cdot (\rho_l - \rho_v)}{\rho_l} \cdot D_{int}^3}{v_l^2} \tag{13}$$

It is important to emphasize that the corrected dimensionless numbers: Jakob, Bond and Grashof, have the same physical meaning as their original ones.

However, when predicting boiling in thermosyphons, one major difficulty lays in obtaining the initial departure diameter of the bubble. This term has been extensively studied in the literature, and some authors have demonstrated a relationship between the bubble release frequency and its initial diameter. Different mechanisms such as heat transfer (Ivey [11]; Mikic and Rohsenow [12]), inertia (Ivey [11]; Cole [13]), and natural convection (Zuber [14]) were considered the foundations of these correlations.

Souza [15] observed that the confinement number (Eq. 9), can be expressed in terms of the corrected Jakob number:

$$Co = b_1 \cdot Ja_c^{0,8} \tag{14}$$

where b_1 is a constant associated with the fluid. Thus, by applying Eq. 14 to Eq. 8, one gets:

$$\varphi = C_1 \cdot Ja_c^{0,8} \cdot \frac{\mathrm{Pr}_l \cdot Gr_c}{Bo_c^{1,44}} \tag{15}$$

where C_1 is a constant expressed as a function of a_1 e b_1. In this context, Souza [15] observed that several effects are relevant for liquid-vapor phase change in a pool boiling regime: heat transfer, buoyancy, surface tension and viscous forces.

In a thermosyphon, the pool boiling at a liquid-solid interface occurs when the wall surface temperature is higher than the saturation temperature (which corresponds to the pressure in the liquid). Thus, the heat transfer rate from solid to the liquid can be calculated by:

$$q = h_e \cdot A \cdot (T_w - T_{sat}) \tag{16}$$

where h_e is the heat transfer coefficient for pool boiling. Therefore, by substituting Eq. 7 into Eq. 16, a new heat transfer expression is written in terms of the heat transfer coefficient for pool boiling:

$$h_e = \frac{q}{A \cdot (T_w - T_{sat})} = \frac{q}{A \cdot \varphi \cdot T_{sat}} \tag{17}$$

It is important to note that, in a thermosyphon, there is a critical heat flux at which vapor bubbles coalesce near the tube wall, preventing the working fluid in liquid state from making contact with the wall. At this point, the wall temperature increases rapidly, causing h_e to experience oscillations (Faghri [16]).

Additionally, according to Carey [9], if sufficient heat is added to the system, the liquid near the wall may slightly exceed the equilibrium saturation temperature. Once the temperature is higher at the solid surface, the formation of an vapor embryo is more likely to occur at the solid-liquid interface.

Finally, by substituting Eq. 15 into Eq. 17, the heat transfer coefficient can be represented by:

$$h_e = \frac{1}{C_1} \cdot \left(\frac{Bo_c^{1,44}}{Ja_c^{0,8} \cdot \mathrm{Pr}_l \cdot Gr_c} \right) \cdot \frac{q}{A \cdot T_{sat}} \tag{18}$$

The coefficient C_1 is an experimental parameter, that can be expressed in terms of dimensionless parameters. In this paper, it is expressed as a function of the corrected dimensionless numbers: Bond, Jakob and Grashof, by:

$$C_1 = a \cdot Bo_c^b \cdot Ja_c^c \cdot Gr_c^d \tag{19}$$

The coefficients a, b, c e d were adjusted based on experimental data obtained from thermosyphon operating with water and ethanol as working fluids, for vapor temperatures ranging between 40°C and 70°C, as discussed later in this paper.

3. Results and discussions

3.1. Temperature distribution analysis

Figures 2 and 3 illustrate the temperature distributions over time for the thermosyphon tests loaded with water and with ethanol, respectively. The plots are divided by black dashed vertical lines, corresponding to the three levels of heat power inputs: 20, 40, and 60 W. For each of these tests, the thermal bath inlet temperature $T_{TB,in}$ was maintained at 20 °C, while the outlet temperature, $T_{TB,out}$, increased a little. The temperature lines correspond to the average values of the thermocouples located in each section of the thermosyphon, both for the external wall instrumentation and for the thermocouples located internally in the three sections. Furthermore, the steady-state regime is considered achieved when the temperatures exhibit a horizontally uniform behavior, characterized by the last 3000 seconds before changing the power level.

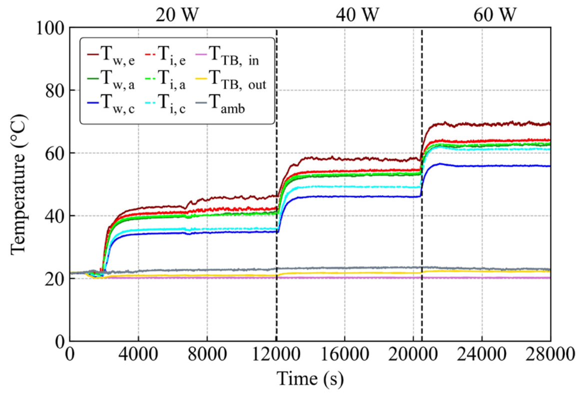

Figure 2. Temperatures of the thermosyphon loaded with a FR of 60% water.

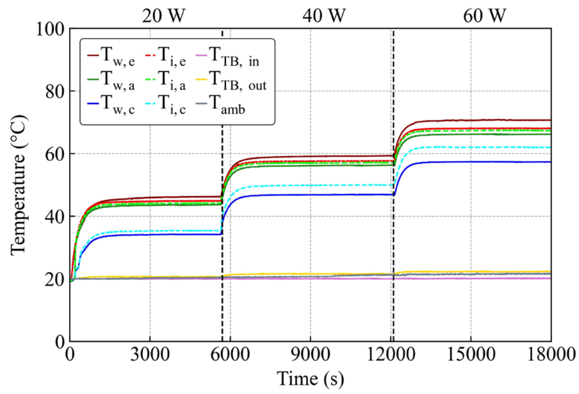

Figure 3. Temperatures of the thermosyphon loaded with a FR of 60% ethanol.

As illustrated in Figures 2 and 3, the evaporator wall temperature is observed to exceed the internal temperature of this same section, thereby indicating the direction of the heat flow. However, for the adiabatic section, the internal and external temperatures are quite similar. In the condensate, the opposite behavior is observed where the internal temperatures exceed the external ones, thereby indicating heat rejection by the coil.

3.2 Heat transfer coefficient

The experimental heat transfer coefficient for pool boiling can be obtained from Eq. 6. It is important to note that during the transient regime, this coefficient exhibits significant fluctuations, potentially reaching very high values. However, in steady-state conditions, the heat transfer coefficient shows more uniform values, which occurs due to the absence of temperature oscillations, as shown in Figs. 2 and 3.

The steady-state data were processed, and the experimental convective heat transfer coefficients were calculated for water and ethanol. Through this data, a linear regression method was applied to obtain the values of the coefficients a, b, c e d. The values obtained for the four constants are, respectively: $1,-1,-2$ e $-0,23$. Thus, the equation that estimates the heat transfer coefficient for pool boiling can be expressed as:

$$h_e = \left(\frac{Bo_c^{2,44} Ja_c^{1.2}}{\mathrm{Pr}_l \cdot Gr_c^{0.77}}\right) \cdot \frac{q}{A \cdot T_{sat}} \qquad (20)$$

Table 2 presents the average values of the experimental heat transfer coefficient for each of the fluids, at the three power levels studied, together with the value estimated from the proposed correlation (Eq. 20) and the relative errors in comparison with the experimental data.

As evidenced by the data presented in Table 2, the two higher values of the relative errors associated with the evaporator heat transfer coefficient are observed at low power levels, of 20 W. For the water and ethanol, these errors are 19% and 27.5%, respectively.

Table 2. Values of $h_{exp.}$ and $h_{correl.}$.

Fluid	Q (W)	T_{sat} (°C)	$h_{exp.}$ (W/m²K)	$h_{correl.}$ (W/m²K)	Error (%)
Water	20	40	519.69	618.76	19.06
	40	53	647.08	584.14	9.73
	60	62	638.02	534.85	16.17
Ethanol	20	44	772.43	560.30	27.46
	40	50	680.79	573.99	15.69
	60	67	649.92	535.64	17.58

An analysis based on dimensionless numbers showed that the Jakob and Prandtl numbers are the most sensitive to variations of the thermosyphon saturation temperature, with the highest values observed at 20W. Actually, at lower power levels, thermal effects associated with sensible heat and the diffusivity of momentum dominate the mechanisms of vapor bubble formation and growth.

In order to be able to compare the correlations in Table 1 with the correlation proposed in this article (Eq. 20), the experimental heat flow and saturation temperature data were used to generate Tables 3 and 4, for water and ethanol, respectively. These tables present the experimental convective heat transfer coefficient data for boiling, organized into three power levels. The convective coefficients estimated by the different correlations are also show for these power levels as well as the relative errors compared to the experimental data. Values in red and with a negative sign indicate that the correlation underestimated the experimental coefficient, while positive values (in black) signal that the correlation overestimated the experimental results.

Table 3. Comparison of convective boiling coefficients in a pool of water for the various correlations.

Water						
Equation	20W		40W		60W	
	h [w/m²K]	Error [%]	h [w/m²K]	Error [%]	h [w/m²K]	Error [%]
Experimental	519,69	- - - -	647,08	- - - -	638,02	- - - -
Proposal Correlation	618,76	19,06%	584,14	-9,73%	534,85	-16,17%
Kutateladze	194,28	-62,62%	361,69	-44,10%	529,79	-16,96%
Labuntsov	287,97	-44,59%	496,91	-23,21%	689,59	8,08%
Imura	1298,70	149,90%	1838,58	184,13%	2273,28	256,30%
Shiraishi	1557,00	199,60%	2110,40	226,14%	2528,42	296,29%

For water (Table 3), the proposed correlation showed the closest results from the experimental data, with errors ranging from 19.06% to -16.17%. These deviations indicate that the model tends to overestimate the coefficients at lower power levels and underestimate them at higher power levels.

On the other hand, the models by Kutateladze and Labuntsov tended to underestimate the heat transfer coefficients. Kutateladze showed large deviations, with errors up to -62.62% at 20W, while Labuntsov presented a smaller deviation at higher power levels, reaching an error of 8.08% at 60W.

The models by Imura and Shiraishi overestimated the heat transfer coefficients at all power levels for water. These models generated errors ranging from 149.90% to 256.30%, indicating that these models are not suitable for water under tested conditions, of heat fluxes below 3800 W/m²K (power levels below 60W). It is worth noting that Jafari et al. [1] recommend these equations for high heat fluxes.

Similarly, an analysis of the correlations using ethanol as the working fluid was conducted based on Table 4.

Table 4. Comparison of convective boiling coefficients in a pool of ethanol for the various correlations.

Ethanol						
Equation	20W		40W		60W	
	h [w/m²K]	Error [%]	h [w/m²K]	Error [%]	h [w/m²K]	Error [%]
Experimental	772,43	- - - -	680,79	- - - -	649,92	- - - -
Proposal Correlation	560,30	-27,46%	573,99	-15,69%	535,64	-17,58%
Kutateladze	107,35	-86,10%	200,87	-70,49%	299,56	-53,91%
Labuntsov	152,49	-80,26%	259,45	-61,89%	359,82	-44,64%
Imura	633,16	-18,03%	909,00	33,52%	1143,93	76,01%
Shiraishi	706,16	-8,58%	971,66	42,73%	1183,49	82,10%

For ethanol (Table 4), it was observed that the proposed correlation underestimates the heat transfer coefficients at all power levels, with errors ranging from -27.46% at 20W to -17.58% at 60W.

The models of Kutateladze and Labuntsov follow the same trend, underestimating the heat transfer coefficients at all power levels. However, these models show larger variations, with errors ranging from -44.64% to -86.10%, indicating that the proposed model showed less discrepancy.

Meanwhile, the models of Imura and Shiraishi underestimate the values at 20W, with errors of -18.03% and -8.58%, respectively. However, as the power increases, these correlations begin to overestimate the convective boiling coefficients, reaching maximum errors of 76.01% and 82.10% at 60W, respectively.

4. Conclusions

This study experimentally investigated the heat transfer coefficient for pool boiling using a stainless steel thermosyphon with an outer diameter of 25.4 mm and an inner diameter of 22 mm. The evaporator and condenser were of 200 mm in length, with a 100 mm of adiabatic section. The thermosyphon was filled with water and ethanol at a filling ratio of 60%. Using internal and external thermocouples, the convective boiling coefficient was experimentally estimated. Based on this experimental data, a linear regression correlation was developed using dimensionless numbers which are used to characterize boiling. Additionally, the data were compared with four well known correlations from the literature, showing that the proposed correlation provided the best fit for both water and ethanol, with a maximum error of 27.05%. The pool boiling correlations without confinement, such as those of Kutateladze and Labuntsov, tend to underestimate the convective coefficients for both fluids. However, the models for pool boiling (Imura and Shiraishi) overestimate the convective coefficient when the fluid is water. For ethanol, these models showed good agreement at low power levels (20W) but deviated as the power increased, indicating that these correlations lose accuracy under higher heat flux conditions. Thus, the proposed correlation proved to be more suitable for both fluids across the investigated power ranges.

5. Acknowledgements

The authors thank the Brazilian National Council for Scientific and Technological Development (CNPq), and the Federal University of Santa Catarina (UFSC).

References

[1] D. Jafari, P. Di Marco, S. Fillippeschi and A. Franco. An experimental investigation on the evaporation and condensation heat transfer of two-phase closed thermosyphons. Experimental thermal

and fluid science 88. 2017: 111-123.

[2] Kutateladze, Heat Transfer and Hydrodynamic Resistance, Energoatomizdat Publishing House, Moscow, Russia, 1990.

[3] D. A. Labuntsov, Heat transfer problems with nucleate boiling of liquids. Therm. Eng., 19 (1972), pp. 21-28.

[4] H. Imura, H. Kusada, J. Oyata, T. Miyazaki, N. Sakamoto, Heat transfer in two-phase closed-type thermosyphons. Trans. Jpn. Soc. Mech. Eng., 22 (1977), pp. 485-493.

[5] Shiraishi, K. Kikuchi, T. Yamanishi, Investigation of heat transfer characteristics of a two-phase closed thermosyphon. Heat Recov. Syst., 1 (1981), pp. 287-297

[6] N. Y. L. Pabón, J. P. F. Mera, G. S. C. Vieira, M. B. H. Mantelli, Visualization and experimental analysis of Geyser boiling phenomena in two-phase thermosyphons. Int. J. Heat Mass Tran., 141 (2019), pp. 876-890.

[7] M. B. H. Mantelli. Thermosyphons and heat pipes: theory and applications. Vol. 1. No. 1. Switzerland: Springer International Publishing, 2021.

[8] T. Bergman, A.S. Lavine, F.P. Incropera, D.P. Dewitt, Fundamentos de Transferência de Calor e de Massa (7th ed.), LTC, Rio de Janeiro (2015)

[9] V. P. Carey. Liquid-vapor phase-change phenomena: an introduction to the thermophysics of vaporization and condensation processes in heat transfer equipment. [s.l.] Taylor & Francis, 1992.

[10] L. H. Cisterna, F. H. Milanez and M. B. H. Mantelli. Prediction of geyser boiling limit for high temperature two-phase thermosyphons. International Journal of Heat and Mass Transfer, v. 165, p. 120656, 2020.

[11] H. J. IVEY, Relationships between bubble frequency, departure diameter and rise velocity in nucleate boiling. International Journal of Heat and Mass Transfer, v. 10, n. 8, p. 1023– 1040, 1 ago. 1967.

[12] B. B. MIKIC, W. M. ROHSENOW, Bubble growth rates in non-uniform temperature field. Prog. Heat Mass transfer, vol. II, p. 283-292, 1962.

[13] R. COLE, Photographic study of boiling in the region of critical heat flux. AIChE J. vol. 6, p.533-542, 1960.

[14] N. ZUBER, Nucleate boiling – the region of isolated bubbles – similarity with natural convection. Int. J. Heat Mass Transfer, vol. 10, p. 53-65, 1963.

[15] F. G. Souza, L. H. Cisterna, F. H. Milanez, M. B. Mantelli, (2023). Geyser boiling experiments in thermosyphons filled with immiscible working fluids. International Journal of Thermal Sciences, 185, 108066.

[16] A. FAGHRI, Heat pipe science and technology. Taylor & Francis, 1995.

Paper ID 105(S1)

TWO-PHASE PRESSURE DROP EXPERIMENTAL STUDY FOR SMALL CAPILLARY TUBES

Kelvin G. Domiciano[1,2*], Mauro Mameli[2], Larissa Krambeck[1], Sauro Filippeschi[2] and Marcia B. H. Mantelli[1]

[1] *Heat Pipe Laboratory, Federal University of Santa Catarina, Florianopolis/SC, Brazil.*
[2]*Department of Energy, Systems, Territory and Constructions Engineering, University of Pisa, Italy.*
**Corresponding author email address: kelvin.guessi@labtucal.ufsc.br*

Abstract

In the present study, pressure drop measurements of a water two-phase flow inside capillary tubes with low mass flow rates under condensation was carried out. The major objective is to understand the mechanics that drive such flows, so that this knowledge can be used to assisting the design of condensers of small two-phase devices, such as miniature loop heat pipes. A simple but interesting workbench, where water vapor flows passively through the capillary tube given by its vapor pressure, was developed. Two capillary tubes were used, one made of copper with 1.01 mm of internal diameter and another of transparent material (PVC) for visualization in order to understand the physics of confined flows. The experimental results shown that the liquid pressure drop plays the major role in such flows, given by the coalescence of liquid forming slugs that occupies the whole internal diameter of the capillary tube, which are pushed along the tube due to the vapor pressure increase. Two techniques for the pressure drop measurement were used: pressure transducers and thermodynamic tables, where the saturation temperature of the working fluid under phase change conditions were the entry parameter. An average difference between the data of 15% was obtained. Therefore, the results showed insightful information for designing new heat pipe condensers.

Keywords: pressure drop, two-phase flows, confined flows, capillary tubes, loop heat pipe

1. Introduction

The use of capillary tubes in phase-change cooling devices, especially for the thermal management of electronic components, has increased over the years with the simultaneous augment of processing power and miniaturization of gadgets. In this context, research resources have been spent in efforts aiming the development of miniaturized heat pipe technologies, where phase change takes place within mini or microchannels.

To properly design mini/micro heat transfer devices able to remove high heat fluxes from electronics, a comprehensive understanding of the physical phenomena responsible for the pressure drops of working fluids flowing in small cross-section channels subjected to vapor/liquid phase change, is of utmost importance.

In the literature, single-phase flow pressure drops within mini and/or microchannels are well characterized, and many correlations are available. Beyond the fluid inertia and viscosity, the pressure drops in two-phase flows are also influenced by the gas-liquid interfacial tension forces, the wettability of the liquid, and the exchange of momentum between both phases [1]. Moreover, in diabatic conditions, the vapor quality must be considered too.

Usually, two-phase flows are considered as a combination of gas and liquid (e.g. air and water) adiabatic parallel flows, so that the pressure drops are mainly the result of the friction forces. Usually, for larger devices, the prediction of pressure drop can be reasonable once the pressure variation due to phase change can be negligible when compared to that of the friction forces.

For small devices, is hard to find a correlation suitable for estimating the two-phase pressure drop, as most of them were developed for large tubes, with high mass flow rates and, besides, do not take into consideration phase changes [2]. Actually, they tend to overpredict pressure drops, especially for small tubes and low mass flow rates [3]. However, in many literatures works, the available two-phase flow correlations are still used for the pressure drop predictions [4–6].

An experimental work of measuring the pressure drops in capillary tubes is carried out. Water in very low mass flow rates, under condensation, are considered. The major objective is to understand the physical mechanisms that rules the pressure drops in capillary tubes. In the proposed apparatus, a capillary copper tube of 1.01 mm and a transparent tube (PVC) of 0.446 mm were used. Heat is removed by natural convection causing the vapor-liquid phase change.

The physics and hypotheses found in the present research are applied to investigate the pressure drop of a loop heat pipe (LHP), bringing a real contribution for the state of the art for scientific community, providing a new approach for the designing of condensers.

2. Experimental workbench

Figure 1 shows the proposed experimental apparatus designed to measure the pressure drop of a capillary tube, in a simple but useful way. The workbench consisted of a boiler with the studied fluid inside. A metallic mesh screen is used in the liquid pool before the boiler exit, to avoid geyser boiling and to separate the vapor from the liquid. The boiler is bottom heated by an electrical resistance using a power supply. The boiler was highly insulated from the environment with a box filled with vermiculite (low thermal conductivity). Also, the exit of the boiler and the sensors were insulated by Armflex® blankets. A mass flow rate of vapor leaves the boiler, entering the capillary tube, being condensed due to external heat transfer by natural air convection, along the tube. Therefore, the pumping of the working fluid through the capillary tube was performed only by the vapor pressure, i.e., such as in real applications including loop heat pipes.

They were used two capillary tubes of 480 mm of length, of different materials: copper and transparent PVC, of 1.01 mm and 0.446 mm of diameters, respectively. The PVC tube allowed for the visualization of the flow. Figure 2 shows a microscopic view of the cross section of these tubes. Four T-type thermocouples were used to measure the temperatures along the experimental apparatus: T_1 located inside the boiler pool, T_2 in boiler outlet, while T_3 and T_4 monitored the inlet and outlet temperatures of the capillary tube (test section). Also, three pressure transducers were used: two in the capillary tube inlet (a differential, Keller® PD-33X, with the atmosphere pressure as the reference and an absolute, Keller® 23SY-Ei); and one absolute (Keller® M5 HB) in the outlet of the test section. The pressure variation between the inlet and outlet of the tube can also be evaluated by thermodynamic tables once the confined flow is in under condensation, i.e., under saturation conditions. The applicability of the temperature approach to accessing the pressure drop along a heat pipe is discussed later in the present manuscript. To guarantee air leakage from the environment to inside the capillary tube, the experiments were performed for inlet pressures above the atmosphere.

The pressure drop measurements were performed only after the flow reached stable condition, which means an average pressure variation of less than 60 Pa, measured by the differential pressure transducer, in one minute. Note that stable condition is more accurate term due to the intrinsic oscillations of the flow around a constant average level. After, for all tests, the stable conditions were achieved, the condensate collected at the end of the capillary tube was weighted during around 300 seconds in order to estimate the liquid mass flow rate.

In the present apparatus, the vapor pressure buildup in the boiler was the driving force mechanism that pushed the two-phase flow along the tube. When liquid was able to form slugs, fulfilling the tube cross section, the friction forces, between liquid and wall, increased. The more the vapor condensed, the larger the friction forces and the larger the boiler vapor pressure. The boiler used in this work was not able to handle too high pressures and, therefore, the average vapor qualities varied between 71% and 84%. Vapor mas flow rate ($\dot{m}=\dot{m}_v$) leaving the boiler was estimated by a heat energy balance, in stable conditions, resulting in:

$$\dot{m} = \dot{m}_v = \frac{q}{h_{lv}} \tag{1}$$

where q is net power input, provided by the input voltage times the electrical current, q = V.I, (discounting the heat losses, q_{loss}), and h_{lv} is the latent heat of vaporization.

By collecting and weighting the condensate at the end of the tube, the vapor quality can be assessed:

$$x_v = 1 - \frac{\dot{m}_l}{\dot{m}_v} \tag{2}$$

The heat loads applied to the copper tube varied from 30.3 to 53.5 W, resulting in mass flow rates from 1.24 to 2.24x10^{-5} kg/s, while 30.72 W (1.25 x10^{-5} kg/s), was applied to the PVC tube.

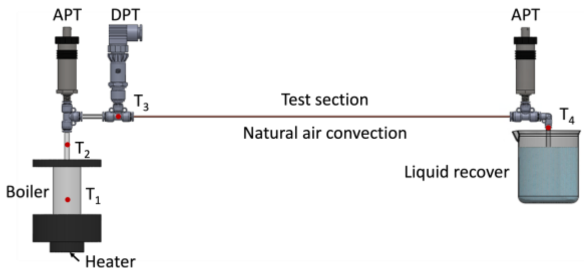

Figure 1. Experimental workbench for the two-phase pressure drop measurement.

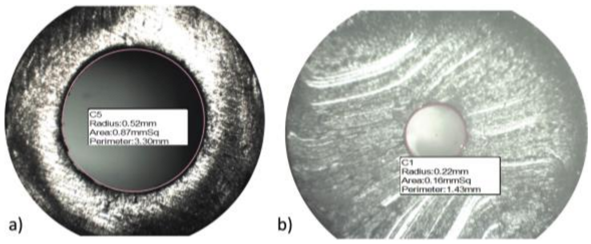

Figure 2. Microscopic image of the internal diameters of the a) copper tube and b) PVC tube.

For estimating the uncertainty of the

experimental measurements (temperature, pressure, voltage, and current), the error propagation method was used, using the following expression [7]:

$$\delta(y)^2 = \sum_{i=1}^{n}\left[\frac{\partial f}{\partial y_i}\delta(y_i)\right]^2 \tag{3}$$

where y_i is the variables that provide uncertainties to the experimental measurement and f is the function regarded to the estimation of the measurement.

As mentioned, besides measuring the local pressure with transducers, thermodynamic tables were used to estimate the pressure, using the saturation temperature as input data. Thus, the local saturation pressure has an uncertainty related to the temperature measurement, i.e.:

$$\delta(p_{sat}) = p[\delta(T)] \tag{4}$$

where δT is the temperature uncertainty given by the thermocouple measurement.

The standard uncertainties of the sensors used in the experimental workbench is shown in Table 1.

Table 1. Standard uncertainties of the sensors used in the experiment.

Measurement	Sensor	Standard uncertainty
Differential pressure	Keller® PD-33X	60 Pa
Absolute pressure	Keller® M5 HB	320 Pa
Absolute pressure	Keller® 23SY-Ei	500 Pa
Temperature	Thermocouples	0.58 °C

3. Physical behavior of the confined flow

Although there is no proper criterion for determining confinement of a fluid flow, the non-dimensional number, Confinement number (*Co*), which as initially proposed for confined boiling flow [8], shall be used for condensation, as recommended by Kew and Cornwell [9] (considered confined if $Co > 0.5$). This non-dimensional parameter is defined as following:

$$Co = \frac{\sqrt{\sigma g(\rho_l - \rho_v)}}{d_h} \tag{5}$$

where σ is the fluid surface tension, g the gravity acceleration, ρ_l and ρ_v are the densities of the liquid and vapor respectively, and d_h is the hydraulic diameter of the capillary tube. The confinement number of the tubes with internal diameters of 1.01 mm and 0.446 mm were 2.47 and 5.56, respectively, therefore in confinement conditions.

As described in the experimental workbench section, the same flow conditions, tested for the copper capillary tube of 1.01 mm in diameter, was performed using a transparent tube (high quality PVC material) to understand the physics behind the confined flow under condensation. For estimating the pressure drop along the capillary tube, stabilized conditions were used, considered achieved when the local pressures reached a constant level while intrinsic fluctuations in the pressure, given by the confined flow, are observed.

Figure 3 shows the absolute inlet pressure as a function of time for water flowing at 1.24x10^{-5} kg/s (30.7 W) inside the PVC tube of 0.44 mm in internal diameter. This graph demonstrates the inlet pressure variation while the fluid flow was visualized and recorded, which the images are shown in Figure 4. Although the heating up starts from the environment conditions, at low pressures and temperature, the plot shows data after boiling was already happening. At around 3500 seconds, the flow reached a stable condition, where the inlet pressure remained at a constant value of around 126 kPa. Some small intrinsic fluctuations are observed due to the sensor noise, which was around ± 100 Pa (checked by measuring liquid single-phase pressure drops). The fluctuations were added to others, with higher intensity, as shown in the zoon view of Figure 3 (4200 to 4700 seconds) where oscillations of up to 600 Pa were observed.

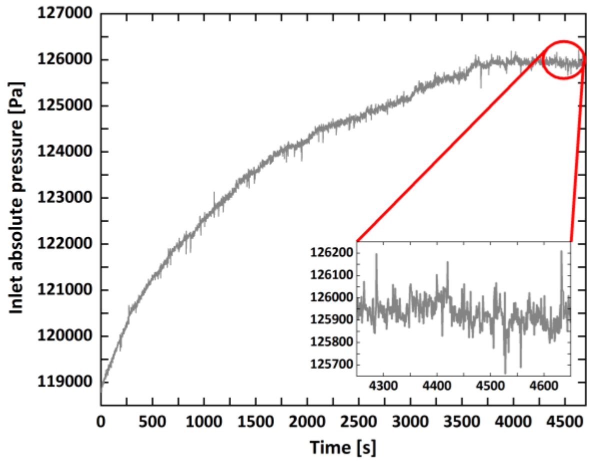

Figure 3. Absolute inlet pressure as a function of time for water flowing at 30.72 W along the PVC tube of 0.446 mm in internal diameter.

The four images within 2 seconds (taken zero as the time for the first picture) obtained from the PVC tube after stable conditions were reached (see Figure 4) helps in the understanding of the confined two-phase flow physical behavior. The average vapor quality of this flow was of around 75%. At the instant zero (0 s, Figure 4a), it can be observed that both fluid phases (liquid and vapor) are flowing in parallel. Although the mass flow rates are small, the very small tube cross section areas results in high vapor flow velocities. However, after only a few milliseconds later, the flow is almost blocked by condensed liquid slugs that fulfills the cross-section areas of the tube. The solid liquid surface tension resulting in liquid wall friction forces that slows down the flow. At Figure 4b, the velocity of the flow is drastically reduced staying in this condition for almost for 1 second, as shown in Figure 4b, c and d. In these moments, due to the low velocity of the fluid, the achieved laminar are clearly observed. The increase in the friction forces between the liquid and the wall requires the vapor pressure to increase to push the liquid plugs, and abrupt increase in the inlet pressure (buildup in the boiler), shown in Figure 3. When the vapor pressure could suppress the static friction force between the liquid and wall, the fluid flowed and the fluid pressure reduced back to the initial condition, as observed in Figure 3 and Figure 4e and f. In these conditions, some turbulences can be seen due to the high vapor velocity.

In general, the confined fluid flow can be characterized by a high velocity flow with low pressure drop, which suddenly is slowed due to liquid slugs, changing its configuration to a low velocity flow with liquid and vapor in series. Also, in such confined flow, a different vapor quality distribution when compared to conventional flows (non-confined ones) can be observed, where values of zero can be assigned to the liquid plugs and one to the region occupied by vapor. The average vapor title is actually a “volume average” between these two values.

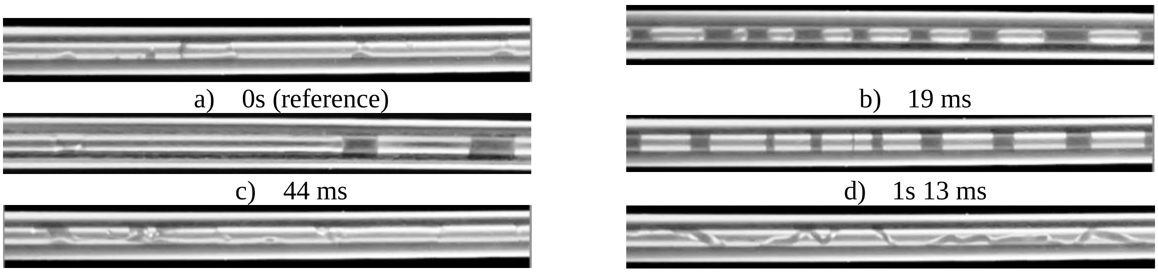

a) 0s (reference)
b) 19 ms
c) 44 ms
d) 1s 13 ms
e) 1s 36 ms
f) 1s 57 ms

Obs. The times are referred to the reference time (t=0), picture a).

Figure 4. Different characteristics of the water flow at 30.72 W along the PVC tube of 0.446 mm in internal diameter, after achieved stabilized conditions.

4. Theoretical pressure drops

The single-phase (liquid or vapor) flow has been extensively studied in the literature and is well characterized by theoretical equations. The expression for estimating the pressure drop of single-phase flows can be written as following [8]:

$$\Delta p = \frac{2 f_k G^2 L}{\rho_k d_h} + \frac{k(\infty)\rho_k {u_m}^2}{2} \quad (6)$$

where L is the tube length, u_m is the mean velocity of the fluid, G is the mass flux, d_h is the internal hydraulic diameter and k (∞) is the incremental pressure defect, which assumes a constant value of 1.28 for fully developed flows. Lastly, f_k is the friction factor, which represents the friction between single-phase (subindex k is for vapor -v- or liquid -l) and wall. Blasius developed the correlation for estimating the friction factor that depends on the flow regime (laminar and turbulent) [10]:

$$f_k = \begin{cases} 16\,\mathrm{Re}_k^{-1} & for\ \mathrm{Re}_k < 2000 \\ 0.079\,\mathrm{Re}_k^{-0.25} & for\ 2000 \le \mathrm{Re}_k < 20000 \\ 0.046\,\mathrm{Re}_k^{-0.2} & for\ \mathrm{Re}_k \ge 20000 \end{cases} \quad (7)$$

where Re_k is the unidimensional Reynolds number that depends on the flow regime, given by:

$$\mathrm{Re}_k = \frac{G j_k d_h}{\mu_k} \quad (8)$$

where j_k is the phase representation, in which for liquid $j_l = 1-x$, while, for vapor $j_v = x$, where x is the vapor quality. μ_k is fluid the viscosity.

Differently from the single-phase, the physics of the two-phase flows are complex and still needs deeper understanding, especially the confined ones. The two-phase pressure drop is influenced by several parameters such as fluid inertia, fluid viscosity, the wettability of the liquid in the surface of the tube, the vapor quality and the interfacial interaction between the vapor and liquid, the vapor and the wall, and the liquid and the wall. The liquid loses velocity due to the friction forces resulting from these interactions.

Most of the works available in the literature studied the pressure drop of two-phase flows along a diabatic tube, i.e., without condensation, where two different fluids are mixed, such as water and air. In these cases, the pressure drops observed are related to the friction between the fluids and between the fluids and the wall. On the other hand, in real applications, the condensation must be considered. Due to the phase-change, the vapor quality decreases while it flows through the tube losing heat, which causes the fluid deceleration (reduction of the fluid velocity), affecting the total flow pressure drops. This deceleration pressure is usually neglected for designing condensers of heat pipes. The importance of this term increases with decreasing the internal diameter of the channel, i.e., for confined flows, the deceleration pressure become even more important. Also, as found studying the physics behind the confined flow, the trapping of liquid slugs when it fulfills the cross-section of the channel must be considered, as capillary forces can be developed. Therefore, the total two-phase pressure drop of confined flows can be estimated by the sum of the following terms: friction between the two phases ($\Delta p_{tp,fr}$), the gravitational force ($\Delta p_{tp,g}$), the acceleration or deceleration of the fluid due to phase change ($\Delta p_{tp,d}$) [1], friction between vapor phase and wall ($\Delta p_{v,fr}$), friction between liquid phase and wall ($\Delta p_{l,fr}$), and the pressure drop due to capillary forces (Δp_{cap}), i.e.:

$$\Delta p_{tp} = \Delta_{v,fr} + \Delta_{l,fr} + \Delta p_{tp,fr} + \Delta p_{tp,g} \pm \Delta p_{tp,d} + \Delta p_{cap} \quad (9)$$

Since the present experimental work was accomplished in the horizontal orientation, the pressure drop due to gravity action can be neglected ($\Delta_{ptp,g} = 0$).

According to Carey [1], the summation of the friction pressure drops ($\Delta p_{tp,fr} + \Delta p_{l,fr} + \Delta p_{v,fr}$) can be estimated by integrating the following expression in the axial direction of the tube with uniform cross-section:

$$-\left(\frac{dp}{dz}\right) = -\phi_k^2\left(\frac{dp}{dz}\right)_k + \left[\left(1-\alpha\right)\rho_l + \alpha\rho_v\right]g\sin\Omega$$
$$\pm\frac{d}{dz}\left[\frac{G^2x^2}{\rho_v\alpha} - \frac{G^2\left(1-x\right)^2}{\rho_l(1-\alpha)}\right] \quad (10)$$

The first term on the right-hand side Eq. (10) provides the total friction pressure drop mentioned ($\Delta p_{tp,fr} + \Delta p_{l,fr} + \Delta p_{v,fr}$), given by the single-phase pressure drop (vapor and liquid, only vapor or only liquid), corrected by the two-phase multiplier (ϕ_k^2). The gravitational pressure drop is the second term ($\Delta p_{tp,g}$), which depends on the void fraction (α), gravity acceleration (g), the angle of the inclination of the tube (Ω) and the phases densities. Lastly, the deceleration or acceleration term ($\Delta p_{tp,d}$), which for the present study is deceleration due to condensation, relies on the vapor qualities and mass fluxes.

The single-phase pressure drop, first right term of Eq. (10), can be estimated by the following expression [1]:

$$-\left(\frac{dp}{dz}\right)_k = \frac{2 f_k G^2 j_k^2}{\rho_k d_h} \quad (11)$$

where f_k is given by Eqs. (7) and (8).

The well-known homogenous model provides the simplest method to determine these friction pressure drops ($\Delta p_{tp,fr} + \Delta p_{l,fr} + \Delta p_{v,fr}$). The model considers that both the vapor and liquid forms a unique flow, with both phases at the same velocity. The two-phase flow properties are estimated by the combination of both single-phase properties. In this way, the two-phase multiplier, ϕ_k^2, is not necessary.

Other models developed in the last years, considered the two-phase multiplier (ϕ_k^2) (see Eq. 10), which basically uses the separated model, with the phases with different velocities. The hypotheses are used: constant properties at an average temperature of the flow, negligible vapor compressibility, and uniform dissipation of the heat along the capillary tube. In this case, the vapor quality changes along the capillary tube, as the condensation process may be approximately linear.

The visualization of the present studied confined flow showed that, when the liquid slugs are trapped between vapor bubbles, the liquid and vapor flows in series, and so have the same velocity. However, for the same flow and at a different instant, the liquid and vapor also presented parallel flows with different velocities (Figure 4a, b, and c).

To determine the total pressure drop, the fluid flow along the tube was split into n discrete volumes, with the pressure drops calculated at each volume. The trapezoidal rule was used to determine the total pressure drop (integrate Eq. (10)):

$$\Delta p = \frac{G^2 v_k}{d_h}\frac{\Delta z}{(n-1)}\times$$
$$\times\left[\left(\phi_k^2 f_k j_k^2\right)_{z_{i-1}} + 2\sum_{i=1}^{n-1}\left(\phi_k^2 f_k j_k^2\right)_{z_i} + \left(\phi_k^2 f_k j_k^2\right)_{z_n}\right] + \quad (12)$$
$$+G^2\left[\frac{x^2 v_v}{\alpha} - \frac{\left(1-x^2\right)v_l}{\left(1-\alpha\right)}\right]_{z_{i-1}} - G^2\left[\frac{x^2 v_v}{\alpha} - \frac{\left(1-x^2\right)v_l}{\left(1-\alpha\right)}\right]_{z_n}$$

where v_k is the specific volume of the liquid (k=l) or vapor (k=v) phases. In Eq. (12), the void fraction is estimated from the Lockhart and Martinelli expression [1]:

$$\alpha = \left[1 + 0.28\left(\frac{1-x}{x}\right)^{0.64}\left(\frac{\rho_v}{\rho_l}\right)^{0.36}\left(\frac{\mu_l}{\mu_v}\right)^{0.07}\right]^{-1} \quad (13)$$

The two-phase multiplier parameter can be evaluated by [11]:

$$\phi_k^2 = \begin{cases} 1 + \dfrac{C}{X} + \dfrac{1}{X^2} & \text{for liquid} \\ 1 + CX + X^2 & \text{for vapor} \end{cases} \quad (14)$$

where C Is the flow constant and X is the Lockhart and Martinelli parameter, given by:

$$X^2 = \left[\frac{(dp/dz)_l}{(dp/dz)_v}\right] \quad (15)$$

The flow constant (C) of Eq. (14) can be estimated by several methods. The two commonly used for designing condenser of heat pipes are used here. The first one was developed by Lockhart and Martinelli (LM) [12]. Based on their data for several working fluids (including water), for adiabatic flows in tubes with hydraulic diameters varying from 1.49 to 25.83 mm, these authors proposed a constant value for C that depended on the liquid and vapor flow regimes. Mishima and Hibiki [13] also proposed a correlation based on adiabatic air-water vertical flows in tubes with diameters from 1 mm to 4 mm. Table 2 provides the C numbers and/or correlations to estimate C, for all two-phase flow regimes. All fluid properties were taken from the software REFPROP®.

Table 2. Constant C estimation parameter

Single-phase flow regimes	C parameter	
	LM	MH
Liquid turbulent Vapor turbulent	20	$21\left[1-\exp\left(-0.333 d_h\right)\right]$
Liquid turbulent Vapor laminar	10	
Liquid laminar Vapor turbulent	12	
Liquid laminar Vapor laminar	5	

5. Experimental results and discussion

To evaluate the quality of the pressure drop measurement and the accuracy of the single-phase friction factor estimation with Blasius expression, Eq. (7), an important for the total pressure drop prediction by Eq. (12), pressure drops for water (in liquid phase) flowing inside both capillary tubes (copper and PVC) were measured, where the liquid was pumped by a precise pump (LongerPump® Model L100-S1-2, head DG-1-B), able to provide low mass flow rates at stable conditions (low oscillations). At the end of the tube, the liquid was collected and weighted with a high-precision scale, to obtain the water mass flow rate with precision.

It should be noted that, to get a precise measurement of pressure drops in confined single-phase or two-phase flows, disturbances of the flow and local pressure drops must be considered, such as contraction, expansion, elbows, and others.

Figure 5 shows the pressure drop theoretical and experimental friction factors, estimated with Blasius expressions, Eq. (7), and calculated by Eq. (6), respectively. For all tests, the flow was considered fully developed, with, therefore, $k(\infty)$ being assumed as 1.28 and with Re lower than 2000, i.e., for laminar flows.

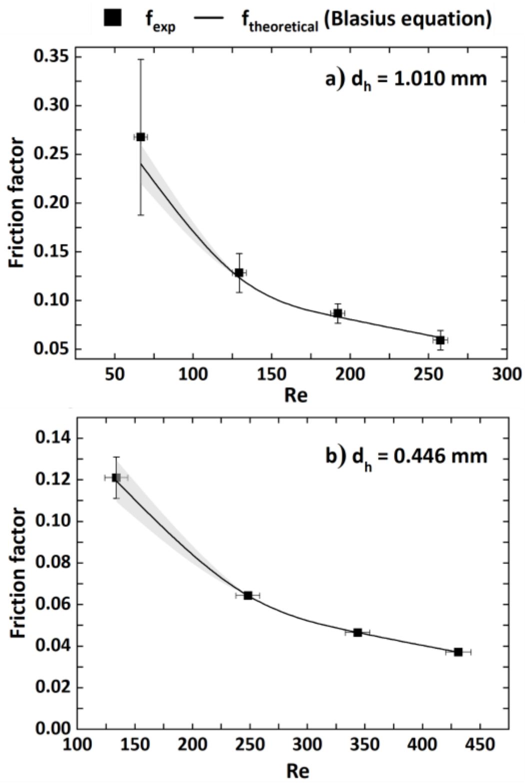

Figure 5. Experimental friction factor estimation for water single-phase flow inside a) a copper tube of 1.01 mm in internal diameter and b) a PVC tube of 0.446 mm in internal diameter.

Since the mass flow rate was experimentally measured, both data (theoretical and experimental) had uncertainties. The experimental uncertainties are shown with errors bars and the theoretical ones by a shadow area. For both capillary tubes, Blasius equation was able to properly predict the liquid single-phase friction factors, which remained between the measurement uncertainties in all tested conditions. The percentage difference between the theoretical data and experimental was from 0.07% to 10.15%, being the lowest values observed for higher Reynolds numbers. This excellent result showed that the Blasius equation is able to predict the friction factor of single-phase flows with high accuracy and that the pressure drop measurement of the present experimental apparatus is reliable.

Figure 6 shows the Experimental pressure drop measured by the pressure transducers and using saturation tables. Theoretical calculations of the friction pressure drop of single-phase vapor and liquid and the friction pressure drop of two-phase flow proposed by Lockhart and Martinelli (LM) and Mishima and Hibiki (MH). The data are plotted as function of the mass flux, mass flow rates (lower horizontal axis) and vapor and liquid single-phase Reynolds numbers, Re_{vo} and Re_{lo} (upper horizontal axis).

From Figure 6, the single-phase vapor flow showed higher pressure drop compared to the liquid one, which is related to the density difference between the phases, i.e., for the same mass flow rate, vapor have much higher velocities compared to liquid.

Both data, obtained from the transducers and saturation table, for the studied two-phase flows, showed low values of pressure drops, being close to the liquid single-phase. However, the trend of all curves showed to be the same, with the pressure drops increasing almost linearly with the mass flow rates, which is reasonable, as the flow regime did not change in this test condition.

Comparing the experimental data with the proposed correlations available in the literature, in which the uncertainties are given by the shadowed areas, all theoretical pressure drops results showed higher values than the data and theoretical vapor single-phase flow. These values shows that, if the friction pressure drop of such flows were of the magnitude predicted by the models, most of mini heat pipe technologies, such as loop heat pipes, would never be able to operate.

In conventional flows (non-confined ones), it is expected that the total friction pressure drop presents larger values than the summation of vapor and liquid single-phase flow pressure drops, as besides the single-phase pressure drops, there is the friction between the phases themselves, when the phases have different velocities in parallel. However, for confined flows, as visualized with the transparent tube, the liquid phase, which presents the highest pressure drops, controls the two-phase flow velocities. Therefore, as shown in Figure 6, the friction pressure drop of confined two-phase flow must be close to the liquid single-phase flow.

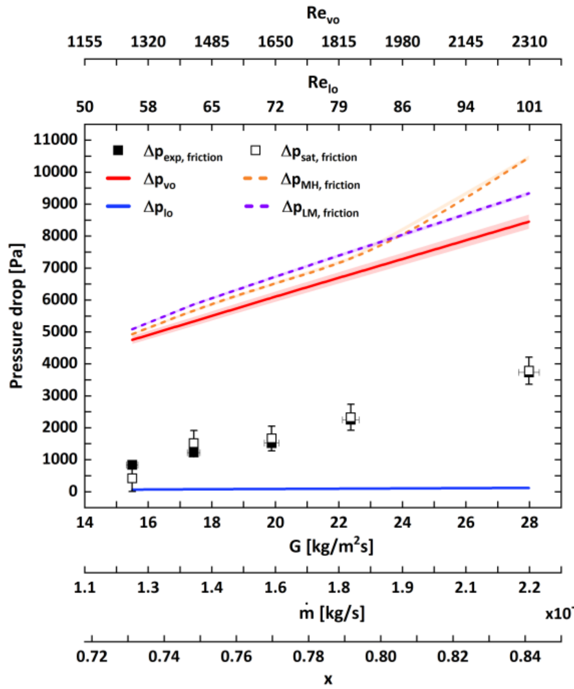

Figure 6. Experimental pressure drop given by the pressure transducers and saturation table. Theoretical calculations of the friction pressure drop of vapor and liquid flowing alone and the friction pressure drop of two-phase flow proposed by Lockhart and Martinelli (LM) and Mishima and Hibiki (MH).

Lastly, from Figure 6, it is clear that the experimental data from the transducer measurement and from the thermodynamic tables matched quite well. The average difference between both data was 15%, with lower discrepancies at higher temperatures. Therefore, these results give powerful insights for estimating the pressure drop of two-phase flows along compact and/or thin heat pipes, in which the use of sensors, such as pressure transducers, drastically affect the thermal performance of such devices. For example, the dead volume caused by pressure transducers sometimes can be larger than the volume of an ultra-thin heat pipe itself, being the measurement of pressure with these sensors unfeasible.

6. Pressure drop analysis of a thin LHP

In order to evaluate the hypotheses mentioned in the present work to explain the physical behavior of confined two-phase flows, data from a thin loop heat pipe (LHP), previously studied, was used as a case to estimate the total pressure drop along the device. The proposed LHP, especially designed for the thermal management of electronics, of 76 x 60 x 0.8 mm^3, is composed of two major sections: an evaporator and a condenser, because, as just the evaporator is insulated from the environment, all the other regions work as condensers, as shown in Figure 7. The LHP has a wick structure in the evaporator and in a fraction of the condenser, which properties, experimentally measured, are shown in Table 3. The device was manufactured by the diffusion bonding of three copper sheets of 0.3 mm thick: two for the external case and one to form the internal channels for the fluid flow. After the diffusion bonding process, a reduction in the total thickness was expected, given by the applied temperature and pressure over the piled plates. For more details about the fabrication procedure, see Domiciano et al. [4,14].

The LHP was tested in the horizontal orientation with 0.14 ml of water as the working fluid. Its temperatures were assessed with T-type thermocouples (*Omega Engineering*®) distributed along the LHP. Increasing heat power inputs, starting with 0.5 W and 1 W, and then with steps of 1 W, were applied to the evaporator, guaranteeing that the temperature of the LHP did not surpass 100 °C.

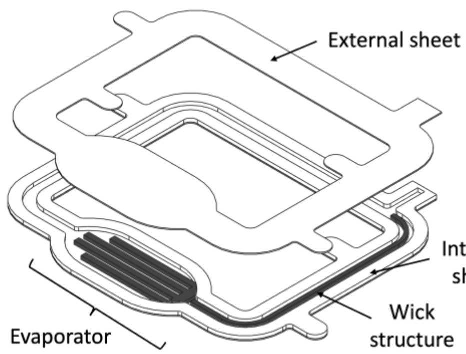

Figure 7. Schematic design of the thin LHP.

Table 3. Main characteristics of developed LHP.

Component	Characteristic
Total dimensions [mm^3]	76 x 60 x 0.8
Evaporator area [mm^2]	37.5 x 20
Vapor grooves area [mm^2]	23.5 x 1.3
Condenser area [mm^2]	180 x 3
Particle average diameter [μm]	49.72 [15]
Porosity [%]	53.46 ± 3.87 [15]
Permeability [10^{-12} m²]	1.99 ± 1.02 [16]
Effective porous radius [μm]	21.04 ± 2.2 [17]

The total pressure drop along the LHP (ΔP_t) can be assumed as the sum of the pressure drop in the evaporator, due to the vapor in the channels (ΔP_{vc}) and the liquid in the wick ($\Delta P_{ev,w}$), and in the condenser, due to the two-phase change (ΔP_{tp}), determined by Eq. (9), and to the liquid in the wick ($\Delta P_{c,w}$), in which the condensate is returned to the evaporator, resulting in:

$$\Delta p_t = \Delta p_{ev,w} + \Delta p_{vc} + \Delta p_{tp} + \Delta p_{c,w} \tag{16}$$

The vapor pressure drop in the channels (ΔP_{vc}) can be estimated by the single-phase pressure drop given by Eq. (11), assuming $j_k = 1$. However, since the LHP channel is rectangular, the friction factor estimation was determined by the following expression, for laminar flow (present case) [8]:

$$f\,\mathrm{Re} = 24\begin{pmatrix} 1 - 1.3553\alpha + 1.9467\alpha^2 \\ -1.7012\alpha^3 + 0.9564\alpha^4 - 0.2537\alpha^5 \end{pmatrix} \tag{17}$$

where α is the channel aspect ratio, given by the ratio between the channel inner thickness and its width. For the single-phase section of the condenser, the hydraulic resistance concept was used, in parallel arrangement, in which some liquid flows in the wick and some in the parallel channels. Lastly, the pressure drop of liquid flowing through a porous media is determined by the well-known Darcy-Weisbach equation:

$$\Delta P_w = \frac{\dot{m}\mu_l L_w}{\rho_l A_w K_w} \tag{18}$$

where $L_{c,w}$, A_w, and K_w are the length, the cross-section area and the permeability of the wick structure, respectively.

For the proper operation of the LHP, the capillary pressure provided by the wick must be larger than the total pressure drop along the device, i.e., $\Delta P_{cap} > \Delta P_t$. To estimate the capillary pressure, the following expression is used:

$$\Delta p_{cap} = \frac{2\sigma}{r_{eff}} \tag{19}$$

where σ is the surface tension and r_{eff} is the effective porous radius of the wick structure.

In Table 4, the capillary pressure of the wick structure estimated by Eq. (19) (ΔP_{cap}), the pressure drop of liquid flowing through the wick structure determined by Eq. (18) ($\Delta P_{ev,w} + \Delta P_{c,w} = \Delta P_w$), and the deceleration pressure drop (ΔP_d) are presented. Also, the total pressure drop, given by Eq. (16), $\Delta P_w + \Delta P_{tp} + \Delta P_{vc}$, is calculated by four different ways, in which the only difference is regarded to the estimation of ΔP_{tp}. The estimation showed that ΔP_{vc} is nearly zero. The first consideration for estimating ΔP_{tp} is considering this term only determined by vapor flowing alone, $j_k = 1$ in Eq. (11) ($\Delta P_{tp,vo}$). Second, considering the two-phase pressure drop given by an average vapor quality of 0.5 in Eq. (11) ($\Delta P_{tp,MHavg}$). Third, assuming the discretization method by Eq. (12) ($\Delta P_{tp,MH}$). Lastly, considering the single phase liquid flow pressure drop plus the vapor flowing with the same liquid velocity ($\Delta P_{tp,lo}$). Besides, based on the LHP experimental data, the pressure drop along the proposed LHP was calculated by the thermodynamic table ($\Delta P_{tp,sat}$), considering the total pressure drop determined by the temperature difference between the evaporator and condenser.

Table 4 shows that most of the pressure drop along the LHP comes from the wick structure (ΔP_w), which is close to the capillary limit (ΔP_{cap}), showing a possible failure of the LHP at 7 W ($\Delta P_w > \Delta P_{cap}$). Considering the two-phase pressure drops, $\Delta P_{tp,vo}$ and $\Delta P_{tp,MH}$ showed the largest values, predicting an earlier failure, at 3 W and 4 W. In the present work, where the liquid pressure drop was considered ($\Delta P_{tp,lo}$), lower values were obtained, showing a possible failure of the LHP at 7 W. Using the average vapor quality ($\Delta P_{tp,MHavg}$), the same prediction of failing at 7 W was obtained. In fact, at this heat load, the LHP showed the onset of operation failure in the experimental results.

Using the thermodynamic table with the actual experimental data ($\Delta P_{tp,sat}$), the data showed that the device started failing at 6 W. Considering average uncertainties of ΔP_{cap} and ΔP_{sat}, around ± 670 Pa and ± 700 Pa, respectively, it is observed that taking the pressure related to the saturation temperature provides good pressure drops prediction, remaining within the uncertainties ranges, showing satisfactory results, without the need for pressure sensors, that would interfere in the thermal performance of the LHP.

These preliminary results must be validated with more experimental data. However, this new approach, never seen in the literature, already showed satisfactory results.

Table 4. Pressure drop results of the proposed LHP. All pressure drops in Pa.

q [W]	$\dot{m}$ [kg/s]	ΔP_{cap}	ΔP_w	ΔP_d	$\Delta P_{tp,vo}$	$\Delta P_{tp,MHavg}$	$\Delta P_{tp,MH}$	$\Delta P_{tp,lo}$	$\Delta P_{tp,sat}$
0.5	1.7E-07	6838	1186	-1.55	2629	1365	1968	1187	177
1	3.5E-07	6760	2086	-4.90	4386	2370	3398	2087	512
2	7.0E-07	6623	3426	-12.71	6456	3795	5188	3423	1269
3	1.0E-06	6487	4350	-18.46	7335	4709	6027	4345	2041
4	1.4E-06	6357	5048	-22.30	7794	5373	6615	5040	3153
5	1.8E-06	6223	5604	-24.87	8087	5895	7043	5595.	5161
6	2.2E-06	6086	6040	-26.73	8288	6300	7463	6031	8680
7	2.6E-06	5963	6456	-28.81	8548	6695	7805	6447	13457

7. Conclusions

In the present study, an experimental workbench was developed to measure the pressure drop of two-phase flows under condensation, with low mass flow rates (lower than $6 \cdot 10^{-5}$ kg/s). A copper tube of 1.01 mm was used to investigate the pressure drop, while a transparent tube (PVC material) of 0.446 mm was used to visualize the flow. The mains conclusions are:

- The single-phase friction factor proposed by Blasius expression showed results with good accuracy, with an average difference between the theoretical results and data within 0.07% to 10.15%
- The visualization flow showed that liquid slugs that fills the cross-section of the capillary tube slows down the working fluid, playing a major role in the friction pressure drop.
- This work demonstrated that the use of thermodynamic tables to obtain the pressure of two-phase flows in saturated conditions is an excellent option for evaluating the pressure drop in thin heat pipes. This is, actually, a novel approach never seen in the literature. An average difference between the data of 15% was obtained.
- Evaluating the pressure drop of an LHP, the approach of using the liquid only pressure drop as the total two-phase pressure drop showed be the best option compared to available correlations in the literature.

8. ACKNOWLEDGEMENTS

Acknowledgments are provided to the National Council for Scientific and Technological Development (CNPq) for the project fundings 405784/2022-8 and 441678/2023-8. The authors acknowledge the Foundation for Research Support of Santa Catarina (FAPESC) for the scholarship under grant number 3003/2021. This study was financed in part by the Coordenação de Aperfeiçoamento de Pessoal de Nível Superior - Brasil (CAPES) - Finance Code 001.

References

[1] V.P. Carey, Liquid-Vapor Phase-Change Phenomena: An Introduction to the Thermophysics of Vaporization and Condensation Processes in Heat Transfer Equipment, CRC Press, 2008.

[2] I.W. Sugita, A.K. Mainil, A. Miyara, General correlation of two-phase frictional pressure drop inside smooth tubes, Heat and Mass Transfer/Waerme- Und Stoffuebertragung, (2024).

[3] W. Qu, I. Mudawar, Measurement and prediction of pressure drop in two-phase micro-channel heat sinks, Int J Heat Mass Transf, 46 (2003) 2737–2753.

[4] K.G. Domiciano, L. Krambeck, J.P.F. Mera, M.B.H. Mantelli, Study of a new thin flat loop heat pipe for electronics, Heat and Mass Transfer/Waerme- Und Stoffuebertragung, (2023).

[5] T. Mizutani, N. Watanabe, S. Aso, K. Sadakata, S. Tanabe, H. Nagano, Experimental and analytical investigation of a 03-mm-thick loop heat pipe for 10 W-class heat dissipation, Int J Heat Mass Transf, 193 (2022) 122950.

[6] N.S. Ramasamy, P. Kumar, B. Wangaskar, S. Khandekar, Y.F. Maydanik, Miniature ammonia loop heat pipe for terrestrial applications: Experiments and modeling, International Journal of Thermal Sciences, 124 (2018) 263–278.

[7] J.P. Holman, Experimental methods for engineers, 8th ed., New York, USA, 2011.

[8] S.G. Kandlikar, S. Garimella, D. Li, S. Colin, M.R. King, HEAT TRANSFERAND FLUID FLOW IN MINICHANNELS AND MICROCHANNELS, Pergamon, 2006.

[9] P.A. Kew, Cornwell. K., Correlations for the prediction of boiling heat transfer in small-diameter channels, Appl Therm Eng, (1997) 705–715.

[10] S.M. Kim, I. Mudawar, Universal approach to predicting two-phase frictional pressure drop for adiabatic and condensing mini/micro-channel flows, Int J Heat Mass Transf, 55 (2012) 3246–3261.

[11] D. Chisholm, A theoretical basis for the Lockhart-Martinelli correlation for two-phase flow, Int J Heat Mass Transf, 10 (1967) 1767–1778.

[12] R.W. Lockhart, R.C. Martinelli, Proposed correlation of data for isothermal two-phase, two-component flow in pipes, Chemical Engineering Process, Vol. 45 (1949).

[13] K. Mishima, T. Hibiki, SOME CHARACTERISTICS OF AIR-WATER TWO-PHASE FLOW IN SMALL DIAMETER VERTICAL TUBES, 1996.

[14] K.G. Domiciano, L. Krambeck, J.P.M. Floréz, M.B.H. Mantelli, Thin diffusion bonded flat loop heat pipes for electronics : Fabrication , modelling and testing, Energy Convers Manag, 255 (2022).

[15] J.P.M. Florez, M.B.H. Mantelli, G.G.V. Nuernberg, F.H. Milanez, Powder Geometry based models for sintered media porosity and effective thermal conductivity, J Thermophys Heat Trans, 28 (2014) 507–517.

[16] J.P. Flórez Mera, M.E. Chiamulera, M.B.H. Mantelli, Permeability model of sintered porous media: analysis and experiments, Heat and Mass Transfer/Waerme- Und Stoffuebertragung, 53 (2017) 3277–3285.

[17] J.P.F. Mera, Heat and Mass Transfer Analysis of a Copper Loop, Universidade Federal de Santa Catarina, 2016.

Paper ID 106(S3)

Antiparallel Flat Plate Pulsating Heat Pipe for the Cooling of Electronic Enclosures

Davis T Vempeny[1], Laxman Kumar Malla[2], Hemanth Dileep[1], Pankaj Srivastava[3], Pallab Sinha Mahapatra[1], and Arvind Pattamatta[1*]

[1] *Indian Institute of Technology Madras, Chennai, India*
[2]*Sri Sivasubramaniya Nadar College of Engineering, Chennai, India*
[3]*Instruments Research & Development Establishment, Dehradun, India*
**Corresponding author's email address: arvindp@iitm.ac.in*

Abstract

A flat plate pulsating heat pipe (FPPHP) is a passive cooling device suitable for heat transfer from flat heat sources. Due to space constraints and design restrictions, placing the condenser section of the FPPHP on the same side of the heat source is not feasible, and research has to be done for the condenser section on the opposite side of the heat source. Moreover, the effect of ambient temperature plays a significant role in the device's thermal performance, and many electronic components operate in the temperature range of subzero temperatures in higher altitudes or polar regions to higher ambient temperatures in deserts. The present study reports an antiparallel arrangement of the FPPHP with the evaporator and condenser on the opposite side, and investigations have been performed in an environmental chamber where the ambient temperature is varied from -20 ºC to 50 ºC. The effect of two FPPHP operating simultaneously attached to an electronic housing has also been reported. Using the present design of the FPPHP, the temperature of the heat source has been maintained below 100 ºC for its safe operation at all ambient conditions and high heat inputs. Further, the effect of wettability modification of aluminum FPPHP surface and the impact of material thermal conductivity is discussed by comparing the results of aluminum FPPHP with a copper FPPHP.

Keywords: Thermal Management, Electronics Cooling, Flat Plate Pulsating Heat Pipe, Thermal Performance

1. Introduction

In the new era of thermal management with continuous miniaturization of electronic components, pulsating heat pipes (PHPs) have been gaining importance because of their advantages, such as simple construction, low cost, excellent thermal performance, flexibility in working fluids, and eco-friendliness [1]. In PHPs, a flat plate pulsating heat pipe (FPPHP) is better for the thermal management of electronics, having flat components with which it would have better contact. An FPPHP mainly consists of an evaporator, condenser, and an optional adiabatic section. A seminal review paper [2] has reported various parameters for improving the FPPHP performance by investigating different working fluids, filling ratios, geometry, materials, internal diameter, etc.

Malla et al. [3] reported the effect of the FPPHP material thermal conductivity testing a copper FPPHP and a steel FPPHP. Jang et al. [4] reported the impact of various asymmetrical channels on the thermal performance of FPPHP and measured thermal performance improvement with an increased pressure difference. Tseng et al. [5] observed that the alternating tube diameters facilitated the early initiation of pulsating motion within the PHPs, reducing thermal resistance. Most of the FPPHP designs studied in the literature have the heat source and the heat sink on the same side of the FPPHP. However, locating the heat source and heat sink on different sides may be necessary due to specific design requirements and space constraints. Winkler et al. [6] studied the performance of an FPPHP with a similar setup and reported an excellent heat spreading capacity. Li et al. [7] proposed an aluminum FPPHP with a centrally placed heat source and an air-cooled heat sink placed on the entire surface of the other side. In both these studies, a single FPPHP was used, and the effect of ambient temperature on performance was not discussed.

In this study, a new antiparallel FPPHP design has been proposed. The FPPHP is called antiparallel because the heat source (evaporator) and the condenser section are on opposite sides of the FPPHP. Two FPPHPs attached to the two opposite faces of a housing mimicking the electronic housing are investigated for thermal performance. The effect of ambient temperatures and the impact of the surface wettability modification and thermal conductivity on the thermal performance is also delineated.

2. Experimental Methodology

Figure 1 shows the exploded view of the FPPHP. Here, the copper heater block mimicking any heat source is the evaporator. It is 158 mm x 35 mm x 10 mm and is heated by placing three cartridge heaters inside it. The FPPHP condenser section is on the opposite face and air-cooled using two 24 V DC axial cooling fans on the cover plate's 40 x 11 pin fins. The

FPPHP plate is made of high-grade aluminum procured commercially, and the required dimensions of the channels are milled using CNC milling. The FPPHP outer dimensions are 182 mm x 100 mm, as shown in Figure 2. Here, the optional adiabatic section is avoided due to the size constraints. The cross-flow of the working fluid is avoided by two O-rings around the mini channels, thereby removing the high gasket resistance in conventional FPPHPs. The evaporator and condenser section heights are 35 and 46 mm, respectively. There are 20 mini-channels interconnected through 10 U-turns, as shown in Figure 2, and each channel's dimensions are 2 x 2 mm^2. The FPPHP's channel hydraulic diameter is 2mm, which satisfies the Bond number (Bo) criterion [8].

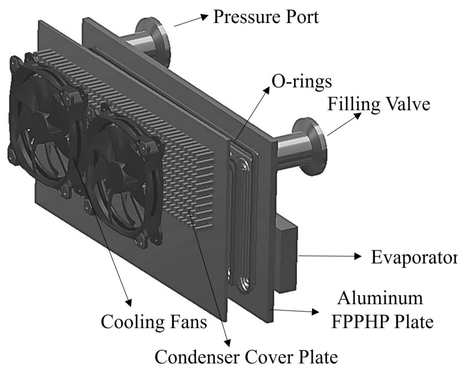

Figure 1. Exploded view of the FPPHP components

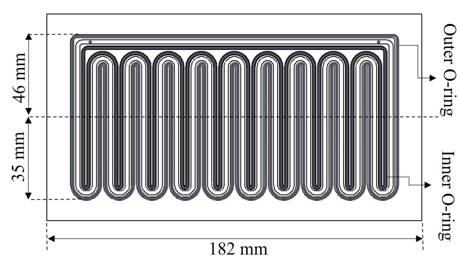

Figure 2. Schematic of the aluminum FPPHP

Figure 3 shows the schematic of typical FPPHP connections during the experiments. The pressure inside the FPPHP is monitored using a pressure transducer attached to the pressure port (Figure 1). The temperature measurements are made through four K-type thermocouples, each connected to the evaporator and condenser section through the thermal adhesive and, in turn, connected to the data logger for recording the measurements. Before starting each experiment, the FPPHP module is completely evacuated using a vacuum pump and vacuuming valve. The working fluid is filled through a micrometer syringe and micro-metering valve arrangement shown in Figure 3. The three vacuuming, micro-metering, and isolation valves are used for filling and vacuuming, as explained in detail in Ref. [9]. The three cartridge heaters in the evaporator blocks are connected to a DC power supply for heat inputs.

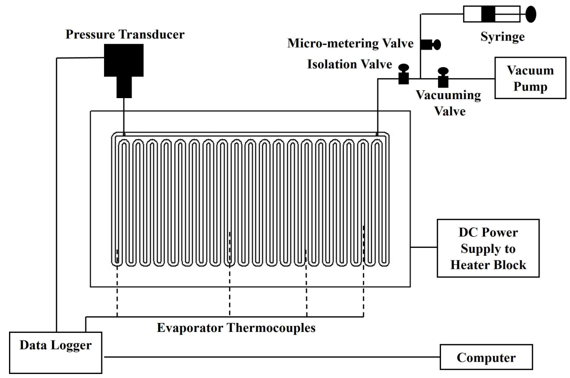

Figure 3. Schematic of the experimental setup

The thermal performance of the FPPHP is investigated at subzero ambient temperatures of -20 ºC to 0 ºC, and Figure 4 shows the actual image of the experimental setup placed inside an environmental chamber. Then, the thermal performance of two aluminum FPPHPs attached to the opposite faces of an electronic housing is studied, as shown in Figure 5. The schematic of the enclosure with two FPPHP is shown in Figure 5 (a), and the actual experimental setup photograph is shown in Figure 5 (b). The enclosure with two FPPHP is also investigated for the effect of ambient temperatures, and the experiments are performed at higher ambient temperatures of 25 ºC to 50 ºC.

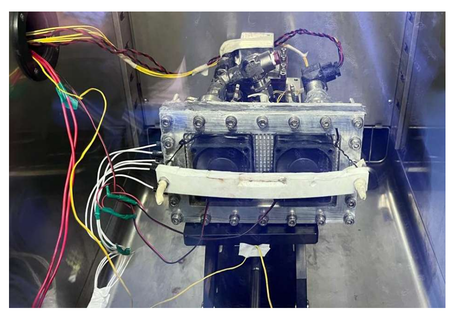

Figure 4. Actual experimental setup inside an environmental chamber for studies at subzero ambient temperatures

The effect of wettability is also studied for the FPPHP. The wettability-modified surface is prepared according to Ref. [10]. The aluminum FPPHP surface is subjected to chemical etching using aqueous HCl solution. Initially, the FPPHP channels are cleaned using deionized (DI) water and sonicated in an ultra-sonicator using a solution of DI water-ethanol-acetone mixture for 10 minutes. Then, the FPPHP is dipped in a 3 M HCl solution for 30 minutes for oxidation. Further, it is washed with DI water and dried in a hot oven for 30 mins. The wettability modification obtained on the aluminum surface made the surface superhydrophilic. Then, the superhydrophilic aluminum FPPHP (SHPL) is tested for thermal performance and compared with the FPPHP without any wettability modification (bare). Further, the effect of material thermal conductivity is discussed by comparing the results of aluminum FPPHP with copper FPPHP. The copper FPPHP is made superhydrophilic by following the exact cleaning procedure and dipping it in a 2 M H_2SO_4 solution.

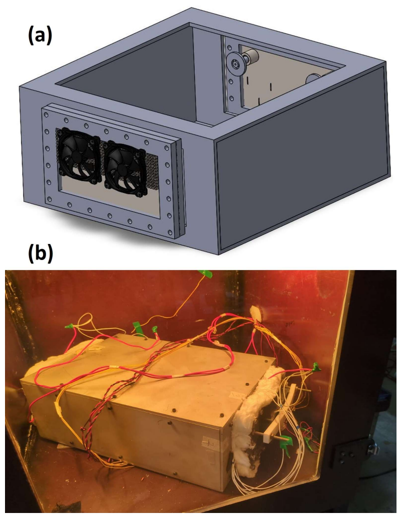

Figure 5. (a) 3-D schematic representation of an electronic enclosure thermally managed by two FPPHPs. (b) Actual experimental setup for studies at higher ambient temperatures with two FPPHPs.

In all the experiments, the working fluid used is ethanol and water mixture in the ratio of 3:1, and the filling ratio is kept at 80%. Before starting the experiments, the FPPHP is put on a leakage test following the procedure mentioned in our previous work, see Ref. [3]. The FPPHP is vacuumed for nearly 12 hours, and once the pressure inside reaches below 10^{-4} bar, the isolation and vacuum valves are sealed shut for the experiments. The isolation valve is closed after the FPPHP's inside pressure becomes steady and the DC power supply is turned on. The heat input (Q_{in}) is varied from 20 W to 60 W with an increment of 10 W. After the pressure and temperatures reach a steady state for a particular heat input, the readings are recorded for 5 minutes at a frequency of 1 Hz. The overall thermal resistance is calculated using the average evaporator temperature (T_{evp}) and the ambient temperature (T_{amb}) as follows,

$$R_{ov} = \frac{T_{evp} - T_{amb}}{Q_{in}} \quad (1)$$

3. Results and Discussions

This section presents the investigation results on the thermal performance of the antiparallel aluminum flat plate pulsating heat pipe (FPPHP) tested for the effect of ambient temperatures, the impact of two FPPHP operating simultaneously attached to an electronic housing, and the effect of wettability modifications on the FPPHP material surface.

3.1 Effect of subzero ambient temperature

Figure 6 (a-c) shows the variation in thermal resistance and evaporator temperatures at the subzero ambient temperatures of -20 ºC, -10 ºC, and 0 ºC. The left y-axis plots the evaporator temperature, and the right y-axis plots the thermal resistance.

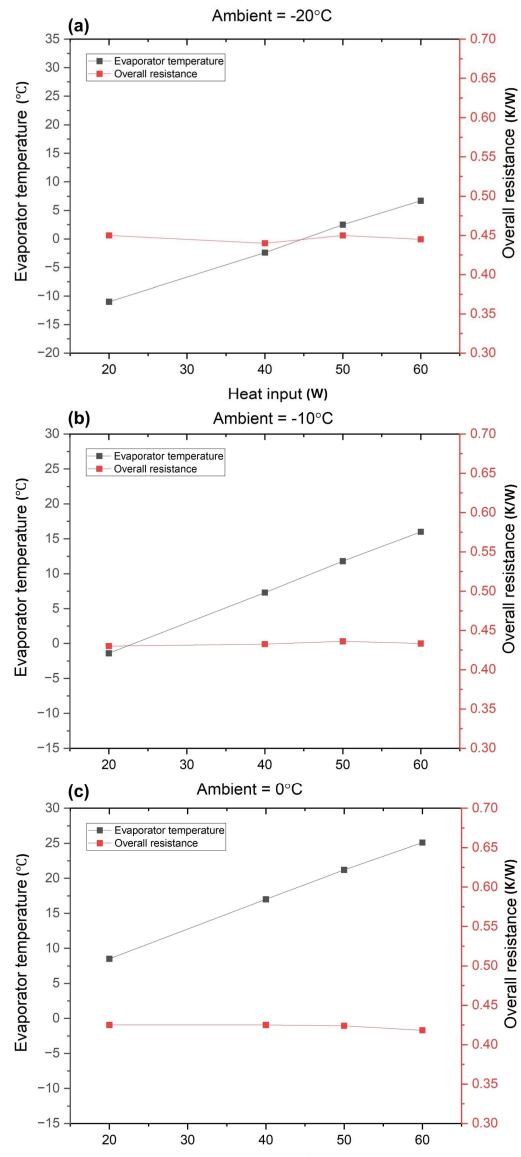

Figure 6. Thermal performance of the FPPHP at subzero ambient temperatures of -20 ºC, -10 ºC, and 0 ºC.

At T_{amb} = -20 ºC (Figure 6 (a)), with the increase in the heat input from 20 W to 60W, T_{evp} increases from -12 ºC to 6 ºC, and the thermal resistance remains constant around 0.45 K/W. At T_{amb} = -10 ºC, T_{evp} increases from -1 ºC to 15 ºC, and the thermal resistance remains constant at around 0.43 K/W. Similarly, at T_{amb} = 0 ºC, T_{evp} increases from 8 ºC to 26 ºC, and the thermal resistance remains constant at around 0.43 K/W. As the heat input increases, the evaporator temperature rises due to more heat available. The thermal resistance remains constant at subzero ambient temperatures as the water content in the working fluid may have frozen, and the oscillations of the working fluid in the form of liquid slugs and vapor plugs may have stopped. The mode of heat transfer from the evaporator to the condenser is only through heat spreading through the FPPHP plate. With further increase in the heat input beyond 60W, the device will perform better and will be able to keep the heat source within safe limits.

3.2 Effect of two FPPHPs attached to housing

This section reports the thermal performance (Figure 7) of two FPPHP attached to the opposite faces of an electronic housing (Figure 5).

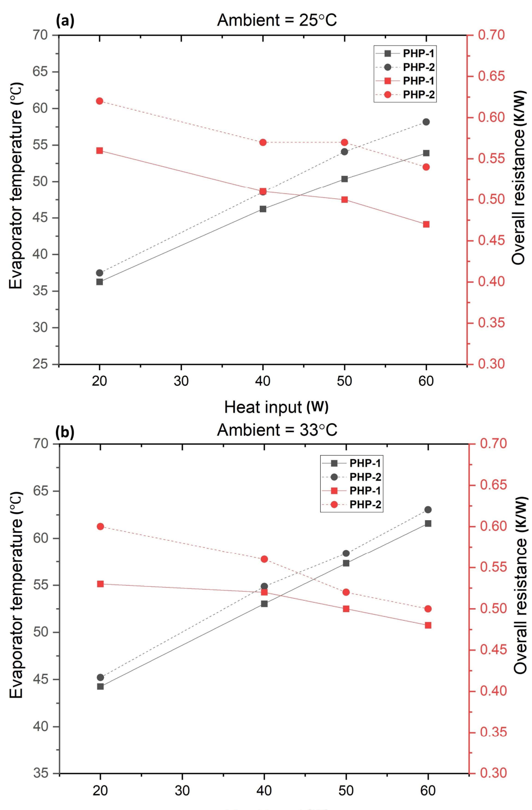

Figure 7. Thermal performance of the two FPPHP attached to the electronic housing and at ambient temperatures of 25 ºC and 33 ºC.

Figure 7 shows the variation of thermal performance parameters with heat inputs for both the FPPHPs at T_{amb} = 25 ºC and 33 ºC. At T_{amb} = 25 ºC, overall resistance decreases with heat inputs for both the FPPHPs. For PHP-1, the resistance decreases from 0.60 to 0.54 K/W as heat input increases from 20 to 60W. The corresponding resistance for PHP-2 is 0.55 to 0.47 K/W. The evaporator temperature rises from 37 ºC to around 55 ºC. Similar trends in the variation of overall resistance and evaporator temperatures with near similar values are observed at T_{amb} = 33 ºC. PHP-2 shows better thermal performance than PHP-1 due to the location proximity of PHP-1 to the environmental chamber wall. PHP-2 condenser was getting comparatively more open space in front to dissipate heat. The overall resistance decreases with heat inputs owing to better pulsation of the liquid slugs and vapor plugs with heat inputs [9].

3.3 Effect of surface wettability modifications

In this section, we present the variation of the thermal performance parameters (Figure 8) with heat inputs at the ambient temperatures of 40 ºC and 50 ºC and for the FPPHP surface to be bare/untreated and superhydrophilic (SHPL).

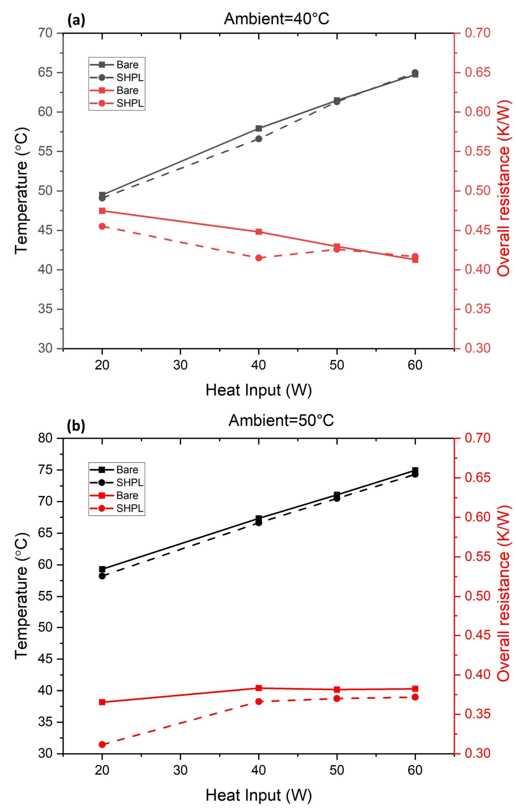

Figure 8. Average thermal performance of the two FPPHPs attached to the enclosure at ambient temperatures of 40 ºC and 50 ºC with surface wettability modifications.

Figure 8 (a-b) shows the evaporator temperature and overall resistance variation with heat input at T_{amb} = 40 ºC and 50 ºC. The superhydrophilic treatment on the FPPHP channel surfaces increases the thermal performance due to the initiation of thin film evaporation [11]. At T_{amb} = 40 ºC and for the bare case, the overall resistance decreases from 0.47 to 0.4 K/W with increased heat input. With superhydrophilic treatment, the maximum decrease in the resistance is 5% at 20W. At T_{amb} = 50 ºC and bare case, the overall resistance remains constant at around 0.37 K/W. With the SHPL treatment, the resistance decreases by a maximum of 20% from the bare case at 20W, and with the increase in heat input, the difference in the overall resistance diminishes. The evaporator temperatures are almost the same for the bare and SHPL cases at T_{amb} = 40 and 50 ºC. At higher heat inputs, the variation of thermal performance between the bare and SHPL cases diminishes, as with heat, there is a thermal degradation of the superhydrophilic coating.

Figure 9 shows the consolidated evaporator temperature and thermal resistance of the PHP-2 at different ambient temperatures at a heat input of 50 KW. The evaporator temperature variations show that the present FPPHP device can keep the heat source at operating temperature limits even at extreme ambient conditions. The overall resistance remains between 0.4 K/W to 0.5 K/W at all ambient conditions.

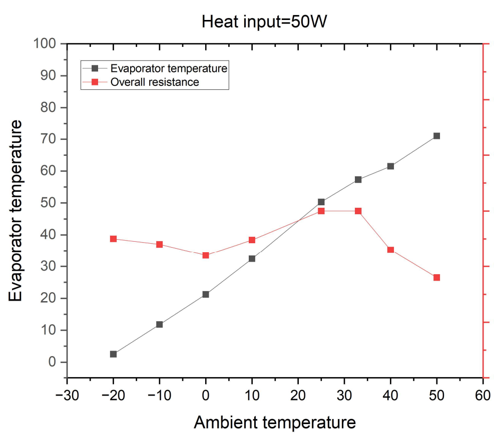

Figure 9. Thermal performance of the bare FPPHP at different ambient temperatures at the heat input of 50W

3.4 Effect of material thermal conductivity

Next, the effect of FPPHP material thermal conductivity has been investigated on the thermal performance of FPPHP. Figure 10 shows the overall thermal performance of the aluminum and copper material FPPHP. The copper FPPHP has the exact dimensions as that of the aluminum FPPHP. The wettability condition for the FPPHP's surface is superhydrophilic. The wettability modification techniques to make the FPPHP surface superhydrophilic have been discussed earlier in section 2. The overall resistance is lower in the aluminum FPPHP than the copper FPPHP at all heat inputs. The overall thermal resistance is decreased by 15 % at 100 W for the aluminum FPPHP. This trend in the graph indicates that the aluminum FPPHP has better thermal performance due to the comparatively lower thermal conductivity than the high conductive copper material FPPHP. The heat spreading through the material will be less in the low thermal conductive FPPHP material. Thus, significant heat transfers through the liquid slug-vapor plug oscillations of the working fluid. This high pulsation of the working fluid leads to a decreased fluid thermal resistance [3].

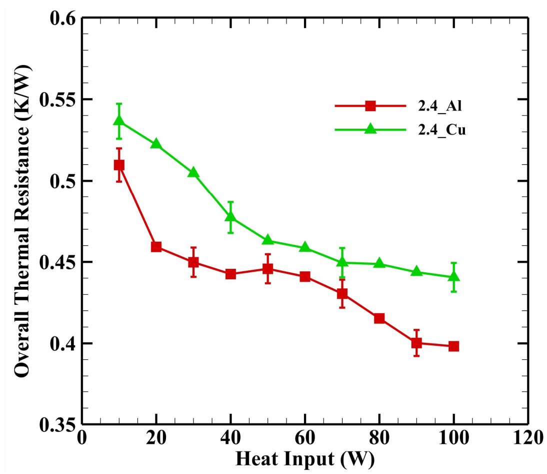

Figure 10. Measured overall thermal resistance for aluminum and copper material FPPHP

4. Conclusions

The present work investigates an antiparallel arrangement of the FPPHP with the evaporator and condenser on the opposite side. The condenser cover plate is air-cooled with multiple pin fins on it. The FPPHP is made of aluminum with 20 mini channels, and the working fluid is an ethanol-water mixture of 3:1 filled at 80%. The experimental investigations are performed in an environmental chamber where the ambient temperature varies from -20 ºC to 50 ºC. The effect of two FPPHP operating simultaneously attached to an electronic housing and the impact of FPPHP surface wettability modifications on the thermal performance is reported at higher ambient temperatures. Using the present design of the FPPHP, the temperature of the heat source has been maintained below 100 ºC for its safe operation at extreme ambient conditions and high heat inputs. The thermal resistance decreases with heat inputs at high ambient temperatures and remains nearly constant at subzero ambient conditions. The superhydrophilic treatment on the FPPHP increases the thermal performance at low heat inputs. However, thermal degradation of the surface treatment occurs at high heat inputs, leading to no increase in thermal performance. The overall thermal performance is better for aluminum FPPHP than copper FPPHP. Moreover, aluminum is lighter in weight and will be more suitable for commercial FPPHP production.

Acknowledgment

The authors express profound gratitude for the financial grant (SP/2021/0532/ME/DRDO/008440) from the Research and Innovation Center - DRDO, IIT Madras Research Park.

References

[1] D. Bastakoti, H. Zhang, D. Li, W. Cai, F. Li, An overview on the developing trend of pulsating heat pipe and its performance, *Appl. Therm. Eng.* 141 (2018) 305–332. doi:10.1016/j.applthermaleng.2018.05.121.

[2] V. Ayel, M. Slobodeniuk, R. Bertossi, C. Romestant, Y. Bertin, Flat plate pulsating heat pipes: A review on the thermohydraulic principles, thermal performances and open issues, *Appl. Therm. Eng.* 197 (2021). doi:10.1016/j.applthermaleng.2021.117200.

[3] L.K. Malla, D.T. Vempeny, H. Dileep, P. Dhanalakota, P. Sinha Mahapatra, P. Srivastava, A. Pattamatta, Thermal performance comparison of flat plate pulsating heat pipes of different material thermal conductivity using ethanol-water mixtures, *Appl. Therm. Eng.* 236 (2024) 121475. doi:10.1016/j.applthermaleng.2023.121475.

[4] D.S. Jang, J.S. Lee, J.H. Ahn, D. Kim, Y. Kim, Flow patterns and heat transfer characteristics of flat plate pulsating heat pipes with various asymmetric and aspect ratios of the channels, *Appl. Therm. Eng.* 114 (2017) 211–220. doi:10.1016/j.applthermaleng.2016.11.189.

[5] C.Y. Tseng, K.S. Yang, K.H. Chien, M.S. Jeng, C.C. Wang, Investigation of the performance of pulsating heat pipe subject to uniform/alternating tube diameters, *Exp. Therm. Fluid Sci.* 54 (2014) 85–92. doi:10.1016/j.expthermflusci.2014.01.019.

[6] M. Winkler, D. Rapp, A. Mahlke, F. Zunftmeister, M. Vergez, E. Wischerhoff, J. Clade, K. Bartholomé, O. Schäfer-Welsen, Small-Sized Pulsating Heat Pipes/Oscillating Heat Pipes with Low Thermal Resistance and High Heat Transport Capability, *Energies*. 13 (2020) 1736. doi:10.3390/en13071736.

[7] C. Li, J. Li, Thermal characteristics of a flat plate pulsating heat pipe module for onsite cooling of high power server CPUs, *Therm. Sci. Eng. Prog.* 37 (2023) 101542. doi:https://doi.org/10.1016/j.tsep.2022.101542.

[8] M. Marengo, V.S. Nikolayev, Pulsating Heat Pipes: Experimental Analysis, Design and Applications, (2018) 1–62. doi:10.1142/9789813234406_0001.

[9] L.K. Malla, P. Dhanalakota, P.S. Mahapatra, A. Pattamatta, Thermal and flow characteristics in a flat plate pulsating heat pipe with ethanol-water mixtures: From slug-plug to droplet oscillations, *Int. J. Heat Mass Transf.* 194 (2022) 123066. doi:10.1016/j.ijheatmasstransfer.2022.123066.

[10] T.M. Thomas, P. Sinha Mahapatra, Fabrication of hierarchically textured aluminum-based superhydrophobic surfaces for anti-frosting application, *Mater. Today Proc.* 56 (2022) 1267–1273. doi:https://doi.org/10.1016/j.matpr.2021.11.211.

[11] L.K. Malla, P. Dhanalakota, H. Dileep, P.S. Mahapatra, A. Pattamatta, Surface wettability modifications and applications in wickless heat pipes, *Surfaces and Interfaces*. 45 (2024). doi:10.1016/j.surfin.2023.103837.

Paper ID 108

Pseudo steady state temperature predictions for a bottom heated pulsating heat pipe utilizing a correlation based tool

K. Nandakumar Chandran[1], Kailash Choudhary[2], Jason Chetwynd-Chatwin[3], June Kee Min[1] and Man Yeong Ha[1*]

[1] *School of Mechanical Engineering, Pusan National University, 2, Busandaehak-ro 63beon-gil, Geumjeong-gu, Busan, 46241, Republic of Korea*
[2] *Rolls-Royce and Pusan National University Technology Centre in Thermal Management, Busan, Republic of Korea*
[3] *Rolls-Royce Plc, Whittle House, P.O. Box 3 , Filton, BS34 7QE, United Kingdom*
**Corresponding author email address: myha@pusan.ac.kr*

Abstract

This work presents the development and validation of a rapid prediction tool for the pseudo steady-state (PSS) temperature of bottom-heated pulsating heat pipes (PHPs). Based on known mass flow rates and intake circumstances, the tool uses lumped parameter modeling to balance heat flows across the coolant, condenser, evaporator, and fluid flow sides of the PHP in order to estimate pseudo steady-state temperatures. The solution algorithm, Kutateladze correlations for PHPs, and details of the iterative heat balance technique are given. The adopted correlation has a considerable impact on the accuracy of anticipated pseudo steady-state temperatures and thermal resistances, as demonstrated by validation against previously published results. For the cases examined, the tool's predictions showed a maximum deviation of 22.37%, demonstrating its potential for quick, cost-effective predictions.

Keywords: Pulsating heat pipe; Pseudo steady state operation; Iterative Heat balance method; Effective thermal resistance; Kutateladze number

1. Introduction

Passive heat transfer is critical in thermal engineering, especially with the increasing need for efficient cooling in miniaturized electronic components. Heat pipes are highly effective as passive heat transfer devices and among its classifications Pulsating heat pipes (PHPs) have become widely popular due to their simple manufacturing process, orientation independence, and effectiveness under variable operating conditions [1,2]. A PHP consists of narrow channels partially filled with a working fluid. When heat is applied to the evaporator section, the fluid forms alternating liquid slugs and vapor bubbles, called a slug-bubble train. Due to the small channel size, surface tension dominates, and capillary action forms these distinct slugs and bubbles. As heat is supplied, the fluid absorbs energy, causing evaporation and forming vapor bubbles. These bubbles create pressure fluctuations, driving the slug-bubble train to move vapor to the condenser and liquid back to the evaporator. This oscillatory motion enables efficient heat transfer through phase change and two-phase flow dynamics [3]. While the precise mechanisms of PHPs remain unclear, prototypes are being applied in sectors like space, chemical, and machine tool cooling [4-6].

To understand the complex physics of PHP operation, various experimental and numerical studies [7-9] have been conducted. Efforts to model PHP behavior range from 1D to 3D simulations, with 1D models requiring a deep understanding of complex fluid dynamics, including the behavior of fluid films and bubble coalescence [10-12]. To minimize the costs and computational time associated with experimental setups, lumped parameter modeling of PHPs was developed and validated. While this approach reduces conventional computational times, it still requires ten times the actual physical time for processing. Currently, it remains a preferred method for understanding PHP transient characteristics, yet for most preliminary design stages, investigating steady-state conditions is more suitable. Indeed, in the case of PHP operations, a Pseudo steady state (PSS) condition prevails [13,14], where the system appears to reach a thermal equilibrium in terms of average heat transfer rates and temperature distributions, but the internal fluid motion and oscillations are still present. Unlike true steady state, where all dynamic fluctuations cease, PSS in a PHP allows for continuous fluid motion and oscillations between phases (liquid and vapor), while the macroscopic or time-averaged quantities like heat input/output and temperature remain relatively constant over time. During PSS, the PHP achieves stable heat transfer performance despite ongoing fluid oscillations driven by intermittent boiling, condensation, and capillary forces.

A tool that focusses on the pseudo steady state thermal characteristics could simplify and be a candidate for quick predictions serving as a resource for decision making. Thus, this study aims to develop a rapid prediction tool for the pseudo steady state temperature (averaged periodically fluctuating temperature) of bottom-heated PHPs, by coupling the principles of heat balance and apt correlation choice which determines the tool accuracy. The primary research objectives of the present work are:

1) To develop a heat balance coupled correlation-based tool for predicting the PSS temperatures in a bottom heated PHP.
2) To validate the tool for one-loop and multi-loop PHP geometrical and working fluid conditions.

The article covers: Sec.2 - methodology (heat balance, correlations, algorithm); Sec.3 - validation with experimental results and tool limitations; Sec.4 - conclusion.

2. Methodology

To develop a bottom heated PHP heat exchanger temperature prediction tool, the authors analyzed heat balances on the coolant, condenser, evaporator, and heat transfer fluid flow sides of the PHP. The tool's current predictive capability relies on known types and mass flow rates , $\dot{m}_h$ and $\dot{m}_c$, of the heat transfer fluids (HTF), coolant inlet temperature (T_{ci}), and steady-state heat transfer value (Q) as inputs. Also the geometrical features of the PHP are prerequisites provided by the user to the tool. The following assumptions were used during the development of tool:

- Both the hot side and cold side heat transfer fluids are single phase.
- PHP is operating at a Pseudo Steady State condition.
- The surface temperature of PHP at condenser and evaporator sides are taken to be the same for PHP working fluids at respective sections.

To grasp the operational logic of tool temperature predictions, refer to Figure 1, which depicts the schematic of a typical two-loop, bottom-heated PHP Heat exchanger.

A counter flow PHP heat exchanger having alternating evaporator and condenser sections, where heat is transferred from a hot fluid to a cold fluid is considered. At the top, the condenser section (blue in colour), where, the cold fluid enters at a temperature,T_{ci} and exits at T_{co}. Whereas, at the bottom hot fluid enters the evaporator section, (red in colour), where the fluid temperature at the inlet is denoted as T_{hi} and the outlet temperature is T_{ho}. The PHP placed in between these two HTFs having effective evaporator section length, L_e, condenser section length, L_e, and adiabatic section length L_a, indicating the geometrical configuration of the PHP. The temperatures T_e^{php} and T_c^{php} represent the temperatures of the PHP outer walls at the evaporator and condenser sections, respectively, which are influenced by the working fluid's heat transfer and oscillatory flow within the pipe.

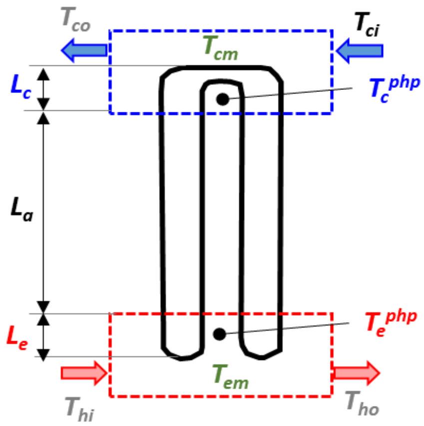

Figure 1. Schematic diagram illustrating a PHP and temperatures used in present study.

With this preliminary understanding of a PHP heat exchanger, in the coming sections the details of heat balance formulations used and algorithm used in current tool development will be discussed.

2.1 Heat Balance Formulations

For a pulsating heat pipe heat exchanger transferring heat from a hot medium to a cold medium operating at a pseudo-steady state temperature the following heat balance must be satisfied at steady state; i.e. the heat entering from the hot fluid equals the heat convected into the PHP surface, transferred through the PHP, convected out, and exiting via the cold fluid. The following steps describe the Heat balance iterative numerical approach employed in construction of the tool.

1) The heat balance at the condenser side is used to determine the coolant's outlet temperature, based on the equation $Q = \dot{m}C_p(T_{co} - T_{ci})$, where C_p represents the specific heat capacity of the coolant at the mean coolant temperature. The mean coolant temperature, T_{cm} is calculated as the average of the outlet and inlet temperatures, given by ($T_{cm} = (T_{co} + T_{ci})/2$). By applying this heat balance, the value of T_{cm} can be deduced via iterations having a minimizing error approach, allowing further calculations related to the heat transfer process within the system.
2) For a specific PHP dimension, the heat transfer coefficient h_c is calculated using the appropriate correlations. In here, the correlation for PHP

condenser side, h_c is evaluated from reference [1] corresponding to condenser side coolant Reynolds number and thermos-physical properties. Heat balance is done for convected lateral surface area of PHP condenser side. This allows for predicting the PSS condenser temperature T_c^{php} at PHP surface by balancing the convective heat transfer into the PHP with the input heat power. This step is crucial for ensuring that the predicted condenser temperature aligns with the actual heat input conditions of the system.

3) By determining T_c^{php} , the corresponding saturation pressure P_c can be calculated, which serves as an essential input for determining properties required to evaluate the individual terms of the Kutateladze number (Ku) correlations. In this study, the Kutateladze number definition is taken as:

$$Ku = \frac{\dot{q}}{h_{fg}\rho_v\{\sigma g(\rho_l - \rho_v)/(\rho_v)^2\}^{0.25}} \quad (1)$$

The appropriate Ku correlation, taken from reference [14] (this is a user choice- he/she could use another correlation), is applied and optimized to obtain the PSS evaporator temperature, T_e^{php}. This, in turn, allows for calculating the saturation pressure P_e which drives the error minimization loop for refinement of the model. Additionally, the secondary Kutateladze number Ku_2 is expressed as:

$$Ku_2 = f(\varphi)\left(\frac{d_i}{L_e}\right)^{l}\left(\frac{L_e}{L_{eff}}\right)^{m}\left(\frac{L_e}{L_c}\right)^{m} Pr^{n} Ja^{p} Bo^{q} Mo^{r} Ka^{s} N^{t} exp(\beta)^{u} \quad (2)$$

where the power and function values are obtained from the reference [14]. This formulation integrates various dimensionless parameters to further refine the predictive model.

4) The final step involves calculating the mean heat transfer fluid temperature, which is derived as the average of the inlet and outlet temperatures of the heat transfer fluid. The same methodology described in points 1 and 2 is followed for calculating this temperature, ensuring that the heat balance and fluid temperature are consistent with the overall energy transfer through the PHP system. The same approach is also applied for determining the mean outlet temperatures at each step, ensuring consistency across all stages of the analysis. to find mean heat transfer fluid temperature ($T_{em} = (T_{ho} + T_{hi})/2$) and the inlet/outlet temperatures similar steps as described in first and second step are utilized.

Throughout the iterative steps, updates of the PHP working fluid's and HTFs' thermo-physical properties, based on temperature and pressure, are computed based on the NIST REFPROP database linked to Matlab.

2.2 Solution Algorithm

The iterative algorithm used to obtain a solution for the PSS temperatures of a PHP is shown in Figure 2.

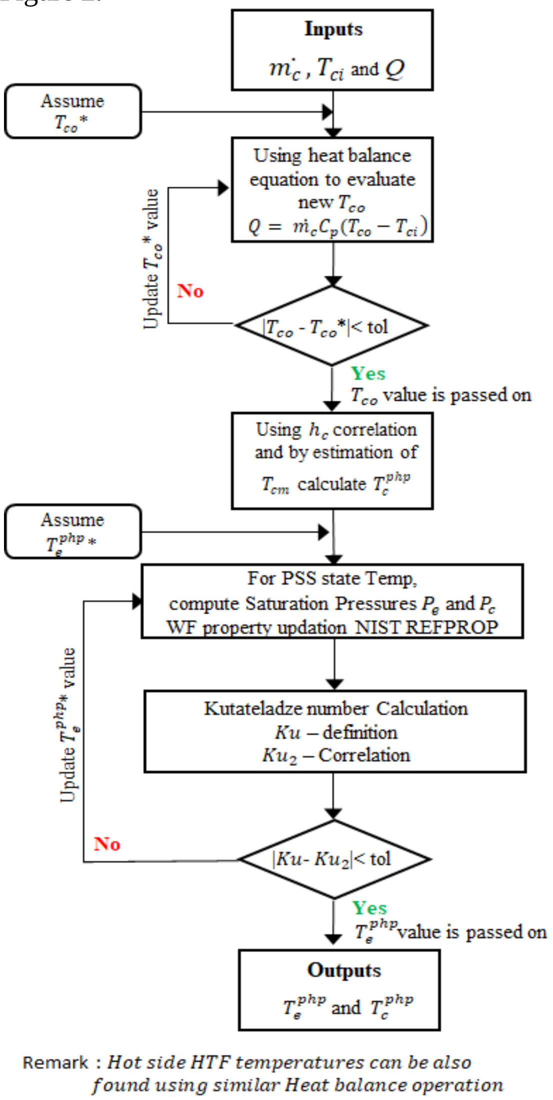

Figure 2. Flow chart of logic of operations used in the algorithm to determine PSS characteristics of PHP.

The "heat balance" algorithm presented above was found to be very stable and converged within a few iterations. The measurable speed of calculations was governed only by the time required for the orbit calculations. The methodology provides a rapid alternative for predicting steady-state temperatures, with accuracy depending on the chosen correlation, and its validation against experimental results is detailed below. It is to be noted that this methodology could also be formulated using known temperatures of cold or hot fluids heat transfer fluids.

3. Results and discussions

The methodology provides a rapid alternative for predicting steady-state temperatures, with accuracy depending on the chosen correlation, and its validation against experimental results is detailed below. Further for the knowledge of the reader the limitations and possible improvements in future to the current tool are also discussed under this section.

3.1 Validation of results

To validate the methodology and to assess the tool's performance, the authors tested it with varying conditions of bottom-heated PHP operation. Specifically, these validations could be considered a set for one-loop PHP and other for multi loop PHP. All of the depicted graphs with present results are plotted against experimental transient condition, for emphasizing that PSS condition's importance.

A) One –loop PHP

The simplest of PHP configuration is a single/one loop which had been investigated mostly to understand the physics of oscillatory and circulatory flow inside PHP during operation. Nevertheless, in the present study also PSS condition of PHPs are evaluated in a single loop configuration at first. Two experimental cases with details of construction and working detailed in Table.1; Set 1 : Khandekar et.al [7] and Set 2: Saha et.al [16] are studied and the results are discussed.

Table 1. Details of chosen PHP experiments for validation (one-loop PHP)

Details	Set I	Set II
Working Fluid	Ethanol	Water
Heat Input	14.8/32.1 (W)	86.62 W
Filling Ratio	60%	40%
Section Lengths (e-a-c)	45/100/45 mm	50/60/30 mm
OD of PHP	4 mm	6 mm
Coolant type	Water 20 ^{0}C	Water 25 ^{0}C
Coolant flowrate	11.33 g/s	14.2 g/s

Figure 3 presents a comparison of the evaporator temperature T_e^{php} and T_c^{php} between Set I experimental and predicted values for two different cases. In Case A for 14.8 W heat input, the experimental evaporator temperature at PSS is recorded as 74.80°C, while the predicted temperature is 83.21°C, resulting in a notable error of 13.3%.

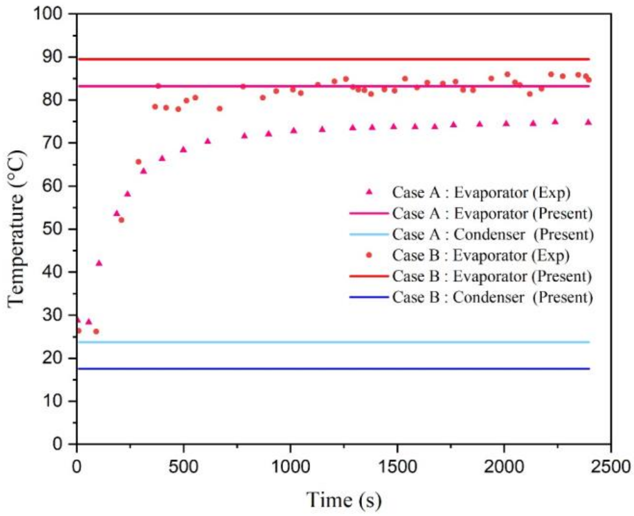

Figure 3. Evaporator and Condenser PSS temperatures against Khandekar et.al [7] Experiment. (Case A: 14.8 W and Case B: 32.1 W)

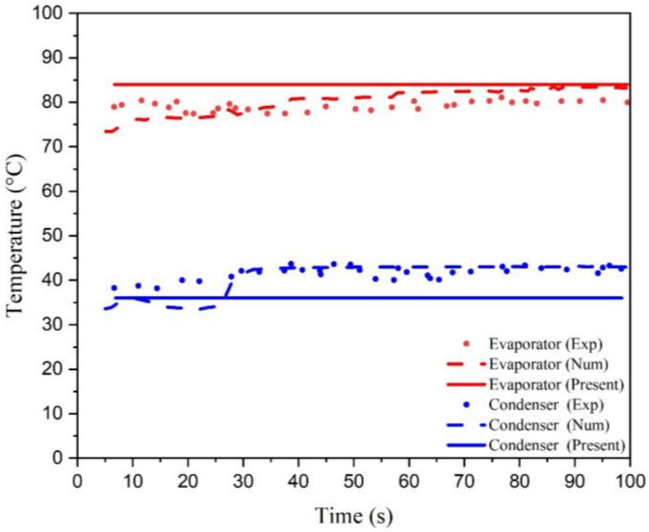

Figure 4. Evaporator and Condenser PSS temperatures for Saha's [16] Experiment. (Numerical results from Opalski et.al [15])

Whereas, in Case B for 32.1 W heat input, the experimental temperature is measured at 83.8°C, and the predicted value is 89.47°C, resulting in a smaller error of 8.89%, indicating improved alignment between the model and the experimental results for this case. An evaluation of thermal resistance (R_{th}) of PHP in the reported literature gives, for Case A, the experimental thermal resistance is recorded as 3.70 K/W, while the predicted value is 4.02 K/W, corresponding to an error of 8.7% and for Case B, the experimental value is 1.98 K/W, while the predicted value is 2.24 K/W, showing a slightly larger error of 11.6%.

Similarly, a comparison of the experimental results from Set II, as shown in Figure 4, reveals that the experimental evaporator temperature at PSS for 86.62 W heat input is recorded as 79.2°C, but the projected temperature is 84.2°C, indicating a considerable inaccuracy of 8.85%. According to an assessment of PHP's thermal resistance (R_{th}) in the published literature, the measured thermal resistance is 0.433 K/W, but the expected value is 0.55 K/W, or an 27.86% inaccuracy. The results of Set I and Set II validations show case the tools capability to predict the thermal characteristics at a reasonable level of accuracy

B) Multi- loop PHP

While single-loop validation tests provide reliable results for understanding the physics, multi-loop PHPs, with their increased number of turns, are more practical and commonly used in real-world applications. This calls on for test of current tool against a multi-loop PHP at varying operating conditions [17], refer to Table 2 for experimental details.

Table 2. Details of chosen PHP experiments for validation (multi-loop PHP)

Details	Set III
Working Fluid	Ethanol
Heat Input	33/44/55 W
Filling Ratio	62.5 %
Section Lengths (e-a-c)	547.8/780/740 mm
OD of PHP	1.9 mm
Coolant type	Water 20 ^{0}C
Coolant flow rate	8.6 g/s
No. of Loops	2 loops/ 3 meanderings

A comparison of the experimental results, as shown in Figure 5, reveals that the experimental evaporator temperature/predicted temperature at PSS is recorded as 66.4°C/ 74.32°C, 68.88°C/ 78.61°C, and 73.38°C/ 85.32°C, respectively, with errors of 17.1%, 19.90%, and 22.37% for heat inputs of 33 W, 44 W, and 55 W. For each of the three cases that were taken into consideration, the thermal resistance (R_{th}) of PHP computed values for 1.68 K/W, 1.32 K/W, and 1.1 K/W at errors of 30.16%, 25.42%, and 21.31%, respectively.

As, a remark, for the above error calculations of temperature prediction, normalization with corresponding coolant is carried out. These results showcase the tool's effectiveness and potential for predictive accuracy improvements, achieving rapid computations in mere seconds. These differences in thermal resistance and temperature predictions reflect the model's varying accuracy across different operational conditions, highlighting areas for further refinement and improvement in correlation use or calibration.

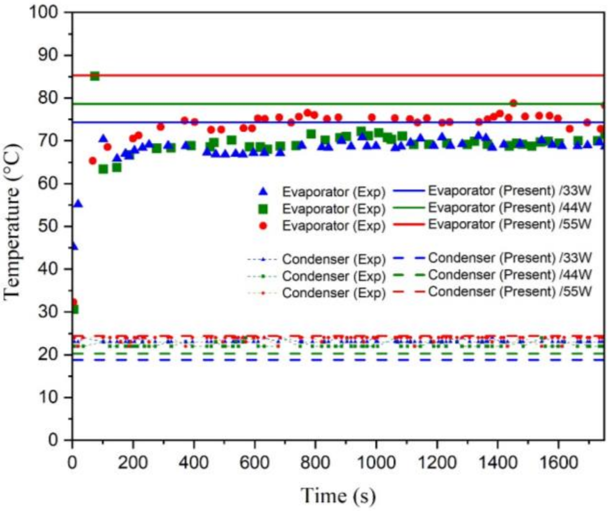

Figure 5. Evaporator and Condenser PSS temperatures against Opalski et.al [15] Experiment. (Varying input power: 33, 44 ,55 W)

3.2 Limitations and Future Improvements

The current methodology heavily relies on empirical correlations like the Kutateladze number and heat transfer coefficient, which depend on experimental conditions, making it difficult to generalize for different PHP designs without recalibration. The model is also limited to steady-state conditions, which may not predict transient behavior during startup or dynamic operation. This can reduce predictive accuracy in real-time or fluctuating heat transfer scenarios, limiting its application in systems with time-varying thermal loads. Furthermore, the model's accuracy decreases due to the lack of consideration for conductive resistance of the pipe material and additional convection at the working fluid-wall interface.

Future improvements could focus on integrating machine learning to adaptively update empirical correlations using real-time data, making the tool more robust for diverse PHP systems. Expanding the model to include multi-phase flow dynamics and non-uniform temperature distributions along the PHP would also enhance prediction accuracy, especially for complex fluids and systems with high temperature gradients.

4. Conclusions

A numerical correlation-based prediction model coupled with iterative heat balance technique was developed to accurately predict the pseudo-steady state thermal characteristics of a bottom heated pulsating heat pipe. The major findings of the study can be summarized as follows:

- A quick prediction model for preliminary design of pulsating heat pipe at various steady state operating conditions is developed
- A Six-step numerical algorithm is formulated and a prediction model based on MATLAB code was developed.
- The experimental validation of the developed tool and its methodology demonstrates that the results are closely aligned, suggesting it as a viable alternative for PHP design considerations.
- The developed prediction model has limitations in terms of selection of appropriate Kutateladze number correlation for estimating pseudo-steady state thermal characteristics (operating temperature and pressure) accurately.

The development of this tool and its methodology will significantly contribute to the efficient design of pulsating heat pipes (PHP) and expedite decision-making in a world where cost-efficiency is paramount. It has the potential to serve as a valuable alternative to coupled system analysis involving PHP components, particularly for evaluating steady-state performance.

References

[1] Faghri, A., 1995. Heat pipe science and technology. Taylor & Francis

[2] Nikolayev, V.S., 2021. Physical principles and state-of-the-art of modeling of the pulsating heat pipe: A review. Applied Thermal Engineering, 195, p.117111.

[3] Khandekar, S., Panigrahi, P.K., Lefèvre, F. and Bonjour, J., 2010. Local hydrodynamics of flow in a pulsating heat pipe: a review. Frontiers in Heat Pipes, 1(2), p.023003.

[4] Mangini, D., Mameli, M., Fioriti, D., Filippeschi, S., Araneo, L. and Marengo, M., 2017. Hybrid Pulsating Heat Pipe for space applications with non-uniform heating patterns: Ground and microgravity experiments. Applied Thermal Engineering, 126, pp.1029-1043.

[5] Ayel, V., Pietrasanta, L., Lalizel, G., Romestant, C., Bertin, Y. and Marengo, M., 2019. Thermo-hydraulic analysis of semi-transparent flat plate pulsating heat pipes tested in 1 g and microgravity conditions. Microgravity Science and Technology, 31, pp.403-415.

[6] Czajkowski, C., Nowak, A.I., Błasiak, P., Ochman, A. and Pietrowicz, S., 2020. Experimental study on a large scale pulsating heat pipe operating at high heat loads, different adiabatic lengths and various filling ratios of acetone, ethanol, and water. Applied Thermal Engineering, 165, p.114534.

[7] Khandekar, S. and Groll, M., 2004. An insight into thermo-hydrodynamic coupling in closed loop pulsating heat pipes. International Journal of Thermal Sciences, 43(1), pp.13-20.

[8] Charoensawan, P. and Rittidech, S., 2004. Closed and Open Looped Pulsating Heat Pipes. In 13th International heat pipe conference, Shanghai, China.

[9] Rouaze, G., Marcinichen, J.B., Cataldo, F., Aubin, P. and Thome, J.R., 2021. Simulation and experimental validation of pulsating heat pipes. Applied thermal engineering, 196, p.117271.

[10] Mameli, M., Marengo, M. and Zinna, S., 2012. Thermal simulation of a pulsating heat pipe: effects of different liquid properties on a simple geometry. Heat Transfer Engineering, 33(14), pp.1177-1187.

[11] Noh, H.Y. and Kim, S.J., 2020. Numerical simulation of pulsating heat pipes: Parametric investigation and thermal optimization. Energy conversion and management, 203, p.112237.

[12] Shafii, M.B., Faghri, A. and Zhang, Y., 2001. Thermal modeling of unlooped and looped pulsating heat pipes. J. Heat Transfer, 123(6), pp.1159-1172.

[13] Das, S.P., Nikolayev, V.S., Lefèvre, F., Pottier, B., Khandekar, S. and Bonjour, J., 2010. Thermally induced two-phase oscillating flow inside a capillary tube. International Journal of Heat and Mass Transfer, 53(19-20), pp.3905-3913.

[14] Kholi, F.K., Park, S., Yang, J.S., Ha, M.Y. and Min, J.K., 2023. A detailed review of pulsating heat pipe correlations and recent advances using Artificial Neural Network for improved performance prediction. International Journal of Heat and Mass Transfer, 207, p.124010.

[15] Opalski, M., Czajkowski, C., Błasiak, P., Nowak, A.I., Ishimoto, J. and Pietrowicz, S., 2024. Comprehensive numerical modeling analysis and experimental validation of a multi-turn pulsating heat pipe. International Communications in Heat and Mass Transfer, 159, p.107990.

[16] Saha, N., Das, P.K. and Sharma, P.K., 2014. Influence of process variables on the hydrodynamics and performance of a single loop pulsating heat pipe. International Journal of Heat and Mass Transfer, 74, pp.238-250.

Paper ID 109(S7)

Additive Manufacturing of Vapor Chamber

Chen K. L[1], Hsu S. C[1] and Kang S. W[1*]

[1] *Department of Mechanical and Electro-Mechanical Engineering, Tamkang University, New Taipei City 25137, Taiwan*
**Corresponding author email address: swkang3114@mail.tku.edu.tw; Tel.: +886-2-2621-5656 (ext. 3279)*

Abstract

This study explores the innovative application of Additive Manufacturing techniques to the design and production of vapor chambers. Utilizing Selective Laser Melting (SLM) to make vapor chambers incorporating Triply Periodic Minimal Surface (TPMS) Gyroid structures to increase thermal performance. The paper presents a detailed investigation of the effects of various porosity settings and fill ratios on the thermal resistance of these VCs. Results demonstrate that the VC with 60% porosity and a 200% fill ratio demonstrated the lowest thermal resistance (0.3948 K/W) at 100W and sustained higher heating powers up to 150W, outperforming other configurations. Furthermore, the study highlights the potential of AM to create intricate, effective thermal management structures that can be tailored to specific application needs, thereby extending the functionality and operational efficiency of vapor chambers. The all-in-one forming capability of AM allows for the seamless manufacturing of uniform evaporator plates, enhancing the integration and performance of the vapor chambers.

Keywords: Additive manufacturing; Vapor chamber; Porous structures; Thermal resistance

1. Introduction

As technology advances, efficient thermal management has become a critical challenge in fields such as aerospace, chemical energy, and sustainable energy. Particularly in modern high-power electronic devices, the miniaturization of components and high heat flux densities have rendered traditional cooling methods, such as natural convection, inadequate. Passive thermal devices such as vapor chamber and heat pipes, which lack moving parts and thus offer high reliability, remain effective solutions for dissipating high heat flux densities despite limitations imposed by gravity and capillary forces.

Vapor chamber (VC) are devices that use the latent heat of an internal working fluid to transfer heat (Figure 1). By incorporating capillary structures within the vapor chambers, these structures utilize capillary forces as channels for liquid return, while also providing effective evaporation paths. Vapor chambers are particularly suited for dispersing heat from a single source over a larger area for cooling purposes. Due to their ability to quickly conduct heat and distribute it evenly across the surface, vapor chamber can prevent local overheating, thereby protecting electronic components from damage. With advancements in manufacturing technology, VC have been widely applied in various fields such as electronic chips, mold manufacturing, and plastic thermoforming. Traditional VC technology typically consists of independently assembled components, which limits the diversity of shapes; they are usually only available in simple curved, varying sizes, or flat casings, restricting design flexibility. Thus, design often needs to revolve around the VC rather than integrating it into the system. However, the development of additive manufacturing technology has opened new possibilities for the design and production of vapor chamber, allowing for a higher degree of manufacturing freedom.

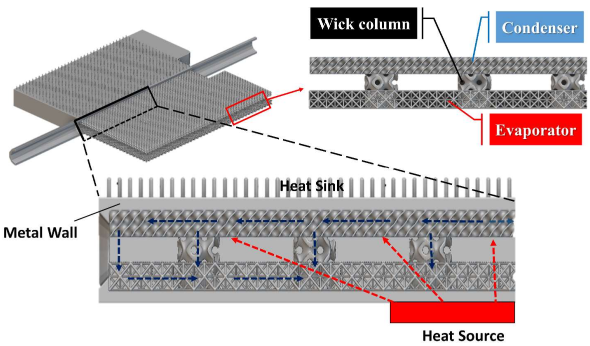

Figure 1 Schematic diagram of vapor chamber.

Powder-bed fusion (PBF) is one of the additive manufacturing technologies. PBF technology mainly uses a high-density focused energy source (such as laser light or electron beam) to sinter or melt material powder (plastic or Metal) into layer of the desired shape [1]. Selective Laser Melting (SLM) is one of the PBF.

Enhancing the performance of vapor chambers has been a focal point of research for many years. This includes increasing flow channel volume, expanding thermal flux range, enhancing overall power, and reducing thermal resistance. These improvements are achieved through the use of various working fluids, designing diverse capillary structures, adjusting fill rates, and optimizing geometric parameters. To minimize flow resistance and maximize capillary forces, controlling the pore structure and geometric parameters is particularly crucial. Additionally, additive manufacturing technology allows for the capillary structures and the base material of the vapor chambers to be integrally formed, enhancing thermal conductivity. However, additive manufacturing is a complex process involving multiple variables, including structural design, equipment precision, laser beam size, and issues with filler clogging, all of which can affect manufacturing outcomes. Despite these challenges, the direct design, optimization, and manufacturing of evaporators through additive manufacturing from the pore scale demonstrate significant potential for improvement and broad application prospects.

Current research on the additive manufacturing of vapor chambers primarily focuses on printing different areas separately and then assembling them through welding [2] However, all-in-one formed vapor chambers, due to printing limitations, offer less control over internal structures and tend to have simpler designs [3]. But it can reduce defects and imperfections that may arise during welding and processing, thereby decreasing contact thermal resistance.

Porous structures in design are primarily categorized into three types: beam-column type, thin-plate type, and triply periodic minimal surface (TPMS) type. The beam-column type, based on a single columnar structure, is frequently utilized in the fields of stress analysis and biomedicine due to its high stiffness-to-weight ratio and excellent elasticity. Thin-plate structures are mainly used to increase heat dissipation area; they exhibit particularly high stiffness in specific directions and, when combined with flexible materials, can provide both elasticity and stiffness, making them ideal for the design of cushioning materials. TPMS are surfaces defined using topological mathematics, characterized by boundaries that change in an orderly and continuous cycle. This smooth boundary structure not only provides structural support but also significantly enhances the feasibility of printing in additive manufacturing [4]. By controlling the thickness and distribution, TPMS structures can create interlocking yet non-intersecting fluid channels. Since TPMS structures have a clear mathematical definition, it allows for precise control over porosity and the fluid flow paths [5].

2. Design and manufacturing of vapor chamber

This study investigates the VC in three parts: the condenser, support columns, and the evaporator. First, we focus on the condenser and support columns. We did not design a separate structure for the condenser; instead, we integrated its space with the support columns, utilizing the surface for condensation, as shown in the Figure 2 below. To enhance condensation efficiency, a TPMS-Gyroid structure was used to create porosity within the support columns. This configuration promotes vapor condensation at the top while the porous structure wicks the condensate back to the evaporator.

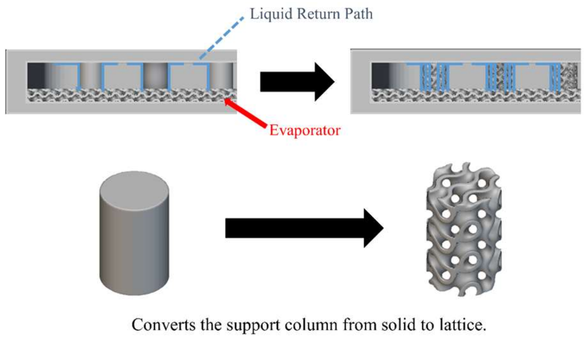

Figure 2. Integrated schematic of the condenser and support.

The advantage of vertical printing is that it avoids the creation of large overhanging spaces, ensuring that all parts have some degree of support during the manufacturing process, which reduces the likelihood of collapse and helps maintain the overall integrity of the VC. Additionally, this approach reduces the number of support columns needed, thereby increasing the cavity volume between the hot and cold ends. Moreover, vertical printing shortens the post-processing time, as the printed VC must be cut from the printing base. Since the contact area between the vertically printed VC and the base is smaller, the cutting process requires less time.

For the evaporator, much of the VC performance is determined by the capillary structure. Its primary function is to use capillary force to quickly return the condensed liquid from the condenser to the evaporator, thereby completing a stable thermal cycle. This capillary return process is crucial to the performance of the VC. Without the capillary structure, the liquid cannot flow back, leading to a lack of liquid replenishment within the VC, which would negatively impact the evaporation efficiency and thermal conductivity.

Secondly, the capillary structure plays a key role in the temperature uniformity within the vapor chamber. The operation of the VC requires the formation of a uniform temperature field inside to prevent localized overheating. By increasing the liquid return speed, the capillary structure ensures heat exchange balance between the evaporative and condensing regions, reducing the temperature gradient. This is particularly important for applications in high heat flux environments, where any temperature non-uniformity could result in equipment failure or decreased performance.

Moreover, the design of the capillary structure directly affects the thermal resistance of the vapor chamber. Thermal resistance is a critical indicator of the VC's performance, and lower thermal resistance translates into higher heat dissipation efficiency. By optimizing the shape of the capillary structure, the thermal resistance within the VC can be significantly reduced, thereby improving overall heat dissipation capability. Factors such as the choice of capillary structure material, pore size, and porosity all influence thermal resistance. For example, finer capillary pores can provide stronger capillary forces, facilitating faster liquid return. However, overly dense structures may increase fluid resistance, which could hinder liquid flow. Therefore, these factors must be balanced during the design process.

In this study, the VC has dimensions of 62.5 x 62.5 x 5 mm³, with two pipes located on the bottom and right side for powder removal and working fluid filling, respectively. Using TPMS Gyroid structures were designed for the evaporator, with porosity settings of 30% and 60%. Based on the conclusions drawn from the support design and printing strategy, we ultimately designed the support columns as 2 mm diameter cylindrical structures. These were integrated with the TPMS-Gyroid porous structure to balance the working fluid's return capability with the structural strength, enabling the support columns to wick liquid back to the evaporator.

For the arrangement of the support columns, we referred to the optimization research conducted by Zhu et al [6]. on support structures and made design improvements accordingly. The supports were uniformly distributed within the VC with a spacing of 5 mm. The overall structural design and parameters are shown in Figure 3 and Table 1.

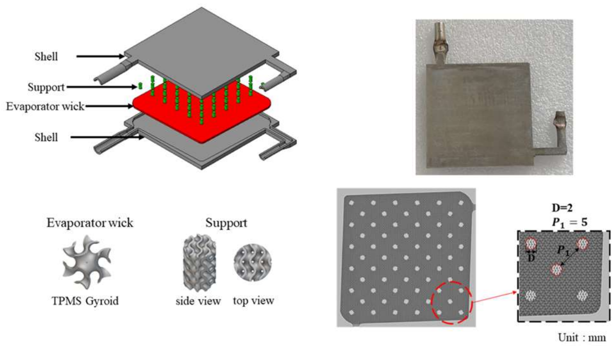

Figure 3. Design and support distribution of vapor chamber.

Table 1. Specifications of VC (unit: mm).

Dimensions of VC (L x W x H)		62.5 x 62.5 x 5			
Evaporator thickness		1			
Wall thickness		1			
Support thickness		2			
Porous structure	Unit cell size	1 x 1 x 1			
	Thickness	0.329	0.205		
	Porosity (%)	30	60		
Filling ratio (%)		200	100	150	200

In the design of porous structures, TPMS-Gyroid were created using nTopology software, which features specialized lattice generation functions that allow for the easy creation of complex lattice structures. The key to porous design lies in the design of the basic unit cell lattice and its structural layout, as each lattice type has its own unique and complex structure. The Figure 4 below shows the continuous structures generated using TPMS lattice designs.

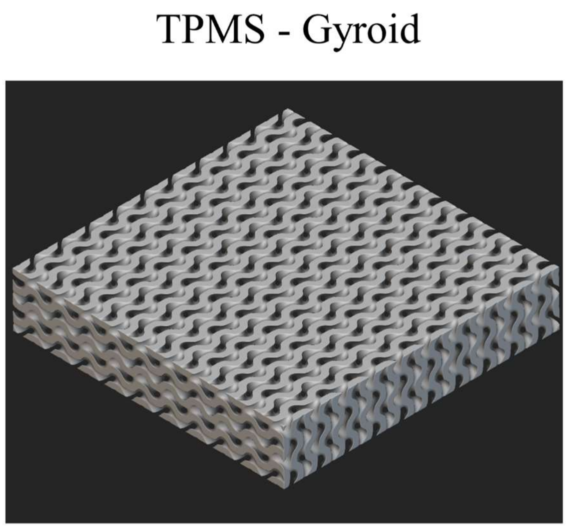

Figure 4. Porous structure patterns.

The study [7] investigated the fluid dynamic properties of lattice structures by varying their porosity. The study found that, compared to random foam structures, the permeability of lattice structures increased by 20% to 80%, and they exhibited thermal performance similar to or even better than foam structures. These results indicate that topological lattice structures are highly suitable for porous designs in heat transfer devices.

The TPMS is a surface described using topological mathematical methods, characterized by its orderly and continuously varying boundaries. This smooth boundary structure not only provides support but also significantly enhances the printability in additive manufacturing. The TPMS structure allows for precise control of porosity and fluid flow paths by adjusting the thickness and distribution [8].

In our study, we selected the TPMS-Gyroid as one of the porous structures for the evaporator. The Figure 5 below shows the design of a single lattice unit, while equation (1) represents its mathematical expression.

TPMS Gyroid

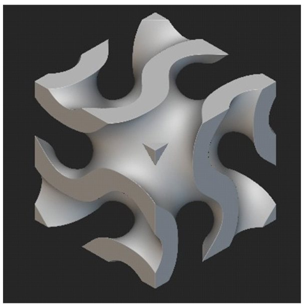

Figure 5. Unit cell lattice of TPMS Gyroid.

$$\sin X \cos Y + \sin Y \cos Z + \sin Z \cos X \qquad (1)$$

In this function, where represents the periodicity of the function, and f(X, Y, Z) = C, When C = 0, a thin-sheet structure (without thickness) is formed. The user can adjust the thickness by setting the value of the constant C.

We use the Tongtai AMP-160 to printing our sample and selected stainless steel (316L) as the material for printing. The machine shown in Figure 6, consists of several key components, including the nitrogen generation system, powder handling unit, and software with printing controls. On the left side of the image is the main machine body, while the right side shows the internal working platform. Table 2 outlines the operational parameters of the AMP-160 machine.

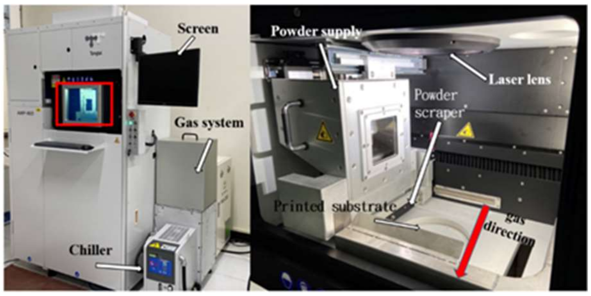

Figure 6. Tongtai AMP-160 AM system.

Table 2. AMP-160 Technical data.

Max laser power	300W
Building volume	Ø160mm x 160mm
Focus diameter	50µm
Building volume	1~10cm^3/hr
Scanning speed	up to 6600 mm/s
Layer thickness	20~100µm
Size accuracy	100µm

When selecting the printing parameters, we referred to previous research [9], which indicates that laser power significantly affects the metal's density and dimensional accuracy. Therefore, we used different parameters for printing the walls and the internal porous structure of the VC, as shown in the Table 3 below.

Table 3. Laser parameters for the wall and wick.

	Laser power (W)	Laser scan speed (mm/s)	Hatch distance (mm)	Slice thickness (mm)	Energy Density (J/mm^3)
Wall	220	900	0.1	0.03	81.5
Wick	100	1000	0.1	0.03	33.3

3. Experiment and result

The experimental setup is shown in Figure 7, while Figure 8 clearly indicates the temperature measurement points and dimensions. The power of the heater is controlled by a power supply, and the condenser is maintained at a stable temperature using a circulating water cooling system. During the testing process, the temperature difference at the inlet and outlet of the cooling water is measured. The VC, once filled and sealed, is placed on the heating end, and a fixed pressure is applied to the condensing end using an electronic pressure loading platform to ensure the VC is securely pressed. After completing the test, a data acquisition system is used to record the temperature data, which is then transmitted to a computer for further analysis to evaluate the performance.

Figure 7. Vapor chamber testing equipment.

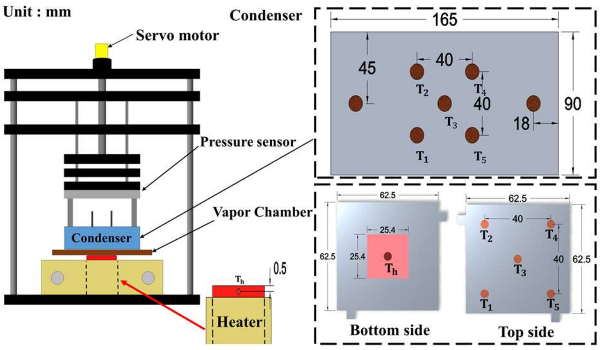

Figure 8. Schematic diagram of testing equipment and temperature measurement points.

T-type thermocouples were used to measure the temperatures at both the heating and condensing ends. The red area on the heating end indicates the contact position of the heater, with an area of 25.4 × 25.4 mm². The blue area on the condensing end represents the contact position of the condenser, with an area of 62.5 × 62.5 mm². The temperatures at the condenser, labeled T_1~T_5, along with the surface temperature of the heating load (T_H), provide key temperature data during the heating and condensing processes.

The working fluid used in the experiment was methanol. During the filling process, a vacuum pump was used to evacuate the chamber to below 1×10^{-2} Torr before injecting a specific quantity of working fluid to achieve the desired fill ratio. A 100% fill ratio is defined as the state where the capillary structure at the evaporator is fully saturated with fluid. We used nTopology software to calculate the porous structure's pore volume, and the fill ratios and corresponding fluid quantities for this study are shown in Table 4.

Table 4. Relationship filling ratio.

Porosity (%)	Structure cavity volume (mm^3)	Fill rate (%)	Filling amount (ml)
30	7876	200	2.16
60	8671	100	1.88
		150	2.83
		200	3.77

To minimize experimental errors, L-shaped insulation blocks were installed around the heater to ensure that the VC is placed in the same position for each experiment (Figure 9). An electronic pressing platform was employed to apply a fixed pressure of 20 kgf, ensuring tight contact between the VC, the heater, and the condenser. To maintain temperature uniformity at the condenser, the water flow rate of the cooling plate was set to 30 LPM, and the water temperature was controlled at 28°C, ensuring consistent experimental conditions across all tests.

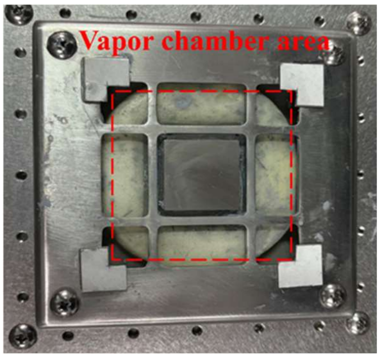

Figure 9. Schematic diagram showing the relationship the heater positioning block.

In the experimental phase, the heater power started at 50W and was gradually increased to 80W, 100W, 120W, 140W, with a maximum of 150W. The system was considered stable when the temperature variation was less than 0.5°C within a 5-minute period. Once the temperature stabilized, the next power level was tested. Additionally, for safe operation and to simulate typical usage conditions, a maximum temperature limit of 100°C ($T_{h,max}$) was set. If the heater temperature exceeded this limit, the experiment would be immediately halted.

The recorded data can be used to calculate the thermal resistance. Thermal resistance is a commonly used method to evaluate thermal performance. The equation (2) for calculating thermal resistance is as follows:

$$R_{system} = (T_h - T_{c,avg})/Q \qquad (2)$$

4. Results and discussion

In this study, five types of VCs were fabricated, The samples were made with a 60% porosity and filled with methanol at 100%, 150%, and 200% capacities. Additionally, for further comparison, a sample was created with 150% methanol fill but maintained at atmospheric pressure, as well as a sample with 30% porosity filled with 200% methanol, as detailed in the Table 5 below.

Table 5. Different sample numbers.

Sample number	Porosity (%)	Filling ratio (%)	Chamber pressure
A	60	100	Vacuum
B		150	Vacuum
C		200	Vacuum
D		150	Atmospheric
E	30	200	Vacuum

Figure 10, Figure 11, and Figure 12 each display the temperature curves for samples A, B, and C, respectively, highlighting the variations due to different fill rates. When testing sample A, a heating power of 100W exceeded the temperature limits, so the sample was tested at 60W and 70W to enhance the interpretability of the data. From the graph, it is observed that the sample exhibits good heat dissipation performance at low heating powers. However, as the heating power gradually increases, a significant change in the temperature curve gradient begins when the power reaches 80W, with a greater increase in the steady-state temperature compared to the rise to 60W and 70W. This indicates that with the increase in heating power, the evaporation rate within the VC accelerates, and the working fluid returning through condensation is insufficient to sustain a large amount of evaporation, leading to an accelerated accumulation of heat. However, due to the low fill rate, the working fluid struggles to support a stable thermal cycle. This results in a sharp decline in heat dissipation efficiency, leading to a significant rise in temperature.

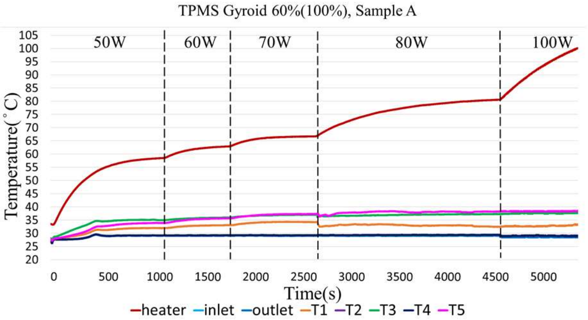

Figure 10. Temperature curve of the sample A.

The sample B demonstrates superior performance. Even when the heating power reaches 120W, it maintains a stable temperature, indicating strong heat conduction capability and stability. This demonstrates that at higher fill rates, samples can operate stably under higher power. During the testing of sample C, two outcomes were observed. One, as shown in Figure 12, featured a noticeable decrease in evaporator temperature and an increase in condenser temperature (highlighted in the top left corner of the diagram). After this phenomenon, the steady-state temperature significantly decreased, ultimately resulting in better performance for this test. The other outcome, as shown in Figure 13, did not exhibit any significant temperature drops, and thus, the performance was poorer .Even at a heating power of 150W, sample C1 maintains a steady temperature, demonstrating enhanced heat conduction abilities and stability. When comparing samples B and C2, the performance difference is minimal, with similar outcomes.

Moreover, Figure 12 reveals a sudden temperature drop at specific moments in both temperature curves. This sharp decline indicates that at that instant, a substantial amount of the working fluid within the VC evaporates, quickly absorbing and removing heat from the heat source, resulting in a sudden decrease in temperature at the evaporator. Simultaneously, the condenser experiences a sudden temperature rise due to the large volume of vapor, which leads to a significant but gradual stabilization of the temperature. This phenomenon reflects the rapid phase change and heat exchange processes within the VC system, highlighting the significant impact of the working fluid's instantaneous evaporation and condensation on system stability and cooling performance. The higher fill rate ensures a more ample supply of working fluid, allowing the system to maintain a stable cooling cycle and effectively control temperature fluctuations even under high power conditions.

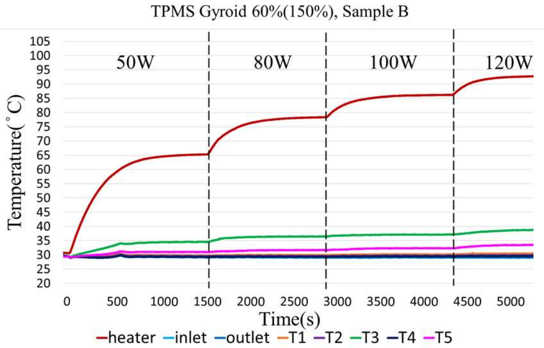

Figure 11. Temperature curve of the sample B.

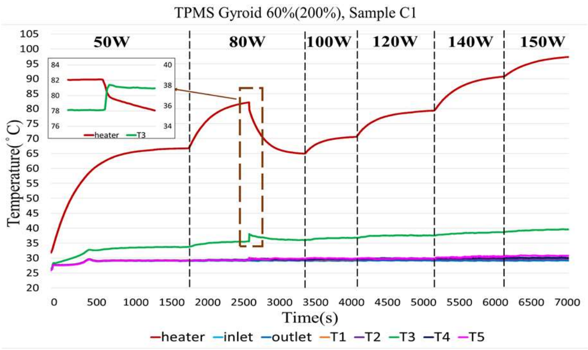

Figure 12. Temperature curve of the sample C1.

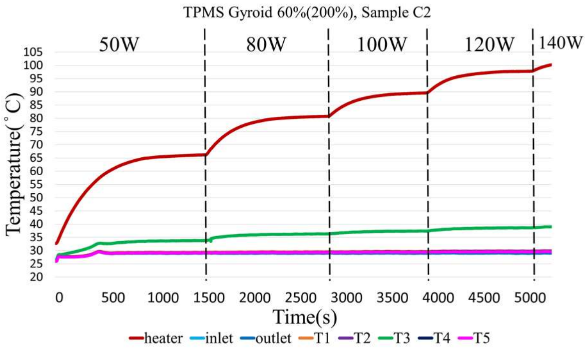

Figure 13. Temperature curve of the sample C2.

Figure 14 compares the thermal resistance of four temperature curves. We use "C1" to denote the scenario where sample C exhibits a noticeable temperature drop, and "C2" where there is no temperature drop. We observe that Sample A has better thermal resistance at power levels between 50 and 80W. However, at 80W, the thermal resistance rapidly increases, and further testing becomes unfeasible. This indicates that due to its lower fill rate, sample A allows the working fluid to boil quickly at lower powers, but encounters a fluid shortage at higher powers.

Sample B shows a decrease in thermal resistance as power increases, with the highest heating power around 120W. Samples C1 and C2 exhibit significant differences; C1 experienced a temperature drop at 80W, significantly reducing its thermal resistance. Notably, at 100W, the thermal resistance reaches its lowest point at 0.4K/W, then increases with further power increases, although it still maintains the best thermal resistance overall.

We speculate that while sample C can operate stably at a power of 150W, excessive boiling above 100W hinders the smooth reflux of the fluid, leading to a reduction in overall performance.

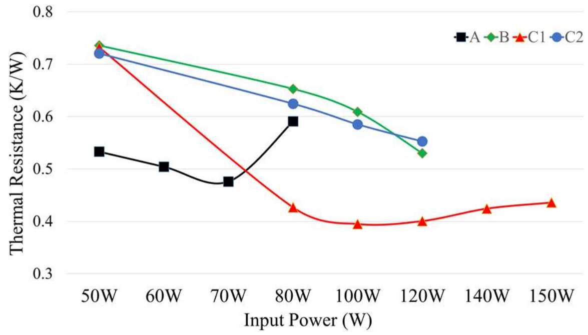

Figure 14. Thermal resistance of the VC with 60% porosity at different fill rates.

We produced sample E with a porosity of 30%, and a fill rate identical to sample C for comparison purposes. Figure 15 shows the temperature changes of the sample E. Comparing this with Figure 12, it is observable that at lower heating powers, the sample E performs better, exhibiting improved cooling effects. However, as the heating power increases, despite the occurrence of sudden temperature drops, the temperature gradient still rises rapidly. Finally, the sample could only be tested up to a maximum power of 120W.

This comparison highlights the impact of the porosity of the capillary structure on performance. While 30% porosity offers a surface area advantage that allows for better performance at lower heating powers—due to faster evaporation rates, helping reduce a temperature, the performance declines as the power increases. With higher power, the rate of fluid evaporation increases, and the denser structure hinders the flow of the working fluid, significantly reducing the heat dissipation efficiency. Even though there are brief temperature drops, the lack of smooth fluid circulation prevents stable temperature maintenance. On the other hand, a 60% porosity provides larger spaces that facilitate smoother fluid flow, thereby sustaining more stable and superior heat transfer performance at higher heating powers.

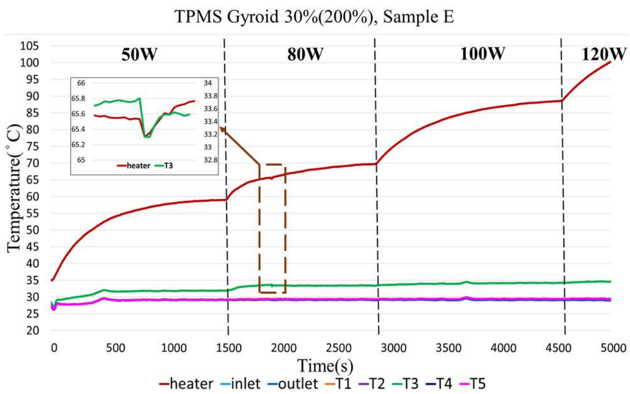

Figure 15. Temperature curve of the sample E.

To test the reliability of VC made using an all-in-one integrated manufacturing approach, we conducted long-term tests on sample B at a weekly frequency. Figure 16 shows the thermal resistance error results from these tests. All thermal resistance errors were within 10%, with no significant upward or downward trends, indicating that these errors are due to experimental operational discrepancies. From this testing, we infer that sample B has good seal integrity, capable of maintaining long-term airtightness and repeated usability.

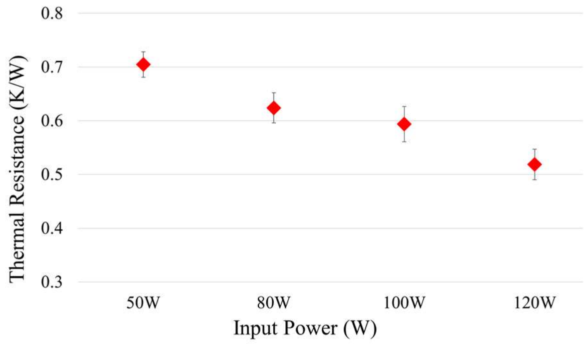

Figure 16. Range of thermal resistance errors in reliability tests.

To assess the performance of the VC in the event of a leak, we fabricated sample D, identical to sample B, but did not perform vacuum processing during filling, thus maintaining atmospheric pressure inside and sealing it by welding. Results from Figure 17 reveal that if the VC cannot effectively prevent leaks, the fluid cannot boil at lower temperatures, leading to a significant decline in system performance.

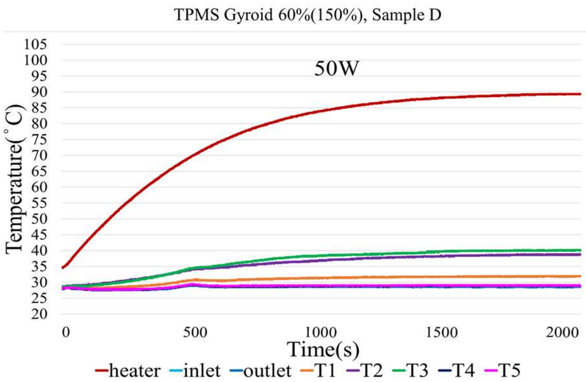

Figure 17. Temperature curve of the sample D.

The Table 6 and Figure 18 summarize the thermal resistance of five different VC, highlighting their variations in thermal management performance. The data clearly show that if a VC is not well-sealed, its thermal resistance will increase, and it will be unable to handle higher heating powers. Sample A, with its lower fill rate, exhibits lower thermal resistance at heating powers between 50W and 80W. However, sample E, due to its denser porosity and higher surface area, produces stronger boiling effects, achieving the lowest thermal resistance at powers between 50W and 70W, but its performance significantly declines when the power exceeds 80W. Sample C, with more porosity and a higher fill rate, can operate at higher powers while maintaining good performance.

Table 6. Thermal resistance table of vapor chambers.

	50W	60W	70W	80W	100W	120W	140W	150W
Sample A	0.5329	0.5041	0.4758	0.5909	X	X	X	X
Sample B	0.7355	X	X	0.6527	0.6089	0.5298	X	X
Sample C	0.7323	X	X	0.4265	0.3948	0.4004	0.4242	0.4358
Sample D	1.1111	X	X	X	X	X	X	X
Sample E	0.5855	X	X	0.4949	0.5819	X	X	X

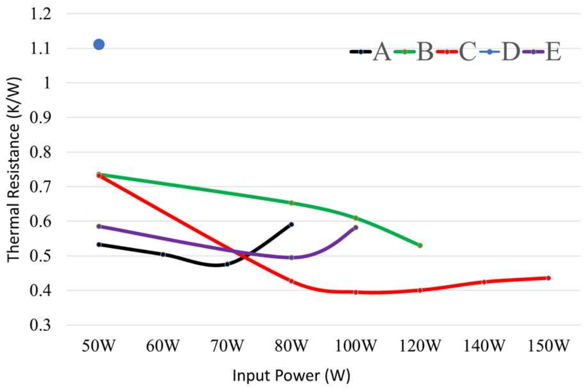

Figure 18 Thermal resistance of vapor chambers.

The TPMS Gyroid structured VCs exhibit distinctly different thermal management capabilities under various porosity and fill rates. Structures with lower fill rates and porosity perform better at lower heating powers, showing improved steady-state temperatures, while those with higher fill rates and porosity can withstand higher heating powers. This versatility makes the TPMS Gyroid structure an ideal choice for different thermal management requirements depending on the application scenario.

5. Conclusion

This study utilized Additive Manufacturing (AM) techniques to fabricate vapor chambers (VCs) and systematically compared the thermal performance of five kinds VC. The capillary structures in the VC were designed using the TPMS Gyroid, setting the porosity at 60% with fill rates of 100%, 150%, and 200%. To verify reliability and test different porosities, samples were also made with chamber pressures at atmospheric levels and with lower porosity rates for comparison. Methanol was used as the working fluid, and the VCs were tested at fill ratios of 100%, 150%, and 200% under varying heating power conditions. The results show that the vapor chamber with sample C exhibited the lowest thermal resistance (0.3948 K/W) at a heating power of 100W. Furthermore, it was able to operate at higher heating powers (150W) compared to other designs. Although the thermal resistance slightly increased (0.4~0.43 K/W), it still remained lower than that of other vapor chamber designs. However, at lower power usage, samples with lower porosity (Samples A and E) exhibit better thermal resistance. Furthermore, the VC maintains consistent performance under prolonged testing, demonstrating that using additive manufacturing techniques to create integrated VC structures is feasible.

And the research can be summarized as follows:

Performance Advantages of TPMS Gyroid Structures:

The TPMS Gyroid structures exhibited significant differences in thermal performance across various porosities and fill ratios. Structures with higher porosity and fill rates (such as 60% porosity at 150% and 200% fill rates) demonstrated lower thermal resistance and could handle higher heating powers with excellent cooling effects. Conversely, structures with lower porosity (such as 30% porosity at 200% fill rate) showed lower thermal resistance under low power heating, highlighting their potential application in low-power thermal management systems. These findings illustrate the ability of TPMS Gyroid structures to be flexibly adjusted to meet diverse cooling requirements based on different application needs.

Potential of AM Technology:

The study showed that AM technology brings unprecedented flexibility and precision to VC design and manufacturing. Additive manufacturing enables the creation of complex three-dimensional periodic structures like TPMS Gyroid, significantly increasing the heat conduction pathways, allowing for faster and more uniform distribution of thermal energy between the evaporator and condenser. This technology not only enhances the design freedom of VCs but also makes it possible to combine different structures and fill ratios, paving the way for the future development of more efficient, customized thermal management systems. The application of AM technology greatly expands the possibilities for VC structural design, especially in fields requiring precise thermal control, offering a highly promising solution.

In conclusion, this research showcases the advantages of the TPMS Gyroid structure, particularly in thermal management systems, where optimal designs can be tailored for different heating power requirements by selecting appropriate porosities and fill ratios. Moreover, additive manufacturing technology provides the technical support necessary to realize these complex structures, significantly enhancing the flexibility and efficacy of VC designs. These achievements indicate that combining additive manufacturing with innovative structural design will lay a solid foundation for the development of future efficient thermal management systems.

6. ACKNOWLEDGEMENTS

We would like to thank National Science and Technology Council (NSTC), Taiwan, Republic of China, for supporting and funding the development of our research with project number 112-2221-E-032 -026.

References

[1] W. E. Frazier, “Metal Additive Manufacturing: A Review,” Journal of Materials Engineering and Performance, vol. 23, no. 6, pp. 1917-1928, 2014.
[2] Z. Gu, H. Liu, K. Yang, et al., “Enhancing heat transfer performance in 3D-printed integrated vapor chamber using composite structures,” Applied Thermal Engineering, vol. 234, 121292, 2023.
[3] S. Ozguc, S. Pai, et al., “Experimental Demonstration of an Additively Manufactured Vapor Chamber Heat Spreader,” 18th IEEE Intersociety Conference on Thermal and Thermomechanical Phenomena in Electronic Systems, 2019.
[4] Wakjira, Y., Cioni, A. & Lemu, H.G. “Current status of the application of additive-manufactured TPMS structure in bone tissue engineering.” Progress in Additive Manufacturing, 2024.
[5] M.B. Hawken, S. Reid, et al., “Characterization of pressure drop through Schwarz-Diamond triply periodic minimal surface porous media,” Chemical Engineering Science, vol. 280, 119039, 2023.
[6] Shuiping Zhu, Yong Li, “Sensitivity and optimization analysis of pillar arrangement on the thermal–hydraulic performance of vapor chamber,” Applied Thermal Engineering, Volume 240, 122246, 2024.

[7] P. Ekade, and S. Krishnan, "Fluid flow and heat transfer characteristics of octet truss lattice geometry," International Journal of Thermal Sciences, vol. 137, pp. 253-261, 2019.
[8] Benjamin W. Reynolds, Conan J. Fee, et al., "Characterisation of Heat Transfer within 3D Printed TPMS Heat Exchangers," International Journal of Heat and Mass Transfer, Volume 212, 124264, 2023.
[9] Chen, K.-L, Luo, K.-Y, et al, "SLM Additive Manufacturing of Oscillating Heat Pipe," *Sustainability*, 15(9), 7538, 2023.

Paper ID 110(S7)

Numerical Simulation of Fluid Dynamics Characteristics in 3D printed TPMS Structures

Senthilkumar S[1], Kishore Bhaskar S[1], Penubarthi Guru Varun[2], Chen K. L[2] and Kang S. W[2]

[1] *Department of Aerospace Engineering, SRM Institute of Science and Technology, Kattankulathur, Chennai 603203, India*
[2] *Department of Mechanical and Electro-Mechanical Engineering, Tamkang University, New Taipei City 25137, Taiwan*
* *Corresponding author email address: swkang@mail.tku.edu.tw; Tel.: +886-2-2621-5656 (ext. 3279)*

Abstract

Heat pipe performance is influenced by fluid properties like permeability, contact angle, capillary action, surface tension, density, viscosity, and vapor pressure. These properties directly impact heat pipe efficiency by enabling fast fluid movement, efficient heat removal from the source, and enhancing capillary action. Optimizing these fluid properties is essential for designing heat pipes that meet specific performance needs, ensuring reliable and efficient thermal management across various applications. This research focuses on numerical study on improving the efficiency of such parameters by using TPMS (Triply Periodic Minimal Surfaces) porous structures. Simulations are carried out for four different TPMS structures namely TPMS Gyroid, Diamond, Octet, and Iso-truss with the unit cell size of 2×2×2 mm3 to understand the dynamic behavior of contact angles and penetration patterns of free-falling water drop of 16 µL in volume. Numerical results of transient drop evolution and its penetration patterns are compared with those of experimental findings and found a reasonably good agreement.

Keywords: Triply Periodic Minimal Surfaces; Porous Structures; Numerical; Contact Angle; Drop

1. Introduction

Heat pipes play an increasingly vital role in managing heat effectively across various applications. In the realm of electronics, such as laptops, desktop computers, and LED lights, they are indispensable for curbing overheating and ensuring optimal performance. Moreover, in the domain of spacecraft thermal management, where temperature fluctuations pose a threat to sensitive electronics, heat pipes are crucial components. Their significance further extends to HVAC systems, power plant cooling setups, and the cooling mechanisms of high-performance CPUs and GPUs in modern computers.

The efficiency and effectiveness of heat pipes hinge greatly on fluid properties like contact angle, permeability, and porosity. The contact angle of the fluid with the inner surface of the heat pipe determines its ability to thoroughly wet the surface, directly impacting the performance of the heat transfer process. Additionally, Liquid behaviour on porous materials is controlled by both bulk penetration and surface spreading [1, 2]. The contact angle of a drop of liquid in contact with the substrate is a characteristic that is influenced by both the fluid and the structure [3]. It is the angle created by the tangent of the drop's outline at the point of contact with the substrate. The dynamic contact angle must be computed or monitored to achieve a delicate balance between drop and surface while absorbing substrates, which is rarely achieved. The contact angle (Θ) quantifies liquid adhesion to surfaces. Notable wetness is indicated by a low Δ value. In many applications, liquid behaviour on porous materials is crucial. In inkjet printing, the contact angle predicts how the dots will spread over the substrate [4]. Membrane liquid penetration is usually measured by the contact angle.

Several experiments have been carried out to examine the phenomenon of drop absorption and spreading on porous surfaces. This research has been conducted utilizing modelling techniques [6,7] or by direct observation [8,7,5]. These studies investigate the effects of substrate pore size and porosity, as well as liquid surface tension and viscosity, on drop spreading and penetration behaviour. The contact angle is affected by the absorption into the substrate, resulting in a reduction as the drop infiltrates the substrate [10, 9, 5, 3]. However, none of these studies are currently looking into the effects of absorption, drop size, and surface tension on the measured contact angle with the TPMS structures. Rather numerical simulations were done for a random CT scanned porous structure and the effects of static contact angle were studied with the help of 2-phase VOF models in OpenFoam [11].

2. Design and Numerical Method

Four models were created namely TPMS Gyroid, Diamond, Octet, and Isotruss with the unit cell size of 2×2×2 mm^3 with the dimensions of 10×10×3 mm^3. using a commercial implicit CAD modeling software nTop as shown in Figure 1.

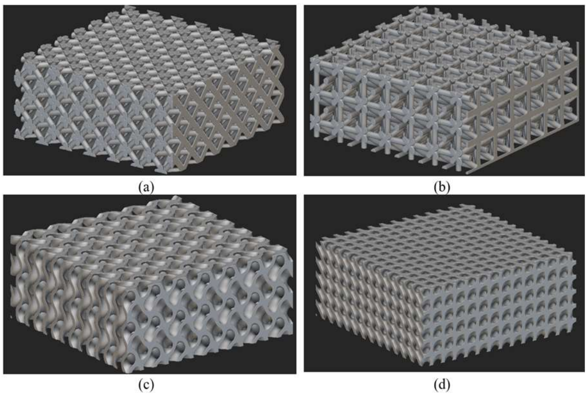

Figure 1. Porous structures designed using nTopology a-Octet, b- Iso-truss, c- Gyroid, d- Diamond.

The following equations were used by the modeler for creating TPMS structures used in this study:

TPMS Architecture	Equation f (x, y, z) = 0
Fischer-Koch S (FKS)	cos(2x)·sin(y)·cos(z)+cos(2y)·sin(z)·cos(x)+cos(2z)·sin(x)·cos(y)
Gyroid (G)	cos(x)·sin(y)+cos(y)·sin(z)+cos(z)·sin(x)
Schwarz primitive (SP)	cos(x)+cos(y)+cos(z)

The static contact angle is to be known before we move forward with the simulation of different structures hence, a 3D-printed flat plat of a water droplet was kept on the surface and the static contact angle was measured to be 53.72°. The below figure shows the experimental results.

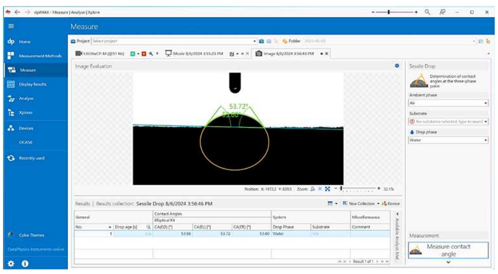

Figure 2. Static contact angle of the solid 3-D printed flat plate measured by dpiMAX goniometer.

To validate the simulation's accuracy, in this experiment, distilled water droplets of 16 microliters were deposited on the porous TPMS-Gyroid structure from a height of 30 mm. The machine employed for this task, the DKSH OCA 15EC contact angle meter, is equipped with a high-resolution camera and precision syringe control. These features are essential for capturing the evolution of the droplet that are in contact with a surface and ensuring accurate volume repeatability. The dynamic Contact angle was measured with the help of the elliptical fit method from the goniometer (Figure 2) and the experimental setup is shown in Figure 3.

Figure 3. Experimental setup (DKSH OCA 15EC contact angle meter).

The boundary conditions and the geometry for validation are given in Figure 3. The following assumptions are used to simulate the drop dynamics:

- Flow type: Transient
- Gravity: 9.81 m/s^2
- Height at which the water was dropped: 30 mm
- Multiphase- VOF model.
- Volume: 16 µL.
- Droplet diameter: 1.529 mm
- Droplet fluid material: Water
- Turbulence model: Laminar

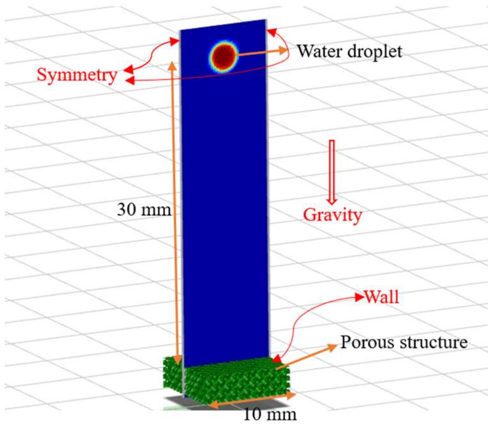

Figure 4. Fluid Domain with Boundary conditions of the numerical model.

The VOF (Volume of Fluid) with transient, multiphase model was used. The tracking interface between different phases is achieved by solving the continuity equation for the volume fraction of phases. For the qth phase, this equation has the following form:

$$\frac{1}{\rho_q}\left[\frac{\partial}{\partial t}\left(\alpha_q\rho_q\right)+\nabla\cdot\left(\alpha_q\rho_q\vec{v}_q\right)=S_{\alpha_q}+\sum_{p=1}^{n}\left(\dot{m}_{pq}-\dot{m}_{qp}\right)\right] \quad (1)$$

In which, m_{qp}- mass transfer from phase 1 to phase 2, m_{pq} is vice versa and the source term is by default 0. However, as there is no phase change occurred in this study, m_{qp} and m_{pq} are equal to zero.

Volume fraction equation is solved by Explicit time discretization:

$$\frac{\alpha_q^{n+1}\rho_q^{n+1}-\alpha_q^n\rho_q^n}{\Delta t}V+\sum_f\left(\rho_q U_f^n\alpha_{q,f}^n\right)=\left[\sum_{p=1}^{n}\left(\dot{m}_{pq}-\dot{m}_{qp}\right)+S_{\alpha_q}\right]V \quad (2)$$

Where,

- n+1 = index for current time step
- n = index for previous time step
- V= volume of cell
- U_f = volume flux through face, based on velocity.
- $\alpha_{q,f}$ = face value of the qth volume fraction, computed from the first- or -second-order upwind scheme.

A geometric reconstruction scheme was used for the interface capture of the two phases of fluids. A single momentum equation is solved throughout the domain, resulting velocity term is shared among the phases. The momentum term shown below is dependent on the volume fractions of all the phases:

$$\frac{\partial}{\partial t}(\rho\vec{v})+\nabla\cdot(\rho\vec{v}\vec{v})=-\nabla p+\nabla\cdot\left[\mu\left(\nabla\vec{v}+\nabla\vec{v}^T\right)\right]+\rho\vec{g}+F \quad (3)$$

Surface tension between air and water was 0.072 N/m and the continuum surface force model was used with the surface tension model on wall adhesion and jump adhesion so that the contact angles are found with both sides being almost the same.

Considering the same boundary conditions the Gyroid structure was replaced with three other different structures namely Diamond, Iso-truss, and Octet of the same unit-cell size can be seen in Figure 1. The volume of water contour in a plane was plotted and the video was obtained, at different time intervals. The droplet dynamic characteristics were captured and then used in a goniometer in this study software as mentioned in [13] was used to find the contact angle at different time.

The fluid domain was finely meshed with a maximum cell size of 0.2 mm and minimum cell size of 0.05mm and with a growth rate of 1.2 with the polyhexa mesh. The surface tension effects are to be captured, so near the top surface of the porous structure the mesh was refined with layers of hexa mesh. The mesh layout can be seen in Figure 5.

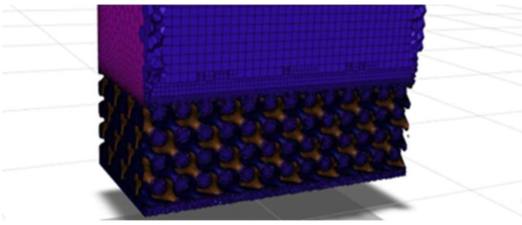

Figure 5. Polyhexa mesh for Gyroid structure.

3. Results and Discussion

The right and left dynamic contact angles, and the average dynamic contact angle between the right and left were plotted from both the experimental and simulated data as in Figure 6 and 7, respectively. In both cases same boundary conditions were used, i.e. volume of the droplet of 16, drop height of 30 mm and, the Gyroid of unit cell size 2×2×2 mm^3.

The comparison of the right and left dynamic contact angles show that it is more agreeable that they are on a similar trend with the angles being almost the same. The average contact angle plot with the trendline with the regression equation shows that the contact angle which is the variable is independent of the mode of obtaining the angles. Both give out R^2 values that are close to each other and hence this numerical model is validated.

The dispersion of the water droplet at different time intervals was recorded in both experimental and numerical analysis and the contours were plotted to compare the dynamic drop evolution patterns. Figure 8 illustrates the spreading pattern of water drop on the Gyroid structure with an initial contact angle of 53.72°.

It can be seen from Figure 8 that the dynamics of the droplet are captured precisely for both experimental and numerical analysis. The error percentage between experimental and numerical results for average contact angle was less than 6% which was agreeable considering the printing thickness difference and surface roughness in real-time models when compared to CAD models which are smooth and uniform.

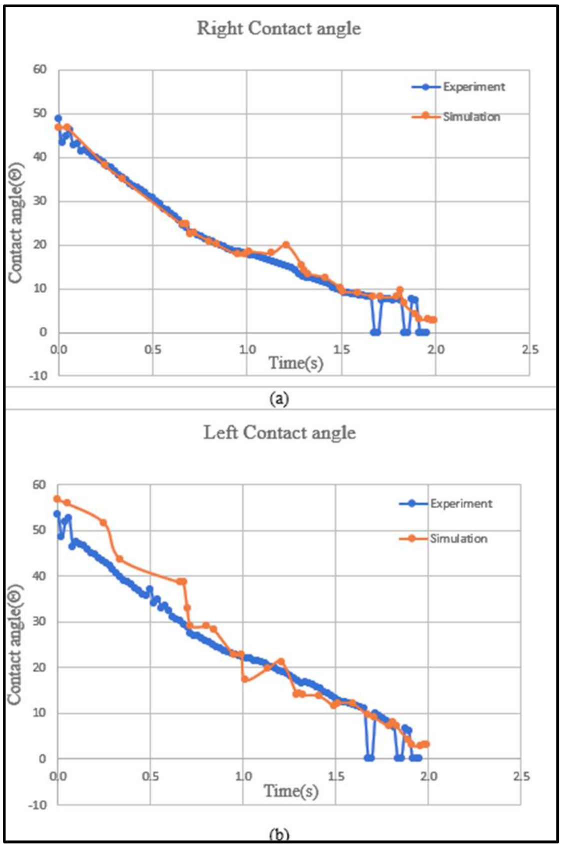

Figure 6. Comparison of dynamic contact angles obtained from both experimental and simulation results for Gyroid structure: (a) Right contact angle (b) Left contact angle.

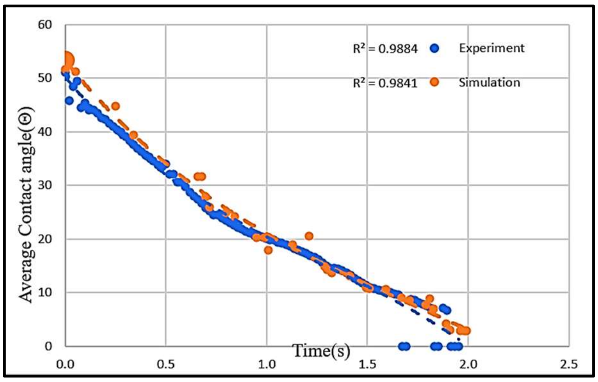

Figure 7. Plot illustrating the average dynamic contact angle of both experimental and simulated results of Gyroid structure

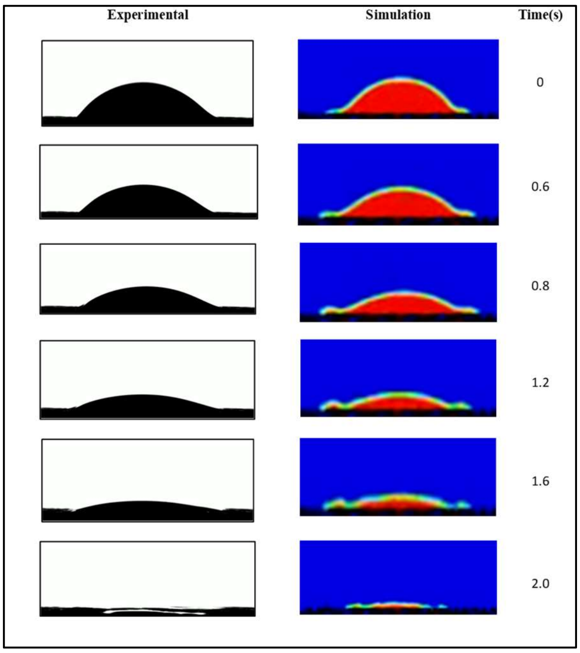

Figure 8. Comparison of water droplet evolution on Gyroid structure results from experiment and numerical simulation.

This study examined how surface wettability affects the time it takes for water droplets to penetrate through four distinct porous structures: gyroid, diamond, octet, and iso-truss. The droplets were discharged from a vertical distance of 30 mm with a radius of 1.529 mm. Although the contact angles were comparable among the structures, there was a substantial variation in the time it took for the droplets to enter each structure. This finding has critical implications for the efficiency of heat pipes.

Figure 9 gives an insight into the inner and outer retention of the water droplet for different porous structures, this helps us visualize the percentage of water that is initially retained on the porous structure before the droplet is fully penetrated. The efficiency of heat pipes, especially micro-channel heat pipes (MCHPs), is significantly affected by the wetting characteristics of the surfaces involved, which has a direct impact on their overall performance. The structures being examined have distinct geometric configurations that result in different levels of surface wettability. These variations have a direct impact on the thermal and flow characteristics of the working fluid inside the heat pipe.

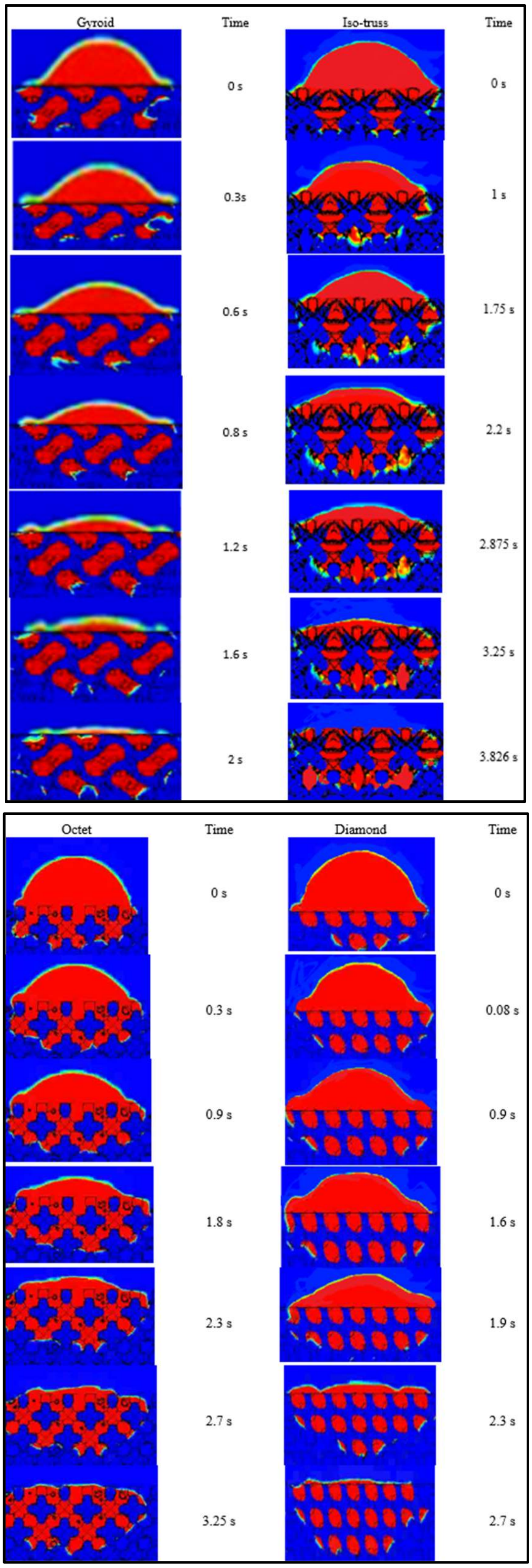

Figure 9. Penetration pattern of the water drop into different TPMS structures at different times: Top – Gyroid & Iso-truss, Bottom – Octet & Diamond.

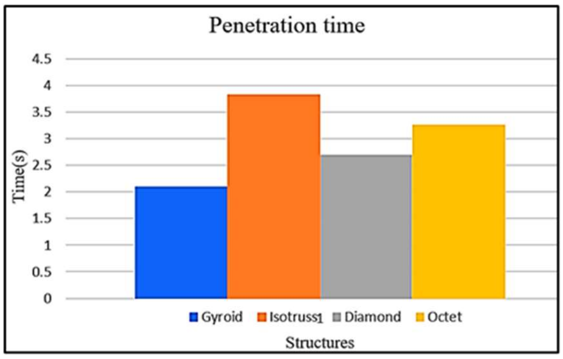

Figure 10. Penetration time for all four structures.

Figure 10 gives an insight into how much time different structures take for the droplet to fully penetrate. This gives us an overall idea about the wettability of different structures.

It can be seen that the droplet had a fast penetration time due to the gyroid's smooth and continuous surface topology. This structure's balance between wettability and permeability plays a crucial role in ensuring a consistent and smooth flow of the refrigerant in the evaporator section of a heat pipe. The heat transfer efficiency is significantly improved with the smooth transition of the liquid film over the surface. This makes it an excellent choice for applications that demand reliable thermal management.

With quick penetration time, the diamond structure, known for its high porosity, was next to the gyroid. Rapid penetration suggests less fluid flow resistance, which might benefit heat dissipation. Increased fluid velocity can reduce thermal isolation, compromising pipe heat retention in some places. This may reduce the effectiveness of sustained heat absorption systems.

The octet structure penetrated longer than diamond and gyroid structures. Reduced fluid flow may indicate higher heat transfer resistance, which might be useful when the heat pipe has to hold heat in some locations to maintain the required temperature differential. Over time, controlled flow through the octet structure can increase thermal performance by uniformly spreading temperature.

The complex lattice construction of the iso-truss structure allowed penetration for the longest time. Higher surface contact and wetness indicate greater thermal insulation. This process may enhance thermal resistance in heat pipes and improve evaporator heat absorption. However, depending on the application, slower flow may delay heat transfer to the condenser portion, reducing heat pipe efficiency.

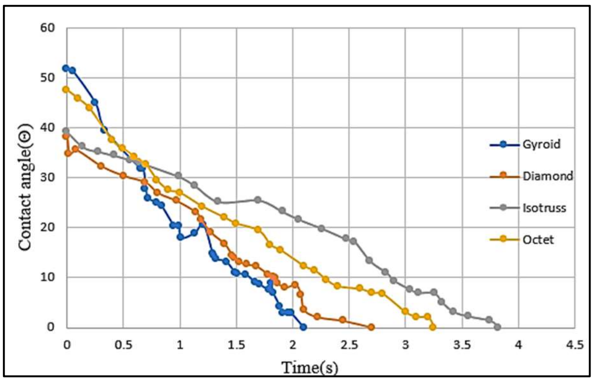

Figure 11. Comparison of the average contact angles for all four TPMS structures.

Through the simulation results, it was found that all four structures exhibit a contact angle in the range of 50° to 30 as shown in Figure 11. It shows the average dynamic contact angle for different structures. With a contact angle range of 52° to 0° and a penetration time of 2 seconds, the gyroid structure has the quickest fluid movement measured. The high initial contact angle suggests a surface that resists wetting, but rapid penetration shows that the droplet quickly wets the surface. By this phenomenon, a refrigerant can rapidly cover and transport heat over the evaporator part of heat pipes, making it ideal for fast heat transmission. This can be easily understood from the the spreading patterns of water drop for various TPMS structures as shown in Figure 12. The videos of these interface patterns between air and water drop video was used to find the dynamic contact angle using Opendrop software.

Octet structure has contact angle in the range of 48° to 0°- and 3.25-second penetration time, slower fluid movement than gyroid. The comparatively smaller initial contact angle and longer penetration duration imply more regulated fluid distribution. Heat pipes need a slower, more constant fluid flow to maintain a steady temperature gradient, hence this trait may improve thermal management over time.

The most fluid-resistant construction is the iso-truss, with a contact angle range of 39° to 0° and a penetration time of 3.75 seconds. Slow penetration suggests a structure that keeps fluid longer, improving thermal isolation, while a lower initial contact angle improves wettability. This tendency could prove useful in applications requiring continuous heat absorption, but it could hinder heat transfer efficiency in quick temperature reaction situations.

The diamond structure balances wettability and penetration time with a contact angle range of 38° to 0° and a penetration duration of 2.75 seconds. It has the lowest initial contact angle, indicating great wettability, but the penetration duration shows fluid spreads slower than in the gyroid structure. The diamond construction is flexible for heat pipes, balancing quick heat transmission with thermal isolation.

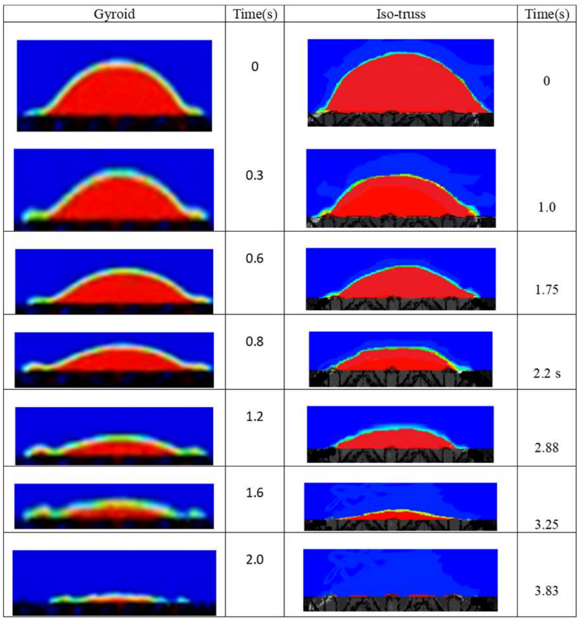

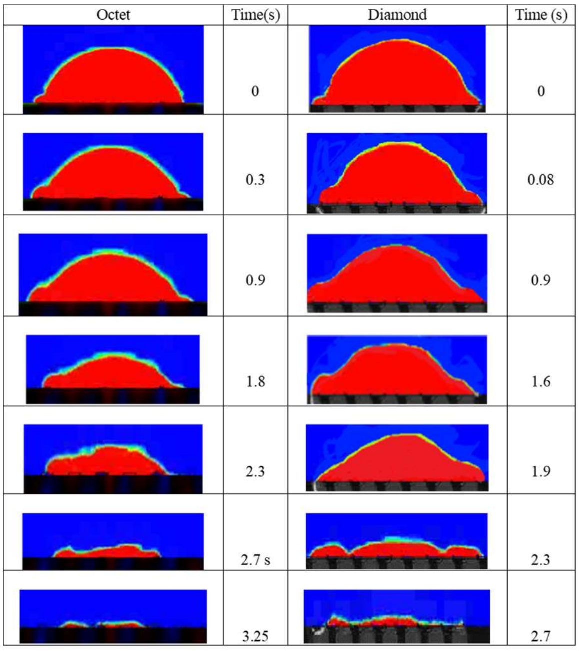

Figure 12. Illustrates the water droplet dispersion behavior for the membrane with a static contact angle of 53.72 for three of the porous structures namely Iso-truss, octet, and Diamond from left to right respectively.

Comparative Analysis: Conventional Porous/Mesh Structures vs. Advanced

Geometric Structures:

Heat pipes commonly employ typical porous or mesh structures, such as sintered powders, metal foams, or wire meshes, to augment capillary action, facilitate fluid distribution, and boost heat transmission. These structures commonly demonstrate favourable wettability, capillary pumping, and thermal conductivity, which renders them very efficient in conventional heat pipe applications. Nevertheless, the effectiveness of their function is mostly determined by their consistent porosity and relatively uncomplicated geometric structure.

On the other hand, the complex geometric structures examined in this research, including Gyroid, Diamond, Octet, and Iso-truss, possess distinct and varied geometries that bring about novel dynamics in fluid penetration and heat transmission mechanisms.

4. Conclusion

This study examined the influence of contact angles and penetration durations on the efficacy of four porous structures namely Gyroid, Diamond, Octet, and Iso-truss for heat pipe applications. The diamond structure exhibited the quickest penetration time of 2.75 seconds and a contact angle range of 38° to 0°, indicating little resistance to fluid flow, therefore rendering it optimal for applications necessitating fast heat dissipation.

The Gyroid structure exhibited rapid penetration in 2 seconds, with a contact angle ranging from 52° to 0°, indicating effective fluid dynamics, ideal for high-performance thermal transfer. On the other hand, the Iso-truss structure exhibited the longest penetration duration of 3.75 seconds and a contact angle range of 39° to 0°, indicating enhanced surface interaction and superior thermal insulation, advantageous for longer heat absorption. The Octet configuration, exhibiting a penetration duration of 3.25 seconds and a contact angle ranging from 48° to 0°, facilitated an equilibrium between fluid dynamics and heat regulation.

In comparison to traditional porous or mesh structures, these advanced geometries have unique advantages. The Diamond and Gyroid configurations provide superior thermal conductivity, whilst the Iso-truss and Octet structures offer improved thermal insulation, rendering them appropriate for diverse thermal management requirements in heat pipe design.

5. ACKNOWLEDGEMENTS

Thanks to NSTC, Taiwan, ROC, for funding our project 112-2221-E-032 -026.

References

1) H. Wijshoff, Drop dynamics in the inkjet printing process, Curr. Opin. Colloid Interface Sci. 36 (2018) 20–27.
2) R.K. Holman, M.J. Cima, S.A. Uhland, E. Sachs, Spreading and infiltration of inkjetprinted polymer solution droplets on a porous substrate, J. Colloid Interface Sci. 249 (2) (2002) 432–440.
3) K. Sarah, H. Ulrich, Short timescale wetting and penetration on porous sheets measured with ultrasound, direct absorption, and contact angle, RSC Adv. 8 (23) (2018) 12861–12869.
4) K. Mielonen, P. Geydt, M. Osterberg, ¨ L.S. Johansson, K. Backfolk, S.-S. Ovaska, T. Laukala, K. Backfolk, Inkjet ink spreading on polyelectrolyte multilayers deposited on pigment coated paper, J. Colloid Interface Sci. 438 (3) (2015) 179–190.
5) S.M. Kumar, A.P. Deshpande, Dynamics of drop spreading on fibrous porous media, Colloids Surf. A Physicochem. Eng. Asp. 277 (2006) 157–163.
6) D. Seveno, V. Ledauphin, G. MArtic, M. Vou´e, J. Coninck, Spreading drop dynamics on porous surfaces, Langmuir 18 (2002) 7496–7502.
7) A. Clarke, T.D. Blake, K. Carruthers, A. Woodward, Spreading and imbibition of liquid droplets on porous surfaces, Langmuir 18 (8) (2002) 2980–2984.
8) V. Andr´e, A. Zosel, Dynamic wetting on porous and non-porous substrates. influence of surface tension, viscosity, and porosity, Ber. Bunsenges. Phys. Chem. 98 (3) (1994) 429–434.
9) L.L. Popovich, D.L. Feke, I. Manas-Zloczower, Influence of physical and interfacial characteristics on the wetting and spreading of fluids on powders, Powder Technol. 104 (1) (1999) 68–74.
10) L. Susana, F. Campaci, A.C. Santomaso, Wettability of mineral and metallic powders: applicability and limitations of sessile drop method and Washburn's technique, Powder Technol. 226 (2012) 68–77
11) Apostolos Kyrloglou, Patrick Giefer, Udo Fritsching, Numerical simulation of droplet dispersion within mesoporous membranes, (2024) https://doi.org/10.3389/fphy.2024.1282122
12) Ansys FLUENT User Guide 2018.
13) Eugene Huang, Adam Skous, Terence Denning, Open Drop: Open-source software for pendant drop tensiometry & contact angle measurements.J. open-source software (2021). doi:10.21105/joss.0260 4.

Paper ID 111(S7)

Experimental Investigation of An Air-Cooled Roll-Bond Flat Thermosyphon Module

Mohsen Khandan Bakavoli[1], Piyatida Trinurak[2], Somchai Wongwises[3], Chi-Chuan Wang[4]

[1] *Departemtn of Mechanical Engineering, National Ynag Ming Chiao Tung University, Hsinchu, Taiwan*
[2] *Department of Mechanical Engineering, Faculty of Engineering, King Mongkut's University of Technology Thonburi, Bangkok, Thailand*
[3] *Department of Mechanical Engineering, Faculty of Engineering, King Mongkut's University of Technology Thonburi, Bangkok, Thailand*
[4] *Departemtn of Mechanical Engineering, National Ynag Ming Chiao Tung University, Hsinchu, Taiwan*
**ccwang@nycu.edu.tw*

Abstract

Due to the high cooling requirements of 5th generation (5G) base stations, conventional metallic heat sinks are not capable of dissipating sufficient heat from these stations. Hence, a new type of air-cooled module is needed to fulfill this task. The roll bond flat thermosyphon (RBFT) is a phase-change solution that is affordable, easy to assemble, and has a high heat transfer coefficient. In the current study, the RBFT module, cooled by natural convection, has been investigated experimentally, considering the effects of filling ratio, working fluids, inclination, and heat loads on the thermal performance of the RBFT module. The results showed that the thermal resistance of the RBFT is around 10% to 25% lower than that of a similar flat plate fin for 100W and 400W heat loads, respectively. The best thermal performance was achieved with 25% and 40% filling ratios for R-600a and R-1233zd, respectively. Additionally, the best thermal performance was observed when the module was installed without any inclination.

Keywords: Roll-bond flat thermosyphon; Air-cooled; Heat dissipation; Natural convection; Thermal performance;

1. Introduction

Due to the boom in mobile communication technologies, 5th generation (5G) base stations are now widely used by many operators. Classical heat sinks with plate fin array configurations are inexpensive and easy to manufacture, but they are limited in heat dissipation [1]. The active antenna unit (AAU) in 5G stations is smaller in size compared to the remote radio unit (RRU) in 4th generation (4G) base stations. However, the 5G AAU consumes significantly more power, most of which is converted into heat [2]. Hence, it is essential to find an alternative to plate fins, which are typically mounted on the back of an antenna's cabinet in 4G RRUs, to dissipate heat from the antenna and prevent overheating that could damage the AAU. The schematic of 4G and 5G base stations is shown in Figure 1.

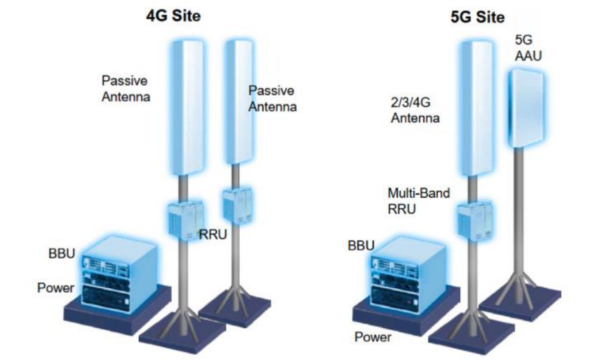

Figure 1. The schematic of 4G and 5G sites [2].

Since the fins of heat sinks are usually made of aluminum, and the thermal conductivity of aluminum cannot fulfill the needs for enhanced heat dissipation, the application of phase-change heat dissipation technologies, such as heat pipes and thermosyphons, has increased. These two technologies leverage the benefits of evaporation and condensation. In a heat pipe, the liquid returns from the condenser to the evaporator by means of surface tension through a wick structure, while in a thermosyphon, or wickless heat pipe, the driving force is gravity, which facilitates the return of the liquid from the condenser [3]. This can be seen in Figure 2.

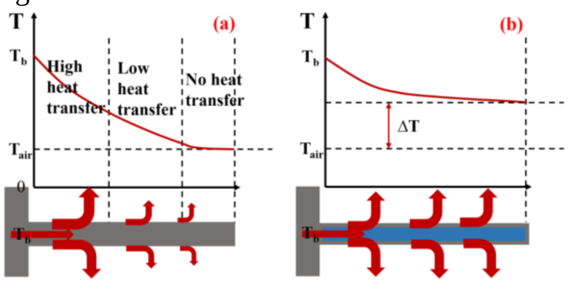

Figure 2. (a) Conventional aluminum fin; (b) heat pipe fin [4].

An innovative solution for the dissipation of heat from the 5G active antenna unit is to replace the aluminum fins mounted on the back of the unit with flat-plate heat pipes.

Several studies have been conducted on roll bond flat heat pipes (RBFHP) and their applications. Deng et al. [1] carried out an experimental study of an RBFT with three different pipe configurations, as well as different filling ratios, to evaluate the effective thermal conductivity. They proposed an optimum design structure and an optimum filling ratio that provide high effective thermal conductivity compared to other cases in their study. In another study, Deng et al. [2] examined the RBFHP using multiple heat sources under natural convection conditions. They investigated the thermal performance based on different filling ratios, heat loads, inclination angles, and heat source distributions. They concluded that there is a relationship between the position of the liquid-vapor interface and the higher heat load source. Khodabandeh [3] studied an RBFT used for cooling a radio base station. Wan et al. [4] studied an RBFHP and concluded that dissipation efficiency was 10% to 55% better than that of a fin heat sink. They also investigated the effect of inclination on the performance of the RBFHP. Sacco et al. [5] proposed a mathematical model for an air-cooled thermosyphon cooling system using roll-bond fins for the condenser part and assessed their results through simulation and experiment, reaching a good agreement. Take et al. [6] studied the capillary limit and thermal performance of an RBHP. They proposed three different designs and found the optimum filling ratio and design. Gradinger and Agostini [7] compared the thermal performance of a classical heat sink and the roll-bond thermosyphon through simulation for forced and natural convection. They stated that the thermal resistance, using free air convection, was 25% to 30% lower for the RBFT compared to the classical heat sink. Gan et al. [8] used a radiator composed of a flat heat pipe as the base and RBFHP as its fins. They compared the thermal performance of the radiator with aluminum fins and RBFHP under different heating powers and air speeds. They showed that the optimum filling ratio for the RBFHP is 35%, and it exhibited a lower thermal resistance than a conventional aluminum fin radiator, whereas the maximum heat dissipation for both cases is the same under natural convection conditions.

2. Experimental Setup

The technique utilized for the manufacturing of these flat heat pipes is called roll bonding. Thus, they are referred to as roll-bond flat heat pipes. The rolling process includes four main steps. Firstly, graphite is printed on two similar plates with the same thickness and material to provide passages for the heat pipe. Then, the two plates are rolled together to bond them. In the next step, an inflation process occurs with compressed air, and the working fluid is charged in. Figure 3 shows the final module and a single RBFT fin.

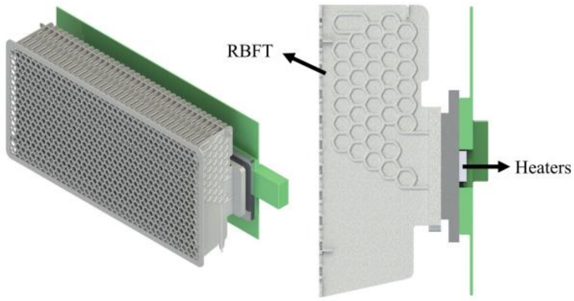

Figure 3. The schematic of the proposed RBFT module.

Figure 4 illustrates the experimental layout. The main components of the setup include the module, the DC power supply, the acquisition module, and the thermocouples. The module is mounted on a platform 1 meter above ground level, inside a room at a constant temperature of 25 ± 1 °C. The heating modules consist of power resistors arranged in 8 pairs in the same location, positioned behind the sample and near the evaporator side to mimic the heat sources in a real cabinet. The module is charged with R-1233zd, a low-pressure and environmentally friendly refrigerant, as the working fluid, and natural convection cooling is chosen as the ambient air condition. The RBFT module consists of 36 aluminum RBFT fins attached to a base block. The interface between the heaters and the module base block is filled with thermal grease (Cooler Master Ice Fusion V2), which has a thermal conductivity of 5 W/mK. The temperature acquisition system includes a data logger (IM MX100 Yokogawa) and 8 T-type thermocouples with a measurement accuracy of ±0.1 °C, which were soldered beneath the power resistors. A Bakelite plate and a polyurethane cover were added to the back of the module and heaters to minimize heat loss and facilitate hanging the sample in the air.

Using a DC power supply (GW Instek PSW 80-40.5), the heating loads start from 100 W for the module and increase to 600 W in 100 W increments after each heat load reaches a steady-state condition. The steady-state condition is defined as when the changes in temperature of each coin are less than 0.1 °C for at least 2 minutes.

The average time to reach a steady-state condition was approximately 40 minutes for each heat load increment. To investigate the temperature distribution of a single RBFT, 12 thermocouples were attached to different locations on the fin during the experiment with various heat loads.

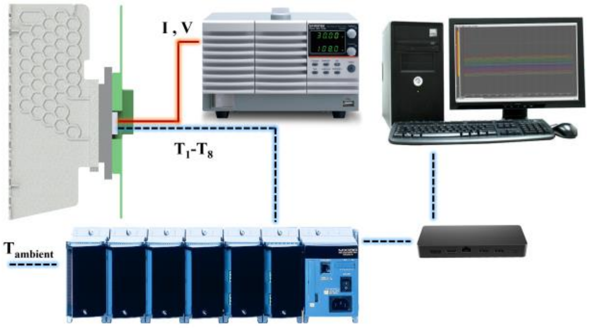

Figure 4. The schematic of the experimental setup.

2.1. Thermal Characterization

The widely used definition for thermosyphons and other passive thermal modules is the filling ratio. The liquid filling ratio for the module can be expressed as equation (1):

$$FR = \frac{V_{liquid}}{V_{total}} \times 100\% \tag{1}$$

The module is charged with R-1233zd under ambient temperature and pressure, with different filling ratios varying from 25% to 50% for the entire module.

The average temperature of the 8 pairs of resistors is considered the evaporator's temperature, as shown in equation (2), while the ambient temperature is also considered the condenser's temperature.

$$T_{evap.} = \frac{\sum_{i=1}^{i=8} T_{Heater,i}}{8} \tag{2}$$

Based on the geometry of the module the equivalent thermal resistance for the module can be defined as equation (3).

$$R_{th} = \frac{T_{evap.} - T_{ambient}}{q} \tag{3}$$

2.2. Uncertainty Analysis

As stated by Holman [9], multiple measurements are taken, each carrying a certain level of uncertainty, with equal probabilities assigned to these uncertainties. The uncertainty in the calculated outcome is then derived from the uncertainties in the primary measurements. The thermal resistance, R_{th}, is calculated based on a particular function of independent variables, including (T_{evap}, $T_{ambient}$, in, I, V), as follows:

$$R_{th} = R_{th}(T_{evap.},\ T_{ambient},\ I,\ V) \tag{4}$$

The Kline and McClintock [10] method was used to calculate the experimental uncertainty as shown below:

$$\varepsilon_{R_{th}}^2 = \left(\frac{\partial \varepsilon_{R_{th}}}{\partial I}\varepsilon_I\right)^2 + \left(\frac{\partial \varepsilon_{R_{th}}}{\partial V}\varepsilon_V\right)^2 + \left(\frac{\partial \varepsilon_{R_{th}}}{\partial T_{evap.}}\varepsilon_{T_{evap.}}\right)^2 + \left(\frac{\partial \varepsilon_{R_{th}}}{\partial T_{ambient}}\varepsilon_{T_{ambient}}\right)^2 \tag{5}$$

The uncertainty calculated from aforementioned equation for the thermal resistance fall within 1.4% to 2.1%.

3. Results and Discussion

This study examined the effects of filling ratio, heating power, inclination angle, and alternative refrigerant on the thermal performance of the RBFT module through experimentation. The impact of each parameter is explained in the following subsections.

3.1. Filling Ratio & Heating Power

In the current study, R-1233zd is employed as a working fluid due to limitations arising from the pressure design of the module and the compatibility of aluminum with this refrigerant. R-1233zd is also favored for its low global warming potential (GWP) and non-ozone-depleting properties, making it an environmentally friendly alternative to traditional high-GWP refrigerants like R-123 or R-134a.

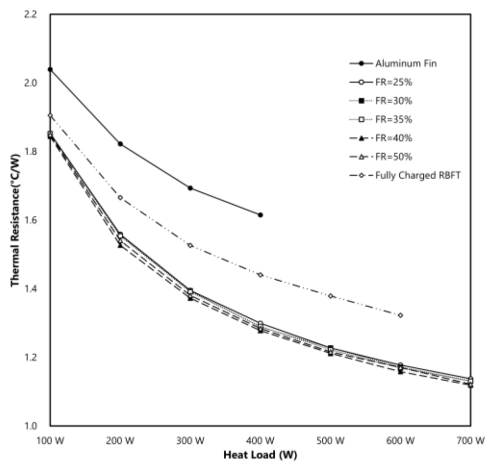

Figure 5. Thermal resistance changes with different heating loads.

In order to evaluate the relationship between filling ratio and the thermal performance of the module, five different filling ratios were considered, and the results were compared with the vacuum condition (aluminum fin) and the fully charged sample to establish a benchmark for assessing the improvement of the RBFT.

From Figures 5 and 6, it can be concluded that the thermal resistance of the module decreases with increasing heating power and filling ratio.

According to Figure 6, the difference in thermal resistance between filling ratios of 25% and 40%, which is considered the optimum filling ratio, is approximately 1%, 1.4%, and 1.7% for low, moderate, and high heat flux, respectively.

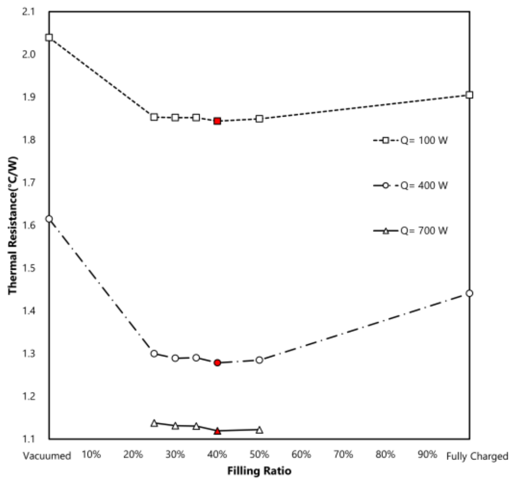

Figure 6. Variation of thermal resistance with different filling ratios and optimum filling ratio.

Since it is expected that the filling ratio affects performance more significantly, this unusual behavior of the RBFT module can be explained as follows. The RBFT single fin is divided into two parts: the bottom side, which functions like a classical fin, and the top part, which is an RBFT. Accordingly, a portion of the heat is dissipated from the fin part, which may affect the start-up time of the RBFT.

Another reason can be derived from the temperature distribution on a single RBFT, gathered using 12 thermocouples attached to its surface. As shown in Figure 7, the temperature differences between thermocouples number 4, 5, 6, and 7 are nearly the same, at around 98 to 98.5 °C for the high heating power (600 W), while the temperatures of thermocouples number 8 and 9 are approximately 3 °C and 6 °C lower, respectively. The temperatures of thermocouples number 1, 2, and 3 are 93.8 °C, 92 °C, and 95 °C, respectively.

Based on the temperature distribution, we can conclude that the fin operates effectively in the lower and middle parts where thermocouples 4 to 9 are attached. However, for the top section where thermocouples 1 to 3 are attached, the temperature distribution is not uniform. The thermal resistance of the RBFT module decreases by 10% for low heating power and by 26.3% for moderate heating loads compared to a classic aluminum fin.

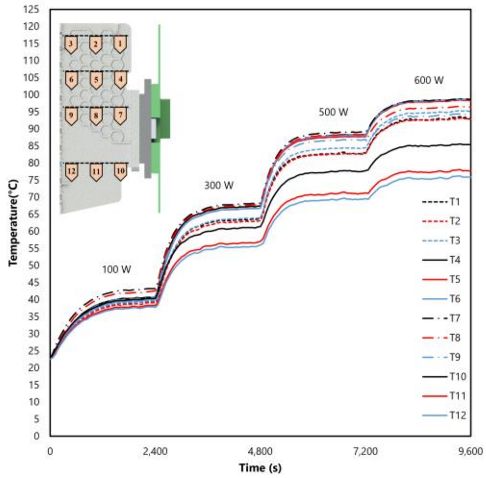

Figure 7. Temperature distribution of a single RBFT fin.

3.2. Inclination Angle

The AAU of 5G is installed outdoors, and the RBFT is also mounted to dissipate the heat generated in the 5G AAU; thus, the module may tilt due to external forces such as wind. Therefore, investigating the inclination angle of the RBFT module becomes important. The schematic of the angles examined for the module is depicted in Figure 8, which includes 60°, 75°, 85°, 90°, 95°, 105°, and 120°.

According to the experimental results for a given filling ratio shown in Figure 8, the optimal functioning angle for this module is 90°. The graph indicates that for low heat loads, the difference in thermal resistance at different angles compared to the vertical position is greater than for moderate and high heating powers. As the heat load increases, the thermal resistance of the module declines for all angles.

On one hand, when the sample is tilted from the vertical position to 60°, the interface between the liquid and vapor phases increases, which should enhance the thermal performance of the module. On the other hand, the airflow inside the pitch between the RBFT fins decreases, as the air flows through the bottom of the module, and some of the heated air is reflected towards the fin by the top part of the bakelite plate behind the tested module. Consequently, the temperature of the fin surface may increase.

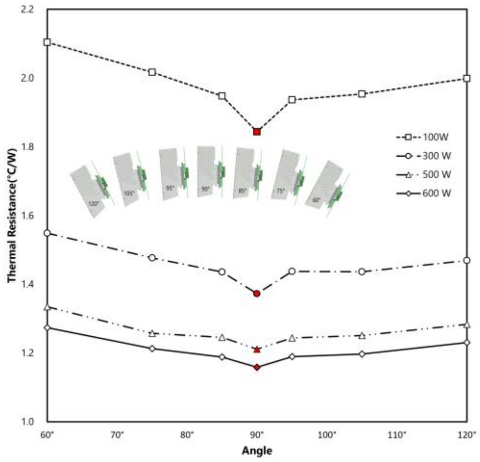

Figure 8. Thermal resistance vs. tilt angle and the optimal working angle of the module.

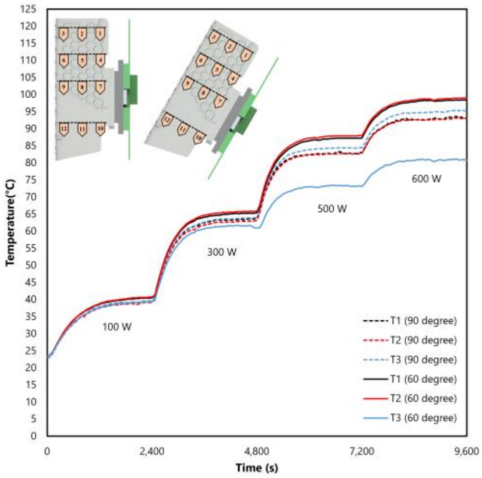

Figure 9. Temperature distribution comparison of thermocouples 1 to 3 in 60° and 90° position.

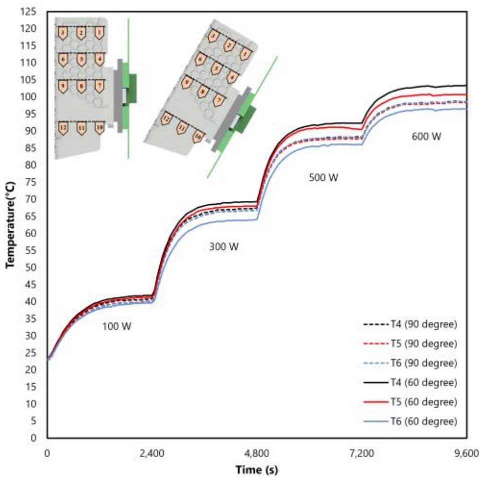

Figure 10. Temperature distribution comparison of thermocouples 4 to 6 in 60° and 90° position.

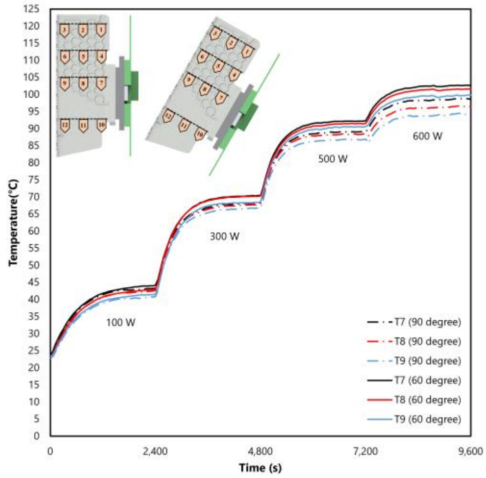

Figure 11. Temperature distribution comparison of thermocouples 9 to 10 in 60° and 90° position.

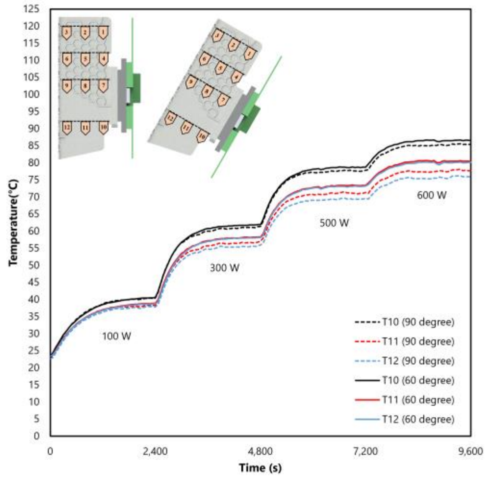

Figure 12. Temperature distribution comparison of thermocouples 10 to 12 in 60° and 90° position.

The temperature distribution, as shown in Figures 9 to 12, illustrates the comparison between the corresponding thermocouples at the 60° and 90° positions for the module.

The reverse situation occurs in the 120° position of the module. Although airflow through the fins increases, less liquid contacts the heaters, resulting in decreased thermal performance of the module. Overall, at a given heat load and filling ratio, the 120° angle indicates a higher thermal resistance compared to the 60° position. This suggests that airflow and natural convection have a dominant impact on the performance of the entire module.

3.3. Alternative Refrigerant

When comparing R-600a (isobutane) with R-1233zd as potential working fluids, several factors need to be considered. R-600a exhibits a higher latent heat of vaporization, leading to greater cooling capacity at lower mass flow rates, whereas R-1233zd operates at lower pressures, making it suitable for low-pressure systems like the present RBFT module. In terms of environmental impact, R-600a has a very low global warming potential (GWP) of approximately 3, while R-1233zd, with a GWP below 1, is similarly environmentally friendly.

However, safety is a key differentiator: R-600a is a flammable refrigerant (A3 classification), requiring stringent safety measures, which limits its application in certain environments. In contrast, R-1233zd is non-flammable (A1 classification), offering more flexibility in industrial applications. Both refrigerants demonstrate energy efficiency benefits, with R-600a being widely used in small-scale systems like domestic refrigeration due to its high efficiency, while R-1233zd is more suitable for large-scale systems such as chillers and heat pumps.

The choice between these refrigerants depends on the specific application requirements, balancing environmental considerations, safety, and thermodynamic performance. Figure 13 demonstrates the thermal resistance versus heating power for R-1233zd and R-600a as alternatives for different filling ratios. While the best filling ratio for the module filled with R-1233zd is 40%, the thermal resistance of the module filled with R-600a is highest at this filling ratio. According to the results, the optimum filling ratio for R-600a is 25%. The figure of merit is a suitable scale for choosing the proper alternative refrigerant.

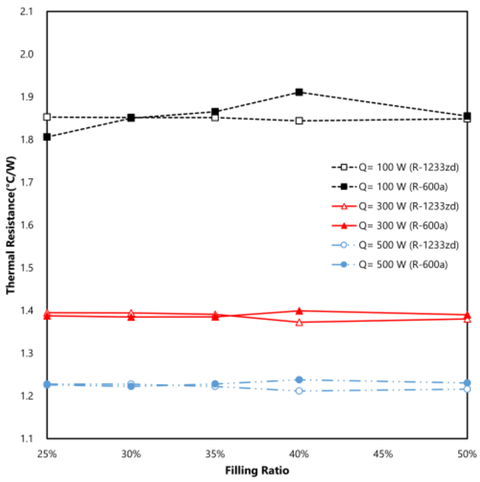

Figure 13. The effect of different refrigerant, filling ratio, and heating powers on thermal resistance.

4. Conclusions

Overall, the following points can be extracted from the current experimental investigation:

Despite some design deficiencies, the module can dissipate a heat load of 600 W with a temperature of less than 110 °C.

Since the optimum filling ratio for R-1233zd is 40% and only shows around a 2% improvement at high heat loads, it is prudent to consider large-scale production costs associated with charging the module with refrigerant. Therefore, it is suggested to sacrifice this small improvement in favor of production cost and consider a filling ratio between 25% and 30%.

The best working angle for this module is 90°; however, some modifications to the sample may lead to better performance.

R-600a can be used as an alternative to R-1233zd; however, safety and pressure issues related to the module should be considered.

5. ACKNOWLEDGEMENTS

We want to appreciate the financial support from the Taiwan Ministry of Science and Technology under grant number 111-2221-E-A49-090-MY3. We also would like to express our sincere gratitude to Cooler Master Co. for their invaluable support in providing the experimental module used in this study. The last author acknowledges KMUTT for providing a Distinguished Visiting Professorship during a short visit to the Mechanical Engineering Department, KMUTT.

References

1. Deng, L.Q., et al., *Fabrication and thermal performance of a novel roll-bond flat thermosyphon.* Applied Thermal Engineering, 2020. **181**.
2. Deng, L.Q., et al., *Thermal study of the natural air cooling using roll bond flat heat pipe as plate fin under multi-heat source condition.* International Journal of Thermal Sciences, 2023. **183**.
3. Khodabandeh, R., *Thermal performance of a closed advanced two-phase thermosyphon loop for cooling of radio base stations at different operating conditions.* Applied Thermal Engineering, 2004. **24**(17-18): p. 2643-2655.
4. Wan, Y., et al., *Experimental Study of Composite Heat Pipe Radiator in Thermal Management of Electronic Components.* Energies, 2024. **17**(12).
5. Sacco, R., et al., *A multiscale thermo-fluid computational model for a two-phase cooling system.* Computer Methods in Applied Mechanics and Engineering, 2014. **282**: p. 239-268.
6. Take, K., Y. Furukawa, and S. Ushioda, *Fundamental investigation of roll bond heat pipe as heat spreader plate for notebook computers.* Ieee Transactions on Components and Packaging Technologies, 2000. **23**(1): p. 80-85.
7. Gradinger, T.B. and F. Agostini, *Assessment of Two-Phase Cooling of Power Electronics Using Roll-Bonded Condensers.* Journal of Thermal Science and Engineering Applications, 2015. **7**(1).
8. Gan, K., et al., *Development and experimental study of a 3-dimensional enhanced heat pipe*

radiator for cooling high-power electronic devices. Applied Thermal Engineering, 2024. **238**.

9. Holman, J.P., *Experimental methods for engineers*. 8th ed. McGraw-Hill series in mechanical engineering. 2012, Boston: McGraw-Hill/Connect Learn Succeed. xix, 739 p.

10. Kline, S., *McClintock, 1953. Describing Uncertainties in Single-Sample Experiments.* Mechanical engineering, 1953. **75**(3): p. 3-8.

Paper ID 112(S2A)

Comparative Study on Operational Characteristics of Polymer Pulsating Heat Pipes in Different Orientations

Zhengyuan Pei and Yasushi Koito*

Kumamoto University, Kumamoto, Japan
* *Corresponding author email address: koito@gpo.kumamoto-u.ac.jp*

Abstract
Flow patterns and heat transfer characteristics of the polymer PHP with HFE-7100 were compared in horizontal, vertical, and sideways orientation modes. Extended experiments were conducted with visualization. In the experiments, the temperatures at evaporator and condenser sections of the PHP were controlled, and the temperature distributions of the PHP were obtained using thermocouples. At the same time, the oscillating flow of the working fluid was captured with a high-speed camera. In the vertical orientation mode, the oscillating flows of the liquid slugs and vapor plugs of various lengths were found in the PHP. In the horizontal and sideways orientation modes, only long liquid slugs and vapor plugs were oscillating in the channel. When the filling ratio of the working fluid was around 60%, the operational characteristics of the PHP were substantially the same. However, in the sideways orientation modes, the thermal performance of the PHP was decreased when the filling ratio was decreased from 60% to 40%.

Keywords: Polymer pulsating heat pipe; Hydrofluoroether, Gravitational force; Thermal design

1. Introduction

When an appropriate amount of working fluid is enclosed in a serpentine channel, and then both ends of the channel are respectively heated and cooled, an oscillation flow of liquid slugs and vapor plugs of the working fluid is induced in the channel. A pulsating heat pipe (PHP) uses this oscillation phenomenon and transports heat passively from a heated to a cooled section. Traditionally, the PHPs are made of metal materials [1–3]. Copper and aluminum are often used as metal materials. However, in recent years, polymer materials are also used to fabricate the PHPs [46]. The use of polymer materials reduces the cost and weight of the PHPs. Besides, polymer materials make it possible to develop mechanically flexible and electrically non-conductive PHPs, which are advantages over metal PHPs.

In the authors' previous study [7], it was found that the distribution of liquid slugs and vapor plugs within a polymer PHP is greatly affected by the gravitational force when hydrofluoroether-7100 (HFE-7100) is used as the working fluid. When the PHP is oriented vertically, liquid slugs flow down and vapor plugs flow up, resulting in a completely separated distribution of the working fluid within the channel. In the present study, extended visualization experiments were conducted to compare the operational characteristics of the polymer PHP at different orientations. Fluid flow patterns and heat transfer characteristics of the PHP were compared in horizontal, vertical, and sideways orientation modes.

2. Experimental methods

A polymer PHP and an experimental apparatus were essentially the same as those shown in the authors' previous paper [8]; thus, their brief overviews are shown here. Figure 1 shows the schematic diagram of the PHP. A serpentine channel body of the PHP was fabricated directly onto a polycarbonate (PC) sheet with a thickness of 0.12 mm. In the serpentine channel body,

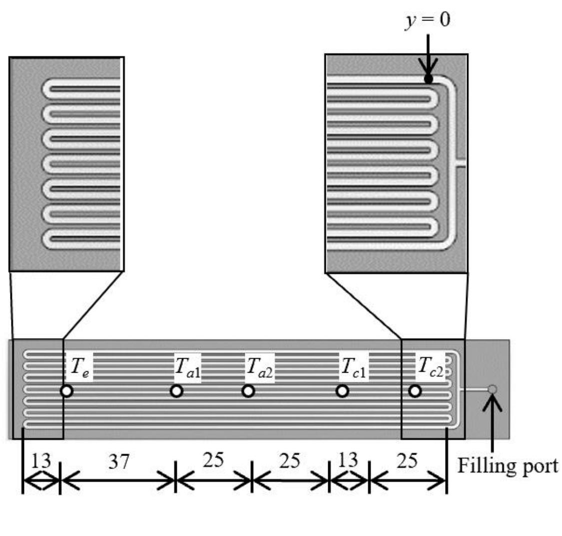

Figure 1. Schematic diagram of the polymer PHP.

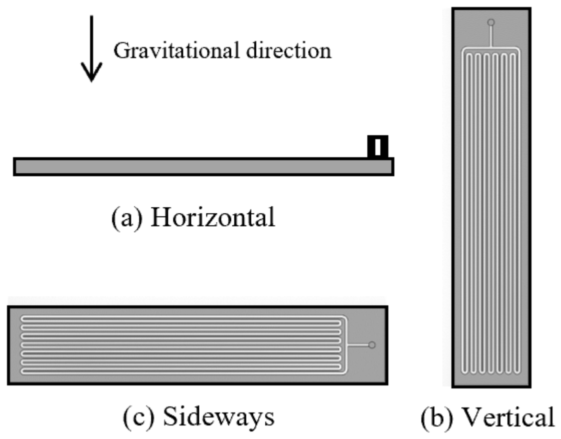

Figure 2. Orientation modes.

fourteen parallel channels were designed, and their ends were connected to form a serpentine channel. The cross-section of the channel was 1.3 mm wide and 1.1 mm high. The serpentine channel body was fabricated with a 3D printer using acrylonitrile butadiene styrene (ABS) filament. The outer surface of the serpentine channel body was chemically treated to maintain airtightness.

In the experiment, heating and cooling jackets were mounted on the PC sheet side of the PHP. Cooling water was supplied to the cooling jacket, while heating water was supplied to the heating jacket. Temporal changes in the temperatures at the evaporator (T_e), adiabatic (T_{a1}, T_{a2}), and condenser (T_{c1}, T_{c2}) sections were measured using thermocouples. At the same time, the oscillating flow of liquid slugs and vapor plugs of the working fluid was captured using a high-speed camera. Temperature measurement points are also shown in Figure 1. Video analyses were conducted using a video analysis software. Hydrofluoroether-7100 (HFE-7100) was used as the working fluid. Figure 2 shows (a) horizontal, (b) vertical, and (c) sideways orientation modes. The experiments in the horizontal orientation mode were already conducted in the authors' previous study [9]. The extended experiments were conducted in the vertical and sideways orientation modes.

3. Results and discussion

Figure 3 compares the flow patterns in the (a) vertical and (b) sideways orientation modes. The vertical axis is the distance (y) from the end of the condenser section, and the horizontal axis is the time from the start of video analyses. y = 0 is

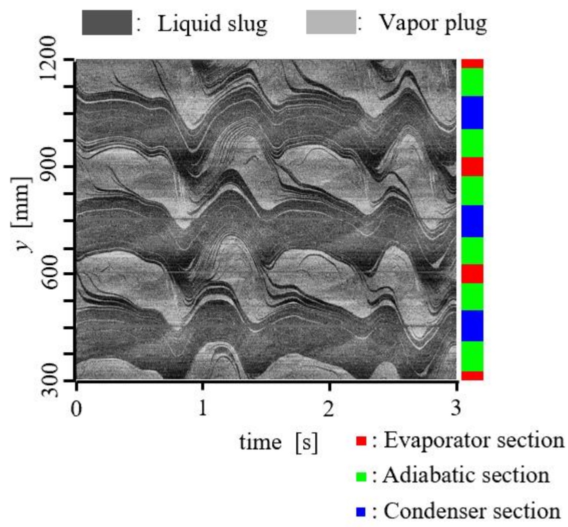

(a) Vertical (V = 59.7%)

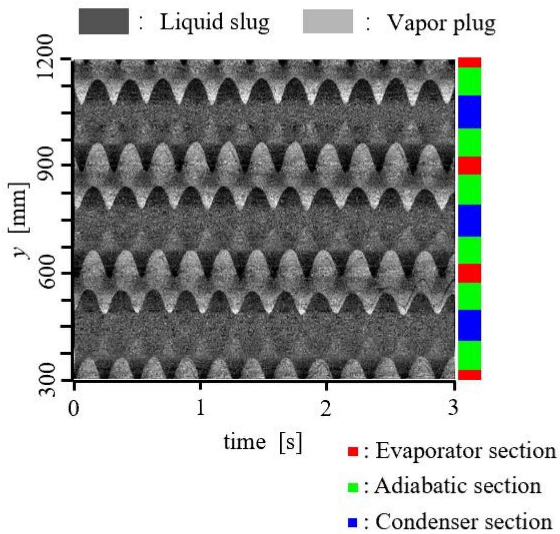

(b) Sideways (V = 64.7%)

Figure 3. Flow patterns in the PHP.

indicated in Figure 1. The evaporator, adiabatic, and condenser sections are also indicated using red, green, and blue colors, respectively. The dark region is liquid slugs, while the light color implies vapor plugs. In the vertical orientation modes, liquid slugs and vapor plugs of various lengths were distributed, and their randomly oscillating flows were found in the serpentine channel. In the sideways orientation mode, on the other hand, only long liquid slugs and vapor plugs were oscillating in the channel. In addition, the long liquid slugs and vapor plugs were oscillating in every two channels with almost the same amplitude, period, and center of oscillation. Under the condition that V was around 60%, almost the same flow patterns of liquid slugs and vapor plugs

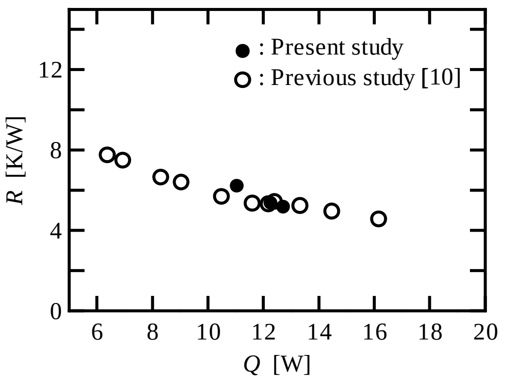

Figure 4. Thermal resistance of the PHP (vertical orientation mode).

were also obtained in the horizontal orientation mode. The details are shown below.

The thermal resistance (R) of the heat pipe was evaluated by

$$R = \frac{T_e - T_c}{Q} \quad (1)$$

where Q is the heat transfer rate of the heat pipe, T_e and T_c are the temperatures at the evaporator and condenser sections of the PHP, respectively. The Q value was obtained from an enthalpy balance of the cooling jacket, and T_c was the average of T_{c1} and T_{c2}.

Figure 4 shows the R values in the vertical orientation mode. The experimental results obtained in the present study are compared with those in the previous study [10]. Note that the polymer PHP with the same dimensions was used in these studies. In the present study, the evaporator temperature of the PHP was controlled by using a heating jacket, and the results in Figure 4 were obtained by changing V as 44.5%, 59.7%, and 64.7% at T_e = 89°C. In the previous study, on the other hand, the PHP was heated using an electrical heater. The electrical power to the heater was changed from 9.0 W to 19.0 W at V = 65.7%, and the results in Figure 4 were obtained. The heating methods were essentially different between the present and previous studies; however, no clear difference was found in R between these studies, which implies that the operational characteristics of the polymer PHPs are hardly affected by the difference in the heating method.

Figure 5 compares the oscillation characteristics of long liquid slugs for the sideways and horizontal [9] orientation modes. The comparison was made at around V = 60% regarding the position of the center of oscillation

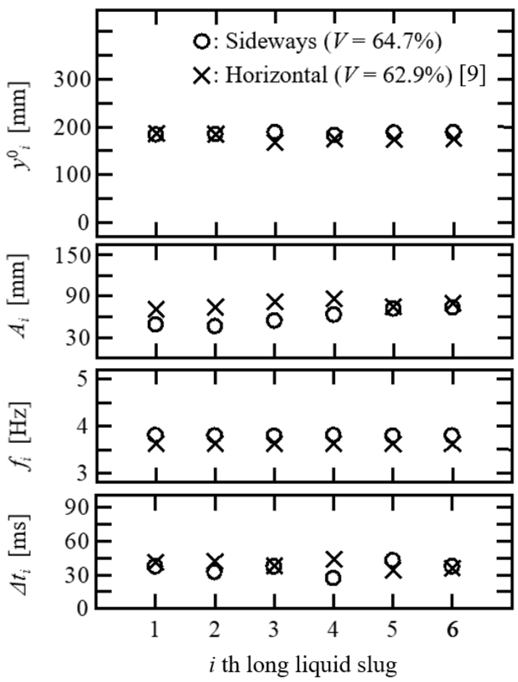

Figure 5. Comparison between sideways and horizontal orientation modes when V was around 60%.

(y^0_i), amplitude (A_i), frequency (f_i), and time difference (Δt_i) of the i th long liquid slug, which was counted from the side closest to y = 0. y^0_i is the distance from the end of each channel on the evaporator side. Δt_i was defined by a time difference between the i th and i+1 th long liquid slugs except for Δt_6. The time difference between the 6th and 1st long liquid slugs was used for Δt_6. As mentioned earlier, the flow patterns of liquid slugs and vapor plugs were almost the same in the sideways and horizontal orientation modes. Moreover, it was confirmed that all the long liquid slugs were oscillating with almost the same values of y^0_i, A_i, f_i, and Δt_i. The Q values for the sideways and horizontal orientation modes were 7.4 W and 8.1 W, respectively. Although slight differences were found in Figure 5, these Q values confirmed that the operational characteristics of the PHP were substantially the same at around V = 60% in the sideways and horizontal orientation modes.

Figure 6 shows the flow pattern in the sideways orientation mode at V = 40.6%. Although the oscillations of liquid slugs and vapor plugs were still observed, the center of oscillation varied with time, which implies that the oscillation became unstable when V was decreased from 60% to 40%. In the horizontal orientation mode, however, continuous oscillations like Figure 3 (b) were

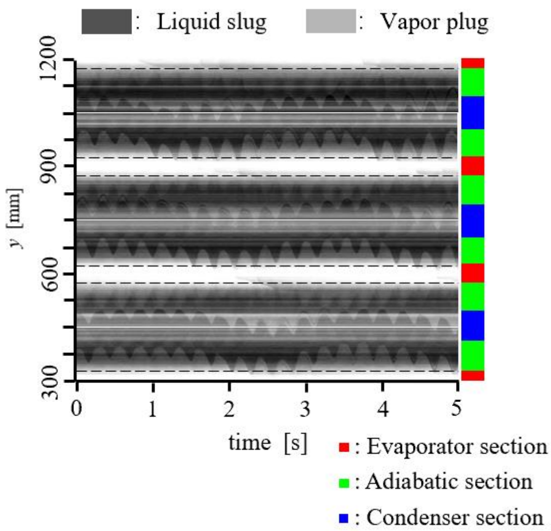

Figure 6. Flow pattern in the sideways orientation mode (V = 37.7%).

observed at V = 37.7% with almost the same position of the center of oscillation. The Q values for the sideways and horizontal orientation modes were 7.7 W and 11.0 W, respectively. These values were obtained at V = 37.7% and 40.6%, respectively. Differing from the horizontal orientation mode, the oscillation became unstable in the sideways orientation mode at around V = 40%, resulting in the decrease in the thermal performance of the PHP.

4. Conclusions

The operational characteristics of the polymer PHP with HFE-7100 were compared in horizontal, vertical, and sideways orientation modes. In the vertical orientation mode, the liquid slugs and vapor plugs of various lengths were distributed, and their randomly oscillating flows were found in the serpentine channel. In the horizontal and sideways orientation modes, on the other hand, only long liquid slugs and vapor plugs were oscillating in the channel. When the filling ratio of the working fluid was around 60%, the operational characteristics of the PHP were substantially the same in the horizontal and sideways orientation modes. However, in the sideways orientation mode, differing from the horizontal orientation mode, the thermal performance of the PHP was decreased when the filling ratio was decreased from 60% to 40%.

5. Acknowledgements

This work was supported by JSPS KAKENHI Grant Number 22K03947.

References

[1] P. Sakulchangsatjatai, M. Siritan, R. Wanison, and N. Kammuang-Lue, Correlation to predict thermal characteristics of pulsating heat pipes with long evaporator section. Applied Thermal Engineering, 2024. 254: 123868.

[2] A. Kumar, S. Singh, R. Kumar, and A. Kumar Das, Evaluation of thermo-fluidic performance of micro pulsating heat pipe with and without evaporator side surface structures. Applied Thermal Engineering, 2024. 249: 123470.

[3] W. Wang, T. Liu, J. Guo, B. Li, H. Zhang, Y. Cai, F. Zhao, and D. Liu, Experimental investigation on the thermal performance of high-concentrated photovoltaic module utilizing the thermal sink of a novel Fan-shaped plate pulsating heat pipe. Applied Energy, 2025. 377: 124365.

[4] J. Lim and S.J. Kim, Fabrication and experimental evaluation of a polymer-based flexible pulsating heat pipe. Energy Conversion and Management, 2018. 156: p. 358.

[5] T. Arai and M, Kawaji, Thermal performance and flow characteristics in additive manufactured polycarbonate pulsating heat pipes with Novec 7000. Applied Thermal Engineering, 2021. 197: 117273.

[6] A.A. Alqahtani, S. Edwardson, M. Marengo, and V, Bertola, Performance of flat-plate, flexible polymeric pulsating heat pipes at different bending angles. Applied Thermal Engineering, 2022. 216: 118948.

[7] Z. Pei and Y. Koito, Fluid distributions and flow characteristics in a polymer pulsating heat pipe: visualization experiments using HFE as a working fluid. Proceedings of the 33rd International Symposium on Transport Phenomena, 2023. 105.

[8] Y. Koito, H. Yoshida, and Z. Pei, An experimental study of a polymer pulsating heat pipe 3D-printed on a thin polymer sheet. Multiphase Science and Technology, 2021. 33(4): p. 31.

[9] Z. Pei and Y. Koito, Experimental analyses of flow pattern and heat transfer in a horizontally oriented polymer pulsating heat pipe with merged liquid slugs. Frontiers in Heat and Mass Transfer, 2024. (under review).

[10] N. Nagasato, Z. Pei, and Y. Koito, Flow patterns and heat transfer characteristics of a polymer pulsating heat pipe filled with hydrofluoroether. Frontiers in Heat and Mass Transfer, 2024. 22: p. 49.

Paper ID 114

Current development of the thermal hydraulic code AC²/ATHLET for the high-temperature heat pipe simulation

Daniel Eckert[1*], Fabian Weyermann[1] and Jörg Starflinger[2]

[1] *Gesellschaft für Anlagen- und Reaktorsicherheit (GRS) gGmbH, Cologne, Germany*
[2] *Institute of Nuclear Technology and Energy Systems (IKE), University of Stuttgart, Stuttgart, Germany*
**Corresponding author email address: daniel.eckert@grs.de*

Abstract

For the analysis of heat pipe-cooled micro modular reactors, the thermal hydraulic code AC²/ATHLET is currently extended for the high-temperature heat pipe simulation. Property packages for sodium and potassium are available in the latest program version. The current development state of the heat pipe module for horizontally orientated heat pipes is presented here. It includes models for the capillary pumping, the radial heat transfer, the phase change, axial pressure drop and horizontal pooling. Two demonstration cases were simulated. 1) The heat pipe of a reactor concept was simulated at different power levels. The result matches very well the analyze of the INL. 2) An experimental investigation of a potassium heat pipe was simulated and compared with the test results. It was shown that the 1-D heat pipe simulation module can be used for the efficient prediction of the temperatures within horizontal high-temperature heat pipes.

Keywords: High-temperature heat pipe; Transient 1-D simulation; Thermal hydraulics, Reactor safety analyze

1. Introduction

Heat pipe-cooled micro modular reactors (HP-MMR) are small, mobile systems designed for off-grid or micro-gird operations [1–4]. Utilizing passively working, alkali metal-filled heat pipes (HP) for core heat removal, such concepts avoid high pressures in the core region [5]. The core consists of a solid steel monolith, which is perforated to contain a high number of fuel rods and heat pipes (see Figure 1). The heat pipes are connected to a primary heat exchanger to supply heat to the energy conversion unit during regular operation. The energy conversion unit is a Brayton cycle which is either based on air or super-critical CO_2. The length of the integrated HPs can be up to several meters [3,4]. They operate at high temperatures for thermal efficiency and are often filled with sodium or potassium [6]. An annular wick or a screen-covered grooved wick is often preferred due to their low flow resistances [7,8]. The local power production differs within the core. Different heat pipe power classes can be defined based on the radial position [9]. Due to the high number of heat pipes, the failure of one or multiple heat pipes is likely and the regular operation should be possible to continue though one or even two adjacent heat pipes fail [9].

Numerical tools are required for the safety assessment and analysis of HP-MMR [10,11]. The 1-D code THROHPUT was developed for the analysis of liquid metals during operation and start-up from solid state [12]. HPTAM is a 2-D heat pipe simulation software considering axial and radial flow [13]. SOCKEYE is a currently developed 1-D heat pipe analyze application based on the thermal hydraulic code RELAP-7 [14]. Shi et al. presented a 1-D, 3-field heat pipe model that accounts for vapor, liquid film and liquid droplets [15].

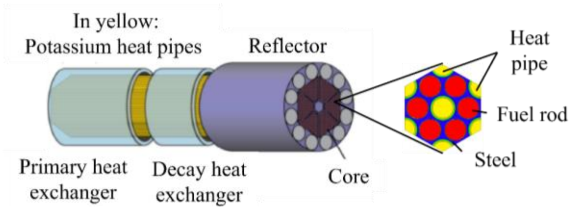

Figure 1. HP-MMR design [4].

The thermal hydraulic code AC²/ATHLET is part of the program package AC² developed by GRS [16]. It can be used for the transient simulation of the cooling circuit of a nuclear power plant and it enables the analysis of transients and design basis accidents [17]. For the transient simulation and analyze of HP-MMRs, AC²/ATHLET is currently extended for the heat pipe simulation. The goal is an efficient high-temperature heat pipe module that enables the transient simulation of heat pipes and predicts the thermal resistance and the operation limitations. It should be able to simulate different wick types, orientations, and filling ratios. A fluid property package covering liquid and vaporous potassium has recently been implemented [18], whereas sodium already existed as a fluid option in the beginning of the project. Hence, the two most relevant high-temperature heat pipe fluids, sodium and potassium, are available in the latest version of AC²/ATHLET.

This publication describes the current development state of the heat pipe module. The modelling for horizontally orientated heat pipes is presented and simulation results are compared to data from the literature.

2. Models and methods

AC²/ATHLET employs a transient, two-fluid model with conservation equations for mass, momentum, and energy for each phase on a one-dimensional grid [19]. The six solution variables are the temperatures of each phase T_v and T_l, the volumetric flow rate of each phase $w_v A$ and $w_l A$, the pressure p and the mass quality x.

The heat pipe module assumes the liquid inside the wick structure at the cylindrical heat pipe container and additionally within the vapor core if the wick is super-saturated and pooling occurs. The total flow cross section area A (Equation 1) is the sum of the cross-section area of the vapor core A_{vc} and the open flow area of the wick A_w (Equation 2). If the wick is an annulus behind a screen, A_w consists of the open flow area of the screen structure A_s and the annulus cross section area A_a. Here, D_w is the inner wick diameter, D_a is the inner annulus diameter, $D_{c,i}$ is the inner container diameter, and φ is the porosity.

$$A = A_{vc} + A_w \tag{1}$$

with

$$A_{vc} = \frac{\pi}{4} D_w^2$$

$$A_w = \begin{cases} \varphi \frac{\pi}{4}\left(D_{c,i}^2 - D_w^2\right) & homogen.wick \\ A_s + A_a & annulus\ wick \end{cases} \tag{2}$$

with

$$A_s = \varphi \frac{\pi}{4}\left(D_a^2 - D_w^2\right)$$

$$A_a = \frac{\pi}{4}\left(D_{c,i}^2 - D_a^2\right)$$

Two void thresholds α_0 and α_1 are defined which correlate to a flat interface and a maximal bent interface respectively (see Figure 2 and Equation 3). Here, $n_p(D)$ is the volumetric pore density per unit length at the diameter D, $V_{p,max}$ is the hemispherical volume of a pore, r_p is the effective pore radius of the wick structure. The porosity φ is utilized as a surface porosity for the prediction of n_p. The threshold α_2 (Equation 4) correlates to the inner position of the annulus if the heat pipe has an annulus behind a screen wick. α_2 is irrelevant for a homogeneous wick.

$$\alpha_0 = \frac{A_{vc}}{A}; \qquad \alpha_1 = \alpha_0 + n_p(D_w) \cdot V_{p,max} \tag{3}$$

with

$$n_p(D) = \frac{\varphi D}{\pi r_p^2 A}; \qquad V_{p,max} = \frac{2}{3}\pi r_p^3$$

$$\alpha_2 = \frac{A_{vc}+A_s}{A} + n_p(D_a) V_{p,max} \tag{4}$$

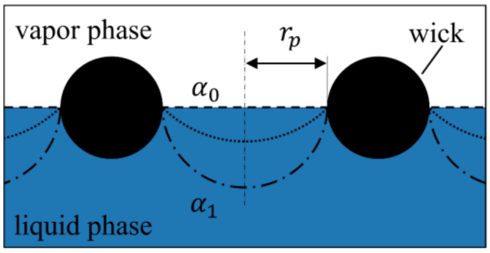

Figure 2. Interface in a pore.

In case of a super-saturated wick in a horizontally orientated heat pipe, a flat pool and a flat interface in the pores are assumed as shown in Figure 3 (Left). Here, θ is the central angle, c is the chord length, and a is the arc length. Figure 3 (Right) shows the assumed cross section only used by the heat transfer model in the case of pooling, which will be described further below.

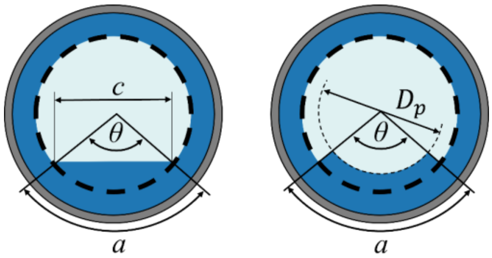

Figure 3. Cross section of a heat pipe with horizontal pool: (Left) Assumed phase distribution; (Right) Radial heat transfer model.

The liquid momentum conservation (Equation 5) includes the liquid density ρ_l, the liquid velocity w_l, the time t, the length s, the gradient of pressure p and the capillary pressure difference Δp_{cap}, the standard gravity force $\vec{g}$, the liquid friction term F_l, the interfacial friction F_δ,the momentum exchange due to phase change M_δ, and the liquid level force F_{LL}. The closure terms are described in detail below.

$$\frac{\partial(1-\alpha)\rho_l w_l}{\partial t} + \frac{\partial(1-\alpha)\rho_l w_l^2}{\partial s} = (1-\alpha) \cdot \left[-\frac{\partial(p-\Delta p_{cap})}{\partial s} + \rho_l \vec{g} + F_l + F_\delta + M_\delta + F_{LL}\right] \tag{5}$$

The gradient of Δp_{cap} enables the capillary pumping of the liquid. Δp_{cap} is based on the surface tension σ, the effective pore radius of the wick structure r_p, and the factor $f_{cap}(\alpha)$ which expresses the shape of the interface based on the void (see

Equation 6). It is equal to zero if the wick is super-saturated and the interface is assumed to be flat ($\alpha \leq \alpha_0$). On the other hand, it is equal to one if the wick is sub-saturated and the interface is assumed to be bend to its maximum ($\alpha \geq \alpha_1$). In between a smooth transition is realized based on the sinus-shaped function $f_{sin}(\alpha)$ shown in Figure 4. It is assumed that the capillarity in a sub-saturated wick is always active even in a partly filled annulus.

$$\Delta p_{cap} = \frac{2\sigma(T_l)}{r_p} f_{cap}(\alpha) \quad (6)$$

with

$$f_{cap}(\alpha) = \begin{cases} 0 & \alpha \leq \alpha_0 \\ f_{sin}(\alpha) & otherwise \\ 1 & \alpha \geq \alpha_1 \end{cases}$$

$$f_{sin}(\alpha) = 0.5 \cdot \left[1 + \sin\left(\frac{\pi}{2} \cdot \frac{\alpha - 0.5(\alpha_0 + \alpha_1)}{\alpha_1 - 0.5(\alpha_0 + \alpha_1)}\right)\right]$$

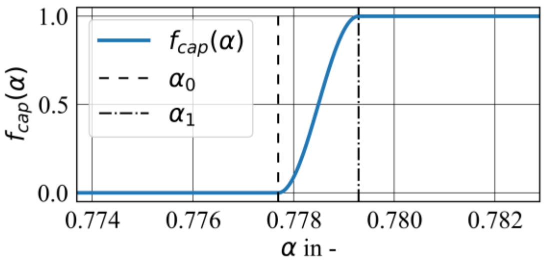

Figure 4. Capillary factor $f_{cap}(\alpha)$ of the reference heat pipe.

If Δp_{cap} is greater than zero, AC²/ATHLET is able to distinguish between a vapor pressure p_v which is now exclusively equal to the solution variable p and the liquid pressure p_l:

$$p_v = p \quad (7)$$

$$p_l = p - \Delta p_{cap} \quad (8)$$

The liquid flow through an annulus or a groove wick can be expected to be slow and laminar [20], and is computed based on Darcy's law (Equation 9) with the permeability K and the liquid viscosity μ_l. The pressure drop of flow through porous wicks is computed including an inertia term with the drag coefficient $C_E = 0.55$ [20].

$$F_l = \begin{cases} -\frac{\mu_l \varphi w_l}{K} & \text{annulus wick} \\ -\frac{\mu_l \varphi w_l}{K} - \frac{C_E}{\sqrt{K}} \rho_l w_l |w_l| & \text{porous wick} \end{cases} \quad (9)$$

If the wick is not super-saturated ($\alpha_0 \leq \alpha$), it is assumed that the wick bears the momentum exchange with the vapor and F_δ and M_δ are equal to zero. If the wick is super-saturated, the liquid will bear a fraction of it based on the factor ω (see Equation 10). M_δ is calculated by Equation 11 with the phase change flux ψ_δ which is negative for condensation. The computation of F_δ (Equation 12) considers the pressure drop per unit length in the vapor F_v (described further below in Equation 21).

$$\omega = \begin{cases} 0 & \alpha_0 \leq \alpha \\ \frac{c}{c + (2\pi - \theta) D_w} & \alpha < \alpha_0 \end{cases} \quad (10)$$

$$M_\delta = \omega w_v \psi_\delta \quad (11)$$

$$F_\delta = \omega \frac{-\alpha}{1-\alpha} F_v \quad (12)$$

Pooling in horizontally orientated pipes creates a geodetic force perpendicular to the pipe axis. Its effect on the liquid momentum is expressed by the liquid level force F_{LL} [21].

The solution variable T_l, which the computation of the liquid enthalpy is based on, is the temperature at the liquid center line with diameter D_l (defined by Equation 13) with the interface diameter D_δ (Equation 14). The radial heat transfer through a not super-saturated wick is predicted based on a conduction model considering the radial thermal resistance R. To model the radial heat transfer in the liquid energy conservation equation, the radial heat transport is split into two parts. One between the inner container wall with diameter $D_{c,i}$ and the liquid center line (Equation 15) and another between the liquid center line and the interface at diameter D_δ (Equation 16). The effective wick conductivity k_{eff} is computed based on a correlation from Table 3.4 in Faghri's book [20].

$$D_l = \frac{D_{c,i} + D_\delta}{2} \quad (13)$$

$$D_\delta = \begin{cases} \sqrt{\alpha \frac{4}{\pi} A} & \alpha \leq \alpha_0 \\ \sqrt{D_w^2 + \frac{4}{\pi\varphi}(\alpha A - A_v)} & \alpha_0 < \alpha \leq \alpha_2 \\ \sqrt{D_{c,i}^2 - \frac{4}{\pi}(1-\alpha) A} & \alpha_2 < \alpha \end{cases} \quad (14)$$

$$R_{c,i-l} = \frac{\ln\left(\frac{D_{c,i}}{D_l}\right)}{2\pi\, k_{eff}} \quad (15)$$

$$R_{l-w/\delta} = \frac{\ln\left(\frac{D_l}{\max(D_\delta, D_w)}\right)}{2\pi\, k_{eff}} \quad (16)$$

If the wick is super-saturated, the additional thermal resistance between the inner wick surface and interface is approximated by the conduction model in Equation 17. The assumed phase distribution is shown in Figure 3 (Right) with the inner, horizontal pool diameter D_p.

$$R_{w-\delta} = \frac{\theta}{2\pi} \cdot \frac{\ln\left(\frac{D_w}{D_p}\right)}{2\pi\, k_l} \quad \text{if } \alpha < \alpha_0 \quad (17)$$

The phase change mass flux at the interface $\dot{m}_\delta$ is predicted based on kinetics theory (Equation 18) using the specific gas constant R_m and the accommodation factor $\hat{\sigma}$ [22,23]. Latter is user-provided and often assumed to be equal to one for liquid alkali metals. The free interfacial area per unit length a_{int} is approximated by Equation 19.

$$\dot{m}_\delta = \frac{\hat{\sigma}}{1-0.4\hat{\sigma}} \sqrt{\frac{1}{2\pi R_m}} \left[\frac{p_{sat}(T_{l,\delta})}{\sqrt{T_{l,\delta}}} - \frac{p}{\sqrt{T_v}}\right] \qquad (18)$$

$$a_{int} = \begin{cases} (2\pi - \theta)a_{int,0} + c & \alpha < \alpha_0 \\ a_{int,0} & \alpha_0 \le \alpha \le \alpha_2 \\ \pi D_\delta & \alpha_2 < \alpha \end{cases} \qquad (19)$$

with

$$a_{int,0} = \varphi\pi \max(D_\delta, D_w)\left[1 + f_{cap}(\alpha)\right]$$

The interfacial temperature $T_{l,\delta}$ is computed based on an energy balance assuming a quasi-steady state at the interface. The implicit Equation 20 with the phase change enthalpy Δh is solved numerically.

$$\Delta h\, \dot{m}_\delta\, a_{int} = \frac{(T_l - T_{l,\delta})}{R_{l-\delta}} \cdot \pi D_\delta \qquad (20)$$

The pressure drop of the vapor flow due to friction (Equation 21) is predicted based on a Darcy friction factor f_v considering the laminar and the turbulent case of flow within a smooth pipe. The hydraulic diameter D_h is computed with Equation 22 considering different states.

$$F_v = \frac{1}{2} f_v \frac{\rho_v}{D_h} |w_v| w_v \qquad (21)$$

with

$$f_v = \max\left[\frac{64}{Re_v}, \frac{0.316}{Re_v^{0.25}}\right]$$

$$Re_v = \frac{w_v D_h}{\nu_v}$$

$$D_h = \begin{cases} D_w & \alpha_0 \le \alpha \\ \frac{(2\pi - \omega)D_w + c}{\alpha A} & \alpha < \alpha_0 \end{cases} \qquad (22)$$

Azimuthal symmetry (exception horizontal pooling) and identical temperature of liquid and wick are assumed. Nucleate boiling in the wick is neglected. The axial heat conduction in the wick and the wall is neglected since it is insignificant for low values of $K_{c,eff}$ [24], which is the case for high-temperature heat pipes. Here, k_c is the thermal conductivity of the container.

$$K_{c,eff} = \frac{k_c}{k_{eff}} \qquad (23)$$

The heat conduction module of AC²/ATHLET is used for the computation of the radial heat conduction in the heat pipe container [19].

For the computation of the fluid flow within the heat pipe, AC²/ATHLET applies a finite volume method. The solution of the equation system and the time integration is based on a linear-implicit Euler method in combination with a polynomial extrapolation up to the order 3 allowing error-controlled, adaptive time step size regulation [19].

3. Demonstration case 1: MMR heat pipe

3.1. Setup

The simulation of one heat pipe of the Special Purpose Reactor from Los Alamos National Laboratory [4] is used to verify the heat pipe module by comparing it to the analysis of the Idaho National Laboratory (INL) [9]. The parameters are listed in Table 1. According to [9], the fill is 100 g. Our analysis requires 120 g to saturate the entire wick and to create a little reservoir. The rods and the steel monolith are neglected, and heat is applied directly to the heat pipe container based on the axial power profile of the rods. The reactor concept utilizes an annulus heat exchanger to transfer heat from the heat pipe to the air inside the secondary system driving a Joule process. Latter is neglected and the heat exchanger is modelled with a fill and a pressure boundary condition (see Figure 5). The heat exchanger parameters are based on the analysis of the INL.

Heat pipe operation at five power levels were simulated (see Figure 6). Each was simulated for 5000 s to reach a stationary state and a change in power lasted 10 s. The power levels cover the following five cases [9]:

- Low power core region (3.7 kW)
- Medium power core region (4.5 kW)
- High power core region (5.4 kW)
- High power with 1 adjacent failure (6.3 kW)
- High power with 2 adjacent failures (7.3 kW)

Table 1. Heat pipe specifications.

Working fluid & mass	120 g Potassium
Orientation	Horizontal
Heat Pipe length	4 m
Inner heat pipe diameter	15.75 mm
Wall and wick material	S316
Wall thickness	2.0 mm
Wick type	Annulus behind screen
Annulus thickness	0.7 mm
Screen thickness	0.3 mm
Effective pore radius	15 µm
Screen Porosity	0.706
Heat Exchanger	Annulus with air flow
Air inlet temperature	452 °C
Air mass flow rate	20.12 g/s
Heat transfer coefficient	326 W/(m²K)

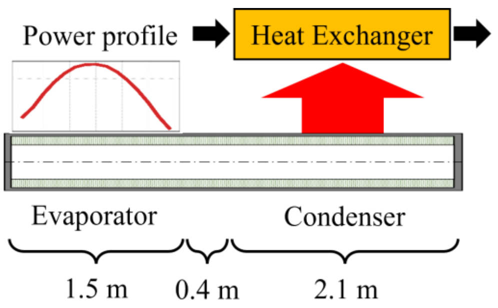

Figure 5. Demonstration case 1.

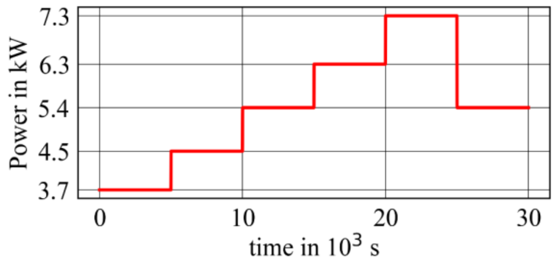

Figure 6. Course of the power. Power change within 10 s between each level.

3.2. Results

The steady state reached for 4.5 kW after 9000 s is presented. The axial velocity profile of the counter-current flow is presented in Figure 7. The adiabatic section can be identified by the zone in which the velocity gradients are zero.

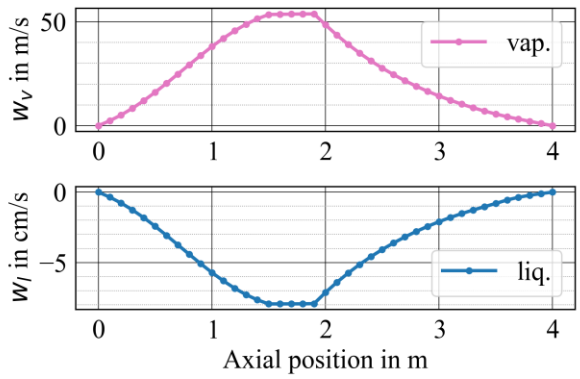

Figure 7. Axial velocity profile at 4.5 kW

The axial temperature profile at different radial positions is compared to the analysis of the INL in Figure 8a. The temperatures match generally very well. There is a difference in the prediction of the axial temperature drop on the vapor flow path. The simulation predicted a drop of 2.5 K and the INL analysis predicted around 4.5 K. Within the condenser both results predicted a near isothermal T_v profile due to pressure recovery. Figure 8b compares the radial temperature difference through the container wall ΔT_c or the wick ΔT_w (see Equation 24 and 25 respectively), which are nearly identical with the result of the INL.

$$\Delta T_c = T_{c,o} - T_{c,i} \tag{24}$$

$$\Delta T_w = T_{c,i} - T_v \tag{25}$$

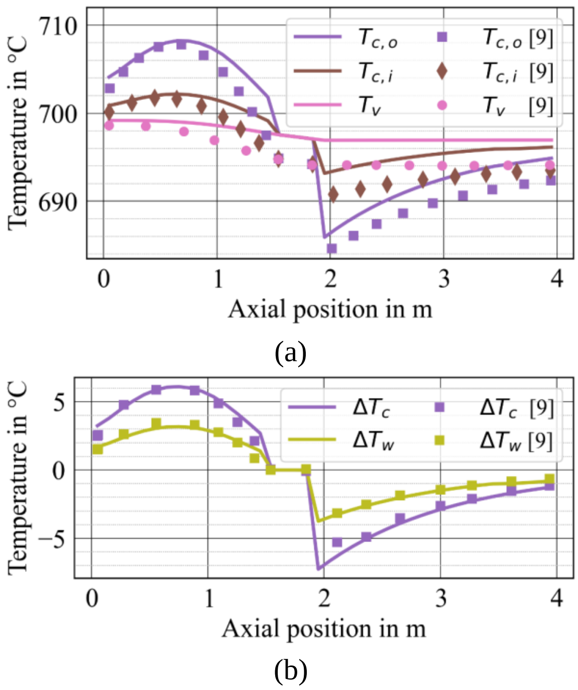

Figure 8. Comparison of the results for 4.5 kW with the result of the INL [9]: (a) Axial temperature profile at different radial positions; (b) radial temperature difference.

Figure 9 shows the pressure distribution in the phases. p_v is significantly affected by the pressure drop due to friction and due to acceleration. Deacceleration caused pressure recovery in the condenser. 25% of the capillary margin are consumed by the pressure losses. The wet point is around position 3.5 m and a small pool is predicted at the condenser end cap (see Figure 10a). As expected for the capillary pumping process, the void increases in the liquid flow direction and its value is between α_0 and α_1 (see Figure 10b).

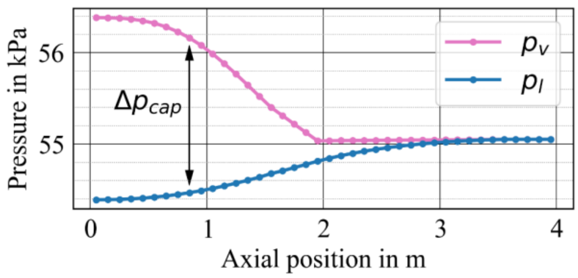

Figure 9. Axial pressure profile at 4.5 kW

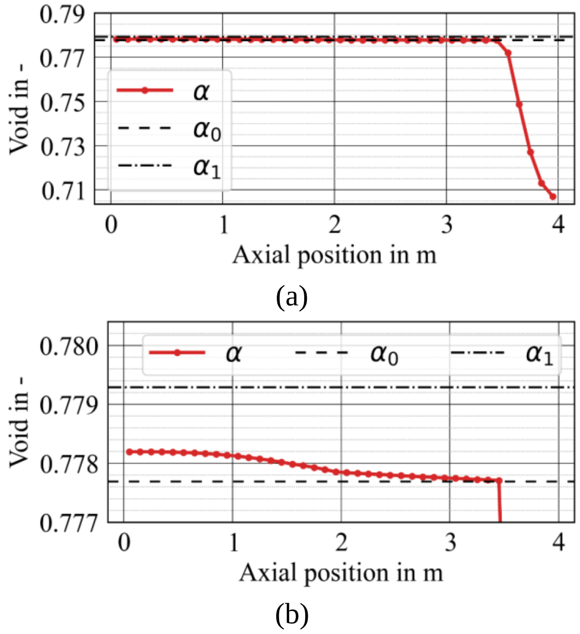

Figure 10. (a) Axial profile of the void at 4.5 kW. (b) detail view on active capillary pumping zone.

The thermal resistance of a heat pipe R_{HP} can be computed considering the power Q, the average outer container temperature of the evaporator $\bar{T}_{c,o}(evap.)$, and the average outer condenser temperature $\bar{T}_{c,o}(cond.)$ (see Equation 26). The axial thermal resistance R_{ax} considers the average vapor temperatures in the same fashion (Equation 27). Figure 11 presents the temporal course of R_{HP}, R_{ax}, and T_v in the adiabatic section. R_{HP} decreases with respect to higher power levels. The reason is the lower R_{ax} due to the higher saturated vapor density at higher operation temperatures.

$$R_{HP} = \frac{\bar{T}_{c,o}(evap.) - \bar{T}_{c,o}(cond.)}{Q} \tag{26}$$

$$R_{ax} = \frac{\bar{T}_v(evap.) - \bar{T}_v(cond.)}{Q} \tag{27}$$

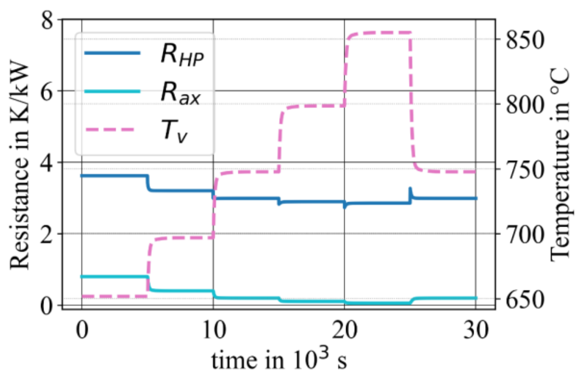

Figure 11. Thermal resistance and heat pipe temperature at power levels 3.7, 4.5, 5.4, 6.3 and 7.3 kW.

4. Demonstration case 2: Heat pipe experiments

4.1. Setup

Experiments of Wang et al. [25] were analyzed by Tien at al. [26] and they were simulated with the presented heat pipe module. The setup consists of a heat pipe, an electrical heater coil, insulation, thermocouples on the container wall at different axial positions, and an inclination apparatus. The cooling was provided by natural convection of the ambient air and radiation. Table 2 shows the parameters. According to the designer, the amount of filling is 15 g. Resulting from our analysis, much more is required to saturate the wick and thus, we interpreted the value as additional fill. We found the total liquid mass of 94 g by considering an evaporator pool mass of 15 g and additional liquid in the wick which is saturated up to the capillary pumping height. The filling process was assumed to happen at 100 °C with a vertically orientated heat pipe.

Table 2. Heat pipe specifications.

Working fluid & mass	94 g Potassium
Orientation	Horizontal
Heat Pipe length	0.8 m
Inner heat pipe diameter	21 mm
Wall and wick material	S316
Wick type	Wrapped screen 300 mesh
Wall / Wick thickness	4.5 mm / 4 mm [26]
Heat sink	Ambient air

The simulation model is similar to the one of demonstration case 1, but with a linear axial heating profile at the evaporator and without a heat exchanger model (see Figure 12). While experiments with different orientations were conducted, only three experiments of a horizontal, air-cooled heat pipe at different power levels were simulated and are discussed here. The heat transfer to the ambient air was approximated by assuming a homogeneous cooling profile. This approach was also done by [26].

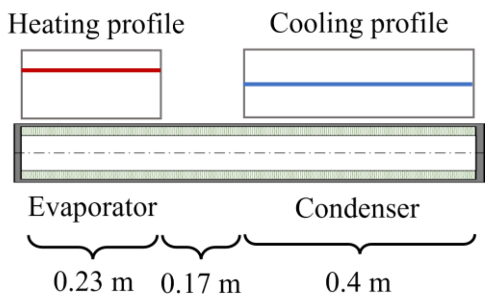

Figure 12. Demonstration case 2.

4.2. Results

The calculated axial temperature distribution is compared to the experimental data [25] and the simulation results of Tien et al. [26] in Figure 13. In general, they match very well. The temperatures at the positions 50 mm and 200 mm are outside the evaporator section and the experimental data shows a significant temperature difference between the two positions, which may be caused by a inhomogeneous axial heating power distribution [26]. Both simulations did not predict this, but predicted isothermal conditions in the evaporator, with temperatures between the two experimental data points respectively.

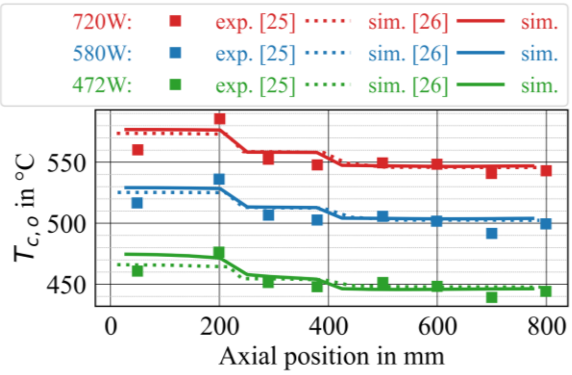

Figure 13. Axial temperature profile during the experiments [25], from [26] and our results.

The predicted thermal resistances are compared to calculated values based on the experimental temperatures and to calculated values based on the temperatures of [26] in Figure 14. The relative error of our analysis is presented in Table 3.

Table 3. Relative error.

472 W	580 W	720 W
19%	-5%	6%

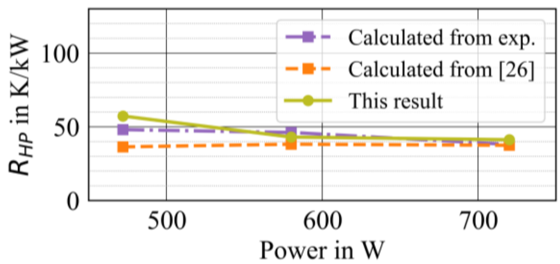

Figure 14. Thermal resistance.

5. Discussion

Regarding the results of demonstration case 1 and the comparison with the INL analysis, the correct implementation of the radial conduction model was verified. The axial vapor temperature profile depends on the axial vapor pressure. The INL analysis utilized probably another friction correlation. Regarding the results of demonstration case 2, the thermal resistances at 580 W and at 720 W were predicted very accurately and the value at 472 W was overpredicted to some extent. The verification with the INL analyze, and the simulation of the experiments showed that the presented heat pipe module can simulate a high-temperature heat pipe with good accuracy.

Multiple implemented models can affect the local temperatures and R_{HP}. The implemented conduction model can be interpreted as the upper limit of the radial thermal resistance of a wick since convection would enhance the radial heat transfer. Other relevant factors are the pressure drop of the vapor, the horizontal pool model, and the thermal conductivity of each of the liquid, the wick, and the container material. More experimental data should be used for the validation, which is also necessary for testing different operation conditions such as other orientations and heat transfer limitations.

The prediction of Δp_{cap} is not based on the geometry of the interface in a pore and a steeper and sharper increase with respect to α can be expected for a geometry-based model (see Figure 15a). Consequently, the presented model overestimates α within the bounds α_0 and α_1 and the liquid film thickness is little underestimated. However, this has no significant effect on other models, since the misprediction of the interface position is limited to r_p, which is tiny compared to the wick thickness of a typical heat pipe. We found that using a smooth function such as the proposed $f_{sin}(\alpha)$ can improve the numerical performance of AC²/ATHLET significantly compared to using a more realistic, geometry-based correlation. Larger time step sizes could be simulated as shown in Figure 15b, which significantly accelerates the iterative time integration and helps the efficient analysis of long operation periods. The total computational time consumption was significantly reduced (see Table 4). The predicted temperatures and the predicted thermal resistances were identically by both program versions respectively.

Table 4. Single-thread time consumption for Demonstration case 1.

$f_{cap}(\alpha)$ based on $f_{sin}(\alpha)$	3 min
$f_{cap}(\alpha)$ based on geometry	7 h 50 min

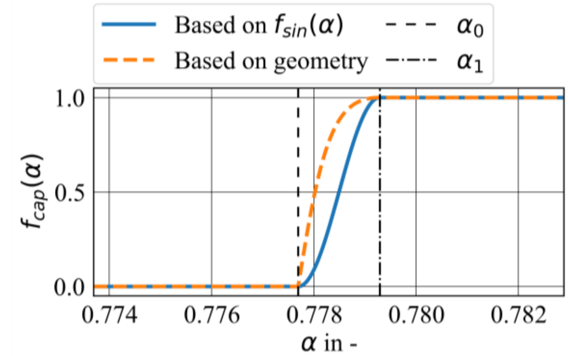

(a)

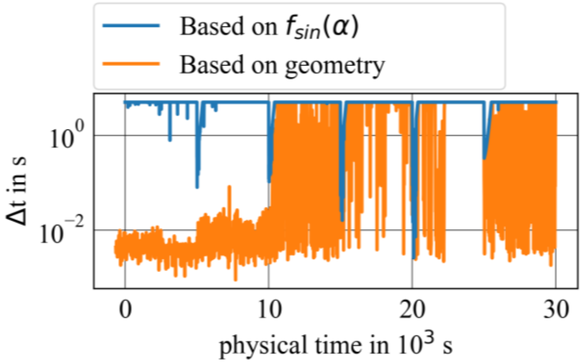

(b)

Figure 15. Comparison of using $f_{sin}(\alpha)$ with using an expression based on the pore interface geometry [14]: (a) prediction of $f_{cap}(\alpha)$; (b) time step size Δt (upper limit 5 s) for demonstration case 1.

6. Conclusions

The thermal hydraulic code AC²/ATHLET is currently extended for the simulation of high-temperature heat pipes to analyze micro modular reactors. The current state of the heat pipe module enables the transient simulation of horizontally orientated heat pipes. The modelling includes the capillary pressure difference, the radial heat transfer based on a conduction model, the phase change at the free interfacial area, the axial pressure drop, and the horizontal pooling.

Two demonstration cases were presented: 1) A potassium heat pipe of a reactor concept was simulated and compared to the result of the Idaho National Laboratory for verification. 2) An experimental investigation of a high-temperature heat pipe was analyzed.

Further, a simple and smooth sinus-based function, $f_{sin}(\alpha)$ for the prediction of Δp_{cap} was presented. Utilizing it instead of a more realistic, pore geometry-based correlation can improve the numerical performance, while it does not affect the result. Concluding, the presented heat pipe module enables the efficient analysis of horizontal high-temperature heat pipes.

The heat pipe model will be further developed and validated on the basis of experiments, which are planned at IKE, University of Stuttgart.

7. Acknowledgements

The MISHA project was funded by the German Federal Ministry of Education and Research (BMBF) based on a decision by the German Bundestag under the project number 02NUK074.

8. References

[1] International Atomic Energy Agency (IAEA), Advances in Small Modular Reactor Technology Developments International Atomic Energy Agency (IAEA), 2022.

[2] W. Bo, X. Shunhao, W. Bin, W. Weibing, L. Yongchao, L. Tong, H. Shaochun, Z. Jiayi, and W. Mengyao, Review of Recent Research on Heat Pipe Cooled Reactor. Nuclear Engineering and Design, 2023. 415: p. 112679.

[3] Westinghouse Electric Company, Westinghouse eVinci™ Micro Reactors Energize Canada's Carbon-Free Efforts (17th March 2022).

[4] P. R. Mcclure, D. I. Poston, V. R. Dasari et al., Design of Megawatt Power Level Heat Pipe Reactors, LA-UR-15-28840 Los Alamos National Laboratory (LANL), 2015.

[5] E. Wang, T. Ren, and L. Li, Review of Reactor Conceptual Design and Thermal Hydraulic Characteristics for Heat Pipe in Nuclear Systems. Frontiers in Energy Research, 2023. 11: p. 1264168.

[6] B. H. Yan, C. Wang, and L. G. Li, The Technology of Micro Heat Pipe Cooled Reactor: A Review. Annals of Nuclear Energy, 2020. 135: p. 106948.

[7] I. Yilgor and S. Shi, Modeling and Investigation of Three Types of Wick Structures in Heat Pipe Microreactor Applications. Transactions of the American Nuclear Society, 2021. 124(1): p. 710.

[8] D. P. Guillen and C. G. Turner, Assessment of Screen-Covered Grooved Sodium Heat Pipes for Microreactor Applications. Nuclear Technology, 2022. 208(8): p. 1301.

[9] J. W. Sterbentz, J. E. Werner, A. J. Hummel et al., Preliminary Assessment of Two Alternative Core Design Concepts for the Special Purpose Reactor, INL/EXT-17-43212 Idaho National Lab.(INL), Idaho Falls, ID (United States), 2018.

[10] C. Mueller and P. Tsvetkov, A Review of Heat-Pipe Modeling and Simulation Approaches in Nuclear Systems Design and Analysis. Annals of Nuclear Energy, 2021. 160: p. 108393.

[11] Z. Tian, C. Wang, K. Guo, D. Zhang, G. H. Su, W. Tian, and S. Qiu, A Review of Liquid Metal High Temperature Heat Pipes: Theoretical Model, Design, and Application. International Journal of Heat and Mass Transfer, 2023. 214: p. 124434.

[12] M. L. Hall, Transient Thermohydraulic Heat Pipe Modeling: Incorporating THROHPUT into the CÆSAR Environment. AIP Conference Proceedings. 2003, Albuquerque, New Mexico (USA).

[13] J.-M. Tournier and M. S. El-Genk, A Heat Pipe Transient Analysis Model. International Journal of Heat and Mass Transfer, 1994. 37(5): p. 753.

[14] J. E. Hansel, R. A. Berry, D. Andrs, M. S. Kunick, and R. C. Martineau, Sockeye: A One-Dimensional, Two-Phase, Compressible Flow Heat Pipe Application. Nuclear Technology, 2021. 207(7): p. 1096.

[15] S. Shi, Y. Liu, I. Yilgor, and P. Sabharwall, A Two-Phase Three-Field Modeling Framework for Heat Pipe Application in Nuclear Reactors. Annals of Nuclear Energy, 2022. 165: p. 108770.

[16] F. Weyermann, D. Eschricht, and A. Wielenberg, AC2-2023 User Manual, GRS - P - 15 / Vol. 0 Gesellschaft für Anlagen- und Reaktorsicherheit (GRS) gGmbH, 2023.

[17] Gesellschaft für Anlagen- und Reaktorsicherheit (GRS) gGmbH, ATHLET 3.4.0 Program Overview, 2023.

[18] D. Eckert, Implementation of Potassium as a Working Fluid into ATHLET, TB-ECD-01-23 Gesellschaft für Anlagen- und Reaktorsicherheit (GRS) gGmbH, 2023.

[19] P. Schöffel, A. Di Nora, D. Eckert et al., ATHLET 3.4.1 Models and Methods, GRS-P-1/Vol. 4 Rev. 9 Gesellschaft für Anlagen- und Reaktorsicherheit (GRS) gGmbH, 2024.

[20] A. Faghri, Heat Pipe Science and Technology: Second Edition (Global Digital Press, Columbia, Mo., 2016).

[21] D. von der Cron, Alternative Formulierung der Wasserspiegelkraft in ATHLET, TN-VDC-20/01, 2020-05.

[22] J. Safarian and T. A. Engh, Vacuum Evaporation of Pure Metals. Metallurgical and Materials Transactions A, 2013. 44(2): p. 747.

[23] R. Lenhard, N. Holešová, and K. Kaduchová, Numerical Investigation of the Influence of Size, Condensation and Evaporation Coefficients on the Power of the Heat Pipe. Joint 21st International Heat Pipe Conference and 15th International Heat Pipe Symposium. February 5-8, 2023, Melbourne, Australia.

[24] A. Faghri and M.-M. Chen, A Numerical Analysis of the Effects of Conjugate Heat Transfer, Vapor Compressibility, and Viscous Dissipation in Heat Pipes. Numerical Heat Transfer, Part A: Applications, 1989. 16(3): p. 389.

[25] C. Wang, L. Zhang, X. Liu, S. Tang, S. Qiu, and G. H. Su, Experimental Study on Startup Performance of High Temperature Potassium Heat Pipe at Different Inclination angles and input powers for nuclear reactor application. Annals of Nuclear Energy, 2020. 136: p. 107051.

[26] Z. Tian, C. Wang, J. Huang, K. Guo, D. Zhang, X. Liu, G. H. Su, W. Tian, and S. Qiu, Code Development and Analysis on the Operation of Liquid Metal High Temperature Heat Pipes under Full Condition. Annals of Nuclear Energy, 2021. 160: p. 108396.

Paper ID 115(S2A)

Effect of bending angle on the thermal performance of a polymeric flat plate pulsating heat pipe

Marco Marengo[1*], Ayse Candan Candere[2], Francois Clemens[3], Nicolas Miché[3], Marco Bernagozzi[3], Mehmet Saglam[2], Anastasios Georgoulas[3], Orhan Aydin[2]

[1] *Department of Civil Engineering and Architecture, University of Pavia, Pavia, Italy*
[2]*Department of Mechanical Engineering, Karadeniz Technical University, Trabzon, Turkey*
[3] *School of Architecture Technology and Engineering, Advanced Engineering Centre, University of Brighton, Brighton, United Kingdom*

**Corresponding author email address: marco.marengo@unipv.it*

Abstract

In response to the rising popularity of foldable electronics, Flexible Pulsating Heat Pipes (FPHPs) have emerged as a potential, adaptable and efficient solution for smart thermal management. This study experimentally investigates the performance of a novel FPHP with asymmetric channels at various bending angles. Four bending angles (0º, 30º, 60º, and 90º) were tested to observe the effect on the thermal resistance, evaporator temperature, pressure, and the underpinned two-phase flow dynamics. All experiments were conducted under constant filling ratio of 50% and heating power range of 4-32W using a compatible working fluid (FC-72). The tested FPHP was fabricated utilizing the stereolithography (SLA) technique. Results indicated that the required start-up temperature at the evaporator increases when the position of the condenser section is changed from vertical to 90° bending. Additionally, as the heating power increases, the thermal resistance variations are similar for 0°, 30°, and 60° bending angles, whereas the thermal performance deteriorates at 90°. The excessive bend at 90° results in a significantly increased flow resistance, affecting the internal flow. This results in a sudden increase of the evaporator temperature and pressure, leading to dry-outs. The maximum operating heating power is 32W for 0º, 30º, and 60º, while it reduces to 20W for 90º.

Keywords: Pulsating heat pipe, Flexibility, Manufacturing method, Flow visualization

1. Introduction

The increasing demand for miniaturised and high-speed electronic components in industries ranging from power electronics to aerospace systems has led to a proportional increase in heat flux dissipation requirement [1-2]. Failures in electronic devices are often caused by factors such as high temperature, humidity, vibration, and dust as shown in Figure 1. Around 55% of these failures are due to inadequate thermal management [3]. Therefore, an effective cooling method integrated with advanced design and manufacturing is essential to achieve uniform heat distribution and reduce the risks associated with overheating.

The Pulsating Heat Pipe (PHP) is a passive heat transfer device that operates thanks to the phase change of the working fluid. The temperature difference between the evaporator and condenser sections, in combination with capillary forces, creates a corresponding pressure gradient, which induces the oscillation motion of liquid slugs and vapour plugs within the capillary-sized channels of the pipe. The PHP has gathered a considerable interest in advanced cooling technologies due to its high heat transfer performance, rapid thermal response, compact form factor and simple construction [4].

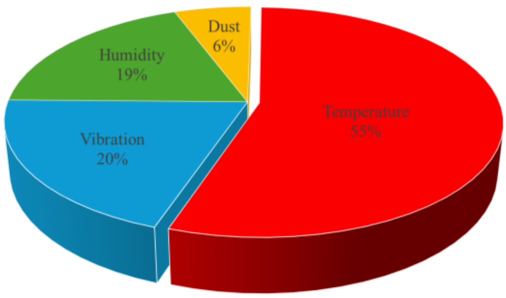

Figure 1. Main causes of electronic failures [3].

PHPs are usually made from rigid materials such as copper, aluminium, glass, and silicon [5-8]. However, there is a technical challenge in implementing non-flexible PHPs as a heat sink for foldable displays and wearable devices [9]. Therefore, the fabrication of a thin, flexible, and lightweight PHP is an important requirement for bendable electronic applications. In this context, Flexible Pulsating Heat Pipes (FPHPs) made from polymer materials can be implemented in foldable systems as a thermal management device.

This study delves into the experimental investigation of the impact of bending angle on the thermal performance of a FPHP at a constant filling ratio (50%). The considered FPHP is subjected to bending angles of 0°, 30°, 60°, and 90°, with FC-72 serving as the designated working fluid. Additive manufacturing technology is utilised to fabricate the device.

2. Experimental set-up and procedure

A scheme of the experimental setup is shown in Figure 2. The evaporator and condenser sections are securely fixed to aluminium plates to ensure the integrity of the heat source and heat sink components. Two Kapton strip heaters are placed in the evaporator section (Omega-KHLVA-104/10, 40W/28V) and connected to a DC power supply (EA-PS 2042-10B, 160W). In the condenser section, two heat sinks are used for the liquid loop system. The loop was maintained at 20 ºC to ensure a constant cooling temperature for the aluminium heat sinks. Two thermocouples are situated at the inlet and outlet of the heat sink respectively. The filling port and pressure transducer are affixed to a port located in the condenser section. A high-speed camera (Ximea XiQ) is also placed to capture the flow images at the adiabatic section.

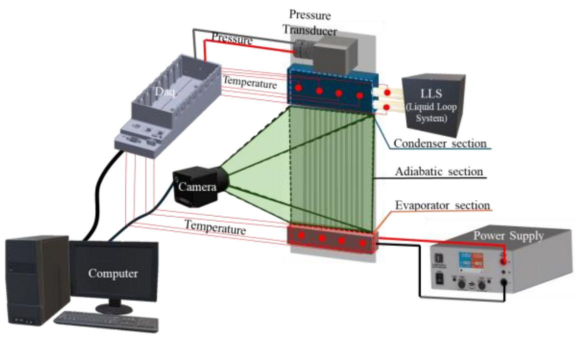

Figure 2. Experimental set-up.

In this study, the FPHP was fabricated using an Anycubic Photon M3 Max Stereolithography (SLA) printer with Anycubic Flexible Tough Resin. The SLA 3D printing process enabled the seamless production of the FPHP, thus eliminating the necessity for layering or bonding processes. Moreover, the FPHP was constructed from a transparent resin, permitting the visualisation of the two-phase flow patterns. Figure 3 presents the fabricated flexible pulsating heat pipe. The experimental setup and procedure are described in detail in a previous work by the present Authors [10].

Figure 3. Illustration of the fabricated flexible polymeric pulsating heat pipe.

The proposed FPHP has asymmetric channel pairs and comprises six turns. Each turn has channel widths of 2.5 mm and 3.4 mm, with a depth of 1 mm. The overall dimensions of the FPHP are 260 mm in length, 98 mm in width, and 2.5 mm in thickness. The dimensions of the FPHP and channel widths are depicted in Figure 4.

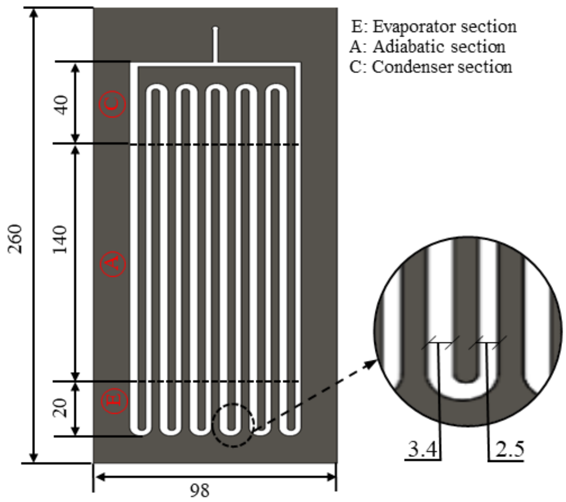

Figure 4. FPHP configuration with geometric details.

As shown in Fig. 5, four distinct bending angles have been selected to evaluate the performance of the polymeric FPHP. In all bending configurations, the evaporator section remains stationary at vertical orientation, while the condenser section undergoes bending via an appropriate hinge mechanism.

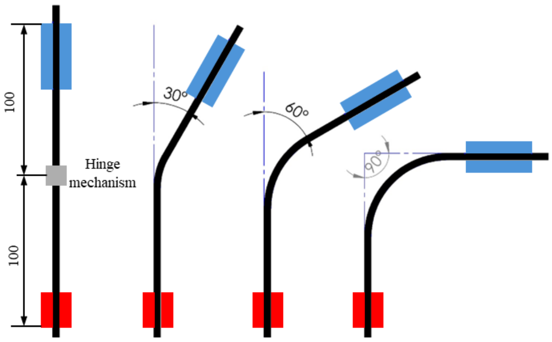

Figure 5. Schematic of bending configurations of the tested FPHP.

The FPHP undergoes a three-step preparation process before the experimental setup is activated. First, the working fluid is degassed to remove non-condensable gases by heating and vacuuming. Next, the FPHP is evacuated with a turbomolecular pump until the internal pressure is reduced to 1 Pa. Lastly, the working fluid is transferred into the FPHP by utilising the pressure difference between the tank and the evacuated FPHP. The mass of the working fluid charged to the FPHP is observed using a high-precision laboratory balance.

After completing the above procedures, the liquid loop system connected to the heat sink is activated in the condenser section of the test area. The power supply is activated to ensure heat input to the evaporator section. The initial heating power is set to 4 W and is gradually increased in 4 W increments. Temperature measurements and flow images are recorded when pseudo-steady-state conditions occur. Ten thermocouples (T-type) are uniformly distributed between the condenser and evaporator sections of FPHP. In each section, four thermocouples contact the front surface of the FPHP, and one thermocouple contacts the back surface. The temperatures in the evaporator and condenser sections are used to calculate the thermal resistance (R_{th}).

$$R_{th} = \frac{T_e - T_c}{Q} \tag{1}$$

where T_e and T_c are the average temperatures of the evaporator and condenser sections respectively and Q is the heating power. The heating power supplied to the heaters is determined by equation (2).

$$Q = V \times I \tag{2}$$

where V and I are electrical voltage and current, respectively. The uncertainty in thermal resistance calculations was assessed following the method by Kline and McClintock [11]. This approach yielded a maximum uncertainty of 5.5% in the thermal resistance, given a temperature uncertainty of ±0.2°C and maximum accuracies of 0.3% for voltage and 0.2% for current.

3. Results and discussion

Figure 6 presents the effect of bending angle on the FPHP through the relationship between thermal resistance and heating power. The degree of deformation at the adiabatic section of the FPHP directly affects thermal resistance and the heating power required for the FPHP activation. A distinct reduction in thermal resistance is observed at 0° (vertical), compared to other bending angles, when the heating power reaches 8W, indicating the initiation of FPHP. On the other hand, as the heating power increases, the changes in the thermal resistance values follow a similar trend at 0°, 30°, and 60° bending angles. However, the thermal resistance of the FPHP positioned at a 90° does not show a significant decrease as the heating power increases. The performance of the FPHP deteriorates in that extreme configuration due to the excessive bending. At a bending angle of 90°, disrupts the uniform distribution of liquid slugs and vapour plugs and leads to uneven heat distribution. This causes partial blockages or constrictions in the channels, restricting flow movement. It also affects the contact quality between the liquid and the FPHP walls, resulting in poor wetting and a reduced effective heat transfer area. All these facts in turn result to an increase of the thermal resistance with a corresponding increase in the power input.

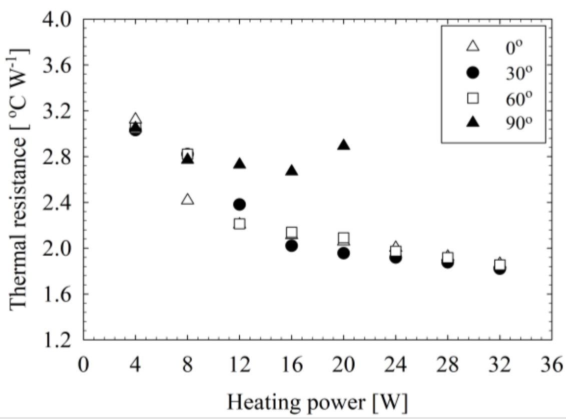

Figure 6. Plot of thermal resistance versus heating power, for different bending angles.

Figures 7a, b, c, and d illustrate high speed camera snapshots at a heating power of 16W for bending angles of 0°, 30°, 60°, and 90°, respectively. These characteristic images are used to analyse the overall flow structure as a function of the bending angle in the tested FPHP. In the vertically positioned FPHP orientation (0^{o}), there is consistent movement of liquid and vapour along all the channels, directed towards the condenser section, with the dominant observed two-phase flow regime being churn-annular flow.

At a bending angle of 30^{o}, the flow structure reveals that the thin-film evaporation process in the evaporator section is notably efficient. In the configuration with low bending angles, the gravity assists the liquid in returning to the evaporator. This provides sufficient liquid for the inner wall of the evaporator, maintaining a stable liquid film. When the FPHP is positioned at a 60^{o} bending angle, a more pronounced impact on the flow resistance is observed. The increased bending angle hinders the smooth transport of vapour plugs towards the condenser. This increased flow resistance not only slows down the liquid-vapour movement, but also disrupts the flow uniformity as some channels become inactive. On the other hand, the suppression of flow motion does not result in a significant change in thermal resistance and evaporator temperature compared to 0^{o} and 30^{o}.

At a bending angle of 90°, the motion of the liquid slugs and vapour plugs are almost completely diminished. The high flow resistance due to the horizontal positioning of the condenser section hinders the ability of vapour bubbles to push the liquid forward. Therefore, the liquid-vapour alignment is seen in only one or two channels. The thin liquid film evaporation process is not effective under these conditions, as the lack of proper condensation leads to the drying of the FPHP, further increasing thermal resistance. This drying indicates that the FPHP's ability to sustain continuous flow oscillations is compromised at this sharp bending. The flow of liquid back into the evaporator is quite insufficient and this causes the oscillation motion to stop or slow down considerably.

This observation highlights the crucial role of gravity in the thermal performance of the FPHP at a bending angle of 90°. In this configuration, where the evaporator is positioned vertically and the condenser horizontally, it becomes increasingly difficult for the force of gravity to overcome the flow resistance imposed by the bending angle.

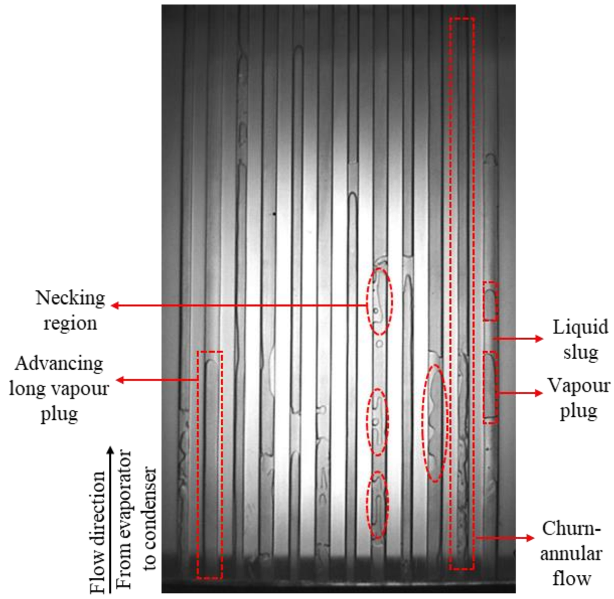

(a)

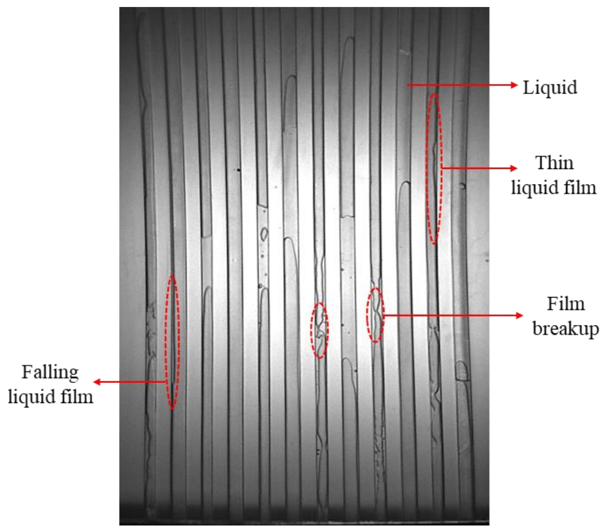

(b)

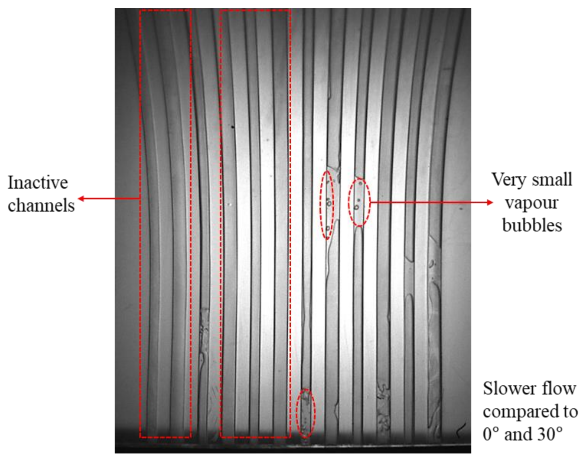

(c)

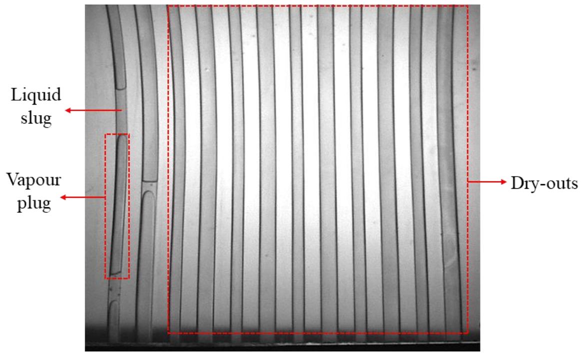

(d)

Figure 7. The flow images at a heating power of 16W for bending angles of 0º (a), 30º (b), 60º (c), and 90º (d).

Figure 8 displays the changes in the evaporator temperatures across four different bending angles. At 8W heating power and 30º, 60º, and 90º bending angles, the evaporator temperature exhibits an increasing and decreasing trend. Temperature fluctuations occur due to low amplitude oscillations and intermittent start-stop movements. As heating power increases, the FPHP encounters higher flow resistance at 90-degree, resulting in higher temperature values. This causes the FPHP to stop operating, resulting in a sudden temperature rise in the evaporator section. The experiment concludes at 20W for a 90º bending angle, while the maximum heating power reaches 32W for bending angles of 0º, 30º, and 60º.

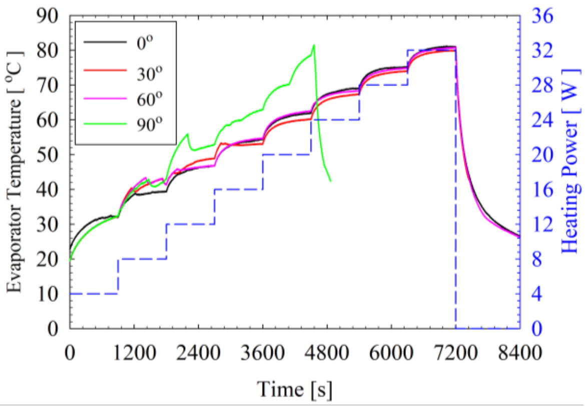

Figure 8. Temporal variation of spatially averaged evaporator temperatures for the tested FPHP for different bending configurations.

Considering the pressure transducer readings at the condenser section, at bending angles of 30º and 60º, the induced flow resistance causes an overall reduction in the pressure, as seen Figure 9, which gradually reduces the driving force that facilitates the working fluid movement. This weakened force affects the minimum heating power required to initiate the operation of the tested FPHP. On the other hand, the 90º bending configuration has the opposite effect, where the significantly increased flow resistance causes substantial temperature, and pressure increases due to the hindered liquid-vapour movement. Therefore, the condensation and evaporation processes are adversely affected, leading to dry-outs.

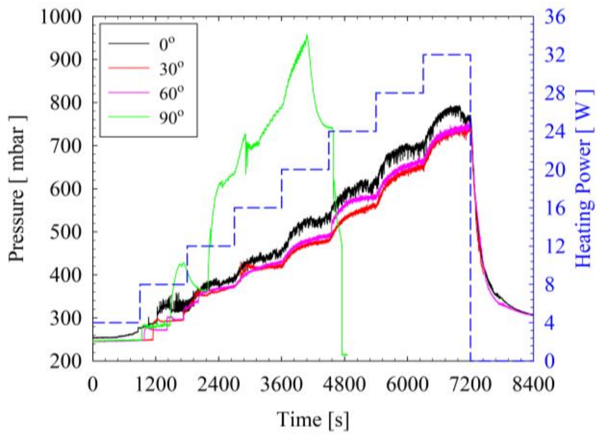

Figure 9. Pressure transducer readings at different heating powers and bending angles.

4. Conclusions

The thermal behaviour of a flexible polymer-based pulsating heat pipe fabricated via additive manufacturing was experimentally analysed using FC-72 as the working fluid. The study aimed to investigate how the bending angle affects the performance of a polymeric FPHP. The main findings of the investigation are summarised below:

- The heating power required for initiation of the FPHP is significantly affected by the increase of the bending angle.
- All FPHP channels appear to be active at smaller bending angles, but as the bending angle increases the corresponding increase of the flow resistance disrupts the liquid-vapour transport, leading to inactive channels and reduced flow uniformity.
- At a 90° bending angle, the uniform distribution of liquid and vapour in the FPHP disrupts. This results in increased thermal resistance which in combination with the insufficient gravity support, leads to a significant reduction in oscillation and dry-outs.
- At bending angles of 30° and 60°, the flow resistance leads to pressure losses, reducing the driving force for fluid movement and to an

increase at the heating power threshold for the FPHP activation. Conversely, at 90°, the higher flow resistance causes sharp rises in temperature and pressure by obstructing liquid-vapour movements, which further increases thermal resistance.

5. ACKNOWLEDGEMENTS

The authors sincerely thank the Scientific and Technological Research Council of Turkey (TUBITAK) for its financial support through the 2214-A International Research Fellowship Programme.

References

[1] H. Tang, Y. Tang, Z. Wan, J. Li, W. Yuan, L. Lu, Y. Li, and K. Tang, Review of applications and developments of ultra-thin micro heat pipes for electronic cooling. Applied Energy, 2018. (223): p.383-400.

[2] M. Fazli, S. A. A, Mehrjardi, A. Mahmoudi, A. Khademi, and M. Amini, Advancements in pulsating heat pipes: Exploring channel geometry and characteristics for enhanced thermal performance. International Journal of Thermofluids, 2024: p. 100644.

[3] Z. He, Y. Yan, and Z. Zhang, Thermal management and temperature uniformity enhancement of electronic devices by micro heat sinks: A review. Energy, 2021. (216): p.119223.

[4] D. Bastakoti, H. Zhang, D. Li, W. Cai, and F. Li, An overview on the developing trend of pulsating heat pipe and its performance. Applied Thermal Engineering, 2018. (141): p.305-332.

[5] X. Cui, Y. Zhu, Z. Li, and S. Shun, Combination study of operation characteristics and heat transfer mechanism for pulsating heat pipe. Applied Thermal Engineering, 2014. 65(1-2): p.394-402.

[6] V. M. Patel and H. B. Mehta, Influence of working fluids on startup mechanism and thermal performance of a closed loop pulsating heat pipe. Applied Thermal Engineering, 2017. (110): p.1568-1577.

[7] X. Liu, L. Xu, C. Wang, and X. Han, Experimental study on thermo-hydrodynamic characteristics in a micro-oscillating heat pipe. Experimental Thermal and Fluid Science, 2019. (109): p.109871.

[8] M. Kumar, R. Kant, A. K. Das, and P. K. Das, Effect of surface tension variation of the working fluid on the performance of a closed loop pulsating heat pipe. Heat Transfer Engineering, 2019. 40(7): p.509-523.

[9] J. Lim and S. J. Kim, Fabrication and experimental evaluation of a polymer-based flexible pulsating heat pipe. Energy Conversion and Management, 2018. (156): p.358-364.

[10] A. C. Candere, N. Miché, M. Bernagozzi, M. Saglam, A. Georgoulas, O. Aydin, and M. Marengo, A novel fabrication method for polymeric flat plate pulsating heat pipe via additive manufacturing. Applied Thermal Engineering, 2024. (241): p.122398.

[11] S. J. Kline and F. A. McClintock, Describing uncertainties in single-sample experiments. Mech. Eng, (1953). (75): p.3–8.

Paper ID 118(S8)

Enhancing the Performance of Single-Loop Pulsating Heat Pipe by Creating a Novel Asymmetry

Anoop Kumar Shukla[1*], and Subrata Kumar[2]

[1,2] *Indian Institute of Technology. Patna, Bihar, India*
**Corresponding author email address: anoop_2021me20@iitp.ac.in*

Abstract

This study aims to improve the performance of a pulsating heat pipe (PHP) by introducing asymmetry through the insertion of a copper wire into one column of a single-loop PHP. Five PHP configurations were tested: one with a uniform internal diameter (ID) of 2.5 mm (UPHP), one with dual diameters (2.5 mm and 1.8 mm ID) geometrically asymmetric PHP (GAPHP), and three with a uniform ID of 2.5 mm but different wire diameters (0.7 mm, 1.2 mm, and 1.7 mm) inserted into one column (WAPHP). Made of borosilicate glass, these PHPs were evaluated using visualization techniques and thermal resistance calculations. The study varied filling ratios, inclination angles, and heat loads to assess performance. Results showed that the WAPHP with a 1.2 mm wire diameter performed best at a 60% filling ratio, exhibiting superior startup, delayed dry-out.

Keywords: Pulsating heat pipe; Wire inserted asymmetry; Flow visualization; Thermal resistance

1. Introduction

The escalating demand for efficient thermal management solutions in industries has spurred significant attention towards pulsating heat pipes (PHPs) among experimental and theoretical researchers. It finds its use from solar to cryogenic applications [1-4]. Geometric parameters such as cross-sectional shape and the number of turns, operational parameters like inclination angle (IA) and check valve configuration, and physical parameters such as filling ratio (FR) and working fluid properties play pivotal roles in determining PHP performance.

The primary goal of pulsating heat pipe (PHP) studies is to optimize thermal performance and ensure orientation independence. In this endeavour Sedighi et al. [5] proposed an asymmetric design with an extra branch in the evaporator section, promoting one-directional fluid circulation. Chein et al. [6] developed a nonuniform flat plate PHP capable of horizontal operation at a filling ratio (FR) $\geq$ 60%. Kwon and Kim [7] investigated optimal diameter ratios for asymmetry. Liu et al. [8] numerically assessed the startup and heat transfer performance of single and dual-diameter PHPs. Markal et al. [9] studied the effect of double cross-sectional ratios on the performance of a flat plate PHP, finding that gradually constricted geometry enhanced flow circulation and maintained orientation-independent performance. Liu et al. [10] tested a large-area cryogenic heat pipe with multiple heat sources, which operated effectively within a temperature range of 80 to 120 K. Shukla et al. [11] studied the startup and thermal efficiency of a two-loop PHP with alternating asymmetric diameters, showing superior performance compared to uniform two-loop PHPs.

Due to the strong coupling between geometry and thermo-hydrodynamics in PHPs, the study of asymmetric channels is greatly important. So far, such asymmetry has been engineered through manufacturing processes. However, the current study presents a novel approach: crafting an asymmetric single loop PHP by inserting a copper wire within a channel. Notably, this PHP is constructed from borosilicate glass to facilitate visualization. The comparison has been conducted between this novel PHP, termed the wired asymmetric PHP (WAPHP), a geometrically asymmetric PHP (GAPHP), and a uniform PHP (UPHP). Effective thermal resistance and flow visualization are two methods used to estimate the performance of both PHPs.

2. Experimental setup and methodology

Five different single-loop PHPs were manufactured using borosilicate glass. The uniform PHP (UPHP) has a uniform inner diameter (ID) of 2.5 mm and an outer diameter (OD) of 8.9 mm. Geometrically asymmetric PHP (GAPHP) features an asymmetric diameter of 2.5/8.9 mm ID/OD and 1.8/7 mm ID/OD respectively. Wired asymmetric PHP (WAPHP) maintains similar dimensions to the UPHP except incorporating three copper wires with diameters of 1.7 mm, 1.2 mm, and 0.7 mm diameter for creating asymmetry, as illustrated in Fig. 1.

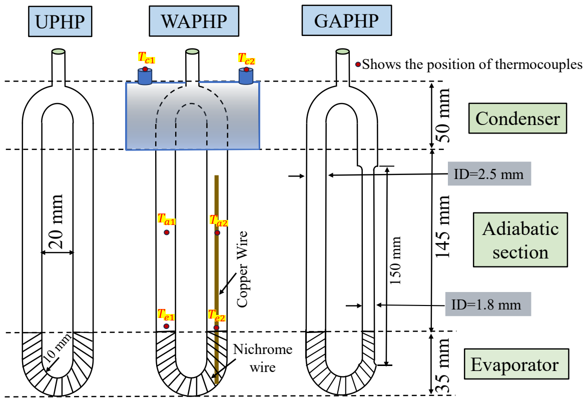

Figure 1. Schematic of PHP configurations.

The diameters of the copper wires were selected to ensure that the equivalent diameter (1.7 mm) and the hydraulic diameter (0.7 mm) of the annular region of the WAPHP match that of the smaller diameter of GAPHP. Both the wire and the asymmetric section of the GAPHP had a length of 150 mm. The diameters of the PHPs were chosen based on the Bond number criteria given by [5, 12, 13].

$$(Bo)_{crit} = \sqrt{\frac{D_{crit}^2 . g . \ (\rho_l - \rho_v)}{\sigma}} \leq 2$$

The schematic of experimental setup is shown in Fig. 2. Deionized (DI) water served as the working fluid, and the system was evacuated using a vacuum pump with a capacity of 0.2 Pa. After degassing, DI water was introduced into the inlet manifold. The condenser housing was constructed from a 5 mm thick acrylic sheet, and the coolant flow rate was maintained at 20 kg/hr, regulated by a rotameter. The evaporator section was created by uniformly wrapping nichrome wire around it. Temperature and pressure data were recorded using a DAQ system integrated with a LabView program, with a sampling rate of 10 Hz. Video recordings were captured at 100 and 200 fps using a high-speed camera. The experiment began with an initial heat load of 5 W, which was then gradually increased in increments of 5 W. Since the system is uninsulated, heat loss occurs from both the evaporator and the adiabatic sections. As a result, the actual heat absorbed by the system is always less than the heat supplied from the DC source. Therefore, in this study, the thermal performance calculations are based on the heat transferred to the coolant flowing through the condenser section.

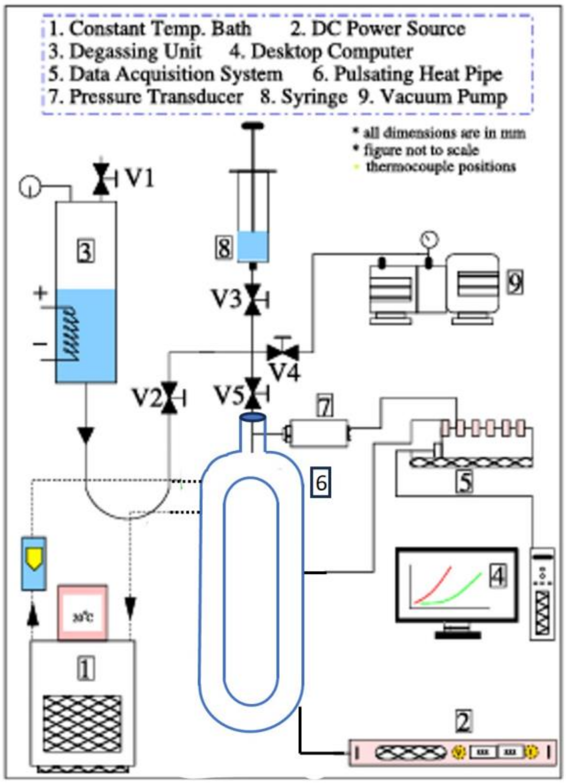

Figure 2. Experimental setup.

3. Data reduction and uncertainty analysis

The locations of thermocouples have been shown in Fig. 1. A total of six thermocouples have been used in the experiment. Time as well as spatial averaging has been performed for the evaporator and condenser temperature as follows:

$$T_{e,1} = \frac{1}{n} \sum_{j=1}^{n} T_{e,1,j} \ ;$$

Similarly, for $T_{e,1}, T_{ci}$ and $T_{c,o}$.
Spatial averaging is performed as follows:

$$T_e = \frac{T_{e,1} + T_{e,2}}{2} \text{ and } T_c = \frac{T_{c,i} + T_{c,o}}{2} \qquad (1)$$

The equivalent thermal resistance ($R_{th,eq}$) is commonly utilized as a metric to assess the thermal performance of PHP. Lower thermal resistance indicates superior heat transfer performance. This equivalent thermal resistance was calculated based on the heat transfer through the condenser to the coolant (i.e. Q_c). Q_c represents the heat that is reliably entering the system. The equivalent thermal resistance for the system, measured between the evaporator and condenser sections, can be defined using the following formula [11, 14]:

$$R_{th,eq} = \frac{T_e - T_c}{Q_c} \qquad (2)$$

The values of T_e and T_c are determined using Eq. 1. The Value of Q_c is determined using relation $Q_c = \dot{m}C_p(T_{c,o} - T_{c,i})$. Where $\dot{m}$ is the mass flow rate of coolant and C_p is the specific heat of coolant water.

Measured parameters are subjected to the uncertainty hence the uncertainty in $R_{th,eq}$ has been calculated. The DC source has an uncertainty of 0.1% + 300mV for the voltage readings and 0.1% + 7.5 mA for the current readings. The T-type thermocouples used in this experiment has an uncertainty of $\pm$ 0.4% or $\pm$ 0.5°C, whichever is greater. The expression for the uncertainty in Q_{in} and R_{th} can be calculated as follows:

$$\frac{w(Q_{in})}{Q_{in}} = \sqrt{\left(\frac{\delta V}{V}\right)^2 + \left(\frac{\delta I}{I}\right)^2}$$

$$\frac{w(R_{th,eq})}{R_{th,eq}} = \sqrt{\left(\frac{w(T_e)}{T_e - T_c}\right)^2 + \left(\frac{w(T_c)}{T_e - T_c}\right)^2 + \left(\frac{w(Q_{in})}{Q_{in}}\right)^2}$$

In this study, the heat input and equivalent thermal resistance were subject to maximum uncertainties of 3.7% and 6.1%, respectively.

4. Results and discussion

The study used filling ratios (FRs) and inclination angles (IAs) to analyze flow visualization and thermal performance in PHPs. Introducing a wire to create asymmetry significantly enhanced performance compared to uniform and dual diameter PHPs. The wire affects flow dynamics by introducing additional physical interactions, adding complexity to the internal flow. High-speed photography and data signals revealed that the wire induces pressure differences, aids in bubble nucleation, acts as a heat source, assists in liquid droplet transport, and dampens slug oscillations. These effects are further detailed in the following sections.

4.1. Impact of Wire on system start-up

Bubble nucleation and growth drive the start-up of the PHP when the evaporator is filled with liquid. This process needs a certain level of wall superheat, which is typically higher on smooth glass surfaces. However, the wire in the evaporator offers rougher surfaces, creating easier nucleation sites for bubbles by providing cavities for trapped gases or vapor. Fig. 3 shows the comparison of start-up time for different PHP configurations. It can be observed that the WAPHP having wire diameter (d_w) of 1.7 mm shows the best start-up performance.

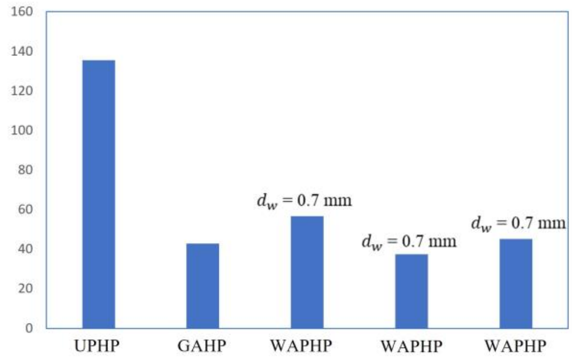

Figure 3. Start-up time comparison for the different PHP configurations at 40% filling ratio.

Easy bubble nucleation additional capillary forces are the main reason for the enhanced start-up performance of the WAPHP.

4.2. Impact of Wire on system dry-out

Fig. 4 shows the temperature vs. time plot for the different PHPs. It can be observed that dry-out occurred at 40 W and 45 W for UPHP and GAPHP, respectively. However, in the case of WAPHP, no dry-out occurred up to a heat load of 65 W. Beyond this point, the experiments were halted for safety reasons. The main reasons for the delayed dry-out in WAPHP are that the wire helps prevent the formation of hot spots in the evaporator section at high heat loads by conducting heat through it, and it also aids in the movement of liquid back to the evaporator.

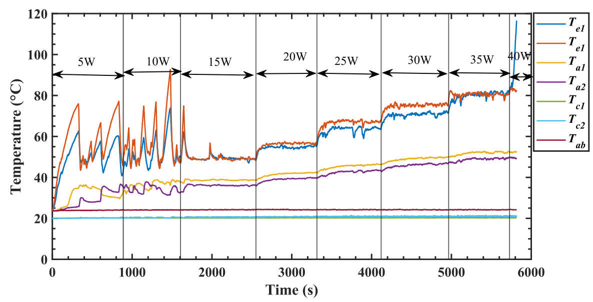

(a) UPHP

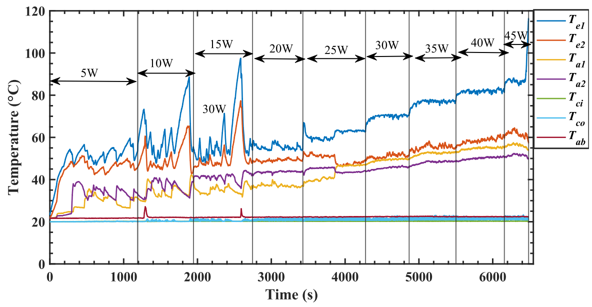

(b) GAPHP

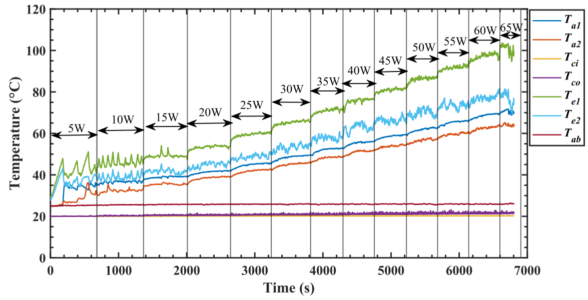

(c) WAPHP ($d_w = 1.2\ mm$)

Figure 4. Temperature vs time plot for different PHPs at 50% filling ratio.

4.3. Thermal performance

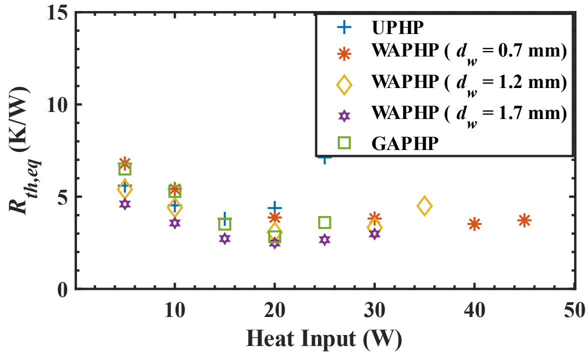

(a) 40% filling ratio.

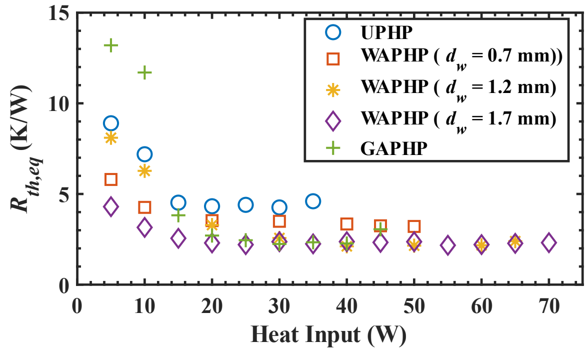

(b) 50% filling ratio.

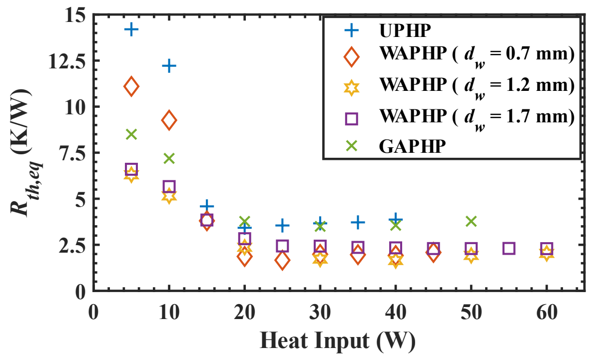

(c) 60% Filling ratio.

Figure 5. Variation of $R_{th,eq}$ with filling ratios at IA = 90°.

The Thermal performance of PHP depends on the various operating parameters. Fig. 5 illustrate the variation of thermal performance of the tested PHP configurations with the filling ratios at 90° IA. It is evident from Fig. 5 that the best performance was achieved with the WAPHP having a wire diameter of 1.2 mm at a 60% filling ratio.

The effect of inclination angle on the equivalent thermal resistance at 60% filling ratio is depicted in Fig. 6. The WAPHP (d_w = 1.2 mm) shows superior performance at 60° and 30° inclination angles compared to the UPHP and WAPHP.

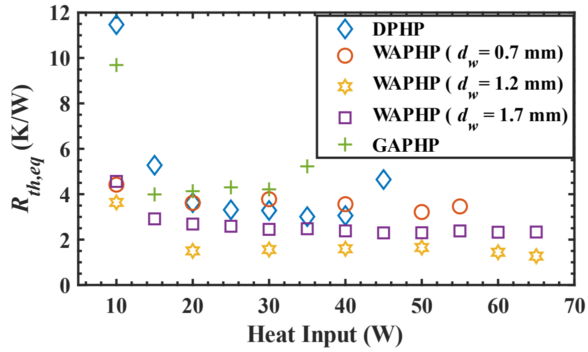

(a) Inclination angle = 60°

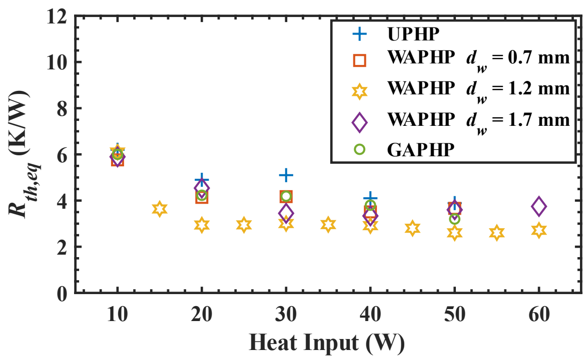

(b) Inclination angle = 30°

Figure 6. Variation of $R_{th,eq}$ with filling inclination angles.

5. Conclusions

The study investigated the impact of different filling ratios, inclination angles, and heat loads on PHP performance, using water as the working fluid. The research primarily aimed to assess how the wire influences the flow dynamics within the PHP and to evaluate its overall thermal performance. The WAPHP shows better start-up performance as well as delayed dry-out compared to the UPHP and GAPHP. The thermal performance index R_{th} was minimum in case of WAPHP (d_w = 1.2 mm) at 60% filling ratio among all the tested PHPs. The WAPHP continued to function effectively at inclination angles of up to 30°, without any degradation in performance. The results of these novel asymmetric PHPs are promising, offering a simple and efficient solution from a manufacturing perspective.

References

[1] Ashouri, Milad, Mohammad H. Ahmadi, S. Mohsen Pourkiaei, Fatemeh Razi Astaraei, Roghaye Ghasempour, Tingzhen Ming, and Javid Haj Hemati. "Exergy and exergo-economic analysis and optimization of a solar double pressure organic Rankine cycle." Thermal Science and Engineering Progress 6 (2018): 72-86.

[2] Faghri, Amir, and Zhen Guo. "Integration of heat pipe into fuel cell technology." Heat Transfer Engineering 29, no. 3 (2008): 232-238.

[3] Tian, En, Ya-Ling He, and Wen-Quan Tao. "Research on a new type waste heat recovery gravity heat pipe exchanger." Applied Energy 188 (2017): 586-594.

[4] Liang, Qing, Yi Li, and Qiuliang Wang. "Effects of filling ratio and condenser temperature on the thermal performance of a neon cryogenic oscillating heat pipe." Cryogenics 89 (2018): 102-106.

[5] Sedighi, A. Amarloo, M. Shafii, Experimental investigation of the thermal characteristics of single-turn pulsating heat pipes with an extra branch, Int. J. Therm. Sci. 134 (2018) 258–268.

[6] K.H. Chien, Y.T. Lin, Y.R. Chen, K.S. Yang, C.C. Wang, A novel design of pulsating heat pipe with fewer turns applicable to all orientations, Int. J. Heat Mass Transf. 55 (2012) 5722–5728.

[7] G.H. Kwon, S.J. Kim, Operational characteristics of pulsating heat pipes with a dual-diameter tube, Int. J. Heat Mass Transfer 75 (2014) 184–195.

[8] Y. Liu, D. Dan, M. Wei, S. Zheng, J. Sun, Numerical investigation on the start-up and heat transfer performance of dual-diameter pulsating heat pipes, Appl. Therm. Eng. 236 (2024) 121709.

[9] Markal, Burak, et al. "Effect of double cross sectional ratio on performance characteristics of pulsating heat pipes." International Communications in Heat and Mass Transfer 127 (2021): 105583.

[10] Liu, Chenpeng, et al. "Experimental study on temperature uniformity and heat transfer performance of nitrogen loop heat pipe with large area and multi-heat source." Applied Thermal Engineering 210 (2022): 118344.

[11] Shukla, Anoop Kumar, Est Dev Patel, and Subrata Kumar. "Study of an asymmetric dual loop pulsating heat pipe: Visualization and parametric analysis." Applied Thermal Engineering (2024): 122842.

[12] Khandekar, Sameer. "Thermo-hydrodynamics of closed loop pulsating heat pipes." (2004).

[13] White, E. T., and R. H. Beardmore. "The velocity of rise of single cylindrical air bubbles through liquids contained in vertical tubes." Chemical Engineering Science 17.5 (1962): 351-361.

[14] Patel, Est Dev, and Subrata Kumar. "Thermal performance of a single loop pulsating heat pipe with asymmetric adiabatic channel." Applied Thermal Engineering 219 (2023): 119541.

Paper ID 124(S4)

Heat transfer performance of a prototypically 8 m-long two-phase closed thermosyphon for spent fuel pool passive cooling

Sergio Iván Cáceres Castro[1]*, Rudi Kulenovic[2], Jörg Starflinger[3]

[1,2,3,] *Institute of Nuclear Technology and Energy Systems, University of Stuttgart, Stuttgart, Germany*
**sergio.caceres@ike.uni-stuttgart.de*

Abstract

This study investigates the heat transfer performance of an 8 m-long prototype two-phase closed thermosyphon designed for the passive cooling of nuclear spent fuel pools, with deionised water as the working fluid. The filling ratio was varied between 10% and 100%, and heat-source temperatures ranged from 45 to 80 °C This experimental study provides valuable data on the operation of long thermosyphons, aiding in the validation and improvement of numerical models simulating passive residual heat removal in nuclear plants. The results indicate that optimal heat transfer performance was achieved at a 30% filling ratio, with the thermosyphon initiating operation at a heat-source temperature of 50 °C. Additionally, the heat transfer coefficient in the evaporator section showed a decline at lower filling ratios. Compared to previous studies, it was found that increasing the length of the evaporator section from 1 m to 2 m resulted in a 35% improvement in heat transfer at temperatures above 55 °C. The length of the adiabatic section had minimal impact at 30% and 40% filling ratios, but at lower ratios, it caused dry patches and reduced performance. There were only slight variations at 50% filling ratio.

Keywords: thermosyphon; filling ratio; stainless steel-water; passive cooling

1. Introduction

The 2011 Fukushima Daiichi nuclear disaster fundamentally reshaped the approach to reactor safety, particularly concerning Nuclear Spent Fuel Pool (NSFP) cooling during severe accidents. The disaster, triggered by a blackout and subsequent failure of backup generators, led to meltdowns in three reactor units. In the NSFP, the water level decreased rapidly due to the unavailability of the active heat removal system. This incident highlighted the need for passive residual heat removal systems in NSFP designs, as traditional electrically powered cooling methods are not operating during blackouts. The International Atomic Energy Agency (IAEA) emphasised in its report "Safety of Nuclear Power Plants: Design SSR-2/1 (Rev. 1)" [1] the importance of reliable cooling systems, where thermosyphons as a passive solution were recommended.

In the meantime, several research groups have researched the potential of two-phase closed thermosyphons for passive NSFP cooling. Studies by Kusuma et al. [2; 3], Choi et al. [4] and Grass et al. [5], among others, have explored various methodologies and yielded different insights into the performance of thermosyphons in these settings. However, despite the progress in understanding the thermal properties of thermosyphons, their performance capabilities remain highly variable. Detailed experimental data on their heat transfer performance, especially for long thermosyphons, are still lacking.

In response to this knowledge gap, experimental investigations were conducted at the Institute of Nuclear Technology and Energy Systems (IKE) to comprehensively understand the optimal heat transfer characteristics of long thermosyphons designed for NSFP cooling. In parallel, the Gesellschaft für Anlagen- und Reaktorsicherheit (GRS), a co-operation partner in joint R&D projects with IKE, has been improving its modelling capabilities. This effort involves the development of the AC²/ATHLET code, which simulates relevant phenomena within nuclear power plants, including passive residual heat removal using thermosyphons. The partnership also aims to improve the ATHLET thermal-hydraulic code system by integrating the modelling of thermosyphon and heat pipe operations into the AC²/ATHLET code [6; 7].

This paper focuses on the experimental investigation of the heat transfer performance of a prototypical 8 m-long thermosyphon designed for large-scale NSFP cooling applications. By varying key parameters such as the heat-source temperature, the heat-sink temperature, and the filling ratio, this study aims to address aspects that have not been extensively explored for long thermosyphons in the context of NSFP cooling. Additionally, the influence of the evaporator and adiabatic section lengths is investigated by comparing the results with previous studies on similar thermosyphons. These findings are crucial for developing safer and more efficient passive cooling systems, contributing to advancements in nuclear safety and reactor technology. Moreover, the results will support further development and validation of the mechanistic ATHLET model for 8 m long thermosyphons.

2. Experimental setup and procedure

2.1 Test rig

Figure 1 illustrates a schematic representation of the experimental setup used to examine the heat transfer characteristics of an 8 m-long thermosyphon. The experimental setup consisted mainly of a test thermosyphon and two separate water circuits for heating and cooling. The thermosyphon was constructed from 1.4301 stainless steel with internal and external diameters of 35 and 38 mm, respectively.

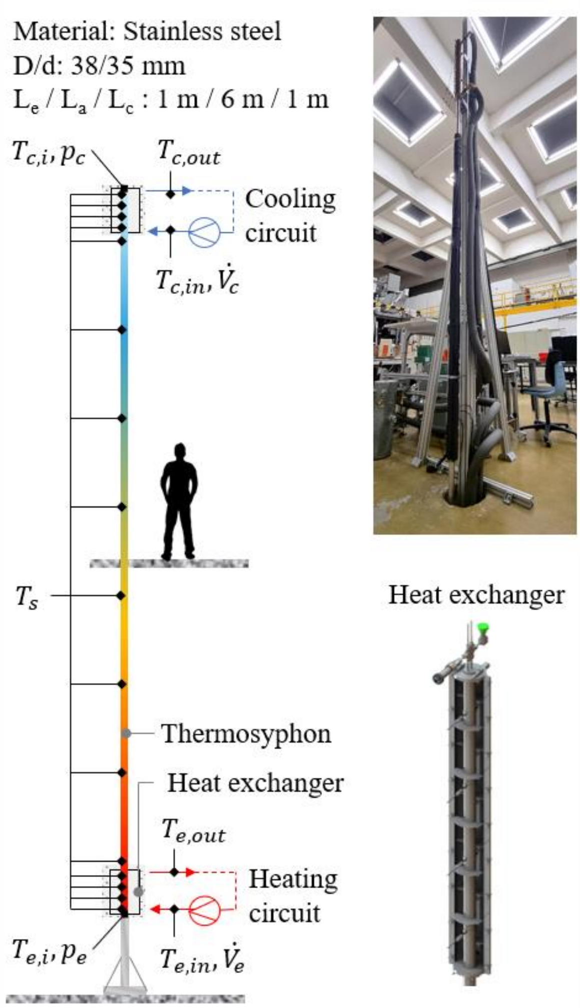

Figure 1. Schematic representation of the experimental test rig and arrangement of the measuring instrumentation.

Both the evaporator and condenser sections of the thermosyphon were equipped with 1 m-long double-pipe heat exchangers, which served as the heat source and heat sink, respectively. These heat exchangers were connected to water-operated thermostats. The adiabatic section and the heat exchangers were insulated with 19 mm thick Armaflex XG insulation to minimise ambient influences on the thermosyphon.

For the 8 m-long thermosyphon, the outer surface temperature T_s was measured at various heights utilising 16 resistance thermometers PT100, with a Class A accuracy of ± (0.15 + 0.002*T RD). Furthermore, two sheathed resistance thermometers PT100 were positioned within the thermosyphon to measure the internal temperatures $T_{e,i}$ and $T_{c,i}$ of the evaporator and condenser sections, respectively. Absolute pressure transmitters PAA-33X with an accuracy of ± 0.15 % FS were situated at the base of the evaporator and the top of the condenser section to measure the internal pressure p_e and p_c of the thermosyphon. The inlet and outlet temperatures $T_{e,in}$, $T_{e,out}$, $T_{c,in}$ and $T_{c,out}$ of both heat exchangers were acquired using sheathed resistance thermometers PT100. The inlet flow rates $\dot{V}_e$ and $\dot{V}_c$ of both heat exchangers were determined using ultrasonic flowmeters with an accuracy of ± (0.7 % RD + 0.7 % FS). Keysight data logger 34980A and LabVIEW computer software were employed for the data acquisition.

2.2 Test conditions and data reduction

The thermal conditions of the experiments followed the pool water temperatures specified in "Kerntechnischer Ausschuss" (KTA) 3303 [8] for the design of fuel pool heat removal systems: 45 °C (normal operation), 60 °C (abnormal or malfunctioning operation), and 80 °C (accidental operation). Accordingly, the experiments in this study were conducted for heat-source temperatures within this range. A summary of the experimental parameters is presented in Table 1. A total of 107 experiments were conducted. with a minimum duration of 5 min for each case.

Table 1. Variation of parameters in experiments.

Parameter	Unit	Value
Volume flow	l/min	10
Filling ratio	%	10, 20, 30, 40, 50, 70, 100
Heat-source temperature	°C	45, 50, 55, 60, 70, 80
Heat-sink temperature	°C	20, 30
Measuring frequency	Hz	0.5

A brief overview of the calculations for the most important thermal variables is provided below. The fluid properties were derived by the International

Association for the Properties of Water and Steam (IAPWS) [9]. The heat transfer rate $\dot{Q}$ of the double-pipe heat exchangers in the evaporator and condenser section is given by.

$$\dot{Q} = \rho\, c_p\, \dot{V}\, (T_{out} - T_{in}) \quad (1)$$

where ρ is the fluid density, c_p is the isobaric heat capacity, $\dot{V}$ is the volume flow, and T_{out} and T_{in} are the outlet and inlet flow temperatures of the double-pipe heat exchangers. The average heat transfer coefficients in the evaporator section $\bar{h}_{e,exp}$ and in the condenser section $\bar{h}_{c,exp}$ are calculated using equations (2) and (3).

$$\bar{h}_{e,exp} = \frac{\dot{Q}_e}{A_e\, (\bar{T}_{w,e} - T_v)} \quad (2)$$

$$\bar{h}_{c,exp} = \frac{\dot{Q}_c}{A_c\, (T_v - \bar{T}_{w,c})} \quad (3)$$

where $\dot{Q}_e$ and $\dot{Q}_c$ are the input and output heat transfer rates in the evaporator section and condenser section, A_e and A_c are the outer areas of the thermosyphon evaporation section and condenser section, $\bar{T}_{w,e}$ and $\bar{T}_{w,c}$ are the mean wall temperatures in the evaporator section and the condenser section, and T_v is the vapour temperature inside the thermosyphon. The thermal resistance R_{th} of the thermosyphon is determined using the following equation

$$R_{th} = \frac{\bar{T}_{w,e} - \bar{T}_{w,c}}{\dot{Q}_c} \quad (4)$$

The uncertainty analysis was conducted for the heat transfer rate and the heat transfer coefficient, followed by the "Guide to the Expression of Uncertainty in Measurement by International Organization for Standardization" [10].

$$\delta\dot{Q} = \sqrt{\sum_{i=0}^{n} \left(\frac{\partial \dot{Q}}{\partial x_n} \cdot \delta x_n^2\right)^2} \quad (5)$$

$$\delta\bar{h} = \sqrt{\sum_{i=0}^{n} \left(\frac{\partial \bar{h}}{\partial x_n} \cdot \delta x_n^2\right)^2} \quad (6)$$

$$\delta R_{th} = \sqrt{\sum_{i=0}^{n} \left(\frac{\partial R_{th}}{\partial x_n} \cdot \delta x_n^2\right)^2} \quad (7)$$

where $\delta\dot{Q}$, δh and δR_{th} represent the error propagations of the considered equations (1) - (4), x_n is the independent measured variable and δx_n is the uncertainty of each used measurement device.

3. Results and discussion

3.1 Optimal filling ratio

Experiments were conducted under the thermal conditions specified in Table 1 to determine the maximum heat transfer rate of the test thermosyphon. Figure 2 illustrates the heat transfer rate in the condenser, denoted as $\dot{Q}_c$, as a function of the filling ratio V^+ for heat source temperatures $T_{e,in}$ from 45 °C to 80 °C and 20 °C (top) and 30 °C (bottom) heat-sink temperatures $T_{c,in}$.

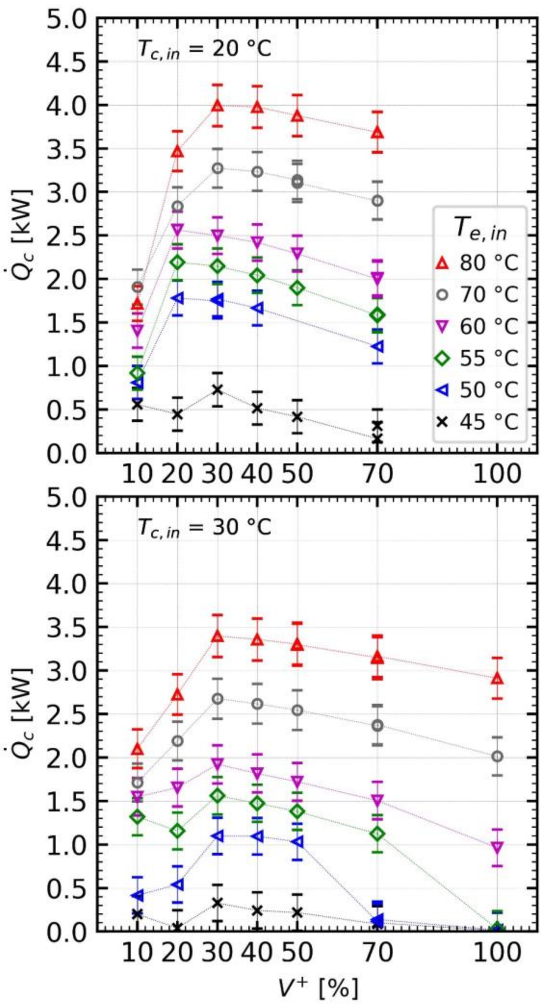

Figure 2. Heat transfer rate $\dot{Q}_c$ vs. filling ratio V^+ at different heat-source temperatures $T_{e,in}$ for 20 °C (top) and 30 °C (bottom) heat-sink temperature $T_{c,in}$.

At a heat-sink temperature of 20 °C, the thermosyphon did not operate at a heat-source temperature of 45 °C. However, at a heat-source temperature of 50 °C and filling ratios between 20% and 40%, the thermosyphon began to operate, achieving a heat transfer rate of approximately 1.7 kW. For heat-source temperatures ranging from 50 °C to 80 °C, the heat transfer rate increased as the filling ratio decreased from 100 to 30%.

For heat-source temperatures from 50 to 60 °C, the results demonstrated an increase in the heat transfer rate for all filling ratios, reaching an individual maximum for the 20% and 30% filling ratios. Notably, for the 70 °C and 80 °C heat-source temperatures, the highest heat-transfer rate was reached at a 30% filling ratio. A maximum heat transfer rate of approximately 4.0 kW was achieved at 80 °C heat-source temperature, 20 °C heat-sink temperature and 30% filling ratio. A similar trend was observed for the 30 °C heat-sink temperature.

In Figure 2, the heat transfer rate of the thermosyphons is discussed, providing insight into whether the thermosyphon is operating or not. However, the figure does not indicate whether the thermosyphon operates steadily or with fluctuations. Two parameters were selected to evaluate the operational stability of the thermosyphon: the mean wall temperature in the evaporator section $\overline{T}_{e,w}$ and the inner temperature at the top of the condenser section $T_{c,i}$. Figure 3 presents the mean wall temperature in the evaporator section $\overline{T}_{e,w}$ (left column) and the inner temperature at the top of the condenser section $T_{c,i}$ (right column) as functions of the heat-source temperature $T_{e,in}$ for various filling ratios V^+ and a heat-sink temperature $T_{c,in}$ of 20 °C. Conditions where the thermosyphon did not operate were excluded from the plot. The bars of the data symbols in the diagrams indicate the minimal and maximal temperature fluctuations during the measurement.

At 10% and 20% filling ratios, it was observed that the evaporator wall temperature is higher for the 10% filling ratio compared to the 20% filling ratio. Additionally, for heat-source temperatures above 55 °C, fluctuations of up to approximately 10 °C in the wall temperature were detected. This increase in temperature variation suggests that, for brief periods, the thickness of the falling condensate film approached zero, leading to the formation of dry spots or local dry-outs in the upper part of the evaporator, as described by Mantelli [11].

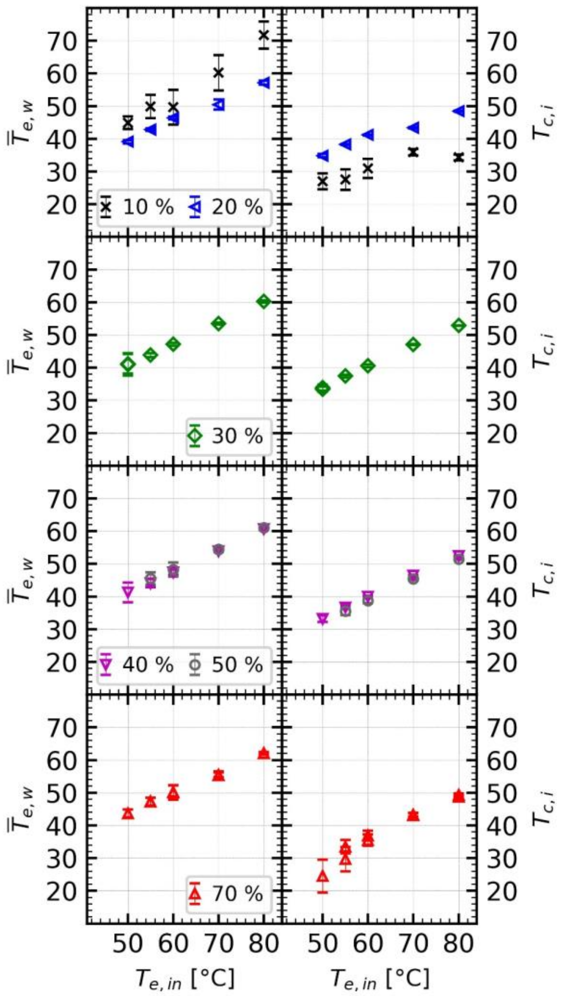

Figure 3. Mean evaporator wall temperature $\overline{T}_{e,w}$ (left column) and condenser inner temperature $T_{c,i}$ (right column) vs. heat-source temperature $T_{e,in}$ at different filling ratios V^+ for 20 °C heat-sink temperature $T_{c,in}$.

At the 30% filling ratio, the thermosyphon exhibited slight fluctuations in the evaporator wall temperature at a heat-source temperature of 50 °C. Notably, during this initial operation phase, the thermosyphon did not reach a steady state, indicating that a continuous, uniform falling film had not yet formed. As a result, the liquid film intermittently broke into rivulets within the evaporator, causing intermittent dry patches. However, as explained by Faghri [12], such localised dry spots on the evaporator wall do not typically result in significant heat transfer limitations, as the wall temperature is expected to stabilise over time. This behaviour was further evidenced by the steady-state thermal performance observed at higher heat-source temperatures of 60 °C to 80 °C. Similar behaviour was reported in previous studies by Cáceres et al.

[13], involving a 3 m-long thermosyphon with identical 1 m-long evaporator and condenser sections.

At 40%, 50%, and 70% filling ratios, a similar operational pattern to that of the 30% filling ratio was observed, characterised by minor fluctuations and eventual stabilisation at higher heat-source temperatures. However, at 70% filling ratio, increased oscillations in the inner temperature of the condenser were detected. These temperature fluctuations can be primarily attributed to bubble surges in the evaporator and the impact of liquid slugs against the thermosyphons's condenser end cap, indicating that the geyser boiling phenomenon occurred. When the heat input was increased to a heat-source temperature of 60 °C, nucleate boiling occurred, allowing the system to reach steady-state temperatures.

3.2 Average heat transfer coefficient in the evaporator section

Figure 4 illustrates the average experimental heat transfer coefficient in the evaporator section $\bar{h}_{e,exp}$ as a function of the heat-source temperature $T_{e,in}$ for different filling ratios V^+ and heat-sink temperatures $T_{c,in}$ of 20 °C (top) and 30 °C (bottom). Conditions where the thermosyphon did not operate were excluded from the plot. For each heat-sink temperature, starting with the highest filling ratio of 70% at 20 °C and 100% at 30 °C, the heat transfer coefficient initially increased as the filling ratio decreased to 30% and its value reached about 3.2 kWm^{-2}K^{-1}. However, at lower filling ratios of 10% and 20%, the heat transfer coefficients were reduced compared to 30%. This deterioration can be attributed to the decreased liquid volume and wetted area in the evaporator section as the filling ratio decreased, leading to partial dry-out in the upper part of the evaporator section, as described in Section 3.1. The maximum partial dry-out occurred at the lowest filling ratio of 10%. Consequently, the boiling heat transfer coefficient at this filling ratio was lower than that observed at a 30% filling ratio.

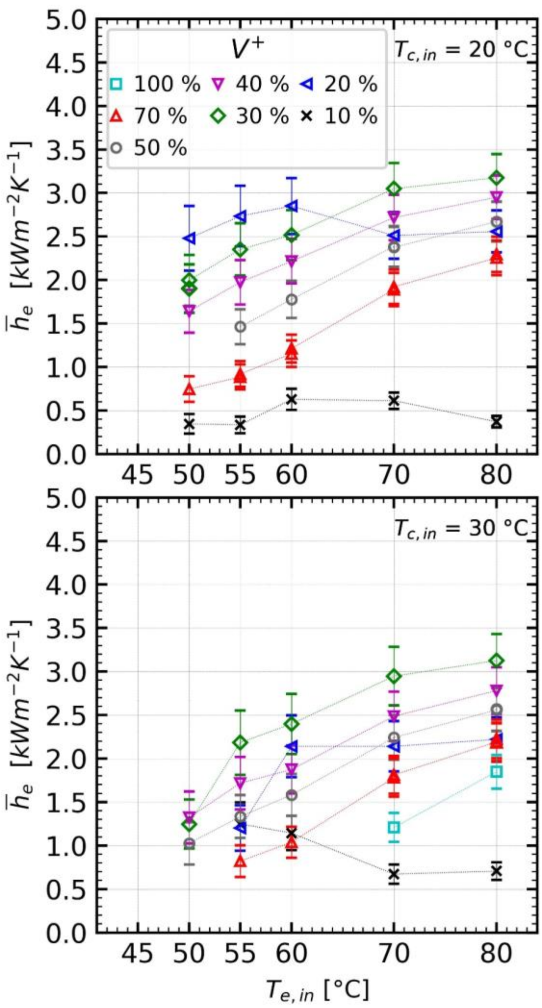

Figure 4. Average experimental heat transfer coefficient in the evaporator $\bar{h}_{e,exp}$ vs. heat-source temperature $T_{e,in}$ at different filling ratios V^+ for 20 °C (top) and 30 °C (bottom) heat-sink temperature $T_{c,in}$.

3.3 Average heat transfer coefficient in the condenser section

Figure 5 illustrates the average experimental heat transfer coefficient in the condenser section $\bar{h}_{c,exp}$ as a function of the heat-source temperature $T_{e,in}$ for different filling ratios V^+ and heat-sink temperatures $T_{c,in}$ of 20 °C (top) and 30 °C (bottom). Conditions where the thermosyphon did not operate were excluded from the plot. For 20 °C heat-sink temperature, a relatively constant value of approximately 3.0 kWm^{-2}K^{-1} was observed. In contrast, at a heat-sink temperature of 30 °C, higher heat transfer coefficients up to 6 kWm^{-2}K^{-1} were recorded. This increase in heat transfer performance is attributed to the reduction in the temperature difference between the saturated vapour temperature and the condenser surface temperature. The smaller temperature difference at 30 °C results in a thinner condensate film, reducing heat conduction resistance. This phenomenon is further evidenced by the higher heat transfer coefficients observed at the 10% filling ratio, where the limited liquid volume in the thermosyphon further decreases the film thickness, leading to higher heat transfer coefficients.

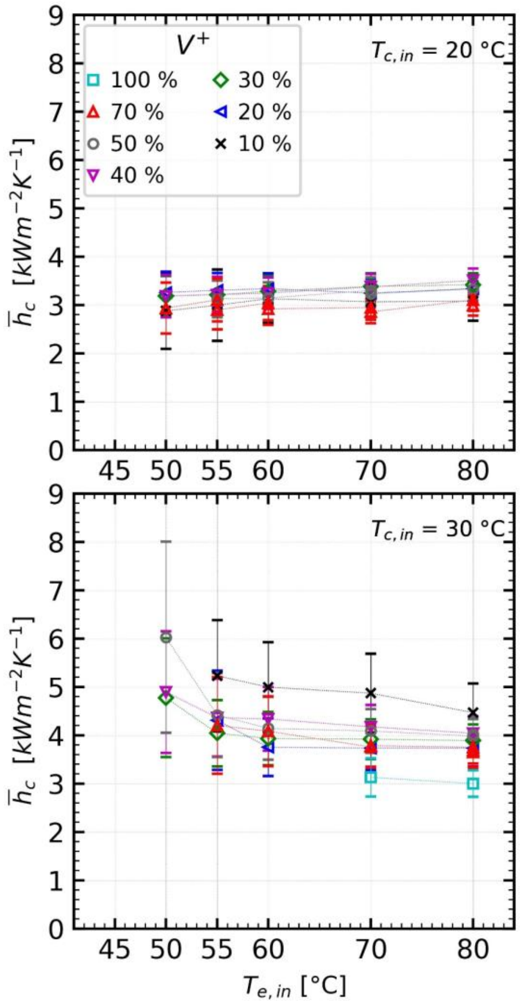

Figure 5. Average experimental heat transfer coefficient in the condenser $\bar{h}_{c,exp}$ vs. heat-source temperature $T_{e,in}$ at different filling ratios V^+ for 20 °C (top) and 30 °C (bottom) heat-sink temperature $T_{c,in}$.

3.4 **Overall thermal resistance**

Figure 6 illustrates the mean overall thermal resistance of the test thermosyphon R_{th} as a function of the heat flux q_e for different filling ratios $V^+$and heat-sink temperatures $T_{c,in}$ of 20 °C (top) and 30 °C (bottom). Conditions where the thermosyphon did not operate were excluded from the plot. For both 20 °C and 30 °C heat-sink temperatures, it was generally observed that the thermal resistance decreased with increasing heat-source temperatures, except at the 10% filling ratio. As discussed in Section 3.2, the decrease in the heat transfer coefficient in the evaporator section at this low filling ratio was attributed to local dry-out, which consequently led to an increase in the thermal resistance. It can be observed that thermal resistance remained relatively stable and reached its lowest values of about 0.006 KW^{-1} at the 20% and 30% filling ratios for both investigated heat-sink temperatures.

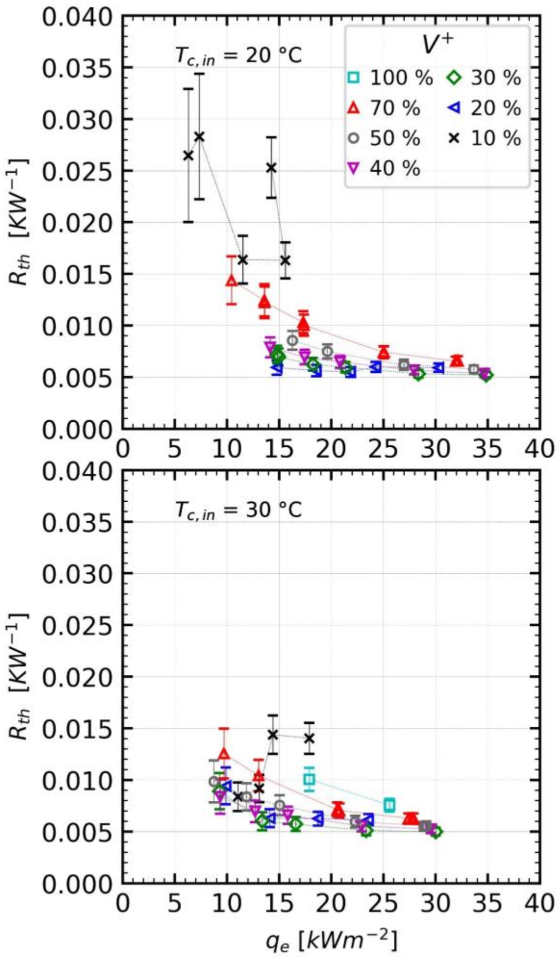

Figure 6. Mean overall thermal resistance R_{th} vs. heat flux q_e at different filling ratios V^+ for 20 °C (top) and 30 °C (bottom) heat-sink temperatures $T_{c,in}$.

As previously discussed and demonstrated in earlier studies [13–15], at a 20% filling ratio, increased heat input may lead to the undesirable formation of local dry-outs due to the low liquid content. Consequently, based on these observations, a 30% filling ratio was considered the most suitable for achieving steady-state thermosyphon operation under the investigated thermal conditions. Steady-state operation is defined as the state where no fluctuations occurred due to intermittent operation, partial dry-out or geyser boiling, as discussed in Section 3.1.

3.5 **Influence of evaporator section length**

The results of this study were compared with those of a previous investigation conducted by Cáceres et al. [16] to assess the influence of the evaporator section length. In their study, the same 8 m-long thermosyphon used in this work featured an extended evaporator section length of 2 m, while the condenser section length remained unchanged at 1 m. Figure 7 depicts the percentage ratio of the heat transfer rate for a 2 m-long evaporator section to that of a 1 m-long evaporator section, plotted against the heat-source temperature $T_{e,in}$ at various filling ratios V^+ for a heat-sink temperature $T_{c,in}$ of 20 °C. Positive values in the plot indicate an increase in heat transfer rate with the longer evaporator section, and negative values indicate a decrease. Conditions where the thermosyphon did not operate were excluded from the plot. Generally, an increase in the heat transfer rate was observed at heat-source temperatures above 55 °C when a longer evaporator section was used. This enhancement can be primarily attributed to the doubled heat transfer area, which allowed a higher heat input at the same heat-source temperatures.

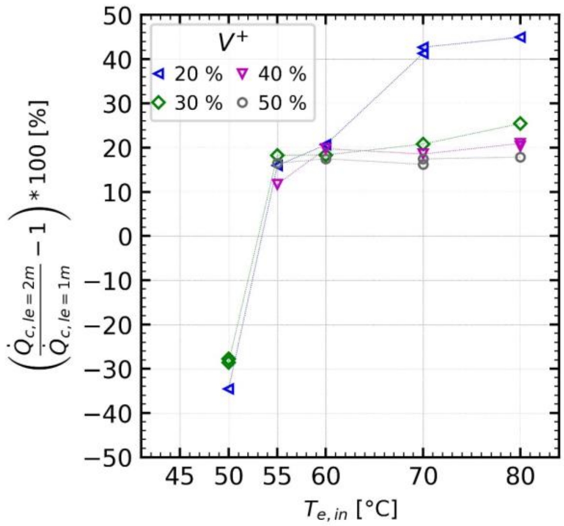

Figure 7. Percentage ratio of heat transfer rates $\dot{Q}_c$ of an 8 m-long thermosyphon with 1 m resp. 2 m evaporator section vs. heat-source temperature $T_{e,in}$ at different filling ratios V^+ for 20 °C heat-sink temperature $T_{c,in}$.

In contrast, at lower heat-source temperatures, a reduction of the heat transfer rate of up to 35% was observed. This reduction is likely due to the thermosyphon failing to achieve operation with the extended 2 m-long evaporator section under these lower thermal conditions. In contrast, the thermosyphon with a 1 m-long evaporator section reached operation.

3.6 **Influence of adiabatic section length**

Similar to the approach described in Section 3.5, the influence of the adiabatic section length was evaluated by comparing the results of this study with those from a previous investigation conducted by Cáceres et al. [13], applying a 3 m-long thermosyphon with 1 m-long sections for the evaporator, adiabatic, and condenser. Figure 8 presents the percentage ratio of the heat transfer rates for both configurations.

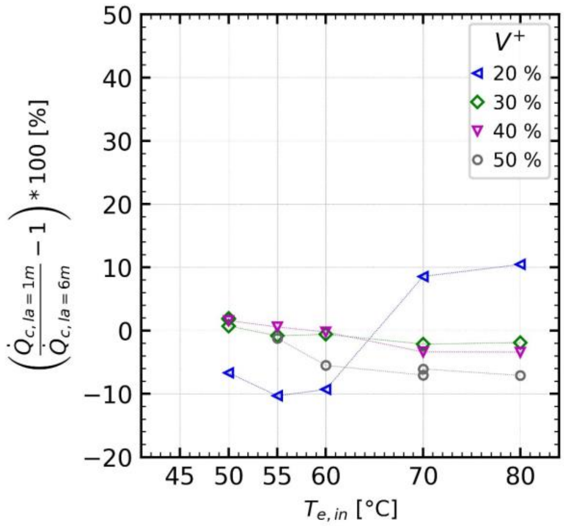

Figure 8. Percentage ratio of heat transfer rates $\dot{Q}_c$ of a 3 m long thermosyphon with 1 m adiabatic section resp. an 8 m long thermosyphon with 6 m adiabatic section vs. heat-source temperature $T_{e,in}$ at different filling ratios V^+ for 20 °C heat-sink temperature $T_{c,in}$.

Starting with a 20% filling ratio, a decrease in the heat transfer rate of approximately 10% was observed at lower heat-source temperatures of 50 to 60 °C. The heat transfer rate improved by about 10% as the heat-source temperature increased. As previously mentioned, partial dry-out may occur at low filling ratios and high heat inputs. For the thermosyphon with a 6 m-long adiabatic section, the probability of forming longer dry patches in the upper part of the evaporator section increases, which can deteriorate the heat transfer coefficient in the evaporator and, consequently, reduce the overall heat transfer rate.

At 30% and 40% filling ratios, the ratio of heat transfer rates remained relatively constant around zero, indicating that the influence of the adiabatic section length was negligible under these conditions. For a higher filling ratio of 50%, the heat transfer rate for the thermosyphon with a shorter adiabatic section showed a slight decrease, suggesting minimal sensitivity to adiabatic length variations at higher filling ratios.

4. Conclusions

The experimental investigation on the heat transfer capacity of a prototypically 8 m-long straight thermosyphon for nuclear spent fuel pool passive cooling has led to several conclusions:

1. The thermosyphon exhibited its highest thermal efficiency at a 30% filling ratio, initiating operation at a heat-source temperature of 50 °C and achieving a peak heat-transfer rate of approximately 4.0 kW at 80 °C.

2. An increase in the heat transfer coefficient in the evaporator was observed as the filling ratio decreased to 30%, reaching a maximum of 3.2 $kWm^{-2}K^{-1}$ at 80 °C.

3. At the filling ratios of 10% and 20%, a deterioration in the heat transfer coefficient was linked to partial dry-out.

4. Extending the evaporator section from 1 m to 2 m improved the heat transfer rate at heat-source temperatures above 55 °C, due to the increased heat transfer area. However, at lower temperatures, the thermosyphon with the extended section failed to achieve steady-state operation, resulting in a 35% reduction in heat transfer rate.

5. The adiabatic section length had a negligible effect on heat transfer at 30% and 40% filling ratios. At low filling ratios, the longer adiabatic section led to dry patches, reducing performance, while at 50% filling ratio, only slight variations were observed.

This investigation offers a dataset for numerical model developments and validation of numerical simulations on 8 m-long thermosyphons. In future work, the experimental results will be used to validate and improve the code system ATHLET incorporating the modelling of the thermosyphon bundle operation as an integral component of the AC^2 code.

5. ACKNOWLEDGEMENTS

The presented work was funded by the German Federal Ministry for the Environment, Nature Conservation, Nuclear Safety and Consumer Protection (BMUV, project no. 1501612A) on basis of a decision by the German Bundestag.

References

[1] INTERNATIONAL ATOMIC ENERGY AGENCY. 2016, Safety of nuclear power plants: Design. Specific Safety Requirements No. SSR-2/1 (Rev. 1).

[2] M. H. Kusuma, N. Putra, A. R. Antariksawan, R. A. Koestoer, S. Widodo, S. Ismarwanti and B. T. Verlambang, Passive cooling system in a nuclear spent fuel pool using a vertical straight wickless-heat pipe. International Journal of Thermal Sciences, 2018. 126: p. 162–171.

[3] M. H. Kusuma, N. Putra, A. R. Antariksawan, Susyadi and F. A. Imawan, Investigation of the Thermal Performance of a Vertical Two-Phase Closed Thermosyphon as a Passive Cooling System for a Nuclear Reactor Spent Fuel Storage Pool. Nuclear Engineering and Technology, 2017. 49(3): p. 476–483.

[4] J. Choi, C. Lim and H. Kim, Fork-end heat pipe for passive air cooling of spent nuclear fuel pool. Nuclear Engineering and Design, 2021. 374: p. 111081.

[5] C. Grass, R. Kulenovic and J. Starflinger, Experimental study on heat transfer characteristics of long two-phase closed thermosiphons related to passive spent fuel pool cooling. in Joint 19th IHPC and 13th IHPS, 2018. Pisa, Italy.

[6] C. Graß, A. Krüssenberg, R. Kulenovic, F. Weyermann, J. Starflinger and A. Schaffrath, Detailed Experimental and Analytical Study on Long Two-Phase Closed Thermosiphons Related to Passive Spent-Fuel Pool Cooling. in International Conference on Nuclear Engineering - ICONE, 2018. London, England.

[7] A. Krüssenberg, A. Schaffrath, A. Wielenberg, M. Kirsch, S. I. Cáceres Castro, R. Kulenovic and J. Starflinger, Long straight closed two-phase thermosiphons - Experiments of IKE and validation of ATHLET models. in International Topical Meeting on Nuclear Reactor Thermal-Hydraulics, Operation and Safety - NUTHOS, 2024. Vancouver.

[8] Kerntechnischer Ausschuss. 2015-11, KTA 3303:2015-11. Heat removal systems for fuel assembly storage pools in nuclear power plants with light water reactors.

[9] International Association for the Properties of Water and Steam. 2012, R7-97(2012): Revised Release on the IAPWS Industrial Formulation 1997 for the Thermodynamic Properties of Water and Steam.

[10] ISO. 1995, Guide to the expression of uncertainty in measurement - Part 1: Introduction.

[11] M. B. H. Mantelli, Thermosyphons and Heat Pipes: Theory and Applications Springer International Publishing, 2021).

[12] A. Faghri, HEAT PIPES: REVIEW, OPPORTUNITIES AND CHALLENGES. Frontiers in Heat Pipes, 2014. 5(1).

[13] S. I. Cáceres Castro, M. Kirsch, R. Kulenovic and J. Starflinger, Experimental investigation of the heat transfer characteristics, operating limits, and temperature distribution of a prototypically 3 m long two-phase closed thermosyphon for spent fuel pool passive cooling. Experimental and Computational Multiphase Flow, 2024. 6(3): p. 229–241.

[14] D. Jafari, S. Filippeschi, A. Franco and P. Di Marco, Unsteady experimental and numerical analysis of a two-phase closed thermosyphon at different filling ratios. Experimental Thermal and Fluid Science, 2017. 81: p. 164–174.

[15] A. J. Robinson, K. Smith, T. Hughes and S. Filippeschi, Heat and mass transfer for a small diameter thermosyphon with low fill ratio. International Journal of Thermofluids, 2020. 1-2: p. 100010.

[16] S. I. Cáceres Castro, R. Kulenovic and J. Starflinger, Experimental investigation on the heat transfer capacity of a prototypically long straight thermosyphon bundle for nuclear spent fuel pool passive cooling. in International Conference on Nuclear Engineering - ICONE, 2024. Prague, Czech Republic.

Paper ID 125

Performance Evaluation of a Bi-porous Wicked Flat Miniature Loop Heat Pipe

Chandan Nashine[1], Toni Kumari[1], and Manmohan Pandey[1*]
[1] *Indian Institute of Technology Guwahati, India*
**Corresponding author email address:manmohan@iitg.ac.in*

Abstract

This study presents the fabrication and testing of a bi-porous nickel wicked flat evaporator miniature loop heat pipe. The device demonstrated successful startup at a heat load of 10 W and efficiently removed up to 270 W using methanol as the working fluid. The transient thermal response of the heat pipe was analyzed across various heat loads, revealing stable operation throughout the tested range. The device's thermal resistance decreased with the rising heat load, reaching approximately 0.3°C/W at 270 W. This reduction in thermal resistance is attributed to enhanced vapor flow rates that improve heat transfer performance. Additionally, the condenser's thermal resistance exhibited an initial increase due to underutilization at low heat loads but decreased as mass flow rates improved with higher loads. The evaporator heat transfer coefficient increases with an increase in heat load. Overall, the findings highlight the effective thermal management capabilities of the bi-porous nickel wicked flat evaporator miniature loop heat pipe.

Keywords: Miniature loop heat pipe; Flat evaporator; Bi-porous wick; Nickel wick; Thermal resistance

1. Introduction

Loop heat pipes (LHPs) are innovative thermal management solutions that utilize phase change to transport heat away from critical components efficiently. Unlike traditional heat pipes, LHPs are designed to function effectively in microgravity environments, making them ideal for aerospace applications [1]. Their flexible mounting options and minimal thermal resistance are crucial for high-performance electronics. Miniature loop heat pipes (MLHPs) are one of the most reliable, passive two-phase cooling techniques used for the thermal management of high-power electronics [2-3].

Recent advancements have emphasized the importance of flat evaporators in LHP design. Flat evaporators offer a larger heat exchange surface area, which is especially advantageous for modern electronics known for their compact designs and high-power densities. Integrating flat evaporators eliminates the need for extra transfer surfaces, reducing overall thermal resistance and improving system efficiency [4-7].

The wick plays a vital role in heat dissipation by providing the necessary evaporation surface area [8]. The wick's design parameters, material, and working fluids must be carefully assessed to ensure optimal system performance [9]. The porous wick must have a high capillary driving force to overcome pressure drops and ensure sufficient liquid return. This requires minimizing effective pore radii. However, the wick must also have low hydraulic resistance for high flow rates, which requires high porosity, large pore radii, and an efficient pore structure [10]. Balancing capillary pressure and permeability is challenging due to their opposing dependence on pore size. Bi-porous wicks represent a significant advancement in LHP technology. Engineered with two distinct pore sizes, these wicks enhance capillary action and reduce thermal resistance compared to traditional single-porous wicks [11]. Research shows that bi-porous wicks effectively manage liquid-vapor separation, improving overall LHP performance under varying conditions. The larger pores facilitate vapor flow, while the smaller pores maintain necessary capillary forces, ensuring reliable liquid supply to the evaporator surface during high heat flux conditions [12].

Therefore, bi-porous wicked structures are incorporated in some recent studies to overcome the challenge of poor pore connectivity and required permeability. The evaporator structure of MLHP can be of different types, such as cylindrical, flat, and disk-shaped [13]. Since MLHP is mostly preferred for cooling electronic equipment, it is easier to mount a flat evaporator directly over the heat source. Flat evaporator MLHP can be directly mounted over the heat source and does not require any saddle for the evaporator assembly. Thus, flat evaporator structures are generally preferred for the thermal management of electronic packages [14].

Therefore, a bi-porous wicked flat evaporator MLHP is developed in the current work to solve the challenge of poor pore connectivity and required permeability. The evaluation of bi-porous wicked flat miniature loop heat pipes is a promising area of research in thermal management technology. By addressing existing challenges and utilizing recent advancements in wick design and fluid dynamics, this research seeks to improve the reliability and efficiency of cooling solutions for next-generation electronic devices.

2. Methodology

The Nickel wick was directly sintered over the evaporator base plate to reduce the thermal contact resistance between the wick surface and the evaporator plate. The sintering of the nickel powder was done at 850°C for 2 hours.

2.1. Fabrication

The bi-porous wick was composed of a mixture of nickel powder of granule size less than 50 microns mixed with salt (sodium chloride) 15% by volume and 15% graphene nano-particles (5-10 nm). The silicon oil was used as a binder and pore former to fabricate the wick. The graphene provides better strength to wick, which makes it suitable for machining ability easily for making grooves.

Figure 1 shows the fabricated flat evaporator for MLHP. Figure 2 shows the fabricated MLHP test section. The copper tubing was brazed in the evaporator section. Table 1 shows the details of MLHP parameters.

Figure 1. Fabricated bi-porous Nickel wicked evaporator

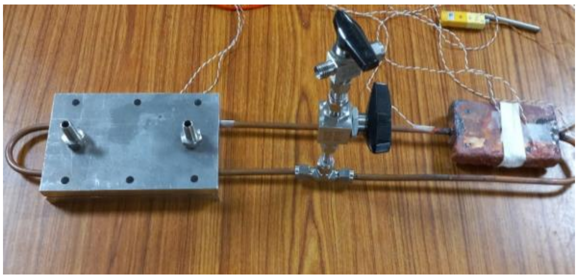

Figure 2. Assembled MLHP device

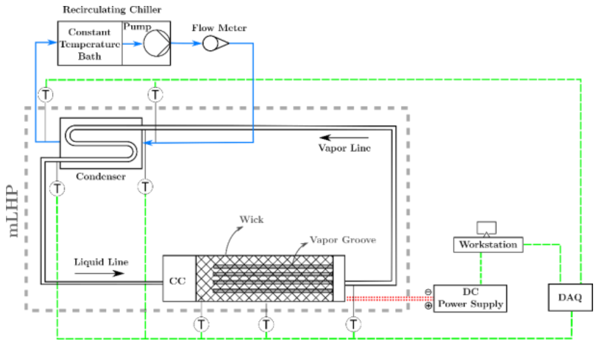

Figure 3. Experimental setup

2.2. Charging

The MLHP was first evacuated using a rotary vane pump up to 10-2 Torr. Further, the device was charged with methanol. The charging ratio was kept at 50%.

Table 1. Experimental parameters of MLHP.

Base-Plate Material	Copper
Wick Material	Nickel Powder size <50 µm
Charging Ratio	50%
Working Fluid	Methanol
Transport lines	ID=4 mm OD=6 mm
Overall Length	590 mm
Pore Radius of Wick	<10 µm
Porosity of wick	50%

2.3. Experimental setup

Figure 3 shows the experimental setup of MLHP. A DC power supply was used to supply power to the flat ceramic heater mounted over the evaporator base plate. T-type thermocouples were placed at different locations of MLHP. NI-DAQ was used to record the temperature data measured. A pin-finned heat sink was mounted over the condenser region. A recirculating chiller was used to maintain the heat sink temperature constant. High conductive thermal paste was used to mount the heater over the evaporator plate. The experiments were performed at 20°C sink and 23°C ambient temperatures. The Experimental investigation of MLHP is performed using methanol as the working fluid.

3. Results and discussion

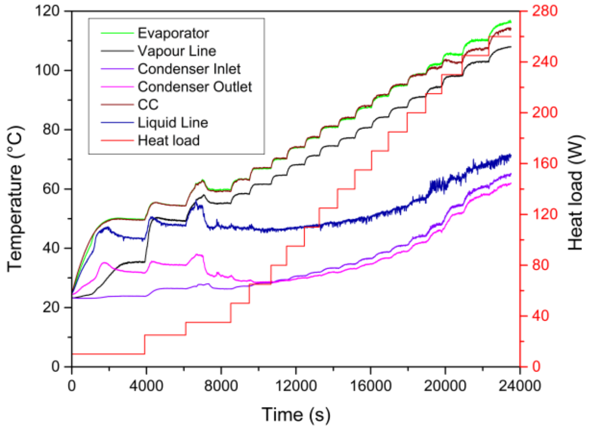

Figure 4. Transient response of MLHP at different heat load

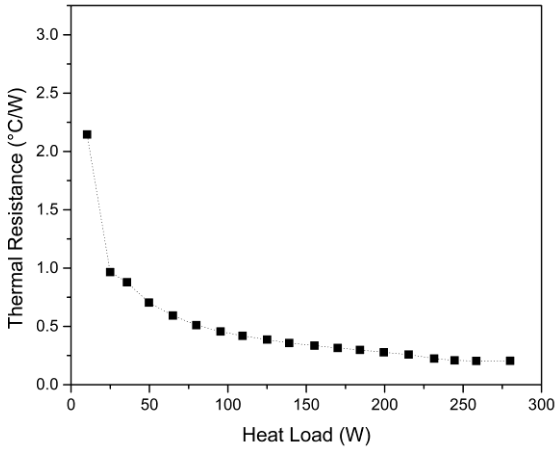

Figure 5. Effect of heat load on thermal resistance of MLHP system

Figure 4 shows the transient thermal response of MLHP at various heat loads. The device showed a successful start-up at 10 W. The MLHP was capable of removing 270 W of heat load. The MLHP shows stable operation in all heat loads. When the heat load rises, the evaporator vaporizes more working fluid. This process absorbs heat from the liquid, raising the evaporator's temperature. The saturation temperature of the working fluid increases with rising pressure, which is also elevated by increased vapor production. Figure 5 shows the effect of heat load on the thermal resistance of the MLHP system. The thermal resistance decreases with an increase in heat load. At 270 W heat load, the thermal resistance of the MLHP was around 0.3°C/W. When the heat load increases, the evaporator vaporizes more working fluid. This results in a higher vapor flow rate, which improves heat transfer and reduces thermal resistance. The increased vapor mass flow efficiently transports heat to the condenser, leading to better LHP performance. Figure 6 shows the variation of evaporator thermal resistance with heat load. The thermal resistance of the evaporator in the MLHP initially decreases with increasing heat load but eventually stabilizes. The evaporator's wick structure uses capillary forces to draw liquid from the condenser. As the heat load rises, these capillary forces become more efficient, ensuring quicker liquid replenishment and efficient heat transfer. The capillary pressure adjusts dynamically to accommodate the higher vapor flow, reducing thermal resistance. Eventually, with continued increases in heat load, the wick reaches its maximum capillary pumping capacity. This occurs when the meniscus within the wick is reduced to the size of the wick material's pores. Beyond this point, further increases in heat load do not significantly improve liquid return rates or vapor flow, stabilizing thermal resistance.

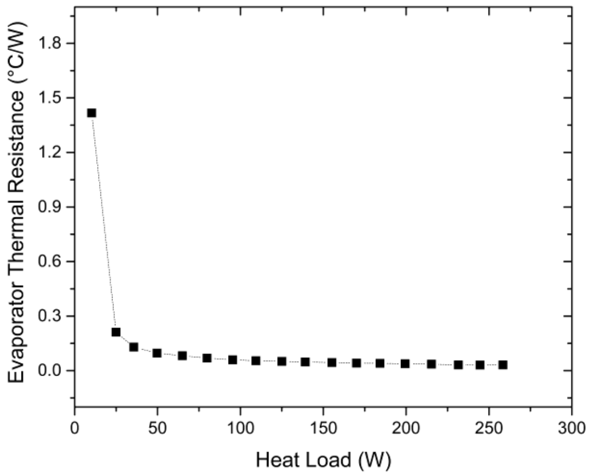

Figure 6. Effect of heat load on evaporator thermal resistance

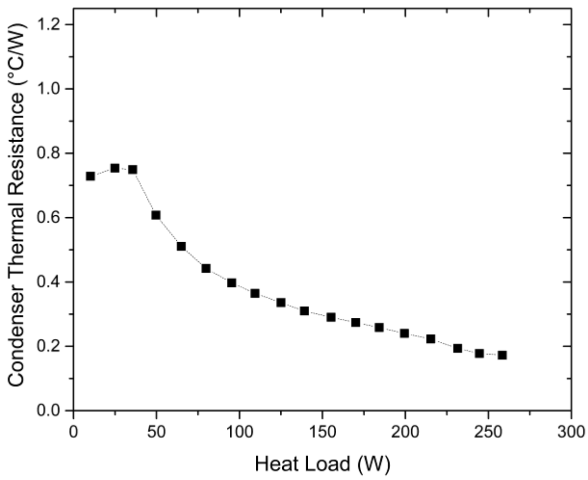

Figure 7. Effect of heat load on condenser thermal resistance

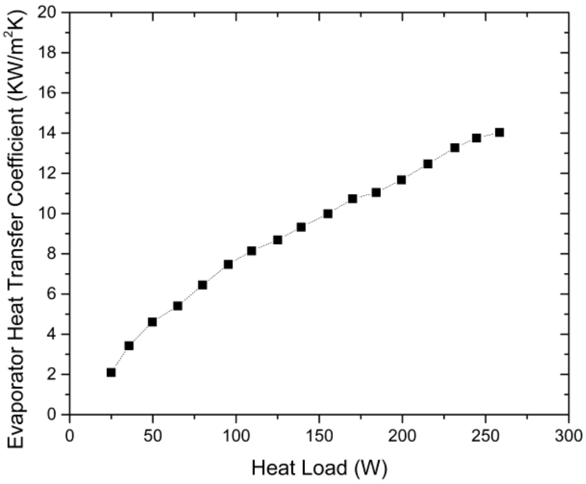

Figure 8. Variation of evaporator heat transfer coefficient with heat load

Figure 7 shows that the condenser thermal resistance decreases with increased heat load. At low heat loads, the condenser operates inefficiently due to underutilization. The liquid exiting the condenser is near the sink temperature, limiting its ability to remove heat from the vapor. This underutilization increases thermal resistance, leading to higher system temperatures. Also, the working fluid's mass flow rate is low at low heat loads. This can force the compensation chamber to increase its temperature significantly to compensate for heat leaks from the evaporator. The higher compensation chamber temperature contributes to increased thermal resistance in the condenser. Figure 8 shows the variation of the evaporator heat transfer coefficient with the heat load. As the heat load increases, the evaporator heat transfer coefficient also increases. When the heat load rises, the evaporator vaporizes more working fluid. This increased vapor production boosts the vapor mass flow rate, enhancing overall heat transfer efficiency. The higher vapor flow improves convective heat transfer from the evaporator surface, resulting in a higher heat transfer coefficient.

4. Conclusion

A novel bi-porous capillary wicked evaporator-based miniature loop heat pipe was fabricated and tested. The working fluid used was methanol. The developed MLHP device demonstrated effective thermal management capabilities across varying heat loads. The device successfully initiated operation at low power levels of 10 W and maintained stable performance while efficiently handling high heat loads up to 270 W at a sink temperature of 20 °C. The thermal resistance of the MLHP decreases with increased heat load. The thermal resistance was found to be around 0.3°C/W at 270 W heat load. The observed decrease in thermal resistance with increasing heat load highlights the importance of vapor flow dynamics and capillary action in optimizing heat transfer within the system. These results indicate that bi-porous wick structures are promising for advancing flat loop heat pipe technology, providing practical solutions for applications requiring reliable and efficient thermal management.

5. Acknowledgement

This work was partially funded through Grant No. CRG/2020/006333 by SERB, DST, Govt. of India. Financial support was provided to the first author by the Technology Innovation Hub (TIH), IIT Guwahati.

References

[1] Ahmed S, Pandey M, Kawaji M. Loop heat pipe design: an evaluation of recent research on the selection of evaporator, wick, and working fluid. Journal of Thermal Science and Engineering Applications. 2022 Jul 1;14(7):070801.

[2] Nashine, C. and Pandey, M., 2021. Thermo-hydraulic modelling of miniature loop heat pipes. In Proceedings of the 26thNational and 4th International ISHMT-ASTFE Heat and Mass Transfer Conference December 17-20, 2021, IIT Madras, Chennai-600036, Tamil Nadu, India. Begel House Inc..

[3] Ahmed, Shahnawaz, Chandan Nashine, and Manmohan Pandey. "Thermal management at microscale level: detailed study on the development of a micro loop heat pipe." Micro and Nano Engineering 16 (2022): 100150.

[4] Szymanski, Pawel, Richard Law, Ryan J. McGlen, and David A. Reay. "Recent advances in loop heat pipes with flat evaporator." Entropy 23, no. 11 (2021): 1374.

[5] Xiong, Kangning, Yanqiu Huang, and Shuangfeng Wang. "Experimental research on the thermal performance of a flat evaporator loop heat pipe with a new composite wick." Applied Thermal Engineering 246 (2024): 122927.

[6] Nam, Bomi, and Wukchul Joung. "Heat transport characteristics of a flat-evaporator loop heat pipe for use in a thermal management system of electric vehicles." International Journal of Heat and Mass Transfer 227 (2024): 125553.

[7] Zhao, Tianyuan, Zhengyuan Ma, Zikang Zhang, Weizhong Deng, Rui Long, Wei Liu, Lei Ma, and Zhichun Liu. "Experimental investigation of a loop

heat pipe with a flat evaporator and cupric oxide nanofluids as working fluid." Energy Reports 7 (2021): 7693-7703.
[8] Nashine, Chandan, and Manmohan Pandey. "Theoretical modelling of miniature loop heat pipe." In ASTFE Digital Library. Begel House Inc., 2022.
[9] Kumari, Toni, Chandan Nashine, and Manmohan Pandey. "Fabrication of a cost-effective bi-porous composite wick for loop heat pipes." In North-East Research Conclave, pp. 117-124. Singapore: Springer Nature Singapore, 2022.
[10] Kumari, Toni, and Manmohan Pandey. "Study of Physical Characteristics of a Bi-porous Composite Capillary Wick for a Flat Miniature Loop Heat Pipe." In Conference on Fluid Mechanics and Fluid Power, pp. 211-221. Singapore: Springer Nature Singapore, 2022.
[11] Nashine C, Mohaddin NA, Sarma SK, Pandey M. Experimental studies on sintered bi-porous wicks for loop heat pipe. in joint 21st IHPC and 15th IHPS conference. Melbourne, Australia.
[12] Nashine, Chandan, Nadaf Arman Mohaddin, Rohit Kumar, Sandip Kumar Sarma, and Manmohan Pandey. "Development and Characterisation of Bi-porous Metallic Wick for Loop Heat Pipes." In North-East Research Conclave, pp. 125-132. Singapore: Springer Nature Singapore, 2022.
[13] Anand AR, Jaiswal A, Ambirajan A, Dutta P. Experimental studies on a miniature loop heat pipe with flat evaporator with various working fluids. Applied Thermal Engineering. 2018. 144: p. 495-503.
[14] Somers-Neal, Shawn, Tatsuki Tomita, Noriyuki Watanabe, Ai Ueno, and Hosei Nagano. "Experimental investigation of a 10 kW-class flat-type loop heat pipe for waste heat recovery." International Journal of Heat and Mass Transfer 231 (2024): 125865.

Paper ID 126(S3)

Identifying Niche of Heat Pipe Technology in Electric Vehicle Battery Cooling Applications

Randeep SINGH[1]*, Takeshi KOSHIO[1], Harutoshi HAGINO[1], Phan Thanh LONG[1], Tsuyoshi OGAWA[1], Tien NGUYEN[1], Masataka MOCHIZUKI[1], Thanudej AUSSAWINWONG[2], Charoenrath CHANSIRISATHAPORN[2], Kanokwan CHAICHANA[2]

Fujikura Ltd, 1-5-1 Kiba, Koto-Ku, Tokyo 135-8512, Japan
[2] *Fujikura Electronic Components (Thailand) Ltd, 68/1 Moo 4, Lamphun 51000, Thailand*
* *E-mail: randeep.singh@jp.fujikura.com*

Abstract

In this paper, passive cooling approaches based on heat pipes has been considered to enhance thermal management of electric vehicle (EV) battery system. Heat pipe based passive system with high effective thermal conductivity and flexibility to be implemented in constrained spaces has been applied at cell, module and pack level to resolve hot spot, integration, system complexity and leakage hazard related issues in existing battery packs. Thin heat pipes have been applied directly on prismatic cells to cool terminal externally, and current collector internally providing 2-5 °C temperature reduction at these heat generation sites. In another case, heat pipes help to improve thermal uniformity on cell surface by more than 5 times of baseline metal interspace plate design. Cooling of battery module bus bar by heat pipes diffuse hot spots, and provide thermal uniformity from module top to bottom. At pack level, heat pipes helped to simplify overall mechanical design of the battery pack by downsizing cold plates thereby reducing system complexity and thermal uniformity to within 5 °C. Specifically, this work extends the concept of hybridization of two-phase technology, based on heat pipes, with single-phase technology, predominately based on liquid cooling, to extend performance, functionalities and operational regime of cooling solutions for vehicle battery packs. In summary, heat pipes will help to improve overall reliability, performance and safety of air and liquid cooling systems in electric vehicles.

Keywords: Li-ion battery, Electric vehicle, Heat pipe, Two-phase cooling, battery pack, terminal cooling

1. Introduction

Battery Electric Vehicles (BEVs) are expected to completely replace Ignition Combustion Engine (ICE) Vehicles by 2050 timeline [1] depending on regional interests, people affordability, government support and more importantly technical innovations to make these vehicles more greener and price affordable for common people. Effective thermal management of battery systems in electric vehicles is very critical for driving range, fast charging, driving comfort and long term reliability of battery system. Figure 1 presents the simplified form of vehicle electric power train with charging system from inlet port to battery, and discharging system (or traction system) from battery to motor [2].

Electric vehicle, in contrast with engine vehicle, have more specific and specialized cooling needs. Specific needs because of high sensitivity of electronics and electrical systems to temperature. Engine vehicle generally uses materials, which have high tolerance to wider temperature ranges. Specialized needs because of exclusive requirements and design customization needed per system functionalities and specifications. Overall electric propulsion system consists of electric system (like cables, connector, fuse, motor), electronic system (like inverter, converter, OBC) and electrochemical system (like Li-ion batteries).

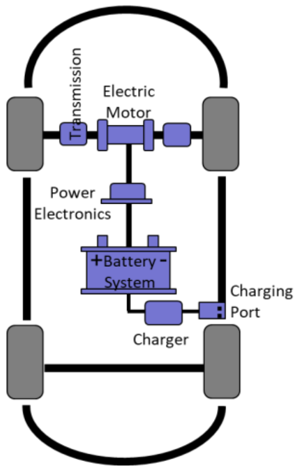

Figure 1. Electrified propulsion system in electric vehicle showing battery system and motor along with control electronics

Each of these categories have very specific cooling requirements due to different materials, chemistry and functions of these systems. Additionally, each system even in similar categories have diverse thermal challenges owing to their electrical architecture (or simply design), location in car (front, back, in-cabin, under-cabin) and cooling method (air-base, liquid-base, conduction to chassis). Cooling requirements of these devices could be dictated by material temperature limits (SiC chip have higher temperature limits than Si chip), criticality of system (autonomous drive system need higher redundancies than infotainment system) and sometime mere system cost (to avoid replacement costs).

Most components of electric drive train requires thermal management for performance and longevity. Electrical (e.g. e-motors) and electronic systems (e.g. IGBTs – inverter, converters) can sustain higher operating temperatures (~ 100 to 150°C) than electrochemical systems like battery cells (~ 40 °C) [3]. Lithium-Ion cells, in either prismatic, cylindrical or pouch form, are invariably used for automotive batteries owing to their high energy density and better charging-discharging efficiency. For good calendar life and performance of Li-ion battery, temperatures should be maintained within narrow temperature range ~ 25 to 40 °C. For the battery electric vehicle (BEV), the range can reduce by 18% when driving on hot summer day (+35 °C, 40% RH) and by 36% when driving on cold winter day (~ -10 °C, 90% RH), due to cabin and battery thermal management. Based on aforesaid facts, it can be safely asserted that thermal management of automotive batteries is very critical for vehicle range (economy), performance and lifetime cost.

In light of above discussion, it is important to understand that existing state of cooling technology in vehicle has been mainly developed to manage engines and other mechanical systems, and therefore could not provide an efficient migration to vehicles with significant electric built (plug in hybrids - PHEVs, battery electric vehicles - BEVs). Battery systems in EVs are mainly cooled by cold plates with circulating liquid coolant that dissipate heat to remotely located radiator assembly. The system is effectively adaption of engine cooling mechanism however thermal needs and temperature sensitivity of batteries are very different than engines. Particularly, with the increasing energy density of battery systems and requirements to achieve 90% of state of charge within the time it need to fill gas in ICE (ignition combustion engine) vehicles, the thermal management for batteries is attracting attention for technically more innovation and economically more cost-effective system. Particularly, batteries need to maintain their temperature in very narrow bandwidth of 25-30 °C (with max of 40 °C for Li-ion based cells) which means that they might need heating during sub-zero climatic conditions, and cooling systems need to maintain more precise temperature control to achieve better longevity and reliable operation for battery systems. Cooling system enhancements based on heat pipes [4-8], loop heat pipes [9-11], phase change materials [12, 13] have been proposed and investigated by different researchers which could support to affect development of thermal management systems for next generation vehicular batteries. It is important that new technologies including two phase technologies based on heat pipes should consider some of critical factors to make proposed cooling solutions practically viable for implementation in actual mass produced electric vehicles. These includes:

1) *Space constraints*: battery systems are very densely packed and any new improvements need to critically consider available space for integration.
2) *Weight impact*: Automotive OEMs are very critical about running cost (or energy consumption) from every gram of added weight even if implanted technology show improvements.
3) *Added Cost*: This would be the prime factor for technology consideration unlike in high performance computing industry where performances are more critical than added costs. Generally, in automotive, cost images are judged on the basis of number of degree reduced for every added dollar cost.
4) *Performance Gains*: It is critical to judge performance metrics with respect to existing baseline system. Unlike computing sector, where every degree reduction in temperature is important, in automotive, two number gains are important to start considering new technologies for development.
5) *System Long-Term Reliability*: long term reliability and production quality of the enhancement technologies are important for practical considerations

In the present work, we have attempted to identify domains where two phase technology based on heat pipes could help to enhance thermal performance of the existing battery cooling systems. It is not attempted neither recommended that heat pipes could replace existing air or liquid cooling battery systems completely, but through their passive operation and superior thermal conductivity, heat pipe technology have potential to solve existing issues of hot spots, thermal gradient/non-uniformity, elevated operating temperatures during stress conditions, cooling system weight, leakage hazard and so on. Particularly, hybridization or optimum mixing of two phase and single phase technologies have potential to provide cooling design breakthroughs in area of battery thermal management.

2. Vehicle Battery System

Electric vehicle battery system in overalls comprises of battery cell modules and related control electronics [14] as shown in Figure 2. Cells are generally derived from Li-ion technology with different form factors (cylindrical, prismatic, pouch). Battery electronics consists of control devices to manage and monitor battery stacks, and includes cell management controller (CMC), battery management system (BMS), battery junction box (BJB) and associated high voltages cabling and connectors. Cooling system is largely considered part of mechanical hardware of the battery pack, and extend beyond battery system to include liquid flow loop and radiator units located elsewhere in the vehicle, and shared with other cooling loops meant to manage electro-mobility power electronics (OBC, Inverter, Converter) and autonomous drive assistance systems (ADAS), depending on vehicle cooling architecture. The current paper is mainly concentrated on cooling of the battery cells modules at cellular, module or pack level.

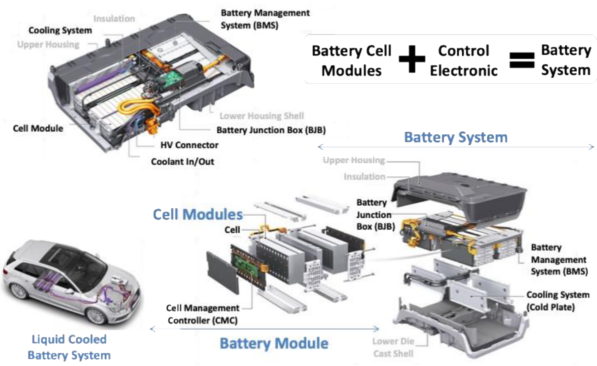

Figure 2. Vehicle battery system details [14]

2.1. Datacenter Analogy

While reviewing different technologies for battery system cooling, it is convenient to derive an analogy between vehicle battery system and high performance data center:

1. Battery modules arranged in pack while server racks arranged in data center facility both represents a modular approach
2. Battery modules have low heat density battery cells, and high heat density management systems (BMS, BJB) whereas data center rack have low power density auxiliary chips (MPU, power management) and high power main chipsets (CPU, GPUs)
3. In both types, heat collection from sources and dissipated remotely using designed facility (pump, manifolds, coolant distribution, radiator/chiller)
4. Both systems need to adapt in real time to changing operating and environmental conditions

There would be some stark difference between two systems, however current analogy could help to take some of the lessons learned from mature data center technology and consider it for battery pack cooling design.

3. Battery Thermal Generation

Heat is generated by battery cell via electrochemical reactions inside cell during charging/discharging (reversible heat), and via joule heating owing to current flow inside the conductive elements i.e. bus bars, terminals, current collectors, connectors (irreversible heat). More than 65-75% of generated heat is irreversible with remaining 25 to 35% reversible heat [15] depending on ambient temperatures. General tendency for battery heat is to increase with reducing ambient temperatures owing to inverse relation of cell internal resistance with temperature.

Traditionally, cells are arranged in module with the individual cooling systems (cold plates) which are then housed in the battery pack (Figure 3).

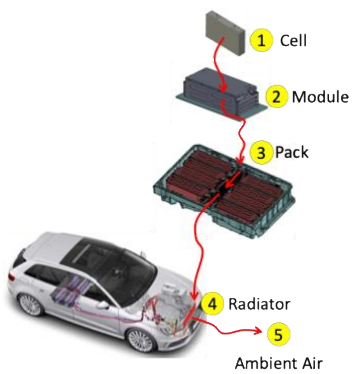

Figure 3. Thermal dissipation flow from cell to ambient as ultimate heat sink

Overall cells are connected in series and parallel combinations to achieve an overall pack voltage between 400 (current) to 800 V (next generation). Max current from 300 to 1000 A is possible to handle by EV battery packs depending on OEM, region and pack concept [16]. Typical cell voltage is ~ 3.7 V with capacity (ampere-hour) depending on cell size, type and pack concept (4.8 Ah cylindrical cells for Tesla Model Y, 55.6 Ah pouch cells for Kia EV6, 72 Ah prismatic cells for Audi Q8 e-tron) [17]. Under given operating conditions, battery cell could generate heat in wider spectrum ranging from 5-10 W for optimal operations, 50-100 W for sudden accelerations/discharging and fast charging conditions. With such wider range of heat generation, it is generally difficult to consider battery thermal mass capacity in cooling design, particularly for high end EVs with ultra fast or fast charging features. For reference, based on simple heat capacity calculations, fast discharge/charge from/to battery pack could fill thermal capacity (25 to 40 °C) of Audi e-tron battery within 4 min or less.

Battery module on an average considers heat dissipation of 100-200 W in their cooling system design (Figure 4) which is on the higher end of the spectrum when compared to different electronics and electric systems in EVs.

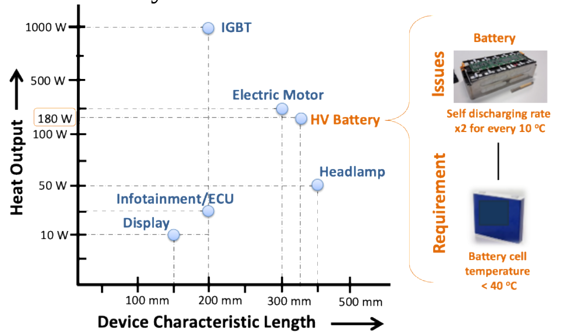

Figure 4. Heat output from different systems in EVs

From cooling system design viewpoint, the heat flux from battery modules/pack is on lower end ~ < 1 W/cm^2, however volumetric heat density for high voltage modules is high 100 kW/cm^3 (Figure 5).

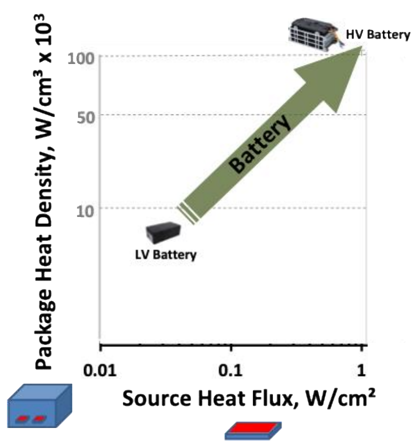

Figure 5. Heat flux versus package heat density for battery modules

In this case, the cooling system design need to concentrate heavily on the heat removal/transfer function to collect large amount of low flux heat from large pack (more than 1 x 2 m^2) area and transport/dissipate it to remotely located (> 2 m in some instances) radiator/chiller unit.

4. Battery Cooling Requirements

Concentrating on the electrochemical cellular makeup of the battery system (i.e. excluding associated electronics and electrical systems), cooling of the battery cell is required to satisfy different needs:

1) *Temperature Control*: Cooling system is expected to efficiently remove heat generated inside battery cells as a results of electrochemical reactions (reversible heat due to reactions in electrodes/electrolyte) and joule heating (irreversible heat due to current flow) during charging and discharging of the Li-ion matrix. For EVs, heat output per cell can vary from 5 to 50 W depending on cell geometry, charging/discharging rates (nominal versus fast charge) and ambient temperature. Target of the cooling system is to maintain battery pack as close to optimum temperatures of 20-25 °C for lithium-ion batteries
2) *Thermal Uniformity*: Thermal management system is expected to keep pack thermal gradient within 5 °C or better. Cell internal resistance show high dependence on their operating temperatures, and thus overall electric characteristics and pack range is affected by thermal non-uniformities.
3) *Safety***:** A thoroughly cooled battery system provide safety against thermal runaway and thus overall security against catastrophic failures related to elevated temperatures including fire hazards.
4) *Long Term Reliability***:** Battery life has direct dependence on its operating and storage temperatures [18]. As temperature of battery rises above permissible limits of 40 °C (for Li-ion cells), the extent of chemical reactions inside battery increases resulting in consequences of self-discharging, chemical aging and premature failures of the cells due to water loss and corrosion [19].

5. Battery Cooling Architecture

This section will review existing state of art of battery cooling system for electric vehicles to outline design attributes, mode of heat transfer and cooling concepts. It is important to understand the complexity of the EV battery system to appreciate challenges that any technology including heat pipe or vapour chambers would have to face in order to successfully implement in such rigid, rigorous and constrained atmosphere. Figure 6 represents a very simplified schematic of battery cooling system that outlines two different circuits that are available to dissipate heat generated by battery pack; 1) thermal dissipation directly to forced air cooled radiator (heat sink) when cooler ambients allows to maintain cell temperature less than 25 °C threshold, and 2) heat dissipation to chiller cooled by vapour compression system (VCS) when ambient temperatures are high or battery pack is undergoing fast charging/discharging sequences. In this case, VCS will have a separate two phase loop to dissipate battery heat to ambient via air cooled radiator.

Battery pack cooling design philosophy is based on number of factors including, but not limited to:

1. Nominal pack heat generation
2. Fast charging power (kW) which is generally higher for European OEM than Asian OEMs
3. Charging curve (maximum current, charging time) that directly affect overall heat generation
4. Battery packaging (cell to module, cell to pack)
5. Mode of cooling (air, liquid, two-phase, immersion)

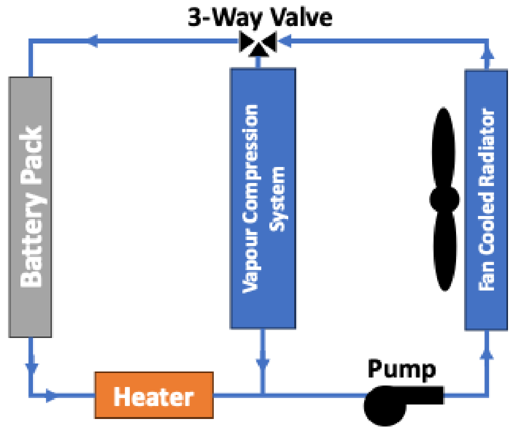

Figure 6. Schematic of battery cooling system immersion)

Depending on the vehicle class and maker, different cooling mechanism and architectures could be use to cool EV battery pack. On the lower end of the performance spectrum, air cooling provides simple and low cost cooling solution for low power battery packs. Figure 7 present air cooling for Lexus UX 300e [20] that uses chilled air circulated by fan in close circuit to dissipate heat from battery pack. Air cooling system has capacity limitation and low efficiency, and could sometimes results in dust contamination which could degrade system performance overtime. Cell to pack density with air cooling is lower due to larger ducting spaces need for circulating air.

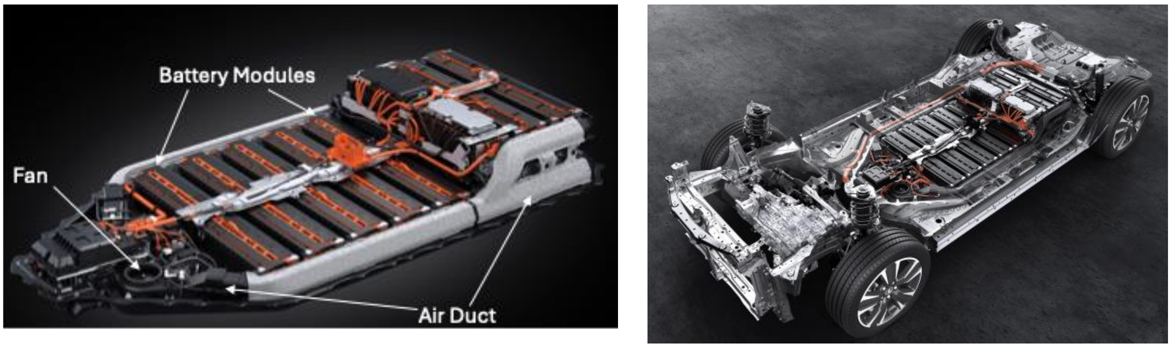

Figure 7. Air cooled Li-ion battery pack in Toyota Lexus UX 300e [20]

Liquid cooling, on the other hand, provide precise temperature control, high heat capacity and adaptation to changing cooling needs however system is complex, poses high demands on leakproof over vehicle life span, have high installation and maintenance costs. Generally, water based coolant (mix of water with ethylene glycol or propylene glycol) is used due to good performance, anti-freeze ability and cheap cost. Battery cells could be cooled from bottom side (Figure 8) or sides (Figure 9 & 10). Both approaches have their pros and cons, with the bottom cold plate [21] help to provide good isolation protection for high voltage batteries, and low connectivity/installation complexity by separating electric flow infrastructure and cooling system. Cold plate contacting cell sides would provide more efficient cooling due to larger contact surface area [22], however system usually tends to be complicated (Figure 9). Traditional methodology of bottom cooling of prismatic cells, and side cooling of cylindrical cell has been combined in innovative approach [23] to cool prismatic cells from side where cooling system provide structural support for pack as well (Figure 10). This approach would provide high cell to pack density, better cooling and economical structural approach with low complexity.

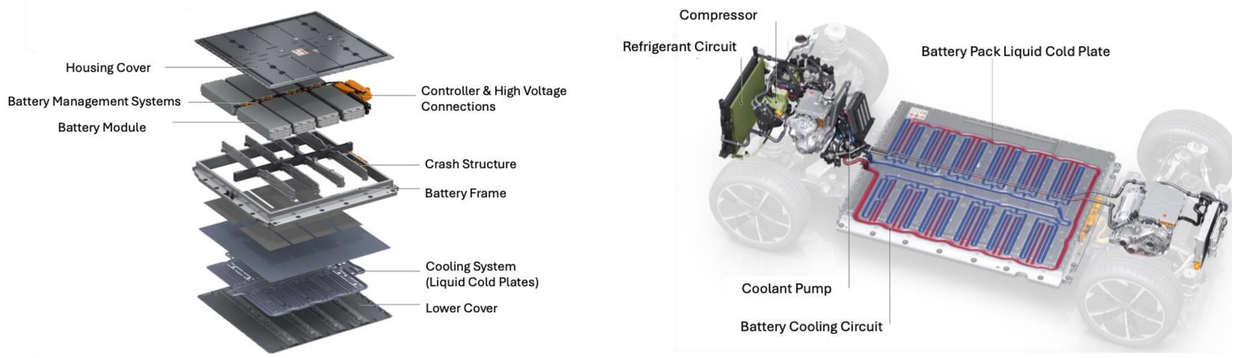

Figure 8. Liquid cooled battery pack in Audi Q4 e-tron [21]

Figure 9. Liquid cooling system for Tesla Model S battery pack [22]

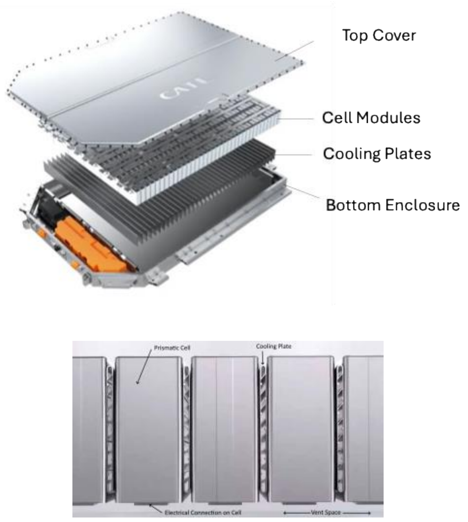

Figure 10. Liquid cooled battery pack with cooling system integrated in structures (CATL Qilin) [23]

Approach of direct refrigerant (two-phase) pumped cooling [24] has been attempted by some OEMs (Figure 11) where cooling efficiencies and capacities better than single phase liquid cooling could be achieved but at added complexity (difficulty in controlling temperature), system cost and environmental impacts (refrigerant leakage). Refrigerants like R134a and R1234yf has been in common use in such systems. High end carlines with ultra-fast charging features and operating in extreme temperature conditions could facilitate from this approach.

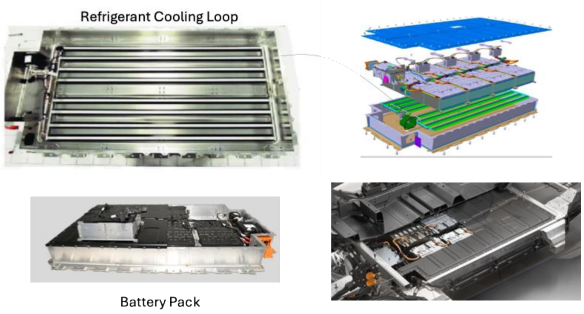

Figure 11. Refrigerant cooling system for battery pack of BMW i3 [24]

Immersion cooling have been attracting a lot of technical attention in data centers and recently in vehicle battery system due to their versatility to cool number of electronic/electrical system arranged in 3D manner. For battery pack cooling, the technique have been tried by limited and very specialized vehicles till now [25], however the approach is being developed by different institutes, [26] and as more experience is accumulated, it is expected to be available for more general carlines. Cooling efficiencies for immersion cooling is good when there are multiple heat sources including battery cells and battery electronics arranged in compact setting, however leakage control, system weight, system cost, serviceability are some of issues that need to be looked into more details. Figure 12 present immersion cooling system in its current state of art in market. Techniques like phase change material based cooling has been investigated by different companies/researchers however still the method is mainly explored in academic setting and difficult to apply for actual application unless clear advantages over approaches in practices are outlined.

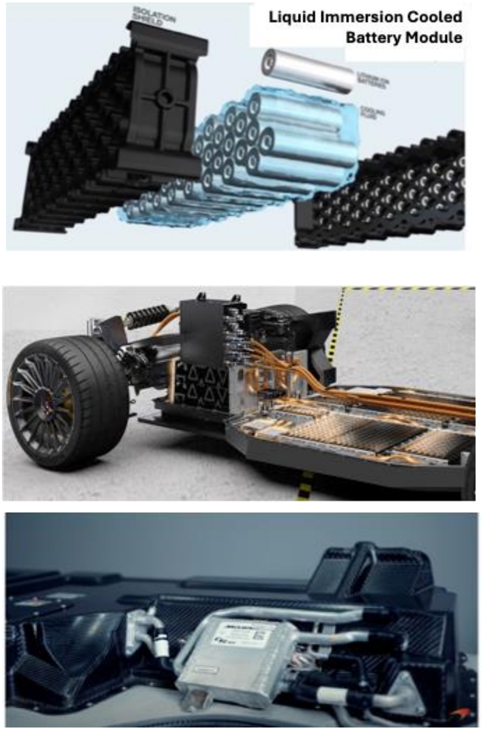

Figure 12. Immersion cooled battery pack [25]

6. Battery Cooling Enhancements with Heat Pipes

Existing thermal management architectures for electric vehicle battery packs have been primarily influenced by the cooling approaches for electric drive components including power electronics (on-board charger, traction inverter, power converter), motor and autonomous drive assistance system (ADAS) which are mostly liquid cooled. As discussed in previous section, air cooling is generally limited to low power battery systems in basic EV models and poses limitations for fast charging and adverse ambient conditions. Liquid cooling offers a safer thermal control options and could be readily implemented owing to the presence of liquid loop in the vehicle, and decades long experience with liquid cooling of engines (in ignition combustion engine (ICE) vehicles). Battery pack needs a dedicated liquid flow without influence from other components of e-drive due to temperature sensitive behaviour of battery cells, and its influence on pack longevity and operational performance. As explained earlier, battery pack can have a dedicated liquid loop with separate battery radiator, or this can share loop with power electronics through flow distribution control system.

Liquid based loop can control cooling capacity with the aid of temperature modulated flow control by pump system, and offer options to switch between structural based cooling (using thermal mass of battery system) for optimal drive modes, and high capacity liquid cooling (using liquid loop) for sudden acceleration/discharging and fast charging modes.

Said that, liquid cooling have performance to cost competitiveness however not always adequate in fulfilling cooling needs of battery packs under stress situations. Most of cabin base in EVs are occupied by battery modules arranged in single pack, and customarily cooled by low-end cold plates positioned under the modules. Such cooling system poses safety issues from liquid leakage in high voltage areas, presents temperature gradient within/amongst modules, have heavy weight due to extend of liquid coolant and cold plate volume, and have high system complexity (multiple cold plate integration and connectivity). In this section, we will look at some of these issues, and provide potential cooling enhancement solutions based on heat pipe based two phase technologies. It is important to emphasis that heat pipes would normally serve to enhance the thermal performance of existing cooling system, through their high effective conductivity and passive operation, and not meant to completely replace it. Although performance would be major need to effect introduction of heat pipes, however in certain instances, benefits of weight reduction, safety against leakage and/or addressing pack mechanical connectivity/complexity can support heat pipe implementation in the battery pack.

Cold plate technology can be mainly applied at the module or pack level (Figure 13) due to size, form factor, manufacturing limitations and integration complexities (die casted, extruded or CNC machined) of these devices which are generally in planar or plate form. For attachment directly to module, these are generally attached at bottom for single cold plate per module basis and sometime side when two modules sandwich one cold plate. Connecting multiple cold plates in overall pack for flow distribution introduces challenges against leak proofing and fault diagnostics. Single dedicated cold plate for overall pack help to address connectivity issues, however at the expense of manufacturing, logistics and integration complexities.

From thermal standpoint, the design and location of cold plate could provide cooling to only one side/face of the battery cell (Figure 13) through layers of thermal interface materials (minimum two locations), electrical isolation and pack enclosures. Figure 14 presents the breakdown thermal resistance from cell terminal to battery radiator that clearly shows that bulk of thermal flow obstruction lies close to generation areas inside cell. This means targeting efficient heat dissipation device closer to cell generation areas, although difficult to implement, would provide best cooling benefits in the form of temperature drops.

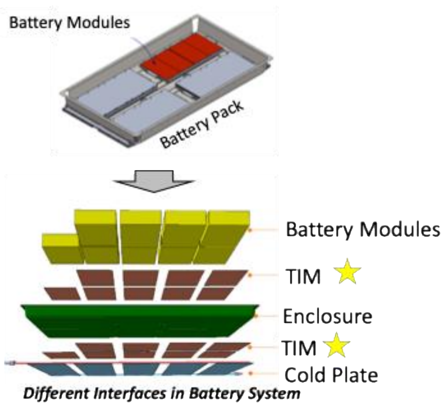

Figure 13. Exploded view of battery pack showing different thermal interfaces

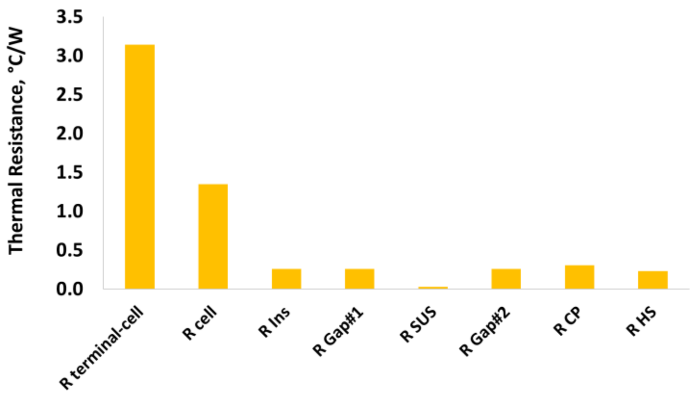

Figure 14. Thermal resistance breakdown for thermal propagation from cell to radiator/heat sink.

Current design of liquid cooling presents high temperature gradient from cooled to uncooled face that is elevated during stress phases like fast charging when extend of release heat from cell terminals and jelly roll increases exponentially. Battery cells have low effective thermal conductivity (18 – 30 W/m.K) that impede heat flow from cell interiors (electrolyte, electrodes) and exteriors (terminal, contacting point with bus bar) [27]. Generally, electric connections (terminal, bus bar) where most of joule heat is generated are lined opposite to cold plate connection side. Additionally, internal joule heat generated at current collector have to be released through complicated and long winding path through cell terminal at top, to cold plate at the bottom of cell. Part of electrochemical heat is released to larger sides area along the cell thickness which is partially attempted to be released by using conductive spacer plates (with isolation layers for maintaining electric flow integrity). In summary, cold plate location is far from heat generation sites and not thermally optimal, but represents best compromise when considering available space, electrical safety and mechanical integration in pack. Extending this discussion further, Figure 15 presents the comparison of different cooling approaches for fast charged battery pack with different configurations and loading sequences. It is evident that standard liquid cooling at pack or module level would not be able to sustain cell temperatures below 40 °C limit. Introducing heat pipe thermal connection between cells to cold plate for modules based or pack based battery packaging could benefit by keeping cell operating temperatures in safety limits. In this analysis, it is estimated that heat load output from cell would triple, than nominal, during fast charging cycle.

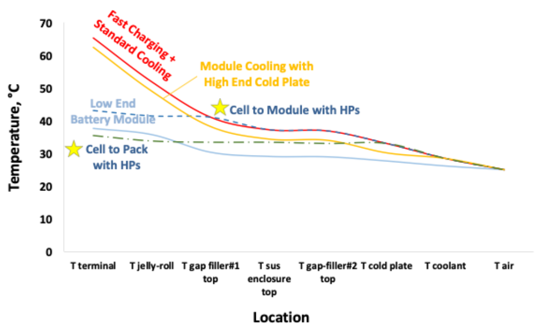

Figure 15. Temperature evolution for battery pack with different cooling method including heat pipe enhancements

Further in this section, cases are discussed to outlay methods in which heat pipes could improve cooling for battery packaging in EVs, starting from cell to pack levels.

6.1 Cell Terminal Cooling

Figure 16 depicts two different methods to cool cell terminal – externally (left) or internally (right). For cell exterior cooling, heat pipe was soldered attached to positive and/or negative terminals with electrical isolation layer at condenser interface to avoid short circuiting. Based on simulation results, which were verified by actual lab experiments, heat pipes were able to reduce terminal temperature by 1 to 3 °C (depending on number of heat pipes and terminal type). Gains with heat pipe was higher at positive terminal due to large output heat at this terminal owing to incoming current [28] as evident in Figure 17.

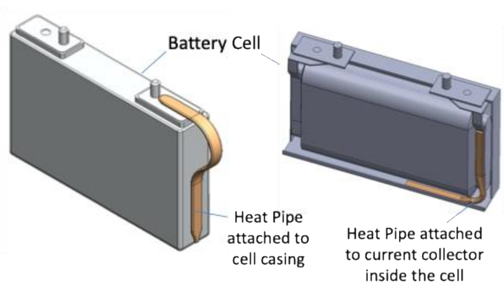

Figure 16. Methods to cool cell terminal (left) and cell current collector (right) using heat pipes [28, 29]

With cell interior cooling at current collector sites, both overall cell temperature reduction and thermal uniformity was more superior, with jelly roll temperature drop by more than 5 °C for extreme stress situations during fast charging [29]. For experimental verification, heat pipe was attached to source area by mechanical adhesion while keeping dielectric gap at one end of heat pipe using isolation layer.

The challenging aspects of heat pipe integration was bending of heat pipe with sharp radii (for terminal area) and in 3D fashion (for current collector area) to obey space limitations both externally and internally to cell. In both instances, heat pipe(s) attempted to reduce thermal gradient along the height of the cell (with cold plate based cooling at cell bottom). Such gradient results from heat generated at cell terminal, cell current collector as well as external mounted electronics/electrics around cells (cell control unit – CDU, current bus bar, battery management system – BMS).

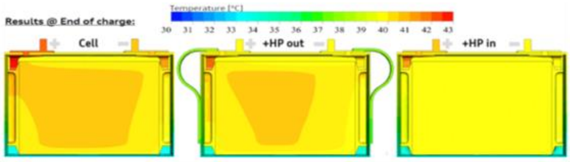

Figure 17. Comparative results for cooling cell terminal extremally and internally using heat pipes [29].

6.2 Intercellular Thermal Gradient Improvement

As depicted in Figure 17, thermal gradient on the sides of the cell can result due to thinner geometry (< 1 to 2 mm) and lower thermal conductivity of the interspace plates. For high voltage batteries under fast charging conditions, these gradients could exceed safer temperature limits for Li-Ion cells or in other words, baseline design would not allow fast charging possibility without any thermal enhancement. In this case, heat pipes could provide high effective thermal conductivity to interspace plates thereby reducing overall gradients by more than 5 times of baseline design at single cell heat dissipation of 100 W. Figure 18 presents module integration concept (left) and actual prototype of heat pipe cooling plates using 4 heat pipes with diameter 6 each [30].

The concept uses cold plate on the side of battery module rather than bottom due to difficulties of routing heat pipes at the bottom side, and availability of space at sides that could allow such idea in practice, wherever space exists on the module side. For this concept, the complexity of interfacing and integration of heat pipes plates between module and cold plate in actual application could be overpowering and need to be considered for simplifications.

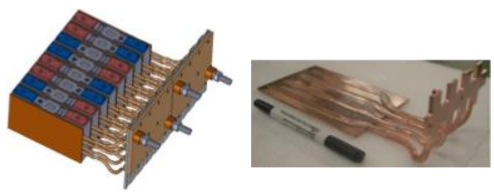

Figure 18. (left) Heat pipe based module cooling enhancement, (right) Heat pipe intercellular plates to reduce gradient on sides of prismatic cells

6.3 Module Bus Bar Cooling

The notion of cell terminal cooling could be extended to cool battery module bus bar using heat pipe(s) as shown in Figure 19. Such design is able to provide twofold advantages [31]; 1) suppress thermal gradient (and hot spots) from top to bottom of cells (or module), and 2) reduce working temperature for module electronics (battery management system) and electrical (bus bar) system located on top of the module. In other words, heat pipe based system could help to channel heat release by electronics and terminals on top of module to the original cold plate housed at bottom side. Diameter 8 heat pipes were attached on either side (positive and negative respectively) bus bars using mechanical fasteners. To avoid short circuiting, heat pipes were coated with polyimide based isolation with dielectric strength exceeding 2 kV. Generally, under fast charging condition, top to bottom temperature gradient of more than 10 °C can exist across cell. By implementing heat pipes into the module bus bar, these gradients were reduced to less than half of original values.

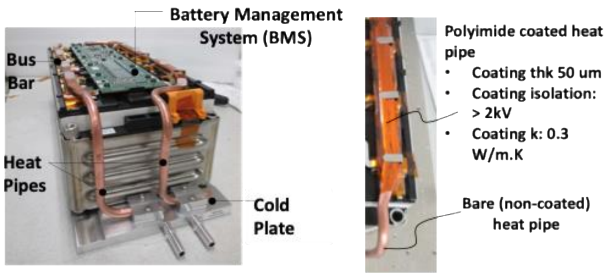

Figure 19. Battery module bus bar cooling using heat pipes

6.4 Pack Mechanical Simplification

Figure 20 present cooling approach for battery pack with heat collection using heat pipe carrier plates and heat transfer to radiator area using significant downsized cold plate loop. Each heat pipe carrier plate was more than 600 mm long with condenser area ~ 50 mm, and was required to transfer 240 W heat load from 1.5 share of battery modules per heat pipe carrier plate. Heat pipe plate was able to provide temperature uniformity within ±5 C and significant temperature reduction (~ 40 ° C) compared to metal Aluminum plate design (Figure 20). Pack level cooling approach is readily easy to apply and integrate in the vehicle without any major mechanical changes.

In this case, two-phase systems based on heat pipes could extend significant advantages to improve temperature uniformity, simplify mechanical design of pack by reducing cold plate size and connectivity between multiple cold plates, reduce overall system weight owing to cold plate downsizing and coolant charge reduction, and improve safety against leakage in high voltage area by keeping downsized cold plate out of battery enclosure through low water charged heat pipes in the vicinity of pack [32].

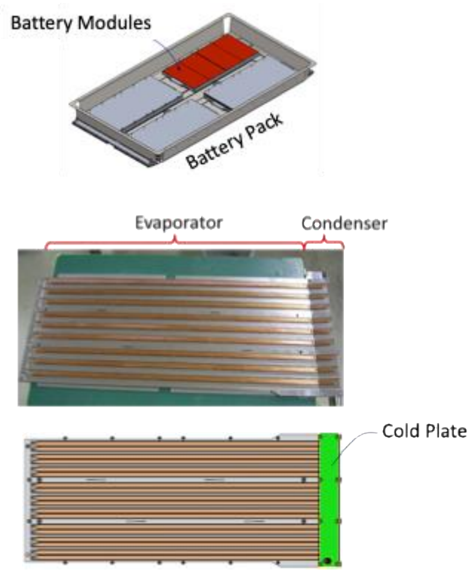

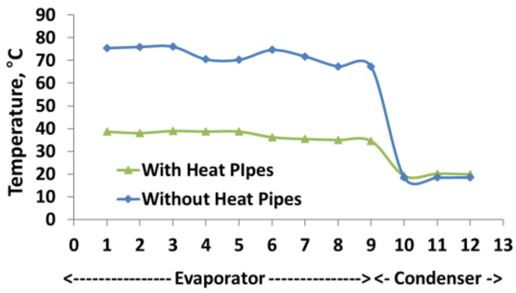

Figure 20. (Top) Heat pipe carrier plate for cooling battery pack with prismatic cells, (Bottom) Pack temperature evolution with and without heat pipes

It should be noted that mix of two phase and single-phase system, as outlined above, would provide most performance and cost optimum approach for battery cooling.

Fully two-phase system are high performance but integration and cost intensive. Similarly, fully single-phase system are bulky, complex and low performance (particularly thermal non-uniformity close to battery cells). The innovative aspect of using heat pipes in battery cooling is hybridization of two-phase and single-phase systems to improve performance and simplify design. The concept can be extended for battery pack with cylindrical cells as shown in Figure 21.

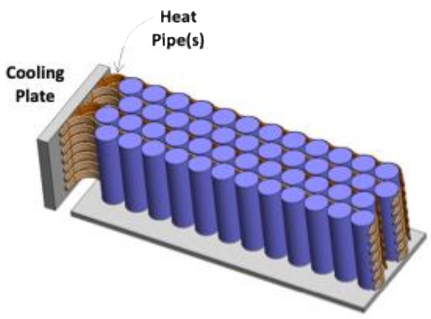

Figure 21. Heat pipe based cooling of battery pack with cylindrical cells

7. Heat Pipe Development for Battery Cooling

Application of heat pipe for battery thermal management need some specific technological advances in performance and structures of heat pipe to make them viable for implementation in vehicle environment. These areas include:

1. *Longer heat transfer distances*: For module and pack cooling, heat pipes are needed to be more than 250 mm (genuine length in consumer electronic cooling) that requires development of wicking structure with superior wicking properties (to promote faster liquid transfer, high capillary pressure for fluid circulation) Figure 22 presents combined wick structure for heat pipe for higher heat capacity and long distance heat transport.
2. *Condenser development*: In battery packs, the heated area is generally 4-5 time larger than heat sink area (contrary to electronic cooling) which need development of condensation heat transfer coefficient through methods like micro texturing of wick surfaces.
3. *Electric Isolation*: High voltage battery modules need dielectric layering between evaporator and condenser to avoid short circuit discharges. This could be done by isolation coatings which are high temperature tolerable and reliable against vibration over extended time period.
4. *Structural Strength*: Automotive environment need ability for cooling system to sustain structures under impact loading and vibration environments. Appropriate wall and wick strength need to be achieved by optimal design and manufacturing parameters.
5. *Complex Forming*: Space restriction requires heat pipe to be bend with sharp radii and complicated 3D shapes. Wick design and tube cross section need to be consider to maintain fluid continuum and structures over lifetime.

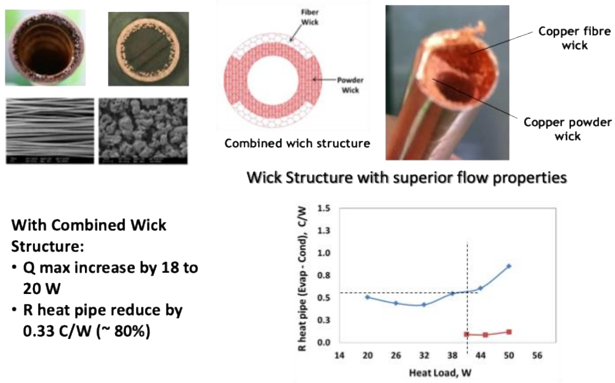

Figure 22. Heat pipe wick development for long distance heat transport.

8. Conclusions

The work have identified niche for heat pipes in improving thermal management ability of existing battery cooling systems:

1. Cell level terminal/current collect cooling tend to reduce heat resistance close to generation site and thus addressed hot spot issues
2. Cell side cooling using heat pipe interspace plates were able to improved cell thermal uniformity
3. Module bus bar cooling concept could reduced hot spots on battery bus bar and thus improved thermal uniformity of overall battery module
4. Pack cold plate downsizing helped to reduce complexity of battery pack cooling system, reduce system weight, improve thermal homogeneity and reduce leakage hazards.

In summary, heat pipe based passive system will provide system with high runtime reliability, better thermal uniformity and more safety for battery cooling in electric vehicles.

References

[1] I. Veza, M. Z. Asy'ari, M. Idris, V. Epin, I.M. R. Fattah, M. Spraggon, Electric vehicle (EV) and driving towards sustainability: Comparison between EV, HEV, PHEV, and ICE vehicles to achieve net zero emissions by

2050 from EV, Alexandria Engineering Journal, Vol 82, 2023, Pp 459-467, https://doi.org/10.1016/j.aej.2023.10.020

[2] R. Singh, T. Oridate, T. Nguyen, Drive Train Cooling Options for Electric Vehicles, Frontiers in Heat and Mass Transfer, Tech Science Press, DOI: 10.32604/fhmt.2024.050744

[3] A. Jeckel, Battery Thermal Management: Key to Performance, Durability and Safety, Proc. of the 7th International Conference on Thermal Management for EV/HEV, 13 – 15 Feb, 2018, Berlin, Germany

[4] R .Singh, G. Lapp, J. Velardo, P. T. Long, M. Mochizuki, A. Akbarzadeh, A. Date, K. Mausolf, K. Busse, Battery Cooling Options In Electric Vehicles With Heat Pipes, Frontiers in Heat and Mass Transfer (FHMT), 16 (2), 2021, DOI: 10.5098/hmt.16.2, ISSN: 2151-8629

[5] J. Huang, S.S Naini, R. Miller, D., Rizzo, K., Sebeck, Development of a heat pipe–based battery thermal management system for hybrid electric vehicles, Proceedings of the Institution of Mechanical Engineers Part D–Journal of Automobile Engineering, 2020, 234(6), 1532–1543

[6] D. M. Weragoda, G. Tian, A. Burkitbayev, K. H. Lo, T. Zhang, A comprehensive review on heat pipe based battery thermal management systems. Applied Thermal Engineering, 224, 2023, 120070

[7] M. Bernagozzi, A. Georgoulas, N. Miche, M. Marengo, Heat pipes in battery thermal management systems for electric vehicles: A critical review. Applied Thermal Engineering, Vol. 219, 2023, 119495

[8] A. Afzal, R. K. A. Razak, A. D. M. Samee, R. Kumar, U. Agbulut, S. G. Park, A critical review on renewable battery thermal management system using heat pipes Journal of Thermal Analysis and Calorimetry (2023) 148:8403–8442 https://doi.org/10.1007/s10973-023-12100-9

[9] M. Mochizuki, Y. Saito, K. Mashiko, T. Raay, R. Singh, High Power Heat Removal by Heat Pipes & Two Phase Heat Transfer for Electric Vehicle, Proc. 53th Japan Heat Transfer Symposium, 2016.

[10] R. Singh, T. Nyugen, Loop Heat Pipes for Thermal Management of Electric Vehicles, Journal of Thermal Science and Engineering Applications, Vol.14, 2021, 061010-1

[11] M. Bernagozzi, A. Georgoulas, N. Miché, C. Rouaud and M. Marengo, A Novel Loop Heat Pipe Based Cooling System for Battery Packs in Electric Vehicles, 2020 IEEE Transportation Electrification Conference & Expo (ITEC), Chicago, IL, USA, 2020, pp. 251-256, doi: 10.1109/ITEC48692.2020.9161607.

[12] A. Wazeer, A. Das, C. Abeykoon, A. Sinha, A. Karmakar, Phase change materials for battery thermal management of electric and hybrid vehicles: A review, Energy Nexus, Vol 7, 2022, 100131, ISSN 2772-4271, https://doi.org/10.1016/j.nexus.2022.100131

[13] A. H. Alami, H. M. Maghrabie, M. A. Abdelkareem, E. T. Sayed, Z. Yasser, T. Salameh, S.M.A. Rahman, H. Rezk, A.G. Olabi, Potential applications of phase change materials for batteries' thermal management systems in electric vehicles, Journal of Energy Storage, Vol. 54, 2022, 105204, ISSN 2352-152X, https://doi.org/10.1016/j.est.2022.105204

[14] Audi Technical Portal, Drive Train, Hybrid Technologies, https://www.audi-technology-portal.de/en/drivetrain/hybrid-technologies/audi-a3-e-tron_en (accesses on 30 September, 2024)

[15] K. An, P. Barai, K. Smith, P. P. Mukherjee, Probing the Thermal Implications in Mechanical Degradation of Lithium-Ion Battery Electrodes, 2014, J. Electrochem. Soc. Vol.161(6), A1058, DOI 10.1149/2.069406jes

[16] U.S. Department of Transportation, Charger Types & Speeds, https://www.transportation.gov/rural/ev/toolkit/ev-basics/charging-speeds#:~:text=Level%201%20equipment%20provides%20charging,6%20hours%20for%20a%20PHEV (assessed on 30 September, 2024)

[17] International Energy Agency, Global EV outlook 2024, Trends in Electric vehicle batteries, https://www.iea.org/reports/global-ev-outlook-2024/trends-in-electric-vehicle-batteries

[18] T. Utsunomiya, O. Hatozaki, N. Yoshimoto, M. Egashira, M. Morita, Self-discharge behavior and its temperature dependence of carbon electrodes in lithium-ion batteries, Journal of Power Sources, Vol 196, Issue 20, 2011, Pp 8598-8603, ISSN 0378-7753, https://doi.org/10.1016/j.jpowsour.2011.05.066.

[19] F. Leng, C. Tan, M. Pecht, Effect of Temperature on the Aging rate of Li Ion Battery Operating above Room Temperature, Sci Rep 5, 12967 (2015). https://doi.org/10.1038/srep12967

[20] Lexus, Toyota Newsroom, https://newsroom.lexus.eu/ux-300e-first-all-electric-lexus-offers-class-leading-quality-and-10-years-peace-of-mind-on-battery/ (assessed on 30 September 2024)

[21] Audi Media center, https://www.audi-mediacenter.com/en (assessed on 30 September 2024)

[22] Battery design, https://www.batterydesign.net/2022-tesla-model-y-4680/ (assessed on 30 September, 2024)

[23] Green car reports, https://www.greencarreports.com/news/1136313_catl-details-next-gen-cell-to-pack-battery-tech-with-disruptive-water-cooling-design (assessed on 30 September 2024)

[24] F. Schoewel, E. Hockgeiger, BMW Group, München, The high voltage batteries of the BMW i3 and BMW i8, AABC 2014, February 3- 7, 2014, Atlanta

[25] Auto innovations, https://www.auto-innovations.net/technical-articles/27451-immersed-cell-batteries-as-the-next-step (assessed on 30 September 2024)

[26] C. Roe, X. Feng, G. White, R. Li, H. Wang, X. Rui, C. Li, F. Zhang, V. Null, M. Parkes, Y. Patel, Y. Wang, H. Wang, M. Ouyang, G. Offer, B. Wu, Immersion cooling for lithium-ion batteries – A review, Journal of Power Sources, Vol. 525, 2022, 231094, ISSN 0378-7753, https://doi.org/10.1016/j.jpowsour.2022.231094

[27] Y. Jiang, J. Huang, P. Xu, P. Wang, Axial and radial thermal conductivity measurement of 18,650 Lithium-ion battery, Journal of Energy Storage, Volume 72, Part C, 2023, 108516, ISSN 2352-152X, https://doi.org/10.1016/j.est.2023.108516

[28] J. Kleiner, R. Singh, M. Schmidt, L. Komsiyska, G. Elger, Influence of heat pipe assisted terminal cooling on the thermal behavior of a large prismatic lithium-ion cell during fast charging in electric vehicles. Applied Thermal Engineering, 188, 2021, 116328.

[29] J. Kleiner, F. Lambauer, R. Singh, L. Komsiyska, M. Hinterberger, Experimental study of cell integrated heat pipe cooling with a lithium-ion cell emulator. Journal of Energy Storage, 56, 2022, 105808. https://doi.org/10.1016/j.est.2022.105808

[30] J. Smith, R. Singh, M. Hinterberger, M. Mochizuki, Battery thermal management system for electric vehicle using heat pipes, Int. J. Therm. Sci. 134 (December 2018) 517-529.

[31] R. Singh, Vehicle Thermal Management Using Heat Pipes, 2019 IEEE CPMT Symposium Japan (ICSJ), Kyoto, Japan, 2019, pp. 75-78, doi: 10.1109/ICSJ47124.2019.8998747

[32] Singh, G. Lapp, J. Velardo, P. T. Long, M. Mochizuki, A. Akbarzadeh, A. Date, K. Mausolf, K. Busse, Battery Cooling Architectures for Electric Vehicles Using Heat Pipes Proc. Of Joint 19th IHPC and 13th IHPS, Pisa, Italy, June 10-14, 2018

The papers of each researcher in The Joint 22nd International Heat Pipe Conference & 16th International Heat Pipe Symposium